BNL-77977-2006-V1-V2
FORMAL REPORT

Conceptual Design Report

December 2006

National Synchrotron Light Source II

BROOKHAVEN NATIONAL LABORATORY

CONTRIBUTORS

James Ablett[2]; Andrew Ackerman[2]; Rudy Alforque[2]; Marc Allaire[2]; Dario Arena[2]; Alfred Baron[11]; Deborah Bauer[2]; Ronald Beauman[2]; Joanne Beebe-Wang[2]; Johan Bengtsson[2]; Scott Berg[2]; Lonny Berman[2]; Wayne Betts[2]; Richard Biscardi[2]; Michael Blaskiewicz[2]; Alexei Blednykh[2]; Michael Borland[1]; Ivan Bozovic[2]; Natasha Bozovic[2]; Clement Burns[15]; Jill Carney[2]; Lawrence Carr[2]; Robert Casey[2]; Yong-Chul Chae[1]; Mark Chance[3]; Chris Channing[2]; Barrett Clay[2]; Scott Coburn[2]; Donna Cotrel[2]; David Dale[2]; Leo (Bob) Dalesio[12]; Dennis Danseglio[2]; Roger Dejus[1]; Steven Dierker[2]; Elaine Dimasi[2]; Michael Dudley[13]; Paul Dumas[10]; Ove Dyling[2]; Louis Emery[1]; Ken Evans-Lutterodt[2]; Martin Fallier[2]; Richard Felter[2]; Conrad Foerster[2]; Horst Friedsam[1]; GEI Consultants; George Ganetis[2]; Diane Gifft[2]; Gilbane Building Company; Nick Gmur[2]; Thomas Gog[1]; Colin Gordon Associates; Weiming Guo[2]; HDR Architecture, Inc.; Edwin Haas[2]; Diane Hatton[2]; Richard Heese[2]; Oliver Hignette[5]; John Hill[2]; Steve Hoey[2]; Chris Holmes[2]; Hsiao-Chuan Hseuh[2]; Eugene Hu[2]; Zahid Hussain[6]; Steve Hulbert[2]; Chris Jacobson[13]; P.K. Job[2]; Erik Johnson[2]; Peter Johnson[2]; Thomas Joos[2]; Marvin Kirshenbaum[1]; Stephen Kramer[2]; Michael Kretschmann[2]; Samuel Krinsky[2]; Tony Kuczewski[2]; Jeff Landgraf[2]; Jerome Lauret[2]; Cathleen Lavelle[2]; George Leskody[2]; Joseph Levesque[2]; Alan Levine[2]; The LiRo Group; Vladimir Litvinenko[2]; Alfredo Luccio[2]; Yun Luo[2]; George Mahler[2]; Nickolay Malitsky[2]; Greg Markovich[1]; Jorg Maser[1]; Thomas McEvaddy[2]; Wuzheng Meng[2]; Lisa Miller[2]; James Mills[2]; Simon Mochrie[17]; Christoph Montag[2]; Paul Montanez[2]; Payman Mortazavi[2]; Boaz Nash[2]; Kathleen Nasta[2]; James Misewich[2]; Christie Nelson[2]; Paul Northrup[2]; Jennifer O'Connor[2]; Paul O'Connor[2]; Satoshi Ozaki[2]; David Paveglio[2]; Igor Pinayev[2]; Sal Pjerov[2]; Boris Podobedov[2]; Dennis Poshka[2]; QED, Inc.; George Rakowsky[2]; Mohan Ramanathan[1]; Deepak Raparia[2]; Alan Raphael[2]; Viswanath Ravindranath[1;2]; Harald Reichert[7]; Ruben Reininger[16]; Howard Robinson[2]; Ian Robinson[14]; Kathleen Robinson[2]; Lydia Rogers[2]; James Rose[2]; Doris Rueger[2]; Brian Rusthoven[1]; Cecilia Sanchez-Hanke[2]; Alec Sandy[1]; Mike Schaeffer[2]; Dieter Schneider[2]; Christian Schroer[4]; Timur Shaftan[2]; Sushil Sharma[2]; Qun Shen[1]; Wuxian Shi[3]; Deming Shu[1]; Yuri Shvyd'ko[1]; John Sidarous[1]; Peter Siddons[2]; Nikolaos Simos[2]; Om Singh[1]; John Skaritka[2]; Anatoly Snigirev[5]; Ivan So[2]; Tammy Stein[2]; Peter Stephens[13]; Chris Stelmach[2]; Vivian Stojanoff[2]; Robert Sweet[2]; Peter Takacs[2]; Toshiya Tanabe[2]; Nathan Towne[2]; Emil Trakhtenberg[1]; Dejan Trbojevic[2]; Triad Project Management; V.J. Associates; VitaTech Engineering; Elio Vescovo[2]; Dong Wang[6]; Fuhua Wang[6]; Jie Wei[2]; Joseph Woicik[9]; Qiong Wu[2]; Lin Yang[2]; Zhijian Yin[2]; Li-Hua Yu[2]; James Yeck[2]; Zhong Zhong[2]; Peter Zuhoski[2].

[1]Argonne National Laboratory

[2]Brookhaven National Laboratory

[3]Case Western Reserve University

[4]Dresden Technical University

[5]European Synchrotron Research Facility

[6]Lawrence Berkeley Laboratory

[7]Max Planck Institute, Stuttgart

[8]Massachusetts Institute of Technology

[9]National Institute of Standards and Technology

[10]SOLEIL

[11]SPring-8

[12]Stanford Linear Accelerator Center

[13]State University of New York, Stony Brook

[14]University College, London

[15]Western Michigan University

[16]University of Wisconsin

[17]Yale University

CONTENTS

Chapter 6 Lattice and Accelerator Physics

Chapter 7 Storage Ring System

Chapter 8 Radiation Sources

Chapter 9 Control System

Chapter 10 Global Support Systems

Chapter 11 Experimental Facilities

Chapter 12 Research and Development Program

Chapter 14 Environment, Safety and Health, and Quality Assurance

Chapter 15 Radiation Safety and Shielding

ACRONYMS AND ABBREVIATIONS

A	Ampere
Å	Angstrom
ADC	analog to digital converter
ADT	array display tool
AFM	atomic force microscope, also called SFM
ALS	Advance Light Source
ANL	Argonne National Laboratory
ANSI	American National Standards Institute
APD	avalanche photodiode
APPLE	Advanced Planar Polarized Light Emitter
APPS	Accelerator Personnel Protection System
APS	Advanced Photon Source
ARPES	angle-resolved photoemission system
ASHRAE	Am. Soc. Heating, Refrig, & Air Cond. Engineers
ASIC	application-specific integrated circuit
ASTM	American Society for Testing and Materials
ASME	American Society of Mechanical Engineers
AWG	American Wire Gauge
BAG	Bayard-Alpert Gauge
BBA	beam based alignment
BDNY	Building Code of New York
BDA	beam defining aperture
BLM	beam loss monitor
BM	bending magnet
B–M	Bjorken and Mtingwa
BPM	beam position monitor
B–SR	booster-to-storage ring
BT	beamline team
CA	channel access
CAD	computer aided design
CCG	cold cathode gauge
CDI	coherent diffractive imaging
CDW	collimator dispersing wavelength
CEM	channel electron multiplier
CESR	Cornell Electron Storage Ring
CMLOG	operator electronic log
CMR	colossal magnetoresistance
CMS	chemical management system
CNM	Center for Nanoscale Materials
CNS	central nervous system
CNT	carbon nanotube
COAF	closed orbit amplification factor
COD	closed orbit distortion
CPGM	collimated plane grating monochromator
CPMU	cryogenic permanent magnet undulator
CPU	central processing unit
CRL	compound refractive lens
CVD	chemical vapor deposition
CVS	Version Control System
CXD	coherent x-ray diffraction
CXDI	coherent x-ray diffractive imaging
CXS	coherent x-ray scattering
DA	dynamic aperture
DAC	digital to analog converter
DART	Days Away, Restricted, Transfer
DB	database, dry bulb
DBD	database definition
DBA	double bend achromatic
DCCT	Direct Current Current Transformer
DCM	double-crystal monochromator
DCT	database configuration tool
DDS	direct digital synthesizer
DEI	diffraction enhanced imaging
DIAMOND	British National Synchrotron
DI	deionized
DMM	digital multi meters
DOF	depth of field
DOS	Density of States
DP	display page
DRO	dielectric resonator oscillator
DSP	digital signal processor
DW	damping wiggler
EDM	extensible display manager
EELS	electron energy loss spectroscopy
EIA	Electronic Industries Alliance
ELF	extremely low frequency
EMI	electromagnetic interference
EMR	experience modification rate
EPICS	Experimental Physics and Industrial Control Sys.
EPR	ethylene propylene rubber
EPS	equipment protection system
EPU	ellipticially polarized undulator
EPW	elliptically polarizing wiggler
ESD	emergency shutdown
ESH	environmental safety and health
ESRF	European Synchrotron Radiation Facility
EUV	extreme ultraviolet
EXAFS	extended x-ray absorption fine structure
FAPM	fixed-aperture photon mask
FCT	fast current transformer
FDI	Fresnel diffraction imaging
FEA	finite element analysis
FEL	free electron laser
FFT	Fast Fourier Transform
FHC	facility hazard categorization
FHVC	fast horizontal and vertical corrector
FOE	front optics enclosure
FPGA	field programmable gate array
FTIR	Fourier Transform Infrared
FWHM	full width at half maximum

FZP	Fresnel zone plate
GbE	gigabit ethernet
GHe	gaseous helium
GISAXS	grazing incidence small angle x-ray scattering
GM/CA-CAT	a beamline at APS
GUI	graphical user interface
GV	gas valve
Gy	Gray, a unit for measuring radiation
(H)	horizontal measurement
H	Henry, a measure of inductance
HEPA	high efficiency particulate air
HMI	human interface
HMTM	Hazardous Material Transportation Manual
HOM	higher order mode
HP	high pressure, high purity, horse power
HPS	hazardous production material
HTSC	high temperature superconductor
HTSCU	high temperature superconducting undulator
HVAC	heating, ventilating, and air conditioning
IBS	intra-beam scattering
ID	inner diameter
IOC	input/output controller
IOT	inductive output tube
ISO	International Organization for Standardization
ISF	Intermediate scattering function
IT	information technology
IVPMU	in-vacuum permanent magnet undulator
IVU	in-vacuum undulator
IXS	inelastic x-ray scattering
KB	Kirkpatrick-Baez
KM	knob manager
LCLS	Linac Coherent Light Source
LCP	left circular polarization
LDDM	laser doppler displacement meter
LEBT	low energy beam transport
LEED	Leadership in Energy and Environmental Design
LEEM	low energy electron microscopy
LHe	liquid helium
Linac	linear accelerator
LID	long insertion device
LLRF	low level radio frequency
LN_2	liquid nitrogen
LOI	letters of intent
LPDOS	Local Partial Density of States
LPG	low pressure gas
LPPS	Linac Personnel Protection System
LTS	low temperature superconductor
LVS	layout vs. schematics
mA	milli-Amps
m	meter, or milli, if a prefix
M	million, or mega-
MLM	multilayer mirror
MBE	molecular beam epitaxy
MCI	maximum credible incident
MCL	multichannel line
MCP	multichannel plate
MEDM	motif editor display manager
MGU	minigap in-vacuum undulator
MLL	Multilayer Laue Lens
MO	master oscillator
MOKE	Magneto-Optic Kerr Effect
MRAM	magnetic random access memory
MRT	microbeam radiation therapy
MTF	Modulation Transfer Function
MTJ	magnetic tunnel junctions
MXTM	magnetic x-ray transmission microscope
n	nano, 1 x 10^{-9}
nC	nanoCoulomb (measure of electrical charge)
NE-CAT	a beamline at APS
NEG	Non-Evaporable Getter
NFPA	National Fire Protection Administration
NIM	normal incidence monochromator
NPE	natural phenomenon event
NRTL	Nationally Recognized Testing Laboratory
NSE	neutron spin echo
OD	outer diameter
ODH	oxygen deficiency hazard
OHSAS	Occupational Health and Safety Adm. Standards
OPI	operator interface
OSA	order sorting aperture
OSHA	Occupational Safety and Health Administration
PAT	Photon Activation Therapy
PCI	phase contrast imaging
PDB	Protein Data Bank
PDP	parameter display page
PDS	power density structure
PEEM	photoelectron emission microscopy
PFN	pulse-forming network
PGM	plane grating monochromator
ph/s	photons per second
PHA	preliminary hazards analysis
PID	proportional integral derivative
PLC	programmable logic controller
PM	permanent magnet
PMS	position monitoring system
PPM	pure permanent magnet
PPMS	physical properties measurement system
PPS	personnel protection system
PRF	pulse repetition frequency
PSD	photon stimulated gas desorption; also, position sensitive detector
ps	picosecond
psf	pounds per sq ft
PSF	Point Spread function
PSM	pulse step modulation
PTS	permanent threshold shift
PV	process variable
PX	protein or macromolecular crystallography
PZT	piezoelectric transducer
QAM	quality assurance manager
QPU	quasi-periodic undulator
rad	radian

RCP	right circular polarization
RDB	relational database
RF	radio frequency
RFI	radio frequency interference
RGA	residual gas analyzer
RH	relative humidity
RIE	reactive ion etching
RL	refrigerator/liquefier
RMS	root mean square
RTOS	real-time operating system
SAA	satellite accumulation area
SAD	safety assessment document
SAXS	small angle x-ray scattering
SBMS	Subject-Based Management System
SCL	single-channel line
SCRF	superconducting radio frequency
SCU	superconducting undulator
SCW	superconducting wiggler
SF	synchrotron footprinting
SFMs	scanning (atomic) force microscope, also AFM
SID	short ID
SIP	sputter ion pump
SMR	spherical mounted retro-reflector
SNC	State Notation Compiler
SNL	State Notation Language
SNR	signal-to-noise ratio
SOE	Second Optic Enclosure
SPPES	spin polarized photoemission studies
SPring-8	Japanese National Synchrotron
SR	synchrotron radiation, also storage ring
SRW	synchrotron radiation workshop
STM	scanning tunneling microscope
STXM	scanning transmission x-ray microscope
SVD	singular value decomposition
SXU	soft x-ray undulator
TBA	three-bend achromatic
TC	thermocouples
TEM	transmission electron microscopy
THz	terrahertz
TIA	Telecommunications Industry Alliance
TIG	tungsten inert gas
TMCI	transverse mode coupling instability
TMP	turbomolecular pump
TRC	total recordable cases
TSP	titanium sublimation pump
TXM	transmission x-ray microscope
UBPM	user beam position monitors
UHR	ultra high resolution
UHV	ultra high vacuum
UPS	uninterruptible power supply
USAXS	ultra small angle x-ray scattering
UV	ultraviolet
(V)	vertical measurement
VLS	variable line spacing
VPU	variable polarization undulator
VUV	vacuum ultraviolet
WBS	white beam slit
WFG	waveform function generator
XANES	x-ray absorption near-edge structure
XAS	x-ray absorption spectroscopy
XES	x-ray emission spectroscopy
XMCD	x-ray magnetic circular dichroism
XPCS	x-ray photon correlation spectroscopy
XRMS	x-ray resonant magnetic scattering
YAGC	yttrium aluminum garnet cerium

LIST OF FIGURES

LIST OF TABLES

1 EXECUTIVE SUMMARY

1.1 Introduction

Brookhaven National Laboratory has prepared a conceptual design for a world class user facility for scientific research using synchrotron radiation. This facility, called the "National Synchrotron Light Source II" (NSLS-II), will provide ultra high brightness and flux and exceptional beam stability. It will also provide advanced insertion devices, optics, detectors, and robotics, and a suite of scientific instruments designed to maximize the scientific output of the facility. Together these will enable the study of material properties and functions with a spatial resolution of ~1 nm, an energy resolution of ~0.1 meV, and the ultra high sensitivity required to perform spectroscopy on a single atom.

The overall objective of the NSLS-II project is to deliver a research facility to advance fundamental science and have the capability to characterize and understand physical properties at the nanoscale, the processes by which nanomaterials can be manipulated and assembled into more complex hierarchical structures, and the new phenomena resulting from such assemblages. It will also be a user facility made available to researchers engaged in a broad spectrum of disciplines from universities, industries, and other laboratories.

1.2 Scope

The project scope includes the design, construction, installation, and commissioning of the accelerator hardware, civil construction, and central facilities required to produce a new synchrotron light source. It includes a highly optimized electron storage ring, full energy injector, experimental beamlines and optics, and appropriate support equipment, all housed in a new building. Specifically, the main scope elements include:

- an electron gun and a short linac, where an electron beam is generated and accelerated to 200 meV
- the transport system to the booster
- the booster storage ring, where the electrons from the linac are accelerated to 3 GeV for injection into the main storage ring
- the transport system to the main storage ring
- the main storage ring, where a 500 mA current of electrons are stored at an energy of 3 GeV and sent through insertion devices and bend magnets to produce synchrotron radiation
- a suite of initial beamlines and supporting instrumentation
- the ring building, central lab office building, auxiliary lab office buildings, and mechanical equipment rooms, comprising the conventional facilities and supporting utility infrastructure

1.3 Capabilities

NSLS-II is a synchrotron with a highly optimized design that will produce world leading levels of brightness and flux and small beams, over a very broad energy range, extending from the far IR to the very hard x-ray region. The main performance characteristics are given in Table 1.1.

Table 1.1 Main Performance Characteristics of the NSLS-II Storage Ring.

Electron energy [GeV]	3.0
Stored current [mA]	500
Stability of average current [%]	<1
Horizontal emittance [nm-rad]	0.55
Vertical emittance [nm-rad]	0.008
Average brightness [ph/s/0.1%bw/mm^2/mrad^2] in the 2 keV to 10 keV photon energy range	>10^{21}
Average flux [ph/s/0.1%bw] in the 2 keV to 10 keV photon energy range	>10^{16}
Horizontal electron beam size [μm]	38.5
Horizontal electron beam divergence [μrad]	14.2
Vertical electron beam size [μm]	3.05
Vertical electron beam divergence [μrad]	3.22
Stability of electron beam in position and direction [%]	<10
Number of straight sections for insertion devices	27
Number of bend magnet sources	30

1.4 Cost and Schedule

The Total Estimated Cost (TEC) of NSLS-II is $678.2M. The Total Project Cost (TPC) is $775.2M. The schedule for construction will lead to start of operations in FY2014.

1.5 Acquisition Strategy

The acquisition strategy relies on Brookhaven Science Associates (BSA), the Department of Energy Managing and Operating (M&O) contractor for Brookhaven National Laboratory, to directly manage the NSLS-II acquisition. The design, fabrication, assembly, installation, testing, and commissioning for the NSLS-II project will be largely performed by the BNL/NSLS-II scientific and technical staff. Much of the subcontracted work to be performed for NSLS-II consists of hardware fabrication and conventional facilities construction.

2 PROJECT OVERVIEW

2.1 Introduction

The unique properties of synchrotron radiation, such as wide-energy tunability, high brightness, extreme collimation, polarization, and time structure, have enabled a number of new and important techniques since the early days of their use in the 1960s. Today's synchrotron light sources are the products of several generations of advances in light source technology.

Most recently, medium energy light sources, occupying the ~2.5 to 3.5 GeV middle ground between low energy and high energy storage rings, have rapidly gained popularity. These machines are distinguished by having a combination of high operating current, low beam emittance, and advanced ID technology. Five such facilities are currently operating and twenty-one more are either in design or under construction around the world.

The utility of the medium energy synchrotrons has been extended by technological progress in many areas, including: shimming of undulator magnets to increase high harmonic content; higher harmonic RF-cavities to extend beam lifetime; bunch-by-bunch feedback systems to control instabilities at high beam current; beam orbit control for high beam stability and reproducibility; in-vacuum, small gap, short period undulators to generate hard X-rays at relatively low electron beam energy; superconducting bend magnets to shift the X-ray spectrum to higher energy; and continual full energy top-off to extend the effective beam lifetime and eliminate thermal cycling of storage ring and X-ray beamline components. Among these, progress in undulator technology is especially important, as it boosts the bright radiation output of the medium energy machines into the most heavily used 5 to 20 keV range. Undulators on the three high energy machines are still required to reach up to the 50 keV and above range required for some experiments.

The performance goals of NSLS-II are motivated by the recognition that major advances in many important technology problems will require scientific breakthroughs in developing new materials with advanced properties. Achieving this will require the development of new tools that will enable the characterization of the atomic and electronic structure, the chemical composition, and the magnetic properties of materials with nanoscale resolution. These tools must be nondestructive, to image and characterize buried structures and interfaces, and they must operate in a wide range of temperatures and harsh environments.

In order to meet this need, NSLS-II has been designed to provide world leading brightness and flux and exceptional beam stability. The brightness is defined as the number of photons emitted per second, per photon energy bandwidth, per solid angle, and per unit source size. Brightness is important because it determines how efficiently an intense flux of photons can be refocused to a small spot size and a small divergence. It scales as the ring current and the number of total periods of the undulator field (both of which contribute linearly to the total flux), as well as being inversely proportional to the horizontal and vertical emittances (the product of beam size and divergence) of the electron beam. Raising the current in the storage ring to obtain even brighter beams is ultimately limited by beam-driven, collective instabilities in the accelerator. Thus, to maximize the brightness, the horizontal and vertical emittances must be made as small as possible.

The conventional approach to designing storage rings for low emittance leads to geometries with many magnetic elements. Achieving small emittances in such lattices results in large nonlinearities in the beam dynamics that ultimately place limits on the lifetime and the minimum achievable size of the emittance.

An alternative to achieving very small emittances which avoids the difficult nonlinearities is based on the use of damping wigglers (a specialized wiggler with a long period and high field). The concept of using damping wigglers for achieving small emittance has previously been employed on storage rings for high

energy physics and is incorporated in the designs of all the lepton damping rings required for the various projects of high energy linear colliders. The approach of NSLS-II is to employ a bare lattice with relatively modest nonlinearities and to use damping wigglers to achieve an unprecedented low emittance. This is quite innovative, as no currently operating synchrotron utilizes damping wigglers.

Fully maximizing the effect of damping wigglers in reducing the emittance requires low-field bending magnets and a number of damping wigglers. As a result, NSLS-II has been specifically designed for their incorporation. Because of their lower field, the bending magnets will be excellent sources of radiation in the VUV and soft x-ray range, as well as world leading sources of infra-red radiation. In addition to damping the beam, the damping wigglers will also produce high energy x-rays with much higher brightness and flux than conventional bending magnets and will be used in place of the bending magnets for experiments requiring hard x-rays. As such, the design of NSLS-II is quite innovative and distinct from other synchrotrons in that most of the synchrotron radiation is produced by insertion devices in the non-dispersive straight sections, rather than by the bending magnets, as is the case in all other synchrotrons. As a result, the emittance growth due to synchrotron radiation is minimized.

The performance of NSLS-II will be nearly at the ultimate limit of storage ring light sources set by the intrinsic properties of the synchrotron radiation process. The facility will produce x-rays more than 10,000 times brighter than those produced at NSLS today. The superlative character and combination of capabilities will have broad impact on a wide range of disciplines and scientific initiatives in the coming decades, including new studies of small crystals in structural biology, a wide range of nanometer-resolution probes for nanoscience, coherent imaging of the structure and dynamics of disordered materials, greatly increased applicability of inelastic x-ray scattering, and properties of materials under extreme conditions.

Commissioned in 1982, the existing National Synchrotron Light Source (NSLS) provides essential scientific tools for 2,300 scientists per year from more than 400 academic, industrial, and government institutions. Their myriad research programs produce about 800 publications per year, with more than 130 appearing in premier journals. It was designed in the 1970s and is now in its third decade of service. It has been continually upgraded over the years, with the brightness increasing fully five orders of magnitude. However, it has reached the theoretical limits of performance given its small circumference and small periodicity, and only a small number of insertion devices are possible. For the productivity of the large NSLS user community to continue and even increase, and in order to tackle the “grand challenge” problems of tomorrow, it is essential that NSLS be upgraded to provide much higher average brightness and higher flux.

The National Synchrotron Light Source II (NSLS-II) facility will be constructed as a replacement for the present NSLS. NSLS-II will fill the gap in the nation’s capabilities by enabling the study of material properties and functions, particularly materials at the nanoscale, at a level of detail and precision never before possible. To achieve this, NSLS-II will provide photon beams having ultra high brightness and flux and exceptional stability. NSLS-II will also provide advanced insertion devices, optics, detectors, robotics, and a suite of scientific instruments.

The combination of brightness, flux, and stability of NSLS-II will provide the world’s finest capabilities for x-ray imaging. NSLS-II will enable the study of materials with ~1 nanometer (nm) spatial resolution and with ~0.1 milli-electron volt (meV) energy resolution. It will be possible to focus both soft and hard x-rays to a spatial resolution of ~1 nm and to perform spectroscopy on a single atom. With the development of novel “lens-less” imaging, it will be possible to capture x-ray images with a spatial resolution of ~1 nm. This resolution and sensitivity is unprecedented in x-ray imaging. If there is any doubt that this is needed for our future energy security, one only need remember that all the elementary steps of energy conversion (charge transfer, molecular rearrangement, and chemical reactions), both for fossil fuels and for critical renewable energy sources, take place on the nanoscale, and many of these steps involve a combination of complex physical, chemical, and often biological, transformations.

The unique characteristics of NSLS-II will enable exploration of the scientific challenges faced in developing new materials with advanced properties, including: the correlation between nanoscale structure

and function, including the profound effects of confinement, finite size, and proximity; the mechanisms of molecular self-assembly, which produces exquisite molecular structures in both the living and nonliving worlds; and the science of emergent behavior, one of the grand scientific challenges.

2.2 Work Breakdown Structure

The NSLS-II project has been organized into a Work Breakdown Structure (WBS). The WBS contains a complete definition of the project's scope and forms the basis for planning, executing, and controlling project activities. The Project WBS is shown in Figure 2.1. Elements are defined as specific systems/deliverables (WBS 1.3–1.7), project management (WBS 1.1), research and development (WBS 1.2) or pre-operations (WBS 1.8) consistent with discrete increments of project work and the planned method of accomplishment

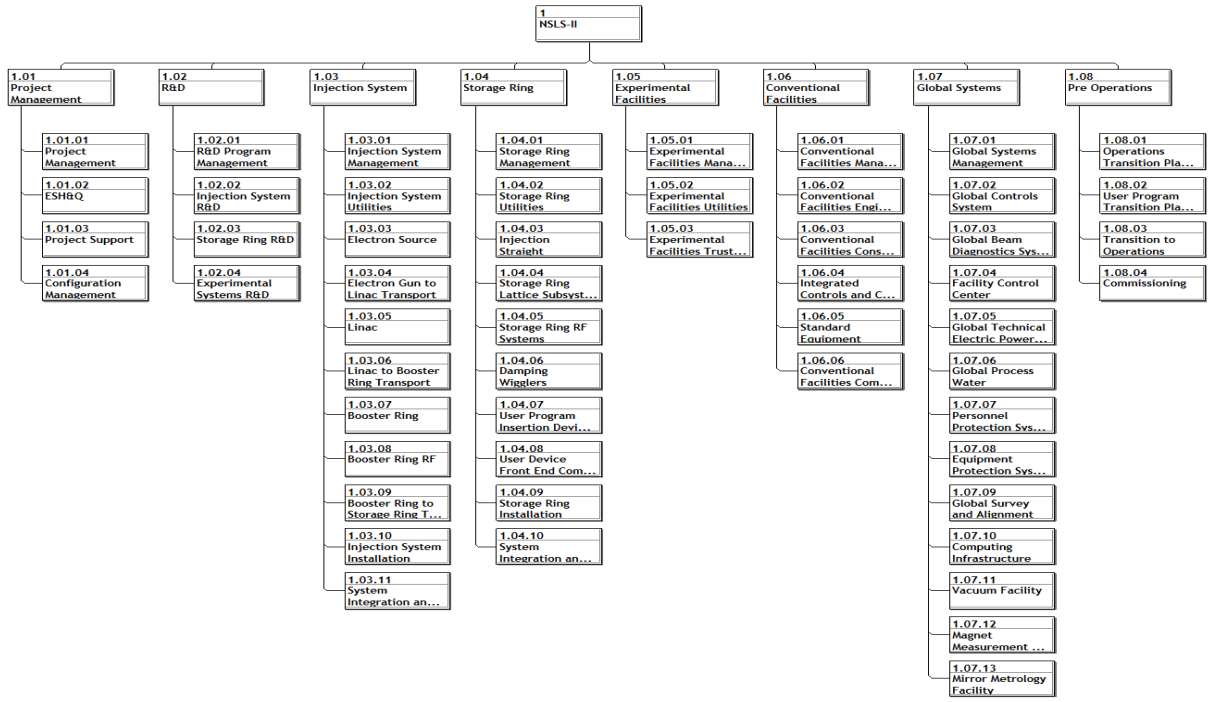

Figure 2.1 Work breakdown structure for the NSLS-II project:

1.01 Project Management – Project Office administrative and management activities that integrate across the entire project (management, regulatory compliance, quality assurance, safety, project controls, etc.)

1.02 Research and Development – R&D activities as necessary to support the delivery of project objectives

1.03 Injection System – All phases of design, procurement, installation, and commissioning of the injection system

1.04 Storage Ring – All phases of design, procurement, installation, and commissioning of the storage ring

1.05 Experimental Facilities – All phases of design, procurement, installation, and commissioning of the suite of beamlines and instruments included in the project scope

1.06 Conventional Facilities – All phases of design, procurement, installation, and commissioning of the conventional facilities including preparation of the site and provision of all utility systems

1.07 Global Systems – All phases of global systems that integrate across subsystems including management of interfaces

1.08 Pre-Operations – Materials, equipment, services, etc. for integrated testing and commissioning

2.3 Cost and Schedule

A preliminary high-level summary of the cost of the NSLS-II project, at the second level of the work breakdown structure, is given in Table 2.1

Table 2.1 Level 2 Cost Breakout for the NSLS-II Project.

NSLS-II Level 2 Cost Element	Cost (AY $M)
1.1 Project Management and Support	53.5
1.3 Injection System	34.1
1.4 Storage Ring System	138.0
1.6 Conventional Facilities	200.1
1.7 Global Systems	22.9
Contingency (35% of TEC cost elements excl. Exp. Facilities)	157.0
1.5 Experimental Facilities (includes contingency)	72.6
NSLS-II Total Estimate Cost (TEC)	678.2
1.2 R&D	35.9
1.8 Pre-operations	61.1
Total Other Project Costs	97.0
NSLS-II Total Project Costs (TPC)	775.2

A preliminary Level 0 milestone schedule to construct NSLS-II is shown in Table 2.2.

Table 2.2 Preliminary Level 0 Milestone Schedule.

Major Milestone Events		Preliminary Schedule
CD-0	(Approve Mission Need)	4th Qtr, FY2005
CD-1	(Approve Alternative Selection and Cost Range)	2nd Qtr, FY2007
CD-2a	(Approved Long Lead Procurement Budget)	2nd Qtr, FY2007
CD-2b	(Approve Performance Baseline)	1st Qtr, FY2008
CD-3a	(Approve Start of Long-lead Procurement)	1st Qtr, FY2008
CD-3b	(Approve Start of Construction)	1st Qtr, FY2009
CD-4a	(Approve Initial Operations)	2nd Qtr, FY2013
CD-4b	(Approve Start of Operations)	3rd Qtr, FY2014

3 SCIENCE AT NSLS-II

The science case for NSLS-II was presented in the proposal submitted for Critical Decision 0 (Approval of Mission Need), which was approved on August 25, 2005. Subsequent to this, in the process of carrying out the conceptual design for NSLS-II, the details and capabilities of the facility have become clearer. In particular, the capabilities of likely beamlines and the science they will enable have become much better defined. Several of these beamlines were examined in some detail, notably those beamlines expected to have especially high scientific impact and those that exploit the high brightness of NSLS-II. In this chapter, we briefly mention some experiments that could be carried out on those beamlines, to provide some context for the conceptual designs discussed later in this document. Note that these examples are not meant to be exhaustive, but rather represent a sampling of the diverse and exciting science that NSLS-II will enable.

3.1 Hard X-ray Nanoprobe

As discussed in Section 11.4, a hard x-ray nanoprobe beamline at NSLS-II will be designed and optimized to enable the production and use of a beam of hard x–ray photons with a minimum beam size in the nanometer range. As such, it will be a world-leading instrument, enabling spatially resolved versions of many powerful structural and spectroscopic x-ray techniques with unprecedented resolution. In particular, it will allow the study of nanomaterials which today play important roles in many diverse scientific fields, opening up a wide range of scientific problems ranging from studying the structure and function of catalytic nanoparticles, to the mapping of strain in buried grain boundaries, to determining the structure of single molecule devices.

Some of the possibilities of such an instrument can be illustrated more concretely by considering a potential experiment on carbon nanotube devices. Carbon nanotubes are among the most studied nano objects. Furthermore, many of the interesting properties of CNTs—metallic or semiconducting transport properties, electroluminescence, photoconductivity, etc.—depend sensitively on their structure. A single-walled CNT can be regarded as a single layer of graphite that has been rolled up into a cylindrical structure.

In general, the CNT is helically wrapped, and a chiral vector can be defined to reflect the way in which the graphite sheet self-registers around the tube. Depending on the chirality [3.1.1], the nanotubes are either metallic or semiconducting. Preparation of CNT samples results in a distribution of nanotube diameters and chiralities, and each fabricated device that randomly selects one from this distribution consequently contains a nanotube with an unknown structure. Currently, the best way to determine the structure of an individual CNT is with electron diffraction [3.1.2, 3.1.3], though this results in damage to the tube. This method also suffers from the drawback that it is very difficult to carry out such a study when the nanotube is buried under a gate electrode structure (as is typically the case), or under a protective barrier, as shown in the device structure in Figure 3.1.1.

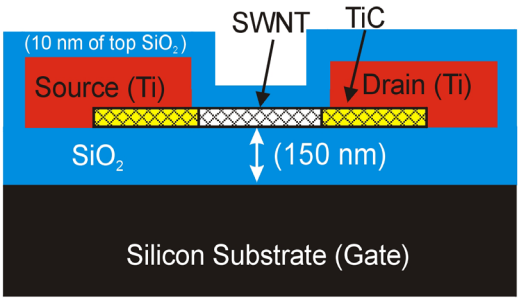

Figure 3.1.1 Schematic of a CNT device in which the nanotube structure is obscured. Such CNTs could be probed with the proposed nanoprobe beamline at NSLS-II.

Figure 3.1.2 shows an SEM image of an actual device. Any protective coatings or support membranes of significant thickness make electron diffraction difficult, so it is almost impossible to compare directly the measured electron transport properties of a given functioning CNT device and its structural properties. As mentioned, a further disadvantage of electron diffraction is that it is a destructive probe of the nanotube structure, so the structural characterization becomes the last step. Although the extent of the damage that an x-ray nanoprobe will induce in a sample has not yet been experimentally resolved, it appears that it will be possible, in at least some cases, to study the structure in situ, with the device in operating conditions. To determine the feasibility of such studies at NSLS-II, the x-ray scattering from a single nanotube has been calculated.

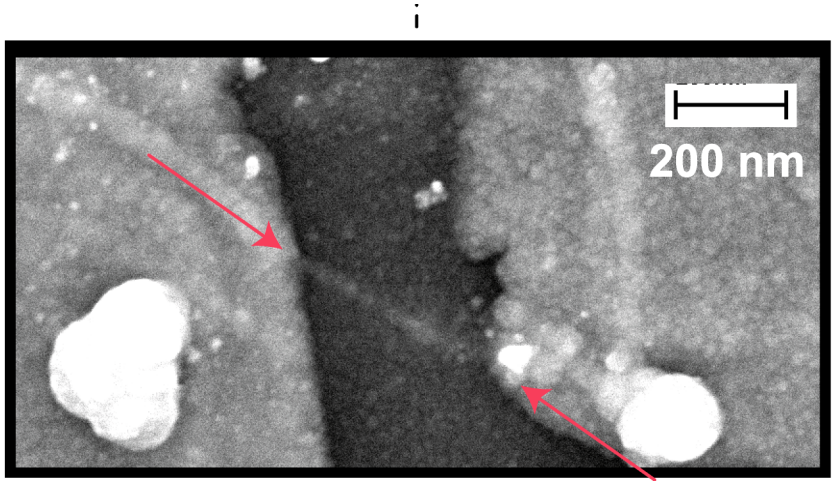

Figure 3.1.2 Scanning electron microscope image of a device.

The model used is illustrated in Figure 3.1.3. A single CNT is illuminated by a perpendicular x-ray polarized parallel to the tube. The diffraction pattern is recorded by a 1024 × 1024 pixel detector array, positioned at a distance d = 20 cm; the pixel area is 100x100 μm^2. The number of counts N recorded by the detector at pixel $\vec{R}$ is given by:

$$N(\vec{R}) = I_{sc}\Delta t = I_0\,\Delta t\,(A_p / A_0)\,(r_0/\mathrm{R})^2\,P(Q)[(\sum_j f_j \cos\phi_j)^2 + (\sum_j f_j \sin\phi_j)^2 \qquad (3.1.1)$$

where I_{sc} is the scattered intensity (number of photons per second impinging on the detector); Δt is the accumulation time; I_o is the incident intensity (number of photons per second impinging on the illuminated area A_0 of the CNT under study); $A_p = R^2\Delta\Omega$ is the (effective) area of the detector and $\Delta\Omega$ is the solid angle that it subtends; $r_0 = 2.8\times10^{-6}$ nm is the classical (Thomson) electron radius; $\vec{R}$ = (X, Y, Z) = (d, mb, nb), where m, n = -215, …, 216 and b = 200 μm specifies the pixel position; $P(Q) = 1 - (\mathbf{e_o}\ ,\ \mathbf{s'}\ )^2$ is the polarization factor, $\mathbf{e_o}$ is the direction of polarization of synchrotron light and $\mathbf{s'} = \vec{R}/\mathrm{R}$ is the direction of scattered light; $fj(Q)$ is the atomic scattering (form) factor of the atom at r_j, calculated ab initio and tabulated in the literature; $\mathbf{Q} = \mathbf{k} - \mathbf{k'}$ is the momentum transfer where $\mathbf{k}$ and $\mathbf{k'}$ are the momentum of the incident and the scattered x-ray photon respectively; and $\phi_j = (Q, r_j)$.

Figure 3.1.3a shows the scattering geometry used in the calculations, with a single-walled (3,3) armchair nanotube illuminated. Figure 3.1.3b shows the resulting diffraction pattern.

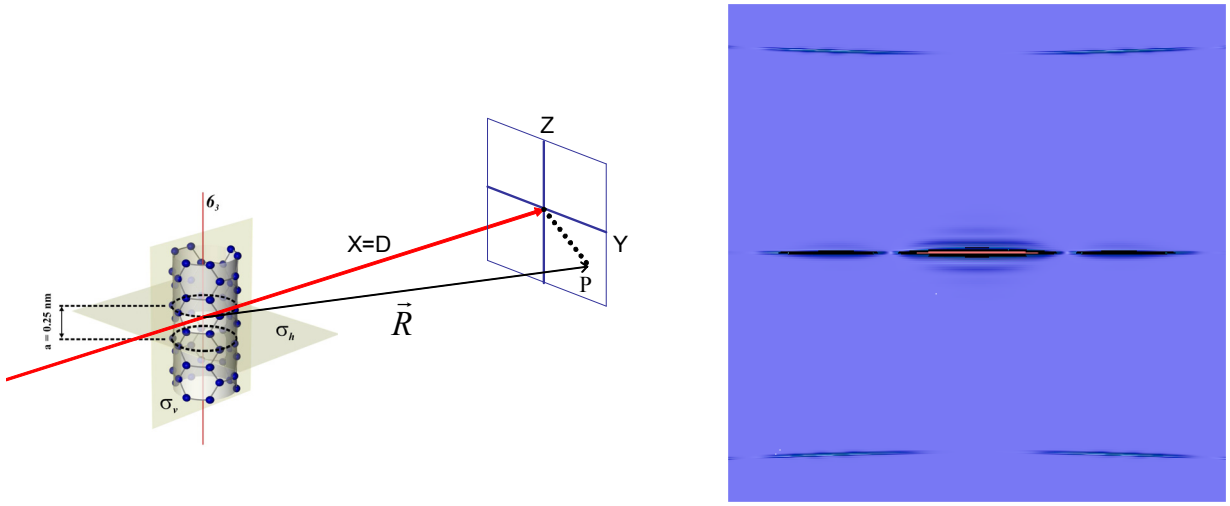

a **b**

Figure 3.1.3 **a**) A single nanotube—here, a (3,3) armchair CNT—is shown illuminated by an x-ray beam, and the diffraction is recorded on a flat screen. **b**) The corresponding x-ray diffraction pattern.

Taking the performance of a 3 m U19 device at NSLS-II and utilizing diffractive optics capable of delivering photons into a 25 nm x 1 nm spot and making reasonable assumptions for the efficiency of these optics and their associated pre-optics, we find that these model calculations give intensities of 10,000 cps in the central maxima and 1,250 cps in the secondary maxima of the diffraction pattern shown in Figure 3.1.3b.

These results illustrate that one will have the sensitivity at NSLS-II to address this important class of problems, understanding the structure of the nanotubes in a real gated device and hence directly connecting their structure to the performance of a given device. Further, the technique will be sensitive to the presence of single dopant atoms on the tube—and to their precise location, as shown in Figure 3.1.4. These capabilities will be revolutionary in the study of such single-molecule devices.

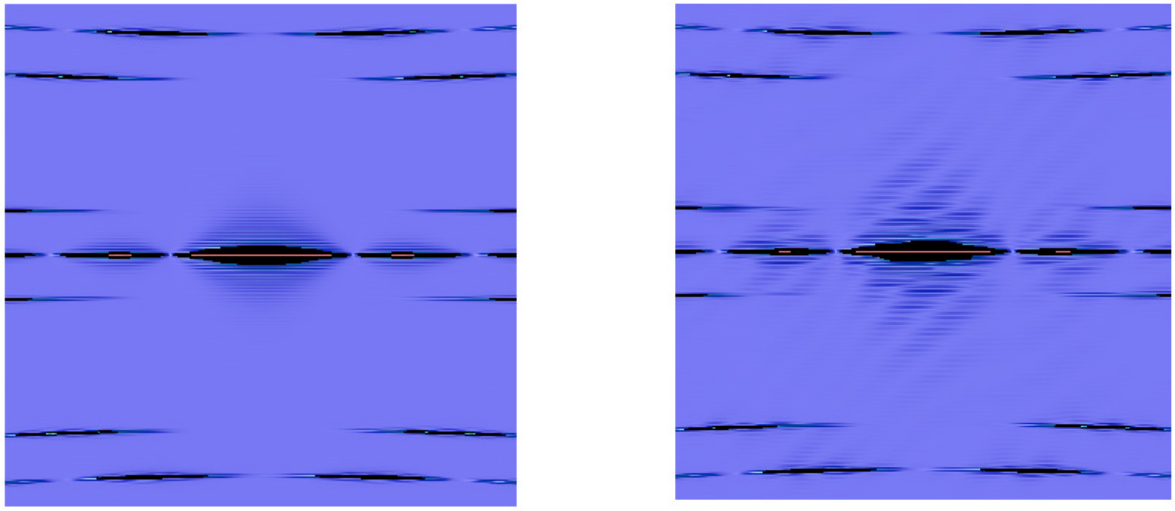

a **b**

Figure 3.1.4 X-ray diffraction from **a**) chiral (4,2) nanotube; **b**) the same, but with one Au atom adsorbed to the side at z = 0.

As a further example of the power of a nanoprobe at NSLS-II, we next calculate the fluorescence from a single Fe atom embedded in a Si matrix. This represents the ultimate limit of a catalytic nanoparticle, which in practice is likely to be made up of tens of atoms.

We first calculate the flux onto a 1 nm spot. To do so, we assume the source properties of NSLS-II with the fully built out complement of damping wigglers, so that the emittance is 0.55 nm-rad. Taking the performance of a 3 m U19 CPMU insertion device occupying a 5 m straight, we calculate the flux delivered onto an optic with a physical aperture of 100 μm. As discussed in Chapter 12, the likely optic for such a beamline is a multi-layer Laue lens (MLL) or a kinoform lens. Both are diffractive, and therefore chromatic, optics; hence, in order to achieve a 1 nm focus they require highly monochromatic beam. In particular, the required bandpass is 3×10^{-5} for a working distance of ~1 mm. Allowing for the reduction in flux associated with this narrow bandpass, together with expected efficiencies for a high-heat-load monochromator, the high-resolution monochromator and the focusing optic, we find that the flux delivered into a 1×1 nm spot is $\sim10^{11}$ ph/s—a very significant number.

Calculating the resulting fluorescence intensity from this flux is relatively straightforward and is given by $I=I_0\omega(\Omega/4\pi)\sigma_{pe}e^{-\mu t}$, where I_0 is the incident flux; ω, the fluorescent yield (=0.35 for Fe), Ω, the collection solid angle of the detector; σ_{pe} the photoelectric cross-section for Fe ($=1.12\times10^{-6}$ nm^2 at 10 keV for Fe K-edge); and the factor $e^{-\mu t}$ accounts for absorption of incoming and outgoing photons in the Si matrix. We ignore this latter factor in these calculations, which is a good approximation for silicon thinner than 1 absorption length (~100 μms at 10 keV). Putting in these numbers, one finds that the fluorescence signal from a single Fe atom is a very respectable ~1,000 cps. Of course there will be background, such as Compton scattering from the silicon, but it should be possible to discriminate against this and thus it will be possible to perform imaging and spectroscopy from a single Fe atom.

In fact, the variation in cross-sections is relatively small for different atomic species. For example, the same calculation for Er L-edge fluorescence for a single Er atom embedded in Si (a problem with relevance to the optoelectronics industry) gives an intensity of 5,000 counts per second with the same assumptions. Thus it should be possible at NSLS-II to perform single-atom imaging and spectroscopy for essentially any atom in the periodic table.

References

[3.1.1] R. Saito, M. Fujita, G. Dresselhaus, and M.S. Dresselhaus, Electronic structure of graphene tubules based on C_{60}, *Phys. Rev. B*. **46** 1804 (1992).

[3.1.2] N. Hamada, S. Sawada, and A. Oshiyama, New one-dimensional conductors: Graphitic microtubules, *Phys. Rev. Lett*. **68** 1578 (1992).

[3.1.3] M. Y. Sfeir, T. Beetz, F. Wang, L. Huang, X.M.H. Huang, M. Huang, J. Hone, S O'Brien, J.A. Misewich, T.F. Heinz, L. Wu, Y. Zhu, and L.E. Brus, Optical Spectroscopy of individual single-walled carbon nanotubes of defined chiral structure, *Science* **312** 554 (2006).

3.2 Coherent X-Ray Scattering

The National Nanotechnology Initiative recognizes the rapidly growing importance of nanostructures, and the potential that future developments in this area have for major breakthroughs in the fundamental and applied sciences and in technology. On this scale—as on all others—imaging is clearly one of the most important characterization tools to connect form with function. In the previous section, real-space imaging was discussed. Coherent x-ray scattering offers an attractive alternate route to solving the structure of nanoparticles with very high spatial resolution—by working in reciprocal space, illuminating the structure with coherent light, and inverting the resulting image. The technique places very high demands on the

coherent flux from the source and as a result NSLS-II is expected to provide an important advance in the field.

On the highest resolution scale, x-ray crystallography provides excellent 3D representations of the molecular structure for materials that can be crystallized. For noncrystalline samples less than 50 nm thick, aberration-corrected transmission electron tomography promises to provide 3D images at 0.1 nm resolution. X-ray microtomography is presently capable of 3D imaging at 60 nm resolution, and is likely to develop further to resolutions of 30 nm. However, it is limited to thin samples at these high resolutions, due to depth-of-field effects. There is, therefore, a significant gap, in that none of these techniques can image samples thicker than a hundred nm and with high spatial resolution.

Coherent diffractive imaging promises to be a powerful microscopic method for imaging noncrystalline or finite-size objects at high spatial resolution, in thick samples and beyond the resolution limit set by x-ray optics. We show here that for very radiation-resistant materials, true atomic imaging with a resolution as small as 0.1 nm may be possible using NSLS-II.

The idea is to determine the spatial distribution of electron density $\rho(r)$ in a noncrystalline sample by measuring its far-field coherent x-ray diffraction pattern. It is analogous to x-ray crystallography, but with two important distinctions. First, the diffraction pattern is a continuous function in reciprocal space for a noncrystalline or finite-size sample, as opposed to discrete Bragg peaks for a bulk crystal. This allows the application of an iterative oversampling phasing algorithm for phase retrieval and structure determination. Second, the method requires an intense coherent x-ray beam incident on the sample to preserve the phase information in the diffraction pattern and overcome the lack of periodicity in the sample.

Here we summarize the requirements on the source for imaging an object of size L with spatial resolution d. One can show that the required incident coherent intensity, I_o (ph/s/cm^{-2}), for determining the reconstructed 3D structure with acceptable signal to noise in time Δt is given by

$$I_o\Delta t = 20\pi^3/(3r_o^2Ln_o^2d^3f^2\lambda^2) \approx (3\times10^{-20}\ gm^2/cm^2)/(Ld^3\lambda^2\rho^2) \qquad (3.2.1)$$

where n_o is the atom density (atoms/cm^3), f is the scattering amplitude (~Z, the atomic charge), λ is the wavelength, and ρ is the mass density (gm/cm^3). This shows that the coherently scattered signal scales with ρ^2 and d^3 and is proportional to sample thickness, L. Table 3.2.1 gives $I_o\Delta t$ required to image a 1 μm^3 volume with 1 nm resolution for materials having a range of densities from light (carbon) to heavy (gold). The dose equivalent is also given in Table 3.2.1 and discussed below.

Table 3.2.1 Coherent Diffraction Measurement Considerations at NSLS-II. Required coherent flux density, equivalent dose, and measurements times for unfocused and focused radiation from NSLS-II, for imaging a 1 μm^3 volume of different materials with 1 nm resolution.

Material	$I_o\Delta t$ (ph/μm^2)	Dose (Gray)	Measurement Time NSLS-II Unfocused	Measurement Time NSLS-II Focused
Carbon (Z = 6)	7.1 x 10^{12}	4.3 x 10^9	14 hours	20 seconds
Cobalt (Z = 27)	1.6 x 10^{11}	3.0 x 10^9	19 minutes	0.4 seconds
Ruthenium (Z = 44)	8.7 x 10^{10}	2.0 x 10^9	10 minutes	0.2 seconds
Gold (Z = 79)	3.5 x 10^{10}	0.95 x 10^8	4 minutes	0.1 seconds

With NSLS-II, the coherent flux at 8 keV will be 6×10^{12} ph/s after the Si monochromator, which will provide the appropriate longitudinal coherence. The transverse coherence lengths will be 65 μm and 819 μm in the vertical and horizontal, respectively, at 25 m from the source. Thus, the incident coherent intensity in the required bandwidth will be 1.4×10^8 ph/s/μm^2. The times required to collect the diffraction patterns for the examples above range from 4 minutes to 14 hours.

The incident coherent intensity can be increased by focusing while still meeting the coherence requirements. This is because the divergence angle of the coherent radiation from NSLS-II is 14 μrad in the horizontal and 3.2 μrad in the vertical, whereas the smallest detection angle is $\lambda/(1.4L) = 110$ μrad. For a focused beam size of about 4L, the gain in coherent intensity for the case of 1 μm is a factor of about 2600. This reduces the time to measure the diffraction patterns to from 0.1 to 20 seconds, as shown in Table 3.2.1.

The requirement of an intense x-ray beam for coherent diffraction measurements may cause radiation damage to the sample, which would ultimately limit the tolerable dose, and thus the achievable spatial resolution. Table 3.2.1 shows the required dose depends only weakly on composition and density.

Several studies have shown that radiation-damage effects in biological specimens at a given dose depend on the spatial resolution of interest. At atomic resolution, it is commonly accepted that a dose of 2×10^7 Gy is enough to destroy crystalline order in protein crystals. At much lower resolutions, however, much higher x-ray dosages of 10^{10}-10^{11} Gy can be tolerated at cryo-temperatures. These radiation-damage limits are purely empirical, and are for biological specimens only. The x-ray radiation tolerance for inorganic materials has been less well studied, but indications are that it can be a factor of 100, or more, higher than for biological materials.

Table 3.2.2 shows the required dose and measurement times for imaging such a $(10\ \mu m)^3$ volume of different materials with 0.3 nm resolution. Carbon is included since, for example, carbon nanotubes have been shown to be very radiation resistant – at least 100 times higher than for biological materials. A $(10\ \mu m)^3$ volume of carbon nanotube bundles could thus be imaged with 0.3 nm resolution. Such experiments will complement the single molecule diffraction experiments discussed above. The required time is reasonable, at a few minutes or less for most materials. It should be noted that no losses have been taken into account for the monochromator (other than accounting for its bandwidth), focusing optics, or beamline windows, and the detector quantum efficiency has been assumed to be 100%. In addition, the finite readout and storage rate for area detectors has been neglected. In practice, these losses, plus the overhead from detector readout, might increase the measurement time by a factor of ~ 5. These will combine to give measurement times of ~ 10 minutes, which are still reasonable.

Table 3.2.2 Required Coherent Flux Density, Equivalent Dose, and Measurement Times. Values are for unfocused and focused radiation from NSLS-II, imaging a $(10\ \mu m)^3$ volume of different materials with 0.3 nm resolution.

Material	$I_o \Delta t$ (ph/μm²)	Dose (Gray)	Measurement Time NSLS-II Unfocused	Measurement Time NSLS-II Focused
Carbon (Z = 6)	2.6×10^{13}	1.6×10^{10}	52 hours	2.2 hours
Cobalt (Z = 27)	5.9×10^{11}	1.1×10^{10}	1.2 hours	2.9 minutes
Ruthenium (Z = 44)	3.2×10^{11}	7.4×10^{9}	37 minutes	1.5 minutes
Gold (Z = 79)	1.3×10^{11}	3.5×10^{8}	15 minutes	37 seconds

This analysis has shown that for radiation-resistant nonbiological material, such as nanostructures, nanocomposite materials, magnetic materials, and others, the physical, chemical, and magnetic imaging of materials with atomic spatial resolution will be possible at NSLS-II.

One example of an area where this will have tremendous impact is that of inorganic open-framework materials, such as zeolites. These porous materials can have superior catalytic or sorption properties. The latter might be especially important for hydrogen storage applications. These materials often occur as powders with poor crystallinity, so conventional x-ray diffraction can have limited applicability. In addition, their catalytic activity is often due to other species, such as transition metal atoms, absorbed on their high surface area interior. These active atoms are often heterogeneously distributed throughout the porous material, so, once again, conventional diffraction is ineffective.

For example, nickel succinate is a 3D porous open framework structure. The pores are 0.8 nm in diameter and the pore–pore spacing is 2.3 nm. Imaging this structure with 0.3 nm resolution using NSLS-II will clearly reveal the pore structure and atoms lining the pore surface.

Some other applications of coherent diffractive imaging in the material sciences include: 1) imaging the complex tangle of dislocation lines that are responsible for work hardening; 2) imaging the cavities inside duplex steels that are responsible for their very high uniform extension; 3) 3D imaging defect structures in magnetic multilayers; 4) tomographically imaging misfit dislocations at interfaces, free of the thin-film elastic relaxation processes that distort the images obtained by transmission electron microscopy; 5) imaging the 3D arrangement of Orowan dislocation loops which, by entanglement with particles, provide the dispersion-hardening of copper alloys; 6) imaging precipitates in metal–matrix composite materials; and 7) imaging electronic or spintronic device elements for future computing schemes, such as quantum computing.

For very radiation-resistant materials, true atomic imaging with a resolution as low as 0.1 nm may be possible. With NSLS-II, this will require measurement times on the order of 10 minutes × $(3)^3$, or about 4.5 hours for a 10 μm^3 sample, which is not unreasonable.

3.3 X-Ray Photon Correlation Spectroscopy (XPCS)

X-ray photon correlation spectroscopy also utilizes the very high coherent flux at NSLS-II, in this case to probe the equilibrium or steady-state dynamics of condensed matter. In this endeavor, the XPCS technique offers the significant strengths of being able to study length scales shorter than can be achieved with optical techniques and longer time scales than can be achieved via neutron scattering. Even on optically accessible length scales, it permits the study of opaque and metallic samples, presenting new opportunities for studies of colloidal and other soft-matter systems.

XPCS involves creating a partially coherent x-ray beam, which is allowed to impinge upon a sample. The dynamics of any fluctuations within the sample are then determined by characterizing the intensity autocorrelation function, $g_2 = g_2(Q,t)$, of the resultant x-ray speckle pattern versus delay time (t) and wave vector (Q). In a certain sense, this may be thought of as the time-resolved counterpart to coherent diffraction discussed above. Importantly, the quantity $g_2(Q,t)$ is related to the sample's normalized intermediate scattering function (ISF) $[f(Q,t) = S(Q,t)/S(Q,0)]$ via $g_2(Q,t) = 1+A[f(Q,t)]^2$, where A is the optical contrast. The ISF (equivalent to the sample's Q- and t-dependent density–density autocorrelation function) is a quantity of central interest for any condensed matter system, and is usually key in comparing theory to experimental results.

However, PCS is much more challenging with x-rays than with light. This is due to a combination of the fact that there are many fewer photons in x-ray beams from even the brightest synchrotrons than from laser sources, and the fact that x-ray scattering cross-sections are invariably many times smaller than light scattering cross-sections. As a result, the crucial aspect of any XPCS experiment is generally the signal-to-noise ratio.

The XPCS SNR is linearly proportional to the source brightness. Since the brightness of NSLS-II will exceed by a factor of 30 that of any source in existence today, the corresponding SNR will be about a factor of 30 higher. NSLS-II will drive a revolution in the kinds of samples that will be accessible to XPCS studies. Interestingly, while the SNR scales linearly with brightness, it only scales as the square-root of the sample time (which should be a few times smaller than the sample's correlation time). It follows that for samples of a given scattering strength, meaningful XPCS measurements will be possible at NSLS-II on time scales that are about 10^3 times faster than currently possible anywhere. Since the current state-of-the-art for diffuse scattering measurements (not from liquid crystal Bragg peaks, or surface specular reflection) corresponds to sample times of about 1 millisecond, we expect time resolutions at NSLS-II of 1 microsecond or less to be

feasible, which will enable entirely new science. Indeed, with a time resolution of 0.1 microseconds, it may be possible, in favorable circumstances, to overlap with neutron spin echo measurements.

There are several classes of XPCS experiments that will be possible at NSLS-II but are impossible at current facilities. These include:

Membrane Dynamics. Studies of the dynamics of membrane-based complex fluid phases, consisting of oil–water and an amphiphilic surfactant. Such phases—including the sponge phase and the bicontinuous microemulsion phase, for example—have been the subject of intense interest over the past 20 years, not least because of their possible utility in enhanced oil recovery applications. There are detailed predictions for the equilibrium dynamics of such phases for the wave vectors most characteristic of these materials, namely wave vectors at and near the peak of the static scattering. However, these dynamics are typically too slow for neutron spin echo (NSE) measurements and occur at wavevectors that are too large for optical studies. The faster time scales made accessible by the enhanced brightness of NSLS-II will enable XPCS studies to test these predictions.

Nanoparticles in Suspension. Studies of the collective dynamics of suspensions of nanoparticles. At NSLS-II, it will be possible to study fluctuation dynamics of smaller nanoparticles than is possible now. This will, for example, permit studies of the motions of nanoparticles confined within block copolymer matrices, or on surfaces. Such studies will be critical in understanding the processes underlying how small particles self-assemble into potentially, technologically useful structures. Especially interesting will be studies examining mixtures of differently-sized nanoparticles of differing compositions, which can self assemble into a variety of different structures, depending on their relative sizes, and which it may be possible to selectively probe via anomalous scattering methods.

Polymer Dynamics. A longstanding question in polymer science concerns so-called *reptation*, which is the process by which polymers in an entangled polymer melt diffuse. The enhanced brightness of NSLS-II will permit XPCS studies on shorter length scales than is now possible, allowing such studies to critically examine the reptation model and relaxations associated with reptation in polymer melts in a much more direct fashion—by actually looking at the polymer motion—than has been possible previously.

Surface Fluctuations. Surface XPCS studies carried out at NSLS-II will probe shorter length scales and faster time scales than are possible now and will therefore elucidate the dynamical behavior of thin liquid and polymer films, and permit definitive answers to questions concerning the role of surface roughness in quenching dynamical fluctuations, or of a polymer's radius of gyration in determining a polymer thin film's capillary mode spectrum.

3.4 Small Angle X-Ray Scattering (SAXS)

Small angle x-ray scattering can provide information on sample inhomogeneities in the nm range, providing, for example, information about the shape and size of macromolecules, characteristic distances of partially ordered materials, pore sizes, etc. SAXS is capable of delivering structural information on macromolecules between 5 and 25 nm, and of repeat distances in partially ordered systems of up to 150 nm. USAXS (ultra-small angle x-ray scattering) can resolve even larger dimensions. Present trends in the field are toward extending the technique both to longer length scales and, through the use of flow cells, to faster time scales, a trend that will accelerate with the availability of the high-brightness beams at NSLS-II. In this section we provide several examples of research areas in which a state-of-the-art SAXS instrument at NSLS-II will have significant impact.

3.4.1 Dynamical Events in Biological Macromolecular Solutions

Macromolecular crystallography has provided much of our knowledge about the function and interaction of various proteins and other biomolecules. However, these functions often depend on flexibility of the molecule, and on environmental parameters such as pH and ion concentration. Furthermore, in cases where the molecule is flexible or is insoluble in water (such as membrane proteins), crystallization may be difficult. In such cases, structural studies in solution, where flexibility is natural and solution parameters can be controlled, can complement or even replace crystallographic studies.

In this context, there have been two recent developments in the instrumentation and data analysis of small angle solution scattering, namely, micro-fabricated flow cells and the low-resolution shape reconstruction algorithms. These advances, combined with NSLS-II beams, will provide new insights into the function, control, and dynamics of individual macromolecules and large molecular complexes.

Micro-fabricated flow-cell mixer is a technology that allows sub-millisecond-resolution time-resolved x-ray scattering measurements. In particular, the continuous-flow diffusion mixer (Figure 3.4.1) [3.4.1, 3.4.2] has the potential to provide μs time-resolution. This device produces thin laminar flow sheets of solutions. Dynamical events are triggered as the solutions mix by diffusion between the solution sheets, and one follows the events in time by measuring at different positions downstream. For instance, to generate a protein-folding event, denatured protein is injected into the central channel, sandwiched between buffer solutions. As the protein and buffer solutions flow downstream, the denaturant diffuses out of the protein layer. Once the denaturant concentration drops below a threshold, the protein folds back to its functional conformation. The solution mixer can also trigger other biochemical reactions by a similar mixing of reactants.

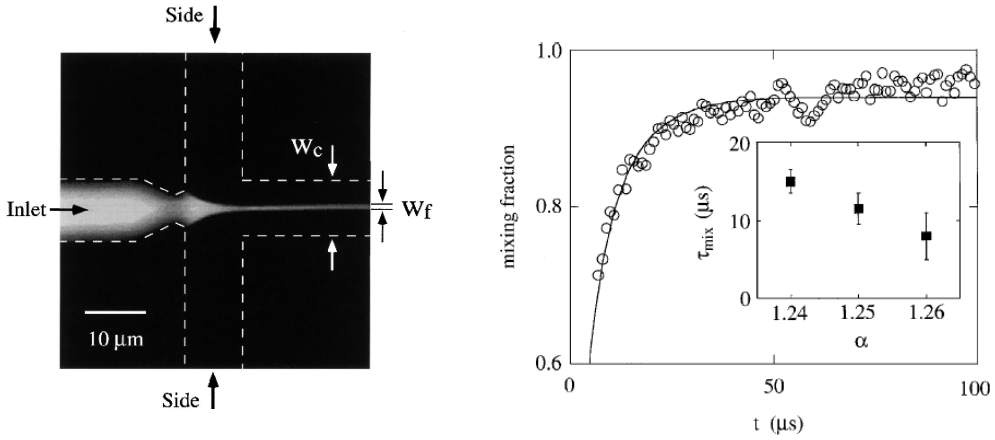

Figure 3.4.1 Fluorescence image of a continuous-flow cell, (left) and its intrinsic time resolution (right). Time resolution is on the order of ~10 μs [3.4.1]. X-ray studies in such cells will be possible at NSLS-II. The fluorescein-labeled inlet flow is bright in the image. Currently, limited by x-ray beam size and intensity, the mixers used for x-ray experiments are larger (50–100 micron channels) and the time resolution is on the order of 1 millisecond.

However, the potential of solution-mixers for SAXS measurements can only be fully realized when the device is used with very high brightness x-ray beams. This is because the time-resolution that the mixers can provide is limited by the beam size. An intense and small beam not only allows a smaller overall dimension of the solution layers and reduces sample consumption, but also improves the time resolution. Note that radiation damage effects are mitigated because the sample is continually renewed by the flow.

The second development is a handful of shape determination algorithms [3.4.3, 3.4.4] that have excited renewed interest in solution scattering. The basic idea behind these methods is that although the molecules in solution are randomly oriented and much of the structural information is lost in the isotropic average, some information that is characteristic to the shape envelope of the biomolecules remains in the measured one-

dimensional scattering curve. This may suffice to define a low-resolution shape envelope. In many cases, the subunits that make up a protein complex, for example, are rigid and their atomic structures are known. Solution scattering can then provide a useful tool for putting the pieces of this puzzle together to reveal the functional structure of the protein complex; by knowing the shape of components, one reduces the degrees of freedom in the model, and the overall shape determination becomes much more reliable.

Solution mixers are already being used, in combination with size characterization provided by simple SAXS analysis, to study protein folding on a time scale of milliseconds. With smaller, brighter x-ray beams to improve the time-resolution and the more sophisticated data analysis outlined above, low-resolution movies may be created to capture events such as the assembly and functioning of molecular machines, for the first time.

3.4.2 Structures in Model Membranes Submerged in Water

Many of the most intriguing biological processes, such as cell recognition, signal transduction, chemical sensing, and transportation, take place in the membranes of cells and organelles. Yet, progress in membrane research has been painfully slow, mainly because of the difficulty of crystallizing membrane proteins and a lack of alternative structural characterization tools.

Progress is being made slowly in preparing model systems for x-ray structural studies of biological membranes. A very promising model system is substrate-supported single bilayers [3.4.5] that resemble native cell membranes. A lipid bilayer of biologically relevant composition can be spread on a flat substrate so that Grazing Incidence SAXS (GISAXS) can be carried out to probe the structures embedded in the bilayer, such as membrane proteins. This technique applies to both fluid-like membrane structures and 2D membrane protein crystals, if such crystals are available [3.4.6].

It is important to note that lipid bilayers are stable only in an aqueous environment and disintegrate instantly in air because of the lower surface energy when the hydrophobic lipid chains are exposed to air. While keeping the membrane under water is advantageous because the solution provides many possibilities to control the membrane structures, it also leads to experimental problems because of absorption issues and because it gives rise to significant background scattering. The experiments therefore must be done with high energy x-rays (>20 keV for less x-ray absorption) and relatively small samples (<1 cm long) illuminated at grazing incidence. The latter implies the need for a small beam size in the direction perpendicular to the model membrane. For instance, at the water–Si interface, the critical angle is 0.064º, at 20 keV. The vertical beam size must therefore be less than 10 microns in order not to overfill a sample that is 1 cm long. In the case of semi-crystalline structures, the beam footprint may need to be limited to be comparable to the horizontal beam size (<1 mm) so that in-plane powder average can be effectively performed. The beam height in this case will therefore need to be less than 1 micron.

These requirements present instrumentation challenges for scattering experiments on model membranes under water. Not only must the x-ray beam be intense enough so that the scattering from the extremely thin (~5 nm thick) lipid film can produce high-quality data, but the beam divergence must also be smaller than usual so that the instrument can access the same q-range as instruments operating at lower x-ray energies (note that for the same scattering angle, the q value is inversely proportional to x-ray energy). Routinely carrying out these experiments will only be possible at NSLS-II.

Studies on lipid membranes under water are just beginning (Figure 3.4.2) [3.4.7, 3.4.8], with the promise of emulating bulk SAXS and crystallography studies. At NSLS-II, they will provide a generic tool for studying membrane structures that are relevant to biology.

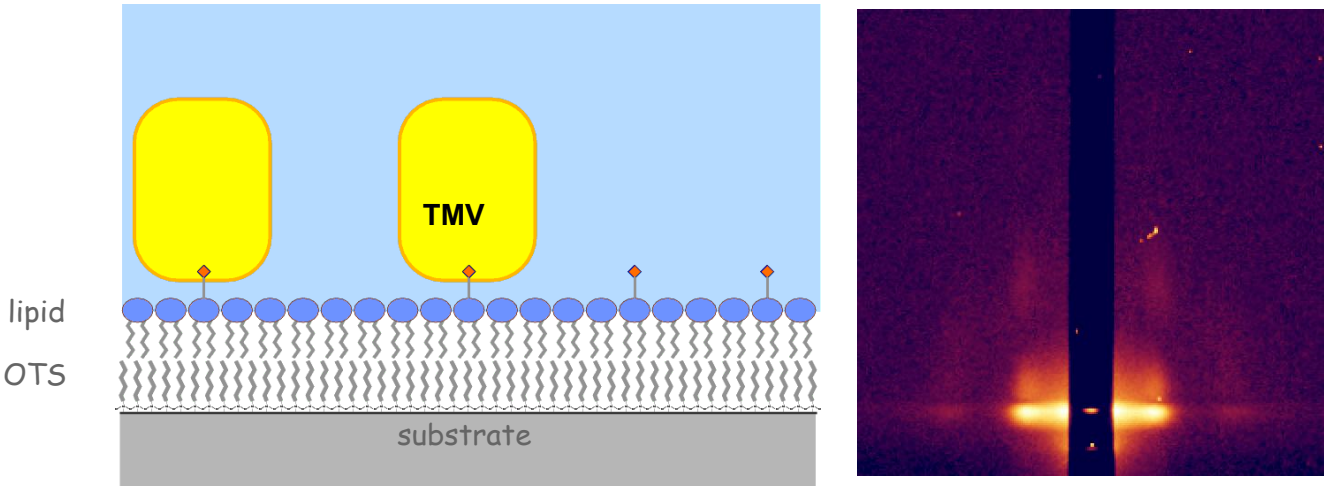

Figure 3.4.2 Schematic of self-assembled arrays of tobacco mosaic virus adsorbed onto a lipid film under water (left), and (right) GISAXS pattern from the formed arrays [3.4.8]. Membrane proteins also can be attached to the lipid film, provided the appropriate ligands (red dots in the schematic) in the lipid layer provide anchorage. Currently, the data quality is limited by the x-ray intensity at the sample and the divergence of the x-ray beam.

3.4.3 Molecular and Supra-Molecular Organization in Micro-Textured Materials

Microbeam-based techniques, such as microbeam diffraction and microbeam x-ray fluorescence, in effect provide a scanning probe microscope for studying the internal textures in materials. Unfortunately, producing a microbeam inevitably requires focusing the beam and thus increasing beam divergence, making scanning SAXS measurements problematic. However, as a result of the exceedingly high brightness at NSLS-II, the x-ray beam divergence will remain low even after focusing and scanning. SAXS studies of textures with underlying supra-molecular-scale structures, as in polymers and liquid crystals, will become possible.

There are two areas in which microbeam SAXS will be very useful. The first is for studies of biomaterials, such as bones and hair, which exhibit hierarchical structures. Microbeam SAXS/WAXS reveals the organization of the material on the molecular and supramolecular levels and helps to elucidate the relationship between the structure and the properties of the materials, as, for instance, in diseased tissues.

The second area is in-situ characterization of materials used in devices. Soft materials such as liquid crystals and polymers do not exhibit long-range structural order and their structures very often depend on the local environment, such as the presence of interfaces and temperature distribution. Therefore they cannot be studied as bulk materials. High energy x-rays may also prove useful in this area, since these materials are often buried under other materials.

References

[3.4.1] J.B. Knight, et al., *Phys. Rev. Lett.* **80** 363 (1998).
[3.4.2] L. Pollack, M.W. Tate, A.C. Finnefrock. C. Kalidas, S, Trotter, N.C. Darnton, L. Lurio, R.H. Austin, CA Batt, S.M. Gruner, and S.G.J. Mochrie, *Phys. Rev. Lett.* **86** 4962 (2001).
[3.4.3] D.I. Svergum, *Biophys. J.* **76** 2879 (1999).
[3.4.4] P. Chacon, F. Moran, J.F. Diaz, E. Pantos, and J.M. Andreu, *Biophys. J.* **74** 2760 (1998).
[3.4.5] E. Sackman, *Science* **271** 43 (1996).
[3.4.6] H. Tahlberg, D. Fotiasis, S. Scheuring, H. Remigy, T. Braun, K. Mitsuoka, Y. Fujiyoshi, and A. Engel, *FEBS Lett.* **504** 166 (2001).
[3.4.7] C.E. Miller, J. Majewski, T. Gog, and T.L. Kuhl, *Phys. Rev. Lett.* **94** 238104 (2005).
[3.4.8] L. Yang, M. Fukuto, and S. Wang, in preparation.

3.5 Inelastic X-Ray Scattering (IXS)

The previous sections discussed the use of the very high brightness of NSLS-II to probe the structure and dynamics of condensed matter. In this section, we discuss a technique that utilizes the very high flux to study dynamics on very fast time scales (ps to fs) by working in the energy domain—namely, inelastic x-ray scattering.

IXS is a momentum-resolved technique for studying dynamics and excitations in condensed matter systems. Of increasing importance, IXS has been used to study excitations ranging from phonons in solids, to sound modes in liquids and polymers, to plasmons in simple metals, to complex electronic excitations in strongly correlated electron systems. Further, there are many new, as yet largely unexplored, areas to which the technique could well make important contributions, including surface dynamics, excitations in extreme environments, time-resolved studies, and non-equilibrium dynamics.

As a technique that probes one of the fundamental response functions of condensed matter, namely $S(q, \omega)$, IXS is an extremely powerful method for addressing some of the most important questions in science today. Its principle limitation to date has been the dearth of active instruments in the world, and the very low count rates achievable on such instruments. Despite these limitations, IXS has the intrinsic advantages of a weak cross-section (so that multiple scattering effects are negligible) and the ability to study very small samples. This latter attribute has been used, for example, to study phonons in high Tc compounds (in MgB_2, in plutonium micro crystals, etc.), for which larger, neutron-sized crystals are simply not available. Further, there is no need to deuterate samples, as there is for inelastic neutron scattering from many soft-condensed-matter systems. As a result, given sufficient availability of instruments and reasonable count rates, IXS should have an impact at least as large as that of triple-axis neutron spectrometry, its direct analog. IXS beamline(s) at NSLS-II, as discussed in Section 11.5, will feature unprecedented resolution and count rates and thus are expected to offer the potential for high scientific impact.

As Figure 3.5.1 shows, IXS offers the ability to probe excitations over a range of energy and momentum transfers, q, that cannot be studied with other techniques. For instance, light scattering with an energy of ~1 eV has a maximum momentum transfer of about 10^5 cm^{-1}; much smaller than a typical Brillouin zone boundary, which is ~10^8 cm^{-1}. While neutrons can reach higher q values, they have only an extremely weak coupling to electronic excitations, and are therefore not ideal probes of these excitations. Electron Energy Loss Spectroscopy is very sensitive to surface modes, and is thus complementary to IXS, which observes primarily volume modes. Further, IXS has the advantage of a wider range of accessible momentum transfers, since EELS is limited by multiple scattering effects to relatively small momentum transfers. In addition, EELS requires high vacuum and so is incompatible with certain environments, such as liquids or systems under high pressure. It is also incompatible with strong electric or magnetic fields.

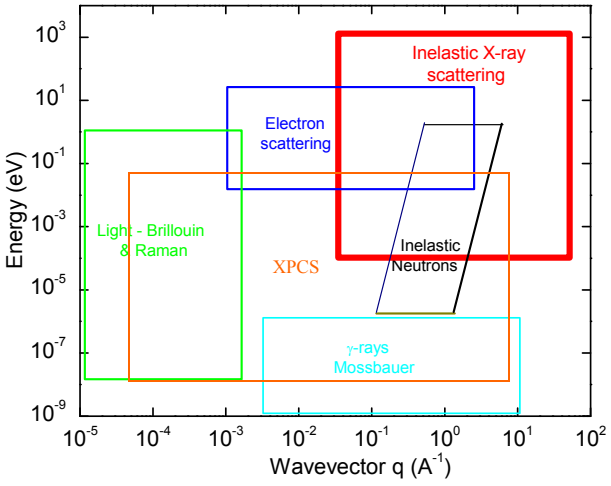

Figure 3.5.1 Probing the Dynamic Response of a System. IXS (red outlined area) covers a range of wave-vector and energy transfers that are inaccessible with other techniques.

With the inherent strengths of the technique and the increasing brightness of synchrotrons, IXS has grown as a technique, with impact in diverse fields of science. NSLS-II will play a key role in pushing this trend still further. Below, we discuss two energy transfer regimes.

3.5.1 Very High-Resolution Inelastic X-Ray Scattering

The capabilities of NSLS-II will allow for a dramatic improvement in the state-of-the-art for IXS instruments, and indeed this is one of the principal goals for the facility. A novel feature of the proposed inelastic spectrometers at NSLS-II is that they will operate at high energy resolutions but utilize moderate photon energies—in contrast to the existing instruments around the world that operate with photon energies on the order of 20 keV and higher.

It is natural to ask what the implication of operating at lower photon energies is on the expected phonon intensities. A useful estimate of the phonon x-ray cross-section has been provided by Sinn [3.5.1], who estimated that the intensity of single phonon scattering for small momentum transfers, q, in a mono-atomic elemental solid was

$$I = I_0 \frac{r_0^2 \hbar^2 c^2}{2e} (\delta q)^2 \frac{1}{E_i^2} Z^2 n_0 \ell_{abs} \frac{k_B T}{M v^2} \ , \qquad (3.5\text{-}1)$$

where the symbols have their usual meaning, the sample is one absorption length, ℓ_{abs}, thick (which results in the largest possible signal) ν is the speed of sound in the solid, and n_0 is the number density in the solid. From this, if one compares two instruments with the same momentum resolution, δQ (note that $\ell_{abs} \propto E_i^3$), one finds that, to a reasonable approximation, $I \propto E_i$, assuming that in all cases the sample is 1 absorption length thick. Thus, operating at 10 keV instead of 20 keV will result in a cross-section that is smaller by a factor of two. However, as noted in Section 11.5, the performance of the source, as measured in ph/s/meV, is significantly better at lower energies than at high energies (see Figure 11.5.2). That is, the pre-factor I_0 (the incident intensity) is significantly higher, and this more than makes up for the reduction in cross-section.

For the spectrometer based on the asymmetric optics scheme proposed in Section 11.5, one can estimate the flux on the sample from a 3 m U19 CMPU device at NSLS-II. Taking into account expected efficiencies of the various focusing optics and the high-resolution monochromator itself, one obtains a flux on the sample of ~10^9 ph/s at 9.1 keV with a 0.1 meV bandpass. This compares favorably with existing high-resolution inelastic spectrometers. For example, the new instrument at Sector 30 at APS delivers ~10^9 ph/s on the sample at 1.5 meV energy resolution from a 4.8 m U30 device, and BL35XU at SPring-8 delivers ~5×10^9 ph/s on the sample at 1.5 meV resolution from a 4.5 m U35 undulator source. Thus the incident intensity is expected to be comparable to existing instruments, but with more than an order of magnitude better energy resolution. Note also that because the absorption length is smaller at these lower energies, only very small volumes of sample will be required.

As an example, consider the case of indium, a low-temperature superconductor (T_C = 3.4 K). It has an absorption length of 10 μm at 10 keV. With the new instrument discussed here, one could measure the phonons in indium relatively easily. Equation 3.5-1 predicts count rates at small q will be ~5 cps (and this will increase at larger momentum transfers, since the phonon cross-section varies as q^2). Note that a lower limit for detectable count rates in an inelastic experiment is typically ~5×10^{-3}, given by the electronic noise level of the detector. Thus, this intensity (5 cps), at this resolution, should provide the sensitivity to observe subtle changes expected in phonon lifetimes as the superconducting state is entered and scattering pathways are removed by the opening of the superconducting gap. This in turn sheds direct light on the electron–phonon coupling which controls the superconducting pairing mechanism. With this understanding in hand, experiments at NSLS-II will turn to high-temperature superconductors for which the pairing mechanism

remains a mystery. These ultra-sensitive phonon measurements should reveal unambiguously if phonons are indeed involved in the superconducting state of the high-temperature superconductors.

There are numerous other systems that require very high-resolution measurements of dynamical modes. These include:

Structural phase transitions. These transitions are frequently driven by a phonon mode going "soft," that is, driven toward zero energy. In cases where such soft modes are present, one needs to measure the phonon softening to as low an energy as possible. As the transition is approached, the phonon energy becomes progressively lower. In addition, frequently there is also elastic scattering appearing, so that very high energy resolution is needed to separate the phonon from this so-called "central peak." An example of a relevant current problem in this field is that of shape memory alloys, and a subset of the general problem of martensitic phase transitions. These latter—which occur in steel—have been dubbed the world's most economically important metallurgical transition [3.5.2]. While shape memory alloys underlie many technologically relevant applications, including military, medical, safety, and robotics applications, the details of the physics that underlies these transitions remain to be explored. The IXS instrument at NSLS-II proposed here, with the ability to study phonons at very high resolution and in very small samples, will make dramatic contributions to this field.

Dynamics of CDW transitions. **C**harge **d**ensity **w**aves form in a wide variety of systems. There are at least two mechanisms that can drive such a transition. One is due to electron–phonon interactions, as, for example, in the classic CDW system, $NbSe_3$, and the other is due to electron–electron interactions in strongly correlated systems, as may be the case in the transition metal oxides, for example. CDWs are characterized by a two-component order parameter, given by the amplitude and phase of the density wave. There are excitations associated with each component, known as amplitudons and phasons, respectively. However, these are excitations of the electronic system, and inelastic neutron scattering is thus not well suited to their study. Inelastic x-ray scattering is thus the probe of choice. However, phasons are gapless and consequently have low energies at small momentum transfers; to study them will require extremely high resolution, coupled with high intensity.

Thermoelectric materials. These are materials which produce a voltage difference across the material in the presence of a temperature difference (and vice versa). They thus offer great potential in future energy applications. However, while many materials, including simple metals, are thermoelectric, most produce only a very small voltage for a given gradient. To be efficient, such materials must have very low thermal conductivity. A great deal of activity is currently underway to find good ways of doing this. One method is to modify the structure so as to reduce the phonon lifetimes by disorder or by putting "rattlers" into an open structure. Nanostructured materials offer particular promise in this regard. However, to date very little has been done to measure phonon linewidths in these materials, or even to study them theoretically. IXS at NSLS-II will make it possible for these linewidths to be studied, even in very small samples, and for parametric studies to be performed.

3.5.2 Moderate Resolution Inelastic X-Ray Scattering

In addition to the very high-resolutions discussed above (1 meV and 0.1 meV), NSLS-II will also have a very large impact in the science carried out at more moderate energy resolutions. With moderate resolution, defined here as 10 to 100 meV, one is able to probe the dynamics of electronic excitations as well as higher energy phonons. These electronic excitations include collective modes, such as plasmons, single-particle-type excitations such particle-hole pair creation in a Fermi-liquid, and excitations across various gaps (such as the charge transfer gap, Hubbard gap, superconducting gap, or band gap). The energy, dispersion, and lifetime of such excitations play an enormously important role in determining the properties of essentially all of the materials of current interest in condensed matter physics.

In addition, in many cases it is possible to carry out resonant IXS (RIXS) in which the incident energy is tuned to the energy of a particular excitation at an absorption edge. This type of scattering can increase the cross-section by more than two orders of magnitude in certain cases, greatly extending the applicability of the technique. Such resonant scattering also offers atomic and initial state selectivity that allows for much additional information about an excitation, which can be crucial to identifying the nature of the excitations.

Much of the current work has focused on copper-based compounds, including 2D systems containing copper oxide planes, and 1D chain compounds. One area of great interest is the study of Mott insulators such as the high temperature superconductor parent compounds, in an attempt to understand how the Mott gap and other excitations evolve as a function of doping. An understanding of this area is important for studies of the high temperature superconductors in particular, and many highly correlated systems in general. As an example of this work, M. Z. Hasan et al. [3.5.3] have looked at the evolution of the Mott gap with doping dependence in both hole and electron-doped superconductors, and find that the phase diagram for these systems is directly related to the measured Mott gap, indicating a relation between the pseudogap and the Mott charge gap.

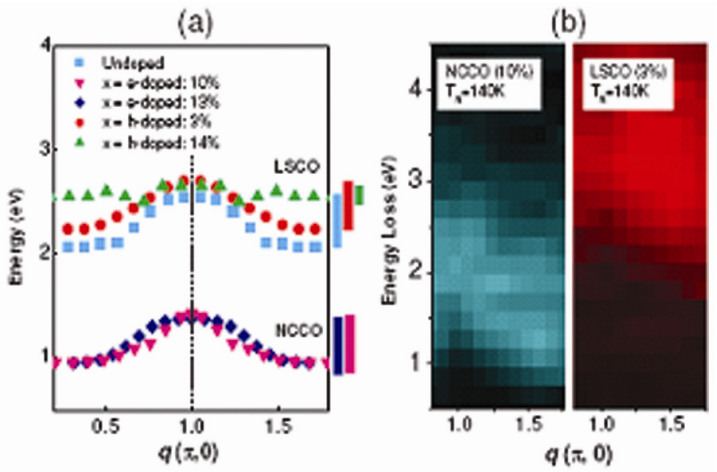

Figure 3.5.2 **a**) Mott gap in doped cuprates. **b**) Systems with the same Neel temperature but different doping.

From M. Z. Hasan, et al. [3.5.3]

As discussed in Section 11.5, the proposed medium energy resolution instrument will feature a number of significant advances over the existing instruments. Principal among these will be the higher intensities resulting from the larger fluxes available at NSLS-II, and improved resolution and throughput resulting from the adoption of a novel detection scheme involving a position sensitive detector. These advances will mean that studies can be made in much greater detail at much higher-resolution than has been possible to date. A key area that these new capabilities will address is that of in the so-called mid-IR range in the cuprates (few hundred meV). Presently this is impossible to study with x-rays because of the presence of a large elastic line that obscures the weak inelastic signal out to several times the resolution half-width. With resolutions of ~50 meV, and better, that will be possible at NSLS-II, this difficulty will be overcome and it will be possible to study this important region for the first time. Several interesting phenomena occur in this energy range, including spin-waves and electronic excitations. Optical measurements that are confined to the center of the Brillouin Zone have revealed that sum rules in this spectral region are broken on going through the superconducting transition [3.5.4]. This in turn suggests that some of the condensation energy comes from a lowering of the kinetic energy of the electrons. However, these results remain somewhat controversial and poorly understood. Inelastic x-ray scattering will provide the first momentum-dependent information on this spectral region and may well be central to the problem of high-temperature superconductivity.

References

[3.5.1] H. Sinn, *J. Phys. Condens. Matter* **13** 7525 (2001).
[3.5.2] C.M. Wayman, and J.D. Harrison, *JOM* **41**(9) 26 (1989).
[3.5.3] M. Z. Hasan, et al. cond-mat/0406654.
[3.5.4] H.J.A Molegraaf, et al., *Science* **295** 2239 (2002).

3.6 Soft X-Ray Resonant Scattering: XRMS and RIXS

As discussed in Chapter 8, NSLS-II will be a superb source of soft x-rays. Conceptual designs for two beamlines are presented in Sections 11.7 and 11.8. These are optimized for high resolution and high flux, respectively. In this and the following section, we discuss some of the science drivers for these beamlines, beginning with the high-resolution beamline.

In the soft x-ray range, resonant processes at relevant core levels can enhance scattering amplitudes by orders of magnitude. Such resonant enhancements lie at the core of recent increased interest in the exploitation of soft x-rays for the investigation of wide classes of materials, including technologically relevant compounds and alloys and advanced nanoscale materials. Further, the wavelength of soft rays (~0.5 nm to a few nm) is well matched to many interesting and useful length scales, including those that occur intrinsically in many materials and those that have been engineered.

In particular, scattering studies in the soft x-ray range are uniquely suited to examining some of the most important issues surrounding correlated electron systems, spintronic materials, engineered ferromagnetic alloys, nanopatterned structures, advanced fuel cell electrodes, candidate hydrogen storage materials, and many other scientifically or technologically relevant materials. A large portion of the periodic table can be investigated via the use of soft x-rays, including the 3D transition metal L edges, rare-earth M4,5 edges, and the K edges of C, N, and O. There are strong resonant enhancements in the vicinity of these dipole-allowed absorption edges. In addition, polarization-dependent studies, which are more practical with advanced undulators and novel end station designs, can reveal underlying order in the charge, spin, and orbital degrees of freedom in the system.

X-ray Resonant Magnetic Scattering and Resonant Inelastic X-ray Scattering are two scattering techniques whose use in the soft x-ray range has increased considerably in recent years. XRMS and RIXS are both photon-in, photon-out techniques, and have a number of advantages over electron-based spectroscopies and scattering processes. For example, the probe depth of XRMS and RIXS is much longer because the measurements are not affected by the relatively short mean free path of electrons. Furthermore, photons are not affected by electric and magnetic fields and multiple scattering events are negligible in the soft x-ray range.

XRMS exploits magnetic sensitivity in diffraction patterns to extract element-specific information on magnetic ordering processes, on length scales from microns down to a few nm. While soft x-rays do not have the Q-range to probe the magnetic alignment of atoms in such structures and devices, the length scales of soft x-ray scattering are matched ideally to multilayer spacings, domain patterns, and feature sizes of current lithography techniques [3.6.1]; see, for example, Figure 3.6.1. XRMS is particularly well suited to studies of engineered thin films and multilayers, as the element-specific magnetism in individual layers can be separated. Indeed, the depth profile of the element-specific magnetic moment across an interface can be deduced from analytic models of specular and diffuse reflectivities [3.6.2].

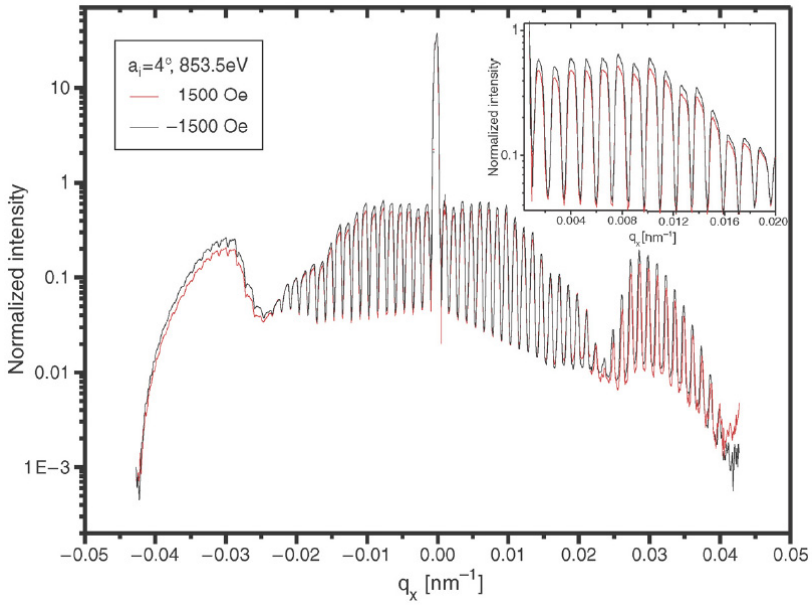

Figure 3.6.1 XRMS diffuse scan from an artificially structured magnetic micro-structure (FeNe alloy islands, 0.3×3 μm, 5 μm pitch). Note the large dynamic range of the scattering and the dozens of satellite reflections on either side of the specular peak. Source: [3.6.7].

The exceptional properties of NSLS-II will enable the implementation of soft x-ray beamlines with unsurpassed brightness, small photon spot size, energy resolution, and polarization control. These characteristics will be crucial in designing and ultimately using the next generation of XRMS and RIXS instrumentation. RIXS is inherently a very low-count-rate technique, and improvements in brightness and spot size translate directly to improved detection efficiency. In XRMS, the most valuable information is attained often only at high-momentum transfer or in off-specular scans. In both instances, the count rate at current instruments is often at the noise floor of the detectors.

In many complex oxides and intermetallic compounds, cooperative phenomena among the charge carriers result in charge, spin, and orbital ordering. Soft x-ray scattering is an ideal technique to study these ordered phases. For the transition metal oxides, XRMS in the soft x-ray range directly interrogates the valence states of the relevant transition metal d-orbitals and the oxygen s- and p-orbitals. Fractional order diffraction peaks in XRMS scans appear on the onset of orbital ordering. The peak intensity, which is correlated with the order parameter of the phase transition, can be measured as external parameters (e.g. fields, temperature) are manipulated [3.6.3]. In multi-layered structures of complex oxides, XRMS can probe interface-specific issues such as changes in the transition-metal valence state and modifications introduce by interfacial strain. Finally, careful modeling of XRMS scans can reveal unexpected phases that develop at interfaces, such as the development of anti-ferromagnetic insulating phases at the surface of otherwise metallic manganites [3.6.4].

Unlike XRMS, for which the energy of the scattered photons is not analyzed and hence only elastic scattering processes dominate the signal, RIXS directly examines inelastic processes by utilizing a soft x-ray spectrometer to resolve the energy of the emitted photons. The energy lost in the scattering process, which is measured in a RIXS experiment, can reflect important parameters such as the local partial density of states of an atomic species in a complex compound, low energy excitations (such as d–d interactions), and charge transfer from surrounding ligands.

As RIXS is an element-specific, local probe, it is an ideal technique to examine the low energy excitation spectra of correlated electron systems. As mentioned above, such systems are extremely sensitive to perturbations such as charge density, magnetic and/or electric fields, and temperature, particularly near phase transition boundaries. For example, in some “colossal magnetoresistance” manganites, at low temperatures the electron charge density self-organizes into stripe domains, resulting in a charge-ordered insulating phase [3.6.5]. Application of a magnetic field can drive such materials into a ferromagnetic metallic phase [3.6.6]. The mechanism governing the magnetic field–induced phase transition is thought to be increased

hybridization imposed by the alignment of valence spins; such a mechanism would change the valence structure of these materials. While such changes would be apparent in valence band spectra recorded with ARPES, the relatively large magnetic fields required (~several Tesla) preclude such measurements; such a limitation does not apply to RIXS. Furthermore, some degree of momentum resolution is available in RIXS, as the incident and emitted photon have well-defined directions and the projection of the momentum transfer can be varied by rotating the sample.

The momentum resolution combined with exceptionally good energy resolution of modern RIXS instruments will enable important and novel investigations into the still-unresolved mechanisms of high temperature superconductivity in cuprates. In such materials, the superconducting state at finite temperatures appears to be finely balanced with the competing dynamic stripe-order phase [3.6.6]. It has recently been suggested that spectral evidence of such dynamic stripe fluctuations might be accessible in momentum-resolved energy loss spectra [3.6.7] (see Figure 3.6.2). While the resolution required for such measurements is beyond the capacity of current-generation RIXS beam lines and spectrometers, the advanced capabilities of the NSLS-II XRMS/RIXS beam line, combined with a state-of-the-art RIXS spectrometer, will help unravel interactions between superconductivity and competing ordering phenomena in cuprates and related materials.

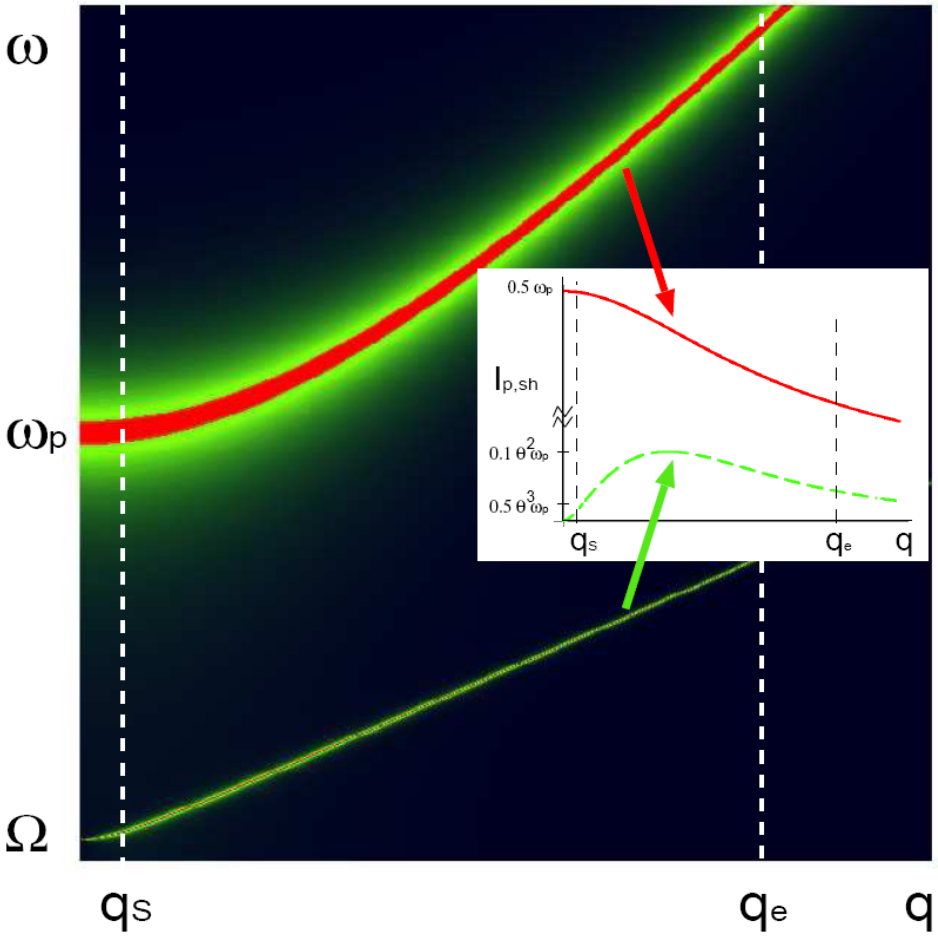

Figure 3.6.2 Electromagnetic absorptions in the "nearly ordered" superconductor, as seen by electron energy loss spectroscopy as a function of frequency Ω and momentum q. Besides the strong plasmon pole dominating the long wavelength dielectric response, the authors [3.6.7] also find a weak absorption that corresponds to the massive shear photon, giving away the presence of the "dual shear superconductor." This can be regarded as the unique fingerprint of a superconductor characterized by transient translational order extending over distances that are large, compared to the lattice constant. Tests of such theoretical predictions should be uniquely possible using resonant inelastic x-ray scattering at NSLS-II.

References

[3.6.1] A. Remhof, et al., Shining light on magnetic microstructures. *Superlattices and Microstructures* **37**(5) 353 (2005).
[3.6.2] S. Roy, et al., Depth profile of uncompensated spins in an exchange bias system. *Phys. Rev. Lett.* **95**(4) (2005).
[3.6.3] P. Abbamonte, et al., Crystallization of charge holes in the spin ladder of Sr14Cu24O41. *Nature* 1078 (2004).
[3.6.4] J.W. Freeland, et al., Full bulk spin polarization and intrinsic tunnel barriers at the surface of layered manganites. *Nature Mat.* **4**(1) 62 (2005).
[3.6.5] S. Mori, S. C.H. Chen, and S.W. Cheong, Pairing of charge-ordered stripes in (La,Ca)MnO3. *Nature* **392**(6675) 473 (1998).
[3.6.6] H. Kuwahara, et al., Spin-charge-lattice coupled phase transitions in bandwidth-controlled systems: (Nd,Sm)(1/2)Sr1/2MnO3. *Phys. Rev. B* **56**(15) 9386 (1997).
[3.7.7] V. Cvetkovic, et al., Observing the fluctuating stripes in high Tc superconductors. cond-mat/0607402 v1, 2006.

3.7 Soft X-Ray Coherent Scattering and Imaging

Like their counterparts in the hard x-ray region, soft x-ray imaging and coherent scattering are extremely photon-hungry techniques in which brightness is a crucial parameter. This is because such techniques utilize only the transversely coherent portion of the undulator beam, in both the vertical and horizontal planes. The high flux soft x-ray beamline, discussed in section 11.8, will produce a heretofore unprecedented (flux) × (energy resolution) × (spot size) figure of merit from 200 to 2200 eV in the soft x-ray range, with either fixed selectable polarization (linear, circular, or elliptical) or fast-switching between two selected polarizations. Figure 3.7.1 elucidates the high brightness of the EPU45 undulator beam by showing the number of transverse coherent modes it contains as a function of photon energy over the range to be covered by the high-flux undulator beamline. The number of modes varies from 3 at 200 eV to somewhat over 10 at 2 keV, where a single mode corresponds to a fully transverse coherent photon beam. This degree of transverse spatial coherence is very high, and in fact is more than ~10 times greater than competing synchrotron sources in the United States.

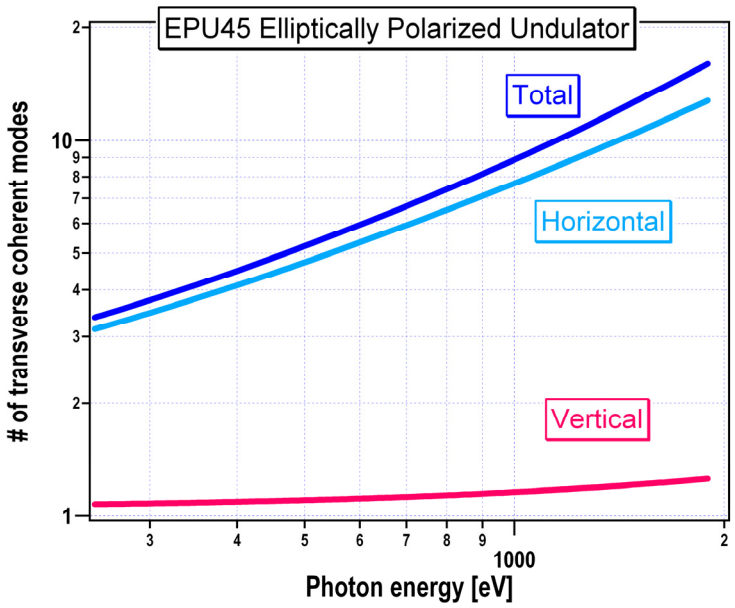

Figure 3.7.1 Coherent modes in the EPU45 beam. Vertical, horizontal, and total number of transverse coherent modes contained in the EPU45 beam as a function of photon energy.

These source properties, coupled with the state-of-the-art high flux soft x-ray beamline described in Section 11.8, will enable the next generation of experiments in soft x-ray microscopy and coherent scattering/imaging, i.e., those experiments that would suffer from impractically low signal rates using existing sources or are simply impossible, owing to the lack of selectable beam polarization. The types of scientific problems in coherent imaging/scattering to be addressed include nanoscale and mesoscopic imaging of noncrystalline samples (e.g., large cells and magnetic domains), time correlation spectroscopy of fluctuations in materials, and 3D imaging of granular materials. For soft x-ray microscopy, the problems to be addressed range from simultaneous spectroscopic (electronic) and microscopic (structural) measurements on nano- and mesoscopic length scales (e.g., of single nano-elements, nanocontacts, or nanomagnets), to understand isolated behavior and differences between boundaries/interfaces and bulk systems.

The design of the beamline described in Section 11.8 prioritizes photon flux over resolving power, in a tradeoff between transverse coherent flux and energy resolution or longitudinal coherence, the latter determining (among other things) the depth of field of a focused beam. The conceptual design has yielded a soft x-ray beam with, for example, a photon flux of a few × 10^{13} ph/s with a resolving power greater than 3000 for energies between 200 eV and 2.2 keV. By a simple change of grating, it can produce a flux greater than 10^{12} ph/s with a resolving power greater than 12000 over this photon energy range. In both cases, a focused 1-sigma spot size of 2.5 microns (H) by 1.3 microns (V) (see Figure 11.8.8) is achieved. Given the degree of transverse spatial coherence described above (~10 modes), the flux on sample for coherent scattering experiments will be in the 10^{11} to 10^{12} range, which represents a very significant improvement compared to existing U.S. soft x-ray coherence beamlines. For soft x-ray microscopies in which the beam is focused (e.g., with zone plates), if the efficiency of the focusing optic is on the order of 10%, we estimate a flux of 10^{10} to 10^{11} ph/s in the focused spot, which is again a quite significant improvement over existing soft x-ray beamlines. The extremely high flux-on-sample values described here will lead directly to reduced counting times, which currently limit the overall duration of soft x-ray coherent scattering/imaging and microscopy experiments. As described in Section 11.8, this may also drive the need for faster scanning stages in the case of scanning probe microscopies. Achieving significantly shorter measurement times for an image is also quite beneficial in minimizing nonstatistical fluctuations arising from unavoidable drifts in beamline or endstation components.

An example where this tremendous increase in coherent flux will have direct benefit is in the study of domain fluctuations in **c**olossal **m**agneto**r**esistance manganites. These materials are known to exhibit complex

low-temperature ground states in which the occupancy of the electronic orbitals varies from site to site in a periodic manner. These structures are known as "orbitally ordered." However, for reasons that are not at all clear, they do not attain long-range order at low temperatures, instead forming short-range ordered domain states. It is believed that the origin of these domains, and their dynamics, lies at the heart of the CMR phenomena. Very recently, coherent scattering has been used to observe the speckle pattern arising from these domains. Figure 3.7.2 shows one such pattern taken at ALS on beamline 12.0.2, utilizing the resonant enhancement at the Mn L-edge to give the scattering contrast for the orbital domains. The speckle pattern in Figure 3.7.2 was taken at low temperatures where the scattering is strongest; after binning, the count rate is approximately 50 counts per speckle.

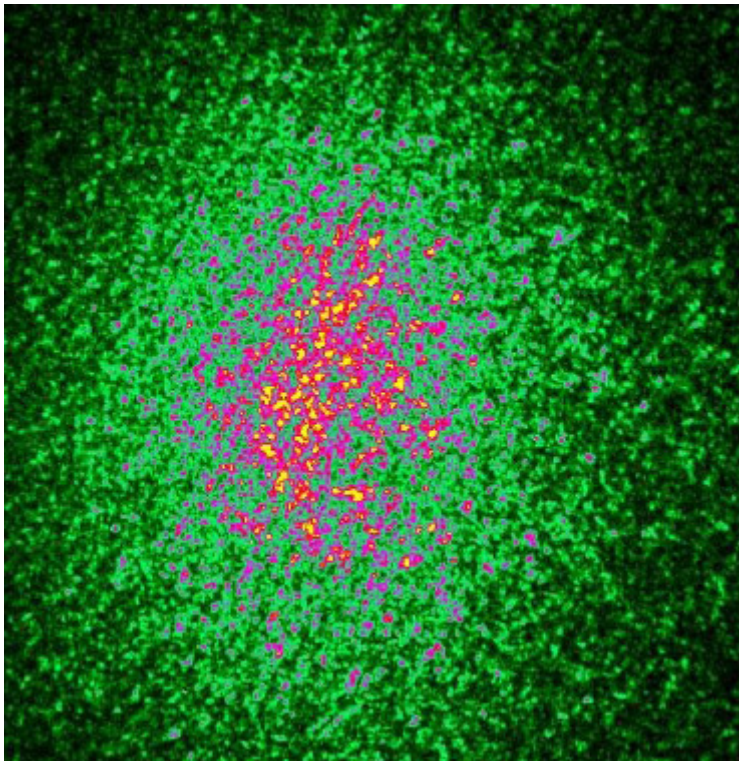

Figure 3.7.2 Speckle pattern from soft x-ray coherent scattering, from a sample with short-range orbital order. Data were taken at low temperatures at ALS [3.7.1].

Intensity corresponds to about 50 counts per speckle. Coherent intensities are expected to be a factor of 1000 higher at NSLS-II, allowing similar data to be taken close to the phase transition and the dynamics of the process to be studied for the first time.

At NSLS-II the coherent flux is expected to be 1,000 times larger; this will transform such experiments. In particular, it will become possible to make similar measurements close to the transition where the scattered intensity is very weak. Further, it should be possible to carry out XPCS measurements with such data, rather than the static measurements shown here, and study the dynamics of this important transition for the first time—an enticing prospect.

Finally, as stated above, the ability to select the polarization of the EPU45 photon beam adds an important variable to any of the experiments and techniques intended for this beamline. For tiny focused beams, the ability to select the polarization of the photon beam without altering its position or angle is crucial for any type of dichroism experiment (linear or circular) in order to illuminate only one selected spot on the sample. For magnetic-sensitive coherent scattering experiments, the ability to select the handedness of the beam polarization is essential, since the magnetization of the sample must remain fixed in order to avoid magnetization-induced changes to the domain structure of the sample and hence to the scattering pattern. The arguments for the advantages of fast-switching polarization capability are even greater, since the other experimental variables cannot be changed at the high rates necessary to detect tiny dichroic signals.

References

[3.7.1] J. Turner, K.J. Thomas, K. Chesnal, M. Pfeiffer, J.P. Hill, and S. Kevan, unpublished data.

3.8 Macromolecular Crystallography

Few fields have seen as dramatic an impact of synchrotron radiation as have the life sciences—in particular, macromolecular crystallography, where the technique has literally been transformed. Here we discuss the future impact NSLS-II will have on this surging field.

Understanding the living cell is the utmost challenge of modern biology. The expectation that a deeper understanding of the biological process can be achieved, once the three-dimensional structure of countless molecules and their functional roles have been conquered, is the driving force behind the revolution structural biology is undergoing today.

3.8.1 Macromolecular Crystallography Has Transformed Biology

Structural biology, perhaps especially x-ray crystallography, has transformed our understanding of biological processes. It was x-ray diffraction that provided the first clues to the structure of the DNA double helix 50 years ago. Nowadays numerous cellular mechanisms are described at a molecular level. Examples of these are protein synthesis, RNA transcription, DNA replication, immune response, enzymatic metabolism, signal transduction, cellular division, and the production of energy, to name just a few. In addition, structural biology has had a dramatic impact on the development of new drugs, wherein drug designers count upon being able to look in three dimensions at the molecular fit of their proposed drug into the active site of its target enzyme.

The principal tool to provide this knowledge for 25–30 years has been macromolecular x-ray crystallography (referred to as PX, the *P* for *protein*). New concepts and new equipment from many disciplines have provided a nearly exponential increase in productivity, as follows. Genetic engineering and protein cloning provide specimens. Crystal-growth screening methods and cryo-preservation improve this picture. Synchrotron radiation and the MAD method provide better data and a direct phasing vehicle. Modern detectors provide extremely accurate data very quickly. And finally, the computer industry's proven ability to obey Moore's Law lubricates the whole of this discipline. We're truly in a golden age for PX. Together these advances enhance two aspects of the research: increasingly difficult problems can be approached and solved with higher quality results, and human effort is decreased for each project, thereby making each individual more productive.

The growing use of synchrotron sources for macromolecular crystallography has increased the pressure on existing facilities to upgrade existing, or construct new, sources and beamlines. As of June 2006, more than three structures out of four deposited in the Protein Data Bank were solved using synchrotron data (see Figure 3.8.1), and this fraction keeps increasing. To some extent, the recent growth in structure depositions results from recent organized efforts in structural genomics. However, not only these projects, but also hypothesis-driven investigations launched by other structural biologists, or drug-target studies performed by pharmaceutical scientists, all benefit from the availability of brighter x-ray sources and the improved quality of instrumentation and methods that we see today. All of the power of the method has driven researchers to attempt increasingly difficult scientific problems, especially structures of large macromolecular assemblies and membrane proteins. Indeed, the size and complexity of macromolecules that can be studied has increased by an order of magnitude in the last roughly 15 years. There is no sign of this trend changing and it is certain that the brighter beams of NSLS-II will be in intense demand by this community to continue to push such developments.

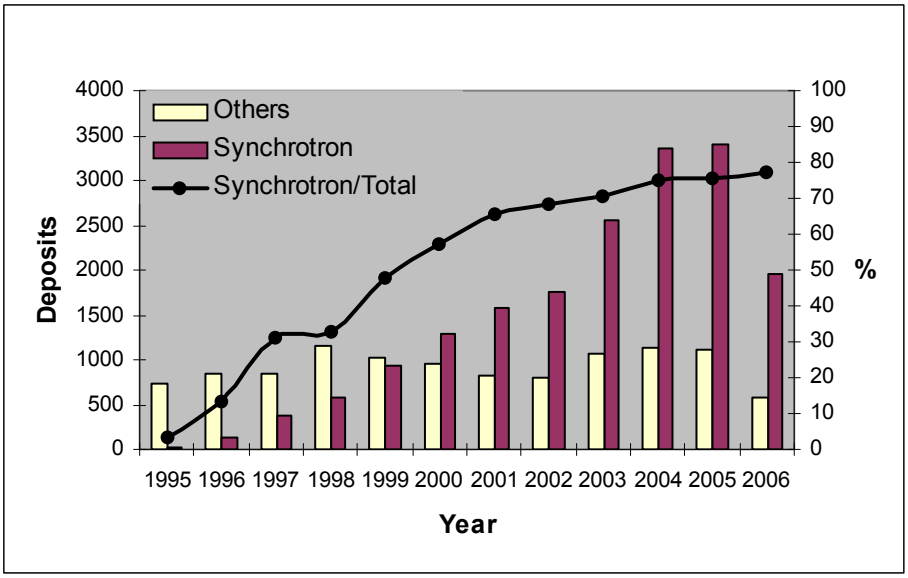

Figure 3.8.1 Evolution of Deposits to the Protein Data Bank (PDB).

Source: BioSync (http://biosync.rcsb.org/BiosyncStat.html)

3.8.2 The Most Difficult Problems Are the Most Interesting

These large structures represent the pinnacle of the structural biologist's craft. Picturing these large assemblies, firstly at the level of interactions among macromolecules, then at the level of atoms of the macromolecule interacting with a substrate, gives detailed information about the machinery of the cell. A great example is the three-dimensional structure of the bacterial ribosome, the protein synthesis apparatus of the cell, consisting of 150,000 atoms, in 53 proteins and three chains of ribosomal RNA, interacting with three tRNA molecules. Determination of this structure was an amazing *tour de force*. At least four major research groups used at least six synchrotron sources in multiple visits each to provide the model we have now of the whole particle and its two individual subunits [3.8.1–3.8.6]. Also in this category are the structures of virus particles, which have possible application in treatment of diseases and nanotechnology. These studies illustrate the difficulties of working with crystals in large complexes. Weak diffraction, close spacing of the reciprocal lattice, and radiation-sensitive crystals all conspired to make x-ray data collection possible only at synchrotron radiation sources.

The work on the voltage-dependent K^+ channel, for which Roderick MacKinnon, Rockefeller University, was co-awarded the 2003 Nobel Prize in Chemistry, is a perfect illustration of the exciting science obtained from structural studies on membrane proteins. Among other processes, these "life's transistors" control electrical activity in nerve and muscle. MacKinnon's work revealed a model for control of the passage of potassium ions through the pore in response to changes in cell membrane voltage (see Figure 3.8.2).

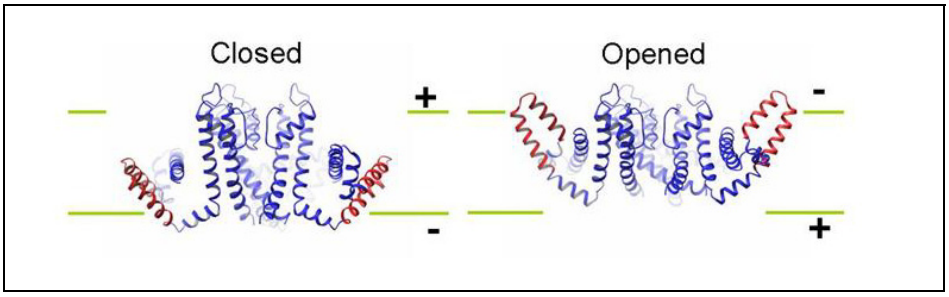

Figure 3.8.2 Model for control of potassium ions through a channel in the cell membrane, in response to changes in the cell membrane voltage. From the work of Prof. Roderick MacKinnon, Rockefeller University.

Membrane proteins perform many cellular functions and responses, representing about 30% of all proteins produced in a cell (making them quite interesting to the pharmaceutical industry). Although a number of investigators have reported structure determinations of macromolecular assemblies of membrane proteins, e.g., nutrient uptake across Gram-negative bacteria [3.8.7, 3.8.8], a serious impediment to all such work is that membrane proteins are notoriously difficult to produce and crystallize, providing small crystals that diffract poorly. To address this issue, structural genomics efforts specifically targeting membrane proteins have recently been launched. NSLS-II will provide the frequent access to a bright x-ray source required to solve these challenging problems.

3.8.3 NSLS-II Will Have a Major Impact on Structural Biology

There are numerous challenges in macromolecular crystallography that will benefit from NSLS-II. The two highest priorities are to handle very small crystals, and to treat very large molecular assemblies; this is where dramatic progress in structural biology will lie. Investigators in the Northeastern United States are at a serious disadvantage: neither the current NSLS, nor CHESS at Cornell University, can provide the small beam size with high intensity and excellent collimation that is required for this sort of progress. The ultrahigh source brightness of NSLS-II, in combination with anticipated developments in optics, detectors, and computing power, will allow structural biologists to tackle macromolecular assemblies of exceptional complexity, bringing our understanding of the macromolecular machinery of the cell to an unprecedented level. Also, in selected cases, time-resolved studies of macromolecular dynamics and interactions down to microsecond time scales or beyond will be possible, adding an additional dimension to the value of the results.

Many types of research effort will benefit. These will include small labs (ease of use, high-level staff support, training for inexperienced users), the large programmatic structure groups (rapid access, they take a role in planning and continued development of the facility, they will exploit new capabilities), the inventors of new methods (access for true experimentation, collaborations), and the pharmaceutical labs (automation, remote participation, efficient routine PX).

References

[3.8.1] Ban, et al., *Science* **289** (2000) 905.
[3.8.2] Harms, et al., *Cell* (2001) 107, 679.
[3.8.3] Wimberly, et al., *Nature* **407** (2000) 327.
[3.8.4] Pioletti, et al., EMBO **20** (2001) 1829.
[3.8.5] Yusupov, et al., *Science* **292** (2000) 883.
[3.8.6] B.S. Schuwirth, et al., *Science* **310** (2005) 827.
[3.8.7] Shultis, et al., *Science* **312** (2006) 1396.
[3.8.8] Pawelek et al., *Science* **312** (2006) 1399.

3.9 High Energy X-Rays

The use of high energy x-rays, defined here as those above ~50 keV, has grown in recent years to service what is now a diverse and continually growing community. As discussed in Section 11.12, the use of a 6 T wiggler source will provide a superb, intense source of x-rays out to 100 keV and beyond. Here we outline several possible programs that could utilize such a source at NSLS-II.

3.9.1 Earth and High-Pressure Science

The evolution of the Earth and other planets is a vast process lasting billions of years, involving huge amounts of materials (crystalline and molten silicates, metals, and volatile constituents), at temperatures from near absolute zero to several thousand degrees, and pressures from a fraction to millions of atmospheres. The present state of the Earth, as well as its evolution through time, is governed by the properties of these materials. Their properties at the relevant conditions of pressure, temperature, and stress dictate the red and blue regions of a seismic tomographic image (Figure 3.9.1), or control the depth and time history of earthquakes. These materials also define the frequencies of the oscillations of the Earth and the rate that plates slide over the surface. With the symbiotic development of synchrotron radiation and high-pressure techniques, experimental studies of such materials are experiencing an unprecedented surge of breakthroughs that were deemed inconceivable a decade ago. Synchrotron sources have fundamentally altered the nature of high-pressure experimentation, from reconnaissance study with limited capabilities to high-precision study with comprehensive material characterization over a wide range of pressures and temperatures. In particular, rheological properties, phonon-related properties, and the dynamics of chemical reactions can now be investigated at very high pressures and temperatures. By studying the materials of which the Earth is made, high-pressure research using synchrotron high energy x-rays has contributed significantly to understanding of the phenomena, processes, and state of the Earth. This information allows addressing issues that range from the chemical heterogeneity of the Earth's interior to the processes responsible for deep-focus earthquakes.

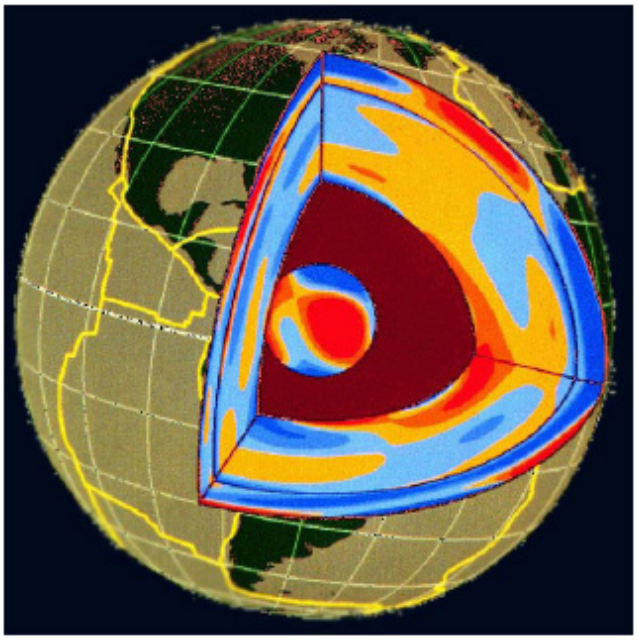

Figure 3.9.1 Seismologist's view of the Earth. Red regions indicate slow sound wave velocities, blue are fast. This structure may represent the flow patterns of hot (slow) material rising with sinking cold (slow) regions. Actual association of fast with either thermal or chemical variations requires high-pressure laboratory data.

3.9.2 Strain Mapping and Materials Science

Understanding and accurately calculating the stresses/strain field distribution is fundamental in the design engineering of static/cyclic load-bearing components. Often of equal importance, however, is the residual stress distribution that is present in the absence of external forces. Such residual can dramatically alter (for good or ill) a component's load capacity and resistance to failure. For example, compressive (tensile) surface stresses tend to retard (accelerate) the surface-initiation and growth of cracks. To compound the problem, the residual stress distribution is extremely difficult to experimentally characterize, offers little or no external evidence of its existence, and is often recognized only a posteriori, after failure.

The interaction between residual stresses (incurred during fabrication or duty-to-duty cycle fatigue) and applied stresses accounts for the failure of most structural engineering elements. However, many of the most

powerful techniques to probe this are explicitly destructive and involve theoretical modeling of the strain fields accompanying material removal (e.g., hole drilling and layer removal). Conventional x-ray and neutron scattering have traditionally been the only direct, nondestructive methods for strain profiling as a function of depth into a material. The short penetration depth of conventional x-ray analysis limits its use to the very near surface (<0.01 mm) region. The weaker scattering of the neutrons allows deep penetration (to tens of mm); however, it also precludes sampling volumes of less than about 1 mm^3. Thus, until recently there was a large hole in the spatial scale and resolution routinely accessible by direct/nondestructive methods of strain-field depth profiling (Figure 3.9.2).

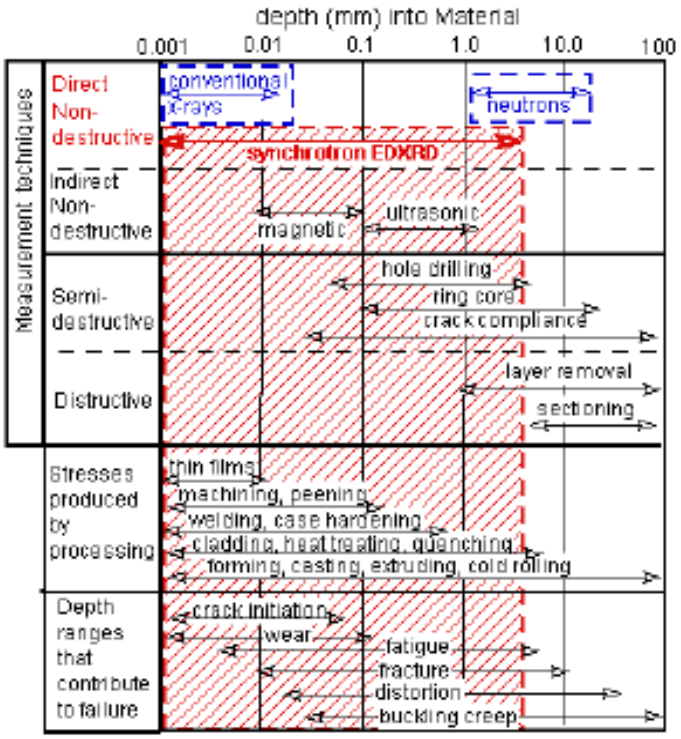

Figure 3.9.2. Residual strain (RS) sources, relevance, and means-of-measurement as a function of depth below the surface of a material. The summary is divided into: (top) the RS measurement techniques; the materials processing origins of RS (center); and the classes of material-component failure that can result from RS (bottom). The conventional x-ray and neutron scattering methods are indicated. The red-shaded region emphasizes the crucial range/relevance of high energy x-ray strain mapping.

In recent years, high energy synchrotron radiation x-ray diffraction techniques have emerged to fill this gap. These techniques have been applied to a number of problems, including applications to strain field mapping in the vicinity of fatigue cracks. High beam intensity has allowed the investigation of small diffraction volumes buried deep inside material specimens. At NSLS-II, one could create a 3D strain mapping facility that would be unique in the world.

Such a facility will have the capabilities to perform 3D strain mapping on large test specimens and actual components from real-world systems. Moreover, the ability to subject the specimens to large in-situ dynamic and static stresses, extreme temperatures, and corrosive/hostile environments will integrate into the facility. Specimens with the equivalent thicknesses (in terms of x-ray absorption) of 40 mm of steel will be strain mapped deep in their interior as well as on the surface. With this facility, the details of the residual, load-induced, and thermally induced strain distributions, as well as their interactions, can be mapped in three dimensions, bringing new insights into the failure modes of these components.

3.9.3 Medical Imaging and Radiation Therapy (MRT, DEI, and PAT)

Medical imaging and radiation therapy has a long tradition at the NSLS wiggler beamline X17B. At NSLS-II it will be possible to target specific techniques of synchrotron medical research that will reach the

stage of human studies in the foreseeable future, and could then be translated to clinical applications using bremsstrahlung sources. Examples include Microbeam Radiation Therapy, Diffraction Enhanced Imaging, and Photon Activation Therapy.

MRT is a major synchrotron medical tool developed at NSLS. Irradiation with arrays of parallel, very thin planes of x-rays was shown to be tolerated by normal tissues, including the central nervous system, at very high doses of up to several hundred Gy. MRT beam arrays were also shown to preferentially damage tumors when used at very high doses. Although the underlying mechanisms of MRT effects are not well understood, they clearly involve the recovery of both the microvasculature and the glial systems. In particular, microvasculature repair seems to be facilitated by endothelial and other support cells surviving between the individual microbeams. The method, developed in early the 1990s at the NSLS X17B1 superconducting wiggler, has also been pursued since 1996 at ESRF. Recent studies indicate that the tissue-sparing effect of microbeams stays strong with beams as thick as 0.68 mm. The study also showed that MRT could be implemented by using two arrays of parallel thick-beams aimed at the target from perpendicular angles to interlace, producing a nonsegmented solid beam at the target while exposing the surrounding healthy tissues only to microbeams (Figure 3.9.3).

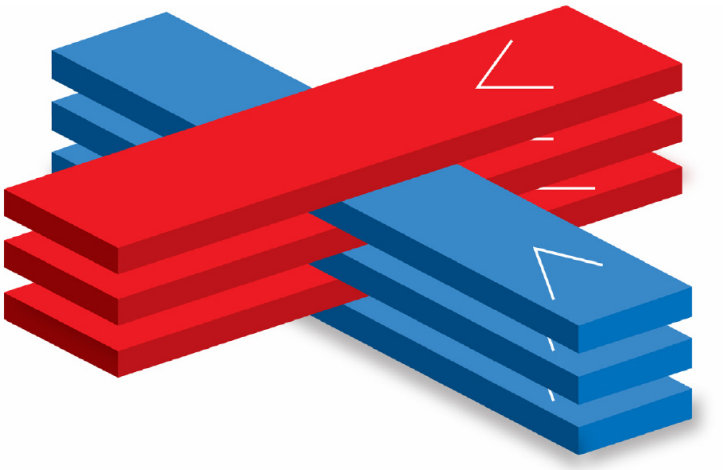

Figure 3.9.3 Model of Microbeam Radiation Therapy (MRT). Interlaced microbeams produce an unsegmented beam in the target but spare surrounding tissue.

MRT at NSLS-II will benefit from the beam's high energy and high intensity, which are essential to allow the beamline to be used for clinical studies. In particular, the beamline will make possible the use of a heavily filtered beam (e.g., one with a half-power energy of 150 keV to improve dose penetration) at a dose rate of 2000 Gy/s. This dose rate will allow the delivery of a therapeutic dose (e.g., 200 Gy incident dose) in a fraction of a heartbeat. The current X17B1 beam provides about 40 Gy/s at 12 keV half-power energy. Another major advantage of an MRT setup at NSLS-II will be the ability to allow for implementation of clinical MRT, accommodating all auxiliary functions, such as the physician's control area and medical imaging for patient positioning into the beamline infrastructure.

Diffraction Enhanced Imaging is another method developed at NSLS. DEI's angular sensitivity enables the gradient of the x-ray index of refraction to be measured, as well as the yield of "small-angle scattering" (extinction contrast). In DEI, a collimated monochromatic x-ray beam is passed through the subject as in conventional radiography. A silicon crystal (analyzer) is placed between the subject and the detector. The analyzer discriminates small-angle x-ray scattering and introduces sensitivity to refraction occurring within the subject. Variations in the subject's density and morphology refract the x-rays, generally in the sub-microradian range. The analyzer converts these subtle angle variations into intensity variations. Thus DEI enhances soft-tissue imaging, which lacks contrast in traditional x-rays and CT. DEI at NSLS-II will benefit from the beamline's high beam energy and intensity that could be used to image subjects as large as a human

head in a reasonable time in the CT mode, using beams of about 60 keV. This kind of work is impossible for implementation at the current NSLS.

Photon Activation Therapy was also developed at NSLS. PAT is based on the principle that absorption of radiation dose in tissue can be enhanced by administering contrast agents, including heavy elements, to the tissue and then irradiating the tissue with an X-ray beam in which the energy spectrum is concentrated above the K-edge of the contrast element. Inducing a photoelectric effect in a stable high Z atom localized to tumor cell DNA generates the emission of short-range, low energy Auger electrons that act like an energy sink in the DNA, severely damaging both strands, and so increasing the effective radiation dose to tumors**.** Such damage is associated with significantly less repair than single-strand breakage. The biological efficacy of Auger electron emission induced by synchrotron radiation was reported in PAT studies with iodine. The method can also be used with agents that do not target the cell nucleus, to enhance the dose localization in the target.

3.10 Hard X-Ray Imaging

X-ray imaging covers a wide range of techniques and applications and is likely to be among the most prominent techniques in use at NSLS-II. It is impossible here to do justice to the breadth of science that may be covered—ranging from materials science, to life science, to nanoscience. Here we simply mention a few of the techniques that will be utilized and list some likely applications. At NSLS-II, x-ray imaging might be expected to focus on the following core experimental techniques: 1) phase-contrast imaging, in both static and time-resolved modes, 2) diffraction-enhanced imaging capability, 3) coherent Fresnel diffraction imaging, and 4) image retrieval and tomographic 3D reconstruction as an integral part of the facility.

A good portion of the scientific program requires a highly coherent x-ray beam in an energy range of 7–50 keV, and a large field of view with minimal source-size smearing. In addition, time-resolved imaging experiments could make use of the pulsed nature of the NSLS-II synchrotron x-rays with an aim to achieve a single-pulse temporal resolution of ~50 ps and a simultaneous high spatial resolution of ~1 μm.

3.10.1 Phase-Contrast Imaging (PCI)

Phase-contrast x-ray imaging is a coherence-based technique that makes use of the edge-enhanced effects in near-field Fresnel diffraction and allows detections of weakly absorbing features in a specimen that are not observable in conventional absorption-based x-ray radiography. The spatial resolution with PCI is generally limited by the detector spatial resolution of 1–10 μm, which is well suited for many biological, medical, and materials science applications. A KB mirror system is planned to provide a projection-imaging capability that will allow increased spatial resolution down to 0.1–1 microns, if necessary.

Phase sensitivity directly depends on the distance between source and specimen, and between specimen and detector, thus leading to the requirement of a long beamline for PCI applications. In addition, a long beamline provides an unobstructed larger field of view, which will be needed for imaging larger specimens in materials and medical sciences. Based on the designs and experiences of the existing synchrotron beamlines in the world, a 300 m beamline at NSLS-II will provide a phase sensitivity of 2 mrad within the typical spatial resolution of 1 μm, and will be able to detect minute refractive angular deviations of <1 μrad. These specifications will represent the state-of-the-art in worldwide x-ray PCI capabilities.

Phase contrast imaging will be the workhorse facility of the XRI beamline, perhaps contributing to 60 to 70% of scientific research. Examples of research include: fracture mechanics of composites and biological materials, materials microstructure/properties such as deformation and sintering; bone and cartilage growth and formation; small animal and soft tissue research on vascular and pulmonary functions; porosity distribution in foods; structure and development of plant seeds; characterization of geological structures and microfossils; cement mortar research; structure and development of foams; granular packing of non-

equilibrium systems; time-resolved studies of internal complex fluid flow and fluid sprays; and multi-phase fluid flow using particle image velocimetry.

3.10.2 Diffraction Enhanced Imaging

Diffraction enhanced imaging, discussed above in the context of high energy x-rays, makes use of a high quality crystal analyzer to detect refracted or small-angle-scattered x-rays from the specimen. Because of high angular selectivity of the crystal analyzer, DEI can image very minute phase shifts due to density inhomogeneity in the specimen. In addition, in ultra-small-angle-scattering (USAXS) mode, it can be used to image density inhomogeneities and fluctuations at a given spatial frequency of interest. Technically, DEI can be set up in one or all of three regimes: a) top of analyzer rocking curve for scattering background rejection, b) side of analyzer rocking curve to convert refraction-angle into intensity contrast, and c) far from analyzer rocking curve on direct beam to pick up USAXS signals at a given scattering angle. Examples of DEI applications include: microstructures and defects in materials; deformation, sintering, and crack formations; porosity in bones and calcification effects; soft tissue and vascular network detections in x-ray radiographs; and diagnosis of cancerous tumors in soft tissues.

3.10.3 Coherent Fresnel Diffraction Imaging (FDI)

Coherent Fresnel diffraction imaging involves collecting Fresnel or in-line holograms in near-field regimes and reconstructing original nonperiodic objects by image retrieval techniques. Compared to PCI, discussed in 3.10.1, coherent FDI seeks to record a complete set of Fresnel diffraction fringes at a greater detector-to-specimen distance, which allows quantitative determination of an object's density function and permits spatial resolution reaching well beyond the detector pixel resolution. When working in the intermediate regime of a few Fresnel zones, FDI essentially becomes the far-field coherent diffraction imaging technique, as discussed in Section 3.2. Examples of potential applications include: structures of large biological functioning units (e.g., tissues, myocytes, muscles, bones, cartilage, etc.); identification of organelles and critical protein assemblies in biological cells; self-assembly of macromolecule arrays with nanotemplates and nanogrids; structural imaging of multi-unit inorganic/small-molecule/biomolecule composites; noncrystalline nanoparticles such as nanoclusters and nanowire assemblies; structural imaging of precipitates and defects in engineering materials; and topographic imaging of domain growths in ferroelectrics.

4 ACCELERATOR OVERVIEW

This chapter describes the main requirements and features of the NSLS-II accelerator complex, focusing on the philosophy and the approach used to select the NSLS-II ring lattice, injection scheme, and main components. Based on the considerations presented here, we believe we have arrived at an optimal, or near-optimal, design. This description is brief, and important details of the individual systems and subsystems are presented in other chapters of this CDR.

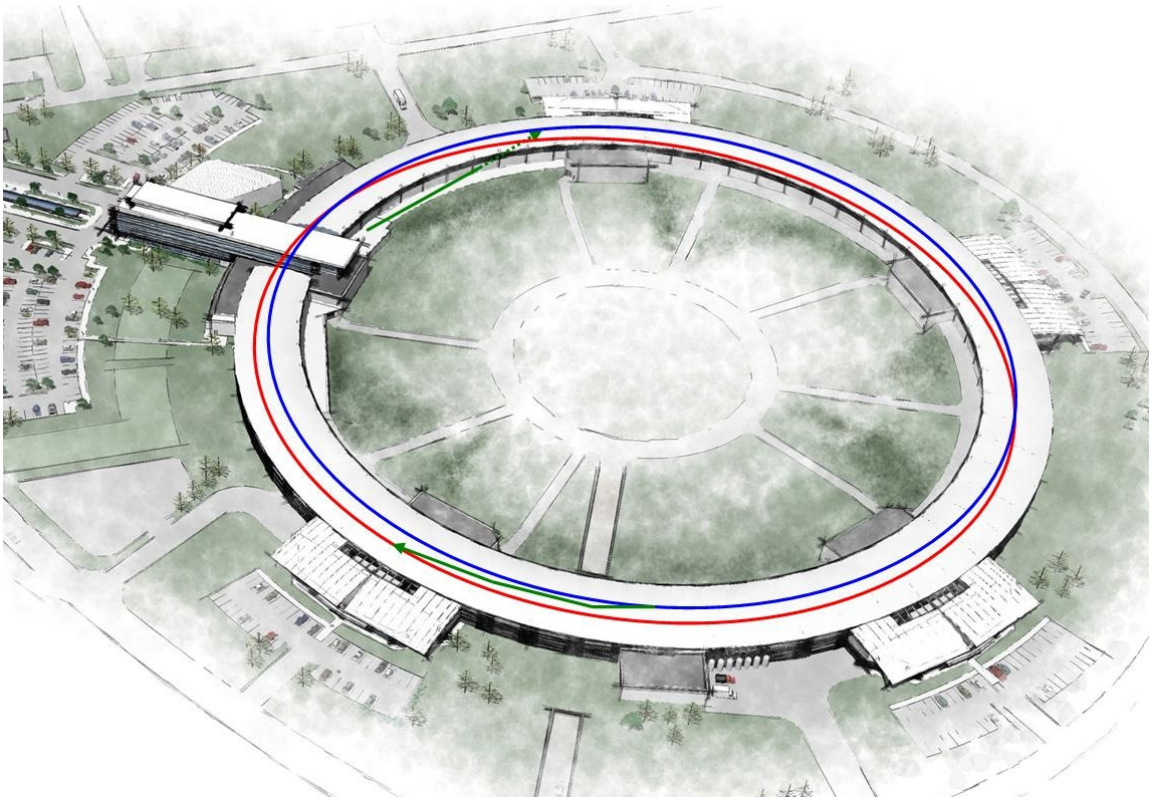

Figure 4.1.1 Schematic layout of the NSLS-II accelerators: a 200 MeV linac, a 3 GeV booster ring, and the 3 GeV storage ring. The booster and the storage ring share the same tunnel.

4.1 Scope of the Accelerator Complex

NSLS-II is designed to deliver photons with average spectral brightness in the 2 keV to 10 keV energy range exceeding 10^{21} ph/mm^2/mrad^2/s/0.1%BW. The spectral flux density should exceed 10^{15} ph/s/0.1%BW in all spectral ranges and with a peak value approaching 10^{16} ph/s/0.1%BW for photon energies around 2 keV. This cutting-edge performance requires the storage ring to support a very high-current electron beam (I = 500 mA) with sub-nm-rad horizontal emittance (down to 0.5 nm-rad) and diffraction-limited vertical emittance at a wavelength of 1 Å (vertical emittance <8 pm-rad). The electron beam will be stable in its position (<10% of its size), angle (<10% of its divergence), dimensions (<10%), and intensity (±0.5% variation). The latter requirement provides for constant thermal load on the beamline front ends.

A schematic layout of the NSLS-II accelerators is shown in Figure 4.1.1. Electrons generated in the linac are accelerated to 3 GeV in the booster. The accelerated electrons are periodically added to the electron beam circulating in the storage ring to keep the stored current nearly constant in time, a process know as top-off injection. This chapter presents the main parameters of the accelerator systems and main subsystems for NSLS-II and descriptions of the considerations and process that led to their optimization.

4.1.1 Physics Design and Parameters of NSLS-II

4.1.1.1 Storage Ring

Everywhere possible, NSLS-II will use known, reliable, and cost-effective solutions for its subsystems. Examples of such subsystems extend from a simple low-energy linac to the ring and booster RF systems, which are commercially available. Subsystems that are not critical to NSLS-II performance will be based on the simplest, most robust, and best-proven technologies. Hence, all magnetic elements of the accelerators have a significant margin in their design, but are not over-designed. Only the few subsystems that are crucial for attaining the ultimate NSLS-II performance require cutting-edge technologies and engineering solutions.

The overall layout of the storage ring and beamline is shown in Figure 4.1.2 and in more detail in Figure 4.1.3. The chosen lattice meets the challenge to provide record-low electron beam emittance. The choice of large-radius bending magnets enhances the effectiveness of damping wigglers to reduce the emittance. The lattice is optimized to meet the required performance within budget and size constraints.

As described in this chapter, the optimized storage ring lattice consists of 30 DBA cells, with straight sections alternating in length between 5 m and 8 m. There are thus 15 super-periods for the lattice. The lattice functions of one DBA cell (one half super-period) are shown in Figure 4.1.4. Each straight section is achromatic and has four quadrupoles at each end. These quadrupoles provide for ideal matching of the optic functions (β_x, α_x and β_y, α_y) and tune advances ($\Delta\nu_{x,y}$) in the straights to compensate the strong influence of the IDs on the linear lattice [4.1.1]. The total number of quadrupoles per super-period is 24. Each super-period also has five chromatic sextupoles per DBA cell and eight geometric sextupoles per straight section (i.e., 26 sextupoles per super-period). All quadrupoles and sextupoles in the SR will have individual power supplies, which will be fully utilized for high-precision, beam-based alignment and for experimental verification and correction of the quadrupole alignment errors [4.1.2]. The main parameters of the storage ring are summarized in Table 4.1.1.

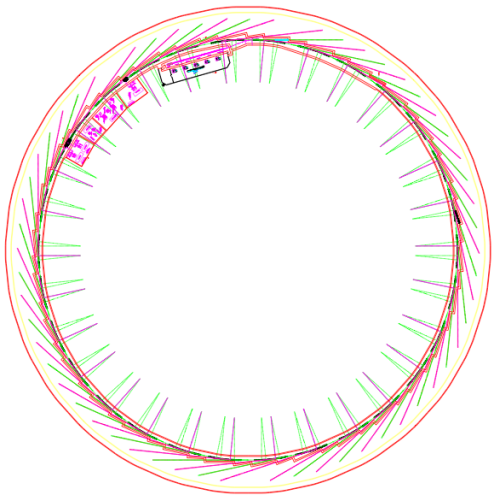

Figure 4.1.2 Geometry of the NSLS-II light source and its beamlines; green and magenta lines indicated the ID and dipole beamlines.

Figure 4.1.3 Three DBA cells (one and a half super-periods) with short (5 m) and long (8 m) straight sections.

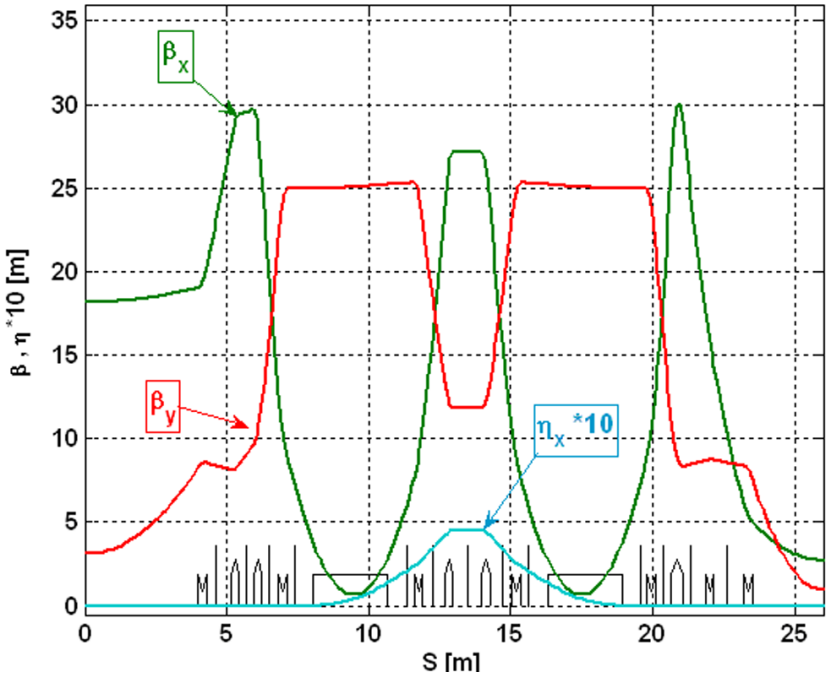

Figure 4.1.4 Lattice functions of half of an NSLS-II storage ring super-period.

Table 4.1.1 Main Parameters of the NSLS-II Storage Ring

Energy [GeV]	3
Circumference [m]	780
Number of DBA cells	30
Number of 8 m straights	15
Beta-functions in the center of the 8 m straights: β_x, β_y [m]	18, 3.1
Number of 5 m straights	15
Beta-functions in the center of the 5 m straights: β_x, β_y [m]	2.7, 0.95
Number of dipoles	60
Number of quadrupoles	360
Number of sextupoles	390
Circulating current at 3 GeV, multi-bunch [mA]	500
Radio frequency [MHz]	499.46
Harmonic number	1300
Number of bunches at 80% fill	1040
Nominal bending field at 3 GeV [T]	0.4
Dipole critical energy at 3 GeV [keV]	2.4
Total Bending magnet radiation energy loss [keV]	286.4
Radiation energy loss per damping wiggler [keV]	129.3
Vertical emittance [nm-rad]	0.008
Horizontal emittance of bare lattice [nm-rad]	2.1
Horizontal emittance with three 7 m 1.8 T damping wigglers [nm-rad]	0.9
Horizontal emittance with eight 7 m 1.8 T damping wigglers [nm-rad]	0.6
Momentum compaction factor	3.7×10^{-4}
Bunch length, RMS, natural [mm, ps]	2.9, 10
Energy spread, RMS	0.05 –0.1%

The 3 GeV storage ring is designed to be a reliable light source of hard and soft x-rays with average spectral brightness and flux in the target energy range from ~10 eV to ~20 keV, significantly exceeding all synchrotron light sources currently operating or under construction. All of its components are designed with an operational safety margin of more than 20%. The parameters of the magnets and their tolerances are specified in Section 7.1. None of the magnet parameters goes beyond well-established standards. The stability and alignment requirements are challenging but achievable (Section 6.1.2.4), as demonstrated at the Swiss Light Source. To achieve these tolerances, the clusters of quadrupoles and sextupoles will be assembled on individual girders, as shown in Figures 4.1.5 and 4.1.6. Their magnetic centers will be aligned precisely with respect to the girder fiducials using the vibrating wire technique. The pre-aligned girders will then be moved into the ring tunnel and installed. The alignment tolerances between girders are less critical than between individual elements.

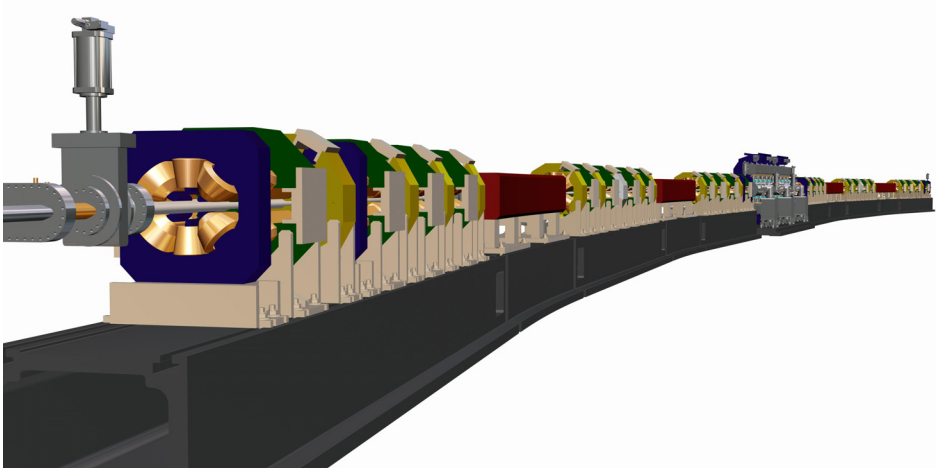

Figure 4.1.5 3D-view of the SR super-period comprised of two DBA cells and two straight sections (half of the 8 meter straight is shown at each end). The super-period has bilateral symmetry with respect to the center of the long or short straight section.

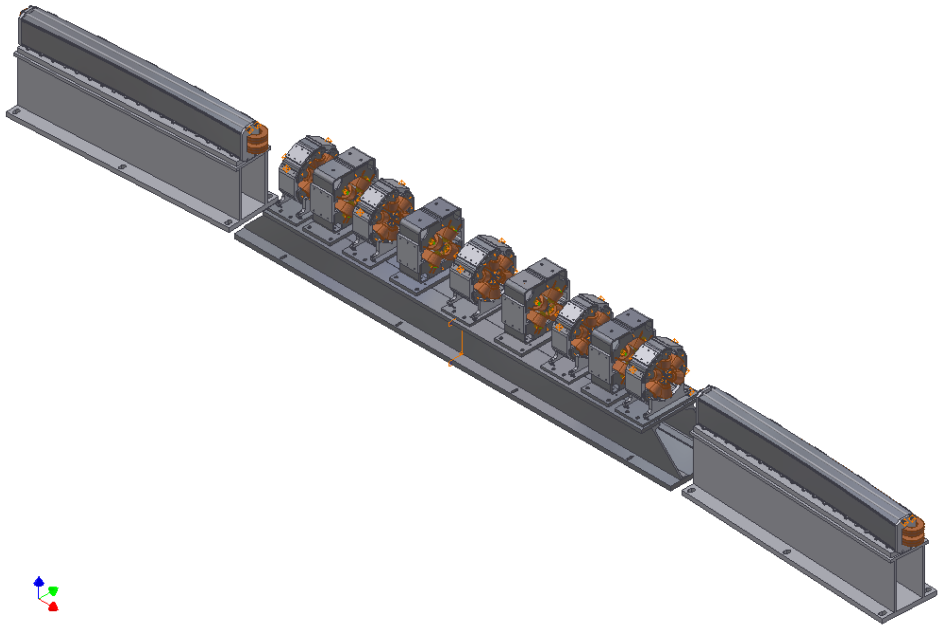

Figure 4.1.6 3D view of a standard DBA cell with bilateral symmetry. It consists of two dipoles, four quadrupoles, and five sextupoles. All quadrupoles and sextupoles are located on a single low-height rigid girder.

The girders are designed with natural resonant frequencies >60 Hz to avoid amplification of low-frequency floor vibrations. The orbit feedback system will damp beam motion below 60 Hz. A local feedback system will steer the ID photon beam in the beamlines, where high stability is required.

The necessity for relatively long lifetime and large dynamic aperture require the very nonlinear, sextupole-dominated, ultra low emittance SR lattice to be very robust and capable of tolerating manufacturing

and installation errors. Furthermore, the presence of high-field and short-period undulators at the relatively low energy of the SR imposes an additional, very strong nonlinear component on the lattice, which changes when users change the undulator gaps. The four quadrupoles per ID provide the capability of minimizing the linear impact of these IDs, restoring much of the corrected nonlinear dynamics behavior of the beam.

The NSLS-II storage ring will be equipped with a full set of beam diagnostics and feedbacks necessary for prompt commissioning and reliable operation of this cutting-edge facility. The diagnostics will monitor closed beam orbit position, tunes, beam current and lifetime, filling pattern, beam emittances, bunch length, position of the photon beam in insertion devices, coherent bunch instabilities, and distribution of beam losses around the ring. It will allow for the measurement and study of parameters for the linear and nonlinear optics (including lattice functions, chromaticities, local and global coupling, momentum compaction, and magnet and RF system parameters [4.1.2]), to measure the beam energy spread as well as impedances of vacuum chambers, and to use beam-based alignment relative to the quadrupoles and sextupoles. Beam diagnostics and feedbacks will include at least the following:

- two high-precision DCCTs and two bunch-to-bunch current monitors
- 226 beam position monitors (seven BPMs with sub-μm sensitivity per cell plus two BPMs per each installed ID, with average and single turn capabilities) plus photon BPMs (two per ID) paired with 210 regular orbit correctors. These correctors will provide regular (slow) orbit feedback.
- a set of fast correctors with feedback bandwidth of 100 Hz, for each ID
- monitors of both transverse tunes and synchrotron tunes
- diagnostic undulator equipped to monitor horizontal and vertical emittances of electron beam
- dual-sweep streak-camera with picosecond resolution for measuring the bunch length
- beam loss monitors

All the diagnostics listed above are non-interceptive. A few interceptive diagnostics (such as flags) will be used for commissioning purposes. (See complete descriptions in Section 7.8.)

NSLS-II will use CESR-B type superconducting RF (SRF) 500 MHz cavities. In addition, passive cavities operating at the 3rd harmonic (1.5 GHz) will be used to increase the bunch length and improve the beam lifetime. Initially, the RF system will be comprised of two 500 MHz cavities and a single harmonic cavity installed in an 8 m straight section. A single 310 kW klystron amplifier will drive each of the main ring cavities through a 350 kW rated circulator and load (see Section 7.5 for further detail on the RF system and its cryogenics). When the facility is fully built out with insertion devices, two additional RF cavities (for a total of four) and one additional harmonic cavity (for a total of two) will be required. These additional devices will occupy one additional 8 m straight section.

Of the 1,300 RF buckets, only 80 to 90% will be filled. The remaining buckets will stay empty, serving as a clearing gap for ions. The presence of the ion clearing gap impacts the beam lifetime and improves its stability (see detailed discussion in Section 6.2.7).

4.1.1.2 Injection System for the Storage Ring

Due to the relatively short lifetime of the electron beam (~3 hours), full-energy top-off injection is required. Injections will be very brief (milliseconds) and occur about once per minute. In contrast with the previous generation of light sources based on high-energy storage rings, the short lifetime of NSLS-II means that it cannot perform at its target level if the injector is not readily available. Thus, it is imperative that the injector be a very robust and reliable device. This requirement led to the selection of a full energy booster for the injector. In addition, the booster is placed in the same tunnel as the main ring to remove the cost associated with an external building to house the booster (Figure 4.1.7). The booster also has a low power consumption of only approximately 100 kW.

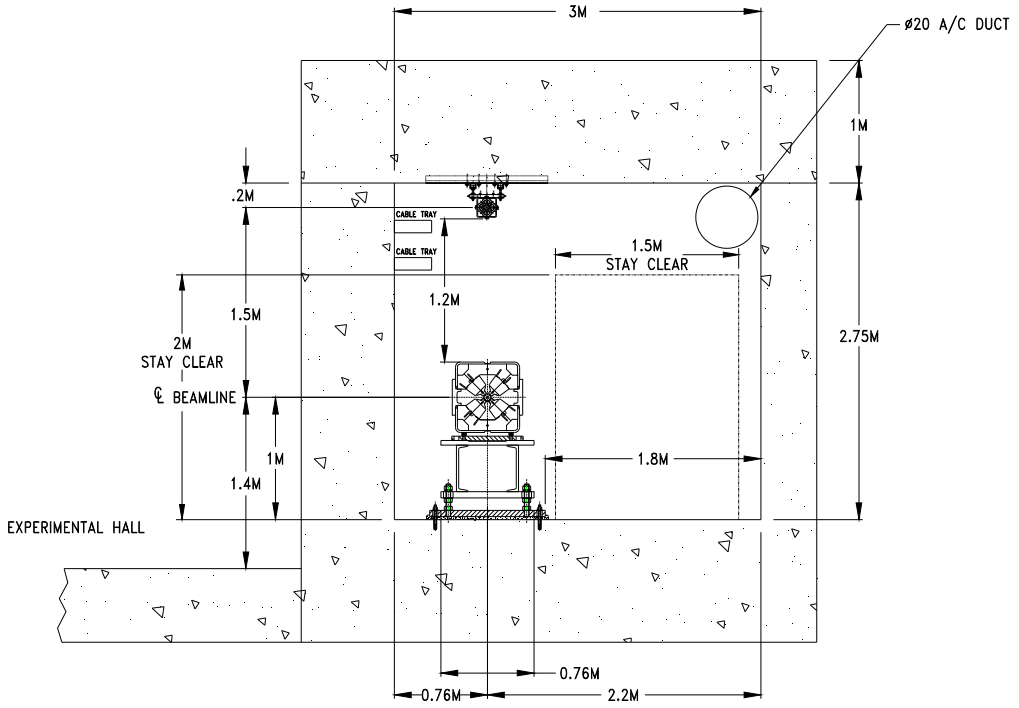

Figure 4.1.7 Schematic layout of the storage ring and the full energy booster in the same tunnel.

The main parameters of the injector are given in Table 4.1.2 and a detailed description is given in Chapter 5. A 200 MeV linac with thermionic triode electron gun will serve as the injector for the booster. For straightforward commissioning and reliable operation, the injector will be equipped with a full set of beam diagnostics (DC and fast current transformers, 75 BPMs, four fluorescent flags, 30 loss monitors, fire-wire, and streak-cameras); see Section 5.11 for details. The linac, booster, and storage ring are connected by transport lines, described in Sections 5.3 and 5.10.

Table 4.1.2 Main Parameters of the NSLS-II Injector.

Booster	
Injection energy [MeV]	200
Nominal energy [GeV]	3
Circumference [m]	780
Ramping repetition rate [Hz]	1
Acceleration time [sec]	~0.4
Radio frequency [MHz]	499.46
Total number of cells	15
Total number of bending magnets (combined function)	60
Total number of quadrupoles	96
Dipole field at injection / extraction [T]	0.053 / 0.7
Energy loss per turn at 3 GeV [MeV]	0.5
Natural emittance at 3 GeV [nm-rad]	11.5
Linac	
Nominal linac energy [MeV]	200
Frequency [GHz]	2.998
Pulse repetition rate [pps]	1
Pulse charge [nC]	7

The booster RF system (Section 5.8) will be based on a five-cell "PETRA" (room temperature, copper) cavity that will provide 1 MV accelerating voltage, which is sufficient for the acceleration and required energy acceptance. An 80 kW IOT transmitter will be used to provide the 50 kW of power required for the cavity.

4.1.1.3 Photon Sources

The NSLS-II storage ring has 27 straight sections available for insertion devices (one 8 m straight section will be used for the injection and two for the RF system). An 8 m straight section can also accommodate two short undulators whose radiation is separated by a local angular bump (so-called canted undulators). NSLS-II will host a variety of different types of undulators and wigglers that will generate high brightness and high flux beams of hard and soft x-rays. A full description of these IDs and their performance, together with that of the bending magnets, is given in Chapter 8. The storage ring lattice is designed to withstand the influence of a complete set of insertion devices set to arbitrary gap (field) values in the fully developed facility (see Section 6.1.2.8).

NSLS-II will use damping wigglers (see Section 4.2) for two purposes [4.1.3]:

1. to reduce horizontal beam emittance to the desired level while minimizing the number of cells of the lattice and thus the circumference (and cost) of the storage ring
2. to serve as broadband sources of very bright and high flux x-rays superior to conventional bend-magnet sources

4.1.1.4 Mechanical Design and Magnets

Many of the mechanical designs for NSLS-II are now conventional technology for third-generation light sources. Most of the NSLS-II storage ring uses extruded aluminum vacuum chamber with short (about 15 cm) stainless steel inserts for fast feedback orbit correctors. This vacuum chamber provides for in-situ bakeout to 130°C using pressurized hot water circulated within the cooling water channel of the Al profile. Synchrotron radiation is either extracted to a user beamline or intercepted by a localized water-cooled copper absorber (see Section 7.4). All bellows in the storage ring vacuum chamber will be RF shielded to provide low impedance and low losses. The most complex are the vacuum chambers for the insertion devices, especially those for in-vacuum undulators with flexible transitions. These devices are described in Section 7.4.3. Vacuum pressure of 1×10^{-9} Torr will be provided by 240 ion vacuum pumps, 180 titanium sublimation pumps, and about 250 NEG pumps distributed around the ring, IDs, and front ends. The ring vacuum system will have 90 gate valves. The pressure and the residual gas content in the storage ring will be monitored by 270 ion gauges and by 104 residual gas analyzers.

Stainless steel will be used for the booster vacuum chamber (Section 5.7), transport lines, and linac. The low ramp-rate of the booster allows us to use simple elliptical vacuum chambers. A suite of vacuum pumps, vacuum gauges, and RGAs will be used to support and monitor vacuum at the 10^{-7} Torr level.

The main parameters of the magnets for the booster and storage ring are discussed in detail in Sections 5.6 and 7.1, respectively. A number of pulsed elements (kickers and septa) are also used in NSLS-II, as described in Sections 5.9 and 7.6.2.2.

Among the most challenging requirements are those associated with the precise alignment of magnetic elements in the storage ring. Another challenge is the design of the girder system, which must be as rigid as possible to reduce vibration of the elements that results in low-frequency noise in the position and angle data from the x-ray beams. The solutions for these challenging problems are described in Section 7.2.

4.2 Optimization of the NSLS-II Design

The pre-conceptual design of NSLS-II [4.2.1] was based on 24 triple-bend achromatic cells (TBA24) with a circumference of 630 m. Further extensive studies [4.2.2] demonstrated that this lattice, with a horizontal emittance of 1.5 nm-rad, was not robust. The dynamic aperture for this lattice collapsed in the presence of realistic errors. Further studies explored possibilities of various lattices (DBA vs. TBA), radii of curvature, and circumferences, as well as damping wigglers.

The performance goals for the current NSLS-II lattice, including the effects of all realistic errors and of small gap undulators, are listed in Table 4.2.1. They are based on analyzing alternative designs for NSLS-II and on the experience of the most advanced operational mid-energy light sources (such as the Swiss Light Source [4.2.3]).

Table 4.2.1 Goals for the NSLS-II Lattice.

Beam lifetime [hours]	~3
2D dynamic aperture [mm-mrad] [2]	~25 x 25
Energy aperture [%]	~±3
Horizontal emittance at 3 GeV with damping wigglers [nm-rad]	~0.5
Horizontal geometrical aperture for injection [mm]	~±20

Sextupole-dominated lattices of modern low-emittance synchrotron light sources are intrinsically non-linear and do not allow the traditional approach of designing a linear lattice and later retrofitting it with the appropriate number of sextupole families. Instead, nonlinear aspects of the lattice must be addressed from the very beginning of the lattice design through continuous iterations of both linear and nonlinear elements. Furthermore, for convergence of these iterations to a robust (i.e., operational) lattice, the following decisions are vital: the number and locations of beam position monitors (BPMs) and correctors, target BPM accuracy, the scheme for orbit correction, and methods for beam-based alignment. Details on the process of selecting an operational lattice for NSLS-II are in Section 6.1.

This process of proper lattice design is labor intensive and lengthy. As a result, only a very limited number of lattices can be studied in sufficient detail. To streamline the NSLS-II design process and to avoid dead ends such as the "zero-dynamic aperture desert," the restrictions given in Table 4.2.2 were imposed on the choices for the lattice cell in the presence of realistic errors and IDs.

Table 4.2.2 Restrictions on the NSLS-II Linear Lattice Design.

Chromaticity per cell, ξ_x	≤ 3
Maximum β-functions [m]	≤ 30
Maximum η-functions [m]	>0.3
Maximum β-beating: $\Delta\beta_x/\beta_x$, $\Delta\beta_y/\beta_y$ [%]	≤5%, ≤1%
Maximum tune-spread per cell: $\Delta\nu_x$, $\Delta\nu_y$	<0.05, <0.002
Transverse alignment accuracy of quadrupoles, sextupoles and BPMs [μm]	±30
Roll-off errors for quadrupoles, sextupoles and BPMs [mrad]	≤ 0.5

Within the framework above, the following design philosophy was pursued to attain sub-nm horizontal emittance for NSLS-II:

- use a lattice with reasonable natural emittance (~2 nm-rad) and robust dynamic aperture
- keep achromatic conditions in the straight sections so IDs reduce emittance, and also to avoid additional nonlinear 3D driving terms

- use damping wigglers to reduce emittance
- limit total losses of synchrotron radiation to 1 to 2 MeV per turn to limit electrical power consumption
- increase bending radius to maximize impact of damping wigglers while keeping emittance under control
- monitor the cost

Using a larger radius for the bending magnets causes a modest increase in the ring's circumference and some increase in the maximum dispersion, resulting in reduced sextupole strengths. Our studies showed that it is possible to keep the bare emittance under control while increasing the bending radius of the dipole magnets. Increasing the bending radius reduces the dipole field ($B_o = pc/e\rho_o$) and (in the case of the same coil cross-section) reduces the power consumption.

The approach of using damping wigglers to achieve low horizontal emittance has been used previously in accelerators designed for high energy physics, but it has not been widely used for light source designs. Usually the use of damping wigglers is associated with large synchrotron radiation losses and large consumption of RF power. This is not the case for NSLS-II – the use of a large bending radius proportionately reduces the radiation losses from both the bending magnets (U_{bends}) *and* the damping wigglers. This is a unique feature of the NSLS-II design. The emittance for a given total loss per turn from synchrotron radiation (U_{total}), i.e., for a given RF power, decreases with the increase of the radius of curvature:

$$\varepsilon_{nat} \cong \varepsilon_{bare} \cdot \frac{U_{bends}}{U_{total}};\ U_{bends} \cong 88.5\left[keV\right] \cdot \frac{E^4\left[GeV\right]}{\rho_o[m]},$$
$$U_{bends}(@3GeV) \cong \frac{7.17\left[MeV\right]}{\rho_o[m]} \qquad (4.2\text{-}1)$$

where ε_{bare} is the emittance of the bare lattice (without wigglers) and ε_{nat} is the natural emittance in the presence of damping wigglers [4.2.4].

This approach to emittance control is straightforward and has a rather modest effect on the vertical dynamic aperture (see Section 6.1). The fact that the damping wigglers at NSLS-II will be also very bright, high-intensity sources of broadband x-rays makes this approach even more attractive.

Using this design approach, two promising lattices, the TBA24 (bending radius of 18 m) and the DBA32 (bending radius of 15.3 m), emerged in the early stages of the conceptual design development. Both lattices at the time of consideration had circumference ~750 meters with bare natural horizontal emittance between 1.8 and 2 nm-rad. Both could go well below 1 nm-rad with the use of damping wigglers and clearly indicated a potential for robustness.

A key advantage of lattices based on a DBA cell compared to a TBA cell is that, for lattices with comparable bare emittance, the DBA cell allows significantly more straight sections for user IDs while having a similar number of magnets and circumference. Lattices based on a DBA cell are thus preferred, and further studies were focused on selecting the optimum number of DBA cells.

Table 4.2.3 shows the key parameters used in selecting the optimum size DBA lattice. All lattices considered had a super-period of two cells, with alternating straight section lengths of 8 m and 5 m, and a bend magnet radius of 25 m (the optimum choice of bend magnet radius is discussed in the next section). A straight section length of 8 m is required in order to inject in a single straight, as well as to accommodate two RF cavities and one harmonic cavity in a single straight. The second straight section length of 5 m was chosen as a compromise between having longer IDs and minimizing the storage ring circumference. Shorter straights are also conducive to having smaller beta functions, and hence smaller beam sizes, as discussed in Chapter 6. Achieving very small beam sizes is especially beneficial in enabling the photon beam to be focused down to a 1 nm spot size, as discussed in Chapter 11. As discussed generally in the next section, and shown in Table 6.1.3 and Figure 6.1.3 for the choice of a DBA30 lattice with 25 m bend magnet radius, eight 7 m long damping wigglers are sufficient to achieve nearly the full emittance reduction that can be achieved from

damping the beam. Thus, eight of the 8 m straights are assumed to be occupied by damping wigglers. Table 4.2.3 shows the resulting expected straight section utilization.

As discussed in Chapter 11, the DBA30 lattice will provide nearly the same number of beamlines, when the possibility of canting multiple independent undulators per straight is included, as exist on the present NSLS x-ray and VUV storage rings. This will enable NSLS-II to accommodate a user community comparable in size to that of the existing NSLS. The DBA30 lattice will also achieve nearly the same performance as the DBA32. We carried out a parametric estimate of the cost savings from reducing the number of lattice cells from 32 to 24, and found a cost reduction of ~$16M (including all burdens, escalation, and contingency) per super-period (two cells). Overall, we find that the DBA30 lattice with a circumference of 780 m provides a good compromise between many competing parameters and goals (cost, length and number of user IDs, and performance).

Table 4.2.3 Storage Ring Parameters for Number of DBA Lattice Cells Varying from 32 to 24.

Lattice	DBA32	DBA30	DBA28	DBA26	DBA24
Circumference [m]	822	780	739	697	656
Bend magnet radius [m]	25	25	25	25	25
Straight sections [n x (m)]	16x(8, 5)	15x(8, 5)	14x(8, 5)	13x(8, 5)	12x(8, 5)
Horizontal emittance, ε_x (bare) [nm-rad]	1.7	2.1	2.6	3.2	4.1
Horizontal emittance, ε_x (full set of damping wigglers) [nm-rad]	0.5	0.6	0.7	0.8	1.1
Straight Section Utilization					
8 m straights					
RF and injection	3	3	3	3	3
Damping wigglers	8	8	8	8	8
Undulators	5	4	3	2	1
5 m straights					
Undulators	16	15	14	13	12

4.2.1 Large-Radius Bends and Intrabeam Scattering (IBS) Limits

Following the choice of a DBA30 lattice, studies were carried out to determine the optimum bend magnet radius and number of damping wigglers. As the bare emittance is reduced, it ultimately becomes limited by the effects of intra-beam scattering. Therefore, an important part of our studies was related to the issue of the ultimate IBS-limited emittance for the lattice with fixed synchrotron radiation losses per turn. Even though the detailed calculations of the single and multiple intrabeam scattering on the beam lifetime and the beam emittance were performed using appropriate computer codes (see Section 6.2), the conclusions reached are very similar to those that could be derived using analytical formulae for these processes. Furthermore, such an approach allowed rapid parametric studies and avoidance of multiple, labor intensive trial-and-error lattice designs. Well-known synchrotron radiation integrals for radiation damping and quantum excitation [4.2.4] and the IBS formula for flat electron beam [4.2.5] can be used to calculate the equilibrium energy spread σ_δ and horizontal emittance ε_x:

$$\begin{aligned} \sigma_\delta^{\,2} &= \tau_E\left(D_{\delta\ SR} + D_{\delta\ IBS}\right); \quad \delta = \frac{E - E_0}{E_0}; \\ \varepsilon_x &= \tau_x\left\langle H \cdot D_{\delta\ SR}\right\rangle + \tau_x\left\langle H \cdot D_{\delta\ IBS}\right\rangle; \\ H &= \frac{1}{\beta_x}\left[\eta_x^{\,2} + (\beta_x\eta_x' - \beta_x'\eta_x/2)^2\right] \end{aligned} \tag{4.2-2}$$

where E_o is the energy of the electron beam, E is the energy of individual electrons, and τ_E and τ_x are the damping time of energy (synchrotron) oscillations and horizontal betatron oscillations, respectively. $D_{\delta\ SR}$ and $D_{\delta\ IBS}$ are relative energy diffusion coefficients caused by quantum fluctuations of synchrotron radiation (i.e., causing so-called natural emittance) and by the intrabeam scattering, respectively. The H-function is the well-known connection between emittance growth and the energy diffusion coefficients.

The energy diffusion induced by IBS can be expressed in the following terms:

$$D_{\delta\ IBS} = \frac{N_e r_e^{\,2} c}{2^5 \pi \gamma^3 \varepsilon_x \sqrt{\varepsilon_y \beta_y(s)}\,\sigma_s} f(\chi_m(s)); \quad f(\chi_m) = \int_{\chi_m}^{\infty} \frac{d\chi}{\chi} \ln\left(\frac{\chi}{\chi_m}\right) e^{-\chi};$$

$$\chi_m = \frac{r_e m^2 c^4}{b_{\max} \Delta E_{acc}^{\ 2}}; \quad b_{\max} \cong n^{-1/3}, \tag{4.2-3}$$

where $\gamma = E_o/mc^2$ is the relativistic factor of the electron ($\gamma \approx 6{,}000$ for 3 GeV electrons), $N_e = I/N_b/e$ is the number of electrons per bunch, m is the mass and r_e is the classical radius of an electron, c is the speed of light, and σ_s is the electron bunch length. $f(\chi_m)$ is the scattering integral depending on the following parameters: ΔE_{acc} is the energy acceptance (in the location of scattering) and n is the density of electrons (see [4.2.5] for details of the definition). As shown in Figure 4.2.1, this function depends very slowly (logarithmically) on its parameter χ_m. For the case of NSLS-II, variations of horizontal emittance (by an order of magnitude, from 0.2 nm-rad to 2 nm-rad) change the value of $f(\chi_m)$ by only ±20%.

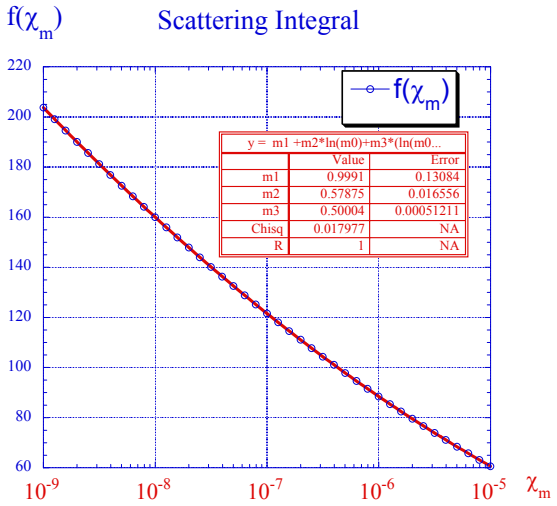

Figure 4.2.1 Dependence of the scattering integral on the maximum scattering parameter χ_m.

The NSLS-II designs have a number of parameters that are either constant or have very small variations. First, vertical emittance will be held at the diffraction level for 1 Å radiation ($\varepsilon_x \approx 8$ pm-rad). Second, both low emittance and low energy spread are paramount for the attainment of the required spectral brightness at high harmonics and in the hard-x-ray range (see Chapter 8), which led to a natural selection of a separate function lattice (i.e., there is no field gradient in the dipoles) and constant ratio of synchrotron and horizontal damping times:

$$\tau_E \cong \frac{\tau_x}{2} \cong \frac{1}{f_o} \cdot \frac{E_o}{U_{total}}; \tag{4.2-4}$$

where $T_o=1/f_o$ is the revolution time of electrons around the ring. Thus the damping time is simply proportional to the ring circumference and to the ratio between the beam energy and total losses on synchrotron radiation E_o/U_{total}. Third, the bunch length in NSLS-II will be kept about constant (between 3 mm and 4.5 mm,) by various means, including its lengthening by harmonics cavity (see Section 6.2.7).

Equations (4.2-2) and (4.2-3) can be solved with respect to the natural emittance ($\varepsilon_{nat} = \tau_x \langle H \cdot D_{\delta\ SR} \rangle$; i.e., the beam emittance in the absence of the IBS) using weak dependence of the scattering integral on the beam emittance:

$$\varepsilon_{x\ total} \cong \frac{\varepsilon_{nat}}{2}\left(1+\sqrt{1+\frac{4\varepsilon_{IBS}^{\ 2}}{\varepsilon_{nat}^{\ 2}}}\right), \tag{4.2-5}$$

where ε_{IBS} is the minimum emittance that can be achieved in a given lattice for a given current per bunch $I_b=eN_ef_o$:

$$\varepsilon_{IBS} = \sqrt{\frac{\tau_x N_e r_e^{\ 2} c}{2^5 \pi \gamma^3 \sigma_s}\left\langle H(s)\frac{f\left(\chi_m(s)\right)}{\sqrt{\varepsilon_y \beta_y(s)}}\right\rangle}\ . \tag{4.2-6}$$

The expression for ε_{IBS} (Eq. 4.2-5) can be easily evaluated for any given lattice and bunch parameters, and it naturally has very weak (square root) dependence on the bunch length, bunch current, and damping time, and even weaker (4^{th} power root) dependence on vertical emittance. Overall, this number is a good measure of the ultimate emittance one can approach with realistic beams. For all realistic TBA24 and DBA24 through DBA32 lattices and related beam parameters under consideration (and maximum total losses limited to 1 MeV per turn), the value of ε_{IBS} was between 0.2 nm-rad and 0.25 nm-rad, thus setting the natural limit for attainable emittance. Naturally, increasing the power losses by a factor of two to 2 MeV per turn would further reduce ε_{IBS} by $\sqrt{2}$.

The dependence of the beam emittance on the natural emittance also sets a natural scale for the bending magnet radius. As shown in Figure 4.2.2, reduction of the natural emittance below ~*(2-3)*ε_{IBS} is increasingly ineffective at reducing ε_{x_total} and is increasingly expensive as the circumference grows.

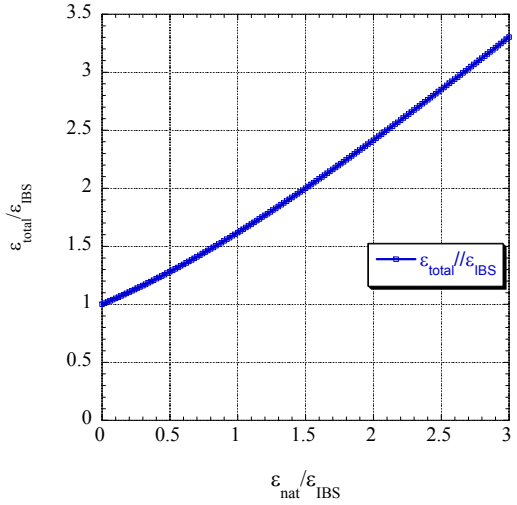

Figure 4.2.2 Dependence of the horizontal beam emittance (given by Eq. 4.2-6).

Reduction of the natural emittance by a factor of two from $2\varepsilon_{IBS}$ to ε_{IBS} (by roughly a doubling of the bending magnet radius) results in only a 33% reduction in emittance. A further doubling of the bending magnet radius only results in a 23% further emittance reduction. Hence, the optimum choice for the natural emittance is about 2 to 3 times ε_{IBS}. When combined with (Eq.) 4.2-1, this yields a simple expression for the optimum power radiated by the bending magnets:

$$U_{bends} = (2-3)U_{total}\frac{\varepsilon_{IBS}}{\varepsilon_{bare}} \quad . \tag{4.2-7}$$

For the 3 GeV NSLS-II storage ring, with total synchrotron radiation losses of 1 MeV per turn, this ratio also gives an optimum range for the radius of the bending magnets:

$$\rho_o[m] = (2.4-3.6)\frac{\varepsilon_{bare}}{\varepsilon_{IBS}} \quad . \tag{4.2-8}$$

Thus, the present DBA30 lattice with a bare emittance of ~2.1 nm-rad and ε_{IBS} ~0.25 nm-rad ($\varepsilon_{bare}/\varepsilon_{IBS} \sim 8.4$) has an optimum bending magnet radius ~25 m.

A bend magnet radius of 25 m is rather large compared to that at other synchrotrons. For example, the existing NSLS x-ray ring bend magnet radius is 6.9 m. As a result, the bend magnet critical energy at NSLS-II will be ~2.4 keV, compared to a critical energy of 7.1 keV for the bend magnets at the existing NSLS x-ray ring. As discussed in Chapter 8, this makes the NSLS-II bend magnets less attractive as sources of high flux, hard x-rays (>4 to 5 keV). However, they will be excellent sources of VUV and soft x-ray radiation. Furthermore, the damping wigglers will also serve as radiation sources for beamlines, and their brightness and flux will be about 100 times greater than would be provided by bend magnets with a small radius.

Finally, the parameters for the damping wigglers (see Chapter 8) were determined by a combination of the following effects (with the assumption that $U_{total} >> U_{bends}$):

- The wiggler magnetic field, B_w, in the damping wigglers should not be very high because it will increase the energy spread according to $\sigma_\varepsilon \propto \sqrt{B_w(T)}$, which will reduce the brightness of high harmonic radiation from the undulators.
- The wiggler period should not be too large, in order to serve as a source of very bright broadband x-rays.
- It should not be too small, to keep nonlinear effects under control.
- The wiggling angle and horizontal β-function should be limited to avoid excitation of horizontal emittance in the damping wiggler caused by $H \cong \beta_x \theta_w^2$.

As the result of optimization, damping wigglers with 1.8 T peak field and 10 cm period were selected. These damping wigglers provide synchrotron radiation losses of 18.5 keV per meter. The initial configuration of NSLS-II will have three 7 m long permanent magnet wigglers. This will achieve an emittance below 1 nm-rad. All damping wigglers will have fixed gap and field and will also serve as excellent sources of user radiation. The final configuration allows up to eight damping wigglers, with which the horizontal emittance will reach a value below 0.6 nm-rad.

4.2.2 Emittance and Lifetime

Electron beam lifetime is an important parameter of the NSLS-II light source. It defines the frequency of top-off injections and, ultimately, defines the radiation environment and necessary shielding. The lifetime has a strong dependence on the energy acceptance of the storage ring. For low-emittance light sources, the energy

acceptance depends not only on the linear compaction factor α_1 (in NSLS-II, higher order compaction factors are not important, $\alpha_1/\alpha_2 \approx 3.7\times10^{-4}/4.1\times10^{-4} = 92\%$) and the parameters of the RF system (harmonic, voltage, synchronous phase), but also may depend on nonlinear coupling and the vertical gap in IDs.

Here we will focus on two unusual phenomena in the lifetime dependences for the NSLS-II storage ring, and their consequences:

- For a given energy acceptance, the beam lifetime depends very weakly on the value of the horizontal emittance (within the range from 0.2 nm-rad to 2 nm-rad).
- Lifetime dependence on the energy acceptance is approaching the fourth power of the latter.

Conventional wisdom says that lowering the beam emittance in an electron storage ring leads to a proportional reduction of the lifetime. This conclusion can be drawn from the following formula [4.2.5]:

$$\frac{1}{\tau_{Touschek}} = \frac{N_e r_e^2 c}{8\pi\cdot\sigma_x\sigma_y\sigma_s\cdot\gamma^2\cdot\delta_{acc}^3} D(\xi); \qquad \xi = \left(\frac{\delta_{acc}}{\gamma\sigma_\theta}\right)^2;$$
$$D(\xi) = \sqrt{\xi}\left\{-\frac{3}{2}e^{-\xi} + \frac{\xi}{2}\int_\xi^\infty \frac{\ln u\cdot e^{-u}}{u}du + \frac{1}{2}(3\xi - \xi\ln\xi + 2)\int_\xi^\infty \frac{e^{-u}}{u}du\right\} \tag{4.2-9}$$

where $\delta_{acc} = \Delta E_{acc}/E_o$ is the relative energy acceptance, σ_θ is the transverse angular spread (dominated by horizontal oscillation for the NSLS-II case), $\sigma_{x,y} = \sqrt{\beta_{x,y}\varepsilon_{x,y}}$ are the transverse RMS beam sizes, and $D(\xi)$ is the scattering integral causing loss of the electrons.

Nevertheless, direct use of this formula (integrated over the NLSL-II circumference) gives a lifetime dependence (shown in Figure 4.2.3) which shows very weak lifetime variation in a (0.2, 2.0) nm-rad interval, and (exponential!) lifetime growth for emittances below 0.2 nm-rad. This dependence has a very solid physics foundation [4.2.6].

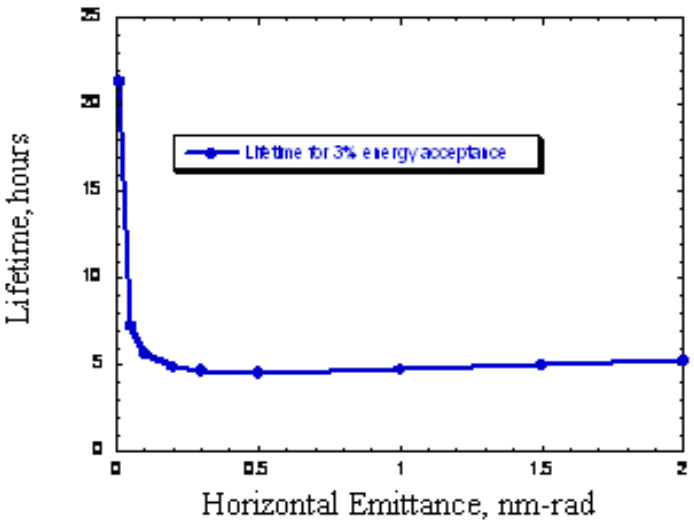

Figure 4.2.3 Dependence of the beam lifetime in NSLS-II on horizontal emittance for 0.008 nm-rad vertical emittance and fixed uniform 3% energy acceptance.

The main loss mechanism for ultra relativistic electrons ($\gamma >>1$, $\gamma_{NSLS\text{-}II}$ ~6000) in storage rings comes from the mechanism first described by Touschek. The simple picture can be presented as follows: In the co-moving frame (i.e., that moving with the electron bunch), two electrons execute betatron oscillations having transverse momenta $\pm p_t$ (in the case of a flat beam, mostly in the horizontal direction: $p_x = \pm\gamma mcx'$). They then scatter on each other and transfer the momenta ($p_s = \pm\gamma mcx'$) in the direction of motion (s-direction). The

Lorentz transformation into the laboratory frame gives a relativistic boost to p_s momenta by a factor of γ and generates an energy deviation of $\Delta E \approx \pm\gamma^2 mcx'$. If the energies of the scattered electrons are outside the energy acceptance ($\gamma^2 mcx' > \pm\Delta E_{acc}$), then the electrons may get lost. For most storage rings, the angular RMS spread of the electrons,

$$\sigma_\theta(s) = \sqrt{\varepsilon_x\left(1+\alpha_x^2(s)\right)/\beta_x(s) + \varepsilon_y\left(1+\alpha_y^2(s)\right)/\beta_y(s) + \eta'^2(s)\sigma_\delta^2}\,, \tag{4.2-10}$$

is sufficient for such a process to occur (note that σ_θ is a function of azimuth s). But for storage rings with extremely low emittances (in the NSLS-II case, sub-angstrom emittances), only the far tails of the electron distribution $f(\theta) = \exp\left(-\theta^2/2\sigma_\theta{}^2\right)/\sqrt{2\pi}\sigma_\theta$ can cause such processes, and the lifetime of such beams increases with the decrease of the emittance. Formally, this dependence can be seen from a formal evaluation of the $D(\xi)$ function, shown in Figure 4.2.4.

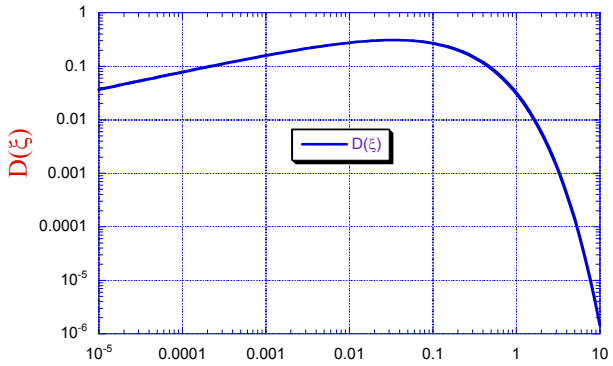

Figure 4.2.4 Dependence of the loss integral D(ξ) on the parameter ξ: D(ξ) is a rather slow function of ξ for ξ <*0.01*, flat in the range *0.01*<ξ <*0.1*, and falls exponentially for ξ >0.1. (nearly a Gaussian dependence).

For NSLS-II, ξ spans the range from $2\text{x}10^{-3}$ to 2 (the large range is an indication of very strong variation of the β-function with s). The explanation of the lifetime dependence shown in Figure 4.2.3 is very straightforward: while reduction of the horizontal emittance increases the electron density $\propto 1/\sqrt{\varepsilon_x}$, it also increases $\xi \propto 1/\varepsilon_x$ and, as a result, increases the portion of the ring where $\xi > 0.1$ and the losses are exponentially suppressed. Figure 4.2.5 shows that for the range of NSLS-II parameters under consideration, the beam lifetime exhibits an extremely weak dependence on the horizontal emittance, but a very strong dependence on the energy acceptance. As shown by the fit in Figure 4.2.6, the lifetime of NSLS-II is proportional to the fourth power of the energy acceptance. In contrast, storage rings having larger emittances and operating in the regime of ξ <0.01 typically have a power dependence on the energy acceptance of about 2.7. This strong dependence for NSLS-II, again, comes from the fact that large values of the ξ-parameter (where losses are suppressed) are important for the reduction of the losses and increase of the lifetime of NSLS-II. This underlines the importance of a large energy acceptance for NSLS-II.

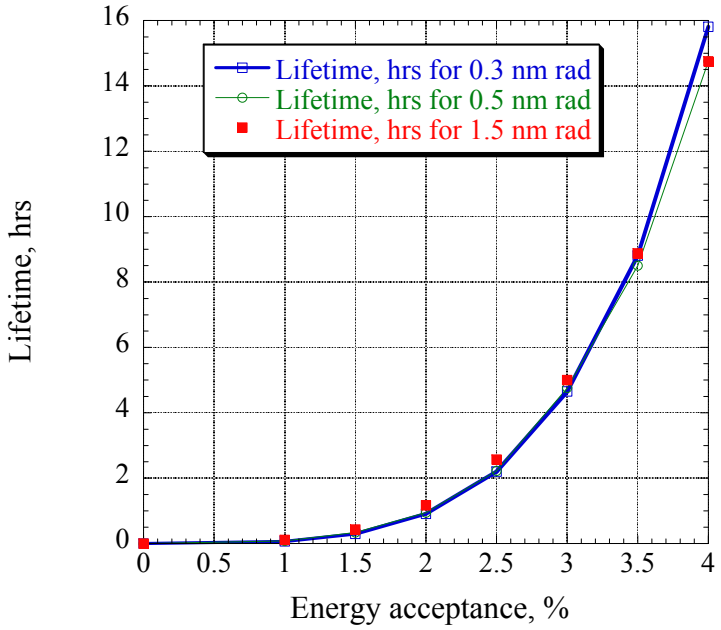

Figure 4.2.5 Dependencies of the beam lifetime on the energy acceptance for horizontal emittances of 0.3, 0.5, and 1.5 nm-rad and vertical emittance of 0.05 nm-rad. Note: the bunch length is assumed to be constant.

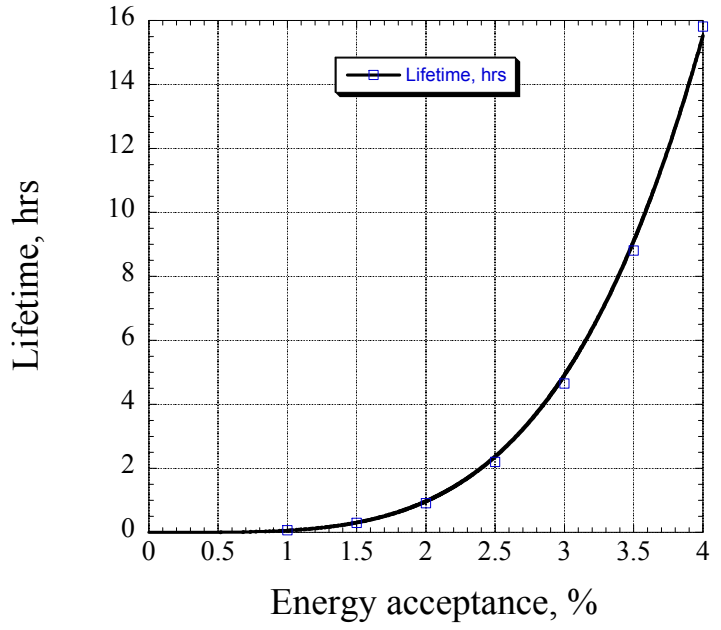

Figure 4.2.6 Fit of the beam lifetime dependence to the fourth power of the energy acceptance for horizontal emittance of 0.3 nm-rad and vertical emittance of 0.008 nm-rad.

Detailed calculations in Section 6.2.6 show features similar to those discussed in this chapter, supporting the assertion that reduction of the horizontal beam emittance at NSLS-II will not adversely affect the beam lifetime.

At the same time, any reduction of the energy acceptance for NSLS-II would have a substantial impact: a 19% reduction of the energy acceptance reduces the lifetime by a factor of two. Because of this, intense and detailed studies of the effects of the lattice and insertion devices on the beam lifetime were carried out, as reported in Chapter 6.

4.2.3 Collective Effects

Collective effects, described in detail in Section 6.2, have two distinct subgroups: instabilities and effect on the beam parameters (IBS and lifetime). We touched on the latter in the previous section. In this section, issues related to beam instabilities will be briefly reviewed.

The studies of beam instabilities were based both on well-established theoretical estimations as well as on detailed calculations of specific impedances using the code GdfidL for the most convoluted structures (such as RF cavities and ID transitions). GdfidL was also used intensively for calculating the impedance budget for the ring with resulting longitudinal impedance values of $(Z/n)_o \sim 0.4\ \Omega$.

The impedance model was used for estimating instability thresholds or their growth rate for the following: CESR-B SRF cavity, 720 m of Al vacuum chamber with ±12.5 mm vertical gap, 60 meters of copper shielding for in-vacuum undulators with gap of ±2.5 mm, and transverse (1 MΩ/m; Q = 1, 30 GHz) and longitudinal (R_s = 30 kΩ, Q = 1, Z/n = 0.4 Ω) broadband impedances to represent transitions and other imperfections in the vacuum chamber.

The studies of instabilities were performed for the most conservative case of short electron bunches (i.e., without the use of harmonic cavities). These conservative estimates predict that an electron beam with the NSLS-II parameters will be stable, with only one exception: the transverse coupled bunch instability has a threshold ~15 mA (with 500 mA required) at zero value of vertical chromaticity (see Section 6.2.3.3 for details). The studies using computer tracking predicted that increasing the chromaticity to at least +4 will stabilize the 500 mA beam. Being prudent, we include a well-known multi-bunch feedback system in the list of instrumentation for the NSLS-II storage ring. This feedback system will guarantee the suppression of this and other multi-bunch instabilities.

References

[4.1.1] T. Shaftan, J. Bengtsson and S. Kramer, "Control of Dynamic Aperture with Insertion Devices," http://accelconf.web.cern.ch/AccelConf/e06/PAPERS/THPLS091.PDF

[4.1.2] J. Safranek, "Experimental Determination of Linear Optics Including Quadrupole Rotations," http://accelconf.web.cern.ch/AccelConf/p95/ARTICLES/FAB/FAB11.PDF; also, J.A. Safranek, "Beam-Based Accelerator Modeling and Control," Proc. of Beam Instrumentation Workshop 2000, AIP Conf. Proc. 546, pp. 23–34.

[4.1.3] S. Krinsky, J. Bengtsson, and S. Kramer, "Consideration of a Double Bend Achromatic Lattice for NSLS-II," http://accelconf.web.cern.ch/AccelConf/e06/PAPERS/THPLS090.PDF

[4.2.1] NSLS-II CD-0 proposal, http://www.bnl.gov/nsls2/docs/PDF/NSLS-II_CD-0_Proposal.pdf

[4.2.2] S.L. Kramer, and J. Bengtsson, "Dynamic Aperture Optimization for Low Emittance Light Sources," http://accelconf.web.cern.ch/AccelConf/p05/PAPERS/RPAE057.PDF; and J. Bengtsson, "Control of Dynamic Aperture for Synchrotron Light Sources," http://accelconf.web.cern.ch/AccelConf/p05/PAPERS/MPPE020.PDF

[4.2.3] http://sls.web.psi.ch/view.php/about/index.html

[4.2.4] J. Murphy, *Data Book on Synchrotron Light Sources*, ver. 4, May 1996, BNL 42333, Upton, NY.

[4.2.5] J. LeDuff, "Single and Multiple Touschek Effects," Proc. of CERN Accelerator School, Rhodes, Greece, 20 Sept. – 1 Oct., 1993; Ed.: S.Turner, CERN 95–06, 22 November 1995, Vol. II, p. 573.

[4.2.6] V.N. Litvinenko, "Review of Ring-Based Light Sources," Proc. of ICFA Future Light Sources Workshop, April 2–5, 1999, APS, Argonne, IL.

5 INJECTION SYSTEMS

5.1 Introduction

The NSLS-II injection system must meet several user requirements:

- maintain a stable level of the ring current in order to maintain a constant intensity to experiments and heat load on beamline optics
- minimize frequency of interruptions of user experiments, especially for those involving long scans that cannot accommodate interruptions in beam intensity
- minimize the disturbance of the beam during and immediately after injection due to the residual orbit perturbation from an incompletely closed injection bump and/or transients in fast magnets
- minimize bunch-to-bunch variation of current in order to minimize intensity-correlated orbit oscillations due to uneven bunch patterns [5.1]
- fill the storage ring from zero to full charge in a minimum amount of time

These requirements must all be accomplished in a way that is as transparent to the users as possible. They are summarized in Table 5.1.1.

Table 5.1.1 User Requirements.

Stability of average current	<1%
Time between injections	>1 min
Bunch-to-bunch variation of current	<20%
Time to fill ring from zero to full charge	<5 min

To achieve these requirements, NSLS-II will utilize a full-energy injection system that will operate in top-off mode with minimal disturbance to the circulating beam. The technical specifications for the NSLS-II injection system are summarized in Table 5.1.2.

Table 5.1.2 Storage Ring Parameters Related to the NSLS-II Injector.

Parameter	Value
Energy [GeV]	3.0
Circulating current [A]	0.5
Circumference [m]	780
Revolution period [μs]	2.6
RF frequency [MHz]	499.46
RF wavelength [m]	0.6
Circulating charge [μC]	1.3
Total number of buckets	1300
Number of filled buckets at 80% filling	1040
Charge per bucket [nC]	1.25
Current per bucket [mA]	0.48
Lifetime [min]	180
Interval between top-off cycles [min]	1
Current variation between top-off cycles [%]	0.55
Current variation between top-off cycles [mA]	2.75
Charge variation between top-off cycles [nC]	7.15

As follows from Table 5.1.2, the NSLS-II injection system must supply approximately 7 nC of charge once per minute, assuming a lifetime of 3 hours. For single-bunch injection mode and a moderate repetition rate of a few Hz, replenishing this amount of charge would take a few seconds, occupying a significant fraction of the overall beam time. Therefore, multi-bunch injection is adopted, leading to minimal disturbance for user experiments and lower power consumption by the injection system.

The main ring contains 1,300 RF buckets at 500 MHz. To alleviate the problems of ion trapping in the stored electron beam, approximately 1/5 of the buckets must be left empty. The exact number of buckets to fill is difficult to predict and will be determined empirically during commissioning. Feedback systems and the ultimate vacuum conditions in the ring will determine what requirements will be imposed on the bunch structure. In any case, to keep the current constant with high accuracy, considerable flexibility and accuracy must be built into the bunch transfer timing system, the single-bunch capability, and the current and bunch structure measurement system of the main ring.

5.1.1.1 Injection Sequence

The initial fill occurs at the rate of 1 Hz, and nominally 40 bunches are transferred to the main ring nominally at each injection (this number can be increased to 100 or more bunches) to fill consecutively 1,040 of the 1,300 RF buckets available. Bunch trains from the injector enter the ring in sequence, starting with the front of the ring train and stepping sequentially back in time along the ring train until the end is reached, then skipping over the empty section and starting again at the head of the train, until the required current has been established.

Assuming the same amount of charge per injection (7 nC per bunch train) as for top-off mode, the duration of the initial fill will be about 3 minutes with the injection system running at a 1 Hz repetition rate.

5.1.2 Ring Injection Scope

There are several possible basic schemes for the injection system that can meet the requirements stated above. One is to use a full-energy linear accelerator, which would require no booster synchrotron at all; another is to use a booster synchrotron fed by a small linac.

A full-energy linac would provide flexible injection operations and present no technically challenging problems. The disadvantage would be the high cost for the linac and the additional cost of a building to house the linac and transport line. In addition, a full-energy linac is likely to have a lower reliability and higher operations cost than a full-energy booster. A high reliability injection system is especially important for NSLS-II, given its short beam lifetime. For these reasons, a full-energy booster was selected as the NSLS-II injector.

Two approaches were considered for the design of the NSLS-II booster. In the first, a "compact" booster design was developed [5.2] and its cost was estimated. It was shown that a booster of 170 meters circumference, housed in a separate building, could satisfy the requirements for injection into the storage ring. In the second approach, the booster was located in the storage ring tunnel. This results in a much larger circumference for the booster, but most of this is taken up by small stainless steel vacuum pipe. Comparing both approaches revealed a substantially higher total cost for the compact booster due to the extra costs of constructing and shielding a separate building to house it. Therefore, the NSLS-II design employs a booster in the same tunnel and with the same circumference as the storage ring.

The large circumference of the booster (780 m) has the added benefit of simplifying injection and extraction. Due to the long revolution periods (2.5 μsec) of both the booster and the main ring, rise and fall times of the pulsed magnetic components are quite relaxed. It also results in a relaxed booster lattice together with excellent quality of the extracted beam at 3 GeV.

On the other hand, the large booster circumference necessitates keeping the energy of injection into the booster sufficiently high to avoid beam losses at injection, for example, due to gas scattering. The 200 MeV linac is thus specified for injection into the booster.

Two transport lines will be constructed: one to connect the linac to the booster and a second to connect the booster to the main ring. A full set of beam diagnostics will be installed for commissioning and routine operations of the injection system.

In this section we describe all the components of the NSLS-II injection system in the following order: linac and electron gun, linac-to-booster transport line, and booster with booster-to-storage ring transport line.

5.2 Linac

5.2.1 Scope

The NSLS-II storage ring requires approximately 7 nC of charge to be delivered in top-off mode once every minute to replace charge lost through Touschek scattering. This charge should be delivered in a single booster cycle, so that the storage ring beam is disturbed only for the duration of the ring damping time (tens of milliseconds) each minute. Details of this will be presented later in this section. In addition, future storage ring requirements may include single camshaft bunch or timing bunches for user experiments or machine studies. To meet these requirements, two modes of linac operation are envisioned: single-pulse mode with about 1 nC charge per bunch, and multi-bunch mode, where a few tens of bunches of more than 100 pC of charge are delivered.

To have sufficient lifetime in the booster at injection in the presence of gas scattering, an energy of 200 MeV is specified for injection into the booster. To inject bunch trains into a booster with a 500 MHz RF system, a 3 GHz linac bunch structure must fit into the booster buckets of ~1 ns length, separated by 2 ns.

The booster is located in the same tunnel as the storage ring, which results in a large booster circumference. To minimize the booster cost, the aperture of the magnets is kept small. To keep the injection efficiency high given the small magnet aperture, a reasonably small emittance is required. Likewise, a small energy spread is needed to prevent beam loss in the high-dispersion regions of the booster lattice. An

additional requirement is that the linac be able to provide sharp edges to the electron bunch train, to avoid injecting electrons into the ion clearing gap.

Thales and ACCEL have produced turn-key linac systems for Soleil and Diamond, respectively. The Soleil linac, using CERN "LIL" 3.5 m structures, has a smaller energy spread that meets the NSLS-II design specification. An approach similar to the Soleil linac is used as a baseline and described below (Figure 5.2.1). The Diamond injector uses the DESY 5.2 m accelerator structures, resulting in a slightly longer linac. To keep both options open in the preliminary design phase, the linac building has been designed to accommodate either four 5.2 m tanks or five CERN 3.5 m structures.

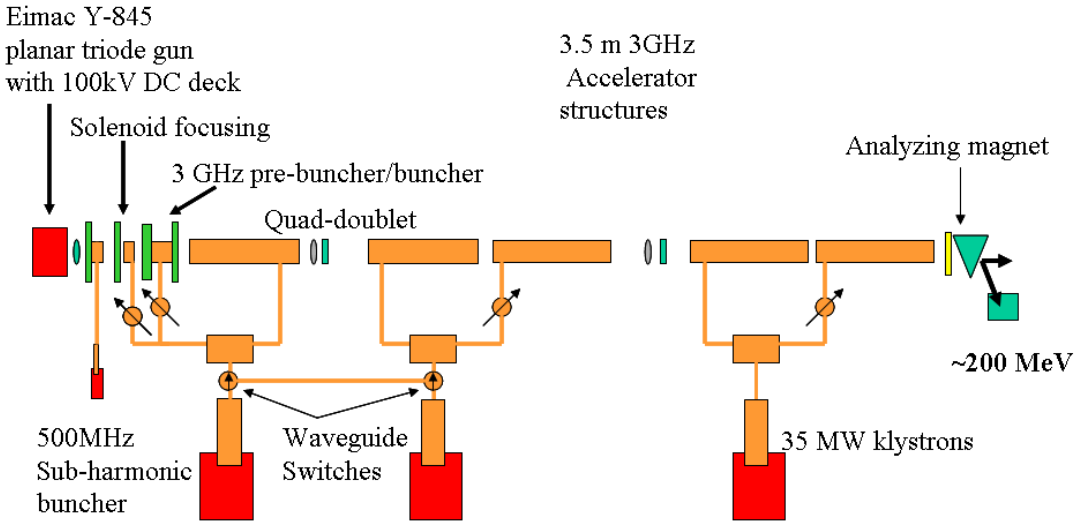

Figure 5.2.1 Layout of the 200 MeV linear accelerator.

The injector consists of the following subsystems:

- 100 kV triode gun (e.g., Eimac Y-845) with a 500 MHz modulation at the gun grid and high-voltage deck
- four shielded lenses, situated between the gun and the buncher
- a 500 MHz subharmonic pre-bunching cavity with ± 25 kV modulation
- a 3 GHz pre-bunching cavity with ± 10 kV modulation (100 W power)
- a 3 GHz stationary wave buncher surrounded by two shielded coils (1.2 m long, 5.5 MW, energy gain of 15 MeV)
- five traveling wave-accelerating structures at 3 GHz in the $2\pi/3$ mode and with a length of 3.5 m (flange to flange)
- a Glazer lens between the buncher and the first accelerating structure
- two focusing doublets
- three Klystrons (TH2100, 35 MW) and their modulators.
- low-level RF controls

5.2.2 Physics Design and Parameters

Although a range of parameters will meet the requirements, we focus here on a specific case of approximately 200 pC per bunch in bunch trains of 40 bunches, to provide details on the injector design. Allowing for faster initial fills and for losses in the injection process, a sufficient margin will be considered at the detailed linac design stage.

The energy spread must be controlled throughout the acceleration process. The maximum horizontal size of the beam injected into the booster (Section 5.5) is dominated by the energy spread. For $\varepsilon = 100$ nm-rad (2σ emittance) and maximum $\beta_x = 25$ m, the zero-dispersion beam size is 1.6 mm. At the maximum dispersion, $\eta = 0.75$, and energy spread, $\Delta E/E = 0.5\%$, the contribution to beam size is $\Delta\sigma_x \approx \eta\Delta E/E \approx 3.75$ mm.

Recent experience at SOLEIL [5.3] has shown that industry can produce turn-key linac systems that meet these specifications. Because the approach taken may differ significantly from one machine to the next, only the salient points of a generic linac are presented.

A planar triode electron gun, the EIMAC Y845 [5.4], is used with a fast-pulser cathode driver. In single-bunch mode, the cathode is pulsed to create ~1 ns pulses of ~0.5 nC. The DC gun inherently has small energy spread. However, to compress the gun pulse for acceleration in the 2.998 GHz linac and capture it in the 500 MHz booster RF, we need to prevent nonlinearities in the RF from increasing the energy spread beyond the 0.5% (RMS) requirement. This translates into a requirement on the length of the micro-bunches exiting the linac to be less than 11 ps.

To create these short bunches, a bunching system is required. First, a 500 MHz subharmonic buncher is used to compress the charge into bunch lengths less than 1 ns to match the 500 MHz booster bucket. This is followed by a 2.988 GHz pre-buncher that micro-bunches the 1.5 ns bunch train to $\leq$ 11 ps bunches within the linac buckets. A final buncher simultaneously accelerates the electrons to 3 MeV to increase capture efficiency. In bunch-train mode, the cathode is pulsed on for the duration of the train, up to 200 ns, and is bunched in the process described above. During the preliminary design phase, system performance will be confirmed by E-Gun [5.5] and Parmela [5.6] simulations, and cathode driver experiments at the NSLS electron gun test stand.

The main accelerator is comprised of 3 GHz traveling wave structures, with an energy gain of:

$$E[MeV] = 12.5\sqrt{P[MW]} \tag{5.2-1}$$

The accelerating structures being considered obtain 52 MeV per tank for an input power of 17.5 MW. Using readily available 35 MW klystrons, the first klystron is power split, with about 5.5 MW feeding the 3 GHz pre-buncher and buncher. The latter has an energy gain of more than 15 MeV. The remaining power feeds the first linac structure. Individual waveguide phase shifters and attenuators are used for adjusting amplitude and phase between elements.

The remaining four tanks are powered by two klystrons for an energy gain of an additional 52 MeV each. Thus, a total of 255 MeV energy gain is possible. For redundancy, two waveguide switches can connect the second klystron to power the two bunchers and first tank. In this scheme, an energy of 170 MeV can be achieved if one klystron fails. This will be explored in the preliminary design phase.

The bunch charge and train current—although not beyond that which has been achieved in other applications [5.3, 5.7]—is sufficient to warrant close attention to beam-loading issues. For traveling wave tanks, the voltage induced along the bunch train on short time scales (compared to the fill time of the cavity) is given by:

$$V_b = -ir_0L[(1-\tau^{-1})(1-e^{-x\tau}) + xe^{-x\tau}] \tag{5.2-2}$$

where r_0 is the shunt impedance, τ the attenuation constant in nepers, L the length of the tank, and x the ratio t/t_f, where t is the time duration of the macro-pulse and t_f the fill time of the structure.

For forty 200 pC bunches separated by 2 ns (100 mA), this corresponds to about 2% in the correlated energy spread along the bunch train. There are several methods of reducing this beam loading. For a given beam current, the beam loading compensation can be achieved by sending the beam during the filling time of

the second structure. This approach has been successfully implemented at SOLEIL [5.7] for a 300 ns long train current of 9 nC. Alternatively, the effect of beam loading can be diminished by lengthening the macro-pulse, either by simply lengthening the pulse and proportionally reducing the charge per bunch, or by pulsing the gun once every fourth, sixth, or eighth 500 MHz bucket with constant charge per bunch to reduce the effect by the corresponding factor. For example, by filling every sixth ring bucket (12 ns bunch separation), the average current is 21mA and the energy spread due to beam loading drops to 0.4%. This last method may require a sophisticated cathode modulation system, which has not yet been developed.

5.2.3 Klystron Modulators and Power Supplies

Pulsed 3 GHz high-power klystrons are a mature technology and several manufacturers can meet or exceed the 35 MW power requirement. The klystrons are powered by pulsed modulators. The traditional approach is to use Pulse Forming Networks with hard-tube (thyratron) switches to produce RF pulses between 2 and 4 microseconds long. NSLS has recently designed and built such a modulator for the 45 MW tube installed at its DUVFEL facility. Our own experience and studies of reliability at SLAC/PEP-II and Pohang Light Source have shown that the Mean Time Between Failure and Mean Time To Repair of the PFN/hard tube modulator dominate the linac downtime, with rates three times those of the klystron tube and its filament/core bias power supplies [5.8, 5.9]. For this reason, solid-state modulators are being explored for NSLS-II. Several competing designs have been developed for both medical linacs and the X-band International Linear Collider. One such example is the design by Scandi-nova [5.10], which uses a multi-turn primary pulse transformer, reducing the modulator voltage from about 40 kV to 3 kV, further increasing reliability by limiting the high voltage to only the pulse transformer and klystron cathode assembly in the oil tank [5.11]. These systems are also between one-half and one-third the size of similar PFN-type modulators. The decision to use a solid state or a PFN-hard tube modulator will be made during the preliminary design phase.

The 500 MHz subharmonic pre-buncher requires about 6 kW (for a shunt impedance of 250 kΩ) to reach 36 kV. This is well within the range of solid-state RF amplifiers.

The 3 GHz pre-buncher is a single cell with ±10 kV modulation, requiring only 100 W of RF power.

The 3 GHz final buncher is a standing wave structure, requiring 5.5 MW of RF power, and delivering an energy gain of 15 MeV.

The low-level RF can be a duplicate of the DUVFEL RF system [5.12], with a master clock in common with the booster and storage rings driving a 2.988 GHz DRO-based synthesizer whose output is split and feeds direct I/Q modulators for the amplitude and phase control of the individual klystrons. The 500 MHz will be derived from the booster RF that is synthesized in a similar way. Complimentary I/Q demodulators can be used to down-convert to baseband and close amplitude and phase loops around the cavity fields.

5.3 Beam Transport to Booster

This section describes the transport line from the injector linac to the booster. This transport line contains a complete set of diagnostics required for commissioning, operation, and maintenance of the linac.

5.3.1 Structure of the Linac-to-Booster Transfer Line

The linac is located on the same level as the booster. In the next phase of design we will determine whether the linac is installed on floor supports or suspended from the ceiling.

The transfer line from the linac to the booster is shown schematically in Figure 5.3.1. The first bending magnet deflects the electron beam toward the booster and will be used as an energy spectrometer. When the

magnet is switched off, the electron beam does not enter the ring tunnel. This design allows early commissioning of the linac, while the assembly of the booster and ring is ongoing. Twiss parameters in the transport line are matched to those in the booster injection point.

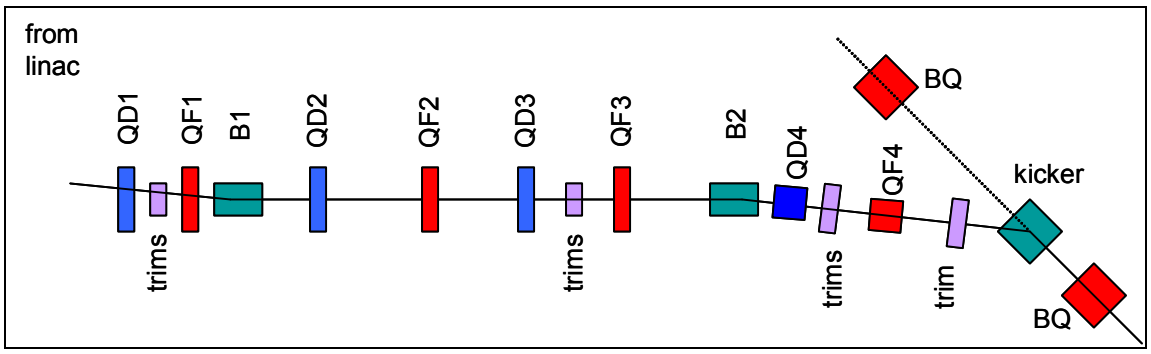

Figure 5.3.1 Layout of the linac-to-booster transfer line.

The machine functions of the transfer line are shown in Figure 5.3.2. Four pairs of correctors provide adjustment of the electron trajectory in the transport line and proper aiming of the injected beam. The main parameters of the magnetic elements are listed in Table 5.3.1. The injection kicker is installed just before the booster quadrupole in the injection straight. The kicker is of the same design as that used in the storage ring.

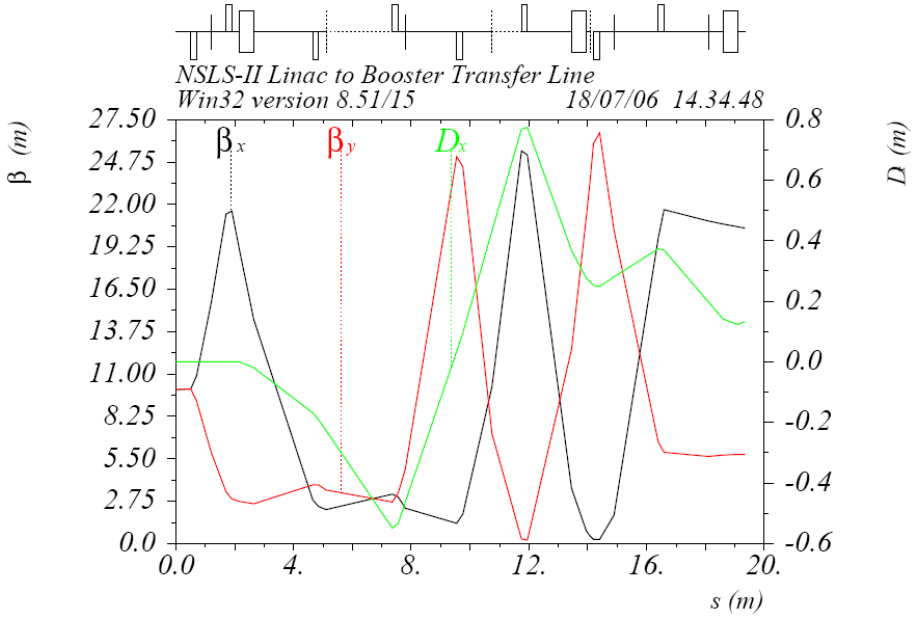

Figure 5.3.2 Beta and dispersion functions of the linac-to-booster transport line.

Table 5.3.1 Magnet Characteristics.

	Dipole	Quadrupole	Kicker	Corrector
Number required	2	8	1	4
Field strength at 200 MeV	0.8 T max	3 T/m max	0.2 T	
Effective length [m]	0.5	0.2	0.5	0.2
Gap height or diameter [mm]	50	50	50	50

5.3.1.1 Linac-to-Booster Power Supplies

Four families of power supplies will power the magnets that provide the pathway from the 200 MeV linac to the booster. The power supplies (listed in Table 5.3.2) are connected to two dipoles, four quadrupole pairs, and four vertical / horizontal correctors.

Table 5.3.2 Linac-to-Booster Power Supplies.

Function	Quantity	Volts	Amps
Dipole	2	20	300
Quadrupole	8	6	200
Trim	8	20	20

The supplies will stay at the nominal setpoint only during the ring fill. For energy savings, it is anticipated that the supplies' output will be lowered during the dwell time in top-off mode and brought back to the operating point slightly before the fill cycle.

5.3.1.2 Power Supply Control

Each transfer line power supply will be set by its analog programming interface. Either a micro-controller or PLC could be used to control the supply. Analog output voltages from the control system will be used to control the current setpoint of the supply, and the digital-to-analog converter will have a resolution of at least 16 bits. Both supply output voltage and current will be read back by medium-speed analog-to-digital converters with a resolution of 16 bits. Monitoring of the supply outputs should be able to detect transients as short as 1 ms. Long-term monitoring of drift will be done by an independent external shunt connected to a high-precision analog channel.

5.3.1.3 Interlock

An external power distribution unit will be installed in each power supply rack and will contain a primary contactor that can be controlled remotely and independently. This contactor will be controlled by the personal safety system and will be independent of the power supply controller. Each power supply will have its own circuit breaker and power receptacle. The breaker will be sized to withstand turn-on in-rush power and to limit steady-state current to the line cord rating.

5.3.1.4 Dipole Power Supply Specification

Two dipole bending magnets are used to deflect the beam into the booster. The magnets are 0.5 m long, operate at 0.8 T, and have a 50 mm aperture. The proposed coil configuration has an electrical resistance of 42 mΩ and will be run at 250 A and 10.5 V. The supply selected is a 6 kW unit capable of producing 300 A and 20 V.

5.3.1.5 Quadrupole Power Supply Specification

There are four pairs of focusing and defocusing quadrupoles, each powered by a separate power supply. The magnets are 0.2 m long, operate with a gradient of 3.0 T/m, and have a 50 mm aperture. The proposed coil configuration is air-cooled and has an electrical resistance of 16 mΩ, operating at 150 A and 2.4 V. The supply selected will be capable of supplying 200 A and 6 V.

5.3.1.6 Corrector Power Supply Specification

Each of the four corrector magnets has separate horizontal and vertical coils, powered by separate supplies. The magnets are 20 cm long and have a resistance of 50 mΩ and inductance of 13 mH. Each magnet is connected to its supply with #10 AWG wire and is expected to be within 100 feet of the load for a lead resistance of less than 20.4 mΩ. The magnets will be powered by linear bipolar power supplies capable of supplying 20 A and 20 V.

5.3.1.7 Kicker Power Supply Specifications

A high-voltage power supply designed to operate in constant current mode will charge the HV capacitors of pulse-forming networks. Injection kicker specifications are described in more detail in Sections 5.9 and 5.10.2.

5.4 Diagnostics/Instrumentation for Linac

Table 5.4.1 shows beam diagnostics for the electron source, linac, and transfer line to the booster.

Table 5.4.1 Linac Diagnostics.

System	Quantity	Monitor Type	Measured beam parameter
Electron source	3	Wall current monitor	intensity, longitudinal beam characteristics
Linac	3	Fluorescent screens	position, profile
	2	Current transformers	intensity
Linac-to-booster transfer line	5	Fluorescent screens	position, profile
	1	Current transformers	intensity
	2	Faraday cup	intensity
	3	4-button pick-ups	position

5.4.1 Electron Source Instrumentation

The gun diagnostics consist of three resistive **w**all **c**urrent **m**onitors to observe the longitudinal profile of the electron bunches after the gun, pre-buncher, and buncher. The WCM is formed by equally spaced broadband ceramic resistors mounted on a flexible circuit board, wrapped around a short ceramic break [5.13].

5.4.2 Linac Diagnostics

A schematic of diagnostics for the linac is shown in Figure 5.4.1. The bunch charge, produced by the gun and accelerated by the linac, is monitored by two in-flange **i**ntegrated **c**urrent **t**ransformers [5.14]. Placed after the first section and at the linac exit, the current transformers will monitor beam losses in the linac. Three flags installed between the linac tanks will be used to observe the transverse profile and the position of the electron beam [5.15].

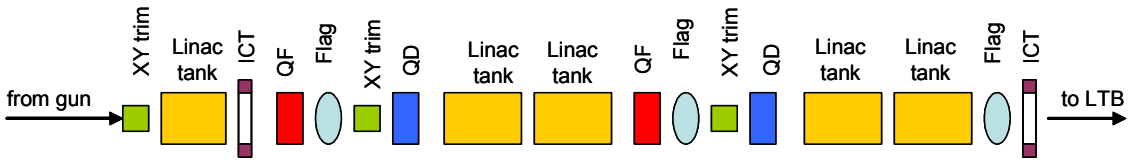

Figure 5.4.1 Schematic of the linac diagnostics.

5.4.3 Linac-to-Booster Transport Line Diagnostics

The linac-to-booster transport line is shown schematically in Figure 5.4.2. The first bending magnet is used to steer the beam either to the booster or to an energy spectrometer or emittance measurement set-up. The beam dumps will include Faraday cups for charge measurement.

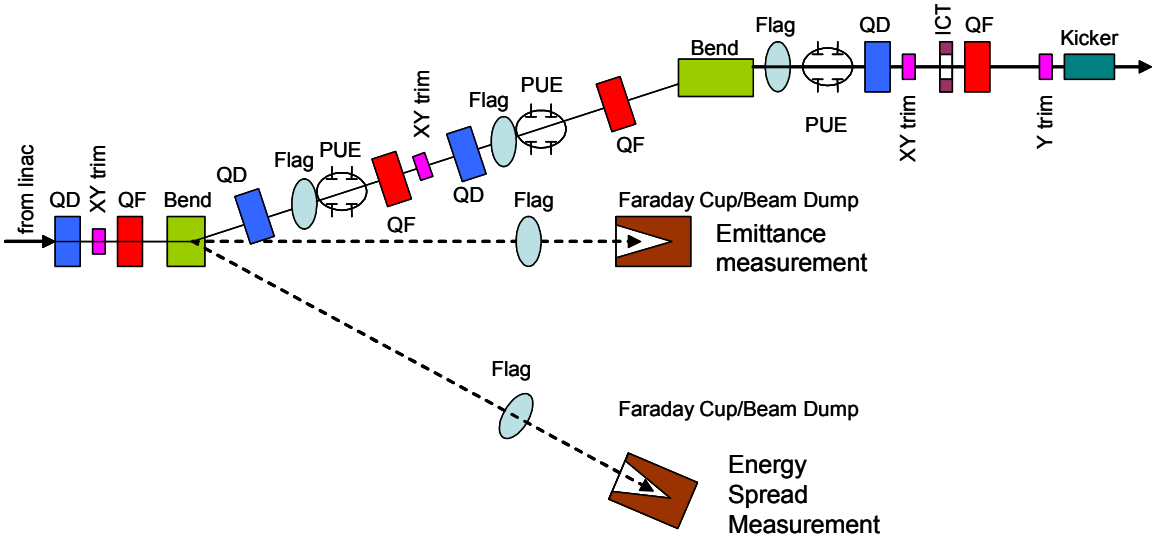

Figure 5.4.2 Diagnostics for the linac-to-booster transport line.

Three flags in the transport line itself will be used to measure electron beam size and position. The beam trajectory during normal operations is monitored by three pick-up electrodes equipped with log-ratio beam position monitors [5.16, 5.17]. An ICT will measure the amount of charge passing through the transport line.

5.5 Booster

The NSLS-II booster is required to produce a 3 GeV bunch train with a charge of about 7 nC at a repetition rate of 1 Hz and a geometric emittance below 30 nm-rad. Injection in the booster ring takes place at an energy of 200 MeV. The booster magnetic field and RF voltage are ramped for 400 ms to accelerate the electron beam from the injection energy to the nominal energy of 3 GeV. At the highest point of the ramp, the electron beam is extracted from the booster and injected into the main ring.

Two alternative booster configurations were considered during the NSLS-II booster design. A compact booster, residing in a separate building, was compared with a booster sharing the same tunnel with the storage ring. Comparison revealed a substantially higher cost for the compact booster due to the cost of constructing and shielding a separate building. Therefore, a booster located in the storage ring tunnel was selected.

The concept of placing the booster in the same tunnel as the storage ring was suggested and successfully implemented at the Swiss Light Source (SLS) [5.18, 5.19, 5.20]. This layout was subsequently adopted by other facilities, namely CANDLE [5.21] and ALBA [5.22], and is being considered for the Taiwan Light Source [5.23]. The main advantages of such a layout are in the low cost of lattice elements—together with relaxed tolerances for their design and installation, low power consumption, and excellent output beam parameters. The main disadvantages are an inability to service the booster independently from the main ring, and the potential impact of stray fields from the ramping booster magnets on beam orbit in the storage ring. The success of the SLS injector, which has achieved nearly 100 percent injection efficiency, has shown the same-tunnel booster design to be highly reliable and optimal in cost and performance.

Two alternatives were considered for placing the NSLS-II booster with respect to the storage ring. In the SLS case, the booster is positioned on the inner wall of the storage ring tunnel. The main disadvantage of this layout is the extra cost due to increasing the width of the storage ring tunnel to accommodate the booster ring. In addition, the booster-ring transport line blocks the pathway between the two rings on a scale of tens of meters. Also, the requirement that the inner wall be sufficiently rigid and stable increases construction costs. Consequently, the NSLS-II booster will be placed 1.5 m above the main ring. This is sufficient to not interfere with the ring subsystems and yet still allow easy access to the booster elements for installation and commissioning.

Putting the booster above the storage ring motivates a special arrangement of the booster magnets to provide accessibility for installing insertion devices. It is important not to place the booster elements above the storage ring straight sections. In turn, this defines the symmetry of the booster lattice to be identical to that of the storage ring. In addition, optimization of the overall system cost requires the number of magnetic elements and power supplies for the booster lattice to be minimal.

The design of the booster provides an effective solution that can meet the requirements of the NSLS-II injector.

5.5.1 Lattice

Based on the considerations discussed in the introduction to this chapter, the booster lattice incorporates 60 dipoles, with additional focusing magnets. All booster magnets are arranged to avoid having them above the storage ring straight sections (Figure 5.5.1). A single period consists of only a small number of magnetic elements, similar to that of the existing NSLS booster [5.24].

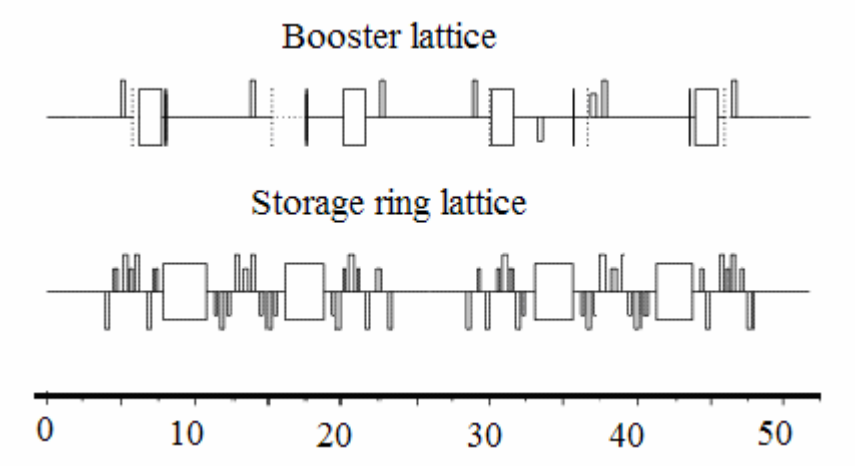

Figure 5.5.1 Layout of the booster and the ring periods plotted on the same scale (meters).

The lattice is designed with twelve identical cells together with three modified cells containing families of quadrupole correctors. Phase advances per cell are chosen as 74° and 40° for horizontal and vertical planes,

respectively. This results in a sufficiently low horizontal emittance of 11.5 nm-rad at the nominal energy of 3.0 GeV. The booster lattice is presented in Figure 5.5.2.

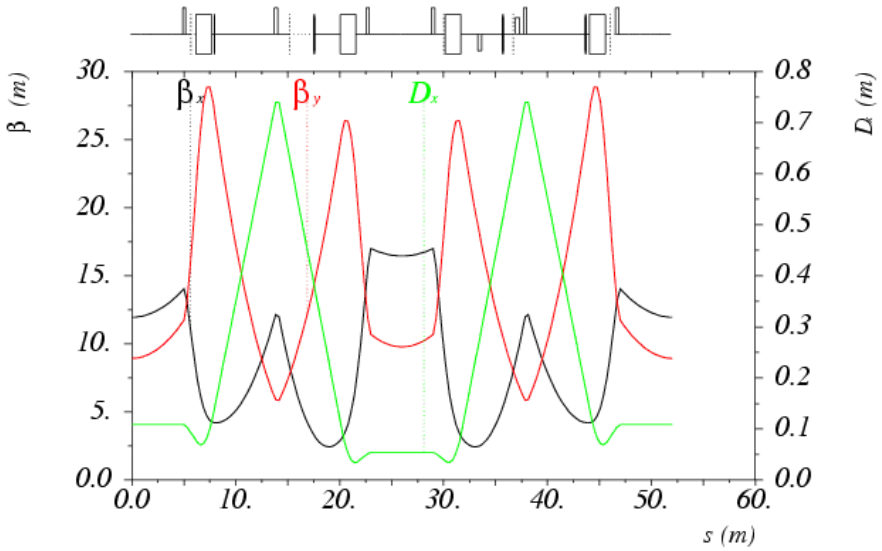

Figure 5.5.2 A single period of the booster lattice.

The lattice consists of 30 long (6 and 10 m) straight sections with low dispersion (less than 15 cm) suitable for installation of RF cavity, injection, and extraction systems. Due to the sparse lattice structure and long circumference, dispersion grows to a relatively high value, which simplifies chromaticity correction. Beta-functions are limited to 30 m, which corresponds to the maximum injected beam size of about 2 mm RMS in the vertical plane.

The lattice is composed of a single family of combined-function dipoles together with two families of quadrupoles, Q1 and Q2. Two separate power supplies for the booster quadrupoles provide the freedom to optimize the lattice and control tunes, dispersion, and chromaticity. A regular cell is shown in Figure 5.5.3a. An additional six weak quadrupoles QC (K_1 <0.5 m^{-2}) are distributed in three super-periods (two per super-period) for fine tuning of the lattice parameters. A modified cell with additional quadrupole correctors is shown in Figure 5.5.3b.

Chromaticity correction is implemented by introducing two sextupoles per booster super-period, shown as SF and SD in Figure 5.5.3. Separate power supplies for both sextupole families enable independent adjustments of horizontal and vertical chromaticity. The possible merging of sextupoles and quadrupoles in the dispersive region into a single combined-function magnet will be addressed in future optimization of the booster lattice.

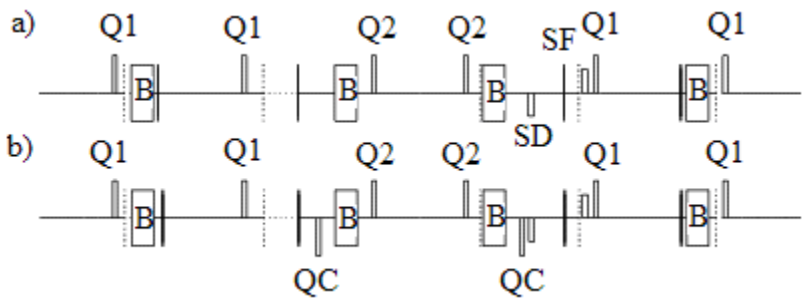

Figure 5.5.3

a Regular cell.

b Cell with quadrupole correctors.

B = bends; Q1, Q2 = main quadrupoles; SF, SD = sextupoles; QC = quadrupole trims; dashed line = beam position monitor; solid line = combined orbit corrector.

A working point in tune space was chosen to avoid low-order resonances (Figure 5.5.4) and to provide a large dynamic aperture. Also, the chosen tunes favor smaller orbit amplification factors.

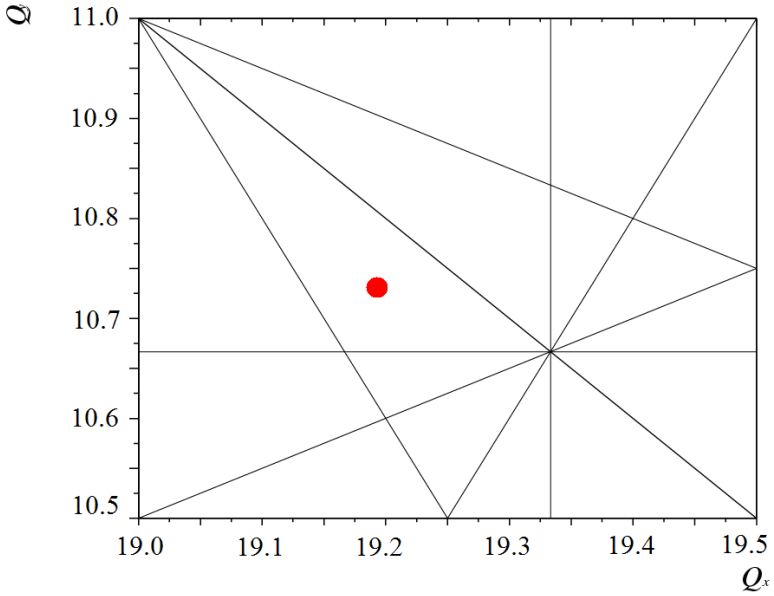

Figure 5.5.4 Working point on the tune diagram, including resonances up to the third order.

The computed DA for the bare lattice is shown in the left panel of Figure 5.5.5. The lattice tunes were chosen according to the tune scan shown in the right panel of Figure 5.5.5. Optimization of the DA has led to a sufficiently large value: the developed lattice has a momentum aperture of about ±3% together with a DA of 190 mm-mrad (H) and 140 mm-mrad (V). This is larger than the physical aperture presented by the vacuum chamber (black ellipse in the figure). Optimization of the booster DA was done using the TRACY-2 code. The additional quadrupoles help control the tunes within the area corresponding to about an integer tune.

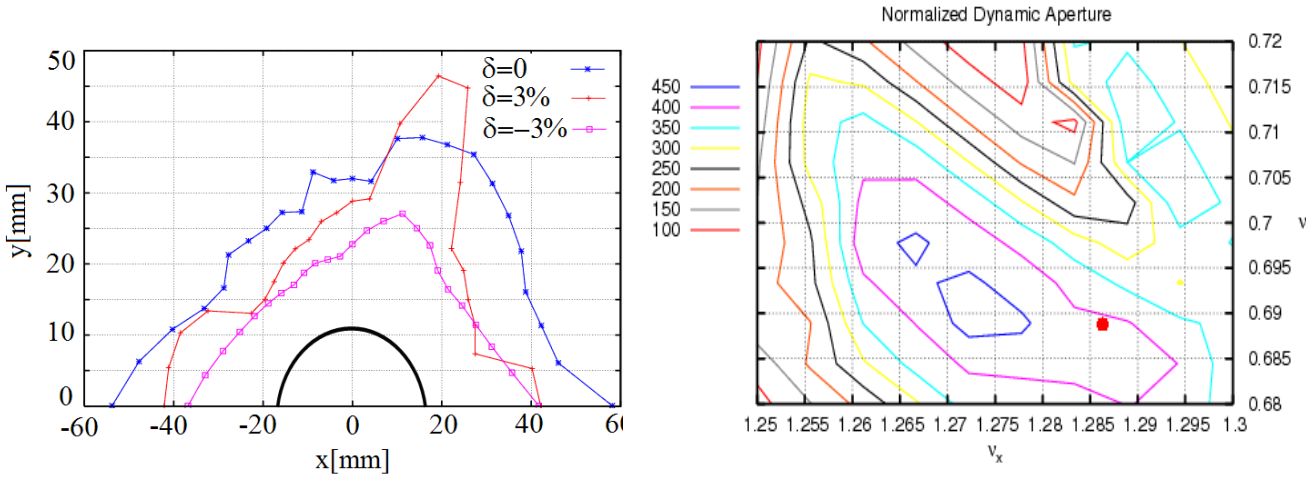

Figure 5.5.5 (left) Dynamic aperture for on-momentum and ±3% momentum deviation tracking. (right) Tune scan used to optimize the DA: a large area of robust solutions is present; the chosen working point is shown as a red circle.

For estimates of chromaticity driven by eddy currents, we used a formalism developed in [5.25]. For the given lattice parameters, the estimated maximum value of the sextupolar moment is 0.66 m^{-3}. Corresponding calculated values of chromaticity are +0.3 horizontally and –2 vertically, which is much smaller than the

natural chromaticity (–21.7 in both planes) and can be compensated by local modification of the sextupole ramp.

Expected RMS beam sizes along the machine are plotted in Figure 5.5.5. These values correspond to parameters of the beam injected from the linac ($\varepsilon_{x,y}$ = 100 nm-rad, σ_γ/γ = 0.5%).

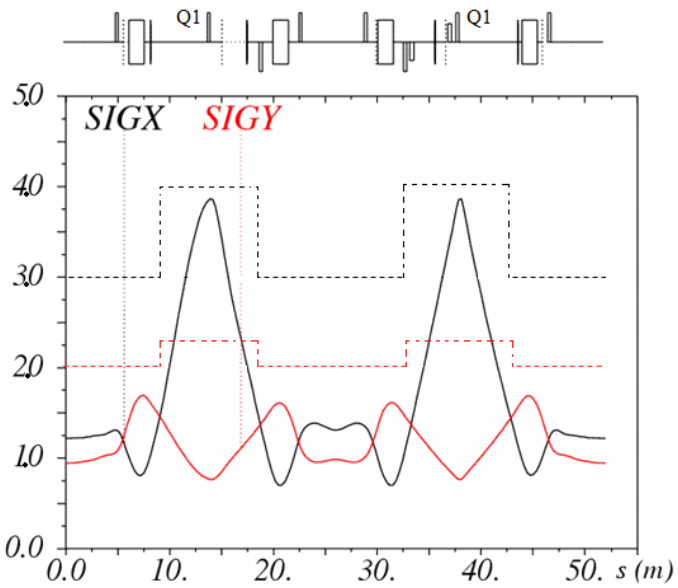

Figure 5.5.6 Injected beam sizes are plotted in mm. Maximum horizontal beam size is determined by dispersion. Dashed lines correspond to the full physical aperture scaled down by a factor of 10.

Note that the maximum horizontal beam size occurs in the quadrupoles Q1, following the behavior of the dispersion function (Figure 5.5.2). Consequently, we increase the size of the vacuum chamber in the dispersive region, providing clearance of about 10 times the RMS size of the injected beam in both planes. Further optimization of the stay-clear aperture will receive attention in our future studies.

The following tolerances for the magnet alignment and fields were assumed (Table 5.5.1). Tolerances on the magnet parameters were developed using analytical estimates that assumed random errors in all magnets. As the table shows, the developed lattice is relaxed with respect to the magnet errors.

Table 5.5.1 Field and Alignment Tolerances for the Booster Magnets.

Parameter	Value
Quadrupole transverse displacement [mm]	0.15
Dipole transverse displacement [mm]	0.15
Relative bend dipole field error [RMS %]	0.1
Relative bend quadrupole field error (corresponding to 0.05 tune shift) [RMS %]	0.9
Relative quadrupole field error (corresponding to 0.05 tune shift) [RMS %]	1
Dipole roll error [mrad]	2
Quadrupole roll error [mrad]	2

Orbit correction is implemented using 75 beam position monitors and 60 horizontal and 60 vertical trim magnets, producing a maximum deflection angle of 1 mrad. The trim fields will follow the energy ramp, enabling orbit correction at all energies. The developed trim–BPM arrangement allows correcting the booster orbit down to a 0.8 mm maximum deviation in each plane. This requires only 0.2 mrad (RMS) in the corrector strength, making its design simple, with low magnet weight and size. This orbit correction system results in alignment tolerances for the dipoles and quadrupoles of 150 μm in displacement and 2 mrad in roll angle.

These tolerances can be relaxed even further, at the expense of slightly larger orbit deviations, by further optimizing the trim arrangement.

The main parameters of the chosen booster lattice are summarized in Table 5.5.2. The parameters of the SLS booster are also listed, for comparison.

Table 5.5.2 NSLS-II (3 GeV) and SLS (2.4 GeV) Booster Lattice Parameters.

Parameter	NSLS-II	SLS
Energy range [GeV]	0.2 – 3.0	0.1 – 2.4
Circumference [m]	780	270
Emittance [nm-rad]	11.5	9
Repetition rate [Hz]	1	3
Mode of operation	multi-bunch	single-bunch
Radiation loss per turn [keV]	500	233
RF frequency [MHz]	500	500
Magnet power [kW]	150	150
RF voltage [MV]	1.0	0.5
Over-voltage	2.0	2.15
RF acceptance [%]	±1	±0.43
Beam current [mA]	3	1
Momentum compaction	5.7×10^{-4}	5×10^{-3}
Tunes: x, y	19.19, 10.73	12.41, 8.38
Chromaticity: x, y	–21.7, –21.7	–15, –12
Damping times: x, y, E [ms]	22, 31, 19	11, 19, 14

The booster circumference is kept the same as that of the storage ring in order to ease synchronization of the injected beam with the stored beam. Accurate computation of the booster ring circumference, including a realistic field model of the magnets, will be a subject of future developments. We will also explore the possibility of reducing the booster circumference by the length equivalent to a single RF bucket, resulting in potential simplification of the ring injection timing.

The large booster circumference increases the cost of the vacuum system. We have chosen the value of the booster vacuum to be at least 10^{-7} Torr on average, providing an elastic gas scattering lifetime of 3.5 seconds at the injection energy, and inelastic gas scattering of more than 15 minutes throughout the energy ramp.

The repetition rate of the booster was chosen to fulfill the injection requirements and maintain low power consumption.

An RF voltage of 1 MV provides an RF acceptance of about 1% at the extraction energy. Damping times are suitable for operation at 1 Hz. Assuming that the beam stays in the machine for about 400 ms, the emittance and the energy spread are fully damped at extraction (Figure 5.5.7).

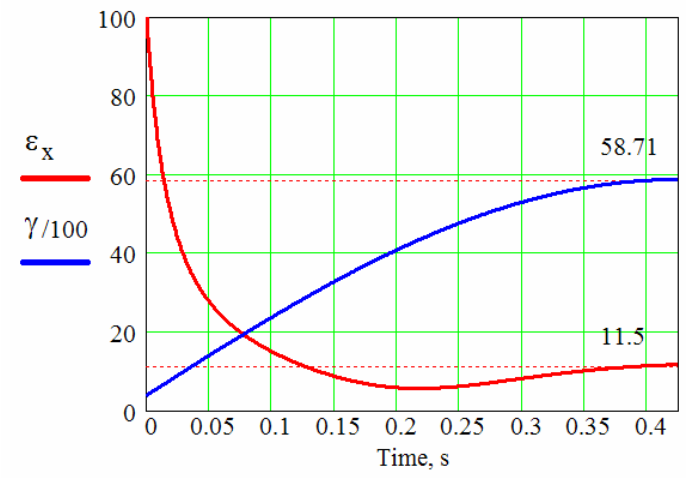

Figure 5.5.7 Evolution of horizontal emittance (red, nm-rad) during energy ramp (blue, scaled down by a factor of 100).

Average booster power consumption is only about 75 kW at 1 Hz and is substantially less in top-off mode, when the booster is required to produce a bunch train only once a minute.

5.6 Conceptual Design of Magnets and Hangers

5.6.1 Booster Ring Magnet Design Considerations

As at SLS, the NSLS-II booster shares the same tunnel as the storage ring. The large booster circumference leaves ample space to accommodate magnets of modest field. Unlike SLS, the booster magnets reside directly over the storage ring; this feature is unique to the NSLS-II design. Because of this, water-cooled magnets would present a source of potential leaks above the main ring. These considerations, together with the goal of minimizing system costs, led us to design for operation without water cooling. The following paragraphs present a summary of the work on individual magnetic components that yielded the physics requirements of the present booster lattice configuration. Optimization and refinements in individual components are anticipated during the next phase of preliminary design. Table 5.6.1 lists some basic parameters for the NSLS-II booster magnets.

Table 5.6.1 Booster Magnet Parameters.

Magnet	Number of magnets	Length, m	Strength
Dipole	60 (1 family)	1.5	0.7 T, –2.1 T/m*
Quadrupole	60 (1 family)	0.3	9.3 T/m
	30 (1 family)	0.3	10 T/m
	6 (3 families)	0.3	<0.5 T/m
Sextupole	15 (1 family)	0.2	200 T/m^2
	15 (1 family)	0.4	200 T/m^2
Orbit corrector	60 (x and y)	0.2	<1 mrad

*Quadrupole gradient in combined-function dipole

The following paragraphs in this section present a partial list of booster magnet design considerations. For the conceptual design these considerations are global in nature and will evolve into more specific parameters during the next phase of preliminary design.

Critical lift and installation safety issues will be of extreme importance because the booster is suspended directly over the storage ring. Handling and rigging safety issues for magnet installation and maintenance

personnel will be addressed and the reference design will be in compliance with the laboratory's critical lift policy.

Electrical and all other safety issues will be addressed during preliminary design. The designs of the magnet, magnet power cable connections, and magnet instrumentation and controls will all comply fully with the requirements of the Nationally Recognized Test Laboratory.

The average current density in the coil section of the booster ring magnets was selected to be less than or equal to 2.5 A/mm^2. Electrical, magnetic, and mechanical design optimization will be performed for the reference design of the 1 Hz, H-type combined function dipole, quadrupole, and sextupole magnets to assess the impact of tunnel temperature on the operation of these magnets and to assure that the air-cooled magnets will function reliably with no chance for thermal runaway.

The NSLS-II booster dipole is a combined-function magnet with quadrupole field component introduced by the shape of the poles. This requirement will affect the sequence of dipole magnet fabrication and installation in the tunnel.

Booster ring magnet reference designs will be developed to minimize fabrication costs, provide high operational reliability, and minimize the power consumption of individual components as well as the overall magnet systems.

To assure precise alignment and field quality of the lattice components, it is necessary to develop reference magnet designs and stable mechanical assemblies. These will be integrated into a standardized, stable, low-vibration kinematic support system that can be safely installed and easily surveyed while suspended from the ceiling of the NSLS-II tunnel.

3D magnetic modeling will be performed to determine what level of impact, if any, ramping of the NSLS-II booster ring may have on beam orbit in the storage ring. The results of this modeling study will be appropriately incorporated into the reference designs for the storage ring and booster ring magnets.

Vacuum chambers will be incorporated into each booster magnet to facilitate modular component installation and enhance the safety and simplicity of magnet installation. Orbit correctors can be assembled around the vacuum chamber and simply secured to the ceiling of the tunnel.

These design concepts and considerations will be refined during the next phase of preliminary engineering design, and engineering prototypes of the reference magnets will be produced and evaluated. The final design will ultimately be implemented by the magnet manufacturer and approved by NSLS-II project staff.

5.6.1.1 Conceptual Design of the Booster Dipole Magnet

5.6.1.1.1 Dipole Magnetic Design Parameters

The NSLS-II booster ring will be equipped with 60 dipole magnets 1.5 m long with 0.7 T field in the nominal gap of ~25 mm, for an electron energy of 3.0 GeV. The dipole magnets are H-type, with a curved laminated yoke. The nominal radius of orbit curvature in the bending magnets is 14.56 m; the electron beam is bent by 6.0 degrees with a beam sagitta of 19 mm. The booster dipoles are combined-function magnets with a quadrupole component permanently superimposed in the dipole field by the pole face geometry. Therefore, the magnet must be curved to match the beam orbit, so that the beam is always on the axis of the quadrupole component. The coil was designed by considering the number of turns, the height of the pole gap, and the specifications of the power supply.

Calculations of the magnetic field were made to optimize the pole contours and the quality of the magnetic field. Due to the low-duty cycle for energy ramping, air-cooled coils may be used with a current density of less than 2.5 A/mm² in the copper conductor. This choice will reduce utility costs and improve the

overall reliability of the NSLS-II magnet system. The magnet yokes are made of AISI 1006 low-carbon steel sheet, 1.5 mm thick. The magnet parameters are listed in Table 5.6.2.

Table 5.6.2 Booster Dipole Parameters.

Dipole length [m]	1.5
Radius of curvature [m]	14.58
Nominal gap [mm]	25
Pole width [mm]	60
Dipole field [T] (injection–extraction)	0.046–0.698
Quadrupole gradient [T/m]	–2.112
Dipole resistance [mΩ]	15
Dipole inductance [mH]	12
Dipole PS peak current [A]	355
Number of turns per pole	20
Square conductor size [mm]	12.7
Tolerances	
On magnetic length, for $\Delta\phi$ = 0.1 mrad [mm]	1.4
On gradient, for $dQ_{x,y}$ = 0.05 [%]	0.9
On x-position, for $\Delta\phi$ = 0.1 mrad [mm]	0.3

To test the feasibility of the booster dipole design, magnetic modeling was performed. Figure 5.6.1 illustrates a 2D magnetic model of the dipole cross-section with the B-field flux shown in light blue lines. The developed design satisfies the specifications listed in Table 5.6.2 within an acceptable margin.

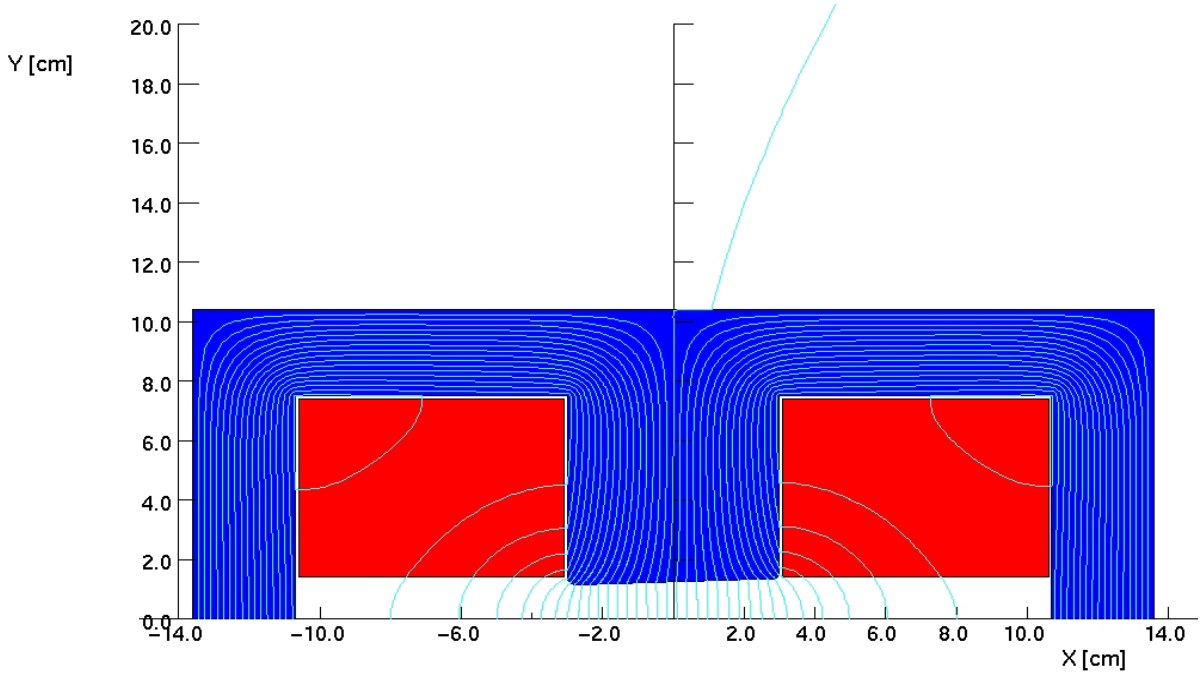

Figure 5.6.1 Dipole magnetic model.

5.6.1.1.2 Mechanical Design of the Booster Dipole Magnet

The dipole laminations are keyed and welded together to form two rigid yoke halves. Bracket yoke clamps are attached to the keys near the parting surface. The mechanical assembly is shown in Figure 5.6.2.

The excitation coils consist of solid copper conductors, 12.7×12.7 mm. The conductor is insulated using layers of fiberglass with a minimum thickness of 0.6 mm around each conductor to form a minimum of 1.2 mm turn-to-turn insulation. An additional 2.0 mm of fiberglass around the outside of the coil forms the ground plane insulation. The coil will be vacuum impregnated with radiation-resistant epoxy resin. The coils will be high-potted up to 5 kV to detect defects in the inter-turn and ground plane insulation of the coil. The coils are installed into the yoke halves and then the yoke halves are keyed and bolted together around a section of booster vacuum chamber. Magnet hanger brackets are attached to the top yoke block in preparation for installation.

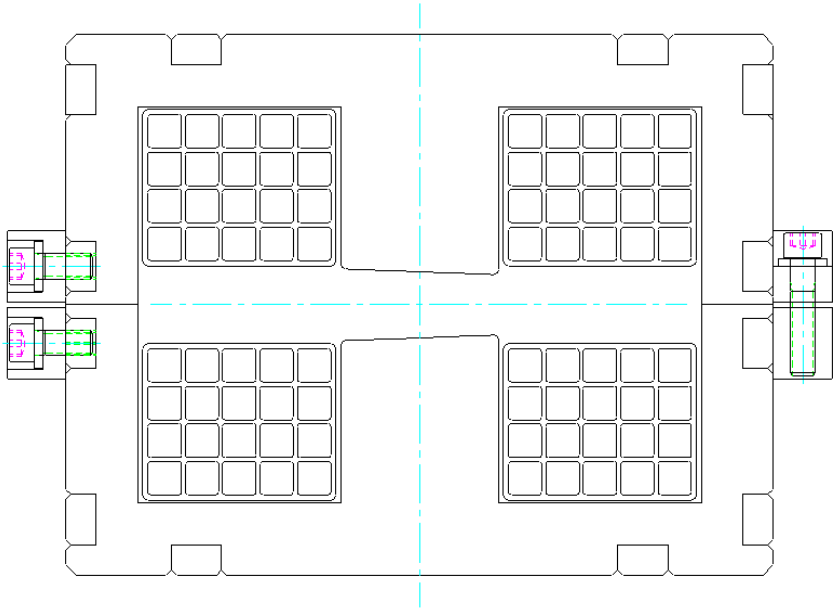

Figure 5.6.2 Cross-section of the booster dipole magnet. Note the magnet yoke clamping method.

5.6.1.2 Conceptual Design of the Booster Quadrupole Magnet

5.6.1.2.1 Quadrupole Magnetic Design Parameters

The NSLS-II booster will be equipped with 96 quadrupole magnets energized in three families of power supplies. Ninety of the 96 quadrupole magnets are required to yield a gradient of 10 T/m at 3 GeV, with inhomogeneity of the gradient field of less than 0.1% inside the beam tube. The quadrupoles will have an aperture of 35 mm. The field quality is consistent with the specified gradient throughout the required transverse region. The magnetic cores are made of AISI 1006 low-carbon steel sheet, 1.5 mm thick. The parameters of the quadrupole magnets are listed in Table 5.6.3.

Table 5.6.3 Booster Quadrupole Magnet Parameters at 3 GeV.

Quantity	96
Maximum field gradient [T/m]	10
Magnetic length [m]	0.3
Aperture [mm]	35
Peak current [A]	76
Number of turns per pole	16
Square conductor size [mm]	6.3
Gradient: extraction, injection [T/m]	9.3, 0.62 (1 family of 60) 10.0, 0.67 (1 family of 30) (6 individually powered quadrupoles)

To test the feasibility of the booster quadrupole design, magnetic modeling was performed using OPERA-2D. Figure 5.6.3 shows a 2D magnetic model of the quadrupole cross-section with the B-field flux shown in light blue lines. The developed design satisfies the specifications shown in Table 5.6.3 within an acceptable margin.

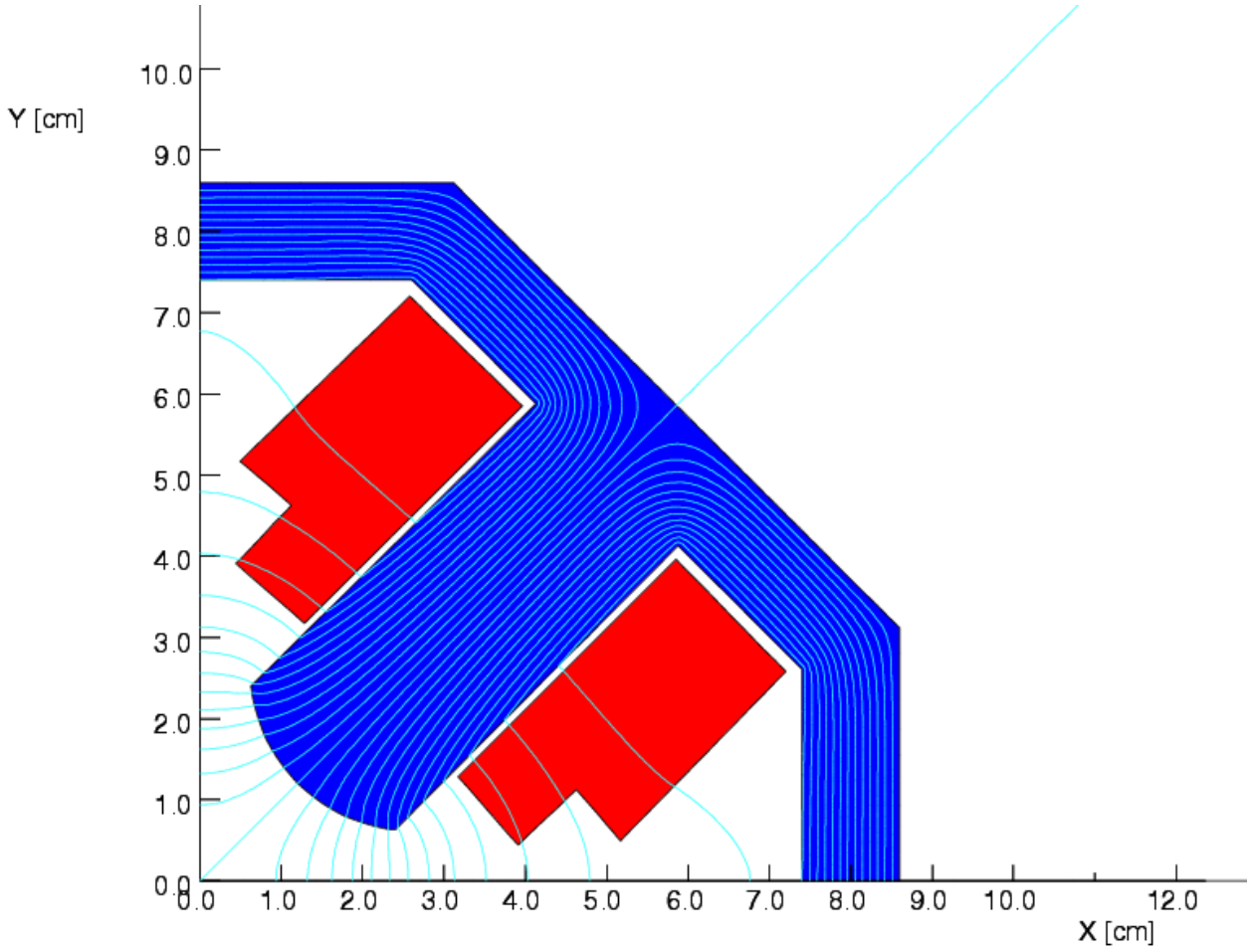

Figure 5.6.3 NSLS-II booster quadrupole magnet model. B-field flux lines shown in light blue.

5.6.1.2.2 Mechanical Design of the Booster Quadrupole Magnets

The top and bottom halves of the quadrupoles are pinned and bolted together to form a flux-return yoke. To install the coil on the quadrupole, the magnet core is divided into four quadrants. A square copper conductor, 6.3×6.3 mm, was selected for winding the excitation coils. Vacuum-impregnated fiberglass with radiation-resistant epoxy more than 1.0 mm thick will provide interstitial conductor insulation. At least 1.5 mm additional vacuum-impregnated epoxy fiberglass will provide ground plane insulation. The coils will be high-potted up to 5 kV to detect defects in the inter-turn and ground plane insulation of the coil.

Fabrication and assembly concepts have been studied, resulting in the conceptual magnet design shown in Figure 5.6.4.

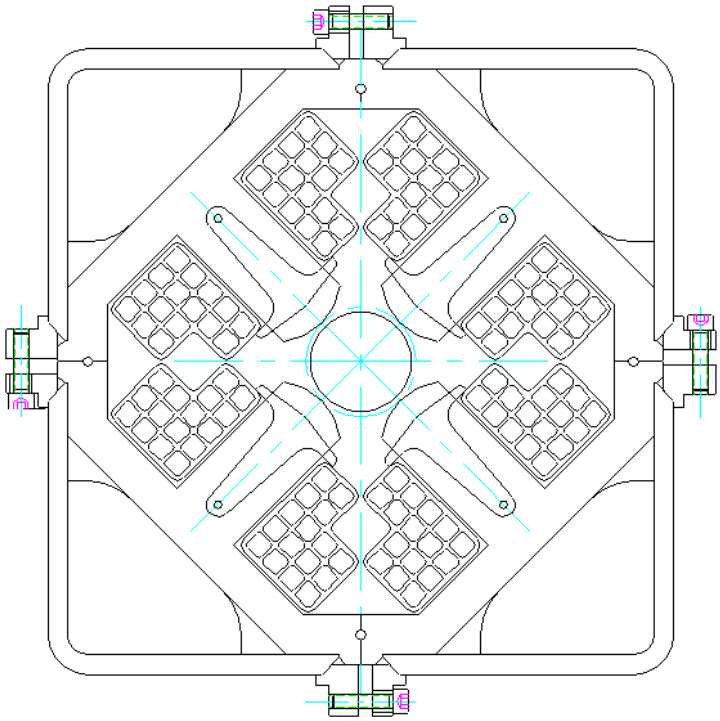

Figure 5.6.4 NSLS-II booster ring quadrupole magnet cross-section.

5.6.1.3 Sextupole Magnets

5.6.1.3.1 Sextupole Magnetic Design Parameters

The 30 sextupole magnets are divided in two families of magnets that are 0.4 m and 0.2 m long. The bore diameter of 35 mm gives a minimum clearance of 2 mm between the vacuum chamber and the adjacent poles. All sextupole magnets are required to yield strength of 200 T/m^2 at 3 GeV, with inhomogeneity of the field strength of less than 0.1% inside the beam tube. The maximum current density in the conductor will not exceed 2.5 A/mm^2. The laminated magnet yokes are made of AISI 1006 low-carbon sheet steel, 1.5 mm thick. These parameters are shown in Table 5.6.4.

Table 5.6.4 Booster Sextupole Parameters at 3 GeV.

Magnetic length [m]	0.4	0.2
Quantity	15	15
Aperture [mm]	35	35
Sextupole strength [T/m^2]	200	200
Peak current [A]	47.4	47.4
Number of turns per pole	6	6
Square conductor size [mm]	6.3	6.3

To test the feasibility of the booster sextupole design, magnetic modeling was performed. The figure below illustrates a 2D magnetic model of the sextupole cross-section, with the B-field flux shown in light blue lines. The developed design satisfies the specifications shown in Table 5.6.4 within an acceptable margin.

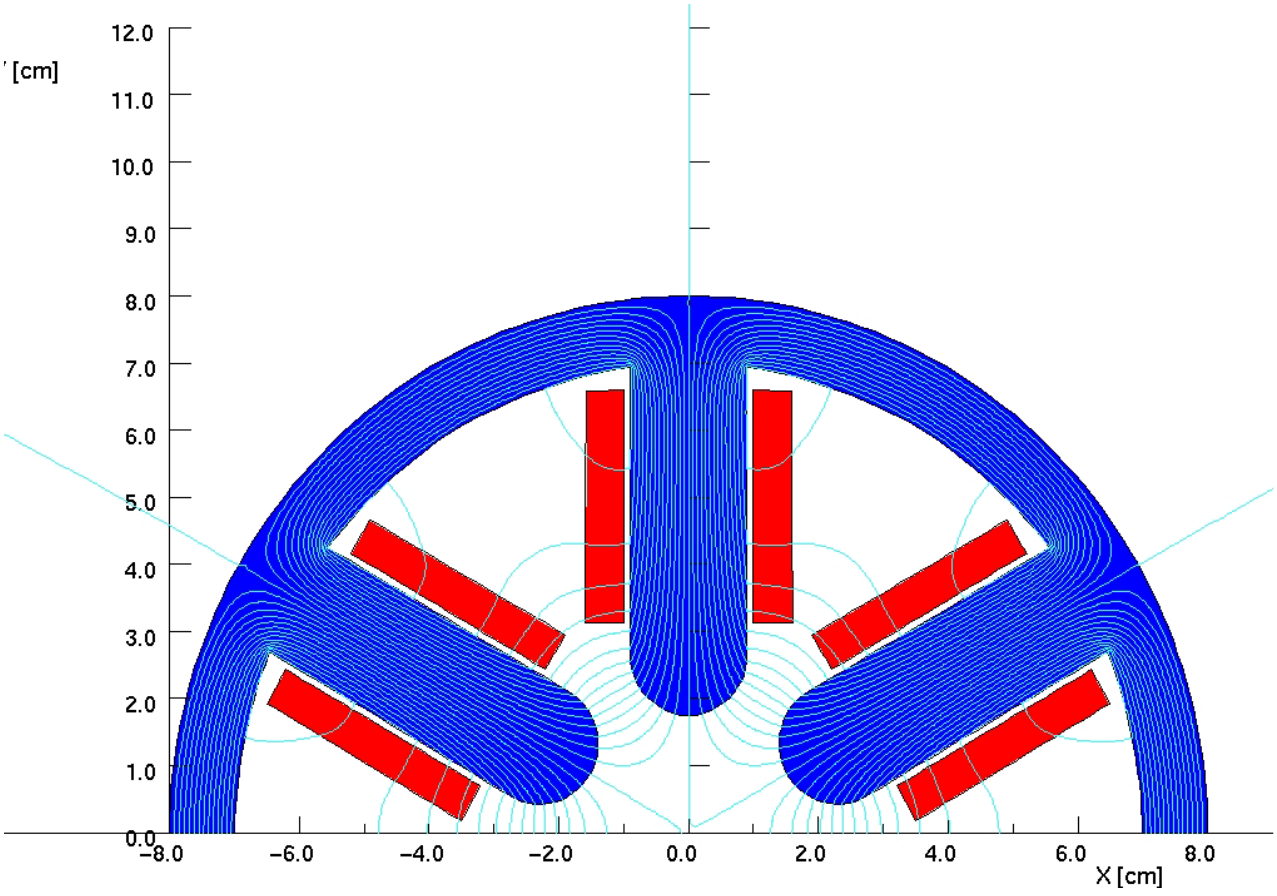

Figure 5.6.5 Magnetic model of the booster sextupole.

5.6.1.3.2 Mechanical Design of the Sextupole Magnet

The 30 sextupole magnets of the booster ring come in two lengths: 0.40 m and 0.20 m. To simplify sextupole fabrication and reduce costs, a standardized cross-section was selected for use with the two magnet yoke lengths.

The magnet yoke is composed of laminated, AISI 1006 low-carbon sheet steel, 1.5 mm thick. The laminated iron yoke is pinned and welded to form identical sextuplets. A square copper conductor 6.3×6.3 mm was selected for winding the excitation coils. The conductor is wrapped with fiberglass to provide a minimum of 1.0 mm turn-to-turn insulation. An additional 1.5 mm of fiberglass is wrapped around the windings to form the ground plane insulation. The coils are then vacuum impregnated with radiation-resistant epoxy resin. The coils will be high-potted up to 5 kV to detect defects in the inter-turn and ground plane insulation. To assemble the magnet, each sextupole coil will be secured to a sextuplet. The coil and sextuplet assembly are then keyed and bolted together around a flanged length of booster vacuum chamber to form the flux-return yoke. A 2 mm (minimum) clearance between the vacuum chamber and the adjacent poles is maintained to provide thermal insulation during chamber baking and to prevent the transmission of vibrations from the vacuum chamber to the magnet.

Studies of fabrication and assembly concepts have resulted in the design that is shown in Figure 5.6.6. This design will be refined during the next phase of the project.

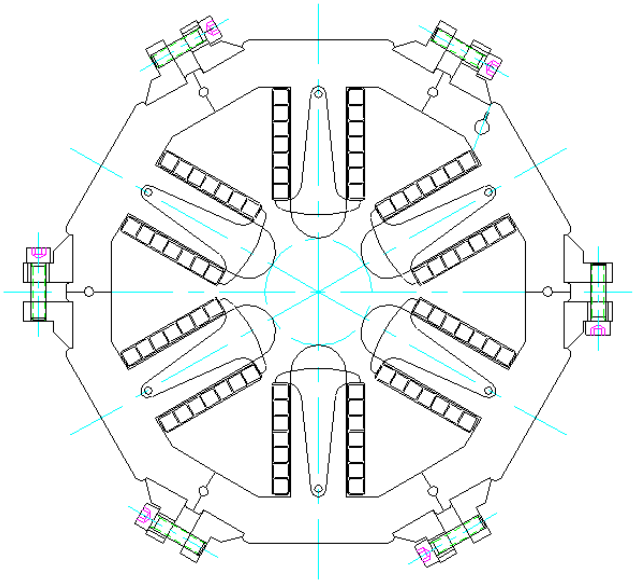

Figure 5.6.6 NSLS-II booster ring sextupole magnet cross-section.

5.6.1.4 Booster Corrector Magnets

The NSLS-II booster will be equipped with 60 combined vertical and horizontal corrector magnets. The field strength of the corrector magnet is selected to deliver about 1.0 mrad of steering to the electron beam at 3 GeV. In the booster, a conventional window-frame style corrector will be assembled around the beam tube. The corrector yoke will be made of 0.5 mm thick steel sheet. The correctors will follow the ramping excitations of the other magnetic components of the booster. The maximum booster corrector excitation current will be 15 A. The booster corrector magnets will be powered by separate bipolar power supplies.

5.6.2 Booster Magnet Installation

The NSLS-II booster presents a number of challenges for tunnel installation, survey, vibration and magnetic isolation, and servicing. We plan to finish installing portions of the booster lattice before the start of storage ring installation, so that booster commissioning may begin in parallel with storage ring installation. Booster commissioning will occur during the evening shift, while the storage ring is installed during the day.

In contrast to the storage ring, the sparse density of the booster magnets makes the concept of girder support uneconomical. Instead, sections of Unistrut U-channel will be cast into sections of the tunnel roof.

Strut assemblies will be secured to the Unistrut tracks. Most of the individual magnets will be mounted to the ceiling using methods depicted in Figure 5.6.7.

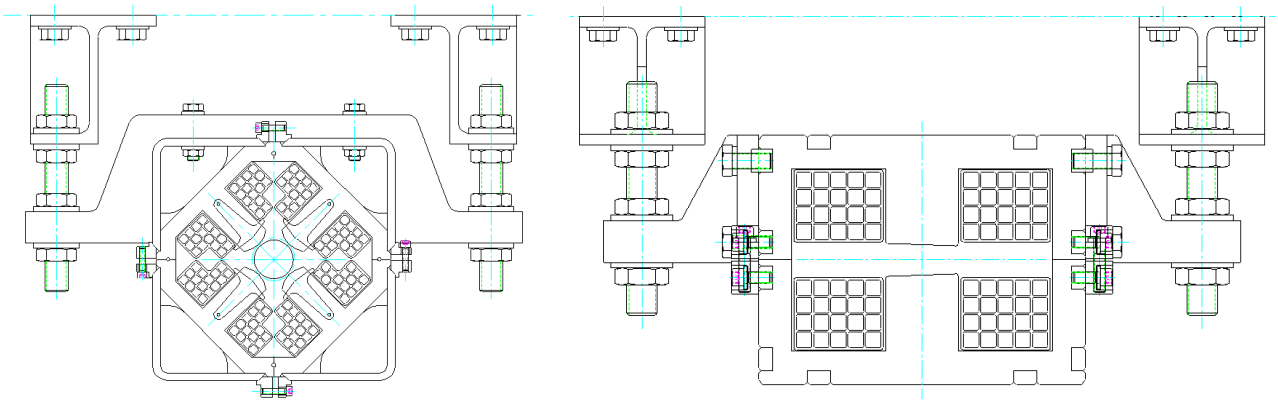

Figure 5.6.7 The 2D CAD cross-sections of the magnet hanger system for the booster magnets. This view shows a quadrupole (left) and dipole (right) magnet mounted to the tunnel ceiling.

This system can be used to provide rigid mounting of individual magnets to the tunnel ceiling. This hanger mounting technique is a low-cost version of the strut systems first developed at ALS, where all the magnets and girders are rigidly mounted using struts. There is ample experience at BNL in the use of ceiling-mounted accelerator systems.

The hanger system shown in Figure 5.6.8 provides a cost-effective and rigid yet versatile solution for mounting and surveying magnetic components.

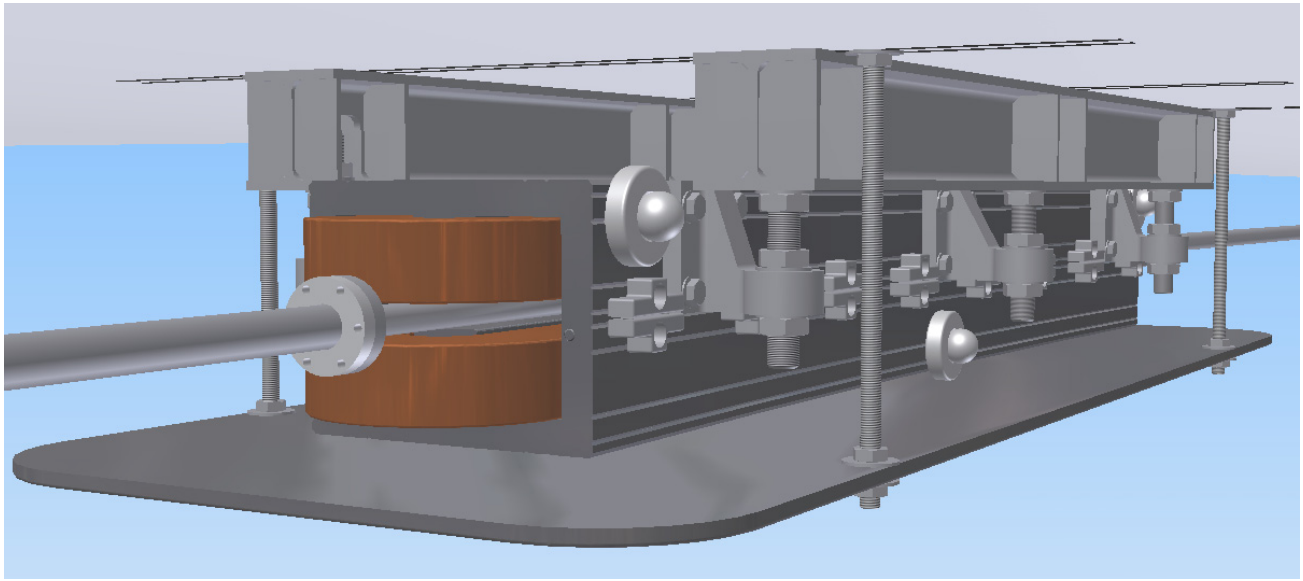

Figure 5.6.8 Field isolation plate secured beneath the dipole magnet. Note that the laser tracker survey targets are magnetically affixed in the fiducial cups that are secured to the aisle side of the magnet. These targets will be reused and will allow all the booster magnets to be surveyed from below using laser trackers in the tunnel aisle.

The plate mounted beneath the assembly magnetically isolates the storage ring components from the ramping booster elements. Magnetic modeling to determine the effectiveness of the isolation plates will be conducted. The use of an isolation plate or steel enclosure around the dipole will be evaluated to ensure appropriate ring isolation without distorting the magnetic fields of the booster ring elements.

The magnets will be pre-surveyed and laser tracker target cups will be mounted to the outside of the iron yoke. These will be used to locate the magnet axis relative to the booster lattice axis during installation. Fiducialization of each magnet will be achieved by conventional alignment methods, e.g., by locating and then securing the fiducials relative to the mechanical center of each dipole and multipole.

The installation of the booster magnets must follow strict engineered lifting procedures that are compliant with the BNL Critical Lift Policy. Special equipment will be designed to aid in the installation of the booster lattice components to minimize safety risks. Figure 5.6.9 shows one of several industrially produced lifting devices that are being considered for booster installation and servicing.

Figure 5.6.9 Possible lifting device for booster installation and servicing.

Some transporter models are steered with the aid of a thin sensor-detectable strip adhered to the floor, forming an electronic track that controls side-to-side motion of the transporter to help prevent collisions with the tunnel wall or storage ring lattice components.

One unit that has been considered as a possibility is the Model 71 4500-lb Electric Side-Loader Truck manufactured by the Raymond Corporation. It can shuttle sideways along the 1.8 m wide tunnel aisle carrying a magnet.

Once the booster magnets have been shuttled to their prescribed location, the side-loader will lift them straight up until they clear the top of the main storage ring. The side loader's vertical mast moves forward, projecting the magnet radically outward to its approximate position. Final positioning is accomplished by a BNL-designed screw-driven scissor lift with 2D translational capabilities, as shown in Figure 5.6.10.

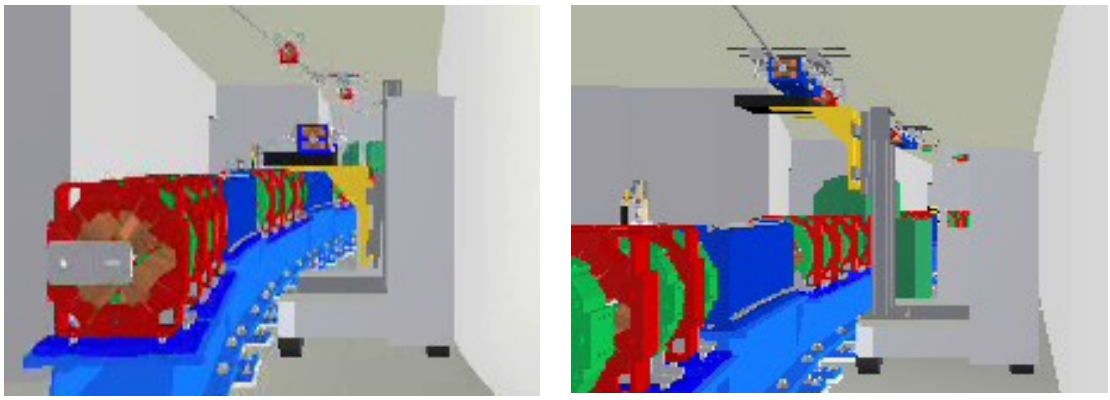

Figure 5.6.10 Procedure of booster magnet installation. Left: The transporter delivering a booster dipole magnet to its point of installation. Right: Platforms may be added to the transporter system to allow access to the booster ring components for ease of installation, survey, and servicing.

No single model side-loading transporter may have all the features that are needed for NSLS-II. Further investigation will address desirable custom options, adaptations, and safety features—such as ergonomics, tunnel egress, critical lift issues, and the incorporation of extendable manned platforms.

5.6.3 Booster Power Supplies

The power supplies are designed to ramp from a low current at injection to a higher current at extraction (Figure 5.6.11). The shortest total ramp time for both up and down ramps is 1 second. The time between ramp cycles can vary from milliseconds to minutes. This longer time between cycles will be used for top-off operations. All power supplies will have at least a 20% operating current margin.

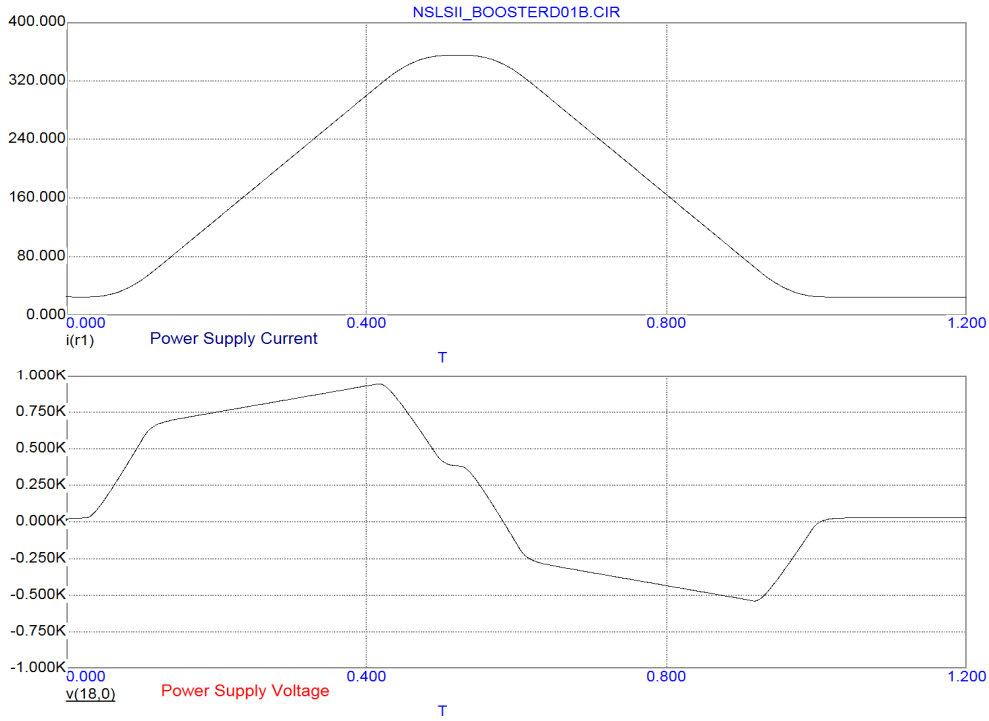

Figure 5.6.11 Dipole power supply current and voltage waveforms for 3.0 GeV operation.

All power supplies will be capable of programmable ramping profiles, which will be stored in a Waveform Function Generator All profiles will be synchronized by a global timing system. Figure 5.6.12 shows the block diagram for the dipole power supply.

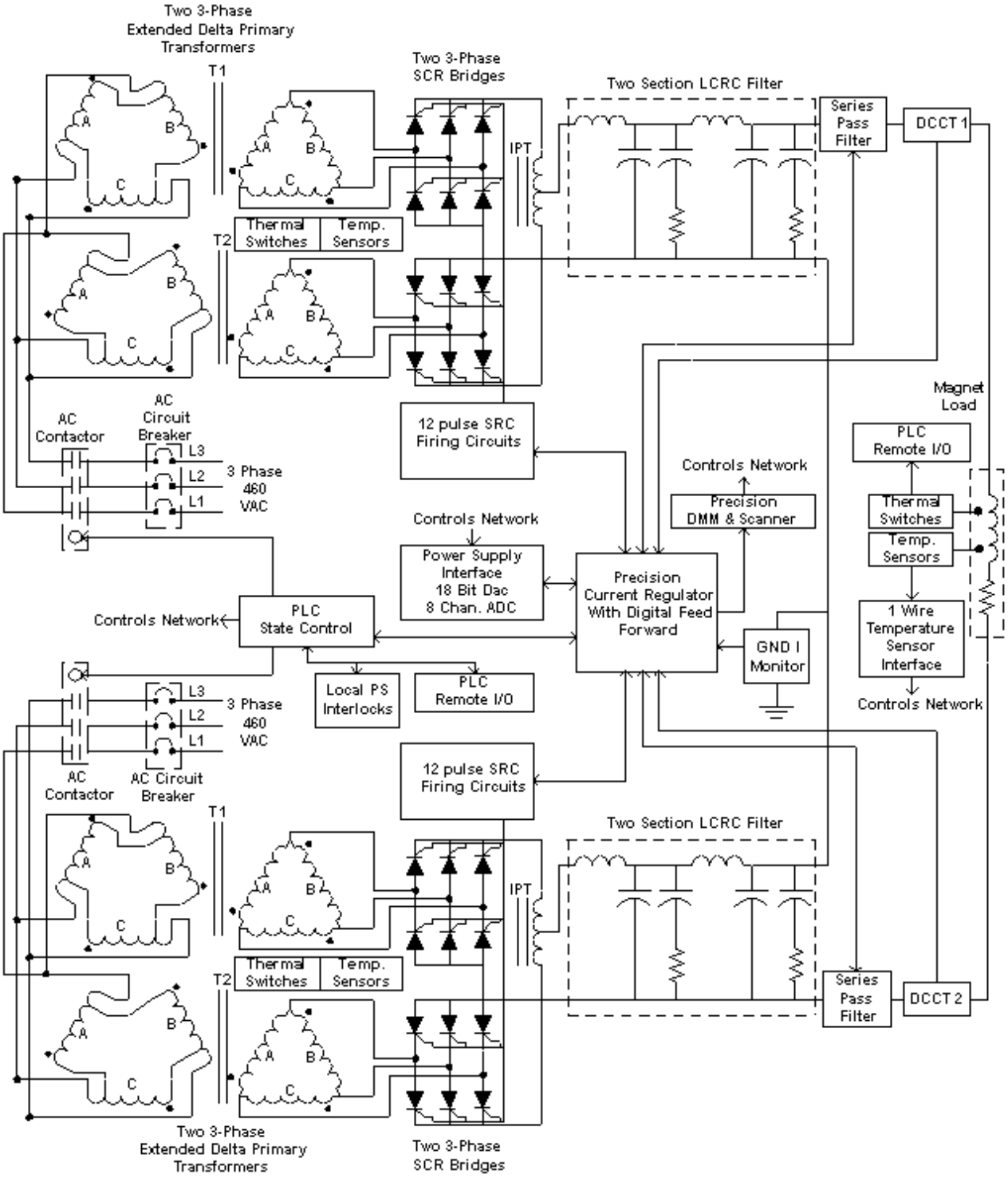

Figure 5.6.12 Dipole power supply block diagram.

The booster power supplies are listed below and discussed in detail in the rest of this section. The anticipated power consumption of the power supplies is quite low. The booster ring power supplies consume only 150 kW over a 1-second fill cycle. During top-off with a 1-minute cycle between fills, the average power usage is estimated to be 23 kW. Table 5.6.5 lists the specifications for the different power supply families, for comparison.

- B-PS – 60 dipole magnets in series circuit
- Q1-PS – 60 quadrupole magnets in a series circuit
- Q2-PS – 30 quadrupole magnets in a series circuit
- QC-PS1 to QC-PS13 – 2 quadrupole magnets in a series circuit, 3 separate circuits
- SF-PS – 15 sextupole magnets in a series circuit
- SD-PS – 15 sextupole magnets in a series circuit
- BH-PS1 to BH-PS60 – 60 horizontal correction dipole circuits
- BV-PS1 to BV-PS60 – 60 vertical correction dipole circuits

5.6.3.1 B-PS – Main Dipole Power Supply

The B-PS circuit consists of 60 dipole magnets, each 15.7 mΩ and 12 mH. The operating current is ~355 A for 3.0 GeV. Cabling between the magnets and the return bus will use 650 MCM flexible copper cable with a resistance of 0.11 Ω and inductance of 1.4 mH. The power supply load is 1.06 Ω and 0.72 H. The B-PS current and voltage waveforms for 3.0 GeV operations can be seen in Figure 5.6.11. The electrical diagram for this power supply is shown in Figure 5.6.12. This power supply is a unipolar, two-quadrant, current-regulated supply. It will use two 12-pulse SCR converters in series, with the center point connected to ground. This configuration will reduce the voltage rating on various converter components. Each converter will have a ripple current to low levels. The power supply will be able to run in the invert mode while ramping down. This produces a negative voltage and recovers the stored energy in the magnets.

A combined digital and analog control system will control the operation of the B-PS power converter. The power supply will have a precision current regulator using a DCCT as the current feedback device. The digital controls will use a feed-forward system to improve the overall reproducibility on the ramp. A PLC will be used for state control (on/off commands and interlocks).

5.6.3.2 Q1-PS and Q2-PS – Quadrupole Power Supplies

The Q1 and Q2 circuits will share a power supply. The power supply will be able to run in the invert mode while ramping down, which produces a negative voltage and recovers the stored energy in the magnets. The Q1 circuit consists of 60 quadrupole magnets, each 21 mΩ and 2.7 mH. Cabling between the magnets and the return bus will use #1 AWG flexible copper cable with a resistance of 0.86 Ω and inductance of 1.4 mH. The Q1 power supply load is 2.12 Ω and 0.16 H.

The Q2 circuit consists of 30 quadrupole magnets, each 21 mΩ and 2.7 mH. Cabling between the magnets and the return bus will use #1 AWG flexible copper cable with a resistance of 0.75 Ω and inductance of 1.4 mH. The Q2 power supply load is 1.38 Ω and 82 mH. The operating current for both circuits is ~76 A for 3.0 GeV.

Q1-PS and Q2-PS are unipolar, two-quadrant, current-regulated supplies. Each power supply will consist of a 12-pulse SCR converter with a single-stage LCRL passive filter and a series pass active filter (see Figure 5.6.13). A combined digital and analog control system will control the operation of the power converter. This power supply will have a precision current regulator using a DCCT as the current feedback device. The digital controls will use a feed-forward system to improve the overall reproducibility. A PLC will be used for state control (on/off commands and interlocks).

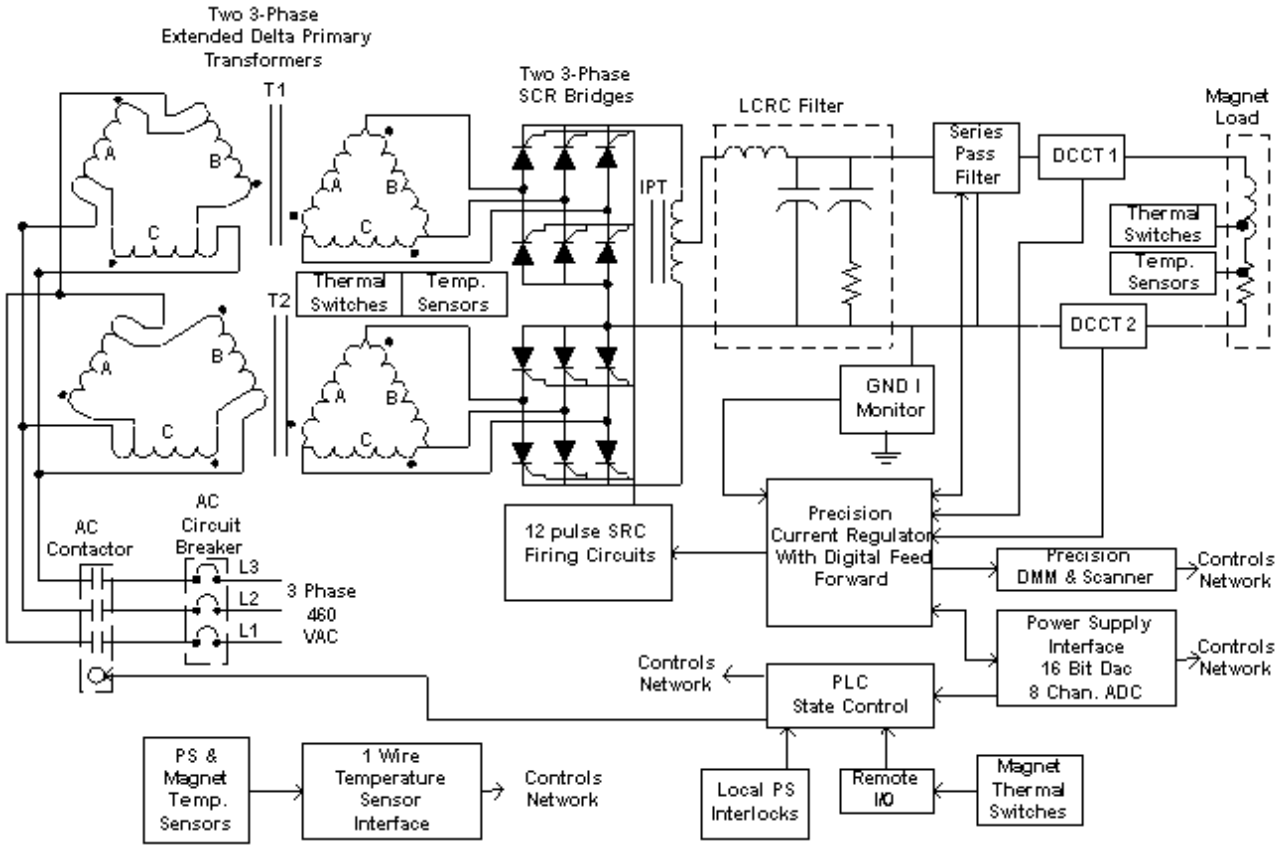

Figure 5.6.13 Q1 and Q2 quadrupole power supply block diagram.

5.6.3.3 QC-PS – Quadrupole Power Supply

There are three QC circuits, each consisting of two quadrupole magnets, each 21 mΩ and 2.7 mH. The operating current is ~76 A for 3.0 GeV. Cabling between the magnets and the return bus will use #1 AWG flexible copper cable with a resistance of 50 mΩ and inductance of 0.1 mH. The power supply load is 92 mΩ and 5.4 mH. There also are three QC power supply circuits.

QC-PS is a unipolar, single-quadrant, current-regulated, switch-mode power supply. It will use a series pass output stage. An analog control system will control the operation of QC-PS. The power supply will have a precision current regulator using a DCCT as the current feedback device. The digital controls will use a feed-forward system to improve overall reproducibility. A micro-controller or PLC will be used for state control (on/off commands and interlocks).

5.6.3.4 SF-PS and SD-PS – Sextupole Power Supplies

The SF and SD circuits will share a power supply. Both circuits consist of 15 sextupole magnets. Each SF magnet is 7.1 mΩ and 0.54 mH, and each SD magnet is 14.1 mΩ and 1.1 mH. The operating current for both circuits is ~47 A for 3.0 GeV. Each circuit has the same cabling between the magnets and the return: #1 AWG flexible copper cable with a resistance of 0.69 Ω and inductance of 1.0 mH. The power supply load for the SF circuit is 0.8 Ω and 8 mH.

SF- and SD-PS are unipolar, single-quadrant, current-regulated, switch-mode power supplies (Figure 5.6.14). A combined digital and analog control system will control the operation of the power converter. These power supplies will have a precision current regulator using a DCCT as the current feedback device.

The digital controls will use a feed-forward system to improve overall reproducibility. A PLC will be used for state control (on/off commands and interlocks).

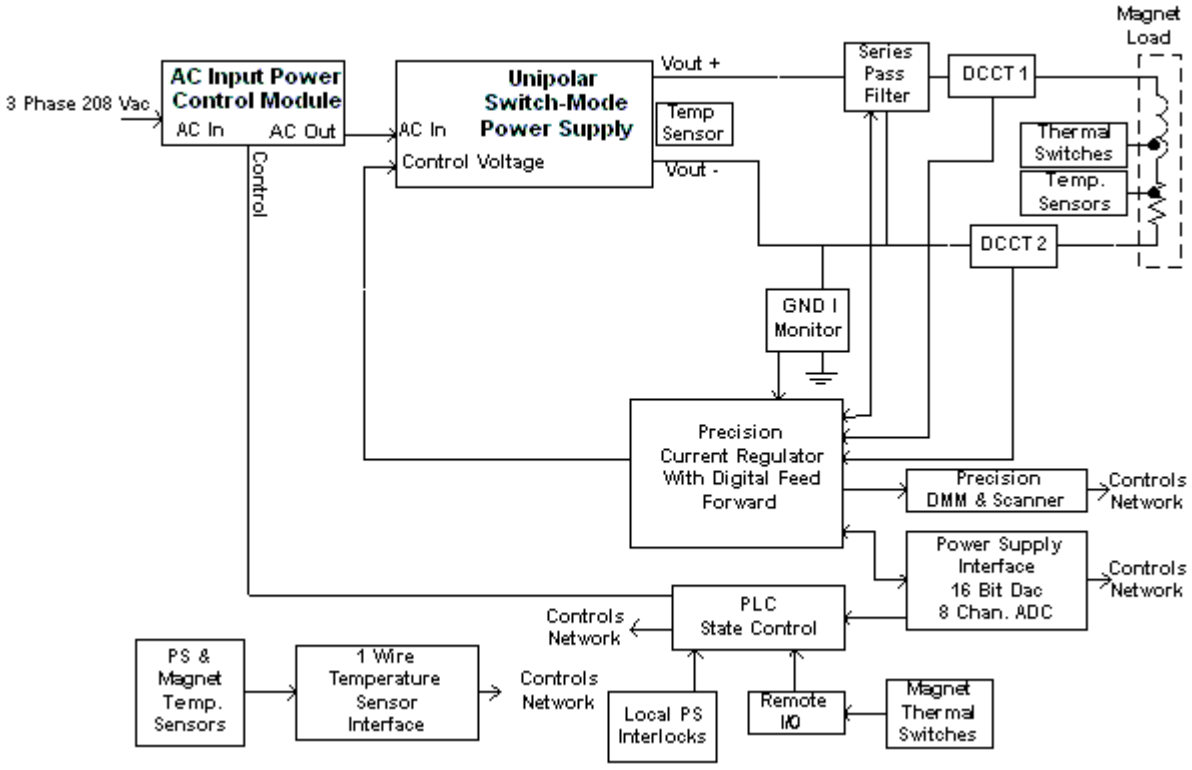

Figure 5.6.14 SF and SD sextupole power supply block diagram.

5.6.3.5 BH-PS & BV-PS – Dipole Corrector Power Supply

This circuit consists of one coil set located in each horizontal/vertical corrector magnet. Each coil set is 90 mΩ and 50 mH. The operating current is ~15 A for 3.0 GeV. The cabling from the coil sets to the power system will be #10 AWG flexible copper cable, routed through the tunnel ceiling into the equipment area above the main tunnel. The power supply is located just above the magnet in the equipment area. The cabling has a resistance of 90 mΩ and inductance of 0.1 mH. The power supply load is 0.18 Ω and 50 mH.

The power supply is a bipolar, four-quadrant, current-regulated linear power supply, controlled by an analog system. The power supply will have a precision current regulator using a shunt as the current feedback device. A micro-controller or PLC will be used for state control (on/off commands and interlocks).

5.6.3.6 Power Supply Interlocks

All power supplies will have sufficient interlocks to prevent the power supply from damage due to changes in cooling conditions, AC power disturbances, and out-of-range setpoints. All magnet coils will have an over-temperature interlock if damage can occur due to a change in cooling or operating conditions. All power supplies will have an electrical safety interlock that will prevent the power system from turning on if the machine safety system requirements so warrant.

5.6.3.7 Electrical Safety

All power supplies will conform to the latest BNL safety requirements, especially concerning arc flash protection. Whenever possible, NRTL-listed equipment will be used.

5.6.3.8 Cable Tray

The cable tray for the magnet circuits will be located inside the main tunnel, on the ceiling. All cables will be tray-rated. Power cables will be arranged to minimize pickup from other circuits. All power cables will be separated from signal cables. All cables and trays will meet NEC requirements.

5.6.3.9 Power Supply Instrumentation

Redundant DCCTs or shunts will be used to confirm the power supply current reproducibility. High-precision DMMs and scanners will be used to monitor the power system current, the redundant current sensor, and the analog current setpoint. This equipment will ensure long-term stability and reproducibility. Temperature monitoring of the magnet coils and power system environment will be accomplished using low-cost digital temperature sensors. With such system, a problem can be identified before it becomes an emergency, making it possible for repairs to be scheduled more conveniently and economically.

5.6.3.10 Power Supply Controls

Each booster power supply circuit will require a Waveform Function Generator. These VME device cards will be located in a control system's VME chassis, mounted in one of the power supply system racks. The WFGs will generate the reference current profiles, input analog data, and perform digital state control and status readbacks. A timing system will be needed to synchronize all the WFGs. The output of the WFGs is connected via fiber optics to a Power Supply Interface. The PSI has a precision digital-to-analog converter for generating the reference current, and a multi-channel analog-to-digital converter for inputting power system signals. The PSI also has digital IO for state control and status readbacks of the power supply.

The other controls will include the operation of the high-precision DMM and scanner, and readout of the digital temperature sensors.

Table 5.6.5 Power Supply Specifications.

	B	Q1	Q2	QC	SF	SD	BH and BV
AC input power: 3-phase… at max. P.S. rating	460 VAC ~808 AAC	460 VAC ~37 AAC	460 VAC ~23 AAC	208 VAC ~15 AAC	208 VAC ~21 AAC	208 VAC ~21 AAC	1-phase; 208 VAC ~2.4 AAC
Peak power [kW] at 3.0 GeV	372	16.6	11.2	2.7	4.0	4.3	
DC maximum output current – Imax [ADC]	450	100	100	150	65	65	+20
DC minimum output current – Imin [ADC]	1	1	1	1	1	1	-20
DC output voltage [VDC]	300	250	150	20	75	75	±20
Operating quadrants	2; (V+, I+), (V–, I+)	2; (V+, I+), (V–, I+)	2; (V+, I+), (V–, I+)	1: (V+, I+)	1; (V+, I+)	1; (V+, I+)	4: (V+, I+), (V–, I+), (V–,I–) & (V+, I–)
Small-signal –3-db bandwidth [kHz]	0.5	1	1	1	1	1	1
Large-signal –3-db bandwidth [Hz]							3
Stability (8 h – 10 s) – referred to Imax [ppm]	40	200	200	200	200	200	5000
Stability (10 s – 300 ms) - referred to Imax [ppm]	20	200	200	200	200	200	5000
Stability (300 ms – 0 ms) – referred to Imax [ppm]	10	100	100	200	100	100	5000
Absolute accuracy – referred to Imax [ppm]	100	200	200	100	200	200	5000
Reproducibility long term – referred to Imax [ppm]	50	100	100	200	100	100	500
Current ripple – referred to Imax [ppm at 60 Hz or greater]	25	25	25	10	25	25	20
Resolution of reference current	16 bit + 1 LSB	16 bit + 1 LSB	16 bit +1 LSB	16 bit + 1 LSB	16 bit + 1 LSB	16 bit + 1 LSB	16 bit + 1 LSB
Resolution of current measured – fast sampling (at 200 μsec)	16 bit + 1 LSB	16 bit + 1 LSB	16 bit + 1 LSB	16 bit + 1 LSB	16 bit + 1 LSB	16 bit + 1 LSB	14 bit + 1 LSB
Resolution of current measured – slow sampling (at 16.67 msec)	22 bit + 1 LSB	22 bit + 1 LSB	22 bit + 1 LSB	22 bit +1 LSB	22 bit + 1 LSB	22 bit + 1 LSB	22 bit + 1 LSB

5.7 Beam Chambers and Vacuum System

5.7.1 Scope

The booster ring vacuum system provides the acceptable vacuum pressure for the beam within the vacuum chambers in the booster. The vacuum system includes all vacuum chambers, vacuum pumps, vacuum instrumentation and diagnostics, vacuum controllers, and connecting wiring. The vacuum chamber design, materials, and processes are described in Section 5.7.2. The estimated gas load, pumping scheme, and expected pressure distribution in the booster are given in Section 5.7.3. The vacuum monitoring and control are explained in Section 5.7.4.

An average pressure below $1x10^{-7}$ Torr (see Section 5.5.1) is needed within the booster to minimize the induced beam loss and the resultant ionizing radiation that result from bremsstrahlung scattering. The booster vacuum system will be designed with sufficient pumping capability to achieve vacuum pressures in the 10^{-8} Torr range. The booster ring vacuum system includes an array of chambers, pumps, diagnostics, and regulation devices placed and selected for optimal performance and low maintenance and long, trouble-free operation. Most of the booster vacuum chambers will be constructed from seamless stainless steel tubing and will utilize Conflat flanges.

5.7.2 Mechanical Design

5.7.2.1 Approach to Booster Vacuum System Design

The full-energy booster synchrotron will be located above the storage ring in the same tunnel and consequently will have the same circumference as the storage ring. This choice will be less costly than a compact booster, due to savings in civil construction cost, even though the cost of the vacuum systems will be higher due to longer beam tube length and many more pumps. The mounting and service of the vacuum systems will also be more challenging.

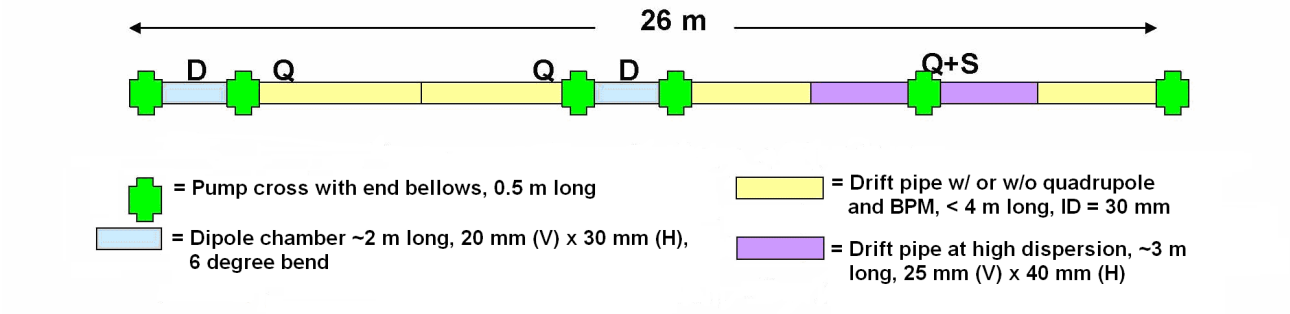

Figure 5.7.1 Schematic layout of vacuum chambers in a 26 m booster half-cell.

The booster vacuum will be divided into 15 sectors of 52 m each, coinciding with the length of the synchrotron cells. The layout of a standard half-cell is shown schematically in Figure 5.7.1. In each 26 m half-cell, there are two dipole chambers, several straight drift pipes, and five pump crosses with bellows. The injection, extraction, RF, and diagnostics will be housed at the long drift pipe regions. The 15 vacuum sectors are isolatable from each other, and from injection, extraction, RF, and diagnostic sections, with radiation-resistant EPDM-sealed gate valves. Conventional ultra high vacuum technology will be implemented. High

vacuum will be achieved with 30 l/s sputter ion pumps distributed around the booster ring. An aluminum foil window at the end of the booster-storage ring transfer line may separate the booster high vacuum from the storage ring ultra high vacuum.

5.7.2.2 Vacuum Chamber Design

The booster will accelerate the 200 MeV bunch train from the linac to the full energy of 3 GeV at 1 Hz repetition rate. To minimize the eddy currents during the fast ramping fields (and the associated sextupole effect), the vacuum chambers will be made of thin-wall stainless steel. A wall thickness of about 1 mm is sufficiently strong for a dipole chamber with an elliptical cross section of 20 mm (V) × 30 mm (H), while having sufficiently low eddy currents. The 60 dipole chambers will be about 2 m long with a bending radius of 14.3 m. They will be made from seamless tubing, drawn and pushed into elliptical shape, then roll-curved to give the 6 degree bend angle. The ends of the dipole chambers will be tapered from elliptical to round cross-section and welded to Conflat flanges. The maximum stress and deflection of the dipole chamber under the external atmospheric pressure occurs at the top and bottom of the chambers. Using ANSYS analysis, the stress and deflection are found to be 2500 psi and 0.1 mm, respectively (Figure 5.7.2), which is well within acceptable ranges with large safety margins. To reduce eddy currents further, the dipole chambers can be made of Inconel 625 material with thinner walls, which has higher yield strength, lower magnetic permeability, and a resistivity 60% higher than stainless. Inconel 625 can be TIG-welded to the stainless flanges with ease. The additional cost of fabricating the dipole chambers from Inconel is small, since the total length of the dipole chambers is approximately 15% of the overall length.

The straight drift pipes around the high-dispersion quadrupole will also have an elliptical shape to accommodate the required large horizontal aperture. The vacuum chamber size in these regions is 40 mm (V) × 25 mm (H). The balance of the beam pipes will be made of 1 mm wall, 32 mm OD tubes of round stainless steel. To simplify the fabrication, alignment, and mounting of the beam pipes, the BPMs and the quadrupole chamber will be part of the drift pipes. Two drift pipes in each half-cell will have a precision-machined block welded to one end for mounting the BPM buttons. Two pump crosses with bellows will bracket each dipole chamber and there will be one pump cross in the middle of the long drift section. Conflat flanges (size DN38) will be used throughout the booster ring.

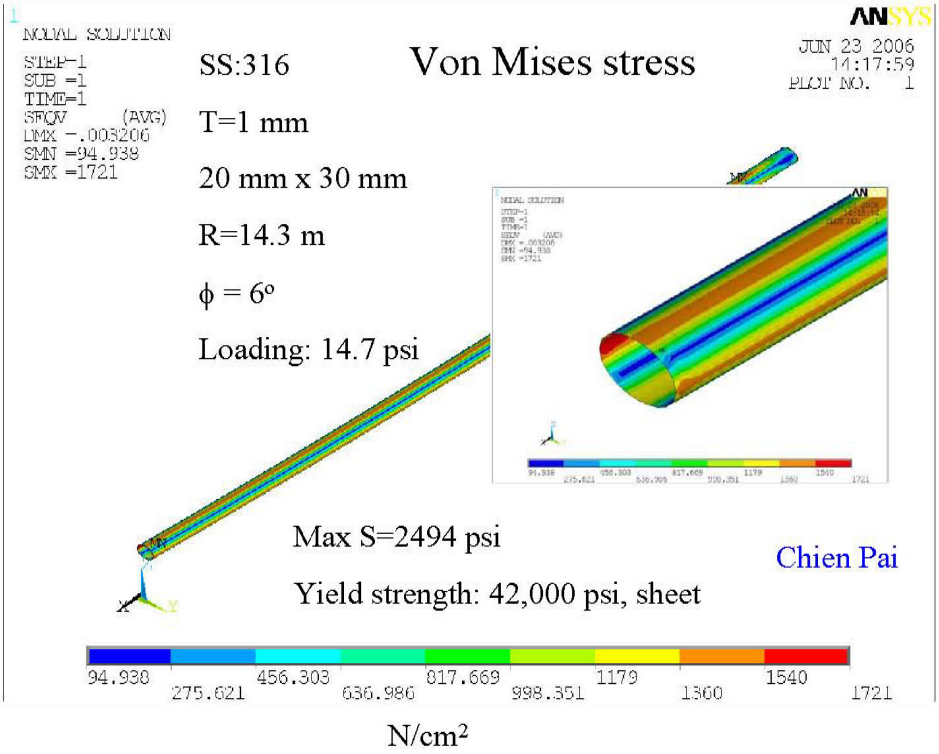

Figure 5.7.2 Calculated stress of the thin-wall bending chamber under vacuum load. The high stress is at the side of the tube along the horizontal plane with maximum stress of less than 2500 psi. The calculated deflection is ~0.1 mm.

After proper chemical cleaning, the completed chambers and drift pipes will be vacuum degassed at 450ºC in a vacuum furnace for several days to remove any trace of surface contaminants and to reduce outgassing, eliminating the need for in-situ baking. The chambers and the pipes are then assembled into the magnets, welded with end flanges, and tested prior to installation in the tunnel. Once they are installed and connected to other beam pipes, two gate valves will be mounted at the end of booster cell, so each cell can be pumped down to high vacuum. Additional gate valves will be used to isolate the RF, injection, extraction, and diagnostics from the regular vacuum sectors. High-precision BPMs will be incorporated into the vacuum chamber. It also will contain tapered transitions, flanges, bellows, additional ion pumps, and ceramic breaks.

5.7.3 Vacuum Pumping and Pressure Distribution

The thermal outgassing of the clean stainless chamber surface will be less than $1x10^{-10}$ Torr-l/s/cm^2, 24 hours after pumping down. This is equivalent to a total thermal gas load of ~$7x10^{-5}$ Torr-l/s for the whole booster ring, excluding contributions from RF, injection, extraction, and diagnostics. The pressure in the booster will also be influenced by the synchrotron radiation-induced desorption. Assuming a 3 mA beam at the energy of 3.0 GeV in the booster during the 0.4 sec acceleration cycle, the total synchrotron radiation power on the vacuum chamber wall is about 700 W, concentrated at the downstream end of the dipole chambers, with a linear power density less than 8 W/m. No observable temperature rise at the chamber wall is expected.

The total photon flux during acceleration is approximately 2×10^{18} ph/s. Assuming a PSD yield of $\eta = 1\times10^{-3}$ mol/ph, the total photon-desorbed gas load will be about 6×10^{-5} Torr-l/s, which is comparable with the thermal desorption gas load. Desorption yield of $\eta = 1\times10^{-3}$ mol/ph can be achieved with an integrated dosage of 10^{19} ph/meter, reached in a few hours of continuous booster operation. Both the thermal- and photon-desorbed gas load will be handled with the five 30 l/s ion pumps in each half-cell. The pressure distribution in a standard half-cell section is plotted in Figure 5.7.3, with an average pressure about 1.5×10^{-7} Torr. Due to the limited conductivity of the small-diameter beam pipes, the average pressure will improve with shorter pump

spacing, rather than with larger ion pumps. The pressure will improve rapidly to low 10^{-8} Torr within a week, since η decreases with integrated beam dose and thermal outgassing decreases with time.

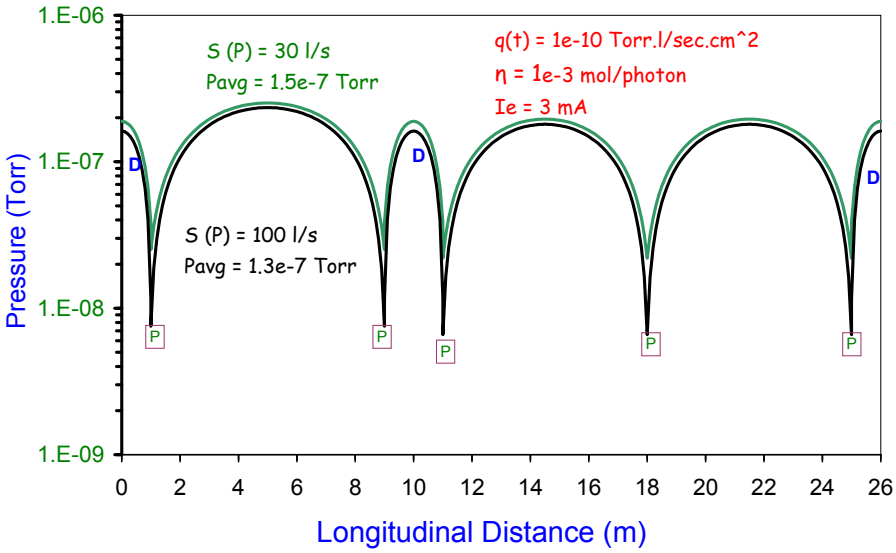

Figure 5.7.3 Pressure distribution in a standard booster half-cell section from both thermal desorption and photon-stimulated desorption. Each half-cell will have five 30 l/s ion pumps, with two ion pumps bracketing each dipole chamber and one ion pump in the middle of the long drift pipe. Due to the limited linear conductance of the small diameter beam pipes, the average pressure only decreases by 15% if 100 l/s ion pumps are used in place of the 30 l/s pumps.

The booster ring vacuum sectors will be roughed down from atmospheric pressure with portable turbo-pumps (TMP) backed with dry mechanical pumps before transferring to the sputter ion pumps. Two right-angle, all-metal valves will be mounted at each vacuum sector for roughing, bleed-up, and for other vacuum diagnostics. Long manifolds will connect the TMP to the booster ring mounted on the ceiling of the storage ring tunnel. The TMP stations will have their own vacuum gauges and an electro-pneumatic valve to isolate the TMP from the vacuum section in the event of pump or power failures. The TMPs will be manually isolated with valves, once each booster ring sector is at high vacuum. Large ion pumps of about 200 l/s, identical to those deployed in the storage ring, will provide sufficient UHV pumping speed at the long straight sections for RF cavities, injection, extraction, and diagnostics.

5.7.4 Vacuum Monitoring and Controls

Power supplies and controllers for linac and booster vacuum systems will be located in the satellite electrical racks outside the storage ring shielding. Commercial dual ion pump controllers and vacuum gauge controllers with local and remote capabilities will power, monitor, and control the ion pumps and vacuum gauges, and interface with the PLC and control computers. Ion pump currents and the vacuum gauges will provide information on the pressure distribution in the booster ring.

5.7.4.1 Vacuum Monitoring

The booster vacuum will be monitored and interlocked with the ion pump current and the vacuum gauge readings. Each 52 m vacuum sector will have a convection-enhanced Pirani gauge (TCG), two inverted-magnetron cold cathode gauges as the primary gauges, and ten 30 l/s ion pumps. Additional vacuum gauges will be installed to protect the cavity and the kickers. Residual gas analyzer heads will be installed at special straight sections for diagnostics during operation and maintenance periods. A residual gas analyzer head may be mounted on the portable TMP stations to assist the pumpdown and troubleshooting of regular vacuum sections. Table 5.7.1 presents a list of booster vacuum devices, together with those for linac and beam transport lines.

Table 5.7.1 List of Vacuum Components for the Linac and Booster Vacuum Systems.

	IP (30 l/s)	IP (200 l/s)	TCG	CCG	TMP	RGA	GV
E-gun	2	2	2	2	1	1	2
GtL		2	1	2	1		2
Linac		8	4	8	1	1	2
LtB	4		2	4	1		2
Booster	150	8	19	38	8	5	19
BtSR	6		1	2	1	1	2
Total	162	20	29	56	13	8	29

5.7.4.2 Vacuum Controls

The vacuum control system will interface with vacuum devices while being part of the machine control. Due to the high radiation levels in the tunnel, all the vacuum devices will be located at the satellite control racks. These vacuum devices (such as gauge controllers, ion pump controllers, RGA, etc.), with local and remote capabilities, will communicate with the machine control system through RS232 or Ethernet links for remote monitoring, operation, and control. The low-level vacuum control will consist of dedicated vacuum programmable logic controllers. Each PLC has both digital and analog I/O modules with inputs from various vacuum devices, and provides the logic for the operation of the sector gate valves, the interlocks for other subsystem devices, and generation of the beam permits. For the gate valve control, a voting scheme with inputs from the setpoint contacts of several ion pumps will be used to initiate the interlock functions, therefore minimizing false triggering due to the failure of a single pump.

5.8 RF Acceleration System

5.8.1 Introduction

The booster RF acceleration system must capture the bunch train injected from the 3 GHz linac, accelerate it to 3 GeV, and transfer the bunch train to the storage ring RF buckets at 500 MHz (Table 5.8.1).

Table 5.8.1 RF and Beam Parameters for the Booster.

RF frequency [MHz]	500
Loss per turn (3 GeV) [keV]	493
Overvoltage	2
Accelerating voltage [MV]	1
Momentum compaction	5.7×10^{-4}
Bunch charge [pC]	200
Number of bunches	40
Nominal beam power for top-off [kW]	1.3

The requirement for 1 MV eliminates using a single one-cell cavity at 500 MHz. Rather than using two or more single cells, the five-cell PETRA cavity was chosen [5.26]. The cavity parameters are given in Table 5.8.2. The cavity geometry is shown in Figure 5.8.1.

Table 5.8.2 Parameters for the Five-Cell PETRA Cavity.

Shunt impedance [MΩ]	14.5
Cavity power (copper losses for 1 MV) [kW]	35
Beam power (7 nC) [kW]	1.3
Total RF power [kW]	37
Maximum voltage (for 75 kW copper losses) [MV]	1.5

The power source will be a modified broadcast induction output tube (IOT) transmitter capable of 80 kW at 500 MHz, used at Diamond and other synchrotron light sources. A circulator is necessary between the transmitter and the cavity.

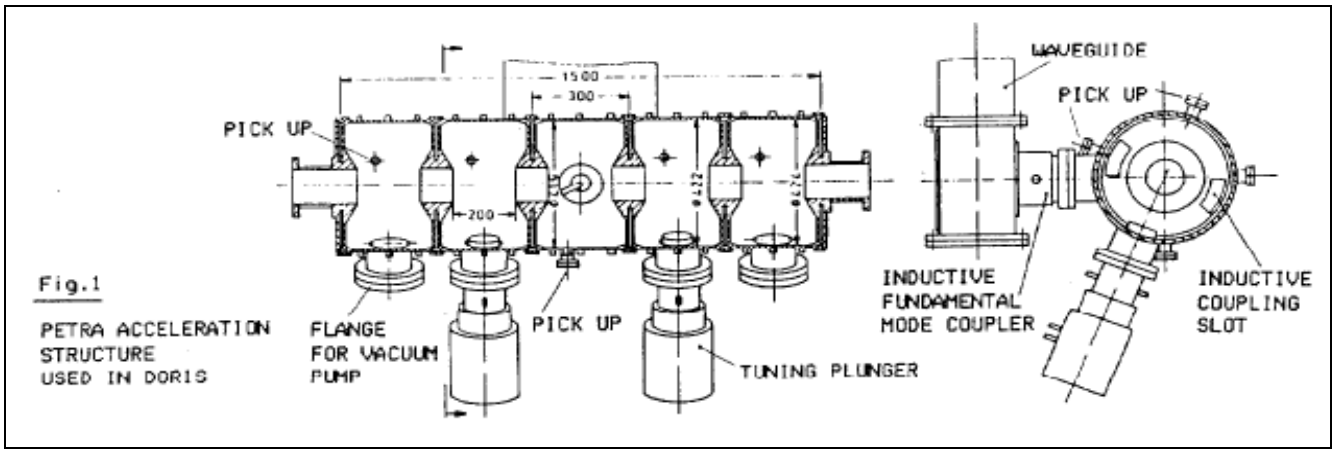

Figure 5.8.1 The five-cell PETRA cavity.

The IOT transmitter utilizes a broadcast IOT tube. Several IOTs can provide 80 kW at 500 MHz, including the THALES TH793, E2V e2v2130, and Communication and Power Industries K5H90W. Tube parameters for the TH793 are given in Table 5.8.3.

Table 5.8.3 Tube Parameters for TH793 Inductive Output Tube Transmitter.

Beam voltage [kV]	36
Beam current [A]	3.2
Maximum output power [kW]	90
Maximum collector dissipation [kW]	70

Two options are available to provide the 115 kW DC power to the IOT transmitter: a standard broadcast transformer-rectifier or a Pulse-Step-Modulated switching power supply. The PSM supply has lower ripple, which results in lower residual modulation of the beam and a lower stored energy. These attributes, combined with the fast turn-off capability, eliminate the need for a hard-tube crowbar circuit.

The 1 MV of accelerating voltage provides a 1% bucket height at the top energy of 3 GeV. At the injection energy of 200 MeV, this can provide a greater than 6% bucket height, so that the injected beam energy spread is limited by the physical and dynamic apertures in the booster, not the RF system. The booster separatrix for the injection and extraction energies is plotted in Figure 5.8.2.

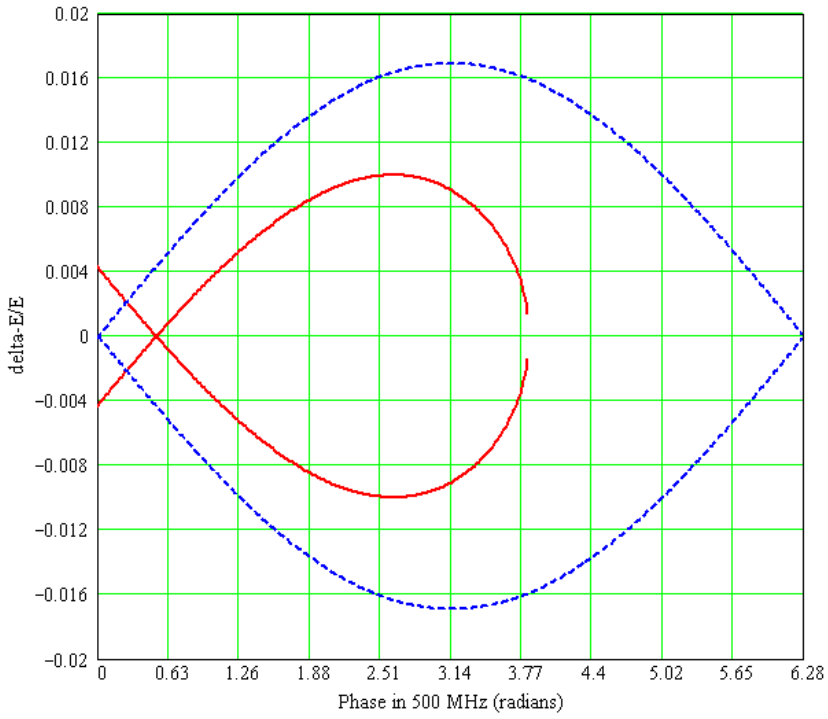

Figure 5.8.2 RF separatrix for 1 MV RF field, with radiation loss (red curve) and without (blue curve). Note that it provides about 1% bucket height at the top energy of 3 GeV.

5.9 Injection and Extraction System

The booster injection system consists of a single kicker located in a low-dispersion 6 m booster straight. The kicker design is the same as that of the kicker for the storage ring injection system.

The booster extraction system includes a kicker and a septum, located in the straights adjacent to a booster dipole magnet. Parameters of the pulsed magnets are summarized in Table 5.9.1.

The calculated trajectory of the beam extracted toward the booster-to-storage ring transport line is shown in Figure 5.9.1. After passing the kicker, deviation of the trajectory at the septum entrance reaches 15 mm, suitable for bending the beam toward the extraction channel. Sufficient margin will be provided for the pulsed magnet strength, assuring lossless beam extraction.

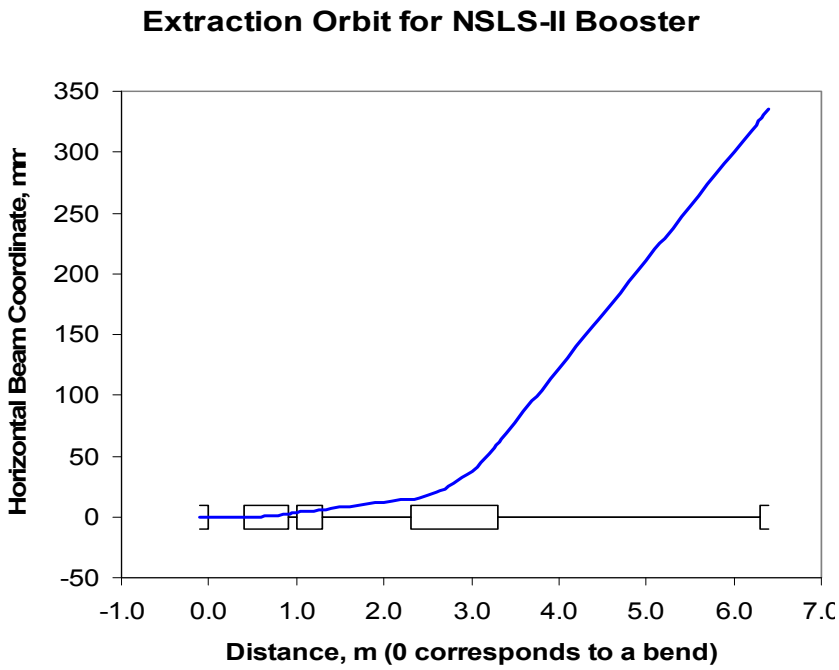

Figure 5.9.1 Beam trajectory at the booster extraction.

Table 5.9.1 Booster Pulsed Magnet Parameters.

System Component	Specification
Injection Kicker Magnet	
Magnetic length [m]	0.5
Deflection angle [mrad]	150
Field at 200 MeV [T]	0.2
Extraction Septum	
Minimum septum thickness [mm]	2
Effective length [m]	1
Bending angle [mrad]	80
Peak field at 3 GeV [T]	0.8
Extraction Kicker Magnet	
Number	1
Length [m]	0.5
Bending [mrad]	10
Field at 3 GeV [T]	0.2

5.10 Beam Transport to Storage Ring

5.10.1 Structure of the Booster-to-Storage Ring Transport Line

The transfer line from the booster to the storage ring is shown in Figure 5.10.1.

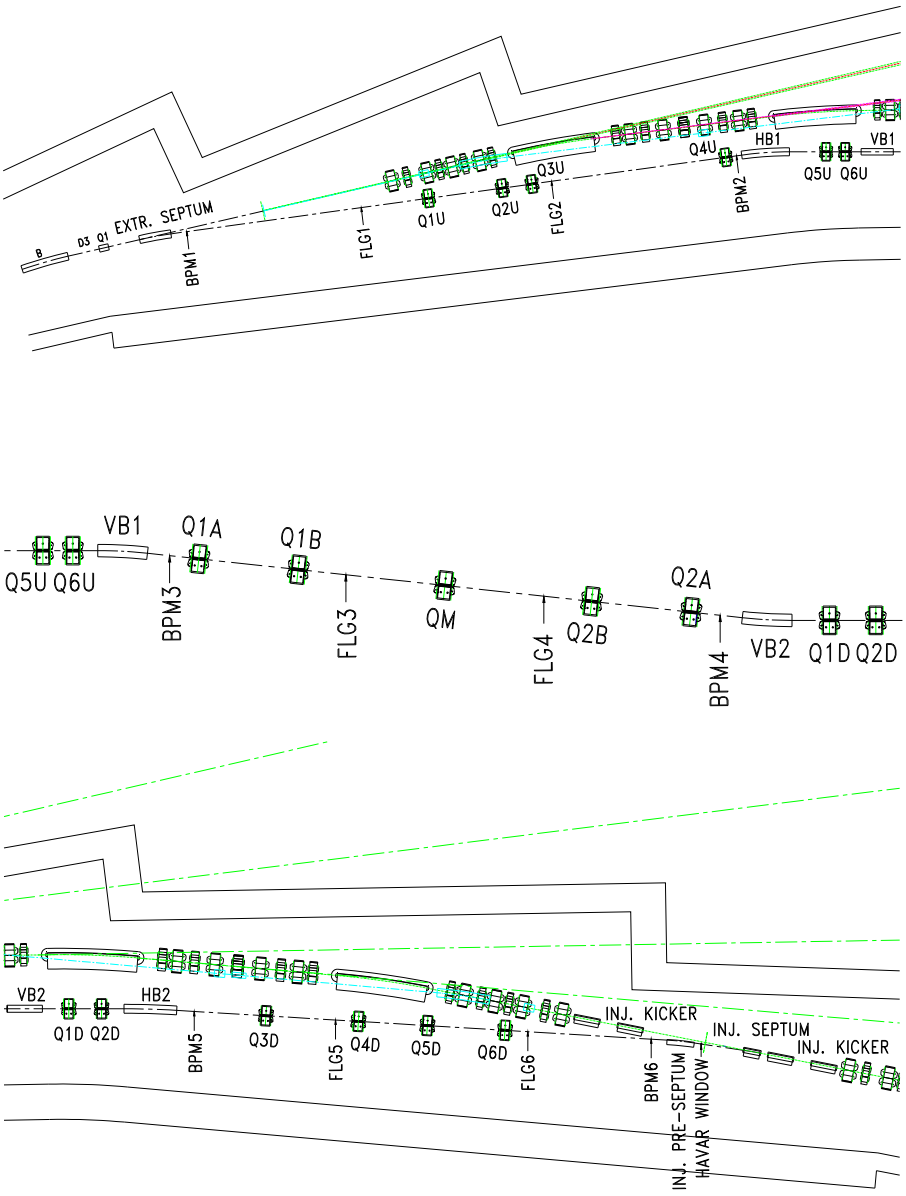

Figure 5.10.1 Beam trajectories through the booster-to-storage ring transport line. Top-to-bottom, figures show views from above, side, and above, respectively.

Conceptually, the transport line consists of three parts. The first part starts from the extraction septum and ends by the first horizontal dipole. Four quadrupoles located between these two elements preserve full achromaticity of the beam transport, canceling the horizontal dispersion at the end of the dipole.

The second part corresponds to a vertical dog leg, which is made fully achromatic as well, by using five quadrupoles located between two vertical dipoles. The vertical dispersion is matched to zero value at the end of the second part.

The third part, like the first one, serves as an achromatic bend, bringing the beam to the injection septum in the storage ring.

Quadrupole doublets inserted in the dispersion-free regions help to match the beta functions between various parts of the transport line and optimize the beta functions at the injection point.

Three pairs of trim magnets (two for each part of the transport line) are included for adjustment of the beam trajectory in the transport line. Six flags, accompanied by six beam position monitors, will be used to measure the beam position and size (Table 5.10.1).

Table 5.10.1 Magnet Parameters of the Booster-to-Storage Ring Transport Line.

	Dipole	Quadrupole	HV Trim
Number required	4	17	6
Field strength at 3 GeV	<0.8 T	<25 T/m	<1 T
Length [m]	1-1.5	0.3	
Gap height or diameter [mm]	35	35	–

In summary, the trajectory of the electron beam matches the storage ring injection straight, with the help of four bending magnets. Matching of the machine functions is accomplished with 17 quadrupoles. The machine functions are shown in Figure 5.10.2, and beam sizes along the transport line are shown in Figure 5.10.3.

5.10.2 Booster-to-Storage Ring Transport Line Power Supplies

Power supplies for the transport line magnets are listed in Table 5.10.2.

Table 5.10.2 Booster-to-Storage Ring Transport Line Power Supplies.

Function	Qty.	Volts	Amps	Magnet supplies
Dipole	4	7.3	175	BX-B1 to 4
Quadrupole	17	20	150	BX-QD1 to 8, LB-QF1 to 9
Trim	6	20.0	20.0	BX-V1 to 6, BXH1 to 6
Extraction kicker	1	12000	0.100	BXEKF
Septum	2	800	1.500	BXISH1, BXISH2
Injection Kicker	1	5000	0.100	BXIBF

The supplies will be operated around a static operating point, eliminating the need for significant voltage head room. For energy savings, we anticipate that the supply's output will be lowered during the dwell time in top-off mode and brought back to the operating point slightly before the top-off cycle. Unmodified commercial power supplies are currently used at NSLS in its transfer lines and are analog programmed by 14-bit digital-to-analog converters. The supplies are operated in current mode with shunt feedbacks.

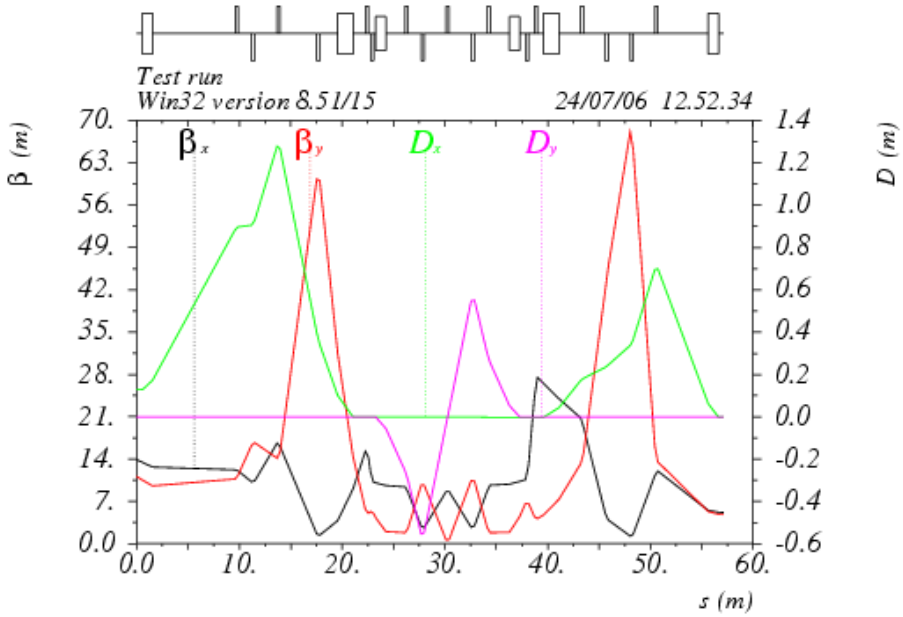

Figure 5.10.2 Twiss parameters along the B–SR transfer line.

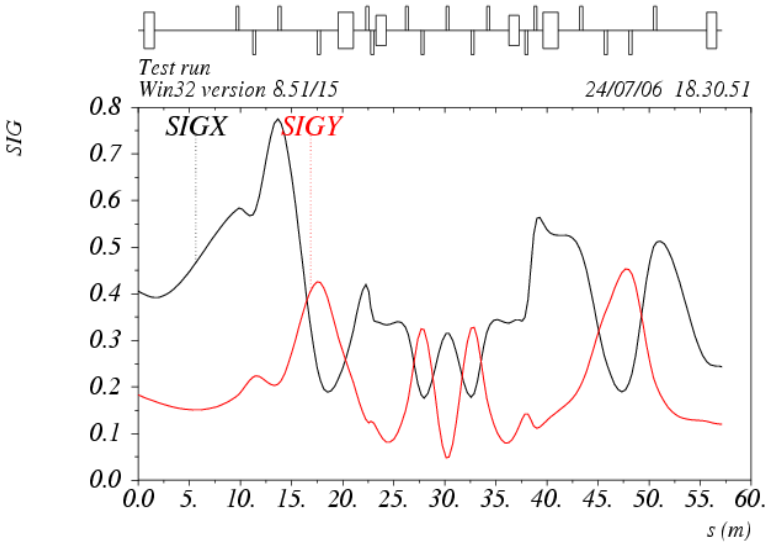

Figure 5.10.3 RMS beam sizes along the B–SR transfer line.

5.10.3 Power Supply Control

Either a micro-controller or PLC will provide an analog input to power supply programming interface and control the setpoint with a DAC resolution of at least 16 bits. Both the output voltage and current will be read back by a 16 bit ADC with a speed greater than 1 kHz.

Long-term monitoring of drift will be done using an independent external shunt connected to a high-precision analog channel.

5.11 Diagnostics and Instrumentation

5.11.1 Scope

This section describes diagnostics and instrumentation for the booster ring. The following parameters will be monitored:

- orbit
- working point (tunes in both planes)
- circulating current and filling pattern
- emittances
- beam losses around the booster
- bunch length

Booster diagnostics are summarized in Table 5.11.1.

Table 5.11.1 Beam Diagnostics for the Booster Ring.

Monitor	Quantity	Beam parameter
DC current transformer	1	Beam current
4-button pick-ups	75	Beam position
Fluorescent flags	4	Injection position, profile
Stripline set and amplifier	2	Betatron tune
Loss Monitor	30	Beam losses
Fast current transformer	1	Filling pattern
Optical beamline with streak-camera	1	Bunch length
Firewire camera	1	Beam position, profile

5.11.2 Flags

Four fluorescent flags will be used to observe shape and position of the injected electron beam during the first turn. The flag material will be YAG:Ce. This was chosen because it results in an excellent resolution of the beam image and exhibits high sensitivity and high radiation hardness.

5.11.3 Orbit Correction

The booster orbit will be monitored with 75 pick-up electrodes instrumented with RF BPM receivers. RF BPMs are widely used for accelerators and have the specifications shown in Table 5.11.2 [5.27]:

Table 5.11.2 RF BPM Specifications.

Beam intensity range [dB]	>75
Input signals	+5 dBm –70 dBm, 50 Ω
Operating frequency [MHz]	60 to 800
Noise RMS [mV]	<2 (1 kHz BW) @ +5 dBm
	<5 (1 kHz BW) @ –35 dBm
	<50 (1 kHz BW) @ –60 dBm
Linearity error (on-center) [mV]	<5 (+5 dBm to –35 dBm)
Output [V]	±10
Button sampling	2 k sample/s with external clock
Power supply	+15 V, <200 mA; –15 V, <40 mA

5.11.4 Current Measurement

The booster current will be measured with a parametric current transformer, such as the one manufactured by Bergoz [5.28]. Its radiation-hardened sensor head is equipped with 30 m cable and its inner diameter of 115 mm is sufficient to fit over the flange. The parametric current transformer has the following specifications:

Table 5.11.3 Booster Current Monitor Specifications.

Full scale ranges	±20 mA, ±200 mA, ±2 A, ±20 A
Range control	2 TTL lines
Output [V]	±10
Output bandwidth (–3 dB)	8 kHz in 20 mA range, 10 kHz other ranges
Response time (at 90%) [μs]	<50
Resolution [μA/Hz$^{1/4}$]	<5
Output accuracy [%]	±0.1
Linearity error [%]	<0.1
Output impedance [Ω]	100

The filling pattern will be monitored with an in-flange, fast current transformer. For example, the Bergoz FCT has the following specifications [5.29]:

Table 5.11.4 Filling Pattern Specifications for the Fast Current Transformer.

Turns ratio	20:1
Nominal sensitivity [V/A]	1.25
Rise time (typ.) [ps]	200
Droop [%/μs]	<6
Upper cutoff frequency (–3 dB typical) [MHz]	1750
Lower cutoff frequency (–3 dB) [kHz]	<9.5
Position sensitivity [%/mm]	<0.2
Minimal L/R time constant [μs]	17
Maximum charge per pulse (pulses<1 ns) [μC]	0.4

5.11.5 Bunch Length Measurement

The synchrotron radiation from one of the bends will be used for bunch-length measurements with the help of a streak camera [5.30]. Its specifications are shown in Table 7.8.3.

5.11.6 Tune Measurement System

The fractional tune measurement system will be based on real-time spectral analysis of the signal induced on the strip-lines by the electron beam. Electron beam motion will be excited by broadband noise generator with fixed cutoff frequencies. The real-time spectrum analyzer will be used to observe tune evolution along the ramp.

5.11.7 Beam Loss Monitors

The beam loss monitors will have two p-i-n photodiodes mounted face to face for coincidence detection of charged particles. Coincidence counting makes them insensitive to the synchrotron radiation photons. The widely used Bergoz BLM specifications are as follows [5.31]:

Table 5.11.5 Beam Loss Monitor Specifications.

Single particle detection efficiency [%]	>30
p-i-n photodiode surface [mm^2]	7.34
Maximum count rate [MHz]	>10
Spurious count rate [Hz]	<0.1
Output	positive TTL, 50 Ω
Cable driving capability	>200 m RG213
Power supply	+5 V, 170 mA; –5 V, 80 mA; +24 V, 1 mA
Size [mm]	69 x 34 x 8

5.11.8 Visible SR Diagnostics

The synchrotron radiation from the bending magnet will be used for beam observation with CCD cameras. The beam image will be analyzed for the emittance measurements and also will provide information on the beam position and stability during the ramp.

References

[5.1] http://accelconf.web.cern.ch/AccelConf/e04/PAPERS/THPLT186.PDF
[5.2] T. Shaftan, et al., “Design of 3 GeV Booster for NSLS-II,” Proc. of PAC-2005, p. 3473.
[5.3] A. Setty, et al., “Commissioning of the 100 MeV Preinjector HELIOS for the SOLEIL Synchrotron,” EPAC06.
[5.4] EIMAC, CPI, Eimac Division, Palo Alto, CA.
[5.5] W. B. Herrmannsfeldt, “EGUN – An Electron Optics and Gun Design Program,” SLAC 331, 1988.
[5.6] Parmela, ver. 3, by Lloyd M. Young , Documentation by James H. Billen, Los Alamos Nat. Lab.
[5.7] C. Christou, et al., “Commissioning of the Diamond Pre-Injector Linac,” EPAC06.
[5.8] C.W. Allen et al., “PEP-II Hardware Reliability,” SLAC-PUB-10835.
[5.9] S.S. Park et al., “Reliability Analysis of the PLS Klystron-Modulator System,” Proc. of the Second APAC, Bejing, 2001.
[5.10] http://www.sc-nova.com/

[5.11] W. Crewson, "A new solid-state high-power pulsed modulator," 5th Modulator-Klystron Workshop for Future Linear Colliders MDK-2001 Geneva, 25-27 April 2001.
[5.12] J. Rose, et al., "Radio-Frequency Control System for the DUVFEL," PAC03. http://epaper.kek.jp/p03/PAPERS/TPAB006.PDF
[5.13] B. Fellenz, and J. Crisp, "An Improved Resistive Wall Monitor," Proc. of Beam Instrumentation Workshop 1998, AIP Conf. Proc. 451, pp. 446–453.
[5.14] http://www.bergoz.com
[5.15] E. Johnson, W.S. Graves, and K.E. Robinson, "Periscope Pop-In Monitor," Proc. of Beam Instrumentation Workshop 1998, AIP Conf. Proc. 451, pp. 479–484.
[5.16] http://www.gmw.com/beam_diagnostics/Bergoz/bpm/pdf/GMW-DS-BPM-UHV-50_B.pdf
[5.17] A. Kalinin, "Log-Ratio Beam Position Monitor," Proc. of Beam Instrumentation Workshop2002, AIP Conf. Proc. 648, pp. 384–392.
[5.18] G. Mülhaupt, "A Few Design Considerations for Injector Synchrotrons for Synchrotron Light Sources," Internal Report ESRF/MACH-INJ/94-13, ESRF Grenoble 1994A.
[5.19] W.D. Klotz, G. Mülhaupt, "A Novel Low Emittance Lattice for High Brilliance Electron Beams. Workshop on Fourth Generation Light Sources, 1992, Stanford, CA
[5.20] W. Joho, M. Munoz, and A. Streun, "The SLS booster synchrotro," *Nucl. Instrum. & Meth. A* 562 (2006), p.1.
[5.21] V. Tsakanov, et al., "Status of the 3 GeV CANDLE Synchrotron Light Source Facility project," Proc. of EPAC-2004, Lucerne, p. 2254.
[5.22] D. Einfeld, et al., "Progress of the Synchrotron Light Source ALBA," Proc. of PAC-2005, Knoxville, TN, p. 4203.
[5.23] G.-H. Luo, et al., Design Consideration of a Booster for Taiwan Photon Source, Proc. of PAC-2005, Knoxville, TN, p. 2992.
[5.24] J. Galayda, et al., "The NSLS Booster Synchrotron," Proc. of PAC-1979, p. 3839.
[5.25] M. Munoz and V. Joho, Eddy current effects in the SLS booster: http://**sls**bd.psi.ch/pub/**sls**notes/tmeta9810/**eddy**.html
[5.26] H. Gerke, H.P. Scholz, M. Sommerfeld, A. Zolfaghari, "Das Petra Cavity," Interner Bericht DESY PET-77/08, August 1977.
[5.27] http://www.bergoz.com/products/MX-BPM/MX-BPM.html
[5.28] http://www.bergoz.com/products/NPCT/PCT-downloads/files/NPCTflyer.pdf
[5.29] http://www.bergoz.com/products/FCT/d-fct.html
[5.30] http://sales.hamamatsu.com/en/products/system-division/ultra-fast/streak-systems.php
[5.31] http://www.bergoz.com/products/BLM/BLM.html

6 LATTICE AND ACCELERATOR PHYSICS

6.1 Lattice and Beam Dynamics

The storage ring lattice is designed to provide a stable, closed orbit on which the electron beam can circulate with long lifetime and efficient injection of beam from the booster. This injection will be capable of filling the ring from zero beam current to the operating values ($\leq$500 mA) in a short time, as well as to provide top-off injection to maintain a constant level of beam current ($<\pm$0.5% variations) and thus provide a constant radiated beam power on the users' beamline components, with low thermal distortions.

The electron beam will be damped by the synchrotron radiation to a small beam emittance lower than that of any storage ring light source currently operating or under construction. The photon beams radiated from undulators will, therefore, have lower emittance and higher brilliance, surpassing any existing light sources in the 2 to 10 keV range in focused beam flux on small specimens.

6.1.1 Physics and Design Goals for the Storage Ring Lattice

The design of the NSLS-II storage ring is driven by goals required to achieve the baseline performance as well as challenge goals that will provide the potential for future upgrades of beam performance. The challenge goals will keep NSLS-II at the frontier of the field for an extended time. Table 6.1.1 lists the required and challenge goals.

Table 6.1.1 Goals for the NSLS-II Design.

Beam Property	Required Goal	Challenge Goal
Ultra low horizontal emittance [nm-rad]	$\leq$1.5 (achromatic)	$\leq$0.5
Vertical emittance [nm-rad]	0.010	0.008
Stored currents [mA]	500	750
ID straights for undulators	$\geq$21	$\geq$25
Electron beam stability [μm]	1	<1
Top-off injection current stability (Δt $\geq$2 min) [%]	<1	<0.1

Several lattices have been studied over the past few years. As work progressed, it became clear that the Double Bend Achromatic lattice could meet the emittance goals while providing an increased number of insertion device straight sections. To achieve our low emittance goals, we maintain achromatic arcs and install damping wigglers in the extra ID straight sections to enhance the SR power without significantly increasing the quantum excitation of the electron beam [6.1.1]. This process yields a net reduction of the beam emittance proportionally related to the ratio of dipole-radiated power to the DW-radiated power, reducing the beam emittance up to five-fold without significantly impacting the DA performance of the ring.

The minimum emittance for a DBA lattice with 2M dipole magnets and electron energy $E_0=\gamma mc^2$ is given by

$$\varepsilon_0^{\min} = \left(7.7\times10^{-4}\, nm-rad\right)\gamma^2 / M^3 . \qquad (6.1\text{-}1)$$

The achievable emittance for a realistic lattice design is about twice this minimum value. The momentum compaction is

$$\alpha = \frac{\pi^2}{6M^2}\frac{2\pi\rho_0}{C}, \tag{6.1-2}$$

where ρ_0 is the dipole magnet bending radius and C is the ring circumference. Note that the momentum compaction increases linearly with bend radius.

The emittance ε_w with damping wigglers is related to that without damping wigglers, ε_0, by $\varepsilon_w \approx \varepsilon_0/(1+U_w/U_0)$, where U_w / U_0 is the ratio of the energy lost per turn in the wigglers to that lost in the dipoles. For NSLS-II, we chose to have a large dipole bending radius. This reduces the energy radiated in the dipoles, which means we need to radiate less energy in the wigglers to reduce the emittance by a given factor.

To be more precise, consider a wiggler of length L_w having bending radius ρ_w and period λ_w centered in the insertion section. The ratio of the fractional energy spread with the wiggler to that without is

$$\frac{\delta_w}{\delta_0} = \sqrt{\left[1+\frac{L_w}{2\pi\rho_0}\frac{4}{3\pi}\left(\frac{\rho_0}{\rho_w}\right)^3\right]\left[1+\frac{L_w}{4\pi\rho_0}\left(\frac{\rho_0}{\rho_w}\right)^2\right]^{-1}}, \tag{6.1-3}$$

and the ratio of the emittance with the wiggler to that without is

$$\frac{\varepsilon_w}{\varepsilon_0} = \frac{1+f}{1+\frac{L_w}{4\pi\rho_0}\left(\frac{\rho_0}{\rho_w}\right)^2}. \tag{6.1-4}$$

The fluctuation factor, f, is given by

$$f = \frac{2C_q\gamma^2}{3\pi^2\varepsilon_0}\frac{L_w\rho_0}{\rho_w^3}\left[\frac{K_w^2}{5\gamma^2}\langle\beta_x\rangle + \frac{\eta_0^2}{\beta_{x0}} + \beta_{x0}\eta_1^2\right], \tag{6.1-5}$$

where $C_q = 3.84\times10^{-13}$ m, and strength parameter $K_w = \lambda_w\gamma / 2\pi\rho_w$. The horizontal beta function is given by $\beta_x(s) = \beta_{x0} + s^2/\beta_{x0}$, where $s = 0$ is the center of the wiggler and insertion, and $\langle\beta_x\rangle$ denotes the average value of β_x in the wiggler. We express the dispersion function in the wiggler in the form $\eta(s) = \eta_w(s)+\eta_0+\eta_1 s$, where $\eta_w(s)$ is the sinusoidal dispersion generated by the wiggler itself, and $\eta_0+\eta_1 s$ is the dispersion generated by errors elsewhere in the ring. Eq. (6.1-5) can be used to determine a tolerance on the dispersion in the insertions arising from errors.

As at ESRF, the NSLS-II lattice has alternating high and low horizontal beta function straight sections for insertion devices. A large value of β_x is desired at the injection septum. Small β_x is desired in undulators for beamlines designed to focus the radiation down to a small spot. The vertical beta function should be small in undulators to optimize brightness. In fact, it is essential that β_y not be large in any of the insertion devices. The linear tune shift produced by an undulator or wiggler is

$$\Delta\nu_y = \frac{\langle\beta_y\rangle L_w}{8\pi\rho_w^2}. \tag{6.1-6}$$

Small β_y keeps the tune shift within acceptable limits. We have bounded the straight sections with quadrupole quartets in order to provide a local correction for the modification of the betatron functions and phases due to undulator or wiggler focusing.

The tune shift with amplitude due to nonlinear undulator or wiggler focusing is

$$\frac{d\nu_y}{dJ} = \frac{\pi \left\langle \beta_y^2 \right\rangle L_w}{4\lambda_w^2 \rho_w^2}. \tag{6.1-7}$$

To minimize the effect of the nonlinear focusing on dynamic aperture, it is essential to have small β_y in the insertion devices.

This is the approach taken for NSLS-II [6.1.2]. A DBA with 30 periods was chosen as the lattice structure, with a natural emittance of 2.1 nm. One cell of the lattice, shown in Figure 6.1.1, comprises half a super-period with reflection symmetry about the right or left hand end of the cell. The lattice functions have been optimized to achieve achromatic arcs, low emittance and modest chromatic sextupole strengths, small Closed Orbit Amplification Factors, and desired betatron functions in the long and short straight sections, which are required for small impact on the DA of the IDs, as given by Eq. (6.1-6 and 6.1-7). The working point tune was selected for optimization of the sextupole correction of the nonlinear driving terms that limit the DA, as well as reduced COAF and instability sensitivity. The dipole magnets have been optimized (bend radius ρ_0 = 25 m, B_0 = 0.399 T at 3 GeV) to enhance the reduction of the beam emittance with the DWs. Although the bare lattice doesn't quite meet the required emittance goal (2.1 nm instead of 1.5 nm), this goal is exceeded with only one 7 m DW installed and operated at a peak field of 1.8 T.

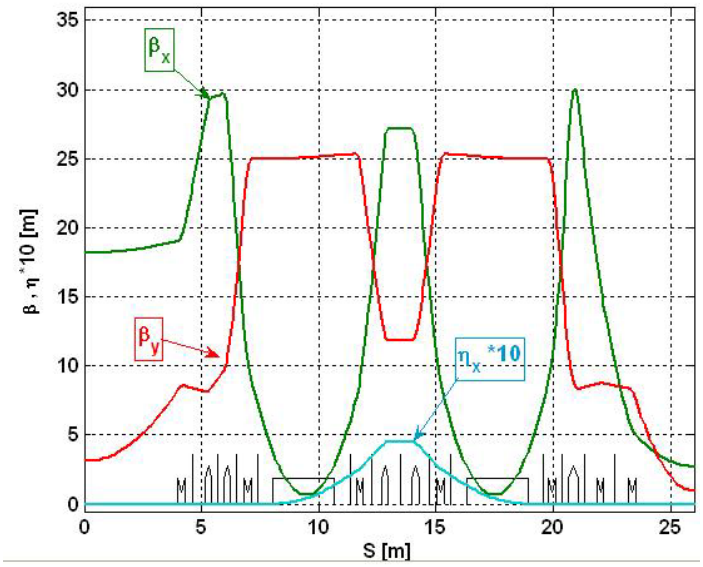

Figure 6.1.1 The lattice functions for one-half of a DBA period. A super-period consists of this cell reflected about either ID center: 8 m on the left-hand side or 5 m on the right.

The impact of DWs on the emittance and the energy spread, given by Eq. (6.1-3 and 6.1-4), is shown in Figure 6.1.2 for the designed ρ_0 = 25 m and a stronger dipole with 1.5 times the field (2/3 the bend radius). This calculation also assumes no significant spurious dispersion in the straight section, since the individual quadrupole powering in this lattice should allow the dispersion to be corrected cell-by-cell for any dipole variations. The gain in undulator brightness resulting from the smaller emittance provided by more damping wigglers is somewhat reduced by the increased energy spread of the beam, especially at x-ray energies corresponding to higher harmonics of the undulator. Increasing the bend radius from 16.68 m to 25 m reduces both the emittance as well as the energy spread. Continuing to increase the bend radius to larger values is

increasingly less effective at reducing the emittance as it approaches the IBS limit, and at the same time increasingly expensive, as it increases the circumference of the ring. As discussed in Chapter 5, a bend radius of 25 m is about optimal for NSLS-II. The installed RF power also provides a practical limit to the gain from more damping wigglers, since the beam lifetime will be reduced if the radiated power exceeds the installed power necessary for sufficient RF bucket height.

An additional advantage of the low-field dipoles is that their radiated photon energy will be lower than many of the planned ID beams and therefore they will have less impact on the photon beam position monitors used in feedback systems, e.g., as seen at APS [6.1.3]. The photon energy separation between the two beams will allow filters to be used to absorb the dipole beam while the ID photon beam passes through.

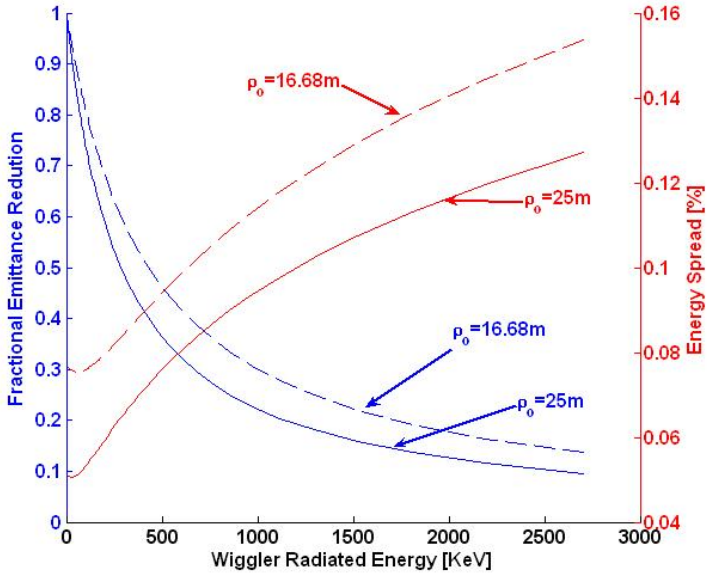

Figure 6.1.2 The fractional reduction of the ring emittance and the increase in energy spread for dipole magnets of bend radii: ρ_o = 25 m (proposed for NSLS-II) and ρ_o = 16.7 m dipole that could yield a shorter circumference lattice.

Table 6.1.2 lists the design parameters for this 15 super-period DBA (15×2) lattice. The choice of low dipole field restricts the photon beam energies radiated by the dipoles to 2.4 keV critical energy at 3 GeV. The dipole radiation will provide very bright VUV and soft-x-ray beams. Hard x-rays will be available from the installed DWs (10.8 keV critical energy) with high brilliance and flux.

Table 6.1.2 Storage Ring Parameters.

Energy [GeV]	3
Circumference [m]	780
DBA cells	30 (15 x 2)
Bending radius [m]	25.019
RF frequency [MHz]	499.46
Momentum compaction	0.000368
Tune: ν_x, ν_y	32.35, 16.28
Natural chromaticity: ξ_x, ξ_y	–100, –41.8
Maximum dispersion [m]	0.45
High-beta 8-m straights: β_x, β_y [m]	18, 3.1
Low-beta 5-m straights: β_x, β_y [m]	2.7, 0.95
Dipole radiated energy loss [keV]	286.5
Dipole critical energy [keV]	2.394

Figure 6.1.3 shows the expected reduction of the emittance as one to eight 7 m DWs are added to the ring.

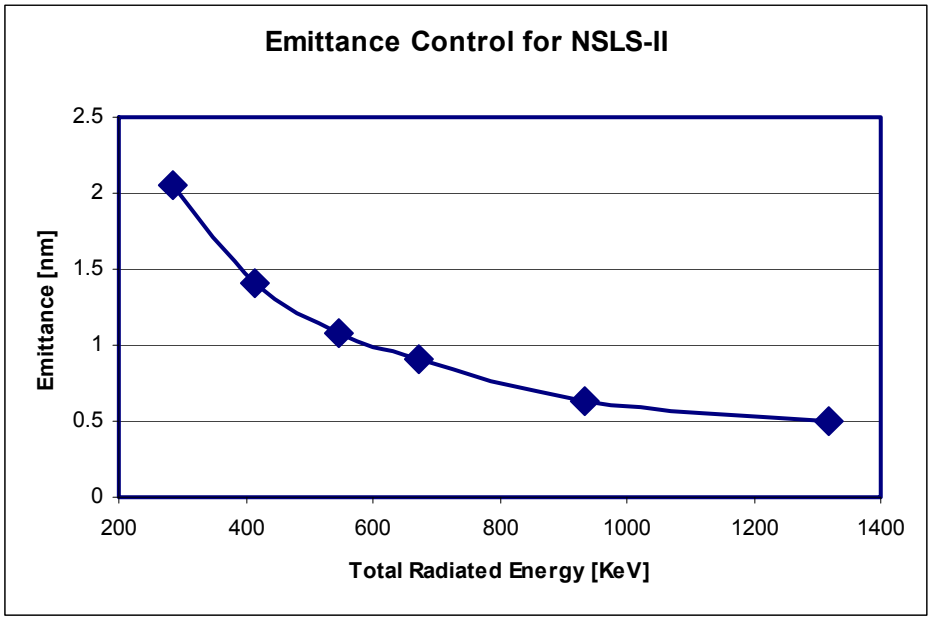

Figure 6.1.3
Emittance reduction for NSLS-II as 0, 1, 2, 3, 5, and 8 DW (7 m each) are installed and operated at 1.8 T peak field.

Table 6.1.3 compares the basic lattice properties with those obtained with 21 or 56 m of DWs installed in the ring. All of these DWs will have a fixed gap and will be available to drive user beamlines.

Table 6.1.3 Effect of Three and Eight 7 m Damping Wigglers on Beam Properties at 3 GeV.

	Zero DWs	Three 7 m DWs (21 m)	Eight 7 m DWs (56 m)
Energy loss [keV]	287	674	1320
RF voltage (3% bucket) [MV]	2.5	3.1	3.9
Synchrotron tune	0.0079	0.00876	0.0096
Natural emittance: ε_x, ε_y [nm-rad]	2.1, 0.01	0.91, 0.008	0.50, 0.005
Damping time: τ_x, τ_s [ms]	54, 27	23, 11.5	12, 6
Energy spread [%]	0.05	0.089	0.099
Bunch duration [ps]	10	15.4	15.5

The lattice shown in Figure 6.1.1, like that at ESRF, has low and high beta function straight sections. However, we have increased the length of the high-β_x straight section to provide for injection, space for RF cavities, and space for longer DWs and user IDs. The drift space between quadrupole magnets is 8 m. The space available for insertion devices is 7 m. The magnet layout for the long ID straight section, with 8 m inner quadrupole spacing, is shown in Figure 6.1.4. Half the long ID is shown with reflective symmetry about the centerline (left-hand side). There are a total of eight quadrupoles (Q1, Q4×2) and eight sextupoles (S1, S4×2) in each ID straight section. Although they are considered as four families of focusing strengths, they will be independently powered to account for magnet-to-magnet differences and for the possibility of shifting the symmetry condition for improved photon beam focusing. The four quadrupole families provide sufficient parameters for correcting the local distortions of the linear lattice when IDs are installed or when the gaps are changed by the users [6.1.4, 6.1.5]. The four families of sextupoles in each long ID are required in order to correct the nonlinearity of the lattice arising from the strong chromatic sextupoles located in the dispersive

regions. For certain working points, some sextupoles have small strengths. These might be dropped from a future optimized design.

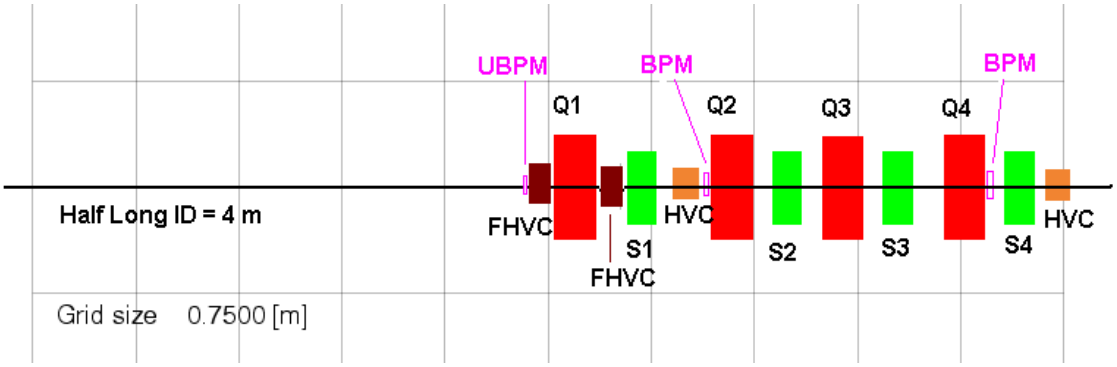

Figure 6.1.4 Layout for half of a long ID straight section, with reflection symmetry on left side.

The short ID straight section layout is shown in Figure 6.1.5. The short ID has a 5 m drift between the inner quadrupoles and is similar to the long ID in layout of the quadrupoles and sextupole families. Differences include additional drift between quadrupoles to reduce the chromaticity, while providing the increased focusing needed for the lower beta functions. To meet the maximum gradient values, one quadrupole (Q33) must be longer than those in the long ID straight section.

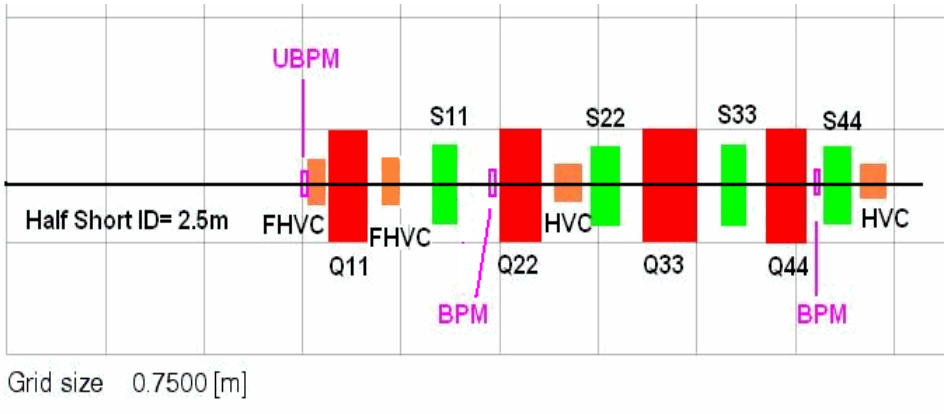

Figure 6.1.5 Layout for half of a short ID straight section, with reflection symmetry on left side.

Two slow horizontal and vertical closed-orbit correction magnets are included in each ID straight section (some also include a skew quadrupole winding). For the purposes of this conceptual design,, we assume independent corrector magnets, as shown in Figures 6.1.4 and 6.1.5. Also shown are two beam position monitors to be used for closed-orbit correction. When a user ID is installed in the ring, it is assumed that two pairs of fast horizontal and vertical correctors and a pair of user BPMs will also be installed. These will be optimized for the aperture of the ID vacuum chamber to yield increased sensitivity to orbit motion and the increased frequency of correction for fast orbit motion required for the ID beamline. To accomplish this will require some advanced engineering, but there is adequate drift space provided. The FHVCs and UBPMs will be used as part of a local feedback system to provide submicron photon beam stability up to 100 Hz. Since the four FHVCs will provide a closed bump, the possibility of adding a photon beam position signal to the feedback system will also be available, without that signal impacting the beam for other users.

Figure 6.1.6 shows the magnet layout for the dispersion region of the lattice with the dipoles included. This region has four quadrupoles in two families and five sextupoles in three families. These magnets give some flexibility for optimizing the dispersion function for reduced chromatic sextupole strength. The third chromatic sextupole allows the linear chromaticity to be compensated, while reducing the higher-order chromatic terms. As in the ID straight sections, two BPMs are included close to the quadrupoles near the ends of the girder. This is to provide improved alignment of the magnets on the girder using a beam based alignment of the BPM to the quadrupoles magnetic center. A third BPM is included near the QF quadrupole (near the maximum dispersion point). This BPM will be used for accelerator physics measurements of the dispersion and beta functions, when needed, and will improve the orbit correction for random alignment errors. Also included are three discrete HVC correctors that will be used for static and global orbit correction. However, since the vertical beta function is small in the middle corrector, only a horizontal correction power supply will be provided in this corrector.

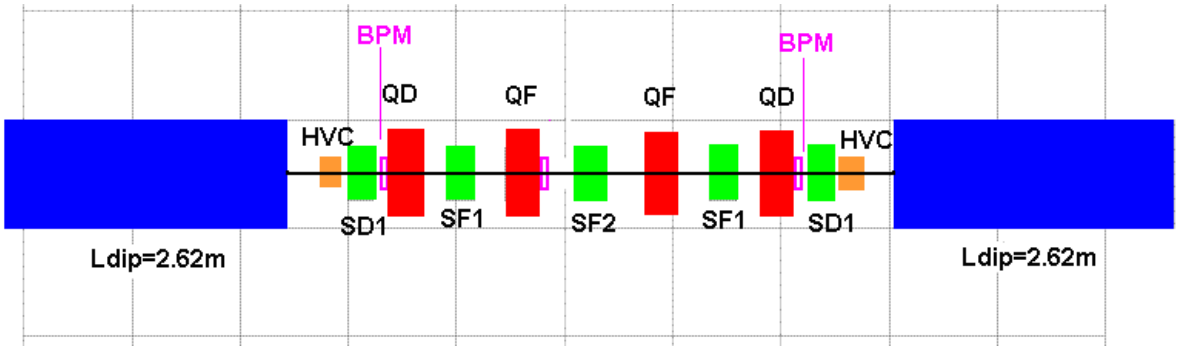

Figure 6.1.6 Layout for the dispersion section, including the two dipole magnets.

Table 6.1.4 lists a summary of the basic storage ring beam components and BPMs in the lattice design and closed-orbit control. Details on the maximum values and tolerances of these magnets are listed in Section 8.1.1.

Table 6.1.4 List of Magnets and BPMs for the NSLS-II Storage Ring.

No. of Elements	Type of Element	Length [m]
60	Dipole	2.62
330	Quadrupole (S)	0.3
30	Quadrupole (L)	0.4
30	Sextupole (L)	0.30
120	Sextupole (M)	0.25
240	Sextupole(S)	0.20
180	H+V Corrector (30 H only PS)	0.15
30	H+V + SQ Corrector (1 SQ per cell)	0.15
210	BPM electronics	0.05
≤20 (initial)	Fast H+V Corrector (as required)	0.10
≤10 (initial)	User ID BPM (2 per ID)	0.10

6.1.2 Nonlinear Dynamics

6.1.2.1 Guidelines

One of the main design challenges for a strongly focusing lattice is to obtain adequate dynamic aperture for injection and Touschek lifetime[1]. As the required strength of the chromatic sextupoles increases, the DA can be improved by introducing extra families of geometric and chromatic sextupoles. However, once the sextupoles become too strong, this is no longer feasible. Eventually, cross terms generate higher-order terms, and when more families are introduced, the lattice will become pathological [6.1.5]. To avoid this, the following guideline has been provided for the linear optics design:

- horizontal chromaticity per cell, $\xi_x \sim 3$,
- peak dispersion, $\eta_x \sim 0.3$ m.

Similarly, we have adopted the guidelines for the DA summarized in Table 6.1.5. This is a conservative approach[2] to satisfy the requirements for the injection aperture for efficient top-off, as well as to ensure sufficient Touschek lifetime.

Table 6.1.5 Dynamic Aperture Guidelines.

	Horizontal and Vertical Dynamic Acceptance [mm·mrad]	Horizontal Dynamic Aperture [mm]	Momentum Acceptance [%]
Bare lattice (2.5 degrees of freedom[3])	~25	±20	**±3**
"Real" lattice (3 degrees of freedom[4])	~20	±15	**±3**

This also provides some leeway for magnetic alignment and field tolerances, and nonlinearities due to insertion devices, which, when included, perturb the symmetry of the linear optics and diminish the cancellation of the nonlinear effects, reducing the DA.

6.1.2.2 Sextupole Scheme

The linear lattice has a chromaticity of $\xi_{x,y}^{(1)} \sim (-100, -42)$ and a natural momentum spread of ~0.1% leading to a tune spread of $\Delta\nu_{x,y} \sim (0.1, 0.04)$, which must be corrected[5]. The linear chromaticity is given by

$$\xi_{x,y}^{(1)} = \mp\frac{1}{4\pi}\sum_{k=1}^{N}\left[(b_2L)_k - 2(b_3L)_k\eta_{x,k}\right]\beta_{(x,y),k}, \tag{6.1-8}$$

where (b_2L), (b_3L) are the integrated quadrupole and sextupole strengths, and β and η are the beta function and dispersion, respectively at the quadrupoles and sextupoles, k. The driving terms for linear chromaticity from sextupoles are shown in Figure 6.1.7. Three mirror symmetric chromatic families are introduced inside the dispersion section and 4+4 geometric families in the short and long straight sections, i.e., a total of 11

[1] For medium energy rings: ~3 GeV.

[2] Based on the experience from the Swiss Light Source conceptual design, i.e., a highly nonlinear lattice [6.1.6] with straightforward commissioning [6.1.7], excellent top-off injection efficiency [6.1.8], and stability [6.1.9].

[3] With δ (momentum deviation) treated as a parameter, i.e., the adiabatic approximation.

[4] In particular, with synchrotron oscillations.

[5] Moreover, a positive linear chromaticity in the range 0–5 is required to stabilize the head-tail instability.

sextupole families. While a few of the families in the matching sections tend to be weak, they have been left as place holders until a more comprehensive optimization has been completed. Independent power supplies for all the quadrupoles and sextupoles are provided, to allow for local optics correction [6.1.10–6.1.16] and control of residual nonlinear resonances [6.1.17].

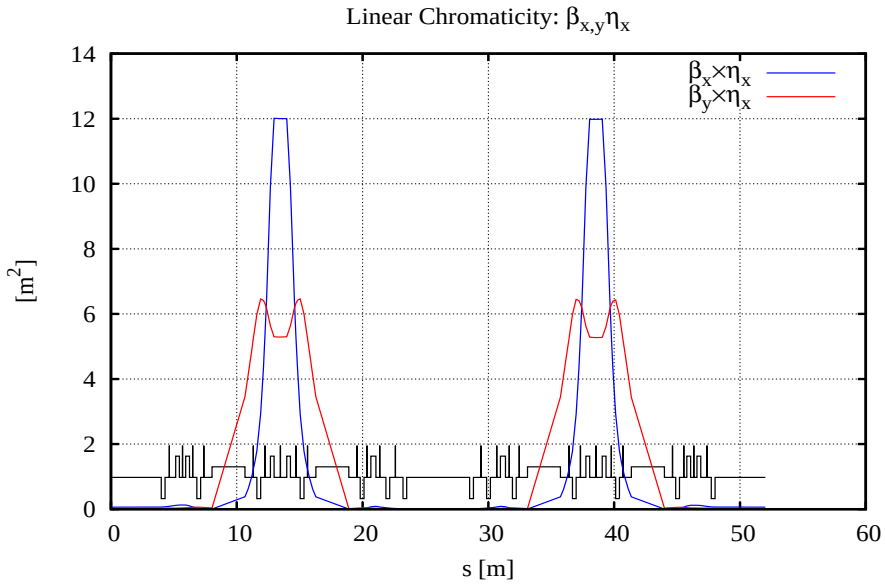

Figure 6.1.7 Driving terms for zeroing linear chromaticity with sextupoles, $\beta_{x,y}\,\eta_x$.

After linear chromaticity has been zeroed, the nonlinear chromaticity may be a limiting factor. The second-order chromaticity is given by 0:

$$\xi^{(2)}_{x,y} = -\frac{1}{2}\xi^{(1)}_{x,y} + \frac{1}{8\pi}\sum_{k=1}^{N}\left\{2(b_3L)_k \frac{\partial\eta_{x,k}}{\partial\delta}\beta_{(x,y),k} - \left[(b_2L)_k - 2(b_3L)_k\eta_{x,k}\right]\frac{\partial\beta_{(x,y),k}}{\partial\delta}\right\} \tag{6.1-9}$$

The driving terms are shown in Figures 6.1.8 and 6.1.9. Clearly, small variations of the sextupole locations may lead to large changes of the nonlinear chromaticity[6]. In particular, the rather large second-order horizontal dispersion leads to a substantial residual cubic term in the horizontal chromaticity [6.1.19] as discussed in Section 6.1.2.3. As a further refinement, this term should be controlled by including the driving term in the linear optics optimizations.

[6] As noted from numerical simulations for the DIAMOND conceptual design [6.1.18].

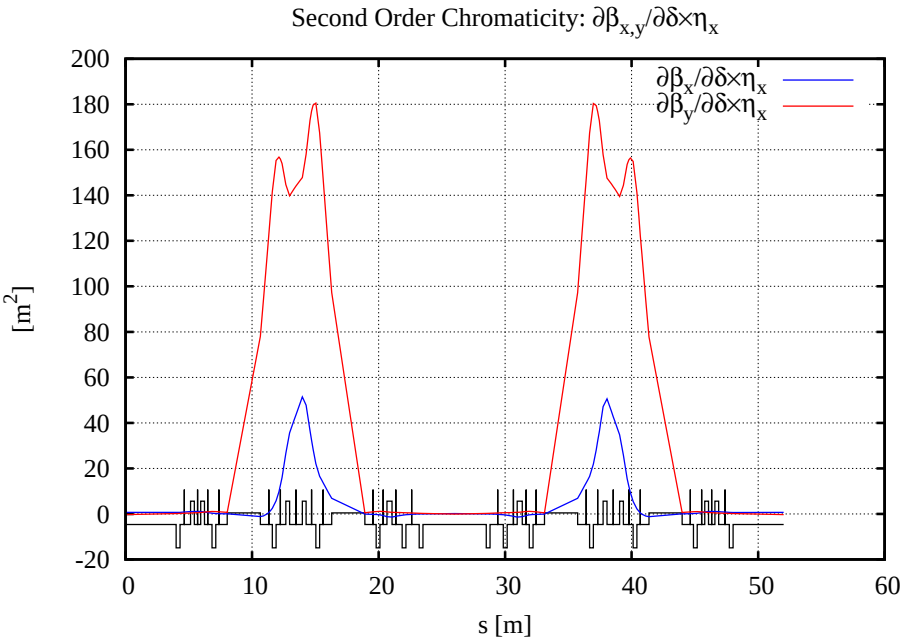

Figure 6.1.8 Driving terms for second-order chromaticity, $\partial\beta_{x,y}/\partial\delta\times\eta_x$.

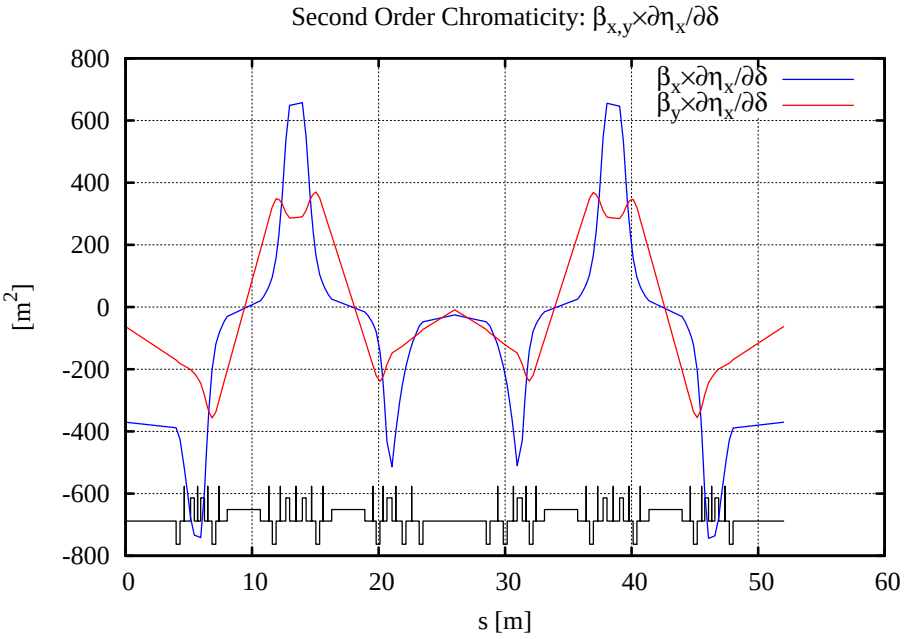

Figure 6.1.9 Driving terms for second-order chromaticity, $\beta_{x,y}\partial\eta_x/\partial\delta$.

6.1.2.3 Dynamic Aperture Optimization

The Poincaré map has the formal Lie series representation [6.1.17]:

$$\mathcal{M} = e^{:h:}\mathcal{M}_{\text{linear}} \tag{6.1-10}$$

where $\mathcal{M}_{\text{linear}}$ is the linear one-turn map, and the Lie generator h represents the nonlinear kicks transferred to the entrance of the lattice. In particular, the first-order generators have the form:

$$h_3 = \sum_J h_{jklmp} (2J_x)^{(j+k)/2} (2J_y)^{(l+m)/2} \delta^p e^{i\left[(j-k)\phi_x + (l-m)\phi_y\right]} + \text{c.c.},$$
$$h_{jklmp} = h^*_{kjmlp} = \sum_{n=1}^{N} (b_3 L)_n \beta_{xn}^{(j+k)/2} \beta_{yn}^{(l+m)/2} \eta_x^p e^{i\left[(j-k)\mu_{xn} + (l-m)\mu_{yn}\right]} \quad (6.1\text{-}11)$$

where J, ϕ are the action-angle variables and β, μ the beta functions and phase advances at the sextupoles, n.

In contrast to the linear case, the long-term stability now depends on: $\mathcal{M}_{\text{linear}}$ (i.e., the tune), h, and the initial conditions. In other words, for a systematic approach, the Lie generator and the working point have to be optimized simultaneously. We have implemented a generalized third-order achromat by introducing 11 sextupole families to the super-period, and minimized h over two super-periods, i.e., four DBA cells, for a range of cell tunes. At each working point with optimized sextupole strengths, we evaluated the DA by tracking. To the second order in the sextupole strengths, there are:

- 2+3+2 chromatic terms
- 5+8 geometric terms (modes)
- 3+3 tune shift with amplitude and momentum

This is a total of 26 terms[7] (see Table 6.1.6 for an inventory). These are minimized by varying the sextupole strengths using the following automated method[8] [6.1.5]:

1. For a given cell tune, the Lie generator h and its parametric dependence on the sextupole strengths (i.e., the Jacobian) are calculated for $J_{x,y}$ and δ at the anticipated DA.
2. The norm of $||h||$ is minimized[9] and the DA is evaluated by tracking.
3. The cell tune is changed by adjusting the quadrupoles in the matching sections and steps 1–3 are repeated.

The off-momentum aperture is included by using a weighted average for the DA at δ = 0, ±3%. A robust solution is obtained by establishing a broad local maximum for the DA. The tune scan presented in Figure 6.1.10 shows a broad maximum for the DA centered near (ν_x, ν_y)=(2.115, 1.105) per super-period.

[7] The corresponding overconstrained system of nonlinear equations for the sextupole strengths can be minimized because of symmetry and the fact that the higher order terms are due to cross terms of the lower order.

[8] Feasible only because of the use of symmetry and the fact that the higher order terms appear due to cross terms of the lower order.

[9] In particular, a least-square of the individual terms.

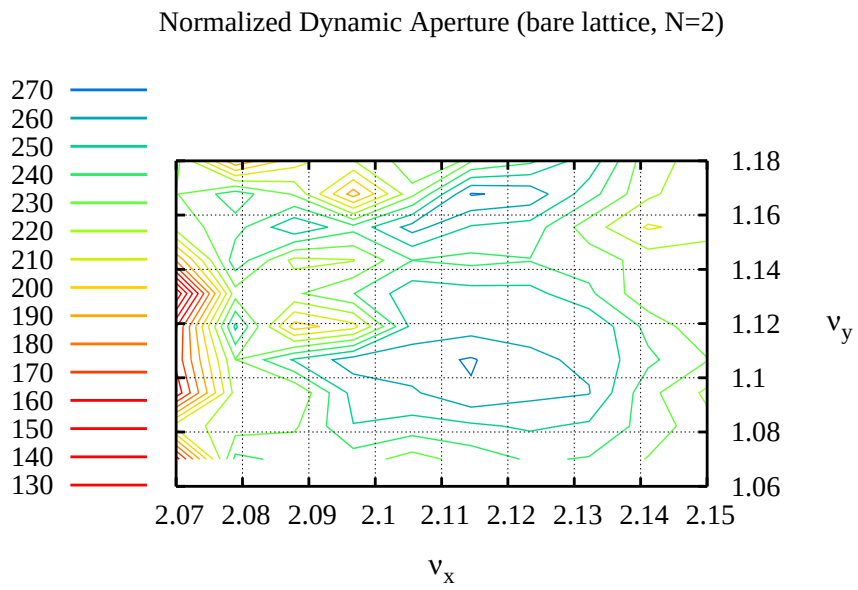

Figure 6.1.10 Normalized DA ($\mathrm{Area}/\sqrt{\beta_x \beta_y}$) vs. tune per super-period.

The resulting DA is shown in Figure 6.1.11, for $\delta = 0, \pm 3\%$.

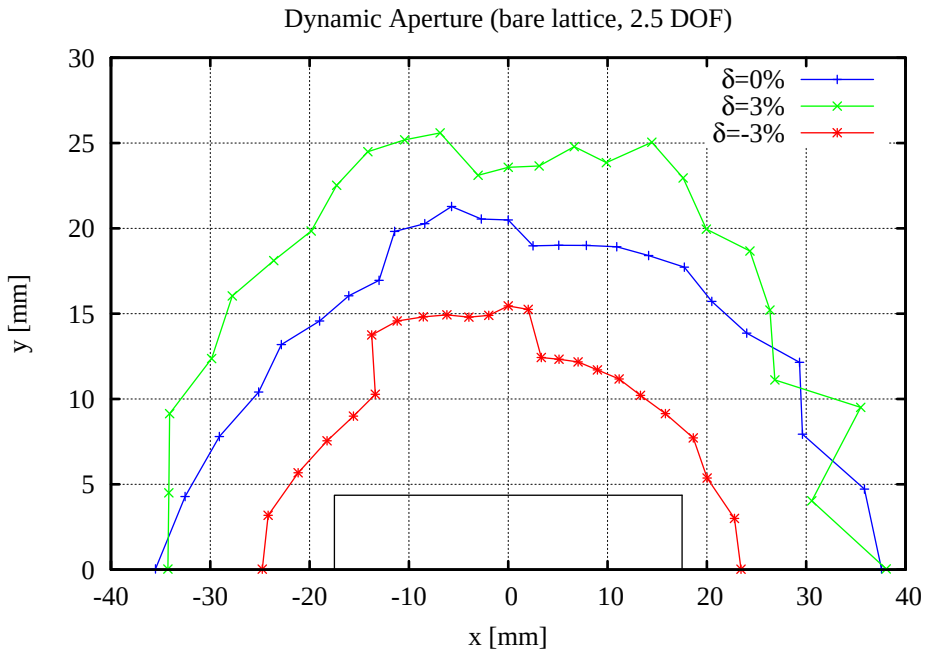

Figure 6.1.11 DA for $\delta = 0, \pm 3\%$ for the optimized tune and sextupoles at the center of the long straight section (i.e., at injection), $\beta_{x,y}$ = (18.2, 3.2) m.

The linear chromaticity is zeroed, and the residual nonlinear chromaticity is shown in Figure 6.1.12.

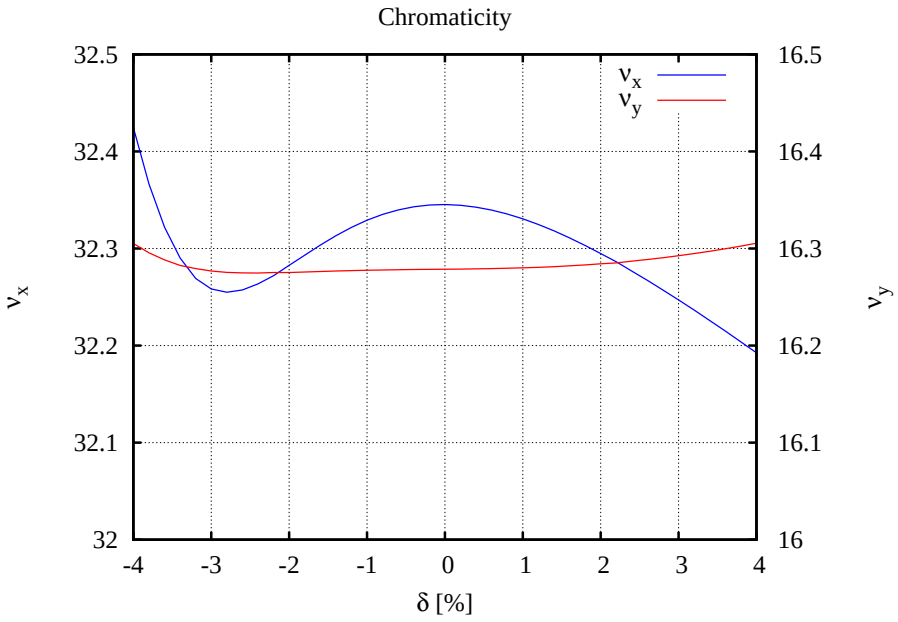

Figure 6.1.12 Residual nonlinear chromaticity for the optimized tune and sextupoles.

As mentioned earlier, the horizontal chromaticity has a substantial cubic term originating from h_{10002} driving second-order dispersion. The crossing between the horizontal and vertical tunes during synchrotron oscillations should be avoided in further optimizations. Otherwise, the Touschek lifetime can be affected. The amplitude-dependent tune shifts are shown in Figures 6.1.13 and 6.1.14, and the residual Lie generators are listed in Table 6.1.6.

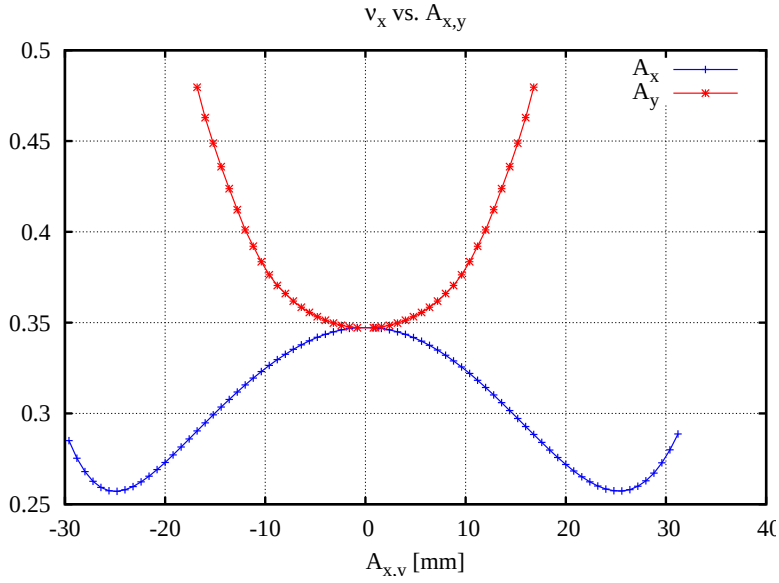

Figure 6.1.13 Horizontal tune, ν_x, vs. transverse amplitude (x_0, y_0) at the long straight section for A_x = (x_0, y_0~0) and A_y = (x_0~0, y_0).

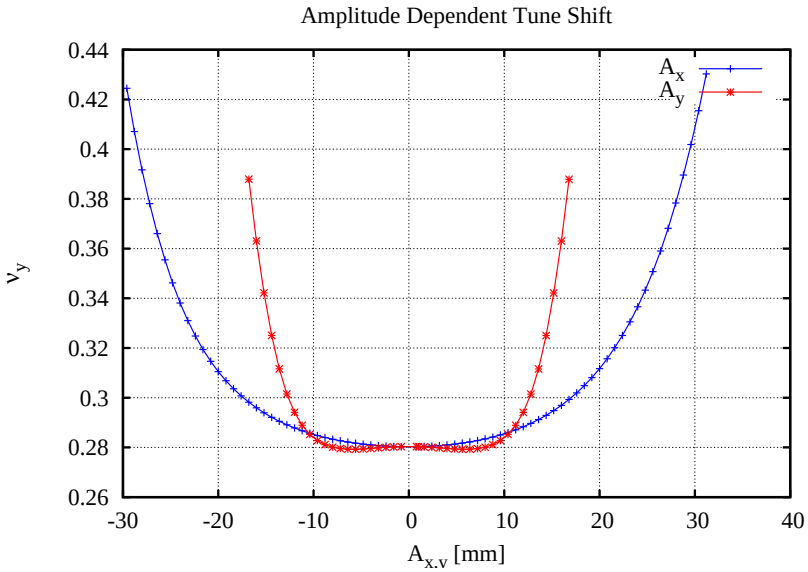

Figure 6.1.14 Vertical tune, ν_y, vs. transverse amplitude (x_0, $y_{0)}$ at the long straight section for: A_x = (x_0, y_0 ~0) and A_y = (x_0 ~0, y_0).

A frequency map [6.1.15] shows diffusion rate as a function of amplitude or tunes. The diffusion rate, as defined by

$$D(\nu_x, \nu_y) = \log_{10}\left(\sqrt{(\Delta\nu_x)^2 + (\Delta\nu_y)^2}\right), \tag{6.1-12}$$

is an indicator of chaotic behavior, where $\Delta\nu$ is the tune change between the first and second half of the particle tracking with initial amplitude $J_{x,y}$. The frequency map for the optimized working point and sextupole settings for zero linear chromaticity is shown in Figure 6.1.15, with the diffusion parameter plotted as a color-weighted value. Note that increased diffusion occurs at A_x ~25 mm and A_y ~8 mm, because $\partial\nu/\partial A = 0$. Hence, as a further refinement, it could be avoided by also controlling the derivative of the amplitude-dependent tune shifts at these large amplitudes.

Table 6.1.6 Residual Normalized Lie Generators.

Lie Generator	Effect	Normalized Value
$\lvert h_{11001}\rvert$	$\partial\nu_x/\partial\delta$	1.6×10^{-11}
$\lvert h_{00111}\rvert$	$\partial\nu_y/\partial\delta$	1.3×10^{-12}
$\lvert h_{10002}\rvert$	$\partial\eta_x/\partial\delta$	3.3×10^{-6}
$\lvert h_{20001}\rvert$	$\nu_x \pm \nu_s$	6.0×10^{-7}
$\lvert h_{00201}\rvert$	$\nu_y \pm \nu_s$	3.5×10^{-8}
$\lvert h_{21000}\rvert$	ν_x	6.4×10^{-7}
$\lvert h_{10110}\rvert$	ν_x	1.5×10^{-7}
$\lvert h_{30000}\rvert$	$3\nu_x$	2.1×10^{-8}
$\lvert h_{10020}\rvert$	$\nu_x - 2\nu_y$	5.4×10^{-8}
$\lvert h_{10200}\rvert$	$\nu_x + 2\nu_y$	7.1×10^{-7}
$\lvert h_{20110}\rvert$	$2\nu_x$	2.2×10^{-8}
$\lvert h_{31000}\rvert$	$2\nu_x$	8.8×10^{-8}
$\lvert h_{40000}\rvert$	$4\nu_x$	7.4×10^{-9}
$\lvert h_{20020}\rvert$	$2\nu_x - 2\nu_y$	3.4×10^{-7}

Lie Generator	Effect	Normalized Value
$\lvert h_{20200}\rvert$	$2\nu_x + 2\nu_y$	1.3×10^{-9}
$\lvert h_{11200}\rvert$	$2\nu_y$	5.5×10^{-8}
$\lvert h_{00310}\rvert$	$2\nu_y$	1.5×10^{-7}
$\lvert h_{00400}\rvert$	$4\nu_y$	2.3×10^{-8}
$\lvert h_{22000}\rvert$	$\partial\nu_x/\partial J_x$	1.1×10^{-6}
$\lvert h_{11110}\rvert$	$\partial\nu_{x,y}/\partial J_{y,x}$	1.3×10^{-7}
$\lvert h_{00220}\rvert$	$\partial\nu_y/\partial J_y$	6.9×10^{-7}
$\lvert h_{22001}\rvert$	$\partial^2\nu_x/\partial J_x\partial\delta$	7.0×10^{-7}
$\lvert h_{11111}\rvert$	$\partial^2\nu_{x,y}/\partial J_{y,x}\partial\delta$	3.7×10^{-7}
$\lvert h_{00221}\rvert$	$\partial^2\nu_y/\partial J_y\partial\delta$	7.6×10^{-8}
$\lvert h_{11002}\rvert$	$\partial^2\nu_x/\partial\delta^2$	3.9×10^{-6}
$\lvert h_{00112}\rvert$	$\partial^2\nu_y/\partial\delta^2$	1.1×10^{-7}

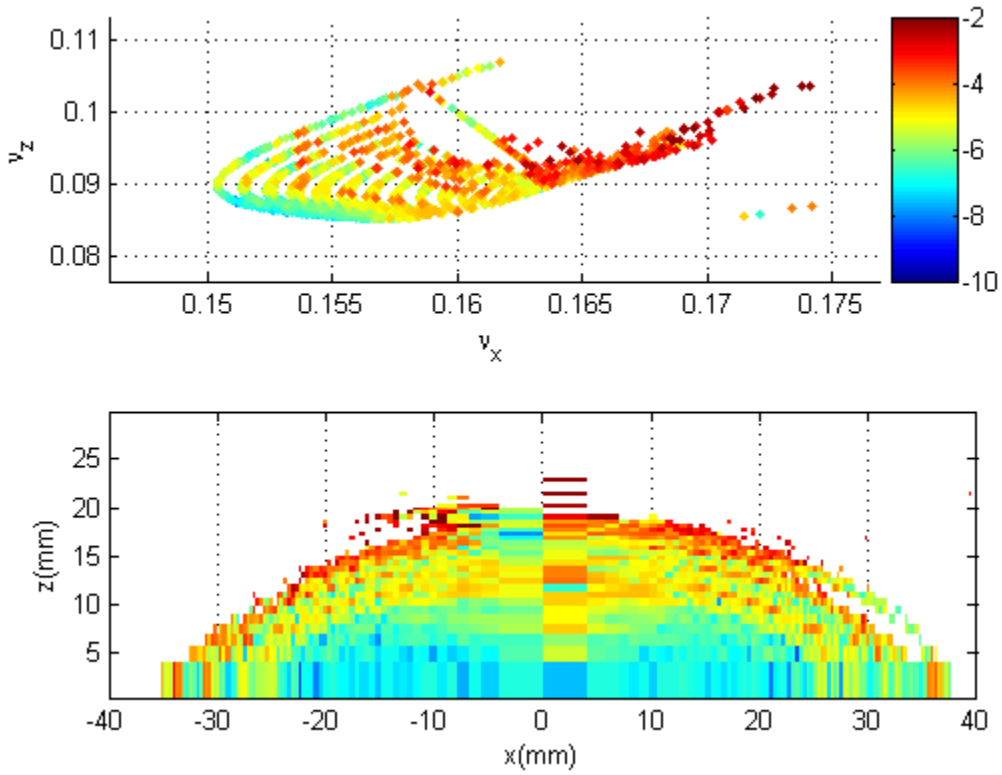

Figure 6.1.15 Frequency map vs. transverse amplitudes at the Long Straight Section, $\beta_{x,y}$ = (18.2, 3.2) m.

6.1.2.4 Impact of Alignment and Field Tolerances on Dynamic Aperture

Systematic and random magnetic field errors further reduce the DA, and their impact has been evaluated by simulations. Figure 6.1.16 shows the impact on the DA as the random quadrupole gradient errors are increased for all the quadrupoles of the lattice. At a relative RMS error of $\Delta b_2/b_2 \approx 5\text{x}10^{-4}$, they reduce the DA by ~20%, which is taken as the tolerance level for the quadrupole powering errors.

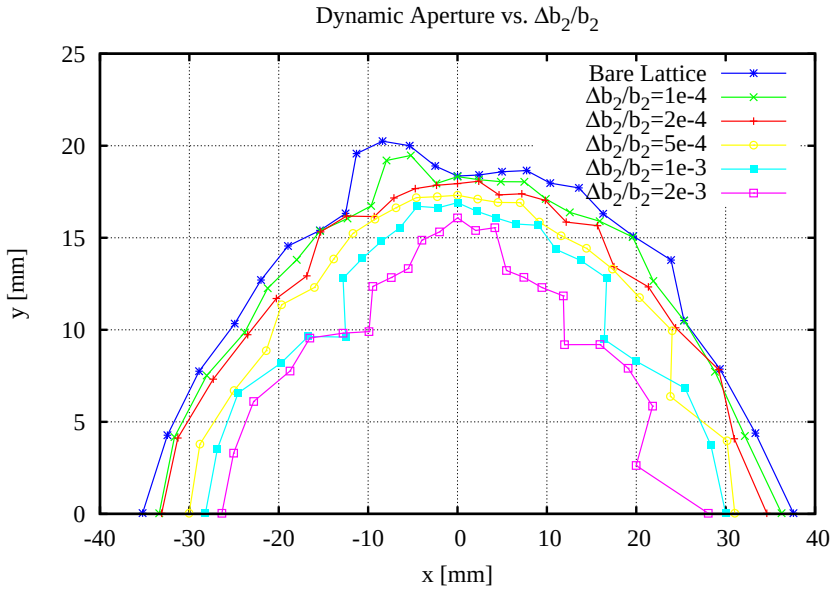

Figure 6.1.16 DA sensitivity versus the fractional gradient errors in the quadrupoles.

This reduction in DA originates from distortions of the linear optics at the sextupole magnets that perturb the influence of the carefully balanced sextupole strengths that were chosen to minimize the nonlinear driving terms. The resulting RMS beta and phase advance beats at the sextupoles can therefore be used as a tolerance level, regardless of their source [6.1.20]. These latter tolerance levels, as well as the gradient tolerance level, are listed in Table 6.1.7.

Table 6.1.7 Optics Tolerances for Robust DA of the NSLS-II Lattice.

Location	At the Quadrupoles	At the Sextupoles		
Parameter	$\left(\Delta b_2 L / b_2 L\right)_{\text{rms}}$	$\left(\Delta\beta_{x,y} / \beta_{x,y}\right)_{\text{rms}}$	$\left(\Delta\nu_{x,y}\right)_{\text{rms}}$	$\left(\Delta x_{\text{cod}}, \Delta y_{\text{cod}}\right)_{\text{rms}}$
Tolerance	$\sim 5\times10^{-4}$	$\sim (0.02, 0.03)$	$\sim (0.003, 0.01)$	$\sim (50, 50)$ μm

Similarly, a tolerance level can be specified for the residual Closed-Orbit Distortions at the sextupoles, which introduce beta and phase advance beats proportional to the sextupole gradients times the COD offset. This impact on the DA was simulated by introducing random transverse alignment errors to all the sextupoles and is shown in Figure 6.1.17 vs. the RMS error. At a level of $\sigma_x = \sigma_y$ ~50 μm, the DA area is reduced by about 20%. These RMS values can be taken as the tolerance level for the misalignments and residual COD at the sextupoles that must be maintained by the global orbit correction system (see Table 6.1.7).

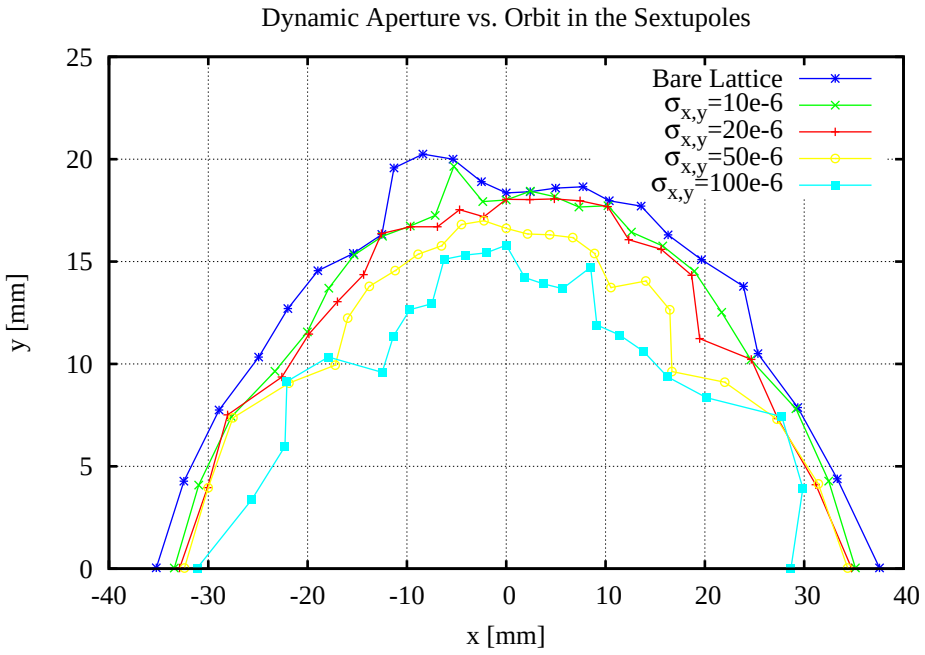

Figure 6.1.17 DA sensitivity to transverse alignment errors of the sextupoles.

Correspondingly, the required transverse magnet alignment tolerances are summarized in Table 6.1.8, assuming the COD errors are corrected using the seven BPMs and seven correctors of the lattice. Details on the global orbit correction scheme are given in Section 6.1.2.5.

Table 6.1.8 Transverse Magnet Alignment Tolerances.

	Δx RMS [μm]	Δy RMS [μm]	Roll RMS [m-rad]
Dipole	100	100	0.5
Girder	100	100	0.5
Quadrupoles	30	30	0.2
Sextupoles	30	30	0.2

The magnetic field error tolerances are specified in terms of the normal and skew multipole coefficients (b_n, a_n), defined by the normalized transverse magnetic field expansion:

$$\frac{1}{(B\rho)}\left[B_x(x,y) + i\,B_y(x,y)\right] \equiv \sum_n (b_n + i\,a_n)(x+i\,y)^{n-1} = \sum_n (b_n + i\,a_n)\,e^{i(n-1)\varphi} \qquad (6.1\text{-}13)$$

where $n = 1,2,3,\ldots$ are the dipole, quadrupole, sextupole, … components, respectively.

In particular, the multipole errors, $\Delta B_n^{(N)}$, relative to the desired field component, b_N, are normalized at a reference radius R and defined by[10]

$$\Delta B_n^{(N)}(R) \equiv R^{n-N}\,\frac{\Delta b_n}{b_N} \quad or \quad \Delta A_n^{(N)}(R) \equiv R^{n-N}\,\frac{\Delta a_n}{b_N} \qquad (6.1\text{-}14)$$

[10] Using the peak B-field for insertion devices.

where $(\Delta b_n, \Delta a_n)$ are the multipole field errors.

The tolerances for the multipole errors are given in Table 6.1.9 using values achieved at the SLS facility [6.1.21, 6.1.22]. The impact is an additional ~20% DA reduction for the lattice with the previously defined alignment tolerances. Future work will include parametric studies for a more precise specification.

Table 6.1.9 Tolerance Levels for RMS Normalized Multipole Errors.

Magnet Type	Normalized Field Error (R = 28 mm)				
Quadrupoles	$\Delta B_2^{(2)}$	$\Delta B_3^{(2)}$	$\Delta A_3^{(2)}$	$\Delta A_3^{(2)}$	$\Delta A_3^{(2)}$
	2.5x10^{-4}	2.8x10^{-4}	2.9x10^{-4}	1.9x10^{-4}	1.4x10^{-4}
Sextupoles	$\Delta B_3^{(3)}$	$\Delta B_4^{(3)}$	$\Delta A_4^{(3)}$	$\Delta B_5^{(3)}$	
	5.0x10^{-4}	5.2x10^{-4}	4.9x10^{-4}	3.5x10^{-4}	

Note: Based on tolerances from SLS.

Similarly challenging is the impact of the linear optics distortions from the insertion devices listed in Table 6.1.10. In particular, the proposed superconducting undulators will substantially affect the nonlinear dynamics in the vertical plane due to their short period (see Section 6.1.2.8). The effect of elliptically polarized undulators on the DA remains to be studied. Table 6.1.11 lists the allowed multipole field tolerances for these undulators [6.1.25]. The potential configuration includes the following IDs:

- CPMUs in the 5 m straights
- CPMUs in the 8 m straights
- DWs in the 8 m straights
- EPUs in the 8 m straights[11]

Details on the impact of these insertion devices and the control of their nonlinear terms are presented in Section 6.1.2.8.

Table 6.1.10 Insertion Device Parameters and Their Impact on the Vertical Tune.

ID	λ_u [mm]	B [T]	K_u	L_u[m]	Gap[mm]	$\Delta\nu_y$
SCU (2+1)	14	1.7	2.2	2	~5	0.002
CPMU (3)	19	1.24	2.2	3	5	0.002
DW	100	1.8	16.8	7	~11	0.028
EPU	~40	0.88	(3.3, 3.3)	~4	~6.5	TBD

Table 6.1.11 RMS Normalized Field Errors for Insertion Devices (CPMU, R = 20 mm).

Multipole	$\Delta B_3^{(1)}$	$\Delta A_3^{(1)}$	$\Delta B_4^{(1)}$	$\Delta A_4^{(1)}$
Random	6.6x10^{-7}	6.6 x10^{-7}	2.2 x10^{-8}	2.2 x10^{-8}

Note: Based on tolerances from the Swiss Light Source.

[11] Presumably as 2×1 m canted devices; see Table 6.1.14.

6.1.2.5 Control of Closed-Orbit Distortions

While essentially a linear problem, effective orbit control is crucial for robust DA[12] and orbit stability. From a DA point of view, the main objective for the global orbit correction system is to establish and maintain an orbit at the magnetic centers of the sextupoles (to avoid breaking the symmetry of the linear optics), to within ~50 μm (see Table 6.1.7). As a rough guideline, the BPMs should be spaced by ~90º in phase advance and placed close to the sextupoles. With a horizontal DBA cell tune of ~1.1, about six BPMs per cell should provide good coverage. In order to center the orbit in all the BPMs, one corrector for each BPM is needed. In theory, the DA can be restored if the BPM is at the sextupole magnetic center, 0. The number of correctors can be reduced in the vertical plane, since the cell tune is only ~0.5. From the horizontal phase advance (Figure 6.1.18), it is clear that at least one BPM is required in each of the dispersive and straight sections.

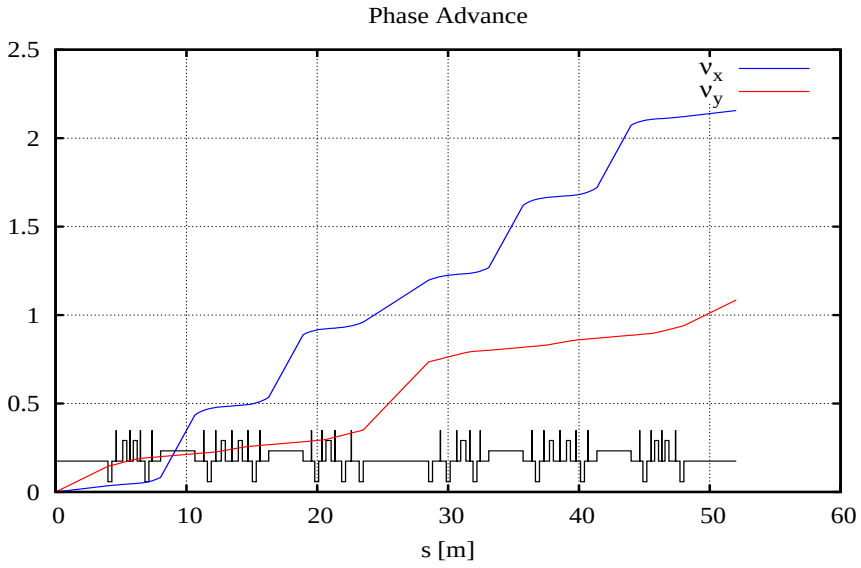

Figure 6.1.18 Normalized Phase Advance for one super-period.

Figures 6.1.19 a and b show the corrected horizontal and vertical RMS closed-orbit distortions (for 1,000 seeds) due to 100 μm RMS random horizontal and vertical quadrupole misalignment errors, with the (H-BPM×H-Corrector, V-BPM×V-Corrector) = (7×7, 7×6) baseline configuration outlined in Section 6.1.1. Clearly, the resulting orbit is well within the guidelines of Table 6.1.7. Note that a BPM is included at the center of each DBA. With some fine tuning of the BPM placement, this BPM can be removed, leading to a (6×6, 6×6) configuration. The BPM buttons will be kept for optics checks during commissioning. Beam-based alignment [6.1.29, 6.1.30] with BPMs at the end of the girders will make it possible to reduce orbit errors below the survey and alignment tolerances for the girders, particularly since the alignment tolerances for the magnetic centers on the girders are tighter than the girder alignment in the tunnel.

[12] To avoid the collapse of DA observed in the ALS CDR [6.1.26], eventually addressed by "Global Matching of the Normalized Ring" [7.1.10–7.1.15].

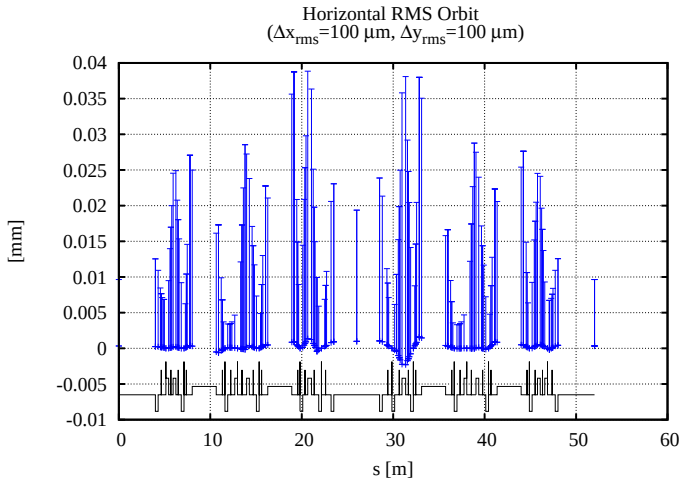

Figure 6.1.19 a Corrected horizontal RMS COD (over 1,000 seeds) for one super-period.

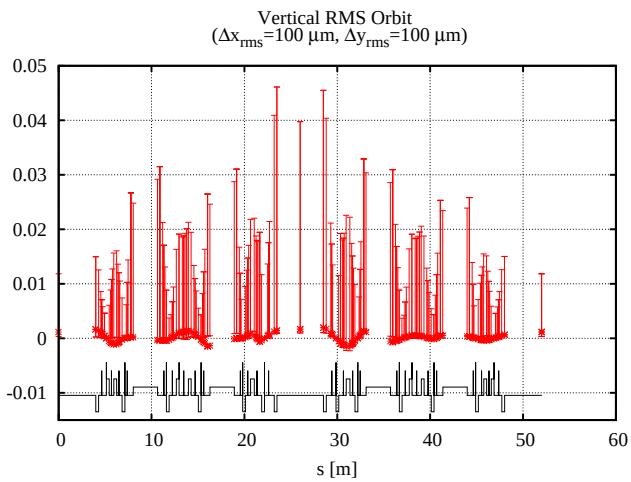

Figure 6.1.19 b Corrected vertical RMS COD (over 1,000 seeds) for one super-period.

Although placing the BPMs close to the sextupoles reduces the residual COD at the sextupoles, the BBA resolution is better for quadrupole centering (<10 μm both H and V) by at least a factor of three [6.1.28]. This allows for orbit centering beyond the magnet alignment tolerance on the girder. Therefore, we have adopted the (7×7, 7×6) correction scheme, with the BPMs close to the quadrupoles for BBA with a resolution of 10 μm. The impact on the DA of the corrected COD resulting from the alignment tolerances[13] listed in Table 6.1.8 is shown in Figure 6.1.20 (for 10 random seeds). Clearly the (7×7, 7×6) orbit correction system provides adequate DA, and provides margin for error.

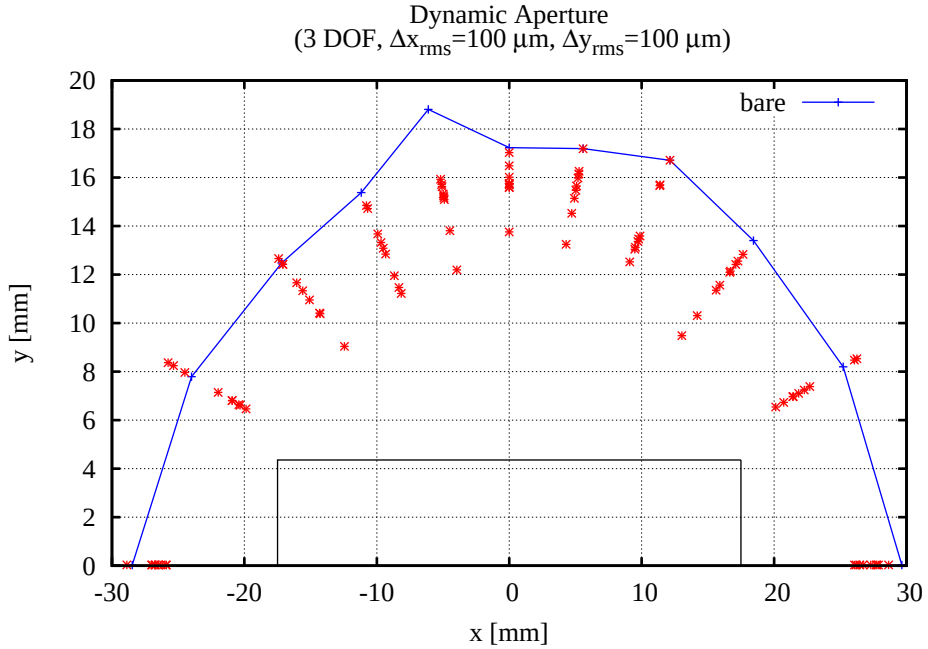

Figure 6.1.20 DA for lattice with transverse misalignment errors, according to Table 6.1.8. These CODs are corrected with the baseline (7×7, 7×6) system.

[13] Except for roll errors, to be treated later.

6.1.2.6 Control of Vertical Beamsize

The vertical beamsize is given by

$$\sigma_y = \sqrt{\beta_y \varepsilon_y + (\eta_y \sigma_\delta)^2} \tag{6.1-15}$$

where β_y and η_y are the vertical beta function and dispersion, ε_y is the vertical emittance, and σ_δ is the momentum spread. The design goal is $\varepsilon_y \sim 0.01$ nm-rad, corresponding to $\sigma_y \sim 5$ μm in the short straights. The non-vanishing vertical emittance originates from:

- linear coupling of the horizontal emittance due to roll errors of the quadrupoles and vertical orbit displacement in the sextupoles,
- and vertical dispersion due to roll errors of the dipoles and linear coupling of the horizontal dispersion.

Local control of the vertical beamsize is straightforward. In particular, by controlling the off-diagonal beam response matrix elements given by [6.1.29]:

$$\begin{aligned}
\frac{\partial y_k}{\partial p_{x,i}} &= -\frac{(\Delta a_2 L)_j \sqrt{\beta_{x,i}\beta_{x,j}\beta_{y,j}\beta_{x,k}}\cos\left(\left|\mu_{x,i\to j}\right| - \pi\nu_x\right)\cos\left(\left|\mu_{y,j\to k}\right| - \pi\nu_y\right)}{4\sin(\pi\nu_x)\sin(\pi\nu_y)} + O(\Delta a_2 L)^2, \\
\frac{\partial x_k}{\partial p_{y,i}} &= -\frac{(\Delta a_2 L)_j \sqrt{\beta_{y,i}\beta_{y,j}\beta_{x,j}\beta_{y,k}}\cos\left(\left|\mu_{y,i\to j}\right| - \pi\nu_y\right)\cos\left(\left|\mu_{x,j\to k}\right| - \pi\nu_x\right)}{4\sin(\pi\nu_x)\sin(\pi\nu_y)} + O(\Delta a_2 L)^2
\end{aligned} \tag{6.1-16}$$

for a dipole kick, $p_{(x,y),i}$ at i, due to a skew quadrupole $(a_2 L)$ at j. produces an orbit change $(\Delta x_k, \Delta y_k)$ at a BPM located at k. Similarly, the local control of the vertical dispersion is done by:

$$\Delta\eta_{y,k} = -\frac{(\Delta a_2 L)_j \eta_{x,j}\sqrt{\beta_{y,j}\beta_{x,k}}\cos\left(\left|\mu_{x,j\to k}\right| - \pi\nu_x\right)}{2\sin(\pi\nu_y)} + O(\Delta a_2 L)^2 \tag{6.1-17}$$

The driving term for the linear coupling is shown in Figure 6.1.21, whereas the driving term for vertical dispersion is similar to the one for vertical linear chromaticity, (see Figure 6.1.7). We have found that adequate control is obtained by introducing one skew quadrupole:

- in each long matching section
- in one of the dispersion cells for each super-period

for a total of 15 + 15 = 30 skew quadrupoles for the full lattice. The corresponding (linear) $82{,}110\times 30$ system of equations

$$\left[\frac{\partial \overline{\mathrm{x}}}{\partial \overline{p}_y}, \frac{\partial \overline{\mathrm{y}}}{\partial \overline{p}_x}, \Delta\overline{\eta}_{\mathrm{y}}\right]^{\mathrm{T}} = S \cdot \overline{(\Delta a_2 L)} \tag{6.1-18}$$

was solved in a least-square sense by the Singular Value Decomposition method. The vertical dispersion after correction for the coupling introduced by the roll errors in Table 6.1.8, is shown in Figure 6.1.22. It turns out that the vertical emittance can be corrected significantly below $\varepsilon_y \sim 0.01$ nm-rad. To optimize the Touschek

lifetime, a vertical dispersion wave[14] is introduced to obtain the desired vertical beamsize, e.g., η_y = 5 mm $\Rightarrow \sigma_y \sim \eta_y \sigma_\delta = 5$ μm (see Figure 6.1.23). Since it is straightforward to measure the beam response matrix and vertical dispersion on the real storage ring, the correction algorithm implemented for this simulation will eventually be used for commissioning as well.

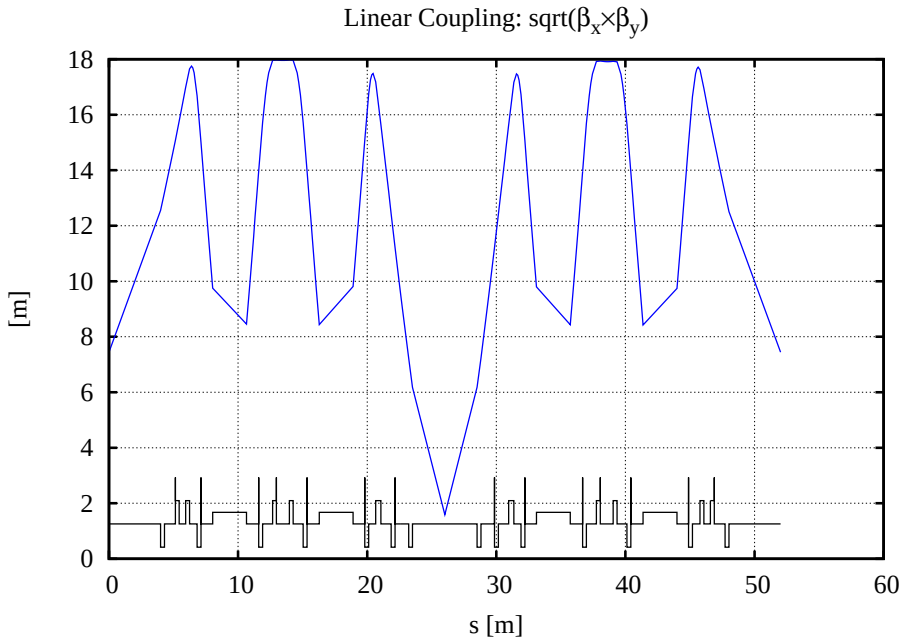

Figure 6.1.21 Driving term for linear coupling, for one super-period.

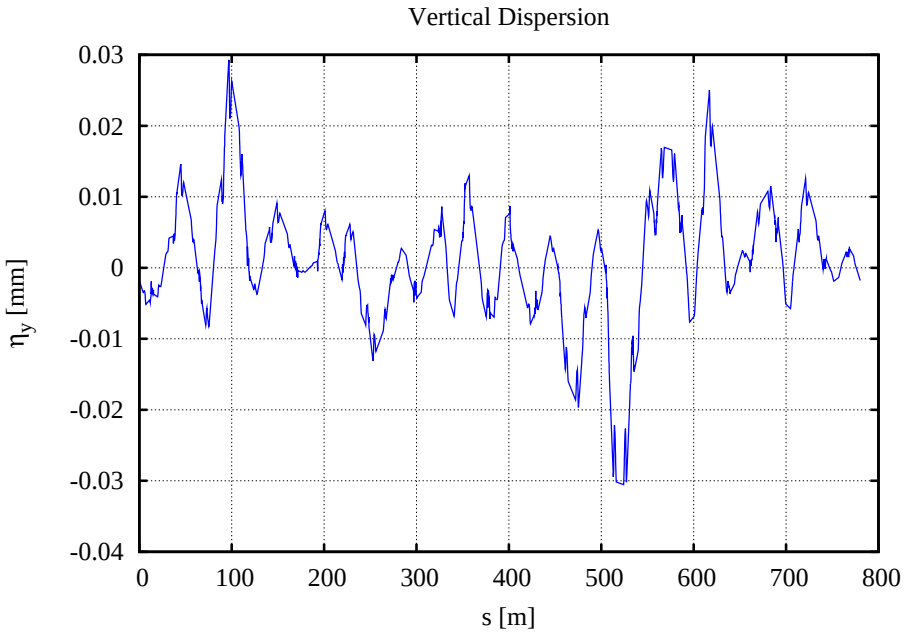

Figure 6.1.22 Corrected vertical dispersion for the quadrupole and dipole roll tolerances.

[14] To avoid affecting the dynamics 0.

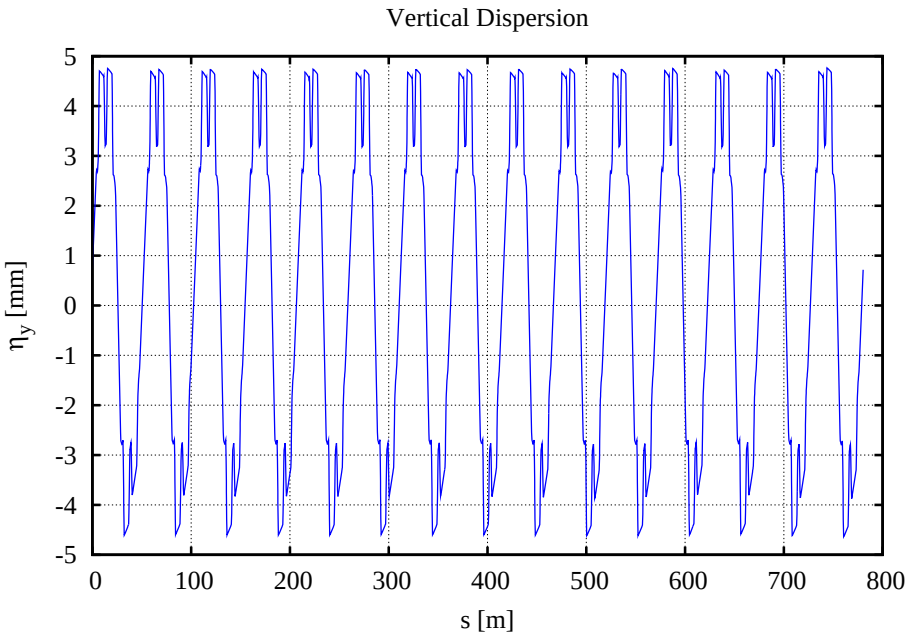

Figure 6.1.23 Corrected vertical dispersion with a residual 5 mm dispersion wave for vertical beamsize control.

6.1.2.7 Robustness of DA

The introduction of alignment errors in the lattice leads to orbit distortions, which generate magnetic field errors due to feed-down in the multipoles. These errors are summarized in Table 6.1.12. A robust DA requires that the global orbit correction system maintains the orbit centered in the sextupoles, since feed-down leads to gradient errors. To correctly evaluate this impact, correlations between magnet-magnet alignment errors, e.g., from girder misalignments, need to be included. Also, real magnets are not pure dipoles, quadrupoles, or sextupoles, requiring systematic and random multipole errors to be included. A detailed study of the individual maximum tolerance levels of these multipole errors remains to be done, but the realistic values listed in Table 6.1.9 have been used to evaluate the impact on the DA.

Table 6.1.12 Effect of Mechanical Tolerances on the Magnetic Field Quality.

	Dipole	Quadrupole	Sextupole
Horizontal orbit		horizontal dipole error	gradient error
Vertical orbit		vertical dipole error	skew quadrupole error
Roll error	vertical dipole error	skew quadrupole error	skew sextupole error

Also, due to the nonlinear chromaticity, tracking for at least one synchrotron oscillation period is required to obtain realistic estimates of the DA, since the off-momentum particle will be slowly crossing betatron resonances, which may limit the stability to smaller amplitudes. The design goal for the RF acceptance is ±3%. To obtain a conservative estimate of the momentum aperture, an RF voltage sufficient to produce a 4% bucket height was used to evaluate the DA. The impact on the DA and momentum aperture is shown in Figures 6.1.24 – 6.1.26, where the black-outlined rectangle (Figure 6.1.24) represents the physical aperture of the lattice, propagated to the center of the long straight section. The 10 seeds shown represent 10 lattices generated with randomly distributed alignment and multipole errors having RMS values given by the tolerance values and corrected for COD, as described above. The tracked particles undergo synchrotron

oscillations, but do not radiate. Since the radiation damping will also lead to the crossing of resonances, it should also be included in refined studies.

Low-emittance lattices tend to have a small linear momentum compaction, α_1, requiring the second-order term, α_2, to be included for a proper evaluation of the RF bucket, which becomes distorted and reduces the momentum acceptance [6.1.31]. The source of this distortion is a second stable fixed point, which has an energy offset given by the ratio:

$$\alpha_1/\alpha_2 \approx 3.7\times10^{-4}/4.1\times10^{-4} = 92\% . \qquad (6.1\text{-}19)$$

Since it only becomes important for ratios <20%, it will not pose a problem for this lattice[15]. This is further demonstrated by the phase space for the longitudinal Hamiltonian (shown in Figure 6.1.27), including terms to α_3, as well as the radiation loss of 35 m of damping wigglers.

To summarize, the DA guidelines from Table 6.1.5 are easily met for the bare lattice, as well as when the impact of realistic alignment and field tolerances, listed in Tables 6.1.8 and 6.1.9, are included in the lattice model using the correction schemes described above.

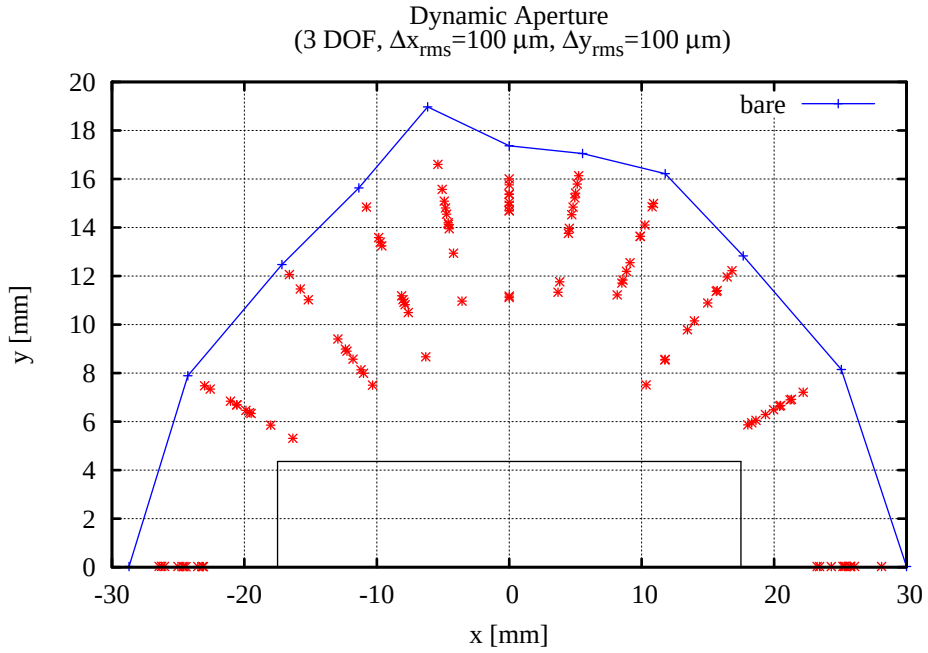

Figure 6.1.24 DA for a "realistic" lattice (10 seeds) with engineering tolerances and corrections. The black outline indicates the physical aperture.

[15] An advantage of the achromatic straights for the DBA lattice.

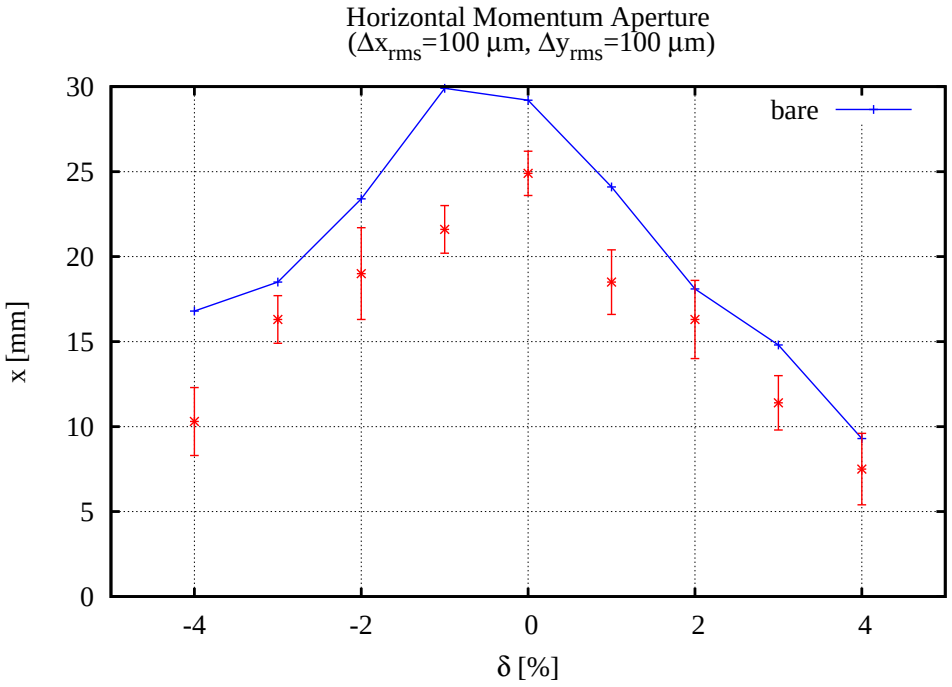

Figure 6.1.25
Average and RMS horizontal momentum aperture for a "realistic" lattice (10 seeds) with engineering tolerances and corrections.

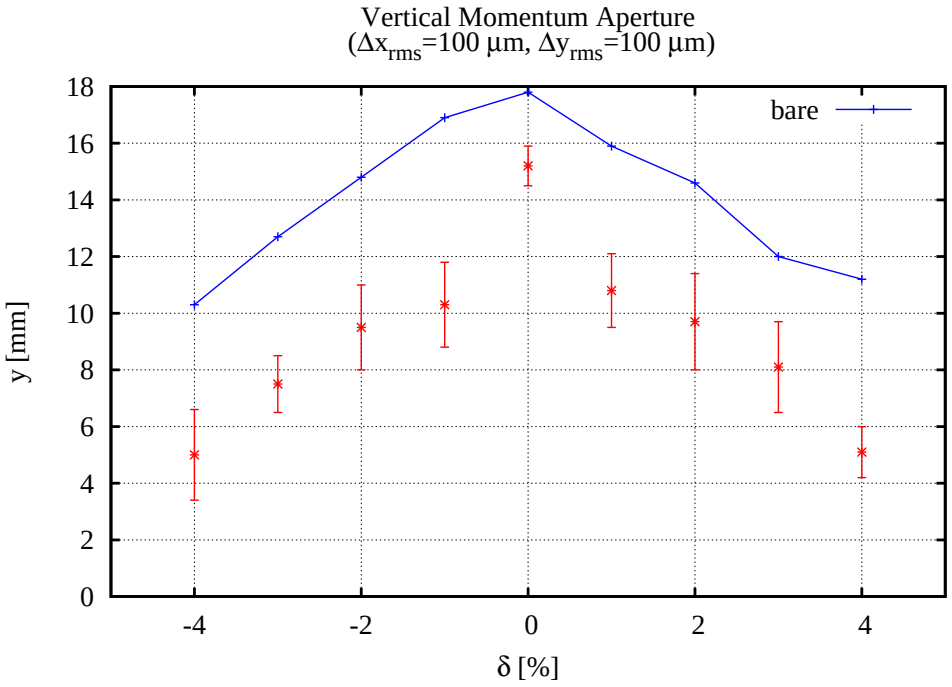

Figure 6.1.26
Average and RMS vertical momentum aperture for a "realistic" lattice (10 seeds) with engineering tolerances and corrections.

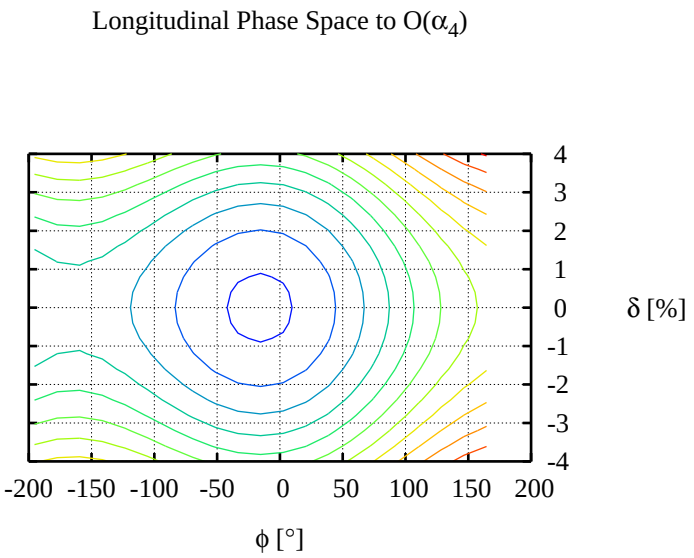

Figure 6.1.27 Longitudinal phase-space, including the radiation loss from damping wigglers.

6.1.2.8 Control of Impact from Insertion Devices

The Hamiltonian for an ID averaged over one undulator period, λ_u, is given by [6.1.32, 6.1.33]:

$$\langle H \rangle_{\lambda_u} \approx \frac{p_x^2 + p_y^2}{2(1+\delta)} - \frac{B_u^2 y^2}{4(B\rho)^2(1+\delta)} + \frac{\pi^2 B_u^2 y^4}{3(B\rho)^2 \lambda_u^2 (1+\delta)} - \delta + O\left(p_{x,y}^4\right) \tag{6.1-20}$$

with phase-space coordinates $\vec{x} = \left[x, p_x, y, p_y, \delta, c\Delta t\right]$, peak field B_u, and magnetic rigidity $(B\rho)$[16]. Note that both the leading-order linear and nonlinear effect scales with $1/(B\rho)^2$, i.e., the effect is reduced with the energy squared for a given undulator field, B_u. The term quadratic in y introduces a vertically focusing term with the integrated gradient

$$(b_2 L) \approx -\frac{B_u^2 L_u}{2(B\rho)^2} \tag{6.1-21}$$

i.e., quadratic in B_u. The beta-beat at location i due to integrated quadrupole kicks, $(\Delta b_2 L)_j$, is given by:

$$\frac{\Delta\beta_{(x,y),i}}{\beta_{(x,y),i}} = \sum_{j=1}^{N} \frac{(\Delta b_2 L)_j \beta_{(x,y),j} \cos\left(\left|2\mu_{(x,y),i\to j}\right| - 2\pi\nu_{(x,y)}\right)}{2\sin\left(2\pi\nu_{(x,y)}\right)} + O(\Delta b_2 L)^2 \tag{6.1-22}$$

where β, μ, ν are the beta functions, phase advance, and tune. Similarly, the phase-beat is given by:

$$\Delta\mu_{(x,y),i} = -\sum_{j=1}^{N} \frac{\mathrm{sgn}\left(\mu_{(x,y),i\to j}\right)(\Delta b_2 L)_j \beta_{(x,y),j} \left(\sin\left(2\pi\nu_{(x,y)}\right) + \sin\left(\left|2\mu_{(x,y),i\to j}\right| - 2\pi\nu_{(x,y)}\right)\right)}{4\sin\left(2\pi\nu_{(x,y)}\right)} + O(\Delta b_2 L)^2 \tag{6.1-23}$$

[16] $(B\rho) \approx 10.007$ T-m at 3 GeV.

and the total tune shift is given by

$$\Delta\nu_{(x,y)} = \pm\frac{1}{4\pi}\sum_{j=1}^{N}\left(\Delta b_2 L\right)_j \beta_{(x,y),j} + O\left(\Delta b_2 L\right)^2 \tag{6.1-24}$$

The parameters for the proposed insertion devices are summarized in Table 6.1.10 and the impact of three DWs on the linear optics is shown in Figure 6.1.28, where the beta-beat is rather obvious.

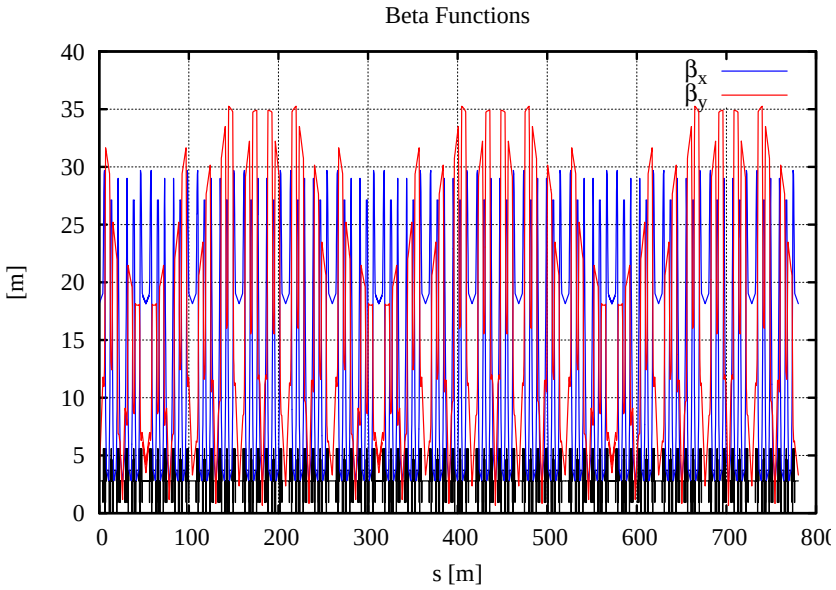

Figure 6.1.28 Perturbed beta functions of the lattice with three DWs installed.

The perturbation of the optics is corrected by adjusting the quadrupole quadruplets in the matching sections. With four quadrupole strengths as parameters, it is expected[17] that the beta- and phase advance beat can be removed in both planes. In particular, the optics deviations at all of the lattice sextupoles, *i,* are represented in a linearized system of equations that includes the focusing impact of all installed IDs $(\Delta b_2 L)_j$. These equations are given in matrix form by

$$\left[\left(\frac{\Delta\beta_{(x,y)}}{\beta_{(x,y)}}\right)_i, \Delta\mu_{(x,y),i}, \Delta\nu_{x,y}\right]^{\mathrm{T}} = A\cdot\left[\Delta\bar{b}_2\, L\right] \tag{6.1-22}$$

which was solved using an iterated SVD algorithm[6.1.34, 6.1.35], see Figure 6.1.29. The corrected beta and phase advance beats satisfy the optics tolerances specified in Table 6.1.7.

[17] If the parameters are independent.

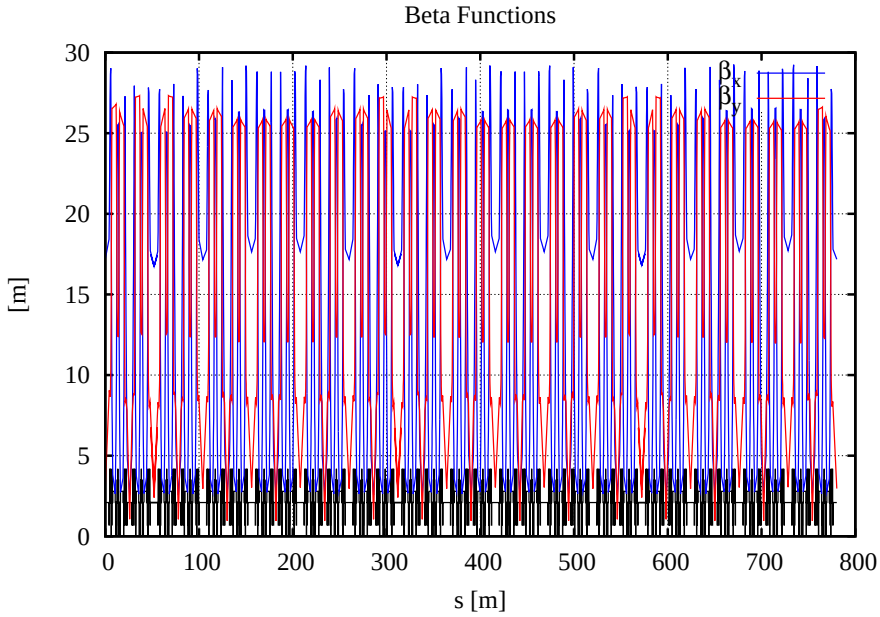

Figure 6.1.29 Corrected beta functions for the lattice with three DWs installed.

The leading order nonlinear part of the ID focusing contains an octupole-like term in the vertical plane which drives amplitude dependent vertical tune shift and $2\nu_y$ and $4\nu_y$ resonances. Table 6.1.13 presents a comparison of the magnitude of the main driving terms from the IDs with those from sextupoles in the lattice.

Table 6.1.13 Lie Generators from the Sextupole Scheme and a Single ID.

Lie Generator	Effect	Sextupole Scheme	DW (Long Straight)	CPMU (Short Straight)	CPMU (Long Straight)	SCU (Short Straight)	SCW (Short Straight)	EPU
h00220	$\partial\nu_y/\partial J_y$	606.9	1,089.2	1,102.6	3,681.3	1,259.6	TBD	TBD
h00310	$2\nu_y$	76.2	52.3	6.9	379.1	39.5		
h00400	$4\nu_y$	46.6	58.7	13.7	228.3	11.3		

The effect on the DA of a lattice with corrected magnet misalignment errors and one ID (one at a time for the DW, CPMU, and SCU IDs) is shown in Figure 6.1.30. While there is a substantial reduction of the vertical DA when one CPMU or SCU is introduced, nevertheless the DA remains outside the physical aperture and it does not degrade significantly as additional devices are included (Figure 6.1.31).

Although the long straight sections are primarily planned for machine components and DWs, there will be four uncommitted long straights. The high power radiated by a 7 m DW raises the question of the feasibility of splitting the wiggler into sections, which could be canted, yielding multiple lower-power beamlines from one long ID. Also, the potential of inserting multiple short undulators with canting in the long IDs is being considered as a method for obtaining more than four beamlines from the uncommitted long straight sections. In principle, one can introduce a small angular separation of the photon beams with three or four corrector magnets that bend the electron beam in the straight section by an angle θ, with little perceived impact. However, this adds horizontal dispersion to the achromatic straight section, which reduces the effectiveness of the DW in lowering emittance.

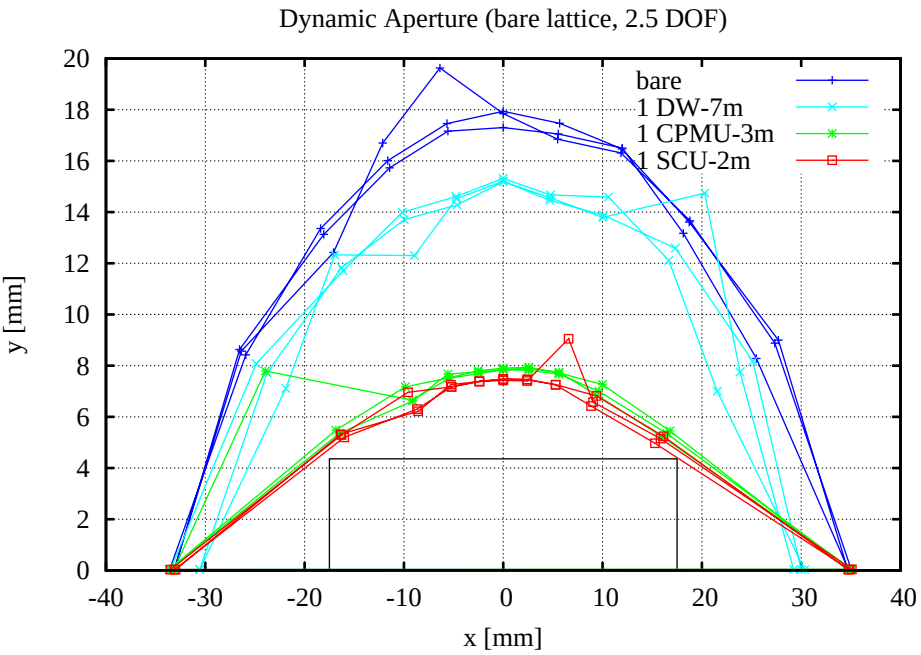

Figure 6.1.30 DA for the lattice with transverse alignment errors (for three seeds) and a single ID, one type at a time, for DWs, CPMUs, or SCUs.

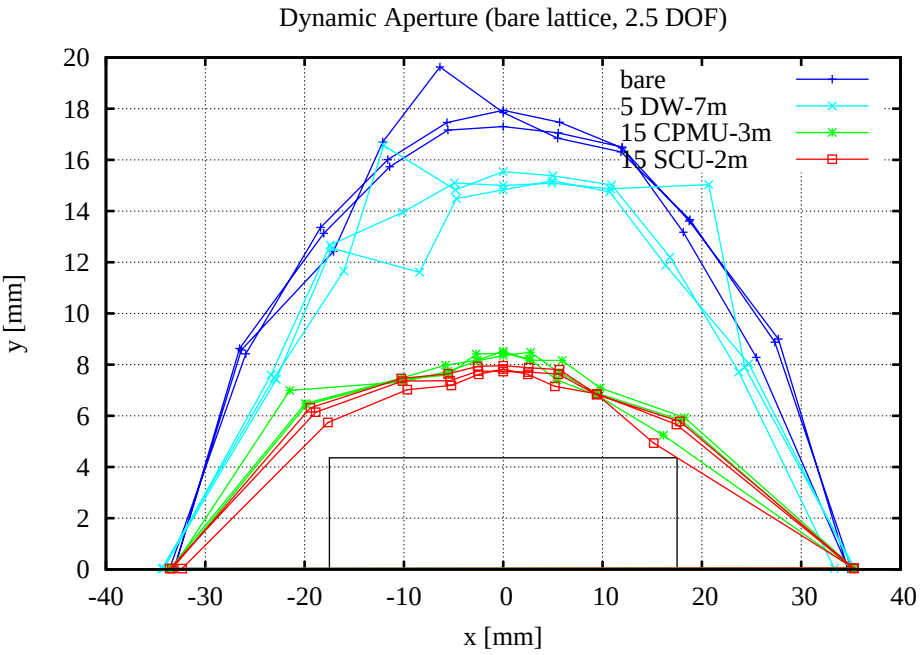

Figure 6.1.31 DA for the lattice with transverse alignment errors (for three seeds) and multiple IDs, one type at a time for five DWs, 15 CPMUs, or 15 SCUs.

A preliminary evaluation of the feasibility of canting of the IDs to yield either two or three separated photon beams per straight section is summarized in Table 6.1.14. We have found that a two-way canting angle of ≤3 mrad contributes with a few mm of horizontal dispersion and increases the emittance by less than 10%. For a three-way canting angle of 3 mrad, the emittance increase is >20%. For the undulators, this impact is considerably less, since they only provide a small amount of damping. These results were obtained with corrected optics using the four quadrupoles in matching sections.

Table 6.1.14 Emittance Increase Due to Canting of the DW and the CPMU Undulator.

Configuration	Cant Angle ($\theta/2, -\theta, \theta/2$) [m-rad]	Cant Angle ($\theta, -\theta, -\theta, \theta$) [m-rad]	Peak η_x [mm]	σ_δ [%]	ε_x [nm]
Bare Lattice				0.051	2.04
5×7 = 35 m DWs				0.090	0.66
5×(2×3.5) = 35 m DWs	1.5, -3, 1.5		6	0.090	0.71
	2.5, -5, 2.5		10	0.090	0.80
5×(3×2.33) = 35 m DWs		1, -1, -1, 1	3	0.089	0.67
		3, -3, -3, 3	8	0.089	0.80
35 m DWs + 1×2 = 2 m CPMU				0.089	0.64
35 m DWs + 1×(2×1) = 2 m CPMU	1, -2, 1		3	0.089	0.64
8×7 = 56 m DWs				0.094	0.48
8×(2×3.5) = 56 m DWs	1.5, -3, 1.5		6	0.094	0.54

6.1.2.9 Future Work in Lattice and Beam Dynamics Issues

The work presented here shows that the present lattice is very robust for the errors and realistic magnets and IDs studied to this point. Additional work is needed to evaluate 1) the implications of going to higher energy, 2) tailoring by, and refocusing for, multiple IDs per straight, and 3) corrections for longer IDs. This involves the following tasks.

- scan the individual field tolerances for maximum allowable values
- study the impact of multipole errors in the IDs
- evaluate the DA for the complete set of alignment and field errors with a full complement of IDs and corrections
- Move the working point to avoid crossing of the horizontal and vertical tune off-momentum, to avoid a reduction of Touschek lifetime when roll errors are introduced. Changing the sextupole values has already shown promise in avoiding this tune-crossing by reducing the second-order chromaticity.
- evaluate the acceptable range of positive linear chromaticity for head–tail stabilization
- reduce the nonlinear chromaticity by controlling second-order horizontal dispersion in the linear optics design
- evaluate the impact of a reduced number of BPMs and correctors
- evaluate the impact of removing one quadrupole family in the short matching sections
- evaluate the impact of removing 1+1 sextupole families in the short and long matching sections
- evaluate the impact of elliptically polarizing undulators and provide guidelines for their integration into the lattice
- evaluate the Touschek life time for a realistic lattice, i.e., with vertical apertures, misalignments and field errors, insertion devices, and related corrections
- evaluate the phase-space dynamics with radiation damping (one damping time) for a realistic lattice
- study the injection dynamics of the stored beam bump and the injected beam pulse
- evaluate the feasibility of reducing the amplitude-dependent tune shifts from the IDs, by introducing octupoles

References

[6.1.1] H. Weidemann, NIM **A266**, p. 24 (1988).
[6.1.2] S. Krinsky, et. al., EPAC06, p.3487 (2006).
[6.1.3] G. Decker, and O. Singh, *Phys. Rev. STAB* **2,** p. 112801 (1999).
[6.1.4] S. Krinsky, J. Bengtsson, and S. Kramer, "Consideration of a Double Bend Achromatic Lattice for NSLS-II," pp. 3487–3489, EPAC06.
[6.1.5] J. Bengtsson, "A Control Theory Approach for Dynamic Aperture," pp. 3478–3480, EPAC06.
[6.1.6] J. Bengtsson, W. Joho, P. Marchand, G. Mülhaupt, L. Rivkin, and A. Streun, "Increasing the Energy Acceptance of High Brightness Synchrotron Light Storage Rings," *Nucl. Instr. Meth. A* **404**, 237–247 (1998).
[6.1.7] A. Wrulich, et al., "Commissioning of the Swiss Light Source," pp. 224–226, PAC01.
[6.1.8] A. Wrulich, et al., "Achievements of the SLS Commissioning," PSI. Scientific Report 2001 Vol. VII, 2002.
[6.1.9] M. Böge, "Achieving Sub-Micron Stability in Light Sources," pp. 211–213, EPAC04.
[6.1.10] J. Bengtsson, and E. Forest, "Global Matching of the Normalized Ring" Workshop on Effects of Errors in Accelerators, their Diagnosis and Corrections," Corpus Christi, TX, Oct. 3–8, 1991.
[6.1.11] J. Bengtsson, and M. Meddahi, "Modeling of Beam Dynamics and Comparison with Measurements for the Advanced Light Source (ALS)," pp. 1022–1024, EPAC94.
[6.1.12] D. Robin, G. Portmann, H. Nishimura, and J. Safranek, "Model Calibration and Symmetry Restoration of the Advanced Light Source," pp. 971–973, EPAC96.
[6.1.13] J. Safranek, "Experimental Determination of Storage Ring Optics Using Orbit Response Measurements," *Nucl. Instr. and Meth. A* **388**, 27-36 (1997).
[6.1.14] D. Robin, C. Steier, J. Safranek, and W. Decking, "Enhanced Performance of the Advanced Light Source through Periodicity Restoration of the Linear Lattice," pp. 136–138, EPAC00.
[6.1.15] J. Laskar, L. Nadolski, D. Robin, and C. Steier, "Global Dynamics of the Advanced Light Source Revealed through Experimental Frequency Map Analysis," *Phys. Rev. Lett.* **85**, 558–561 (2000).
[6.1.16] J. Bengtsson, "X-Ray Ring Optics: the Inverse Problem," NSLS Tech Note 540 (2005).
[6.1.17] J. Bengtsson, "The Sextupole Scheme for the Swiss Light Source (SLS): An Analytic Approach," SLS Note 9/97 (1997).
[6.1.18] Diamond Synchrotron Light Source: Report of the Design Specification," CCLRC (2002).
[6.1.19] S.L. Kramer, S. Krinsky, and J. Bengtsson, "Comparison of Double Bend and Triple Bend Achromatic Lattice Structures for NSLS-II," pp. 384–386, EPAC06.
[6.1.20] J. Bengtsson, "On the NSLS-II Dynamic Aperture: Robustness," NSLS-II Tech Note 8 (2005).
[6.1.21] A. Streun, "SLS Dynamic Acceptance Degradation due to Magnet Multipole Errors," SLS-TME-TA-1998-0002 (1998).
[6.1.22] E.I. Antokhin, et al., "Multipoles of the SLS Storage Ring: Manufacturing and Magnetic Measurements," IEEE Trans. of Appl. Super. vol. 12, no. 1, 51–54 (2002).
[6.1.23] J. Safranek, C. Limborg, A. Terebilo, K.I. Blomqvist, P. Elleaume, and Y. Nosochkov, "Nonlinear Dynamics in a SPEAR Wiggler," *Phys. Rev. ST* **5,** 010701 (2002).
[6.1.24] C. Steier, G. Portmann, and A. Young, "Commissioning of the First Elliptically Polarizing Undulator at the ALS," pp. 2343–2345, EPAC00.
[6.1.25] B. Singh, and A. Streun, "Limits for Normal and Skew Sextupole and Octupole Field Errors in the First (I_1) and Second (I_2) Field-Integrals of Insertion Devices planned for SLS," SLS-TME-TA-2001-0170 (2001).
[6.1.26] "1-2 GeV Synchrotron Radiation Source Conceptual Design Report," LBNL PUB-5172 (1986).
[6.1.27] G. Portmann, D. Robin, and L. Schachinger, "Automated Beam Based Alignment of the ALS Quadrupoles," pp. 2693–2695, EPAC96.
[6.1.28] S.L. Kramer, "Beam Based Alignment," NSLS-II Tech Note (2006).
[6.1.29] J. Bengtsson, and I. Pinayev, "NSLS-II: Control of Vertical Emittance," NSLS-II Tech Note (2006).

[6.1.30] C. Steier, D. Robin, A. Wolski, G. Portmann, and J. Safranek, "Coupling Correction and Beam Dynamics at Ultralow Vertical Emittance in the ALS," pp. 3213–3215, PAC03.
[6.1.31] D. Robin, E. Forest, C. Pellegrini, and A. Amiry, "Quasi-Isochronous Storage Rings," *Phys. Rev. E* **48**, 2149–2156 (1993).
[6.1.32] L. Smith, "Effect of Wigglers and Undulators on Beam Dynamics," LBL-21391 (1986).
[6.1.33] Y. Wu, V.N. Litvinenko, and J.M.J. Madey, "Lattice and Dynamic Aperture of the Duke FEL Storage Ring," pp. 218–220, PAC93.
[6.1.34] T. Shaftan and J. Bengtsson, "Impact of Insertion Devices on the NSLS-II lattice," NSLS-II Tech. Note (2006).
[6.1.35] T. Shaftan, J. Bengtsson, and S. Kramer, "Control of Dynamic Aperture with Insertion Devices," pp. 3490–3492, EPAC06.

6.2 Collective Effects

6.2.1 Introduction

In this section, we discuss the effect of multi-particle interactions [6.2.1] on the electron beam in the NSLS-II storage ring. The storage ring has 500 MHz RF and a revolution period of 2.6 μs. The baseline design configuration corresponds to filling 80% of the RF buckets and leaving a 20% gap to allow for ion clearing. In this case we have M = 1040 bunches, each containing $N_e = 7.8\times10^9$ electrons ($N_e e$ = 1.25 nC) corresponding to a total average current $I_{av} = MN_e e/T_0$ = 500 mA and a single-bunch current $I_0 = N_e e/T_0$ = 0.5 mA. For an RMS bunch duration σ_t = 15 ps, the peak bunch current is $I_p = N_e e/\sqrt{2\pi}\sigma_t$ = 33 A.

Limitations on the single bunch current result from the short-range wakefield (broadband impedance). The longitudinal microwave instability depends primarily on the impedance of the vacuum vessel. The transverse mode coupling instability depends on the resistive wall impedance and the geometric impedance due to changes in the vacuum chamber cross-section.

Limitations on the total average current arise from the long-range wakefield (narrowband impedance). The longitudinal coupled-bunch instability is predominantly driven by the longitudinal higher-order modes in the RF cavity. The transverse coupled-bunch instability is primarily due to the resistive wall and the transverse higher-order modes in the RF cavity.

The most accurate approach to estimating the instability thresholds for NSLS-II is to carry out computer simulation tracking studies using the wakefields determined by numerical calculations of the wakefield for each component comprising the storage ring. This is a large effort that is now underway. Here, we shall provide estimates of the instability thresholds using a simplified model of the ring impedance, which has been developed based on impedance calculations performed to-date and on the experience at existing storage rings [6.2.2], especially APS and ESRF. We also present results of impedance calculations obtained thus far using the electromagnetic simulation code GdfidL [6.2.3].

In addition to the wakefield effects mentioned above, we also discuss intrabeam scattering. We report estimates of the Touschek lifetime resulting from single scattering, and of the increase in emittance due to multiple scattering.

We plan to use third-harmonic Landau cavities to increase the bunch length and synchrotron tune spread. Lengthening the bunch will be useful in raising the longitudinal microwave instability threshold, increasing the Touschek lifetime and reducing the effect of intrabeam scattering on the emittance. Increasing the bunch length and synchrotron tune spread improves the effectiveness of positive chromaticity in raising the single and coupled bunch transverse instability thresholds. The beam dynamics issues involved in the operation of the Landau cavities will be addressed.

6.2.2 Wakefields and Impedance

We provide a short overview of wakefields and impedance [6.2.4, 6.2.5] to clarify the approach we plan to adopt. Consider a point charge q (the drive particle) traveling very close to the speed of light in the z-direction through a vacuum enclosure displaced from the design trajectory by $\vec{r}_d$. A unit test charge travels at a distance s behind the first (see Figure 6.2.1) on a trajectory parallel to the z-axis but displaced by $\vec{r}_t = (x, y)$. The change of momentum $\Delta\vec{p}$ of the second particle, caused by the electromagnetic field of the first, is given by

$$\Delta\vec{p} = \int_{-\infty}^{\infty} dt \left[\vec{E}\left(\vec{r}_t, z, t\right) + c\,\hat{z} \times \vec{B}\left(\vec{r}_t, z, t\right) \right]_{z=ct-s} . \tag{6.2-1}$$

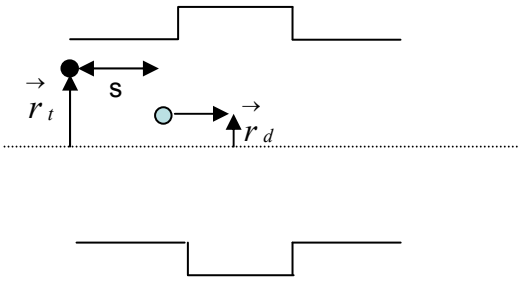

Figure 6.2.1. A drive particle *d* leading a test particle *t* through a vacuum structure.

For $\vec{r}_t = \vec{r}_d = 0$, we define the longitudinal wakefield $w_{\parallel}(s)$ [volt/coul] by

$$w_{\parallel}(s) = -\frac{c}{q}\Delta p_z = -\frac{1}{q}\int_{-\infty}^{\infty} dz E_z\left(z, t = \frac{z+s}{c}\right), \tag{6.2-2}$$

and the longitudinal impedance $Z_{\parallel}(k)$ [ohms] is determined by the Fourier transform,

$$Z_{\parallel}(k) = \int_{-\infty}^{\infty} \frac{ds}{c} w_{\parallel}(s) e^{iks} . \tag{6.2-3}$$

For a Gaussian bunch containing N_e electrons, the energy loss is $\Delta E = \kappa_{\parallel}(eN_e)^2$ and the power loss is $P = \kappa_{\parallel} I_0^2 T_0$, where the energy loss factor $\kappa_{\parallel}$ [V/C] is given by

$$\kappa_{\parallel} = \int_{-\infty}^{\infty} \frac{cdk}{2\pi} \mathrm{Re}\, Z_{\parallel}(k) e^{-k^2\sigma_s^2} . \tag{6.2-4}$$

The transverse wakefield [V/C-m] is

$$\vec{w}_{\perp}\left(s,\vec{r}_t,\vec{r}_d\right)=\frac{c}{q}\Delta\vec{p}_{\perp}=\frac{1}{q}\int_{-\infty}^{\infty}dz\left[\vec{E}\left(\vec{r},z,t\right)+c\,\hat{z}\times B\left(\vec{r},z,t\right)\right]_{t=\frac{z+s}{c}}. \tag{6.2-5}$$

The transverse impedance $\vec{Z}_{\perp}$ [Ω/m] is determined by the Fourier transform,

$$\vec{Z}_{\perp}\left(\vec{r}_t,\vec{r}_d,k\right)=\frac{-i}{c}\int_0^{\infty}ds\,\vec{w}_{\perp}\left(\vec{r}_t,\vec{r}_d,s\right)e^{iks}. \tag{6.2-6}$$

When the vacuum enclosure has reflection symmetry about the xz and yz planes, the transverse wakefield vanishes for $\vec{r}_t=\vec{r}_d=0$ and the first terms in a Taylor expansion yield [6.2.6],

$$w_x\left(s,x_t,x_d\right)\cong w_{Dx}\left(s\right)x_d+w_{Qx}\left(s\right)x_t \tag{6.2-7}$$

$$w_y\left(s,y_t,y_d\right)\cong w_{Dy}\left(s\right)y_d-w_{Qy}\left(s\right)y_t \tag{6.2-8}$$

where w_D is the dipole wakefield and w_Q is the quadrupolar wake. The dipole and quadrupolar impedances are determined by the Fourier transforms

$$Z_x\left(x_t,x_d,k\right)\cong Z_{Dx}\left(k\right)x_d+Z_{Qx}\left(k\right)x_t \tag{6.2-9}$$

$$Z_y\left(y_t,y_d,k\right)\cong Z_{Dy}\left(k\right)y_d-Z_{Qy}\left(k\right)y_t \tag{6.2-10}$$

The coherent betatron tune shift in a Gaussian bunch of N_e electrons produced by the transverse dipole impedance is approximately given by

$$\Delta\nu_{x,y}=\frac{e^2N_e}{4\pi E}\sum_j\beta_{x,y,j}\kappa_{x,y,j}, \tag{6.2-11}$$

where E is the electron energy and $\beta_{x,y,j}$ is the average value of the betatron function at the j^{th} impedance element and $\kappa_{x,y,j}$ [V/C-m] is the kick factor of the j^{th} element defined by

$$\kappa_{x,y,j}=\frac{c}{\pi}\int_0^{\infty}dk\,\mathrm{Im}\,Z_{Dx,y,j}\left(k\right)e^{-k^2\sigma_s^2}. \tag{6.2-12}$$

In a similar manner the quadrupolar impedance contributes to an incoherent tune spread. Some authors employ the effective impedance $\left(Z_{x,y}\right)_{eff}$ defined by

$$\left(Z_{x,y}\right)_{eff} = \frac{\int_{-\infty}^{\infty} dk\, Z_{D\,x,y}(k) e^{-k^2\sigma_s^2}}{\int_{-\infty}^{\infty} dk\, e^{-k^2\sigma_s^2}} \tag{6.2-13}$$

The kick factor is related to the effective impedance by

$$\kappa_{x,y} = \frac{c}{2\sqrt{\pi}\sigma_s} \mathrm{Im}\left(Z_{D\,x,y}\right)_{eff} . \tag{6.2-14}$$

To estimate instability thresholds, we use a model in which the impedance is comprised of a broadband resonator plus the resistive wall. The analytic forms for the wakefield and impedance of these elements are summarized in Table 6.2.1.

Table 6.2.1 Analytic Expressions for Impedance and Wakefield.

Resonator	
$Q' = \sqrt{Q^2 - 1/4} \qquad k_r' = k_r Q'/Q$	
$w_\parallel(s) = \frac{ck_r R_s}{Q_s}\exp\left(-\frac{k_r s}{2Q_s}\right)\left[\cos k_r' s - \frac{1}{2Q_s'}\sin k_r' s\right]$	$w_\perp(s) = \frac{ck_r R_\perp}{Q_\perp'}\exp\left(-\frac{k_r s}{2Q_\perp}\right)\sin k_r' s$
$Z_\parallel(k) = \frac{R_s}{1 - iQ_s\left(k/k_r - k_r/k\right)}$	$Z_\perp(k) = \frac{k_r}{k}\frac{R_\perp}{1 - iQ_\perp\left(k/k_r - k_r/k\right)}$
$\kappa_\parallel = \frac{\omega_r R_s}{2Q_s} \qquad (k_r\sigma_s << 1)$ $\kappa_\parallel = \frac{\omega_r R_s}{4\sqrt{\pi}\,Q_s^2\left(k_r\sigma_s\right)^3} \qquad (k_r\sigma_s >> 1)$ $\left(Z/n\right)_0 = R_s\left(\omega_0/\omega_r\right)$	$\kappa_\perp \cong \frac{1}{\sqrt{\pi}}\frac{cR_\perp}{Q_\perp}\left(k_r^2\sigma_s\right) \quad (k_r\sigma_s << 1)$ $\kappa_\perp \cong \frac{c}{2\sqrt{\pi}\,\sigma_s}\frac{R_\perp}{Q_\perp} \qquad (k_r\sigma_s >> 1)$
Resistive Wall [6.2.7]	
$s_0 = \left(2b^2/Z_0\sigma_{cond}\right)^{1/3}$	
$w_\parallel(s) \cong \frac{-cZ_0 L}{4\pi\sqrt{2\pi}\,b^2}\left(\frac{s_0}{s}\right)^{3/2} \qquad (s >> s_0)$	$w_\perp(s) \cong \frac{cZ_0 s_0 L}{2\pi b^4}\sqrt{\frac{2s_0}{\pi s}} \qquad (s >> s_0)$
$Z_\parallel(k) \cong \frac{(1-i)Z_0 s_0 L}{4\pi b^2}\sqrt{k\,s_0} \quad (0 \le k << 1/s_0)$	$Z_\perp(k) \cong \frac{2}{kb^2}Z_\parallel(k) \quad (0 \le k << 1/s_0)$
$\kappa_\parallel \cong 1.2\frac{cZ_0}{4\pi}\frac{L}{2\pi b^2}\left(\frac{s_0}{\sigma_s}\right)^{3/2}$	$\kappa_\perp \cong 0.58\frac{cZ_0}{4\pi}\frac{2s_0 L}{b^4}\sqrt{\frac{s_0}{\sigma_s}}$
Extreme Anomalous Skin Effect [6.2.8]	
$s_0 = \left(Bb\right)^{3/5}/\sin\left(\pi/10\right)$ $B = 3^{1/6}2^{-4/3}\pi^{-1/3}Z_0^{-1/3}\left(l/\sigma_{cond}\right)^{1/3} \cong 3.9\times10^{-7}\,m^{2/3}$ (Cu @ 4 K, specular reflection)	
$w_\parallel(s) \cong \frac{-2cB\,Z_0 L}{3\pi\,\Gamma(1/3)b}s^{-5/3} \qquad (s >> s_0)$	$w_\perp(s) \cong \frac{2cB\,Z_0 L}{\pi\,\Gamma(1/3)b^3}s^{-2/3} \quad (s >> s_0)$
$Z_\parallel(k) \cong \frac{\left(1-\sqrt{3}\,i\right)B\,Z_0 L}{2\pi\,b}k^{2/3} \quad (0 \le k << 1/s_0)$	$Z_\perp(k) \cong \frac{2}{b^2\,k}Z_\parallel(k) \quad (0 \le k << 1/s_0)$
$\kappa_\parallel = 0.16\frac{cZ_0}{4\pi}\frac{L}{\pi b^2}\left(\frac{s_0}{\sigma_s}\right)^{5/3}$	$\kappa_\perp \cong 0.21\frac{cZ_0}{4\pi}\frac{2s_0 L}{b^4}\left(\frac{s_0}{\sigma_s}\right)^{2/3}$

6.2.3 Estimates of Instability Thresholds

To estimate the instability thresholds, we considered an approximate model of the storage ring impedance, including the long-range wakefield due to the longitudinal and transverse higher-order modes in the CESR-B cavities. The storage ring vacuum chamber is approximated by 720 m of aluminum with a vertical half-aperture of 12.5 mm. We also included 20 in-vacuum undulators, each with 3 m copper chambers of vertical half-aperture 2.5 mm. The geometric impedance due to cross-section changes in the vacuum vessel is approximated by longitudinal and transverse broadband resonators. The parameters for the resonators are based on experience at other storage rings [6.2.2, 6.2.9], especially APS and ESRF, as well as on the impedance calculations we have performed to date. We believe the model is conservative and that it may be possible to build NSLS-II with lower impedance. The details of the impedance model are presented in Table 6.2.2, and some key parameters needed in the estimation of instability thresholds are given in Table 6.2.3.

Table 6.2.2 Impedance Model.

CESR-B cavity higher-order modes (see Tables 6.2.4 and 6.2.5.)	$\beta_x = 18m$
720 m of aluminum with half-gap of 12.5 mm and β_{av} = 7.6 m:	$\kappa_{\|\|} = 4.0 V/pC \quad \kappa_y = 0.68\, KV/pC/m$
60 m of copper with half-gap of 2.5 mm and β_{av} = 2 m:	$\kappa_{\|\|} = 1.3 V/pC \quad \kappa_y = 5.6\, KV/pC/m$
Transverse broadband impedance with f_r = 30 GHz, R_y = 1 MΩ/m, Q_y=1, and β_{av} = 7.6m	$\kappa_y = 19\, KV/pC/m$
Longitudinal broadband impedance with $f_r = 30GHz$, $R_s = 30k\Omega$,	$\left(\mathrm{Im}Z_{\|\|}/n\right)_0 = 0.4\Omega \quad \kappa_{\|\|} = 35V/pC$

Table 6.2.3 Parameters for Threshold Calculations

Energy, E [GeV]	3
Revolution period, T_0 [μs]	2.6
Momentum compaction, α	3.7×10^{-4}
Energy loss, U [keV]	1172
RF voltage, V [MV]	3.7
Synchrotron tune, ν_s	0.0094
Damping time: τ_x, τ_s [ms]	13, 6.5
Energy spread, $\sigma_{\varepsilon 0}$ [%]	0.09
Bunch duration, σ_{t0} [ps]	15

6.2.3.1 Transverse Mode Coupling Instability (TMCI)

An approximate relation [6.2.10] determining the threshold of the TMCI at zero chromaticity is given by

$$\frac{\Delta\nu_y}{\nu_s} = \frac{e I_0^{th}}{2E\,\nu_s\,\omega_0}\sum_j \beta_{yj}\kappa_{yj} \cong 0.7\,, \tag{6.2-15}$$

where I_0^{th} is the threshold bunch current, β_{yj} is the average value of the vertical beta function in the j^{th} element, and κ_{yj} is its kick factor. $E = \gamma mc^2$ is the electron energy and ν_s is the synchrotron tune. Consider a current of 0.5 mA bunch. Using the NSLS-II parameters as described in Table 6.2.3, we find that to be below the TMCI threshold requires

$$\sum_j \beta_{yj}\,\kappa_{yj} < 180\ KV/pC\,. \tag{6.2-16}$$

Using the values of the kick factors and beta functions as specified in Table 6.2.2, we find that $\sum_j \beta_{yj}\,\kappa_{yj} = 160\ KV/pC$. Therefore, 0.5 mA bunches are below the TMCI threshold for zero chromaticity.

6.2.3.2 Longitudinal Microwave Instability

At very low single-bunch current, the longitudinal density is determined by the equilibrium between radiation damping and quantum fluctuations. As the bunch current increases, the longitudinal charge distribution is modified by the wakefield. Below the threshold of the microwave instability, the energy distribution remains unchanged, and the longitudinal charge distribution $f_0\left(\tau/\sigma_{\tau 0}\right)$ is determined by the time-independent solution of the Haissinski equation [6.2.11],

$$f_0(q) = A\exp\left[-\frac{1}{2}q^2 + S\int_q^\infty dq'\int_{q'}^\infty dq''\, f_0(q'')w(q''-q')\right], \tag{6.2-17}$$

where the constant A is chosen to satisfy the normalization

$$\int_{-\infty}^{\infty} dq f_0(q) = 1 \tag{6.2-18}$$

In the case of a broadband resonator with shunt impedance R_s, resonant frequency ω_s, and quality factor $Q_s = 1$, the scaled current is defined by

$$S = \frac{e I_0 R_s \omega_r}{E_0 \nu_s \omega_0 \sigma_\varepsilon} \tag{6.2-19}$$

and

$$w(q) = \exp\left(-\frac{q\omega_r\sigma_{t0}}{2}\right)\left[\cos\left(q\omega_r'\sigma_{t0}\right) - \frac{1}{2\sqrt{0.75}}\sin\left(q\omega_r'\sigma_{t0}\right)\right]. \tag{6.2-20}$$

In Figure 6.2.2, we show the Haissinski distribution for currents of 0.1 mA and 0.4 mA.

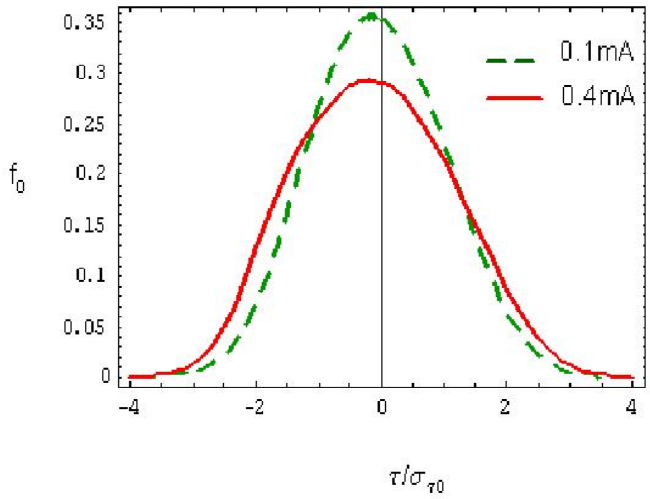

Figure 6.2.2 Longitudinal distribution as determined from the Haissinski equations.

Once the current exceeds the microwave instability threshold, both the energy distribution and the charge distribution are modified and are no longer time-independent. In the case of a broadband resonator with shunt impedance R_s, resonant frequency ω_s, and quality factor $Q_s = 1$, Oide and Yokoya [6.2.12] have shown that the single-bunch current threshold is given by

$$I_0^{th} = \frac{E \nu_s \sigma_\varepsilon}{e R_s (\omega_r / \omega_0)} S(\omega_r \sigma_t). \tag{6.2-21}$$

In Figure 6.2.3, we show the function $S(\omega_r \sigma_t)$ as determined by Oide and Yokoya (solid curve), and by tracking using the computer code ELEGANT [6.2.13] (symbols). A useful fit to the scaling function, in the regime x >0.2, is given by

$$S(x) = 11 + 9.4(x - 0.7)^2 . \tag{6.2-22}$$

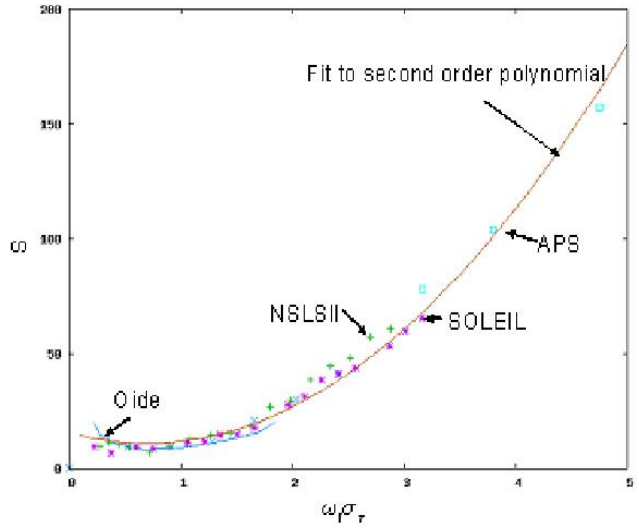

Figure 6.2.3. The scaling function $S(\omega_r \sigma_{t0})$ as determined by Oide and Yokoya (solid curve) and by tracking using ELEGANT (characters). The threshold is defined to be when the energy spread has increased by 5% over the zero current value.

In the limit when $\omega_0\sigma_{t0} >> 1$, the threshold condition becomes

$$I_0^{th} = 9.4\frac{E\nu_s^2}{e\alpha\left(\mathrm{Im}Z/n\right)_0}\left(\omega_0\sigma_{t0}\right)^3, \tag{6.2-23}$$

where $\left(\mathrm{Im}Z/n\right)_0 = R_s\left(\omega_0/\omega_r\right)$. This has the same form as the Boussard [6.2.14] criterion, except that in the Boussard case, the constant 9.4 is replaced by the smaller value $\sqrt{2\pi}$. The reason that the Boussard criterion gives too pessimistic a threshold is that it does not take into account the bunch lengthening due to potential well distortion.

In Figure 6.2.4, we show the dependence of the bunch length and the energy spread as calculated using the program ELEGANT. This shows that 0.5 mA bunches will suffer negligible increase in energy spread due to the longitudinal microwave instability.

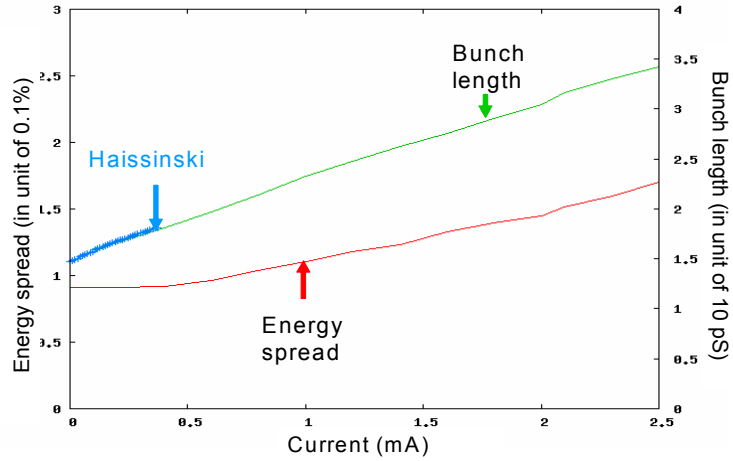

Figure 6.2.4. Bunch length and energy spread for broadband resonator. Resonant frequency $f_y = 30$ GHz, shunt impedance $R_s = 30\ k\Omega$, and $Q_s = 1$. This corresponds to $(\mathrm{ImZ/n})_0 = 0.4\ \Omega$.

6.2.3.3 Transverse Coupled Bunch Instability Driven by Resistive Wall Impedance

As discussed in Section 6.2.3.1, the short-range part of the resistive wall impedance contributes to the single-bunch TMCI. The long-range tail contributes to the transverse coupled bunch instability. A rough approximation to the growth rate of the fastest growing transverse coupled bunch mode driven by the resistive wall impedance (at zero chromaticity) is given by

$$\frac{1}{\tau_{gr}} \cong \frac{ecI_{av}}{2E}\frac{\beta_y}{C}\mathrm{Re}\,Z_\perp^{rw}\left(\omega_0\right)\frac{1}{\sqrt{1-q}}, \tag{6.2-24}$$

where C = 780 m is the ring circumference, β_y is the average value of the vertical beta function in the resistive wall, and q = 0.28 is the fractional part of the vertical tune. Equating the growth time to the radiation damping time provides an estimate of the instability threshold. Using the model parameters given in Tables 6.2.2 and 6.2.3, we find the threshold is at a total average current of 15 mA, far below the design value of 500 mA. Running at positive chromaticity will increase this threshold value.

Particle tracking [6.2.15] has been used to estimate transverse stability thresholds for coupled bunch modes. In these calculations we include both the long-range and short-range resistive wall wakefields as well as the short-range longitudinal and transverse wakefields, as described in Table 6.2.2. To keep the problem

manageable, we assume that all RF buckets contain identical bunches interacting via a single coupled bunch mode. A single bunch is tracked and the effect of other bunches is obtained by appropriate phase shifts under the assumption that the coherent frequency shift is small compared to the characteristic frequency width in the long-range transverse impedance. This should be an excellent approximation for the resistive wall impedance, which dominates the long-range transverse wake. The resistive wall impedance is due to 60 m of Cu with vertical aperture 5 mm and average beta function 2 m, in conjunction with 720 m of Al with aperture 25 mm and average beta function 7.6 m. The broadband transverse resonator has $R_\perp$ = 1 M-Ohm/m with $Q_\perp$ = 1 and 30 GHz resonant frequency at beta function 7.6 m. A longitudinal resonator with R_s = 30 k-Ohm, resonant frequency 30 GHz, and Q_s = 1 dominates the longitudinal impedance.

Three cases were simulated. Case 0 is a "stripped" case with no longitudinal wakes, no quadrupolar wakes (also referred to as detuning wakes), and no third-harmonic RF. Case 1 has the full suite of collective effects but no third harmonic cavity. Case 2 includes a perfect third harmonic cavity. The single-bunch threshold current as a function of vertical chromaticity is shown in Figure 6.2.5. In cases 1 and 2, a chromaticity of 4 allows for an average bunch current of about 0.5 mA and hence for an average stored current of 500 mA. This demonstrates the importance of running at positive chromaticity. Note also that bunch lengthening and enhanced synchrotron frequency spread introduced by the longitudinal wakefield and the third-harmonic cavity increase the effectiveness of positive chromaticity to stabilize the beam.

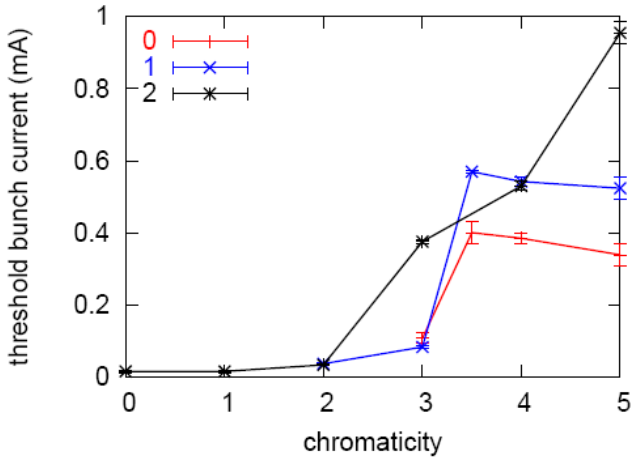

Figure 6.2.5 Threshold single bunch current vs. chromaticity for: (0) no longitudinal wakes, no quadrupolar wakes, and only fundamental RF; (1) all the impedances but only fundamental RF; (2) all impedances as well as fundamental and third-harmonic RF.

6.2.3.4 CESR-B Cavity Longitudinal Impedance and Coupled Bunch Growth Rates

The longitudinal higher-order modes (HOM) in an RF cavity can result in coupling between bunches, leading to unstable synchrotron oscillations. In the case of *M* equally spaced and populated point bunches, the coherent synchrotron frequency Ω_μ of the μ^{th} multi-bunch mode can be approximated by

$$\Omega_\mu - \omega_0 \nu_s = \frac{i e \alpha \omega_0 I_{av}}{4\pi \nu_s E} \sum_{j=-\infty}^{\infty} (M j + \mu) Z_\parallel [(M j + \mu + \nu_s)\omega_0] \qquad (6.2\text{-}25)$$

and

$$(\mu = 0,1,2,\ldots,M-1). \qquad (6.2\text{-}26)$$

A 3D GdfidL [6.2.3] model has been created for the CESR-B cavity [6.2.16]. The model consists of the niobium cavity with the asymmetric beam tubes, warm-to-cold transitions, and ferrite-lined HOM dampers, and it tapers to the 25×50 mm elliptical ring beampipes. The cavity has a fluted beam tube that allows the

lowest dipole mode to be coupled out to the HOM damper. This made it essential to use a 3D model for calculating the HOMs. To benchmark such a complex model, C-Fish [6.2.17] and Superfish [6.2.18] models of the cavity with complex permitivity and permeability were created. The results were compared to GdfidL and to measured data on a ferrite-lined pillbox cavity that was measured on the bench.

The Superfish model approximates the fluted beampipe by a cylindrical tube with the same cutoff frequency. An outline of the cavity geometry with the field lines of the 1586 MHz mode is shown in Figure 6.2.6.

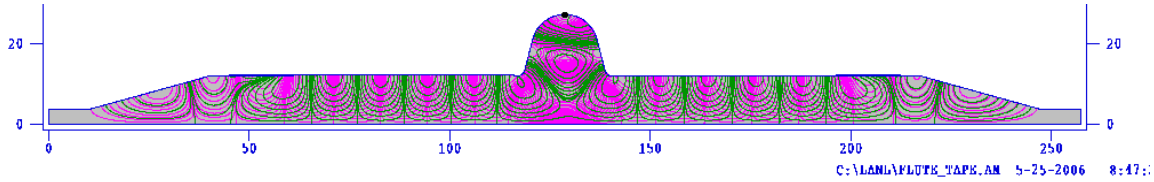

Figure 6.2.6 CESR-B cavity geometry input to C-Fish.

The first eight HOMs calculated are given in Table 6.2.4. Superfish correctly calculates the surface resistivity of niobium as a function of frequency, but only takes the complex permeability and permitivity as a single input. The permitivity of the ferrite load is relatively constant and does not contribute significantly to damping the HOM, but the ferrite permeability properties vary considerably, so specific values (Table 6.2.4) closest to the HOM frequencies were calculated. The ferrite properties were obtained from the Canadian Light Source [6.2.19]. The measurements were made at several discrete frequencies in the band of interest.

Table 6.2.4 CESR-B Higher-Order Longitudinal Modes.

Superfish			**GdfidL**		
Frequency (MHZ)	Shunt Impedance (Ohms)	Q	Frequency (MHZ)	Shunt Impedance (Ohms)	Q
952.4	112	222	950.55	8.14	350
973.32	57.07	332	976.62	54.6	420
1014.85	498	112	1014.38	505	150
1184.65	44.1	43	1181.5	13.2	60
1331.15	38.7	40	1361	65.6	20
1487.5	12.5	53	1481.5	46	40
1586.58	27.8	169	1580	7.5	30

We also performed studies of HOMs in CESR-B assembly using GdfidL code, shown in Figure. 6.2.7. The studies took off from time-domain simulation of 1 pC charge passing through the structure. For the longitudinal impedance computation, the beam is moving on-axis, in comparison with the transverse impedance computation when the beam trajectory is shifted off-axis with an offset taken as 3×STEPSIZE. To get a result for the impedance, which is Fast Fourier Transforming of the wake function with higher frequency resolution, the wakepotenial is computed up to an s-value of 50 meters. Parameters of the ferrite material are taken as $\varepsilon_r = 13.4$, $\mu_r = 0.9$, $\tan\delta_\varepsilon = 0.02$, $\tan\delta_\mu = 2.33$, $\sigma_\varepsilon = 0.05\ \Omega^{-1}/m^{-1}$, and $\sigma_\mu = 46395\ \Omega/m$ at a frequency of 2.8 GHz [6.2.19].

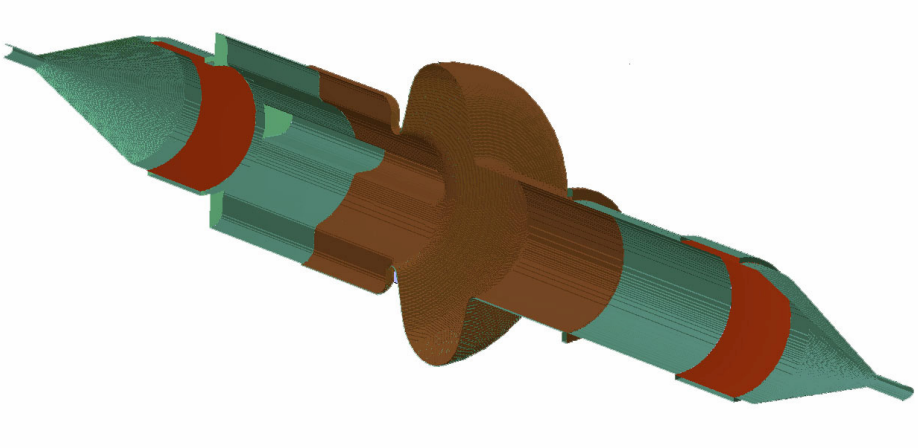

Figure 6.2.7 3D model of CESR-B cavity assembly in GdfidL.

These parameters were used in ZAP [6.2.20] to calculate the growth rates for nominal ring and beam parameters. The maximum growth time was 120 ms for the sum of three cavity impedances, much longer than the longitudinal damping time of 6.5 ms, and so the beam is longitudinally stable for cavity HOMs.

To summarize the CESR-B cavity studies, longitudinal CB growth rates were calculated for the first few HOM of the CESR-B cavity and were found to be below the damping rate, even for three installed cavities without stagger tuning. However, the combination of small-bunch length exciting higher frequency modes and ferrite loss decreasing at higher frequency could lead to unstable modes whose growth rate exceeds the damping rate, so this analysis must be extended to higher frequencies. To enable this, we are pursuing measurements of the ferrite properties to 6 GHz with Ron Hutcheon, who provided the data below 3 GHz that were used in these calculations. This work must also be extended to the third harmonic cavities.

6.2.3.5 CESR-B Cavity Transverse Impedance and Coupled Bunch Growth Rates

The transverse higher-order modes in an RF cavity can result in coupling between bunches, leading to unstable betatron oscillations. In the case of M equally spaced and populated point bunches, the coherent synchrotron frequency Ω_μ of the μ^{th} multi-bunch mode can be approximated by

$$\Omega_\mu - \omega_0 \nu_x = -i \frac{e c I_{av}}{2E} \frac{\beta_x^{cav}}{C} \sum_{j=-\infty}^{\infty} Z_\perp \left[\left(M j + \mu + \nu_y \right) \omega_0 \right], \tag{6.2-27}$$

where $\mu = 0,1,2,\ldots M-1$). The same GdlfidL model used to compute the longitudinal cavity impedances was used to compute the transverse modes. The first 15 modes are listed in Table 6.2.5.

Table 6.2.5 CESR-B Higher-Order Transverse Modes.

Time domain #	Frequency [MHz]	$R_\perp$ [kΩ/m]	$Q_{\perp,load}$
f1	608	2.2	60
f2	653	3.1	60
f3	681	15.6	70
f4	769	1.6	30
f5	864	1.03	50
f6	917	0.72	40
f7	964	0.66	30
f8	1045	0.8	30
f9	1146	1.17	30
f10	1243	2.3	70
f11	1299	0.36	160
f12	1344	0.31	40
f13	1405	0.33	70
f14	1433	0.22	100
f15	1464	0.44	70

The horizontal betatron function is 18 m at the RF cavities. These modes were used in ZAP [6.2.20] to calculate the transverse coupled-bunch growth rates. For 500 mA average current distributed uniformly in all the buckets around the ring and zero chromaticity, the coupled bunch growth time is 40 ms, which is longer than the radiation damping time of 13 ms. Therefore, the transverse cavity modes will not lead to unstable coupled-bunch betatron oscillations.

6.2.4 Impedance Budget

Extensive calculations have been performed of the wakefield and impedance produced by the storage ring components. Results of the calculations are summarized in Table 6.2.6, where we present the longitudinal kick factor (Eq. 6.2-4)], the transverse kick factors (Eq. 6.2-12) and the imaginary part of the longitudinal impedance at low frequency divided by $n = \omega/\omega_0$. The values given correspond to a single element. The number of times a given object is located in the ring is stated.

Table 6.2.6 Calculated Impedance for Storage Ring Components.

Object	Number of occurrences	$\kappa_{\|\|}$ V/pC	$(\mathrm{Im}Z_{\|\|}/n)_0\Omega$	κ_xV/pC/m	κ_yV/pC/m
Absorber	180	3.4×10^{-3}	9.2×10^{-6}	0.5	0.002
Bellows [1]	180	8.7×10^{-3}	124×10^{-6}	0.8	2
BPM	270	20×10^{-3}	47×10^{-6}	0.9	1.1
CESR-B cavity	3	3.6	40×10^{-3}	58	58
Dipole Chamber	60	0.24×10^{-3}	0.5×10^{-6}	0.045	0.0
Flange [1]	300	0.47×10^{-3}	16×10^{-6}	0.141	0.141
Injection Region	1	TBD	TBD	TBD	TBD
SCU chamber geometric	TBD	7.4×10^{-3}	495×10^{-6}	58	190
SCU chamber ease	TBD	5.6×10^{-3}		13	26
IR chamber	-5	TBD	TBD	TBD	TBD
CPMU geometric	TBD	95×10^{-3}	1.1×10^{-3}	136	425
CPMU resistive wall	TBD	66×10^{-3}		112	225
Al resistive wall	1	4.0		272	545
Scraper	2	TBD	TBD	TBD	TBD

[1]Values for bellows and flanges were calculated by Nagaoka [6.2.21] for SOLEIL with σ_s = 6 mm. The values for the CESR-B cavity were calculated using GdfidL with σ_s = 4 mm. The other geometric impedances were calculated with σ_s = 3 mm. The resistive wall and extreme anomalous skin effect estimates were made with σ_s = 4.5 mm. The bunch-length dependence of the wakefields will be determined in future work.

The Al vacuum chamber is taken to be of length 720 m with vertical half-height 12.5 mm. The copper-plated RF shield for the in-vacuum permanent magnet undulator is 3 m long with vertical half-height of 2.5 mm. The superconducting undulator chamber is 2 m long with vertical half-height 2.5 mm and is cold copper in the extreme anomalous skin effect regime [6.2.8]. The vertical resistive wall wake of the elliptic chamber is taken to be 0.8 times the value for the circular chamber and the horizontal wake is 0.4 times the circular value [6.2.22]. Results not yet determined are indicated in the table.

6.2.4.1 Insertion Device Chambers

While most of the components listed in Table 6.2.7 are fairly common and have been successfully used in many machines, we feel that significant attention is warranted for studies and optimization of the impedance due to insertion device chambers. This need is based on experience at modern light sources, where installations of small-gap ID chambers have significantly affected beam dynamics [6.2.24], as well as on the requirements for NSLS-II, which is expected to have a large number of ID chambers (~20) with gap down to 5 mm beam stay-clear. Both the resistive wall component and the geometric component due to the transitions have been studied. Furthermore, in addition to the dipole impedances, which directly cause beam instabilities, we have estimated the quadrupolar component [6.2.25], which results in incoherent frequency shift and indirectly contributes to the instabilities through the Landau damping.

For the purposes of impedance budget we consider two representative ID chamber geometries: 1) a variable-gap, in-vacuum, permanent magnet undulator, and 2) a 5 mm fixed-gap elliptical chamber (4.2 K Cu inner surface) for a superconducting small-gap undulator.

Resistive wall contribution has been estimated analytically. While the inner chamber cross-sections are either complex H-like or elliptical shapes we have conservatively used the formulas in Table 6.2.1 for round cross-sections. It is known [6.2.22] that as the chamber gets flatter (while height is kept fixed), the longitudinal impedance passes through a minimum equal to about 90% of the round-pipe value, while the transverse impedance monotonically approaches ~80% of its round-pipe value. Copper coating and a minimum full gap of 5 mm were assumed for the estimates.

Geometric impedance contributions due to transitions [6.2.26] were calculated using EM code GdfidL [6.2.3] as well as checked against a recently developed analytical approach [6.2.25].

Table 6.2.7 Description of Components.

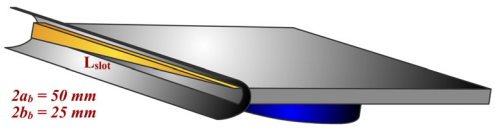	**Absorber** To protect the vacuum chamber and insertion devices in the ring from damage due to synchrotron radiation, photon absorbers are used. The model consists of a regular elliptical beampipe with 50 mm (W) and 25 mm (H), with a rectangular slot 10 mm high, 180 mm long, and 180 mm deep. A triangular copper burr is located inside the slot for synchrotron radiation absorption. It projects 5 mm inside the regular elliptical beampipe.
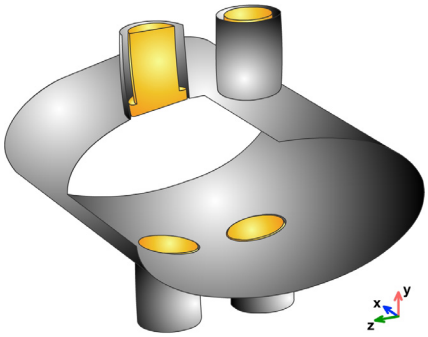	**BPM** Due to excitation of resonant modes in the buttons, the impedance, kick factor, and loss factor depend very strongly on the BPM button geometry. The BPM button geometry can be optimized to reduce impedance contribution and heating, without losing its resolution. To estimate BPM contribution to the transverse and longitudinal impedance, buttons designed for the SOLEIL BPM were modeled on the regular elliptic beampipe for NSLS-II. Results of the transverse impedance were compared with results for the SOLEIL BPM geometry; in both cases, 50 Ω/m was computed.
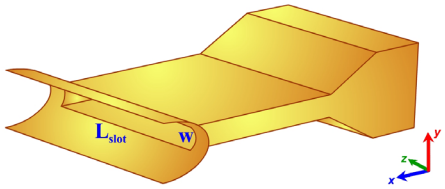	**Dipole Chamber** The dipole vacuum chamber for NSLS-II has an elliptical cross-section. Inside the chamber there is a slot 10 mm high. As was shown by Stupakov [6.2.23], the slot length does not affect the impedance. For this numerical computation, the slot length is taken to be 80 mm. The horizontal impedance of this geometry depends on beampipe radius and height of the slot.
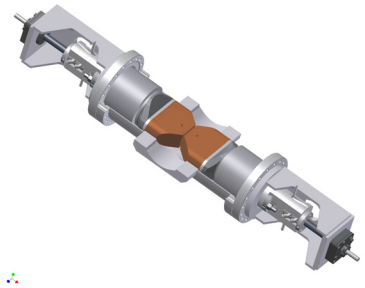	**Scraper-H** From the impedance estimations of other laboratories, horizontal or vertical beam scrapers can produce impedance comparable with that of a rectangular step or a tapered transition with a small angle of opening. Two scrapers of the presented geometry, one horizontal and the other vertical, are under consideration for application in the NSLS-II ring.

6.2.4.1.1 In-Vacuum Undulator

A 3D model of the CPMU [6.2.26] is shown in Figure 6.2.8 (a, top). This model is motivated by the geometry of the X13 Mini-Gap Undulator [6.2.27] currently operating at the NSLS x-ray ring and has been tailored to meet the NSLS-II requirements. The device consists of two magnet arrays of width w_m = 100 mm and thickness 34 mm, located inside a rectangular vacuum chamber of width w_{vc} = 180 mm and height h_{vc} = 170 mm. The tapered transition consists of two parts: 1) a fixed portion between the regular beampipe and the undulator vacuum chamber; and 2) a flexible-height portion with one end fixed to the interior of the undulator vacuum chamber and the other end fixed to the moveable magnet array. The flexible portion only consists of flat upper and lower conductive plates with no side walls. For simplicity in the 3D model, we used a

continuous smooth taper of length 180 mm. Also, due to mesh limitations, we have shortened the magnet section length to 0.5 m.

Figure 6.2.8 (a, bottom) shows the transverse wakepotential for the considered geometry and 3 mm RMS bunch length. The wakepotential has a Gaussian-like part corresponding to mainly inductive broadband impedance, as well as a characteristic long-range tail.

The short-range wakefield in the CPMU is predominantly determined by the tapers; the long-range wake depends on the cross-sectional geometry of the vacuum enclosure and the length of the magnet. The oscillations in the long-range part are due to multiple narrowband impedance resonances that are possible to characterize in terms of waveguide theory [6.2.28]. Due to limitations on the mesh, we have not yet been able to carry out a systematic study of the length dependence.

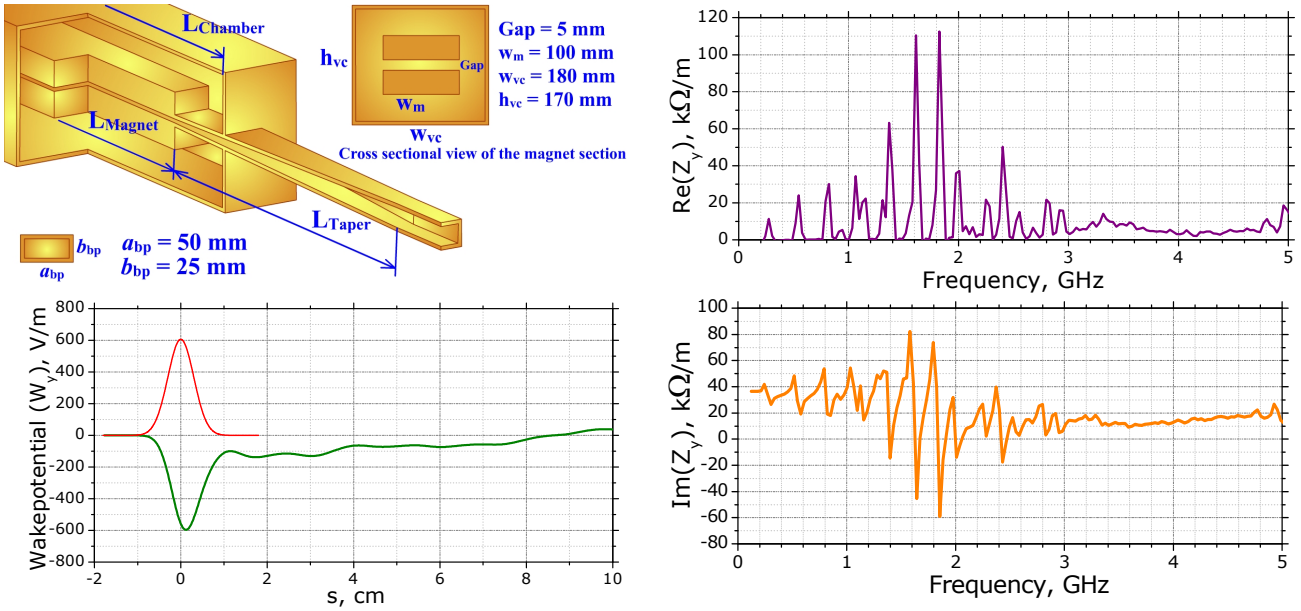

Figure 6.2.8 (a, top) Geometry of CPMU with L_{taper} = 180 mm; (a, bottom) Short-range transverse wakepotential of in-vacuum permanent magnet undulator chamber; (c, top and bottom) Low-frequency behavior of the real and imaginary parts of the transverse impedance of CPMU. Impedances determined by FFT of the computed wakepotential up to s = 7 m.

6.2.4.1.2 Superconducting Undulator

Similar calculations were performed for the elliptic vacuum chamber of a superconducting undulator. The geometry of the tapered elliptic vacuum chamber is shown in Figure 6.2.9 (a, top). The small-gap magnet region of the elliptic vacuum chamber for the superconducting undulator is fixed and has major axis $2a_s$ = 15 mm and minor axis $2b_s$ = 5 mm, with a magnet section length of 2000 mm. The tapers must smoothly transition between the magnet section and the regular beampipe, which has a major axis $2a_b$ = 50 mm and minor axis $2b_b$ = 25 mm.

Transverse impedance in the low-frequency limit and the kick factor for the tapered vacuum chamber are independent of the distance between the tapers. The inner section length was reduced to 100 mm for GdfidL calculations. The resulting wakepotential for 3 mm RMS long bunch and the taper length of L_{Taper} = 180 mm

is shown in Figure 6.2.9 (a, bottom). It corresponds to κ_y = 190 V/pC/m and Im Zy(ω→0) = 6.5 kΩ/m. When we increased the taper length, κ_y and Im $Z_y(\omega \to 0)$ decreased inversely proportional to L_{Taper}. The taper length of the elliptic vacuum chamber is chosen to optimize its contribution to the total impedance as well as space in the ring. Note that resonance peaks are observed inside the vacuum chamber in all cases of the transverse impedance calculations. These peaks are not resolved with a wakefield length of 1.5 m. A more detailed investigation of the electrodynamic properties of the tapered elliptic vacuum chamber uncovered the existence of trapped modes. These modes have been identified and classified [6.2.28]. In principle, these modes may affect multi-bunch dynamics and will be systematically studied.

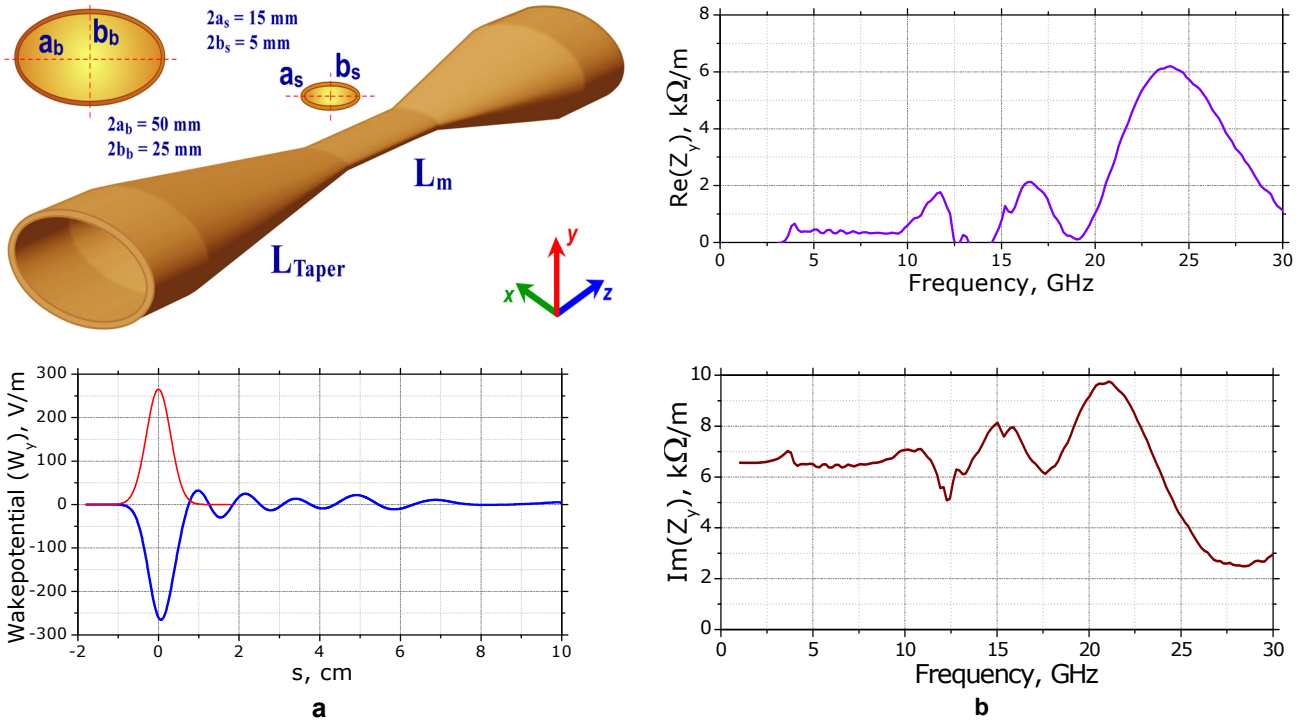

Figure 6.2.9 (a, top) Tapered elliptical vacuum chamber for superconducting small-gap undulator (L_{Taper} = 180 mm). (a, bottom) Transverse wakepotential; (b, top) Real part of the transverse impedance. (b, bottom) Imaginary part of the transverse impedance. Impedances correspond to FFT of the computed wakepotential up to s = 1.5 m.

6.2.4.2 CESR-B Short-Range Wake

CESR-B type superconducting cavities are considered here for acceleration of the beam in the NSLS-II storage ring. Two main 500 MHz RF cavities are required. In addition, one passive 1500 MHz bunch lengthening harmonic cavity will be located in the ring. To avoid additional transitions between the round pipes of cavities and the elliptical regular beampipe, three cavities (two main cavities and one harmonic cavity) are planned for installation in one straight section and the remaining cavities in the other straight section. The complicated nature of the RF cavities will require significant computational resources, to establish the longitudinal and transverse impedances for these assemblies. The most difficult part is a computation of the short-range wakefield for a 3 mm RMS bunch length. These data are required for determining the kick and loss factors.

Investigation of longitudinal and transverse impedances of cavities and transitions [6.2.29, 6.2.30] has begun, using simplified geometries. The first approximation simplifies the geometry of a single cavity as currently installed in the Cornell Electron Storage Ring, CESR. The 3D model of the 500 MHz CESR-B assembly is shown in Figure 6.2.7. Its length is 2.6 m. The geometry consists of the single main 500 MHz RF

cavity with the attached round beampipe of 120 mm on one side, and the fluted beampipe for HOM coupling on the other. Inside the round beampipe, close to the transition on both sides of the structure, ferrite material is located for HOM damping. Our first calculations were done using a thickness of 10 mm, due to the limitations in the mesh size. In the future, calculations will be done for the realistic thickness of 3.2 mm. Parameters of the ferrite material C-48 at different frequencies are taken from a [6.2.19]. They are presented only up to a frequency of 2.8 GHz. Using these data, we have analyzed the contribution to the longitudinal and transverse impedance due to the CESR-B assembly. The RF coupler is not included in these computations. This simplification allows using a quarter of the structure, which drastically reduces required computer resources and computation time.

The current structure has two tapered transitions. The regular beampipe planned for the NSLS-II storage ring has an elliptical cross-section 50 mm wide and 25 mm high. The round beampipe attached to the 500 MHz RF cavity has a radius of 120 mm. To accommodate the difference in cross-sections, smooth transitions must be provided. Their lengths should be calculated to optimize for transverse and longitudinal impedances. Every transition contributes to the impedance. However, in each round beampipe, near each tapered transition, ferrite material is located for HOM damping. Transitions cannot be accurately estimated without including the effects of the ferrite material because the modes generated at discontinuities by a passing bunch can be damped in the ferrite material. Hence, to get approximate impedance data from these tapered transitions, ferrite material should be included in the analysis.

Table 6.2.6 (beginning of Section 6.2.4) presents results of the kick factor and the loss factor for a 4 mm RMS bunch length. These data are a sum of numerical computations in the two separate geometries. The first geometry is a simple RF cavity with attached round and fluted beampipes. On the end of the pipes, "PORT" boundary conditions were specified. The second geometry is a round beampipe, lined with ferrite material, with a radius of 120 mm transitioning by 300 mm tapers on both sides to the regular elliptical beampipe. In this way, the cavity contribution was calculated separately from the rest of the assembly.

6.2.5 Intrabeam Scattering

Small-angle Coulomb scattering within a beam leads to the excitation of betatron and synchrotron oscillations of particles, which usually increases beam emittances in all phase planes. This effect, often called intra-beam scattering (IBS) or multiple Coulomb scattering, is proportional to the beam 3D phase-space density and depends strongly on beam energy, becoming more severe for high intensity, low energy machines.

When IBS is included, the steady-state beam properties with radiation damping are defined by

$$\varepsilon_x = \frac{\varepsilon_{x0}}{1-\tau_x/T_x}, \quad \varepsilon_y = \frac{\varepsilon_{y0}}{1-\tau_y/T_y}, \quad \sigma_p^2 = \frac{\sigma_{p0}^2}{1-\tau_p/T_p}, \tag{6.2-28}$$

where subscript 0 indicates the beam properties in the absence of IBS, $\tau_{x,y,p}$ stand for synchrotron radiation damping times, and $T_{x,y,p}$ are the IBS growth times discussed below. These equations indicate that the IBS effect becomes important when IBS rates are significant in comparison with the radiation damping rates. Because the IBS growth times $T_{x,y,p}$ depend on beam current as well as beam emittances, energy spread, and bunch length, the above equations are coupled, and solving them requires some iterative procedure. Sometimes a fourth equation is added that expresses the current-dependent relation of the bunch length to the energy spread, to account for the potential well distortion. If the vertical emittance is dominated by weak coupling (which is our expectation for NSLS-II), the effect simplifies to 2D, and the second equation is replaced by $\varepsilon_y = \kappa\, \varepsilon_x$, where κ stands for the coupling coefficient.

The basic theoretical framework of IBS effect was established long ago by Piwinski [6.2.31] and Bjorken and Mtingwa (B–M) [6.2.32] using two different approaches. These theories express IBS rise times $T_{x,y,p}$ as

complicated integrals of beam parameters, such as energy and phase space density, as well as lattice properties. The B–M theory has been extended to include arbitrary vertical-horizontal and vertical-longitudinal coupling [6.2.33]. The resulting growth rates are local quantities, and have to then be averaged around the lattice. Many accelerator physics codes include some variations of the B–M approach. In addition to these general procedures which are fairly computer intensive, there exist a number of more approximate formulations of IBS effect that simplify the treatment for certain parameter regimes. For example, Bane [6.2.34] has recently shown the equivalence of the Piwinski and B–M treatments in the regime applicable for high energy machines. In this regime, Bane has found that B–M results reduce to fairly compact expressions for IBS rise times, which we have found useful for NSLS-II.

The IBS approaches mentioned above result in growth times proportional to the so-called Coulomb log factor, equal to $ln(b_{max}/b_{min})$, where $b_{max,\ min}$ are impact parameters, which are not well defined. Often, b_{max} is taken equal to σ_y . To fix b_{min}, a so-called "tail-cut" procedure was suggested by Raubenheimer [6.2.35]. He pointed out that, since IBS results in non-Gaussian beam distributions, tail particles could be overemphasized; therefore, one must chose b_{min} to eliminate interactions having collision rates smaller than SR damping rates.

The NSLS-II emittance is strongly dominated by the IDs and damping wigglers. Rather than assuming some fixed ID makeup, we have calculated IBS effects as a function of radiation losses in the machine, having ε_{x0} vary from the ~2 nm bare lattice value down to about 0.4 nm. The zero-current vertical emittance ε_{y0} was fixed at the diffraction limit for 1 Å x-rays (8 pm-rad), corresponding to κ varying from ~0.5% for bare lattice to about 2% for ε_{x0} = 0.4 nm.

Most NSLS-II calculations have been performed with the code ZAP [6.2.20], which implements the 2D procedure of the B–M theory [6.2.32], i.e., the vertical emittance is assumed dominated by coupling. We used 500 mA for the total ring current, and assumed it uniformly distributed into 80% of the 500 MHz RF buckets. As we changed the amount of radiation losses, the RF voltage was adjusted to keep the RF energy acceptance constant at 3%. Electron beam parameters in the absence of IBS, used as input to ZAP (such as horizontal emittance, energy spread, bunch length, and radiation damping times) were calculated analytically by scaling bare lattice values by the amount of radiation losses. The results given by ZAP are shown in Figure 6.2.10.

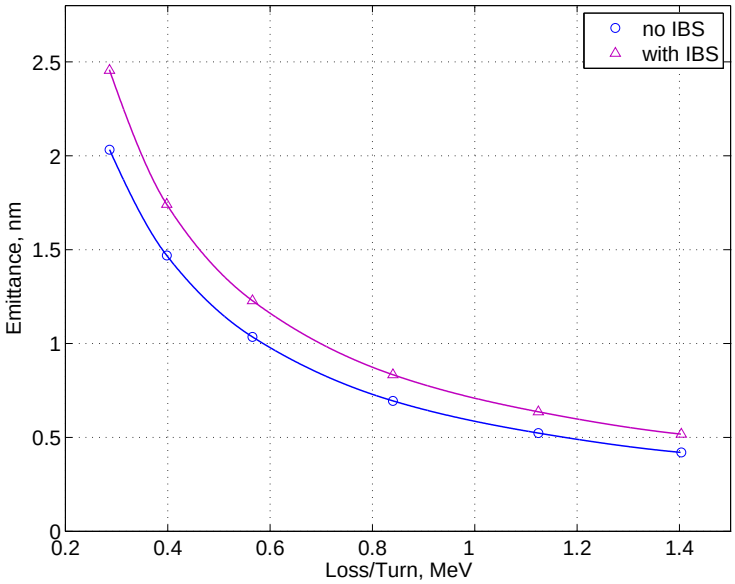

Figure 6.2.10 Horizontal emittance vs. total SR loss.

Note that the IBS-induced relative emittance blow-up does not exceed 20%, and remains fairly independent of the amount of radiation losses (and hence the emittance). This implies that for smaller emittances, increased IBS rates due to denser bunches are offset by the increase in radiation damping. This is quite contrary to a more typical situation in a storage ring light source not dominated by IDs, where

decreasing the emittance by adjusting the lattice (and hence keeping the SR rates fixed) can result in an increase of IBS-induced emittance blow-up. We have also found that the IBS rise times calculated by ZAP are in reasonable agreement (better than 50 %) with the estimates we have done using Bane's formalism.

Note that the results presented in Figure 6.2.10 are based on several conservative assumptions. First, calculations are performed at zero-current bunch length, while in reality the bunch will be longer, due to potential well distortion and the harmonic RF system. At even higher single-bunch currents, used in special operating modes, the microwave instability will result in an even stronger increase in bunch length as well as energy spread, reducing the IBS effect further. In addition, the calculations of Coulomb log that are used in ZAP use $b_{max} = \sigma_x$ and do not include the tail-cut procedure. As a result, the Coulomb log value ZAP assumes for NSLS-II parameters is about 17, while more recent estimates [6.2.33] that include the cut would reduce it to about 10.

We have also done some cross-checks of the bare lattice case using the SAD code from KEK [6.2.36]. SAD has been extensively benchmarked against the experimental results from the ultra-low emittance ATF storage ring. SAD does include the tail-cut, so it results in smaller IBS induced blow-up compared to ZAP. However, when scaled for the Coulomb log, the codes are in good agreement. SAD allows for full 3D treatment of IBS and will be used in the future to study the effects of vertical dispersion for NSLS-II.

To summarize, our calculations to date indicate that under pessimistic assumptions, IBS-induced relative emittance blow-up for NSLS-II should not exceed 20% at nominal bunch intensity and therefore it should not present a problem. Furthermore, we have found the magnitude of the blow-up to be fairly independent of the NSLS-II emittance, since the increased IBS rates for denser bunches are compensated by faster radiation damping. Future studies will include accounting for a more comprehensive ID makeup, considering the effects of vertical dispersion, and further developing some models of bunch lengthening.

6.2.6 Touschek Lifetime

The beam lifetime in most modern synchrotron radiation sources is limited by the Touschek effect, which describes the collision of two electrons inside a bunch, leading to momentum transfer from the transverse (usually horizontal) plane into the longitudinal direction. If the resulting longitudinal momentum exceeds the momentum acceptance of the accelerator, these particles are lost.

The Touschek lifetime is calculated as [6.2.37],

$$\frac{1}{\tau} = \frac{r_e^2 cq}{8\pi e \gamma^3 \sigma_s} \cdot \frac{1}{C} \cdot \oint_C \frac{F((\delta_{acc}(s)/\gamma\sigma_{x'}(s))^2)}{\sigma_x(s)\sigma_{x'}(s)\sigma_z(s)\delta_{acc}^2(s)} ds, \tag{6.2-29}$$

where r_e denotes the classical electron radius, q the bunch charge, σ_s the RMS bunch length, C the circumference of the storage ring, and σ_x (s) and σ_z (s) the RMS horizontal and vertical beam radii, including the dispersion term.

$$\sigma_{x'}(s) = \frac{\varepsilon_x}{\sigma_x(s)} \sqrt{1 + \frac{H(s)\sigma_\delta^2}{\varepsilon_x}} \tag{6.2-30}$$

is the RMS beam divergence for $\alpha_x = 0$, with

$$H(s) = \gamma_x \eta^2 + 2\alpha_x \eta\eta' + \beta_x \eta'^2 \tag{6.2-31}$$

the chromatic invariant. The function F(x) is defined as

$$F(x) = \int_0^1 (\frac{2}{u} - \ln\frac{1}{u} - 2) \cdot \exp(-x/u) du. \quad (6.2\text{-}32)$$

While the Touschek lifetime depends linearly on the bunch length as well as on the vertical beamsize, its dependence on the horizontal beamsize (or emittance) is more complicated. For large horizontal beamsize, the particle density of the bunch becomes very small, thus greatly decreasing the probability of two electrons colliding. On the other hand, a large horizontal emittance results in large horizontal momenta that can be transferred into the longitudinal plane due to a Touschek scattering event. The dependence of the resulting Touschek lifetime on horizontal emittance is illustrated in Figure 6.2.11.

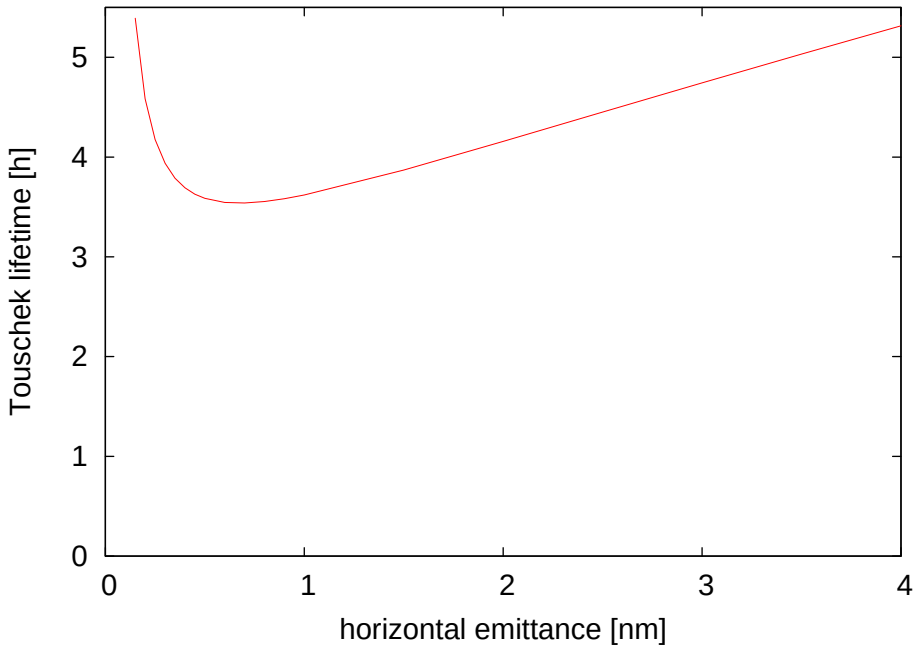

Figure 6.2.11 Touschek lifetime vs. horizontal emittance.

Experience at facilities like ALS and SLS has shown that nonlinear betatron coupling plays a significant role in limiting the momentum acceptance of the storage ring, especially in the presence of small vertical apertures due to small-gap insertion devices. Therefore, tracking has been performed using the TRACY-2 code. Since Touschek scattering occurs near the center of the bunch, the momentum acceptance δ_{acc} needs to be determined for particles starting at a longitudinal position s with coordinates $x = x' = y = y' = 0$. In general, this yields different momentum acceptances δ_{acc}^{+} for positive and δ_{acc}^{-} for negative momenta, resulting in different Touschek lifetimes τ^{+} and τ^{-}. Based on these two results, the total Touschek lifetime τ_{tot} is computed as

$$\frac{1}{\tau_{tot}} = \frac{1}{2} \cdot \left(\frac{1}{\tau^{+}} + \frac{1}{\tau^{-}} \right). \quad (6.2\text{-}33)$$

The Touschek lifetime was calculated for four different combinations of RF voltage and vertical aperture in the long straights, 2.5 MV and 5.0 MV in combination with ±2.5 mm and ±5.0 mm vertical aperture. The resulting momentum acceptances vs. longitudinal start position *s* around the ring are shown in Figure 6.2.12.

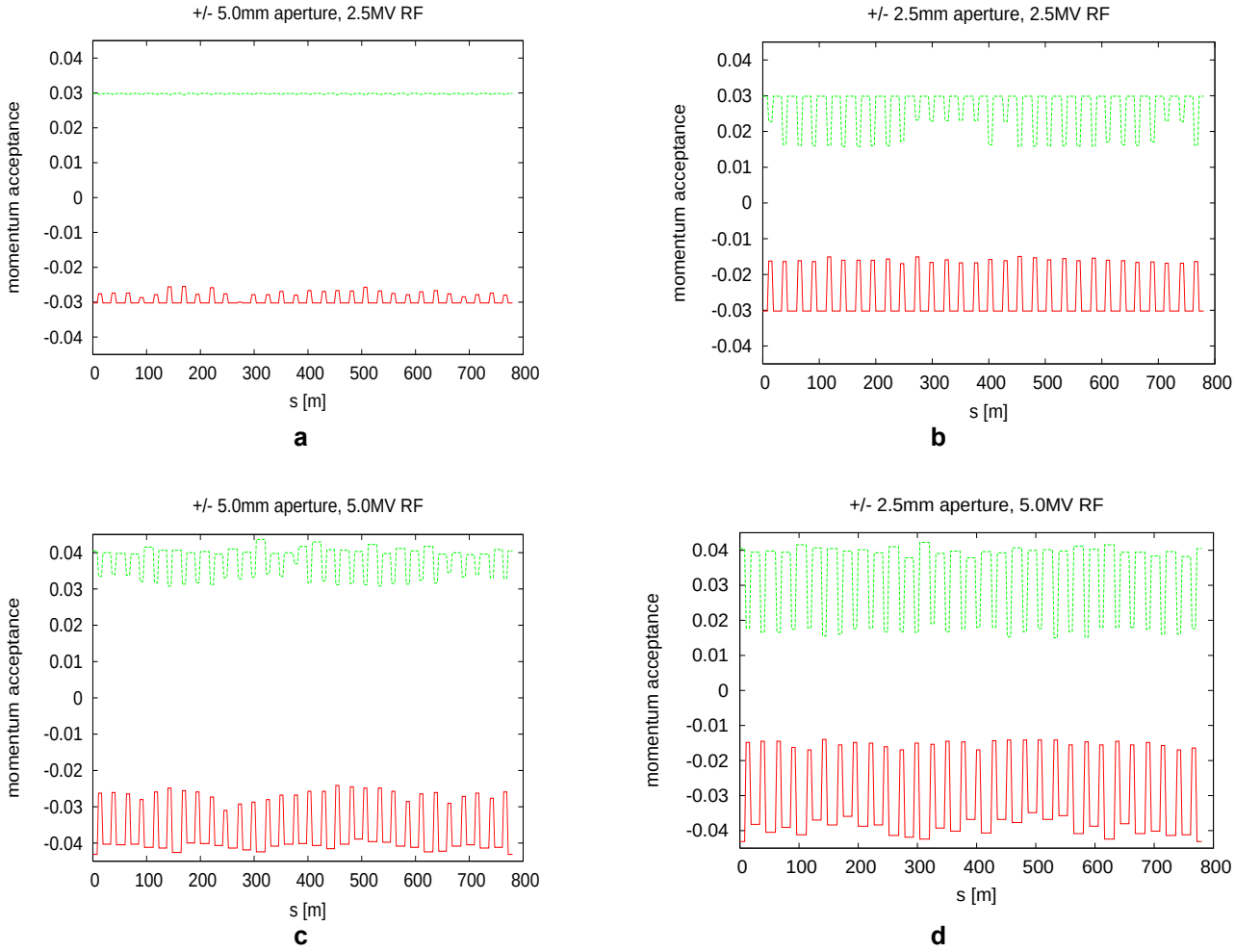

Figure 6.2.12 Momentum acceptance for: a) minimum vertical aperture of ± 5 mm and 2.5 MV RF voltage; b) minimum vertical aperture of ± 2.5 mm and 2.5 MV RF voltage; c) minimum vertical aperture of ± 5 mm and 5.0 MV RF voltage; and d) minimum vertical aperture of ± 2.5 mm and 5.0 MV RF voltage.

At the nominal RF voltage of 2.5 MV, which provides an RF energy acceptance of 3%, the resulting Touschek lifetime with a ±1.5 m long, ±5.0 mm vertical aperture in the short straights is 2.5 hours. When the aperture is reduced to ±2.5 mm, the Touschek lifetime drops by nearly a factor of two, to 1.3 hours. Doubling the RF voltage to 5.0 MV results in a Touschek lifetime of 1.1 hours for the ±2.5 mm aperture, and 3.6 hours for the ±5.0 mm aperture. This counterintuitive behavior is attributed to the decreasing bunch length at higher RF voltage, 2.1 mm vs. 3.0 mm, which results in a higher electron density within the bunch, thus overcompensating the effect of the larger momentum acceptance.

Assuming a constant RMS bunch length of 5.0 mm independent of RF voltage, which may be achieved by damping wigglers, the Touschek lifetimes are 2.2 hours and 4.2 hours for ±2.5 mm and ±5.0 mm vertical aperture, respectively, in the 2.5 MV RF voltage case. At the raised RF voltage of 5.0 MV, these lifetimes increase to 2.7 hours for the ±2.5 mm aperture, and 8.7 hours for the ±5.0 mm aperture.

6.2.7 Landau Cavity

Let us begin by reviewing the operation of a higher-harmonic, bunch-lengthening cavity (HHC) [6.2.38]. The fundamental cavity operates at an angular frequency, $\omega_{rf} = h\omega_0$, where h is an integer and $\omega_0 = 2\pi / T_0$ is the angular frequency of revolution. Assuming the Landau cavity is operating at the n^{th} harmonic of the frequency of the fundamental RF, the voltage seen by an electron with temporal deviation τ is

$$V(\tau) = V_0\left[\sin\left(\omega_{rf}\tau + \phi_s\right) + \kappa\sin\left(n\omega_{rf}\tau + \phi_n\right)\right]. \tag{6.2-34}$$

In the ideal operation of such a cavity, one chooses to satisfy the conditions

$$\begin{aligned} U_0 &= V_0\left[\sin\phi_s + \kappa\sin\phi_n\right] \\ 0 &= \cos\phi_s + n\kappa\cos\phi_n \\ 0 &= \sin\phi_s + n^2\kappa\sin\phi_n, \end{aligned} \tag{6.2-35}$$

where energy loss (U_0) and gain are balanced, and the first and second derivatives of the waveform are set to zero, at zero phase. In this case, the voltage has the form

$$V(\tau) = \cos\phi_s\left(\sin\omega_{rf}\tau - \frac{1}{n}\sin n\omega_{rf}\tau\right) + \sin\phi_s\left(\cos\omega_{rf}\tau - \frac{1}{n^2}\cos n\omega_{rf}\tau\right). \tag{6.2-36}$$

Approximating this for small τ yields the cubic form

$$V(\tau) \cong \cos\phi_s\left(\frac{n^2-1}{6}\right)\left(\omega_{rf}\tau\right)^3 + \sin\phi_s\left(1 - \frac{1}{n^2}\right). \tag{6.2-37}$$

As we will operate the Landau cavity passively, i.e., powered only by the beam, we cannot satisfy all of the ideal conditions. A superconducting cavity, in particular, absorbs very little power, implying that ϕ_n is fixed at $-\pi/2$, a few degrees from the ideal phase. Fortunately, this phase shift has little impact on the bunch profile. Figure 6.2.13 shows an unstretched bunch (blue) plotted with a stretched bunch (red) in a uniform fill with HHC detuning at +82 kHz.

A third-harmonic Landau cavity can be used to increase the electron bunch length without increasing the energy spread. This increases the Touschek lifetime and reduces the effect of intrabeam scattering on emittance. The nonlinear voltage resulting from the use of a Landau cavity results in a large increase in the dependence of the synchrotron tune on the amplitude of synchrotron oscillations. Energy transfer from potentially unstable resonant particles within a bunch to the surrounding nonresonant particles often provides a powerful mechanism for the suppression (Landau damping) of longitudinal coupled-bunch dipole modes. Also, the increase of bunch length can increase the stabilizing effect of positive chromaticity on the transverse dipole oscillations. The increased synchrotron tune spread can also help stabilize the higher-order head-tail modes.

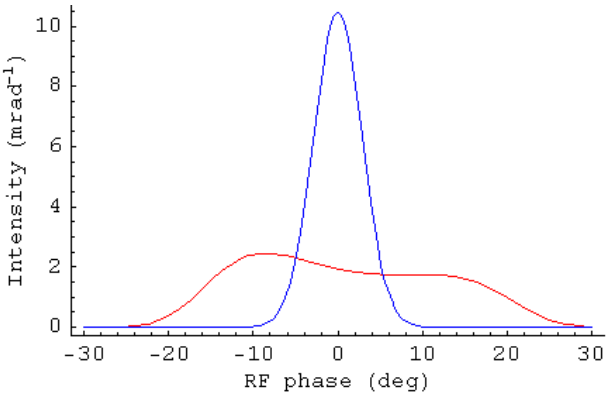

Figure 6.2.13 An unstretched bunch (blue) plotted with a stretched bunch (red) in a uniform fill with HHC detuning at +82 kHz.

If, as expected, there is a gap in the fill for ion clearing, then there will be a periodic transient induced in the cavity fields, causing non-uniform bunch profiles across the bunch train [6.2.39, 6.2.40, 6.2.41]. This effect is proportional to the *R/Q*s of the cavities, which favors superconducting cavities due both to their lower *R/Q* and their higher sustainable fields (requiring fewer cavities). Away from the center of the bunch train, bunches are much shorter and are peaked near the local synchronous phase, which can be a distance from the center of the nominal bucket. These peripheral bunches have shorter Touschek lifetime. This effect was found at ALS [6.2.40] to significantly reduce the overall lifetime of the beam. Figure 6.2.14 shows the bunch profiles for a 90% fill pattern and harmonic-cavity detuning of +82 kHz. Average RMS bunch length is 2.7 times the unstretched length.

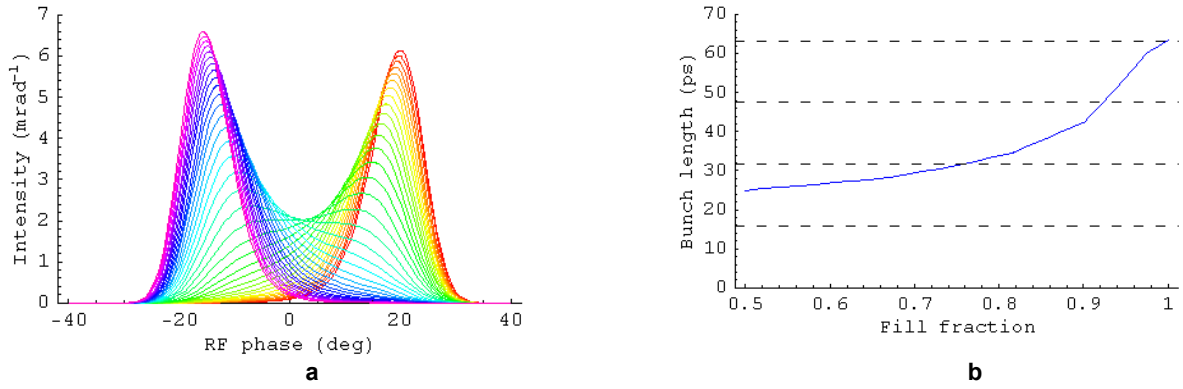

Figure 6.2.14 Bunch profiles**. a)** Along the bunch train for a 90% fill pattern and harmonic-cavity detuning of +82 kHz. **b)** Average bunch length as a function of fill fraction. Dashed lines are placed at multiples of the unstretched bunch length.

The average bunch length varies with the fill fraction. Smaller fill fractions aggravate the variation of bunch shapes along the train. Figure 6.2.14b shows the average bunch length as a function of fill fraction with cavities detuned to 82 kHz. Dashed lines are placed at multiples of the unstretched bunch length.

Bunch lengths vary with position along the train, being greatest near the center. In Figure 6.2.15a, each trace corresponds to a particular cavity field. From bottom to top, the detunings are +120, 105, 92, 85, 82, and 79 kHz. Dashed lines are drawn at multiples of the unstretched bunch length. As HHC fields increase, bunch and lifetimes tend to increase; but bunches that become double peaked, however, can show large RMS bunch length but reduced lifetime. Bunch centroid phases (arrival times) also vary with position along the train. In Figure 6.2.15b, the phase along the train is plotted for a 90% fill and the same fields as in Figure 6.2.15a. The

synchronous phase is a sensitive function of local shifts in the RF wave due to the $(\omega_\gamma t)^3$ inflection; that sensitivity increases with increasing HHC field, even beyond the optimal HHC field.

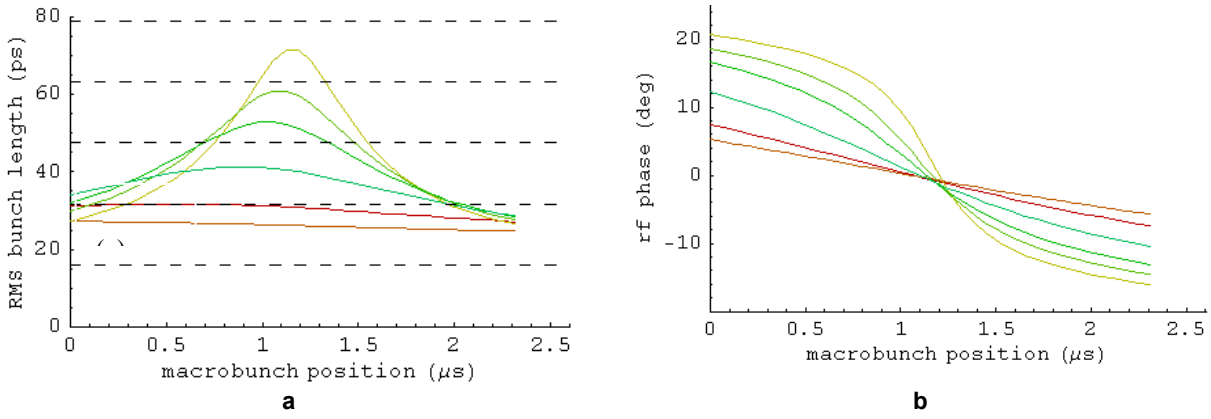

Figure 6.2.15 **a)** Each trace corresponds to a particular cavity field. From bottom to top, the detunings are +120, 105, 92, 85, 82, and 79 kHz. Dashed lines are drawn at multiples of the unstretched bunch length. **b)** Phase along the train is plotted for a 90% fill and the same fields as in **a**.

The HHC field required for nominal bunch stretching is 1.17 MV. Since the maximum sustained fields reached in HHCs developed to date are 0.5 MV per cell in 1500 MHz cavities, three cells are required, either in three single-cell cavities, or two double-cell cavities. The performance plots above were computed assuming three cells. In practice, significantly longer lifetimes are achievable by operating the HHCs at fields slightly higher than the ideal described above, as the NSLS VUV ring is operated now. The useful fields are limited by the onset of higher-order longitudinal instabilities.

The Day 1 configuration employs a reduced number of damping wigglers and consequently requires less main- and harmonic-cavity fields. Since two harmonic-cavity cells are capable of providing 1.0 MV of the 1.1 MV nominally required during this phase, most of the benefit of the HHC is obtained from this one cavity. Figures 6.2.16a and b show the bunch profiles and lengths expected by operating two cells at about 1.0 MV total field, but with the full complement of wigglers. Since the impedance is only that of two cells, the impact of the bunch train on bunch profiles is reduced in proportion. Fill fraction and detuning are 90% and +67.67 kHz, respectively. There is two-fold gain in the average bunch length.

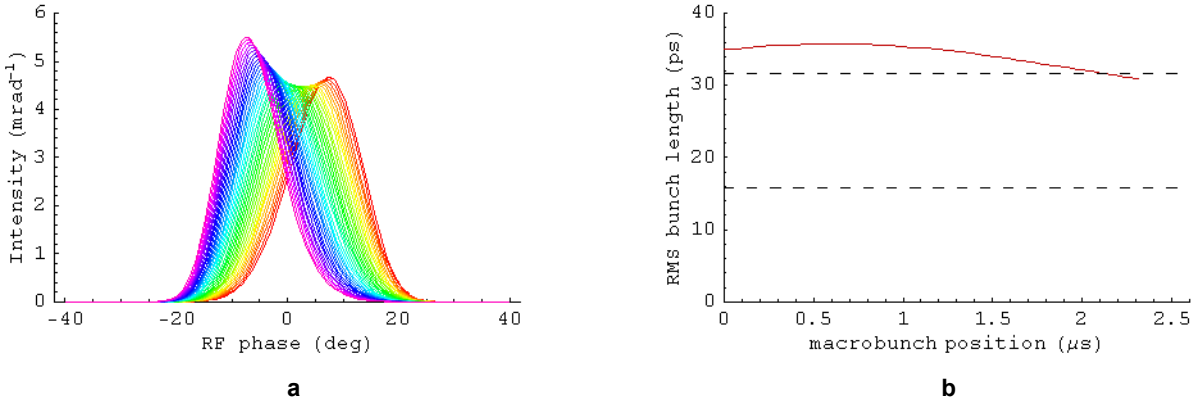

Figure 6.2.16 Bunch profiles (**a**) and lengths (**b**) expected by operating two cells at about 1.0 MV total field, but with the full complement of wigglers.

Compressed bunch operation for timing experiments is possible by detuning the HHC below the RF harmonic, instead of above. The bunch length at small single-bunch currents is reduced to less than half the bunch length without a harmonic cavity. But at finite currents, potential-well distortion by the ring's broadband impedance, and microwave instability, if present, inevitably increases the bunch lengths. The short bunch lengths may also permit higher-frequency, higher-order modes in the HHC and elsewhere to drive coupled-bunch instabilities. Short-bunch operation may drive the need for longitudinal feedback.

NSLS-II can opt to use an active HHC, i.e., HHCs that are powered by conventional amplifiers, such as was done in the NSLS VUV ring. In this configuration, resistive and reactive power are applied to control the phase of the cavity relative to the beam, almost arbitrarily. But the numerical results presented above, and the example of the VUV ring, which uses an active system to set the cavity (a NC cavity) phase to –90 degrees, show that the impact of the difference between –90 degrees and the nominal phase for stretching, even in the uniform-fill case, is insignificant. And in a fill with a significant gap, the improvement in the profiles is swamped by the effect of the periodic transient. Furthermore, an active system would require development of a cavity with an input coupler, could introduce multipacting, and could complicate HOM suppression. For these reasons, a passive cavity has been selected for NSLS-II.

6.2.8 Conclusions

Using a simplified model of the storage ring impedance, we have estimated the instability thresholds for NSLS-II. The longitudinal motion is found to be stable. At zero chromaticity, the transverse resistive wall impedance will make the beam unstable at 15 mA average current. According to simulations, increasing the chromaticity above 4 should provide stability. However, there is concern about the effect on DA at higher chromaticity; therefore, we will also use a transverse feedback system.

We have made significant progress in calculating the impedance of the storage ring using GdfidL. The results obtained thus far are within the envelope of the model we have used to estimate thresholds. Thus, we believe our model is conservative. We plan to complete the calculation of the storage ring impedance and then use the numerically determined wakefields in a tracking code to determine the instability thresholds.

Calculations indicate that the increase of emittance due to intrabeam scattering should be less than 20%. For the present state of the lattice design, the 5 mm full vertical aperture of the in-vacuum undulators reduces the energy acceptance from 3% down to 1.5% at large-dispersion locations. This results in a Touschek lifetime of 2 hrs. We plan to investigate whether further optimization of the working point can reduce the nonlinear coupling and thus increase the Touschek lifetime. Use of a Landau third-harmonic bunch lengthening cavity is planned. This will reduce the effect of intrabeam scattering on the emittance, lengthen the Touschek lifetime to more than 3 hrs, and provide enhanced longitudinal and transverse stability.

References

[6.2.1] A.W. Chao, *Physics of Collective Beam Instabilities in High Energy Accelerators* (Wiley, NY, 1993).

[6.2.2] See, e.g., K. Harkay, R. Nagaoka, J.L. Revol, and T. Nakamura, "A Preliminary Comparison of Beam Instabilities among ESRF, APS, and SPrinG-8 X-Ray Storage Ring Light Sources, Proc. EPAC2002, 1505 (2002).

[6.2.3] W. Bruns, http://www.gdfidl.de.

[6.2.4] G.V. Stupakov, "Wake and Impedance," SLAC-PUB-8683 (2000).

[6.2.5] B. Zotter and S.A. Kheifets, *Impedances and Wakes in High-Energy Particle Accelerators* (World Scientific Publishing Co., Singapore, 1998).

[6.2.6] A. Chao, S. Heifets, and B. Zotter, "Tune Shifts of Bunch Trains due to Vacuum Chambers Without Circular Symmetry," *Phys. Rev. ST-AB* **5**, 111001 (2002).

[6.2.7] K. Bane, and M. Sands, "Short-Range Resistive Wall Wakefields," AIP Conf. Proc. **367**, 131 (1995).
[6.2.8] B. Podobedov, "Extreme Anomalous Skin Effect Wakefields," unpublished.
[6.2.9] Y.C. Chae, "The Impedance Database and its Applications to the APS Storage Ring," Proc. PAC2005, 3017.
[6.2.10] See, e.g., S. Krinsky, "Simulation of Transverse Instabilities in the NSLS-II Storage Ring," BNL-75019-2005-IR.
[6.2.11] J. Haissinski, *Il Nuovo Cimento* **18**, 72 (1973).
[6.2.12] K. Oide and K. Yokoya, "Longitudinal Single-Bunch Instability in Electron Storage Ring," KEK Preprint 90-10 (1990).
[6.2.13] M. Borland, ELEGANT, http://www.aps.anl.gov/Accelerator_Systems_Division/Operations_Analysis/software.shtml
[6.2.14] D. Boussard, CERN LABII/RF/INT/75-2 (1975).
[6.2.15] M. Blaskiewicz, "The TRANFT User's Manual," unpublished.
[6.2.16] J. Kirchgessner, Part. Accel. **46**, 151 (1995).
[6.2.17] M. de Jong et al., *J. Microwave Power Electromagnetic Energy* **27**, 136 (1992).
[6.2.18] K. Halbach and R.F. Holsinger, "SUPERFISH-A Computer Program for Evaluation of RF Cavities with Cylinderical Symmetry," *Part. Accel.* **7**, 213 (1976).
[6.2.19] Mark deJong, private communication.
[6.2.20] M.S. Zisman, S. Chattopadhyay, and J.J. Bisognano, "ZAP User's Manual," LBL-21270, UC-28 (1986), 168.
[6.2.21] R. Nagaoka, "Numerical Evaluation of Geometric Impedance for SOLEIL," Proc. EPAC2004, 2038.
[6.2.22] K. Yokoya, "Resisitive Wall Impedance of Beam Pipes of General Cross Section," *Part. Accel.* **41**, 221 (1993).
[6.2.23] G. Stupakov, "Coupling Impedance of a Long Slot and an Array of Slots in a Circular Vacuum Chamber," *Phys. Rev. E* **51**, 3515 (1995).
[6.2.24] E. Karantzoulis, V. Smaluk and L. Tosi, "Broad Band Impedance Measurements on the Electron Storage Ring ELETTRA," *Phys. Rev. ST-AB* **6**, 030703 (2003).
[6.2.25] B. Podobedov and S. Krinsky, "Transverse Impedance of Elliptical Cross-Section Tapers," Proc. EPAC2006, 2973 (2006).
[6.2.26] A. Blednykh, S. Krinsky, B. Podobedov, and J.M. Wang, "Transverse Impedance for Small-Gap Undulators for NSLS-II," Proc. EPAC2006, 2973 (2006).
[6.2.27] P. Stefan et al., "Small-Gap Undulator Research at the NSLS: Concepts and Results." *Nucl. Instr. Meth. A* **412**, 161 (1998).
[6.2.28] A. Blednykh, "Trapped Modes in an Elliptic Vacuum Chamber," *Nucl. Instrum. Meth. A*.
[6.2.29] P.J. Chou, "Numerical Analysis of Higher-Order Modes for Superconducting RF Cavity at SRRC," Proc. Pac2003, 1368.
[6.2.30] P.J. Chou, J. Chen, K.-T. Hsu, C.-C. Kuo, C. Wang, and M.-H. Wang, "Collective Effects in the TLS Storage Ring after the Installation of Superconducting Cavity," Proc. PAC2005, 2360.
[6.2.31] A. Piwinski Tech. Rep. HEAC 74, Stanford, 1974; See Also A. Piwinski in A. Chao and M. Tigner, *Handbook of Acclerator Physics*, World Scientific (1999) 125.
[6.2.32] J. Bjorken and S. Mtingwa, "Intrabeam Scattering," *Part. Accel*. **13**, 115 (1983).
[6.2.33] K. Kubo and K. Oide, "Intrabeam Scattering Formulas for High Energy Beams," *Phys. Rev. ST-AB* **4**, 124401 (2001).
[6.2.34] K.L.F. Bane, "A Simplified Model of Intrabeam Scattering," SLAC-PUB-9226 (2002).
[6.2.35] T. Raubenheimer, *Part. Accel.* **45**, 111 (1994).
[6.2.36] K. Oide, *SAD User's Guide*.
[6.2.37] A. Streun, "Momentum Acceptance and Touschek lifetime," SLS Note 18/97.
[6.2.38] A. Hofmann and S. Meyers, "Beam Dynamics in a Double RF System," Proc. 11th International Conference on High Energy Accelerators, Geneva (Birkhauser Verlag, Basel, (1980), p 160.

[6.2.39] N. Towne, "Stretched Bunch Shapes in the NSLS VUV Ring," Proc. PAC1999 (1999) 2828.
[6.2.40] J.M. Byrd, S. De Santis, J. Jacob, and V. Serriere, "Transient Beam Loading Effects in Harmonic RF Systems for Light Sources," *Phys. Rev. ST-AB* **5**, 092001 (2002).
[6.2.41] A. Blednykh, S. Krinsky, B. Podobedov, J. Rose, N.A. Towne, and J.M. Wang, "Harmonic Cavity Performance for NSLS-II," Proc. PAC2005 (2005) 2544.

6.3 Orbit Feedback System

The linac is located on the same level as the booster. In future design we will determine whether the linac is installed on the floor supports or suspended from the ceiling.

6.3.1 Requirements for Beam Stability

To realize the benefits of the high brightness and small beam sizes of NSLS-II, it is essential that the photon beams are exceedingly stable, assuring constant intensity after apertures, constant photon energy after monochromators, and minimal photon source size and highly precise steering accuracy for focusing on small samples. For example, in the common case of 1:1 focusing optics, positional stability of the photon beam on the sample is directly related to that of the electron beam. The position of the photon beam should be stable to a level of Δ_y/σ_y ~10%. We require beam motion of no more than 10% of beamsize, particularly in the frequency range from ~10 mHz to 100 Hz. This tolerance has been adopted by many synchrotron radiation laboratories. Since the minimum vertical beta function is about 1 m, when we take the vertical emittance as $10^{-10}/4\pi$ m, the vertical beamsize is 2.7 μm RMS. Therefore, the beam position stability should be ~0.3 μm in the short straight section.

6.3.2 Fast Orbit Motion with Feedback Loop On and Off

For the NSLS-II ring with a DBA30 lattice as shown in Figure 6.1.1 (only half a super-period is shown), the performance of a fast, closed-orbit feedback system with 120 BPMs and 120 correction trims was calculated (for BPM positions, see Figures 6.1.4 – 6.1.6).

We averaged over 400 different sets of random numbers for all the quads, assuming they vibrate randomly with uncorrelated RMS displacement of 1 μm. The resulting beam RMS motion $\sigma_{\Delta y}$ is shown in blue in Figure 6.3.1. It is well approximated by the function $14\sqrt{\beta_y[m]}$ μm, which is shown in green.

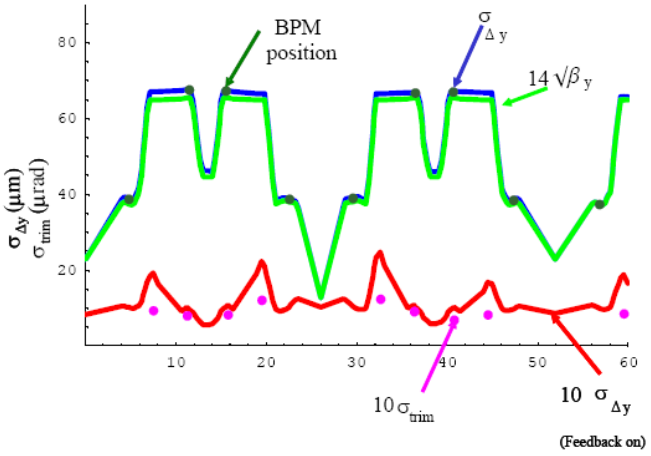

Figure 6.3.1 Open (green) and closed-loop (red) RMS orbit motion and RMS corrector strengths in the feedback loop. The x axis is the distance along the ring circumference, in meters.

For each set of Gaussian random errors for the quad vibration and BPM vibration, all with RMS displacement of 1 μm, the open-loop BPM signal was calculated, then the SVD matrix was used to calculate the corrector strength, and finally the orbit with the feedback loop closed. After averaging over 400 random samples, the residual RMS beam motion shown in Figure 6.3.1 was obtained, represented by the red curve. The open-loop BPM signal and the corrector strength used in the feedback loop are marked by dark green and purple dots, respectively.

The residual orbit is multiplied by a factor of 10 in Figure 6.3.1 to make it visible. The height of the purple dots represents 10 times the RMS strength of the correctors, in units of μrad. The figure shows that the feedback loop reduces the beam motion at the center of the long straight section (z = 0) from 25 μm to 0.7 μm. The maximum RMS corrector strength is on the order of 1.2 μrad.

The tolerance on the floor motion required to keep beam motion within 10% of beamsize was determined using the following assumptions: 1) ε_y = 0.1 nm/4π, 2) all the quads and BPMs mounted on the girders have uncorrelated random vibration of 0.4 μm, and 3) the BPM electronic noise is negligible. Averaging over 400 samples gave the ratio of the vertical beam motion divided by the RMS beamsize as a function of z in the ring, shown in Figure 6.3.2. At the 5 m straight section, the ratio of beam motion over beamsize is 11%. This implies that the tolerance for the quad vibration is <0.3 μm RMS. This calculation ignored the fact that for low-frequency ground motion, the movement of different components mounted on the girders can be correlated, since the sound wavelength at low frequency can be larger than the girder dimension. Actually, simulation for correlated movement of quads mounted on the same girder shows a reduced amplification factor, since the quads moving together tend to cancel each other [6.3.1]. The noise caused by ripples in the power supply corrector magnet current was also ignored. Compared with this effect, the orbit motion due to the vibration of BPMs is much more difficult to suppress. Actually, it is very difficult to reduce the beam motion to much less than the amplitude of the BPM vibration. Similar calculations for horizontal orbit show that if quads and BPMs have random vibration of RMS value 1 μm, the residual RMS value of beam motion is 0.7 μm at the straight sections. Since the horizontal beamsize is much larger than the vertical beamsize, the horizontal requirement is much easier to satisfy than the vertical.

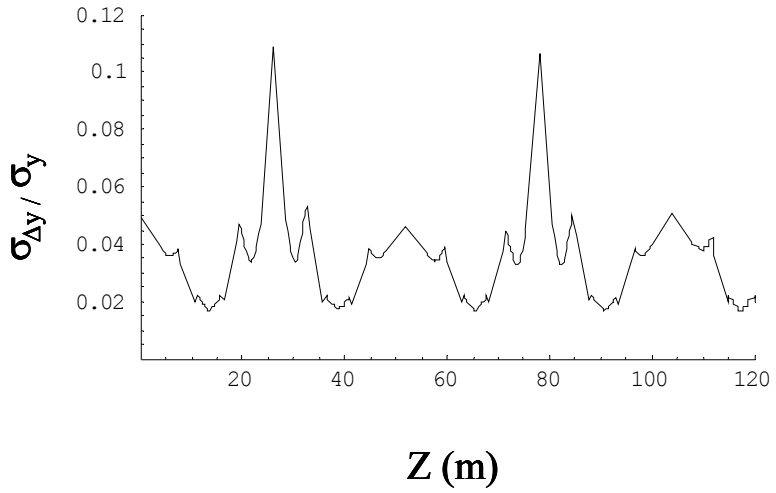

Figure 6.3.2 Closed-loop orbit deviation normalized by beamsize.

The beam motion due to power supply noise in a digital feedback system is determined by the voltage corresponding to the last bit of the power supply and the power supply current noise itself [6.3.1, 6.3.2]. Similar to the vibration simulation, we find that if we require beam motion (due to trim noise at the beam waist where β_y = 1 m) to be less than 0.25 μm, the RMS trim noise should be less than 10 nrad. Hence the

power supply should be accurate to 10 n-rad/0.29 = 30 nrad. If the maximum trim strength is 1 mrad, we need the last digit to be 30 ppm so the RMS noise should be less than 10 ppm.

6.3.3 Ground Movement at the NSLS-II Site

Floor vibration measurement near beamline X5 at the NSLS site on Feb. 22, 2006 is shown in figure 6.3.3. The measurement is the RMS value of vibration above 0.5 Hz. Note that between 10 p.m. (22 hrs) and midnight, the vibration reached a minimum of about 70 nm. It reached a maximum near noontime of about 200 nm. Since the sound speed in concrete is 3 km/s below 0.5 Hz, the effect of the vibration below 0.5 Hz is not critical.

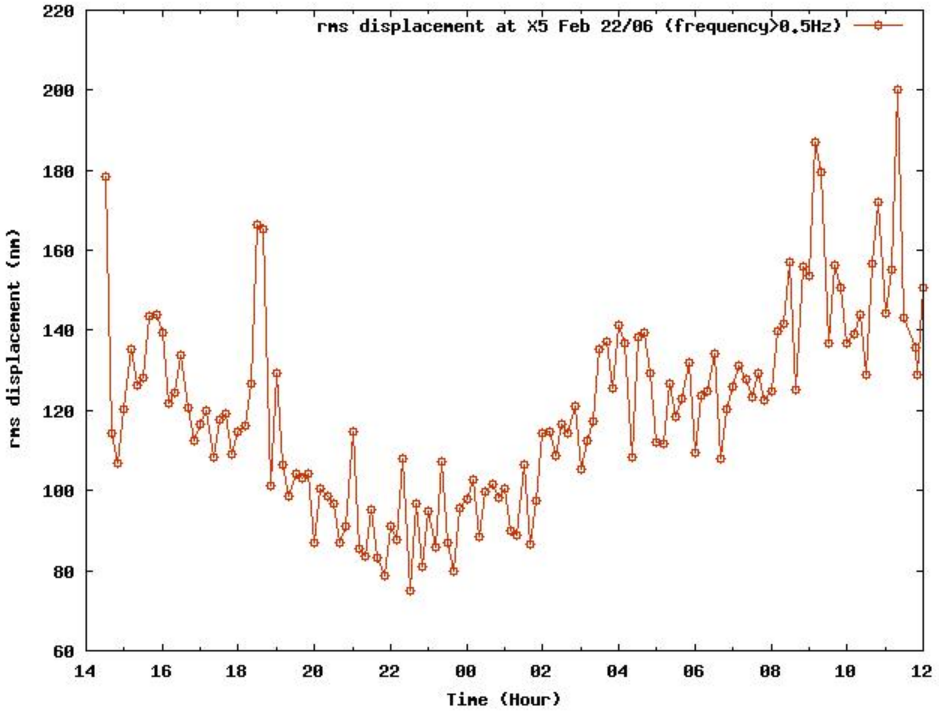

Figure 6.3.3 Floor vibration measurement near beamline X5 at the NSLS site on Feb. 22, 2006.

6.3.3.1 Long-Term Ground Movement

As for long-term ground movement at the BNL site, measurements carried out at RHIC between 1997 and 2002 show the coefficient A in the ATL law is $A \cong 3\times10^{-18}$ $m^2/m/s$ [6.3.4, 6.3.5]. Based on this, we estimate that the RMS movement within the 248 m diameter of NSLS-II over a half-year is about 110 m.

We simulated the performance of the slow feedback system on long-term ground motion using the ATL law [6.3.6] at the NSLS-II site over a half year, with the same set of BPMs and correctors as mentioned in Section 6.3.2. The results are shown in Figure 6.3.4. In this specific example, the maximum ground movement was 250 μm, with an RMS value of 60 μm.

Feedback Loop Off

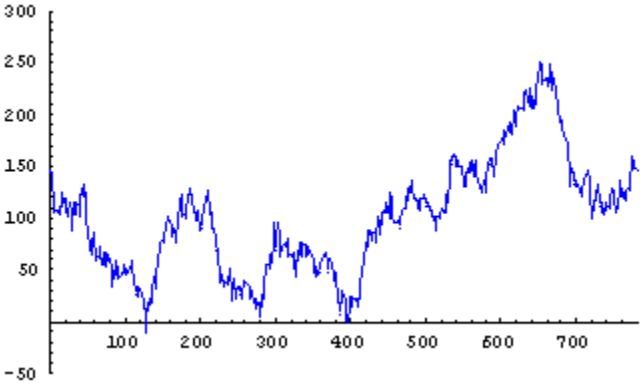

Floor motion around the ring. While the RMS maximum value around the ring for a large number of examples is 100 μm, in this specific example the maximum is 250 μm.

Electron beam motion (vertical) without feedback loop; maximum is 800 μm.

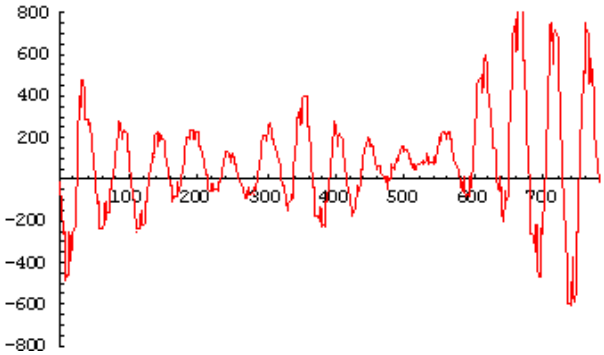

Feedback Loop On

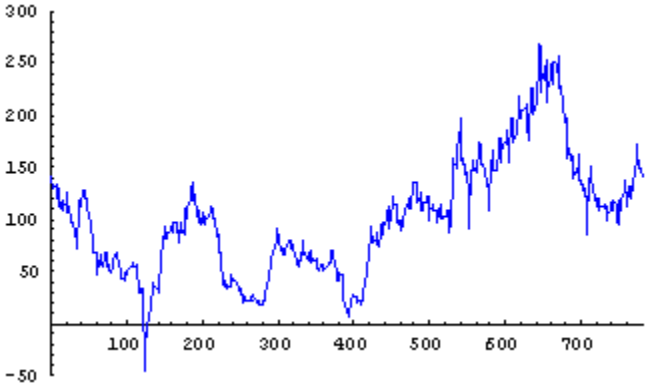

Electron beam motion with the feedback loop on.

Electron beam motion relative to floor (the difference between the two plots on the left) with the feedback loop on; maximum is 60 μm, RMS 12 μm.

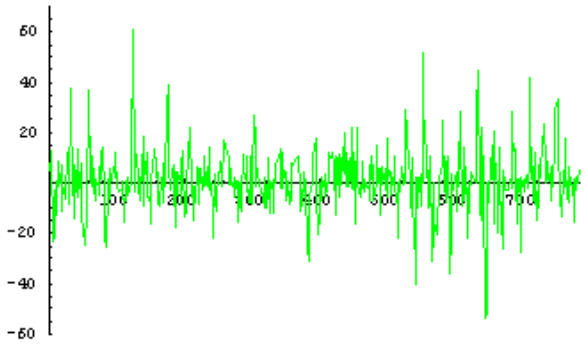

Figure 6.3.4 Simulated long-term ground motion and electron beam motion within half a year, with feedback system on and off. The horizontal axis is the distance along the circumference. Although the x-axis on the fourth plot is difficult to read, it aligns with the x-axis of the plot above it and the same labels apply to both.

The maximum relative movement between the beam and the ground was about 800 μm without feedback; with feedback, it was 60 μm with an RMS value of about 12 μm. Based on the ratio of 250 μm/12 μm, we estimate that, for the RMS value of the maximum ground movement of 110 μm across the diameter, the residual movement is about 5.3 μm over half a year. Hence, according to the ATL law, the residual RMS movement within a day should be reduced to about 0.4 μm.

If the orbit is realigned every six months, then within that half year the required corrector strength for the global orbit correction is about 0.1 mrad. (As mentioned in Section 6.3.2, to feedback on 1 μm movement, the required corrector strength is about 0.1 μrad.) To leave a margin for error, the maximum strength of the corrector is specified to be 0.5 to 1 mrad. As shown in Section 6.3.2, this requires the last bit of the power supply to be 30 ppm. To relax this condition, it is desirable have separate fast and slow feedback systems. This way, the slow feedback system correctors have a maximum strength of 0.5 to 1 mrad to handle the larger long-term motion, and the fast feedback system correctors have a lower maximum strength of 0.15 mrad;

thus, the last digit may be relaxed to 200 ppm. The fast feedback system uses the four correctors SL4, SD1, SD1, and S4 for each half super-period, as mentioned in Section 6.3.2. These correctors are located around stainless steel bellows, and hence can have high frequency response.

6.3.3.2 Temperature Stability

The air temperature stability in the storage ring tunnel is specified to be ±0.1ºC. Due to thermal expansion of the girder and vacuum chamber support system (~12 μm/m/ºC), the BPMs will move about ±1.2 μm. This motion is in the acceptable range everywhere in a super-period except in the 5 m and 8 m straight sections, where the BPM motion is required to be less than 0.3 μm (see Figure 6.3.2). A local feedback system will be used with two correctors on each side of an installed insertion device to stabilize the x-ray beam based on user's supplied feedback on its position. The local and global feedback systems will be decoupled, thus isolating the global orbit correction from the thermal displacements of the BPMs in the straight sections.

6.3.4 BPM Resolution and Noise Floor

A power density spectrum plot of measurement of orbit motion at NSLS using an RF BPM is reported in Figure 6.3.6, with beam motion shown in blue and the noise floor of the BPM in red. The plot shows that above 200 Hz, the beam motion is dominated by the noise floor. Hence, a feedback system with frequency higher than 200 Hz will not improve the orbit stability. The feedback system based on our BPM should have a cut-off point set below 200 Hz. Measurements at NSLS show that the vibration amplitude between 50 Hz and 200 Hz is less than 10 nm, which is negligibly small. Therefore, to relax the requirement on the feedback system bandwidth, the cut-off point is set at 60 Hz. A long-term drift test of the BPM offset is still needed, to show it is sufficiently small (lower than 0.2 μm). BPMs with better performance are available, and work in developing better BPMs is needed.

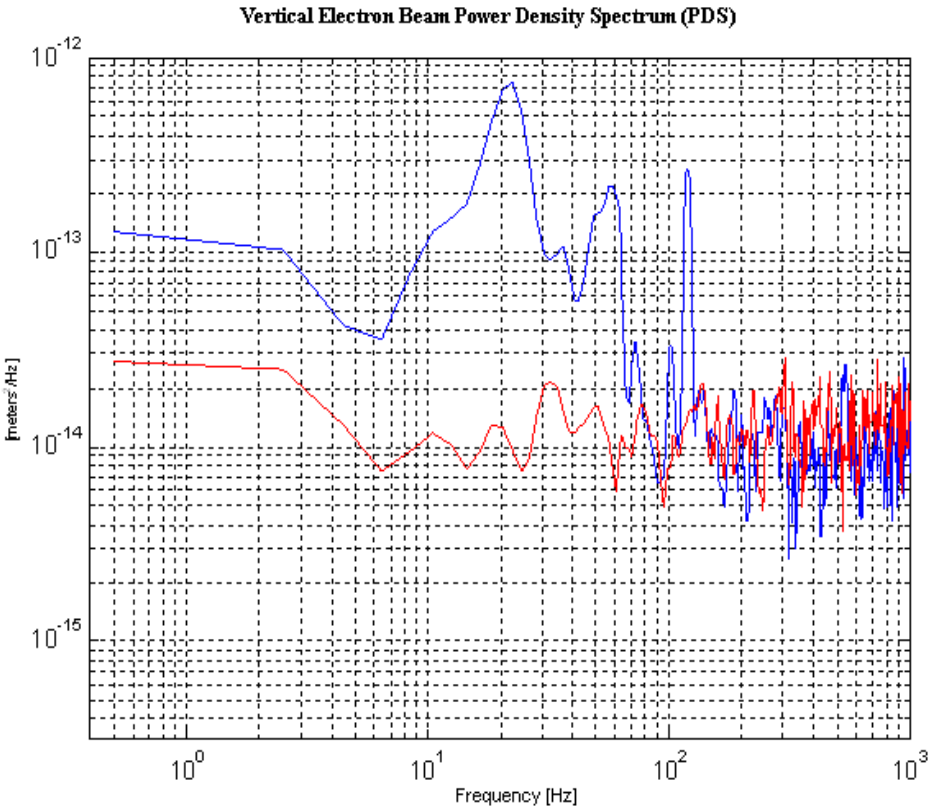

Figure 6.3.5 Power density spectrum of beam motion.

6.3.5 Requirements for the Feedback System

Based on these considerations, the ground vibration of 0.2 μm above 0.5 Hz satisfies the 0.3 μm requirement determined by the feedback system performance calculation presented in Section 6.3.2. However, since the ring tunnel temperature stability of ±0.1°C can only provide 0.5 μm girder stability, it is clearly a rather stringent requirement. As the most stringent requirement comes from the 5 m straight section, R&D work is needed to satisfy this condition. One approach is to develop local feedback systems for these sections and improve the temperature stability in the tunnel.

As mentioned in Section 6.3.4, the measured beam motion coincides with the BPM noise floor for frequencies higher than 200 Hz (see Figure 6.3.2). In addition, since most of the motion comes below 60 Hz, it is desirable to design the feedback system PID circuit to reach a 60 Hz bandwidth.

Because eddy currents are proportional to the thickness and electrical conductivity of materials, only thin laminations (1 mm thickness) or air coils should be used for correctors and the low-conductive materials preferred for vacuum chambers. Eddy currents in vacuum chambers usually impose the most critical bandwidth limitation on the feedback loop [6.3.1].

When designing the feedback system bandwidth, it is crucially important to design the vacuum chamber and power supplies for all the correctors to be used in the fast global feedback system such that they have the same frequency response. For the same reason, all four trims used in any one local feedback system should have the same frequency response. If the vacuum chambers or power supplies are very different for different correctors in the local bumps, or in the global feedback loop, it will be difficult to equalize the trim frequency response. Without excellent equalization, there will be interaction between the different systems; hence there will be instability, which may force us to narrow the bandwidth of the feedback system or lower the gain of the system. In addition, to avoid coupling between the fast global feedback system and the local feedback system, it is important to have at least one additional BPM and four fast correctors in all the straight sections with undulator beamlines, and to be sure that no global feedback system BPMs or fast correctors lie between them.

To maintain the dynamical aperture regardless of long-term ground movement requires the beam to stay within 50 μm of the center of the sextupoles. According to the simulation based on the ATL law, described in Section 6.3.2, if the ring is regularly realigned every six months, this can be achieved. RF frequency will also be used as an additional corrector to compensate for energy drifts.

The analysis in Section 6.3.2 also addresses the maximum strength for the trim correctors. Assuming the mechanical error when realigning the ring is 100 μm, the strength required for the feedback system trims is 120 μrad. Given a factor 2.5 margin, a 0.5 to 1 mrad strength should be sufficient for the slow feedback system. Because the fast and slow feedback systems are separate, and the maximum strength of the fast feedback system is lowered to 0.15 mrad, the analysis on the trims' last digit noise in Section 6.3.2 shows that the last digit can be relaxed to less than 200 ppm of the maximum strength.

References

[6.3.1] M. Borg, PAC '01, talk on IWBS'02, and EPAC 04 paper.
[6.3.2] J. A. Carwardine and F. R. Lenkszus, "Real-Time Orbit Feedback at the APS," p.12, 1997 beam instrumentation workshop at SSRL.
[6.3.3] Heiko Ehrlichmann, private communication (2/2006).
[6.3.4] Vladimir Shiltsev, "Space-Time Ground Diffusion: The ATL Law for Accelerators," DESY-MPY, Notkestrasse 85, 22603 Hamburg, Germany.
[6.3.5] Vadim Ptitsyn, private communication (7/2004).
[6.3.6] A. Walski, and N.J. Walker, Proceedings of 2003 PAC.

7 STORAGE RING SYSTEM

7.1 Storage Ring Magnets

7.1.1 Parameters and Tolerances

The DBA (15×2) lattice consists of 60 dipole magnets with uniform magnetic field and a maximum field of 4 kiloGauss at 3.0 GeV. The dipoles are planned to be run in series with a common power supply. The ring quadrupoles consist of a total of 360 magnets with two different lengths: 30 and 40 cm. These quadrupoles have a maximum gradient strength of 21 T/m at 3.0 GeV. The quadrupoles are individually powered, but the current lattice design assumes 10 families. With an undulator or wiggler installed in a straight section, the pair of four quadrupoles in the ID straight will be used to adjust locally for the tune shift and beta-beat modulation induced by the undulators. This was shown in Chapter 6 to be quite useful in reducing the impact of the IDs on the dynamic aperture of the ring and improving the lifetime and injection efficiency. The four dispersion-region quadrupoles are tuned as two families in the design, but the individual power supplies on each quadrupole will allow tuning out any dispersion beating resulting from differences between the dipoles. With the dispersions below 5 mm (H) and ~1 mm (V), the DW reduction in emittance will be within 10% of the expected values and will decouple energy modulation from the user's x-ray beam.

The sextupoles include 390 magnets with three different lengths: 20, 25, and 30 cm (Table 7.1.1). However, for most tunes found so far, the 25 cm sextupoles could be replaced by 20 cm sextupoles, saving some space for other components. Also, some tunes show that some sextupoles are running at quite low values. These may be eliminated in future designs, but the extra knobs have proven useful for now. The sextupoles are individually powered but the design tuning has assumed 11 families of sextupoles.

Table 7.1.1 List of Storage Ring Magnet Parameters at a 3 GeV Beam Energy, with Basic Tolerances.

Qty.	Magnet Type	Length [m]	B, B', B" [T,T/m,T/m^2]	Field Tol.	Alignment Tol.
60	Dipole	2.62	0.4, 0, 0	0.01%	0.1 mm, 0.5 mrad
330	Quadrupole (S)	0.30	0, 21, 0	0.02%	0.03 mm, 0.2 mrad
30	Quadrupole (L)	0.40	0, 21, 0	0.02%	0.03 mm, 0.2 mrad
30	Sextupole (L)	0.30	0 , 0 , 500	0.05%	0.03 mm, 0.2 mrad
120	Sextupole (M)	0.25	0 , 0 , 500	0.05%	0.03 mm, 0.2 mrad
240	Sextupole (S)	0.20	0 , 0 , 500	0.05%	0.03 mm, 0.2 mrad
120	H & V	0.35	0.03, 0		0.1 mm, 0.02 mrad
30	H & V	0.25	0.03, 0		0.1 mm, 0.02 mrad
30	H only	0.25	0.03, 0		0.1 mm, 0.02 mrad
30	H & V & SQ corrector	0.25	0.03, 0.36, 0		0.1 mm, 0.2 mrad
≤20	Fast H & V corrector	0.20	0.01, 0		
150	Magnet girders				0.1 mm, 0.5 mrad

The alignment and field tolerance errors are still being studied. However, initial testing of the lattice with tolerance that has been achieved at other light sources has shown the DA is robust for individual errors. As with most synchrotrons, the **c**losed-**o**rbit **a**mplification **f**actors contribute the most significant tolerance to be handled. COAFs give the RMS closed-orbit distortion around the ring per unit of RMS alignment error (assumed to be a random Normal distribution) for all the quadrupoles in the ring. The COAF for this lattice is shown in Figure 7.1.1 for one cell and has an average value in each plane of greater than 50. This means a 100

μm RMS alignment error in the quadrupoles will yield an average closed-orbit distortion of >5 mm. This closed orbit error in the sextupoles contributes to a nonlinear focusing error in the lattice, which breaks the sextupole strength settings that yield the large DA.

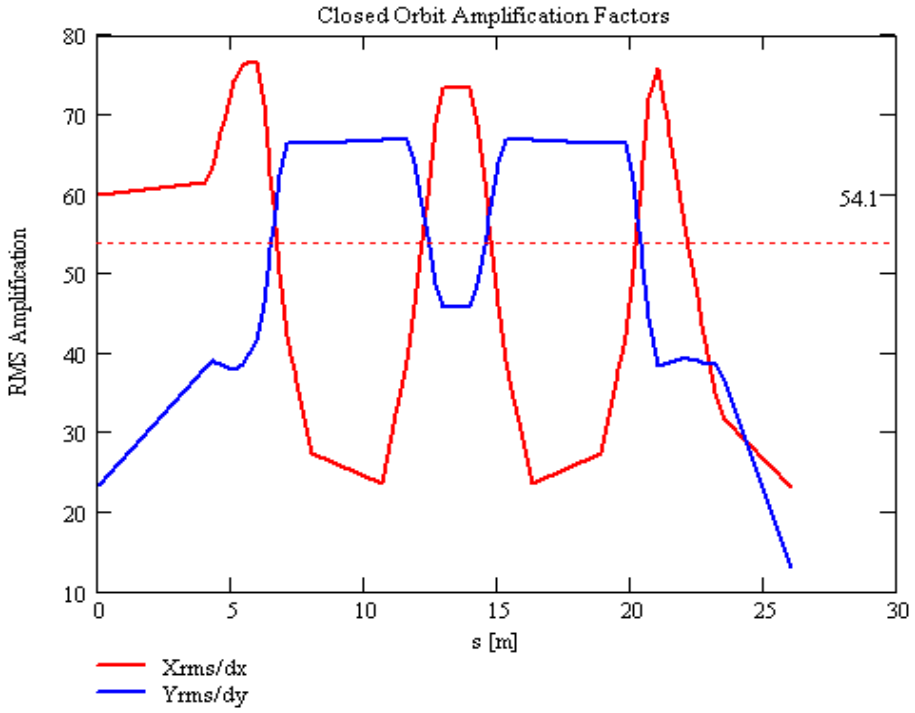

Figure 7.1.1 RMS expected closed-orbit amplification factors for random alignment errors in the quadrupoles of the lattice.

Figure 7.1.2 shows the impact of random quadrupole alignment errors of 100 μm with correction to the BPMs located close to the high beta-function quadrupole magnets. We have corrected the orbit to the BPMs with an assumed ideal Beam-Based Alignment. The DAs for 20 different starting seeds for the random alignment offsets are shown. The DA remains adequately large and is more than sufficient for injection and lifetime.

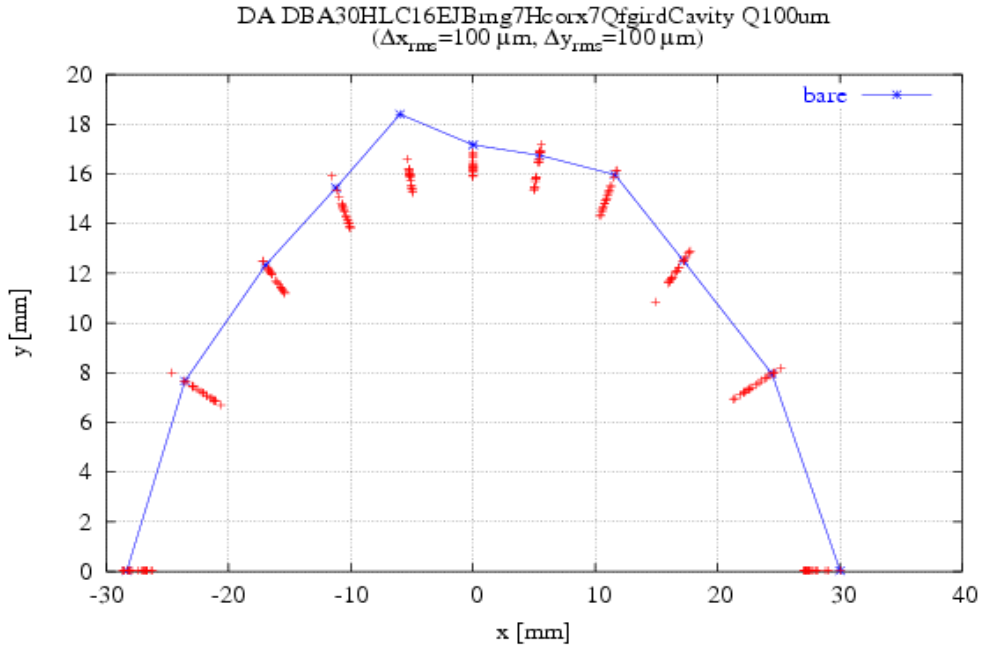

Figure 7.1.2 DA with 100 µm quadrupole alignment tolerances corrected with ideal BBA (zero relative alignment error) BPMs located at the quadrupoles. Each point represents the DA for one of 20 seeds (sample lattices). It includes synchrotron oscillations, and is for 2 K turns around the lattice.

Adding a 30 µm random alignment tolerance of the BPM-to-quadrupole magnetic center yields little additional reduction of the DA, as shown in Figure 7.1.3, and is more than adequate. This random offset of the BPMs is equivalent to a BBA resolution of the BPM center relative to the quadrupole magnetic center, which could be much better than the 30 µm assumed in Figure 7.1.3, as described below.

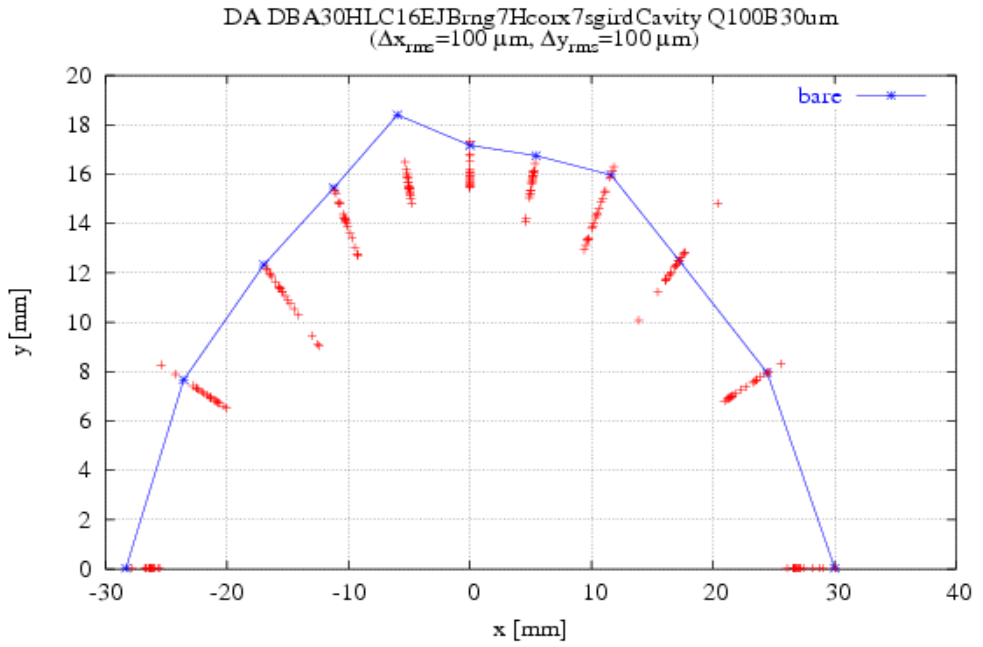

Figure 7.1.3 DA with 100 µm quadrupole alignment tolerances corrected with 30 µm BBA tolerance for BPMs (20 random seeds shown, with synchrotron oscillations).

We have assumed that the BPMs are close to the quadrupoles, since they are the source of the closed-orbit distortions in the sextupole magnets that cause the reduction of the DA. The two BPMs on a girder are aligned to the centers of the neighboring quadrupole magnetic center using the BBA procedure, which has become common at many synchrotrons. This method uses a beam bump to vary the beam position (x, y) in the quadrupole and its neighboring BPM. If that quadrupole has its strength modulated (ΔK_2), then the magnitude of the closed-orbit distortion measured by the BPMs is (X_m, Y_m). The BPM reading that yields a null in (X_m,

Y_m) is then the magnetic center of this quadrupole, as measured by the BPM. With two BPMs on a girder, the beam can be magnetically centered to all elements on the girder using the magnetic alignment instruments: pulsed wire, vibrating wire, and/or rotating coils. Therefore we specify the alignment tolerances for the magnetic elements in terms of: 1) an alignment tolerance of centers one to another, 2) alignment of girder ends one to another and a common roll error of the girder, and 3) a BBA alignment tolerance of the BPMs to their neighboring quadrupole. The sensitivity of the closed-orbit distortion amplitude to the quadrupole modulation ($\Delta K_2 L$) and beam offset relative to the quadrupole center position, (x_c, y_c), is given by:

$$X_m(s) = \frac{\sqrt{\beta_x(s)\,\beta_x(quad)}}{2\sin(\pi Q_x)}\left(\Delta K_2\, L\right)x \geq 5.2\,\left(\Delta K_2\, L\right)x \tag{7.1.1-1}$$

and

$$Y_m(s) = \frac{\sqrt{\beta_y(s)\,\beta_y(quad)}}{2\sin(\pi Q_y)}\left(\Delta K_2\, L\right)y \geq 7.2\left(\Delta K_2\, L\right)y \tag{7.1.1-2}$$

where we assume the smallest beta function at a quadrupole and the average beta function at the BPMs. We assume that the closed-orbit amplitude is measurable to the resolution of the BPMs, ~1 μm, and the modulation is 3% of the quadrupole strength; the magnetic center should be measured in the neighboring BPM with an accuracy of better than

$$\sigma_{xc} \leq 8\ to\ 10\,\mu m \quad and\ \sigma_{yc} \leq 15\,\mu m\,. \tag{7.1.1-3}$$

Consequently, the random tolerances on the magnet-to-magnet alignment in Table 7.1.1 will be greater than the BBA resolution. However, we have assumed the BBA resolution of 30 μm in Figure 7.1.3, which is two to three times greater than achievable.

The impact of the larger values for the girder alignment tolerances were evaluated assuming that either end of the girder is aligned to an RMS level (random Normal distribution Δx, Δy). This misalignment of the girders contributes a correlated misalignment error in all magnets and BPMs on the girder. The sensitivity to this type of error is shown in Figure 7.1.4, where the Girder Amplification Factor is shown. The GAF is defined as the RMS closed-orbit distortion per unit of RMS girder misalignment. This shows a reduction in the averaged COAF (Figure 7.1.1) by a factor of 4X (H) and 5X (V). The GAF values at the center of the short straight section are 4.8 in the horizontal and 2.3 in the vertical plane, compared to 22.5 and 12.0 for the COAF, respectively. However, correcting for the assumed 100 μm girder alignment tolerances yields almost complete restoration of the DA (without BPM errors), since the correlations of the quadrupole misalignments are easier to remove by BBA alignment to the quadrupoles on the misaligned girders.

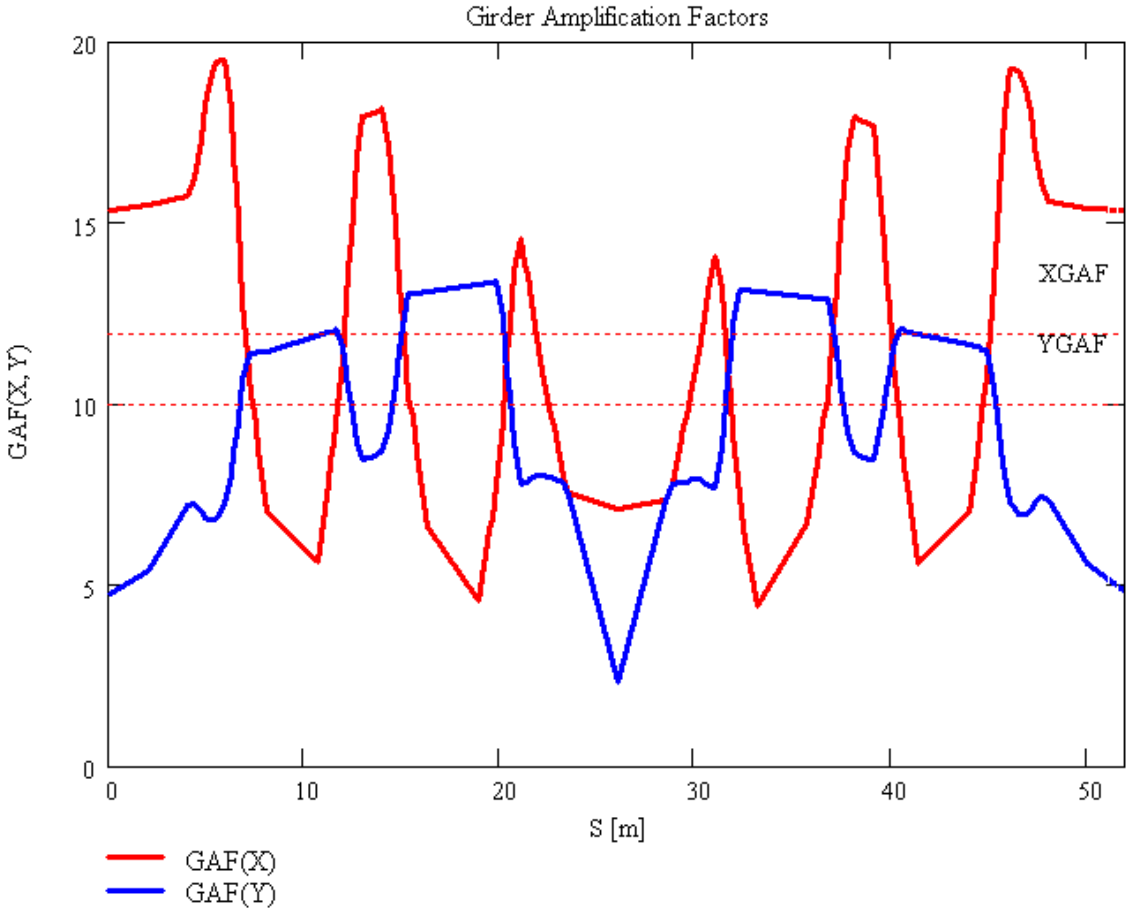

Figure 7.1.4 Girder Amplification Factors for one period of the storage ring. The average GAF values are 12 (H) and 10 (V).

The corrected DA is shown in Figure 7.1.5 for 100 μm RMS random girder alignment tolerances, where no other errors are assumed in the BBA resolution for the BPMs, nor for quadrupole misalignments on the girder. The complete analysis of the DA with all alignment and field tolerances is presented in Section 61.2. The COAF and GAF presented here will also be used to estimate the orbit stability resulting from magnet vibrations in Section 7.2.2.

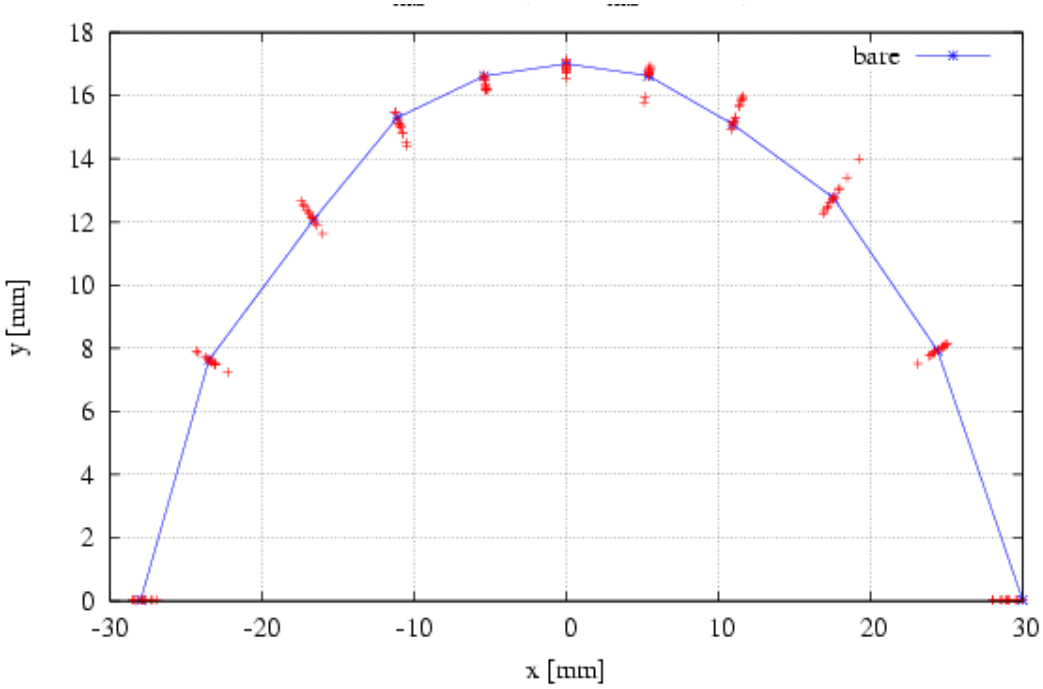

Figure 7.1.5 DA for 10 seeds (lattices) with 100 μm RMS girder alignment tolerances corrected using the BPMs with zero error in the BBA resolution.

7.1.2 Conceptual Magnet Design

7.1.2.1 Storage Ring Lattice Magnet Design Considerations

The magnet lattice is designed with a 30 superperiod DBA (double bend achromat) structure for a machine with 3.0 GeV full-energy top-off injection and a beam emittance of 0.5 nm-rad. The 780 m storage ring will contain 1,040 magnets. This quantity is comprised of 60 bending dipoles, 360 quadrupoles, 390 sextupole magnets, and 230 corrector magnets. To ensure acceptable dynamic aperture for the electron beam, the required magnetic field and alignment tolerances are the two primary considerations in the design. All the dipole magnets are connected in series and are energized by a single power supply. Individual trim power supplies will be used to provide 1% field adjustment. All quadrupoles and sextupoles will be individually powered. Storage ring magnets are summarized in Table 7.1.2.

Table 7.1.2 Storage Ring Magnet Specifications at 3.0 GeV.

	Dipole				Slow	Fast
	35 mm	63 mm	Quadrupole	Sextupole	Corrector	Corrector
Number of units	50	10	360	390	210	<20
Bending angle [deg]	6	6	0	0	±0.07	±0.01
Clear bore aperture [mm]	35	63	55	64	150	150
Dipole field [T]	0.4	0.4	0	0	0.04	**0.01
Field gradient [T/m]	0	0	21	0	*0.36	0
Sextupole field [T/m^2]	0	0	0	500	0	0
Field quality in GFR - 20x40 [mm]	$1x10^{-4}$	$1x10^{-4}$	$2x10^{-4}$	$5x10^{-4}$	$1x10^{-3}$	$1x10^{-2}$
Nominal operating current [A]	360	360	108	182	20	20
Cooling type	water	water	water	water	air	air
Maximum temperature rise [°C]	10	10	10	10	20	20

*Skew quadrupole component, 30 each required

** At 100 Hz

In this section, we present designs of the individual magnets. Optimization and refinements will occur during the next phase of detailed design.

The following paragraphs in this section present a partial list of lattice magnet design considerations. For the conceptual design these considerations are global in nature and will evolve into specific design parameters for the next phase of preliminary or "reference" design.

The average current density in the coil cross-section of the storage ring magnets was selected to be less than or equal to 2 A/mm^2.

Deionized water will be used to limit the magnet coil temperature rise to within 10ºC, with a pressure drop across each magnet of less than 4 bar.

The NSLS-II storage ring multipole field quality and alignment requirements preclude the use of multifunctional sextupoles; therefore, only discrete corrector magnets are used in the storage ring. However, the corrector magnets are designed to be multifunctional.

The magnetic alignment requirements of the multipoles exceed those of achievable assembly tolerances. Therefore, these magnets are aligned magnetically and then fixed to a rigid girder for installation in the storage ring tunnel.

The storage ring magnet reference designs are being developed to minimize fabrication costs, provide high operational reliability, and minimize the power consumption by individual components as well as overall magnet systems.

To assure magnetic field quality and stable alignment it is necessary to produce a reference design that will be an extremely accurate, stable, and robust mechanical assembly.

The supports for the multipoles will be optimized to reduce vibration amplification.

Methods will be developed to precisely monitor magnet position in the tunnel and assure the required multipole magnetic alignment, despite environmental effects such as variations in tunnel temperature and local tunnel settling.

The detailed design will address a low-cost yet reliable means to integrate the multipole magnets into a vibrating wire magnet-to-magnet alignment system and a means to transfer magnetic field center locations precisely to survey targets on the magnet girder.

Handling and rigging safety issues for magnet testing and installation personnel will be addressed and the reference design will comply with BNL's Critical Lift Policy.

Electrical and all other safety issues will be addressed in the next phase of design. The design of the magnets, the power cabling from the magnet-to-cable connections on the girders, and the magnet instrumentation and controls will be fully NRTL compliant.

We anticipate further optimization of magnetic length and increase in drift space between the multipoles to accommodate corrector magnets without altering the lattice.

Electrical, magnetic, and mechanical design optimization will be performed for the reference design of the relatively low-field-strength 0.4 T dipole magnet to assure high field quality requirements for the C-type magnet cross-section.

3D magnetic modeling will be performed to determine what level of effect, if any, the ramping of the NSLS-II booster ring may have on the magnetic fields of the storage ring magnets. The results of this modeling study will be appropriately incorporated into the reference designs for the storage ring and booster ring magnets.

Extensive 3D modeling and design optimization is anticipated for both the 21 T/m gradient quadrupole and the 500 T/m^2 gradient sextupole to assure high field quality and extremely critical alignment requirements for both multipoles while accommodating the synchrotron's x-ray extraction lines and the vacuum chamber, as well as to minimize or eliminate the effects of crosstalk between neighboring magnets and correctors.

These design concepts and considerations will be refined by both the Laboratory and Industrial resources during the next phase of design, resulting in a preliminary or "reference" design. The final magnet design will be developed by the magnet manufacturer and approved by the Laboratory.

First-order 2D magnetic modeling, as well as mechanical fabrication and assembly methods, have been studied, resulting in conceptual magnet designs that are shown in the following sections.

7.1.2.2 Dipole Magnet Conceptual Design

7.1.2.2.1 Scope and Physics Design Parameters

A unique attribute of NSLS-II is the use of dipole magnets with two different size apertures. This requirement is necessary to accommodate a significant and growing community of users that require lower energy infrared and THz radiation. To serve this important community, a 63 mm aperture concept has been chosen, to allow the extraction of long-wavelength light from the dipole magnet [7.1.1, 7.1.2].

The NSLS-II storage ring will be equipped with 10 dipole magnets having a gap of 63 mm, and 50 dipoles having a gap of 35 mm. Each dipole will have a magnetic length of 2.62 m with a field 0.4 T at an electron energy of 3.0 GeV. The radius of curvature of the bending magnet is 25 m; it bends the electron beam 6.0° with a sagitta of 35 mm. The dipole magnets are C-type with a curved laminated flux return yoke (Figure 7.1.6).

Investigations of beam dynamics have established that the good-field region accommodates the dynamic aperture. The designed magnetic cross-section will accommodate the vacuum chamber with a 1 mm clearance between the magnetic poles and either side of the vacuum chamber.

Calculations of the magnetic field were made to optimize the pole contours and the quality of the magnetic field, which for a dipole magnet must have a field nonhomogeneity of $\Delta B/B \leq \pm 0.01\%$ over a good-field region of 40×20 mm.

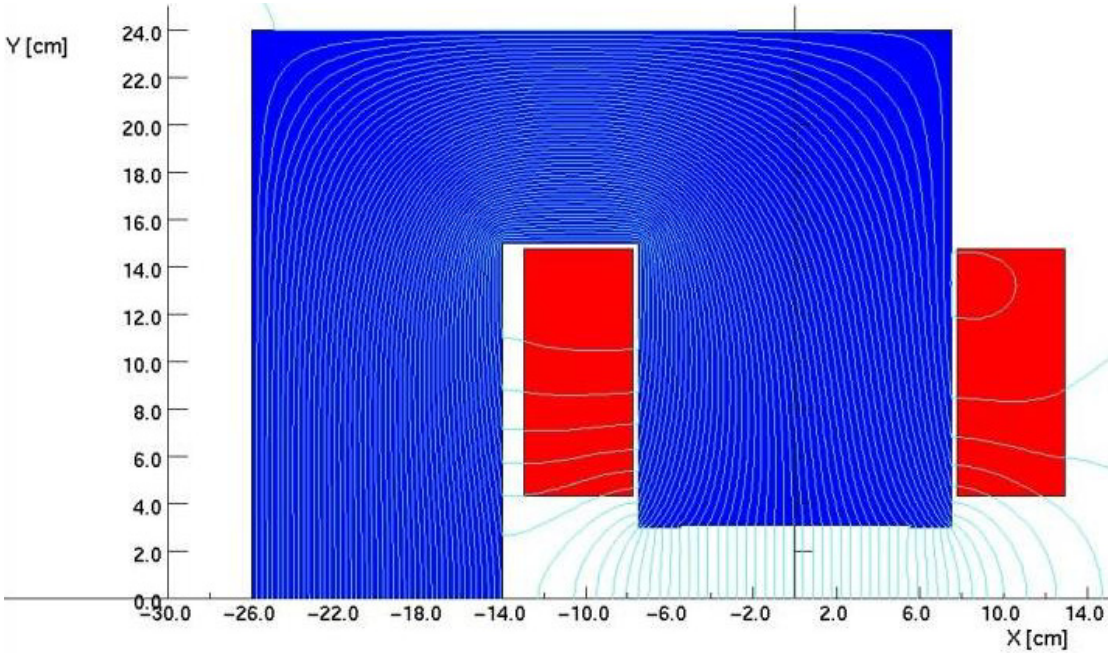

Figure 7.1.6 Ring Dipole Flux model.

The storage ring dipoles are designed so that both aperture magnets may be connected in series with a single power supply. Minor differences between the two aperture magnets shall be corrected by independently powered trim coils located on each dipole The ten large aperture dipoles will be installed into the storage ring in pairs; each pair shall comprise the adjacent bending magnets in a single cell, and there will be five cells equally distributed around the storage ring.

A list of the conceptual design dipole parameters is found in Table 7.1.3.

Table 7.1.3 Dipole Magnet Conceptual Base Line Design Parameters

	Storage Ring 35 mm Dipole	Storage Ring 63 mm Dipole
Number of units	50	10
Energy [GeV]	3.0	3.0
Bending angle [deg]	6	6
Clear bore aperture [mm]	35	63
Dipole field [T]	0.4	0.4
Field quality	$1x10^{-4}$	$1x10^{-4}$
Good-field region [mm]	40 x20	40 x20
Magnetic length [mm]	2,620	2,620
Nominal operating current [A]	360	360
Number of Ampere-turns	11,520	20,160
Number of turns / magnet	32	56
Total Inductance of the magnet [mH]	13	38
Current density in conductor [A/mm²]	3.5	2.4
Max. temperature rise [°C]	10	10
Max. pressure drop [bar]	4.0	4.0
Voltage/magnet	11.4	14.5
Nom. power per magnet [kW]	4.2	5.4
Iron length [mm]	2,585	2,557
Lamination thickness [mm]	1.5	1.5

7.1.2.2.2 Mechanical Design of the Dipole

Fabrication and assembly concepts have been studied, resulting in the magnet design concepts shown in Figures 7.1.7 and 7.1.8.

The laminated magnet yokes are composed of 1.5 mm thick AISI 1006 low-carbon steel sheet. The permeability of the core material deviates by about 5% from the production value. The laminations must be shuffled to ensure a uniform magnetic property.

The coils for the 35 mm dipoles are made up of square hollow copper conductors, 13×13 mm, with an interior diameter of 9 mm. The coils for the 63 mm dipoles are made up of rectangular hollow copper conductors, 13×16 mm, with an interior diameter 8.5 mm. The water channels of the hollow conductor coil pancakes are connected in parallel to provide adequate cooling to maintain the increase in coil temperature to less then 10°C.

Fiberglass that is vacuum impregnated with highly radiation-resistant epoxy exceeding 1.0 mm in thickness will provide interstitial conductor insulation. An additional 1.5 mm (minimum) of vacuum-impregnated epoxy fiberglass will provide ground plane insulation. The magnet will be high-potted up to 5 kV to detect defects in the insulation.

Dipoles of either aperture that are not used as SR sources will use a single dipole vacuum chamber design. The chamber will allow damping wiggler radiation to pass through. The larger aperture IR dipole vacuum chamber will have a minimum internal aperture of 50 mm.

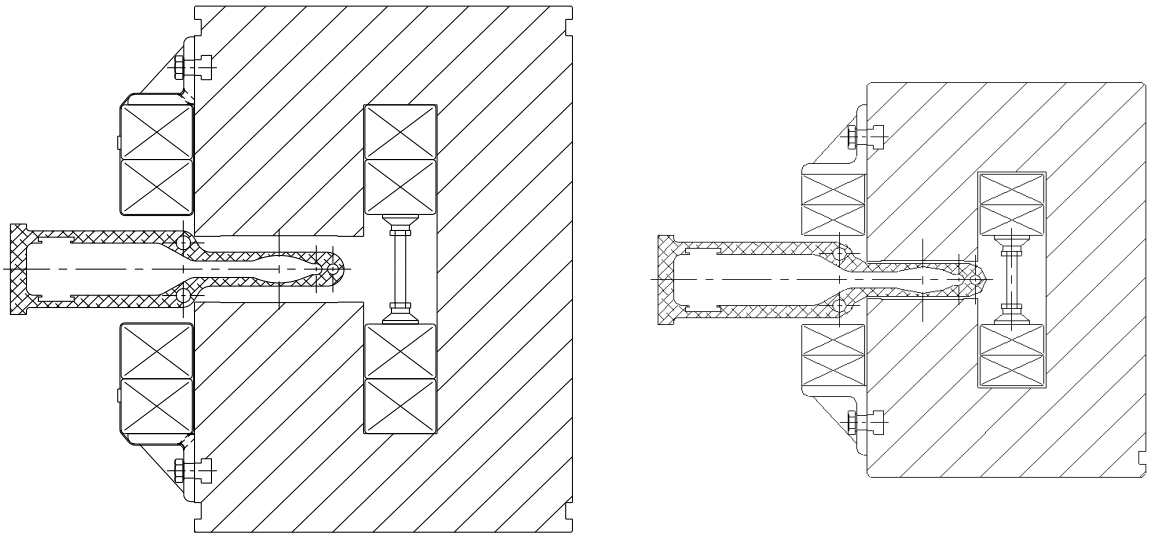

Figure 7.1.7 Storage Ring Dipole cross-sections, aligned on the centerlines, with coil, coil support system, and vacuum chamber. On the left is the 63 mm dipole; on the right is the 35 mm dipole.

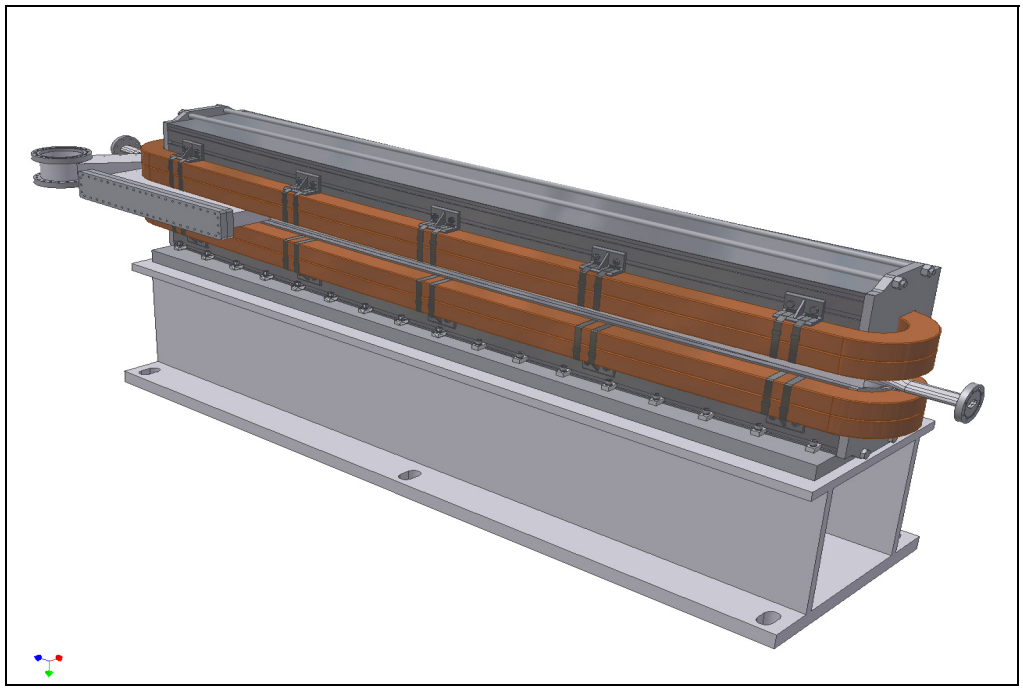

Figure 7.1.8 The 63 mm aperture dipole design concept with an IR beam extraction vacuum chamber installed.

The 60 dipole magnets are connected in series with a single highly stable magnet power supply with low-ripple current. The dipole magnet and its power supply are connected by 650 MCM power cables. The dipole cabling will be designed to avoid loops that could induce errors in the dipole circuit.

7.1.2.3 Quadrupole Magnet Conceptual Design

7.1.2.3.1 Scope and Physics Design Parameters

The storage ring has 360 quadrupole magnets, each with an individual power supply. The field gradient homogeneity in a region 40×20 mm is required to be better than 0.02%. The geometry of the vacuum chamber determines the bore radius of the quadrupole magnet. In modeling studies (Figure 7.1.9), the design of the quadrupole magnet is constrained by the need to accommodate the antechamber of vacuum vessel.

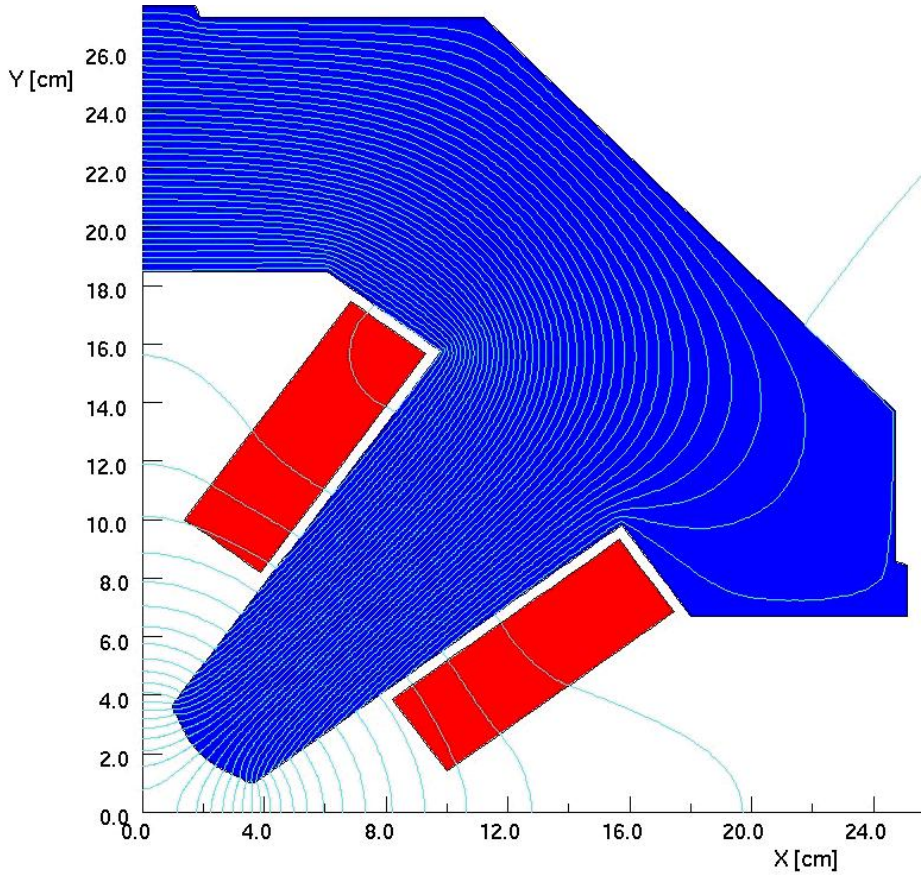

Figure 7.1.9 Quadrupole Magnet Analytical Model.

To provide a path for synchrotron radiation exiting dipoles and insertions devices, the antechamber must extend into the horizontal mid-plane of the magnet yoke. To assure symmetry, the horizontal back leg on either side of the quadrupole has been removed to accommodate the antechamber of the vacuum chamber. Therefore, the top and bottom halves of the quadrupoles are not connected with a flux-return yoke; each half is connected mechanically with nonmagnetic stainless steel spacers accommodating the vacuum chamber. The quality of the gradient in one-quarter of the geometry has been examined. The poles and shims are optimized with a 2D approximation. Further modeling will be done to ensure that the requirements for higher-order multipoles (Table 6.1.9) are met. Figure 7.1.10 presents the mechanical design. Table 7.1.4 lists the conceptual design parameters.

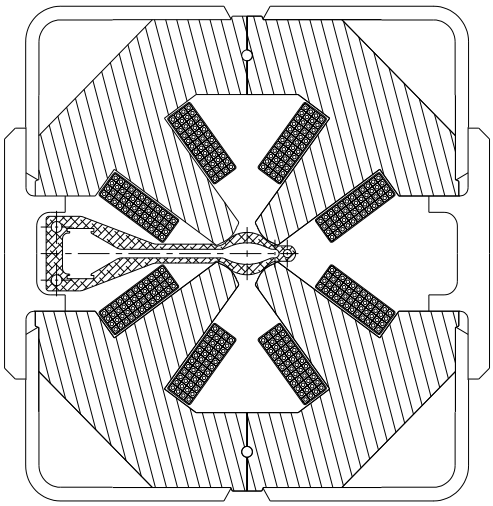

Figure 7.1.10 Conceptual design for NSLS-II storage ring quadrupole magnet cross-section with water-cooled coil and vacuum chamber.

Table 7.1.4 Quadrupole Magnet Conceptual Design Parameters

	30 cm SR-Quadrupole	40 cm SR-Quadrupole
Number of units	330	30
Energy [GeV]	3.0	3.0
Clear bore aperture [mm]	55	55
Maximum field gradient at 3.0 GeV [T/m]	21	21
Field quality	2×10^{-4}	2×10^{-4}
Good field region [mm]	40 x20	40 x20
Magnetic length [mm]	300	400
Nominal operating current [A]	108.2	108.2
Number of Ampere-turns	25,956	25,956
Number of turns / magnet	192	192
Total resistance of the magnet at 30°C [Ω]	0.092	0.112
Total inductance of the magnet [mH]	51.8	68.8
Current density in conductor [A/mm^2]	2.7	2.7
Number of parallel cooling circuits	4	4
Temperature rise [°C]	5	7
Pressure drop [bar]	4	4
Voltage / magnet [V]	9.95	12.12
Iron core length [mm]	245	345
Lamination thickness [mm]	1.5	1.5
Quadrupole alignment tolerance [μm]	30	30

7.1.2.3.2 Mechanical Design of the Quadrupole

The magnetic cores are made of low-carbon steel sheet, AISI 1006, 1.5 mm thick. To install the coil on the magnet the magnet core is divided into four quadrants. A 2 mm (minimum) clearance between the vacuum chamber and the adjacent poles is used to maintain thermal isolation during chamber baking. This gap is maintained to prevent the transmission of vibration from the vacuum chamber. A hollow copper conductor, 7.4×7.4 mm, with a 4 mm diameter water channel, was selected as a base for winding the excitation coils. Fiberglass that is vacuum impregnated with radiation-resistant epoxy at least 1.0 mm thick will provide interstitial conductor insulation. An additional 1.5 mm of vacuum-impregnated epoxy fiberglass will provide ground plane insulation. The magnet will be high-potted up to 5 kV to detect defects in the insulation. Four water channels are connected in parallel to maintain the temperature increase of the coil to be less than 10°C.

7.1.2.4 Sextupole Magnet Conceptual Design

7.1.2.4.1 Scope and Physics Design Parameters

The storage ring is equipped with 390 sextupole magnets, each connected to an individual power supply. The sextupole field homogeneity in a region 40×20 mm is required to be better than 0.05%. The geometry of the vacuum chamber determines the bore radius of the sextupole magnet. The design of the sextupole magnet is constrained by the need to accommodate an antechamber. The sextupole has been designed with three-fold symmetry with one horizontal air gap where the back leg has been removed to accommodate the antechamber of the vacuum chamber. Therefore the three segments of the sextupole are not connected with a flux-return yoke; each triplet is connected mechanically with a stainless steel spacer to accommodate the vacuum chamber.

The poles and shims are optimized with a 2D approximation. Further modeling will be done to ensure that the requirements for higher-order multipoles (Table 6.1.9) are met.

Table 7.1.5 Sextupole Magnet Conceptual Design Parameters.

	20 cm Sextupole	25 cm Sextupole	30 cm Sextupole
Number of units	240	120	30
Clear Bore aperture [mm]	66	66	66
Sextupole field [T/m^2]	500	500	500
Field quality	5×10^{-4}	5×10^{-4}	5×10^{-4}
Good-field region [mm]	40 x20	40 x20	40 x20
Magnetic length[mm]	200	250	300
Nominal operating current [A]	199.7	199.7	199.7
Number of Ampere-turns	28,757	28,757	28,757
Number of turns / magnet	144	144	144
Conductor cross-sectional area [mm^2]	51.3	51.3	51.3
Total resistance of the magnet at 30°C [Ω]	0.0276	0.0324	0.0372
Total inductance of the magnet [mH]	8.6	10.8	12.9
Current density in conductor [A/mm^2]	3.9	3.9	3.9
Temperature rise [°C]	7.5	5.1	6.3
Pressure drop [bar]	4	4	4
Voltage / magnet	5.03	5.89	6.77
Iron length [mm]	136	186	236
Laminae thickness [mm]	1.5	1.5	1.5
Sextupole alignment tolerance [μm]	30	30	30

The quality of the sextupole field in one half of the geometry has been modeled (Figure 7.1.11). The field quality is consistent with the specified sextupole field throughout the required transverse region. The bore diameter of 66 mm was determined by specifications of field quality and the spatial constraint between the vacuum chamber and the poles and coil geometry. The base of the pole is widened to prevent saturation in that area at high field excitations.

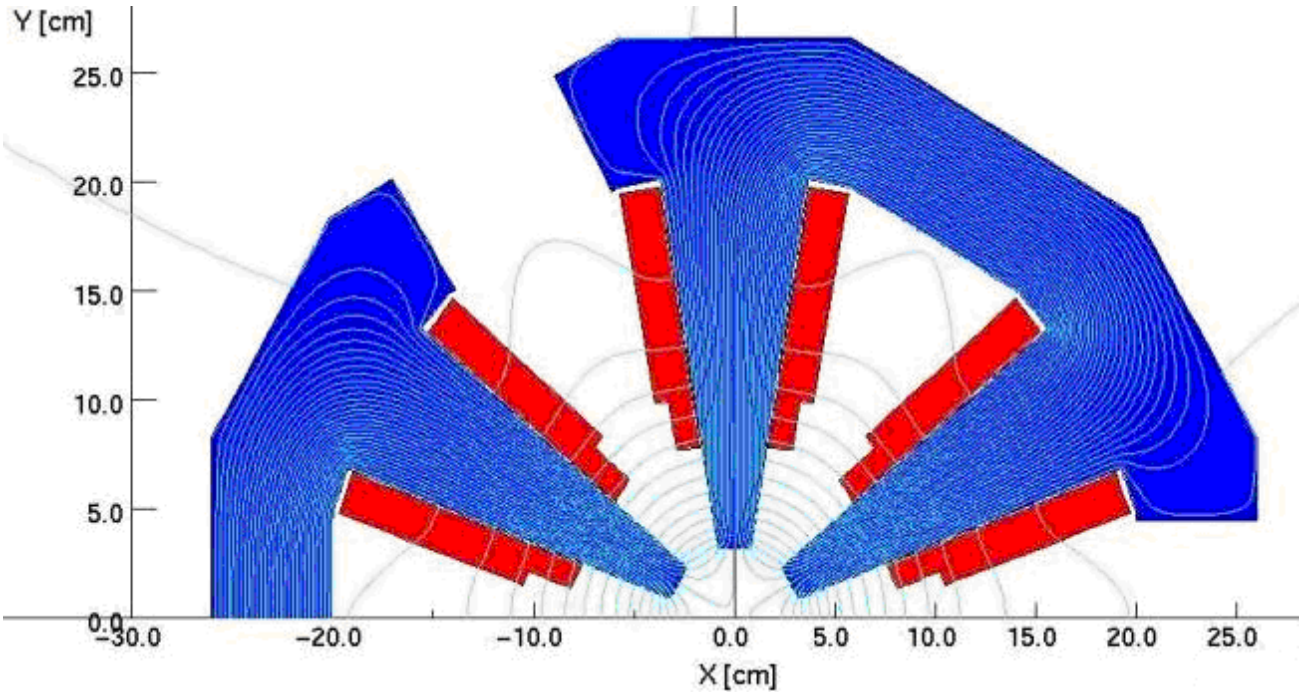

Figure 7.1.11 Sextupole magnet analytical model.

7.1.2.4.2 Mechanical Design of the Sextupole

The 390 sextupole magnets of the storage ring come in three lengths: 0.30 m, 0.25 m, and 0.2 m. To install the coils on a sextupole magnet, the magnet with three-fold symmetry must be divided into six identical segments (Figure 7.1.12). A 1 mm minimum clearance between the vacuum chamber and the adjacent poles is used to maintain thermal isolation during chamber baking. This gap is maintained to prevent the transmission of vibration from the vacuum chamber. The magnetic cores are made of steel sheet, AISI 1006 low-carbon, 1.5 mm thick. A square hollow copper conductor, 8×8 mm, inside diameter 4 mm, will be used in the coils, which are insulated with fiberglass at least 1.0 mm thick that is vacuum impregnated with highly radiation-resistant epoxy. Three water-cooling channels are connected in parallel on the sextupole magnet to distribute the power and to maintain the temperature increase of the coil to less than 10ºC.

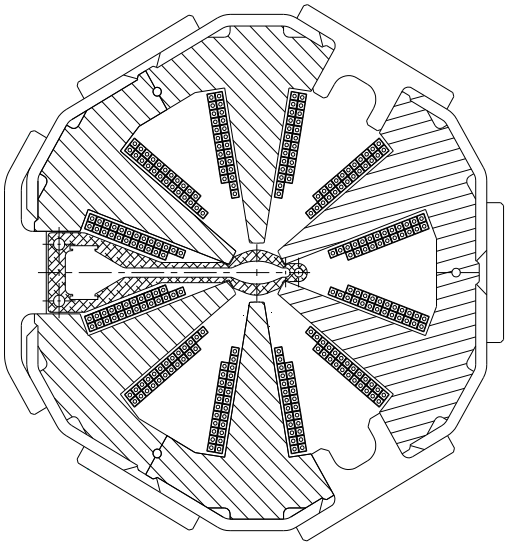

Figure 7.1.12 Conceptual design of the storage ring sextupole magnet cross-section depicting magnet yoke, the water-cooled coil, and the position of the vacuum chamber.

7.1.2.5 Correction Magnet Conceptual Design

In addition to the primary lattice magnets, the NSLS-II storage ring has corrector magnets. The correctors will be used to adjust the beam orbit and correct for alignment errors. The correctors will also be used as part of both global and local feedback systems. The conceptual design calls for 230 correctors to be installed at the start of operation.

Unlike other light sources, where steering correction can be integrated into combined-function lattice sextupoles, the precise alignment and field quality requirements of the NSLS-II sextupoles prevent the use of this combined function multipole, so only discrete correctors may be used.

There will be three types of correction magnets in the storage ring. The first type is a slow corrector operating with vertical and horizontal steering fields up to 400 Gauss from DC to less than 50 Hz. Ninety of these correctors will be located around the aluminum vacuum chamber. The maximum operational frequency of these correctors will be determined as part of the NSLS-II R&D program, as we study and optimize the corrector's field interaction with the vacuum chamber. Thirty of these correctors will possess skew quadrupole windings to deliver a maximum DC field gradient of 0.36 T/m.

A second type of corrector will be used for both static steering and dynamic global feedback. One-hundred-twenty of these correctors will have a DC component providing a maximum field of 320 Gauss for up to ±1.2 mrad vertical and horizontal steering as well as a dynamic component of ±0.15 mrad steering at up to 100 Hz. These correctors will be located around stainless bellows at either end of the dipole magnets.

A third type will be fast correctors providing a maximum field of 100 Gauss at a frequency up to or exceeding 100 Hz. At the start of operations twenty of these correctors will be used for local feedback and will be located around stainless steel sections of vacuum chamber or bellows. Two of these correctors will be located at either end of an insertion device, such as an undulator.

The geometry of the corrector magnets is highly dependent on the shape of the vacuum chamber around which they are assembled, and their location in the lattice. Several designs are being considered: the C-shaped dipole, a window frame-or box-shaped X–Y type corrector, and an APS-style corrector magnet. Silicon steel lamination 0.5 mm thick was selected for the magnet assembly, to suit the rate of charging of the corrector magnet.

Many factors must be considered in the corrector magnet design. The design of a corrector magnet will be specific to its required function, the space constraints of the specific locations in the lattice, and how the

corrector accommodates and interacts with the vacuum chamber design at its required location. Design options such as APS-style correctors are compact in size but tend to be rich in harmonics; the box-style correctors around the vacuum chamber have good field quality but tend not to use available space as efficiently, and have larger stray fields. Analytical modeling of the C-shaped correctors reveals that viable solutions exist for each corrector location. Specific design selection for each discrete corrector will be made during the next phase of design.

Injection magnets such as septum and kicker magnets are discussed in Section 5.9.

References

[7.1.1] Creagh, D., et al., "An Infrared Beam-line at the Australian Synchrotron," SRI-2006.
[7.1.2] Katoh, M., et al., "Coherent Terahertz Radiation at UVSOR-II," SRI-2006.

7.1.3 Storage Ring Power Supplies

These power supplies are designed to stay at a fixed current except for the fast dipole correctors. Most of the power supplies will be able to do simple ramps that will take 5 to 60 seconds from zero current to maximum current. These ramps will be software generated. The fast dipole correctors will be part of a beam-based feedback system. All power supplies will have at least a 20% margin in operating current. Listed below are the numbers of power supplies that will be required.

- B1-PS – 60 dipole magnets in series a circuit (50 small-aperture and 10 large-aperture magnets)
- Quad.3-PS1 to 330 – 330 quadrupole magnet circuits
- Quad.4-PS1 to 30 – 30 quadrupole magnet circuits
- Sext.2-PS1 to 240 – 240 sextupole magnet circuits
- Sext.25-PS1 to 120 – 120 sextupole magnet circuits
- Sext.3-PS1 to 30 – 30 sextupole magnet circuits
- B1Trim-PS1 to 60 – 60 B1 dipole trim magnet circuits (trim coils located on the B1 main dipoles)
- SKQ-PS1 to 30 – 30 skew quadrupole magnets circuits
- BH-PS1 to 90 – 90 intermediate speed horizontal dipole corrector magnet circuits
- BV-PS1 to 60 – 60 intermediate speed vertical dipole corrector magnet circuits
- FGBH-PS1 to 120 – 120 fast global horizontal correction dipole circuits
- FGBV-PS1 to 120 – 120 fast global correction dipole circuits
- FIBH-PS1 to 20 – 20 fast insertion horizontal correction dipole circuits
- FIBV-PS1 to 20 – 20 fast insertion vertical correction dipole circuits
- Total number of slow power supplies – 841
- Total number of intermediate-speed power supplies – 150
- Total number of fast power supplies – 280

7.1.3.1 B PS – Main Dipole Power Supply

This circuit consists of 50 small-aperture dipole magnets and 10 large-aperture dipole magnets, for a total of 60 magnets. The small-aperture magnets are 0.032 Ω and 13 mH. The large-aperture magnets are 0.040 Ω and 35 mH. The operating current for both magnets is ~360 A for 3.0 GeV. The cabling between magnets and the return will use 650 MCM flexible copper cable with a resistance of 0.162 Ω and inductance of 1.4 mH. The power supply load is 2.162 Ω and 1.001 H.

The power supply is a unipolar, two-quadrant, current-regulated supply. It will use two 12-pulse SCR converters in series with the center point connected to ground. This configuration will reduce the voltage to ground at the magnet load and reduce the voltage rating on various converter components. Each converter will

have a two-stage LCRL passive filter and a series pass active filter. This is required to reduce the ripple current to low levels (see Figure 7.1.13). The power supply will be able run in the invert mode while ramping down. This produces a negative voltage.

A combined digital and analog control system will control the operation of the power supply. The power supply will have a precision current regulator using a Direct Current Current Transformer as the current feedback device. The digital controls will use a feed-forward system to improve overall reproducability.

A PLC will be used for state control (on/off commands and interlocks).

Main Dipole Power Supply Specifications

AC input power	▪ 3-phase 460 VAC ~683 AAC
DC maximum output current – Imax	▪ 450 ADC
DC minimum output current – Imin	▪ ~1 ADC
DC output voltage	▪ 1100 VDC
operating quadrants	▪ 2: (V+, I+) & (V-, I+)
small-signal – 3 db bandwidth	▪ 500 Hz
stability (8 h–10 s) – referred to Imax	▪ 40 ppm
stability (10s–300 ms) – referred to Imax	▪ 20 ppm
stability (300 ms–0 ms) – referred to Imax	▪ 10 ppm
absolute accuracy – referred to Imax	▪ 100 ppm
reproducability long term – referred to Imax	▪ 50 ppm
current ripple – referred to Imax	▪ 5 ppm 60 Hz and greater
resolution of reference current	▪ 18 bit ±1 LSB
resolution of current measured – fast sampling	▪ 16 bit ±1 LSB at 200 μsec
resolution of current measured – slow sampling	▪ 22 bit ±1 LSB at 16.67 msec

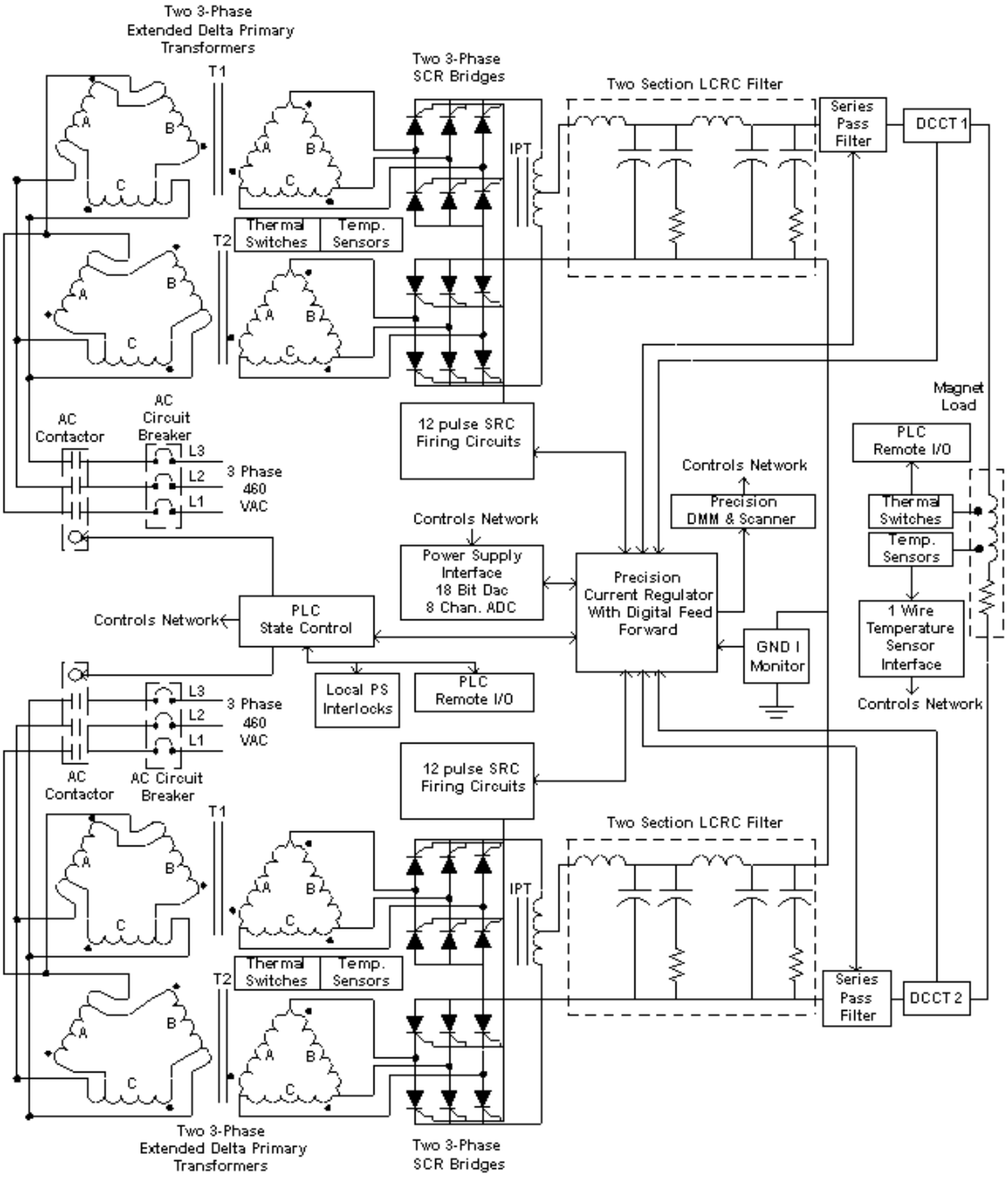

Figure 7.1.13 Dipole power supply block diagram.

7.1.3.2 Quad. 3 PS and Quad. 4 PS – Quadrupole Power Supplies

These circuits will use one power supply for each magnet. The magnet load parameters are close enough to use a single power supply for the two quadrupole magnet types. There are a total of 360 magnet circuits. The Quad.3 magnet is 90.0 mΩ and 50 mH. The Quad.4 magnet is 110.0 mΩ and 69 mH. The operating current is ~108 A for 3.0 GeV. The cabling between the magnets and power supply will be 250 MCM flexible copper cable. The power supplies will be located above the magnets in the equipment area. The cabling has a resistance of the 6 mΩ and an inductance of 0.1 mH. The worst-case power supply load is 116 mΩ and 69 mH.

The power supply is a unipolar, single-quadrant, current-regulated switch-mode design. The power section is a commercial voltage-controlled switch-mode programmable power supply with high output bandwidth (~1 kHz). These supplies have a 3 kW output power. They fit in a standard 19 inch electronics rack and are only 3.5 inches high. These power supplies are air-cooled. A precision analog regulator to control the current will be developed in-house. The power supply will use a DCCT as the current feedback device. To minimize current ripple, an additional output filter will be used. An AC input module will turn the power supply on and off. A microcontroller will be used for state control (on/off commands and interlocks). See Figure 7.1.14 for a block diagram of the Quad/Sext power supply.

Quadrupole Power Supply Specifications

AC input power	▪ 3-phase 208 VAC ~11 AAC
DC maximum output current - Imax	▪ 150 ADC
DC minimum output current – Imin	▪ ~0.5 ADC
DC output voltage	▪ 20 VDC
operating quadrants	▪ 1: (V+, I+)
small-signal – 3 db bandwidth	▪ 300 Hz
stability (8 h–10 s) – referred to Imax	▪ 200 ppm
stability (10s–300 ms) – referred to Imax	▪ 200 ppm
stability (300 ms–0 ms) – referred to Imax	▪ 100 ppm
absolute accuracy – referred to Imax	▪ 200 ppm
reproducability long term – referred to Imax	▪ 100 ppm
current ripple – referred to Imax	▪ 15 ppm 60 Hz and greater
resolution of reference current	▪ 16 bit ±1 LSB
resolution of current measured – fast sampling	▪ 16 bit ±1 LSB at 200 μsec
resolution of current measured – slow sampling	▪ 22 bit ±1 LSB at 16.67 msec

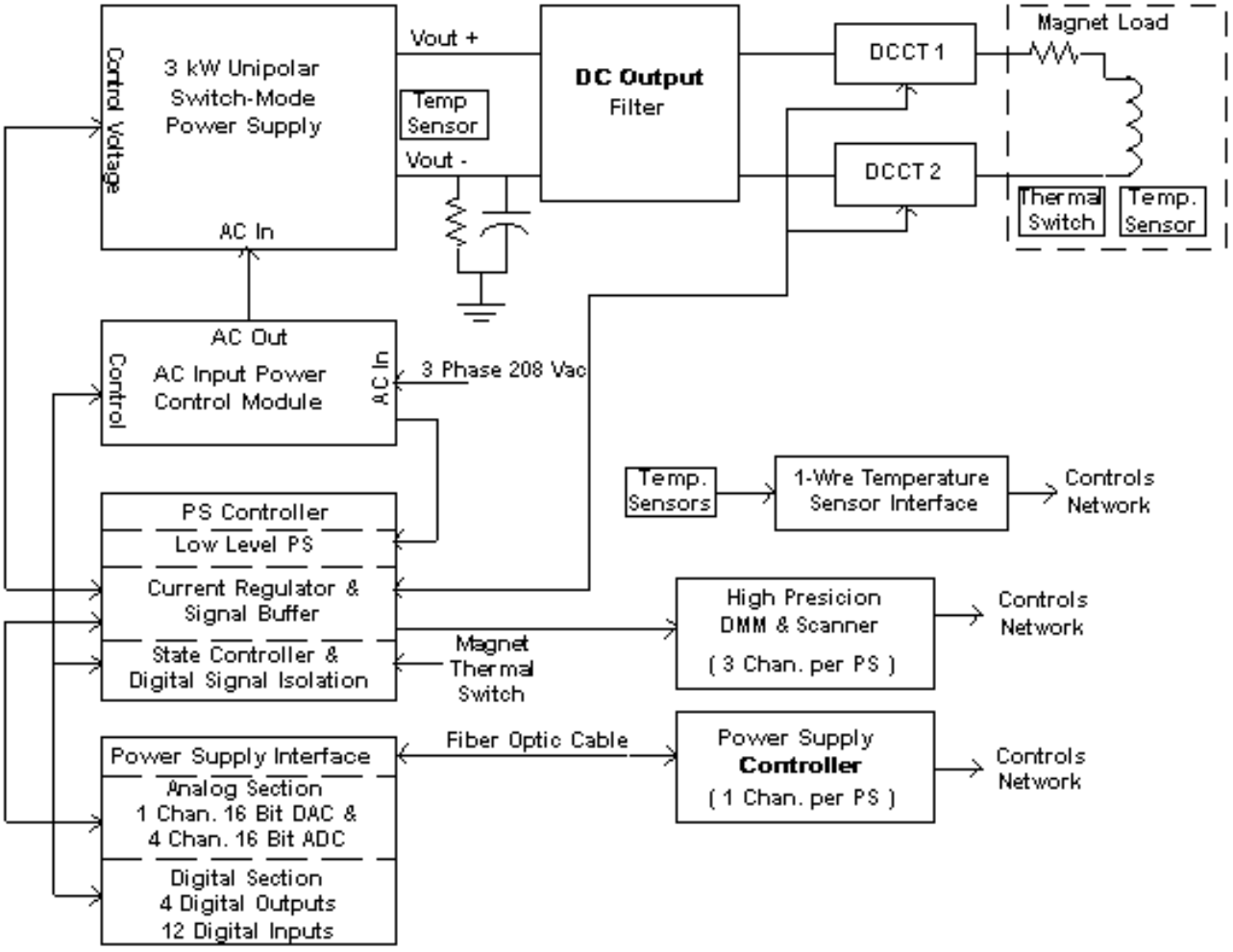

Figure 7.1.14 Unipolar current regulated switch-mode design power supply.

7.1.3.3 Sext. 2 PS, Sext. 25 PS, and Sext. 3 PS – Sextupole Power Supplies

These circuits will use one power supply for each magnet. The magnet load parameters are close enough to use a single power supply for the three sextupole magnet types. There are a total of 390 magnet circuits. The Sext.2 magnet is 27 mΩ and 9 mH. The Sext. 25 magnet is 32.0 mΩ and 11 mH. The Sext. 30 magnet is 37.0 mΩ and 13 mH. The estimated operating current is ~200 A for 3.0 GeV. The cabling between the magnets and power supply will be 350 MCM flexible copper with a resistance of 4 mΩ and inductance of 0.1 mH. The worst-case power supply load is 41.0 mΩ and 13 mH. The power supplies will be located above the magnets in the equipment area.

The supply is a unipolar, current-regulated switch-mode design, identical to that for the quadropoles. The power section is a commercial voltage-controlled, switch-mode programmable power supply with high output bandwidth (~1 kHz). These air-cooled power supplies have an output power rating of 3 kW. They fit in a standard 19 inch electronics rack and are only 3.5 inches high. A precision analog regulator to control the current will be developed in-house. The power supply will use a DCCT as the current feedback device. To minimize current ripple, an additional output filter will be used. An AC input module will turn the power supply on and off. A microcontroller will be used for state control (on/off commands and interlocks).

Sextupole Power Supply Specifications

AC input power	■ 3-phase 208 VAC ~11 AAC
DC maximum output current – Imax	■ 250 ADC
DC minimum output current – Imin	■ ~0.5 ADC
DC output voltage	■ 12 VDC
operating quadrants	■ 1: (V+, I+)
small-signal – 3 db bandwidth	■ 300 Hz
stability (8 h–10 s) – referred to Imax	■ 200 ppm
stability (10s–300 ms) – referred to Imax	■ 200 ppm
stability (300 ms–0 ms) – referred to Imax	■ 100 ppm
absolute accuracy – referred to Imax	■ 200 ppm
reproducability long term – referred to Imax	■ 100 ppm
current ripple – referred to Imax	■ 15 ppm 60 Hz and greater
resolution of reference current	■ 16 bit ±1 LSB
resolution of current measured – fast sampling	■ 16 bit ±1 LSB at 200 μsec
resolution of current measured – slow sampling	■ 22 bit ±1 LSB at 16.67 msec

7.1.3.4 B1 Trim PS and SKQ PS – B1 Trim Coil Set Power Supplies

The B1 Trim PS circuit consists of the trim coil set located in the B1 dipole magnet. The coil set is 3.11 Ω and 26 mH. The SKQ power supply circuit consists of a corrector coil set located TBD; this coil set is estimated at 3.0 Ω and 5 mH. The operating current for both power supplies is ~2 A for 3.0 GeV. The cabling from the coil set to the power supply will be # 14 AWG flexible copper, routed through the tunnel ceiling into the equipment area above the main tunnel. The cabling has a resistance of 0.355 Ω and an inductance of 0.1 mH. The power supply is located above the magnet in the equipment area. The worst-case power supply load is 3.465 Ω and 0.026 H.

The bipolar, 4-quadrant, current-regulated linear power supply fits in a standard 19 inch electronics rack and is 5.25 inches high. An analog system will control its operation. The power supply will have a precision current regulator using a shunt as the current feedback device. A microcontroller will be used for state control (on/off commands and interlocks).

B1 Trim PS and SKQ PS Power Supply Specifications

AC input power	▪ 1-phase 120 VAC ~1.1 AAC
DC maximum output current – Imax	▪ +5 ADC
DC minimum output current – Imin	▪ –5 ADC
DC output voltage	▪ ±20 VDC
operating quadrants	▪ 4: (V+, I+), (V–, I+) , (V–, I-) & (V+, I–)
small-signal – 3 db bandwidth	▪ 10 kHz
large-signal bandwidth	▪ ~5 Hz
stability (8 h–10s) – referred to Imax	▪ 1000 ppm
stability (10s–300 ms) – referred to Imax	▪ 500 ppm
stability (300 ms–0 ms) – referred to Imax	▪ 100 ppm
absolute accuracy – referred to Imax	▪ 2000 ppm
reproducability long term – referred to Imax	▪ 1000 ppm
current ripple – referred to Imax	▪ 20 ppm 60 Hz and greater
resolution of reference current	▪ 16 bit ±1LSB
resolution of current measured – fast sampling	▪ 14 bit ±1 LSB at 200 μsec
resolution of current measured – slow sampling	▪ 22 bit ±1 LSB at 16.67 msec

7.1.3.5 BH PS and BV PS – Corrector Coil Set Power Supplies

The BH and BV Corrector PS circuits consist of the corrector coil set located in an HVC magnet. Each coil set is 0.09 Ω and 50 mH. The SKQ power supply circuit consists of corrector coil sets located TBD. This coil set is estimated at 3.0Ω and 1 mH. The operating current for both power supplies is ~15 A for 3.0 GeV. The cabling from the coil sets to the power supplies will be # 10 AWG flexible copper cable, routed through the tunnel ceiling into the equipment area above the main tunnel. The cabling has a resistance of 0.140 Ω and an inductance of 0.1 mH. The worst-case power supply load is 0.230 Ω and 0.050 H. The power supply is located above the magnet in the equipment area.

The BH and BV power supplies are bipolar, 4-quadrant, current-regulated linear PS that fit in a standard 19 inch electronics rack and are 5.25 inches high. An analog control system will control their operation. Each will have a precision current regulator using a shunt as the current feedback device. These corrector power supplies are part of an intermediate-speed beam position feedback system. A microcontroller will be used for state control (on/off commands and interlocks).

Corrector Coil Set Power Supply Specifications

AC input power	▪ 1-phase 208 VAC ~2.6 AAC
DC maximum output current – Imax	▪ + 20 ADC
DC minimum output current – Imin	▪ – 20 ADC
DC output voltage	▪ ±200 VDC
operating quadrants	▪ 4: (V+, I+) , (V–, I+), (V–, I–) & (V+, I–)
small-signal – 3 db bandwidth	▪ 10 kHz
large signal – bandwidth	▪ ~5 Hz
stability (8 h–10 s) – referred to Imax	▪ 1000 ppm
stability (10s–300 ms) – referred to Imax	▪ 500 ppm
stability (300 ms–0 ms) – referred to Imax	▪ 100 ppm
absolute accuracy – referred to Imax	▪ 2000 ppm
reproducability long term – referred to Imax	▪ 1000 ppm
current ripple – referred to Imax	▪ 20 ppm 60 Hz and greater
resolution of reference current	▪ 16 bit ±1 LSB
resolution of current measured – fast sampling	▪ 14 bit ±1 LSB at 200 μsec
resolution of current measured – slow sampling	▪ 22 bit ±1 LSB at 16.67 msec

7.1.3.6 FIBH PS and FIBV PS

The FIBH and FIBV fast insertion corrector power supply circuits consist of the corrector coil set located in a fast insertion HVC magnet. These magnets are located in the insertion region on either side of an insertion device. Each coil set is estimated at 1.5 Ω and 13 mH. The operating current for the power supplies is ~5 A for 3.0 GeV. The cabling from the coil sets to the power supply will be # 14 AWG flexible copper, routed through the tunnel ceiling into the equipment area above the main tunnel. The cabling has a resistance of 0.355 Ω and inductance of 0.1 mH. The worst-case power supply load is 1.86 Ω and 0.013 H. The power supply is located above the magnet in the equipment area.

The bipolar, 4-quadrant, current-regulated linear power supplies fit in a standard 19 inch electronics rack and are 5.25 inches high. An analog control system will control their operation. The power supply will have a precision current regulator using a shunt as the current feedback device. These corrector power supplies are part of a fast beam position feedback system. A microcontroller will be used for state control (on/off commands and interlocks).

Fast Insertion Corrector Power Supply Specifications

AC input power	■ 1-phase 208 VAC ~2.6 AAC
DC maximum output current – Imax	■ +6 ADC
DC minimum output current – Imin	■ -6 ADC
DC output voltage	■ ±72 VDC
operating quadrants	■ 4: (V+, I+) , (V–, I+), (V–, I–), & (V+, I–)
small-signal – 3 db bandwidth	■ 10 kHz
large signal – bandwidth	■ 100 Hz
stability (8 h–10 s) – referred to Imax	■ 1000 ppm
stability (10s–300 ms) – referred to Imax	■ 500 ppm
stability (300 ms–0 ms) – referred to Imax	■ 100 ppm
absolute accuracy – referred to Imax	■ 2000 ppm
reproducability long term – referred to Imax	■ 1000 ppm
current ripple – referred to Imax	■ 20 ppm 60 Hz and greater
resolution of reference current	■ 16 bit ±1 LSB
resolution of current measured – fast sampling	■ 14 bit ±1 LSB at 200 μsec
resolution of current measured – slow sampling	■ 22 bit ±1 LSB at 16.67 msec

7.1.3.7 FGBH PS and FGBV PS

The FGBH and FGBV fast global corrector power supply circuits consist of the corrector coil set located in a fast global HVC magnet. The coil set is not yet designed. The operating current, coil resistance and coil inductance is TBD. The cabling from the coil sets to the power supply will be flexible copper, routed through the tunnel ceiling into the equipment area above the main tunnel. The power supply is located above the magnet in the equipment area.

Plans are to use a bipolar, four-quadrant, current-regulated linear power supply. It will fit in a standard 19 inch electronics rack. An analog control system will control their operation. The power supply will have a precision current regulator using a shunt as the current feedback device. This corrector power supply is part of a fast beam position feedback system. A microcontroller will be used for state control (on/off commands and interlocks).

Fast Global Corrector Power Supply Specifications

AC input power	■ TBD
DC maximum output current – Imax	■ TBD
DC minimum output current – Imin	■ TBD
DC output voltage	■ TBD
operating quadrants	■ 4: (V+, I+), (V–, I+), (V–, I–), & (V+, I–)
small-signal – 3 db bandwidth	■ 10 kHz
large signal – bandwidth	■ 100 Hz
stability (8 h–10 s) – referred to Imax	■ 1000 ppm
stability (10s–300 ms) – referred to Imax	■ 500 ppm
stability (300 ms–0 ms) – referred to Imax	■ 100 ppm
absolute accuracy – referred to Imax	■ 2000 ppm
reproducability long term – referred to Imax	■ 1000 ppm
current ripple – referred to Imax	■ 20 ppm 60 Hz and greater
resolution of reference current	■ 16 bit ± 1 LSB
resolution of current measured – fast sampling	■ 14 bit ± 1 LSB at 200 μsec
resolution of current measured – slow sampling	■ 22 bit ± 1 LSB at 16.67 msec

7.1.3.8 Power Supply Interlocks

All power supplies will have sufficient interlocks that will prevent the power supply from becoming damaged due to changes in cooling conditions, ac power disturbances, and nonstandard operating conditions.

All magnet coils will have an over- temperatures interlock if there is a change in cooling and/or operating conditions.

All power supplies will have an electrical safety interlock that will prevent the power supply from turning on if the machine safety system requires it.

7.1.3.9 Power Supply Instrumentation

Redundant DCCTs or shunts will be used to confirm the power supply current reproducability.

High-precision DMMs and scanners will be used to monitor the power system current, the redundant current sensor, and the analog current set point. This equipment will ensure long-term stability and reproducability.

Temperature monitoring of the magnet coils and power system environment will be accomplished using low-cost digital temperature sensors. With such system, a problem can be identified before it becomes an emergency, making it possible for repairs to be scheduled more conveniently.

7.1.3.10 Power Supply Controls

The slow power supplies will require software generated current references for each power supply. The Power Supply Interface has a precision DAC for generating the reference current and a multi-channel ADC for inputting PS signals. The PSI also has digital IO for state control and status read backs of the PS.

A VME device card will be used to communicate between the control system and the PSI. This card will be located in a control system's VME chassis that will be mounted in one of the power supply system racks. This card will generate the reference current profiles, input analog data, and perform digital state control and status readbacks. The output of the device card is a fiber optics cable that connects to a PSI.

The other controls will include the operation of the high-precision DMM and scanner and readout of the digital temperature sensors.

7.1.3.11 Electrical Safety

All power supplies will conform to the latest BNL safety requirements, especially concerning arc flash protection. Whenever possible, NRTL-listed equipment will be used.

7.1.3.12 Cable Tray Cable Routing

The cable tray for the dipole magnet circuits will be located in the equipment area above the main tunnel. The cable will drop through the tunnel ceiling at each cell, where it will connect to two dipole magnets. There will also be a tray along the inside wall of the main tunnel only in the area of the cell. This tray will be located in a different area then the booster cable tray. The dipole cables will be installed with a twist to prevent pickup from the booster circuits. All cables will be tray-rated cables. Power cables will be arranged to minimize pickup from other circuits. All power cables will be separated from signal cables. The quadrupole, sextupole, and corrector cables will be routed through conduit in the main tunnel ceiling. The power supply racks will be located above the conduits. The cable going through the conduit will run in the cable tray mounted on the inside wall until it is connected to the magnet. All cables and trays will meet NEC codes.

7.1.3.13 Power Supply Racks

All storage ring power supplies except for the dipole will be mounted in sealed Nema 12 electronics racks. These racks will have a maximum of six 3-kW power supplies installed in them. These racks will also have power supply controls and instrumentation installed in them. At each cell location there are 10 racks. The racks will be located above the magnets they supply power to. A water-to-air heat exchanger will cool a set of two or three racks. Cooled air will flow through the power supplies and circulate back to the heat exchanger. The heat exchanger will use chilled water and have the outlet temperature regulated (Figure 7.1.15).

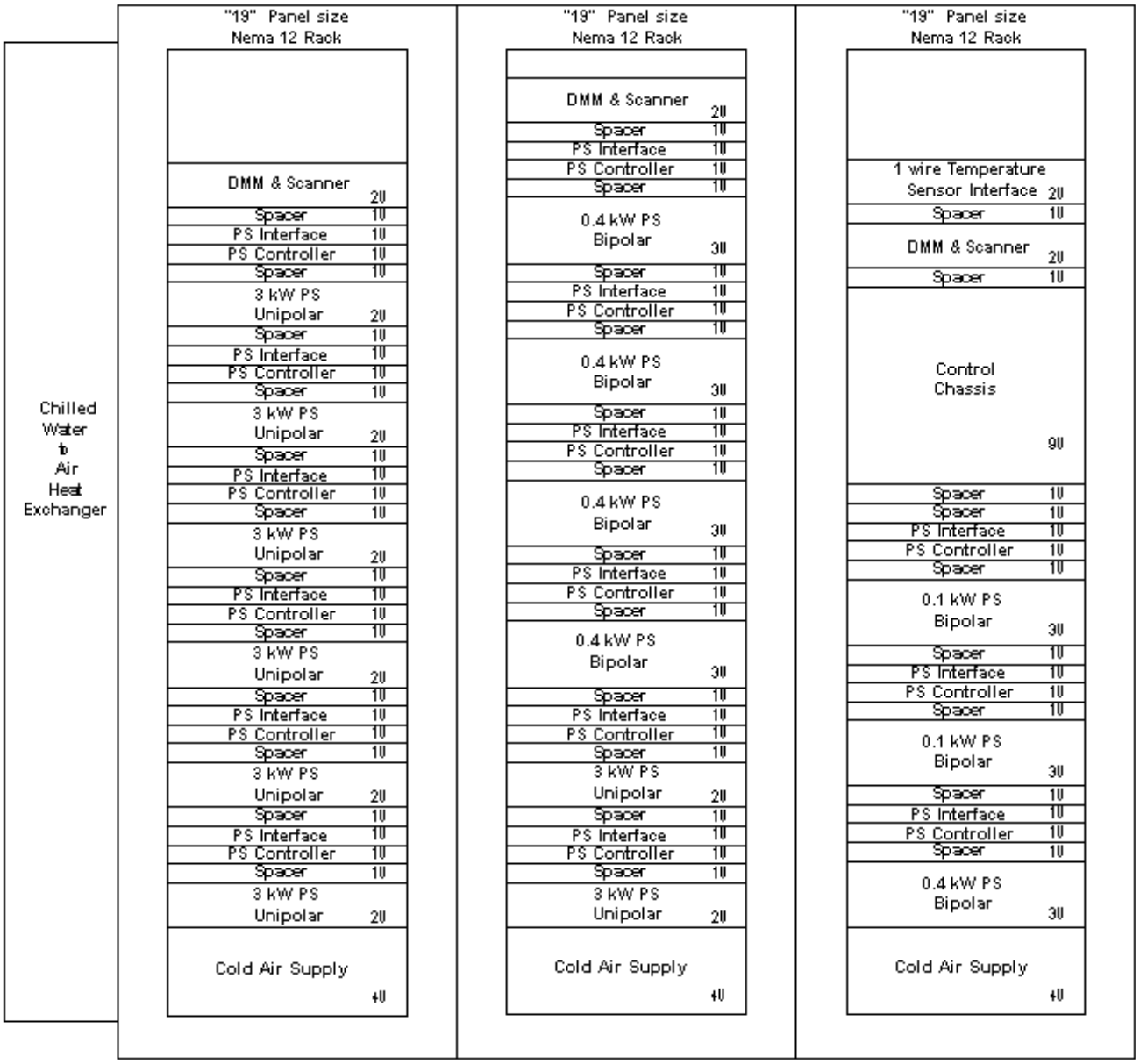

Figure 7.1.15 Single magnet power supply rack layout.

7.2 Magnet–Girder Support System

7.2.1 Scope

This section describes alignment tolerances, stability requirements, and conceptual design of the storage ring magnet support system. Specifications for magnet alignment and stability are established from analysis of the storage ring nonlinear dynamics. Functional requirements of the girder supports are presented and design features for meeting these requirements are discussed. Various sources of ambient motion affecting the stability of the support system are identified and design solutions to mitigate their effects are discussed

7.2.2 Alignment Tolerances and Stability Requirements

The alignment tolerances for the ring magnets impact the ring performance in several ways. Magnet alignment is necessary to be able to store the electron beam with the design emittance and lifetime (i.e., sufficient dynamic aperture, DA). First, there is a relative magnet-to-magnet alignment tolerance to a line relative to the rigid girder. Second, there is an alignment tolerance specified for the transverse position of the ends of the girder and its roll angle and longitudinal position (six parameters), as it is installed in the tunnel. The girder misalignment introduces a correlated offset of the magnets. For this conceptual design, we took the achieved magnet-to-magnet alignment values from recently commissioned light sources as our specification and calculated the impact on the DA. Future studies will further explore these sensitivity to these tolerances, along with the tolerance on magnetic field errors. The current tolerances are listed in Table 7.1.1. The impact of tolerance errors is discussed in Section 7.1.1.

The stability of closed-orbit position is critical to providing a constant flux in the user beamlines (i.e., intensity through slits and mirror systems). There are several sources of steering that cause large closed-orbit motion (relative to the user beamline): power supply fluctuations, energy modulations, and alignment variations due to vibrations of the magnets. We only consider the last effect here. The magnet motions that are of most concern are those of the quadrupole transverse position, dipole longitudinal position, and roll angle. This closed-orbit motion is the result of the large COAF, discussed in Section 7.1, which determined the magnitude of beam motion per unit of transverse motion of the quadrupoles, assuming that all quadrupole motions were uncorrelated in location around the ring, as well as uncorrelated in time. Here we discuss in more detail the time variation of the beam orbit due to quadrupole and dipole motion and the impact this has on the user beam.

To estimate the magnitude of the resulting orbit motion, we need to know how the quadrupoles are shifted around the ring. This depends on the noise source that generates this motion, as well as its coupling to the magnets through their support system (girders and floor). The simplest model of these magnet vibrations is just the random fluctuations of the magnet centers by a common tolerance level and assuming this impact will be the same at any frequency of vibration. This tends to overestimate the impact on the beam motion, since it ignores correlations that will smooth the distortions, as well as the synchrotron radiation damping that will damp the beam to the shifted closed orbit. This latter effect will mean that for frequencies greater than $F_{x,y} \approx 1/\tau_{x,y}$, where $\tau_{x,y}$ are the transverse damping times, the effective beam emittance will grow, while the centroid orbit shift will be reduced from that estimated from the random closed-orbit shift calculation.

We place a limit on the amplitude of magnet motion to be that which contributes to an RMS orbit shift equal to 10% of the RMS beam size in that plane. These sizes are shown in Table 7.2.1 for beam at the center of the two ID straight sections (long and short, LID and SID):

Table 7.2.1 Beam Size at the Center of the ID Straights for 0.5 nm-rad (H) and 0.008 nm-rad (V) Emittance.

	LID Straight (8 m)	SID Straight (5 m)
σ_x [μm]	96	37
σ_y [μm]	5	2.7

The closed orbit at the center of the short straight section for 2,000 random seeds is shown in Figure 7.2.1, for the ring quadrupoles shifted by Gaussian random values with RMS values of (ΔX = 0.163 μm and ΔY = 0.023 μm). Each point represents a different sampling of the random fluctuations of the quadrupole centers at any frequency with that amplitude, and includes all of the nonlinear elements in the calculation.

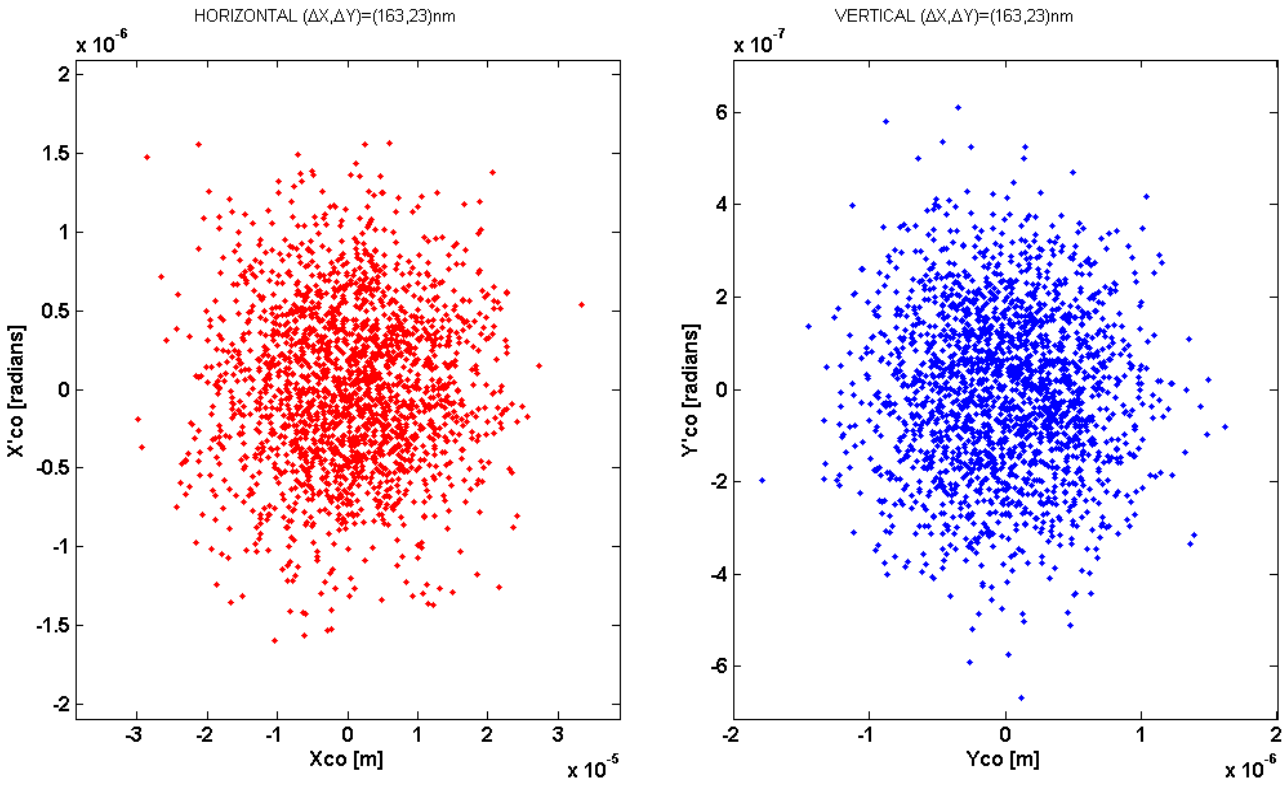

Figure 7.2.1 The horizontal and vertical closed-orbit in the LID straight for 2,000 seeds with RMS random quadrupole center shifts of ΔX = 0.163 and ΔY = 0.023 μm.

The RMS horizontal and vertical beam orbit shifts were 19.4 and 0.5 μm, respectively, or 10% of the RMS beam size in the LID. These RMS values give a very conservative tolerance for quadrupole vibration tolerances. At frequencies above the damping frequency, $F_{x,y}$, this calculation gives an estimate of the emittance dilution.

$$\Delta\varepsilon_x / \pi = \frac{1}{n}\sqrt{\sum x^2 \sum x'^2 - \left(\sum x\, x'\right)^2} \tag{7.2-1}$$

where x and x' are closed orbit and slope from each seed and the sum is over all seeds. The effective emittance dilution shown in Figure 7.2.1 is only 1% horizontal and 1% vertical of the emittance plane, or $\Delta\varepsilon_x$ = 5.1 pm and $\Delta\varepsilon_y$ = 0.09 pm, representing a small increase in the damped beam emittance.

Since the dipole magnets do not have gradients, their transverse motions have little impact on the closed-orbit motion. However, longitudinal position fluctuations of the dipoles will also create a horizontal beam motion and the roll angle will create a vertical closed-orbit motion. Using a similar random distribution analysis, we set a tolerance level for the RMS fluctuations of the dipole longitudinal position, ΔS <2 μm, and the dipole roll angle of $\Delta\theta$ <0.1 μrad. These tolerances, together with the quadrupole levels set above, contribute increases of the RMS closed-orbit motions of 11% and the effective emittance dilution of

$$\Delta\varepsilon_x = 5.6 \text{ pm and } \Delta\varepsilon_y = 0.12 \text{ pm.} \quad (7.2\text{-}2)$$

Because the magnets are not supported independently but on girders, magnetic center fluctuations will be correlated. In Section 7.1.1 the effect of random misalignment of the girders was considered and the closed-orbit Girder Amplification Factor was computed to be 3 to 5 times less than the COAF for the quadrupoles, for independent fluctuations. The GAFs in the long ID straight sections are 15.4 μm (H) and 7.1 μm (V). In the short ID straight sections the GAFs are 4.8 μm (H) and 2.3 μm (V). To maintain an RMS closed-orbit fluctuation of ~10% of the RMS beam size in the LID would require random girder fluctuations of less than 0.62 μm (H) and 0.07 μm (V). The tolerances for the SID would be 0.77 μm (H) and 0.12 μm (V). This shows the reduction in tolerance levels for vibrations coming from the correlation of the magnet vibrations, compared to the random quadrupole tolerance, and that the random model tends to yield a worst-case tolerance level estimate for vibrations.

Another model for quadrupole magnet center fluctuations attempts to include a magnet-to-magnet spatial correlation based on a ground movement model of a plane wave passing through the ring. This model was implemented in the accelerator design code BETA-ESRF [7.2.1]. The horizontal and vertical quadrupole motions are then calculated from the amplitude and wavelength (λ) of the wave. The increase in the effective emittance can be calculated from the closed-orbit shift around the ring using Eq. (7.2-1). Since there will be a dependence on the direction of the wave relative to straight sections, several phases relative to the lattice orientation have been considered, to estimate the maximum impact. The wavelength varies as a function of frequency, which depends on the knowledge of the speed of propagation. We assumed V = 270 m/sec for both S and P waves (see Section 7.2.3.5.1 for measurement for the BNL site). The impact on the beam's closed-orbit shift is then estimated by displacing the center of each quadrupole on the corresponding point of the plane wave. The effective amplitude of the closed-orbit distortion is estimated by sampling the closed orbit around the ring, instead of for different seeds. No consideration for the girders is taken, nor is there any damping of the wave or the beam assumed. Figure 7.2.2a shows the tolerance level for the horizontal (pressure, P) wave amplitude versus frequency ($f = V/\lambda$), for an effective emittance dilution that is 1% of the beam emittance, or 5 pm.

Figure 7.2.2b shows the tolerance level for the vertical (shear, S) wave amplitude versus frequency ($f = V/\lambda$), for an emittance dilution that is 1% of the beam emittance, or 0.08 pm. Clearly, as the wavelength exceeds the ring diameter of 248 m (f<~2 Hz), the entire ring moves in phase and the closed-orbit impact becomes small; the tolerance becomes quite large. Above 20 Hz (H) and 10 Hz (V), the amplitude tolerance becomes almost independent of frequency, about at the levels where ΔX = 0.08 μm and ΔY = 0.04 μm.

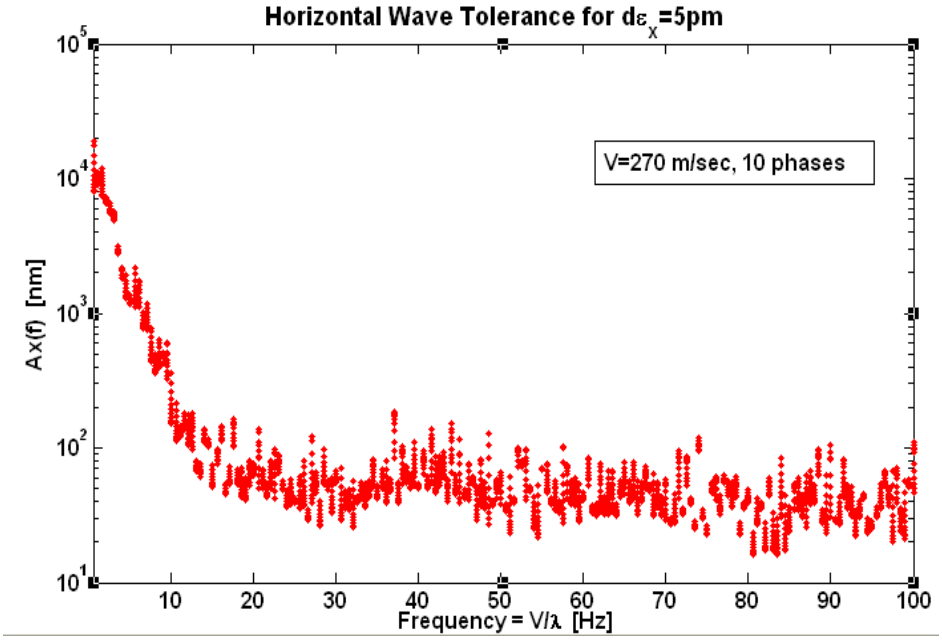

Figure 7.2.2 a The tolerance level for a horizontal wave amplitude, in nm, yielding a 5 pm emittance dilution, assuming a wave velocity of 270 m/sec.

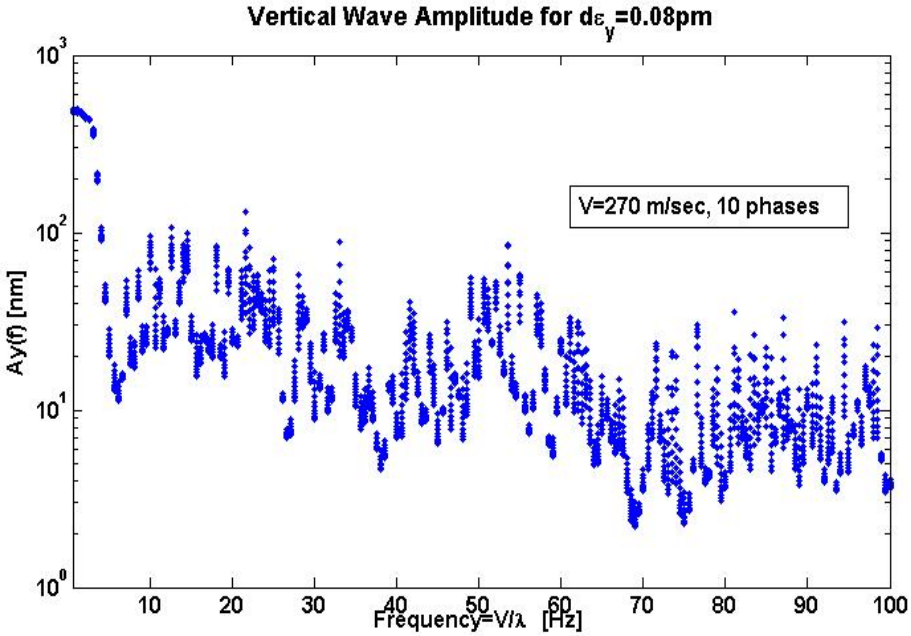

Figure 7.2.2 b The tolerance level for a vertical wave amplitude, in nm, yielding a 0.08 pm emittance dilution, assuming a wave velocity of 270 m/sec.

At frequencies below the 2 Hz level, clearly this model will yield very large tolerances, since all the ring magnets move together. In the low-frequency range (up to ~50 Hz), the global feedback system will take out most of the closed-orbit motion independent of the source term, to a level limited by the BPM and corrector electrical noise level. Above 50 Hz, the centroid motion becomes less obvious, but the beam emittance will be diluted by the effective emittance resulting from the magnet motion.

In summary, the magnet stability tolerances estimated with these models show the worst-case being the random model for the ~10% vertical beam size. However, the effective emittance contribution of this is 1% of the beam emittance and could be relaxed at least by a factor of 2, to about 0.050 μm. These tolerance limits, for the magnets only, are listed in Table 7.2.2. All other tolerances are readily achievable with careful design of girders and the accelerator floor. However, a global feedback system is planned, to ensure that orbit stability is achieved even if these tolerances cannot be achieved. Based on the calculations in Section 6.3, this feedback system will handle random quadrupole fluctuations as large as 0.3 μm vertically.

Table 7.2.2 Magnet Stability Tolerances for AC Closed-Orbit Stability, without Feedback Correction.

Tolerance Limits	ΔX RMS Quads	ΔY RMS Quads	X (LID) RMS (ε_x)	Y (LID) RMS (ε_y)
Random motion	<0.163 μm	<0.023 μm	9.4 μm (5.1 pm)	0.5 μm (0.09 pm)
Random girder motion	<0.62 μm	<0.070 μm	9.4μm (5.1 pm)	0.5 μm (0.09 pm)
Plane wave <5Hz	>2 μm	>0.1 μm	(5 pm)	(0.08pm)
Plane wave >10Hz	~0.08 μm	~0.04 μm	(5 pm)	(0.08 pm)
Additional limits	**ΔS RMS Dipole**	**Δθ RMS Dipole**		
Random motion	≤2 μm	≤0.1 μrad	10 μm (0.006 nm)	0.58 μm (0.12 pm)

7.2.3 Conceptual Design of the Magnet–Girder Support System

7.2.3.1 Functional Requirements

The storage ring girders in a cell provide common mounting platforms for different set of magnets, as shown in Figure 7.2.3. Multipole magnets are mounted on girders number 1, 3, and 5. Dipoles are mounted on separate girders, numbered 2 and 4, because of their height difference and less stringent alignment and stability requirements.

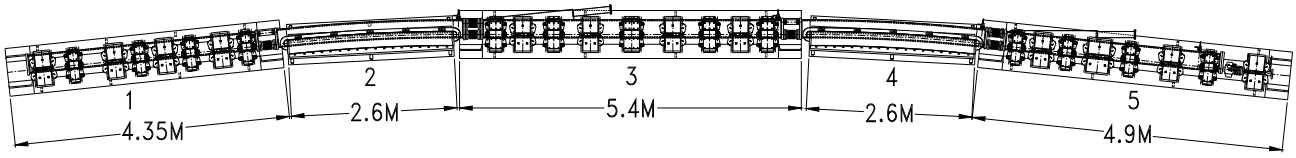

Figure 7.2.3 NSLS-II girders in one cell of the storage ring.

General functional requirements of the magnet–girder support system are given as follows:

1. Raise the centers of the magnets to the nominal beam height of 1 m. This height was chosen based on stability considerations that are discussed in Section 7.2.2.
2. Provide a stable platform for assembling and aligning the magnets outside the tunnel. The stringent alignment tolerances can only be met by precision alignment techniques (see Section 7.2.3.3) requiring out-of-tunnel assembly and alignment. The magnet alignment must remain unperturbed during the transportation and installation of the magnet–girder assemblies in the tunnel.
3. Meet girder-to-girder alignment requirements, both during the initial alignment and subsequently to compensate for long-term floor settlement.
4. Meet dynamic stability requirements under expected ambient floor motion, flow-induced vibrations, and temperature fluctuations of the tunnel air and process water.

In addition, the overall width of the magnet–girder support system must be less than 1 m, for ease of transportation and assembly in the tunnel. The support design must also be cost effective without sacrificing speed of installation and alignment.

7.2.3.2 Main Conceptual Design Features

In many recent light sources the girders have been precisely fabricated with very stringent top surface tolerances (~15 μm flatness) and with T-slot type alignment features. Magnets, built with equally tight tolerances, are fastened directly to the girder's top surface without an interface of alignment hardware. After a careful examination of this approach, we decided to design NSLS-II girders and magnets with conventional tolerances, and to use a vibrating-wire alignment technique for aligning the magnets to ~30 μm precision.

A typical girder with its mounting pedestals is shown in Figure 7.2.4. The nominal length is 2.6 m for the dipole girders and 4.35 to 5.4 m for the multipole girders. The girders are approximately 0.8 m wide and 0.4 m high. They are fabricated by welding commercially available plates and channels of thicknesses ranging from 1 to 2 inches. After welding, the girders are stress-relieved by commercial vibratory stress-relief equipment.

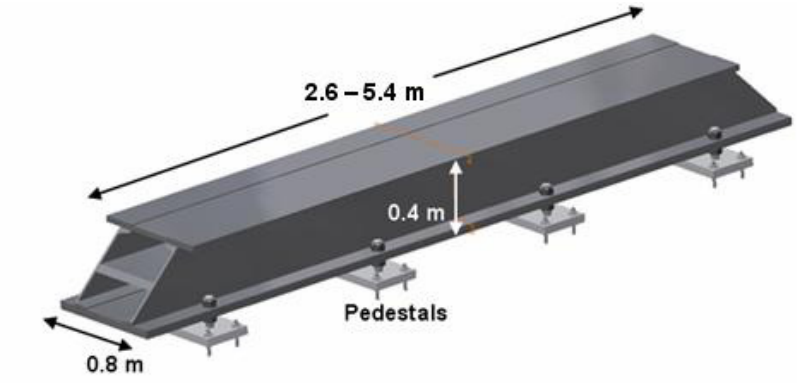

Figure 7.2.4 Conceptual design of the NSLS-II storage ring girder.

The girders are mounted on four 2-inch-thick pedestals that are grouted to the floor with nonshrinking epoxy grout. For mounting and height adjustment, eight 2 inch-diameter bolts with spherical washers are used. The girder is thus over-constrained in order to minimize static deflection and raise the first natural frequency of the magnet–girder assembly. A similar over-constrained scheme has been used successfully at SPring-8 [7.2.2] and will be implemented at the ALBA light source [7.2.3].

7.2.3.3 Magnet–Girder Assembly and Alignment

NSLS-II lattice magnets have magnetic alignment tolerances that exceed mechanical assembly tolerances and the ability of conventional alignment techniques to locate the magnetic components within the required tolerances. Therefore, a vibrating wire alignment technique, originally developed at Cornell University [7.2.4] and subsequently adopted at SLAC, will be used. It has been shown that this technique is capable of aligning magnets on the same girder to within 10 μm.

In this alignment technique, a generator supplies a varying current in the wire and the field of the magnet causes the wire to vibrate. Adjusting the current frequency puts the driving forces in resonance with the wire's vibrating modes. This creates standing waves on the wire that are detected by optical wire sensors. In this way, the null center of the magnet can be located to within a few microns. Laser trackers are then used to transfer the position of the wire to the tracker cups on the girder.

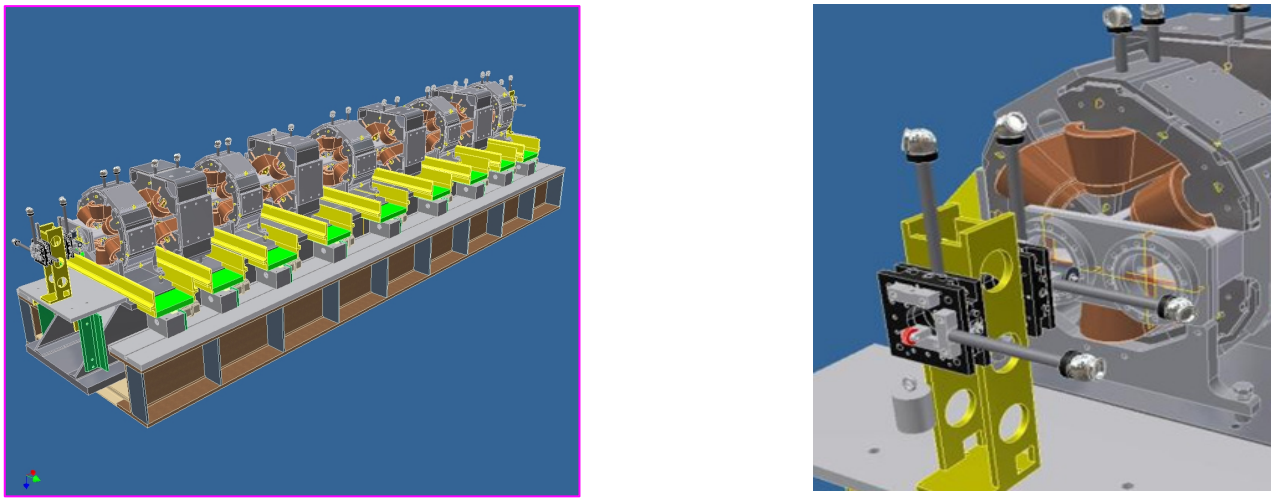

Figure 7.2.5 Left: Vibrating wire alignment system mounted on the girder. Right: Special brackets with wire movers, wire locators, and laser tracker fiducials are attached to either end of the girder.

Initially, the magnets will be installed and aligned on the girder with a laser tracker. The top-half of the multipole magnets will then be split and the vacuum chamber will be installed. The ends of the chamber will be sealed with Mylar caps. The caps will have small holes in either end to allow the ends of the vibrating wire to protrude through while a positive purge of dry nitrogen gas is maintained.

A clean wire will be installed into the vacuum chamber prior to bakeout and conditioning. Vibrating wire support brackets will be attached to either end of the magnet girder assembly and the wire will be secured to X–Y translation stages mounted on these brackets (Figure 7.2.5). After the top half of the magnets are reassembled, their iron cores will be supported on precisely computer-controlled positioners (such as cam movers). The roll angles of the magnet cores will be brought to within ±0.2 mrad tolerance by using magnet positioners and digital inclinometers. For each magnet the sag of the stretched wire is compensated by using translation stages to introduce a vertical offset in the wire's position. The magnet is aligned by moving it to a "null" position that stops the wire from vibrating. The core of the magnet is then fastened to its support frame.

7.2.3.4 Installation of the Magnet–Girder Assembly

A transporter system with self-contained air pads will be used to transport the girder–magnet assemblies from the alignment laboratory into the storage ring tunnel for final installation.

During the early phases of girder installation, the multipole girders will be installed prior to the dipole magnets. The wire support brackets will be left attached for the entire installation process. The air pad system will cushion any shocks to the girder during transport, assuring accurate magnet location. The girder transporter will locate the girder over the eight pedestals studs that will affix the girder to the tunnel floor.

Instrumented torque wrenches will be used in conjunction with laser trackers to precisely offload the girder from the air pads onto the pedestals' studs. Once the girder is fixed to the floor and prior to dipole installation, in-situ vibrating wire measurements will be repeated to confirm alignment of the magnets. These measurements will be discontinued when it is established that the magnet alignment was not disturbed during transportation and alignment.

7.2.3.5 Mechanical Stability of the Magnet–Girder Support System

Sources affecting the mechanical stability of the support system include ground settlement, ambient floor motion, flow-induced vibrations, and thermal transients. These sources can be categorized in terms of the

frequency range—*fast* when greater than a few Hz or *slow* when operating at frequencies lower than one Hz. Sources are also categorized based on the time-scale of the excitation, as being short (<1 hour), medium-term (<1 week), or long-term (>1 week). Short-term sources include natural and cultural ground vibrations, flow-induced vibrations, and power supply jitters. Thermal transients due to temperature changes of the cooling water or the tunnel air, as well as gravitational and tide effects, constitute medium-term sources. Floor settlement or seasonal temperature changes, which may have direct impact on the alignment of components, are considered to be long-term effects. Cultural noise or human activity is typically observed in the frequency range of 1 to 100 Hz. Ground motion from ocean waves or tides is centered at about 0.2 Hz.

7.2.3.5.1 Medium- and Long-Term Stability

Over the years, various studies have been performed at the BNL site and in the vicinity of NSLS-II to characterize the subsurface conditions. Drill-core data show that the soil at the site consists mainly of medium coarse sand with traces of silt and, in some cases, traces of clay and gravel. The shear wave velocity in the top sand layer is about 270 m/sec. The bedrock lies at a depth of approximately 430 m beneath the site. Therefore, the BNL site, including the NSLS-II site, is classified as a very deep site with relatively soft soil. The soil consisting of glacial sands is well settled and, based on the drill-core results, exhibits limited scatter in key properties (coefficient of variation ~0.18). This is important, in that the differential movement (or settlement) in the soil supporting NSLS-II is expected to be of the order of 10 μm /10 m / year. To ensure that this is the case, a detailed study of ground settlement based on finite element analysis will be performed, taking into account both the site soil conditions and the facility layout.

7.2.3.5.2 Short-Term Stability

Short-Term Stability – Ambient Ground Motion

Ambient ground motion measurements near the NSLS-II site were taken from August 31 through September 1, 2006. Data measured at the following locations at BNL were used for a comparison of the NSLS-II site with the ALS, ESRF, and SPring-8 sites:

1. Microscopy suite of the Center for Functional Nanomaterials currently under construction
2. Foundation of a light stand near CFN, not stiffened by the presence of the building
3. A remote location near the northeast corner of BNL
4. Experimental hall of NSLS directly beneath the X1 beamline

The RMS (4–50 Hz) amplitudes of the ground motions in vertical, north–south, and east–west directions are given in Table.7.2.3. The most important value is that of the microscopy laboratory at CFN, where the RMS amplitudes are 20 nm or lower in all directions. The lower values, compared to those at the free-field at CFN and at the remote northeast BNL location, are indicative of the stiffening effect of the CFN building and the floor. The ambient ground motion at the floor of NSLS X1 beamline is considerably higher at 18 and 30 Hz, due most likely to rotating mechanical equipment.

Table 7.2.3 RMS (4-50 Hz) Ground Motion near the NSLS-II Site.

Location	Time	Vertical (nm)	North–South (nm)	East–West (nm)
Microscopy lab at CFN	7:30 pm	20	12	19
Free-Field at CFN	11:40 pm	24	41	38
Remote location near the northeast corner of BNL	Noon	21	25	26
Beamline X1 at NSLS	Midnight	71	12	13

Figure 7.2.6 shows the vertical log mean of site vibrations at the NSLS-II site expressed as PSD, compared with similar data from ALS, ESRF, and SPring-8. Shown also are PSD spectra measured at NSLS beamline X1 just after midnight, the "free-field" location near CFN, and the microscopy suite at CFN identified by the black arrow. The legend indicates the RMS amplitude using summation between 4 and 50 Hz, except for the NSLS-II log mean, which is summed with a 6 Hz lower cutoff because of contamination by the instrumentation noise floor at lower frequencies. The RMS amplitudes for ALS, ESRF, and SPring-8 were calculated in the 2 to 100 Hz band.

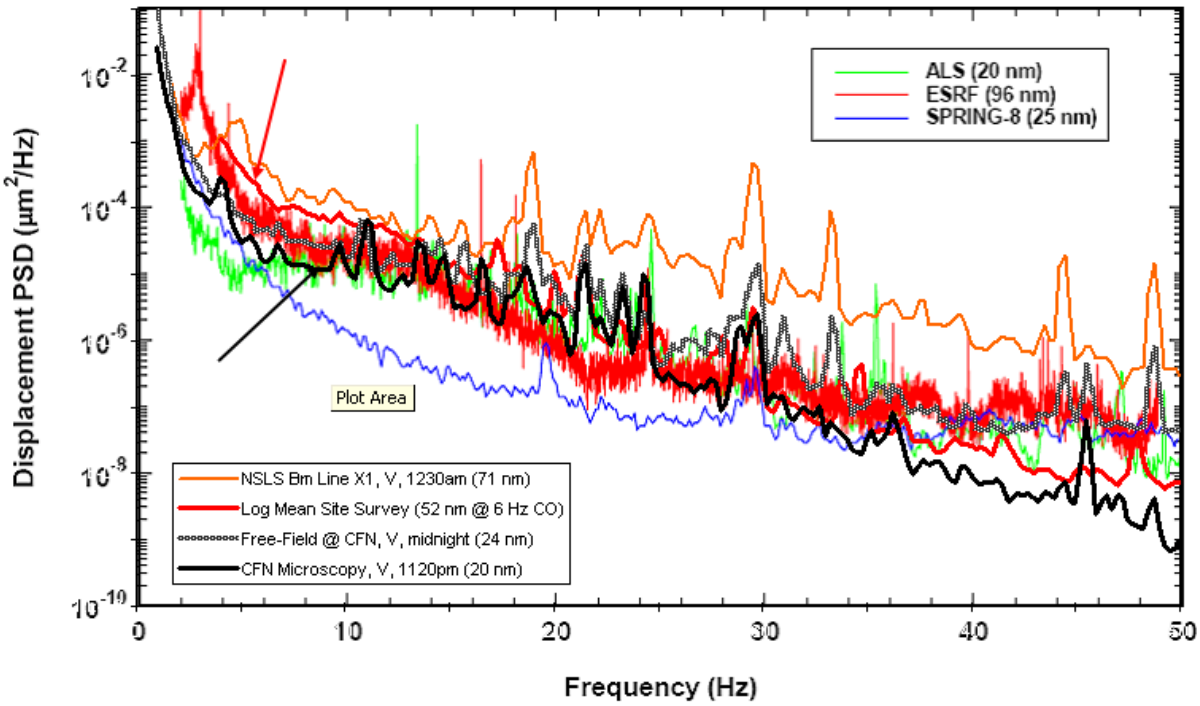

Figure 7.2.6: Comparison of PSDs of vertical ground motions at various locations near the NSLS-II site and at ALS, ESRF, and SPring-8 light sources [7.2.5].

The vibration measurements indicate the presence of local noise sources at ~18 and 30 Hz in the NSLS building. Further vibration measurements are planned to identify and eliminate these local sources of vibration. In addition, the CFN measurements show that the installation of the NSLS-II storage ring and experimental hall will significantly stiffen the site. The floor vibration levels of the NSLS-II storage ring are then expected to be comparable to those of the other light source facilities.

7.2.3.6 Resonant Frequencies of the Girder Support System

Although the NSLS-II magnet–girder assembly fastened to the pedestals is a complex dynamical system, its important design features can be understood by a simple 1D oscillator shown in Figure 7.2.7a.

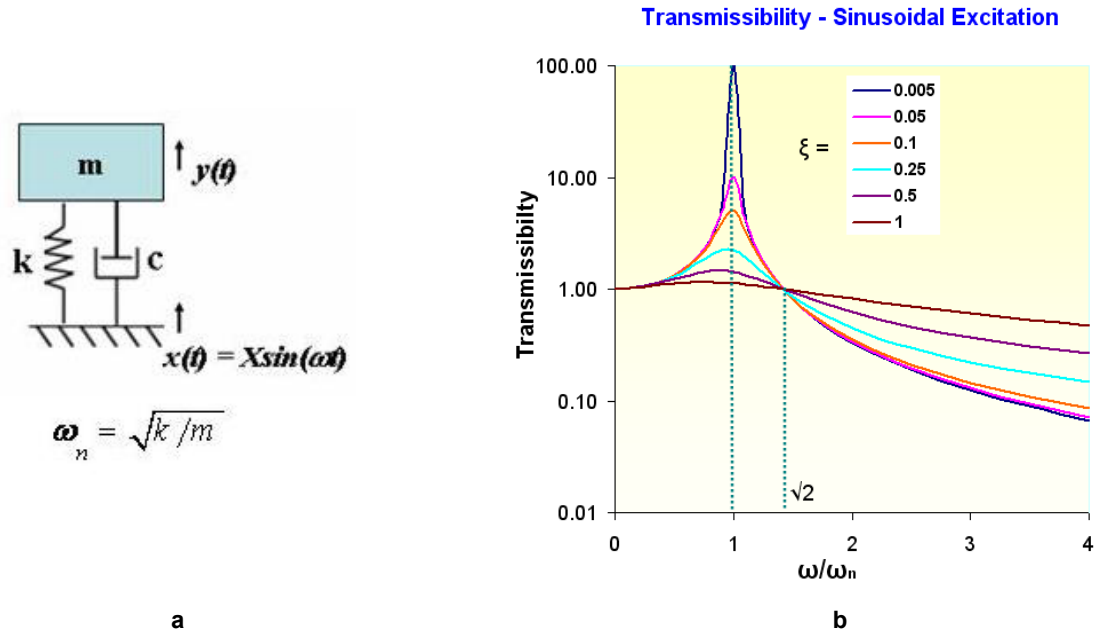

Figure 7.2.7 **a**) 1D oscillator; **b**) transmissibility plot.

For such an oscillator, the natural frequency is

$$\omega_n = \sqrt{k/m} \tag{7.2-3}$$

and the vibration amplification (or transmissibility) is given by

$$Transmissibility = Y/X = \sqrt{\frac{4\xi^2(\omega/\omega_n)^2 + 1}{[1-(\omega/\omega_n)^2]^2 + 4\xi^2(\omega/\omega_n)^2}} \tag{7.2-4}$$

where the fraction of critical damping, ξ, is given by

$$\xi = \frac{c}{2\sqrt{mk}} \tag{7.2-5}$$

Transmissibility curves, obtained from Eq. 7.2-4 for different values of critical damping, ξ, are plotted in Figure 7.2.7b. There is no significant vibration amplification (transmissibility ≈ 1) when the natural frequency, ω_n, is substantially greater than the excitation frequency, ω. The ambient ground motion reduces sharply as $1/\omega^4$, as shown in Figure 7.2.6, and its amplification above 30 Hz can be ignored. Several investigations have been carried out on the dynamic response of the magnet–girder support systems using vibration measurements and finite element modal analyses. These studies have shown that it is quite difficult to raise the lowest natural frequency of the support system to greater than 20 Hz if elaborate alignment mechanisms are used either between the girder and its pedestals or between the girder and the magnets. When such alignment mechanisms are used, then the internal structural damping (ξ = 0.02 to 0.04) of the support

system is insufficient to reduce the floor motion amplification to an acceptable level. External damping devices, either active or passive, are then used, such as viscoelastic damping pads at APS and ESRF.

For the NSLS-II magnet–girder support system, a lowest natural frequency of greater than 50 Hz will be obtained by eliminating elaborate alignment mechanisms, and by lowering the beam height to 1 m. Short, stiff threaded rods will be used for height adjustment only. Transverse alignments will be made by precise but removable alignment mechanisms. Finite element model analysis of the NSLS-II magnet–girder assembly shows that the lowest two natural frequencies are 68.7 Hz and 94.3 Hz. The corresponding mode shapes, rolling and twisting of the girder, are depicted in Figure 7.2.8.

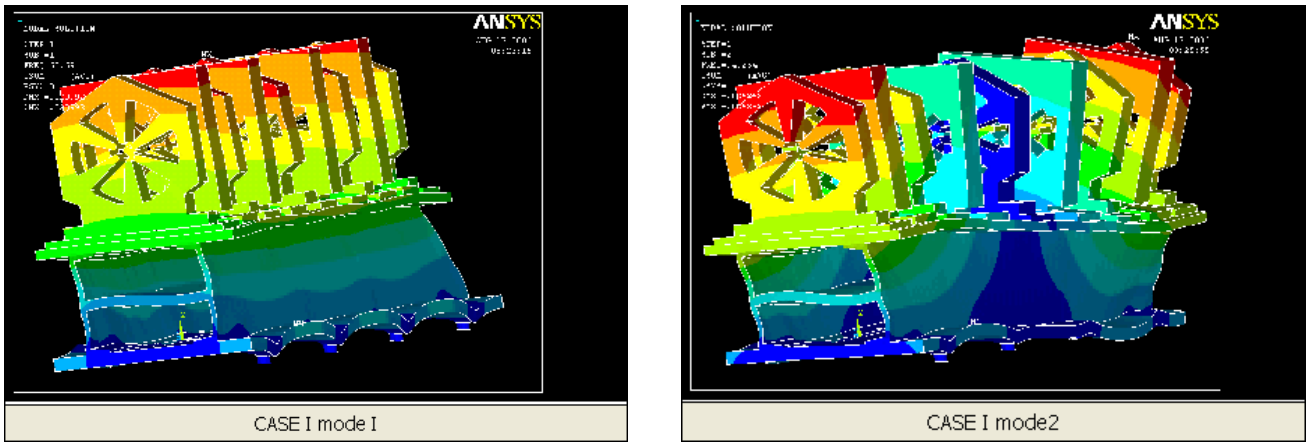

Figure 7.2.8 Mode shapes of the NSLS-II magnet–girder assembly: (left) First mode shape, rolling, ω_1 = 68.7 Hz. (right) Second mode shape, twisting, ω_2 = 94.3 Hz.

7.2.3.7 Flow-Induced Vibrations

Flow-induced vibrations of the water headers can be transmitted to the magnets and the vacuum chambers [7.2.6] by flexible hoses and pipes. The effects of flow-induced vibrations will be mitigated by paying close attention to several useful design guidelines, namely:

1. Locate all rotating equipments including fans, blowers, compressors, and pumps outside the storage ring tunnel, preferable tens of meters away from the tunnel floor and ceiling.
2. Keep low flow velocities (less than 2 m/s) in the process water headers.
3. Design header supports to minimize their vibration, such as by integrating viscoelastic dampers in the headers hangers, or by attaching headers directly to the ceiling.
4. Arrange water flow circuits and connection fittings such that sharp bends are eliminated. Special attention is to be given to the routing and clamping of the hoses and tubes that connect the magnets and vacuum chambers to their respective headers.

Analytical models and vibration measurements will be employed to ensure that flow velocities required to regulate the temperature of the vacuum chambers do not induce unacceptable level of vibrations.

7.2.3.8 Thermal Stability

Ambient temperature variations will result in displacements of both the magnets on the girders and the BPMs on the vacuum chambers [7.2.7]. To ensure acceptable thermal deformations of the ring components, process water and tunnel air temperatures will be maintained to within ±0.1ºC of their nominal values, 29.4ºC and 25.6ºC (85ºF and 78ºF), respectively. Air-conditioning temperature cycling of ~1-hour duration will be

maintained in order to take advantage of the thermal inertia of the support system. Thermal insulation of the girder will also be considered as an option to further reduce the effects of temperature transients.

Lowering the beam height from 1.4 m to 1 m would reduce the vertical thermal expansions of the assembly proportionately. In addition, over-constraining each girder to its pedestal at eight locations would minimize thermal bending effects.

7.2.3.9 R&D Program on Stability of the Magnet–Girder Support System

To further improve the mechanical stability performance of the girder support system, the following R&D tasks will be undertaken.

- real-time online measurements and analysis of the NSLS-II ambient ground motion.
- optimization of the stiffness of the magnet–girder assembly (A prototype assembly will be built for this purpose.)
- use of viscoelastic damping devices
- characterization and mitigation of the flow-induced vibrations of the magnets and the vacuum chambers
- investigation of the effect of process water and tunnel air temperatures on the field quality of the storage ring magnets
- assessment of insulating materials to reduce the effects of thermal transients in the tunnel

References

[7.2.1] BETA USERS' GUIDE by L. Farvacque, T.F. Gunzel, J.L. LaClare, A. Ropert.
[7.2.2] K. Tsumaki and N. Kumagai, “Vibration Measurement of the SPring-8 Storage Ring,” IEEE, PAC, 2001.
[7.2.3] L. Nikitina and Y. Nikitin, private communication on ALBA girders, August 13, 2006.
[7.2.4] A. Temnykh, “The Magnetic Center Finding using Vibrating Wire Technique,” CBN 99-22, Cornell University, May 26, 1999.
[7.2.5] S. Sharma, C. Doose, G. Portmann, L. Zhang, K. Tsumaki, and D. Wang, “Ground Vibration Problems at the Light Sources,” 22nd Advanced ICFA Beam Dynamics, SLAC, Nov. 6-9, 2000, SLAC-WP-18, pp. 37-48.
[7.2.6] Nakazato, et al., “Observation of beam Orbit Fluctuation with Forced-Vibrating Magnets and Vacuum Chambers,” MEDSI2002, Chicago, IL 2002.
[7.2.7] L. Emery, “Measurements of Thermal Effects on the Advanced Photon Source Storage Ring Vacuum Chamber,” MEDSI2002, Chicago, IL, 2002.

7.3 Beam Chambers and Vacuum Systems

7.3.1 Scope

The storage ring vacuum system provides and measures the acceptable vacuum pressure within the storage ring and front-end vacuum chambers. The storage ring vacuum system includes all vacuum chambers, vacuum pumps, vacuum valves, bake-out systems, and vacuum instrumentation and control. The storage ring vacuum system extends throughout the storage ring from the booster injection line-storage ring interface to the outer portion of the shield wall where the front end transitions to the user beamline. Vacuum system information for the linac-to-booster transport line, the booster, and the booster-to-storage ring transfer line is discussed in Chapter 5.

Many components such as shutters, photon absorbers, beam scrappers, insertion devices, etc. require or share storage ring vacuum, but only the components whose main purpose is to maintain, monitor, and control storage ring and front end vacuum are included in detail here. The other components are described in their respective sections. Due to many years of accumulated operational experience at NSLS and other synchrotron radiation facilities, a design approach that provides optimal performance at minimal cost will be pursued.

The storage ring vacuum pressure with beam is designed to be less than 1×10^{-9} Torr. At this pressure level, the beam lifetime due to bremsstrahlung and Coulomb scattering is longer than 10 hours. The stored beam lifetime for 500 mA operation will be limited to 2–3 hours by the Touschek lifetime due to the scattering loss of electrons in the bunch. The designed pressure level will provide ample beam lifetime with minimal radiation and beam loss effects.

To achieve the low thermal outgassing and low photon-stimulated desorption, all the vacuum vessels and appendage vacuum components will be made from ultra high vacuum compatible materials. All the vacuum components will be carefully prepared, cleaned, and conditioned using UHV compatible processes.

7.3.2 Mechanical Design

7.3.2.1 Design Overview

There are 30 cells in the storage ring. Each vacuum cell consists of five basic chambers; an upstream straight chamber, a dipole chamber, a mid-section straight chamber, a second dipole chamber, and a downstream straight chamber. There are RF-shielded bellows connecting the chambers. There is a long straight section either 5 m or 8 m long between the cells, for insertion devices and for special components such as RF cavities, injection devices, damping wigglers, and so forth. A typical vacuum cell layout is shown schematically in Figure 7.3.1. The dipole magnet chambers are approximately three meters long and the straight chambers for the multipole magnets 4 to 5 m long. All-metal, RF-shielded gate valves will be employed to isolate each of the 30 cells and the long straight sections between cells.

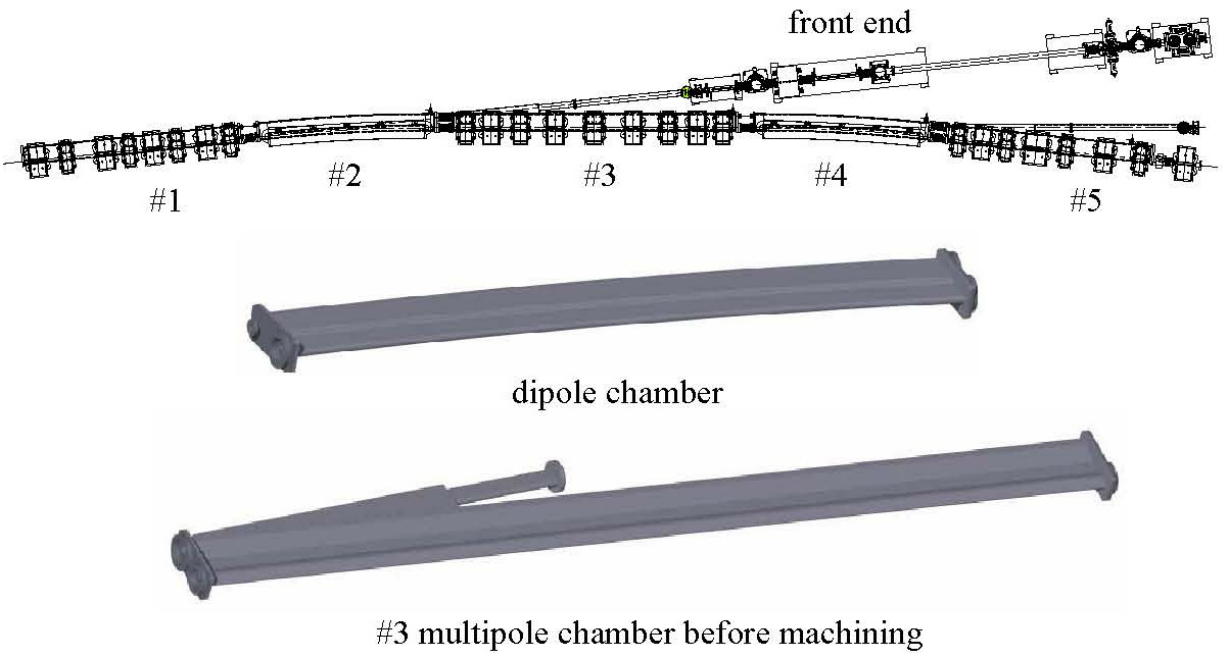

Figure 7.3.1 The layout of the five vacuum chambers in a typical synchrotron cell with two photon exit ports; and the 3D models of dipole magnet chambers, and the #3 straight chamber for multipole magnets.

Most of the storage ring chambers will be made of extruded aluminum with a cross-section similar to that of the APS chambers [7.3.1]. Conflat flanges with copper gaskets will be used throughout the vacuum systems, except for the flanges and seals for beam position monitor buttons, where Helicoflex delta seals will be employed. Water-cooled copper or Glidcop absorbers will be positioned in the storage ring vacuum chambers to absorb the unused photons and high heat loads. The entire set of vacuum cells will be in-situ bakeable to 150°C to remove adsorbents and contaminants. Vacuum bake for the aluminum chambers will be at 130°C using pressurized hot water circulated within the cooling water channels. External heating jackets will be used for the bakeout of the appendage vacuum components.

To achieve fast conditioning after intervention, sufficient pumping capacity is needed. The chambers will use sputter ion pumps, non-evaporable getters (NEGs), and titanium sublimation pumps (TSP) for their main UHV pumping. Following rough pumping, in-situ vacuum bakeout is required, to remove contaminants. Provisions for vacuum bakeout are therefore necessary, and the careful selection of vacuum chamber materials and all other materials that are directly in contact with the vacuum chambers is important. The vacuum chamber design must provide provisions for stability during bakeout and be made with sufficient precision for accurately locating the vacuum chambers and BPM buttons after bakeout. The impedance of the vacuum chamber should be low enough so as not to excite higher-order mode resonances. Smooth cross-sectional transitions between components are required, as are flexible interfaces such as RF-shielded bellows between cell chambers and insertion devices. The design parameters of each vacuum system component must be considered separately and as a whole, as each parameter affects the performance of the overall storage ring vacuum system.

7.3.2.2 Vacuum Chamber Design

The electron beam vacuum chambers differ according to their location within the storage ring. The vacuum chambers will provide adequate ports for heat absorbers, BPM buttons, pumps and exit ports to the front ends. A pronounced antechamber design similar to that of APS [7.3.1] will be used to better distribute vacuum pumping capability. The cell vacuum chambers contain two distinct but connected channels; the

beam channel portion must be continuous, but the antechamber portion may be interrupted at various locations for vacuum valves, bellows, insertion devices, and other devices where the mechanical requirements constrain the use of the antechamber. Ports emanating from the cell chambers will use bi-metal Conflat flanges. The internal beam chamber cross-section will be elliptical, 25 mm vertical by 76 mm horizontal, to allow sufficient beam-to-chamber clearance, except at absorbers, which insert to 25 mm from the storage ring centerline at the outboard side to intercept some unused photons. The antechamber portion of the vacuum chamber is sized for distributed NEG pumping and to fit within the magnets. A slot connecting the beam channel and antechamber portions of the vacuum chamber is sized as large as possible according to the physical requirements of the magnets that the vacuum chamber passes through, and according to constraints given by the wall strength requirements for the vacuum chamber. The chamber cross sections inside the dipole, quadrupole and sextupole magnets are shown in Figure 7.3.2. There will be at least 2 mm clearance between chambers and magnet poles and coils at the closest points to allow adjustment in the chamber supports as well as during in-situ bake. The extruded chamber cross sections and the cross sections after machining are given in Figure 7.3.3. The ANSYS analysis of the stress and deflection due to atmospheric pressure load of the multipole chambers at the sextupole location, which has the thinnest wall, is shown in Figure 7.3.4, with maximum stress of 135 MPa and maximum deflectors 0.6 mm × 2. However, a 3D ANASYS analysis gives maximum stress of 94 MPa and maximum deflection of 0.3 mm × 2, because the chamber wall is machined down to 2.9 mm only at the sextupole locations.

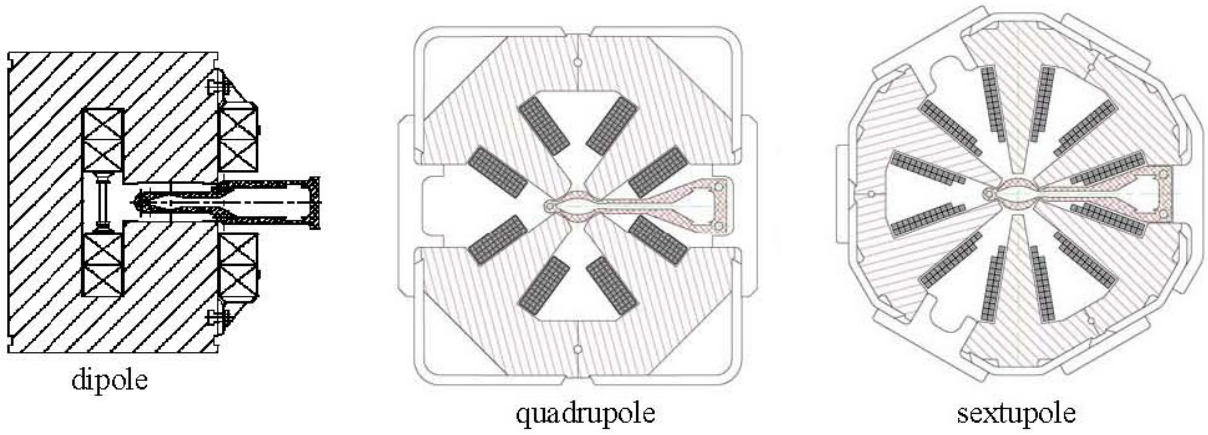

Figure 7.3.2 Storage ring vacuum chamber and magnet cross-sections at dipole, quadrupole, and sextuple interfaces. The beam channel will have a minimum aperture of 25 mm (V)×76 mm (H).

A list of storage ring vacuum chambers for the storage ring is given in Table 7.3.1.

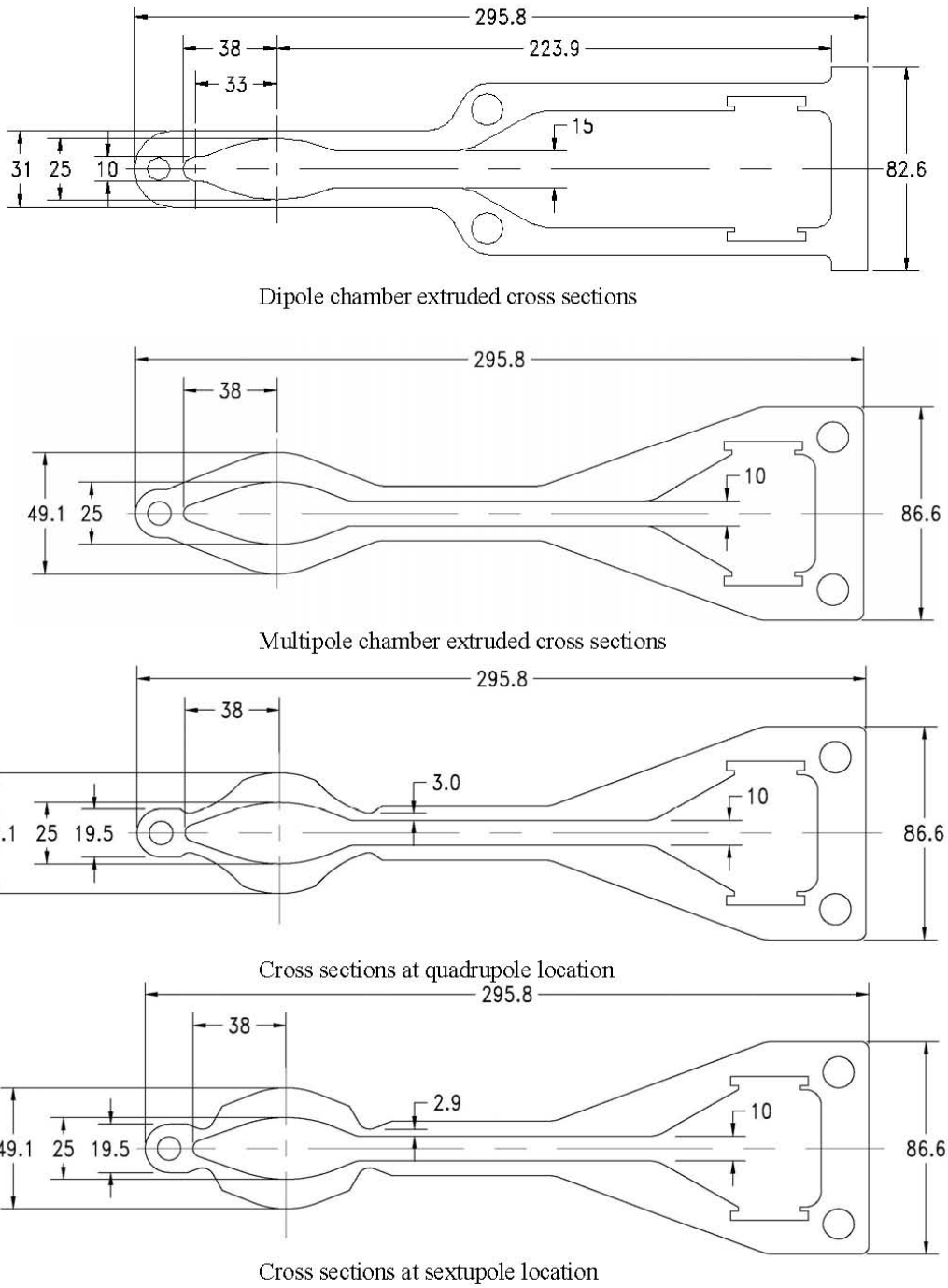

Figure 7.3.3 Storage ring vacuum chambers at dipole, multipole, quadrupole, and sextupole interfaces. The minimum wall thickness at the sextupole location is ~2.9 mm.

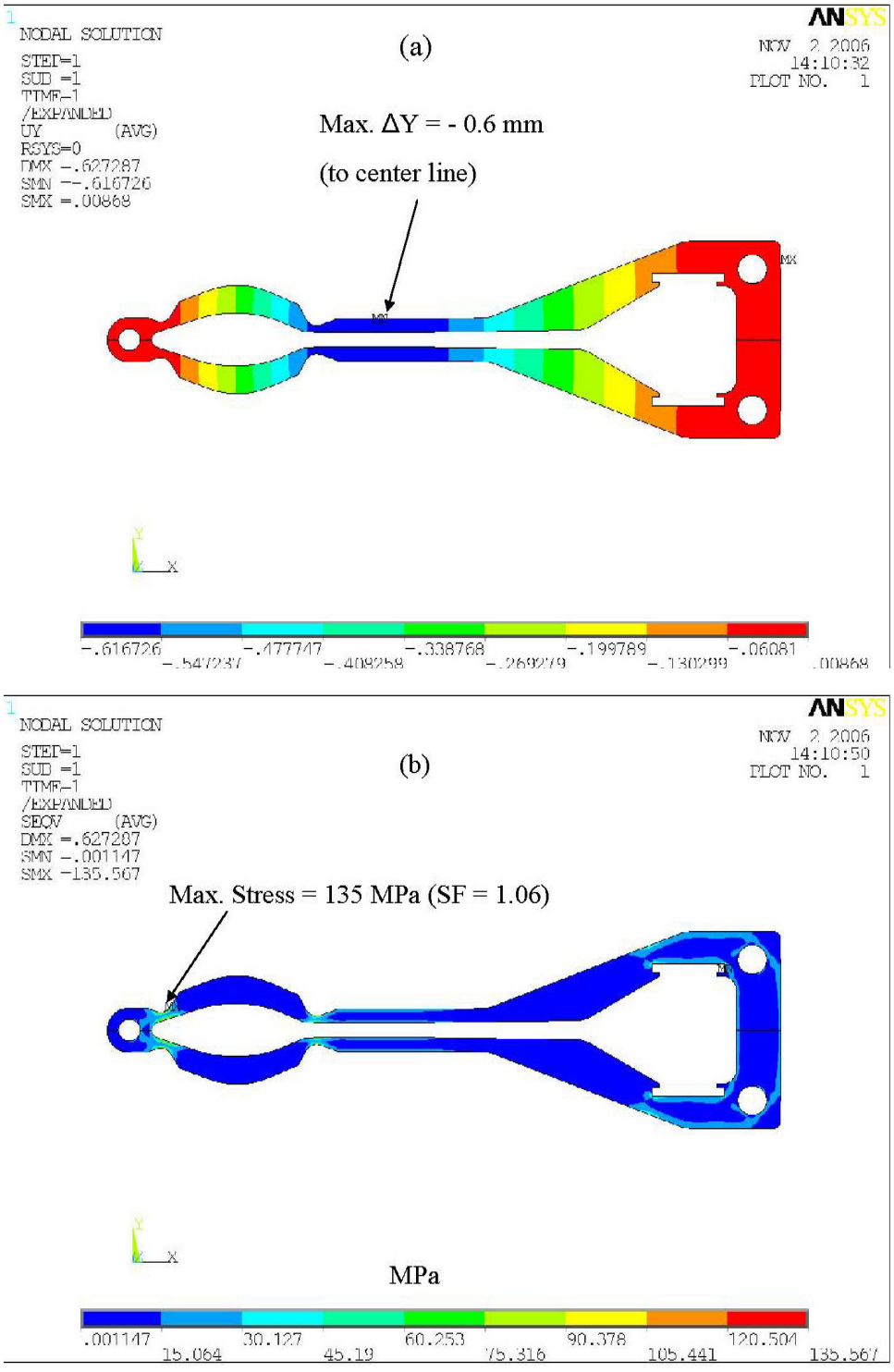

Figure 7.3.4 ANSYS analysis of the deflection and stress of the multipole chamber at the sextupole pole tip locations where the wall thickness is 2.9mm, **a)** the maximum deflection due to atmosphere pressure load is found to be 0.6 mm×2; and **b)** the maximum von Mises stress at this single point is 135 MPa, within the maximum allowable stress of 144 MPa.

Table 7.3.1 Types and Numbers of Vacuum Chambers, Absorbers, and RF-Shielded Bellows in the NSLS-II Storage Ring at Start of Operations.

Description - Type	Length (m)	Quantity
Cell – Bending - #2, #4	3.0	60
Cell – Straight – #1	3.7	30
Cell – Straight – #3	4.8	30
Cell – Straight - #5	4.3	30
Cell – RF–Bellows	0.3	120
Cell - Absorber		210
ID – CPMU & EPU	~4	5
ID – Damping wiggler	~7	3*
ID – SRF cavity	~7	2
ID – Injection kickers + septum	~7	1
ID – Empty 5 m straight	~4	10
ID – Empty 8 m straight	~7	9*
ID – RF-Bellows	~0.3	~60

* Two 4 m beampipes will be used at each 8 m long straight.

7.3.2.3 Pumping at the Photon Absorbers

There are several discrete photon absorbers, as described in Section 7.7.2, in each vacuum cell to intercept and absorb unused photons from the two bending magnets and the upstream insertion devices. The absorbers are located as far from the source of the photons as practicable, to reduce the power density, and thus the peak temperature on the absorber surface. Sputter ion pumps with either NEG cartridges or TSPs will be located at the absorbers to remove as much desorbed gas as possible, thus minimizing the amount of gas diffused back to the beam channel. The maximum gas load from each absorber for the bending magnet radiation is estimated to be $\sim 1\times10^{-6}$ Torr-l/s, as described in Section 7.3.3.2, and can be handled with the combination of a sputter ion pump and titanium sublimation pump. The absorber for the DW radiation fan will intercept ~10 kW of photons, resulting in a gas load of 7×10^{-6} Torr-l/s. This high gas load at the DW absorber will be pumped by the combination of a sputter ion pump and a NEG cartridge pump, which has higher capacity than a titanium sublimation pump.

7.3.2.4 Injection Kicker and Front-End Chambers

Kicker magnets require special ceramic vacuum chambers. The four ceramic chambers will be located in the injection straight section, upstream and downstream of the injection septum magnet to correct the electron beam path as needed during injection to the storage ring. These chambers will be specially designed so that they are able to 1) withstand the stresses of fast magnet actuation, 2) resist fatigue, and 3) maintain vacuum integrity. The internal surface of the ceramic chambers will be coated with a conductive film to reduce impedance for the beam image current and prevent charge buildup [7.3.2]. The film must be thin to minimize the eddy current induced by the fast-pulsing kicker field so as not to disturb the injected beam. A thin window may be used at the injection septum to separate the transport line high vacuum from the storage ring UHV.

There are two photon exit ports at each vacuum cell to extract proper photon beams to the user beamlines: one at straight Chamber 3 for photon beam originating from the upstream insertion device; and the second at the upstream end of straight Chamber 5 for photons from bending magnet 4. The front ends of these exit ports will have high heat load components to intercept the photons before the beamlines are installed or when the beamlines are not in use. The front ends will consist of photon masks, safety shutters, heat absorbers, and fixed and adjustable slits. Vacuum gate valves will also be located in the front ends to allow vacuum isolation of components as needed for maintenance and troubleshooting. The front-end vacuum chambers will be made

of stainless steel. Sputter ion pumps with TSP will be placed in each front-end section as close as practical to the gas sources at the photon mask, safety shutter, and absorbers. Vacuum gauges and residual gas analyzers will be installed at each front end to monitor vacuum quality. Radiation shielding will also be installed at front ends to protect downstream equipment and personnel.

7.3.2.5 RF-Shielded Bellows, Flanges, and Ports

To reduce the broadband impedance of the vacuum chamber wall and to minimize the localized HOM heating, the inner cross-section of the electron-beam chamber should be maintained as smooth as possible. High transverse impedance may cause beam instability, which might put an upper limit on the stored current. The changes in cross-sections of the beam chamber should vary smoothly, with an angle of inclination less than 1/5 for tapered transitions. The height of the steps should be less than 1 mm, in general, and less than 0.5 mm at small-aperture ducts for insertion devices. For vacuum components with cavity-like or discontinuous structure, such as flange joints and bellows, RF contact fingers will be installed to reduce the impedance and provide a smooth path for the beam image current. The opening of the thin slits of these fingers should allow enough pumping of residual gases from behind the slits. Calculations will be made to optimize the design of the thin slits while minimizing the impedance of the chambers. Slots or screens will be implemented at the ports of some ion pump locations to reduce impedance and still provide adequate vacuum pumping. Only RF-shielded gate valves, commercially available, will be used along the storage ring beam channel.

Two types of RF-shielded bellows will be studied for their finger contact force, flexibility, cost, and vacuum and RF properties: the single-finger type with hydro formed bellows used at APS [7.3.3], and the double-finger type with welded bellows used at B-factories and a few SR facilities in Asia. They are shown in Figure 7.3.5. The welded bellows will allow more compression and lateral movement than the hydro-formed ones. The double-finger design may not be as reliable as the single-finger type, but does offer lower contact resistance. The magnetic permeability of both welded and formed bellows must be measured and the eddy current effect calculated, since fast corrector magnets will be mounted at some bellows. The welded bellows will cost more than the formed ones.

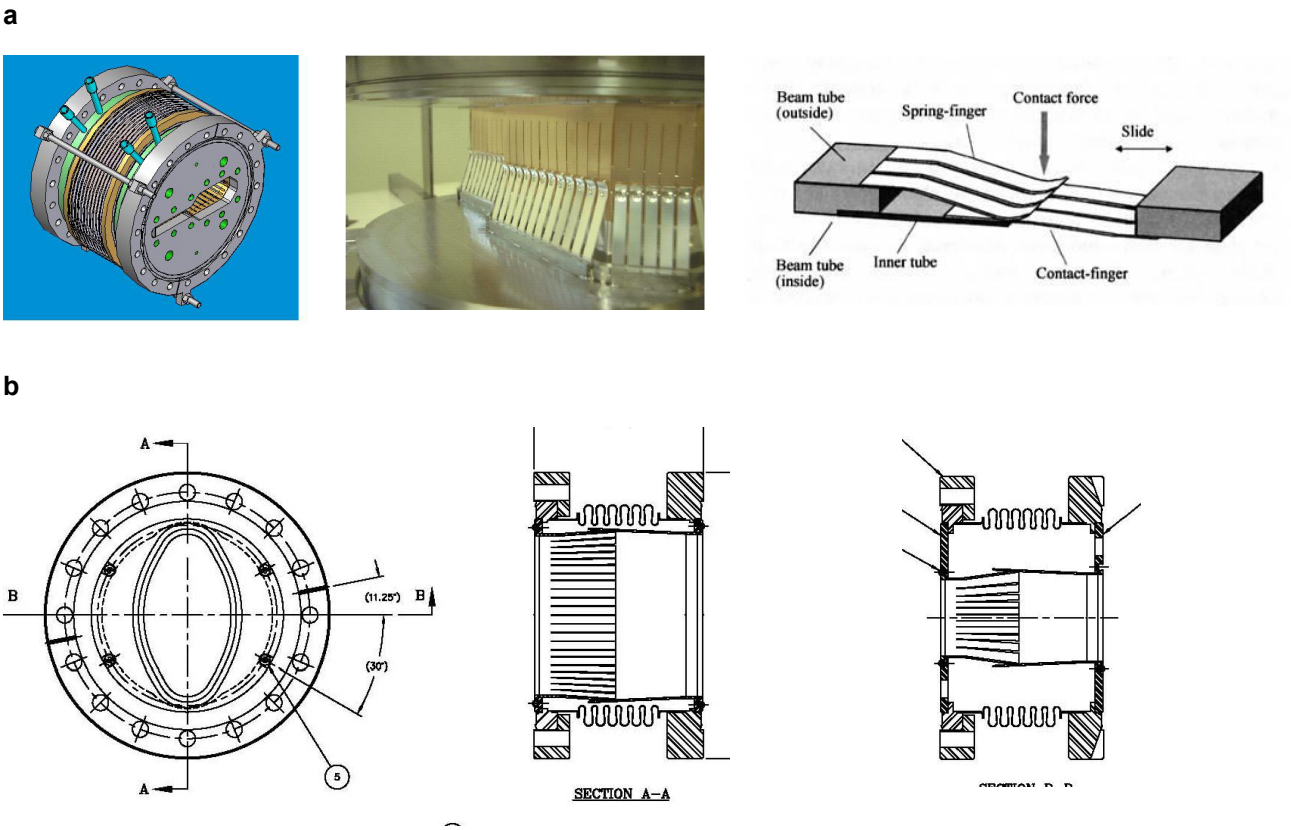

Figure 7.3.5. Two types of RF-shielded bellows: (a, upper row) the ones with welded bellows used in B-factories and BEPC-II with single or double fingers; and (b, lower row) the APS type with single fingers and hydro formed bellows.

Explosion-bonded bi-metal transition flanges, made from 316L stainless steel and A6061-T6 aluminum plates, will be used for the aluminum chambers throughout the storage ring. These Conflat type flanges with aluminum weld neck will be tungsten-inert-gas welded to the cell chambers using a robotic welding machine. They have the standard stainless steel knife-edge sealing face for the copper gaskets and are commercially available. They will form reliable, leak-tight joints with other bi-metal flanges and standard stainless steel flanges of adjacent chambers, bellows and other appendage vacuum components, such as vacuum pumps and gate valves. The bi-metal joints can be in-situ baked up to 250^{o}C.

7.3.3 Pressure Requirements and Distribution

As mentioned earlier, an average beam channel pressure of less than 1×10^{-9} Torr is needed. This pressure will provide ample beam-gas lifetime with minimal radiation and beam loss effects. Beam losses generate radiation according to electron current, energy, and vacuum pressure. At pressures greater than 10^{-9} Torr, both the stored beam lifetime and the life of many of the vacuum pumps will be reduced. Titanium sublimation and NEG pumps have lifetimes that are directly related to the operating pressure; therefore, maintaining this vacuum level in the storage ring improves vacuum component life, stored beam life, and minimizes the amount of radiation produced from bremsstrahlung scattering.

The beam gas scattering loss in the NSLS-II storage ring will depend largely upon the interaction of the beam with heavier residual gas molecules such as CO, CO_2, and Ar due to bremsstrahlung and Coulomb scattering. The gas density inside the vacuum chamber is determined by the installed pumping and by the surface condition of the vacuum chambers and the absorbers, which is bombarded by photons (synchrotron

radiation) generated by the circulating electron beams. During initial ring commissioning, there are severe limitations on the achievable beam current and stored beam lifetime, caused by large pressure increases due to gas species from Photon-Stimulated Desorption. Experience gained during early commissioning of the NSLS x-ray ring showed that residual gas spectra obtained with no stored electrons were typical of a well-baked UHV system. Hydrogen constituted approximately 95% of the residual gas at that time, and the average vacuum was in the 10^{-10} Torr range. The composition of the desorbed gases during initial operation of the x-ray ring was 43% H_2, 25% CO, and 16% each of CO_2 and CH_4. After three months of additional beam conditioning, the PSD rate dropped by a factor of five, and the CO, CO_2, and CH_4 peaks represented much smaller percentages of the total desorbed gas. The PSD rate versus beam conditioning dosage for copper and aluminum chambers [7.3.4, 7.3.5], as measured at NSLS, is shown in Figure 7.3.6. Typical desorption yields after 100 A/hr beam conditioning are used in the pressure simulation. The beam lifetime did not show a corresponding increase with the reduced desorption rate, however.

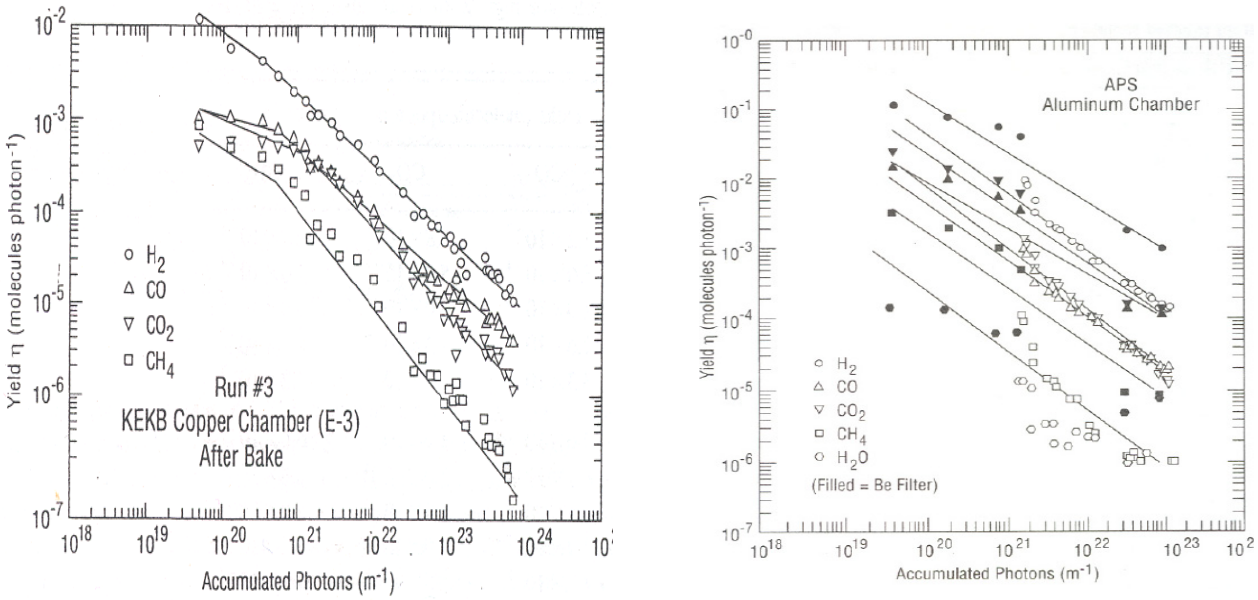

Figure 7.3.6 Comparisons of PSD yields with photon dosages for copper and aluminum. **a)** PSD yields for a 1 m pure copper sample beam chamber at KEKB. **b)** PSD yields for a 1 m extruded aluminum sample beam chamber at APS.

Most of the NSLS-II storage ring vacuum chambers will be fabricated from extruded aluminum and may be exposed to low levels of bending magnet photon radiation. Almost all unused photons will be incident on specially designed water-cooled absorbers. After NSLS-II commissioning and operation, copper, stainless steel, and aluminum PSD will be at almost the same levels.

The 25×76 mm electron beam channel is vacuum pumped using distributed NEG strips in the ante chamber connected by a narrow pumping slot. Two NEG strips are installed in the extruded ante chamber and have a combined pumping speed of 240 l/s/m. The NEG pumps only chemically active gases. Sputter ion pumps are employed to pump the inert gases not pumped by the NEGs. The SIPs are located under the photon absorbers where the majority of PSD occurs. The SIPs provide 400 l/s pumping and are part of a combination SIP/TSP. The TSP provides an additional 500 l/s of pumping for active gases.

Conductance of the electron beam channel is 8 l/s/m. The connecting slot in the extrusion between the NEG ante chamber and the dipole beam chamber is 15 mm high and limits the NEG pumping speed to about

150 l/s/m, in the beam channel. The slot in the extrusion for the quadrupoles and sextupoles is 10 mm high, which yields a conductance of approximately 110 l/s/m in the beam channel.

7.3.3.1 Static Vacuum: Thermal Outgassing

The static pressure distribution in the storage ring will be determined by the amount of thermal outgassing from the internal surfaces in the vacuum chambers. These outgassing rates will depend on the construction materials used and their preparation. After precision cleaning, the chambers will be vacuum-baked and may be glow-discharge conditioned to reduce outgassing and remove contaminants prior to their final assembly into the storage ring magnets and girders. All the chambers and vacuum components in the vacuum cell will be in-situ baked, again to reduce the thermal outgassing. Most of the internal vacuum surfaces along the storage rings are aluminum. The contribution of other materials to the thermal outgassing load is much smaller than that of aluminum wall. Vacuum-baked aluminum outgassing of 1×10^{-12} Torr-l/s/cm^2 is used for thermal gas load modeling. The total thermal gas load is estimated to be 6×10^{-6} Torr-l/s.

7.3.3.2 Dynamic Vacuum: Photon Stimulated Desorption

During operations with stored electrons, specially designed water-cooled Glidcop absorbers will intercept most unused synchrotron radiation. The PSD rate η for vacuum-baked copper and Glidcop has been studied at NSLS [7.3.4] and at other laboratories. An η value of 2×10^{-6} molecules per photon is used for the modeling calculations [7.3.6]. The total photon flux from the storage ring dipole magnets is calculated using Np (ph/s) = $8\times10^{+20}$ [E(GeV)] [I(Amperes)]. For 3 GeV and 500 mA, the total photon flux is $1.2\times10^{+21}$ ph/s. Using these values and converting to gas load yields 7.5×10^{-5} Torr-l/s (or $\sim1.2\times10^{-6}$ Torr-l/s per bending magnet). Thus the total estimated gas load, for both thermal and bending magnet PSD, is 8×10^{-5} Torr-l/s. The undulator radiation will have a narrow fan. It will mostly be collimated and intercepted down at the front end and beamline, and will produce little gas load to the storage ring beam channel. In contrast, the damping wiggler radiation will have a relatively wide fan. Approximately 15% of the DW radiation will be intercepted by the crotch absorber located upstream of the #3 multipole chamber, equivalent to $\sim1\times10^{+20}$ ph/s by each DW. Assuming the same η value of 2×10^{-6} molecules per photon, this corresponds to an additional gas load of 7×10^{-6} Torr-l/s from each DW.

7.3.3.3 Dynamic Pressure Distribution

The pressure rise with beam operation will be determined by the PSD of gases from internal surfaces of the vacuum chamber, and the amount of dynamic pumping. Most synchrotron radiation will be intercepted by water-cooled Glidcop absorbers, which are located downstream of bending magnets and insertion devices. The pressure distributed in a super-period of 52 m was calculated using both Molflow [7.3.7] and Vaccalc [7.3.8] software. The storage ring pressure distribution in the beam channel with 500 mA stored beam current, with no beam current, without TSP, and with only 50% NEG strip coverage, is plotted in Figure 7.3.7. PSD yield of 2×10^{-6} mol/ph, reached after approximately 100 amp-hours of beam conditioning, is used in the calculation. The design average pressure of less than 1×10^{-9} Torr can be reached with the current pumping scheme of distributed NEG, lumped ion pumps, and TSP. The significance of the distributed NEG is clearly illustrated, i.e., a 50% decrease in NEG coverage results in a five-fold increase of average pressure in the electron beam channel. The comparison of the pressure distribution in super-periods with and without DW is illustrated in Figure 7.3.8. The crotch absorber for DW radiation produces a sharp but localized pressure peak, but only a 10% increase in average pressure for that super-period.

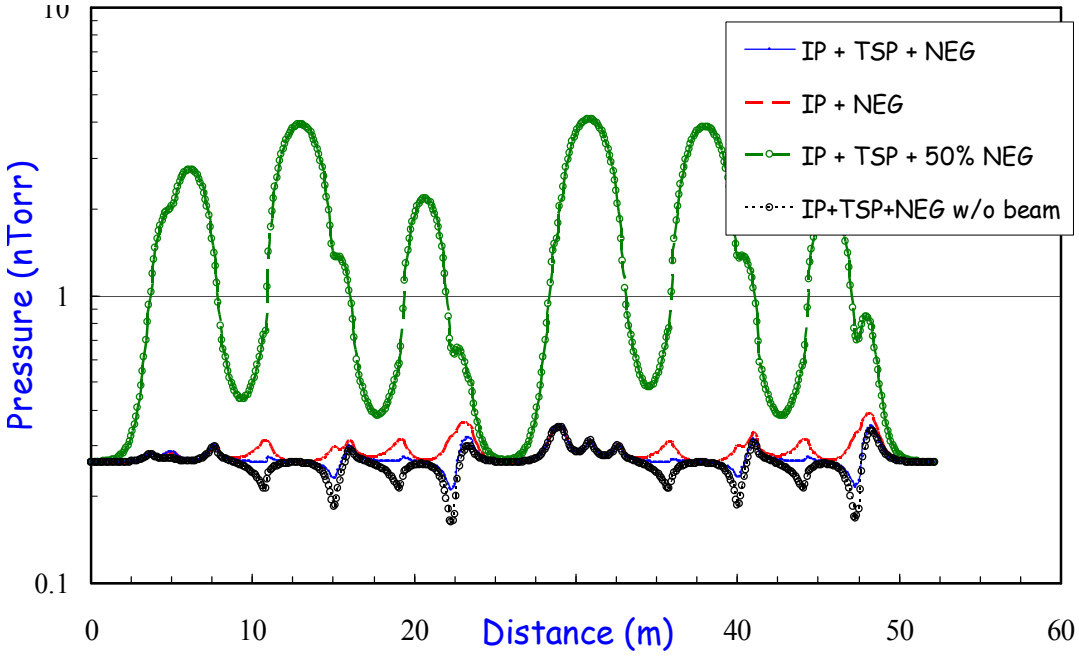

Figure 7.3.7 Pressure distribution inside the electron beam channel in one storage ring super -period without beam (black circles), with 500 mA current (blue line) , without TSP (red line), and with 50% NEG strip coverage (green circle). The average pressure is at ~3×10^{-10} Torr, except when 50% NEG strips are removed, where the average pressure increases five-fold, to 1.5×10^{-9} Torr.

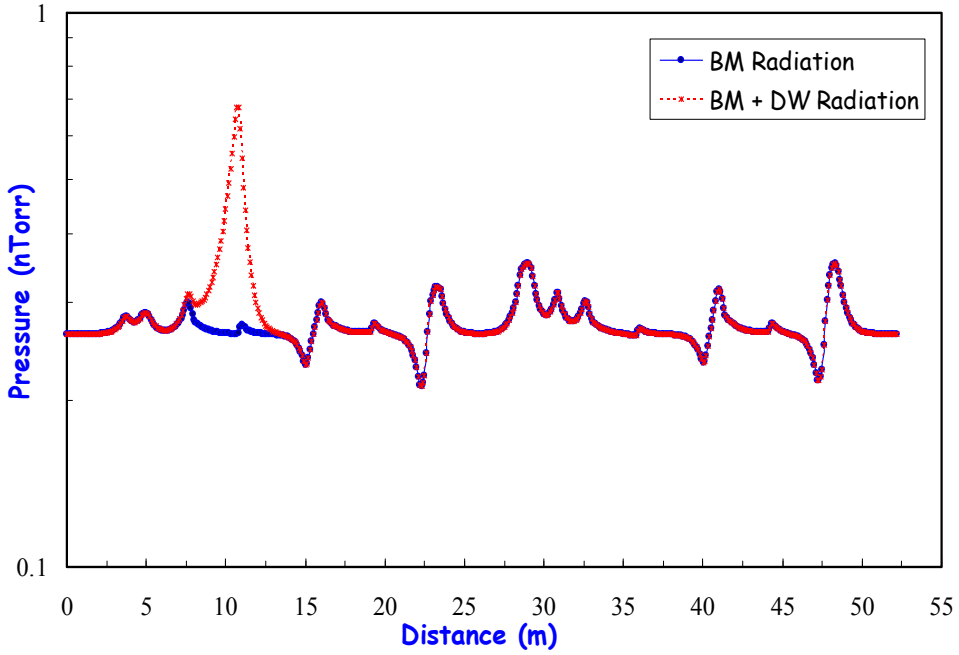

Figure. 7.3.8 Pressure distribution inside the electron beam channel in one 52 m super period with and without a damping wiggler. The crotch absorber intercepting the DW radiation generates a localized peak pressure with a 10% increase on the average pressure.

7.3.4 Vacuum Chamber Materials, Fabrication, and Treatment

Most of the storage ring vacuum chambers will be constructed from extruded A6063-T5 aluminum. This alloy was selected based on a comparison of various properties for commonly used vacuum chamber materials, as described below.

7.3.4.1 Selection of Chamber Materials

There are three common UHV materials suitable for the vacuum chambers of the electron storage ring: stainless steel, aluminum alloys, and OFHC copper, with stainless being preferred for a few new SR facilities in Europe, and aluminum for the new ones in Asia and the U.S. Copper was chosen for storage rings with high energy and high power density, such as the B-factories at SLAC and KEK, and also for its high thermal conductivity and radiation shielding properties. However, copper has the disadvantages of high material and fabrication costs. For the 3 GeV NSLS-II, radiation shielding and thermal conductivity requirements are not as critical as in the higher energy machines. Moreover, most synchrotron radiation from bending magnets will be removed by discrete copper or Glidcop absorbers. Therefore, copper has not been considered a preferred chamber material. The choice between stainless and aluminum for the NSLS-II cell chambers is based on experience at NSLS and APS, plus aluminum's vacuum and mechanical properties, ease of fabrication, and relatively reasonable cost.

One major difference between NSLS-II and other new SR facilities of comparable energy is the large bending magnet radius. The photon fan from the bending magnet will have a small dispersion and will be easily intercepted by discrete absorbers. This allows a narrow chamber geometry design; therefore, the cell chambers can be fabricated from extruded aluminum with uniform cross-sections. The need to accommodate the distributed NEG pumping also favors extruded aluminum, since an antechamber can easily be produced by aluminum extrusion. The cost of extrusion is considerably lower than that of chambers made of stamped stainless plates or machined aluminum plates, although the cost of machining the external chamber profile to fit the magnet poles and the various access ports will be significant. A few important arguments concerning the choice of material are listed and further discussed below.

Table 7.3.2 Electron Storage Ring Chamber Materials and Their Critical Properties.

Specifics	**Aluminum**	**Stainless**	**Copper**
Initial PSD rate	High	Low	Average
Mechanical strength	Acceptable	Excellent	Good
Thermal expansion	Large	Small	Small
Thermal conductivity	Excellent	Poor	Excellent
Weldability	Good	Excellent	Good
Beam impedance	Low	High	Low
Bi-metal flanges	Yes	No	Yes
Cooling channels	Extrusion	Brazed	Brazed
Fabrication cost	Low	Average	Expensive
Ease of in-situ bake	Good	Poor	Good
Radiation shielding	Poor	Average	Excellent

The outgassing of unbaked aluminum is higher than that of stainless, but an in-situ baked aluminum surface has similar or lower outgassing than that of stainless. The initial PSD rate of an aluminum surface is higher than those of copper and stainless. However, aluminum conditions faster and will reach the same PSD rate at a modest integrated beam dosage. The high thermal conductivity of aluminum offers distinct advantages over stainless, both during the in-situ bake and during normal operation. No conductive coatings or strips are needed on aluminum to reduce the chamber wall impedance, whereas stainless chambers may need copper strips and absorbers in certain locations and for mis-steered beam. Therefore, our preferred material to form the cell chambers through extrusion is aluminum A6063-T5 alloy. Stainless-to-aluminum bi-

metal Conflat flanges will be welded to the aluminum chambers, and standard copper seals can be used to form reliable joints between the chambers, bellows, and appendage components.

7.3.4.2 Vacuum Facility

To ensure the necessary chamber surface properties, cleanliness, mechanical quality, and leak tightness, vacuum facilities will be needed for cleaning, welding, assembling, and evaluating the vacuum chambers and other vacuum components for the storage ring and injectors. A dedicated chemical cleaning facility is required to clean the long chambers and other vacuum components. It will consist of four long, stainless steel tanks and a gantry crane capable of handling chambers up to 6 m long and 200 kG in weight. These tanks will provide ultrasonic cleaning with hot water, commercial bio-degradable cleaning agents, and de-ionized water rinse, and are suitable for aluminum, copper, inconel, and stainless chambers and materials. The exact cleaning recipe and process will be based on the chamber material and experience developed at other SR facilities such as NSLS and APS. Programmable robotic welding stations with laminar flow hoods will be set up to weld the cleaned chambers, the sub-assemblies, and the flanges. A Class 1000 clean room with ~100 m^2 floor space is needed for the assembly of the chambers with distributed NEG strips, ion pumps, gauges, absorbers, BPM buttons, and other components.

A facility with these capabilities was established at Argonne National Laboratory for the construction of the Advanced Photon Source. The NSLS-II project is evaluating the potential benefit of using the ANL/APS facility for the production, chemical cleaning, and automatic welding of the cell chambers of the NSLS-II vacuum system. Should this prove impractical for some reason, equivalent facilities will be established at BNL. Even if the ANL vacuum facility is utilized, a small chemical cleaning facility is still needed at BNL for storage ring and beamline vacuum components. The clean room and vacuum bakeout/evaluation stations are still required at BNL for the final assembly and evaluation of the cell chambers. If we do not utilize the APS facility and need to establish all of the capabilities at BNL, then ~2,000 m^2 of space would be required. If the ANL facility is used for production, cleaning, and welding, then ~1,400 m^2 would be required. Building 905 at BNL has been identified as the preferred location for the BNL vacuum facility. This building has more than 2,500 m^2 of space, as well as overhead cranes, and is available for use by the NSLS-II project.

7.3.4.3 Fabrication, Assembly, and Evaluation

Most of the storage ring chambers will be made of extruded aluminum. Immediately after extrusion, the long chamber sections will be stretched to obtain the uniform cross-section and to meet the dimensional requirement. They will then be cut to the designed length. The bending chambers will be formed to the curvature on a hydraulic press with a die of correct radius. To preserve the internal cross-sections, the inner volume of the bending chambers will be filled with DI water and frozen prior to the forming operation. The extruded chambers will be machined at industrial vendors to the appropriate external profiles and to add photon exit ports, access ports for BPM buttons, pumps, absorbers, and other vacuum components. The chambers will then be cleaned at the chemical cleaning facility and sealed in an aluminum bag filled with dry nitrogen gas for storage and further processing.

The aluminum chambers and flange adaptors are welded together with tungsten-inert-gas welding processes, using programmable robotic welding machines. The relative humidity of the laminar hoods over the welding zones will be reduced to less than 50% during welding to minimize oxide growth at the heat zone and to ensure weld integrity. Following welding, the vacuum chambers will be pumped down with a TMP backed by a dry mechanical pump, then checked for leaks using a leak detector with minimum helium sensitivity of 5×10^{-11} Torr-l/s. Specific procedures for repairing each type of weld leak will be developed to ensure that the quality of the chambers is not compromised. The cooling water channels will be leak-checked with vacuum and by sniffing while pressurized. The welded chambers are then brought into the Class 1000 clean room for assembly of peripheral components, such as BPM buttons, NEG strips, pumps, absorbers, and gauges. The chamber end flanges will then be capped with blank flanges.

The assembled chambers will be installed at the evaluation stands for final leak checking and bakeout at 130°C using temporary ovens. The vacuum level and the residual gas composition will be closely monitored during the bakeout, using vacuum gauges and RGAs, to ensure that the chambers remain leak-tight and are free of contaminants. All the pumps, gauges, BPM buttons, absorbers, and thermocouples are to be activated and measured to ensure their proper operation during the bakeout cycle. The possible use of a DC glow-discharge system to clean internal surfaces with an Ar/O_2 mixture during bakeout will be investigated for its merit versus the technical complexity and cost. After bakeout, the chambers will be either at storage vacuum or back-filled with dry nitrogen for the subsequent assembly into magnets and installation in the SR tunnel.

7.3.4.4 Installation, Alignment, and In-Situ Baking

During the machining of the vacuum chambers, all mounting holes for the survey fiducials will be checked against the beam channel cross-sections and the BPM mounting surfaces. To ensure precision alignment, the design of the vacuum chambers and the proposed alignment schemes will be reviewed and approved by the diagnostics, accelerator physics, and alignment and support groups. The required precision of the chamber alignment is ≤0.5 mm in general, and ≤0.1 mm for special parts such as the BPM buttons. The assembled and tested chambers will be installed into the split magnets and aligned using built-in adjustment bolts of the fixed support plates mounted on the girder. After the installation and alignment of individual chamber/magnet girders in the tunnel, the end capping flanges will be removed and the RF-shielded bellows will be installed and connected to the next cell chambers. Two sector gate valves will be mounted and supported on the end flanges of the #1 and #5 chambers of each cell. The magnet buses, cooling water lines, and vacuum equipment cables will then be connected prior to final measurement, pump down, leak check, and in-situ bakeout.

The in-situ bakeout of the storage ring cell in the tunnel will be carried out with pressurized hot water provided by the SR utility system. Additional heating jackets, heating tapes, and thermal insulation are needed for large appendage components, such as gate valves, ion pumps, etc., to ensure uniform temperature distribution, especially at large flange joints where uneven temperatures may result in seal failure and vacuum leaks. The supports for the chambers and the pumps must be adjusted to allow thermal expansion during the bake, while still maintaining and protecting the mechanical stability of the entire system. The storage ring cell will be pumped down with a turbopump backed by a dry mechanical pump during the bakeout. The vacuum level and gas composition will be continuously monitored using cell vacuum gauges and RGAs during the bakeout. The temperature of the chambers will be raised slowly by the hot water system and the heating jackets, and controlled by the bakeout programmable logic controller with inputs from the installed thermocouples on the chamber surface. The entire vacuum cell will be baked at 130°C for 40 hours to remove absorbed water and other contaminants from the surfaces. The sputter ion pumps, the titanium sublimation pumps, the NEG strips, and NEG cartridges will be degassed during the bake, then activated during the ramp down of the bake cycle. The bakeout of the whole cell will be completed in ~3 days, from Day 1 to Day 3, and can be comfortably fitted in a normal work week while still leaving sufficient time for any necessary remedial actions. The vacuum cell will be leak-checked again after the bake, using the cell RGA. The fixed support points on the chambers will be checked and adjusted to their original positions by the survey group to ensure that all the critical components are properly aligned.

7.3.5 Storage Ring Vacuum Pumping

The types and sizes of the pumps to be used at NSLS-II will be standardized throughout all the machine areas as much as possible, to lower the unit cost and to ease routine maintenance in the future. The selection of the pumps will be based on the experience of the existing pumps used in NSLS and other similar SR facilities.

7.3.5.1 Roughing Pumps

A set of TMPs backed by dry mechanical pumps will be used to rough down the vacuum section from ambient pressure to high vacuum, and during in-situ bake before turning on the in-line ultra high vacuum pumps. The TMPs will be connected to the vacuum sections through small, manually operated, all-metal angle valves. TMPs with magnetic or ceramic bearings of ~100 l/s size backed by dry pumps of ~5 l/s are deemed sufficient, since the ultimate pumping speed at the vacuum chambers is limited by the conductance of the chambers, the angle valve, and the flexible hose. TMPs will be manually valved out once the sector reaches ultra high vacuum. Each of the TMP stations will be equipped with vacuum gauges and electro-pneumatic valves to quickly and effectively isolate the TMP from the vacuum section in the event of pump or power failure. A dozen TMPs will be needed during the first phase of NSLS-II construction for component testing and leak checking. These TMPs, due to limited operating lifetime under heavy usage, will be replaced with newer models to meet required ring and beamline vacuum during NSLS-II commissioning and operation. A list of TMPs required for the operations at the storage ring is given in Table 7.3.3.

Table 7.3.3 List of Vacuum Pumps and Gate Valves for the Storage Ring and Font Ends.

	IP 400 l/s	TSP 500 l/s	NEG Lumped 500 l/s	NEG strips*~100 l/s/m	TMP portable	Gate valves
SR	150	150	60	150	10	60
Front end	60	60	0	0	4	30
ID	60	60	60	27	4	
Total	270	270	120	177	18	90

*Each chamber will have a pair of 3–5 m NEG strips for a total length over 1 km.

7.3.5.2 Ultra High Vacuum Pumps

After initial rough down and in-situ bakeout of the vacuum sectors, the system pumping will be transferred from TMPs to ultra high vacuum pumps, including SIPs, TSPs, NEG cartridges, and NEG strips. TSPs and NEGs have high pumping speed for active gases such as CO, CO_2, H_2O, and H_2 with equilibrium pressure down to 10^{-12} Torr; they, however, will not pump inert gases (CH_4, C_2H_6, etc.) nor noble gases (He, Ne, Ar, …). Sputter ion pumps will remove inert and noble gases as well as active gases.

Triode-type SIPs have better pumping speed for noble gases, but they tend to have higher current leakage and are harder to rebuild after electrode saturation. A few noble diode SIPs, with tantalum cathode plates and similar pumping speed as triode pumps for noble gases, will be used to supplement the regular diode-type SIPs, thus avoiding so called “argon instability.” Ion pumps of 30 l/s, 200 l/s, and 400 l/s will be used throughout NSLS-II, with the 30 l/s pumps used at conductance-limited areas such as booster synchrotron and beam transport lines; and the larger pumps at SR absorber and shutter locations. These SIPs will have large anode cells to retain sufficient pumping speeds down to the 10^{-10} Torr range. A DESY-style high-voltage feedthrough, which is less prone to radiation-induced corrosion at the brazing joint, will be used for the ion pumps. Commercial dual ion pump controllers with local and remote capabilities will power and monitor the SIP, by interfacing with the PLC and control computers, through hard wires and Ethernet linkage, respectively. Ion pump currents will supplement the vacuum gauges to provide pressure distribution over the whole ring. However, due to the buildup of leakage current in the ion pump elements, the reliable pressure reading from ion pumps is limited to the mid 10^{-10} Torr range. A list of ion pumps for the storage ring is given in Table 7.3.3.

The large volume of active gases desorbed from the photon absorbers can be efficiently removed from the SR by localized TSPs of ~500 l/s, thus minimizing the quantity of gases diffused back to the electron beam channel. Alternatively, at absorbers for damping wigglers, with a modest increase in cost TSPs may be replaced with NEG cartridges of comparable pumping speed but higher capacity between the reactivations. Both TSPs and NEGs can be activated and reactivated locally or remotely. However, TSPs have the advantage of only generating a brief gas burst during their short sublimation period, while NEG activation

takes longer, during which time a larger amount of hydrogen is produced and must be removed by the portable TMP stations.

Distributed NEG pumping in the form of NEG strips, similar to those employed at the APS storage ring, is planned for use in all cell vacuum chambers. This is deemed efficient to provide linear pumping to the beam channel through the photon exit opening. Dual strips will be mounted on the top and bottom of the antechamber. There will be sufficient clearance between the two mounted NEG strips to allow the passage of photons, even when a beam mis-steers. The mounting of the dual strips will be carefully designed and thoroughly tested to eliminate any potential electrical faults during in-situ bake and NEG activation. The NEG activation is at 400^{o}C for 30 minutes and will be achieved with resistive heating of the NEG strips with ~45 ampere current, carried out at the end of in-situ bakeout or during the machine maintenance period. The two NEG strips together will provide more than 240 l/s per meter pumping speed for active gases such as CO and H_2 even after pumping ~0.1 Torr-l per meter of active gases, corresponding to a few months of beam operation at 10^{-9} Torr pressure.

Some of the ID vacuum chambers will have very small gaps, resulting in limited linear conductance. In these cases it is not effective to simply rely on the lumped pumps located at both ends of the chamber. Sputter-coated NEG thin film has been applied to the inner surface of ID chambers at several SR facilities, notably at ESRF, where 20 ID chambers have been coated and in operation for 5 years, and at Soleil, where most straight chambers have been NEG coated. For narrow-gap undulators at NSLS-II, NEG coating will be considered during the design stage; if appropriate, it will greatly simplify the pumping system design. For long straight sections that are not occupied by insertion devices, distributed NEG strips together with large ion pumps and titanium pumps will be installed to maintain ultra high vacuum.

7.3.6 Vacuum Measurement and Control

7.3.6.1 Monitoring and Control Methodology

The vacuum level in the storage ring, the front ends, and the beamlines will be monitored and interlocked with the ion pump current and with vacuum gauge readings. Residual gas analyzers will also be used for online monitoring and diagnosis. Each vacuum sector will have a convection-enhanced Pirani gauge and two ionization gauges as the primary vacuum gauges. Additional vacuum gauges will be installed to protect the RF cavities and kickers. Vacuum devices such as gauge controllers, ion pump controllers, gate valve solenoids, and valve position indicators—with local and remote capabilities—can be operated through front-panel switches. Their communication with the equipment control system will be through RS232 or Ethernet links for remote monitoring and control. It is anticipated that most of the vacuum controllers will be off-the-shelf items purchased through competitive bids from qualified vendors.

Due to the predicted high level of radiation in the SR tunnel, controllers for vacuum systems will be placed in satellite electrical racks located outside the storage ring shielding structure. Electrical power for vacuum diagnostics and controllers will be standard 115 V AC and 60 Hz. Since vacuum pumps and associated vacuum equipment surrounding the ring vacuum chambers are subjected to synchrotron and bremsstrahlung radiation, radiation-resistant cables and appropriate routing for wire extensions will be employed to minimize radiation damage.

7.3.6.2 Vacuum Gauges

One primary vacuum gauge, a convection-enhanced Pirani gauge, will be installed in each vacuum sector to provide pressure readings ranging from atmospheric pressure down to 10^{-4} Torr. It will also be used for other vacuum equipment protection and interlocking. Two ion gauges, either Bayard-Alpert ion gauges or inverted-magnetron cold cathode ion gauges, will be installed at each SR vacuum section as the primary UHV gauge. The same type of ion gauge will be used for injectors, beam transport lines, front ends, and user

beamlines. Both types of ion gauges have a useable pressure-sensing range down to 10^{-11} Torr and they have been implemented successfully at various synchrotron radiation facilities. CCGs have the advantage of overlapping the lower end of the Pirani gauge range and can be operated through long cables for signal transfer, thus eliminating the necessity of locating electronics nearby. CCG tubes do not have built-in hot filaments and are therefore less susceptible to mishandling and filament breakage during startup and commissioning. The accuracy of CCG readings is normally at ±50%. Moreover, it is difficult to de-gas CCGs once they are contaminated. CCGs are still our choice at this point in the design process. The numbers of vacuum gauges in each area of the storage ring are listed in Table 7.3.4.

Table 7.3.4 Number of Gauges and Residual Gas Analyzers in Various Areas of the Storage Ring.

	TCG*	Ionizing Gauge	Residual Gas Analyzer
SR	30	60	34
Front end	30	60	60
ID	30	60	10
Total	**90**	**180**	**104**

*TCG = convection-enhanced Pirani gauge

Interference with the gauge readings due to the presence of copious electrons, photons, and photoelectrons has been observed at many SR facilities. Therefore, if practically achievable, the gauge tubes will be mounted on elbows at shielded ports on the vacuum chambers to minimize interference and erroneous pressure readings. The gauge tubes will also be installed in areas with minimal stray electrical and magnetic fields. Radiation-hardened material such as Kapton-insulated cables will bridge the short distance between the chamber gauge ports and the cable tray to ensure system reliability. Kapton cables are bakeable up to 200^{o}C. Microprocessor-based multi-gauge controllers will be used to control the vacuum gauges and to provide system monitoring and control through RS232 or an Ethernet bus. The controller will be hardwired to interlocks through PLCs to gate valves and other beam components and subsystems.

7.3.6.3 Residual Gas Analyzers

Quadrupole-type RGAs will be installed to measure the partial pressures of residual gas species at selected locations in the injectors, storage ring, front ends, and user beamlines. Their use will help to identify sources of residual gases, including photon-desorbed gas from chamber walls and absorbers, air leaks, cooling water leaks, oil back-streaming, specialty gases back-streamed from the beamlines, and other contaminants. RGAs with electron multiplier will have partial pressure sensitivity down to the 10^{-13} Torr range. Due to the high cost, RGAs may only be installed at some vacuum sections during the initial phase of NSLS-II operation. The RGAs' quadrupole mass filter RF box, which contains sensitive electronics, may be located near the head and needs to be shielded from synchrotron radiation. The PC-based control units for RGAs, however, will be located at the satellite control racks, to allow easy access for online analysis and maintenance. The number of RGAs estimated for the storage ring and front ends is listed in Table 7.3.4.

7.3.6.4 Vacuum Control and Equipment Protection Systems

The vacuum control system has to 1) monitor and control all the vacuum equipment including gauges, pumps, valves, etc., to ensure that they are operating properly in their appropriate ranges; 2) collect and archive the data for instant display and alarm and for off-line analysis; and 3), most importantly, interlock and protect the storage ring and injector from harm before damage can develop.

The vacuum control system will interface directly with each vacuum device, and as part of the storage ring equipment control and protection systems (EPS). Due to high radiation levels in the storage ring tunnel, all the vacuum devices and the vacuum control system will be located at the satellite control racks. They will be backed by uninterruptible power supplies. Vacuum devices include gauge controllers, ion pump

controllers, chamber and absorber temperature readouts, cooling water flow sensors, and gate valve solenoids. They can be operated via front-panel switches and with the machine control system through RS232 or Ethernet links for high-level monitoring and control. The low-level vacuum controls, consisting of several dedicated PLCs with digital and analog I/O modules, take inputs from the vacuum devices and send out commands through dry contact circuits. The PLCs, with their own microprocessors and operating systems, will be programmed by vacuum system experts and provide the logic for the operation and control of the vacuum devices.

For gate valve control, the PLCs will use a voting scheme, with inputs from the setpoint contacts of several gauges and pumps, to initiate valve interlock and closure, therefore minimizing false triggering due to the malfunctioning of a single gauge or pump. The PLC for the water flow and temperature monitoring system, with direct inputs from thermocouples and flow meters, will read and compare those with the pre-set values. An out-of-range alarm from this PLC will trigger an output to the EPS to abort the beam, thus preventing overheating of the chamber wall or absorbers, due to either the malfunction of the cooling water system or abnormal beam steering. The PLC outputs for the flow meters, the temperature readouts, and gate valve status will be part of input arrays to the EPS, which will be used to determine if conditions are unacceptable. When warranted, the EPS will initiate a fast beam abort by interrupting the low-level RF power to the accelerating cavities. The stored beam would coast inward to a scraper and be lost in a fraction of millisecond.

References

[7.3.1] J. Noonan, J. Gagliano, G.A. Goeppner, R.A. Rosenberg, and D.R. Walters, "APS Storage Ring Vacuum System Performance," Proc. PAC97, p 3552-5 (1998).

[7.3.2] C. Doose, L. Emery, and S.H. Kim, "Investigation of the Surface Resistivity Tolerance of the Kicker Ceramic Vacuum Chamber at APS," Proc. PAC01, p1491-3 (2001).

[7.3.3] J. Jones, S. Sharma, and D. Bromberek, "APS SR Flexible Bellows Shield Performance," Proc. PAC99, p 3095-7 (2000).

[7.3.4] C.L. Foerster, C. Lanni, and K. Kanazawa, "Measurements of photon stimulated desorption from thick and thin oxide of KEKB collider copper beam chambers and a stainless steel beam chamber," *J. Vac. Sci. Technol. A* **19**, 1652 (2001).

[7.3.5] C.L. Foerster, C. Lanni, J. Noonan, and R.A. Rosenberg, "Photon stimulated desorption measurements of an extruded aluminum beam chamber for the Advanced Photon Source," *J. Vac Sci. Technol.* A14, 1273 (1996).

[7.3.6] V. Anashin, et al., "Photodesorption and Power Testing of the SR Crotch-Absorber for BESSY-II," Proc. EPAC98, p. 2163 (1999).

[7.3.7] R. Kersevan, "MOLFLOW User's Guide," Sincrotrone, Trieste Technical Report, ST/M-91/17 (1991).

[7.3.8] M.K. Sullivan, "A Method for Calculating Pressure Profiles in Vacuum Pipes," PEP II AP Note No. 6-94, March 1994. (Vaccalc is a software using the finite differential method for pressure calculation.)

7.4 Beamline Front Ends

7.4.1 Scope

The beamline front ends connect the storage ring to the user beamlines and provide radiation protection to personnel. Most of the front-end components generally reside within the storage ring's shield wall, outboard of the dipole vacuum chamber. The major components of the beamline front-ends are photon masks, shutters, heat absorbers (such as beam-defining apertures and/or slits), fast valves (or other shock wave protection devices), vacuum isolation valves, beryllium windows, or other means of pressure isolation sensors, and diagnostics. Vacuum chambers are also included; however, the chambers are often part of the individual front-end components. Other components, such as filters, may be included depending on the application. The front end usually starts at the exit to the dipole vacuum chamber and usually extends to the beryllium window (if used), where the user vacuum is isolated from the machine vacuum. If a beryllium window is used, it generally is positioned as close as is practical to the outer end of the storage ring shield wall. Also to be considered as important front-end components are radiation shields, i.e., safety shutter shields and bremsstrahlung shields. Vacuum pumps, vacuum sensors, and diagnostics (e.g., for Residual Gas Analysis, to activate fast valves, etc.), heater tape and provisions for bakeout, as well as the vacuum valves are included in the front ends—even though these components are generally considered part of the vacuum system. Steel stands will be designed, as needed, to support the front-end components at the nominal 1 m beam height.

The details of the front-end components will differ based on the radiation source. The front ends may transport x-rays from a bending magnet or from an insertion device. The resulting photons may be collected and directed down a beamline, or absorbed as heat. For the bending magnet beamlines, the front-end designs can differ according to the angle (in mrad) of radiation and number of apertures (and therefore beamlines) in each heat absorber that allows synchrotron radiation to pass through. For insertion device front ends, the type of insertion device used (e.g., undulator or wiggler), and its magnetic properties (field strength, length of field, periodicity, etc.) determine the radiation output parameters (e.g., radiation fan, output power density, and total radiated power). The heat-absorbing-components in each front end therefore need to be set according to the radiation source parameters. These parameters are selected according to the research needs of the scientific program served by each beamline. The front-end components and the arrangement of components therefore will differ somewhat according to the specific front end.

The vacuum aspects of the front ends include the gas loading (including outgassing loads from the heat absorbers) and pumping characteristics. The front-end vacuum system must maintain and measure acceptable vacuum pressures within the vacuum chambers in the front end and must be compatible with the storage ring vacuum. Vacuum isolation valves are included to allow the removal and replacement of front-end components. Since there is no vacuum isolation during operations between the front ends and the storage ring, the front ends share machine vacuum from the exit of the storage ring chamber to the beryllium window (or other vacuum isolation provision). The vacuum system may differ slightly between beamline magnets and front ends. The vacuum system components must function in conjunction with the front-end components, however. Therefore, some front-end vacuum system aspects are included in this section as they relate to the front end components.

Vacuum isolation provisions between the front end and the downstream beamline are necessary. For hard x-ray beamlines, this usually takes the form of a beryllium or a CVD diamond window, which is under consideration for NSLS-II. However, for beamlines such as VUV and soft x-ray beamlines, as well as the hard x-ray beamlines that cannot tolerate the presence of a window (due to its potential to introduce optical artifacts into the transmitted beam), "vacuum isolation" must be implemented without a solid window separating the front end and beamline vacuum spaces. A differential pumping stage can address this requirement. A commercially available device, which could permit a downstream beamline to operate at a

pressure as high as 10^{-4} Torr while still preserving a pressure of 10^{-9} Torr in the front end, is used on several beamlines at APS for this purpose. This device consists of an inline ion pump with internal throttles to limit conductance, yet it offers a sizable clear aperture for the beam.

Note that the inclusion of such a device between the front end and the beamline does not obviate the need for sensitive pressure diagnostics along the beamline, as well as protective measures such as fast-closing valves in case of accidental vacuum breaks along the beamline.

7.4.2 Mechanical Design

Six front-end configurations are currently anticipated, based on radiation source type and concomitant characteristics of output, geometry, and power loading. The six sources are 1) superconducting wigglers, 2) cryogenic permanent magnet undulators, 3) superconducting undulators, 4) damping wigglers, 5) normal conducting and permanent magnet insertion devices, including soft x-ray undulators and elliptically polarized wigglers, and 6) bending magnet beamlines. Figure 7.4.1 shows a conceptual layout of the mechanical design for a typical hard/soft x-ray beamline front end.

The storage ring lattice constrains the length available for insertion devices. Fifteen 5 m straight sections and twelve 8 m straight sections are available for insertion devices. The design parameters for the various radiation sources currently expected at NSLS-II are given in Chapter 8.

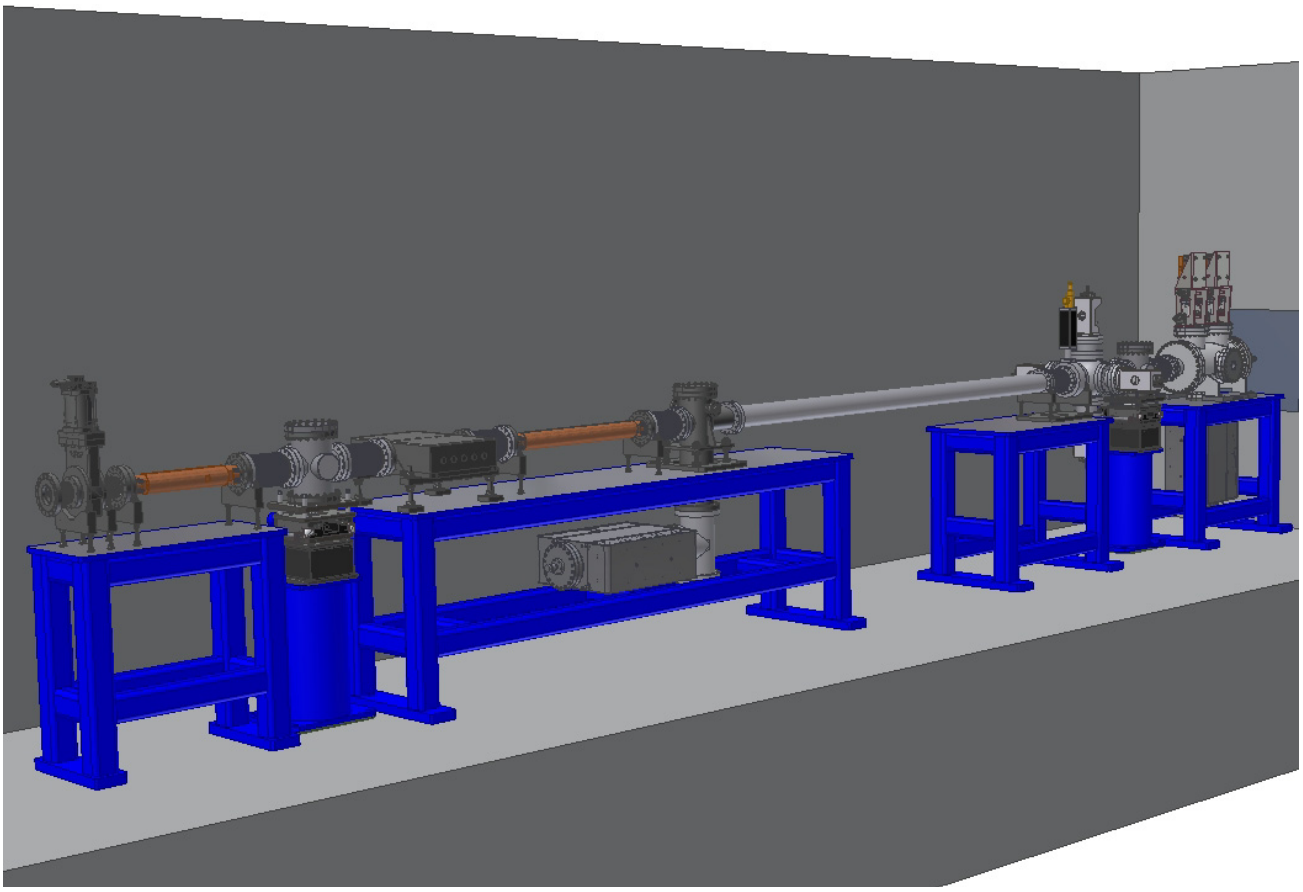

Figure 7.4.1 Typical layout of a hard or soft x-ray beamline front end. From left to right: UHV gate valve, fixed aperture photon mask, first, photon beam position monitor (BPM1), collimator, photon shutter, four-way cross for ion pump, spool, fast valve, beam defining aperture, second photon beam position monitor (BPM2), and safety shutter.

7.4.3 Vacuum Components/Enclosures

The front end will consist of numerous ultra high vacuum chambers that house heat absorbers, beam diagnostics, and personnel protection devices, along with beam chambers to transport the photon beam from the electron storage ring to the experimental beamlines. These chambers and ducts will be constructed from 304L stainless steel tubes and weldments, where applicable, and will be joined to adjacent components using commercially available Conflat flanges, copper gaskets, and UHV hardware. Fabrication of chambers and ducts will be from stainless steel utilizing TIG-welded construction.

Because the front ends share the storage ring vacuum, front-end and SR vacuum pressures must be compatible. A pressure of 10^{-9} Torr therefore must be maintained in the beamline front ends during machine operations. To achieve these pressures, a combination of UHV components and procedures, in addition to bakeout of the front-end subsystem, will be employed. The chambers and beam ducts will be designed to withstand a bakeout temperature of 200°C, to accelerate the release of gases. We expect that an integral bakeout system will be incorporated in the beamline front end, to enable the capability of in-situ bakeout. Commercially procured equipment to accomplish this task within the stated parameters will be selected.

Each front end will employ a commercially available UHV all-metal gate valve. This valve will be used to separate the front-end from the SR vacuum for bakeout, maintenance, and during installation of the front end. Additionally, this valve will be used in combination with a commercially procured UHV fast-closing valve to protect the SR vacuum in the event of a vacuum breach from the beamline. The fast valve should close in less than 15 msec and have a leak rate of less than 7.5×10^{-10} Torr-l/s when closed. We plan to use this isolation valve in combination with a water-cooled bending magnet photon shutter [see Figure 7.4.2(c)] to accept the synchrotron radiation at the exit ports where no front end is installed.

Referring to Figures 7.4.2a and 7.4.2b, two ion pump/titanium sublimation pump combinations are planned, located strategically in each beamline front end. In order to minimize any residual gas species generated by the photon beam impinging on a surface, a 400 l/s ion pump/TSP pair will be installed near the photon shutter locations. An additional 400 l/s ion pump/TSP pair will be installed at the safety shutter due to the relatively long distance (approximately 5 m) between the photon shutter and the safety shutter—a section of the beamline front end that would otherwise have no dedicated vacuum pumping.

The front end configuration shown in Figure 7.4.2a reflects our current thinking of what is required to serve a beamline supporting a hard x-ray nanoprobe instrument. It includes a combination of a fixed mask and moveable slits to define the beam size as close to the undulator as possible. This is not likely to be necessary for most beamlines, and so they will only have a beam defining aperture, as shown in Figure 7.4.2b. This is an example of some of the differences that may be required in the design of front ends to optimally serve each beamline.

The front ends for beamline ports that have not yet been allocated will be configured with a photon shutter, gate valve, and bremsstrahlung beam stop, as shown in Figure 7.4.2.c. Once a beamline port is allocated, the front ends will be configured to meet the specific requirements of the beamline it will serve. Since those requirements may vary for different beamlines, the detailed design and construction of front ends will occur as part of the design and construction process for each beamline.

An all-metal right-angle valve will be located between the photon shutter and the fast-closing valve. Attached to this valve will be a fitting with both an ion gauge and an RGA to monitor the total and partial pressures of the front-end vacuum. At the remaining port of the cross, a valve will be installed (to be used in combination with the right-angle valve) to allow for venting and pump-down when replacing either the ion or RGA gauge filaments. Additionally, installation of a vacuum valve between the fast-closing valve and the second BPM is planned to allow for separate venting/pump-down of the downstream portion of the front end.

To allow for transverse offsets in front-end hardware, thermal expansion and/or contraction, and to allow for sufficient flexibility in the alignment of front-end devices, an appropriate number of welded bellows assemblies will be part of the front-end vacuum system.

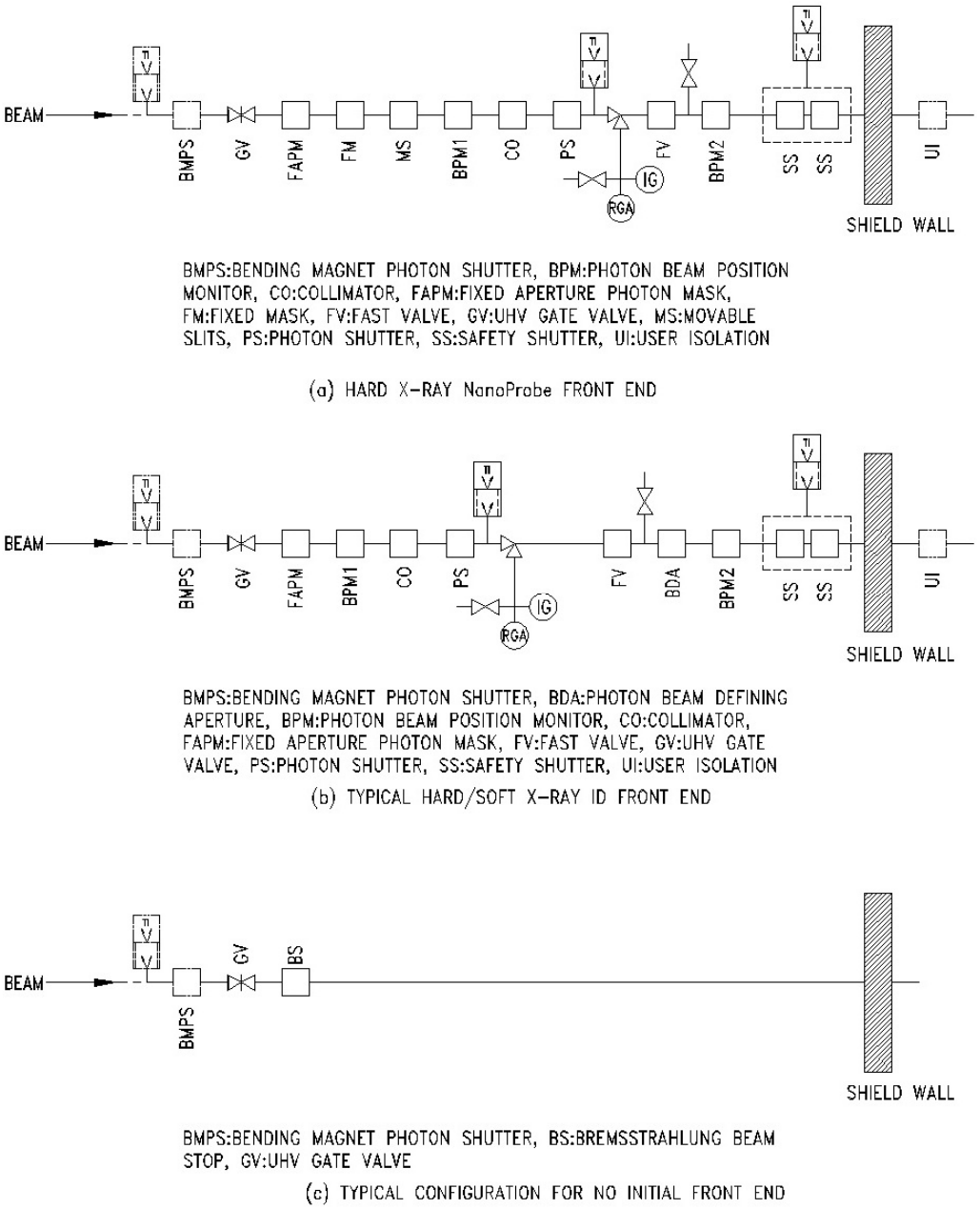

Figure 7.4.2 Front-end schematic representation of: **a)** the Hard X-Ray NanoProbe front end, **b)** typical Hard/Soft X-Ray insertion device front ends, and **c)** exit ports with no initial beamlines.

7.4.3.1 Heat Absorbers

Heat absorbers are front-end devices consisting of components whose function is to absorb the synchrotron radiation produced by the SR bending magnets or IDs. These absorbers are needed to: 1) stop dipole radiation in the exit ports that have no front ends, 2) prevent uncooled surfaces in the front ends from being impacted by a mis-steered beam, 3) protect the uncooled safety shutter shielding blocks, and 4) completely prevent the photon beam from being transported beyond the front end. The heat-absorbing devices needed to accomplish these tasks are a bending magnet photon shutter, a fixed aperture photon mask, and a photon shutter.

Heat-absorbing front-end components are designed based on the horizontal and vertical angular divergence and the power density distribution of radiation produced by each insertion device, as well as on temperature criteria. As an example (referring to Chapter 8), for the CPMU device at a distance of 15 m from the source, the peak heat flux of the insertion device radiation is approximately 11.6 W/mm^2, with a total power of 11.1 kW at 3.0 GeV and 500 mA. We assume that an electronic active-interlock system will be used to reasonably limit the electron beam orbit so that the photon beam cannot illuminate any uncooled surfaces of the storage ring vacuum chamber. For thermal calculation purposes, we assume that there is a ±2 mm offset to accommodate beam deviations in position and minor manufacturing and alignment errors. The electron beam may also have an angular steering error of ±1 mrad.

Since the storage ring isolation valves are uncooled, dedicated heat absorbing devices capable of protecting the valves from the incident dipole magnet radiation are required. A bending magnet photon shutter will be installed upstream of the UHV isolation gate valve, which is the first vacuum component in the front end (see Figure 7.4.2a). Due to the rather low power density produced by the dipole magnet radiation, a normal incidence, water-cooled device will be sufficient. For heat-absorbing devices that experience relatively low peak temperatures (less than 200˚C), OFHC copper will be the material of choice for all heat absorbing surfaces. We anticipate that the BMPS, which is not a high heat flux device, will meet this criterion and that it will be possible to procure and install a commercially available version.

The **f**ixed-**a**perture **p**hoton **m**ask is the first front-end component that may be impacted by the photon beam. The FAPM protects front-end components that are not designed to withstand the thermal loading of the photon beam, in the case of beam mis-steering. For this reason, the photon mask must close when the front-end vacuum valves close. For commonality, the initial overall engineering design approach for the FAPM and the photon shutter will be similar. The heat absorbing surfaces of the FAPM will be designed from a single solid piece of Glidcop to handle the high heat flux of the insertion devices. To accommodate the dissipation of the full insertion device power, the aperture of the FAPM will be tapered on all four sides. The mask will be designed such that when the final geometry is fixed, the converging aperture will taper to 7.5 mm (V)×30 mm (H) at the downstream end of the device. Integrally machined cooling passages on all four sides will provide pathways for the flow of coolant. Since the FAPMs will be designed to withstand vacuum forces, a separate vacuum chamber will be unnecessary. Also, since the FAPMs will be infrequently subjected to the full ID power, a higher peak temperature will be allowed than for similar masks that are cyclically loaded.

Recent experimental results at both APS and ESRF have concluded that for Glidcop devices, a maximum calculated temperature of 500˚C is sustainable for 10,000 thermal cycles [7.4.1]; therefore, this will be our thermal design criteria for high heat flux devices which are not cyclically loaded. From preliminary photon shutter thermal calculations, a 4° (70 mrad) angle of incidence to the nominal should provide adequate thermal loading reduction for the FAPM heat-absorbing surfaces. Careful calculations and detailed study will be carried out in the preliminary design phase to ensure that the devices are optimized for the high heat loads encountered.

The photon shutter is a device that can be opened to allow photons to be directed down each beamline. One method to accomplish this would be to tilt a photon shutter similar in design and construction to the FAPM so that one of the inclined, heat-absorbing surfaces completely intercepts the photon beam when the photon shutter is in the closed position. To minimize design and fabrication costs, all heat-absorbing surfaces of the photon shutter will be designed and fabricated from Glidcop, similar to the FAPM. As with the FAPM, integrally machined cooling passages will provide coolant flow to remove the thermal load. Figure 7.4.3 illustrates a conceptual design for the photon shutter (*PS* in the figure). In addition to the cooling passages on the horizontal heat absorbing surfaces (as shown in the figure), the photon shutter would have an additional set of machined cooling passages adjacent to each vertical heat-absorbing surface. During the design phase, the requirements for each photon shutter will be considered carefully for each application. A photon shutter design that can accommodate most or all front-end applications will be considered, to minimize engineering and design labor, to keep manufacturing costs low, and to maintain commonality of components wherever possible.

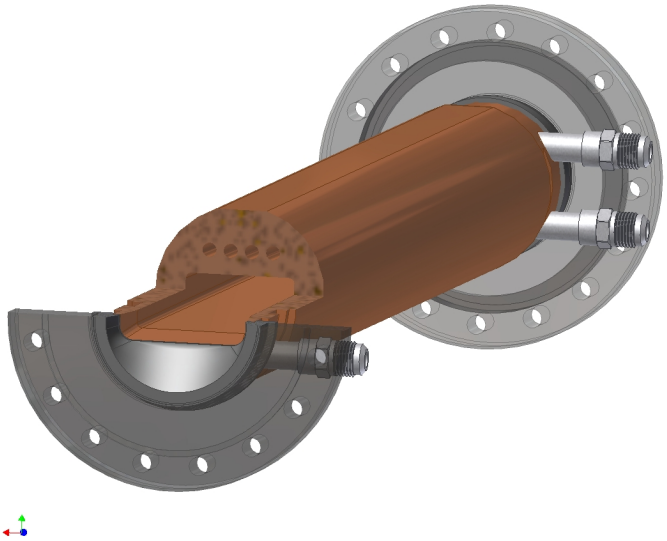

Figure 7.4.3 Conceptual design of the NSLS-II photon shutter.

Preliminary calculations indicate that an angle of incidence of 4˚ between the nominal photon beam centerline and the inclined surface of the photon shutter aperture will allow us to maintain the design specification for Glidcop of $T_{max} \leq 450$˚C. Figure 7.4.4 shows the results of a steady-state, 2D finite element computation for the CPMU device listed in Table 7.4.1, at 3.0 GeV and 500 mA and a distance of 17 m from the source. That figure shows the thermal gradient that results from completely intercepting the ID radiation with the heat absorber directly in the photon beam path. This simulation was computed using a heat transfer coefficient of ~1.6 W/cm^2/˚C for each cooling channel. The final optimized design of the photon shutter must recognize that the 4˚ inclined surface incorporated in the simulations includes both the angle the device is rotated through to close off the photon beam, as well as the angle of inclination of the heat-absorbing surface.

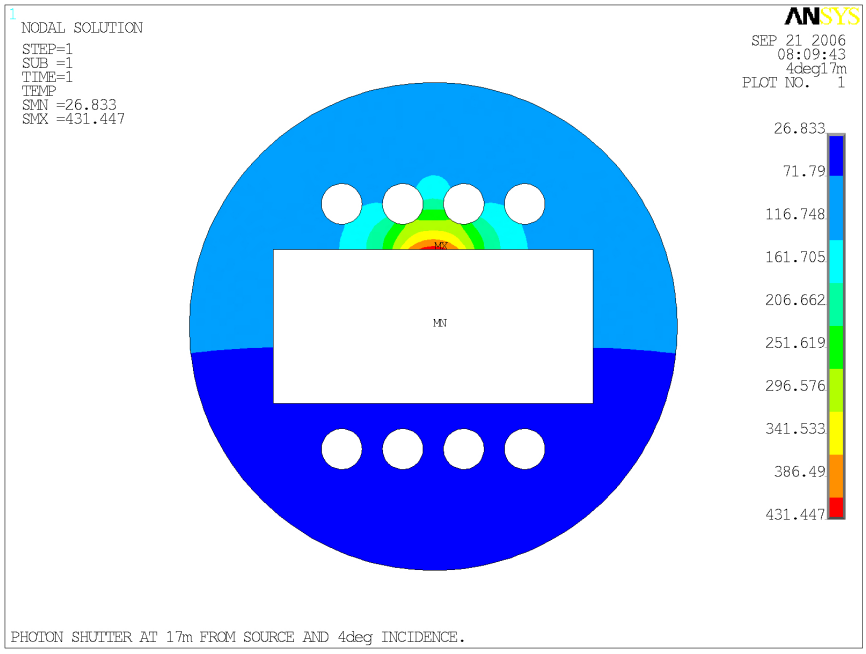

Figure 7.4.4 Steady-state temperature distribution from 2D finite element analysis simulation of the photon shutter. Temperature units are degrees Centigrade.

Additional specific requirements for beamline front ends that require specialized collimating or beam-defining apertures downstream of the FAPM will not be specified until those beamlines are designed. We nevertheless expect, however, that one additional photon-collimating aperture will be needed in most front ends. Therefore, a generic BDA will be included as a placeholder in these front ends until specific requirements are developed. Any additional photon collimating devices will be located in the individual beamlines outside of the x-ray ring's outer shield wall.

7.4.3.1.1 Hard X-Ray Nanoprobe Beamline Masking Requirements

The Hard X-ray Nanoprobe Beamline has unique requirements. Two additional BDAs (listed as moveable and fixed masks in Figures 7.4.2a and 7.4.5) are currently planned for this beamline front end. The first BDA downstream of the FAPM in the Nanoprobe Beamline front end (in Figure 7.4.5, listed as "1st fixed mask") will be located as close to the undulator source as possible. This BDA is fixed in space and serves as a guard, reducing the size of the initial undulator x-ray beam to the desired maximum beam size accepted by the beamline. The second absorber (listed as "2nd moveable mask" in Figure 7.4.5) is not fixed. It can be moved into the beam for a high-spatial-resolution mode and removed for high-flux mode. When in the beam, it provides a beam-defining horizontal constriction equal to the vertical FWHM extension of the beam. When removed, it passes the full beam unobstructed. These two additional absorbers are shown without the other front-end components in Figure 7.4.2. For an x-ray wave length of 1 Å (~12.4 keV), the following values were used to help estimate the absorber geometric requirements.

horizontal source size, σ_x	▪	84.5 μm
vertical source size, σ_y	▪	4.3 μm
horizontal source divergence, σ'_x	▪	18.2 μrad
vertical source divergence, σ'_y	▪	1.8 μrad
length of undulator, L	▪	5 m

In this application, placement of the first absorber at 14 m or less and the second absorber at 15 m or less from the undulator is desired for best optical properties of the photon beam. The aperture openings for the first absorber are calculated to be X1 ≈ 1400 μm and Y1 ≈ 300 μm. For the second absorber, the settings calculated are X2 ≈ 180 μm and Y2 ≈ 2 mm. The need for further vertical collimation at the second absorber in this beamline is currently not required; therefore, we will consider a design for this device similar to those in use at APS.

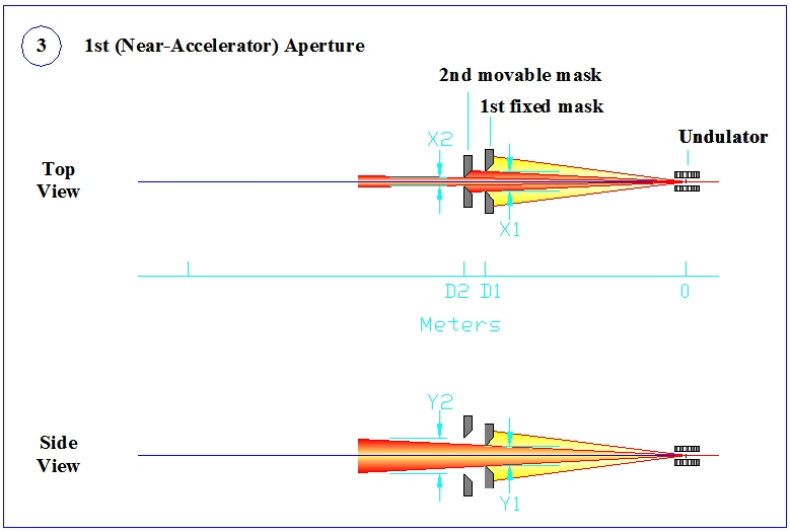

Figure 7.4.5 Absorber geometry for a nanoprobe beamline front end.

7.4.3.2 Radiation Protection

At times during storage ring operations, it will be necessary to access the experimental hutch (for example, to set up equipment and change samples). It will also be necessary to assemble and maintain the beamline apparatus when there is stored beam in the accelerator. To accomplish these tasks, a remotely actuated safety shutter will be required as one of the front-end components. For redundancy purposes, this component will consist of two identical tungsten shielding blocks housed in a single UHV-compatible vacuum chamber in each front end. The shielding blocks may be inserted into (or retracted from) the path of the bremsstrahlung radiation cone. There will be no need to provide active cooling for this device because the photon shutter, which is located upstream of this device, will completely absorb the synchrotron radiation.

The remotely actuated safety shutter device is a required part of a beamline personnel protection system, which should absorb the bremsstrahlung radiation, thus providing protection from ionizing radiation for personnel downstream of each shutter. From calculations, a thickness of 20 cm of tungsten is required to attenuate the bremsstrahlung radiation in the forward direction. Ray-tracing will be required to determine the transverse dimensions of the tungsten shielding. Additionally, lead collimators will be provided in each front end to confine the bremsstrahlung cone in the downstream experimental area. From calculations, a thickness of at least 30 cm of lead for the collimators will be required to attenuate the bremsstrahlung radiation in the forward direction. As with the tungsten shield of the safety shutter, ray-tracing will be performed to determine the minimum transverse dimensions of lead required. For exit port chambers that have no initial complement of front-end components, it will be necessary to install a bremsstrahlung beam stop as close as possible to the storage ring vacuum isolation valve (see Figure 7.4.2c).

A byproduct of the bremsstrahlung/lead collimator interaction is the production of neutrons that ultimately must be shielded. The concrete used in the shielding wall is a very effective neutron shielding material; however, there will be beampipe penetrations through the shield wall that must be considered. Void volumes between the shield wall and front-end beampipe penetrations will be filled with concrete and lead, to terminate the transit of photons and neutrons beyond the shield wall. For exit ports with no front end, the shield wall window will be completely filled with concrete.

7.4.3.3 Diagnostic Equipment

To correct for unwanted mechanically and electrically induced electron beam motions, two x-ray beam position monitors will be designed and installed in each front end as part of an orbit feedback system. These BPMs will detect photon beam position and supply information to an active feedback system that will correct the electron beam orbit. We anticipate that two gapped, blade-type BPMs will be installed to detect any closed-orbit instabilities. By utilizing two x-ray BPMs in each front end, it will possible to correct for both angular and displacement steering errors. To more accurately measure any angular steering error, it is most desirable to take advantage of the increased lever arm by placing the second x-ray BPM as far downstream as possible within the confines of the front end enclosure.

7.4.3.4 Interlocks

The two safety shutters and the photon shutter will provide a redundant means of absorbing the full synchrotron power and bremsstrahlung radiation in the beam. The Personnel Protection System will monitor the position of these devices to provide personnel at the beamline safety from prompt radiation. The Equipment Protection System will control the sequencing and control of front-end devices and prevent damage from occurring. The EPS will prevent damage to front-end components by sensing position, water flow, and vacuum, then taking action by operating components or dumping the beam, when appropriate.

To protect the storage ring vacuum from any inadvertent pressure rise due to front-end or beamline component failures, various interlock sequences will be implemented. Two possible scenarios in which an air-to-vacuum leak in the front end would corrupt the SR vacuum are mentioned here as examples: 1) a slow air-

to-vacuum leak due to faulty bellows or a leaking weld in a vacuum chamber, and 2) a catastrophic vacuum leak due to a failure in a beamline.

If monitoring of the vacuum quality (see Figure 7.4.2a) indicates a slowly increasing pressure, the origin of this pressure rise will be investigated and repaired during a regularly scheduled maintenance period. Should the pressure in the front end reach the ion gauge set point of approximately 5×10^{-7} Torr, the EPS will first signal the insertion device on the offending beamline to open its gap, thereby eliminating the high heat flux on any front-end components. The bending magnet photon shutter will then be actuated to provide dipole radiation protection to the uncooled isolation valve when it has been moved into the closed position. Finally, first the photon shutter and then the safety shutters will be the last devices instructed to close. With the storage ring isolation valve in the closed and sealed position and Personnel Protection System in place, ring operations will be allowed to continue unhindered by the vacuum leak in the front end. The front end or beamline experiencing such vacuum difficulties would be repaired during a regularly scheduled maintenance period. Note that all of these front-end actions will be taken in the background while facility operations continue unhindered.

In the case of a catastrophic leak, once the fast closing valve is triggered by a pressure exceeding 5×10^{-6} Torr in the front end or beamline, the EPS will send the appropriate signals to dump the stored electron beam. Triggering of the FV will simultaneously close the BMPS, isolation gate valve, and safety shutters. Operations may resume when proper sealing of the isolation gate valve has been verified and the vacuum leak in the front end or beamline has been isolated from the SR vacuum.

These two vacuum leak management strategies are the assumed baseline modes of operation in the event of an air-to-vacuum leak in the NSLS-II front ends. At present, we are aware of an ongoing evaluation at APS of a fast closing photon shutter that would be capable of handling the power densities generated by the planned NSLS-II insertion devices. This heat-absorbing device is, in principle, capable of closing in approximately 15 ms. One clear advantage of installing a device such as this in the beamline front end is that it would be possible to continue SR operations in the event of a catastrophic beamline vacuum leak rather than dumping the stored electron beam. The strategy to be employed in this scenario is as follows:

1. The EPS simultaneously signals the fast closing photon shutter to close and the fast valve to close.
2. The EPS then signals the offending insertion device to begin opening its gap.
3. Once the insertion device gap has been fully opened, reducing the insertion device heat flux to a level that the BMPS can safely manage, the BMPS receives a signal to close, to protect the storage ring isolation valve from incident dipole radiation.
4. The EPS then simultaneously signals the isolation valve to close and seal, and the safety shutters to close.
5. Once the SR isolation valve is sealed, the EPS disables the affected front end while the insertion device remains in the open position. The front end must be repaired during a regularly scheduled maintenance period.

As a preliminary estimation, we have determined that to reduce the heat flux developed by an ID to the same order of magnitude as the dipole magnet radiation, each insertion device will need to have its gap fully opened in the event of a catastrophic vacuum leak. A precondition of employing the vacuum leak strategy just described will require that all ID mechanics are designed to be sufficiently robust such that the gaps between magnet arrays can be fully opened in the least time practicable. Note that in this alternative scenario, we assume that the leak rate through the fast valve is small enough that the SR vacuum stays within acceptable limits until the isolation valve is completely closed and sealed. Thus, during the preliminary design phase, it will be important to determine the precise time required to open the ID gap to a state that will enable the BMPS to safely handle both the reduced ID power and the dipole magnet power.

7.5 Storage Ring RF Systems

The large dipole radius (25 m) and the medium energy (3 GeV) of NSLS-II results in very low radiated energy from the bending magnets (288 keV/turn). This increases the effectiveness of 8 damping wigglers to reduce the bare emittance of 2.1 nm-rad to 0.5 nm-rad. The RF system power requirement for NSLS-II is determined primarily by the power radiated by the damping wigglers. This makes it possible for us to stage the RF system installation to parallel the installation of damping wigglers and user insertion devices.

The small momentum compaction (0.0037), an RF frequency of 500 MHz and high RF voltage results in small bunch lengths of ~4 mm. This contributes to a short Touschek-dominated lifetime of <2 hours. To improve lifetime to greater than 3 hours, a third harmonic bunch lengthening cavity is included in the baseline design.

The storage ring RF system consists of the 500 MHz Superconducting RF cavities, their associated klystron tube amplifiers and power supplies, the passive SCRF third harmonic Landau (bunch lengthening) cavity, the liquid helium cryogenic plant, and the master clock, frequency synthesizers, digital I/Q cavity controllers, and RF distribution system that make up the low-level RF.

7.5.1 Physics Requirements and Design Parameters

The RF system must provide sufficient momentum acceptance (bucket height) so as not to be the limiting factor in the storage ring acceptance. In addition, with the small momentum compaction of the low emittance lattice leading to very short bunches, and the accompanying short lifetime, a third harmonic (1500 MHz) RF system is used to lengthen the bunches to increase the Touschek lifetime from <2 hours to >3 hours. The Landau cavity also increases the dependence of the synchrotron tune on the oscillation amplitude providing Landau damping, which can suppress bunch instabilities. The required RF power is the sum of the beam radiated power in the dipoles, damping wigglers, and user IDs. There is no unique approach to meeting the RF requirements; in fact, the frequency choice of 500 MHz is within a broad range of frequencies in which RF sources and cavity designs exist and that would meet the physics requirements. Three frequencies within this broad range, 352 MHz, 476 MHz, and 500 MHz, have been used successfully in third-generation light sources. The operating frequency of 500 MHz has been selected here due to the availability of existing SCRF cavity designs, commercial RF transmitters, and the large number of 500 MHz systems in use at light sources around the world. This translates into mature technologies and lower development costs. A summary of the ring parameters related to the design of the RF system is shown in Table 7.5.1.

Table 7.5.1 RF and Beam Parameters for the NSLS-II Storage Ring.

RF frequency [MHz]	499.46
Circumference [m]	780
Harmonic number	1300
Loss per turn (assuming 5 undulators, 21 m of DW, and dipole losses) [keV]	816
RF acceptance [%]	3
Accelerating voltage [MV]	3.3
Momentum compaction	3.7×10^{-4}
Bunch charge [nC]	1.2
Number of buckets filled with charge	1040

The radiation from dipoles and an assumed complement of five undulators and 21 m of damping wigglers result in an energy loss per turn of 816 keV, corresponding to 408 kW power loss at the design current of 500 mA. A 3% momentum acceptance ($\Delta p/p$) is specified to insure sufficient Touschek lifetime of the storage

ring. For 816 keV/turn energy loss this corresponds to an RF voltage of 3.3 MV (see Figure 7.5.1). As insertion devices and damping wigglers are added as the user program is built out, the loss per turn increases to more than 1.6 MeV, and a voltage of 4.8 MV is required to maintain the 3% bucket height.

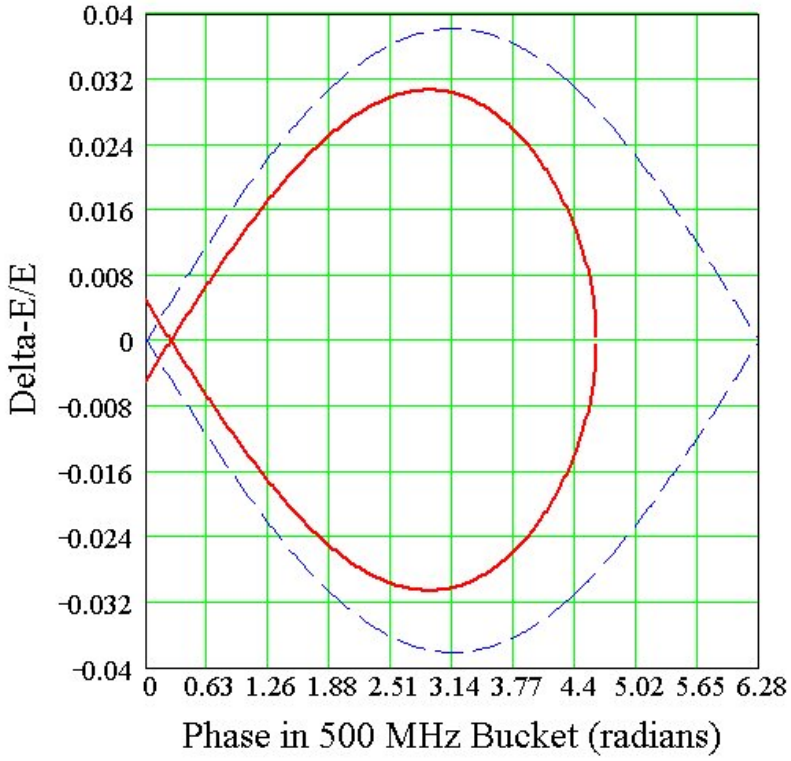

Figure 7.5.1 RF seperatrix for 3.3 MV RF field with (red trace) and without (blue trace) 816 keV/turn radiation losses. The 3% RF acceptance is easily met with two CESR-B cavities.

Thus, the evolution of the RF power requirements over the life of the facility must be taken into account. Table 7.5.2 outlines the initial machine configuration, the capabilities of the RF system, and a reasonable extrapolation as to how this might evolve as insertion devices are added. The exact scenario will be driven by the user requirements and is not fixed at this stage of the machine design.

Table 7.5.2 RF Power Requirements for Dipole Losses and Various Example Insertion Device Configurations.

	Phase 1: Capability of installed RF (270kW/cavity)		Phase 2: Adding 3rd cavity plus purchase 300-kW Transmitter		Phase 3: Add 4th RF station (cavity + transmitter)	
RF power requirements	**#**	**P (kW)**	**#**	**P (kW)**	**#**	**P (kW)**
Dipole	-	144	-	144	-	144
Damping wiggler (9.23 kW / m, 7 m each)	4	259	8	517	8	517
Cryo-PMU (4.17 kW/m, 3 m each)	6	76	6	76	10	127
EPU (4.1 kW/m, 4 m each)	4	66	4	66	5	83
Additional Insertion devices						209
Total		545		803		1080

The initial RF system will consist of two CESR-B cavities, each powered by a 310 kW transmitter. Three cavities will be purchased with the third cavity to be used as a spare in the event of a cavity failure. Two installed cavities can provide up to 5 MV, which exceeds the voltage requirement of 4.8 MV even for the full

complement of insertion devices and the 56 m of damping wigglers envisioned for NSLS-II. However, the power coupler is capable of delivering only ~270 kW of beam power, and so the ring is limited to four damping wigglers and 10 user IDs (or equivalent) by the initially available RF power. Installing a third cavity and transmitter will support a full complement of eight damping wigglers, resulting in the ultimate horizontal emittance of 0.5 nm-rad. Two 500 MHz cavities and one 1500 MHz harmonic cavity (to be described in Section 7.5.3) fit into a single 8 m straight. A second RF straight is reserved for the third and potentially fourth CESR-B cavity and second 1500 MHz cavity to meet the evolving power requirements of NSLS-II as more user IDs are added.

7.5.1.1 Impedance Analysis and Beam Stability

The high beam loading due to 500 mA average stored current requires highly damped structures to prevent beam instabilities. In this regard, the B-factory cavity designs of KEK, PEP-II, and Cornell are attractive and have been studied in detail.

The narrow band cavity impedances have been calculated using the codes GdfidL, SUPERFISH, and CLANS [7.5.1, 7.5.2, 7.5.3]. These codes calculate the longitudinal shunt impedance as

$$R_{sh} = \frac{\left[\mathrm{Re}\left(\int E_z(z) e^{ikz/\beta} dz\right)\right]^2}{2P}, \tag{7.5-1}$$

where P is the power dissipated in the cavity, E_z is the longitudinal electric field either on axis (monopole modes) or displaced with a radial offset corresponding to a dipole mode, quadrupole mode, etc. Here, k is the wave number (ω/c), and β is the ratio of beam velocity to that of light.

The cavities also have transverse impedances that can couple strongly to the beam. The transverse shunt impedance of a cavity is given by the integral of the force acting on the beam, as

$$Z^{\perp} = -i\left(\frac{\int_0^L (\vec{E} + \vec{v} \times \vec{B})_{\perp} ds}{\beta \cdot I_{av} \cdot a}\right), \tag{7.5-2}$$

where L is the cavity length, I_{av} is the average bunch current, and *a* the offset of the beam from the cavity axis. The beam must couple energy into the higher-order transverse mode through the electric field and hence there is a relation between the longitudinal and transverse impedances. The broadband impedance model uses the Panofsky-Wenzel relation,

$$Z_{\perp} = \frac{c}{\omega \Delta^2} \cdot Z_{\parallel}^{(\Delta)}, \tag{7.5-3}$$

where Δ is the offset at which the longitudinal impedance is calculated. The cavity impedances have been calculated for the PEP-II, KEK-B, and CESR-B cavities [7.5.4, 7.5.5, 7.5.6]. All three cavity designs can meet the NSLS-II requirements in terms of attainable voltage and beam power delivered. The SCRF approaches of KEK and Cornell result in lower installed RF power requirements and more efficient operation, attain much lower HOM impedances, and require fewer cavities to achieve the voltage specification. This is particularly important when additional insertion devices are installed which will increase the RF voltage requirement to ~5 MV. The choice for NSLS-II has been narrowed to either the KEK-B cavity or the Cornell CESR-B cavity. Further studies on cost, reliability, and future upgrade potentials in the preliminary design phase will lead to the final choice. For the purposes of this document, the CESR-B cavity is baselined in order

to present self-consistent calculations of system parameters such as RF power and cryoplant requirements, coupled bunch growth rates, system mechanical layouts, and cost. Details of the HOM impedances and coupled bunch growth rates are given in Section 6.2.3.

To meet the initial requirements of 3.3 MV accelerating voltage and 408 kW beam power, two RF cavities with individual klystron transmitters are to be installed. A third cavity to be used as a test cavity / spare will be purchased as part of the baseline machine. It is expected that this cavity will be installed in a future upgrade as additional insertion devices increase the beam power requirement to beyond 2×270 kW, a soft limit of the power couplers in the CESR-B cavities. The CESR-B cavity parameters are given in Table 7.5.3.

Table 7.5.3 CESR-B Cavity Parameters.

Frequency [MHz]	499.46 +/- 0.2
Electric field (normalized to 0.3m) [MV/m]	>8 MV/m
Accelerating Voltage (beam energy gain) [MV]	>2.4 MV
Unloaded Q (at 8MV/m)	$>7*10^8$
Static heat losses [W]	<30 W
Dynamic heat losses (at 4.5k and 8MV/m) [W]	<120 W
Maximum power transferred to beam [kW]	>250 kW
Loaded Q	2×10^5

In addition to coupled bunch instabilities caused by higher order modes in the cavities, the fundamental and harmonic RF systems can cause instabilities where all of the bunches oscillate in unison, the so-called Robinson instabilities. The classical Robinson analysis [7.5.7] is particularly relevant for short and compressed bunch operation of the machine. The resistive Robinson instability is not excited by the cavities. This is due to the fact that the main cavities are detuned below resonance to compensate for beam loading, which strongly damps phase oscillations, while the harmonic cavities' very high quality factor greatly reduces the resistive part of their impedance at the synchrotron frequency, and hence their excitatory (or damping) influence on phase oscillations.

The second observation concerns the reactive Robinson instability. In this instability the static bunch distribution is an unstable fixed point of the longitudinal dynamics, and a perturbation of the bunch pushes it with some growth rate away from that distribution, subsequently damping to one of two stable distributions. In the absence of harmonic cavities, the bunch is marginally unstable. The addition of inductively detuned harmonic cavities for stretched bunches tend to suppress this problem; capacitively detuned harmonic cavities for compressed bunches aggravate the instability. In unstretched or compressed operation, however, the unmitigated instability results in only a small phase shift of the bunch due to the narrow potential well. But for stretched bunches the potential well is wide and flat, and the instability results in gross distortion of the bunches, which must be addressed. A simple cure, first recognized by Miyahara [7.5.8], is to introduce a small-bandwidth feedback of the RF system to the beam. Simulations also show that a reduction of the main-cavity impedance using RF feedback suppresses the instability, although too much feedback excites a higher-order oscillatory instability.

Although glossed over in the discussion to this point, with stretched bunches the classical Robinson picture is not so simply applicable; more involved analyses, such as those by Bosch et al. [7.5.9], and numerical simulations are required to assess the stability of higher-order modes of these bunches. As was just mentioned, the use of RF feedback, which allows the adjustment of the impedance of the main cavities, is a means by which some manipulation of bunch stability is possible. Our experience with the NSLS VUV ring also shows that short-range wakes can have an impact on the stability of stretched bunches, which is further complicated by the varying bunch profiles along the train.

7.5.2 500 MHz RF System

7.5.2.1 500 MHz Cavities

The CESR-B cavity consists of a bulk niobium SCRF single cell with waveguide coupler, a special fluted beampipe to extract the lowest frequency dipole modes, warm-to-cold transition spool pieces for thermal isolation, water-cooled C48 ferrite HOM dampers, and long tapers to transition from the 240 mm cavity bore to the elliptical beampipe. The CESR-B cavity is a "single-mode" cavity. All higher-order modes with the exception of the TM110 dipole mode propagate through the cylindrical beampipe. A fluted beampipe at the opposite end of the cavity has a lower cutoff frequency to allow the TM110 to propagate to the ferrite load. This has only a small effect on the fundamental mode. This allows a shorter attenuation length in the beam tube and a more compact cavity. The cavity assembly is shown in Figure 7.5.2. The layout of two CESR-B cavities plus a single Super3HC harmonic cavity in a single straight is shown in Figure 7.5.3.

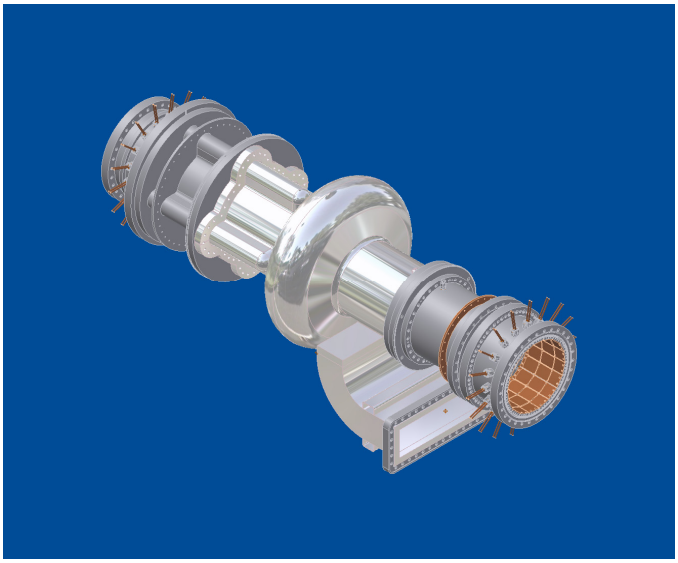

Figure 7.5.2 The CESR-B bare cavity assembly.

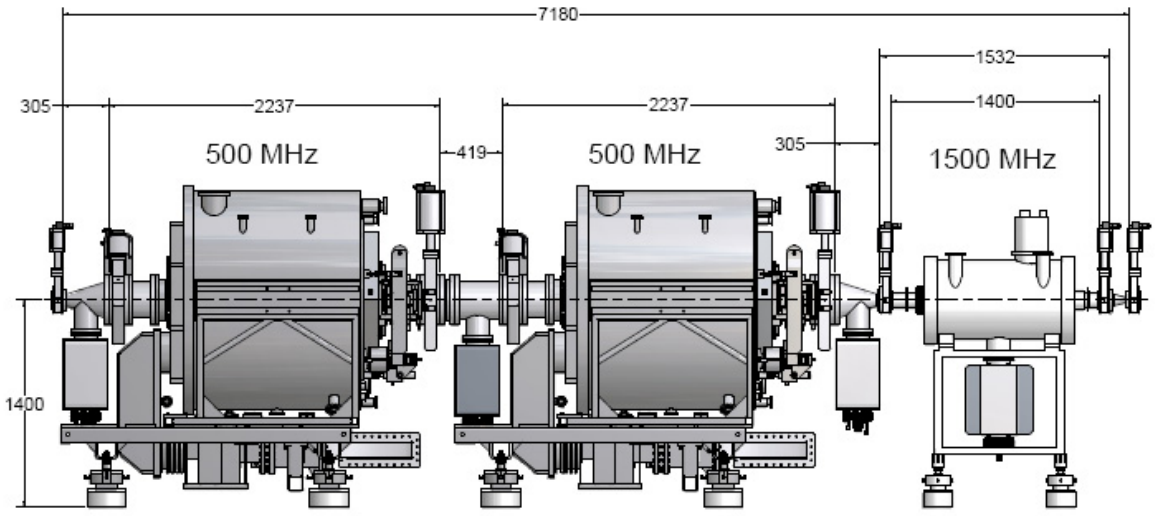

Figure 7.5.3 Layout of two 500 MHz cavities plus one 1500 MHz Landau cavity in a single straight. The tapers from the large cavity beampipe to the ring beampipe are ~300 mm long, limited by the available length in the straight of 7.18 m. A second RF straight is reserved for additional cavities.

7.5.2.2 HOM Damper

The HOM damper consists of C48 ferrite tiles brazed to water-cooled copper backing plates that form a spool piece outside the cryostat. The ferrite is several 500 MHz attenuation lengths away from the SC cavity. There is power dissipated in the ferrite from two sources. First, there is dissipation of the fundamental 500 MHz field driven by the transmitter. This has been calculated with CFISH [7.5.2, 7.5.10] to be less than 100 W at 2.5 MV cavity voltage. Second, the beam also loses energy from wakefields. This loss is given by

$$P_{loss} = k_{\|} \cdot I_0^2 / n \; T_0 \,. \tag{7.5-4}$$

For NSLS-II, $T_0 = 2.6$ μs, $I_0 = 0.5$ A, and $k_{\|}(\sigma_s = 4\text{ mm}) = 3.6$V/pC, resulting in a $P_{loss} = 2.3$ kW. In the worst case, all of this power is lost in the ferrite, which is still a factor of 4 lower than the design limit.

7.5.2.3 KEK-B Cavity Option

The superconducting cavities developed for the KEK-B factory are being considered as an option for NSLS-II, for several reasons. The most significant advantage is the higher power per coupler, which has been demonstrated at KEK to be greater than 400 kW. In principle, two KEK cavities could meet the power requirements for the full complement of damping wigglers and user insertion devices, ~800 kW. The waveguide feed at the top of the cryostat makes the tunnel installation easier, and the coupling can be optimized for various beam currents and cavity voltages by simple spacers on the antennae coupling mounting flanges, as opposed to the fixed coupling of the waveguide feed for the CESR-B approach. A layout of two KEK-B cavities in an 8 m straight is shown in Figure 7.5.4.

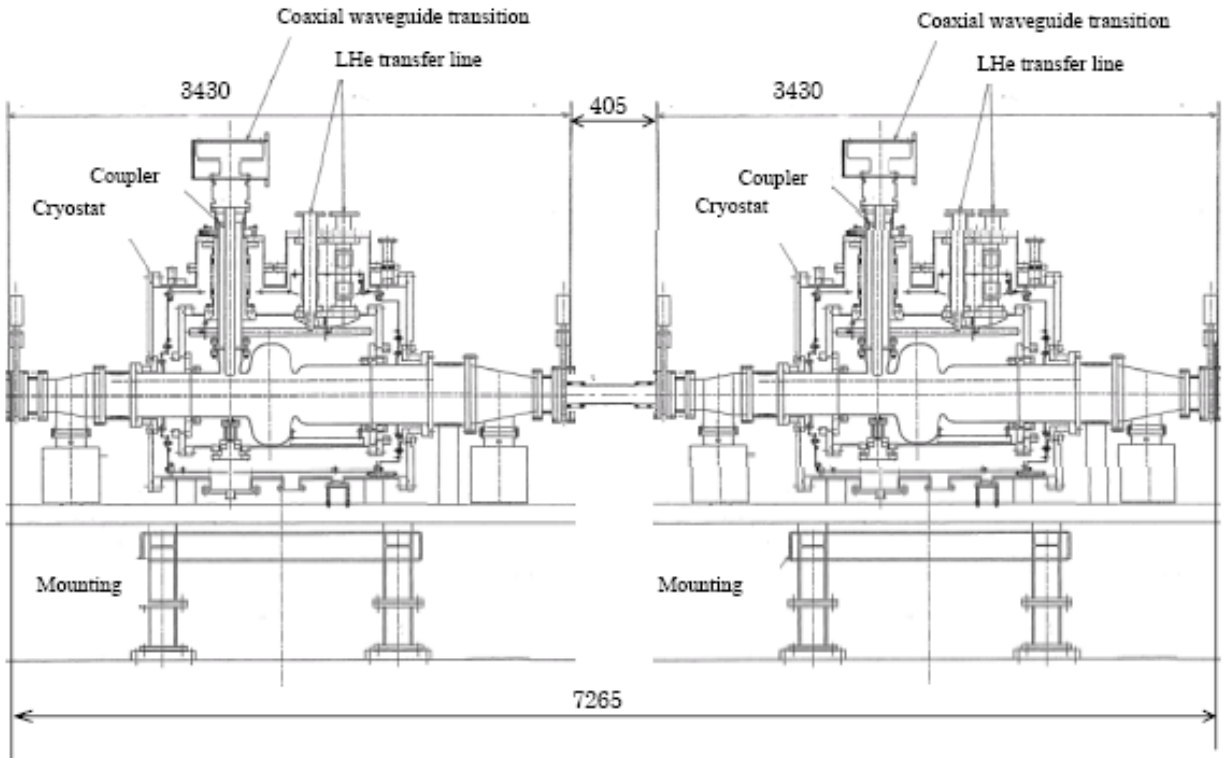

Figure 7.5.4 Installation of two KEK-B SCRF cavities in an 8 m straight.

7.5.2.4 RF Transmitter

The power couplers for SCRF cavities have a wide statistical variation in their power handling capability. Although they have been engineered for high power handling by proper thermal and electrical design, they are prone to multipacting, a resonant electron-avalanche effect that can impose a hard limit on power transmission and cause failure by local heating due to electron loading. The multipacting depends on the secondary-emission coefficient of the surface, which in turn depends on the properties of the bulk material, usually copper or niobium, and surface contaminants, which are usually cryo-pumped organics from the machine vacuum. These contaminants can be present at start-up or accumulate over a period of time, degrading performance and requiring, in the worst case, the cavity to be warmed up with a mild bake to drive off the condensed gases. Experience with the CESR-B cavities has shown transmitted power per coupler in the range of 250–330 kW. A transmitted power of 270 kW is assumed for meeting machine requirements and placing a limit on installed RF power. In addition to the energy losses due to radiation in dipoles, damping wigglers, and undulators, the RF power transmitter and coupler must provide for the HOM losses that are excited by the beam. We are exploring ways of increasing the power per coupler, and will factor this into the preliminary design and choice of transmitter power.

The coupling of the waveguide to the cavity in the ideal case is adjusted so that the cavity presents a matched load to the RF source at the normal operating current and energy. Since there is a phased installation of cavities and insertion devices, this optimal coupling varies over the life of the machine. The KEK-B cavity has an adjustable antennae coupler that, in principle, can be changed to follow the optimal coupling. In practice, this must be done in a cleanroom environment and may be of limited value.

For an aperture-coupled cavity such as the CESR-B, coupling is set during the design and manufacture. Usually coupling is set so the generator is matched to the cavity at the highest expected beam-loading (beam power) of 270 kW. This minimizes the requirement on installed RF power. For the staged installation of insertion devices (RF power required) and RF cavities there is not a single minima, and it is necessary to balance the mismatch over the different phases. For an approximate match to the conditions in Phase 3 in Table 7.5.2, the maximum reflected power in the other three phases is ~10.5 kW. In order to reduce the residual reflected power during commissioning and staged insertion device installation, a 3-stub waveguide tuner will be installed between the circulator and the cavity.

There will be variation of the impedance presented by the cavities to the beam at different times of the machine's life due to the varying number of cavities and insertion devices. RF feedback can be used to reduce (or increase) this impedance; this option is being studied and system layout designed to minimize loop delay to allow its implementation. A minimum transmitter power of 275 kW is required to meet the sum of the radiated, HOM, and reflected power demands. To allow for the case of coupler improvement (coupler is limited by multipacting, not power limitations) or system aging (degradation of klystron output power), the transmitter will be designed for a minimum of 310 kW, allowing up to ~280–300 kW per coupler.

A single 310 kW klystron amplifier will drive each of the main ring cavities through a 350 kW rated circulator and load. Klystrons that meet or exceed this power level are available from three vendors: CPI, Toshiba, and Thompson. The klystron beam power will be provided by a Pulse Step Modulation switching power supply at 55 kV and 12 A. The PSM switching power supplies have the benefit of low stored energy, and fast turn-off capability of the IGBTs, eliminating the need for a crowbar circuit to protect the klystron. The power supply will have redundant switching cards built in, and will operate at full capacity even with several card failures. The RF transmitter will have local control via PLC, with system parameters and control available to the main control system via an Ethernet link. The PLC will also monitor the PSM switch modules, so that failed modules are logged and transmitter repairs can be scheduled for the next maintenance period. The main ring power systems with a rating of 310 kW are beyond the power limit of air-cooled coaxial cable, and will be implemented in WR1800 waveguide. A layout of the RF straight with the associated RF transmitters is shown in Figure 7.5.5.

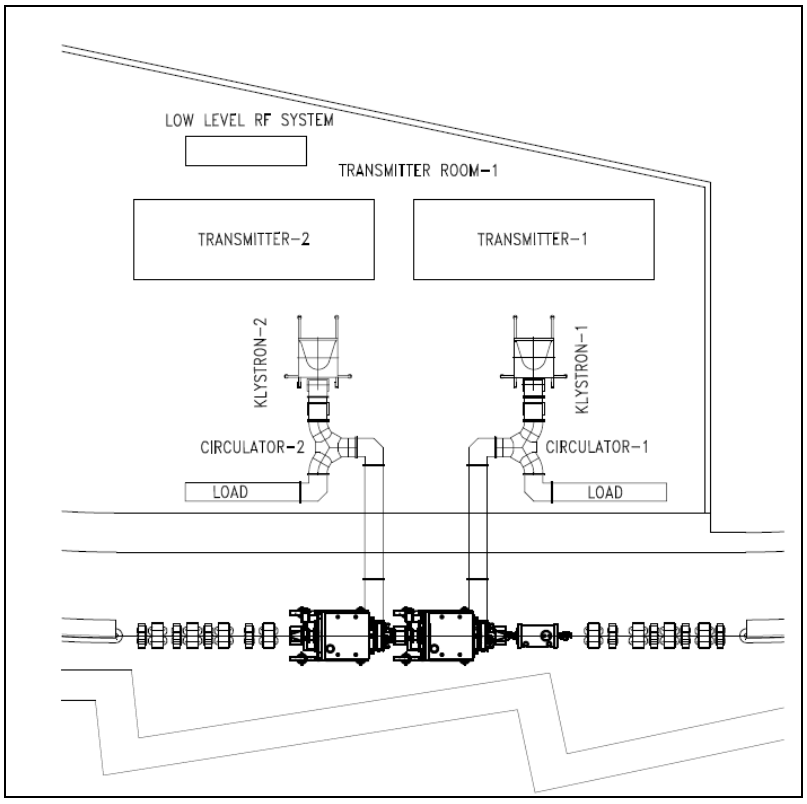

Figure 7.5.5 Layout of an RF straight section with two 500 MHz cavities and their klystron transmitters and a single 1500 MHz harmonic cavity.

An alternative approach of combining several Inductive Output Tube amplifiers to obtain the necessary RF power has been developed at other facilities [7.5.11, 7.5.12]. IOT systems have higher efficiencies and some limited failure tolerance. Likewise several hundreds of high-power transistors can be combined to provide the required power. SOLEIL has recently commissioned such a system at 352 MHz [7.5.13]. Both of these options will be explored in detail during the design phase.

7.5.3 1500 MHz Harmonic Cavity System

A passive 1500 MHz SCRF cavity, such as the BESSY scaled CESR-B [7.5.14] or Super3HC [7.5.15] scaled SOLEIL cavity, has been studied for the Landau cavity in NSLS-II. Both of these cavities can achieve ~0.5 MV per cell, with the BESSY cavity containing a single cell, and the Super3HC containing two cells per cavity. The details of the impact of the Landau cavity have been discussed in Section 6.2.7 on collective effects. Here we will discuss the hardware and system configuration. For this purpose, two cells of the Super3HC Y design will be used in the estimate.

The nominal voltage and phase of the harmonic cavity is that which cancels the slope and second derivative with respect to time of the total RF field. This results in bunches lengthened by approximately the ratio of the harmonic-to-main cavity frequencies. The field required of the harmonic cavity is approximately the reciprocal of that ratio times the main-cavity field, although slightly less due to the non-zero main-cavity synchronous phase that is a consequence of the beam's radiation loss. In practice, this harmonic-cavity field is pushed slightly higher to provide additional stretching, striking a balance between improved lifetime and the eventual onset of longitudinal instabilities. Furthermore, the use of a gap in the ring's fill pattern for ion clearing results in perturbations of the potential wells that vary along the train. As a result, the lengths of most bunches are shortened by these perturbations and the average lifetime is reduced. For these reasons, the harmonic-cavity field and phase require further investigation. Simulations shown in Section 6.2.7 give a

maximum in bunch length for ~1.1 MV of third-harmonic voltage for the initial fundamental cavity voltage of 3.4 MV. This can be met with a single Super3HC cavity. As the number of damping wigglers and user insertion devices increases, the fundamental mode voltage increases to 4.8 MV and an additional third-harmonic cavity will be necessary for optimal bunch lengthening.

7.5.4 Low-Level RF and Beam Control

The specifications of the RF system amplitude and phase requirements are derived in part from the user requirements that the transverse motion of the photon beam is to be <10% of the RMS beam size, and the increase in photon beam size due to emittance dilution of the electron beam is to be <10%. The relation of the photon beam size and jitter to electron beam size and jitter is influenced by the design of a particular insertion device and beamline, which might impose a tighter tolerance on the electron beam stability. The stability required from the RF system to limit the transverse jitter of the electron beam to 10% beam size is derived below. This will be expanded to study the effect on the photon beam in the next phase of design.

The electron beam size is given by

$$\sigma_x = \sqrt{\beta_x \varepsilon_x + \left(\eta_x \delta\right)^2} \ . \tag{7.5-5}$$

Since the residual dispersion in the ID straights is expected to be on the order of 1 mm, and the natural momentum spread ~1×10^{-3}, the dispersive term is negligible and the beam size depends only on the emittance and the beta function at the ID. For the 5 meter straights, $\beta_x = 2.7$ and $\varepsilon_x = 0.6\times10^{-9}$, corresponding to a beam size of 40 microns in the horizontal plane. Similarly, in the vertical plane for $\beta_y = 0.95$ and $\varepsilon_y = 0.6\times10^{-11}$, the vertical beam size is ~2.4 microns. The orbit jitter is given by

$$\Delta_{x,y} = \frac{\Delta p}{p}\eta_{x,y} \, . \tag{7.5-6}$$

In order to restrict the beam jitter to ~10% of beam size with a residual vertical dispersion of 1 mm, the momentum jitter must be less than 2.4×10^{-4}; the horizontal plane is less demanding. For the NSLS-II RF system, this corresponds to a 0.7 degree phase jitter.

The longitudinal beam stability derives in part from timing experiments. Even though these users employ a photodiode detection system to determine the arrival time, the limited bandwidth (~1 kHz) sets strict requirements for the jitter tolerance to be 5% of the RMS bunch length over the frequency range of 500 Hz to 50 kHz. This corresponds to a bunch phase tolerance of 0.12 degrees, for timescales comparable to the synchrotron period this is a tolerance on the RF phase as well. An example of the impact of emittance dilution is from user beamlines employing the radiation of higher harmonics, whose spectral purity and beam spot size depends on the momentum spread and momentum jitter of the electron beam. So it is a requirement of the RF systems to not contribute significantly to energy spread or jitter, either through instabilities or noise. While suppression of instabilities is already a basic requirement of the system, a cap on energy spread provides a constraint on the noise the RF system contributes to the beam.

The magnitude of the effect on the beam of RF phase and amplitude noise depends on whether the source of the RF jitter is random or harmonic (systematic). Sources of noise are broadly classified into continuum sources possessing a continuous and slowly varying (with respect to frequency) spectral density, and spurious sources that possess spectral lines, possibly varying in time. Examples of the former are the continuum component of synthesizer phase noise, amplifier shot noise, and the continuum components of other active devices in the RF system. Examples of the latter are line related and power-supply switching noise, microphonics, and vibration. To assess the impact of, and derive tolerances for, RF-system noise sources, we need to determine the beam's sensitivity to noise from identified sources and derive a tolerance budget. The

sensitivities are to be determined by modeling the RF system's linear response to these sources. Noise magnitudes in existing machines are a starting point for noise intensities, from which sensitivities are used to determine where noise tolerances need to be tightened. This work is in progress, and will be expanded in the preliminary design phase. Digital low-level RF systems have achieved less than 0.1 degree phase and 0.1% amplitude stability [7.5.16], these tolerances should be sufficient for NSLS-II.

7.5.4.1 Master Oscillator and Ring Frequency Synthesizers

The low-level RF and beam control design is at a preliminary stage of defining specifications and architecture. Unlike the power systems, which stay relatively static over long periods of time during the life of the machine and should be transparent to the user, the LLRF and beam control requirements may change several times as the machine evolves, so the design must be flexible. To this end a digital architecture is used. There are several approaches being studied; we present one here as an example. This is similar to the system proposed by Horrabin and Dykes [7.5.17] for Diamond Light Source.

An ultra stable Master Oscillator, offset from the fundamental RF frequency, is mixed with a Direct Digital Synthesizer to provide the ring frequency. This will allow for future implementation of a radial (frequency) feedback loop to stabilize the beam orbit to the sub-micron level. Depending on future considerations, there may be individual DDSs for the booster, ring, and feedback systems, or all systems may be driven by the ring DDS. Separating the systems would allow the booster to synchronize with the linac for injection and then synchronize to the ring for extraction, decoupling the injector from the ring. An example of such a system is shown in Figure 7.5.6. A wide range of Master Oscillator and IF frequencies are feasible, and the exact frequencies would be determined in the design phase.

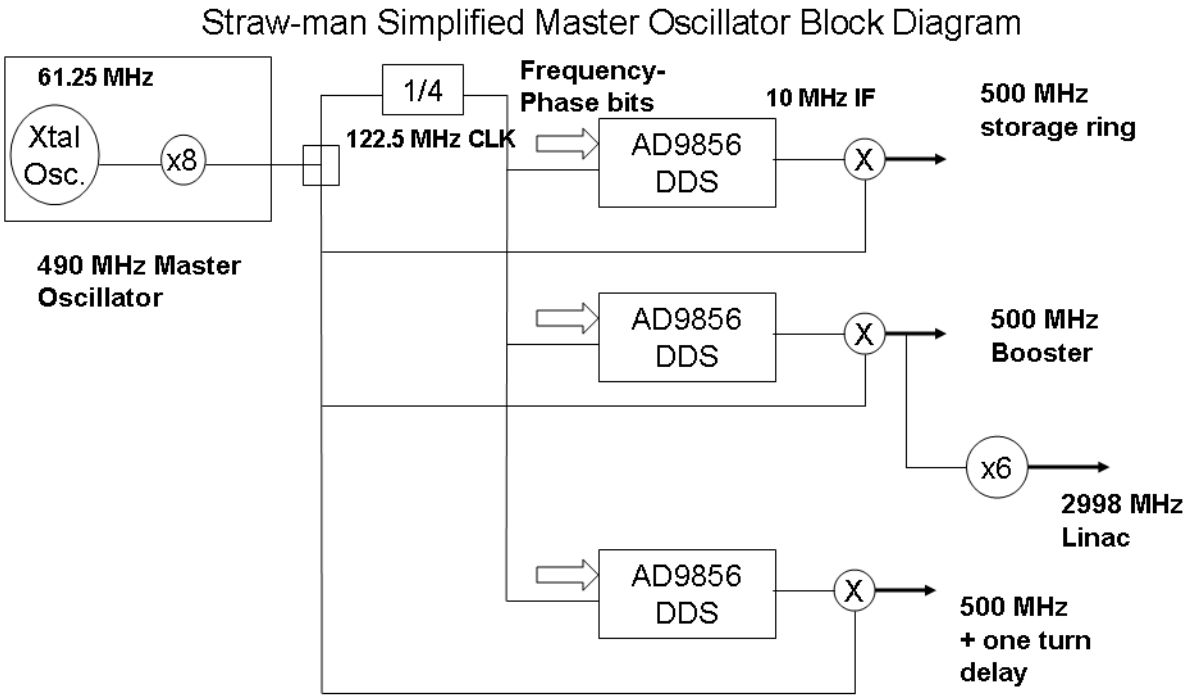

Figure 7.5.6 Example of master oscillator.

7.5.4.2 Cavity Controllers

The cavity-amplifier system has several nested feedback loops to control the amplitude and phase of the RF cavity fields in the presence of beam-loading, mechanical perturbations to the cavity, and residual klystron noise due to power line/DC power supply ripple. The innermost loop is the tuner loop, which tunes the cavity resonance in order to present a purely resistive impedance to the klystron, thus minimizing klystron power. This loop, which is closed around a mechanical tuner, is slow—on the order of 1 Hz. Next is an RF feedback loop that is used to adjust the impedance of the main-cavity accelerating mode. In order to stabilize the cavity fields against fast perturbations, an amplitude and phase loop around the klystron-cavity chain is implemented. Although these can be independent loops, it is more effective to combine them in a common In-phase and Quadrature (I/Q) modulation loop, due to the coupling of the loops by cavity detuning for beam loading.

In addition to the above RF, amplitude, phase, and tuner loops, it may be necessary to implement other loops. A loop for zero-order coupled-bunch-mode feedback from the beam to the RF system to damp Robinson or higher-order longitudinal instabilities may be necessary. A klystron amplitude/phase loop to linearize the klystron, and possibly a feed-forward loop on the anode modulation of the klystron for maximizing klystron efficiency under different operating conditions, may also prove useful.

With the exception of RF feedback, the above loops can be implemented in either analog or digital hardware. Analog systems have the advantage of being simpler and less expensive to produce, and have higher speed and bandwidth. Their disadvantages include the lack of flexibility in changing loop characteristics for varying beam loading, slightly less phase and amplitude accuracy, and DC shifts that are more difficult to control. Digital implementation has the advantage of flexibility, in particular of being able to synthesize the loop filters digitally so that the feedback loops can be programmed for different machine states. Higher accuracy can be achieved, and DC drifts are easier to control. This comes at the price of higher complexity, and requires an additional skill set in high-speed digital design. Careful attention must be paid during the design stage to design in “digital probes” and other debugging tools to monitor and allow trouble shooting of the digital feedback loops.

To maximize the performance of the RF system and allow simple optimization and upgrades over the life of the machine, a digital implementation is our choice for NSLS-II.

The low-level RF cavity field control will be via a digital I/Q modulator-demodulator incorporating up and down conversion, ADCs and DACs interfaced to the digital baseband signal processing, a Field Programmable Gate Array state machine, and interface to the control system. Similar systems have been designed for both hadron and electron machines in recent years [7.5.18, 7.5.19]. A particularly attractive approach is the Cornell design, which has been operating in CESR with the SCRF cavities over the past two years. The system was developed within the VME architecture at Cornell. PC104 and compact PCI architectures for the NSLS-II LLRF system will be explored in the preliminary design phase.

Although the booster RF is simpler because there is only one cavity (no vector sum), and harmonic cavities are easier because they are passive, we assume at this stage that identical storage ring controllers will be used, with the only differences being how they are programmed and their interface with the control system.

7.5.5 Cryogenics

A helium closed-cycle cryogenic system is necessary to provide liquid helium to the superconducting radio frequency cavities. Two 500 MHz (fundamental) and one double cell, 1500 MHz (harmonic) SRF modules for the main storage ring must be maintained at approximately 4.5K during operation of the storage ring and booster. Additional cooling lines and capacity may be needed to cool one 500 MHz SRF cavity to 4.5K for offline development purposes. The cryogenic system includes a refrigerator/liquefier cold box, a main compressor and oil removal system, a recovery compressor and oil removal system, LHe dewars, LHe and liquid nitrogen distributing systems, a gaseous helium management system, cryogenic lines, instrumentation, controls, and safety devices. Each cavity cryostat has a volume of 500 L and stores 400 L of LHe during operation.

7.5.5.1 Factors Influencing Cryogenic System Design

7.5.5.1.1 Single vs. Multiple Refrigerators

The refrigeration system needs to have high reliability with near-zero unscheduled downtime. Using risk and failure analysis criteria, we compared similar systems that use either one large refrigerator or multiple refrigerators. A study to determine the sources of unavailability in existing cryogenic refrigeration systems was undertaken in the past by the TESLA Collaboration at DESY. The results are listed in Table 7.5.4, in order of their occurrence frequency.

Table 7.5.4 Rating of Refrigerator System Unavailability.

Rating	Topic	Example	Multiple Refrigerators
1	External Utility Failure	Electrical power, cooling water, instrument failure	No advantage
2	Blockage by frozen gas or impurities	Air and/or water vapor	Somewhat larger risk tolerance provided
3	Operational problems	Operators, controls, instrumentation,	Greater risk due to more system complexity
4	Single component failure not leading to total plant shutdown	Electrical motor burnout, compressor bearings, leaking oil pump seal, turbine bearing trouble	No advantage over component redundancy within a single refrigerator
5	Catastrophic component failure leading to plant shutdown	Loss of insulation vacuum, rupture of heat exchanger, oil spill into cold process piping	Would have a positive effect

From the information in the table above, we can predict that major downtime will occur as a result of catastrophic component failure, while the effect of any of the other four occurrences is relatively negligible. After consulting with experts and researching other sources that faced similar circumstances, a single refrigerator was selected. To lower risk however, a full inventory of spare components will be required, as well as strict adherence to the individual manufacturer's recommended maintenance schedule.

7.5.5.1.2 Constant versus Variable Loads

The reliability factor is increased by designing refrigerators that are capable of operating efficiently at partial load. When the accelerator is operated at reduced load, or when all modules are not in use, the electrical power and utility usage will be proportionally reduced. This is achieved by automatically modulating the discharge pressure and mass flow rate of the main compressors to match the actual load.

7.5.5.1.3 With or Without External Gas Purity Monitoring System

Gas impurities have an adverse effect on R/L efficiency. Air, for instance, solidifies at approximately 50K. Small solidified air particles can damage the expansion turbine, which runs at a high rotational speed; thus the concentration of impurities in the helium gas must be maintained at less than 10 ppm. The R/L internal adsorber is one source of purification; however, additional external purifiers to further enhance the gas purity level are suggested. At least one external purifier that can operate at partial mass flow rates is recommended. To conserve budget, this has not been included initially, but will installed at a later date, as soon as sufficient budget is available.

7.5.5.2 Mechanical Design Parameters

7.5.5.2.1 Heat Load Budget

There are essentially two types of heat loads: static and dynamic. The static heat loads of the RF cavity cryostats are measured values, recorded by other synchrotron facilities. The dynamic heat loads are calculated based on physics requirements. Heat loads associated with transfer lines, valve boxes, dewar losses, and other components are estimated values based on information provided by vendors, engineering calculations, and professional judgment. Table 7.5.5 itemizes the estimated static and dynamic heat loads of the superconducting cavities and associated cryogenic components at 4.5K.

The waveguides for the 500 MHz cavities operate in liquefaction mode, whereby each requires 5.3 l/hr of LHe for cooling. There is one distribution valve box serving as flow distribution between the LHe dewar and the straight section cryostats.

Table 7.5.5 Cryogenic System Heat Loads Budget and Refrigeration Sizing.

Component(s)	Two Cavities [W]	Three Cavities [W]
500 MHz Cavity (Static + Dynamic (Main Ring)	(25 + 98) x 2	(25 + 65) x 3
RF Valve Box (vendor)	15	15
Wave Guide (NSRRC)	8	12
Harmonic Cavities (Static + Dynamic)	(50 + 50)	(50 + 50)
Transfer lines (0.5 W/m), 50 m	25	25
Dewar loss	5	~5
Subtotal	399	427
R/L with 40% (239 – 268 W) margin	665	712

The projected LN2 required to cool the R/L heat exchangers, SRF modules, and transfer line/valve heat shields is listed in Table 7.5.6.

Table 7.5.6 Cryogenic System Liquid Nitrogen Consumption Estimates.

Component(s)	Two Cavities [L/hr]	Three Cavities [L/hr]
500 MHz cavity	20	30
Harmonic cavities	10	10
Cold Box, 10 pre-cooler	10	10
RF valve box (1)	12	12
Transfer lines (1 W/m), 50 m	12	12
Subtotal	64	74
Margin (20% of subtotal)	13	15
Total	77	89

7.5.5.2.2 Engineering Design Approach

The main storage ring RF systems will initially consist of one 1500 MHz (harmonic) and two 500 MHz (fundamental) Superconducting RF Cavities.

The cryogenic system must operate continuously for at least a full year before scheduled downtime. The design goal, therefore, is to provide a highly reliable and stable cryogenic system supported with required monitoring, alarms, interlocks, and a safety and control system. As the cryogenic system must supply LHe to all of the RF cavities, redundancy of vulnerable components is highly desirable to ensure that continuous operations can be maintained effectively.

Total refrigeration cooling requirements are based on the accumulated heat loads of one double-cell 1500 MHz and two 500 MHz SRF cavities operating simultaneously (see Table 7.5.6). The cryogenic system must minimally provide refrigeration power of 399 W. To enhance reliability, the refrigerator is sized to operate at 60% of its peak cooling capacity, which will reduce wear and tear while providing a comfortable 40% safety margin Therefore, an R/L capable of 700 W cooling capacity (with the LN2 pre cooler) will be specified for this application. The basic cryogenic system flow diagram is shown in Figure 7.5.7.

A single 3,000 L dewar will serve as a buffer storage vessel between the R/L cold box and the RF distribution valve box. The dewar volume is more than twice the volume of total LHe stored in all SRF modules. This reserve volume is estimated to maintain nearly six hours of continuous operation while troubleshooting or minor repairs are being conducted. A carefully planned control system will regulate the LHe production rate to maintain the stored liquid volume in the dewar at the desired level.

A single compressor with an oil removal system will deliver pressurized helium gas to the R/L. An identical compressor/oil removal system will be installed in parallel as a back-up. It must remain ready to operate in the event of an unexpected failure of the main compressor. These two compressors will also alternatively cycle to extend their overall life time. Both compressors will be equipped with a frequency driver to match the cooling load to the compressor's output to maximize system efficiency. A single uninterrupted recovery compressor, along with an oil removal system, will recover the generated boil-off gas in the event of loss of power to the main compressors.

A single gas management system will regulate GHe during various operational conditions. Three $70m^3$ tanks capable of storing all generated GHe during warm-up will be used. Two control valves working in concert will regulate GHe flow between the compressor and helium storage tanks.

A gas purifying/monitoring system is not included at this time but it is suggested for sampling the circulating GHe to monitoring purity levels.

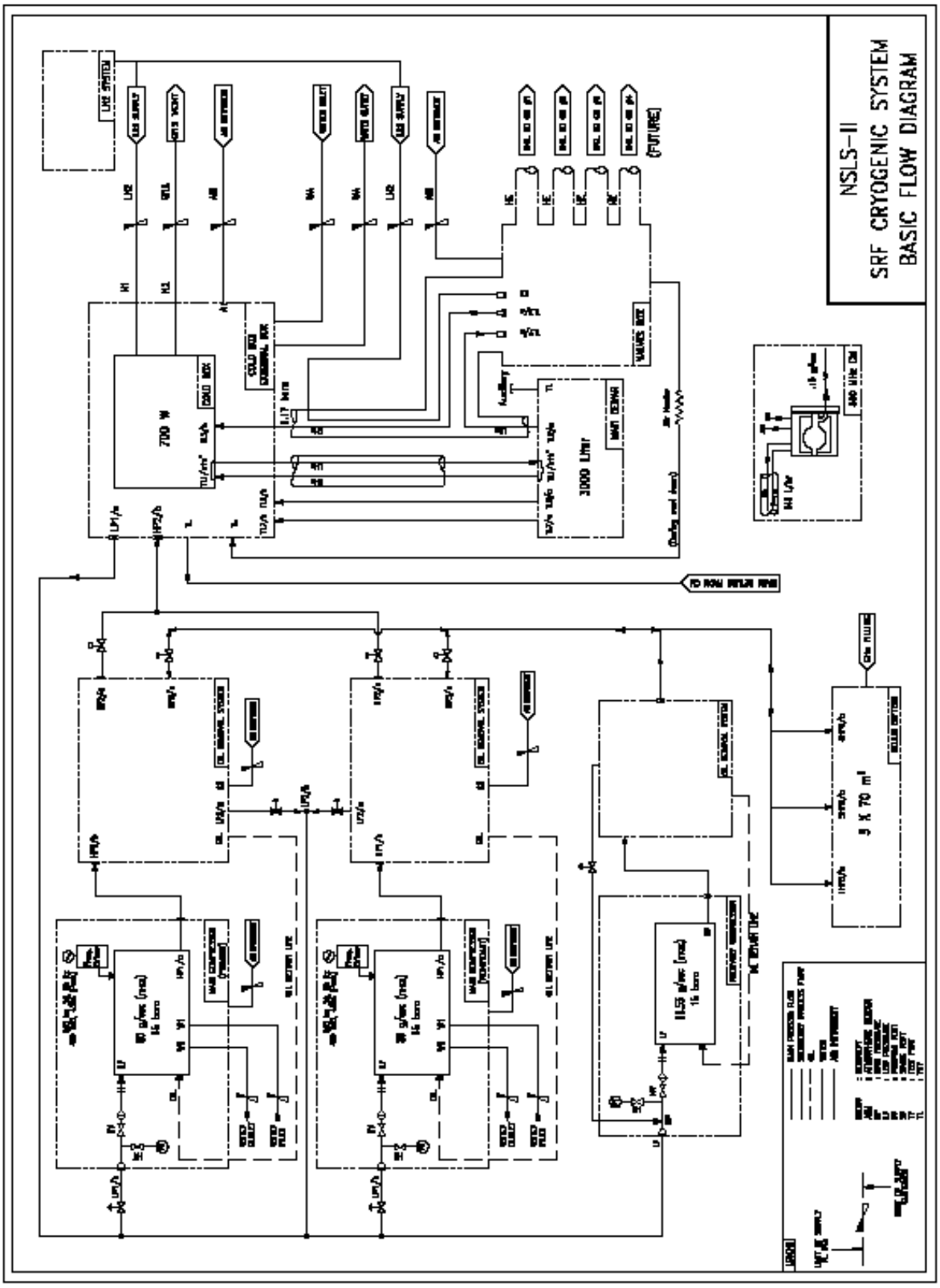

Figure 7.5.7 Basic Cryogenic System Flow Diagram.

As the cryogenic system will be purchased with documentation, as required to meet NSLS-II requirements, interfaces with SRF cryostats and machine control system will be developed during the overall system design. In summary, the major components of the cryogenic system include:

- two screw-type helium compressors and oil removal sets equipped with frequency drivers, where one will act as hot standby
- one turbo-expander type refrigerator–liquefier cold boxes with maximum combined cooling capacity of 700 W
- one gas management system consisting of three carbon steel warm GHe tanks (70 m^3 each)
- one main LHe dewar (3000 L)
- one cryogenic distribution valve boxes capable of serving four SRF cryo-modules
- multi-channel, vacuum-jacketed, LN2 transfer lines with length and size to be determined later
- single vacuum-jacketed LN2 transfer lines, with length and size to be determined later
- appropriate length/size of vacuum jacketed LN2 transfer line
- stainless steel piping for GHe supply and return
- an 84000 L bulk Liquid Nitrogen storage tank to deliver LN2 throughout the system
- central process and control system (including software, hardware, and standard communication ports to provide intelligent to machine control system)
- the appropriate number and type of warm-cold valves, safety devices
- instrumentation, such as pressure/temperature transmitters, gauges, etc.
- a hazard monitoring and control system

Other features for the closed-loop cryogenic system are briefly described as follows:

- The helium compressor sets will be located in a detached compressor room at sufficient distance from the main building to minimize environmental effects such as noise (72 db at 1 m distance) and vibration to the machine/personnel.
- The refrigerator/liquefier cold box and the main LHe dewar will be located in a “cryogenics room” located adjacent to the inner wall between two RF straight sections.
- Three helium gas buffer tanks (70 m^3 each) will act as make-up and recovery of GHe together with a GHe refill tube trailer, which will be located on a platform adjacent to the compressor room.
- Associated helium gas piping will interconnect the components according to the PID drawing (to be developed later).
- One cryogenic distribution control valve box will supply the SRF cavities with required LHe flow to be located adjacent to an RF straight section.
- Multi-channel vacuum-jacketed lines will deliver LHe and GHe between the R/Ls and the storage dewar.
- LHe will be transferred from the main LHe dewar using a positive pressure difference from the helium dewar through a multi-channel line, or by using a set of vacuum-jacketed transfer lines to the cryogenic distribution valve box, and then through a set of cryogenic flexible transfer lines, to the main SRF modules.
- A 84,000 L LN2 storage tank will supply required LN2 to the cryogenic system and SRF cavities, and will be located outside main building. An automated telemetry system will be used to maintain safe LN2 volume and tank operating pressure (3.0 bar absolute).
- A large capacity, LN2 phase separator will be placed next to the cryogenic room (due to intermittent excess noise level), for delivery of constant pressure LN2 to the SRF modules and to the R/L, which are all sensitive to pressure fluctuations.
- Vacuum-jacketed transfer lines will deliver and distribute required LN2 to the cryogenic room and SRF modules.
- A central control monitoring system located in the cryogenic room will act as interface between operators and various components.
- Installation of O2 monitors and interlock systems in all enclosed areas (tunnel, cryogenic, and compressor rooms) will guard personnel against potential Oxygen Deficiency Hazards.

The following section briefly describes functional characteristics of main components.

7.5.5.2.3 Refrigerator/Liquefier Cold Box

The refrigerator/liquefier cold box is required to reliably produce combined 700 W of refrigeration and LHe at 4.5K. The principle design of R/L is based on a two-turbine, in series, Claude Cycle with six stages of heat exchangers (see Figure 7.5.7). The gas-bearing turbine expander-type 4.5K R/Ls have demonstrated reliability and efficiency during the past 30 years. Commercially-manufactured systems such as Air Liquide's HELIAL and Linde's TFC models have been used by other synchrotron facilities and equipped with comprehensive instrumentation and control systems.

High-pressure helium gas from the compression system enters the cold box system at 298K. Following removal of impurities in the inlet via a <50 micron filter, the flow is fed to a series of heat exchangers that are cooled by the returning low-pressure gas stream. LN2 is used as to pre-cool the first heat exchanger and to help cool the HP stream to 80K. At the outlet of the second heat exchanger, the HP stream is then fed into an 80K adsorber, where air pollutants are removed. The stream exits the particulate filter downstream of the adsorber and is then split into two parts: the gas that is expanded in the two turbines in series (in the so-called Brayton Cycle part), and the gas that is processed in the Joule-Thomson circuit (in the so-called Joule-Thomson cycle part).

The expansion turbines include a stator and a rotor. The rotor consists of a cold wheel, a brake wheel, and a gas bearing. Fully automated R/Ls with control systems driven by PLCs are preferred. Some of the automation features under consideration are:

- automatic re-start of liquefier after a breakdown of electrical power, cooling water, or instrument air
- the capability to start and stop safely at any time and under any condition without requiring special precautions
- remote monitoring capability from onsite or offsite locations
- the capability to perform remote diagnostics and troubleshooting (from onsite or offsite)

7.5.5.2.4 Liquid Helium Storage Dewars

A single 3,000 L LHe dewar is used for liquid storage and to transfer LHe to the SRF modules through the cryogenic distribution valve box via a differential pressure transfer. The main LHe dewar acts as a buffer and stores sufficient liquid during cool-down, warm-up, and normal operation. The 3,000 L capacity was selected to provide at least six hours of uninterrupted operation while minor troubleshooting is being conducted.

The dewar will be constructed using an inner insulated vacuum vessel and an outer vessel, both made of 304 stainless steel. There will be adequate access ports for helium transfer and instrumentation. There will be an additional inlet for feeding the dewar from an external source, should this be necessary. The main parameters and some of the design features are as follows:

- maximum operating pressure: 2 bar absolute
- steady-state operating pressure: 1.2 to 1.6 bar absolute (17.4 – 23.2 psia)
- dewar pressure fluctuation: ±3 mbar (0.0435 psi)
- insulating Vacuum Pressure: $<1.0\times10^{-5}$ mbar, sustainable of >5 years, when dewar is cold
- dewar level fluctuation during steady state operation: ±1% of full scale
- level indicator/sensor resolution: 1% of digital display
- radiation shields will be cooled with helium boil-off (LN2 shields are not permitted). The boil off gas will be sent to compressor suction line, through a series of check valves.
- maximum allowable heat leak, including penetrations and necks: 5 W

- Dual 500 W heaters (removable, one as spare) with one DC power supply/controller installed inside the main liquid dewar for capacity and refrigerators control purposes. The heater load will be controlled by a dedicated PID controller reading the LHe level sensor.
- Heater resolution: ±5 W
- Two superconducting LHe level detectors/sensors (a differential pressure level detector is not acceptable) and one indicator
- Two redundant pressure transmitters will provide remote monitoring of dewar vapor pressure.
- A mechanical pressure gauge with resolution of 0.25% full scale and with a maximum of 2.5 bara full-scale for local measurement of the helium vapor pressure
- The LHe vessels have dual in-line relief valves and a rupture disk to handle vaporized gas in case of catastrophic event such as fire or loss of vacuum. The pressure settings of the burst disk will follow the ASME code.
- The outer vessel will be equipped with vacuum pump-out port, mechanical pressure gauge, and pressure transmitter.

The access ports and penetrations are:

- MCL for transfer of LHe and vapor return between R/L and LHe dewar
- MCL for transfer of LHe and vapor return between the dewar and RF distribution valve box (to be sized for liquid transfer rate during cool down and normal operation of SRF cavities)
- one port for external fill/withdrawal at 500 L/hr flow (for simultaneous operation of three fundamental and one harmonic cavity at a pressure difference of 2 psi)
- one combined for relief/burst disk system and normal warm-up

All other applicable manufacturing and design requirements will be specified during the next design phase.

7.5.5.2.5 Main Helium Compressor Stations

Two oil-lubricated screw-type compressors (one as hot standby) will be designed to feed (at max) 80 g/s at 15 bar absolute of pressurized GHe to the R/L box. On the discharge side of each compressor station, the helium and oil mixture will first undergo separation in the bulk oil separator. At the outlet of the compressor, the temperatures of the helium and oil gas mixture reach about 395K. This is cooled down to 298K in a water-cooled heat exchanger. The helium stream then flows through the final oil removal system, whereby the remaining oil (either aerosols or vapor) is removed. Oil coming from the separator is first cooled by a water-cooled heat exchanger and then re-injected into the compressor.

Each compressor will be equipped with a frequency driver, housed in an external cabinet. The drive motor of the compressor package should therefore be able to control load variation between 20 Hz to 60 Hz (corresponding to one-third to full flow). The screw compressors inherently are low-vibration machines that normally do not require massive foundations. Vibration dampers, however, will be identified and implemented at the time of installation.

A systematic maintenance program will be implemented to reduce the possibility of unscheduled downtime during normal operation.

7.5.5.2.6 Helium Recovery Compressor

An automatically operated screw-type recovery compressor with mass flow rate of at least 11.53 g/s, equipped with uninterrupted power supply, will be used to pump the generated helium gases from warmup or shutdown to the GHe storage tanks without loss of helium. This compressor will have same pressure characteristics (1.05 bara suction and 15 bara discharge pressure) with a minimum flow rate of 4.56 m^3/min. The start time of emergency power will be about 20 s, to avoid the difficulty of starting at high suction pressure.

The recovery compressor will start pumping at about 1.22 bara immediately if the main cryogenic plant shuts down or the suction line pressure drops below 1.08 bara. The recovery compressor will be able to switch to full gas flow automatically when the suction line pressure reaches 1.36 bara again during a 2-hour period. The recovery compressor's start time to achieve full capacity will be set during the operational testing phase.

7.5.5.2.7 Gas Management

Helium inventory in the refrigeration system is automatically adjusted by the gas management system as the refrigeration/ liquefaction load changes. The gas management system will consist of two control valves. One valve automatically sends excess helium to the buffers (for example, during quenches or warmups) One valve adds helium to the system from the buffer tank when the liquefaction capacity is higher than flow recovered from loads.

These two valves work in concert with the bypass recycle valve, which automatically recycles excess flow from compressor discharge to suction. These two valves control the liquefaction and refrigeration rate. A frequency driver will reduce the total cycle mass flow rate in case of excess flow from the compressors.

An automatic pressure-controlled bypass valve will be installed between the discharge line and the suction line of each compressor. This bypass valve will form a closed loop with the main compressors, to maintain and limit the discharge pressure.

Pressure transmitters and indicators with analog or digital output will be installed on both the discharge and suction lines near the main compressors. Similar transmitters will be installed near the suction side of the distribution valves boxes. Both compressors will be equipped with suitable suction and discharge relief valves.

Several spare ports with shut-off valves will be placed on both the discharge and suction lines in the compressor room and also on the high-pressure line near the refrigerators/liquefiers. The makeup/recovery control valves will be in the compressor room. Several other smaller ports will be on both the discharge and suction lines of the compressors and oil removals for gauges, sensors, and gas sampling purposes.

7.5.5.2.8 GHe Storage Tanks

Three tanks, each with water volume of 70 m^3, will serve as GHe recovery and makeup storage volumes. These tanks will be designed for a gauge pressure of 20 bar (290 psig). The maximum operating pressure will be the same as the maximum discharge pressure of the recovery compressors, 15 bar absolute (217.7 psia). The minimum operating gauge pressure is 2 bar (29 psig). The minimum design gauge pressure will be –1 bar for evacuation purposes. The design specifications will include all appropriate ASME Boiler and Pressure Vessel Codes, Section VIII, Divisions I (Unfired Pressure Vessels) and IX (Welding and Brazing Qualification), and Safety Relief Valves. Material and other geometric features will be detailed before purchasing.

7.5.5.2.9 Ballast and Surge Tanks

These tanks will stabilize pressure variations from the refrigerators' operation. Ballast tanks with the same design pressure as the buffer tanks will be installed at the high-pressure inlet side of the refrigerator. The surge tanks will be designed for lower pressure and will be installed near the suction side of the compressor. Both of these tanks will have an approximate volume of five m^3 and will be built with all applicable pressure vessel codes and safety devices.

7.5.5.2.10 Insulating Vacuum Pumping System

All vacuum insulating space must have pressure lower than 10^{-4} Torr for optimum performance. For this reason, a two-stage pumping set is recommended. The primary pump will be a rotary vane roughing

mechanical pump. This pump will be connected in series with a secondary oil diffusion pump, which will be capable of attaining a vacuum level of 10^{-6} Torr at cold conditions. The process controllers will control the vacuum pumps based on information from vacuum relay signals/gauges. The size of this mechanical vacuum pump will be determined based on final design needs. The vacuum pump will have primary vacuum valves and vacuum gauges to allow remote control of the vacuum system.

7.5.5.2.11 Valves

Different types of valves will be used throughout the cryogenic system. All valve seals will be soft seat and replaceable. Warm, noncontrol valves will be vacuum-tight ball valves with elastomer seats and seals or all-metal diaphragm-type refrigeration valves. Cold valves will be of low heat-leak extended stem design. All valves, with the exception of the JT and compressors bypass valves, will be selected without having sonic flow during steady-state conditions.

7.5.5.2.12 Emergency Helium Recovery

In the event of an unexpected or intentional shutdown of the main cryogenic systems, all the LHe in the main dewars, transfer lines, and the main SRF modules will be recovered to the gaseous storage tanks by the recovery compressors' control system.

All SRF modules must be protected against over-pressurization. The cryogenic system will receive a fail-safe signal to initiate securing the SRF modules as follows.

- The helium level/control feed valves in the cryogenic distribution valve box for the SRF modules are turned off.
- The DC heaters in the helium vessel of the SRF modules are turned off.
- The RF power to the SRF modules is turned off.
- The intercept flow valves are turned off.
- The DC heaters in the main LHe dewars are turned off.

7.5.5.2.13 Emergency Power

Cryogenic systems are susceptible to damage from abrupt power losses. Loss of electrical power, for example, could cause an unexpected system shutdown, which would require continuous operation of the recovery compressor to recover generated boiled-off GHe to the helium storage tanks. The recovery compressor, main helium dewars, cryogenic distribution valve box, and the cryogenic electronics of the SRF modules require a sufficient source of emergency power, as does the Oxygen Deficiency Monitoring systems, which must have an Uninterruptible Power Supply system.

7.5.5.2.14 Utilities Requirements

All utilities requirements for individual cryogenic components such as power, current and voltage, water cooling, instrument air, and so forth have been listed in Table 7.5.7.

7.5.5.2.15 Helium Transfer Lines

Single- or multi-channel transfer lines may be used to transfer liquid or GHe to various components such as to/from the main LHe dewar, SRF distribution valve box, or SRF module. There are three different helium gas lines:

- one suction line to transfer low-pressure helium gas from SRF modules (waveguides), valve boxes, the main dewar (in case of relief or burst), and the refrigerators/liquefier to the main compressors

- one discharge line to transfer high-pressure helium gas from the main/recovery compressors to oil removals, to the refrigerators/liquefiers, cold box, and gaseous storage tanks
- one makeup/recovery line between suction/discharge of the compressors and GHe storage tanks

All these lines will be capable of handling the individual required gas flow rate within specified pressure drops, as will be determined during the design stage. The pressure drops for each line correspond to the line geometry and flow conditions and will be calculated as required during the design phase.

The geometric design of these lines will be dictated by pressure drop, state, and flow-rate requirements. The length, outer diameter, inner diameter, and wall thicknesses will be selected to satisfy the design requirements (flow rate, pressures, heat leak, and safety). Seamless, high-quality 316L stainless steel tube will be used to construct the inner and outer sections. The use of copper tubing to carry LN2 for cooling radiation shields will be permitted provided the design conforms to all applicable codes.

Single- and multi-channel lines may be used to transfer LHe between various cryogenic components. These vacuum-jacketed lines are also to be made from high-quality seamless stainless steel tubing. The lines and mating connections of the SCL or MCL will be constructed to have minimum heat leak, will resist damage from thermal expansion and contraction, and will utilize smooth, seamless, low-pressure drop construction.

7.5.5.2.16 Nitrogen Transfer Lines

The LN2 lines will transfer the LN2 from the nitrogen storage tank to various components. There will be different sizes to transfer appropriate flow rate among inter-connecting components. The main line from the LN2 tank to the phase separator and then to the LN2 distribution manifold will be capable of handing a LN2 flow rate of 200 l/hr at <.5 bar pressure drop. The heat loss of the LN2 lines will be specified to have less than 0.5 watt/m at 80K (exclusive of valves and bayonets). All LN2 transfer lines will be the vacuum-jacketed type, and made of seamless stainless steel. The inner lines will be provided with flexible sections to compensate for thermal expansion and contraction.

Suitable keep-full valves will be installed along the fixed lines to ensure single-phase liquid flow to designated components when pressure stability is essential (e.g., SRF modules). The insulating vacuum space of the lines will take into account the relative humidity factor, dew point, and seasonal temperature variations to ensure it is condensation-free at all times. In addition to combined pump-out/burst ports, the line will have pressure and temperature transmitters with digital or analog output signals for monitoring and interlock.

7.5.5.2.17 LN2 Storage Tank, LN2 Phase Separator

An 84,000 L bulk LN2 storage dewar located outside the storage ring will supply LN2 as needed to the helium cryogenic system, as well as to the Liquid Nitrogen Distribution System. The estimated average withdrawal of ~400 L/hr will use 11% of the stored liquid daily. Based on this estimated rate of consumption, the nitrogen tank must be refilled at least twice weekly for an uninterrupted supply of the LN2 to the cryogenic system. Installation of wireless telemetry will ensure an adequate supply of LN2 by the LN2 supplier. This device will provide remote information of the current liquid level and tank's pressure to the central control system. A minimum of two LN2 withdrawals will be specified, one for direct supply to the cryogenic room and one for supply to vaporizers supplying GN2 to the cryogenic room instrumentation. A gas vent line will be installed to vent gas to the outside buildings. Redundant safety devices, such as relief valves, rupture disks, and various sensing devices will ensure maximum operational safety. Incorporating the use of a vertical fin pressure building system will reduce frost and ice buildup.

The supply pressure to the SRF cavities and the refrigerator pre-cooler will fluctuate, due to uneven withdrawal, and also when the tank is being refilled by the delivery truck. Operating pressure of the SRF cavities and the refrigerators' pre-cooler efficiency will be compromised during such conditions. Therefore, a

sufficiently large phase separator (necessary due to the large flow rates) will ensure steady pressure to each SRF cavity, the refrigerators, distribution valve boxes, and transfer line heat shields.

Table 7.5.7 Cryogenic System Utilities Requirements.

Item, (Qty)	Location	Power	Water Needs	Compressed Air	Ventilating Air	Reference
Main compressors and the oil removal systems (2)	Comp. Room	265 kW, 3phase, 60 Hz, 400 VAC, 450 A (Peak Current), interruptible	Chilled: 28 m^3/h, Ti=15C, ΔT=15 CPi (max) = 7barg, ΔP=2.5bar	21 m^3/h	10,000 m3/h	AL
Recovery compressor and the oil removal system (1)	Comp. Room	43 kW , 3 phase, 60 Hz, 400 UPS -VAC, , 20A nominal intensity at 0 load, 64 A nominal intensity at full load. no interruption	Chilled: 4 m^3/h	2 m^3 /h		NSRRC, AL
Refrigerator (1)	Cryo Room	10 kW, 60 Hz, 230 UPS - VAC, interruptible	Deionized: 170 L/h Ti=20-30°C, ΔT=10°C, Pi (min-max) = 3-7 barg	10 m^3/h		NSRRC, AL
LHe dewar (1)	Cryo Room	1kW, 110 VAC (Heaters)	-		-	
RF valve Box (1)	Tunnel Roof	TBD	-	50 m^3 / hr		NSRRC
Multi-channel transfer lines (As required)	Cryo Room	TBD	-	50 m^3/h		
Monitor system and vacuum pump for cryogenic plant (1)	Cryo Room	40 A, 3 phase, 480 volt, no interruption 40 A, 3 phase, 380 volt, interruptible	-	-		NSRRC
Dryer for He purifier system (1)		12 kW, 1 phase, 220 volt, no interruptible	-	4 m^3/h		NSRRC
LN2 phase separator (1)	Near Cryo Room	110 VAC – 60 Hz, 5 A	-	Small amount	-	-

7.5.5.2.18 Cryogenic System Layout

A flow schematic of the cryogenic system is shown in Figure 7.5.7. The two 500 MHz (fundamental) and one double-cell 1500 MHz (harmonic) SRF modules will occupy a single straight section. A designated space in the neighboring straight section is planned for an additional 500 MHz SRF module to be installed later. These two neighboring straight sections were located near the linac and most of the NSLS-II offices, where the fewest beamlines are located.

Currently we envision four rooms dedicated to the RF power supplies and cryogenic systems. These rooms will be adjacent to the RF straight sections, minimizing the waveguide length and heat load from the helium transfer lines between the cryogenic room and SRF modules. Two power supply rooms are directly adjacent to each RF straight section. The cryogenic room is deliberately placed almost at equal distance from each straight section, between the power supply rooms. Another room adjacent to the cryogenic and power supply rooms is planned for testing SRF modules prior to installation, troubleshooting, and for R&D purposes. The compressor room and gas management buffer tanks have been separated and placed farther from the main building, to isolate induced vibration and noise.

The cryogenic room houses the refrigerator, LHe dewar, inter-connecting transfer lines, multi-channel distributing manifolds, and local control system. The adjacent RF test room is dedicated for pre-installation testing and R&D purposes.

7.5.5.2.19 Oxygen Deficiency Hazard Monitoring and Control System

Oxygen Deficiency Hazards are present when atmospheric oxygen content falls below 19.5% by volume. The BNL Standard Based Management System has strict guidelines in compliance with the Occupational Safety and Health Administration Respiratory Protection Standard 29CRF1910.134 (see Table 7.5.8).

The main potential sources of reduced oxygen are from unplanned discharge of cryogens into confined spaces. Liquefied gases such as helium and nitrogen have the potential to cause ODH conditions, since expanded gases can displace air rapidly when released to the atmosphere.

For NSLS-II, a complete ODH analysis is required for each area (tunnel, cryogenic room, and compressor room), for all possible scenarios, in order to plan and put appropriate controls and measures in place. For the purpose of this report, an ODH classification of 1 is assumed, which among several requirements mandates the implementation of personal oxygen monitoring systems.

Table 7.5.8 ODH Control Measures.

	ODH Class				
Environmental Controls	**0**	**1**	**2**	**3**	**4**
1. Warning signs	■	■	■	■	■
2. Ventilation			■	■	■
ODH-Qualified Personnel Controls					
3. Medical approval as ODH-qualified		■	■	■	■
4. ODH training	■	■	■	■	■
5. Personal oxygen monitor		■	■	■	■
6. Self-rescue supplied atmosphere respirator		■	■	■	
7. Multiple personnel in communication			■		
8. Unexposed observer				■	■
9. Self-contained breathing apparatus					■

Multi-channel gas monitoring systems, such as Safe T Net 410 (up to four channels), have been considered for installation in each area. These microprocessor-based controllers are designed to accept up to four combustible oxygen transmitters. Features include digital readout display, LED alarm indication, 4 to 20 mA output, individual low and high alarm, and relay signals for interlock purposes.

7.5.5.3 Preventive Maintenance Programs

The overall availability of the cryogenic system is defined as the ratio of the actual delivery time to the scheduled operating time. Synchrotron light source facilities are normally operated continuously, 24 hours per day, seven days a week, excluding short studies or maintenance periods and one or two extended periods of machine maintenance per year when the facility is shut down for preventative maintenance, upgrades, and repairs. This is necessary to decrease the number of unscheduled breakdowns. Routine preventive maintenance must therefore be conducted according to manufacturers' recommendations, and, for in-house designed equipment, from past operational experience and engineering judgment.

In some cases, vendors' input via remote monitoring systems may be required. Remote monitoring and storage of data may enable technicians to intervene and troubleshoot problems before complete breakdown occurs. The nature and extent of this capability will be defined during the system design phase.

7.5.5.4 Electrical Design and Power Supplies

The cryogenic system for the RF cavities will include power supplies as required; however, prime power is needed for the cryogenic system components such as the refrigerators, liquefiers, diagnostics, controls, etc. For personnel safety systems such as the ODH system, uninterruptible electrical power is also required.

Prime power inputs required for the cryogenic system will be specified as 115 V, 60 Hz AC, 208 V or 230 V 60 Hz AC, and 480 V 60 Hz AC. Electrical wiring and electrical components will be installed according to BNL, NFPA, and OSHA specifications. Wiring and schematics will be developed as needed for documentation and troubleshooting purposes. As applicable, electrical components will be purchased that are NRTL approved.

7.5.5.5 Control System

Process control systems will be driven by PLCs. The process logic architecture is depicted in Figure 7.5.8 (next page). The main PLC controls the entire helium liquefaction system. This PLC can communicate to a flat screen and is capable of providing an alarm, shutdown protection, local display, and other specified control functions. The compressor's PLC will transmit the specified signals to the main control panel, located at the liquefiers via a digital data interface. The compressor's control panels are to be furnished with a remote/local key switch to transfer starting capabilities between the compressor's panel and the main control panels. The CPUs, RAM, interface boards, power supply, and other components will be defined later.

The overall logic control architecture will be defined during the detail design stage when all control functions will be integrated and communicated to the machine control system.

References

[7.5.1] W. Brauns, www.gdfidl.de
[7.5.2] K. Halbach and R. F. Holsinger, "SUPERFISH - A Computer Program for Evaluation of RF Cavities with Cylindrical Symmetry," Particle Accelerators **7** (1976) 213-222.
[7.5.3] D. Myakishev, "CLANS2 - A Code for Calculation of Multipole Modes in Axisymmetric Cavities with Absorber Ferrites," Proceedings of the 1999 Particle Accelerator Conference, NYC.
[7.5.4] R. A. Rimmer et al., "An RF Cavity for the NLC Damping Rings," Proceedings of the 2001 Particle Accelerator Conference.
[7.5.5] S. Mitsunobu et al., "Status and Development of Superconducting Cavity for KEK-B," Proceedings of the 1997 Particle Accelerator Conference.
[7.5.6] J. Kirchgessner, Part. Accel. 46(1):151 1995.
[7.5.7] K.W. Robinson, CEAL-1010, Cambridge Electron Accelerator, Cambridge, MA (1964).
[7.5.8] Y. Miyahara et al., "Equilibrium Phase Instability in the Double RF System for Landau Damping," NIM A-260 (1987 p 518-528.
[7.5.9] R.A. Bosch et al., "Robinson Instabilities with a Higher-Harmonic Cavity," Phys Rev ST-AB **4**, p. 74401 (2001).
[7.5.10] M. de Jong et al., J. Microwave Power Electromagnetic Energy, **27**:136-142, 1992.
[7.5.11] M. Jensen et al., "First Results of the IOT Based 300 kW 500 MHz amplifier for the Diamond Light Source," PAC 2005, Knoxville, TN.
[7.5.12] F. Perez et al., "New Developments for the RF System of the ALBA Storage Ring", EPAC 2006, Edinburgh, Scotland.
[7.5.13] P. Marchand, et al., "High Power (35 kW and 190 kW) 352 MHz Solid State Amplifiers for the SOLEIL Synchrotron," PAC 2005, Knoxville, TN.
[7.5.14] Hanspeter Vogel, ACCEL. Private communication.

[7.5.15] M. Svandrlik, et al., "The Super-3HC Project: An Idle Superconducting Harmonic Cavity for Bunch Length Manipulation," EPAC 2000.
[7.5.16] S. Simrock, "Digital Low-Level RF Controls for the Future Superconducting Linear Colliders," PAC 2005, Knoxville, TN.
[7.5.17] C.W. Horrabin, and D.M. Dykes, "Diamond Low Power RF System," EPAC 96.
[7.5.18] J.M. Brennan et al., "RHIC RF beam control," EPAC-2001.
[7.5.19] M. Liepe, S. Belomestnykh, et al., "A New Digital Control System for CESR-C and the Cornell ERL," PAC 2003, Portland, OR.

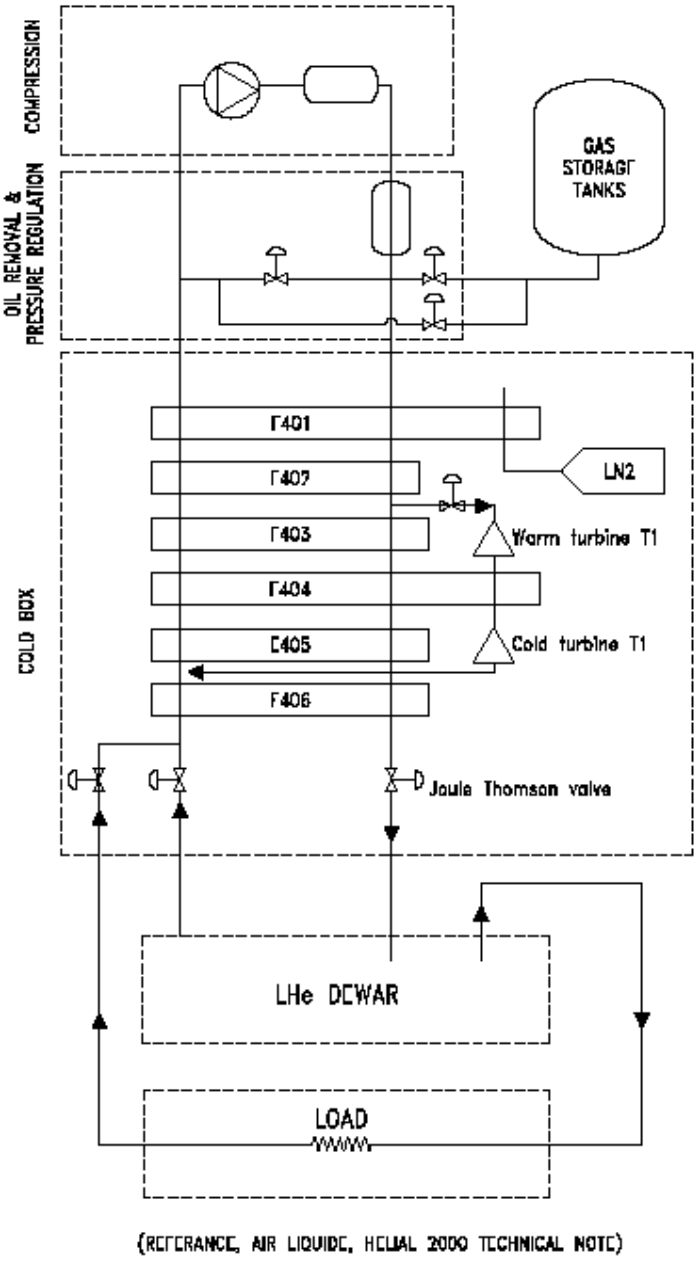

Figure 7.5.8 Cold box, simplified flow diagram.

7.6 Injection System

To minimize disruption to operations, the full-energy injection system will run most of the time in top-off mode. It will also be capable of filling the ring from empty to full charge in a reasonable time.

The injection system consists of a 200 MeV linac, followed by a booster housed in the main ring tunnel and hung from the ceiling above the main synchrotron, as described in Chapter 6. The capability to increase the injector linac energy is built into the design. The large circumference of the booster (780 m) makes injection and extraction a relatively simple operation, due to the long revolution periods (>2.5 μsec) of both the booster and the main ring, at least as far as rise times and fall times of the pulsed magnetic components are concerned.

7.6.1 Injection Sequence

The injection process to fill the ring from zero current occurs at the rate of 1 Hz, and bunches are transferred to the main ring nominally 40 at a time (this number can easily be increased to 100 or more bunches) to fill consecutive about 1,040 of the 1,300 RF buckets available. Bunch groups enter the ring in sequence, starting with the front of the ring train and stepping sequentially back in time along the filled ring bunch train until the end is reached, then skipping over the empty section and starting again at the head of the bunch train, until the required current has been established. Assuming the same amount of charge (7 nC per macropulse) as for the top-off mode, the duration of the initial fill is about 3 minutes with the injection system running at a 1 Hz repetition rate. This value is sufficiently low; therefore, there are no additional requirements for the injection system in terms of the initial fill.

Top-off operation to keep the current within ±0.5% of the nominal value will be the standard operating mode of NSLS-II. The frequency of operation to keep the current within these boundaries depends on the beam lifetime and is expected to take place about once per minute. The injected bunch trains from the booster (nominally 40 buckets), are stepped sequentially around the ring bunch structure. Users expect bunches to stay relatively constant in charge relative to each other (a difference of ±10% has been adopted). We are considering several possible techniques for providing a filling pattern with sufficient uniformity.

7.6.2 Ring Injection Scope

The entire ring injection system consists of four distinct component assemblies: 1) linac and electron gun, 2) beam transport line, 3) the booster, discussed in Chapter 5, and 4) the booster-to-storage ring transfer system. Three of these assemblies are briefly discussed below.

7.6.2.1 Linac and Electron Gun

The first component of the ring injection system is the linear accelerator (linac), including the electron gun, which is a grid-controlled dispenser cathode running at -100 kV, capable of peak pulse currents of up to 1.5 A. The low-energy beam transport system that brings the gun current from the gun to the linac includes four or more focusing solenoids, a subharmonic buncher cavity that imposes the ring/booster RF structure (~500 MHz) on the drifting beam, and a pre-buncher cavity that imposes the linac RF structure (~3000 MHz) on the 500 MHz bunches. At least two fast beam current monitors must be included here, to be able to detect the bunching of the beam at both frequencies before injection into the linac. The gun pulse will nominally be 80 nsec long, supplying 40 buckets of ring charge at 500 MHz.

The linac itself comprises four 2/3π traveling wave iris-loaded waveguide accelerating sections, each driven at 3000 MHz by a single 35 MW peak power non-sledded klystron fed by its associated modulator. The linac output energy is very conservatively rated at 200 MeV, with the typical energy spread from an S-

band linac of ±0.5%. The linac also requires at least four X–Y steering coils, their power supplies, and beam position monitors. It is described in more detail in Chapter 5.

7.6.2.2 Booster-to-Storage Ring Transfer System

The fourth component is the booster-to-storage ring transfer system, which includes the extraction system, the transport line to the ring, and the injection straight in the storage ring. The transport lines need to match the Twiss parameters of the linac or booster beam to the booster or ring acceptance at the injection point. The trajectory of the electron beam gets matched to the storage ring injection straight by four bending magnets. Matching of the machine functions is accomplished with 17 quadrupoles. These transport lines, along with the appropriate numbers of beam current and position monitors and X–Y steering magnets, are described in more detail in Chapter 6.

A long, strong-pulsed magnet close to the circulating beam can perturb the orbit of the circulating beam significantly. To minimize this effect, we keep this magnet as short as possible and construct it as a straight eddy current-shielded type. We will use a second pulsed magnet upstream of the final septum; this will be a longer, higher-field pulsed magnet, farther away from the storage ring beam and constructed of thin silicon steel laminations arranged in a curve following the injected electron beam trajectory. This magnet provides most of the final bend of the transport line. Optimization of these two magnets is still in progress. The injection straight section (Figure 7.6.1) is an 8 m dispersion-free straight in the storage ring containing the entire injection bump. The ring injection hardware consists of 1) a pre-septum with end-field compensated, 750 mm laminated, steel-pulsed dipole (Table 7.6.1) 2), a final eddy current channel shielded septum magnet that is 500 mm long (Table 7.6.1), and 3) four injection kickers that are 750 mm long, (Table 7.6.2).

We are assuming 1) a space between the last ring component and the first kicker at the upstream end of the injection straight, 2) a spacing center-to-center of the first and second kickers to achieve a beam displacement of 15 mm, and 3) a mirror image of the kicker spacing at the downstream end of the ring straight section. This will leave a 3.6 m space, which is enough room for the proposed injection septum configuration, allowing the injection process in horizontal phase space to be achieved (Figure 7.6.1). The final injection septum at the end of the transport line will bend the beam coming from the transport line into a trajectory parallel to the displaced coasting beam in the ring.

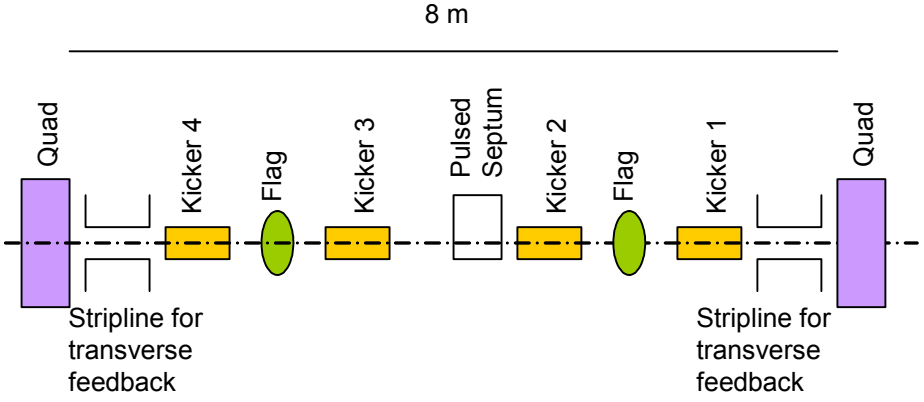

Figure 7.6.1 Arrangement of the injection straight section.

Table 7.6.1 Parameters of the Septum Magnets.

Pre-septum magnet	
Field [T]	1.1
Length[m]	0.75
Angle [mrad]	83
Aperture, H xV [mm]	20 x10
Current Amplitude[kA]	12
Inductance[μH]	1.8
Voltage [V]	600
Pulse shape	100 μsec ½ sine wave
Design	10 mil silicon steel laminations
Final injection septum magnet	
Field [T]	0.9
Length [m]	0.5
Angle [mrad]	45
Aperture, H xV [mm]	20 x10
Current amplitude [kA]	10
Inductance [μH]	1.2
Voltage [V]	600
Injected pulse shape	60 μsec period, full sine wave
Design	Ferrite EBG V270-035A

The ring injection kickers will be run in series from a single capacitor bank and are connected together by low-impedance transmission lines. Experience at NSLS has shown that the insertion impedance of well-constructed transmission lines is insignificant. In this way, with some tuning, the disturbance to the stored beam due to the injection process can be minimized, as any slight mismatch and field jitter are common to all four pulsed magnets.

Table 7.6.2 Parameters of the Injection Kickers.

Ring injection kickers [number)	4
Field [T]	0.193
Length [m]	0.75
Angle [mrad]	14.4
Aperture, H xV [mm]	70 x25
Current Amplitude [kA]	5.34
Inductance [μH]	1.3
Voltage [V]	4,500
Temporal pulse shape	5 μsec at the base, ½ -sine wave
Design	Ferrite CMD 5005

Special attention will be paid to minimizing the disturbance of the stored beam orbit from transients induced by the pulsed magnets. Alternative arrangements of the injection straight section will receive attention in our future studies. Namely, using the Lambertson injection septum with the transport line descending vertically may provide substantial benefits. The Lambertson septum magnet is fed by a DC, not pulsed, power supply, which eliminates a major component of the disturbance for the stored beam orbit. Requirements on the ring dynamic aperture for this injection scheme will be carefully examined.

7.6.3 Injection Simulations

Given the injection straight set-up, we performed simulations of the injected beam dynamics. These studies indicate the design is feasible. To quantify requirements for the injector, three values of the injected beam emittance were used for tracking the electron bunch through the NSLS-II lattice. Initial efforts included modeling the injection process using ELEGANT and determining the ring stay-clear aperture required for injection using TRACY-2. Both of these studies are discussed below. Future work will include calculating tolerances for the injected bunch and estimating the loss budget and loss patterns.

7.6.3.1 Phase Space of the Injected Beam

To determine the minimum acceptance required by the injection process, we simulated the electron distribution in x, x′ phase space after the injection, using the particle-tracking code ELEGANT. In Figure 7.6.2 we plot the result for three different cases of the injected beam with emittance 10, 50, and 100 nm, respectively (Table 7.6.3). For each case, the beta function and injection offset are optimized to reduce the required acceptance. The plot gives the electron distribution for the first five turns indicated by the five colors, as shown by the key. Note that when the emittance increases to 100 nm, as the betatron oscillation amplitude increases, the tune is approaching 0.33; hence, the fourth-turn distribution almost overlaps with the first turn. The horizontal maximum increases from 7 mm to ~10 mm, while the maximum x′ increases from 0.35 mrad to ~0.5 mrad. This simulation showed that storage ring acceptance is adequate for injection of the beam with emittance up to 100 nm. This tracking was done for the bare lattice without RF, synchrotron radiation, or errors. Including those additional effects will be the subject for future work.

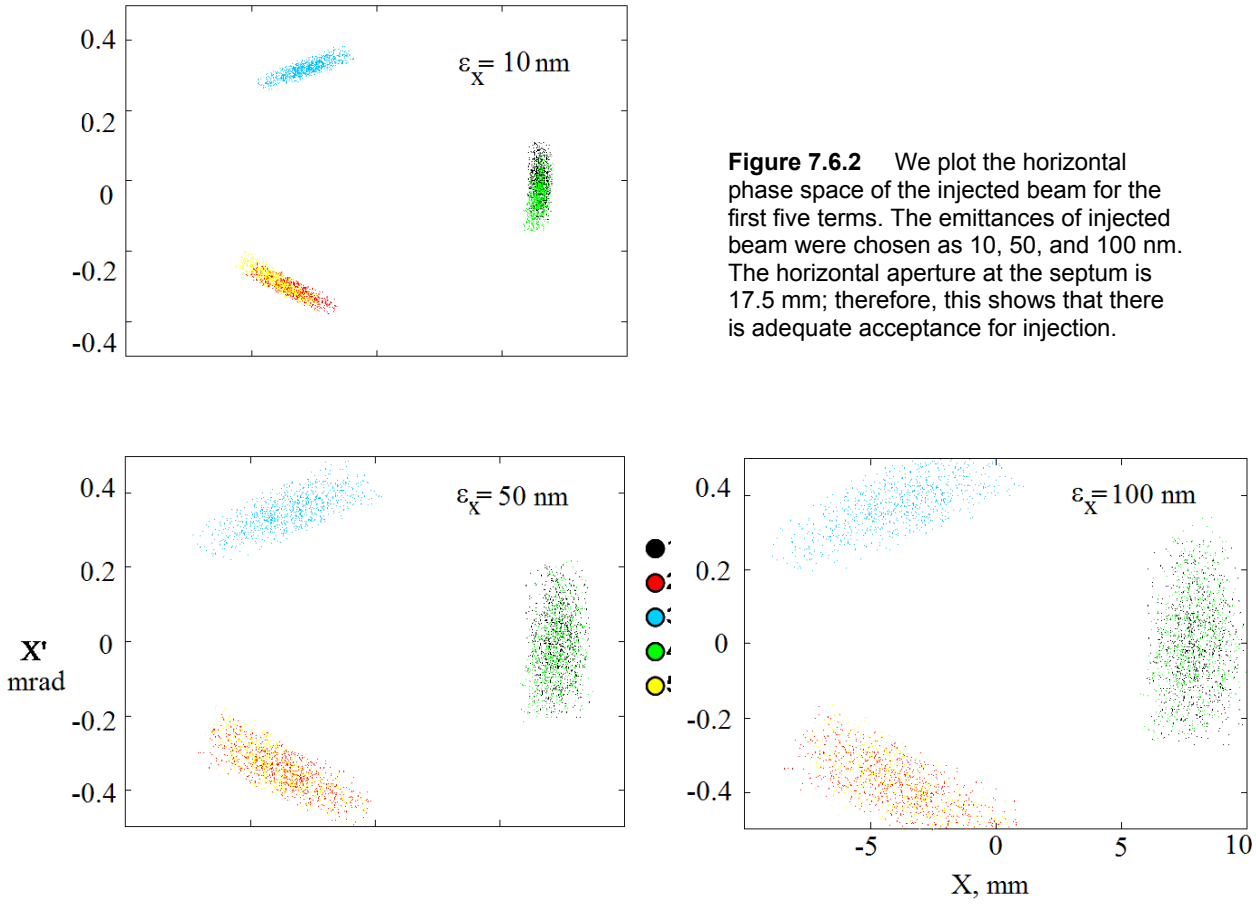

Figure 7.6.2 We plot the horizontal phase space of the injected beam for the first five terms. The emittances of injected beam were chosen as 10, 50, and 100 nm. The horizontal aperture at the septum is 17.5 mm; therefore, this shows that there is adequate acceptance for injection.

Table 7.6.3 Input Beam Parameters. Injected beam is matched to provide minimum stay clear aperture for each value of emittance. $\Delta E/E$ = 0.05% in all cases, vertical beam size calculated with coupling κ = 0.1.

Horizontal emittance (nm-rad)	Initial displacement from stored beam (mm)	3x RMS horizontal beam size (mm)	3x RMS horizontal beam divergence (mrad)
10	6.5	0.62	0.15
50	7.3	1.65	0.27
100	7.9	2.47	0.36

7.6.3.2 Stay-Clear Aperture Required for Injection

Tracking results from InjTrack, a TRACY-2 module for tracking the injected beam at NSLS-II, are presented here. After correcting for errors, we will use the results to define the minimum aperture NSLS-II requires for injection.

The results are tracked with radiation and RF cavity off for the entire lattice, and then the maximum of beam envelope for each cell is plotted in Figures 7.6.3 (H) and 7.6.4 (V). The upper and lower curves correspond to the 17.5 mm septum aperture projected around the ring with $\sqrt{\beta_x(s)/\beta_x^{sept}}$. This is repeated for the vertical plane using the insertion device half-gap of 2.5 mm. Three curves represent required stay-clear aperture for tracking beam with the three emittances of 10, 50, and 100 nm. Results show that our design has sufficient physical aperture for injection. In the future, we plan to extend this analysis by tracking with errors, synchrotron motion, and radiation damping.

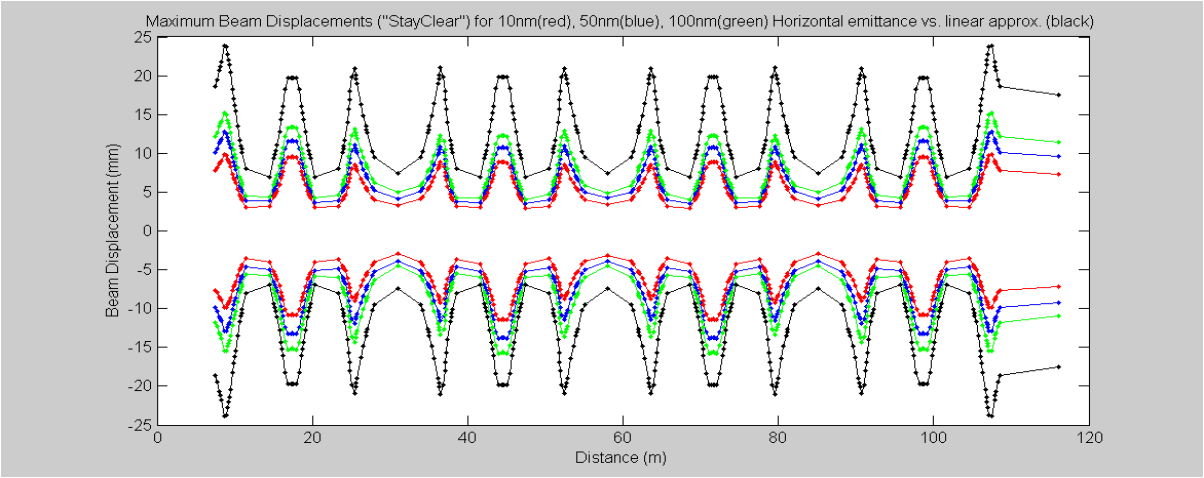

Figure 7.6.3 Beam (H) is injected at an initial displacement of ~17.5 mm (septum location).

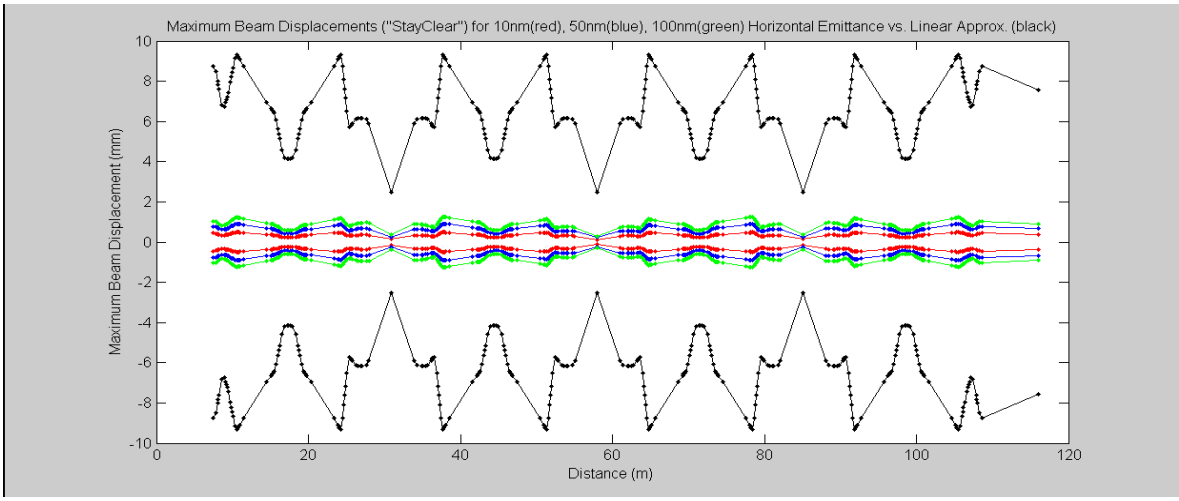

Figure 7.6.4 Injected beam envelope (V). Physical aperture at ID half-gap of 2.5 mm.

Reference

[7.6.1] B. Kalantari, V. Schlott, T. Korhonen, Proc. of EPAC-2004, Lucerne, Switzerland, p. 2882.

7.7 Beam Scrapers and Photon Absorbers

7.7.1 Beam Scrapers

Two pairs of electron beam scrapers will be used for accelerator physics measurements of the aperture and beam lifetime limits. The thickness must be ~$5X_o$ (radiation lengths) for the electron beam. The horizontal blades must be in the same plane and adjustable from full open (vacuum chamber width) to the chamber centerline with a resolution of ~1 μm and a reproducibility of ~5 μm. One location for the horizontal scrapers is in one of the dispersion regions next to the BPM and the SF2 sextupole, where there is high β_x and dispersion. The second location for horizontal scrapers is in the SID between the Q33 and S22 sextupoles, the maximum β_x for the ring. The two vertical scrapers will be placed near the high β_y in the dispersion region (D5A at $\Delta\mu_y \sim\pi/2$ from the injection septum) and the LID (D4B at $\Delta\mu_y \sim 2\pi$ from the injection septum). These scrapers will provide controlled physical apertures to prevent large-amplitude particles (from the injector) from hitting the small-gap undulators, later in the ring. The scrapers will also provide defined apertures for understanding the dynamic aperture and lifetime in the ring.

7.7.1.1 Conceptual Design

To maximize their effectiveness as well as to simplify their engineering design, the two pairs of beam scrapers required will actually consist of four separate units: two horizontal and two vertical scrapers. These scrapers will serve as protective devices for the IDs. They will also be used as diagnostic tools during the commissioning phase and during machine studies.

Previous reports [7.7.1] have indicated that Touschek scattering is the dominant source of ID damage. Work done at APS has shown that scrapers should be located in a low-emittance lattice to effectively protect the IDs. This suggests that the horizontal scrapers should be installed where there is adequate dispersion at the scrapers as well as a large horizontal beta function. Touschek scattering presumably not only imparts a large energy deviation, but also induces large betatron oscillations for the scattered particles. A significant concern, however, is that the scrapers may compromise injection efficiency—or worst yet, may even produce more ID damage if the injected beam hits the scrapers, creating a shower that propagates to the IDs. To address this concern, we will carefully study the development work done at APS.

All four units planned for NSLS-II will share the same engineering design and be built identically—the horizontal and vertical scrapers differing only in the final mounting and installation. Each unit will have two jaws or blades that can move independently from one another, each being driven by precisely controlled stepping motors. The blades will be made of Glidcop, a dispersion-strengthened copper with excellent thermal and electrical properties at elevated temperatures. Each of the blade assemblies will have a water-cooling circuit to minimize thermal expansion of the blades when they are hit by the dipole radiation fan.

Furthermore, to minimize impedance problems, the shape of the blades will be determined by detailed numerical simulation. These studies are still in progress and the results are preliminary. Figures 7.7.1 and 7.7.2 show two views of the design of an existing scraper at APS. The NSLS-II scraper design will be based on this APS design, with appropriate modifications to match the chamber geometry. Figure 7.7.3 shows a preliminary layout of the possible NSLS-II scraper.

Each scraper unit will be mounted directly on the vacuum chamber and the adjustable blades can be repositioned remotely. Once they are in the desired position, however, they must stay in place within the required tolerance.

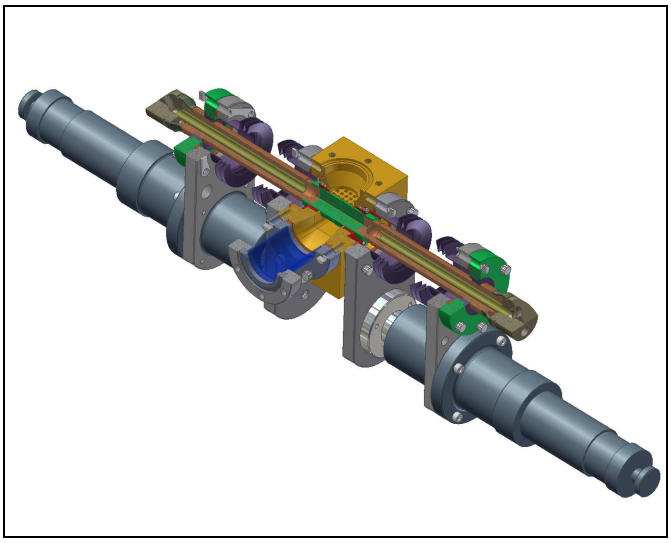

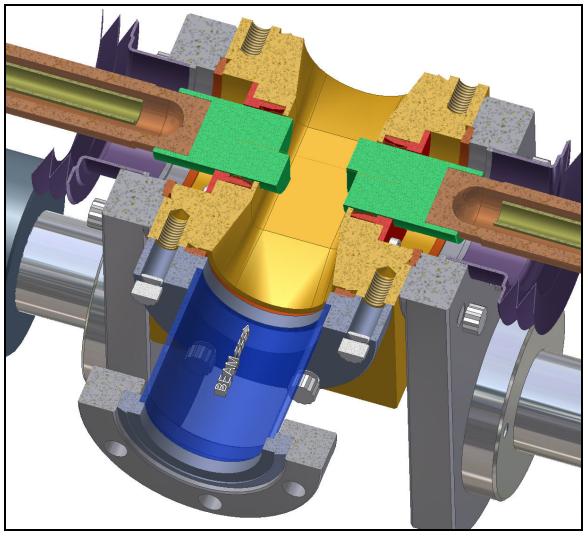

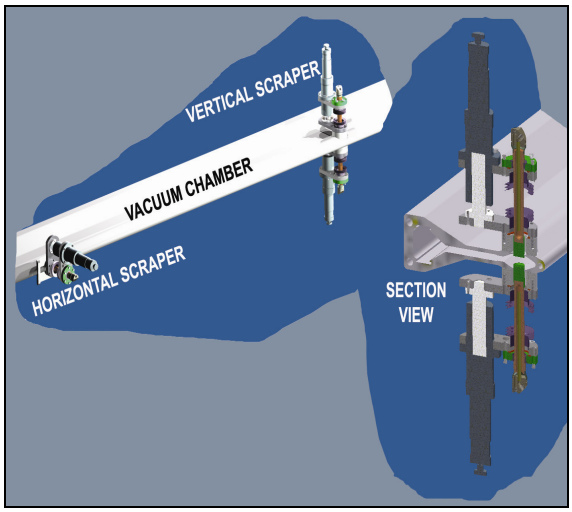

Figure 7.7.1 (top left) Sectional view of APS scraper assembly, round blades (closed).

Figure 7.7.2 (top right) Sectional view of APS scraper assembly, blades partially opened.

Figure 7.7.3 (right) Conceptual layout of NSLS-II scraper (two views)

7.7.2 Photon Absorbers

Discrete photon absorbers will be installed in the vacuum chambers to protect their uncooled surfaces from the radiation fans of the bending magnets and IDs. Shielding the vacuum chambers from radiation fans also minimizes their thermal distortions and leads to better thermal stability of the PUEs attached to the chambers. To protect the chambers from exposure to unintentional beam deviations, PUE interlocks at insertion devices will be set at ± 0.25 mrad [7.7.2]. The positional error budgets consisting of orbit error, mechanical, and survey tolerances will be set at ±2 mm.

As discussed in Chapter 8, the peak power densities of the bending magnets, damping wigglers, and cryogenic permanent magnet undulators are 0.088 kW/mrad^2, 55.30 kW/mrad^2, and 77.86 kW/mrad^2, respectively, for a 500 mA beam at 3 GeV. The power density of the BM is uniform in its horizontal fan of 104.7 mrad (6º) except at the edges. For the DW and CPMU devices, the horizontal power density profiles are shown in Figure 7.7.4. The vertical power density profile, common for all devices, is shown in Figure 7.7.5.

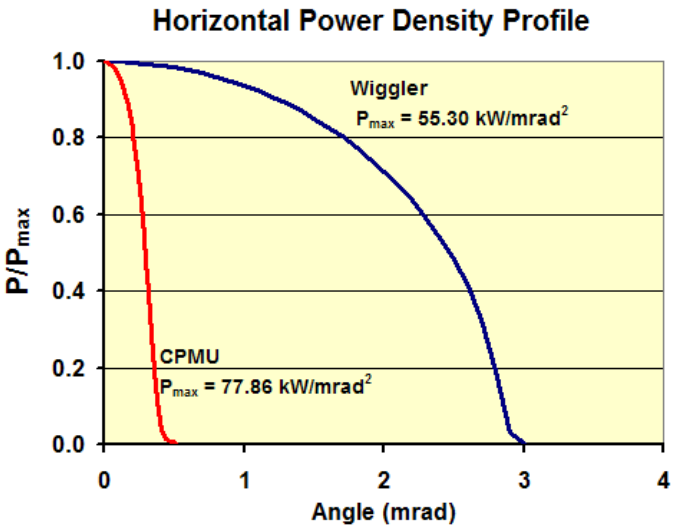

Figure 7.7.4 Horizontal power density profiles, P/P_{max}, of damping wiggler and CPMU. P_{max} is obtained at 500 mA beam current.

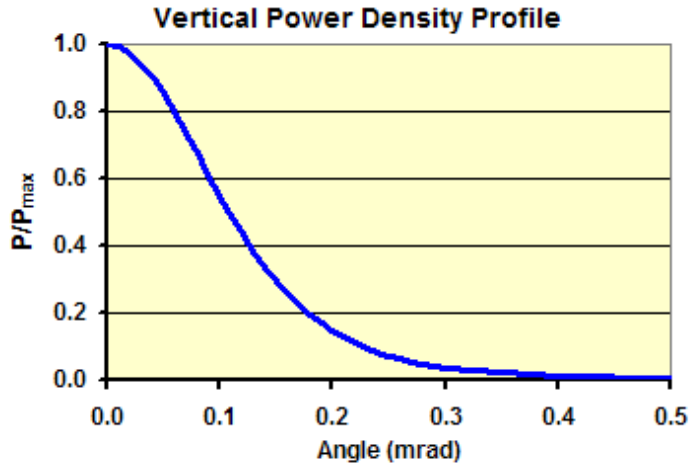

Figure 7.7.5 Vertical power density profile, P/P_{max} for damping wiggler and CPMU.

The CPMU radiation fan is narrow in both directions and can be extracted with adequate clearance through the 76 mm (H) × 25 mm (V) apertures of Chambers 1 and 2 and the 15 mm slot of Chamber 2 (see Figures 7.3.1 and 7.3.3). The BM and DW radiation fans in Chamber 2 (Figure 7.7.6), however, require clipping by two absorbers, namely, a crotch absorber and a wiggler absorber. Because of the high power density of the DW radiation, these absorbers clip the outer edges of the DW horizontal fan just enough to allow the clipped fan to be extracted to the front end.

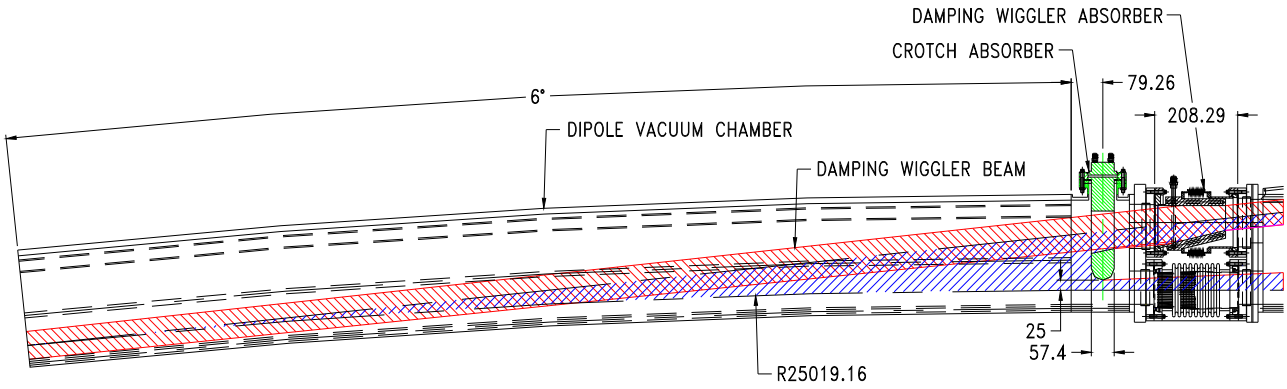

Figure 7.7.6 Clipping of BM and DW x-ray fans by crotch and wiggler absorbers in Chamber 2. The BM radiation fan (blue color) partially overlaps the DW radiation fan (red color).

7.7.2.1 Conceptual Designs of Photon Absorbers

Figure 7.7.7a shows a 3D model of the crotch absorber. The absorber is made from a Glidcop® block with brazed water-cooling channels of OFHC copper. Also brazed to the Glidcop block are a stainless-steel flange and a water manifold. A rectangular slot in the center of this block allows DW or CPMU radiation fans to pass through without interception (only the inboard edge of the DW fan is slightly clipped). The crotch absorber is inserted into the downstream aperture of Chamber 2 such that its nose tip is 5 mm inside the aperture (i.e., 30 mm outboard from the center of the aperture). The tip intercepts a total of 814 W of beam power with a maximum power density of 5.54 W/mm^2. A thermal analysis of the crotch absorber was carried out using ANSYS software. The results, plotted in Figure 7.7.7.2b, show a peak temperature of 102ºC, which is substantially lower than the maximum allowable temperature of 450ºC for Glidcop. OFHC copper would normally be used for a low temperature rise of ~100ºC. However, Glidcop will ensure the dimensional stability of the nose tip after brazing cycles and will allow a slight clipping of the inboard edge of the DW fan.

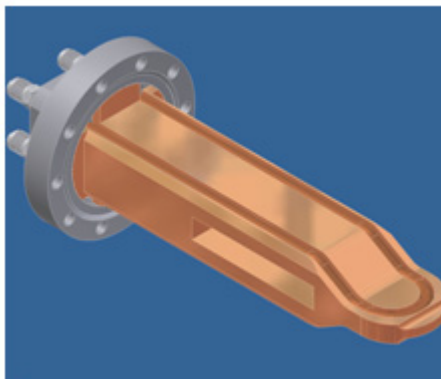

Figure 7.7.7 Crotch absorber.

a) 3D model.

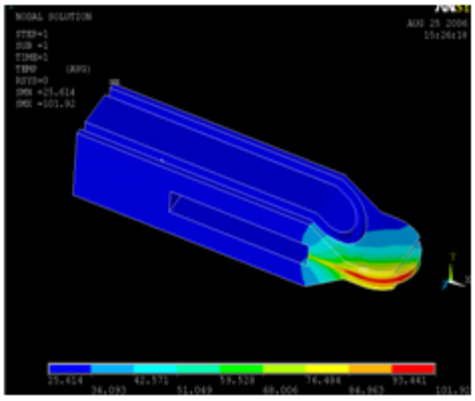

b) Temperature contours from Ansys FE analysis showing a peak temperature of 102ºC.

The damping wiggler absorber, shown in Figure 7.7.8a, fits in the 208 mm space between Chambers 2 and 3 on the outboard side. The upstream end of the absorber is brazed to a flange that mates with the flange of Chamber 2. The downstream end is cantilevered inside a bellows assembly to allow for thermal expansions of the chambers during bakeout. Two water cooling channels are provided on each vertical side of the Glidcop block to absorb power from the outer extents of the horizontal DW x-ray fan at a grazing incidence of

6º. The total power intercepted by the two vertical sides is 11.6 kW, with a peak power density of 47.8 W/mm^2.

An ANSYS FE thermal analysis of the wiggler absorber predicted a peak surface temperature of 398ºC. The temperature profile, plotted in Figure 7.7.7b, shows high temperatures directly under the beam footprint.

Assuming a water flow of 2 GPM in each of the cooling channels, the average bulk water temperature rise will be 5.5ºC.

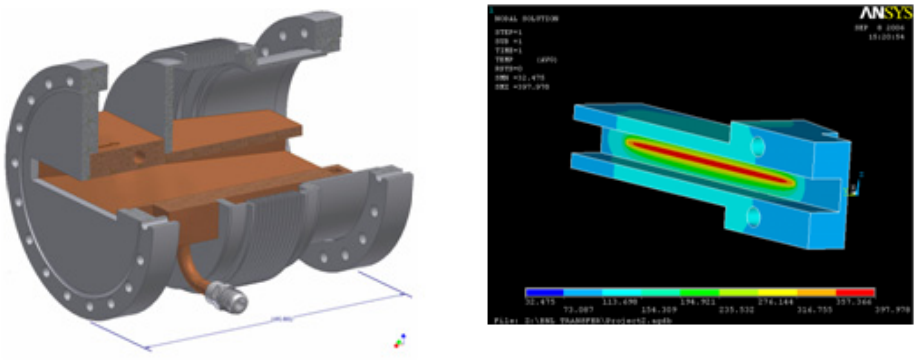

a **b**

Figure 7.7.8 Damping wiggler absorber. **a**) Cut-out of a 3D model showing Glidcop block, cooling channels, bellows, and flanges. **b**) Temperature contours from an ANSYS FE analysis with a peak temperature of 398ºC.

Another crotch absorber will be used in Chamber 4 with a slot width that will allow the user-specified width of the dipole radiation fan to exit to the front end. Additionally, counter-flow and flange absorbers (Figure 7.7.9) will be used in Chambers 1, 3, and 5 to intercept unused dipole radiation fans.

Figure 7.7.9 Counter-flow and flange absorbers for the storage ring vacuum chambers.

References

[7.7.1] Borland, M. "ID Protection with Fast-Moving Scrapers," OAG-TN-2004-050, November 11, 2004.
[7.7.2] V. Ravindranath, S. Sharma, B. Rusthoven, M Gosz, L. Zhang, and J. Biasci, "Thermal Fatigue Life Prediction of Al-15," proceedings, MEDSI-2006 Workshop, SPring-8, Himeji, Japan, May 24-26, 2006.

7.8 Storage Ring Diagnostics and Instrumentation

7.8.1 Introduction

State-of-the-art advanced diagnostics and instrumentation systems are required for a smooth and rapid commissioning and for productive and successful operation of the NSLS-II storage ring. This section provides a list of the monitored parameters, technical solutions with some alternative variants, and the required specifications to achieve these goals. Table 7.8.1 shows a summary of these various instrumentation components.

Table 7.8.1 Beam Diagnostics and Instrumentation for Storage Ring.

Monitor	Quantity	Function
4-button pick-ups	226	Beam position, dispersion, response matrix, turn-by-turn dynamics
Stripline pick-ups	1	Longitudinal and transverse frequency components
RF-drive stripline and amplifier	1	Betatron tune
Loss monitors	10	Beam loss
Fluorescent flags	4	Injection position, profile
Transverse feedback system	1	Suppress beam instabilities
Optical ports for visible radiation	2	To provide light for streak camera, FireWire camera and emittance monitor
Streak-camera	1	Bunch length
DC current transformer	2	Beam current
Fast current transformer	2	Filling pattern
X and Y beam scrapers	2	Machine studies, halo
FireWire camera	1	Transverse beam characteristics
Emittance monitor	1	Transverse emittances
Diagnostics undulator	1	Energy spread, beam divergence, momentum compaction factor
Pinhole camera	1	Horizontal emittance
Counter	1	RF frequency monitor
Photon BPMs	2 per installed undulator	Photon beam angle and position

As a basic policy, whenever possible, we will pursue the utilization of commercial-off-the-shelf devices in order to reduce cost as well to achieve better reliability. Most of the existing diagnostics equipment today already satisfies the basic requirements for NSLS-II and only a few, if any, need further development.

Full utilization of the micron size electron beam requires sub-micron resolution of the orbit monitoring system, in order to provide the required position stability. Priority consideration will be given at the earliest stages of design to provide instruments for the detection and remedy of factors that affect beam quality.

7.8.2 Physics Design and Parameters

The following beam parameters will be monitored:

- closed orbit
- working point (tune for the both planes)
- circulating current and beam lifetime
- filling pattern
- emittance for both planes
- individual bunch length

- position of the photon beam for the insertion devices
- coherent bunch instabilities
- distribution of beam losses around the ring

During beam studies the following parameters will be measured:

- linear optics
- dispersion for both planes
- chromaticity for the both planes
- coupling
- momentum compaction
- energy spread
- beam based alignment of quadrupoles and sextupoles
- nonlinear resonances
- synchrotron frequency
- RF system parameters
- vacuum chamber impedances

7.8.3 Intercepting Diagnostics

Four flags will provide information on the shape and position of the injected beam and will assure proper matching of the injected beam. Two flags will be placed in the injection straight: the first one will be used to observe the incoming beam from the booster. The second flag, installed before the first kicker, will allow observation of the injected beam shape after one turn. The third flag will be installed after the first bend downstream of the injection straight. The fourth flag location will provide data on beam position and the beam approximately half a circumference away from the injection straight. The flag material will be cerium-doped yttrium aluminum garnet, which has excellent resolution (about 30 μm) and radiation stability [7.8.1]. The estimated horizontal beam size coming from the booster is σ_x = 400 μm, and vertical size for 2% coupling is σ_y = 60 μm. If the spatial resolution of the YAG:Ce flag is found inadequate, then optical transition radiation can be used.

To avoid impedance problems, the flag will be designed to ensure a smooth vacuum chamber wall when the screen is fully retracted. Spring-loaded RF-fingers will be used to provide electrical contact in order to avoid trapped modes for the wake fields. A typical flag assembly used at APS is shown in Figure 7.8.1, and the RF fingers are shown in Figure 7.8.2. To use this design we will need only to modify the vacuum chamber aperture to match the NSLS-II geometry.

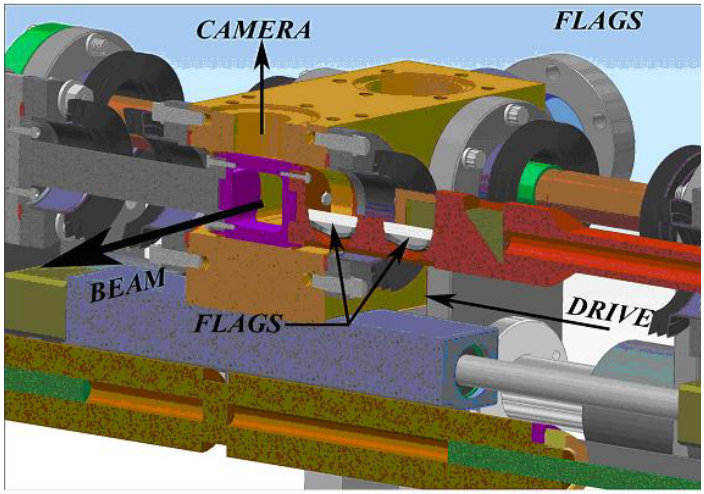

Figure 7.8.1 Design of the flag used for the diagnostic of the electron beam injected into the storage ring.

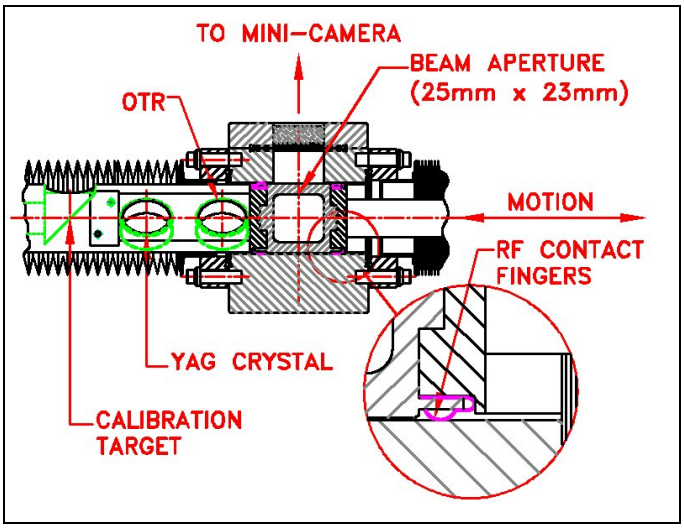

Figure 7.8.2 RF fingers (with detail), providing smoothness in the vacuum chamber.

7.8.4 Circulating Current

7.8.4.1 Filling Pattern Measurement

To maintain uniform fill and mitigate dependence of the BPM receivers on the filling pattern, two in-flange fast current transformers will measure the charge of individual bunches [7.8.2]. They have 1.75 GHz bandwidth with 200 ps rise time. The information obtained will be used in the top-off algorithm. The signal from the FCT will be used as input for top-off safety interlock. Figure 7.8.3 shows a typical in-flange fast current transformer that can be directly mounted on the beam chamber. An elliptical aperture, matching the shape of the storage ring vacuum chamber, will be used (Figure 7.8.4).

Figure 7.8.3
Bergoz In-Flange
Fast Current Transformer.

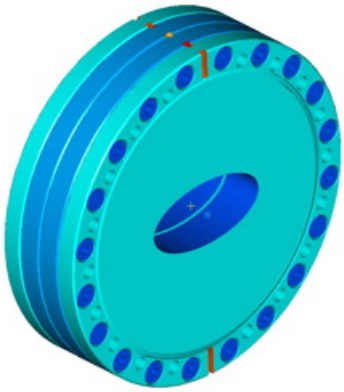

Figure 7.8.4
Elliptical aperture of the
in-flange current transformer
utilized at DESY.

7.8.4.2 DCCT

Two DC current transformers (PCT by Bergoz) will monitor the stored current, providing redundant measurement capability [7.8.2]. The Bergoz New Parametric Current Transformer (Figure 7.8.5) is the latest evolution of the Unser transformer, commonly known as DCCT, developed at CERN in 1966 by Klaus B. Unser.

DCCT has large dynamic range and high bandwidth, making it a versatile device for measuring lifetime and injection efficiency. It is insensitive to synchrotron revolution frequency and bunch fill pattern, with residual modulator ripple being eliminated, thus enabling full bandwidth operation down to a very low current.

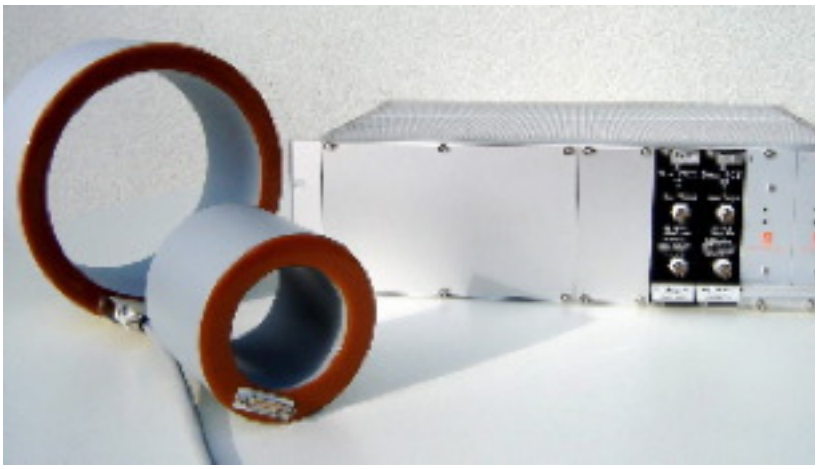

Figure 7.8.5 Bergoz New Parametric Current Transformer.

The NPCT-115-C30-H model has a radiation-hardened sensor and four ranges (±20 mA, ±200 mA, ±2 A, ±20 A) with remote control by TTL signals. Its resolution is better than 5 μA/Hz^{½}. We expect that the NPCT described previously will also be available as an in-flange unit.

7.8.5 RF Diagnostics

7.8.5.1 RF BPMs

The optics of the NSLS-II storage ring is shown in Figure 7.8.6. In the baseline design there will be seven BPMs for each cell. Straights with insertion devices, however, will be provided with two additional BPMs, shown in the figure as user BPMs.

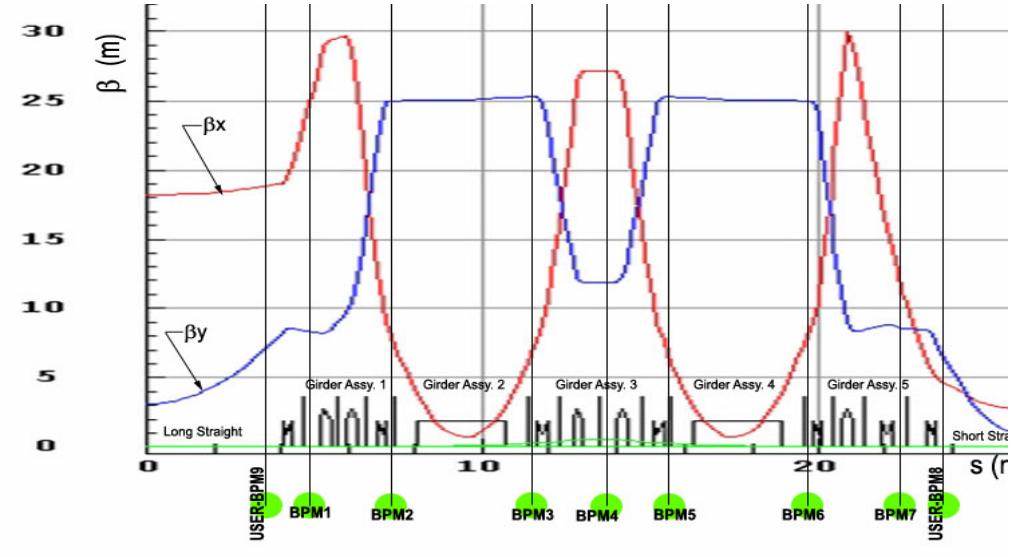

Figure 7.8.6 NSLS-II cell with BPM locations.

The high precision pick-up electrodes will utilize button design and will be diagonally incorporated into the aluminum extrusion vacuum chamber. Figure 7.8.7 shows the cross-section of the basic construction of the four-button pick-up electrodes. An average current of 500 mA circulating in the storage ring is expected to produce –1.1 dBm signal into 50 Ω load at 500 MHz. This estimate is done for a button, shown in Figure 7.8.8, with 5 mm radius and 4 pF capacitance. The buttons are spaced with a distance to the beam of 20 mm. The sensitivities for both vertical and horizontal directions will be established during preliminary design.

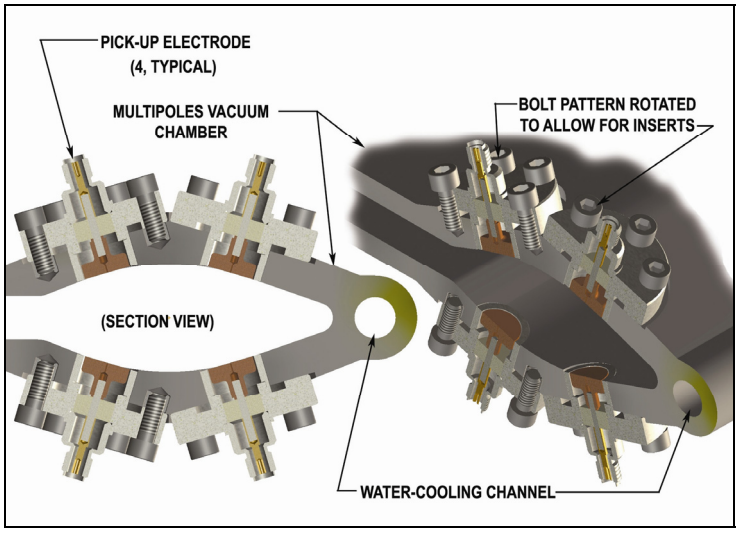

Figure 7.8.7 Four-button, two-plane pick-up electrodes mounted on the vacuum chamber.

Libera Electronic Modules, manufactured by I-Tech [7.8.3, 7.8.4], will process the signal from the BPM buttons. The RMS uncertainty of the beam position is 0.2 μm in 1 kHz bandwidth for the buttons placed on

the 10 mm radius. The digital design of the modules provides the possibility of turn-to-turn beam position measurements with 10 μm accuracy.

The chamber with BPM buttons will be mounted on a girder by precisely machined supports, to provide high stability. Small alignment errors as well as electrical offsets and errors in the BPM system will be accounted for at the commissioning using beam-based alignment, which is straightforward due to the individual power supplies.

The NSLS-II storage ring utilizes very strong sextupoles. This makes it very important to have the orbit of the circulating beam as close as possible to the magnetic centers of the sextupoles. We will rely on highly accurate relative alignment of the sextupoles and quadrupoles on the same girder. In addition, a beam-based alignment procedure will be used for the sextupoles.

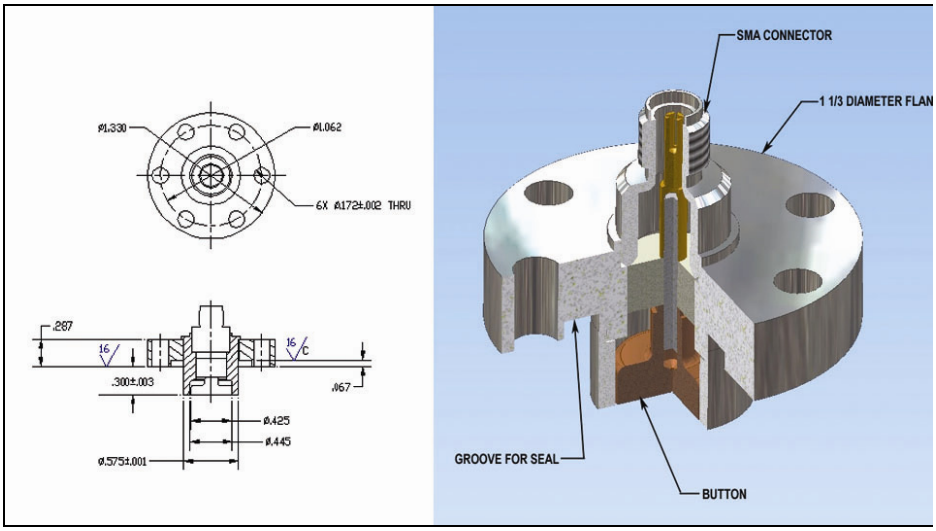

Figure 7.8.8 Design of the BPM button for the storage ring.

7.8.5.2 Tune Monitor

The vertical and horizontal betatron tunes will be monitored using a network analyzer [7.8.5, 7.8.6]. The analyzer's source will be connected to the excitation striplines through a buffer amplifier. The signal from the receiver striplines will be combined with hybrids to produce vertical or horizontal signals, which will be down converted below the revolution frequency and fed to the input of the network analyzer. Such an approach allows utilization of the maximal driving strength and sensitivity of the striplines and makes measurement of the tunes less sensitive to changes in the revolution frequency.

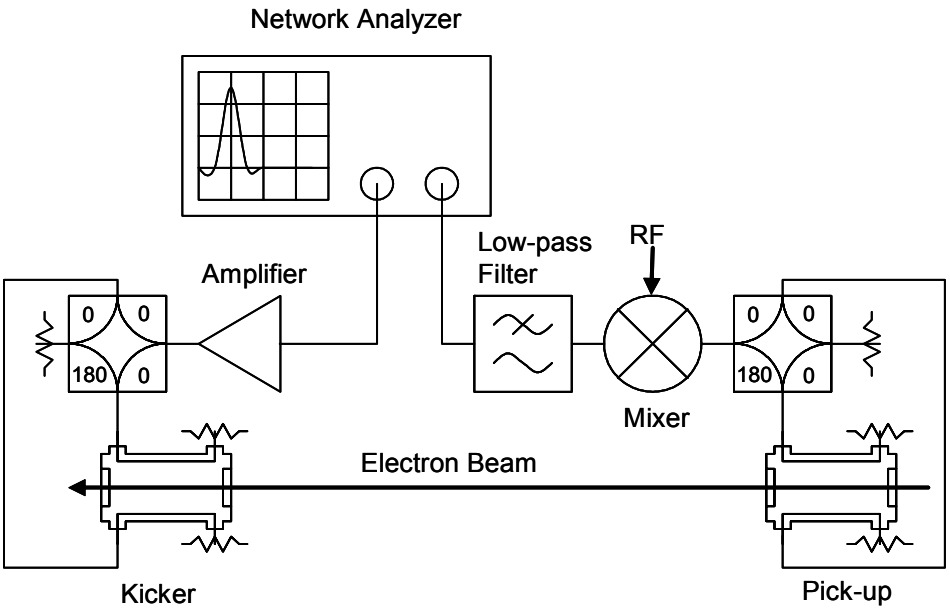

Figure 7.8.9 Layout of the tune measurement system.

An alternative solution can utilize a tune tracker (PLL-based) similar to the one utilized at RHIC [7.8.7].

7.8.5.3 Beam Stability Monitoring

The signal from one of the striplines will be connected to an RF spectrum analyzer. The sidebands observed can be used to analyze electron beam stability and find the synchrotron frequency. Summing the signal from opposite striplines helps to eliminate components with transverse oscillations, while maintaining the signal with phase motion of the electron bunches. The difference signal will be used to observe transverse oscillations of the electron beam.

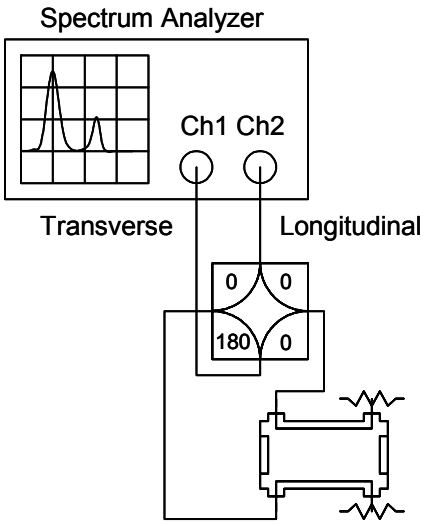

Figure 7.8.10 System for the observation of beam stability.

7.8.5.4 Transverse Feedback System

The resistive wall wake can make the electron beam in the storage ring unstable. Increasing the chromaticity may not be sufficient, due to limitations on sextupole strength resulting from loss of dynamic aperture required for beam lifetime and injection. The required stability can be provided by a digital bunch-by-bunch transverse feedback system [7.8.8, 7.8.9]. A broadband signal measuring the position of the individual bunches will be provided by a stripline pick-up. It will be sampled with a fast ADC (sampling rate 500 MHz). A digital filter will calculate the desired correction signal, which is generated by a DAC. The correction kicks are fed through a broadband amplifier and drive the electron beam using the second stripline.

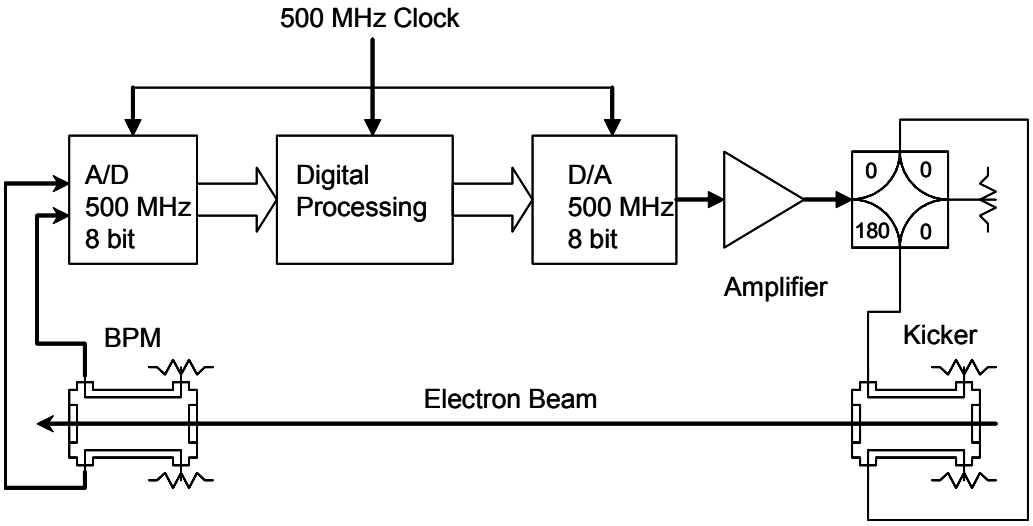

Figure 7.8.11 Conceptual layout of the transverse feedback system.

7.8.6 Synchrotron Radiation Diagnostics

7.8.6.1 Overview

This section describes diagnostics for the NSLS-II storage ring that utilize visible and x-ray synchrotron radiation generated in a bending magnet and an x-ray undulator. Table 7.8.2 shows the types and quantities of diagnostics for the storage ring.

Table 7.8.2 Complement of the Optical Diagnostics for the NSLS-II Storage Ring.

Monitor type	Quantity	Function	Range	Resolution	Bandwidth
Two slit optical interferometer	1	Horizontal emittance Vertical emittance	2.5 nm-rad 8 pm-rad	5 pm-rad 1 pm-rad	100 Hz
Streak-camera	1	Bunch length	10 – 50 ps	2 ps	8 Hz
Photon BPM	2 per beamline	Angle and position of ID radiation	10 mm	0.01 mm	1 Hz
Diagnostics undulator with pinhole camera	1	Horizontal emittance energy spread momentum compaction factor	0.5 – 2.5 nm-rad 0.2 – 2% 10^{-4}		
FireWire camera	1	Beam profile		640x480	120 fps

7.8.6.2 Two-Slit Optical Interferometer

For measuring the ultra low vertical emittance of the storage ring, we plan to use the interferometric method developed at KEK [7.8.10] for measuring ultra small beam sizes. Visible or UV light emitted by the circulating beam passes through a pair of slits separated by distance D and placed at distance L from the source. A lens is used for focusing the diffracted beam on a camera to observe the interference pattern in the far field region. A narrowband filter selects the observation wavelength, λ. The optical set-up is shown in Figure 7.8.12. Due to the non-zero beam size σ, the observed intensity profile will be constructed from the interference patterns coming from the different angles.

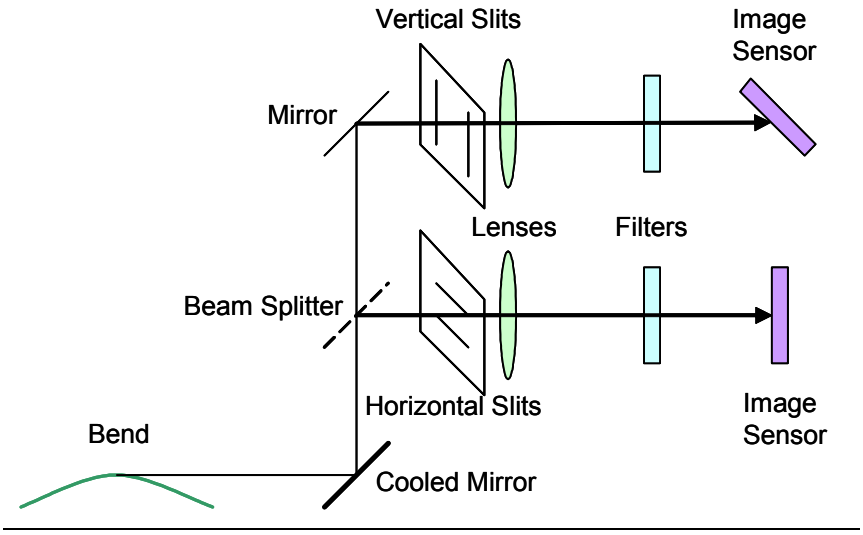

Figure 7.8.12 Layout of emittance monitor utilizing a two slit interferometer. Vertical slits are used for horizontal emittance measurement and horizontal slits are used for vertical emittance measurement. A water cooled mirror is needed to avoid exposure of the image sensors to x-rays.

The interference visibility $V = \dfrac{I_{\max} - I_{\min}}{I_{\max} + I_{\min}}$ is given by the formula [7.8.10]:

$$V = e^{-2\pi^2 (D\sigma / L\lambda)^2} \tag{7.8-1}$$

For synchrotron radiation from the bending magnet, in the vertical plane with a slit width, D, of 16.6 mm and placed at distance L, of 5 m from the source, with observation wavelength, λ, 250 nm, the visibility, V, is expected to be 0.5 for 8 pm-rad vertical emittance and $\beta_y = 25$ m. The calculated intensity profile is shown in Figure 7.8.13. In such conditions, 5% accuracy in the measurement of visibility gives 7% precision of the beam size (and hence emittance) measurements.

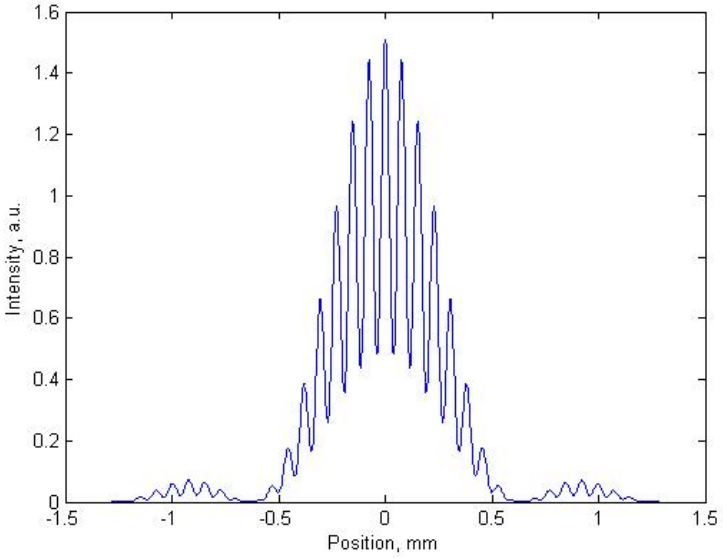

Figure 7.8.13 Calculated profile of the intensity of diffracted light for 1 mm slits. Observation plane is 5 m away from the slits.

7.8.6.3 Bunch Length Measurement

A double-sweep streak-camera Hamamatsu model C5680 [7.8.11], shown in Figure 7.8.14, will be used to measure the longitudinal beam dynamics. Its versatility and high sensitivity make it an excellent choice for monitoring the bunch length with sub-picosecond resolution and studying beam instabilities. The streak camera will be equipped with A1976-01 input optics with an N5716 streak tube. The parameters are shown in Table 7.8.3. The synchroscan feature provides low-phase jitter for synchronous summing of signals and tracking phase dynamics.

Table 7.8.3 C5860 Streak Camera Parameters.

Spectral response characteristics [nm]	200 to 850
Minimal radiant sensitivity [mA/W]	2 at 240 nm, 1 at 820 nm
Synchroscan frequency (factory setting) [MHz]	100
Temporal resolution at 800 nm (FWMH) [ps]	2
Sweep range	200 ps to 1/6Fs (Fs is synchroscan frequency)
Dual time sweep range [s]	10^{-7} to 10^{-1}
Camera resolution [pixels]	1280x1024
Frame rate [Hz]	8
Dynamic range [bit]	12

The streak camera will be shared with the booster. An optical beamline from the booster will be used to transport a beam of synchrotron radiation from the booster bending magnet to the streak camera.

Figure 7.8.14 View of the C5860 streak camera.

7.8.6.4 Photon Beam Position Monitors

Photon beam position monitors similar to the ones used at APS as shown in (Figure 7.8.15) will be used for monitoring radiation from the insertion devices [7.8.12]; the blades, of course, will be designed and optimized to suit the requirements of NSLS-II. The information obtained on the angle and position of the photon beam will be incorporated into the orbit feedback system to provide the beam stability required for user applications. Two photon BPMs will be used for each beamline. The BPM assembly will be mounted on a stable post and its location (elevation and transverse position) will be adjusted with 2D translation stages. Utilizing such devices has been shown to enable pointing stability of the photon beam with peak-to-peak drift of less than 2 μrad over six days [7.8.12].

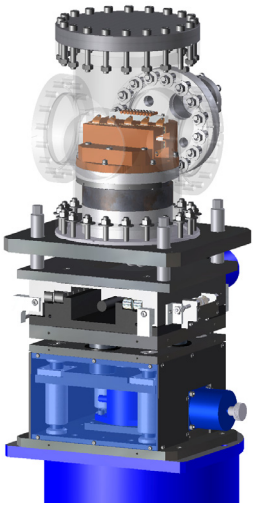

Figure 7.8.15 APS Photon beam position monitor.

7.8.6.5 Optical Synchrotron Radiation

An IEEE1394 camera will be used for observation of the OSR from the electron beam. Such an approach eliminates the need for a frame-grabber and makes display of the beam on the control computer straightforward. The camera has an external trigger capability and exposure control from 10 μsec to 5 sec.

Position sensitive photodiodes that provide signal depending on the location of the center of gravity of the optical beam, can be incorporated into the orbit feedback system as well as results of image processing. The model S2044 (in the right bottom corner of Figure 7.8.16) has 0.6 μm sensitivity and 0.3 μsec rise time. They will be used to monitor beam stability for the IR users.

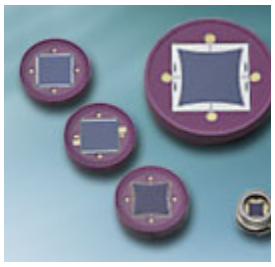

Figure 7.8.16 Position-sensitive diodes by Hamamatsu.

7.8.6.6 Diagnostics Undulator

The diagnostics undulator will allow independent measurement of the energy spread and horizontal emittance. The momentum compaction factor can be also measured. We plan to utilize one of the user beamline undulators in a 5 m straight. This beamline will be equipped with an additional high resolution fluorescent screen and a retractable pinhole (Figure 7.8.17). Use of the radiation from this undulator for diagnostic purposes will be restricted to periods when it is not needed by the users.

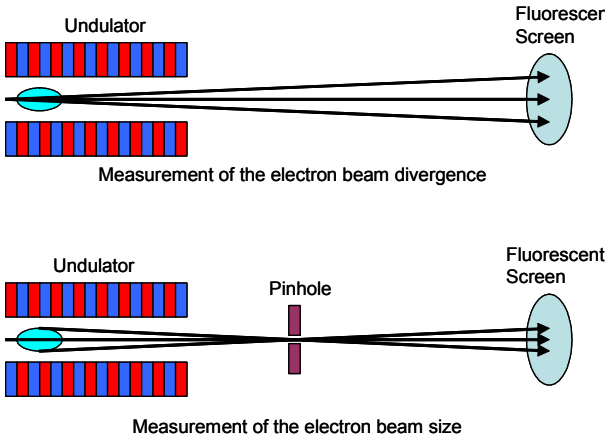

Figure 7.8.17 Beam diagnostics with undulator radiation.

The β-functions in the straight are $\beta_{xmin} = 2.5$ m and $\beta_{ymin} = 1.0$ m. The U19 undulator, proposed for usage, has 19 mm period and 3 m length.

For measuring the divergence of the electron beam, the transverse profile of the undulator radiation will be obtained. In order to increase the system resolution, small undulator K values will be utilized. These will also help to keep the power from higher harmonics low and avoid distortion of the power profile. For $K = 0.3$, the power density of the 3rd harmonic is two orders of magnitude below the power density of the main harmonic. For this value of K, the fundamental wavelength of the undulator radiation will be 0.29 nm and the

divergence due to a diffraction will be $\sigma'_{ph} = \sqrt{\lambda / L} = 9.8\,\mu\text{rad}$, which compares favorably with the horizontal divergence of the electron beam $\sigma'_e = \sqrt{\varepsilon_x / \beta_x} = 14.1\,\mu\text{rad}$ for 0.5 nm-rad emittance.

Inserting a pinhole, which can be realized as a slit, will allow measurement of the horizontal beam size. Knowledge of the divergence and beam size gives one the ability to measure directly the beam emittance (independent of the β-function).

Analysis of the width of the undulator spectrum provides information on the energy spread of the electron beam. It is also possible to measure the momentum compaction factor by observing the shift of the undulator spectrum with revolution frequency [7.8.13].

7.8.7 Other Diagnostics

7.8.7.1 Beam Loss Monitors

NSLS-II will utilize a distributed beam loss monitoring system based on pin-diodes, which are commercially available from Bergoz [7.8.2] (Figure 7.8.18). At least two beam loss monitors per beamline will be used for interlocks. This feature is especially important for the mini-gap undulators.

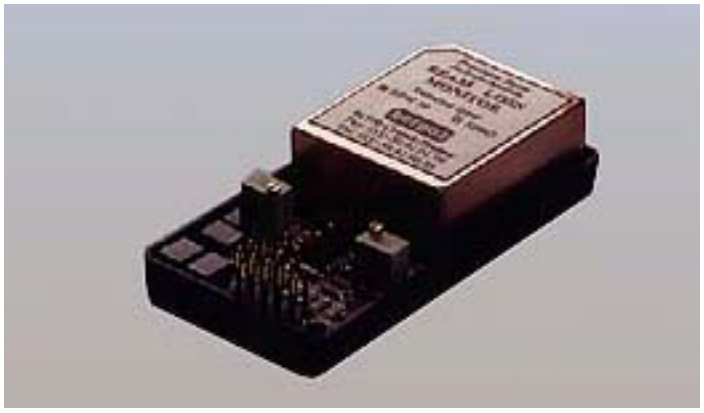

Figure 7.8.18 Beam loss monitor by Bergoz.

The loss monitors have a pulse output (one pulse per lost particle) and are insensitive to the synchrotron radiation photons. The monitors are small and can be easily relocated to the region of interest.

7.8.7.2 RF Frequency Monitor

Signal from the RF master oscillator will be provided to a counter in order to monitor the revolution frequency.

7.8.7.3 Scrapers

Two pairs of two-plane adjustable-position scrapers will be installed on the ring to be used both as protective devices as well as diagnostic instruments for accelerator studies. More details are described in Section 7.7.

One set of scrapers (horizontal and vertical) will be installed in the dispersive section to measure the energy distribution of the electron beam. Another set will be installed in a straight section with zero dispersion in order to have information on the transverse size of the electron beam and eliminate possible beam halos capable of affecting the insertion devices.

7.8.7.4 High-Level Accelerator Modeling

High level accelerator modeling required to extract data on the storage ring lattice from the experimental data [7.8.14]. It is described in the control system section. It will be also used for the development of real time orbit feedback system and coupling correction.

References

[7.8.1] E.D. Johnson, W.S. Graves, and K.E. Robinson, "Periscope Pop-In Beam Monitor," Proc. of Beam Instrumentation Workshop 1998, AIP Conf. Proc. 451, pp. 479–484.

[7.8.2] http://www.bergoz.com

[7.8.3] R. Ursic et al., "Holy Trinity of the Instrumentation Development," Proc. of the 11th Beam Instrumentation Workshop, Knoxville 2004.

[7.8.4] U. Mavric, "Innovative RF Design Unites Benefits of Multiplexed and Multichannel System," Proc. of the 11th Beam Instrumentation Workshop, Knoxville, 2004.

[7.8.5] A.S. Fisher, "Instrumentation and Diagnostics for PEP-II," Proc. Beam Instrumentation Workshop 1998, AIP Conf. Proc. 451, pp. 95–109.

[7.8.6] A. S. Fisher, M. Petree, U. Wienands, S. Allison, M. Laznovsky, M. Seeman, and J. Robin, "Upgrades to PEP-II Tune Measurements," Proc. of Beam Instrumentation Workshop 2002, AIP Conf. Proc. 648, pp. 267–274.

[7.8.7] T. M. Brennan, P. Cameron, P. Cerniglia, R. Connolly, J. Cupolo, W. Dawson, C. Degen, A. DellaPenna, J. DeLong, A. Drees, D. Gassner, M. Kesselman, R. Lee, A. Marusic, J. Mead, R. Michnoff, C. Schultheiss, R. Sikora, and J.Van Zeijts, "Tune Measurement in RHIC," Proc. Beam Instrumentation Workshop 2002, AIP Conf. Proc. 648, pp. 134–149.

[7.8.8] M. Dehler, R. Kramert, P. Pollet, and T. Schilcher, "Commissioning Results of the Multi Bunch Feedback System at SLS," Proc. of EPAC 2004, pp. 2508–2510.

[7.8.9] S.N. Thanos and R. H. Hosking, "ELETTRA Photon Source Beam Stabilization," Proc. Beam Instrumentation Workshop 2002, AIP Conf. Proc. 648, pp. 248–253.

[7.8.10] T. Mitsuhashi, "Measurement of Small Transverse Beam Size Using Interferometry," Proc. of DIPAC 2001, pp. 26–30.

[7.8.11] http://www.hamamatsu.com

[7.8.12] G. Decker and O. Singh, "Beam Stability at the Advanced Photon Source," Proc. of PAC 2005, pp. 3268–3270.

[7.8.13] B. Yang, M. Borland, and L. Emery, "High Accuracy Momentum Compaction Measurement for the APS Storage Ring with Undulator Radiation," CP546, Beam Instrumentation Workshop 2000, American Institute of Physics, pp. 235–241.

[7.8.14] J.A. Safranek, "Beam-based Accelerator Modeling and Control," Proc. of Beam Instrumentation Workshop 2000, AIP Conf. Proc. 546, pp. 23–5.

8 Radiation Sources

This chapter describes the parameters and performance of the radiation sources planned for NSLS-II. Continuing the tradition established by the existing NSLS, they span a very wide spectral range, from the far IR, down to 0.1 meV (equivalent to 1 cm^{-1}), to the very hard x-ray region, more than 300 keV. This is achieved by a combination of bending magnet sources, covering the IR, VUV, and soft x-ray range, and insertion device sources, covering the VUV through very hard x-ray range. They will achieve world leading levels of time average brightness and flux from the far IR through to ~20 keV, only being surpassed above ~20 to 25 keV by the performance of synchrotrons operating at higher energy (6 to 8 GeV).

As discussed in Chapter 6, the NSLS-II lattice contains 30 DBA cells, or 15 superperiods with alternating straight section lengths of 5 m and 8 m. The 5 m straights will have low beta functions and the 8 m straights somewhat higher beta functions. The resulting horizontal and vertical electron beam sizes and divergences in the center of the two types of straights, as well as in the center of the bend magnets, are given in Table 8.1.1. These beam sizes and divergences are already very small, and an option for even smaller beam sizes is discussed in Section 8.3.8. The beta functions also determine the allowed minimum vertical gap of an undulator and non-linear dynamic effects constrain the maximum length of the undulator, L. The minimum undulator gap and the undulator lengths for the devices described in this chapter were all chosen to satisfy these constraints.

All of the source properties described in this chapter assume a fully-damped horizontal emittance value of 0.55 nm-rad. This is the performance value for the NSLS-II storage ring when operating with a full complement of eight 7 m damping wigglers. The initial emittance value will be greater than this value, owing to operation with fewer damping wigglers, as discussed in Chapter 6.

Table 8.1.1 Electron Beam Size and Divergence at NSLS-II.

Type of source	5 m straight section	8 m straight section	Bend magnet
σ_x [μm]	38.5	99.5	44.2
$\sigma_{x'}$ [μrad]	14.2	5.48	63.1
σ_y [μm]	3.05	5.51	15.7
$\sigma_{y'}$ [μrad]	3.22	1.78	0.63

8.1 Insertion Devices

The goal in choosing the set of principal insertion device parameters is to provide a wide overall spectral coverage with insertion devices that target the photon energy ranges of interest for the experimental programs. It is expected that other parameter choices besides those outlined here may be specified to meet the needs of the science program as it evolves over time.

The set of insertion devices described includes hard x-ray, soft x-ray, and VUV undulators, x-ray damping wigglers, and high-energy superconducting wigglers. Their spectral brightness, flux, power, spatial and angular output properties, and polarization performance are described. These IDs produce high-brightness radiation spanning a large photon energy range, from the VUV (~10 eV) to the very hard x-ray (~300 keV). An R&D program focused on developing the required magnetic and mechanical design of these devices is presented in Chapter 12. Their effects on the properties of the NSLS-II storage ring and other accelerator physics issues are presented in Chapter 6.

The set of IDs discussed is not meant to be a complete set. Rather, these devices represent a possible set that might optimize the performance of the beamlines that are ultimately constructed. Once these beamlines are actually chosen, it is anticipated that, consistent with the philosophy of building beamlines dedicated to a given technique, the source will also be individually optimized for each application, as appropriate.

Other types of undulators and/or wigglers besides those discussed in this Chapter will also be considered during the preliminary engineering design phase of the project. These will include in-vacuum EPUs, to reach smaller magnetic gaps and thereby wider photon energy coverage, and quasi-periodicity, for both planar undulators and EPUs. In addition, revolver concepts, figure-8 type undulators, and long-period electromagnetic undulators will be considered. These concepts are discussed further in the description of the undulator R&D program in Chapter 12.

8.1.1 Planar Undulators

The hard x-ray undulators at NSLS-II will be planar designs and will produce linearly polarized radiation.

8.1.1.1 CPMU – U19

The baseline NSLS-II hard x-ray undulator is a Cryogenic Permanent Magnet Undulator with a period of 19 mm, referred to as U19. Cooling the CPMU's magnets to ~150 K increases its peak magnetic field strength by ~13%. Cooling a permanent magnet undulator to achieve higher performance is a quite recent development of the last few years, but has already undergone significant development. There are some remaining issues that require R&D to fully demonstrate a device with the capabilities described here, as discussed in Chapter 12. However, we are confident they can be addressed and so we specify a U19 device as the baseline hard x-ray undulator for NSLS-II.

8.1.1.1 SCU – U14

Superconducting undulator technology requires substantial R&D to demonstrate its viability and so SCUs are not specified as baseline devices for NSLS-II. We do plan to carry out an R&D program focused on pursuing SCUs using high temperature superconducting technology, as described in Chapter 12. If successful, it will enable x-ray undulators to be produced with both shorter periods and higher K than the U19 CPMU device. For example, a 14 mm period SCU, referred to as U14, has ~25% shorter period than U19 but will be able to achieve 10% higher K_{max}. Together, these increase the brightness by a factor of ~2 over that of U19, provide more continuous coverage as the field strength is tuned, and extend the performance to higher energies. The spectral properties of an SCU U14 device are described here in addition to those of the baseline CPMU U19 device in order to give an indication of the performance that would become possible with the successful development of this technology.

8.1.2 Elliptically Polarized Undulators

The NSLS-II soft x-ray and VUV insertion devices will be elliptically polarized undulators. These EPUs provide full ellipticity control of the radiated output from circular through linear, while only marginally reducing the brightness of the linearly polarized output, compared to pure planar undulators of the same period. In addition, these EPUs can also provide linearly polarized output with the polarization axis oriented either horizontally, vertically, or anywhere in between. As discussed in the soft x-ray beamline sections (see Chapter 11), these properties are extremely useful for separating various contributions to a given signal in an experiment.

8.1.2.1 Soft X-ray EPU – EPU45

The total length of the EPU45 undulator is specified as 4 m, corresponding to a single long device. However, this corresponds to only one of two proposed operating modes for these devices. In fact, for the soft x-ray beamlines discussed in Chapter 11, this 4 m total length would be comprised of two ~2 m EPUs and the appropriate steering magnets and diagnostics would be placed between the sections to allow a small (~0.25 m-rad) canting angle for the electron beam between them. As described in more detail in Chapter 11, this configuration will allow the two undulator sections to be set to two different polarizations, e.g., left circular and right circular, or horizontal linear and vertical linear. The angular separation provided by the canting will then permit fast switching between the chosen polarizations of the two EPUs, thereby enabling various types of polarization sensitive experiments to be performed with high sensitivity, as provided by lock-in detection methods for example. The accelerator issues associated with these, and other, canting angles are discussed briefly in Section 6.1 and will be addressed in more detail in the technical design phase of this project.

8.1.2.2 VUV EPU – EPU100

The harmonic content issue is particularly important in the case of the EPU100 owing to the intensity of the n >1 harmonics, which are comparable to or even greater than the n = 1 fundamental, as shown below. As a result, the EPU100, which produces vacuum ultraviolet radiation, will almost certainly need to be quasi-periodic, an issue that will be addressed during the R&D and technical design phases, as discussed in Chapter 12.

8.1.3 Wigglers

Classes of experiments that require continuous x-ray spectra, sizable x-ray beams, or very hard x-rays, such as EXAFS, powder diffraction, x-ray topography, x-ray photoemission, x-ray standing waves, high pressure, and x-ray footprinting, to name some, will benefit from the availability of x-ray beamlines that view damping wiggler sources. Superconducting wigglers will be the preferred source for those experiments requiring very hard x-rays, up to ~300 keV. All wiggler sources at NSLS-II are expected to be in high demand.

8.1.3.1 Damping Wiggler – DW100

The damping wigglers will produce the highest flux of any NSLS-II source out to ~30 keV and will also have excellent brightness. They are expected to be the premier source for experiments above ~5 keV that do not require the ultra-high brightness and small beams produced by the hard x-ray undulators.

8.1.3.2 Superconducting Wiggler – SCW60

The highest energy photons will be produced by very high field, short period, wigglers. The radiation will be broadband with high power at high x-ray energies, covering the 20 to 300 keV energy range. The selected device has a wiggler field of 6.0 T and a period length of only 60 mm so that the flux and brightness are as high as possible. The combination of high field and small period requires a superconducting wiggler design that pushes the limit of presently achievable current density, an issue that will be addressed during the technical design phase. Specifications of other similar high SCWs that are currently in service at medium energy synchrotrons are listed in Table 8.1.2.

Table 8.1.2 Some Working SCWs Similar in Specifications to Proposed and Alternative NSLS-II Wigglers.

Facility	Manufacturer	Field(T)	Period (cm)	# full-field poles
NSLS X17	Oxford	6	17.4	5
BESSY II	Novosibirsk	7	14.8	13
CLS	Novosibirsk	4.2	4.8	25
ELETTRA	Novosibirsk	3.6	6.4	45
MAX lab	Custom	3.5	6.1	47

The SCW60 will outperform other options at energies above 30 keV. The deflection parameter, K, is chosen to be wide enough to generate a large horizontal beam profile of a more than 0.5 m at 50 m from the source point. This allows splitting of the fan into multiple experimental hutches, as discussed in Chapter 11.

8.2 Bend Magnets

The NSLS-II bending magnets will have a relatively low critical energy (2.4 keV), and will be excellent sources for low photon energies, below 10 keV. It is expected that the available bend magnet ports will be allocated primarily to VUV and soft x-ray uses, as well as infrared uses. Those classes of experiments that require access to harder x-rays (energy >~5 keV) are better suited to damping wiggler sources.

The NSLS-II bend magnets will provide very stable beams. The relatively low emitted power simplifies the cooling requirements on the optics, although it does not eliminate the need to provide cooling. The brightness provided by the NSLS-II dipole sources will be three orders of magnitude higher than that of the present NSLS dipoles (extending up to ~12 keV) and their flux will also show some improvement (extending up to ~4 keV), as shown in Table 8.2.1. Indeed, the NSLS-II bend magnets will provide almost twice the flux of the ALS conventional bend magnets (i.e., not the superbends) and offer even larger improvements in source brightness. Thus, aspects of the very successful ALS research programs based on bend magnet illumination can be developed at NSLS-II, although the distribution of beamlines and end stations will be determined by the strengths and interests of the NSLS-II user community.

Table 8.2.1 Comparison of Bend Magnet Sources.

	NSLS-II Bend Magnet		ALS Conventional Bend Magnet		NSLS X-Ray Bend Magnet		NSLS VUV Bend Magnet	
Energy	Flux	Brightness	Flux	Brightness	Flux	Brightness	Flux	Brightness
1000 eV	3.3×10^{13}	1.5×10^{16}	2.1×10^{13}	1.5×10^{15}	1.4×10^{13}	1.3×10^{14}	6.0×10^{12}	1.1×10^{13}
100 eV	2.5×10^{13}	8.0×10^{15}	1.5×10^{13}	7.5×10^{14}	8.0×10^{12}	7.0×10^{13}	1.3×10^{13}	9.0×10^{13}
10 eV	1.3×10^{13}	3.7×10^{15}	7.2×10^{12}	3.4×10^{14}	3.8×10^{12}	2.8×10^{13}	7.7×10^{12}	4.4×10^{12}
1 eV	5.9×10^{12}	1.7×10^{15}	3.4×10^{12}	1.6×10^{14}	1.8×10^{12}	1.3×10^{13}	3.7×10^{12}	2.0×10^{12}
0.1 eV	2.8×10^{12}	8.0×10^{14}	1.6×10^{12}	7.3×10^{13}	8.4×10^{11}	6.1×10^{12}	1.8×10^{12}	9.4×10^{11}

ALS parameters assume top-off mode operation at 500 mA stored current. Flux is in units of ph/s/0.1%BW and brightness is in units of ph/s/0.1%BW/mm^2/mrad^2.

The special considerations required for collecting infrared radiation produced by the bend magnets is discussed in detail in Section 8.4.

8.3 Parameters and Performance of Radiation Sources

The basic parameters characterizing the IDs and bending magnet sources are listed in Table 8.3.1. In the case of the NSLS-II bend magnet, the total power value is actually the power per horizontal mrad.

Table 8.3.1 Basic Parameters of NSLS-II Radiation Sources for Storage Ring Operation at 3.0 GeV and 500 mA.

	U14	U19	EPU45	EPU100	DW100	SCW60	Bend Magnet
Type	SCU	CPMU	EPU	EPU	PMW	SCW	Bend
Photon energy range [keV]	Hard x-ray (1.8–30)	Hard x-ray (1.5–20)	Soft x-ray (0.180 – 7)	VUV (0.008 – 4)	Broadband (<0.010 - 100)	Very hard x-ray (<0.010 – 200)	Soft and low-energy x-ray (<0.010 – 12)
Type of straight section	5 m	5 m	5 m	5 m	8 m	5 m	
Period length, λ_U [mm]	14	19	45	100	100	60	
Total device length [m]	2.0	3.0	4.0	4.0	7.0	1.0	
Number of periods	143	158	89	40	70	17	
Minimum magnetic gap [mm]	5	5	10	10	15	TBD	
Peak magnetic field strength in linear mode, B [T]	1.68	1.14	1.03	1.50	1.80	6.0	0.40
Max K_y*, linear mode	2.20	2.03	4.33	14.01	16.81	33.62	
Peak magnetic field strength in circular mode, B [T]			0.64	1.15			
Max K_y*, circular mode			2.69	10.74			
Minimum $h\nu$ fundamental [keV]	1.79	1.47	0.183	0.0086			
$h\nu$ critical [keV]					10.77	35.91	2.39
Maximum total power [kW]	16.08	11.18	12.09	25.64	64.60	102.55	0.0228
On-axis power density [kW/mrad^2]	103.70	77.86	40.03	26.33	55.30	43.9	0.0879
Horizontal angular power density [kW/mrad]							0.023

*K = 0.934 B[T] λ_u[cm]

8.3.1 Brightness

For many experiments, especially those involving imaging or microscopy, where, for example, the beam must be focused down to a small spot, the key figure of merit of user radiation sources is their time average brightness. This is the flux output per unit bandwidth, per unit source area, and per unit solid angular divergence. Undulators and wigglers are excellent sources of high brightness radiation. The brightness of the base set of radiation sources for NSLS-II is is shown in Figure 8.3.1. For the undulators, the tuning curves of harmonics 1, 3, 5, 7, and 9 are shown. These tuning curves show the variation of the peak brightness of the undulator harmonics as the magnetic field strength, and hence K parameter, is varied from K_{max}, listed for each undulator in Table 8.3.1, down to K_{min} ~0.4.

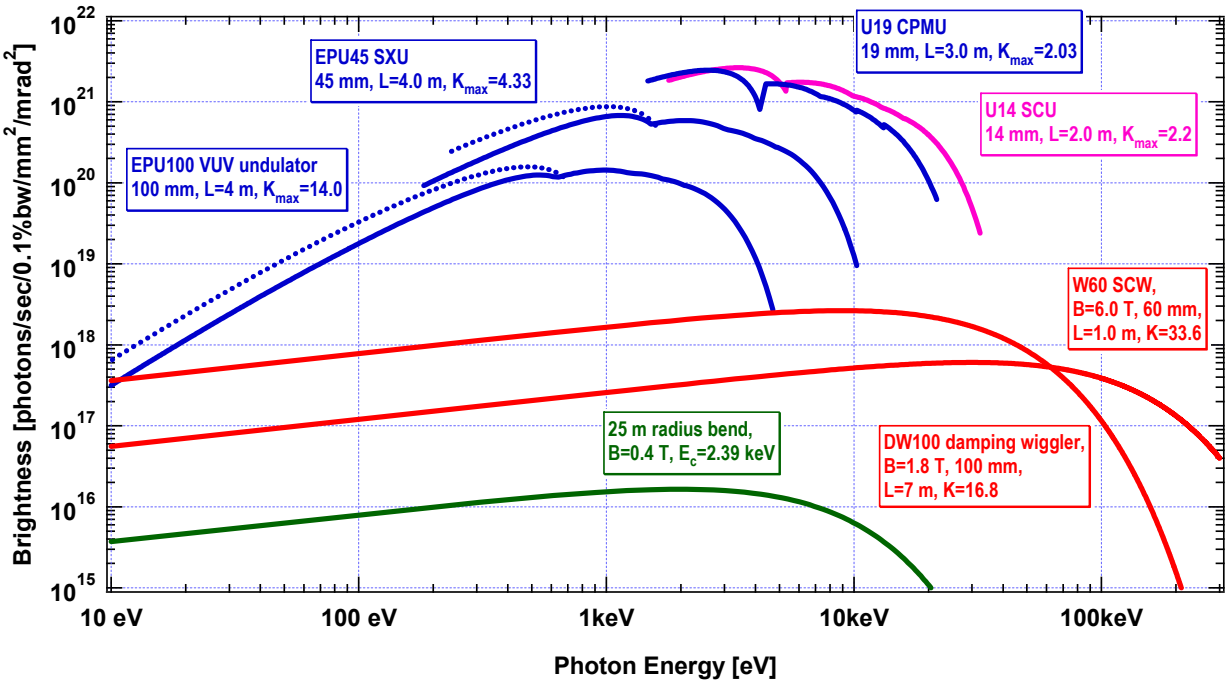

Figure 8.3.1 Brightness vs. photon energy for various devices at NSLS-II. Ring parameters: 3.0 GeV, 0.5 A, ε_h=0.55 nm, ε_v=0.01 nm, energy spread=0.001; Straight section parameters: 5 m length: ε_h=2.7 m, β_v=0.945 m; 8 m length: β_h=18.2 m, β_v=3.09 m; α_h=α_v=η_h=η_v=η'_h=η'_v=0; Bend magnet parameters: β_h=0.65 m, β_v=25.1 m, α_h=0.032, α_v=-0.044, η_h=0.04 m, η'_h=0.056, η_v=η'_v=0.

The brightness of the U14 and U19 hard x-ray undulators is the highest of any devices proposed for NSLS-II. This is due in part to the short period length of these devices, thereby increasing the number of periods contributing to the flux output, and in part to the short output wavelengths compared to the soft x-ray (EPU45) and VUV (EPU100) undulators. For diffraction-limited undulator radiation, which characterizes a good portion of the range of these four undulators, the brightness varies inversely as the square of the output wavelength. Note that the brightness of the hard x-ray undulators (U14 and U19) exceeds the 10^{21} ph/s/0.1%BW/mm^2/mrad^2 level.

The wigglers provide broadband, high brightness sources of x-ray radiation. Each of the wigglers shown in Figure 8.3.1 covers nearly the entire photon energy range shown. The superconducting wiggler SCW60 is optimized for very high-energy x-ray work (i.e., above ~60 keV), while the damping wiggler DW100 is a high-flux, hard x-ray source with smooth spectral output extending down through the soft x-ray and VUV photon energy ranges. Note that the EPU100 undulator and DW100 wiggler devices have the same period length (100 mm) and comparable magnetic field strength (1.5 T for EPU100 vs. 1.8 T for DW100). The difference in their brightness and flux curves, other than their difference in length (4 m for EPU100 vs. 7 m for DW100) arises in the difference between the standard undulator and wiggler flux and brightness formulae: the undulator values represent the peaks (in photon energy) of a widely-varying intensity spectrum, while the wiggler values represent an average value. For use of the low-n harmonics (n = 1, 3, 5, 7, or 9), the undulator formula is most useful, while for the high-n harmonics (n >20 or so), the wiggler formula is more appropriate.

Figure 8.3.1 shows the source brightness of the EPU45 and EPU100, in two polarization modes: helical (or circular), shown as dotted lines, and linear, shown as solid lines. The circular polarized mode has intensity only in the fundamental and is slightly brighter than the linearly polarized mode at the same energy. It is expected that this mode will be used for all work below 2 keV for the EPU45 and below 850 eV for the EPU100, unless linearly polarized light is specifically required.

The NSLS-II bending magnet spectral brightness curve is also shown in Figure 8.3.1. The bending magnet spectrum is a bright source which extends from the infrared to the hard x-ray. These sources will be useful up to a few times the critical energy of 2.39 keV, i.e., up to ~10 keV. The bending magnet brightness peaks at ~2 keV, making it an ideal broadband source in the soft x-ray (0.1–2 keV) and low-energy x-ray (2–5 keV) ranges.

8.3.2 Flux

For those experiments which do not require a very collimated and/or focused beam, the photon spectral flux is the key figure of merit. This is the number of photons per unit bandwidth per unit time. Figure 8.3.2 shows the flux for the NSLS-II radiation sources. The maximum flux is ~1.5×10^{16} ph/s/0.1%BW, reached by the damping wiggler DW100 at ~3 keV. The hard x-ray undulators U14 and U19 reach a flux of ~5×10^{15} ph/s/0.1%BW at an energy of ~2 keV. As discussed in Section 8.2, the bend magnets at NSLS-II will be superlative sources of high brightness and high flux radiation in the VUV and soft x-ray energy range. For both wigglers and bend magnets, a horizontal collection of 3 mrad is typical (Figure 8.3.2), although larger horizontal angular fans—e.g., up to 10 mrad—could be made available, if required.

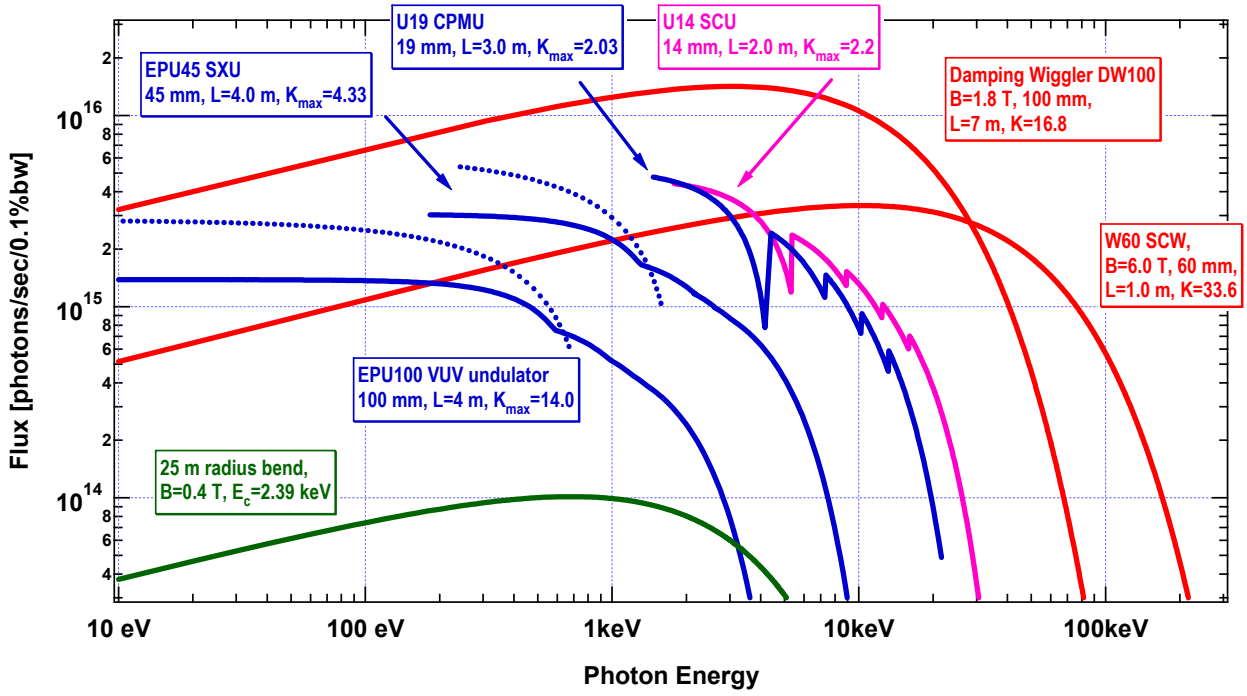

Figure 8.3.2 Flux output of various devices at NSLS-II vs. photon energy. See the caption to Figure 8.3.1 for a listing of accelerator parameters used to calculate the flux curves shown here."

8.3.3 Power

Table 8.3.1 gives the maximum total output power of the NSLS-II radiation sources and Figure 8.3.3 shows how the total output power output of the undulators varies as their K value is changes from K_{min} (taken to be ~0.4) to K_{max}, as given in Table 8.3.1. For reference, the corresponding energy of the photons' radiation in the fundamental as a function of K is also given. The photon energy of harmonic n is n times that of the fundamental.

The total power radiated by the undulators at their maximum K settings (i.e., at minimum magnetic gap) is in the 10–30 kW range. The total power output from the NSLS-II wigglers is higher than that of the

undulators, at nearly 65 kW, while that of the NSLS-II bend magnet is very much less, at only ~23 W per horizontal mrad (see Table 8.3.1). Figure 8.3.3 also shows that the total output power increases by about a factor of 2 when operating in circular mode compared to linear mode for the EPUs. The engineering challenges of handling the high heat loads in the insertion device front ends are detailed in Section 7.4.

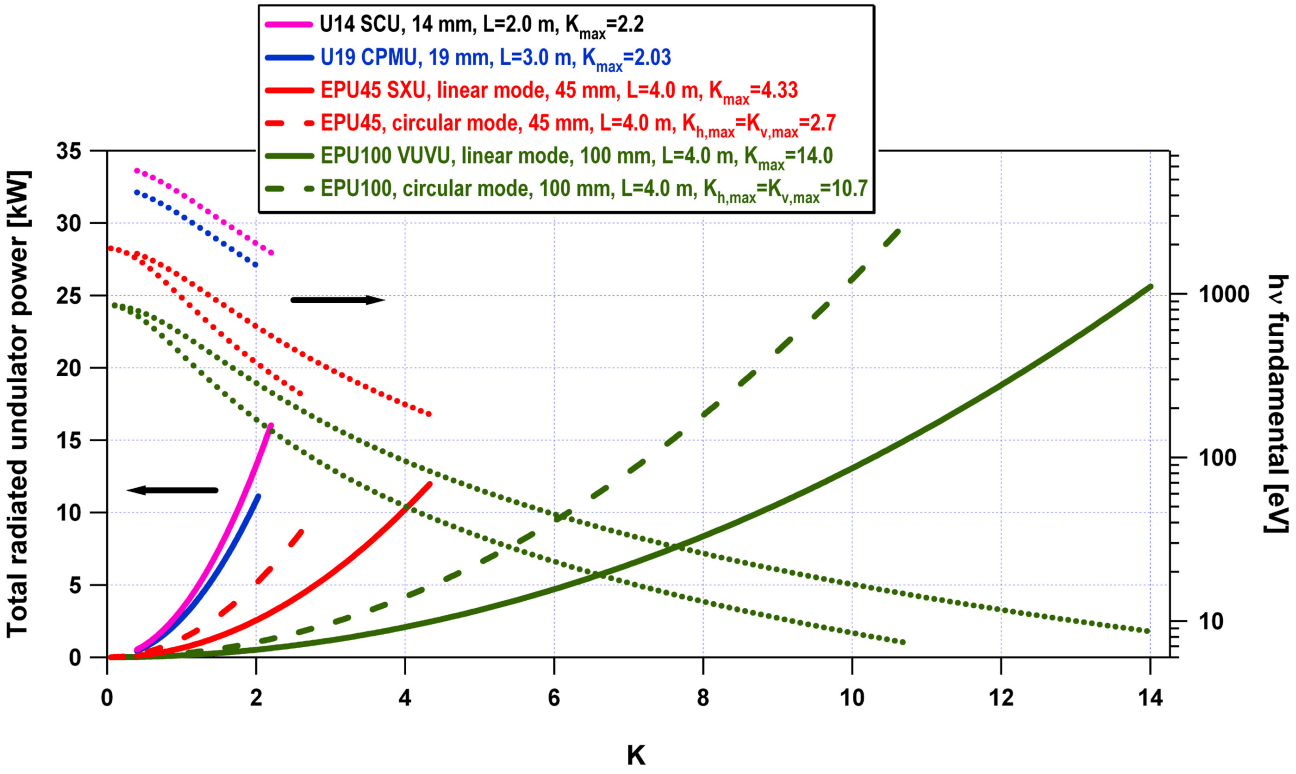

Figure 8.3.3 Total output power of the NSLS-II undulators as a function of the undulator parameter, K.

8.3.4 Power Density

Table 8.3.1 gives the maximum (on-axis) angular power density of the NSLS-II radiation sources; Figure 8.3.4 shows how the maximum angular power density of the undulators varies as their K value changes from K_{min} (taken to be ~0.4) to K_{max}, as given in Table 8.3.1. For reference, the corresponding energy of the photons radiated in the fundamental as a function of K is also given. The energy of harmonic n is n times that of the fundamental. The maximum undulator angular power density radiated by the undulators at their maximum K settings (i.e., at minimum magnetic gap) varies from 25 to 100 kW/mrad^2. The wiggler angular power density output is in the 25–55 kW/mrad^2 range, while the bend magnet value is again very much less, at 88 W/mrad^2.

Figure 8.3.4 also shows that the output angular power density of the EPUs in circular polarization mode is much lower than in linear polarization mode, and has a different dependence on K. This is primarily because in circular mode there are no higher harmonics, just the fundamental. An advantage of the circular polarization mode is the lower output power density, which simplifies the design and operation of high energy-resolution beamlines by reducing the thermal deformations of the optical elements (see Chapter 11).

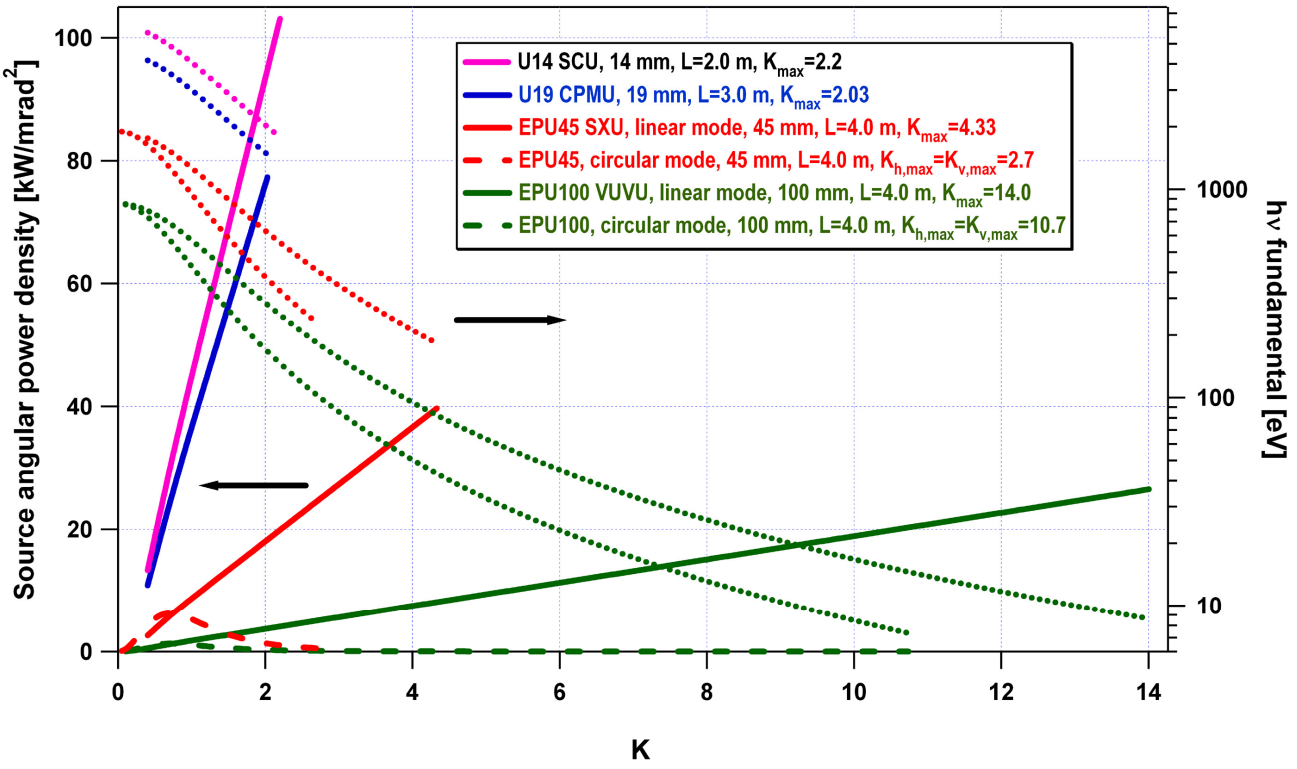

Figure 8.3.4 Angular power density versus undulator parameter, K, for the NSLS-II undulators.

8.3.5 Photon Beam Size

The 1-σ effective photon beam size of the NSLS-II undulators is shown in Figure 8.3.5 as a function of photon energy. The lowest, straight (on a log-log graph) gray lines show the "natural" photon beam size, which is the size of a diffraction-limited photon beam for a zero emittance (and therefore zero size) electron beam. This diffraction-limited, "natural" photon beam size σ_{photon} is given by

$$\sigma_{photon} = \frac{1}{4\pi}\sqrt{2L\lambda} \quad . \tag{8.1-2}$$

One measure of the effective photon beam size, σ_{eff}, is given by the quadrature sum of the electron ($\sigma_{electron}$) and photon, σ_{photon}, contributions:

$$\sigma_{eff} = \sqrt{\sigma_{electron}^{\ 2} + \sigma_{photon}^{\ 2}} \quad . \tag{8.1-3}$$

The green, red, and blue curves show σ_{eff} for the NSLS-II undulators in the vertical and horizontal planes, as labeled. Clearly, the undulator radiation is nearly diffraction-limited in the vertical plane over a wide photon energy range from 10 eV to ~2 keV. The deviation of the effective source size from the natural, diffraction-limited value is due to the contribution of the small, but finite, electron beam size. The effective beam size in the horizontal plane is approximately an order of magnitude greater than the natural, diffraction-limited value at 10 keV, but at 10 eV is nearly diffraction-limited.

It should be noted that the beam sizes shown in Figure 8.3.5 were calculated for the current baseline electron beam sizes given in Table 8.1.1. If it proves possible to use the smaller horizontal beta function in the

5 m straights, discussed in Section 8.3.8, there would be a corresponding reduction the horizontal photon beam sizes shown in Figure 8.3.5, and a corresponding increase in the degree of coherence.

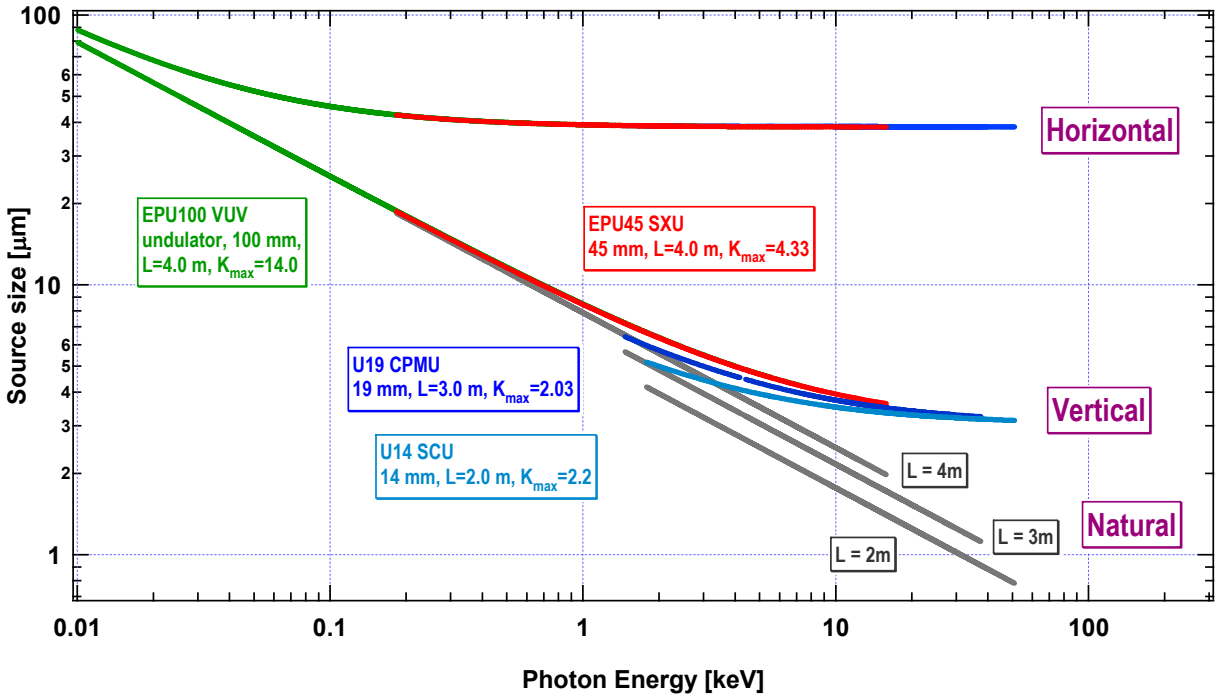

Figure 8.3.5 Photon beam source size in the horizontal and vertical directions for the various NSLS-II devices. The straight (gray) lines represent the diffraction-limited values for the various devices (i.e., the zero electron beam emittance limit).

8.3.6 Photon Beam Angular Divergence

The 1-σ effective photon beam angular divergence of the NSLS-II undulators is shown in Figure 8.3.6 as a function of photon energy. The lowest, straight (on a log-log graph) gray lines show the "natural" photon beam angular divergence, which is the angular divergence of a diffraction-limited photon beam for a zero-emittance (and therefore zero angular divergence) electron beam. The diffraction-limited, "natural" photon beam angular divergence σ'_{photon} is given by

$$\sigma'_{photon} = \sqrt{\frac{\lambda}{2L}} \tag{8.1-4}$$

and the effective photon beam angular divergence σ'_{eff} is again given by the quadrature sum of the electron ($\sigma'_{electron}$) and photon (σ'_{photon}) contributions:

$$\sigma'_{eff} = \sqrt{\sigma'^{\,2}_{electron} + \sigma'^{\,2}_{photon}} \quad . \tag{8.1-5}$$

The green, red, and blue curves in Figure 8.3.6 show σ'_{eff} for the NSLS-II undulators in the vertical and horizontal planes, as labeled. As in Figure 8.3.5 for beam size, Figure 8.3.6 shows that the angular divergence of the undulator radiation from NSLS-II undulators is nearly diffraction-limited in the vertical plane, and only somewhat less so in the horizontal plane, over the wide photon energy range from 10 eV to ~2 keV. The deviation of the effective source angular divergence from the natural, diffraction-limited, value is due in part to the contribution of the tiny, but finite, beam angular divergence of the NSLS-II electron beam. In the

horizontal plane, the effective beam angular divergence is approximately a factor of 2 or 3 greater than the natural, diffraction-limited, value at 10 keV, but is nearly diffraction-limited at 10eV.

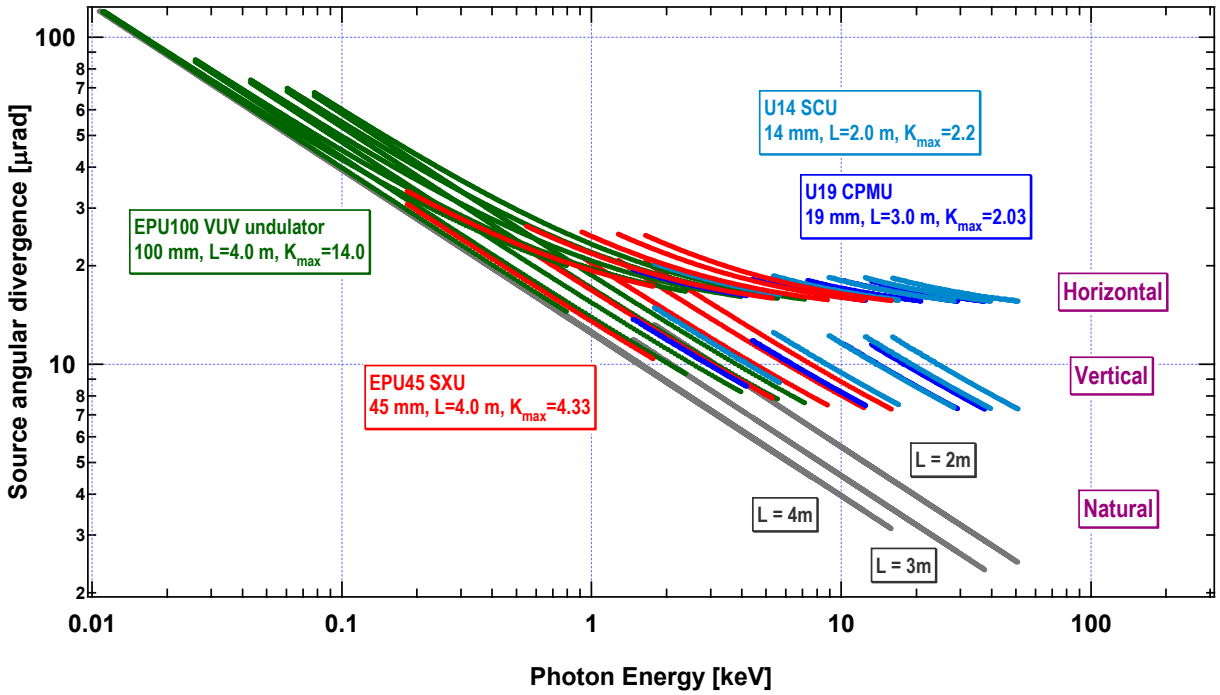

Figure 8.3.6 The angular divergence of the photon beam at NSLS-II devices.

The angular divergence is also limited by the finite energy spread of the electron beam. A noteworthy feature of Figure 8.3.6 is that the angular divergence of the various harmonics for a given undulator is approximately equal to that of the fundamental of that undulator. That is, it appears, empirically, that the angular divergence of undulator harmonic n is given by

$$\sigma'_n \approx \sqrt{\frac{\lambda_1}{2L}} \tag{8.1-6}$$

for n = 1, 3, 5, 7, or 9, in both the horizontal and vertical planes. This value is $\sqrt{\lambda_1}/\lambda_n = \sqrt{n}$ times larger than the natural, diffraction-limited angular divergence.

Thus, the limiting factor governing the vertical angular spread of the U14 and U19 undulators is the finite energy spread of the electron beam, which for the fully-damped case is $\delta E/E \sim 0.001$. Figure 8.3.7 illustrates this effect for the U14 SCU for three values of energy spread: 0, 0.0005, and 0.001. The difference between the natural, diffraction-limited, vertical angular divergence and the curve labeled $\delta E/E = 0$ is the contribution from the finite vertical angular spread of the electron beam. The difference between the $\delta E/E = 0$, $\delta E/E = 0.0005$, and $\delta E/E = 0.001$ curves is the contribution from the specified electron energy spread. Figure 8.3.7 clearly demonstrates that the vertical angular divergence of the U14 fundamental is determined by the combined contributions of the natural and electron beam divergences, but that the vertical angular divergence of the higher harmonics (n = 3, 5, 7, and 9) is mostly determined by the effect of electron energy spread. Note however, as can be seen in Figure 8.3.6, that whereas the effect of energy spread is significant for the U14 and U19 undulators, it has a much smaller effect on the angular divergence of the soft x-ray and VUV undulators.

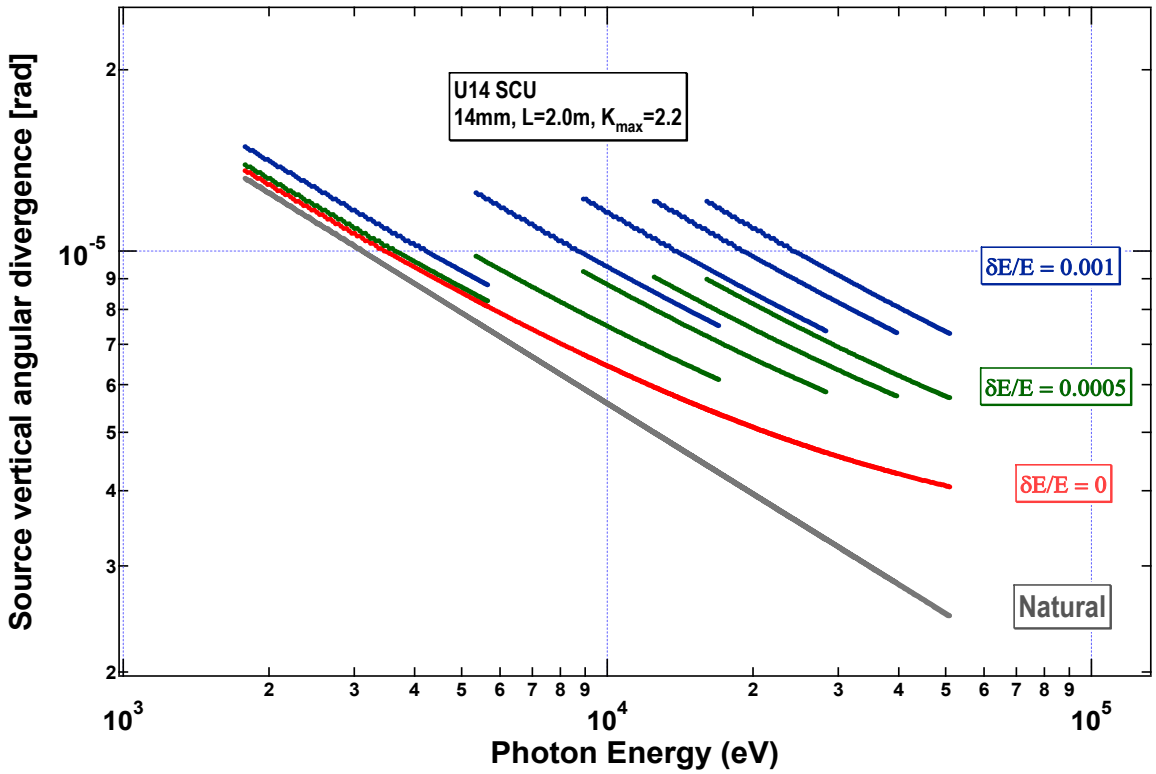

Figure 8.3.7 The vertical angular divergence for the 14 mm SCU device vs. photon energy for different values of the energy spread of the electron beam. The straight (gray) line is the diffraction limit, and the deviation from this line at higher energies for zero energy spread is a result of the finite electron beam divergence.

8.3.7 Effect of Increasing Undulator Length

One way to increase undulator source brightness and flux is to increase the overall length, i.e., to increase the number of undulator periods. Of course, accelerator physical constraints must be obeyed, including the minimum magnetic gap vs. length, the overall maximum ID straight section length, and limits set by collective effects. For a low emittance electron beam, the length dependence of the brightness should be similar to that of the flux, since for a diffraction-limited photon beam the denominator in the brightness expression depends only on the emitted wavelength. It turns out that the linear dependence of brightness vs. undulator length applies only to the case of zero electron energy spread, as demonstrated for the 5th harmonic of the U19 CPMU by the uppermost solid curve in Figure 8.3.8. For non-zero energy spread values, this dependence becomes sublinear. For example, for 0.001% electron beam energy spread, a 2 m long U19 CPMU is 2.1 times brighter than a 1 m long device, but a 6 m long device is only 1.75 times brighter than a 3 m long device. Moreover, the brightness penalty for finite energy spread is rather severe: for 0.001% energy spread, the brightness reduction compared to zero energy spread ranges from a 35% reduction for a 1 m long U19 CPMU to more than 70% reduction for a 7 m long device. For 0.002% energy spread, the corresponding reduction fractions are 60% and 85%.

It is clear that the origin of the energy-spread-related brightness reduction lies mostly in the vertical divergence angle, as pointed out Section 8.3.6 above. This effect is greater for higher harmonics than lower ones. Shown by dotted lines in Figure 8.3.8 are the brightness vs. undulator length curves for the 3rd harmonic at 3.6 GeV electron energy. The zero-energy-spread curves are nearly identical, but the 0.001% and 0.002% energy spread curves are more than 1.5 times brighter than the 5th harmonic curves at 3.0 GeV (solid lines).

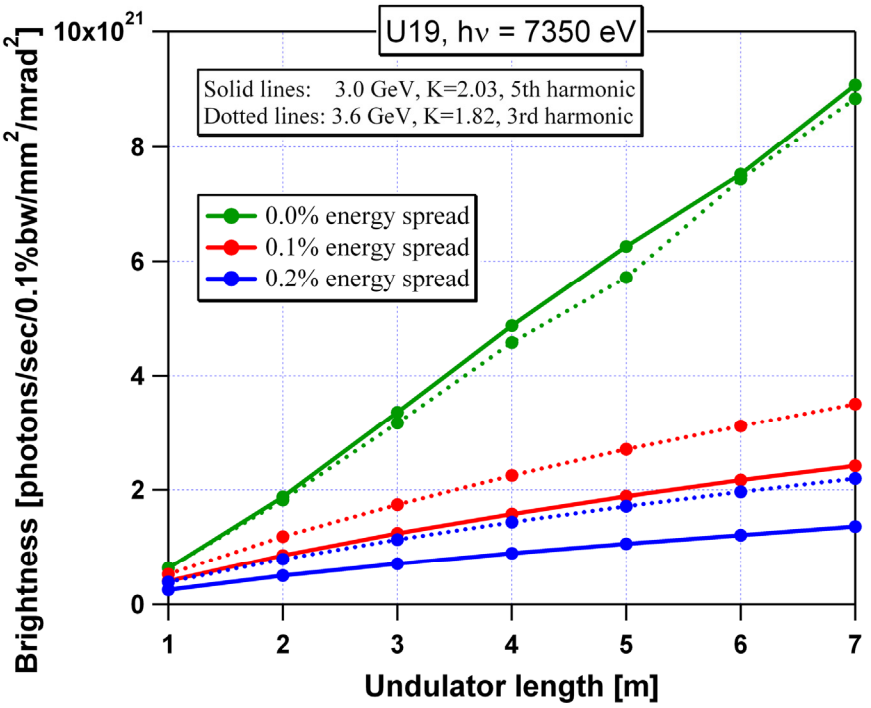

Figure 8.3.8 On-axis brightness of the U19 undulator at 7350 eV photon energy as a function of undulator length, for the 5th harmonic at 3 GeV (K = 2.03, solid lines) and the 3rd harmonic at 3.6 GeV (K = 1.82, dotted lines).

8.3.8 Effect of Possible Reduction of Horizontal β-Function

We are investigating whether the horizontal β-function at the center of the 5m ID straight sections might be able to be reduced by about a factor of 10 from baseline value, i.e., from 2.7 m to ~0.3 m. Although this would only increase the brightness by ~20% for the U19 CPMU and U14 SCU undulators, it would have a significant effect in reducing the horizontal source size from the already unprecedented low value of 38.5 μm (see Table 8.1.1) to an even lower value of 12.2 μm. This would lead to nearly round photon beams, given the vertical size of 3.05 μm. Such tiny and nearly round beams are a decided advantage for microscopy applications, such as the nanoprobe beamline described in Chapter 11.

8.3.9 Options for Multiple U14 or U19 Undulators in a Single ID Straight Section

It may also be feasible to insert multiple U14 or U19 undulators in a single 5 m or 8 m ID straight section by including additional focusing magnets to focus the electron beam in the centers of these multiple undulators and so maintain small beta functions throughout their length. One scenario would enable two 2 m long U14 SCUs to be installed in a 5 m long ID straight section with β_h = 0.3 m and β_v = 0.945 m, as described for a single undulator above. Another scenario would enable either three 2 m long U14 SCUs or two 3 m long U19 CPMUs to be installed in an 8 m long ID straight section, with β_h = 3m and β_v = 3m. The brightness increase for either of these scenarios involving the U19 CPMU at the low energy end of its tuning curve is ~60%, whereas that for scenarios involving the U14 SCU is ~150%. A bigger advantage is the increase in flux, which is linear in undulator length, and thus would increase a factor of 2 for two U19 devices in an 8 m straight and a factor of 3 for three U14 devices in an 8 m straight. This would be especially advantageous for flux-starved experiments, such as those attempting to perform spectroscopy with 0.1 meV energy resolution, as outlined in Chapter 11.

8.3.10 Optimization of Insertion Devices for Specific Beamlines

To maximize overall beamline performance of NSLS-II undulator beamlines, the parameters of the undulator should be matched to those of the beamline, and both should match the experiments that they serve. The specificity of experiments at the various beamlines ranges widely, as does the specificity of the various beamlines. Therefore, the parameters of the undulators shown in this Chapter are intended to be representative choices to serve broad photon energy ranges, and not necessarily the exact values that would be chosen for a specific beamline.

As an example of the optimization process needed to match undulator and beamline parameters, we consider the needs of the Inelastic X-Ray Scattering Beamline. The ultra high resolution IXS experiments would primarily utilize a photon energy of 9 keV and so the undulator parameters should optimize the source brightness at this energy. Figure 8.3.9 shows the brightness of the various harmonics of candidate CPMUs in a photon energy region centered at 9 keV. The CPMUs considered are of fixed overall length (3 m), but with periods of 16, 17.5, 19, and 21 mm, a range which brackets the canonical CPMU period length of 19 mm for U19.

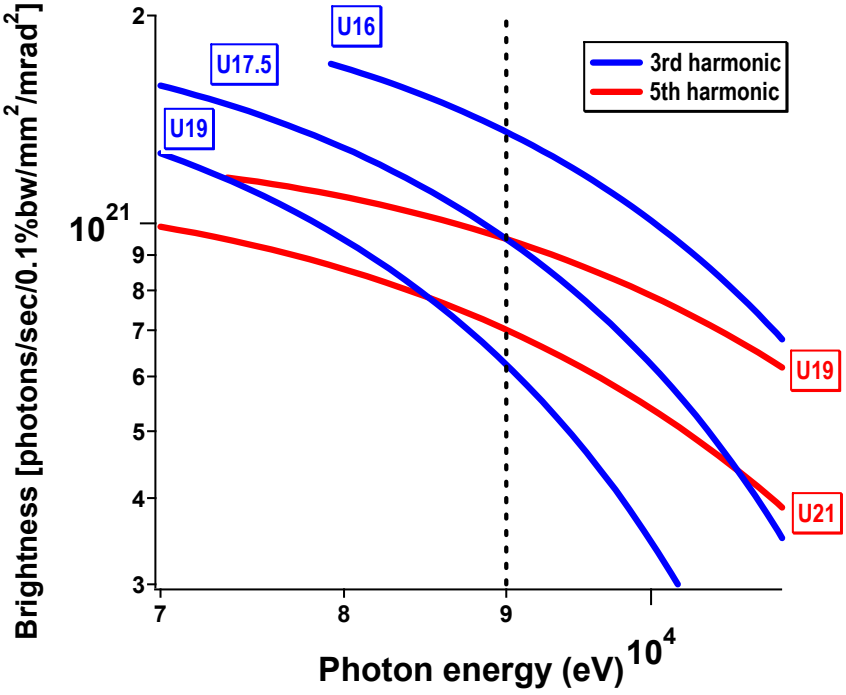

Figure 8.3.9 Possible candidate devices that optimize the brightness of undulators around 9 keV.

Figure 8.3.9 shows the brightness of third and fifth harmonic emission from these candidate CPMUs. Fundamental (first harmonic) emission does not reach 9 keV for any of the CPMU period lengths considered, and the seventh and higher harmonics produce lower brightness at 9 keV than the third and fifth. The optimum undulator parameter choice to maximize source brightness at 9keV is the third harmonic of the 16 mm period CPMU (uppermost blue curve in Figure 8.3.9). Note that it may be possible to further optimize this brightness by going to a slightly shorter period (e.g., 14.5 mm) before the minimum photon energy for the third harmonic exceeds 9 keV. Of course, an additional gain in brightness would also be realized from the third harmonic of the 2 m, 14 mm period superconducting undulator if such a device were to be developed.

The figure of merit for the source for certain experiments, and their beamlines, might be flux rather than brightness. For such experiments, a similar optimization process should occur. The source flux of the various harmonics of candidate CPMUs in a photon energy region centered at 9 keV is shown in Figure 8.3.10. As is

typical of undulator sources, the differences in flux are smaller than the differences in brightness. In this case (and in general), the optimum combination of undulator period length and harmonic is the same for flux optimization and brightness optimization: third harmonic of the 16 mm period CPMU. In the case of flux, the fifth harmonic of the 19 mm period undulator is only slightly inferior to the optimum combination.

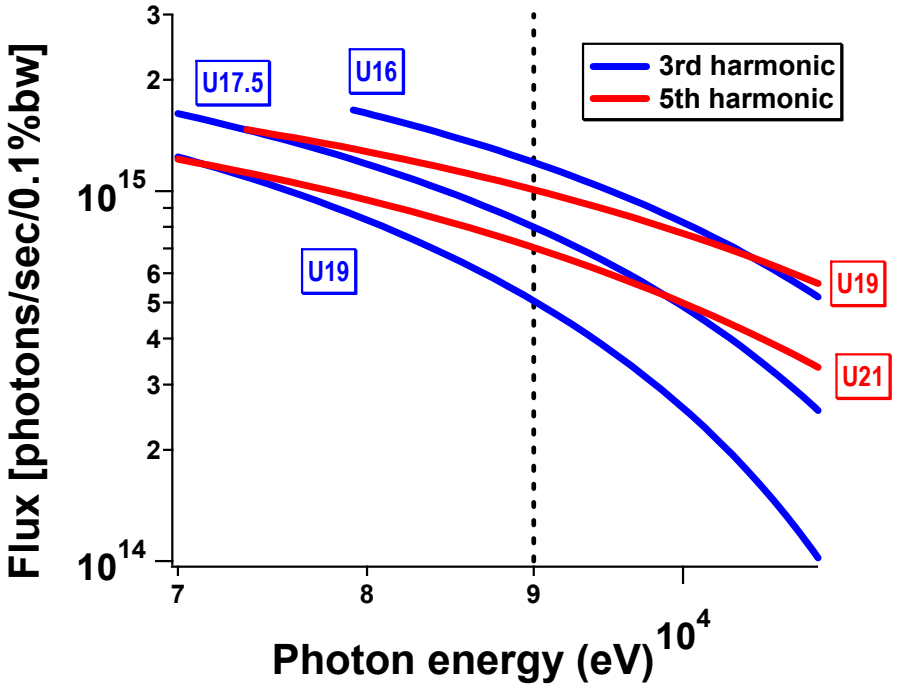

Figure 8.3.10 The source flux of the various harmonics of candidate CPMUs in a photon energy region centered at 9 keV.

.

8.4 Infrared

The intrinsic infrared brightness of most synchrotron storage ring sources is determined entirely by the circulating beam current. This is certainly the case for the low emittance electron beam of the NSLS-II storage ring, and the goal of 500 mA beam current is very attractive from the standpoint of infrared performance. The ring is designed for an extremely stable beam; an important characteristic for the standard rapid-scan interferometric techniques employed in most infrared spectroscopies. But designing an optical extraction configuration that preserves the brightness, while meeting mechanical and accelerator design constraints, can be quite difficult. Typically, the large angular collection needed to achieve an acceptable performance involves nonstandard construction geometries for the dipole chambers. These, in turn, can affect the beam impedance and lead to instabilities. A careful impedance analysis will be integral to the design of any dipole chamber intended for extracting infrared radiation, and efforts are underway to treat this issue quantitatively.

It is well known that dipole (bending) magnets produce infrared radiation by two distinct mechanisms: the conventional synchrotron radiation (bending magnet radiation) is produced in the body of the magnet, whereas edge radiation is produced as electrons enter or exit a dipole's magnetic field [8.4.1]. Infrared beamlines have been built to utilize one or the other of these source types, and sometimes both. For reasons outlined later in this section, we plan to meet most of the source requirements using bending magnet radiation, but also plan to collect and extract edge radiation. The beamline design and performance analysis described in Chapter 11 will take both source types into account.

8.4.1 Bending Magnet Source

The collection efficiency for conventional dipole bend radiation is determined by the natural opening angle for synchrotron radiation in the long wavelength limit. For a wavelength λ and bend radius ρ, the RMS half-angle is defined as:

$$\theta_\lambda = \left(\frac{3}{4\pi} \frac{\lambda}{\rho} \right)^{1/3} . \qquad (8.4\text{-}1)$$

From this expression we see that the large bending radius (ρ ~25 m) of NSLS-II dipoles causes the infrared to be emitted into angles 2.35 times smaller than for the existing NSLS VUV/IR ring (ρ ~1.9 m). Thus, the performance for NSLS-II with 38 mrad extraction would be identical to a 90 mrad extraction from the VUV/IR ring. A study of the NSLS-II dipole design indicates that a horizontal extraction of 50 mrad is achievable (plus an additional 5 mrad on the "negative side", useful for collecting edge radiation). This is based on an infrared extraction where the second dipole in a DBA cell is used in order to stay clear of any potential insertion device beamline (Figure 8.4.1). The large bending radius makes extraction increasingly difficult as one continues toward the second half of a dipole, giving rise to the 50 mrad horizontal collection limit.

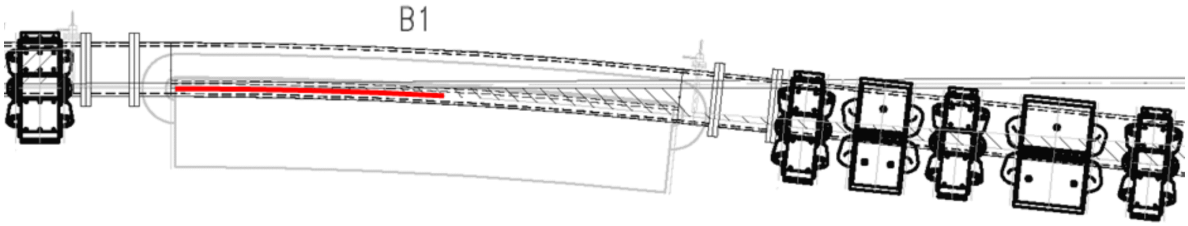

Figure 8.4.1 Drawing of the second dipole magnet in the NSLS-II DBA 30 lattice. Red line indicates the candidate IR source orbit segment. Approximately 50 mrad of horizontal collection appears feasible, including the zero degree segment for edge radiation.

The standard NSLS-II dipole bending magnets allow a vertical chamber dimension of ~25 mm and represent another constraint for infrared, limiting the vertical collection to approximately 16 mrad (the value varies from 12 mrad up to 20 mrad due to the large source depth). While this is adequate for mid-infrared spectroscopy as used in chemical imaging, it limits the performance for far-infrared spectroscopy due to the relatively large angles into which this radiation is emitted. Therefore, we are planning for a second dipole magnet design for use on far-infrared ports. This dipole would have a ~60 mm (or larger) gap and would accept a dipole chamber providing an average 32 mrad of vertical collection (and potentially up to 48 mrad with a larger dipole gap). The need for such a large aperture port becomes even more apparent when one considers the shielding effects of a conducting dipole vacuum chamber. The subject has been treated most thoroughly by Bosch [8.4.2] who confirmed (theoretically) that bending magnet radiation is suppressed for wavelengths greater than an effective cutoff value given by $\lambda_c=(h^3/\rho)^{1/2}$ where h is the chamber height and ρ is the bending radius. The large bending radius of NSLS-II, combined with a standard chamber height of 25 mm, results in a cutoff wavelength of 800 μm, effectively removing the portion of the THz spectral range most important for magnetospectroscopy. This provides another compelling reason for a larger dipole chamber and 60 mm gap dipole magnet. Indeed, increasing the dipole gap an additional 30 mm (to accept a 75 mm vertical height chamber) would shift the cutoff wavelength to beyond 4 mm. In all cases, the detailed dipole chamber design and transitions will require careful study in terms of electron beam impedance and potential instabilities. Our initial impedance analysis for a 50 mm high chamber appears promising and suggests that an even larger (75 mm) chamber would be feasible. However, more detailed calculations will be needed for actual chamber mechanical designs to ensure no instability problems will arise.

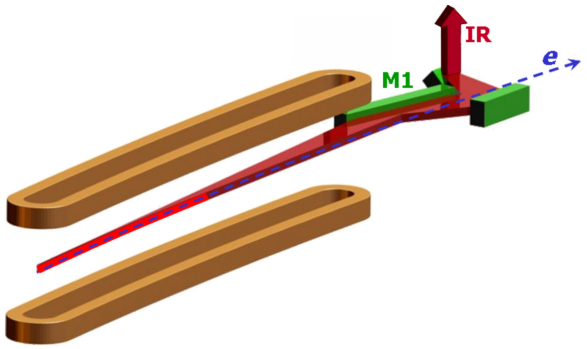

Figure 8.4.2 NSLS-II Infrared Dipole Radiation Extraction. The bright red segment marks the electron beam segment serving as an infrared source. The radiation is collected by a long mirror (M1) and reflected out of the dipole chamber by a second and third mirror combination.

The extraction arrangement for NSLS-II is proposed to have the 1st mirror optic integrated into the dipole chamber construction. The metal mirror can be made to be electrically contiguous with the chamber wall to minimize impedance effects. The oblique angle of incidence and soft x-ray spectrum from the large NSLS-II dipole bending radius limits the local power load on this optic to well under 1 kW/cm^2, such that a special slot or cooling mask may not be required (Figure 8.4.2). Finite element analysis will be performed on candidate mirror materials (e.g., aluminum or copper) to confirm that this heat load can be directly managed without significant optical distortion of the surface. Initial studies of the required optical figure for this 1st mirror suggest that a simple toroidal shape will suffice, allowing conventional diamond turning to be used in its construction (Figure 8.4.3). The remaining optical elements can be either conventional aluminized glass or diamond-turned aluminum to meet specific optical design requirements.

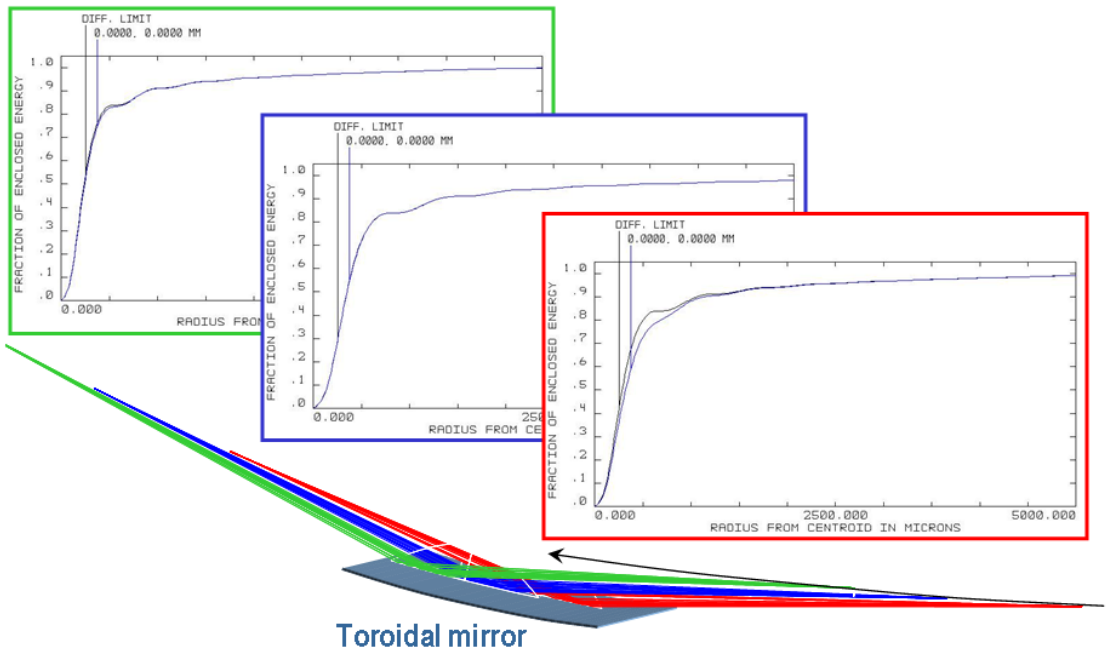

Figure 8.4.3 Extraction Optical Performance. ZEMAX optical analysis for a toroidal first mirror optic when used to focus a dipole bend/arc source at a wavelength of 6 μm (mid-infrared). Near diffraction limited performance is achieved along the entire source length.

A detailed performance comparison for these NSLS-II dipoles and the existing VUV/IR ring dipoles can be made using the standard expressions for dipole synchrotron radiation in the low frequency limit. The flux calculations can be compared to results from other synchrotron radiation source codes such as SPECTRA

[8.4.3] or SRW [8.4.4] to check for consistency. Though some of these calculations are for the photon flux, they can be used for comparing brightness whenever the source's physical dimensions are smaller than the diffraction limit (the case for all IR wavelengths on NSLS-II, and IR wavelengths longer than 10 microns for the existing NSLS VUV/IR ring). We find that all three calculations agree to within 10% for the intrinsic flux of dipole radiation when multiparticle coherence and chamber shielding effects are ignored. Note that one can convert from units of ph/s/0.1%BW to watts per wavenumber, multiplying by 2×10^{-20}. Calculation results are shown in the Figures 8.4.4 and 8.4.5, along with a calculation for an existing port on the VUV/IR ring, indicating that NSLS-II can serve as a highly competitive, and indeed, world-leading, storage ring source for infrared.

Details of these calculation results show that an extraction based on a conventional NSLS-II dipole (average of 16 mrad vertical and 50 mrad horizontal) will be sufficient for mid-infrared spectroscopy, including microprobes and imaging. We envision two options for such mid-infrared extractions. In one option, the beam is divided horizontally to simultaneously serve two or three mid-infrared microprobe end stations. The three collections (in order of entering the dipole) would be (H×V) 15×12 mrad, 15×16 mrad, and 20×20 mrad. The varying vertical aperture is due to the changing distance between the first collecting mirror and the collected source segment as a function of horizontal position (angle). The performance for any of these extractions exceeds the present performance of the NSLS VUV/IR ring over most of the mid-infrared. Only at the long wavelength (low frequency) end of this spectral range are the three extractions distinguishable, with the 20×20 mrad outperforming the other two. But it should be noted that the initial 15×12 mrad collection also includes the zero-degree component, giving this the added feature of edge radiation (not included in the brightness calculation). In the other option, the entire horizontal swath is fed into a single microspectrometer end station based on a focal plane array detector for large area imaging, as described in Chapter 11. The detailed optical system for matching the source to the instrument will be the subject of further research.

In the far-infrared, the brightness for a conventional dipole (16 mrad average vertical extraction) continues to fall away from the ideal value and below the present performance for the NSLS VUV/IR by a factor of 5 at 25 cm^{-1} (400 μm wavelength). The degradation below 10 cm^{-1} becomes even more severe when the shielding effect of the 25 mm high dipole chamber is taken into account. Note that the shielding effect for dipole radiation is a complex subject, and we have taken it into account using a simplified approach. In this approach, it is assumed that radiation unable to couple into a propagating waveguide mode of the chamber is completely lost, and is roughly equivalent to truncating the effective near-field source size to a dimension equal to the chamber height (see [8.4.2], condition 2 for strong shielding). A large-gap dipole enables greater vertical collection efficiency and also shifts the shielding cutoff to lower frequencies. This is illustrated in the brightness calculations of Figure 8.4.5, which includes curves for the standard NSLS-II dipole extraction (50×16 mrad) plus two candidate large-gap dipole extractions (50×32 mrad based on a 50 mm high dipole chamber, and 50×48 mrad based on a 75 mm high dipole chamber). Also shown is the existing performance for the NSLS VUV/IR ring's 90×90 mrad ports plus the very large port beamline at the UVSOR facility (Okazaki, Japan) that represents the most competitive far-infrared beamline elsewhere in the world. (Note: This does not take into account the coherent THz synchrotron radiation mode of operation developed at BESSY and proposed for CIRCE by the ALS/Lawrence Berkeley Lab.) The 50×48 mrad configuration would maintain the NSLS lead in the area of incoherent THz synchrotron radiation, and provide excellent ports for studying aspects of coherent synchrotron radiation production, a subject of great interest for future source development. Any of these ports would offer excellent mid-infrared performance.

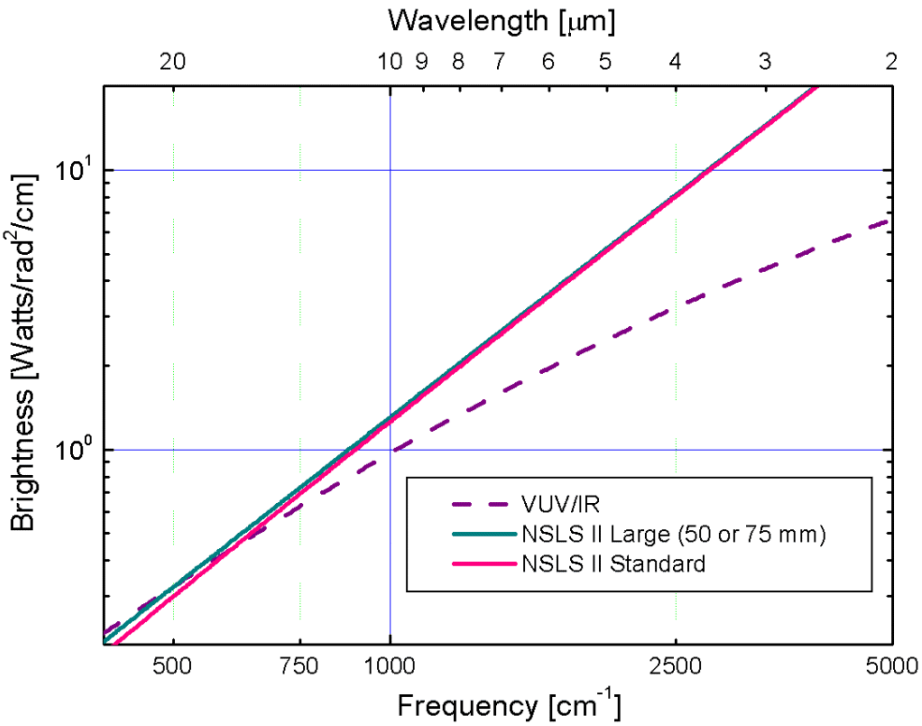

Figure 8.4.4 Calculated NSLS-II brightness for the mid-infrared spectral range, comparing the existing VUV/IR ring with the two proposed for NSLS-II extractions. Note that the lower emittance of NSLS-II leads to brightness improvements over much of this spectral range and that the standard dipole chamber height of 25 mm is sufficient for this spectral range.

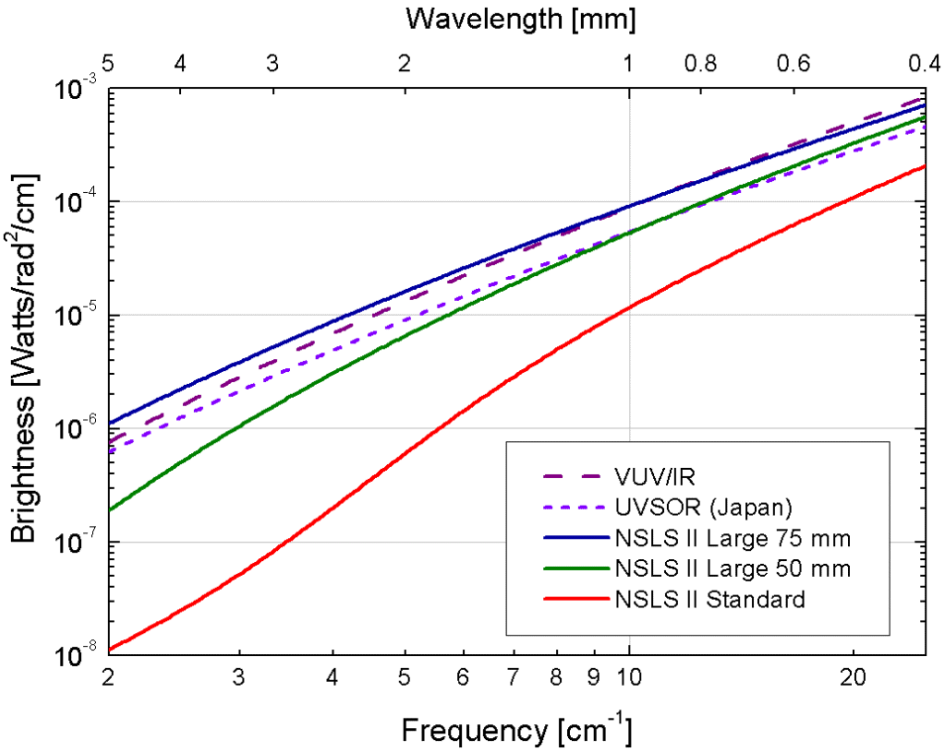

Figure 8.4.5 Calculated NSLS-II brightness for the very far-infrared spectral range, comparing the existing VUV/IR ring with three collection geometries for NSLS-II having vertical dipole chamber heights as shown, plus a high-performance beamline at UVSOR. The cutoff effect of the standard-gap dipole chamber and 16 mrad collection can be clearly seen for wavelengths greater than 1 mm.

8.4.2 Dipole Edge Source

The proposed infrared extraction geometry allows for collection of the zero-degree segment from the dipole (in line with the upstream straight section), including ~5 mrad on the opposite side. This will allow for the extraction of dipole edge radiation [8.4.1]. Dipole edge radiation has characteristics similar to transition or diffraction radiation, e.g., radial polarization. In contrast to bending magnet radiation, the far-field angular distribution for edge radiation is contained mostly within a cone of angle $\theta = 1/\gamma$. This implies an effective source size of $\lambda\gamma$ and a very long formation length of $\lambda\gamma^2$ such that computations designed exclusively for the far-field are no longer accurate. An added complication stems from the fact that dipole edges typically occur in pairs, leading to a ring-like interference pattern that depends on wavelength. The SRW code [8.4.4] includes near-field terms suitable for calculating edge radiation in the ideal case where the ring chamber has no shielding effect on the radiation. An example result from SRW is shown in Figure 8.4.6, and illustrates both edge radiation (ring-like pattern at right) and bend radiation (broad smear extending to left). The actual projection of the beam onto the first mirror optic will be stretched horizontally about a factor of 3 compared to these views (due to the 75° angle of incidence for the radiation).

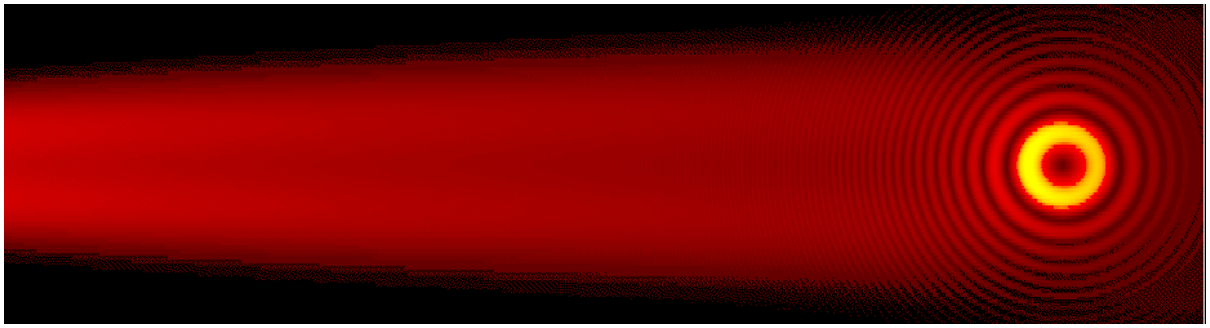

Figure 8.4.6 SRW analysis for 55 mrad (-5 to +50) horizontal and 12 to 20 mrad vertical collection of 6 μm wavelength infrared radiation produced in the leading section of an NSLS-II dipole bending magnet. The ring pattern is due to interference from the back edge of the previous dipole, located 5.6 meters upstream (distance between dipole edges in a DBA cell). The broad stripe of radiation extending to the left is the conventional bending magnet radiation.

Though a few infrared beamlines based on edge radiation exist (e.g., at ANKA/Karlsruhe, SRC/ Wisconsin, and ESRF/Grenoble), the detailed performance at long wavelengths has not been formally demonstrated. There are two reasons to be concerned about the long wavelength performance. First, the radius of the first constructive interference ring moves outward with increasing wavelength such that the collection through a finite aperture will suffer. Second, the large effective source size is expected to cause a shielding (waveguide) cutoff when the wavelength exceeds h^2/R, where h is the chamber height and R is the distance from the source to the collecting aperture [8.4.2]. Our extraction aperture would be situated approximately 3 meters away from the source point and, with a nominal chamber height of 25 mm, the cutoff would begin at a wavelength of ~200 μm such that a significant portion of the very far-infrared would be lost. Edge radiation also introduces complications for mid-infrared microspectroscopy and imaging due to its radial polarization. The source itself is point-like, making it less suitable for illuminating large area focal plane array detectors that are expected to become the standard approach for delivering large area, high-resolution images. For these reasons, our infrared extraction will be based primarily on conventional bending magnet radiation, but we will have the opportunity to exploit the unique characteristics of edge radiation where beneficial.

References

[8.4.1] R.A. Bosch et al., *Rev. Sci. Instr.* **67,** 3346 (1996); Proceedings of the Ninth Nat'l Conf. on Synch. Rad. Instrum., Argonne, IL, (1995.)
[8.4.2] R.A. Bosch, *Nucl. Instrum. & Meth. Phys. Res.* A **482**, 789 (2002).
[8.4.3] T. Tanaka and H. Kitamura, *J. Synch. Rad.* **8**, 1221 (2001)
[8.4.4] O. Chubar and P. Elleaume, *Proc. of the EPAC98 Conference*, 1177 (1998).
[8.4.5] G.L. Carr, *Vibrational Spectroscopy* **19**, 53 (1999); R.P.S.M. Lobo, et al., *Rev. Sci. Instrum.* **73**, 1 (2002).

9 CONTROL SYSTEM

9.1 Introduction and Scope

The control system for NSLS-II is designed to convey all monitor, control, model-based, and computed data from all accelerator, facility, safety, and operations subsystems to accomplish supervisory control, automation, and operational analysis. The scope of the control system extends from the interface of the equipment being controlled through to the designers and operators of the accelerator facility, as well as synchrotron beamline experimenters and staff. The control system includes all hardware and software between these bounds: computer systems, networking, hardware interfaces, and programmable logic controllers.

To provide this comprehensive monitoring, control, and automation, the NSLS-II control system must scale to support 100,000 physical I/O connections and 350,000 computed variables that can be correlated to analyze events and provide data for all control aspects. It must support 1 Hz model-based control, 110 kHz power supply control and readback, 500 MHz RF control, 100 Hz orbit feedback, and 5 millisecond equipment protection mitigation. It also must provide 5 Hz updates to operators of up to 1,000 chosen parameters, provide coherent turn-by-turn orbit data for up to 2^{10} = 1,024 consecutive turns (for FFT), archive up to 6,000 parameters at a rate of 0.5 Hz continually, latch the last 10 seconds of data from all parameters in the storage ring when a fault is detected in the Machine Protection System (MPS), archive up to 2^{10} = 1,024 consecutive turn by turn data for 1,000 parameters at a rate of 10 Hz, and provide pulse-to-pulse beam steering in the linac at 1 Hz.

Our proposed client-server architecture is depicted in Figure 9.1.1. Different levels of access and control reside at distinct layers. At the highest layer (layer 3), access is provided for activities that do not involve moment-by-moment control or monitoring of the accelerator. Layer 3 includes high level physics modeling, making use of live data and data stored in the site Relational Database (RDB in the figure). Experimental activities that do not require synchronization with the ring also reside at layer 3. Layer 2 contains accelerator operation and monitoring activities. Layer 1 contains dedicated equipment controllers, which in turn interface to specific equipment through point-to-point protocols (layer 0).

Communication between subsystems takes place via four distinct buses as indicated. Fast Feedback, MPS, and Global Synchronization buses supply information as implied for the needs of these control operations. Asynchronous information flow which does not require specific transfer rates is achieved by Channel Protocol. This is the most global communication standard in the system and, accordingly, most devices in every layer are identified as channel access clients, servers, or both.

The standard two-layer client server architecture ensures scalability and avoids performance limitations. NSLS-II controls must be built upon a proven tool kit with well-defined interfaces at both the server and client to enable integration and development. It should enable the use of hardware and software already developed for specific light source requirements. The core of the Experimental Physics and Industrial Control System (EPICS) has been chosen as the basis for the control system. Three options for the control system tool kit were reviewed [9.1]: EPICS [9.2], TANGO [9.3], and a commercial SCADA system [9.4]. We concluded that any of these options could be made to work, but with varying levels of functionality, support and cost. However, EPICS has advantages over the other options in three key areas: large user base in the accelerator community, functionality for accelerator-related systems, and support for the required hardware interfaces.

Specific technical requirements, identification of control system user groups, and further details of the system architecture and EPICS toolkit will now be elaborated.

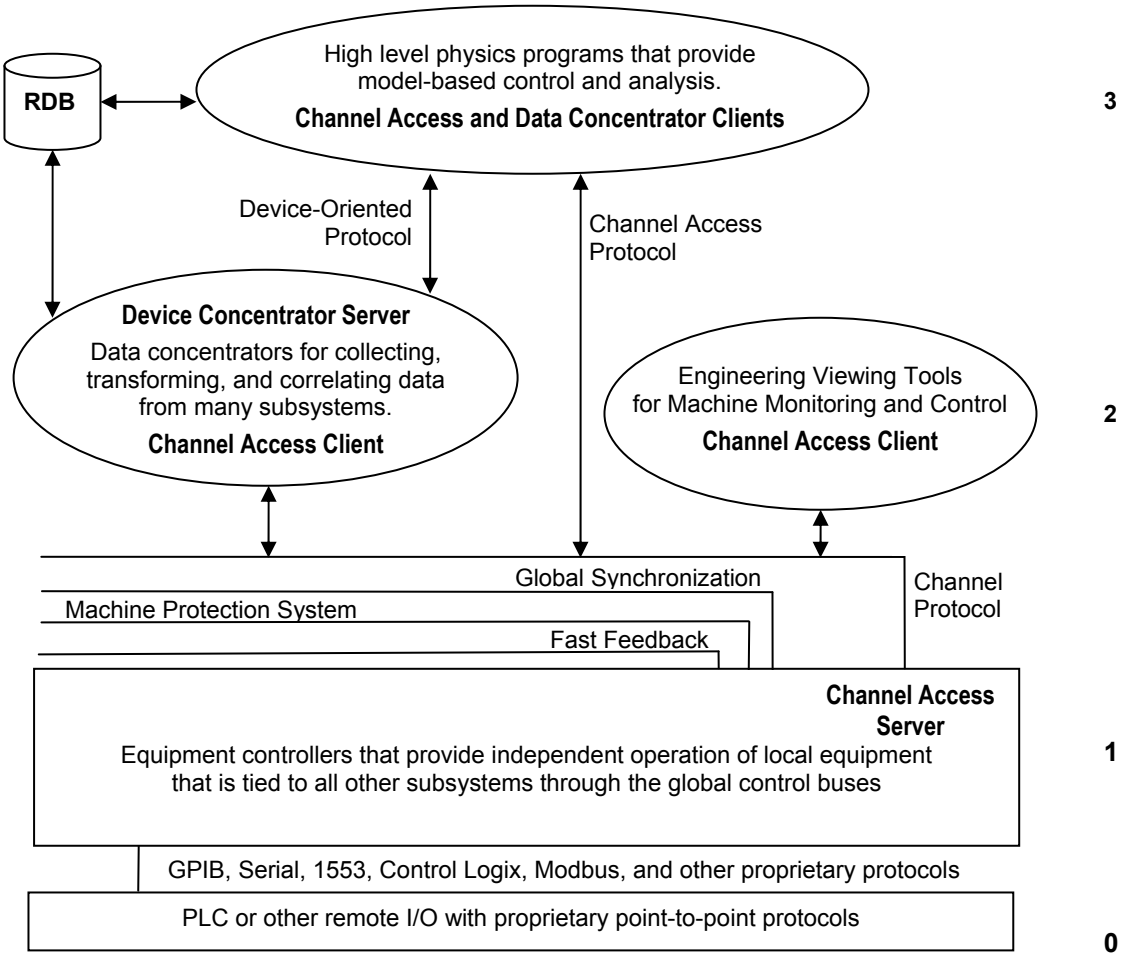

Figure 9.1.1 NSLS-II software architecture.

9.2 Control System Requirements

9.2.1 Technical Requirements

The control system must be modular, incrementally upgradeable, scaleable, and extendable. Expansion of the control system to accommodate the build-up of the accelerator and beamlines from early testing, through installation and commissioning, and during the life of the facility, should not impact the performance. The control system must be available to support all aspects of the project schedule, from component tests during prototyping to beam characterization and optimization at commissioning. To achieve this, the NSLS-II control system is based on open standards and commercial off-the-shelf equipment, whenever possible. Developments needed by NSLS-II are to be accomplished in a manner that meets the project schedule, budget, and performance needs, with consideration for knowledge transfer to the wider accelerator community.

Machine Control

Machine control supports linac control that is synchronized to the master timing system to fill the booster ring with 80 nanosecond pulse trains made up of 40 micro bunches of 2 ns length each. Pulse-to-pulse timing jitter will be less than 80 ps at the 1 Hz rate. The pulse is ramped up to the correct energy in the booster ring over 400 ms. It is then injected into the storage ring. The revolution rate for the booster and storage ring is 2.6 μs. Manual control of orbit trims, quadrupoles, sextupoles, and insertion devices is asynchronous. These are controlled by the operators, accelerator physicists, high level applications, or users. In particular, ~10 Hz write/read is suitable for "turning knobs" for a power supply. The only "fast" process is the fast orbit feedback system with ~100 Hz bandwidth (and feedback systems for coherent bunch instabilities of order MHz). To summarize, the beam bunches in the ring and the injection process are synchronous to the RF, but everything else has its own time scales. Model-based control is used to correct steering, the orbit, tune, linear chromaticity, optics, etc. in the storage ring at 1 Hz.

System Reliability

The control system must have 99.9% availability, 24 hours per day, 365 days per year. Control system modifications that add new functionality will be performed during scheduled down times. New functionality for the operational facility will be tested on equipment test stands before installation. The cryogenic control must achieve even higher standards. Failures or modifications to the cryogenic control system must not result in the loss of temperature control for greater than 15 minutes. Subsystems will be designed to meet system reliability goals using high reliability technology, where required. This includes the use of an uninterruptible power supply, programmable logic controllers, battery backup, and redundant power supplies for VME crates. All subsystems will be designed to achieve operational reliability goals.

Security and Integration across Operator Base

The system must manage access requirements for the different classes of user. It must also incorporate appropriate tools to guarantee security of its computers and network systems. The source of the data should be irrelevant from the point of view of any software designer or user. For example, it should be possible to display data from the control system, from the associated relational database and from an accelerator model on one full-screen synoptic.

9.2.2 Software Requirements

Control system applications must be designed to enable future upgrades to be incorporated economically. Wherever possible, application programs will be provided with command-line options, so that the functionality on offer can be increased by simply running the program with a different set of command line options.

Code Maintenance

All code, control system tools, and applications will be placed under source/release control. A standard tool will be used to control the version of software running and to keep previous versions and an audit trail for changes to released and commissioned software. Accelerator components and signal lists such as: magnetic lengths, min/max currents, calibration coefficients for currents vs. gradients, diagnostics channels, and configuration parameters also will be kept and their versions managed. The data that are also needed by accelerator models are to be kept in a similarly controlled relational database.

Open Standards, Integration, and Ease of Use

The control system will use open standards and an open architecture. The long life expectancy of an accelerator complex implies that the control system will need to evolve to incorporate upgrades and new technology. The control system must enable seamless integration of systems at both the server and client side through well-defined APIs. It is beneficial for the applications that comprise the NSLS-II control system to have a consistent look and feel. Related functions should be linked, to reduce the number of mouse clicks a user has to perform. For example, trends could be accessed by clicking on a process value hotspot displayed on a plant synoptic value. All control system facilities that need to be accessed directly will be accessible via menus, where the menu titles give a clear indication of the facility being called up. It should never be necessary for a user to remember the name of a program or of data files in order to use the system.

Context-sensitive online help facilities should be designed into the system, where feasible. Conscientious attention to common-sense ergonomics during application development will clearly pay dividends for long-term ease of use and will minimize familiarization and training costs for new operators. Production of a concise Style Guide document at an early stage in the development cycle of the project will provide a good ethos for addressing these issues.

9.2.3 Architecture Requirements

The four-layer EPICS-based client-server architecture illustrated in Figure 9.1.1 implies further design considerations for its implementation:

Network

The connection of the control system layers will use standard network components. These should be in a redundant configuration and include provision for network evolution, i.e., the development to GbE standards. Control system network security is to include physical security that limits access to the control network from outside, using gateways and firewalls. It requires appropriate types of password and key protection within the control network with access control to manage who is controlling which operation.

Operator Interface

The operator interface will be either workstations or PCs running Unix or NT, as these are the established standards. The control system should seamlessly integrate with office systems through a gateway process to maintain security.

Equipment Interface

The equipment interface will provide the physical connection to the equipment being controlled through a variety of interfaces. The preferred standards will include VME because of physical and electrical performance, Compact PCI where higher performance backplanes or lower point count make this more cost effective, and PLC I/O for applications where equipment safety is required and speed is not. The control system includes all VME crates and processors, any network hardware required for integrating instrumentation, the timing/event system, all hardware used for fast feedback, and all instrumentation that plugs into the VME crates. When intelligent devices or PLCs are used, it must be clearly stated if the equipment is to be provided by the control system. All cables leading out of the instrumentation at either end are the responsibility of the subsystem.

Relational Database

The control system must include a relational database as a central repository for all configuration information. This should include all static information about accelerator components such as coefficients to calculate field magnetic strength from current. Consideration should be given to extending the database to include all technical information to enable subsequent support and maintenance. At the application level, there should be a unified and seamless interface to both the static and dynamic data.

9.3 Identification of Control System User Groups

The control system must support several user groups, each with varying requirements.

Accelerator Operators

Accelerator operators are the principal managers and users of the control system. It must be a complete and consistent interface for them to perform any function in the accelerator complex. The data and interfaces must be consistent in how data is presented and how equipment is seen to behave. The operation of the accelerators requires real-time control and monitoring of the equipment, archiving, alarm handling, sequencing, backup and restore for routine operation. For these users, alarm and error messages should be supported by information regarding recommended courses of action. The control system should allow the automation of plant operating tasks. It should provide applications that encourage and facilitate the keeping and passing of operation logs, particularly from shift to shift.

Accelerator Physicists

The accelerator physicists' requirements for the control system include all the routine operations of the control system together with the ability to integrate programs developed to support different accelerator models. Functionality is required to allow easy acquisition of data produced as part of an experimental run, and to provide the ability to switch between different accelerator models. Data retrieved from the control system must be acquired with sufficient time accuracy to enable accurate correlation.

Technical Groups

The technical groups require diagnostics to enable maintenance such as calibration and fault finding. Access to the control system is required in the main Control Room, local to the equipment, and potentially in the offices, laboratories and off-site. Applications must provide all diagnostic information necessary to assist in commissioning and debugging of equipment. They must provide useful fault diagnosis facilities to assist with plant equipment maintenance and maintenance of the control system itself (both hardware and software). An easy interface to databases of equipment properties, manufacturers, documentation, cabling data and fault histories is required, as well as access to information clearly identifying the geographical location of equipment and a system of fault prediction facilities to allow for scheduled maintenance of components likely to fail.

Beamline Staff and Experimenters

The end users of the experimental station require a straightforward graphical interface to the control system. They also require good integration of control system parameters with the experimental control and data acquisition systems. This is particularly necessary in the case of synchronizing scanning of a sample with changing a parameter on an insertion device in the storage ring, e.g., the gap of an undulator. Experimenters require clear information on light source status, performance, and timing signals, and may require remote access (i.e., from off site) to experiments and beam-lines.

Control System Engineers

Control system engineers require current and archived data on the status and behavior of the entire control system. Information required includes CPU loading, network loading, application monitoring (for frozen/crashed applications), connectivity status, and reports of any control system faults.

Facility Managers

The control system should be capable of producing operating reports and statistics in a form that can then be imported into software applications (i.e., spreadsheets, web-based tools, etc.) used by management. Information required could include the number of hours of beam time supplied to users and unplanned beam dump statistics – how often these events occur, time taken to restore beam, reason for beam dump, and signs of common modes of failure.

Public Users and Staff

A wide range of other groups will require information from the control system. These include technical and scientific groups on and off site. These groups should be served through a web service as the user interface.

9.4 EPICS Toolkit

EPICS is the result of a collaboration of control groups, across a number of research organizations, to produce a tool kit to build distributed control systems. The resultant tool kit reduces software development and maintenance cost by providing: configuration tools in place of programming, a large user base of proven software, a modular design that is expandable, and well defined interfaces for extension at all levels.

Worldwide, EPICS has a very large user base for a variety of accelerators, detector systems, astronomical projects, and industrial processes. Most recently, EPICS has been successfully deployed at the Diamond Light Source, the Spallation Neutron Source at ORNL, and the Australian Synchrotron Project. It is being used for the LINAC Coherent Light Source at SLAC, the Shanghai Light Source, and the multi-faceted accelerator facility JPARC at Jaeri.

The use of EPICS on a diverse range of projects means that there is a large base of drivers and hardware support already available. The existence of these makes interfacing of the underlying systems less dependent on software development.

The EPICS tool kit is supported through the collaboration with software distribution and documented through the web. There are EPICS training courses run each year by many groups in the collaboration, and there are two EPICS workshops rotating through the U.S., Europe, and Asia each year; a number of individuals and companies are also available to provide support and training.

9.4.1 Structure of an EPICS Control System

EPICS embodies the standard client server model for a distributed control system, and shown in Figure 9.4.1. The user consoles are one class of client that receives and processes information. The servers are the source of information and in the general case, the interface to the equipment being controlled. The clients and servers are physically connected using network technology and they communicate with the EPICS protocol Channel Access.

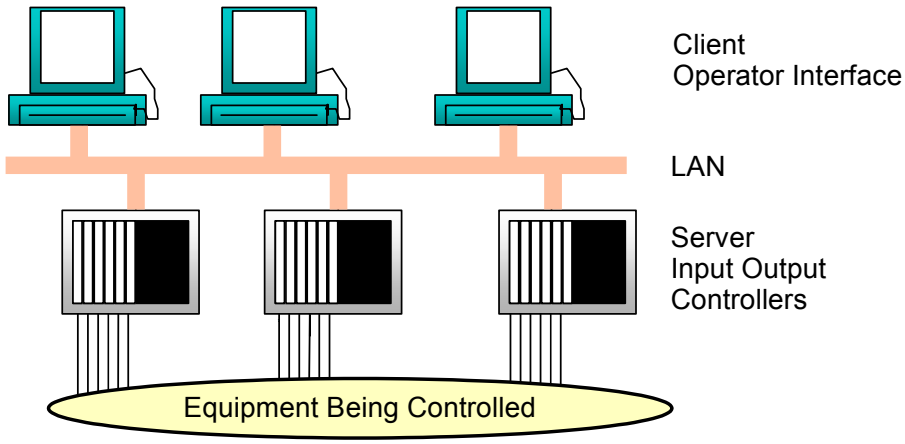

Figure 9.4.1 EPICS model.

9.4.2 EPICS Servers

The physical realization of EPICS servers is typically as multiple embedded VME systems, which are called IOCs, Figure 9.4.2. IOCs interface to the equipment being controlled, for which EPICS supports a large range of physical interface standards, protocols, and devices. IOCs also support the use of an event timing signal, to time-stamp transactions and enable synchronous acquisition or control across multiple IOCs.

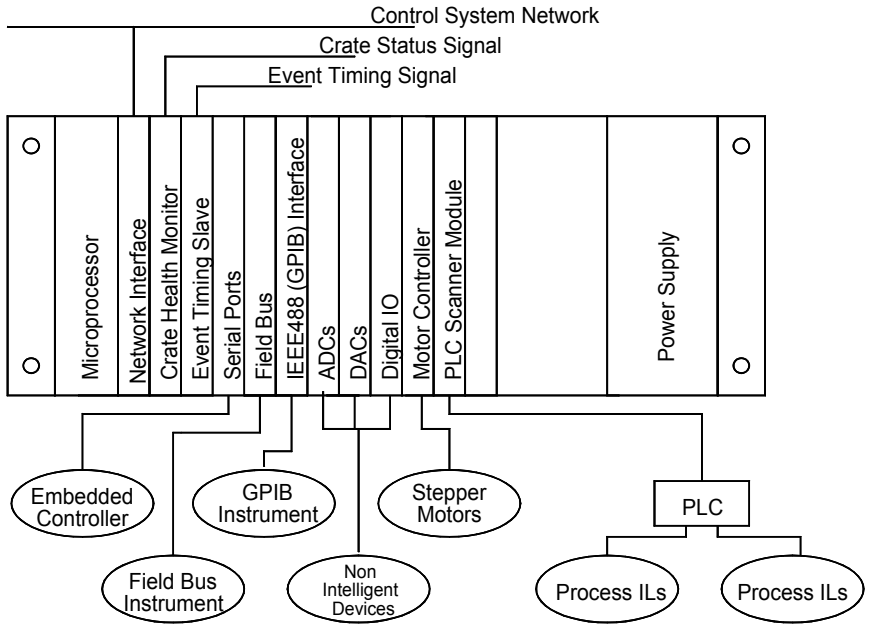

Figure 9.4.2 Example EPICS IOC.

9.4.3 Server Side Processing

Within the IOC, the CA server communicates with the Process Database, which uses the Record Support, Device Support, and Driver Support layers to interface to the plant, Figure 9.4.3. The communication from the EPICS client, over CA to the database, can be by synchronous call and reply or by the client establishing a monitor whereby the server asynchronously serves the data. The update of monitors can be on a periodic basis, on change of data, or on external event.

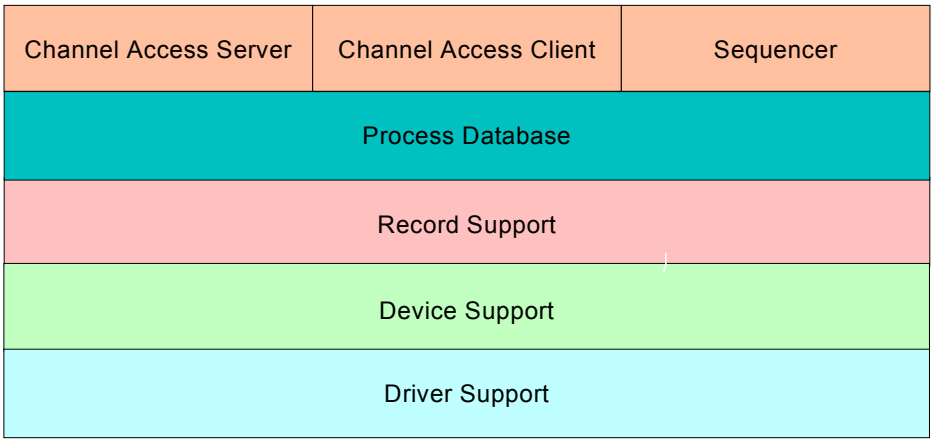

Figure 9.4.3 EPICS IOC data model.

The process database is a memory resident database that defines the functionality of the IOC. The database uses the Record Support layer to perform the processing necessary to access IO, perform data conversion, check alarms, and update monitors. The IO operations are carried out through the Device Support layer, which handles equipment specific protocols, and through the Driver Support layer, for the hardware interfaces. The structure provides support for interfacing to embedded controllers, field buses, IEEE488 (GPIB), DACs, ADCs, Digital IO, stepper motors, PLCs, power supplies, and a range of instrumentation.

Within the Input/Output Controller there is also a CA client to facilitate IOC-to-IOC communication. This is realized by linking process information from one process database to a process database on another IOC.

An IOC also contains a Sequencer to perform Finite State Machine control on the process database. The sequencer logic is defined as SNL, which is compiled to C code, then to an executable to run on the IOC. This allows for easy production on complex sequences, such as switching through the steps in bringing on a piece of equipment.

A standalone version of the CA server is available, which can be integrated into other systems without the process database and support layers. This facilitates integration of self-contained systems into EPICS, one example being the integration of LabView systems.

9.4.4 EPICS Clients

The client side of EPICS is realized on either Unix workstations or PCs running Windows and is called the OPerator Interface (OPI).

In the standard EPICS model, the OPI application programs interfaced directly to the CA client. This has limitations in that it only provides access to the dynamic control data through the CA API and so limits seamless integration of data from other sources, e.g., a RDB. The EPICS toolkit provides a suite of applications for the OPI. Among the choices for the core tools are: a synoptic user interface for control and monitoring (EDM), an Alarm Handler, an Archiver for recording and retrieving the historical state of the control system, a backup and restore facility to take snapshots of parameter settings, a knob manager to provide attachment of physical knobs to parameters and a parameter plotting tool. There is support within EPICS for the scripting languages Jython, Matlab, Tcl/Tk, Perl, and LabView. Data can be further served up to web pages through a CGI server.

9.4.5 EPICS Development Environment

The functionality of a control system built with EPICS is defined in three places: the Operator Interface, the Process Database, and the Sequencer logic. EPICS provides a number of tools to develop each of these which do not require software development. The OPI applications can be produced by a number of interface-generating tools, one of which is EDM. These tools allow for control objects to be placed on pages and animated with a connection to the control parameters. There are both text and graphical tools to produce the Process Database, which involves selecting records and drivers, and linking them to process data and alarms. The Sequencer logic is produced from SNL, which can be defined as text or, more recently, in a graphical form.

9.4.5.1 Distributed Development

Each developer will work on either a Linux PC or a Windows PC. These will be networked to a development file server providing read-access to all the necessary development tools and applications (VxWorks, RTEMS, Matlab, XAL EPICS base and extensions, configuration and database files, etc.), see Figure 9.4.4.

Modifications will only be made to local copies of applications, which will then be checked in to a branch of the CVS repository to enable any changes to be backtracked. When the application has been fully tested and is stable, this branch will become the main development branch for the control system.

A central boot server will be used to provide all the necessary files required by the local IOCs for booting. These files will be generated from the CVS repository. This will ensure that all IOCs are running a consistent and stable version of the control system. The contents of the central boot server will be mirrored on boot servers located in the control room, which will provide local booting of the IOCs.

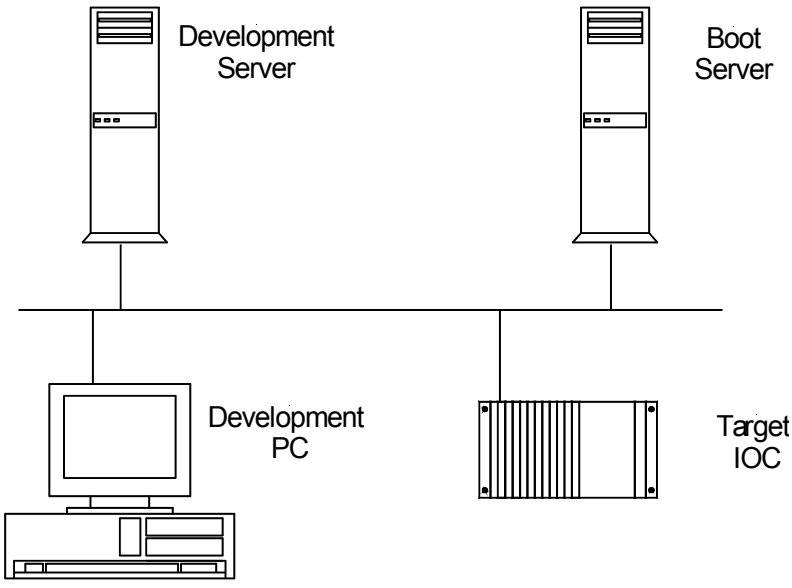

Figure 9.4.4 Distributed development structure.

File Management with CVS

CVS [9.5] is a version control system for keeping track of all modifications to project source code files. CVS is widely used in both open source and proprietary software development projects, and is generally

considered to be the best freely available, full-featured version control tool. Two features make CVS particularly suited to collaborative development across any network, including the Internet:

- Multiple developers can edit their own working copies of files simultaneously. CVS then deals with combining all the changes and notifying developers when there are conflicts.
- Developers have remote access to source code file repositories. Project members can obtain and modify project files from virtually anywhere.

CVS is a client-server system. The CVS repository is maintained on a server; clients run on users' machines and connect to the server via the network (or Internet). Clients are available for nearly all platforms, including Unix, Windows, Macintosh, and any Java-based platform. CVS allows project members to:

- Check out source files and directories
- View differences between versions of files
- View change log history and comments
- Commit changes made in their local copies of the source files to the main source code repository
- Update their local project files when they want to remain in sync with changes committed by other project members

CVS has proven very beneficial to many other accelerator projects in the world, and there is a very large CVS knowledge base within the EPICS community.

9.4.5.2 Application Development

Most application requirements can be met through the standard tools discussed in this section. Where more intelligence is required at the application level, there are EPICS interfaces to all the popular programming languages. The preferred solution will be to use C/C++, Java, or scripting languages to minimize the number of supported languages.

C/C++. C, and C++ are high-level programming languages that have become the de facto standard for portable open systems solutions on Unix/Linux platforms, with C++ usage increasing due to the popularity of Object-Oriented design and programming. Both languages have been widely used both for the EPICS baseline product and for driver software and other applications built on top of the baseline. For the NSLS-II Control System, the emphasis will be on re-use of existing software. Improvements are expected to meet NSLS-II requirements.

Tcl/Tk, Python/Jython. Tcl and Python are widely-used open-source scripting languages. They have simple and programmable syntax and can be either used as a standalone application or embedded in application programs. Tk and Python are Graphical User Interface toolkits that can be used for rapid development of powerful GUIs. Tcl/Tk and Python are highly portable, running on essentially all flavors of Unix (Linux Solaris, IRIX, AIX, *BSD*, etc.), Windows, Macintosh, and more. Tcl/Tk and Python are well supported and extensively used on many EPICS-based projects, particularly for GUI development.

Java. Java is an object-oriented interpretative programming language with a built-in Application Programming Interface that can handle graphics and user interfaces. Java can be used to create standalone applications. However, a more important use is in the development of applets, programs that can be embedded in a Web page. The growth of the Internet, together with Java's hardware independence, has made the language essential for web-based developments.

Currently, Java performance issues mean its usage will only be considered for applications where response time is unimportant. Generally, though, Java solutions providers are seeking to improve performance with developments such as just-in-time compilers and Java processors. If these developments yield effective performance improvements during the development phase of the NSLS-II project, then Java's importance to the project will increase.

9.4.5.3 Server Development

Development of EPICS at the server level is required potentially in three places, namely record and device support, database, and state notation language.

9.4.5.4 Record and Device Support

While there is extensive record and device support available for EPICS, addition of unsupported hardware will necessitate the development of Device and possibly Record Support layers. The EPICS toolkit provides well-defined interfaces to each of these layers and examples to aid development. Device development is carried out in C within the standard EPICS development environment.

Building and developing EPICS requires either the VxWorks [9.6] or RTEMS development environment. VxWorks is currently only available for Windows or Solaris. However, given that the development environment is based on the GNU tool chain, it should be possible to run the RTEMS tools on Linux. The preference will be to standardize on one operating system for development, preferably Linux.

Database Configuration Tools

There are several Database Configuration Tools available. These DCTs allow designers to create EPICS databases by implementing them visually with a "block diagram and link wire" approach, similar to that used in electronic schematic design packages.

NSLS-II will use VisualDCT [9.7] as its database configuration tool. VisualDCT is an EPICS database configuration tool written in Java. It can therefore run under any operating system that supports a Java Runtime Environment. It was developed to provide features missing in existing configuration tools and to make databases easier to understand and implement.

The database development cycle will involve importing the EPICS runtime database into the central relational database to have a single repository of all control system information. VisualDCT has a powerful database parser, which allows existing DB and DBD files to be imported with ease. The parser detects syntax errors in databases, as well as defective visual composition data or its absence. Faults in DB files are safely handled and do not raise any critical errors. VisualDCT automatically lays out all objects that have no visual composition data and saves all visual data as comments to maintain backward compatibility. The output from VisualDCT is also a DB file, with all comments and record order preserved.

Visual DCT has been written within the EPICS community specifically to support EPICS, and is available free to EPICS database developers. However, some development of VisualDCT required to add some missing functionality will need to be undertaken.

State Notation Language / Sequencer Tools

The sequencer is a tool within EPICS that allows the implementation and control of one or more state machines on the IOC. The state machines are created using EPICS SNL. SNL has a C-like syntax, with constructs for building state machines. Once the SNL source code has been written, a SNC pre-processes it into "C" code and then compiles it to create an object file which the sequencer runs in the IOC.

9.4.5.5 Client Tools and Middleware Data Servers

Client tools are available at level 2 of the control system architecture. Clients at this level can directly access all channels in the control system through the Channel Access protocol. These data are time stamped by the Event System for reconstruction of accurate time sequences or correlation of events. At this level, client tools can use data from the IOCs directly, use control system data along with accelerator equipment information for model-based physics applications, or provide computed or correlated data to other clients.

9.4.5.6 Console Applications

The EPICS software package offers comprehensive operator display applications, which include:

- Extensible Display Manager
- Channel Archiver and Archive Viewing Tools
- Strip Chart Tool (StripTool)
- Array Display Tool (ADT)
- Parameter Display Page (DP)
- Alarm Handler
- Knob Manager (KM)
- Operator Electronic Log (CMLOG)

These applications will be used to supply operator display facilities, which will include the following functions.

Operator Menu Bar

This will provide rapid single-click access to all key operator facilities.

Plant Synoptics

These full-screen plant schematic diagrams will provide operators with an at-a-glance indication of plant conditions. Each process value displayed on a synoptic will constitute a "hotspot"; clicking on a hotspot will produce a pull-down menu providing access to further information and control actions relevant to that process value. Typically, a text description of the signal, the units of measurement, alarm limits, maximum and minimum, trend, alarm history, wiring information, operator comment and web access to online help might be provided. By this means, plant synoptics will act as the launch platforms which allow operators to access a wide variety of data in a seamless manner.

Ease of navigation will be considered during the detailed design stage for plant synoptics. An overall Synoptic Menu will be provided, which lists all synoptics grouped by functional area, presenting a clear hierarchy. In addition, where appropriate, plant synoptics will contain links to other associated synoptics. The design aim will be that operators should be able to navigate around the hierarchy without the constant need to return to the Synoptic Menu. Plant synoptics will be designed to have a simple, uncluttered appearance so as not to present more information to the operator than can reasonably be taken in.

Control Panels

Usually sized smaller than full-screen, control panels will be available with a wide variety of control widgets (radio buttons, slider bars, data entry fields with data validity checking, etc.) to allow users to apply control actions to the plant.

Control panels can be configured such that a single slider bar is used to control simultaneously a number of control outputs. Mathematical functions are available to define how these combined control outputs operate in relation to one other.

User-Configurable Tabular Displays

Operators will be able to configure their own sets of tabular displays showing closely-related accelerator parameters. Facilities will be provided to save these user-configured displays with a user-chosen name, and to recall the display from a list presented in a pull-down menu.

System Status Indicators

These schematics will show the status of IOCs, operator monitors, printers, etc. They will also display the health of key applications—so that, for example, operators are made aware quickly if alarm processing stops due to an alarm server program crash.

Operator Comments Facility

This will allow operators to enter lines of text comment for any plant input—to record, for example, when an input is not reading correctly due to a known fault. The presence of an operator comment for a process variable will be clearly indicated on any synoptic which displays that process variable. Individual comments will be easily readable via a suitable control panel, and it will also be possible to collate lists of comments (e.g., all operator comments entered during a shift).

Signal Information Panel

Only a subset of the process variables will be displayed on plant synoptics. However, operators require rapid access to information about any process variable and the Signal Information Panel satisfies this requirement. The panel will provide a Search section and a Display section. The Search section will enable the user to carry out a name search on the relational database, using a name mask to search for either an EPICS database record name or an EPICS record descriptor. Clicking on one of the returned search results will enable the user to request further information (e.g., trend, alarm history, operator comment, etc.).

Message Logging

The CMLOG package available with EPICS will be used to provide a distributed message logging system. This package can be used by any application or system that needs to log messages to centralized log files and display distributed messages to users. The CMLOG package supports C++, C, and CDEV application interfaces for logging messages and has C++ application interfaces for searching/retrieving messages from a dedicated logging server. Applications may send a selection rule to the server to select a subset of log messages for viewing; these rules can be in a form similar to C logic syntax or in a form similar to SQL.

A sample Message Log Browser (an X-Windows Motif application) is included with the CMLOG package. An additional browser will be developed using the supplied application interfaces once detailed requirements are established during the detailed design phase of the project.

9.4.5.7 Alarm Handling

The EPICS Alarm Handler package will be used to provide the following facilities:

An alarm list allows the users to view and manipulate current plant alarms. The alarm list will incorporate the following facilities:

- Indication of alarm acknowledgement state.
- Alarm message which includes EPICS record name, descriptive text, alarm value and date/time of alarm generation.
- Removal of acknowledged alarms from the Alarm List when they are no longer in the alarm state.
- Access to a menu-based set of facilities from each alarm in the Alarm list. The menu would give access to further information about the alarmed signal, including:
  - Trend
  - Alarm history
  - Access to a synoptic which includes the alarmed signal.

- Web access (e.g., a link to a text page with more details about the alarm condition and possible corrective action)
- Operator-selectable alarm inhibition to prevent use of the Alarm List from being disrupted by non-genuine alarms (e.g. "flickering" alarms being generated by a faulty switch). The names and descriptions of inhibited signals will be viewable on a separate list, from where it will be possible to de-inhibit each signal.
- Association of each alarm with a plant area, along with the ability to display only alarms for a particular plant area.
- Color indication of alarm severity.

All alarm messages will be logged to a text file for interrogation and archiving purposes. An alarm log viewer will be available, with various filtering options such as date/time, alarm severity, input name, etc. Provision will be made for audible alarm tones, driven from software using wav files. A separate alarm tone will be available for each alarm severity. An alarm banner window will be available to display a configurable number of recent alarms in a dedicated window at the top or bottom of the screen. Alarms can be acknowledged via the banner without having to call up the main Alarm List.

9.4.5.8 Archiving

The EPICS software toolkit offers comprehensive short, medium, and long-term data collection, archiving and retrieval through the EPICS Channel Archiver package. This package will be used to provide the following facilities. For long-term archiving, the archiver provides support for:

- Data retrievable in tabular and trend form
- A data quality indicator associated with each item of data
- Data compression to minimize the size of archive files
- Dumping of data to removable storage media, for long-term storage
- Loading of archive data from removable storage media for data analysis
- Timely warning to operators when archive data collection is compromised by a "disk full" condition on the archive server
- Variable data collection intervals for archiving
- A mechanism for easily configuring large numbers of process variables for archiving (e.g., by use of name masks)
- Facilities for collecting data in user-definable data sets, where data sets can include files as well as process variable data

The Historical Data Collection provides for short- to medium-term data collection offering the following features:

- Data retrievable in tabular form and trend form
- Data quality indicator associated with all data
- Variable data collection intervals
- Mathematical functions (e.g., averaging, MIN-MAX, etc.) applicable to historical data

A wide variety of data retrieval and data management tools are available with the standard Channel Archiver package, including:

- Retrieval via scripting tools, provided by the Channel Archiver Scripting Interface. Tcl, Python or Perl can be used to develop automation of archive handling.
- Retrieval via native tools, with Xarr/Striptool for UNIX-based systems and WinBrowser for Win32 systems. WinBrowser also provides data export in spreadsheet format or in a format suitable for the Matlab data analysis and modeling package.
- Retrieval via a web server plug-in, offered by the CGIExport client, which allows users to browse the archive via any web browser. File download in spreadsheet or Matlab format is supported by this plug-in.

- Command-line tools provided by the ArchiveExport/ArchiveManager component, providing commands to manage archives and to export data to a spreadsheet, to Matlab or to the GnuPlot plotting utility program.
- The Archive Engine component of the Channel Archiver package includes a built-in Web server. By using this feature, current operational parameters can be viewed and interactive configuration can be carried out via any Web browser.

9.4.5.9 Plotting

The StripTool program will be used for displaying trends of current and archived data. The key features of the StripTool program are:

- A StripTool chart displaying recent live data can be scrolled back to view archive data.
- Data acquisition via both Channel Access and CDEV, thereby allowing trending of both EPICS and non-EPICS data on the same axes.
- Ability to drag signals from synoptic diagram (drawn using MEDM) into a graph window.
- Flexible configuration options, including logarithmic and linear transformations, sampling rate, graph refresh rate, plot colors, grid lines, graph legend coloring, and plot line width. The trend can also be easily reconfigured to make one or more plot curves invisible without removing the plot configuration information for that curve.
- Trends can be printed and trend data saved to file.
- Trends are customizable via X resources, giving access to a wider set of configuration options than those offered by the standard StripTool configuration facilities.

9.4.5.10 Automatic Sequencing

For increased operational efficiency, and in support of a demanding accelerator availability requirement, the control system will include the capability of automatic sequencing, including decision making. These sequences could include automatic run-up procedures, automatic fault-recovery sequences, and automatic data-taking routines. The system will provide simple tools for defining sequences as experience is gained and will be capable of monitoring the status of automatic sequences, annunciating problems encountered in sequences, and intervening or overriding sequences if necessary.

9.4.5.11 Data Server

Computed data and aggregate data are to be done with consideration to overall performance metrics. Where it is reasonable, these data are to be created once in a server and provided to other clients in the control system. Examples of this are first turn data, ring current, and emittance measurements.

9.5 NSLS-II Control System Applications

In addition to the capabilities described above, existing toolkits will enable the following site-specific applications and interfaces to be developed for NSLS-II.

9.5.1 Physics Applications Rapid Prototyping

Rapid prototyping of physics applications is supported through a number of programming language interfaces to the Channel Access protocol. These include: analysis packages such as Matlab, Labview andMathmatica; scripting languages such as Jython, Pearl, Tcl/TK, and SWIG; and programming language

interfaces such as: Java, C, and C++. Applications that are prototyped in this environment can be migrated into the standard EPICS front end controllers and the XAL environment for operations. (Figure 9.5.1).

9.5.2 Model-Based Physics Applications

Model-Based Physics applications must be available for all phases of commissioning. The system should be capable of operating in online and predictive modes. A RDB must contain the model parameters needed for the model based control. A physics modeling system will be needed to provide an interface between the control system and standard codes such as Tracy2, Elegant, or RING. These codes can mathematically model the behavior of various accelerator systems. They can be used to aid understanding of the machine, as well as being a vital tool for optimizing and operating a complex accelerator.

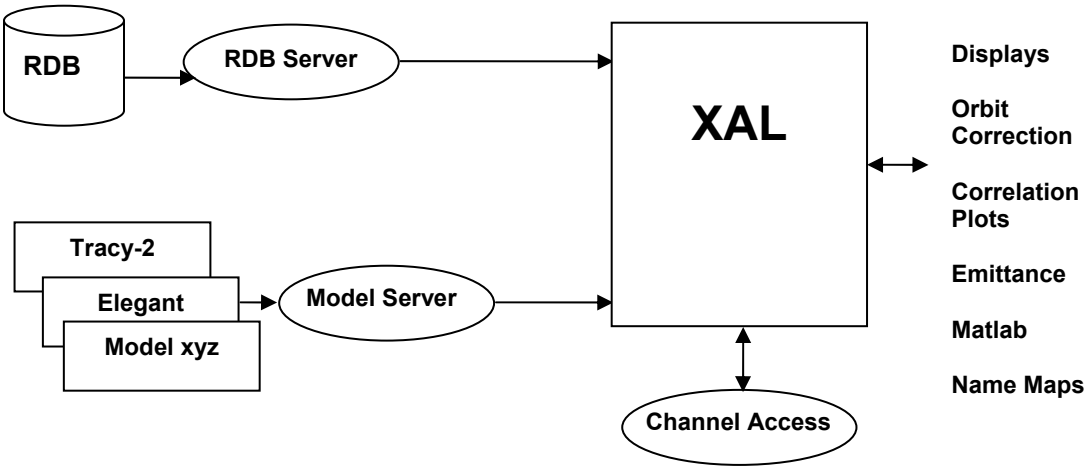

Figure 9.5.1 High-level application architecture.

XAL – the Model-Based Control Framework

NSLS-II will use a toolkit framework and applications developed in the framework, such as XAL, which is in use at SNS. NSLS-II will be able to leverage SNS developments for a faster start, but additional development will be necessary to tailor these approaches to NSLS-II.

Relational Database

ORACLE will be used as the main data store for all beamline component information that is needed for model-based control. Tools will be provided to enter this data, produce reports, and create files needed for run-time control.

Online Mode

Real-time magnet and RF data will be passed to the modeling system. Computed values of Twiss parameters, Q values, chromaticity, momentum compaction factor, etc. will be made available to the rest of the control system or to Accelerator Physics applications.

Predictive Mode

In this mode, offline magnet and RF values are supplied to the modeling system rather than real-time data. This will allow predictive and "look-and-see" experiments to be performed using the machine model to predict the behavior of the accelerator.

Middleware Data Servers

Middleware data servers will be provided to separate the data collection from the visualization layers. All client applications that collect data from the control system that result in the production of new data will be served to multiple, distributed clients. The distribution of this data is done over a standard protocol such as Corba. Alarm information, orbit, archive data, and emittance are some examples of data that may be produced by clients and served to other clients.

9.5.3 I/O Controllers / Equipment Interfaces

The I/O controllers and equipment interfaces must support the wide range of applications that are encountered in an accelerator control system. To minimize integration, training, and maintenance costs, this hardware should be limited to a solution that can meet each class of hardware integration needed. The front-end computers will run a Real-Time Operating System. The RTOS candidates are vxWorks and RTEMS. Although vxWorks runs on a wide variety of CPUs and provides much functionality, it does not provide source code without a prohibitive investment. RTEMS is an open-source RTOS that requires more man-power to wield. Several EPICS sites now support RTEMS. Control at this level of the architecture can be done at the rate of 1 kHz with latencies of 33 μsec. Dedicated data and timing buses are required to achieve this level of performance over distributed controllers.

High-Speed Signals

High-speed signals such as RF, image diagnostics, and beam position signals may be processed with an FPGA to produce results that are used by the control system at a slower rate. These devices may operate on data into the MHz range and be used to analyze high-speed signals from LLRF, Beam Position Monitors, and Power Supply Controllers. These may be implanted as single device controllers that are equipped with dedicated processors to run EPICS and provide the interface to the control system, an FPGA to process the signal, a high-speed interface between the FPGA and the control system, and an interface to the timing system. These device controllers may control a single device or a set of devices. A standard architecture that includes a Power PC with a PCI or PCI interface in the Coldfire format is a candidate for this application.

Low Latency Response I/O

I/O that requires the control system to respond in the minimum time (known as high-density I/O) requires an instrumentation bus that provides interrupts on an external trigger and reasonable data transfer times between I/O boards. This can be implemented using either VME or PCI.

High-Reliability IO

Applications such as vacuum interlocks, flow switch interlocks, and cryogenic control require high reliability control of simple processes. A Programmable Logic Controller will be provided for these applications. All data from the PLC shall be available through the control system. The Control Logix PLC in conjunction with the Flex-I/O line could provide this function at a reasonable price. In any case, one PLC family will be chosen as the NSLS-II standard. These PLCs will be integrated into the control system through an IOC.

9.5.4 Global Control System

9.5.4.1 Buses

The control system must provide some global communication that requires higher performance than is available in a commercial network. NSLS-II requires: an Event System for synchronizing data acquisition and control; a high-speed data network for providing beam-steering data to all ring power supplies for orbit correction; and a Machine Protection System that is a fast-response bus provided for mitigation against failures that greatly impact the operation of the facility by either producing excessive radiation or causing equipment damage. We will evaluate the systems available from other laboratories and select one that meets our requirements.

9.5.4.2 Event System

The Event System, also referred to as a timing system, provides all beam and RF synchronization for all control and data acquisition. The event system provides a master pattern of events that reflect the operation mode of the machine. It provides the synchronization needed to control the beam injection into the ring for initial fill and top-off. The event system may also communicate data that are required for operation and data correlation, as well as data communicated to the subsystems that change with the mode of the machine. Examples include time stamp/pulse ID, machine mode, and global machine status.

The timing system is required to provide control of the beam transfer from the electron source to the storage ring and provide diagnostic equipment and beamline equipment with synchronization signals. The most recent light sources [8] have made use of commercial equipment and built on equipment designed by other light sources, often in collaboration with industry; it is envisaged that the same approach will be adopted for NSLS-II.

Fast Timing

The task of a timing system is to synchronize all the relevant components in an accelerator complex. One part of this task is to control the injection by triggering the particle source and firing the transfer line components, such as injection- and extraction-pulsed magnets, at the correct times. Also, beam diagnostic components such as beam position monitors and current transformers must be synchronized to the passage of the beam. This has to happen with fine time resolution, to RF frequency, clock precision, and low jitter, and is termed Fast Timing.

Event System Signals

Other tasks for the timing system are related to synchronizing components where the resolution is more relaxed. Examples include triggering the magnets for an acceleration ramp, triggering operational sequences such as the filling of the storage ring, BPM acquisition, feedback timing, insertion device control, and supplying the distributed control system with time synchronization for control and correlation of data. The time resolution for these tasks is less demanding; these tasks are often termed Events. Event Signals will be produced with a precision set by the storage ring revolution period and with predictable jitter.

Timing System Components

In designing the accelerator timing system, it is important to consider what has been used at other recently constructed sources and the integration into the EPICS control system. The time-stamp system already exists within the EPICS infrastructure and can be used in conjunction with the Event System, which was developed at APS [9] and enhanced by SLS and, more recently, DIAMOND. The APS/SLS Event System can be used to

meet all slow timing requirements. The Event System is fully EPICS compatible and the required VME modules are available.

Table 9.5.1 Diamond Version of the SLS Version of the APS Event System Specification.

Events	8-bit code – 255 events
Resolution	8 ns
Event TX trigger	Hardware input, software, Event Ram Clock.
Event RX output	Hardware output, software (EPICS record process)
Transmission medium	Gigabit Ethernet

The requirements for fast timing are more specific to a particular accelerator dimensions and operation. Two options are available for the hardware for fast timing, the KEK TD4V as a VME module delay generator and the Stanford Research DG535 as a self-contained instrument. Each is available with EPICS drivers to provide the controlled delays.

Table 9.5.2 Fast Timing Hardware Options.

	KEK TD4V	Stanford Research DG535
Form	VME 6U	Bench / Rack mounting
Delay	16 Bit / RF clock	0 to 1000 s – 5 ps steps
EPICS Support	Yes	Yes, via GPIB
Channels	1	4
Jitter	4.5 ps at 508 MHz	<60 ps

System Structure

Figure 9.5.2 gives an overview of the Event System and Fast Timing control. The Event Generator receives a start signal from the RF clock gated with a line frequency component. Events are then sent to all IOC Event Receivers for timestamp synchronization and to output relevant event signals or process EPICS records. The fast-timing IOCs will require a fast clock and trigger derived from the RF source, but fast sequences can also be initiated upon receipt of an event.

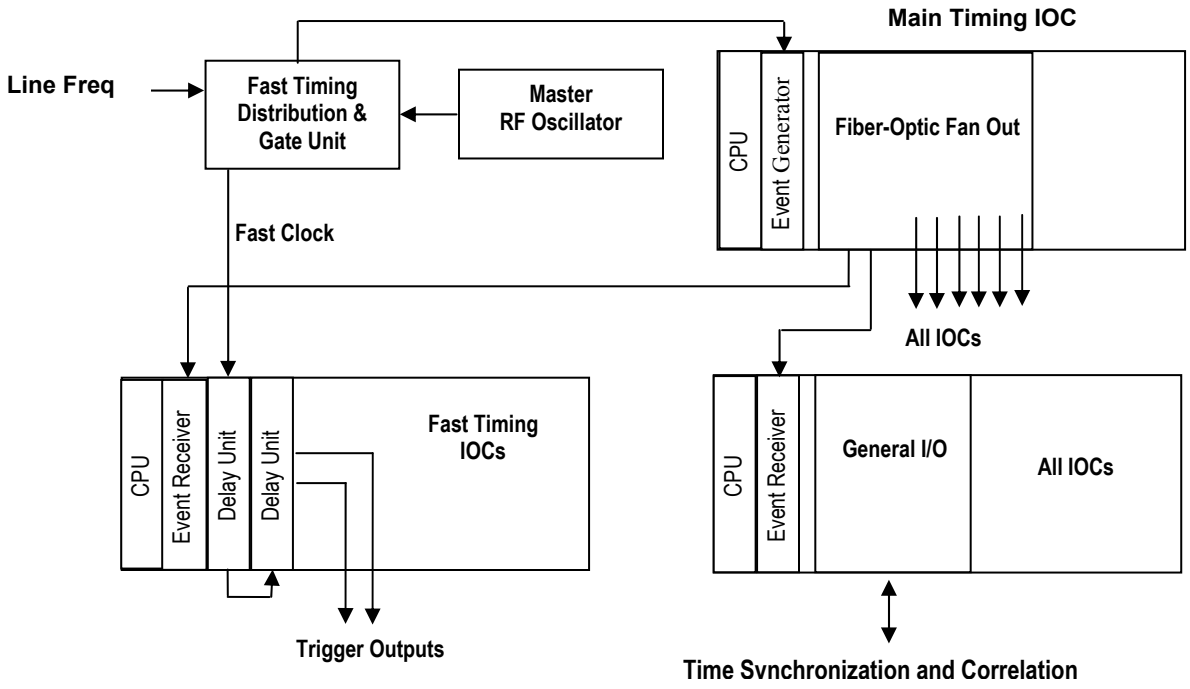

Figure 9.5.2 Block diagram of the Event System and Fast Timing.

Signal Distribution

The Fast Timing and Event signals will be distributed over fiber-optic cable for reasons of noise immunity and distance capabilities. Further investigation is needed into the delay drifts that could be introduced by the fiber installation from temperature differentials and the standardization of length-induced delays in a facility the size of NSLS-II.

Fast Feedback

A beam position stabilizing system is required to maintain orbit stability to within 10% of beam dimension and to provide dynamic correction of low-frequency orbit disturbances. The proposals presented here are very much based on the work on Diamond, APS [9.10], ALS [9.11], and SLS [9.12].

9.5.4.3 Global Feedback

The feedback system will use measurements of the position of the electron beam in the storage ring and the photon beams in the beamline front-ends. This information will be compared against a reference orbit and the error used to calculate desired corrections to be applied to corrector magnets in the storage ring.

The response matrix relates the effect of small changes in corrector magnet fields to the resulting changes in the particle beam orbit as measured at chosen BPMs. By inverting the response matrix the relationship that maps orbit perturbations to changes in corrector magnet fields is obtained. For small orbit errors, this relationship is assumed to be linear and time-invariant. Different objectives, such as correcting the orbit in an rms sense or correcting specific locations, can be achieved by choice of BPM and corrector locations and by applying different weights to correctors or BPMs when computing the inverse response matrix.

Performance

Two global feedback systems, operating in parallel, are proposed to correct orbit errors on NSLS-II, namely a Slow system, correcting DC drift, and a Fast system, correcting beam disturbances to 100 Hz. These systems will use data from both the electron and photon BPMs and operate on either or both of the steering magnet or fast correctors. For both systems, the BPMs need to be sampled synchronously, which will be achieved using Events distributed to the IOCs.

Table 9.5.3 Feedback System Comparisons.

	Correcting Feedback	Update Rate Feedback
Slow	DC drift	0.1 Hz
Fast	0.2 mHz –100 Hz	2 KHz

Slow Correction

The Slow correction will correct the orbit at 10 second intervals, using the desired correctors and BPMs to compensate for slow changes in the orbit. This will maintain the user-steered orbit applied at the beginning of each fill. Communication to the BPM and Steering IOCs will use the EPICS CA communication mechanism. The slow correction will be realized as a dedicated application running on either a console or a computer server.

Fast Correction

Fast correction is not possible through EPICS CA mechanisms because of insufficient bandwidth. It will be realized at the IOC level on separate feedback processor boards dedicated to this function. This involves partitioning the correction calculation across the 30 Steering IOCs to calculate the correction values for the steering elements local to that IOC. Each steering IOC requires access to all the BPM values, to give flexibility in the correction algorithm. This requires a high speed connection to share data between the 30 BPM IOCs and 30 Steering IOCs. Two potential solutions for this are to use either reflective memory or network broadcasts.

EPICS process variables will be used to control the feedback process, by downloading algorithms to the feedback processors and setting coefficients and update rates.

9.5.5 Reflective Memory

Reflective memory is an off-the-shelf solution to distribute information across multiple computer systems without requiring processor time. It enables BPM data to be written to the reflective memory module in each of the BPM IOCs and appear in memory in all the Steering IOCs. In the system shown in Figure 9.5.3, an event received by all BPM IOCs would cause the photon and electron BPM values to be read by the feedback processor and written to the reflective memory board for each of the 30 IOCs. The data would propagate to all the steering IOCs and when all values are received, the feedback calculation would be carried out on the Steering IOC to produce the new steering settings. These values would then be written to the steering elements in conjunction with the slow system values received through EPICS process variables.

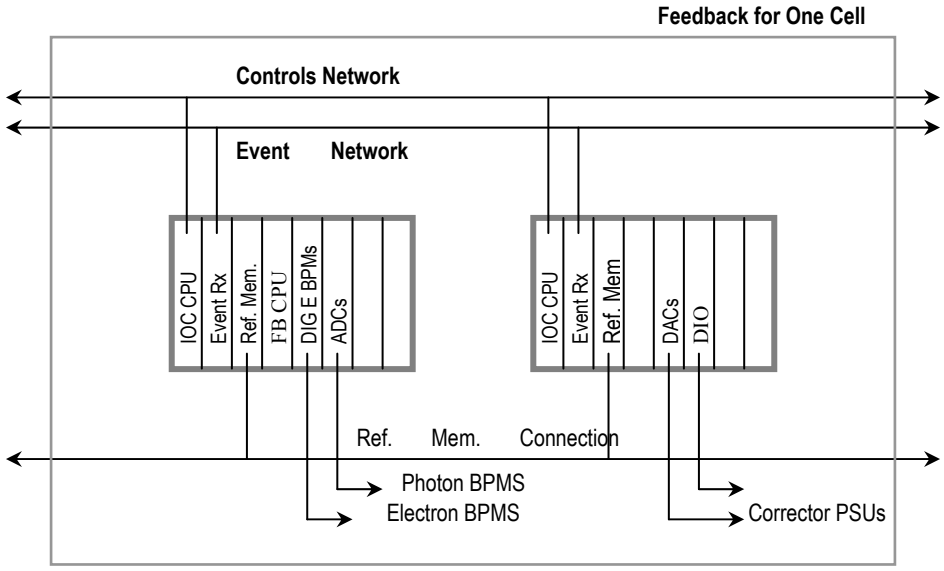

Figure 9.5.3 Reflective memory structure for one cell.

Commercially available reflective memory sizes and update rates provide for moving multi-megabytes per second across tens of boards, and so should easily meet the requirements of this application.

Network Broadcast

In the Network Broadcast system each of 60 feedback processors in the BPM and Steering IOCs is connected to a private network with a central switch in a star configuration. The feedback processor in each of the BPM IOCs reads the BPM values and broadcasts them over the network to be received by each steering IOC. The broadcasts take place simultaneously but do not collide, because the switch buffers each packet as it receives it. The switch then forwards the packets to all the Steering IOCs.

In the system shown in Figure 9.5.4, an event received by all BPM IOCs would cause the photon and electron BPM values to be read by the feedback processor and broadcast over the private network. When each of the 30 broadcasts has been received by all of the Steering IOCs, the calculation would be carried out on each Steering IOC to produce the new steering settings. These values are then written to the steering elements in conjunction with the slow system values received through EPICS process variables.

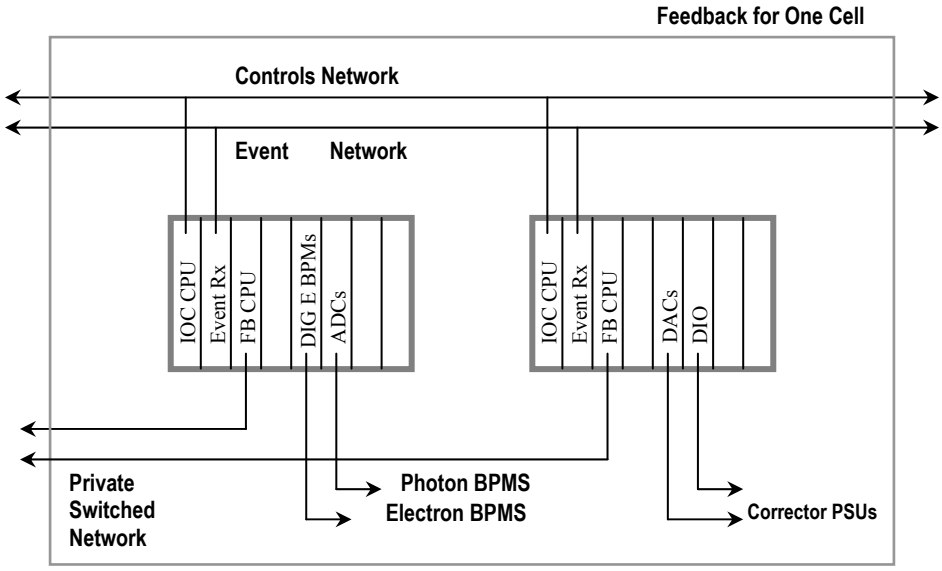

Figure 9.5.4 Network broadcast structure for one cell.

This option is cheaper in terms of hardware because it alleviates the need for the reflective memory boards, but incurs a development overhead to produce software for the broadcasting. The performance achievable using broadcasts also needs to be determined, to establish whether it would meet the requirements of this application.

Feedback Processor

On the Steering IOC, the calculation to produce the new steering values from BPM values and the inverse response matrix needs to be carried out. The time available to carry out this calculation is dependent on the desired update rate, the time to acquire and distribute the data, and the time for the correction to propagate through the steering power supply, magnet and vessel to the beam. While the current generation of PPC processors offers similar performance as DSP processors, in terms of operations per second, they do not have the architectural feature of DSP processors for signal processing intensive calculations. However, the performance available from current PPC makes them suitable to carry out the feedback calculations at a price advantage over DSP processors.

9.5.6 Machine Protection

The control system must monitor beam envelope and other operational parameters that determine if the beam is threatening to damage equipment. Detection and reaction to dangerous conditions must be completed within 3 msec.

9.6 Equipment Protection System

The beamlines at NSLS-II are expected to handle x-ray beams with very high power and power densities. Therefore, care must be taken to design the beamline with components that can handle these power loads. Any component that has to handle these high levels of power has to be monitored. The beamline Equipment Protection System provides a means of monitoring the components which, when jeopardized, can cause

component failure. The EPS has the responsibility to act on alarm conditions by mitigating the situation that has caused the alarms.

9.6.1 Functionality

Every beamline EPS will monitor and interlock the devices in the front end and the beamline.

All front ends at NSLS-II are expected to have two safety shutters, one photon shutter, and a few masks (see Section 7.4). In addition, the front end will also have vacuum inline valves to provide vacuum isolation. The front end is also expected to have a fast valve to provide a conductance limitation during a vacuum accident. Most beamlines will also have an x-ray exit window as part of the front end. These x-ray windows will provide a vacuum isolation but will transmit the x-ray beam. Certain beamlines, such as the soft x-ray beamlines, are expected to share the storage ring vacuum with the front end providing the interface. In such cases, the fast valve, along with the rest of the inline vacuum valves, provides the isolation needed in case of accidents.

Due to the large power loads, all components in the front end that intercept the beam will have water cooling. These components are typically the fixed mask, photon shutter, and exit windows. The water flow will be monitored by flow meters and the signals will be fed to the EPS. All vacuum valves will be pneumatically operated. All vacuum valves will be operated by the EPS and have their positions monitored (see Sections 7.3.6.4 and 7.4.3.4).

Most beamlines are expected to have some beam conditioning optics upstream of their monochromator. The beam conditioning optics will see the large power of the beam and as such will be interlocked by the EPS. Beamlines are also expected to have vacuum valves, which will also be controlled by the EPS.

It is expected that the beamline portion of the EPS system will be customized to suit the condition of the specific beamlines.

9.6.2 Design Specification

The design of the EPS is expected to be robust. The system will be based on programmable logic controllers. The hardware used will be the same as used in the beamline Personnel Protection System (Section 9.7) and the Accelerator Personnel Protection System (Section 9.8). PLCs provide excellent customization capability and also extensive diagnostics.

The sole function of the EPS is to provide protection from damage of equipment due to synchrotron radiation. As such, the EPS will consist of only one PLC per beamline. Each beamline will have its own EPS system. The EPS system will consist of three parts – front-end EPS, beamline-specific EPS, and command/ control of PPS components such as shutters and station doors. The front-end portion of the EPS is expected to be similar on most beamlines, while the beamline portion of the EPS will be customized to each beamline. Similarly, for the command/control of PPS components, the front-end shutters will be identical in all beamlines; however, additional shutters on the beamline will be beamline specific.

All front-end components that intercept the synchrotron beam will have water cooling of the components. The water flow of the components will be monitored by the EPS via flow meters. The EPS will be in alarm state if the flow drops below a specified setpoint. Depending on the location of the component it monitors, it will command the photon shutter to close and for cases where the flow is upstream of the photon shutter it will request the stored beam to be dumped.

All vacuum valves in the front end will also be controlled by the EPS (see Sections 7.3.6.4 and 7.4.3.4). Setpoints from vacuum controllers will be provided to the EPS, which will be used to determine when it is permissible to allow opening of the valves. The EPS will determine when it is necessary to close a valve, and will do so if it senses a vacuum alarm based on the vacuum setpoint to the system.

For specific beamlines, the EPS will be customized based on the user requirements for that beamline. Besides monitoring the water flow and controlling the vacuum valves, the EPS system may be used on beamlines to monitor other variables such as temperature, position, and so forth.

The EPS system will be used to control the actuation of the shutters. The EPS will monitor the status of the PPS for each shutter and, when a permit is available, it will accept requests to open the shutters. The EPS system will be responsible for sequencing the shutters in cases that involve a combination of photon shutters and safety shutters. All station doors that are automated will also be operated by the EPS.

9.6.3 Interface

The EPS system will have human Interfaces (HMI) located at the main location of the hardware, which is expected to be located directly above the front end on top of the storage ring tunnel. In addition, there will be a minimum of one HMI per beamline at the beamline stations.

The EPS provides the command and control functionality for the beamline PPS. It receives the status information of the PPS and, based on that, can operate the shutters. The PPS, in addition, can request the shutter to close and the EPS system will then command the shutter to close. In the event the shutter does not close within a specified time, as determined by the PPS, the PPS will initiate an emergency shutdown (ESD) situation.

The EPS also interfaces with the Accelerator Equipment Protection System. When the EPS detects a fault condition it signals the Machine Protection System to remove the stored beam. Example fault conditions include front-end water flow issues and vacuum issues. To protect the front-end components, the EPS will request that the MPS drop the beam. In some rare instances, problems in the beamline water cooling of components or beamline vacuum issues could also make the EPS request that the MPS dump the stored beam. The EPS provides only equipment protection and as such it does not interface to the APPS.

The EPS system will have an EPICS interface to the control system. The EPICS interface will provide both the main control room and the beamlines a complete overview of the status of each beamline. The data from the EPICS interface will also be logged and archived by the central computing systems.

The EPICS interface to the EPS will be both read and write. The write functionality will be controlled by the EPICS Channel Access Security. This is essential to isolate the possibility of accidental control of the wrong beamline EPS via the control system.

9.7 Personnel Protection System

NSLS-II will produce intense light from IR, UV, and hard x-rays. Beamlines are designed to use either the bending magnet radiation or the radiation from insertion devices located in the straight sections of the storage ring. Beamlines may have more than one station along the beamline for every port. These stations are expected to work in parallel or sequentially.

The Personnel Protection System is an engineered system that provides a means to ensure that personnel are not exposed to the radiation in the beamline. At NSLS-II, the role of the PPS is specifically to protect personnel from prompt radiation that is present only when there are stored electrons in the storage ring. The PPS is an engineered interlock system and is expected to monitor the various devices installed in the beamline for personnel safety and to provide emergency shutdown in case of breach of the interlock.

The PPS system, along with the required shielding in the beamlines, is expected to provide personnel safety during routine operation of the facility.

9.7.1 Functionality

Beamlines will consist of stations where synchrotron radiation is expected to be admitted. The beamline stations are expected to be made of lead-lined walls and roof, as appropriate for the particular radiation characteristics. These stations will house beamline optical components or beamline experimental equipment. The stations are expected to be large enough for personnel to work with the equipment inside.

The beamlines will have one or more shutters based on the particular layout, which is expected to vary from beamline to beamline. However, the functionality of the shutters, from the Personnel Protection System perspective, is expected to be the same and they will be monitored by the PPS. All x-ray beamlines will have shutters in the front-end area inside the storage ring shield wall (see Section 7.4). The bremsstrahlung radiation emitted by the synchrotron can only be stopped by heavy metal elements such as tungsten or lead. The heavy metal device that stops the bremsstrahlung radiation is referred to as the safety shutter. For the sake of safety, the shutter is expected to be redundant. The synchrotron beam, consisting of very high total power and power density, will be stopped by a device that is water cooled, made of copper or alloys of copper, and referred to as the photon shutter. These three devices, the two safety shutters and the photon shutter, will form a shutter cluster and their positions are monitored by the PPS.

Along the beamline are beamline optical elements that will condition the beam, including, for example, monochromators and mirrors. These devices change the characteristics of the synchrotron radiation. The radiation passing through the monochromator will, in most cases, be displaced in either the vertical plane or the horizontal plane from the incident radiation and only a small fraction of the incident radiation with a band pass (of about 0.1% or less) will be passed, with little or no power. In such cases the shutters, located downstream of the monochromator, will be called monochromatic shutters. They will be made of heavy metal and will be much shorter than the safety shutters. Once again, these monochromatic shutters are expected to be redundant for safety and will be monitored by the PPS.

A major role for the PPS will be to provide a means of ensuring that no personnel are inside beamline stations when the station is opened to synchrotron radiation. Prior to admitting the synchrotron radiation inside these stations, a search of the area has to be performed by a human. It is expected that the station search will be performed by one person only. There will be PPS devices called “search boxes” inside the station which must be visited as part of the search. Search boxes are strategically placed to ensure that during the search all parts of the station are either visible or visited by the search personnel and no person is left behind inside the station. The search is completed when the station door is closed. The PPS will then lock the door.

Once the search process is started the PPS will start a beacon and audio signal inside the station, warning all personnel to exit. This signal is expected to last for some time, on the order about 20 to 30 seconds after the station door is closed. The function of the beacon and audio signal is to warn any personnel overlooked by the search person of impending danger. There will be very distinct emergency shutdown buttons placed inside the station which, when pressed, will instantly remove the presence of the prompt synchrotron radiation hazard. In addition, there will be also emergency egress buttons inside the station to unlock and open the door.

9.7.2 Design Specifications

The PPS will be designed to be robust and provide the emergency shutdown functionality to provide personnel safety from prompt radiation. Like the EPS, the PPS is expected to be based on programmable logic controllers. PLCs have numerous advantages over the relay logic scheme of interlocks. They can be reprogrammed to reflect changes in configurations and also have numerous diagnostics. The use of PLCs in safety system is very common now.

All devices attached to the PPS are expected to be designed to be fail-safe—that is, in case of failure the device will fail in such a manner as to either remove the hazard or remove the permit to generate or maintain the hazard.

Every beamline PPS will be designed under the same guidelines. The PPS will consist of two PLCs, referred to as chains A and B. The two PLCs will provide redundancy and will independently monitor all the devices.

All shutters will have two switches, one for chain A and one for chain B. There will be switches to monitor the closed and open positions. Similarly, all station doors will be monitored with two switches, one each for chains A and B.

At beamlines, there will be circumstances when a device such as a mask or photon beam stop is provided to absorb the power of the beam, while the radiation safety is provided by lead shielding as collimators or radiation stops. In such cases, the integrity of the masks and beam stops cannot be compromised, as they, in turn, protect the lead shielding which provides the personnel safety. In these cases, the mask or beam stop will be monitored by the PPS to ensure that it is not compromised. In most cases, the water flow to these components will be monitored independently by chains A and B of the PPS.

All PPS equipment will be clearly identified, and secured in locked cabinets. Cabling for the PPS equipment to field devices will be on separate closed raceways, which will be used exclusively for the PPS. All power to the PPS will be provided by uninterruptible power supplies, which will be backed up by generators.

9.7.3 Interface

The PPS must interface with numerous systems. The primary functionality of the PPS is to monitor and provide emergency shutdown.

To provide emergency shutdown, the PPS interfaces to the Accelerator Personnel Protection System. The PPS will remove a permit to the APPS to operate the storage ring. In the event of the removal of the permit by the PPS, it is the responsibility of the APPS to remove the hazard by dropping the dipole power supply and the RF to the storage ring systems.

The APPS will monitor the positions of the front-end shutters located inside the storage ring shield wall. The APPS will fan-out the status of the shutters to the PPS. There will be a provision in the APPS to remove the PPS interactions for a specific beamline. This is expected to be in the form of a Kirk Key in an interface box between the PPS and APPS for each beamline. The APPS will monitor the closed positions of the front end shutters when the PPS is not available and will remove the storage ring permit if it experiences any “not closed” activity. When the PPS is available, the APPS will ignore the status of the shutters. This scheme will allow installation, maintenance, and validation of the PPS to take place while the machine is in operation.

All PPS functions will be monitored and data archived using the control system at NSLS-II. It is expected that EPICS will interface to the PPS PLCs to monitor their functionality. The EPICS interface will be read-only; there will be no writing to PLCs from the EPICS interface. Changes to the PLC operating codes will be possible from the field devices or when the PLC software is downloaded to the PLCs during routine validation of the system.

All command and control functionality for the PPS will reside with the EPS for the beamlines and front ends. The EPS will interface to the PPS and will receive signals from the PPS prior to operation of the shutter. In the event the EPS malfunctions, the ESD procedure of the PPS will activate and will remove the permit for the machine to operate. The PPS will only provide the ESD functionality and hence it expected to be simple and easy to maintain and validate.

9.8 Accelerator Personnel Protection System

As it relates to personnel protection, the NSLS-II facility consists of an electron gun and linac enclosed in a shielded area, and a main storage ring/booster enclosed in a heavily shielded tunnel. There are also numerous beamline experimental stations located on the perimeter of the accelerator tunnel. Protection from beamline radiation will be provided by the Personnel Protection System (discussed in the previous section), from linac radiation by the Linac Personnel Protection System (discussed in this section), and from radiation from the main ring/booster by the Accelerator Personnel Protection System (also discussed in this section).

9.8.1 Linac/Gun Personnel Protection System

The Gun/Linac area will contain linac accelerating sections where electrons emitted from the gun will be accelerated to an energy level for injection into the booster. The radiation hazards present during linac operation are two-fold, resulting from: 1) a high level of RF present in the linac sections that can accelerate free electrons and produce ionizing radiation fields, and 2) the acceleration of electrons to the full linac energy. RF power is supplied through klystron amplifiers powered by pulse modulators. Turning off the RF power will stop the production of radiation.

The Linac Personnel Protection System is specifically designed to protect personnel from radiation which is present only during linac operations. The LPPS is an engineered interlock system and is expected to monitor the various devices installed in the linac for personnel safety and provide emergency shutdown in case of breach of the interlock.

9.8.1.1 LPPS Functionality

A major role for the LPPS is to provide a means of ensuring that no personnel are inside the linac when the gun is on or the klystrons are pulsing. Prior to Linac operation, a search of the area has to be performed by a human. It is expected that the linac search will be performed by one person only. There will be LPPS devices called “search boxes” inside the linac, which must be visited as part of the search. The search boxes are strategically placed to ensure that during the search all parts of the linac are either visible or visited by the search personnel and no person is left behind inside the linac area. The search is completed with the closing of the linac door. The person searching will lock the door when the search is completed and use a Kirk Key system to complete the search process.

Once the search process is completed, the LPPS system will start a beacon and audio signal inside the linac, warning all personnel to exit. This signal is expected to last on the order of about 60 to 120 seconds after the linac door is closed. The function of the beacon and audio signal is to alert any personnel who have been overlooked by the search person and trapped inside.

Emergency shutdown buttons which are very distinct will be placed inside the linac; when pressed, a shutdown button will instantly remove the radiation hazard.

9.8.1.2 LPPS Design Specifications

The LPPS will be designed to be robust and provide the emergency shutdown functionality for providing radiation safety to personnel in the linac area. The LPPS is expected to be based on programmable logic controllers. PLCs have numerous advantages over the relay logic scheme of interlocks. A PLC can be reprogrammed to reflect changes in configurations and also has numerous diagnostics. The use of PLCs in safety systems is very common and is an accepted practice at accelerator facilities across the United States.

All devices attached to the LPPS are expected to be designed to be fail-safe—in case of failure the device will fail in such a manner to either remove the hazard or remove the permit to generate/maintain the hazard.

The LPPS system will consist of two PLCs, referred to as chains A and B. The two PLCs will provide redundancy and independently monitor all the devices. To immediately stop the production of radiation, power to the modulator power supplies will be removed redundantly. This will be accomplished through the use of AC contactors, one for chain A and one for chain B.

Two critical devices will prevent radiation from entering the main ring from the linac: 1) the linac-to-main-ring stop, and 2) the bending magnet located upstream. The linac-to-main-ring stop will have two switches to monitor the closed and open positions, one switch each for chains A and B. The bending magnet upstream of the stop will be redundantly monitored for current and voltage by both chains. When the magnet is not powered it will prevent electrons from entering the accelerator tunnel area. All linac doors also will be monitored with two switches, one tied into each chain.

All LPPS equipment will be clearly identified and secured in locked cabinets. Cabling for the LPPS equipment to field devices will be separated in raceways. All power to the LPPS will be provided from an uninterruptible power source, backed by generators.

9.8.1.3 LPPS Interface

All LPPS functions will be monitored and data will be archived using the NSLS-II control system. It is expected that EPICS will interface to the LPPS PLCs to monitor their functionality. The EPICS interface will be only read-only; there will be no writing to the PLCs from the EPICS interface. Changes to the PLC operating codes will only be possible locally.

9.8.2 Storage Ring/Booster Personnel Protection System (APPS)

The storage ring and booster will coexist inside the same tunnel. The Accelerator Personnel Protection System interlock will be required to serve both the storage ring and booster. Radiation hazards during normal operations and conditioning are produced from multiple sources under different operational conditions. Operation of the RF accelerating cavities, both booster and main ring, can produce high radiation fields from secondary emissions that are accelerated by high RF fields. This radiation can be produced without electrons injected or stored in either ring.

The electron beam injected from the linac is another hazard, and, finally, stored beam in either the booster or main storage ring will produce synchrotron and bremsstrahlung radiation. The APPS must protect personnel from all conditions.

9.8.2.1 APPS Functionality

The APPS protects personnel from radiation hazards by 1) ensuring that no one is left inside the ring enclosure before operations that will produce radiation and 2) by providing a means of emergency shutdown of components, enabling personnel to stop the production of radiation in an emergency.

The ring enclosure is physically very large and will be divided into six searchable sections. Each section will be separated by a physical barrier in the form of a gate. Before operations begin, each section will be physically searched by a human. Once the search process is completed, the APPS system will start a beacon and audio signal inside the section being secured, as a warning to any overlooked personnel to exit. This signal is expected to last on the order of 60 to 240 seconds after the section gate is closed.

Emergency shutdown buttons, which have a very distinct appearance, will be placed inside the tunnel. When pressed, a shutdown button will instantly remove the radiation hazard.

The gates, along with Kirk keys, will be part of a system to allow controlled access to parts of the ring under defined conditions while other sections remain secured. With the APPS, beam will be dumped to allow authorized personnel controlled access to the ring sections while ensuring that no electron beam can be

injected. Access will be monitored via a remote TV camera hookup to the control room. Each person entering the ring must remove a Kirk key; this inhibits the radiation source. A physical search of the section will be required before operations and radiation production can be resumed.

The first application of this concept defines an area around the RF accelerating cavities. The booster and storage ring cavities will need to be powered with RF for conditioning but without injected electron beam. The APPS will ensure no personnel are in the vicinity of the RF cavities during conditioning, while inhibiting electron beam from being injected into the ring. If the area is breached, the RF power source will be immediately shut off, redundantly.

During injection, while the linac-to-main-ring stop is open, if the storage ring area is breached the APPS interlock must dump stored beam and reach back to the LPPS to shut down the linac modulators.

The APPS may also be required to monitor conditions required for top-off operation of the injector. These conditions have not been determined but could include requiring a minimum stored current before top-off mode is enabled and requiring the dipole current to be at the proper energy level.

The APPS will also monitor the status of the front-end ports and will dump the beam if a port is open and the PPS detects a breach of an experimental station.

All APPS conditions and access modes are displayed and controlled from a dedicated rack in the control room.

9.8.2.2 APPS Design Specifications

The APPS will be designed to be robust and provide the emergency shutdown functionality to ensure personnel safety for the storage ring/booster area. The APPS is expected to be based on programmable logic controllers. PLCs have numerous advantages over the relay logic scheme of interlocks. A PLC can be reprogrammed to reflect changes in configurations and also has numerous diagnostics. The use of PLCs in safety systems is very common and is an accepted practice at accelerator facilities across the United States.

All devices attached to the APPS are expected to be designed to be fail-safe—in case of failure the device will fail in such a manner to either remove the hazard or remove the permit to generate/maintain the hazard.

The APPS system will consist of two PLCs, referred to as chains A and B. The two PLCs will provide redundancy and will independently monitor all the devices. To immediately stop the production of radiation, power to the RF plate power supplies and low level RF will be removed redundantly both for storage ring RF and booster RF. This will be accomplished through the use of AC contactors, one for chain A and an RF switch for chain B. The redundant means for dumping beam will also shut off the main dipole power supply through the AC contactor with both chains A and B.

The storage ring tunnel circumference is large; to avoid ground loops and EMC effects on APPS signals, fiber optic transmission of bus signals (one for each chain) will connect field I/O blocks around the ring to the main PLCs located in the control room. The control room PLCs will also connect to the RF and dipole power supply via a fiber optic I/O bus to avoid interference and corruption of signals.

The system will be designed for testability and will have built-in test features. The concept of diversity will be applied where possible.

The APPS main ring doors, emergency stops, and section gates have two switches, one each for chains A and B. All APPS equipment will be clearly identified and secured in locked cabinets. Cabling for the APPS equipment to field devices will be separated in raceways. All power to the APPS will be provided from an uninterruptible power source, backed by generators.

9.8.2.3 APPS Interface

The PLC program will incorporate a circular buffer of each scan that is triggered by an interlock breach. The buffer will be retrieved via EPICS to troubleshoot problems. All APPS functions will be monitored and data will be archived using the NSLS-II control system. It is expected that EPICS will interface to the APPS PLCs to monitor their functionality. EPICS will read data from a dedicated group of registers that reflect conditions and I/O points in the PLCs. The EPICS interface will be separate from the I/O bus. The EPICS interface will be only read-only; there will be no writing to the PLC from the EPICS interface. Changes to the PLC operating codes will only be possible locally.

9.9 Beamline Controls and Data Acquisition

9.9.1 Introduction

The NSLS-II accelerator control system will be in an isolated network by itself and each beamline is expected to have its own network to connect its computers and its hardware. Connections between these systems will be designed to provide the integrated flow of information between the accelerator and end stations that is needed to meet the requirements for beam monitoring and stability.

All insertion device beamlines require control of the insertion devices [9.13] which are located in the controls network. In addition beam position information, as well as numerous other signals, is needed from the accelerator control system. Similarly, beamline information, along with intensity and beam position from the beamlines, will be needed in the accelerator control system to provide continuous control of the beam.

The infrastructure needed for the exchange of information between the beamlines and the accelerator will be built into the facility. It is anticipated that single-mode fiber will be employed to connect the beamline EPICS hardware and accelerator EPICS hardware. Every beamline will be provided with a dedicated single-mode fiber bundle from the beamline to the accelerator control system racks located on top of the storage ring. In addition, there will dedicated single-mode fibers to the main control room, where some of the timing hardware is expected to be located. These single-mode fibers will be used to provide high-precision timing signals to synchronize the beamline experiments with the arrival of the x-ray beam.

Data exchange between the beamline and the accelerator EPICS systems, which do not require a very fast data rate, will be provided through an EPICS channel access process variable gateway system. This system will reside in the accelerator control system and will have an additional network connection to each of the beamline networks. This way the control, as well as data readbacks, can be accomplished with a high level of security without jeopardizing the integrity of the accelerator or beamline control systems. Such schemes have been used successfully at other facilities, such as APS and BESSY.

The development of the EPICS software for the beamline will be conducted in parallel with the accelerator to ensure that they are consistent and the exchanges of data between the two are seamless.

The beamlines will have their own computers and servers for data acquisition and control. There will be large storage capacity at the beamlines, and a central storage and backup service, with large disk farms, will be available as well. There will be 10 gigabit redundant network structure built into the facility. Each beamline network will be redundantly connected to a central computing facility, which will have a firewall to provide secure access to the outside world.

The offices in the LOBs will also have computing capability. Each LOB will be on a different network and will be serviced by a central computing facility. The LOBs will also be serviced by 10 gigabit network infrastructures. The centralization of data collected from the beamline will allow a user to retrieve data from multiple beamlines for analysis. Data reduction and analysis software will be developed by, and available from, the central computing services.

The variety of information exchange between the various control systems related to the needs of the experimental facilities is schematically indicated in Figure 9.9.1. Patterned after the system at APS [9.14], this system will be based on EPICS process variables, as discussed above.

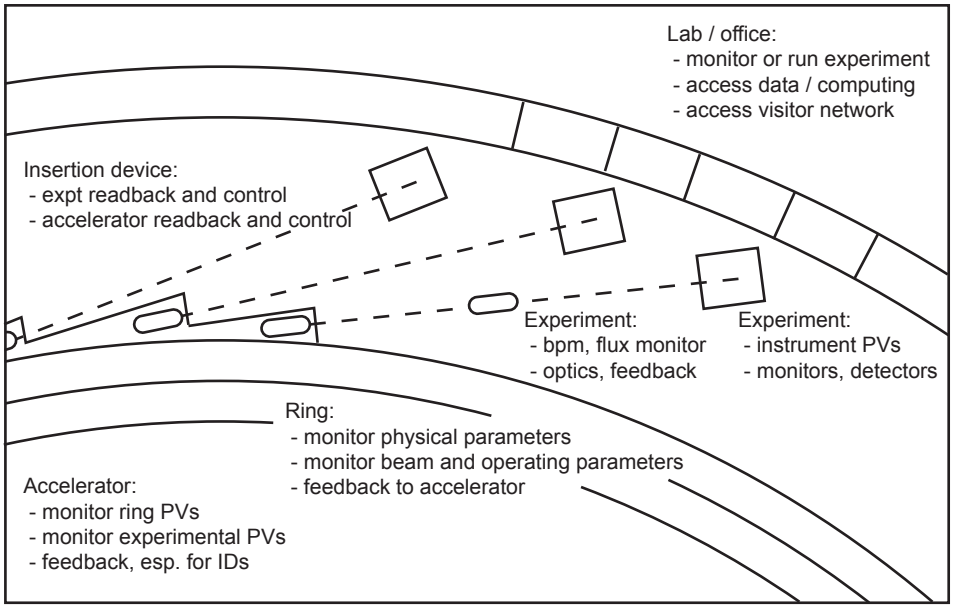

Figure 9.9.1 Activities requiring information distribution in experiment hall.

9.9.2 Design Concepts

From the point of view of the beamline and end station, the requirement is that every beamline have at least one dedicated EPICS IOC controlling its insertion devices and intercepting other information from the facility. For many of the hard and soft x-ray facility beamlines, EPICS will be used as a standard to control optics and beamline motors also. Specialized equipment may have different control systems, which may exist as additional EPICS clients or may in some cases be independent. It will be beneficial for the EPICS IOCs to be of a standardized hardware type. VME is a current favorite, due to its reliability, but the availability of drivers in the future and the improvements in PC-based hardware may cause the latter to be more favorable some years from now. The standardization of beamline server hardware will be assessed during the years preceding beamline commissioning and a standard will be chosen. The same requirements we have today must be satisfied. Hardware must be robust and reliable. A large basis set of scalers, motor indexers, analog and digital I/O, multi-channel analyzers, and so on must be in use. Pre-existing EPICS support for the hardware will be a third criterion.

The network as seen from the beamline is illustrated in Figure 9.9.2. As an example, a Linux PC running Medm GUIs may serve as the operator interface, while a VME CPU serves as the IOC for the beamline control system. Beam transport components with PVs that need to be available to the facility are connected to this network. (The insertion devices, on the other side of the shield wall, are networked separately.) A server acting as router, firewall, and PV gateway connects this sector or beamline network to the experimental network, to other beamlines, and to the other facility networks. The PV gateway controls all permissions necessary to establish who has control permission vs. read-only permission of the PVs.

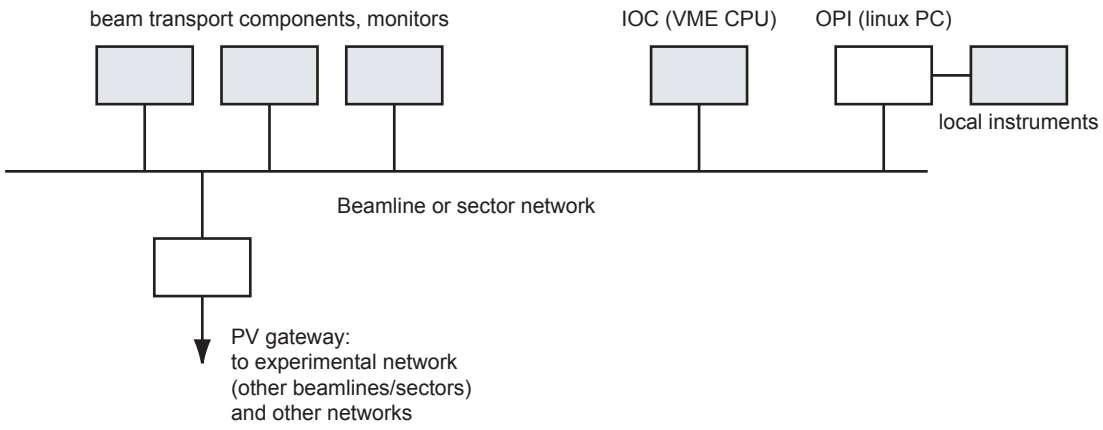

Figure 9.9.2 Sector networks make important process variables (PVs) available to the entire facility through a PV gateway. IOC=input/output controller, OPI=operator interface (as Medm GUI).

We anticipate that the system will be designed so by default read-access is available for everything, everywhere. This way, there will be no need to make assumptions during the initial configuration as to which machines' PVs and monitor values need to be communicated between the accelerator and the experiment hall. Finally, local instrumentation can be assembled on private networks as desired by the users of the individual beamlines. Specialized detectors and other instrumentation controllers may be interfaced to the beamline controls as applicable, particularly as EPICS clients.

9.9.2.1 Considerations for Accelerator–End Station Information Exchange

The accelerator monitoring complex will have far too much information in it to be useful to users as raw PVs. The accelerator group will design simple ways of mapping and colorizing the status of the accelerator with respect to beam excursions, pressure, temperature, and other sensor readouts, and make this digested information available as a monitoring system that the experimenters will be able to use. This will allow the beamline staff and users to gauge where problems may be coming from. It will also provide a unified way for the experimental division to log local beam stability in connection with pertinent information about the ring stability. This information will be provided as part of the general control system information.

The following elements will be expected to provide useful data from the beamlines back to the operations staff:

- position monitors (beams and pipes)
- ambient conditions (pressure, temperature, cooling water flow)
- status of insertion device and recent history (i.e., feedbacks triggered)
- beam figure of merit (quality after optics as defined by the end stations' needs: divergence, angular motions, spatial motions, energy drift).

It will be beneficial to create more generalized "status" readouts for beamlines as well as for the accelerator.

9.9.2.2 Design of the Main EPICS Node at Each Beamline

Resident on the experimental network and associated with each beamline, there will be a CPU running an EPICS IOC and a Linux PC configured with control GUIs and administrative scripts for that beamline. These computers will be quite similar across the NSLS-II complex, since many upstream beam components and interfaces to the gateways and other networks will be common. These computers, and the configuration to interface with facility networks and information buses, will be centrally administered. Giving each beamline a similar, centrally managed system benefits operations by allowing a standard set of tools and debugging

know-how to be applied everywhere. One important concern is cybersecurity requirements. Even if the experiment network is within a firewall, the laboratory will require certain security scans. Uniformity of the beamline machines on this network will make it easier for staff to provide patches and fixes consistent with both security and smooth operations.

EPICS tools alone are sometimes insufficient for scientific data acquisition. Synchrotron beamlines have diverse needs, such as dedicated detector drivers, reciprocal space calculation, spectroscopic tools, and visualization tools for imaging. The end station equipment will be so varied that a top-down attempt at standardization would be very harmful. Thus, each beamline is expected to instrument itself in an independent way. Still, NSLS-II users and staff will benefit from having as much common support as is reasonable to interface different experimental systems and connect them to the EPICS platforms. Many different data acquisition platforms can be clients of the EPICS system. For example, LabView and Spec are widely used control and data analysis systems.

9.9.3 Support for Large Data Sets and Data Analysis Software

All synchrotron experiments have evolved toward faster data acquisition and larger data files, as shown in Table 9.9.1. Drivers for this trend include position- and energy-sensitive detectors and area detectors; beam focusing that enables mapping and energy modes; and high brightness leading to faster sample throughput.

Furthermore, the nm-scale beams and fast data acquisition possible with the very high brightness of NSLS-II have the potential to turn many more experiments into imaging experiments. Microbeam imaging and high resolution macromolecular crystallography already accumulate >250 Gb data sets for typical runs. When nanobeams are employed in imaging experiments, characterization of micron-scale areas will result in 500 GB to 5 TB datasets. For example, with five imaging or PX style beamlines accumulating 1 TB/week and 16 other beamlines collecting 250 GB/week, a total of 9 TB/week would be generated. In 20 weeks of such operations, 180 TB of data would be collected. Significant facility infrastructure, including fast networks and central scientific computing support, must be designed to collect and archive these large data streams. Making sense of such large amounts of data will require sophisticated data analysis, mining, and visualization software even for the expert user. In order to continue the trend of recent years of synchrotron science extending into new fields and new user communities, it will be necessary for this to be readily accessible to the non-expert user as well.

Table 9.9.1 Typical data rates and total data collected in representative experiments

Representative Experiments	MB/sec Live	MB/day Run	Total Run
X-ray scattering, single channel detector	0.0002 to 0.002	2.5	15 MB
SAXS or crystallography, area detector	0.3	400 to 1,200	1.2 to 2.4 GB
EXAFS	0.00005	3	10 MB
Quick-EXAFS	0.1	3,000	3 GB
High pressure, energy dispersive	0.03	1,000	2 GB
High pressure, angle dispersive	0.03	1,000	2 GB
PX, bend magnet	1	52,000	260 GB
PX, insertion device	10	260,000	260 GB
IR spectroscopy, micro-spectroscopy	0.0000.5 to 0.0005	12 to 60	12 to 60 MB
Microbeam XRD, single channel detector	0.001	40	160 MB
Microbeam XRD, area detector	0.3	5,000 to 30,000	12 to 130 GB
Scanning transmission x-ray micro-spectroscopy		2 to 30	50 MB
Fast 2D detector	> 30		> 250 GB
10 nm beams for scanning modes	0.3	5×10^6 to 5×10^{10}	500 GB to 5 TB

9.9.3.1 Data Server Facility

To manage the volume and diversity of user data at NSLS-II, a dedicated data server facility will be established. The data server will have 200 TB of redundant storage, expandable as future requirements increase, and rolling over on a week-to-month timeframe as users collect their data. The physical location and architecture of the disk system can be designed in a number of ways, either distributed among beamlines or in a central farm, but a key feature must be that the data is dropped transparently from the experiment and then can be retrieved later under the direction of a dedicated data management staff. Significantly, many users will be active at more than one beamline. Data dropped to the server can be deposited with a time and source (beamline) stamp so that successive drops are never overwritten. Users will have an authentication allowing them to access the data site and retrieve data they may have generated from any of the NSLS-II beamlines. A selection of protocols and tools might be developed to retrieve data: web-based tools, secure shell gateways, dedicated client/server tools, etc. This facility is advantageous for the beamline operations staff, who will not have to manage disk farms and user authentication from offsite. It is advantageous for users, who will have a well-supported, global interface connecting them to their data. And the data will be protected from being lost or overwritten, since a uniform database management scheme will protect it, distribute it, and log all transactions.

9.9.3.2 Data Analysis Concepts

The experimental communities naturally need a variety of data analysis tools, which each community is accustomed to generating on its own. This often leads to isolated analysis efforts that are not well coordinated across the community. Without good analysis and visualization software, only the most expert users can benefit from the beamlines. Because NSLS-II has the capability to specialize in nanobeam imaging, it should be expected that very large numbers of non-expert users will be interested in characterizing their materials in straightforward ways. For this, dedicated and well supported software is essential.

NSLS-II will support software experts who are responsible for developing creative analysis and visualization solutions, as well as performing extensive quality control checks to ensure that the results are reliable and can be trusted. By working closely with beamline staff, this team of professional programmers will greatly enhance the ability of the beamline to generate real-time information to assist users in getting the most benefit from their beamtime. In the context of microbeam diffraction, for example, a coarse scan might consist of a thousand diffraction patterns. Rather than “solving” them, the real-time goal might be to determine a figure of merit from them (such as crystallinity or orientation of grains) and create a false-color image of the scanned sample area. By constructing a database that combines the diffraction data with the instrument calibration and operating parameters, it would become possible to query the data across any value in real space, reciprocal space, or environmental variables—in other words, variables that relate to the sample and not to the detection format. This kind of online analysis needs to be programmed by dedicated professionals who can continually add capabilities for new experiments while remaining compatible with the instrumentation and local resources such as the central data server.

References

[9.1] M.T. Heron, and B.G. Martlew, “A Review of Options for the DIAMOND Control System,” Proc. PAC99.
[9.2] EPICS, http://www.aps.anl.gov/EPICS.
[9.3] TANGO, http://www.esrf.fr/computing/cs/tango/tango.html
[9.4] V System, http://www.vista-control.com/
[9.5] CVS, www.cvshome.org
[9.6] http://www.windriver.com/
[9.7] VisualDCT, http://kgb.ijs.si/VisualDCT
[9.8] T. Korhonen, and M. Heiniger, “Timing System of the Swiss Light Source,” Proc. ICALEPCS2001.

[9.9] F. Lenkszus, and R. Laird, "The APS Event System," Proc. ICALEPCS95.
[9.10] J.A. Carwardine, and F.R. Lenkszus, "Real-Time Orbit Feedback at the APS," Proc. BIW98.
[9.11] C. Steier, A. Biocca, E. Domning, S. Jacobson, G. Portmann, and Y. Wu, "Design of a Fast Global Orbit Feedback System for the Advanced Light Source," Proc. PAC 2001.
[9.12] M. Böge, M. Dehler, T. Schilcher, V. Schlott, and R. Ursic, "Global Orbit Feedback System for the SLS Storage Ring," Proc. ICALEPCS 99.
[9.13] M. Ramanathan, M. Smith, J. Grimmer, and M. Merritt, "Overview of insertion device controls at the Advanced Photon Source," *Rev. Sci. Instrum.,* **73** (2002) 1448.
[9.14] M. Ramanathan, M. Smith, N. Arnold, F. Lenkszus, R. Laird, K. Evans Jr., J. Anderson, and K. Sidorowicz, "An overview of the information distribution system at the Advanced Photon Source," *Rev. Sci. Instrum.,* **73** (2002) 1445.
[9.15] http://hpdrc.cs.fiu.edu/Sem-DDS/documentation.html

10 GLOBAL SUPPORT SYSTEMS

10.1 Survey and Alignment

10.1.1 Scope

This section outlines the survey and alignment requirements and the technology and tools for achieving the NSLS-II equipment positioning goals. The required alignment tolerances are defined primarily by the physics requirements of the accelerator. At this stage of conceptual design, these tolerances are not known with high precision; however, similar parameters are available for other light sources of equivalent dimension. Our conceptual design of the survey and alignment system is based on the assumption that the tolerance requirements for NSLS-II will be similar to those of APS, for example. An assessment will be performed, however, during the preliminary engineering design phase to identify any extraordinary position requirements of the accelerator systems, and the survey and alignment system will be modified as necessary to meet them. State-of-the art equipment and methods will be employed, but no new technology will need to be developed to meet the NSLS-II alignment requirements.

Survey and alignment provides the foundation for positioning the beam-guiding magnet structures in all 6 degrees of freedom within the required tolerances. Although the tools and instrumentation available for this task have changed over the years and faster and more accurate measurements are possible, only limited control of the environmental conditions is possible. This ultimately sets an upper limit for the achievable measurement and subsequent control network accuracy.

The scope of the survey and alignment work for NSLS-II includes the following:

- Provision of engineering staff to review the design of components having stringent alignment requirements. Engineering staff trained in state-of-the-art methods, software, and systems will be required to ensure that component designs are consistent with the survey and alignment systems that will be used to obtain the anticipated tight tolerances needed to achieve the desired emittance levels.
- Specification of alignment tolerances for each piece of equipment, and a determination of how to achieve them within the limitations of available equipment and hardware. Procedures, methods, and equipment will be specified.
- Procurement of alignment equipment, measurement equipment and instruments, targets, monuments, and hardware.
- Technical staff to achieve the precise alignment requirements during fabrication, assembly, and field installation. Technical staff trained in the use and calibration of state-of-the-art instruments and systems will be required.
- Provision of calibration equipment and facilities to maintain survey equipment within calibration tolerances.

10.1.2 Tolerances

The required positioning tolerances are an essential part of the survey and alignment design. Those tolerances dictate the instruments and methods necessary to obtain the positioning goals. Table 10.1.1 provides the required global tolerances, while Table 10.1.2 outlines the relative tolerances for the NSLS-II girder-to-girder positioning. These tolerances represent the most stringent requirements for the storage ring.

Table 10.1.1 NSLS-II Required Global Tolerances.

Global tolerances	± 3 mm
Horizontal positioning	± 3 mm
Vertical positioning	± 3 mm

Table 10.1.2 NSLS-II Girder-to-Girder Positioning Tolerances.

Relative tolerances	Girder to Girder
Horizontal positioning	± 0.15 mm
Vertical positioning	± 0.15 mm
Longitudinal	± 0.50 mm
Roll angle	± 0.5 mrad

10.1.3 Design Philosophy

10.1.3.1 Control Network Design

Depending on the size of the system to be constructed, a primary and secondary control network may be required to achieve these tolerances. NSLS-II covers an area of about one-eighth of a square kilometer with a radius of ~124 m and a circumference of ~780 m. The NSLS II construction methodology demands that separate tunnel segments be successively available and ready for installation purposes. This requires that each segment be fitted with an independent preliminary control network terminated by a primary monument at each end suitable for less demanding layout work such as the blue-line survey of the major beamline components, girder supports, and photon beamline layout in the front-end sections [10.1.1]. Only after all segments have been measured, processed by least squares, and analyzed will the final control network be ready for the positioning of the girders. Prior to construction, a calculation of the anticipated error propagation of the primary and secondary control network geometry will be needed.

10.1.3.1.1 Primary Control Network

The primary control network spans the entire accelerator facility and ties the accelerator enclosures into one reference system. It consists of a monument located at the center of the storage ring, a second similar one located at a convenient location in the infield close to the storage ring enclosure, and multiple monuments distributed throughout the storage ring—for instance, at the beginning and end of each separate tunnel segment. The two monuments located in the infield should be very stable. Therefore, they require a deep foundation and a secondary outer shell for temperature stability, as shown in Figure 10.1.1 [10.1.2]. These monuments can also be used by the construction companies for layout and construction surveys.

The central monument usually defines the origin of the local right-handed coordinate system, while the second infield monument provides the orientation of the control network. The storage ring monuments are accessible through penetrations in the roof wall shielding. One of these should be located near the linac so no additional penetrations for the linac are necessary. Depending on the instrumentation used, all of the primary control points should be inter-visible. The spacing between storage ring penetrations is normally guided by the law of error propagation and should not exceed approximately 250 m.

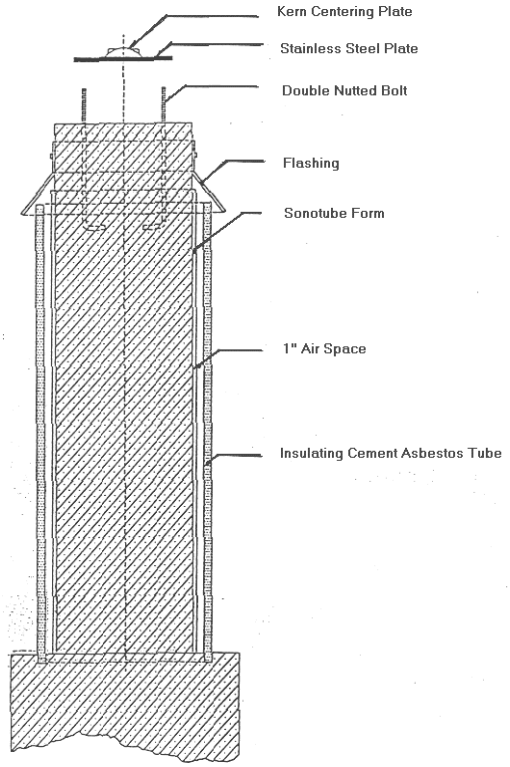

Figure 10.1.1 APS central monument.

The primary control network can be measured as a trilateration network only. Current instruments are able to resolve distances to ±(0.1 + 0.1*D*) [mm], where *D* is the length of the measured distance. This level of accuracy is not attainable with triangulation networks. By using a trilateration network, it should be possible to obtain a control network point accuracy of ±0.3 mm, similar to what has been achieved at APS [10.1.3] and as shown in Figure 10.1.2.

An alternative approach to determine the primary control network utilizes GPS observations for all primary control points. If public reference stations are not conveniently available, a local GPS reference station needs to be established at the storage ring center monument [10.1.4]. This base station supports differential GPS and would also be beneficial for the construction survey, as many survey companies have access to GPS and Real Time Kinematic (RTK) positioning technology. It is expected that utilizing DGPS, millimeter accuracies can be obtained. This approach needs to be further evaluated during the preliminary design phase to determine if it meets the requirements.

Both methods of measuring the primary network are highly dependent on the construction sequence and method, as lines of sight either between the monuments or the GPS satellites are required. This task has to be scheduled after the storage ring tunnel has been built but before the experimental hall enclosure is constructed.

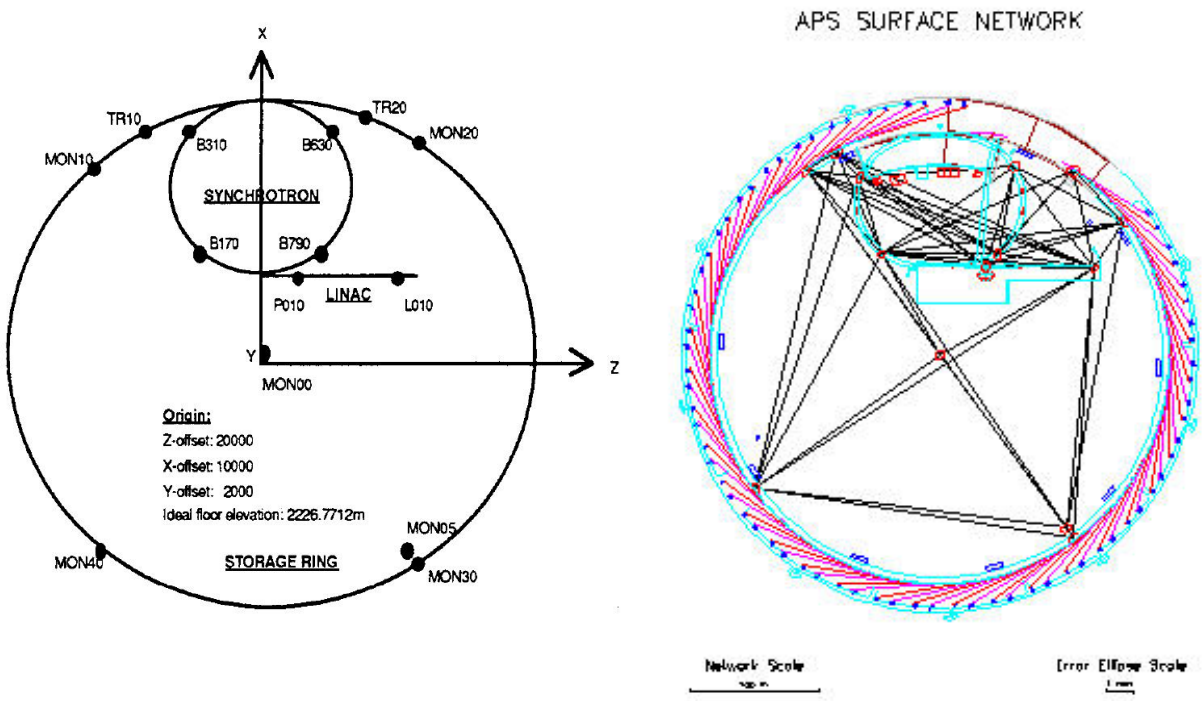

Figure 10.1.2 The APS coordinate system and primary control network.

10.1.3.1.2 Secondary Control Network

The design of the secondary control network is determined by the layout of the storage ring. If, as in the case of APS (see Figure 10.1.3), ratchet doors for each beamline are available, one can extend the secondary control network into the experiment hall, providing a more stable control network design and the means to perform alignment work on beamlines while the machine is operational. The present conceptual design of NSLS-II envisions the installation of similar ratchet doors. Therefore, the secondary control network will be extended to the storage ring enclosure.

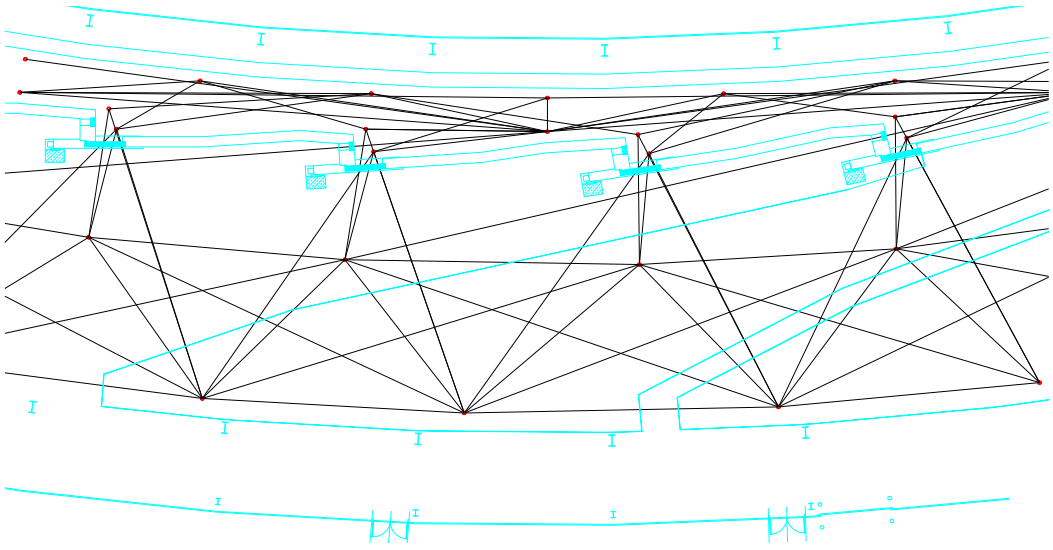

Figure 10.1.3 The APS secondary control network.

Extending the secondary network to the experiment hall floor will benefit the layout work for the individual beamlines while the accelerator is in the commissioning phase. Each BM and ID beamline should receive two control points strategically located at an offset from the ideal beamlines and visible from the storage ring through the ratchet wall openings. Prior to the installation of the ratchet wall collimators the tie between the beamline layout in the front end and the experiment hall has to be established using optical tooling instruments. The marking of the front ends needs to be done while no girders have been placed in the tunnel and is best performed while the quadrupole and girder support locations are being laid out. Otherwise, line-of-sight to these areas will be very restricted and the markings may no longer be possible. The layout of the front-end locations is very important, as it provides the only means to extend the alignment control through the beam ports to the experiment floor.

Laser tracker instruments will be used for measuring the secondary control network, followed by a least squares analysis of the data to produce the final control points prior to setting out the machine components.

Current laser tracker systems obtain point accuracy on the order of ±0.05 mm in a spherical volume with a radius of 10 m around the instrument measurement head. For measuring the secondary control network with laser trackers, the primary control points are included in the measurement process and are part of the data analysis. This constrains the error propagation of the secondary control network to the level achieved by the primary reference network. The primary and segments of the secondary networks must be established, measured, and analyzed before accelerator equipment can be installed. However, sufficient time has to elapse for the concrete to cure before the control network monuments can be considered stable. Installing the floor monuments of the storage ring will necessitate core drilling to recess the target fixtures. The wall-mounted targets will be attached to concrete anchors with threaded inserts.

The secondary storage ring tunnel network should consist of at least four survey monuments located in cross sections of the storage ring spaced 10 m apart, as shown in Figure 10.1.4. An *a priori* error analysis needs to be performed to estimate the optimum locations for these targets and the expected point accuracy. The envisioned tunnel network creates a compact box structure to obtain a stable network geometry. Control points on the infield side of the tunnel are usually always accessible. The control points opposite the aisle should be located such that they will be visible after the girders have been positioned. The floor monuments are measured using common geometric leveling procedures to an accuracy of ±0.1 mm or better. This information, in conjunction with the laser tracker measurements after proper analysis of the redundant data, provides the 3D control network that is used to place the accelerator components. An estimated accuracy of ±0.3 mm should be achievable for the secondary control network.

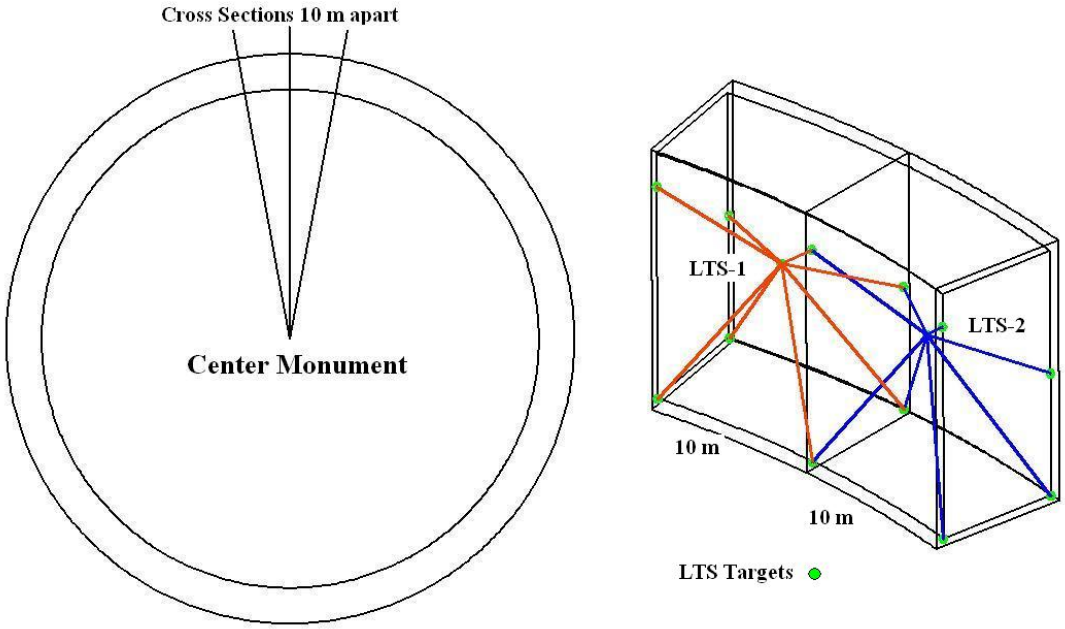

Figure 10.1.4 Sketch of a possible network design.

A variety of monuments for 1.5 inch Spherical Mounted Retro-reflectors are commercially available and can be mounted at the predetermined locations, as shown in Figure 10.1.5. This type of SMR and its accompanying receptors will be used for all survey and alignment work at NSLS-II, where possible.

Figure 10.1.5 Laser tracker 1.5 inch sphere mount.

For both the primary and secondary control network, error propagation calculations will be required before the realization of the reference network. This step provides information about the network density, optimal geometry, and minimum required measurement redundancy without diminishing the point accuracy of the control networks.

10.1.3.2 Elevation Control Network

Similar to the primary and secondary position control networks described in the previous section, we will establish primary and secondary elevation networks that are measured using common geometric level methods employing digital level instruments of proper accuracy.

Most survey instruments are referenced to local gravity. In particular, the leveling process measures elevation differences between two points with respect to the equipotential surface of the geoid. This leads to differences between a local planar system in which the accelerator is constructed and the curved geodetic reference system.

At APS, all accelerators are located in a plane tangential to a best-fitting osculating sphere at the latitude of the center monument. The difference between this sphere and the tangential plane is on the order of 2.3 mm at 175 m from the center monument, the location of the storage ring. GEONET, the software used by APS to reduce these measurements to the reference sphere, takes local deviations into account and adjusts accordingly. In the case of NSLS-II, this may not be an issue, as the booster and storage ring are located in the same enclosure. Both would have approximately the same radii and therefore the same correction factor.

In the NSLS-II storage ring tunnel, the storage ring, the booster ring, and the transport line components will be close to each other. Components will be placed and rough-aligned first, with the components that are farthest from the tunnel entrances placed first. Care must be taken to maintain line-of-sight. To accomplish this, 3D computer graphic modeling will be used. After the heavier components are placed and aligned roughly, fine alignment will proceed using laser tracker and optical level instruments. Some settling of equipment and facilities is anticipated, and it is expected that the alignment adjustment will require checking several times during set-up, commissioning, and initial operation. Therefore, alignment equipment and expertise will have to be maintained in a constant state of readiness.

In any case, for a project the size of NSLS-II with its required high positioning tolerances, measurements for determining elevations and positions will be two distinct and separate operations. Each step requires specialty equipment designed for that purpose. Even if the existing laser trackers provide 3D point information, it is necessary to supplement the vertical information with elevation measurements derived from optical level instruments for increased accuracy.

10.1.3.3 The Lattice

To obtain congruence between the survey network and the lattice layout provided by the machine physicists, the datum of both of these systems must be the same. The six parameters (x, y, z, yaw, pitch, and roll) provided by the lattice for each beam component must be transferred to the Survey group and will be stored in a database that is used for all calculations to set the girders and other accelerator components. The database also contains the fiducial information of each component that needs to be placed. GEONET, a software analysis program originally developed at SLAC for this purpose and developed further at ANL and SLAC, performs these calculations and will be used at NSLS-II.

10.1.3.4 Smoothing

The initial positioning using the reference coordinate system can only be as good as the achieved network accuracy. This accuracy represents an upper limit. However, due to inherent target and instrument errors as well as environmental effects, this limit is not achievable and the actual positioning tolerance in the global system will be less than the obtained control network accuracy. Therefore a smoothing step is required.

For this part of the process, the control network is abandoned and only the local relation between adjacent girders is measured and verified. Instruments with sufficient accuracy, such as laser trackers or special offset measurement devices, can be used for this step. In particular, a comparison between the as-built and the ideal location will provide information about the relative girder position. The girder and magnet fiducial markers will be used in this step. As shown in Table 10.1.2, the girder-to-girder tolerances are relaxed in comparison to the magnet-to-magnet requirements shown in Table 10.1.3. Nevertheless, during the fiducialization process great care has to be taken to obtain the best possible references.

Table 10.1.3 Magnet-to-Magnet Positioning Tolerances.

Relative Tolerances	Magnet-to-Magnet
Horizontal positioning	± 0.05 mm
Vertical positioning	± 0.05 mm
Roll angle	± 0.5 mrad

10.1.3.5 Fiducialization

During the fiducialization process, reference markers are determined with respect to the magnetic axis of the device. These markers are accessible after the magnet has been assembled on a girder and the vacuum chamber has been inserted. At that time, direct access to the magnetic axis is no longer possible and all positioning is performed with respect to these fiducials. Any positioning error during the fiducialization step can only be uncovered after the machine startup, with beam-based alignment methods. Unlike most of the other steps described here, this step does not provide measurement redundancy unless independent repeat measurements are performed.

For components requiring less accurate positioning, referencing to the mechanical axis may suffice. However, for NSLS-II, the magnet-to-magnet positioning tolerances, shown in Table 10.1.3, are exceedingly stringent; therefore, a combination of magnetic and dimensional measurements is required.

Usually, rotating coils or stretched wires are used to establish the beam axis. Once the optimum position of the device is found, the information is transferred from the beam axis to the outside reference markers. This is done for each of the magnets prior to the assembly on a girder. The fiducial information is used in the assembly process. The transfer of the position information from the magnetic axis to the reference point can be performed with a 25–50 μm accuracy, depending on the method used. However, in case of NSLS-II, the accumulation of errors in determining the reference targets, the mechanical assembly of the magnets on the girder, the alignment of the magnets on the girder, and so forth may exceed the required tolerance limits. It is therefore envisioned that all multipoles will be assembled and aligned on a girder using a stretched wire technique [10.1.5]. In this way, the intermediate steps to obtain fiducial information for each magnet separately are circumvented. After this step, the girder will be considered the smallest unit that needs to be placed in the storage ring tunnel.

The girders need to be fitted with permanently mounted SMR receptacles above each of the support feet on both the inboard and outboard side. This is required because the girder will have more than three support feet for reasons of stability and vibration damping. It is envisioned that laser trackers will be used to perform the coordinate transfer from the wire, via a touch-free probe, to the girder fiducials that are used to position the girder and to check for local deformations while aligning the girder in the storage ring tunnel. It is important that there be a defined stay-clear area around each of the girder fiducials. In particular, above each fiducial no obstructions are allowed; doing otherwise would prohibit the use of level rods on these markers.

R&D is planned to carefully evaluate this approach for the magnet alignment and fiducialization prior to construction of NSLS-II.

10.1.4 Implementation

Close coordination between the construction efforts and implementation of the control network must be maintained while NSLS-II is being built. It is also imperative that the survey and alignment team be involved early in the design of the girder and magnet supports and moving systems, because the positioning resolution and performance are directly linked to these devices.

10.1.5 Training

At minimum, operators of survey equipment should have several years of experience in properly handling and operating instruments of that type. Instrument operators will have to work closely with the technicians who will make the required adjustments. In particular, when using laser trackers to provide real-time, online alignment capabilities, Survey and Alignment technicians will apply the required adjustments; these two steps go hand-in-hand. Most laser tracker manufacturers provide onsite training for operating their systems. For the alignment of the front ends and beamlines, optical tooling is required because space is limited. Training in the use of optical tooling instruments is commercially available. All personnel involved with the survey and alignment tasks should have experience and aptitude in the precision alignment of 3D components and hardware.

10.1.6 Component Assembly, Testing, and Calibration

Many of the instruments that are employed for survey and alignment must be tested and calibrated on a regular basis. An alignment and calibration room will be provided for this purpose. This room will be environmentally stable and will have sufficient space for secure storage of all calibration equipment (including a Coordinate Measuring Machine and one or more large surface plates), as well as for the survey instruments themselves. The alignment and calibration room will also have enough additional space to align critical assemblies. Because survey instruments are very delicate, in-house calibration is generally preferred over shipping equipment out to a vendor. Calibration procedures and training are therefore required.

The alignment and calibration room will be large enough for calibration as well as for critical assembly work to be completed in a temperature-stable environment, thus allowing alignment processes to be tested accurately before they are used for the accelerator.

10.1.7 R&D

Two important R&D tasks have been identified. The first is an error analysis of the network configuration, to determine the network layout. It is also important in that step to incorporate the anticipated construction methodology. The second important R&D task determines the magnet measurement process and its effects on the survey and alignment process. If it can be shown that the stretched wire method can be used to position the magnets on girders, then the girder will become the smallest unit that the survey team has to contend with. However, close interaction will be required between the magnet measurement and survey groups. In particular, the girder fiducialization process needs to be established, because special equipment for the touchless wire pickup is required.

References

[10.1.1] H. Friedsam, “The Alignment of the Advanced Photon Source at Argonne National Laboratory,” International Workshop on Accelerator Alignment, CERN, Switzerland, 1993.

[10.1.2] R. Ruland, “Synchrotron Radiation Sources A Primer,” World Scientific Publishing ISBN 981-02-1856-7.

[10.1.3] H. Friedsam, M. Penicka, and S. Zhao, “Status Report on the Survey and Alignment Efforts and Results of the Advanced Photon Source,” International Workshop on Accelerator Alignment, KEK, Japan 1995.

[10.1.4] H. Friedsam, R. Ruland, private communication.

[10.1.5] Z. Wolf, “A Vibrating Wire System for Quadrupole Fiducialization,” SLAC, LCLS-TN-05-11.

10.2 Process Water Systems

10.2.1 Introduction

In order to achieve thermal and mechanical stability in the accelerator and experimental equipment, it is essential that the process water systems provide thermal-hydraulic stability. Therefore, not only must we maintain constant hydraulic conditions; simultaneously, we must remove all generated thermal loads while supplying a thermally stable, ±0.2ºF inlet temperature. To provide the desired parameters, the process systems will be divided into two generic types:

- Aluminum system(s) consisting of only aluminum and stainless steel components, supplying control for the aluminum vacuum chambers (i.e., "beampipes") throughout the rings
- Non-aluminum system(s), consisting of stainless steel components, providing control for all non-aluminum subsystems throughout the rings

10.2.2 Thermal Loads

The actual distribution of the thermal loads is both machine and component dependent. For example, both the storage ring and linac are independent machines with their respective thermal–hydraulic requirements. Also, within the storage ring there are distributed magnets and power supplies, each requiring its own respective parameters. Therefore, we will further divide the non-aluminum system into two separate types, allowing for maximum flexibility and control:

- An independent system for the linac
- Independent systems for the storage ring and its components and constitute subsystems

10.2.3 System Design and Parameters

The linac system will be an independent system supplying a constant pressure and flow with an inlet temperature of approximately 113ºF ±0.2ºF. This system will have a design very similar to the system described for the storage ring, as shown in Figure 10.2.1.

The storage ring design has thirty cells. As two cells constitute a super-period, for both the aluminum and non-aluminum systems the storage ring system has been divided into fifteen repeating sections, with each section having two process water systems, one for the aluminum and one for the non-aluminum needs within that given section.

Each aluminum system, supplying one-fifteenth of the vacuum system, will provide a constant pressure and flow with an inlet temperature of approximately 85ºF ±0.2ºF.

Each non-aluminum system, supplying approximately one-fifteenth of the storage and its subsystems, will provide a constant pressure and flow with an inlet temperature of approximately 85ºF ±0.2ºF. This sectional division will allow for differences in thermal distribution around the ring, and as such, each independent process system can be tailored to the specific thermal needs within its respective section. Also, by distributing the systems, an individual system will be smaller both in size and corresponding pipe runs.

A schematic of a non-aluminum system, using a total of 6 MW thermal loads evenly distributed over the fifteen sections, is shown in Figure 10.2.1. No heat exchanger is needed. "Cold" deionized water is supplied via a common header and pressurized via a 5 HP pump. This flow is controlled by the cold control valve and is then mixed with the hot water returning from the various components and subsystems. This hot water is itself pressurized via a 15 HP pump and is controlled by the hot control valve. Within a few minutes of operations, this hot water is within range and the thermal control is established. We have allowed for an 80

psid pressure drop across the components and magnets, and a 15ºF differential across these same components. The overall system pressure is maintained by a back pressure control valve, thereby setting up a controlled leak of inlet cold water versus outlet hot water. The cold water will be supplied via a common header and all necessary subsystems and water quality control will be carried out at that level.

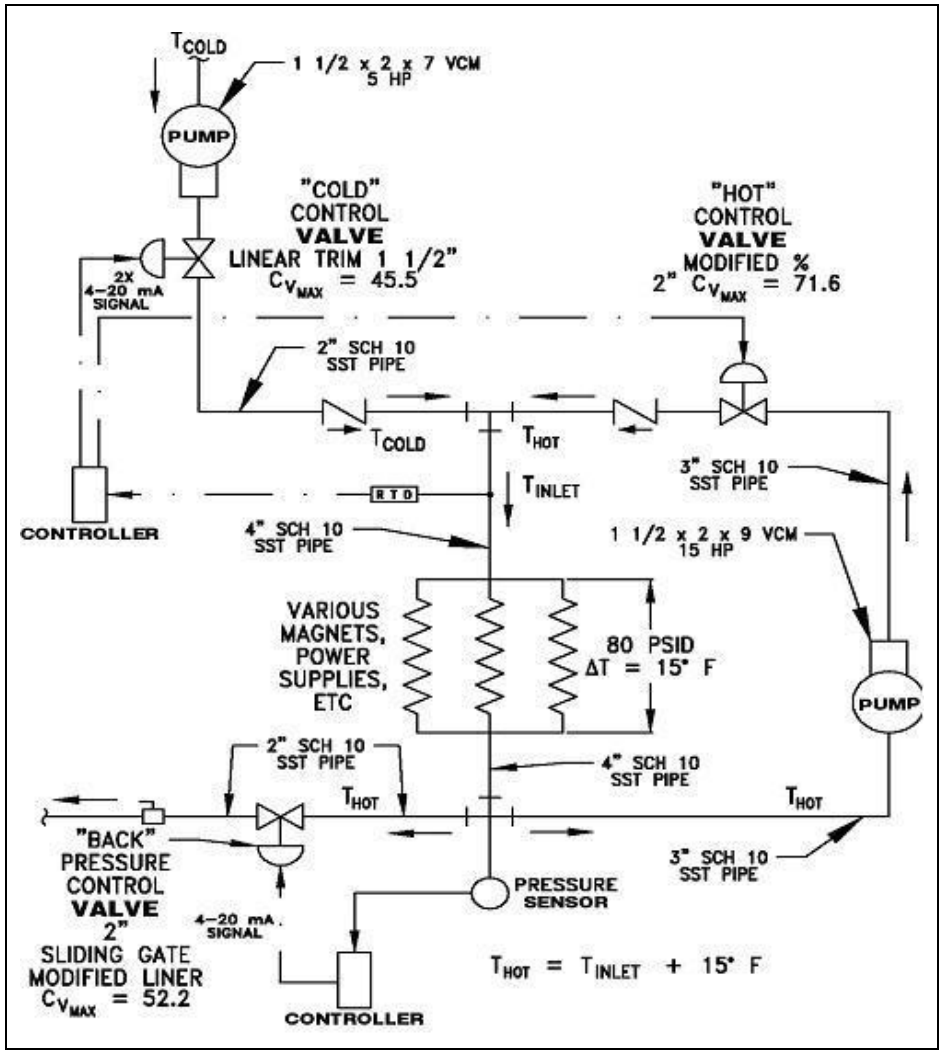

Figure 10.2.1 Non-aluminum process water system (deionized).

A split ranging scheme, which is shown in Figure 10.2.2, maintains the temperature control. The hot valve will be a 2" fail-closed valve with a maximum C_v = 71.6, while the cold valve will be a 1 ½" fail-open valve with a maximum C_v = 45.5.

The actual rate and any off-set in an individual valve's operation will be tailored during its tuning phase, where a standard PID single-loop controller using a split ranging scheme is used.

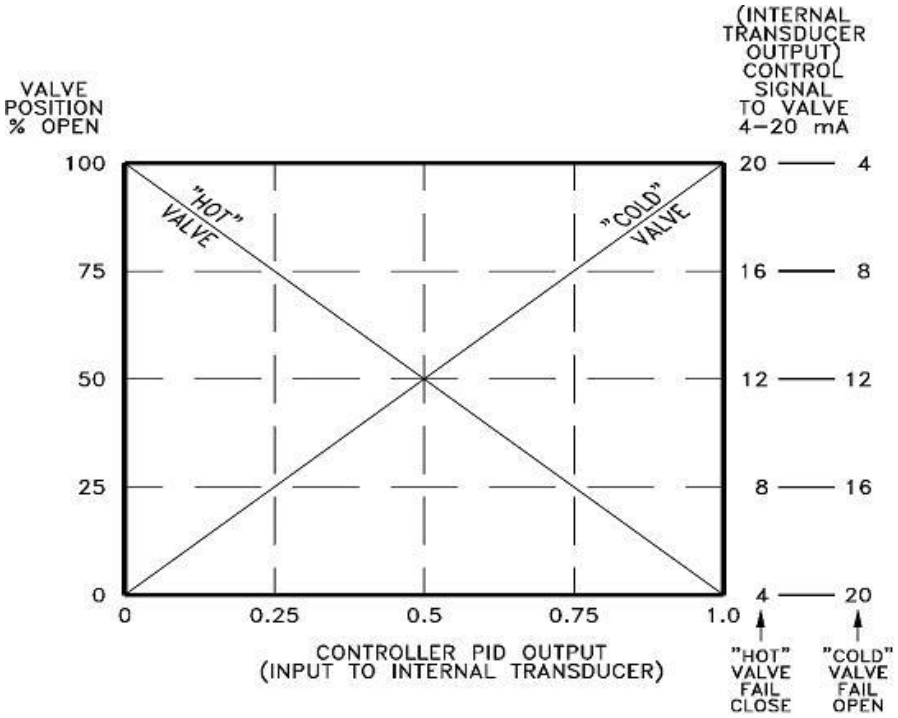

Figure 10.2.2 Control scheme: split ranging.

An aluminum system is shown schematically in Figure 10.2.3. Since the absorbers will absorb most of the thermal load, a total of 75 kW evenly distributed over the fifteen sections was used in sizing the system shown. A heat exchanger is needed, along with a control valve on the cold side of the heat exchanger. A 5 HP pump supplies the necessary pressurization and the system is sized for approximately 2.5 ft/sec through each of the vacuum chamber's flow channels.

Each one-fifteenth section will consist of nine parallel flow paths feeding five straight section beampipes and four dipole section beampipes. Within each beampipe type there is a fixed number of flow channels (or passages).

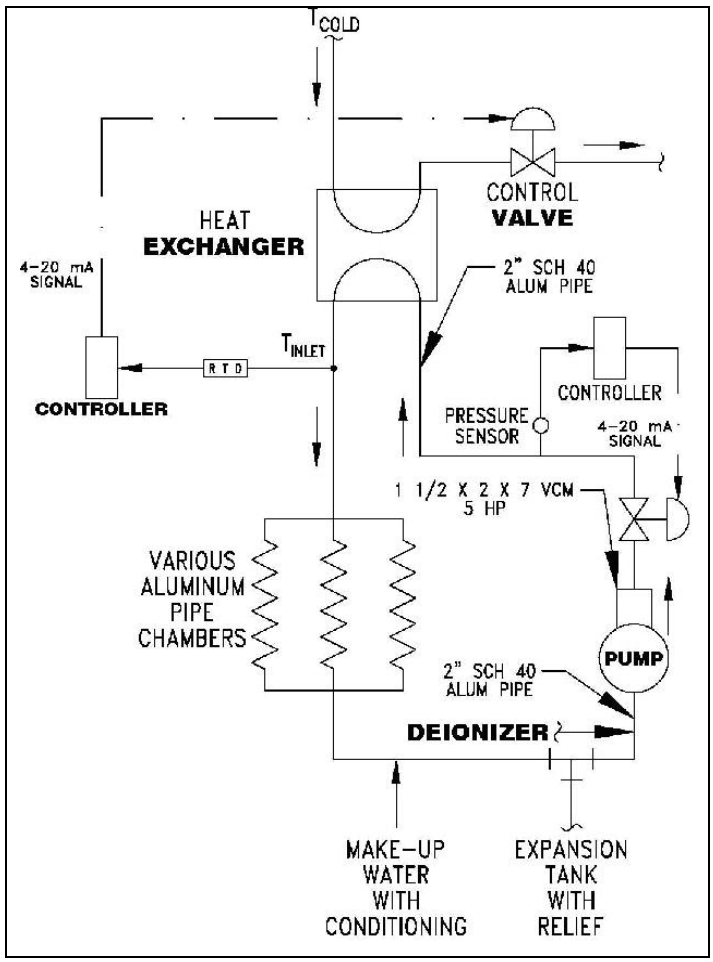

Figure 10.2.3 Aluminum Process System (Independent).

10.2.4 Water Quality Control

The water quality must be maintained in order to minimize any corrosive action that may occur. The following parameters will be maintained:

- Resistivity = 1.0 MΩ-cm ±5%
- pH = 7.5 ±0.2%
- Oxygen concentration = 10–20 ppb ±1 ppb

This water control will be maintained for the non-aluminum (non-linac) systems on a "global" level in the header-supplied cold water. For the linac and aluminum systems, this control will be maintained at the individual system level. For all cases, an industrial stand-alone system will supply the necessary water quality control.

10.2.5 Aluminum Bakeout System

A viable vacuum system must obtain a level of cleanliness that only can be achieved by removing all the entrapped gases within the piping enclosure. Thus, for the aluminum system to achieve its necessary vacuum for operations, a bakeout must be performed. This bakeout will be conducted at a constant 125ºC and will be maintained for the necessary time period as determined by the chamber's exposure to containments. In order to achieve this requirement, each aluminum system will allow for an independent, roll-up, bakeout system to

be connected to it. The aluminum pumping station will be isolated from the chamber and this bakeout system will be connected via a valve.

This bakeout system will consist of a pump, electric heater, and appropriate valving and controls such that a constant flow of 125ºC water will be maintained to the beampipe under consideration. The aluminum pumping stations will have the following design parameters:

- P_{DESIGN} = 150 psig
- T_{DESIGN} = 275ºF

The aluminum system, including the isolation valves, in contact with the bakeout water flow and the beampipes, will be designed for:

- P_{DESIGN} = 200 psig
- T_{DESIGN} = 275ºF

The bakeout system pump/heater will supply water at 150 psig and a temperature of 260ºF (~125ºC). Since the saturation temperature associated with 150 psig is T_{SAT} = 366ºF (@ P = 165 psia), and the operational bakeout temperature is 260ºF, we can see that there is 106ºF subcooling available, thereby ensuring that no change of phase will occur. 260ºF corresponds to a saturation pressure of 35.427 psia, which thus allows for a differential pressure drop of 129 psi before flashing will occur. Once the desired bakeout time has been achieved, the heater will be turned off and the water will be circulated to slowly cool down the beampipe section, thereby effectively ending the bakeout.

11 EXPERIMENTAL FACILITIES

11.1 Introduction

In this chapter, we discuss the conceptual design for the experimental facilities at NSLS-II. These facilities, and the planning for them, have driven and informed the design of both the conventional facilities and the accelerator complex.

We first address beamline development at NSLS-II (Section 11.2). Next we address issues that will confront all beamlines (Section 11.3), including issues of heat load and standard components. We note here that it is expected that at NSLS-II the facility will play an active role in the design and management of most of the beamlines. A benefit of this approach will be the standardization of various components across all similar beamlines.

It is anticipated that each beamline will be optimized for a particular technique—an approach that has proven to be efficient for producing high scientific output. These beamlines will be chosen through a rigorous peer-reviewed process and with the active participation of the user community. The beamlines are likely to be funded through a variety of mechanisms, including the construction project itself, other DOE funding, funding from other federal agencies, and from other sources. In all cases, the facility will play a major role in determining beamline capabilities and design, and ensuring that the development of the beamline portfolio is consistent with the overall strategic plan for the usage of the facility.

Prior to this full peer-reviewed process, we have chosen in the CDR to discuss the design constraints and capabilities for a number of likely beamlines. In particular, we discuss the conceptual design for five beamlines at a reasonably detailed level. These beamlines have been chosen as examples of high-performance beamlines that will take maximum advantage of the state-of-the-art characteristics of the NSLS-II beam. These beamlines would: 1) probe physical and electronic structures with a spatial resolution of 1 nm (Section 11.4, A Hard X-Ray Nanoprobe Beamline); 2) measure excitations in condensed matter, with resolutions down to 0.1 meV (Section 11.5, An Inelastic X-Ray Scattering Beamline); 3) measure the dynamics of soft-matter systems on timescales of microseconds, and image nanostructures to sub-nm precision (Section 11.6, An X-Ray Coherent Scattering Beamline); 4) probe electronic orderings and excitations in transition metal compounds (Section 11.7, A Soft X-Ray Resonant Scattering and RIXS Beamline); and 5) use soft x-rays to image a wide range of samples from biological to chemical to electronic systems, with ~10 nm spatial resolution (Section 11.8, A Soft X-Ray Coherent Scattering Beamline).

Note that the precise missions of these beamlines will likely evolve as their scientific goals and required technical capabilities are further refined by continued interactions with the user community.

Ultimately, of course, NSLS-II will feature a full complement of beamlines serving a wide variety of techniques and user communities. To design the NSLS-II facility appropriately for future development, it is necessary to consider the requirements for these additional beamlines that might have an impact in the conceptual design of the accelerator and conventional facilities. Examples of these requirements include specialized insertion devices for high-energy x-rays, ultra-long beamlines for imaging purposes, beamlines with a particular need for a suite of labs for biological purposes, and so on.

To ensure that the impact of these requirements is properly taken into account, we have carried out conceptual designs of several such beamlines or techniques. Again, the intent here is not that these will be the first beamlines built outside the project scope or that these have the strongest scientific case, but, rather, to explore their implications for the design of the NSLS-II accelerator and conventional facilities.

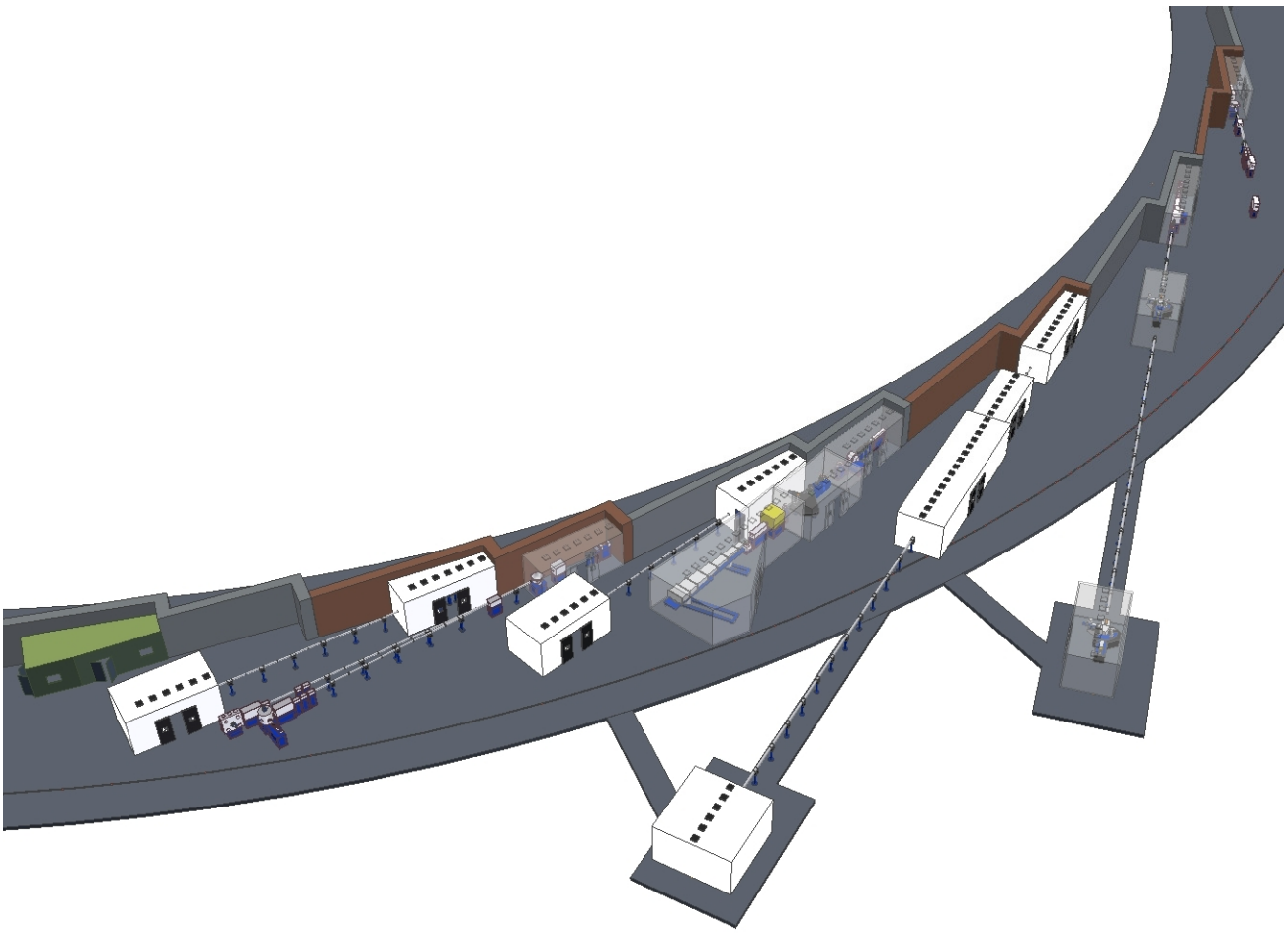

Figure 11.1.1 The experimental floor at NSLS-II showing a number of beamlines. Included here, purely for illustration purposes, are two soft x-ray insertion device beamlines, two bending magnet beamlines, an IR beamline (green enclosure), and three hard x-ray insertion device beamlines.

11.2 Beamline Development at NSLS-II

In this section, we outline the mechanisms and strategies for developing, constructing, and operating the full portfolio of beamlines at NSLS-II. In particular, the guiding philosophy that will be used to develop the strategic plan for NSLS-II will be discussed. In addition, the fully built-out capabilities of the facility are presented, together with a possible distribution of uses of the facility. This latter is purely for the purpose of illustrating the capabilities of the facility. The actual use of the various ports will be determined in the context of a strategic plan that will be developed in the coming years through a process of consultations with the various stakeholders, including the user community, advisory committees, funding agencies, and facility staff.

11.2.1 Strategy for Beamline Development

As a newly constructed third-generation synchrotron, NSLS-II will face a number of challenges and opportunities in developing its beamline portfolio. Specifically, it will be important to optimize the use and maximize the scientific output of the facility to ensure that important needs are addressed and that capabilities are not omitted or needlessly duplicated. To achieve this end, a strategic plan for the use of the facility will be created to guide the development of the portfolio of scientific programs and the experimental facilities

required to support them. As a general philosophy, we anticipate that each beamline will be optimized for a particular technique in order to maximize productivity.

Decisions on approval to construct and operate a particular type of beamline will be made in the context of this overall strategic plan. In addition, the needs and interests of the existing large user community of the current NSLS must be considered in planning for NSLS-II. Their presence means that it is very desirable for the user capacity of NSLS-II to ramp up significantly faster than at other "green field" new facilities without existing user communities. In order to accelerate the growth of user capacity, the strategic plan for NSLS-II will therefore consider opportunities to transition programs and, in some cases, hardware, from NSLS to NSLS-II.

An important component of the strategic plan will be the funding avenues for beamline construction, a number of which are anticipated. The first of these is through the construction project itself. A suite of beamlines will be built as part of the NSLS-II construction project and will deliver state-of-the art user facilities when NSLS-II is commissioned. These beamlines will be constructed and operated by the facility. Beamline Teams will guide the development of these beamlines, as discussed in Section 11.2.1.1. The precise scientific mission, and required capabilities, of beamlines will be determined by continued interaction with the user community.

It is anticipated that a second source of funding for beamline construction will be provided by DOE in the form of Major Items of Equipment (MIE) proposals, and that the facility will bundle a number of beamline proposals together and propose multiple, sequential MIEs to DOE. These will be submitted as early as possible. The MIEs are expected to fund the construction of beamlines that meet needs relevant to the BES mission of DOE. These beamlines would also by guided by BTs and be built and operated by the facility.

A third source of funding that is anticipated is funding from sources other than DOE-BES. Examples include funding from other federal agencies, such as NIH, DOE–BER, DoC, DoD, NSF, and funding from industrial companies. Such sources may fund either specialized equipment, such as end stations, or entire beamlines. In the latter case, the beamline would also by guided by a BT.

11.2.1.1 Beamline Teams

BTs are teams formed to advise the facility on the construction and operation of beamlines. The teams are expected to be comprised of a relatively small number of people who are committed to establishing a beamline to serve a well defined scientific mission. BT members will be closely involved in the specification and design of the beamline and end stations. They will interact strongly with the expected user community—for example through annual workshops—and will be responsive to that community's needs.

BTs will be selected by the facility on the basis of scientific impact, quality of the team, alignment with the NSLS-II strategic plan, utilization of NSLS-II, technical feasibility, and community need. A call for Letters of Intent, LOIs, from potential BTs is expected to be issued shortly after a positive CD-1 decision. Following submission, the various LOIs will be reviewed by the facility and by the Experimental Facilities Advisory Committee (EFAC), who may also chose to utilize external peer review. Upon selection, the BT will work with facility staff to pursue funding and to oversee the beamline design, construction, and commissioning, to ensure that it optimally meets the scientific requirements.

11.2.2 Facility Usage

NSLS-II will have 27 straight sections available for user insertion devices (of the remaining three, one is used for injection and two for RF systems). Of these 27 straight sections, 15 will be 5 m straights and 12 will be 8 m straights. The 5 m straights are expected to be populated with undulators of various types, while most of the 8m straights will be likely populated with damping wigglers and undulators. Of the damping wigglers, the initial build-out is expected to include three 7 m devices. The fully built-out facility would likely include

eight 7 m devices for a total length of 56 m. These devices are likely to be extremely attractive for a large number of users, offering high flux and broad spectra.

Clearly, optimizing the use—and location—of the varied devices that will populate the ring is a many-variable problem. Further enriching the picture is the potential to "cant" devices, allowing multiple devices to be located in a single straight section. With these constraints in mind, we have constructed a picture for the fully built-out facility to illustrate its capacity and provide a guide to its capabilities, and to ensure that the various user communities' needs are met. In doing so, we have used the existing NSLS suite of instruments, user demand, and productivity—as well as the capabilities of existing sources around the world - as a guide to the requirements of the mature facility.

In this strawman arrangement, we have assigned beamlines to particular disciplines and techniques, taking into account such factors as user demand, NSLS-II capability, physical constraints (imposed by the layout of the accelerator), site constraints (for example, possible long beamlines that extend beyond the experimental floor), and scientific constraints (beamlines that address related science questions or use similar techniques are grouped together). This is not meant to reflect any decisions that have been made as to the future development of beamlines, but rather it is an exercise to show the range and capacity of science programs that NSLS-II could host.

Table 11.2.1 summarizes this distribution, where the beamlines have been categorized according to the classification scheme currently in use at NSLS. While these categories are somewhat ambiguous in certain cases, this table nevertheless serves the useful purpose of allowing a comparison with the beamline distribution of the existing NSLS, a mature facility. It shows that NSLS-II can provide a comparable number of beamlines as the NSLS x-ray and VUV rings together provide, when the possibility of canting is included, while providing a similar range of capabilities. The difference, of course, is that at NSLS-II many of the beamlines will be served by insertion device sources (either undulators or wigglers) and therefore will be orders of magnitude brighter than the bending magnet sources currently serving most beamlines at NSLS. Even beamlines served by bending magnets at NSLS-II will be vastly superior to those at NSLS.

Table 11.2.1 Possible Distribution of Beamlines at NSLS-II by Beamline Type. A comparison is made with the existing NSLS facility using the same classification scheme.

		NSLS-II			NSLS		
Category	**Type**	**IDs**	**BMs**	**Total**	**IDs**	**BMs**	**Total**
A	IR/UV/Soft x-ray spectroscopy	1	11	12	3	7	10
B	x-ray spectroscopy	6	3	9	0	9	9
C	soft matter/biophysics scattering	4	0	4	0	8	8
D	hard matter/strongly correlated scattering	9	1	10	3	5	8
E	powder/single crystal/high P/optics	7	3	10	3	8	11
F	Imaging/micro-probe	4	5	9	2	7	9
G	macromolecular crystallography	7	0	7	2	8	10
		38	23	61	13	52	65

The distribution of the beamlines around the ring is shown graphically in Figures 11.2.1 and 11.2.2, which represent the insertion devices and bending magnet usage, respectively.

Although NSLS-II is expected to have a similar number of beamlines as NSLS, the high brightness is expected to increase the throughput of users dramatically for certain types of experiments. Based on this and extrapolating from the current user population of ~2400 users/year at the current NSLS, we estimate that NSLS-II will be able to host ~3500 or more users/year. There is ample evidence from current beamtime oversubscription rates to expect that demand for beamtime at NSLS-II will exceed even this level of service.

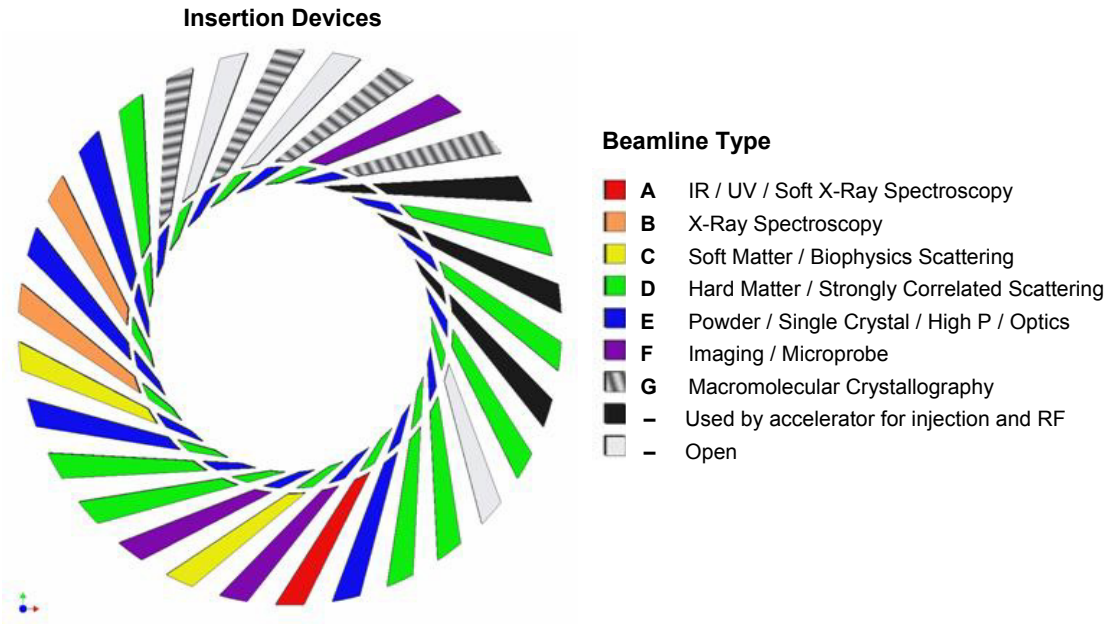

Figure 11.2.1 Possible use of insertion devices, by beamline type at NSLS-II. The inner ring is color coded by the straight section type, with blue indicating 5 m straights, green indicating 8 m straights, and black representing the RF and injector straights that are not available to the user program. Open beamlines are not assigned in this scheme.

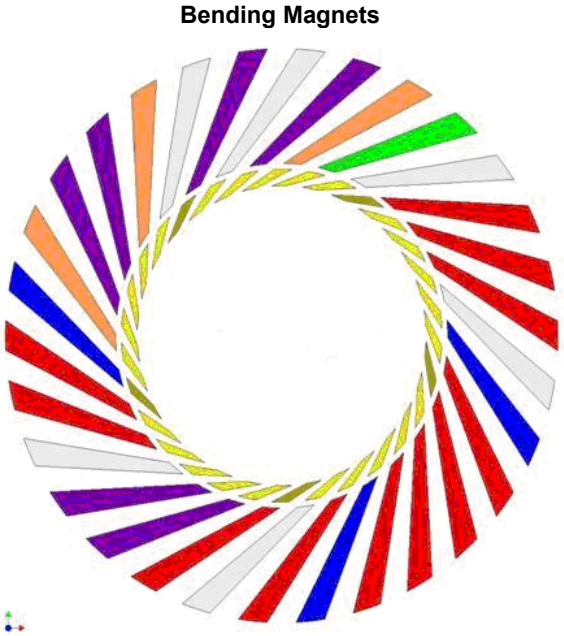

Figure 11.2.2 Possible use of bending magnet beamlines, using the same color key as Figure 11.2.1. The inner ring represents the bending magnet sources, with darker segments signifying large gap dipoles for far-IR sources.

11.3 Standard X-Ray Beamline Components

Standard x-ray beamline components that are addressed in this section consist of filters, slits, photon shutters, double-crystal monochromators, and focusing mirrors. Of these components, the double-crystal monochromators and focusing mirrors have the greatest importance, complexity, and cost.

11.3.1 Double-Crystal Monochromator

Nearly all x-ray beamlines at NSLS-II, regardless of radiation source, will include a double-crystal monochromator in their design. Designs for these are very mature and several commercial versions are available that could satisfy the needs of NSLS-II beamlines. Most monochromators will employ silicon crystals using the (111), (220), or (311) Bragg reflections; some monochromators might employ diamond crystals using the (111) Bragg reflection. For accessing low photon energies, crystals that have larger lattice parameters than silicon or diamond will need to be used, such as germanium, indium antimonide, or, for the lowest photon energies (down to about 1 keV), beryl and YB_{66}. In most cases, both crystals used in the monochromator will be flat, but in some applications the second crystal will be sagittally bent to focus the x-ray beam horizontally. Proven crystal benders are also available commercially.

The mechanics of double-crystal monochromators allow the crystal pair to rotate to provide a range of incidence angles, from a few degrees to as much as 70 degrees, yet still preserve the exit height of the doubly diffracted beam.

Thermal considerations dominate the design aspects of modern double-crystal monochromators, and in view of the extremely high power and power densities of NSLS-II insertion device beams, we will focus most of our attention on these considerations. Thermal issues are associated not only with the first crystal that is impacted by the direct white beam, but also with the second crystal, which may be subjected to parasitic Compton scattered beam from the first crystal and from elsewhere. Appropriate scatter shields and, if necessary, cooling of the second crystal can address the latter effects, but to properly handle the incident heat load on the first crystal requires special measures, usually cryogenic cooling of silicon or the use of water-cooled diamond. In most cases, cryogenic cooling of silicon is employed, usually with liquid nitrogen but sometimes with closed-cycle circulating gaseous helium. This last option is employed on four existing NSLS insertion device beamlines. We anticipate that NSLS-II monochromators that employ cryogenically cooled silicon crystals will use liquid nitrogen. Several recent studies [11.3.1] have established the acceptability of liquid-nitrogen cooled silicon crystal monochromators at higher energy third-generation synchrotron sources, with incident power levels of up to several hundred Watts. Commercial cryogenic cooling systems that are specifically optimized for use with x-ray monochromators are available.

11.3.1.1 Cryogenically Cooled Silicon Monochromator

To gain an understanding of how a cryogenically cooled silicon crystal will be able to withstand NSLS-II ID beams having power levels that are unprecedented for a lower energy, third-generation synchrotron sources. We have examined the performance of a variation of a cryogenically cooled silicon crystal design used on several undulator beamlines at APS, the so-called “hockey puck” crystal design [11.3.2]. The top surface of this crystal is polished and serves as the diffracting surface, and the crystal is cooled from below with flowing liquid nitrogen that makes direct contact with the underside of the crystal, which must therefore be clamped onto a support and sealed. Beneath the crystal are large fins that are in contact with the flowing liquid nitrogen, to enlarge the cooling surface area, Figure 11.3.1. The version of this design that is used at APS includes a milled-out channel beneath the top diffracting surface, to allow the high photon energy components of the APS undulator spectrum to transmit through the diffracting surface and continue past the monochromator, reducing the power absorbed by the crystal. The NSLS-II undulator spectrum will be of much lower energy and the power will be absorbed completely in the top layer of the crystal; therefore, the milled-out channel is unnecessary and has been “filled in” in the design that we are modeling.

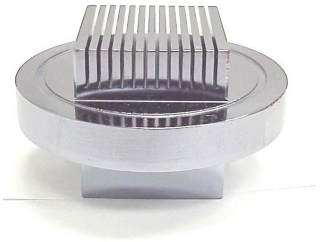

Figure 11.3.1 Photo of a "hockey puck" silicon crystal, upside down. Because it is resting on its diffracting surface, the cooling fins appear on top. The round portion of the crystal clamps onto a cooling manifold, and the circular groove contains a gasket that serves as the seal.

We have carried out initial worst-case calculations based on the 14 mm period superconducting undulator. At 30 m from the source position (a typical monochromator position), the power density for this device can exceed 100 W/mm^2. In this position it has a power of >400 W in a useful beam cross-section 2.4 mm wide and 1.5 mm high. (This is the 4σ beam size for the undulator's fifth harmonic at 8.9 keV, for which the undulator would operate at its highest K, 2.2.) The crystal was subjected to this power load condition (407 W total power) and oriented at an angle of 12.7 degrees to the incident beam, which gives a diffracted photon energy of 8.9 keV for a Si(111) Bragg reflection. Finite element analysis, FEA, shows a maximum thermal slope error, in the scattering plane, of ±10.8 μrad, with the distribution of thermal slope errors in the scattering plane having an RMS value of ~6 μrad. For comparison, the Darwin width for Si(111) at this photon energy is 31.5 μrad. Thus, in this circumstance the thermal distortion is a fraction of the Darwin width, and might be acceptable; its implications are discussed in the following paragraphs. These calculations were repeated after the model was modified with a vacuum isolation window (for hard x-ray beamlines, to separate the storage ring and beamline spaces) of CVD diamond that is 100 μm thick. This window absorbs 16% of the total radiated power in the above-quoted beam dimension, resulting in 343 W of power striking the crystal. The maximum thermal slope error, in the scattering plane, is then ±7.35 μrad, and the slope error distribution has an RMS value of ~4 μrad. Figure 11.3.2 shows the thermal and slope error (in the scattering plane) profiles for these two cases. The maximum crystal temperature is 145K for the unfiltered beam and 127K for the filtered beam; for comparison, the thermal expansion coefficient of silicon crosses zero at 125K.

The implications of these thermal distortions on the brightness of the diffracted beam can be treated individually for each component factor of the brightness, as follows:

Flux. The transmission of flux (compared with the case of no thermal distortion) is given approximately by the ratio of the intrinsic Darwin width to the width of the intrinsic Darwin curve convoluted with the thermal slope error variation; the latter is approximately the quadrature combination of the Darwin width and the RMS thermal slope error. The resulting transmission is about 98% for the unfiltered beam and 99% for the filtered beam. We conclude that the impact of the thermal slope error on the diffracted flux is negligible in either case. Note that the diamond window (100 μm thick) itself absorbs about 10% of the flux at 8.9 keV.

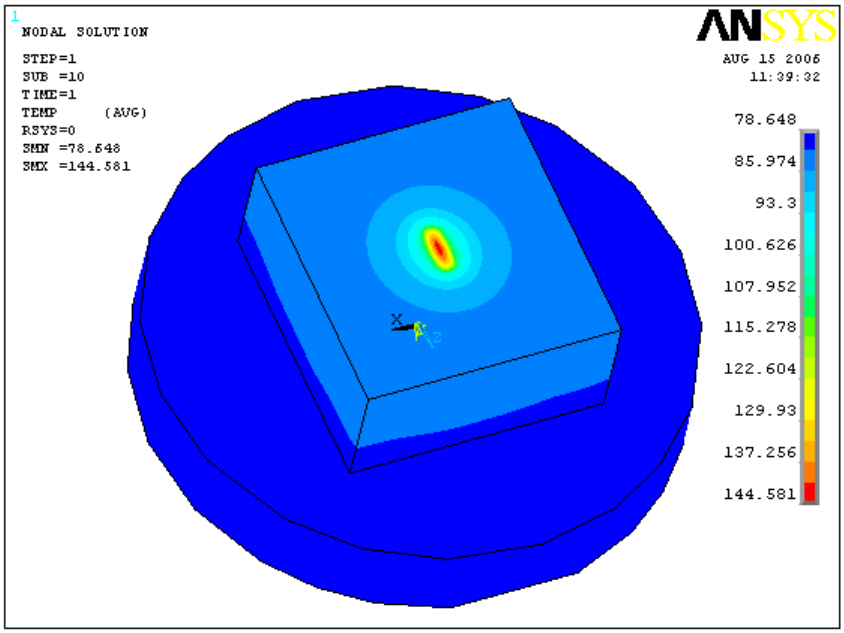

Figure 11.3.2 Profiles of crystal subjected to the NSLS-II undulator power load described in the text.

a)
Thermal profile for unfiltered beam.

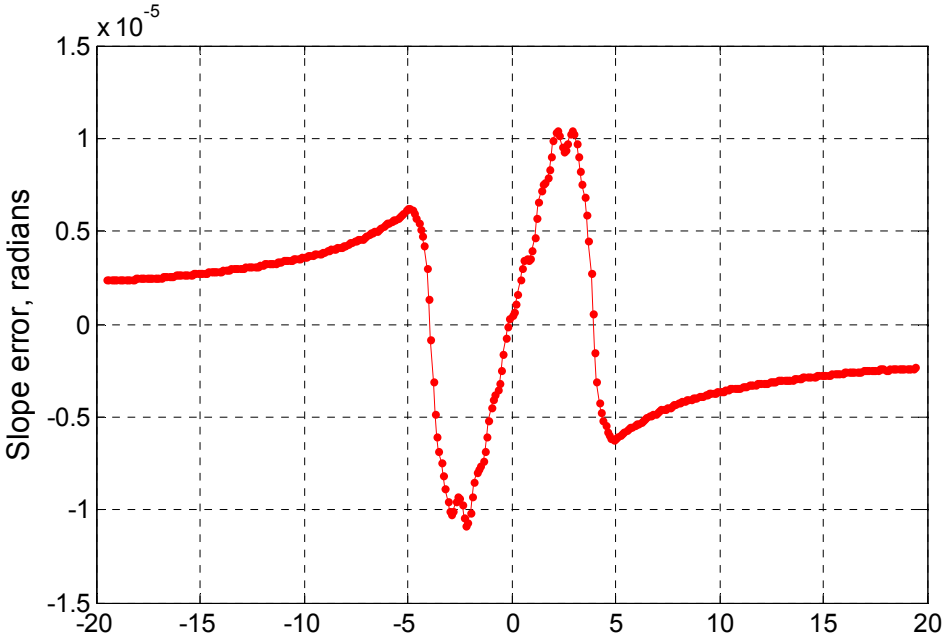

b)
Slope error variation in scattering plane for unfiltered beam. (x-axis is distance from the center in the y-direction, in mm.)

(continues next page)

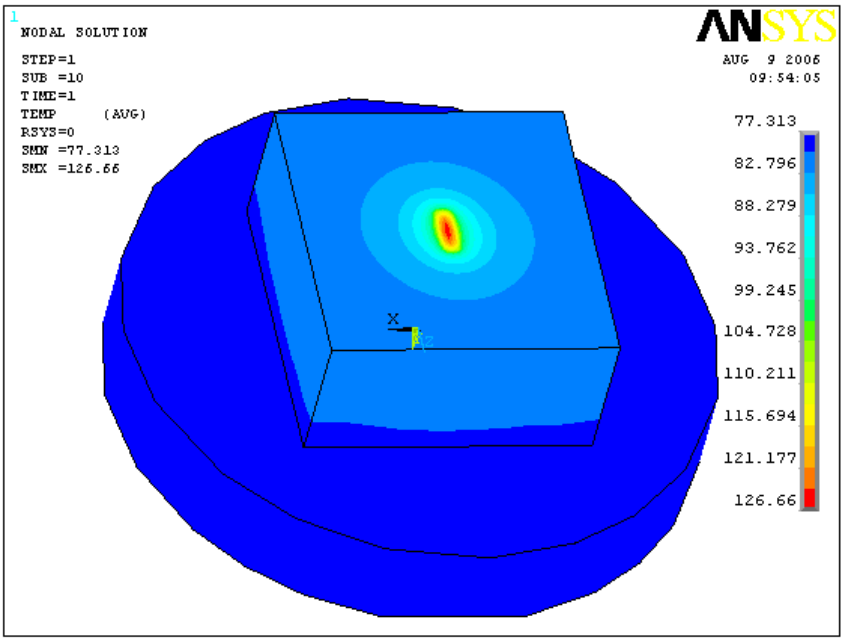

c

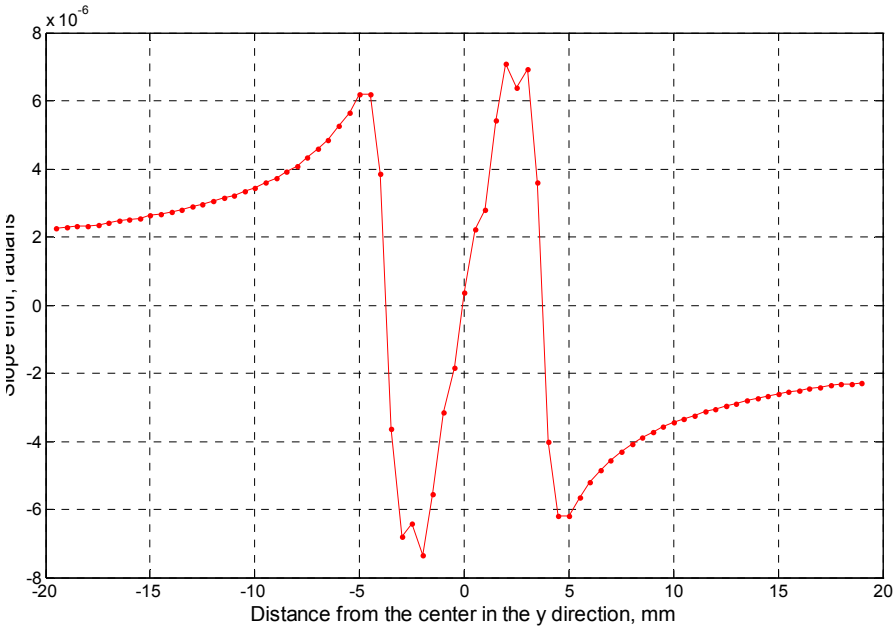

d

Figure 11.3.2 (cont.) Profiles of crystal subjected to the NSLS-II undulator power load described in the text.

c)
Thermal profile for filtered beam.

d)
Slope error variation in scattering plane for filtered beam. The entire extent of the illuminated footprint consists only of the central 6.8 mm in (b) and (d).

Relative wavelength spread. The relative wavelength spread is determined by the range of incidence angles striking the Bragg planes, weighted by the cotangent of the Bragg angle. For flat Bragg planes, the range of incidence angles is given approximately by the quadrature combination of the photon beam opening angle (48 μrad for the case considered here) and the intrinsic Darwin width of 31.5 μrad. When thermal distortion exists, the wavelength spread is broadened further through convolution with the thermal slope error variation. For the cases treated here, the impact is less than 1% and is negligible.

Angular spread. The considerations are the same as for the wavelength spread. The resultant impact of the thermal slope errors calculated for the cases treated here is less than 1% and is negligible.

Position spread. Careful attention must be paid to this aspect of the diffracted beam brightness. Thermal slope errors of monochromator crystal Bragg planes have the same blurring impact on the beam dimension in the vertical plane as mirror figure errors would. It is determined by twice the RMS slope error multiplied by the distance from the monochromator. The effect of a 6 μrad RMS thermal slope error is a blurring of the beam dimension by 240 μm at a distance of 20 m downstream of the monochromator. For an NSLS-II superconducting undulator beamline, these effects might be significant, given that existing state of the art focusing mirrors (with figure errors of 2 μrad or less) will attain vertical focus sizes less than 50 μm. (Mirror issues are discussed in the next section.)

Thus, cryogenic cooling of a silicon monochromator crystal in an NSLS-II superconducting undulator beam appears to be a viable solution to preserving most, but not all, of the aspects of the beam brightness. To compensate the impact of the monotonic thermal distortion variation (see Figures 11.3.2b and d) on the position spread of the diffracted beam in the vertical direction, it should be feasible to mechanically adjust, only slightly, the curvature of the vertical focusing mirror that would typically be used downstream of the monochromator. Such adaptive compensation has been employed successfully in operation of the NSLS beamline X25 for the past 14 years, through mechanical adjustment of the curvature of the silicon crystal [11.3.3]. We will analyze this possibility through ray tracing. Implementing this curvature adjustment method will require the installation of a high-resolution beam profile monitor.

11.3.1.2 Water Cooled Diamond Monochromator

Although less commonly used than silicon, diamond holds particular promise for use as a monochromator crystal in an NSLS-II undulator beam. The superior thermal and mechanical properties of diamond, compared with silicon, are well known, and permit the possibility of using water-cooled, room temperature diamond crystals in high-heat-load applications (although, interestingly, the thermal properties of diamond do also improve at cryogenic temperatures). However, the property that makes diamond more attractive than silicon is its x-ray absorption coefficient. At 8 keV, where NSLS-II undulators would emit substantial power, the 1/e penetration length in diamond is 710 μm, whereas for silicon it is only 70 μm. This is why it is a good approximation to assume that for silicon, the full brunt of the undulator beam power will be absorbed in the top layer of the material. In the case of diamond, however, the absorption of the undulator beam power will be distributed through the material, and if the crystal is thin enough (e.g., ~1 mm), a substantial fraction of the power will be transmitted through the crystal, while the crystal remains thick enough to fully diffract the photon energy of interest. (The required thickness to fully "extinguish" the diffracted x-rays into the reflected beam is several μm.) The resulting thermal distortion of the Bragg planes in the diamond material is reduced significantly, even were diamond's thermal properties to be the same as those of silicon. For these reasons, diamond merits special consideration as a candidate monochromator crystal material in an NSLS-II undulator beamline.

Historically, the major challenge in using diamond crystals in an x-ray monochromator has been the quality of the diamond crystals. Only a few vendors offer diamond crystals of sufficiently high quality. Typically, users must purchase a supply of crystals with no guarantees as to their quality, and determine the quality themselves. Recently, however, ESRF has explored, with a European vendor of synthetic diamond crystals, testing diamond crystals and weeding out crystals of insufficient quality [11.3.4]. The best quality diamonds currently are produced synthetically using a high-pressure, high-temperature process, resulting in crystals of 5–10 mm, from which wafers of perhaps 0.5–1 mm thickness and 5–7 mm cross-section can be sectioned. Wafers with orientation of (001) are the simplest to section and polish, although (111) oriented wafers, which are more useful for monochromators, are also produced. Diamond wafers of this size are relatively costly, typically $20,000 each, and it is usually necessary to purchase extras. The net cost, however, is less than the cost of a cryogenic cooling system.

We carried out initial FEA modeling of diamond crystal monochromators in an NSLS-II undulator beam. The monochromator model is shown in Figure 11.3.3. It consists of a diamond single-crystal wafer of

dimensions 8 mm long (along the beam direction) by 5 mm wide (transverse to the beam direction) by 0.5 mm thick, and is gently clamped atop a water-cooled copper support, using a thin liquid gallium-indium eutectic layer. Because a large fraction of the incident beam power is transmitted by the diamond wafer, the copper support has a hole beneath the crystal wafer that permits the transmitted beam to propagate to a remote beam dump. The hole has dimensions of 6 mm long (along the beam direction) by 3 mm wide (transverse to the beam direction), and therefore there is 1 mm of overlap, all around the hole, between the diamond wafer and copper support, that serves as the thermal contact interface. This design is in use on the Sector 30 (IXS-CDT) undulator beamline at APS. We assumed the same beam parameters as above. For the (111) Bragg reflection of diamond, the Bragg angle at this photon energy is 19.7 degrees. For a diamond wafer 0.5 mm thick oriented at this incidence angle to the undulator beam, 166 W (40% of the total) is absorbed by the crystal and 240 W (60% of the total) is transmitted. In undertaking the calculations, special attention was paid to the volumetric absorbance of the incident beam power; i.e., we did not assume, as we did for the silicon monochromator discussed earlier, that the absorbed power was fully absorbed at the surface layer; we calculated and employed the actual depth profile of the absorbed power.

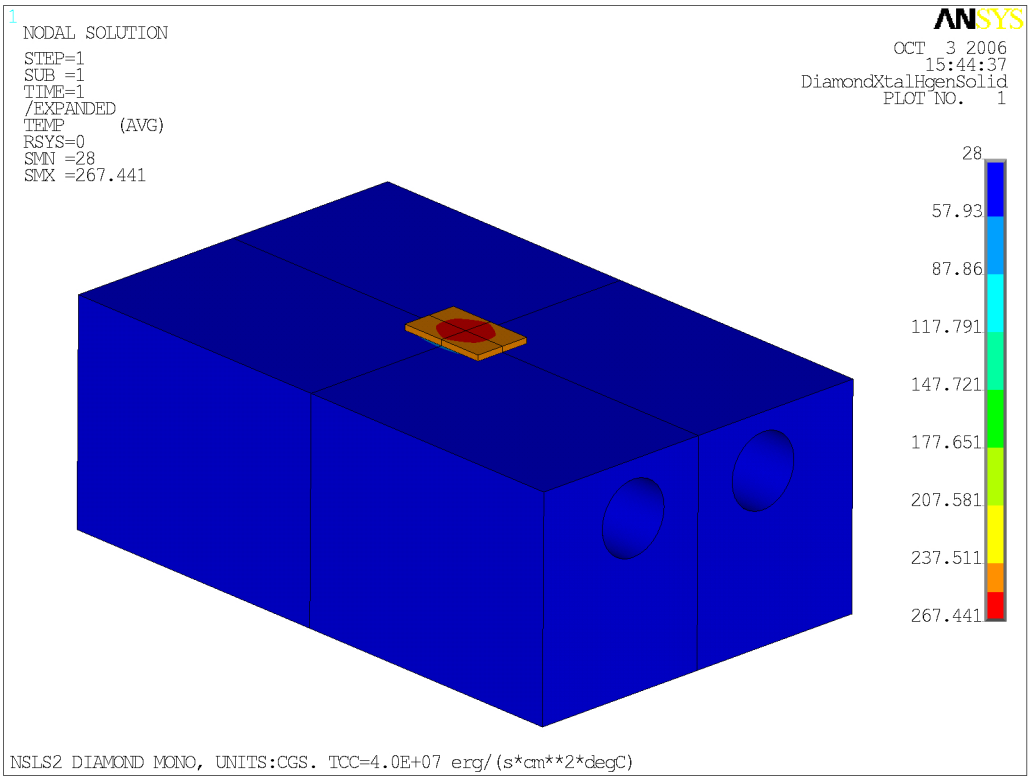

Figure 11.3.3 Model of a diamond wafer atop a water-cooled copper support. The cooling channels through the copper support are shown. The **temperature distribution** is based on the understood heat transfer coefficient of gallium-indium eutectic in contact with solid material.

Figure 11.3.3 shows the calculated temperature distribution in both the diamond wafer and the copper support under these power loading conditions. Of particular note is the enormous difference in temperature between the copper support (which reaches a maximum of 88ºC) and the diamond (which reaches a maximum of 267ºC). This is due to substantial thermal resistance at the interfaces between the gallium-indium eutectic and the diamond, and between the gallium-indium eutectic and the copper; we used a heat transfer coefficient value for these interfaces of 0.04 W/mm^2-ºC [11.3.5]. The resulting diamond wafer thermal distortion map is shown in Figure 11.3.4. Within the beam footprint, the maximum slope error projected into the x-ray scattering plane is ±30 μrad. Compared with the Darwin width of 22 μrad for the (111) Bragg reflection of diamond at 8.9 keV, this is rather severe.

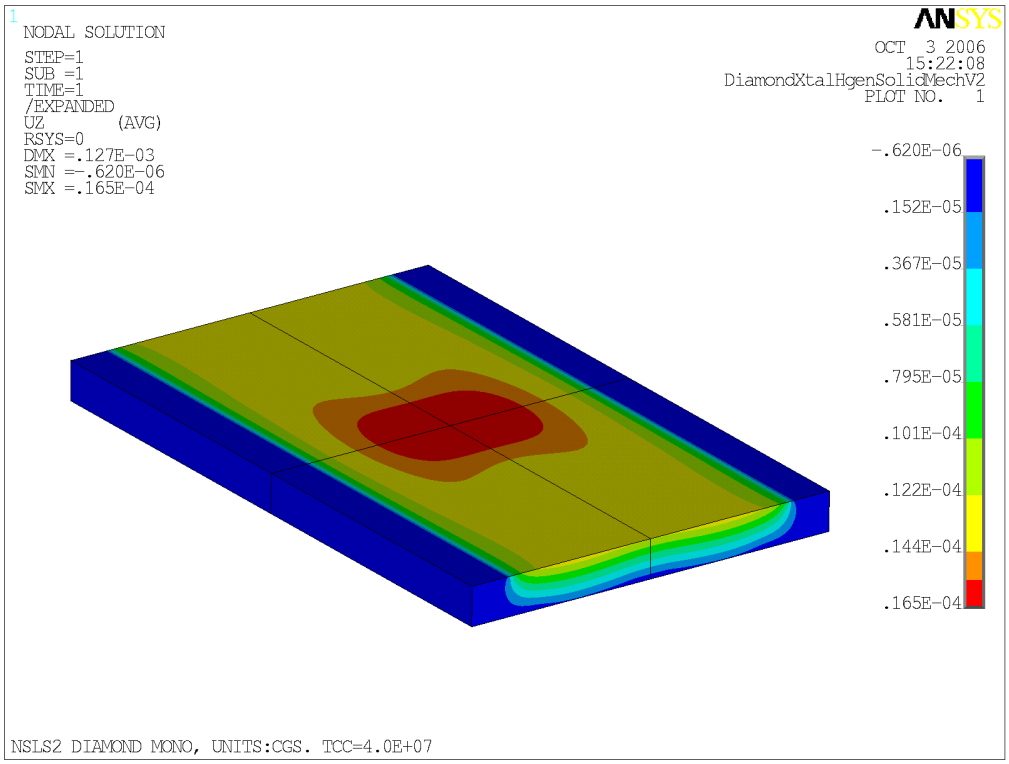

Figure 11.3.4 Calculated **thermal distortion profile** in diamond wafer corresponding to the temperature distribution shown in Figure 11.3.3.

We repeated the FEA calculation after arbitrarily lowering the thermal resistance of the gallium-indium/solid material interfaces, by increasing the heat transfer coefficient by a factor of 10, to 0.4 W/mm^2-ºC, to see what the potential impact of achieving a better thermal contact of the diamond to the copper support via, e.g., brazing might be. The resulting temperature distribution in the diamond wafer is shown in Figure 11.3.5, and its accompanying thermal distortion profile is shown in Figure 11.3.6. The maximum temperature in the wafer is 103ºC (versus 267ºC) and the maximum slope error within the beam footprint projected into the x-ray scattering plane is ±9 µrad (versus ±30 µrad), which is smaller than the (111) Bragg reflection Darwin width. Thus the slope error is greatly improved as a result of the better thermal contact.

This simple exercise reveals the improvement pathways that could be pursued in order to utilize diamond crystal monochromators on NSLS-II undulator beamlines, primarily through measures to reduce the temperature difference between the diamond and its cooled support. The ideal case would be to eliminate the thermal resistance at the interface between the diamond and its support entirely, but this could only be achieved via a monolithic diamond, which is a highly unlikely possibility, although it has been suggested [11.3.6]. More likely measures involve seeking a strain-free braze contact between the diamond and its support, enlarging the contact area (here, the total contact area was 22 mm^2) by obtaining a larger cross-section diamond wafer, or reducing the thickness of the wafer to reduce the absorbed power.

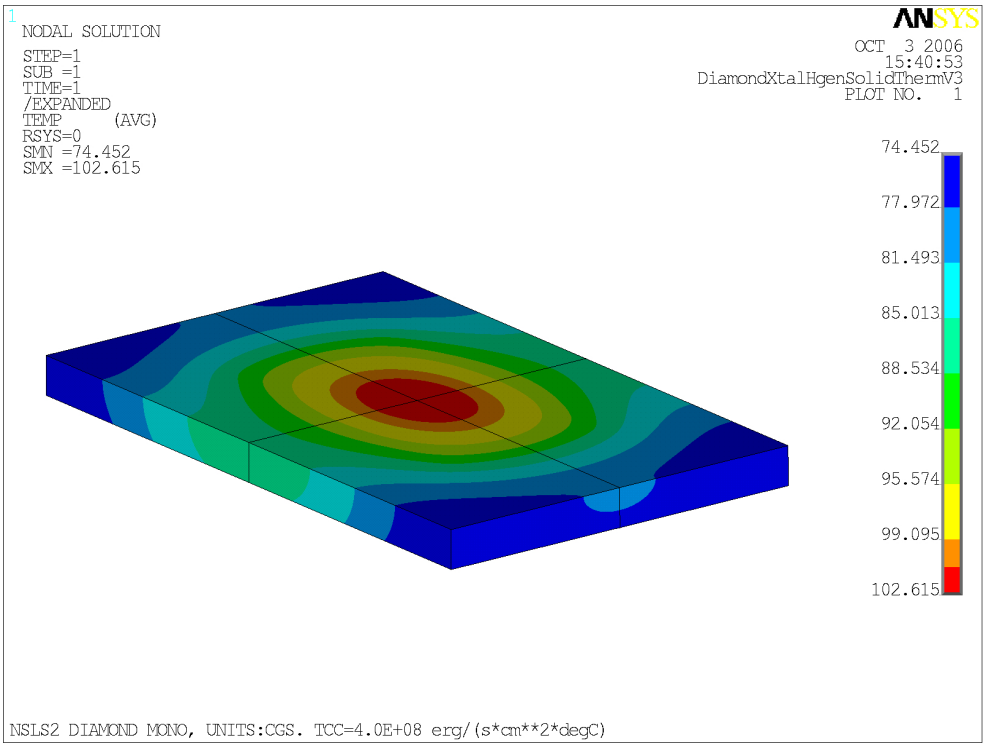

Figure 11.3.5 Calculated **temperature distribution** in diamond wafer assuming a 10 times larger heat transfer coefficient, compared to the distribution shown in Figure 11.3.3.

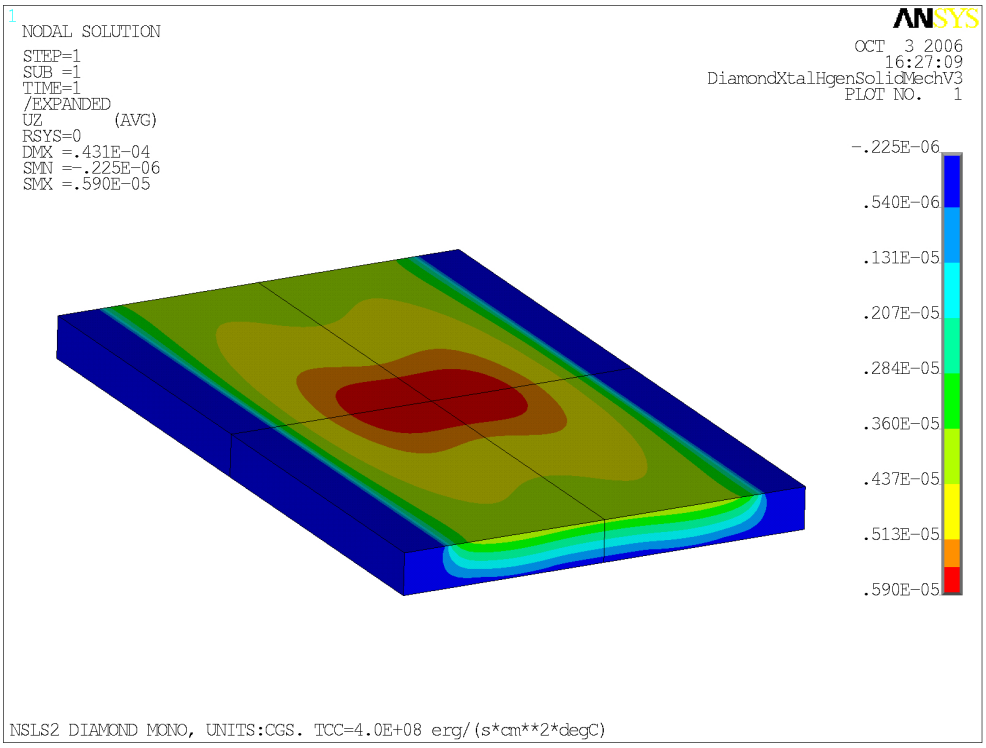

Figure 11.3.6 Calculated **thermal distortion profile** in diamond wafer assuming a 10 times larger heat transfer coefficient, compared to the distribution shown in Figure 11.3.4.

A concern with using diamond crystals is that their small size forces special attention to be paid to the mechanics of positioning the second crystal to center it in the diffracted beam as the monochromator angle is

scanned through its full range. Also, because of diamond's stiffness, its use as a crystal mounted in a sagittal bender that can be curved is rather doubtful.

11.3.2 Focusing Mirror

Many NSLS-II beamlines will use grazing incidence total reflection mirrors to focus the beam in a meridional geometry, with the mirrors used in a monochromatic beam (i.e., downstream of a monochromator). By combining two such mirrors in succession, one to focus the beam horizontally and the other vertically, a low-aberration KB focusing mirror pair configuration is achieved. The low emittance of NSLS-II results in undulator beams of small enough cross-section that KB mirrors with a length shorter than 1 m for horizontal focusing and 0.5 m for vertical focusing could be used. Many commercial versions of such mirrors are available.

To achieve the proper curvature radius (usually several hundred m to a few kilometers) to focus the beam, these mirrors (which are ground and polished flat) are mounted in a bender, that can shape the mirror into a cylindrical or an elliptical cross-section. An example of such a mirror bender system is shown in Figure 11.3.7; this is the focusing mirror system that will be installed on NSLS beamline X25 in the near future. It contains several actuators to orient the mirror and bend it into a cylindrical or an elliptical shape. This particular mirror has a glass substrate and is coated with two different materials, silicon and palladium (each providing a different upper-energy cutoff); other substrates commonly used are silicon and Glidcop, the latter usually for use in a white beam (in which case the mirror is cooled). Either one or the other coating is positioned in the beam at a given time. To realize a KB mirror configuration, two of these in succession are needed, one turned sideways.

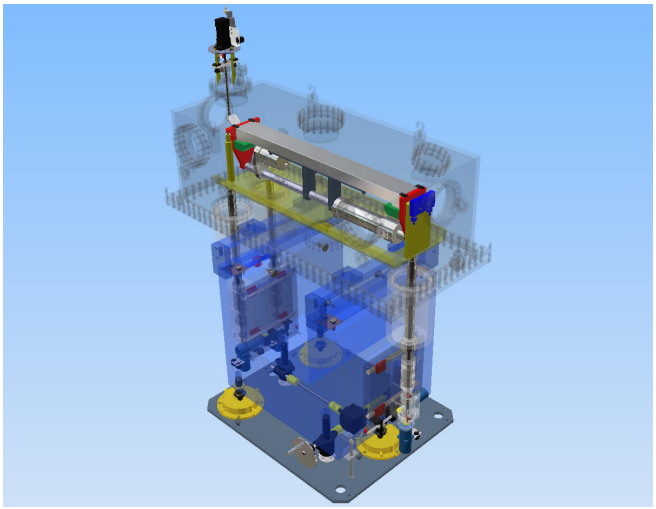

Figure 11.3.7 Focusing mirror system to be installed in the current NSLS beamline X25.

An alternative means of shaping mirrors employs electromechanical methods with segmented bimorph mirrors, where each segment is composed of oppositely biased piezoelectric ceramic plates that are surrounded by polished glass. These mirrors can bend concavely or convexly and be programmed into practically any arbitrary shape. They thereby nullify intrinsic figure errors, to a certain extent, while achieving the desired curvature, through application of an appropriate combination of voltages to the piezoelectric plate electrodes [11.3.7]. These mirror systems also are available commercially, though they tend to be more expensive than conventional, mechanically bent mirrors.

The mirror parameter that will ultimately determine its performance in an NSLS-II beam is figure error. The sensitivity of the performance of an NSLS-II undulator beamline to the figure error is demonstrated in Table 11.3.1. The current mirror figure error, for state-of-the-art mirrors of the size needed for NSLS-II, is ~2 μrad, and there have been recent reports of even smaller figure errors for mirrors of this size; for example, a

figure error of 0.8 μrad was reported for a mirror 78 cm long installed on beamline ID23-1 at ESRF [11.3.8]. In Table 11.3.1, values for the perfect mirror (zero figure error) are shown for comparison, along with intermediate values. The impact of mirror figure error on the performance of the beamline is very clear, particularly in the vertical direction. As discussed in Chapter 12, we have identified challenges and steps that might be taken to achieve sub-100 nrad figure errors in mirror substrates.

Table 11.3.1 NSLS-II Undulator-Based X-Ray Beamline Performance vs. Mirror Figure Error. The red (upper text line in each pair) signifies the "high" demagnification mode for this beamline, and the blue (lower text line) signifies the "low" demagnification mode.

RMS figure error [μrad]	0	0.1	0.5	1.0	2.0
Vertical focus size FWHM [μm]	1.0	2.6	11.8	23.5	47.0
	2.4	6.1	28.3	56.5	112.8
Horizontal focus size FWHM [μm]	15.5	15.8	21.0	32.2	58.5
	33.6	34.2	45.4	69.7	126.7
Monochromatic intensity at 12 keV [ph/s/μm^2]	1.0×10^{13}	4.5×10^{12}	7.9×10^{11}	2.7×10^{11}	7.7×10^{10}
	2.0×10^{12}	8.6×10^{11}	1.5×10^{11}	5.2×10^{10}	1.5×10^{10}

Note: FWHM = Full Width at Half Maximum

11.3.3 Beam Position Monitors

This section addresses beam position monitors that will be used in beamlines for monitoring and stabilizing the position of the monochromatic beam downstream of beamline optics.

A number of beam position monitor designs exist and are in current use, and all of them merit careful attention for use in the NSLS-II beamlines. Commercial versions of these are available. Blade-type monitors have insulated metal blades that graze opposite edges of the beam, and the induced photocurrents in the blades are measured and compared; this indicates the beam position between the blades. This design is intended for use in front ends and could also be used in beamlines. An advantage of this design is that the position monitor material does not intercept the central portion of the beam, which is eventually used in the experimental station. For this reason, blade-type monitors are a good choice for use with VUV or soft x-ray beams. One potential disadvantage of this type is that, because the fringes of the beam are measured, the induced signals in the blades can be very weak, and because the fringes themselves can be diffuse, the position resolution for this design may be modest (up to several μm). When blade-type monitors are used in front ends, as proposed for NSLS-II, the signal is very strong because of the presence of white beam; therefore, this drawback does not apply. Another disadvantage of this design, when used in the downstream sections of beamlines, is that beam-defining slits may be placed upstream of the position monitor, and the slits may decrease the beam dimension to the point where its fringes are not intercepted by the monitor blades. This results in no signal (and therefore no information) from the monitor.

Other beam position monitor designs derive their signals from the entire beam rather than from the fringes. One design, due to R. Alkire [11.3.9]. determines the beam position horizontally and vertically by comparing the doses of radiation scattered from a thin foil placed in the beam path, measured by four PIN diodes placed at 90˚ intervals around the beam. Since the entire beam contributes to the signals, they can be rather strong, and from their relative strengths a determination of the true center-of-mass of the beam can be made. The position resolution of this design is 1–2 μm. This design can be used in the vacuum of the beamline or in the atmosphere of the hutch.

Another design that derives its signal from the entire beam is a split ionization chamber, in which the collector electrode consists of two halves positioned symmetrically relative to the beam centerline. The difference in collector currents measured by these electrodes is due to the position of the beam relative to the electrodes (i.e., the electrode that overlaps more of the beam path will show a higher signal). As in the case of

the quadrant PIN diode monitor described above, the generated signals in this design can be rather strong, and the true center-of-mass of the beam can be determined (two orthogonal pairs of electrodes must be used to determine the beam position in both directions); a similar position resolution for this design of 1–2 μm is obtainable. Because this is a gas-based design, it cannot be used in the vacuum of the beamline, unless it is surrounded by windows.

We envision that NSLS-II beamlines will incorporate two beam position monitors, one placed just downstream of the optical system and the second placed in the hutch. Aside from their use in diagnosing the beam position, they can also be used for stabilizing the beam position, when included in feedback loops in which actuators that adjust the pitch or roll of optical components (such as mirrors, monochromator crystals or gratings) are employed. We anticipate that a position resolution of 1 μm or better will be necessary for many applications. NSLS-II will work with vendors to achieve such resolution. There is no inherent limitation in reaching such resolutions, and it is not expected that R+D on the part of NSLS-II will be required to achieve this.

11.3.4 Other Standard X-Ray Beamline Components

Other standard x-ray beamline components include filters, slits, and shutters. Some commercial versions of these are available, but normally these components are custom manufactured to suit local needs.

Filters can be used to attenuate the low-energy portion of the NSLS-II undulator (or wiggler) spectra, thereby reducing the power load on beamline components. Most existing filters are based on very thin layers of pyrolytic graphite, arranged in a stack in such a way that each filter absorbs a particular amount of power. The power is predominantly thermally radiated away by each graphite layer, from both of its surfaces, as the graphite gets very hot. NSLS beamlines X17, X21, and X25 use such filters to reduce the incident power by as much as 60–70%. We will investigate the efficacy of using graphite filters in NSLS-II insertion device beams.

An alternative choice of filter material is CVD diamond, which can also be used as a vacuum window material [11.3.10] (note that this does not have to be of diffraction quality, as was the case for monochromator crystals discussed above). We considered earlier the use of a diamond window, 100 μm thick, just upstream of a monochromator, in conjunction with the 14 mm period superconducting undulator operating at its highest K value, 2.2. In this circumstance, the window absorbs 16% of the power (64 W) within the 4σ beam dimension of the fifth harmonic of the undulator (2.4 mm wide × 1.5 mm high). The temperature and stress distributions in the window material and the copper mount were modeled using finite element analysis. The maximum temperature in the diamond is 133ºC and the maximum von Mises stress is 553 MPa, well within the tensile strength for diamond of >1200 MPa. Thus, this is an excellent choice of window and filter material for an NSLS-II superconducting undulator beamline.

Motorized slits that are used to define the beam dimension are now very standard components of beamlines and are available either as independently adjusted jaws or as apertures of fixed widths (horizontally or vertically) that can be positioned anywhere in the beam. Often the preference for which kind to use is beamline specific. Normally, slits are located in multiple positions along the beamline. It is prudent to place slits between successive optical components, as well as near the downstream end of the beamline. Commercial versions are available.

Every NSLS-II beamline that has a monochromator will have at least one pneumatically actuated photon shutter placed downstream, designed for the monochromatic beam properties for that particular beamline. Shutter designs will vary in width to meet the needs of individual beamlines, and in shutter material and shielding to handle the radiation spectrum that the shutter will confront. Whereas copper might be acceptable as a shutter material if only synchrotron radiation must be stopped, heavier materials such as Heavimet tungsten alloy would have to be considered if bremsstrahlung radiation must also be stopped. The prospect of redundant photon shutters to stop a monochromatic beam, rather than one shutter, will also be explored.

References

[11.3.1] For example, A. Chumakov, R. Rüffer, O. Leupold, J.-P. Celse, K. Martel, M. Rossat, and W.-K. Lee, *J. Sync. Rad.* **11**, 132 (2004).

[11.3.2] I. Ivanov, G. Rosenbaum, J. Chrzas, R. Fischetti, C.U. Segre, and L.D. Chapman, *Synchrotron Radiation Instrumentation Eleventh US National Conference,* AIP Conference Proceedings 521, edited by P. Pianetta, J. Arthur and S. Brennan, pp. 271–275. New York: American Institute of Physics (2000).

[11.3.3] See Figure 2 of L.E. Berman, *Rev. Sci. Instr.* **66**, 2041 (1995).

[11.3.4] J. Härtwig, private communication, 2006.

[11.3.5] R.C. Blasdell, L.A. Assoufid, and D.M. Mills, ANL/APS Technical Bulletin 24 [1995].

[11.3.6] A. M. Khounsary, R. K. Smither, and S. Davey, ANL/APS LS Note 215, 1993.

[11.3.7] R. Signorato and T. Ishikawa, R&D on third-generation and multi-segmented piezoelectric bimorph mirror substrates at SPring-8, *Nucl. Instr. & Meth. in Phys. Res. A* (467-468), 271-274, 2001.

[11.3.8] D. Nurizzo et al., *J. Sync. Rad.* **13**, 227 (2006).

[11.3.9] R.W. Alkire, G. Rosenbaum, and G. Evans, *J. Sync. Rad.* **7**, 61 (2000).

[11.3.10] H. Blumer, et al. in *Proceedings of the MEDSI06 Workshop*, to be published.

11.4 A Hard X-Ray Nanoprobe Beamline

A hard x-ray nanoprobe beamline would be designed and optimized to enable the production and use of a beam of hard x–ray photons with a minimum beam size in the nanometer range. As such, it would be a world-leading instrument, enabling spatially resolved versions of many powerful structural and spectroscopic x-ray techniques with unprecedented resolution. In particular, it would allow the study of nanomaterials which today play important roles in many diverse scientific fields. This beamline would take maximum advantage of the low emittance beam provided by the NSLS-II lattice. Figure 11.4.1 shows the conceptual layout.

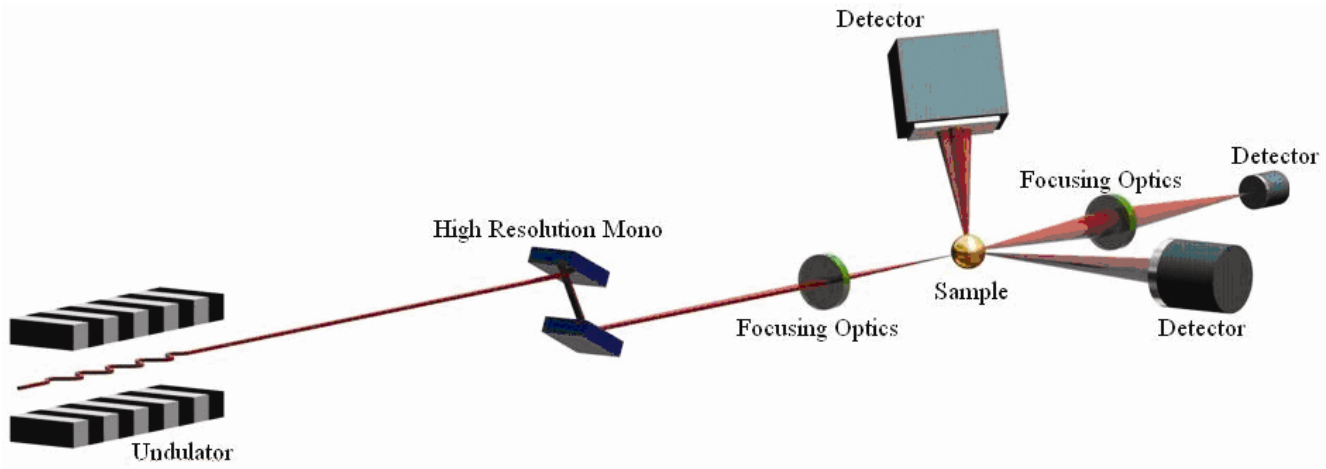

Figure 11.4.1 Conceptual layout of a nanoprobe beamline showing both scanning mode and full-field capability.

The primary experimental techniques for this beamline would likely be scanning nanobeam techniques, but it would also have a limited full-field capability. The limited full-field capability would assist in rapidly locating areas of interest, and would thus allow more efficient use of beam time. For the scanning probe techniques, there are a variety of contrast mechanisms that allow one to extract useful information from the

real-space mapping of a sample. For example, one can spatially resolve the density, elemental composition, crystallographic phase, strain, texture, chemical state, local atomic environment, and magnetization. To access all these aspects of a sample one would need to operate in a number of modes, each of which would place different requirements on the detectors.

First, with a fluorescence detector, one can use fluorescence from the sample to reveal the spatial distribution of individual elements. Second, using a large-area, low-spatial resolution high-sensitivity detector, such as a CCD, one can use diffraction to obtain a spatial map of selected Fourier components of a crystallographic phase, and also a spatial map of the local strain. Third, by scanning the incident photon energy, it is possible to access a number of spectroscopic quantities, such as the local environment from EXAFS and the local chemical state from XANES. Finally, from the back-scattered Compton scattering, one can measure the electron density. This will be especially useful for light elements such as carbon.

11.4.1 Example Experiment on a CNT Device

In Chapter 3, the practicality of carrying out a diffraction experiment on a single carbon nanotube was explored. Here, we outline a procedure that a researcher might follow for such an experiment as a way of illustrating some of the requirements for the nanoprobe beamline. As a first step, when a user brings a sample to the beamline, the local laboratory facilities would be used to align the sample, using a simple optical microscope, onto a sample mount that is pre-aligned with respect to the nanoprobe instrument. Optically aligning the sample on this special mount within a 100-micron sized cube ensures that the sample will be within 100 microns of the x-ray beam when placed in the nanoprobe instrument.

Next, the mounted sample stage is taken through the sample interlock, which keeps the experimental temperature constant within a tight range. Active vibration isolation is turned off. The sample is placed in the instrument mount, device leads are tested, and active vibration isolation is turned back on.

The x-ray beam is turned on and the instrument is brought into full-field mode, with only the low-resolution monochromator inserted. A comparison is made between the optical image and the x-ray full-field image. Next, the high-resolution monochromator is inserted and the instrument is switched to high resolution scanning nanobeam mode. A low-resolution fluorescent scan identifies the metal source and drain contacts, from which the location of the nanotube can be estimated. A high-resolution scan is now performed in this general area to monitor Compton backscattering, and the extra density due to the CNT is observed. With the beam focused on the nanotube, diffraction features characteristic of the nanotube are looked for in the diffraction detector. If none are found, even after an energy scan, the sample is rotated slightly and the alignment procedure repeated. Note that even small rotations can significantly displace the sample at these resolutions.

Once an orientation is found with the beam on the nanotube and a diffraction feature on the diffraction detector, then, since the nanotube is fairly rigid and the diffraction feature is quite broad, it should be possible to scan the sample from source to drain region while continuously monitoring the nanotube diffraction. The nanotube device would then be turned on and the sample scanned again while current is being passed. For this device, infrared photons would be emitted in the central region and a strain difference in the CNT lattice would be observed in the diffraction pattern, consistent with a 100K rise in temperature of that part of the nanotube.

The experiment described above utilizes many of the features the beamline and end stations that are expected to be made available to the user. One important aspect that is not covered by this example is the requirement for EXAFS/XANES capabilities, but other types of samples would require such techniques and they will therefore be implemented.

11.4.2 General Optical Concepts

For scanning mode applications, three optical concepts, referred to as **direct**, **mirror**, and **waveguide** mode, are considered here for achieving a nanometer-size focal spot at the sample position. In addition, a full-field transmission mode with absorption and phase contrast imaging will be implemented to gain an overview of a larger area ($10 \times 10\ \mu m^2$) of the sample before zooming in on smaller features of interest.

Direct and mirror concepts rely on selecting the coherent portion of radiation from the x-ray source and using it to illuminate a high-resolution diffractive/refractive focusing optics, based on Fresnel zone plates, multi-layer Laue lenses, or kinoform lenses. The difference is in the power management of the incident white beam coming from the undulator source, which in the first case will be accomplished by an absorptive filter and in the second case by a mirror.

For both concepts the length of the optical path, and with it the overall length of the beamline, are directly related to the demagnification of the primary source to the final nanometer size focal spot, and the "working distance" between the focusing optics and the sample. An important class of experiments to be conducted on the nanoprobe beamline will involve the detection of radiation back-scattered from the sample, either fluorescence or Compton scattering. This requires an appropriately large solid angle with a substantial component along the optical axes and pointing back towards the focusing optics. Given the spatial extensions of both detectors and focusing optics, a working distance of 10 mm is targeted for this beamline to ensure that necessary instrumentation can be accommodated and practical experiments with back-scattering detection are feasible. Consequentially, an overall beamline length of approximately 100 m is desirable for a beamline operating in one of these modes, as described below.

The waveguide concept, if successful, would significantly reduce the required optical path length by employing a two-stage focusing scheme in combination with the generation of an intermediate diffraction-limited coherent source.

11.4.2.1 Direct Mode

The direct-mode is shown schematically in Figure 11.4.2. The guiding philosophy here is to have as few optical components along the beam path as possible, to preserve the transverse coherence of the beam as much as possible. In this concept a small aperture is placed as close to the primary source (undulator) as practically possible, restricting the beam horizontally to the size of the effective vertical coherent source size $S_{v,coh}$. Some technical design aspects for this "near-accelerator aperture" are presented in Section 11.4.3.6.

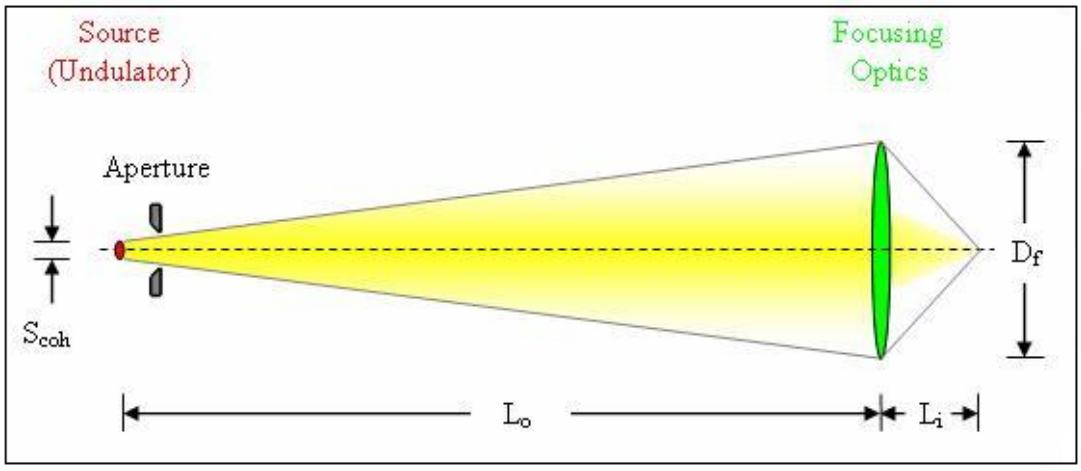

Figure 11.4.2 Direct mode. The coherent portion of the incident beam is selected by an aperture close to the x-ray source and illuminates the focusing optics of diameter D_f at a distance of L_o. The focal spot is located at a distance L_i from the optics.

In terms of the ordinary synchrotron radiation source parameters σ_{xy}, σ_r, and Σ_{xy}—which stand for the particle beam size , the photon beam size, and the size of the combined (effective) source extension—the vertical coherent source size $S_{v,coh}$ is given by

$$S_{v,coh} = \mathrm{FWHM}(\Sigma_y) = 2\sqrt{2\ln 2}\sqrt{\sigma_y^2 + \sigma_r^2} \ . \tag{11.4-1}$$

Thus a near-square, coherent source of dimensions $S_{v,coh} \times S_{v,coh}$ would be generated, which would illuminate the focusing optics placed at a distance L_o from the source. This distance L_o, in combination with the working distance L_i between the focusing optics and the sample, determines the required demagnification of

$$m = \frac{S_{v,coh}}{p} = \frac{L_o}{L_i} \ , \tag{11.4-2}$$

where p is the diameter of the focal spot, ultimately desired to be p = 1 nm.

The diameter D_f of the high-resolution focusing optics should match the transverse coherence length L_T of the incident beam at the position Lo, which is given by

$$D_f = L_T = \frac{\lambda}{2}\frac{L_o}{S_{v,coh}} \ . \tag{11.4-3}$$

Using source parameters for the NSLS-II storage ring in conjunction with one 3 m U19 cryo-cooled permanent-magnet undulator, together with the targeted working distance of 10 mm, the following practical parameters emerge for the direct mode at an x-ray wave length of 1 Å:

Table 11.4.1 Practical Parameters for Direct Scanning Mode, Wavelength 1 Å.

Parameter	Symbol	Value
Horizontal particle beam size	σ_x	38.61 μm
Vertical particle beam size	σ_y	1.62 μm
Photon beam size (λ=1 Å)	σ_r	1.38 μm
Effective coherent vertical source size	$S_{v,coh}$	5.00 μm
Required demagnification	m	5009
Required working distance	L_i	10 mm
Source ↔ optics distance	L_o	50.1 m
Diameter of optics (λ=1 Å)	D	500 μm

The direct mode introduced so far does not include any power management of the incident beam. With the exceptional brightness of the new NSLS-II storage ring, local power densities along the beam path are expected to be large enough to significantly distort optical components and thereby diminish the coherence of the beam. To mitigate these adverse effects, a (high-pass) filter can be inserted into the incident beam to remove unwanted power associated with the lower part of the energy spectrum. This modification is shown in Figure 11.4.3. In the design of the filter, care must be taken to preserve the coherence. A suitable filter material might be highly polished, synthetic or CVD diamond, sufficiently cooled to prevent lattice distortions.

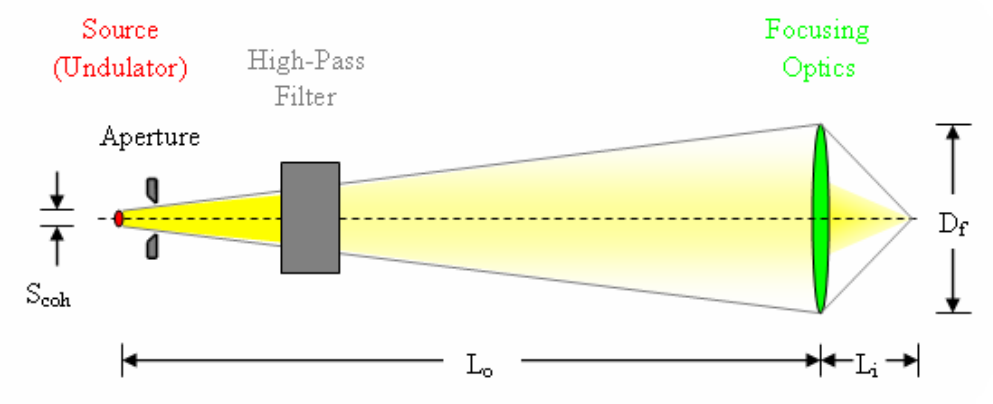

Figure 11.4.3 Modification of the direct mode concept. A high-pass filter in the incident beam reduces the power loading of successive components by removing power associated with the low-energy part of the spectrum.

11.4.2.2 Mirror Mode

An alternative concept to the direct mode, referred to as mirror mode, involves the use of a horizontal mirror system as the power moderating component. In combination with an exit aperture it can act as a spatial filter for the horizontal component of the beam, thereby generating a secondary coherent source downstream of the mirror system which is independent of coherence-diminishing components upstream of it. This concept is shown schematically in Figure 11.4.4. An additional advantage of using a mirror system is to increase the (incoherent) flux due to the larger horizontal acceptance, which is useful for the full-field imaging mode that will be used on the beamline. The disadvantages are, that the total length of the beamline is increased substantially by the distance L_p between the primary and the secondary source and that the coherence associated with the vertical portion of the beam might be adversely affected by figure errors of the mirrors. While the mirror mode constitutes a viable alternative, higher priority will be given to implementing the direct mode for its simplicity and fewer components that could diminish the coherence of the beam.

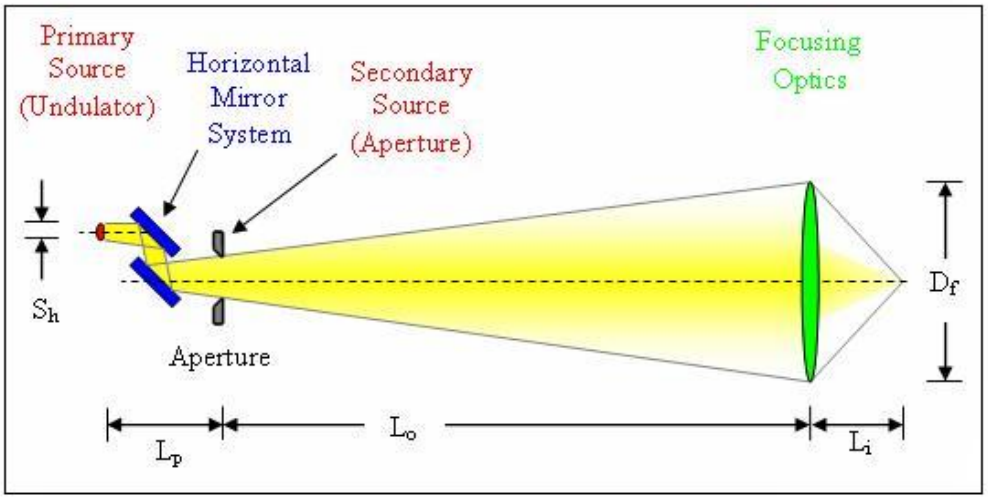

Figure 11.4.4 Mirror mode. A horizontal mirror system in combination with an aperture acts as a spatial filter, generating a secondary coherent source.

11.4.2.3 Waveguide Mode

A novel composite concept, referred to as the waveguide mode, is also being considered. If successful, it promises the advantage of a significant reduction in the required distance between source and experiment, thus allowing for a much shorter beamline to achieve nanometer-size focusing than in the conventional case. Briefly, it involves a two-stage demagnification of the primary source to the final spot size, combined with the generation of a diffraction-limited, coherent secondary source by virtue of an x-ray waveguide. The schematic layout is shown in Figure 11.4.5.

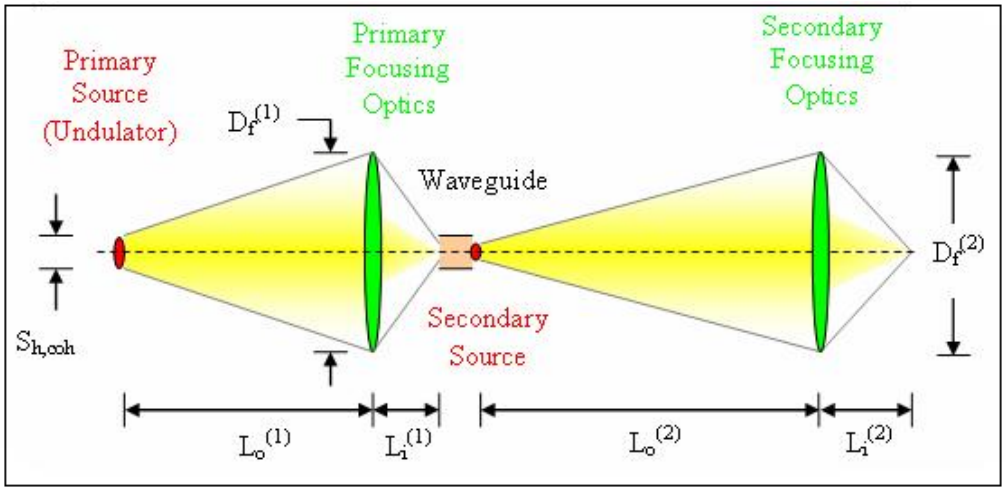

Figure 11.4.5 Waveguide mode. A final nm size focus is achieved by a two-stage demagnification of the primary source; an x-ray waveguide generates an intermediate diffraction-limited, coherent secondary source.

Besides reducing overall length, this system offers the additional advantage that the secondary source isolates the downstream optics from a loss of coherence or vibrational disturbances in the upstream section. In the waveguide mode, the primary focusing optics accepts the full horizontal coherent source size $S_{h,coh}$, given by

$$S_{h,coh} = \mathrm{FWHM}(\Sigma_h) = 2\sqrt{2\ln 2}\sqrt{\sigma_h^2 + \sigma_r^2} \ , \tag{11.4-4}$$

and generates a focal spot of about 50 nm, appropriate to be accepted by the succeeding x-ray wave guide. The demagnification of this stage is determined by

$$m^{(1)} = \frac{S_{h,coh}}{p^{(1)}} = \frac{L_o^{(1)}}{L_i^{(1)}} \ , \tag{11.4-5}$$

where $p^{(1)} \sim 50$ nm is the diameter of the focal spot. The succeeding x-ray waveguide effectively collimates the radiation emanating from this focus, generating a diffraction-limited coherent secondary source which can be further demagnified to the final desired spot size by the second stage.

The diameter of the first stage optics is determined by the transverse coherence length at the position of the focusing element:

$$D_f^{(1)} = L_T = \frac{\lambda}{2}\frac{L_o^{(1)}}{S_{coh}} \ . \tag{11.4-6}$$

Due to the asymmetric source size, the coherence length in the vertical direction is an order of magnitude larger than its counterpart in the horizontal direction, thus $D_f^{(1)}$ is chosen to match the vertical coherent source size $S_{v,coh}$. Furthermore, although the full horizontal source size may be accepted, only a small central portion of it will contribute to the effective coherent photon flux through the focusing optics.

The second stage focusing optics demagnifies the intermediate secondary source generated at the exit of the x-ray waveguide to the desired final nanometer-size focal spot. The required demagnification is

$$m^{(2)} = \frac{p^{(1)}}{p^{(2)}} = \frac{L_o^{(2)}}{L_i^{(2)}} \ , \tag{11.4-7}$$

where $p^{(2)}$ is the diameter of the ultimate focal spot, desired to be p = 1 nm.

Requiring an appropriate working distance of ~10 mm behind the second-stage Fresnel zone plate to perform practical nano probe experiments, the distance $L_o^{(2)}$ between secondary source and optics is $L_o^{(2)} = m^{(2)} L_i^{(2)}$ and the diameter of this optics is

$$D_f^{(2)} = L_T = \frac{\lambda}{2}\frac{L_o^{(2)}}{p^{(1)}} \ . \tag{11.4-8}$$

A practical set of parameters to realize this optical scheme at NSLS-II is given in Table 11.4.2.

Table 11.4.2 Practical Parameters for the Waveguide Scanning Mode.

Parameter	Symbol	Value
Effective coherent vertical source size [μm]	$S_{v,coh}$	5.00
Effective coherent horizontal source size [μm]	$S_{h,coh}$	91.0
Required first-stage demagnification	$m^{(1)}$	1820
Suggested first-stage working distance [mm]	$L_i^{(1)}$	25
First-stage source ↔ optics distance [m]	$L_o^{(1)}$	45.5
Diameter of first-stage optics (λ=1 Å) [μm]	$D_f^{(1)}$	455
Required second-stage demagnification	$m^{(2)}$	50
Required second-stage working distance [mm]	$L_i^{(2)}$	10
Second-stage source ↔ optics distance [m]	$L_o^{(2)}$	0.5
Diameter of second-stage optics (λ=1 Å) [μm]	$D_f^{(2)}$	500

11.4.2.4 Full-Field Transmission Mode

The full-field transmission mode will be utilized to gain an overview of a larger sample area before concentrating on smaller features with the scanning focusing mode. The optical concept for the full-field mode is shown in Figure 11.4.6.

A large condenser zone plate illuminates the sample uniformly over a micrometer-sized area. The diameter of the condenser is chosen to accept a large fraction of the incident undulator radiation. Photons transmitted through the sample are imaged onto an area detector by means of an objective zone plate. Depending on the nature of the sample, both absorption and phase contrast generation can be used to optimize the image.

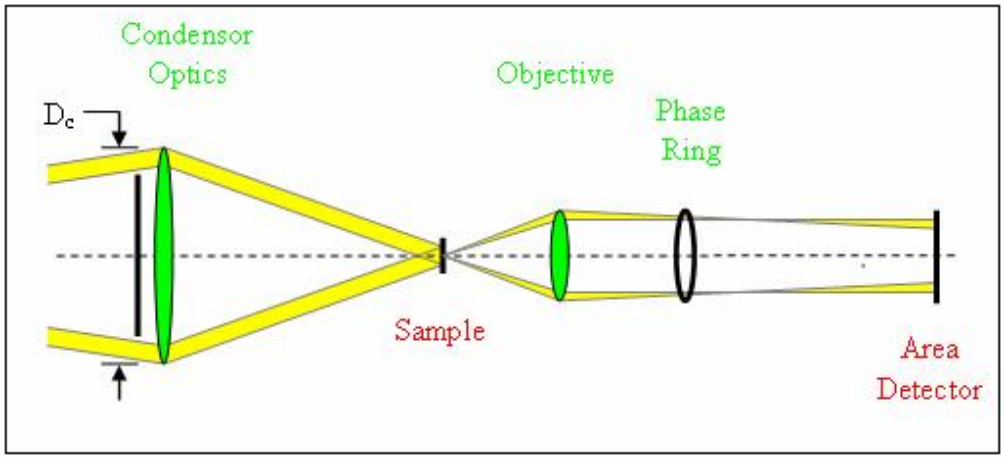

Figure 11.4.6 Full-field transmission mode. A condenser optics illuminates the sample. Transmitted photons are imaged onto an area detector by means of an objective zone plate.

11.4.2.5 Spatial Resolution and Monochromaticity

To achieve nanometer size spatial resolution, a minimum degree of monochromaticity of the x-ray beam incident on the focusing optics is required. In the following argument, Fresnel zone plates are specifically considered, however, similar arguments with similar results hold true for the other optical elements that might be employed in the high-resolution focusing optics.

For a Fresnel zone plate having a total number of zones N, the monochromaticity needs to be better than N^{-1}:

$$\frac{\Delta E}{E} = \frac{\Delta \lambda}{\lambda} \le \frac{1}{N}, \tag{11.4-9}$$

where for a desired focal length (working distance) L_i and an outer zone width, Δr_n, at a particular wave length λ, the required number of zones is given by

$$N = \frac{\lambda L_i}{4\Delta r_N^2}. \tag{11.4-10}$$

By virtue of the Rayleigh criterion, $1.22\ \Delta r_n = 1$ nm. The desired working distance is 10 mm. Therefore the number of zones is of the order of $N \sim 3.8 \times 10^5$ and the associated monochromaticity is

$$\frac{\Delta E}{E} \approx 2.6 \times 10^{-6}, \tag{11.4-11}$$

or approximately 30 meV at 12.4 keV ($\lambda = 1$ Å). In addition to this very high degree of monochromaticity required for extreme focusing, the incident beam divergence has to be preserved by the monochromator, since it was already tailored to fit the high-resolution optics. A monochromator arrangement that can satisfy both conditions is a nondispersive, symmetric, double-crystal combination, using higher-order reflections in near-backscattering geometry. This monochromator concept is further explained below.

11.4.2.6 Choosing Beta for High-Spatial Resolution Optics

The following analysis [11.4.3] shows how beta can be optimized for the maximum coherent flux from an undulator. By definition, for the electron beam the electron source size and angular divergence depend on emittance and beta, as follows:

$$\sigma_y = \sqrt{\varepsilon_y \beta_y} \text{ and } \sigma'_y = \sqrt{\frac{\varepsilon_y}{\beta_y}}. \tag{11.4-12}$$

Substituting these into the expression for effective photon emittance, we find that

$$\overline{\varepsilon_y} = \sqrt{\varepsilon_y \beta_y + \sigma_{ph}^{\ 2}} \sqrt{\frac{\varepsilon_y}{\beta_y} + \sigma'^{\ 2}_{ph}}. \tag{11.4-13}$$

As discussed above, the coherent flux, which is important for zone plate focusing, is proportional to $1/\overline{\varepsilon}$. We thus differentiate with respect to beta to find the extremum:

$$\beta_y = \frac{\sigma_{ph}}{\sigma'_{ph}} = \frac{L}{2\pi}. \tag{11.4-14}$$

For a 3 m undulator, the optimum beta for a zone-plate-based line is independent of wavelength and is 0.5 m.

For asymmetric focusing elements (e.g., KB mirrors or crossed cylindrical refractive lenses), one might assume that the optimum beta function value is not well determined in the nonfocusing direction for a given optic. That is, if one of these optics is focusing in the vertical plane, one might assume that the best beta value in the horizontal would be large, to maximize the acceptance of a given-sized optical element. However, it is likely that off-axis aberrations will couple horizontal source size into vertical image size, leading to the conclusion that source size, not divergence, should be optimized in both directions.

On the basis of these considerations, we chose a small beta, to minimize source size.

11.4.2.7 Consequences of Depth of Focus and Chromatic Optics

The depth of focus, DOF, is given by $\lambda/(\mathrm{NA})^2$. If one defines the optic resolution $\Delta = \lambda/\mathrm{NA}$, then DOF = Δ^2/λ. For a dispersive optic, this puts a constraint on the incident bandwidth of photons in order to not broaden the focus significantly. While solid metal mirrors are non-dispersive, it is not likely that they will reach 1 nm. Many of the likely candidates are dispersive. An example is that of a zone plate, which has $f\lambda$ = constant. For this case, we find $df/f = d\lambda/\lambda = dE/E$. We plot this for a few cases to gain some insight (Figures 11.4.7.a and 11.4.7b.

Figure 11.4.7a shows required bandwidth versus resolution for λ = 0.1 nm (12.4 keV) and for three values of focal length 1 mm,10 mm, and 100 mm. For beamlines of typical length, a reasonable compromise between sufficient experimental working distance and the demagnification required to obtain 1 nm resolution is a focal length of order 10 mm. For this 10 mm focal length, one observes on the plot that a 1×10^{-6} bandwidth is required, significantly narrower than typically available at conventional beamlines. For comparison, a conventional Si(111) monochromator has a bandwidth of 1×10^{-4}. Figure 11.4.7a shows that one can only obtain a 10 nm spot size with this bandwidth. To improve the spatial resolution by one order of magnitude requires a reduction of two orders of magnitude in energy bandwidth.

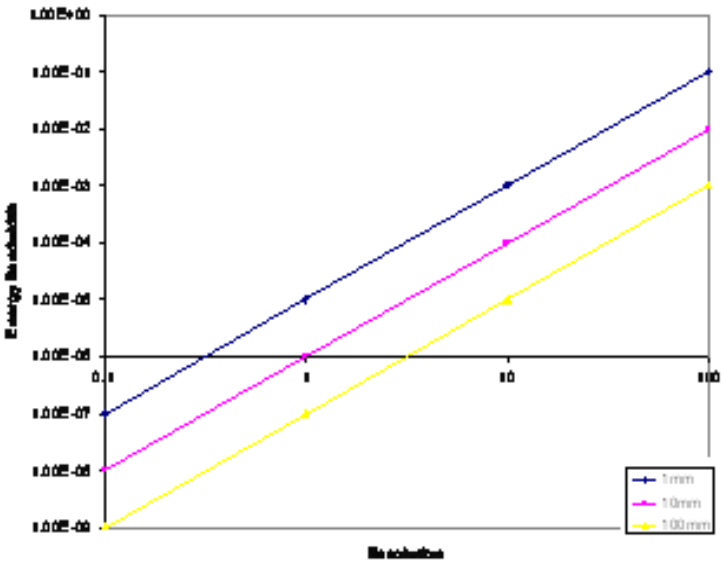

Figure 11.4.7a The energy bandwidth required to obtain a given resolution (in nm) for zone plates of three focal lengths (1 nm, 10 nm, and 100 nm).

Note that at higher energies, the energy bandwidth constraint relaxes. Unfortunately, we gain linearly with photon energy and lose quadratically with spatial resolution, as shown in Figure 11.4.9b, which plots the required energy bandwidth as a function of wavelength from 1.24 keV (λ = 1 nm) to 124 keV (λ = 0.01 nm), for three different resolutions (1 nm, 10 nm, and 100 nm) and for a focal length of 10 mm. One must also consider the energy dependence of the undulator spectrum. Even the relatively modest change from 12.4 keV to 24.8 keV results in a reduction in flux of an order of magnitude, with only a factor of two gained from the relaxed bandpass, thus resulting in a net loss of a factor of five.

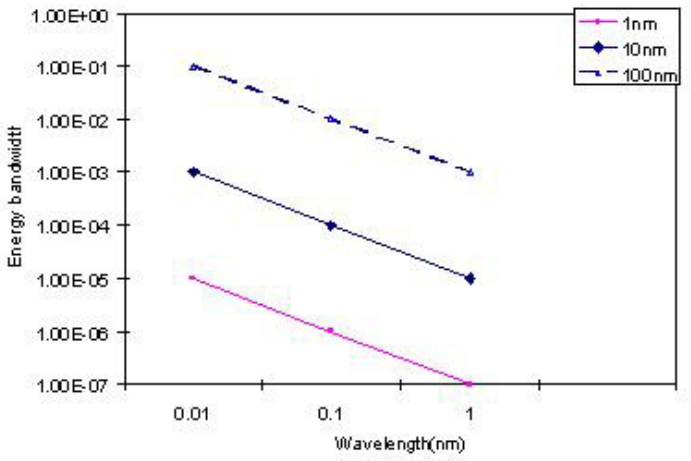

Figure 11.4.7b The energy bandwidth required to obtain various spatial resolutions (1 nm, squares; 10 nm, diamonds; 100 nm, triangles) as a function of photon wavelength.

For the solid refractive optic, the situation is worse by a factor of two in bandwidth. For such optics, $f\lambda^2$ is a constant, so $df/f = 2d\lambda/\lambda$, and all the arguments above can be replicated with an additional factor of two.

In summary, due to the dispersive nature of many of the optics we will consider, we must carefully tailor the bandwidth of incident photons. Due to the quadratic dependence of bandwidth on desired spatial resolution, a relative modest relaxation of resolution results in large reduction in the required bandwidth and hence a large gain in flux on the sample. At a resolution of 10 nm, and a reasonable focal length/working distance of 10 mm, one matches the bandwidth of conventional monochromators. A resolution of 1 nm will be best obtained by reducing the bandwidth, and consequently the flux, by two orders of magnitude relative to this situation.

11.4.2.8 Summary of Optical Concepts

The three optical concepts introduced above for the scanning focusing mode of the beamline (direct mode, mirror mode, and waveguide mode) have certain relative merits and disadvantages. Great advances have been made toward the design and manufacture of coherence-preserving x-ray optical components, such as monochromators, mirrors, and filters. However, in the context of extreme focusing to nanometer-size beams, the limitations for these devices and relative advantages or disadvantages of one component over another still have to be researched further. It is for this reason that, at this stage in the current beamline design, we aim at being able to accommodate all three concepts or combinations thereof, to take advantage of future technical achievements and to have the flexibility of substituting a more favorable component for an outdated or less favorable one.

R&D projects will be initiated or are already ongoing to remove some of the uncertainties regarding coherence preservation of specific components. At APS, for example, a nanoprobe beamline is currently being developed with spatial resolution down to 30 nm or better. Some of the optical components necessary to realize the concepts above will be implemented and tested at the new APS beamline. In particular, a horizontal mirror system and a high-heat load monochromator employed at this beamline are expected to yield a large amount of useful information on which to base further component designs for even better coherence characteristics and higher spatial resolution. Much research at many synchrotron radiation facilities around the world is currently being conducted regarding the use of synthetic or CVD-diamond windows in situations where coherence is an important factor. Calculations are being performed at NSLS-II to explore heat load characteristics of this material and whether new cooling concepts can enhance its coherence capabilities. These proceedings should yield important information helpful in designing a successful power filter appropriate for the brightness of NSLS-II.

The one parameter that has the largest design implications is the length of the optical path, since it determines the experimental locations and thereby the number and distribution of shielding enclosures. Table 11.4.3 lists approximate positions of the effective source and the final focus for the various concepts.

Table 11.4.3 Summary of Characteristics of the Four Modes.

Mode	Effective Source Type	Source Location	Location of Final (1 nm) Focal Spot
Direct	Vertical: Primary	0.0 m	50 m
	Horizontal: Secondary	15 m	
	Tertiary*	35 m	85 m
Modified Direct	Vertical: Primary	0.0 m	50 m
	Horizontal: Secondary	15 m	
	Tertiary*	35 m	85 m
Mirror	Secondary	35 m	85 m
Waveguide	Primary	m	47 m
	Secondary	46 m	

* Even in the direct modes the coherence might not be preserved sufficiently by all optical components. Then a beam-defining aperture downstream of the monochromator will become the effective (tertiary) source.

A shielding enclosure that houses all beam-conditioning components upstream of the 35 m mark (FOE) and two experimental enclosures at around 50 m and 85 m that house focusing optics, sample stages, and detectors, will accommodate all configurations mentioned above. In addition, the concept of having two experimental enclosures with a substantial distance between them allows a dramatic enhancement of phase contrast imaging, when the sample is located in the upstream station while the detector is located in the downstream station.

11.4.3 Nanoprobe Beamline Components

In designing a nanoprobe beamline, the primary effort is to preserve the coherence of the x-ray beam as it passes through the various beam-shaping and beam-controlling components and eventually reaches the sample in a diffraction-limited, nanometer-sized focal spot. At the same time, the photon flux available at the sample position needs to be maximized to ensure that practical experiments can be performed in a timely manner.

The beamline layout features three shielding enclosures, called the A, B, and C stations, as shown in Figure 11.4.8. Station A functions as a First Optics Enclosure, containing the interface to the accelerator, which consists of all beam-conditioning equipment such as slits, mirrors, monochromators, and photon shutters. Its terminal optical component is a beam-defining slit, which can act as a secondary/tertiary source in those optical concepts where coherence preservation of upstream components cannot be relied upon.

The B and C stations, located at around 50 m and 85 m, will house the actual focusing optics, the nanoprobe sample stages, and detectors. Each station can hold a complete set of focusing, sample, and detector optics, or both together can be used in combination to enhance imaging properties of a particular experimental setup. Initially, one set of instruments and detectors will be procured and configured to match a desired optics mode.

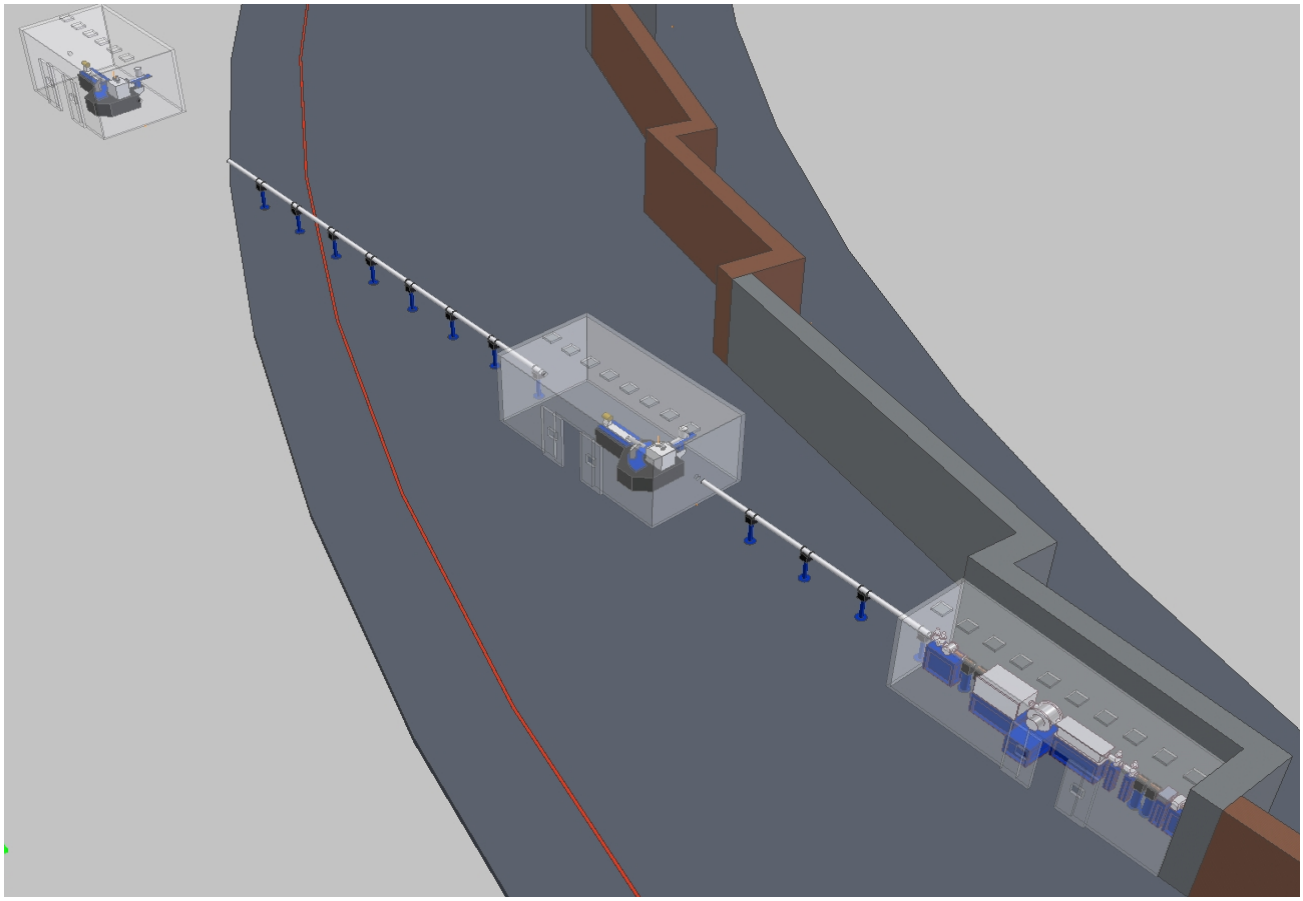

Figure 11.4.8 Overall layout of a hard x-ray nanoprobe beamline.

11.4.3.1 Source

Given the current status of the NSLS-II design, a nanoprobe beamline would be located on a low-β, 5 m straight section of the accelerator, employing one U19 cryogenically cooled permanent-magnet undulator.

The length of this device is presently 3 m. As discussed above, the relevant figure of merit for this beamline is source brightness. If it turns out, during the design phases of NSLS-II, that multiple U19 devices can be accommodated in a single straight, with low β, or SCU U14 devices, these will be the preferred option for this beamline.

11.4.3.2 Layout

The interface between the beamline and the accelerator would be "window-less." A differential pump assembly would largely isolate the beamline vacuum from the accelerator vacuum without the use of a window. A window could potentially diminish the coherence of the x-ray beam; thus, its elimination is one of the coherence-preserving measures. The differential pump assembly is the first component in the A station.

The second component in the FOE is a white beam slit with four slit blades that can be positioned independently around the incident beam. The WBS acts as a variable guard slit, reducing unwanted power and stray scattering into the downstream sections of the beamline, while providing differing aperture sizes to accommodate the various operating modes of the beamline, such as focusing and full-field imaging.

Power management of the very bright white beam generated by the NSLS-II accelerator will be accomplished by a filter assembly and/or a horizontal mirror system. Since the coherence-preserving properties of these two kinds of components are not very well established or characterized at this time, it is expected that they will be used either separately or in conjunction with each other to optimize overall performance for a particular operating mode of the beamline.

A combination of a high heat-load primary monochromator succeeded by a secondary monochromator will enable the selection of photon energy and energy band pass. The assembly is described in more detail below.

The monochromators are followed by a beam-defining slit system with four independent blades. In optical configurations where the coherence-preserving feature of upstream components cannot be relied upon, this slit system will serve as part of a spatial filter, generating a secondary coherent source.

The FOE is terminated by a photon shutter, which allows personnel access to the downstream experimental stations while the x-ray beam is present in the FOE. The FOE is connected to the B station, and the B station is connected to the C station by a beam transport system consisting of shielded beampipe and an in-line ion pump for every 5 m long section.

Instrumentation in the experimental stations consists of a nanoprobe instrument and a suite of transmission and back-scattering detectors.

11.4.3.3 Incident Power Filter

The modified direct mode described earlier relies on an absorptive filter in the incident beam to reduce power loads on the monochromator and focusing optics. To preserve the coherence of the beam, this filter needs to have highly polished, smooth entrance and exit surfaces. These surfaces need to be precisely parallel to each other, and the bulk needs to be perfectly uniform as far as the refraction of x-rays is concerned.

With its high heat conductivity and low thermal expansion, diamond is an attractive material for an incident power filter. Through recent technological advances in the manufacturing of synthetic diamonds, nearly perfect crystals have been grown with a surface roughness of less than 1 nm [11.4.3]. These diamonds are expected to be suitable for x-ray imaging situations where the preservation of coherence is critical. In addition, advances in the production of chemical vapor deposition diamonds might make this material a suitable alternative for coherence applications, although the overall crystalinity is inferior to the synthetic single-crystal diamonds.

Preliminary finite element analysis calculations have been performed to investigate the thermal distortion of diamond for beam conditions in the modified direct mode and using the U19 undulator as a source. Figure 11.4.9 shows a map of local nodal displacements over the copper crystal holder, the crystal, and the actual beam spot of 0.3×0.3 mm^2 (small square in the center) with the temperature held fixed at 20°C at the bottom of the copper block (water cooling). All incident power is assumed to be absorbed. The resulting total range of displacements (red ↔ blue) is about 100 nm.

Close inspection of the map shows that differential displacements within the central beam spot are smaller that 1 nm in this worst-case scenario, leading to only negligible optical phase shifts in the x-ray beam. Thus, coherence of the beam is not expected to be substantially affected.

Further calculation must be performed to study the spectral behavior of a diamond filter of this kind in the context of the particular undulator spectrum. However, the concept appears promising for general use as coherence-preserving power filter and x-ray window.

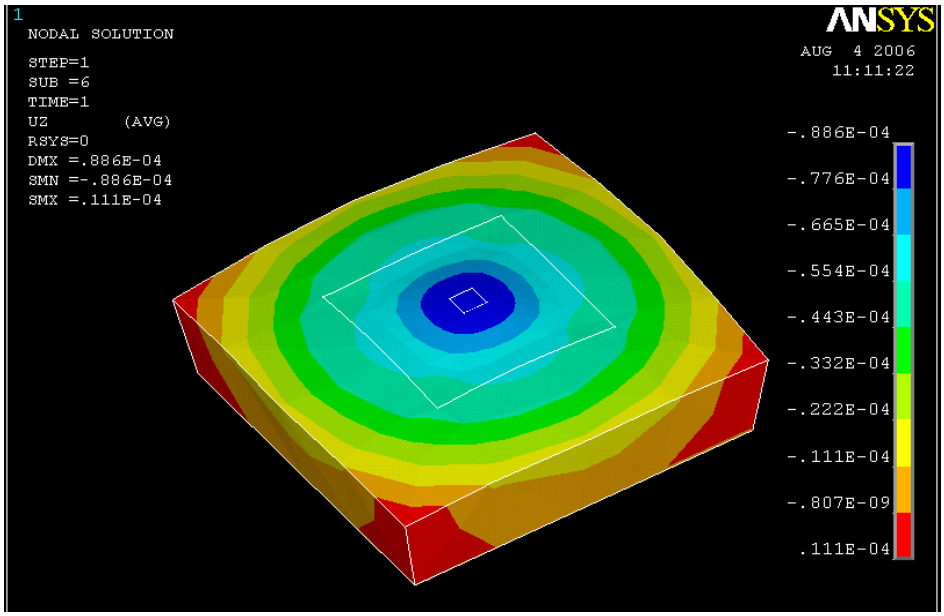

Figure 11.4.9 Contour plot of the nodal displacement along the x-ray beam direction (in mm). The small square in the center marks the extent of the beam; the medium square is the extent of the diamond crystal.

11.4.3.4 Monochromators for a Nanoprobe Beamline

To achieve nanometer-size beams at the desired working distance, the x-ray energy band pass ΔE/E for a nanoprobe beamline needs to be matched to the diffractive focusing optics, as discussed previously. In particular,

$$\cot\Theta_B \Delta\Theta = \frac{\Delta E}{E} = \frac{\Delta\lambda}{\lambda} \le \frac{1}{N} = \frac{4\Delta r_n^2}{L_i}\frac{E}{hc} \qquad (11.4\text{-}15)$$

where Θ_B is the Bragg angle, $\Delta\Theta$ is the incident divergence, N and Δr_n are the number of zones and the outer zone width, and L_i is the working distance between focusing optics and sample. At the same time, the divergence of the incident beam $\Delta\Theta$, already chosen to fit the geometry of the focusing optics, needs to be preserved by the monochromator. A single-stage, double-crystal monochromator arrangement in near back-scattering geometry satisfies both conditions. This arrangement is shown schematically in Figure 11.4.10.

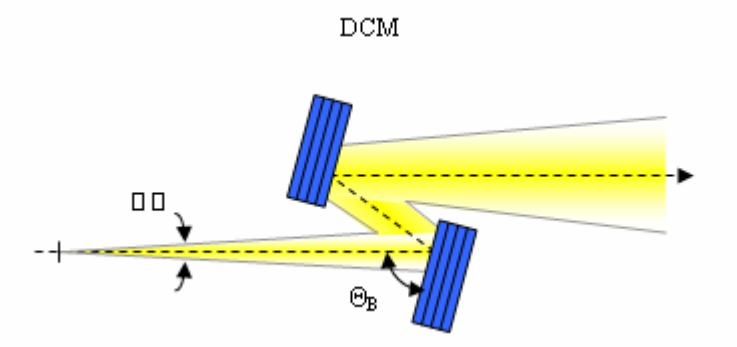

Figure 11.4.10 Basic geometry of the double-crystal monochromator, DCM. The incident divergence is preserved in traversing the monochromator. Near back scattering geometry is necessary to achieve the required energy band pass.

For their favorable thermal and absorptive qualities, water-cooled, symmetric diamond (111) crystals are envisioned for this monochromator, with the sequence of (333), (444), and (555) higher-order reflections providing the reduced band pass and energy scan flexibility. Nevertheless, due to the dependence of the energy band pass on the square of the outer zone width, extreme focusing down to 1 nm can only be achieved for discrete energies, while, with a slight relaxation of the beam size requirement to 2 nm, an extended energy range can be accessed with a single reflection at large working distance. This is indicated in Figures 11.4.11a and 11.4.11b. Here the straight lines indicate maximum band pass boundaries at particular working distances, which cannot be exceeded. The curved lines are actual band pass values generated by the DCM employing a particular reflection and allowing the incident divergence as required by the optical concepts. Where these curved lines dip below a boundary line, focusing to the desired beam size becomes possible.

In the case of a 1 nm beam, three reflections (333, 444, and 555) are necessary to cover an extended but interrupted energy range between 9 keV and 26 keV at a reduced working distance of 4 mm (Figure 11.4.11a). For a slightly larger beam size of 2 nm, the range from 9 keV to 30 keV can becomes accessible with the (333) reflection only, and at 4 nm the (111)-reflection is sufficient to go all the way from 4 keV to 30 keV without change in reflection (Figure 11.4.11b). However, a full range of incident angles, from near 90° to near 0°, is required to achieve this flexibility. This is a requirement that will require careful design of the monochromator.

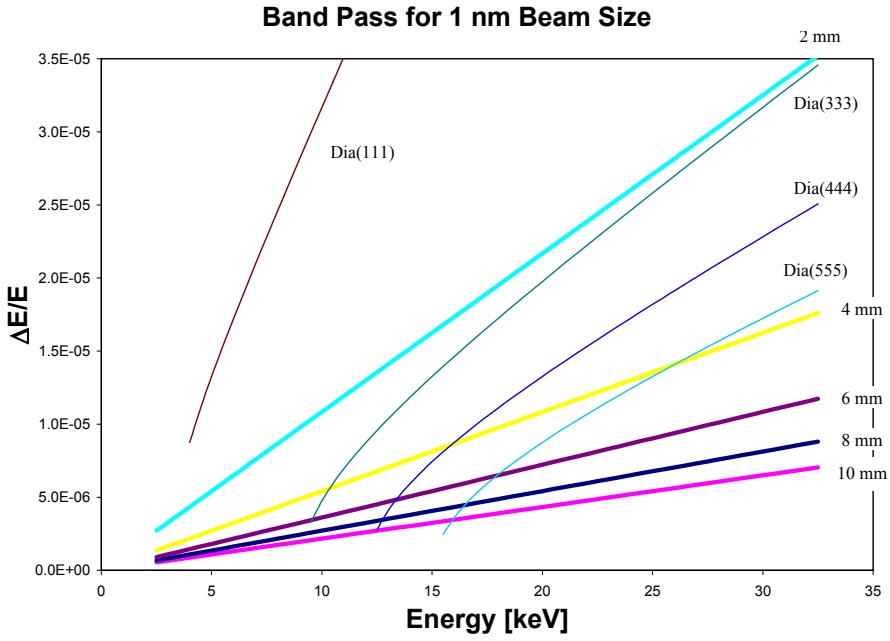

Figure 11.4.11a Band pass boundaries and available band pass values for various reflections of the DCM for a targeted beamsize of 1 nm.

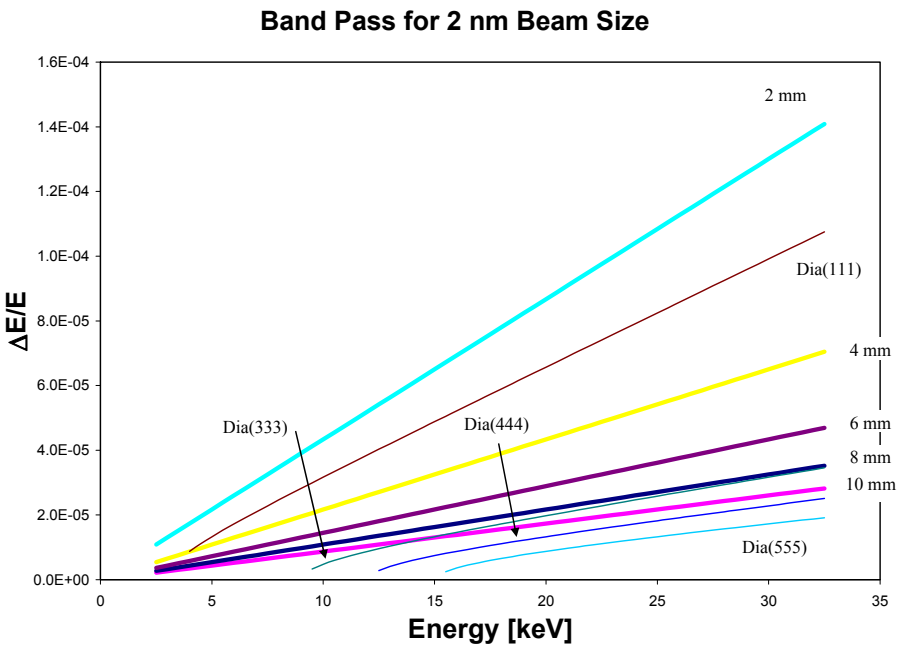

Figure 11.4.11b Band pass boundaries and available band pass values for various reflections of the DCM for a targeted beamsize of 2 nm.

11.4.3.5 The Nanoprobe Instrument

The engineering challenges associated with achieving the sub-nm stability and precision to sample (and optic) positioning stages are severe and will require a dedicated R&D effort. This will be pivotal in the context of NSLS-II, in general, and any nanoprobe beamline, in particular. The specific issues, challenges, and potential approaches are discussed in Chapter 12.

11.4.3.6 Front-End Aperture

The first aperture in a nanoprobe beamline, located in the front end as close to the undulator source as possible, would consist of two separate masks (Figures 11.4.12 and 11.4.13a). The first mask is fixed in space and serves as a guard, reducing the size of the initial undulator x-ray beam to the desired maximum acceptance of the beamline. This maximum acceptance matches the vertical and horizontal FWHM (full width at half maximum) sizes and divergences of the source.

The second mask can be moved vertically to switch between two possible positions. The first position corresponds to a high-spatial-resolution mode of the beamline, while the second corresponds to a high-flux mode. The first position provides a beam-defining horizontal constriction equal to the vertical FWHM extension of the beam, leading to a square-shaped source. When the guard mask is removed, the full beam permitted by the guard mask is passed to the beamline.

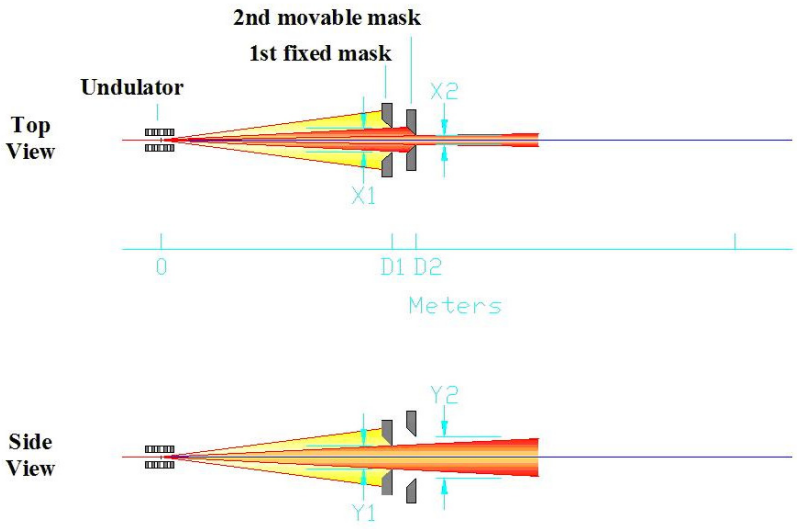

Figure 11.4.12 Geometry of the first aperture.

The locations of the first and second mask will be approximately D_1=14 m and D_2=15 m from the source, respectively. Efforts will be made in the engineering design to reduce these numbers as much as reasonably possible. Given the source parameters described earlier, the sizes of the apertures in the two masks emerge as

horizontal opening, guard mask: $X_1 = 4\Sigma_x + 4\Sigma_x' D_1 \approx 1100\,\mu m$

vertical opening, guard mask: $Y_1 = 4\Sigma_y + 4\Sigma_y' D_1 \approx 400\,\mu m$

horizontal opening, movable mask: $X_2 = \mathrm{FWHM}(\Sigma_y) + \frac{D_f}{L_o} \cdot D_2 \approx 150\,\mu m$

vertical opening, movable mask: $Y2 = 2 \cdot 1\,mm \approx 2\,mm(\mathrm{overall})$

Since the required aperture sizes in both the fixed and the movable mask are relatively small and must endure significant heat loads, fabrication of such apertures to the required tolerances will be an engineering challenge. Manufacturing these will be facilitated by having beam-defining constrictions in different locations along the beam direction for the various sides of the masks. This concept is illustrated in Figure 11.4.13b.

The movable mask features two halves, with the lower half containing a horizontal constriction and the upper half allowing unobstructed passage of the beam.

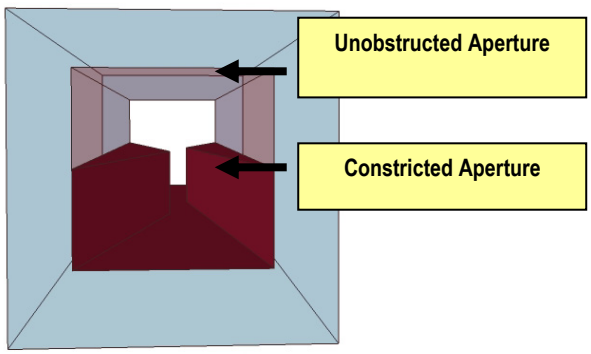

Figure 11.4.13a: Movable mask, beam entrance face.
Lower half with horizontal constriction, upper half straight-through.

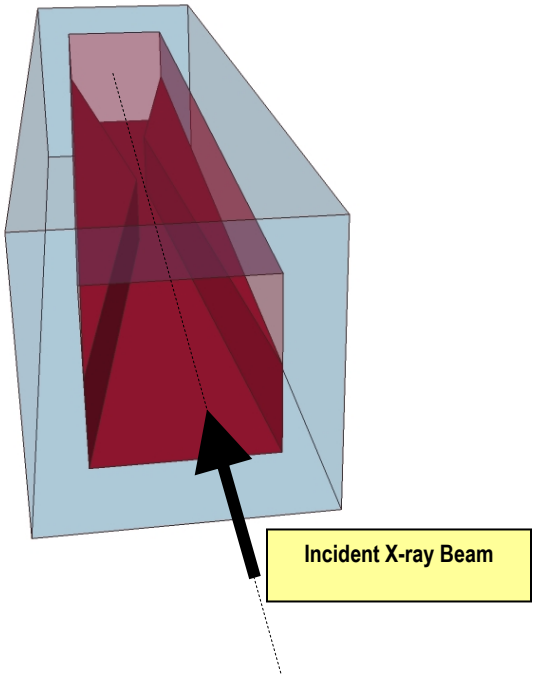

Figure 11.4.13b Movable mask. Points of maximum constriction in the lower half are at different locations along the beam direction for the left and right side.

References

[11.4.1] R. Saito, M. Fujita, G. Dresselhaus, M.S. Dresselhaus, "Electronic structure of graphene tubules based on C_{60}," *Phys. Rev. B,* **46** (1992), pp 1804-1811.
[11.4.2] N. Hamada, S. Sawada, A. Oshiyama, "New one-dimensional conductors: Graphitic microtubules," *Phys. Rev. Lett.,* **68** (1992), pp. 1578-1581.
[11.4.3] Q. Shen, CHESS Technical Memo 01-002, March 8, 2001.

11.5 An Inelastic X-Ray Scattering Beamline

11.5.1 Introduction

Inelastic X-ray Scattering is a momentum-resolved technique for studying dynamics and excitations in condensed matter systems. Of increasing importance, IXS has been used to study excitations ranging from phonons in solids, to sound modes in liquids and polymers, to plasmons in simple metals, to complex electronic excitations in strongly correlated electron systems. Further, there are many new, as yet largely unexplored, areas to which the technique could well make important contributions, including surface dynamics, excitations in extreme environments, time-resolved studies, and non-equilibrium dynamics.

As a technique that probes one of the fundamental response functions of a system, namely $S(q, \omega)$, IXS is an extremely powerful method for addressing some of the most important questions in condensed matter science today. Its principle limitation to date has been the dearth of active instruments in the world, and the very low count rates achievable on such instruments. Despite these limitations, IXS has the intrinsic

advantages of a weak cross-section (so that multiple scattering effects are negligible) and the ability to study very small samples (this latter attribute has been used, for example, to study phonons in high Tc compounds, in MgB_2, and in plutonium micro crystals, etc., for which larger, neutron-sized crystals are simply not available). Finally, there is no need to deuterate samples, as there is for inelastic neutron scattering from many soft-condensed-matter systems. As a result, given sufficient availability of instruments and reasonable count rates, IXS should have an impact at least as large as that of triple-axis neutron spectrometry, its direct analog. IXS beamline(s) at NSLS-II would feature unprecedented resolution and count rates and thus would be expected to offer the potential for high scientific impact.

In this section, we outline the design considerations necessary to construct a state-of-the-art IXS beamline at NSLS-II. We discuss three end stations, each focusing on a different energy-resolution regime: ~50 meV, 1 meV, and 0.1 meV. Of these, 0.1 meV is by far the most challenging, and we discuss a spectrometer based on an entirely new approach utilizing highly asymmetrically cut crystals operating in near-back-scattering. This approach has yet to be demonstrated in a working device and has a number of challenges associated with it. These challenges, and the R&D necessary to address them, are discussed in Chapter 12.

For the purposes of this report, the three end stations are treated as a single beamline, and indeed they could share the same upstream optics and have similar requirements of the undulator. However, although in principle it would be possible to construct all three end stations in series (Figure 11.5.1), in practice this would lead to inefficiencies in operation and in scientific productivity. A more optimized approach would likely move the medium-resolution (50 meV) instrument to it's own, dedicated beamline, with the 0.1 meV and 1 meV end stations sharing a second beamline. This has the advantage of grouping related science and techniques together, as well as providing optimized instruments and sufficient capacity for both regimes. In this scenario, the 50 meV instrument would focus on electronic excitations, while the 0.1 meV and 1 meV instruments would focus on the excitations involving the nuclei (phonons, diffusive modes, etc.), with the 1.0 meV instrument likely to be the work horse instrument, with a relatively high flux, and the 0.1 meV instrument utilized when the very highest resolution is required.

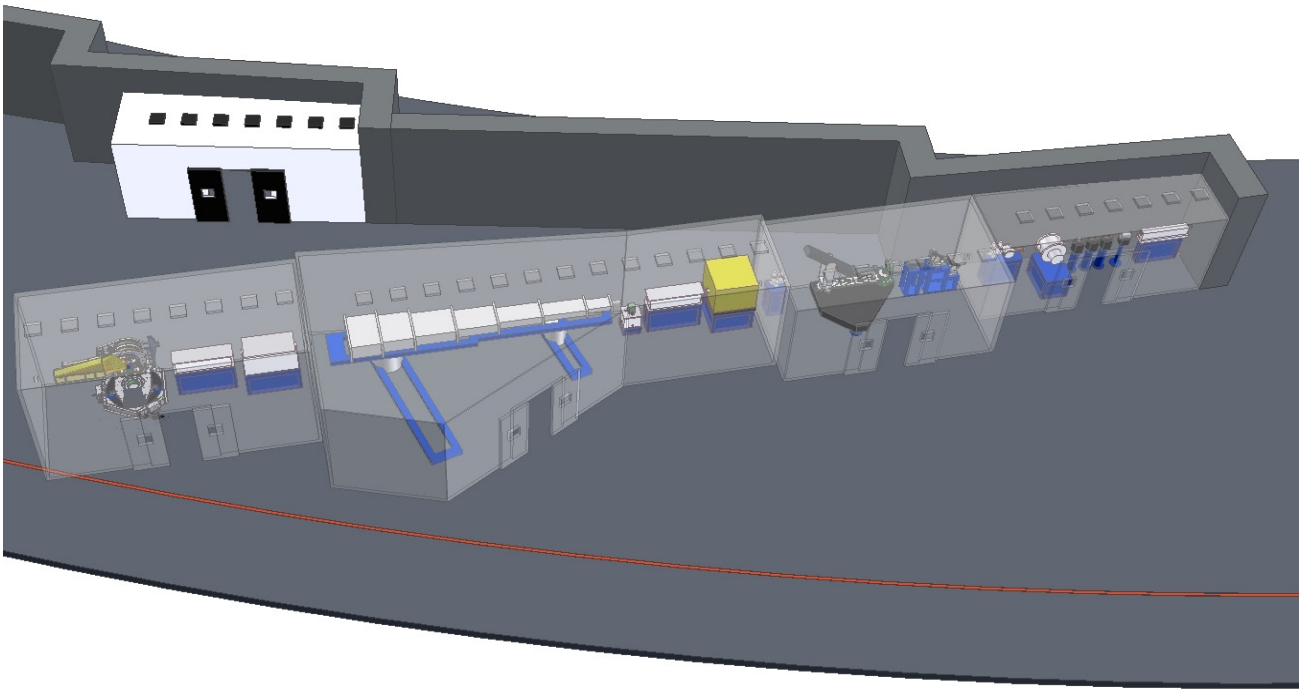

Figure 11.5.1 Three inelastic x-ray scattering end stations shown on a single beamline. These are, respectively, 0.1 meV, 1 meV, and 50 meV instruments, from right to left. Note, however, that these end stations are shown in this way for illustration purposes only. As discussed in the text, a more optimum arrangement would be to have one dedicated straight for the 50 meV and another for the 0.1 meV and 1 meV programs.

11.5.2 Conceptual Design for the Inelastic X-Ray Scattering Beamline

11.5.2.1 Source

The figure-of-merit for a radiation source for an IXS beamline is photons per second per meV. Of the devices considered in this CDR, the 3 m U19 device offers the best performance in this regard in the relevant energy range. However, because of the extreme need for photons for these experiments, it is worth considering further optimization for the IXS beamlines. In particular, longer length devices, if allowed by the machine parameters, improve the incident flux linearly with the length of the device. This is a significant factor for experiments for which a typical scan could easily be 24 hours long. A factor of two then makes a big difference in what can be accomplished in a given beamtime allocation. Such an improvement, or possibly more, may be achievable if accelerator studies during the detailed design phase of the project show that multiple narrow-gap devices can be accommodated in the 8 m straight sections. As shown in Figure 11.5.2, a particularly attractive option would be three 2 m SCU devices in an 8 m straight. This assumes the ability to focus the beam between such devices, which requires careful investigation. The increase in flux, compared to a single 3 m U19 device, would be a factor of five. These beamlines also make a case for yet longer straight sections, if that is possible.

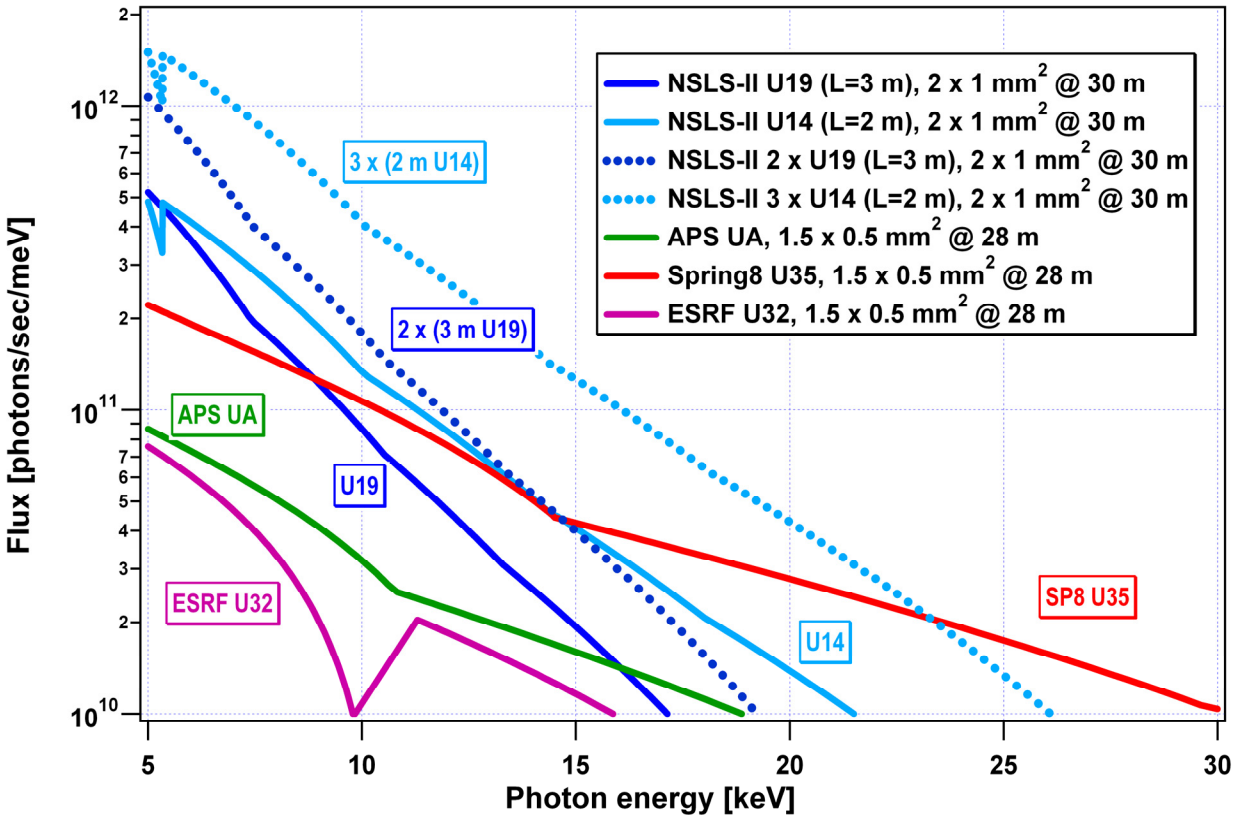

Figure 11.5.2 Comparison of various devices at NSLS-II and elsewhere, as measured in ph/s/meV, the figure of merit for inelastic x-ray scattering beamlines. The advantage of working at lower photon energies is clear. The NSLS-II IXS beamlines would operate around 10 keV and below. The blue dotted curves show the increase associated with placing multiple undulators in a single straight at NSLS-II. The examples shown are two 3 m U19 devices and three 2 m U14 devices and with $\beta_x=\beta_y=3$ m.

11.5.2.2 Beamline Optics

The upstream optics for an IXS beamline are likely to be relatively standard components, including focusing optics and a high heat load monochromator. As discussed elsewhere, this latter will either be a cryogenically cooled Si(111) double-bounce monochromator or a water-cooled diamond monochromator. There would then follow specialized high-resolution monochromators, appropriate to the particular end station served and, if required, appropriate focusing optics to deliver highly monochromatic, focused beam to the sample.

11.5.2.3 End Station I (0.1 meV)

IXS spectroscopy is becoming one of the major techniques for studying vibrational dynamics in solids, liquids, and biological macromacromolecules [11.5.5]. X-ray monochromators and analyzers with meV resolution are the main optical components of IXS spectrometers [11.5.4, 11.5.7, 11.5.18, 11.5.16, 11.5.1].

Single-crystal and multiple-crystal techniques for the meV monochromatization and analysis of x-rays have been developed over the past few decades (for references and reviews see [11.5.8, 11.5.17, 11.5.12]). These techniques all share a basic general property: the higher the required energy resolution, the higher the index of the Bragg reflections used, and thus the higher the energy of photons required. For this reason, photons with E>20 keV are typically used in IXS experiments that achieve meV resolution. To achieve yet higher resolution, that is, approaching ≈ 0.1 meV, with the techniques in use today at high-energy facilities such as ESRF, APS, and SPring-8, then very high-indexed Bragg reflections would be required with incident x-ray photon energies as high as 30 to 35 keV. However, this trend to higher energies conflicts with the basic fact that the brightness of undulators decreases with increasing photon energy, and that the experiments are extremely photon-hungry and can ill afford any reduction in flux. This problem is particularly relevant for NSLS-II, which will be extremely powerful at medium photon energies but not competitive with the higher-energy rings at higher photon energies. Finally, an added disadvantage of the higher energies is that the momentum transfer resolution worsens (for fixed acceptance angle) as the photon energy is increased.

To overcome these problems, and thus to broaden the potential of IXS, an alternative concept of an IXS spectrometer with meV and sub-meV for x-rays in the medium-energy spectral range (5–10 keV) has been proposed [11.5.12]. This approach exploits the effect of angular dispersion in asymmetric Bragg diffraction. One of the advantages of such an approach is that higher energy resolutions are achieved at lower photon energies, typically E<10 keV, a tendency that is consistent with better performance of x-ray undulators at these energies, and with better momentum transfer resolution. It is therefore proposed that the ultra high-resolution instrument at NSLS-II be based on these principles.

Briefly, a monochromator using this scheme requires an arrangement of three crystals, as shown in Figure 11.5.3a, playing the role of a collimator (C), a dispersing element (D), and a wavelength selector (W) in a three-bounce, so-called CDW monochromator. This same monochromator, combined with a parabolic mirror or Kirkpatrick-Baez system with graded multilayer mirrors (M), can also be used as a high-resolution analyzer of scattered radiation from a sample (S in Figure 11.5.3b).

This effect of angular dispersion in backscattering geometry has recently been demonstrated [11.5.15], and the first studies of a prototype CDW angular-dispersive monochromator have been performed [11.5.14], demonstrating an energy resolution of $\Delta E = 2.2$ meV for 9.1 keV photons.

In the following discussion, we outline a conceptual design of an IXS spectrometer utililzing 9.1 keV x-rays, providing an energy resolution of 0.1 meV and a momentum transfer resolution of $\approx 0.1 - 0.4$ nm^{-1}. The spectrometer uses the angular-dispersive (CDW-type) monochromator and analyzer. The concept is based on ideas contained in refs. [11.5.12, 11.5.15, 11.5.14, 11.5.13].

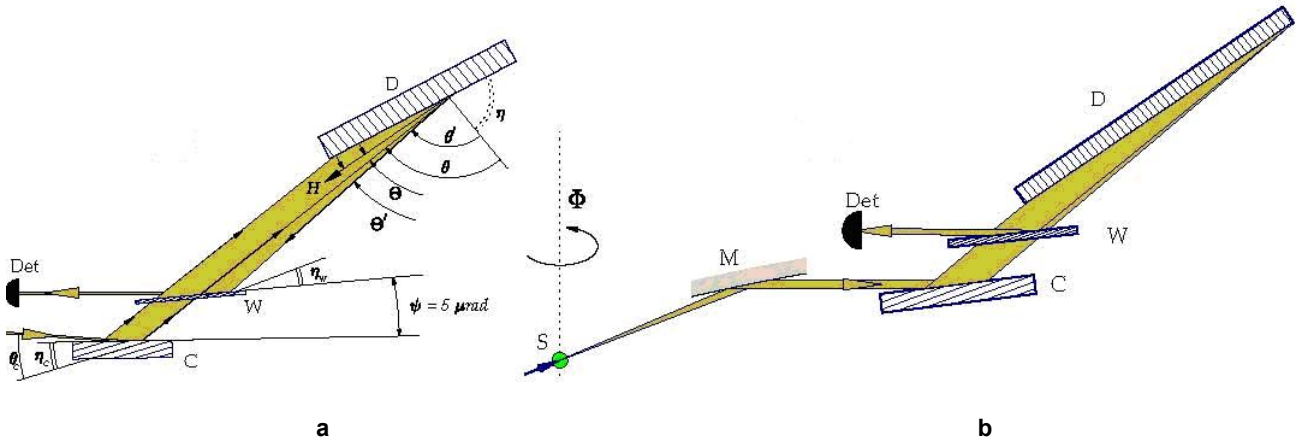

Figure 11.5.3 Schematic of the angular-dispersive backscattering CDW monochromator **a)**, and backscattering CDW analyzer **b)**. [11.5.12, 11.5.14]

11.5.2.3.1 Angular-Dispersive Monochromators

Basic Principle and Features

Any asymmetrically cut crystal diffracting at the Bragg condition behaves like an optical prism, dispersing x-ray photons with different photon energies at different angles. This effect, termed *angular dispersion*, can be used to monochromatize x-rays beyond the limits set by the spectral width of Bragg reflections. For this, in addition to a dispersing element (crystal D in Figure 11.5.3a), two more optical elements are required: a collimator, C, which reduces the angular spread of x-rays incident upon the dispersing element, and a wavelength selector, W. The latter selects x-rays with a desired angular, and hence spectral, spread. Bragg diffraction from single crystals can be used to achieve the required effects of collimation and wavelength selection. The angular dispersion is largest in backscattering. Further, the backscattering geometry is also favorable because the effect of angular dispersion is least affected by the angular spread of the incident radiation here.

The relative energy bandwidth $\Delta E/\mathrm{E}$ of the photons transmitted through the CDW monochromator with the dispersing element in backscattering is given by

$$\frac{\Delta E}{E} = \frac{\Delta\theta'_c + \Delta\theta_w}{2\tan\eta}, \qquad (11.5\text{-}1)$$

where η is the angle of asymmetry, $\Delta\theta'_c$ the angular spread resulting from the collimator, and $\Delta\theta_w$ the angular acceptance of the wavelength selector. Equation 11.5-1 demonstrates an important distinguishing feature of such monochromators: the relative spectral bandwidth $\Delta E/\mathrm{E}$ is independent of the intrinsic spectral width of the Bragg back reflection used. Nor does it depend on the photon energy E. Rather, it simply depends on the strength of the effect of angular dispersion, expressed by tan η, and the geometrical parameters, $\Delta\theta'_c$ and $\Delta\theta_w$. Any Bragg back reflection at any x-ray energy can be used. Importantly, the smaller the photon energy E, the narrower the energy bandwidth, ΔE, that can be obtained. A relative spectral bandwidth of $\Delta E/\mathrm{E} \approx 10^{-6}$ to 10^{-8}, and thus spectral bandwidths of $\Delta\mathrm{E} \approx$ 10 to 0.1 meV at $\mathrm{E} \leq$ 10 keV become possible. A compromise between this requirement for lower photon energy and the higher photon energy favored by smaller photo absorption makes the photon energy range 5 keV $\leq$ E $\leq$ 10 keV most favorable. Here, we have chosen to use 9.1 keV photons for the NSLS-II IXS monochromators and analyzers. We discuss the individual components below.

11.5.2.3.2 CDDW In-Line Monochromator

Despite the merits associated with CDW monochromators, practical difficulties associated with the backscattering geometry make them unwieldy in practice, precisely because of the backscattering geometry; an in-line monochromator would be more practical. Figure 11.5.4a shows such an in-line design, based on the angular dispersion principles. It has two dispersive elements, D1 and D2. The beam is dispersed twice, and therefore the angular dispersion is enhanced by a factor of two. This has the added advantage of then requiring dispersive elements of half the length for the same resolution. The same crystal (labeled C/W) is used as both the collimator and wavelength selection in this scheme.

The spectral function of such a monochromator, with a $\Delta E = 0.1$ meV bandwidth, is shown in Figure 11.5.4b. It has very steep wings, relative to the wings of the spectral function of a single conventional bounce backscattering monochromator. This is an important advantage; frequently, it is the tails of the elastic line (that is, the resolution function) that are the largest source of background in a real experiment, even at very large energy transfers relative to the nominal resolution. Such effects would be significantly reduced by this approach.

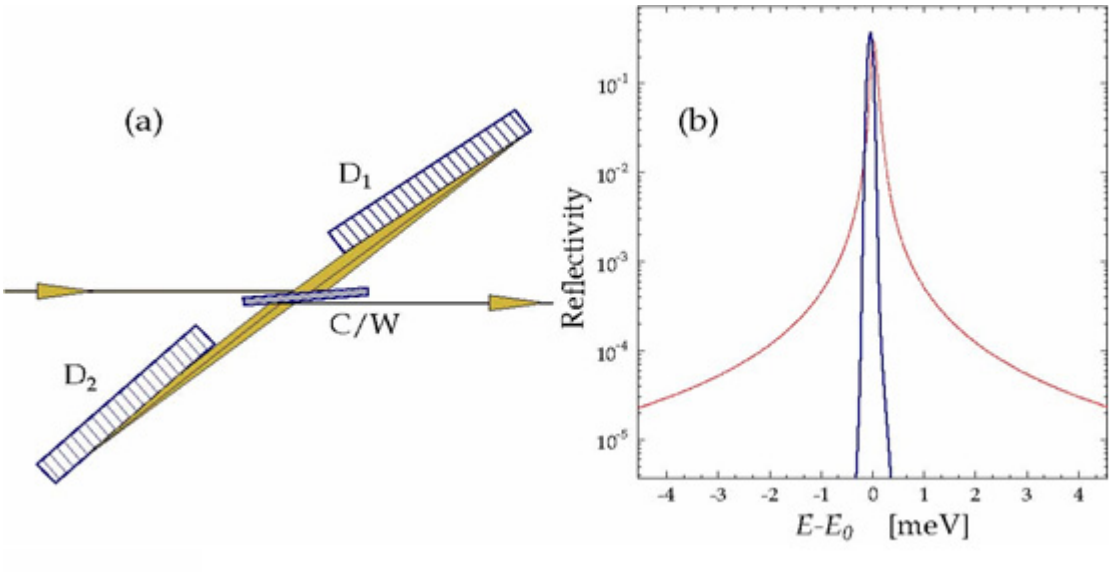

Figure 11.5.4 **a)** Schematic of an in-line angular-dispersive CDDW monochromator [11.5.13].

b) Blue line: dynamical theory calculations for the angular-dispersive CDW monochromator with a $\Delta E = 0.1$ meV bandwidth. Incident photon energy E = 9.1315 keV. Dispersive element: Si(008). Collimator and wavelength selector crystals: Si(220). Red line, shown for comparison: dynamical theory calculations for a single-bounce backscattering monochromator with a $\Delta E = 0.1$ meV bandwidth. Incident photon energy E = 31.02 keV Bragg back reflection Si(1 3 27).

The energy of the photons, selected by the CDDW monochromator, is tuned by varying the temperature of the crystals. The variation of the photon energy with crystal temperature is $\gamma(T) = -23.61(4)$ meV/K at T=300K [11.5.2]. Such an in-line CDDW monochromator is proposed for the IXS beamline at NSLS-II, as shown schematically in Figure 11.5.6.

11.5.2.3.3 Angular-Dispersive Analyzer

As noted earlier, the same optical instrument can be used both as a monochromator and an analyzer. The sole distinguishing functional feature of an analyzer relative to a monochromator is the ability to accept photons in a relatively large solid angle. Typically, an acceptance angle of Υ^2 with $\Upsilon \approx 5$ to 10 mrad is required for IXS experiments. This is a compromise between the required momentum transfer resolution, ΔQ, and the photon flux on the detector. An angular acceptance of $\Upsilon \approx 10$ mrad corresponds to $\Delta Q = 0.46$ nm^{-1} for 9.1 keV photons.

The CDW and CDDW monochromators presented above have an exceptionally large angular acceptance of $\Delta\theta_v = 0.1$ mrad in the vertical scattering plane and $\Delta\theta_h \approx 0.2$. to 0.3 mrad in the horizontal. However, this is still too small an acceptance for the monochromator to be used directly as an analyzer.

Therefore, to utilize either of these optics as an analyzer requires installing collimating optics in front of the analyzer. Collimators are optical elements that collect x-rays scattered from the sample over the required solid angle and deliver them to the analyzer with a reduced angular spread $\leq \Delta\theta_v$ and $\leq \Delta\theta_h$. The basic design concept of the analyzer discussed in this section involves the CDW monochromator and collimating optics integrated into a single instrument, an angular-dispersive x-ray analyzer, as shown in Figures (11.5.3b) and 11.5.6.

11.5.2.3.4 Collimating and Focusing Optics

For the purpose of collecting and collimating medium-energy x-ray photons (5 to 10 keV), it is appropriate to use reflective optics, such as curved grazing incidence mirrors [11.5.6], curved graded multilayer mirrors, KB systems with graded multilayer mirrors [11.5.11, 11.5.9, 11.5.10], or even tapered glass capillaries [11.5.3].

In addition to the requirement of having a rather large angular acceptance Υ, there are certain requirements for the exit parameters of x-rays leaving the collimating optics. First, the angular divergence should match the angular acceptances of the CDW monochromator, $\Delta\theta_v$ and $\Delta\theta_h$. Second, the vertical beam size should not exceed 0.5 to 1 mm (to keep the crystals comprising the angular dispersive analyzer at a manageable length). Optics with such collecting and collimating parameters are commercially available.

The angular divergence of x-rays after the collimating mirror arises from two main contributions, the mirror slope error and the source size contribution. The latter is basically given by the source size (the focal spot size on the sample) S divided by the source-mirror distance. Assuming the distance to be 100 mm (to accommodate the sample environment), the vertical and horizontal focal spot size on the sample should not exceed $S_v \leq 10$ μm and $S_h \leq 20$ to 30 μm, respectively. This requires a focused beam on the sample. Such focusing can be achieved using a commercial focusing system, which is shown schematically on the beamline layout in Figure 11.5.6. While such focusing is certainly a complication, it is also true that, for many experiments, a micro-focused beam is not only a great advantage but a necessity.

11.5.2.3.5 Segmented CDW Analyzer

Achieving a very small energy bandpass of about 0.1 meV requires a very large asymmetry angle, $\eta = 89.5°$, for the dispersing element. This causes an evident technical problem: the dispersive element must be very long, about 2 m, to ensure an angular acceptance of $\Upsilon \leq 2$ to 3 mrad of the analyzer in the vertical plane. The angular acceptance in the horizontal plane can be kept at the level of $\Upsilon_h \leq 10$ to 15 mrad, independent of the beam size.

To overcome the technical problems associated with such an extreme length of the dispersive element, it would be built in independent segments, as shown in Figure 11.5.5 (only three segments are shown). It should be possible to build a 2 m-long dispersive element consisting of about eight to 10 segments, each 20 to 25 cm

long. Note that it is not necessary for the reflecting atomic planes of the segments to be aligned perfectly parallel to each other.

In addition to easing fabrication issues, such a scheme also means that the crystal temperature of a given segment is now only required to be homogeneous to 0.5 mK (corresponding to 0.01 meV energy shift), rather than requiring the same tolerance along an entire 2 m length. Any angular misalignment and temperature shifts of the segments relative to each other will simply result in relative energy shifts of the spectra measured by the different segments. These shifts can be corrected in the data analysis, provided the signal from each segment is recorded independently. For this purpose a position-sensitive detector would be used, as shown in Figures 11.5.5 and 11.5.6. Such corrections are routine in conventional high-energy resolution IXS spectrometers, for which the spectra from multiple analyzers are recorded by independent (point) detectors.

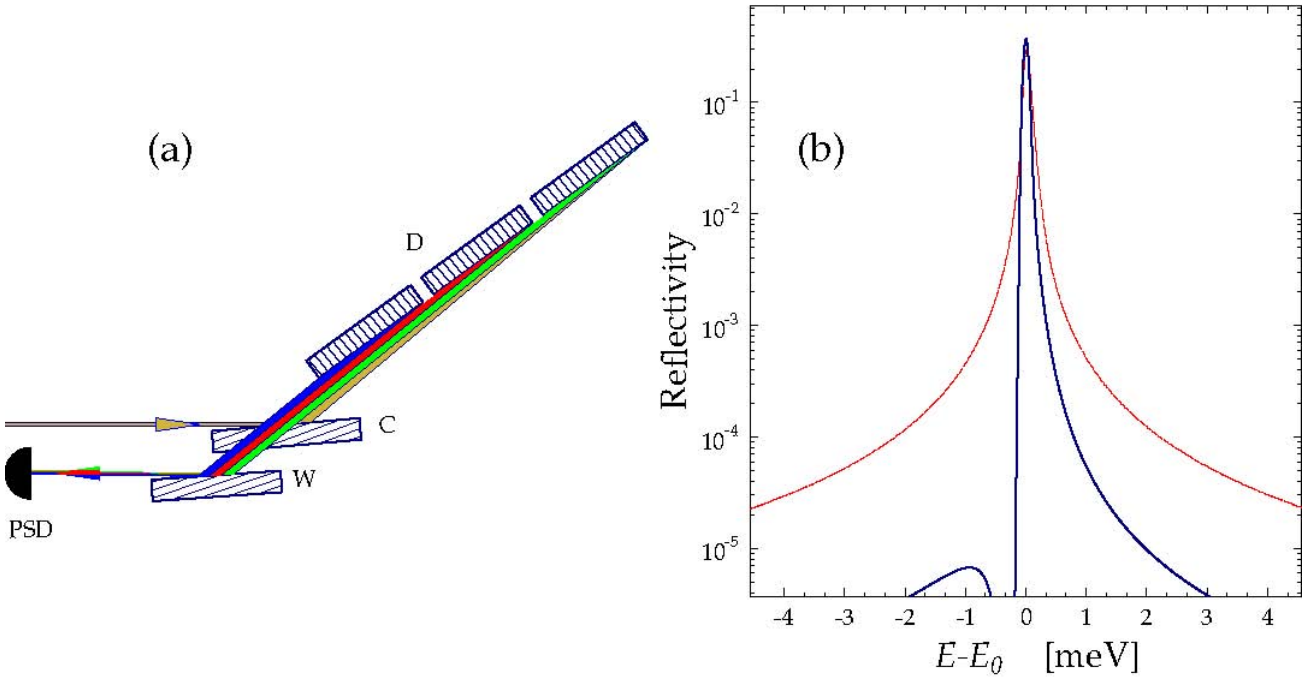

Figure 11.5.5 **a** Schematic of the angular-dispersive CDW backscattering segmented analyzer with the position-sensitive detector, PSD [11.5.13].

b Dynamical theory calculations for the angular-dispersive CDW analyzer with a ΔE = 0.1 meV bandwidth. Incident photon energy E = 9.1315 keV, incident beam angular divergence = 0.1 x 0.2 mrad^2. For comparison, dynamical theory calculations for a single-bounce backscattering monochromator with a ΔE = 0.1 meV bandwidth are shown by the red line.

Figure 11.5.5b shows dynamical theory calculations for the angular-dispersive CDW analyzer with a bandwidth of ΔE = 0.1 meV. The incident photon energy E is 9.1315 keV. Incident beam angular divergence is 0.1 × 0.2 mrad^2, corresponding to the angular divergence of x-rays from the collimating mirror. The spectral function is compared with that of a single-bounce backscattering analyzer of the same resolution, which can be achieved using the high index Bragg reflection Si(1 3 27) and a photon energy E = 31.02 keV. As was the case for the monochromator, the spectral function of the CDW analyzer has much steeper wings relative to conventional approaches, which is a significant advantage.

11.5.2.3.6 Optical Scheme of the IXS Spectrometer

Figure 11.5.6 shows a schematic layout of the entire IXS spectrometer. It comprises the angular-dispersive CDDW in-line monochromator, the focusing mirror, the CDW backscattering segmented analyzer, and the position-sensitive detector. The spectrometer is shown integrated into the IXS beamline, together with other main beamline components: undulator, high heat load monochromator, etc. A possible design of the IXS spectrometer is presented in Figure 11.5.7.

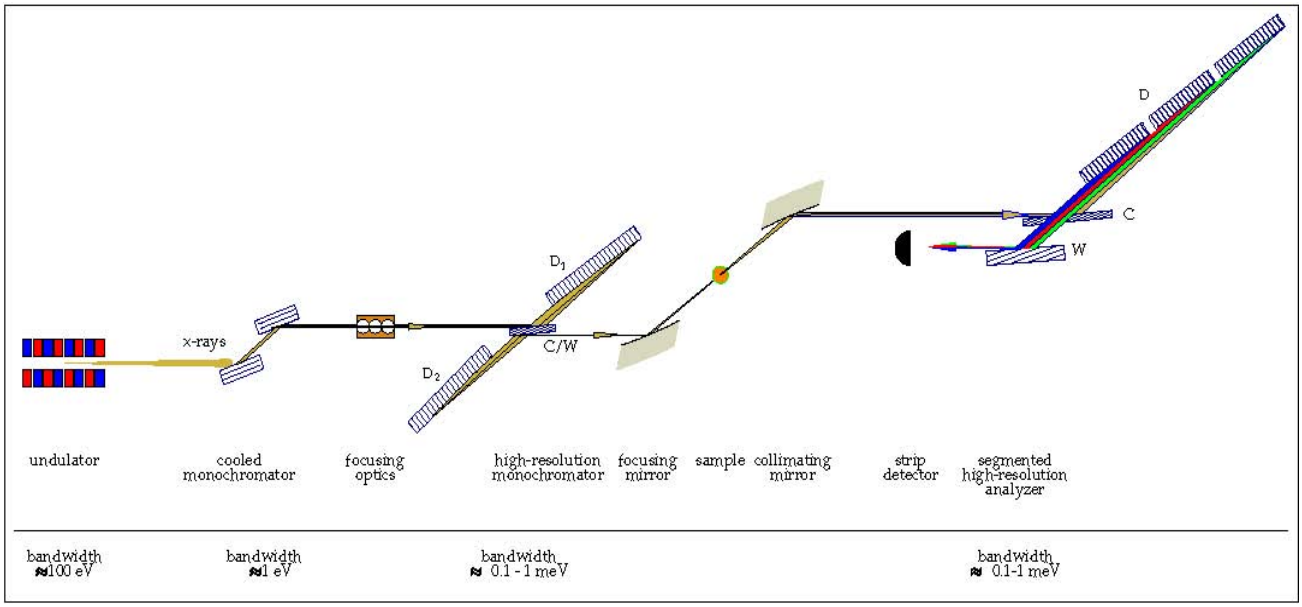

Figure 11.5.6 Optical scheme of the IXS spectrometer with angular-dispersive CDDW in-line monochromator and CDW backscattering segmented analyzer integrated with other main elements of the IXS beamline [11.5.13].

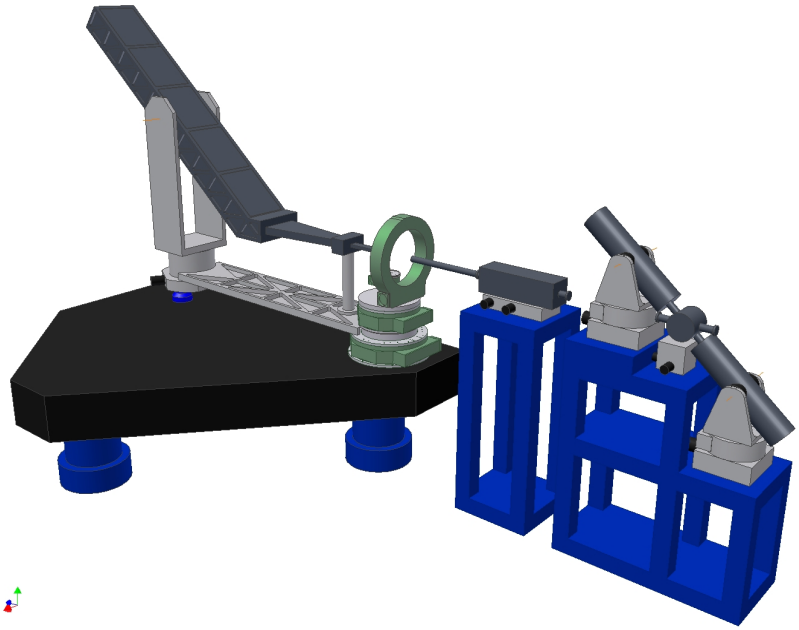

Figure 11.5.7 Possible design of the IXS spectrometer with angular-dispersive CDDW in-line monochromator and CDW backscattering segmented analyzer according to the optical scheme of Figure 11.5.6.

11.5.2.4 End Station II (1 meV)

There currently exist several instruments around the world capable of ~1 to 2 meV energy resolution, notably at ESRF, SPring-8, and APS. Each of these instruments uses backscattering high-order Si reflections (typically, Si[n,n,n] reflections) for analyzers to achieve the appropriate energy resolution. The monochromators used are either also Si(n,n,n) reflections (at ESRF and SPring-8) or high-order reflections utilized in a nested in-line geometry (at APS). To achieve ~1 meV resolution, the photon energy used is in excess of ~20 keV. In principle, one could build a similar instrument at NSLS-II and achieve the same resolution. However, because of the lower storage ring energy at NSLS-II, it would be difficult for such an instrument to be competitive, at these photon energies, with the higher energy third-generation sources.

There are two alternatives to this approach that might be fruitful at NSLS-II.

The first alternative is to again use asymmetric optics discussed above for the 0.1 meV instrument, operating at photon energies of ~9 keV and at smaller asymmetric angles and therefore lower resolutions. The spectrometer itself would look very similar to the one outlined above. The technical challenges associated with such an instrument operating at ~1 meV are significantly more tractable than they are for reaching 0.1 meV. Indeed, as discussed in Chapter 12, the principle has now been demonstrated at 2.2 meV—though there remains a long way to go before a working, high-throughput instrument can be built on these principles. Nevertheless, many of the same advantages described above for the 0.1 meV instrument (sharp resolution functions, good reciprocal space resolution, high flux/meV, etc.) apply equally well here and thus this scheme presents a worthy alternative to the traditional Si(n,n,n)-type approaches of the high-energy rings. Further, the R&D that will be carried out to reach 0.1 meV will necessarily address all of the issues associated with reaching 1 meV. Thus, relatively early in the NSLS-II construction project the answers to the practicality of a 1 meV instrument based on asymmetric optics will be much clearer and one can decide whether to proceed along these lines.

A second alternative would be to move away from Si reflections and utilize other materials with more favorable resolutions at medium energies. As discussed in Chapter 12, such alternatives include sapphire and quartz. There it is stated that inherent limitations in these, and equivalent materials, limited their usefulness at very high resolutions (~0.1 meV). These include very low structure factors and the resulting small reflectivity and large tails in the resolution function. However, the case against such materials is much less clear at resolutions of ~1 meV, and here they may well provide a viable alternative to Si.

In this case, the instrument would look physically similar to the conventional high-resolution instruments with a single-bounce backscattering monochromator and backscattering analyzers. In order to accommodate the large 2θ arm (which would be on the order of 5 to 6 m long), the scattering would be in the horizontal plane. This also greatly reduces the engineering challenges associated with utilizing multiple analyzers. These are commonly arranged in $n \times m$ arrays in which each analyzer is focused onto a dedicated detector (at NSLS-II this might be, say 5×7, with the long side of this array in the scattering plane). This allows data to be collected at multiple points in reciprocal space simultaneously—something that is not simple to do with the asymmetric optics approach. This greatly increases the data throughput—by an order of magnitude, for some experiments. It is difficult to overstate this advantage in a field in which scans routinely take ~24 hrs.

In terms of the analyzer material, one candidate is quartz. As a non-centrosymmetric crystal, quartz offers a number of potential advantages for use as an analyzer material, [11.5.19]. These advantages include providing 184 backscattering reflections between 5–12 keV, many more than the 22 provided by Si, which is of great boon in terms of finding an appropriate reflection if one has to work at a particular energy—for example, a K-absorption edge for a resonance experiment. In addition, quartz has a coefficient of thermal expansion that is three times larger than Si, allowing much greater energy ranges in temperature scans.

Figure 11.5.8 shows some recent results for large-area quartz wafers [11.5.19]. The reflection used was (7, -4, -3, 4) with a Bragg angle of 89.77 at 9.929 keV. When the full 11 cm^2 wafer was illuminated, a resolution of 4 meV was obtained, compared to a theoretical value of 2 meV for a perfect crystal. This

difference was attributed to defects in the quartz associated with strain resulting from the mounting scheme. Figure 11.5.8 show results from two selected areas of the large wafer. It is seen that when an 8×8 mm apparently defect-free area was selected, a resolution of 2.9 meV was obtained, whereas if the beam spot included a defect (dark area in the x-ray topographic image), then the resolution was observed to worsen to 4 meV. However, in addition to the resolution FWHM, another figure of merit for such analyzers is the tails of the resolution function; these were observed to be significantly worse than theoretically expected. Further efforts are required to understand the origin of these tails and to seek to mitigate them.

Such efforts are currently ongoing at SPring-8 (quartz) and APS (quartz and sapphire). If successful, these will offer an alternative route to 1 meV spectroscopy at moderate photon energies. The NSLS-II project will monitor these developments, in addition to carrying out the asymmetric optics R&D for the 0.1 meV effort.

Finally, irrespective of which approach is followed, it is important that the 1 meV instrument cover a wide range in reciprocal space. For example, the scattered intensity from phonons increases with $\sim Q^2$, where Q is the total momentum transfer (though at very large momentum transfers, the Q-dependence of the atomic form factor takes over, driving the intensity to zero). In addition, it is frequently of value to study multiple Brillouin Zones to look for systematic dependencies in the data. For the high photon energy instruments discussed above, this requirement is not too onerous and can be achieved for 2θ scattering angles significantly less than 90°. However, for the photon energies of ~9 keV discussed here, then the requirement that one reach to Q ~8 A^{-1} corresponds to a 2θ angle of ~120°. This presents a problem, because of the horizontal incident polarization and the resulting $cos^2 2\theta$ dependence of the scattering intensity, which reaches zero at 90°.

This problem may be solved by rotating the incident polarization in to the vertical plane by use of two diamond quarter-wave plates. Such arrangements have been shown to be very efficient (~97%) in terms of rotating the polarization, and relatively efficient in terms of transmitted intensity (~40%) at 9.1 keV [3.5.20], and thus should be practical for such purposes.

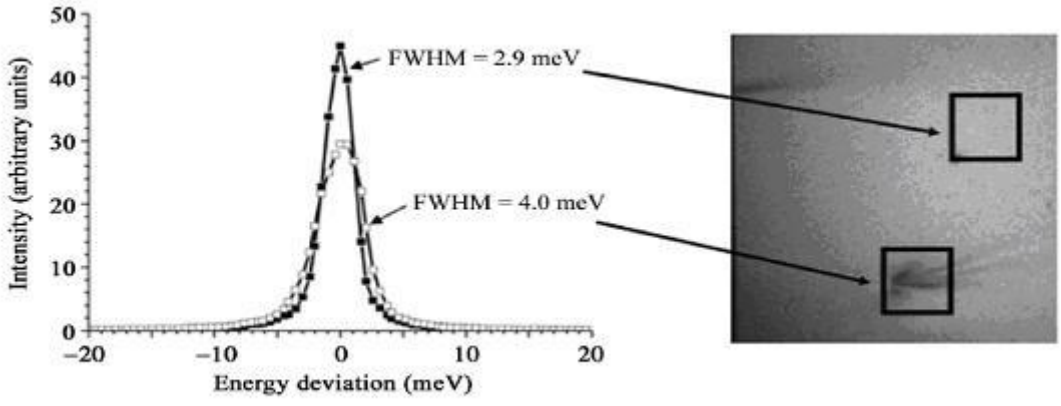

Figure 11.5.8 Quartz offers a potential route to high energy resolutions at medium photon energies. These images show the performance of a quartz wafer at 9.979 keV. The figure shows the energy resolution obtained from two different areas of the same quartz wafer. The right-hand image shows an x-ray topograph of that wafer. The dark spot corresponds to a strain defect believed to be associated with the mounting scheme.

11.5.2.5 End Station III (50 meV)

Achieving ~50 meV bandpass on the incident beam in energy ranges ~5 to 10 keV is a relatively straightforward technical challenge. An example of the state of the art is the MERIX instrument at section 30 at APS, which (at the time of writing) has recently begun final commissioning. This instrument utilizes a four-bounce monochromator of the type shown schematically in Figure 11.5.9. For the reflections show here,

namely Si (800), this device achieves a relatively constant bandpass of ~70 meV and a high spectral efficiency over the energy range 5 keV to 10 keV. By carefully choosing the reflections and mounting multiple crystals simultaneously on the goniometers, it is possible to construct a single monochromator with a number of different resolutions available to the user. Resolutions are chosen by translating the goniometers perpendicular to the beam to select the appropriate crystals. Such an approach gives the user flexibility to choose a higher-flux, lower-resolution mode for part of their experiment, before switching to a high-resolution (and therefore lower flux) mode to examine, for example, a particular feature in more detail. This switch can be made relatively quickly during the course of a single experiment and is therefore highly flexible. Such an approach would likely be followed at an NSLS-II IXS beamline.

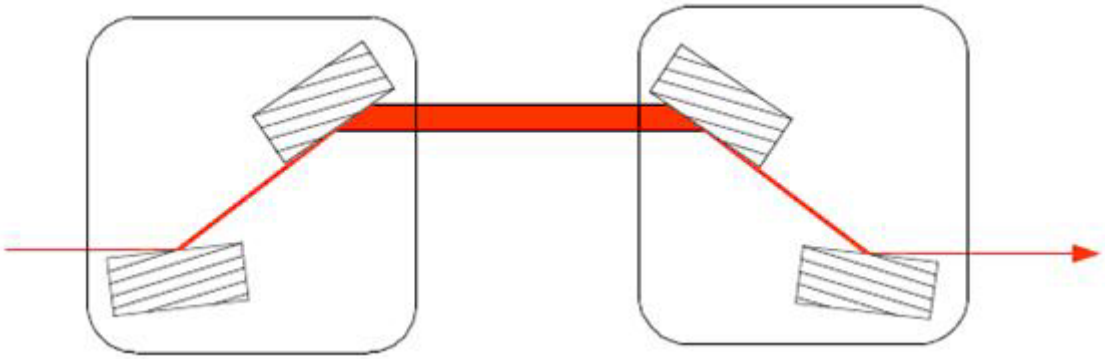

Figure 11.5.9 Medium-energy resolution, constant bandpass monochromator (following Toellner et al., APS [11.5.17]). The use of a four-bounce arrangement of crystals allows a constant bandpass, high-spectral efficiency monochromator (see Figure 11.5.1).

The new Sector 30 beamline at APS also provides a good example of the kind of end station envisaged for the 50 meV instrument at NSLS-II. Figure 11.5.10 shows an illustration of this concept. It features a spectrometer with both horizontal and vertical scattering geometries. This is particularly useful for examining polarization effects in the resonant cross-section, allowing the user to switch between polarization in the scattering plane and perpendicular of the scattering plane, in a single experiment. In addition, the availability of a horizontal scattering geometry allows the accommodation of large sample environments such as pressure cells, cryostats, or superconducting magnets that for various physical reasons only permit horizontal scattering. Finally, having a horizontal scattering geometry available allows the user to position the spectrometer at a 90° scattering angle and thus suppress all the nonresonant elastic scattering. This can greatly increase the visibility of inelastic features at low energy transfers.

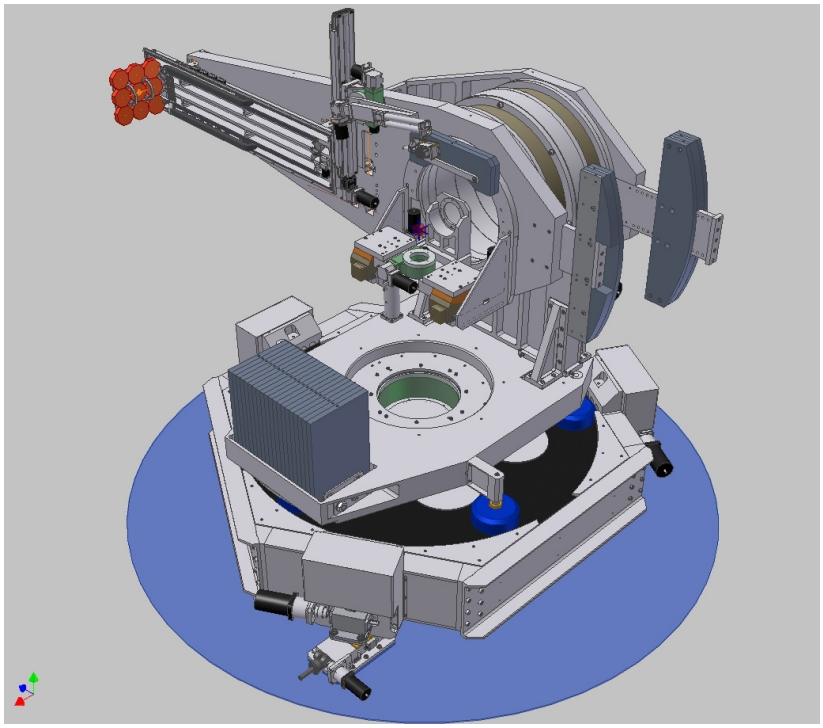

Figure 11.5.10 Possible design for 50 meV IXS end station. Figure shows recently built end station at APS with additional features, including multiple analyzers.

The spectrometer also features 1) a novel counterbalance arrangement to eliminate twisting of the arm as it moves from zero to 90° in the vertical, so the analyzer remains lined up even at the very highest resolutions, and 2) a motorized analyzer stage that allows analyzers of different radii to be used in the same instrument.

There are also several improvements that one would make to such an instrument at NSLS-II. The first would be to take advantage of the increased count rates at NSLS-II relative to existing sources, to carry out polarization analysis of the scattered beam. This has not been attempted before in the hard x-ray regime because of the prohibitively low count rates, but it may be possible at NSLS-II. Such experiments would utilize an analyzer working at 45°; count rates could be expected to be very low, but it may be feasible for certain experiments. If possible, such experiments would provide quantitatively new information, allowing the symmetry of the excitations to be probed directly. This would greatly facilitate the identification of the various observed excitations—something that presently can only be done with theoretical input or by comparison with other techniques, a process that is not always unambiguous.

An additional improvement shown in the figure would be to include multiple analyzers. Such an approach has been utilized in a number of other IXS spectrometers, notably in this energy resolution range at BL12XU at SPring-8. Typically, for such spectrometers the multiple analyzers focus on a single detector and the count rate is increased at the expense of reciprocal space resolution. As discussed below (Section 11.5.3), we are proposing to use position-sensitive detectors to improve both the resolution and data throughput (by simultaneously collecting data for a range of energy transfers). Thus we propose a detector for each analyzer crystal. This would therefore allow data to be taken at multiple q values simultaneously. For single-crystal work, the cut taken by such an area of analyzers through reciprocal space would not be a linear one because the sample is fixed while the data is collected; rather, it would represent a curved path. However, this only allows a slight complication in the data analysis, and by careful choice of scattering angles the impact of this can be minimized. Such an approach would dramatically increase the data rates of the instrument. Also note that similar approaches are routine at spallation neutron sources, where sophisticated software is available to reconstruct the path through (q, E) space in much more complicated geometries than are proposed here. Finally, we note that Figure 11.5.10 illustrated nine analyzers; there is no reason, in principle, that this number could not be extended, though it would be an engineering challenge to handle the associated

additional weight. A conceptual layout for this instrument is show in Figure 11.5.11, in which only a single analyzer is illustrated, for clarity.

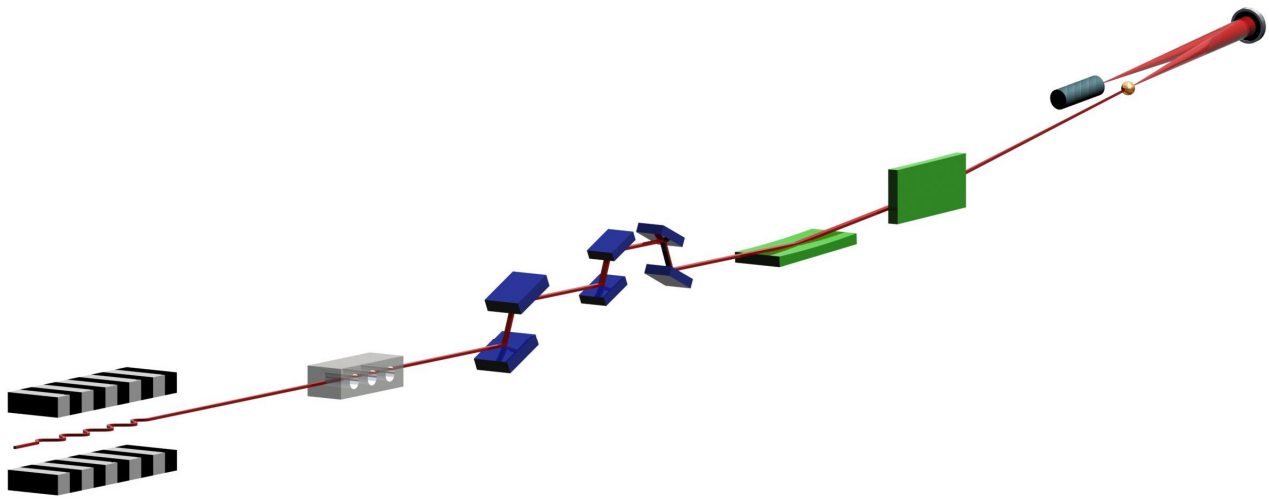

Figure 11.5.11 Conceptual layout for an IXS beamline at NSLS-II. Downstream of the undulator source is a collimating optic (if required), a high heat load monochromator (with eV bandpass), followed by a high-resolution monochromator (meV bandpass), and focusing optics. Downstream of the sample is a large-area analyzer (perhaps multiple analyzers) and a position-sensitive detector (see text).

11.5.3 Strip Detector

To allow for focusing and energy analysis, IXS spectrometers use a so-called Rowland circle geometry. This geometry requires a bent crystal analyzer with a bending radius that is the same as the diameter of the Rowland circle. Bending a perfect crystal causes strain and deformations of the crystal that make-high energy resolution impossible. To circumvent this difficulty, current analyzers use a diced crystal that results in thousands of small, flat, unstrained cubes.

The finite cube size contributes to the energy resolution. To minimize this contribution, one works very close to backscattering. This geometry can cause problems by constraining the sample environment; for example, it makes the use of large magnet cryostats difficult because of the requirement that the detector be near the sample. For Resonant Inelastic X-ray Scattering experiments, the need to be near backscattering is particularly problematic, since the incident energy is also constrained to be near the energy of an x-ray edge. In general, it is not possible to match a backscattering energy with a resonant energy, using the crystals that are currently available. This limitation has meant that high-resolution RIXS studies have been limited to one element (Cu) out of dozens of elements with K and L edges that would otherwise be suitable. Further improvements to this technique are limited by the loss of analyzer area and the inability to create cubes that are sufficiently small.

However, it is possible to circumvent the limit imposed by cube size, using a strip detector. Such a detector consists of pixels approximately 50 microns wide with a length on the order of several mm. Work by Huotari et al. [11.5.21], shown in Figure 11.5.12, has proven the feasibility of this method. As illustrated in Figure 11.5.12, the use of a position-sensitive detector allows one to resolve, spatially, the contributions from the different parts of the diced cube (rather then integrating them all, as is done traditionally with a point detector). Since there is a perfect angle–energy correlation (via Bragg's law), this corresponds to energy resolving the diffracted beam, with the energy resolution now being determined by the intrinsic Darwin width of that reflection (assuming the blocks are, in fact, unstrained). Thus, this approach both improves the energy resolution and relaxes the constraint on being near backscattering. Use of a strip detector would thus enable

high-resolution studies (tens of meV) at all the available edges—in most cases, a 10-fold improvement in resolution. Note that this increase in resolution comes at no loss in signal; in fact, because a position-sensitive detector can collect a range of energy transfers simultaneously, the net data collection rate can be significantly increased relative to point-detector schemes. Thus, the seemingly impossible dual feat of improved resolution and improved data rates is achieved. It will also allow the placement of analyzers closer to the sample, thereby improving the solid angle collected and further increasing the count rates. We anticipate that such schemes will be utilized in the medium-energy resolution instrument at NSLS-II.

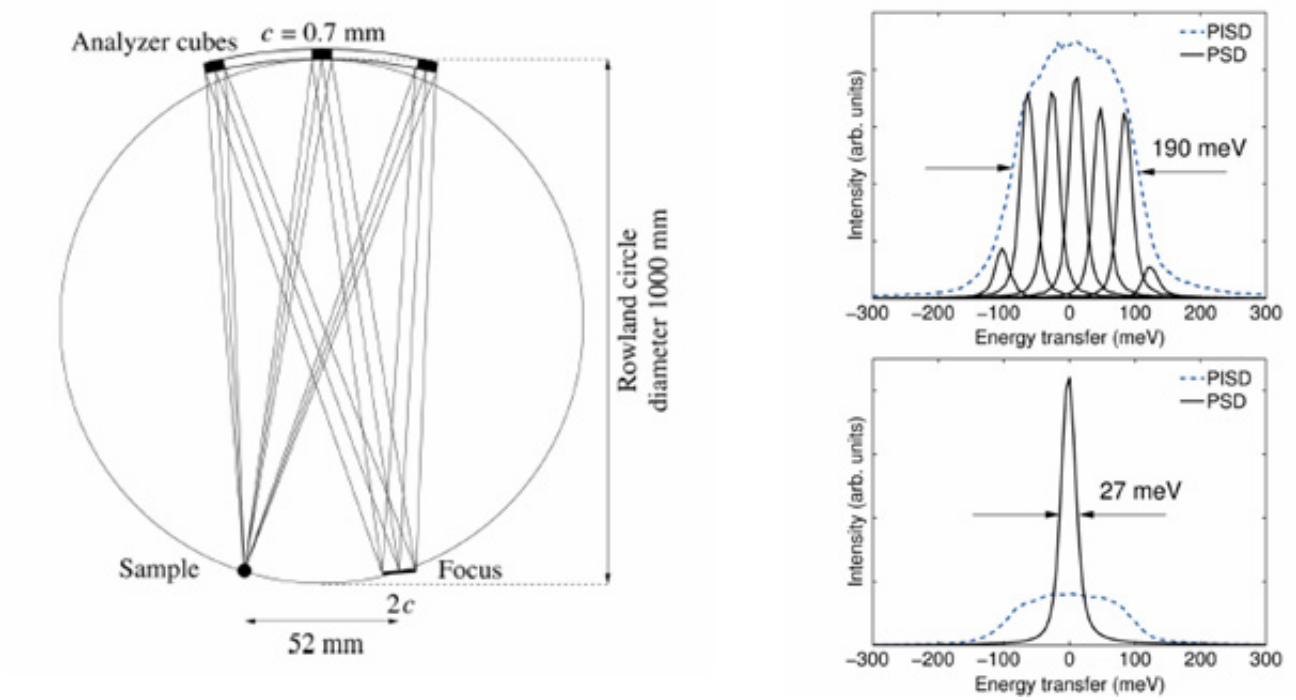

Figure 11.5.12 Rowland Circle geometry and improved resolution due to a strip detector [11.5.21].

11.5.4 Laboratory and Office Space

Several ancillary pieces of equipment would significantly improve the productivity of an IXS beamline and should be available to the users of such a beamline. These include optical conductivity/ellipsometry setups to measure $\sigma(\omega)$ in single crystals in the energy range up to ~6 eV. These measurements provide $\sigma(\omega)$ data that naturally complement the IXS measurement of $S(q,\omega)$ and related quantities that would be performed on the medium-energy resolution instrument and would thus provide a useful, quick cross-check of the data coming off the beamline. Similarly, SQUID magnetronometry and devices such as a Quantum Design PPMS, which provide growth characterization of bulk properties, would be extremely useful. Finally, single-crystal orienting (and possibly) facilities that would allow a sample to be oriented on a goniometer and transferred to the IXS spectrometer would be extremely useful, particularly for the very-high-resolution IXS instruments, which will not have full 6-circle capability and will require pre-orienting of the sample before taking data.

11.5.5 Outstanding Issues

IXS experiments will be among the most photon-hungry experiments performed at NSLS-II. As such, there is a strong case to be made to dedicate a straight section to each end station to optimize the amount of time available for data taking. In particular, the medium-resolution instrument is likely to be well served by a

dedicated set of upstream optics and would comfortably sustain a sufficiently large user community with great enough scientific impact to justify such a development. Finally, these experiments are mostly flux limited, not brightness limited; if, in the context of Title I design, it becomes apparent that longer straight sections are possible and that one could still close the gap in a U19-type device, then the IXS beamline(s) would greatly benefit from such developments. Optics that will be considered include multiple devices in a single straight section with focusing between them; three 2 m SCU devices would be the preferred alternative. Again, in an 8 m straight, accelerator studies need to be performed to determine the impact of such an approach.

References

[11.5.1] A.Q.R. Baron, Y. Tanaka, D. Miwa, D. Ishikawa, T. Mochizuki, K. Takeshita, S. Goto, T. Matsushita, H. Kimura, F. Yamamoto, and T. Ishikawa. Early commissioning of the SPring-8 beamline for high resolution inelastic x-ray scattering. *Nucl. Instrum. Meth. A* **467** 627 (2001).

[11.5.2] A. Bergamin, G. Cavagnero, G. Mana, and G. Zosi. Scanning x-ray interferometry and the silicon lattice parameter: Towards 10^{-9} relative uncertainty? *Euro. Phys. J. B* **9** 225 (1999).

[11.5.3] D.H. Bilderback, S.A. Hoffman, and D.J. Thiel. Nanometer spatial resolution achieved in hard x-ray imaging and Laue diffraction experiments. *Science* **263**(5144):201 (1994).

[11.5.4] E. Burkel. *Inelastic Scattering of X-ray s with Very High Energy Resolution*, Vol. 125 of *Springer Tracts in Modern Physics*. Springer, Berlin, 1991.

[11.5.5] E. Burkel. Phonon spectroscopy by inelastic x-ray scattering. *Rep. Prog. Phys.* **63** 171–232, 2000.

[11.5.6] M.R. Howells, D. Cambie, R.M. Duarte, S. Irick, A.A. MacDowell, H.A. Padmore, T.R. Renner, S. Rah, and R. Sandler. Theory and practice of elliptically bent x-ray mirrors. *Opt. Eng.* **39** 2748 (2000).

[11.5.7] C. Masciovecchio, U. Bergmann, M. Krisch, G. Ruocco, F. Sette, and R. Verbeni. A perfect crystal x-ray analyzer with meV energy resolution. *Nucl. Instrum. Meth. B* **111** 181 (1996).

[11.5.8] T. Matsushita and H. Hashizume. X-ray monochromators. In E. E. Koch, editor, *Handbook on synchrotron radiation*, Vol. 1, pp 261– 314. North-Holland, Amsterdam, 1983.

[11.5.9] Ch. Morawe, P. Pecci, J. Ch. Peffen, and E. Ziegler. Design and performance of graded multilayers as focusing elements for x-ray optics. *Rev. Sci. Instr.*, **70** 3227 (1999).

[11.5.10] V.V. Protopopov, V.A. Shishkov, and V.A. Kalnov. X-ray parabolic collimator with depth-graded multilayer mirror. *Rev. Sci. Instr.*, **71** 4380 (2000).

[11.5.11] M. Schuster and H. Göbel. Parallel-beam coupling into channel-cut monochromators using curved graded multilayers. *J. Phys. D: Appl. Phys.* **28** A270 (1995).

[11.5.12] Yu. Shvyd'ko. *X-Ray Optics – High-Energy-Resol. Appl.*, Vol. 98 of *Optical Sciences*. Springer, Berlin Heidelberg New York, 2004.

[11.5.13] Yu.V. Shvyd'ko. "Advanced designs of angular dispersive x-ray monochromators." *To be published*, 2006.

[11.5.14] Yu.V. Shvyd'ko, U. Kuetgens, H.D. Rüter, M. Lerche, A. Alatas, and J. Zhao. Progress in the development of new optics for very high resolution inelastic x-ray scattering spectroscopy. *Submitted for publication*, 2006.

[11.5.15] Yu.V. Shvyd'ko, M. Lerche, U. Kuetgens, H.D. Rüter, A. Alatas, and J. Zhao. Bragg diffraction of x-rays in asymmetric backscattering geometry. *Submitted for publication*, 2006.

[11.5.16] H. Sinn. Spectroscopy with meV energy resolution. *J. Phys.: Condens. Matter*, **13**(34) 7525 (2001).

[11.5.17] T.S. Toellner. Monochromatization of synchrotron radiation for nuclear resonant scattering experiments. *Hyp. Interact.*, 125:3, 2000.

[11.5.18] R. Verbeni, F. Sette, M.H. Krisch, U. Bergmann, B. Gorges, C. Halcoussis, K. Martel, C. Masciovecchio, J.F. Ribois, G. Ruocco, and H. Sinn. X-ray monochromator with 2×10^{-8} energy resolution. *J. Syn. Rad.*, **3**:62–64, 1996.

[11.5.19] J.P. Sutter, A.Q.R. Baron, D. Miwa, Y. Nishino, K. Tanasaku, and T. Ishikawa*, J. Syn. Rad*. **13** 278 (2006).
[11.5.20] C. Giles, C. Vettier, F. de Bergevin, C. Malgrange, G. Grubel, and F. Grossi, *Rev. Sci. Instr.* **66** 1518 (1995).
[11.5.21] Huotari et al., *J. Sync. Rad.* **12**, 467 (2005).

11.6 A Coherent X-Ray Scattering Beamline (CXS)

11.6.1 Introduction

In this section we discuss the conceptual design of an x-ray beamline that has been designed to take advantage of the extraordinarily high coherent flux that will be provided in the hard x-ray range by NSLS-II. We begin with a few notes on terminology used in this section:

- **Coherent X-Ray Scattering (CXS)** or **X-Ray Coherent Scattering** refers in general to scattering measurements exploiting the coherent nature of the hard x-ray beam.
- **X-Ray Photon Correlation Spectroscopy (XPCS)** or **X-Ray Intensity Fluctuation Spectroscopy (XIFS)** are two terms for the same technique, namely, measurements of the time evolution of fluctuating x-ray speckles, from which characteristic sample decay time(s) are obtained. Hereafter, for brevity, we will refer to this technique as XPCS.
- **Coherent X-Ray Diffraction (CXD)** or **Coherent Diffractive Imaging (CDI)** or **Coherent X-Ray Diffractive Imaging (CXDI)** or *lensless imaging* refer to problems of phase retrieval and object reconstruction based on over-sampled measurements of the scattered intensity

We describe here a beamline with two end stations operating in parallel. The first end station is optimized for coherent x-ray diffraction and large-angle x-ray photon correlation spectroscopy and the second is for small-angle x-ray photon correlation spectroscopy. Finally, we note that diffraction-enhanced imaging and full-field imaging are not part of the scientific mission of this beamline

11.6.2 Conceptual Design of the CXS

The basic concept of the proposed design of the coherent scattering beamline at NSLS-II is to substitute the intrinsic source with a secondary source that is controlled by the end user. This decouples uncertainties of position, stability, and emittance of the synchrotron source from those used for measurements. It also allows multiplexing of the source using horizontally deflecting mirrors so that two stations can be operated in parallel. A secondary source is employed only in the horizontal direction, which serves to enlarge the lateral coherence seen at the sample position and brings the horizontal and vertical coherence lengths closer to each other. For full exploitation of the coherent flux using the natural vertical source size, a moderate amount of vertical focusing can be added.

In its simplest configuration, the optical design can be reduced to a sequence of slits, as illustrated in Figure 11.6.1. Details of the design are presented in subsequent sections. For the time being, note that monochromator crystals and mirrors, the edges of which are used to separate the branches, are omitted from the figure as they do not affect the coherence properties, at least when they act as perfect reflectors. Some of the slits are made to operate in white beam at grazing angle, so these will be designed with a second anti-scatter edge. Some slit pairs have separated blades, comprising slit/mirror or slit/slit pairs, with an offset between the blades, but the effect of this is ignored, as this offset is small compared with the separation of the elements.

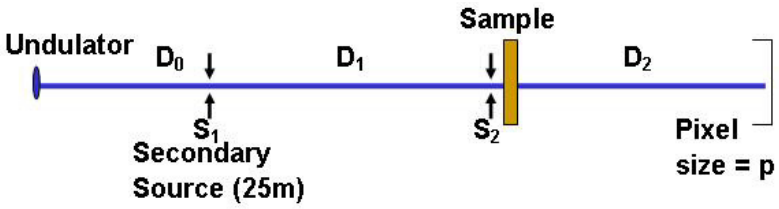

Figure 11.6.1 Schematic layout of a slit-based optical configuration of a CXS beamline.

Four equations relate the slit separations, S_1 S_2, and the distances D_0, D_1, and D_2 between the four optical planes: source (half-width σ_x), secondary slit (separation S_1), coherence-defining slit (S_2 with sample) and the detector (pixel size p).

The pixel size of the detector, p, must be less than half the fringe spacing arising from the sample slit: $\lambda D_2/ S_2 > 2p$. This ensures the speckles are sufficiently over sampled.

A similar equation defines the minimum detector distance needed to put the detector in the far field of diffraction from the sample: the fringe spacing must be wider than the geometric shadow of the sample: $\lambda D_2/ S_2 > S_2$ or $S_2 < \sqrt{(\lambda D_2)}$.

The coherence length at the sample is defined by diffraction from the secondary source. So for the sample to be illuminated coherently, $\lambda D_1/ S_1 > S_2$.

Finally, ray-tracing is used to trace back the minimum size of the synchrotron source itself needed to fill the secondary source with light: $2\sigma_x > S_1 + (S_1 + S_2)(D_0/D_1)$.

All four inequalities are nominal in the sense that the related quantities are distributions that do not cut off abruptly. For example, coherence degrades gradually with the slit separation, not abruptly. Also the throughput of the experiment (flux in the detector) diminishes when the inequalities are optimized, and is highest when they are just satisfied. An optimal design should therefore consider these to be defining equalities. For example, the coherent flux on the sample is best when the coherence length equals the sample size.

Based on these considerations, the following tables summarize the chosen and derived values of these parameters for both the small-angle XPCS branch line (Table 11.6.1) and the coherent diffraction and large-angle XPCS branch line (Table 11.6.2):

Table 11.6.1 Parameters for the Small-Angle XPCS Branch of the Coherent X-Ray-Scattering Beamline.

Item	Value	Comments
Maximum sample-to-detector distance	10 m	For desired maximum wave-vector transfer of 2 nm^{-1}, provides workable window size of ≈ 300 mm
S_2 horizontal slit size	≤ 30 μm	Otherwise in near field diffraction limit
Maximum S_1 secondary source size	80 μm	Using sample to secondary source size = D_1 = (52-27) m = 25 m and S_2 = 30 μm. (The corresponding mirror size is only ≈ 30 mm)
Desired pixel resolution	≤ 70 μm	Matching solid angle subtended by the source at the sample position to the solid angle of the pixels subtended at the sample position and moderately under-resolving speckles as described in the text.

Table 11.6.2 Parameters for the CXD Branch of the Coherent X-Ray-Scattering Beamline.

Item	Value	Comments
Maximum sample-to-detector distance	3 m	Larger separations are not practical because of the need to position area detectors over a range of large scattering angles
S_2 horizontal slit size	$\leq$ 100 μm	
Maximum S_1 secondary source size	70 μm	Using sample to secondary source size = D_1 = (97-29) m = 68 m and S_2 = 30 μm. (The corresponding mirror size is only $\approx$ 30 mm.)
Desired pixel resolution	$\leq$ 20 μm	Coherent fringe resolution on the detector

The division of the beam into two parallel operating stations will not compromise the performance of either one. The coherent part of the beam, even at NSLS-II, is still only a fraction (about 10%) of the total flux of the undulator at 12 keV. Two coherent beams can then be taken from the central cone of the undulator, side-by-side, without any loss of coherent flux. Because a hard edge is required to split the beam, a one-sided secondary source results anyway, so the method works best when a well-defined symmetric double-sided secondary source is utilized. One compromise of such a multiplexed beamline design is that the shared undulator source provides the same spectrum to both stations, and the freedom of either of these to tune the spectrum by varying the gap and/or taper has to be restricted. However, this is compatible with the scientific applications of both branches that are not often expected to require specific tuning of the energy or energy-width. Given that the choice of energy has historically been limited by detector efficiency, which is expected to improve considerably, a good "target" energy for both branches would be 12 keV; the lower energy limit is 7 keV.

The second innovation over previous designs is to extend the length of the beamline beyond the standard value of 60 m. This leads to a general improvement in performance for a number of experimental situations. With longer coherence lengths, radiation sensitive samples will receive less dose and will survive longer in XPCS measurements. This should allow the power of XPCS to be applied to biological samples that are more sensitive to radiation damage. Specifically, XPCS might now be used to study concentrated protein solutions such as the α and β crystallins of the eye. Furthermore, coherent diffraction (CXD) experiments using demagnification to concentrate a coherent beam on a nanoscale sample will attain either larger demagnification ratios (more flux) or create more space for the sample environment. The increased flux density at the sample position will facilitate atomic-resolution CXD. The atomic resolution will allow CXD to examine individual clusters in catalysts, in situ with reactions taking place. The proposed hutch layout for the sector is shown in Figure 11.6.2. Within this overall design concept, there are several additional design requirements:

- Mirrors and monochromators will be water cooled to avoid the vibration and maintenance issues associated with liquid nitrogen.
- Mirror and monochromator surfaces should all be polished to state-of-the-art finishes and figure errors to minimize degradation of the beam brilliance.
- Floor vibrations and ambient temperature fluctuations should be minimized.

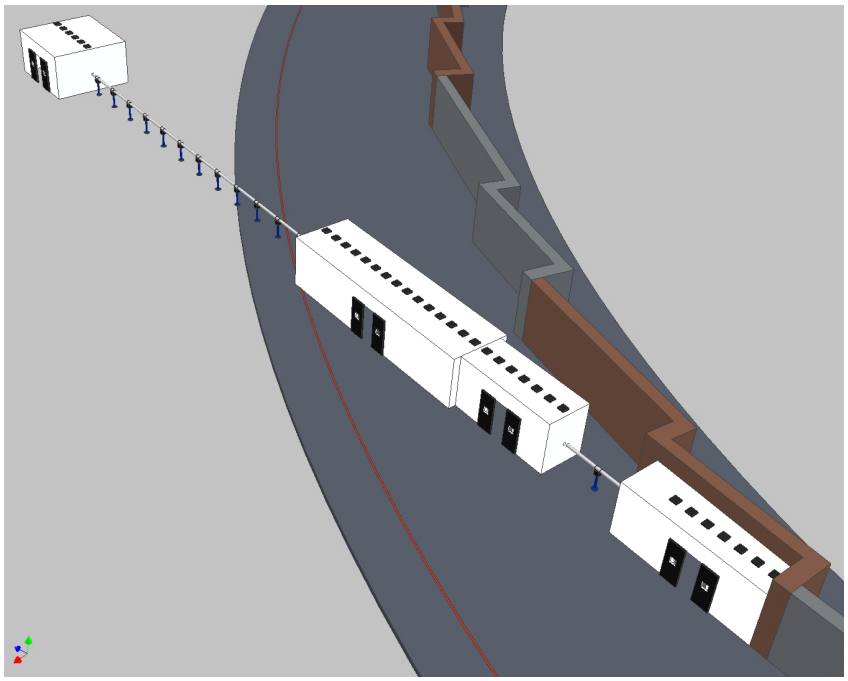

Figure 11.6.2 Proposed floor layout for the coherent scattering beamline at NSLS-II. Proceeding from the storage ring, the first hutches are optics hutches, the next hutch is the small-angle XPCS station, and the last hutch is the coherent x-ray diffraction and large wave-vector transfer XPCS station.

11.6.3 Source

A high-beta 8 m straight is requested with a standard U19 undulator placed at its center. A 3 m device is anticipated initially. We note that we do not require this device to operate at closed gap in the high-beta straight section; the minimum requested K value is K = 1.8 and corresponds to the cross-over from operation at lower x-ray energies on the third undulator harmonic to higher x-ray energies on the fifth harmonic. At the time of writing, the storage ring design parameters in the horizontal direction are: β_x=18.1 m, giving σ_x=100 μm and σ_x' = 5.5 μrad. This assumes the damping wigglers are operating to give the lowest overall emittance of ε_x = 0.55 nm. In the vertical direction, the source parameters are σ_y = 3 μm and σ_y' = 1 μrad.

The additional divergence of the radiation cone from this undulator is expected to be $1/\sqrt{N\gamma}$ = 13 μrad, which dominates the horizontal divergence. The expected typical operations would be at 12 keV, which falls on the fifth harmonic of the U19 tuning curve at K = 1.3. In the optical design presented here, higher harmonics would be cut off by the mirror and lower ones by use of a thin absorber. Such filtering reduces the incident power on the monochromator facilitating water cooling and enables wider bandpass pink beam operations for a small number of potential applications.

The diffraction-limited source sizes and divergences of the photon beam are $\sigma_r = \sqrt{2\lambda L}/4\pi$ = 2 μm and $\sigma_r' = \sqrt{\lambda/2L}$ = 4 μrad. We note, however, that in practice such values are not achieved in the vertical direction at higher harmonics because of the finite energy spread of the electron beam. We take, therefore, at 0.1 nm, the working values for the 1-sigma photon beam sizes ($\Sigma_{x,y}$) and divergences ($\Sigma_{x',y'}$) as Σ_x = 100 μm and Σ_y = 6 μm and $\Sigma_{x'}$ = 15 μrad and $\Sigma_{y'}$ = 12 μrad.

The U19 device is best-suited for these applications among the available devices proposed for NSLS-II. We note, however, that the superconducting mini-gap undulator (SCU) with 14 mm period (U14) is the preferred insertion device for the sector, should it become available as a result of ongoing research and development. The reason for this is quite simple: U14 has the highest proposed brightness in the specified energy range of the beamline (7–12 keV) of the insertion devices proposed. We note, however, that it might not be possible for such a device to reside in a high-beta straight section.

The shared undulator source provides the same spectrum to both branches of the beamline. To give greater flexibility, an upgrade path would be to add a second undulator in-line (tandem) with the first one. This is preferable to canting them, in that when all users agree on the same energy both undulators can be tuned to that energy, doubling the total flux. At other times, users can select their own energy by changing the gap of one of the undulators. This is the approach taken, for example, at the ESRF ID (Troika) beamline.

Finally, we discuss the reasons for choosing the operating x-ray energy of the beamline in slightly more detail. In addition to the explicit λ^2, several factors in the expression for the XPCS Signal to Noise Ratio, SNR, depend on the x-ray energy/wavelength. First, the brightness itself depends on the x-ray energy, as does the detector efficiency: For a 300-micron-thick Si sensor bump-bonded onto an XPCS detector chip, the efficiency would be near unity for x-ray energies up to about 12 keV (0.1 nm); for a similar GaAs or Ge sensor, the efficiency would be near unity beyond 20 keV. The effective sample thickness (W) also depends on energy, in that W should be picked to be more-or-less equal to the sample's x-ray absorption length, which, away from x-ray adsorption edges, varies as λ^{-3}. This factor is not relevant for surface XPCS measurements. Another important advantage of shorter wavelengths (i.e., higher energies), directly related to the energy-dependence of the sample adsorption length, is that sample damage is lower at higher energies. Since the optimum energy may be different for different samples and conditions, the optics of the XPCS beamline will allow for a tunable energy range from ~7 keV to ~20 keV for maximum flexibility.

11.6.4 Optics

Relatively few optics are employed in the design. The main reason for this is that imperfect optics can reduce the coherence in a way that is hard to control. A minimum number of windows are employed and the materials of these are chosen carefully, particularly for windows near the sample. Mirrors and monochromator crystals are made from dislocation-free silicon, germanium, or silicon carbide, polished to the best figure, to minimize the disturbance of the wavefronts passing their surfaces. The mirrors are operated at small angle (3 mrad) so that coatings, which are often not as flat as the substrate, will be unnecessary. Because of the overall length of the beamline, there is enough separation of the branches for sample environmental hardware.

The optical layout of mirrors and monochromators in the two branches is shown in Figure 11.6.3. The layout takes one of the experimental hutches outside the designated ring building walkway, but not outside the perimeter of the lab-office modules. Thus, the building construction associated with the project is kept to a minimum.

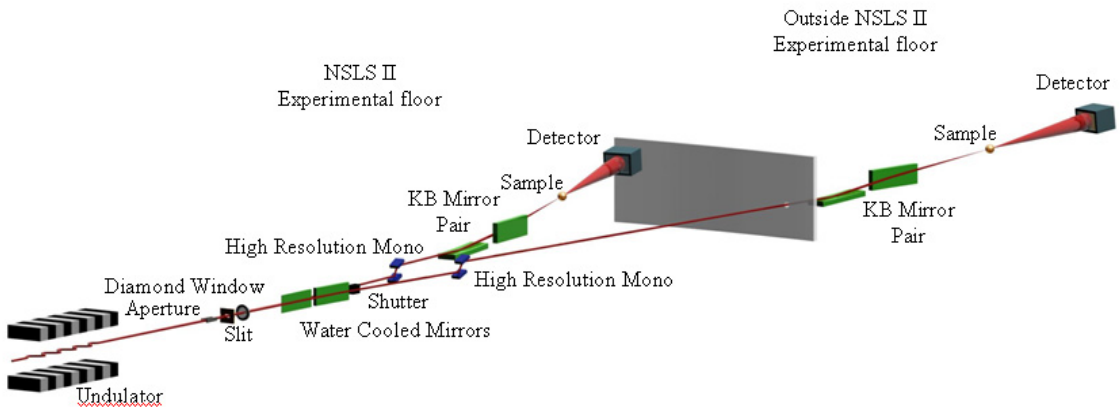

Figure 11.6.3 Conceptual layout of coherent scattering beamline. The two water-cooled upstream mirrors split the beam and feed two end stations simultaneously. The second end station, for XPCS, lies outside the experimental hall, the wall of which is denoted by the gray panel.

Table 11.6.3 lists, in upstream-to-downstream order, the major components comprising the CXS beamline at NSLS-II. Note that locations are approximate.

From the conceptual design outlined in Section 11.6.1.2 and the descriptions in Table 11.6.3, we can make more definitive statements about the required sizes and hence anticipated power loads for several key optical components. The secondary sources (mirrors) define the required horizontal aperture of the beamline. The mirrors for both branch lines each have a projected size of ≈100 μm. (At an incidence angle of 3 mrad, the corresponding mirror lengths are only 3.3 cm.). Summing these two projected sizes and allowing some horizontal offset between the 2 mirrors, we can limit the maximum horizontal aperture of the incoming x-ray beam to ≤500 μm. In the vertical, we must accept a larger portion of the beam because of the increased vertical coherence length. For the fixed vertical aperture, we accept several vertical coherence lengths by choosing a vertical aperture of ≈500 μm. To limit power on the downstream components and also mitigate concerns about placing U19 in a high-beta straight section, we anticipate running for 7 keV ≤E <9 keV on the third harmonic of U19 and for 9 keV ≤E <12 keV on the fifth harmonic. With this restriction and the restriction on the incident beam aperture (500 μm × 500 μm), we can estimate the worst-case power loading and typical power loading on the optical components.

With a minimum energy for the beamline of 7 keV, then the worst case condition is operation on the fifth harmonic at E_5 = 8.5 keV, corresponding to E_1 = 1.7 keV and a U19 K value of ≈ 1.8. The maximum incident angular power density is ≈70 kW/mrad^2. The 500×500 μm aperture at ≈25 m subtends a solid angle of ≈ 0.02 × 0.02 mrad^2, so the power transmitted through this aperture is ≈ 30 W, or 120 W/mm^2.

The next component in the beamline is a brilliance preserving high-pass filter. This might, for example, be composed of a small ≈100 μm-thick diamond crystal, discussed in Section 11.3.4. The power transmitted though such a filter and incident upon the horizontally deflecting mirrors is 20 W. Assuming an incidence angle of 3 mrad, then the incident power density on the mirrors is ≈ 20 W*0.003/(0.5×0.5 mm) = 0.24 W/mm^2, which is well within acceptable limits for mirror side cooling via water.

The final key optical component to consider in the worst case heat load scenario is the monochromator. Each mirror has a projected horizontal size in the beam of ≈100 μm, so the maximum power reflected by the mirror and incident upon the monochromator (ignoring the power at higher x-ray energies that is removed by mirror) is 4 W or, at normal incidence, 80 W/mm^2. The monochromators are at approximately a factor of 50% greater distance from the source than the mirrors are, so the normal power density is reduced to ≈ 40 W/mm^2. At 8.5 keV and for a Si(111) or Ge(111) monochromator, the incidence angle is ≈14º, so the power density is 10 W/mm^2. Further analysis and comparison with power loads on existing operational beamlines are needed to determine whether this power load can effectively be managed with only side cooling by water. The expectation is that it can, and that liquid nitrogen cooling and the maintenance and vibration considerations associated with such optics are not necessary.

For reference purposes, we repeat the above calculations but for the envisioned typical mode of operation, namely, λ = 0.1 nm, which corresponds to E_1 = 2.4 keV and K = 1.3. The power through the fixed aperture is 20 W, the power transmitted through the filter is 11 W, the power density on the mirrors is 0.13 W/mm^2, and the power incident upon the monochromator is 2 W or 3 W/mm^2. These very modest power levels will help ensure the stability of the coherent x-ray scattering beamlines, which is of critical importance.

Table 11.6.3 Principal Components of the Coherent X-Ray-Scattering Beamline at NSLS-II.

Item	Location	Description
U19 (or U14)	0 m	Radiation source
Front end		Beam and bremsstrahlung collimation
Shield wall	23.7 m	
First Optics Enclosure (FOE)	23.7 m (9 × 2.5 m^2)	White-beam radiation shielding enclosure
Differential pump	24 m	Windowless connection to the storage ring for brilliance preservation
Power limiting aperture	25 m	Aperture of (20 × 20) μrad^2
Filter	25.5 m	Brilliance-preserving high-pass filter. Filter material could be single-crystal diamond or a thin, highly polished silicon foil.
Variable aperture (white-beam slits)	26 m	Inboard side of this slit can be used to reduce the illuminated length of the outboard deflecting mirror
Outboard deflecting mirror	27 m	Acts as a low-pass filter and secondary source for the small angle XPCS end station. Deflection angle ≥ 6 mrad. For effective harmonic rejection at the nominal operating condition of λ = 0.1 nm, the mirror should be made of SiC provided it can be finished to a quality corresponding to the best Si mirrors.
Inboard beam-defining slit (white beam)	28 m	White-beam inboard ½ -slit that can be used to reduce the illuminated length of the inboard-deflecting mirror.
Inboard deflecting mirror	29 m	Acts as a low-pass filter and as a secondary source for the coherent diffraction and large angle XPCS end station. Deflection angle ≥ 6 mrad. Mirror materials and coatings will be identical to those for the outboard deflecting mirror.
White-beam and mis-steered pink beam stop	32 m	Critical components needed to prevent inadvertent personnel radiation exposure and equipment damage
PinKBeam shutter	33 m	Single shutter to stop the pink beam from exiting the first optics enclosure
Shielded transport	33–44 m	PinKBeam transport to the second optics enclosure
Second optics enclosure	44 m (4 × 3 m^2)	Contains 2× monochromators and 2× shutters for the end stations
Monochromators (×2)	45 m and 46 m	Small offset, vertical bounce Ge (small angle XPCS) and Si (coherent diffraction and large angle XPCS) monochromators
Shutters (×2)	46.5 m	Independent, pinKBeam capable shutters for the two end stations
Small angle XPCS end station	47 m (15 × 4 m^2)	See Section 11.6.6.1. Nominal sample position is 52 m from the source
Shielded transport	47–97 m	Shielded transport passing through the small-angle XPCS end station and the Laboratory Office Building
Coherent diffraction and small-angle XPCS end station	97 m (6 × 6 m^2)	Distance from the source will be maximized consistent with the hutch being entirely located in the adjoining lab and office complex.

11.6.5 End Stations

11.6.5.1 End Stations for XPCS

The small-angle XPCS station contains three main support platforms: 1) a motorized table (≈ 2 m wide × 4 m long) to support focusing optics and collimating slits, 2) a small motorized optic table (≈ 1 m wide × 4 m long) to support a variety of sample environments, and 3) a long table/double-rail-assembly (2 m wide × 10 m long) for supporting the exit flight path and detectors.

The first optical component in the end station, which is located 47 m from the source, will be a preliminary aperture that restricts the spatial extent of the beam entering the focusing optics. In spite of improving the horizontal coherence by use of the secondary source, there will still be a considerable asymmetry between the horizontal and vertical coherence lengths. In fact, the vertical coherence length at 50 m will be over 200 μm, while the horizontal coherence length will be ≈ 30 μm. For reasons of detector efficiency and to ensure that detection occurs in the far-field (Fraunhofer) diffraction regime, it is important that the effective vertical coherence length be reduced. This will be done with a 1D coherence-preserving vertical focusing optic (a promising option for this is the 1D kinoform lens), that creates a virtual source

upstream of the sample position. A second pair of slits will be located at the focal spot for aperturing of the focal plane. A third and fourth pair of slits will be located near the sample for selecting a coherent fraction of the x-ray beam and for eliminating parasitic scattering produced by the collimating slit. As well as the 1D focusing option described above, we will also require the option to introduce 2D focusing via such optics as Fresnel zone plates or KB mirrors.

A more detailed examination of focusing for XPCS is as follows. First, vertical focusing decreases the vertical dimensions of the illuminated region of the sample, so that the detector lies in the far field of the sample's speckle pattern. The XPCS SNR calculation given above is valid only in this limit. In the near field, the speckle contrast (A) is measured to be less than predicted by the far-field expression. Second, the SNR is maximized when the angular acceptance of the detector pixels equals the angular size of the source, so that with a detector composed of square pixels, the SNR is maximized with equal coherence lengths in the x and y directions.

Because of the very intense x-ray beams at the NSLS-II XPCS beamline, for many possible experiments, especially soft-matter experiments, it will be essential to implement strategies to avoid x-ray sample damage right from the start. We have already discussed that there may be some XPCS SNR advantage in using pink beam, rather than monochromatic beam. However, using pink beam increases the flux on the sample, and thus the sample damage, proportionally with the x-ray bandwidth. Therefore, pink beam should be used judiciously.

Therefore, with regard to the sample area of the small-angle XPCS end station, an important strategy to ameliorate the effects of sample damage follows from the observation that to carry out an XPCS measurement, in fact, it is necessary to illuminate a particular region of the sample for only a few times the sample's relaxation time. After that period the sample's configuration has become completely rearranged. This suggests a flow/translation scheme that moves a new portion of the sample into the x-ray beam on a time scale that is long compared to the sample's intrinsic relaxation time, but short compared to the time for sample damage to occur. For liquid samples, a micro-fluidics-based flow cell will transport fluid in and out of the beam. For solid samples, a rapid translation scheme will be implemented.

The final component in the end station is the detector support assembly, which must be capable of being positioned at any point along the long axis of the flight path support assembly, and it must have motorized stages that allow rapid positioning of the XPCS detector(s) in x and y. The latter translations are necessary because most XPCS-capable area detectors subtend only a relatively small solid angle. So, to perform measurements throughout the region of reciprocal space near it origin, detector translation in x and y is typically required.

11.6.5.2 End Station for CXD

The two coherence end stations will be differentiated by their complementary q-ranges. XPCS experiments can be carried out in both end stations, specifically in a small-angle geometry in the first hutch and at wider angles in the second hutch, using a diffractometer. The detector distance will be considerably longer for the small-angle setup, in which the detector is positioned on vertical and horizontal translation stages. In the CXD hutch, the detector will move on a compound diffractometer detector arm, which for reasons of mechanical strength and available space inside the hutch will be limited to 3 m.

The CXD experiment will consist of a focusing optics table, a diffractometer, and a long (3 m) detector arm. The hutch needs to be large enough for a detector arm of 3 m length to swing on two axes, reaching up to 120º in the vertical and 70º in the horizontal, with polarization losses limiting the horizontal range. (Horizontal detector motion is required for studying in-plane ordering of liquid-like samples and for possible very heavy detectors that can not be attached directly to the detector arm.) The optics table should be incorporated into the diffractometer design so that micron-level stability of the relative positions can be assured.

The first optical component in the end station, which will be located ~100 m (number to be finalized when more building details are known) from the source, is a coherence-defining aperture that restricts the spatial extent of the beam entering the focusing optics. In the vertical, this aperture is determined by the source parameters to be 1.7 mm, while in the horizontal, it is determined by the secondary source, which is adjustable. Typically, S_1~80 μm at D_0=25 m, giving an entrance aperture width of 100 μm. In spite of improving the horizontal coherence by use of the secondary source, there is still a considerable asymmetry between these numbers. It is possible that the full vertical coherence will not be achieved because of the effects of windows or imperfections in the upstream optics. As discussed above for the XPCS end station, it will be possible to introduce upstream collimating optics, for example, a 1D kinoform lens in the monochromator hutch, to increase the flux and reduce the vertical coherence to the range of a few hundred microns.

Immediately in front of the sample position, optics are used to demagnify the source, to concentrate it onto a nanometer-sized sample at the center of the diffractometer. Assuming a 100 m hutch center position, the focus will be located 75 m from the coherence-defining horizontal source and 100 m from the vertical source. The substantial divergence will introduce a degree of (coherent) spherical wave component, or wavefront curvature, in the beam illuminating the sample. The type of optics needed will be defined in the detailed design, but possible choices include KB mirrors, zone plates, or Compound Refractive Lenses, CRLs.

The diffractometer will be a five- or six-circle configuration with a compound detector arm to allow in-plane and out-of-plane scattering geometries. The sample goniometer might employ intersecting phi/chi arcs to give the most clearance around the sample position with limited scanning range. Alternatively, the open kappa geometry could be used. Much emphasis is placed on the amount of clearance in the immediate vicinity of the sample and the center of the goniometer axes,because many probes will be needed to operate in parallel at that point. Space for sample environments would also be shared with these intersecting probes: liquid, gas or vacuum, high pressure, and high or low temperature, for example. A good solution for the sample goniometer might be a “hexapod” that combines very high x-y-z positioning accuracy with phi/chi tilts and a high load-carrying capability (10 kg). Use of a long beamline is also part of the strategy for creating space around the sample, given a fixed choice of demagnification or focal spot size.

It is not expected that a nm-sized sample can be oriented at the center of this diffractometer within a sub-micron-sized beam by the sample rotation axes alone; these would be expected to have a sphere of confusion of at least 20 μm. To take data at multiple orientations of a sample, it will be necessary to guide its x-y-z position as the angles are turned. This will require high-resolution optical microscope objectives trained on the sample from at least two directions. Sample selection and registration by optical microscopy is an essential part of the experiment. Additional x-ray-based registration involving fluorescent markers placed on the sample will be employed as well; for this, a fluorescence detector will also be needed to look at the goniometer axis center.

The detector arm needs to be a flexible configuration that can be adjusted easily. The detector itself (see below), which might be 10 to 20 kg, needs to have a readily adjustable distance from the sample. A flight tube is needed to cut out parasitic scattering, and slits can be used to fine-tune the entrance and exit apertures. It is useful to have the additional ability to rotate the detector around the axis of the diffracted beam direction. This is used to align extended diffraction features with the pixel directions for ease of data analysis.

11.6.6 Detectors

Next to the brilliance of the source, the single most important enabling component of the XPCS branchline is the detector. The three essential features of an XPCS detector are 1) a large number of pixels, 2) high speed, and 3) high x-ray detector efficiency. In addition, it is important for 4) the pixel size to be small enough to partially resolve the speckle in the scattered scattering pattern. Each of these points is discussed in more detail below.

The above considerations reveal the importance of employing a detector with many pixels: The SNR with 10^6 pixels, corresponding to what might reasonably be available on a single detector chip, is 10^3 times improved compared to a single-channel detector. Using 25 or 100 separate chips yields a further SNR improvement by a factor of 5 or 10. It is these very large improvements in SNR from detection in multiple channels that will permit the characterization of short sample relaxation times, even when the number of scattered x-rays per pixel per accumulation time (relaxation time) is far less than 1. Under these circumstances, it will be especially important to discriminate against dark counts.

The detector speed determines the fastest processes that can be studied. Specifically, to be able to study processes occurring on 0.1 microsecond time scales, it is necessary to separately recognize x-rays that are incident in the same pixel separated by 0.1 microseconds. Here it is important to note that the essential output of an XPCS experiment is not the time-dependence of the scattered intensity itself, rather it is $g_2(Q,t)$. Therefore, we are lead to a novel XPCS detector that incorporates an in-pixel auto-correlator. This would allow massively parallel processing of the data and would enormously simplify XPCS data acquisition and data reduction; instead of the formidable task of having to transfer the intensity in each pixel versus time, with a time resolution of 0.1 microsecond, out of the detector to storage for subsequent reduction to $g_2(Q,t)$'s in software—a computational challenge itself, the XPCS detector will determine g_2 pixel-by-pixel in real-time in the detector hardware.

For the case of a coherence length at the sample (after vertical focusing) of 10 microns in both x and y, the maximum XPCS SNR can be achieved for slits set to illuminate about 20 microns. The corresponding speckle size for 12 keV x-ray at a distance $D_2 = 5$ m from the sample is 25 μm. As noted above, the best XPCS SNR is achieved when the speckles underfill the pixels, indicating that a pixel size of 50 microns or somewhat larger would be suitable in the case of a 5 m sample-to-detector distance. A similar value follows from maximizing the expression for the XPCS SNR with respect to the pixel dimension (s) for $D_2 = 5$ m. [Note that $\Delta\Omega = (p/D_2)^2$.] Pixels somewhat larger than 50 μm do not significantly degrade the XPCS SNR. Nevertheless, detectors with the electronics necessary for calculating a correlation function incorporated in each pixel are currently uncertain and may require larger pixels than 50 μm; therefore, hutch dimensions that permit a maximum 10 m sample-to-detector distance have been chosen.

11.6.7 Computing and Controls

Computing requirements for the coherent x-ray scattering beamline are somewhat contingent on developments with detectors. In general, however, we note that both branch lines intend to make extensive use of 2D detectors that produce large volumes of data.

For CXD, powerful computers are needed for efficiently performing phase inversions, but data volumes are not expected to be extraordinarily large. For XPCS, as mentioned in the section above, extensive effort needs to be devoted to performing raw data reduction as close to the sensor element as possible. In fact, significant advances in the experimental program will be achieved by performing all the raw data reduction in the detector itself. If such advances are made, then the computing and data storage requirements for the XPCS program are relatively modest. If such advances are not made, however, then the computing and data storage requirements for XPCS are enormous. In this latter scenario, it is easy to imagine sustained raw data acquisition rates for the XPCS experiments at NSLS-II exceeding gigabytes per second.

11.6.8 Laboratory and Office Space

Typical laboratory and office space is required for the coherent x-ray-scattering beamline. In particular, a simple chemical or wet lab will be required for final preparation of samples before and during beamtime.

11.6.9 Conventional Facilities Requirements

Typical laboratory conventional facilities are required. Specifically:

- Compressed air.
- Chilled air for proportional air conditioned temperature control of the shielded enclosures.
- Deionized water for direct and secondary cooling of beamline optics and heat exchangers. We anticipate cooling mirror and monochromators with low-vibration, gravity-fed water cooling systems that will exchange heat with the direct deionized water supply.
- "House" water for general multi-purpose use.

At this time, we do not anticipate needing liquid nitrogen for cooling optical components but an outstanding issue is whether the monochromators can be cooled efficiently enough with water so that thermal-induced slope errors are within an acceptable range.

11.6.10 Outstanding Issues

One outstanding issue for this beamline concerns the power loads. We estimate the worst case power load on the monochromator first crystals to be 4 W total power and 10 W/mm^2, and the typical power load to be 2 W total and 3 W/mm^2. Analysis and comparison to existing high-performance beamlines needs to be made to determine whether this heat load can effectively be managed with side-cooling via water.

11.7 A High-Resolution Soft X-Ray Beamline for Resonant Scattering and RIXS

The advantages of hard x-rays for scattering include the large penetration depth and high spatial resolution. In the soft x-ray range, resonant processes at relevant core levels can enhance the scattering amplitudes by orders of magnitude. Such resonant enhancements lie at the core of recent increased interest in the exploitation of soft x-rays for the investigation of wide classes of materials including technologically relevant compounds and alloys, and advanced nano-scale materials. Further, the wavelength of soft rays (~0.5 nm to a few nm) is well matched to many interesting and useful length scales, both those that occur intrinsically in many materials and those that have been engineered.

In particular, scattering studies in the soft x-ray range are uniquely suited to examining some of the most important issues surrounding correlated electron systems, spintronic materials, engineered ferromagnetic alloys, nano-patterned structures, advanced fuel cell electrodes, candidate hydrogen storage materials, and many other scientifically or technologically relevant materials. A large portion of the periodic table can be investigated via the use of soft x-rays, including the 3*d* transition metal *L* edges, rare-earth $M_{4,5}$ edges, and the *K* edges of C, N, and O. There are strong resonant enhancements in the vicinity of these dipole-allowed absorption edges. In addition, polarization-dependent studies, which are more practical with advanced undulators and novel end station designs, can reveal underlying order in the charge, spin, and orbital degrees of freedom in the system.

In this section we discuss the conceptual design of a soft x-ray beamline optimized for scattering studies and high resolution spectroscopy. The proposed design considers a single beamline serving two end stations; one is optimized for x-ray resonant magnetic scattering (XRMS) and the other is designed for resonant inelastic x-ray scattering (RIXS). A horizontal switching mirror will be used to divert the beam from one end station to the other. The source for the beamline will be two 2 m elliptically polarized undulators (EPU) in one of the NSLS-II 5 m straight sections. In addition to the standard set of experiments enabled by EPUs, the proposed design will call for independent control of the polarization in the EPUs to provide two separate soft x-ray photon beams. Separation of the two beams is accomplished via inclusion of a small canting angle in

the electron orbit between the EPUs and the novel design of the beamline optics permits separate collection and a coincident focus of the two beams. A mechanical optical chopper would then permit measurements of small, polarization-dependent signals via lock-in amplification.

X-ray Resonant Magnetic Scattering and Resonant Inelastic X-ray Scattering are two scattering techniques whose use in the soft x-ray range has increased considerably in recent years. XRMS exploits magnetic sensitivity in diffraction patterns to extract element-specific information on magnetic ordering processes on length scales from microns down to a few nm. RIXS, in contrast, examines inelastic processes. The energy lost in the process, which is measured in a RIXS experiment, can reflect important parameters such as the local partial density of states of an atomic species in a complex compound, low energy excitations (such as *d–d* interactions), and charge transfer from surrounding ligands. XRMS and RIXS are both photon-in, photon-out techniques, and have a number of advantages over electron-based spectroscopies and scattering processes. For example, photons are not affected by electric and magnetic fields, and multiple scattering events are negligible in the soft x-ray range.

The exceptional properties of NSLS-II will enable the implementation of soft x-ray beamlines with unsurpassed brightness, small photon spot size, energy resolution, and polarization control. These characteristics will be crucial in designing and ultimately using the next generation of XRMS and RIXS instrumentation. RIXS is inherently a very low-count-rate technique, and improvements in brightness and spot size translate directly to improved detection efficiency. In XRMS, the most valuable information is attained often only at high-momentum transfer or in off-specular scans. In both instances, the count rate at current instruments is often at the noise floor of the detectors.

Although XRMS and RIXS have some similarities, they are properly considered as separate and complementary probes of advanced materials. Therefore, the motivation for pursuing these techniques will be presented in separate sections.

11.7.1 Source

We propose that the beamline be equipped with two soft x-ray Elliptically Polarizing Undulators in a 5 m straight section, each approximately 2 m long, which could be operated either in phase as a single 4 m EPU for increased brightness or as two independent EPUs, where the polarization in each EPU would be set independently. The EPUs should be of an APPLE-II type device or an equivalent design that can provide linearly polarized photons, with the polarization axis oriented horizontally, vertically, or at an arbitrary angle in-between. The EPUs should also be able to provide right circular or left circular polarization across an energy range that is matched by the optics of the beamline. Note, the 5 m straight is desired because of the smaller source size.

Present plans for an EPU device for NSLS-II call for a period length of 45 mm and a magnetic gap of 10 mm (see Chapter 8). This would allow it to function as an out-of-vacuum device. However, an EPU42 device, with a period length of 42 mm and a magnetic gap of 8 mm would provide coverage over a slightly wider energy range than the EPU45 device. The EPU42 also has an advantage of a brightness about ~13% higher (averaged over the energy range of EPU45) than the EPU45. However, the 8 mm magnetic gap of the EPU42 may require that it be an in-vacuum undulator, which requires R+D. Absent such a device, the EPU45 would certainly be a good alternate.

As previously mentioned, the 2 m EPUs could be operated in-phase as a single 4 m insertion device. By canting the electron beam slightly through the EPUs (the canting angle is expected to be less than 0.25 mrad) the EPUs could be operated as independent devices and could be used to provide two beams to the end stations, each with a different polarization (e.g., linear and horizontal, or RCP and LCP). These two beams would be focused on the same spot on the sample. An in-vacuum chopper would be included in the beamline, allowing for rapid switching between the two polarizations, possibly at frequencies as high as a few kHz. This approach also eliminates the need to provide rapid polarization switching via movement of the magnetic

arrays in the EPUs, and hence minimizes any perturbations on the electron beam. For this approach to work, appropriate steering magnets and beam diagnostics must be included in the straight section.

The rapid polarization switching would enable the detection of extremely weak signals via use of phase-sensitive lock-in detection. Such approaches have already been exploited for the detection of very small induced ferromagnetic moments in nominally paramagnetic layers adjacent to strong ferromagnets [11.7.1]. Even lower absolute moments could be detected with the increased brightness and higher polarization switching frequencies of NSLS-II. This capability will be extremely useful in detecting small spin-currents in nonmagnetic layers [11.7.2, 11.7.3]. The rapid polarization switching could also be invaluable in detecting weak scattering peaks in orbital-ordered manganites, or in examining other correlated electron systems.

11.7.2 Beamline Design and Optics

11.7.2.1 Introduction and Proposed Design

State-of-the-art optical elements are required to match the very high resolving power achievable with the proposed beamlines at the NSLS-II ring. The XRMS/RIXS beamline will achieve a resolving power $>0.9\times10^5$ at 1 keV with a 5 μm exit slit width and with RMS slope errors of 0.1 μrad over ≈100 mm on the plane optical elements. A spot size with FWHM of less than 5×5 μm^2 requires RMS slope errors of approximately 0.5 μrad along the meridional direction on the sagittal cylinder and the elliptical cylinders used in the proposed design. In the beamline, almost 5×10^{10} ph/s will illuminate a spot with FWHM of less than 6×4 μm^2 (H × V) at 1 keV with a bandwidth of 11 meV. The flux at 1 keV would increase by two orders of magnitude with a different grating delivering a resolving power of 8500 to the same spot size. The requirements for the highest possible resolution and a fixed exit slit over a broad energy range can be fulfilled with the Collimated Plane Grating Monochromator proposed by Follath et al. [11.7.4]. The optical design of the CPGM includes a horizontally deflecting toroidal mirror that collimates along the vertical (dispersion direction) and focuses the beam horizontally at the exit slit. The vertically collimated beam is deflected (vertically) by a plane mirror illuminating the plane grating at an angle of incidence α. The beam dispersed by the grating, at an angle β, is focused onto the exit slit plane by a sagittally focusing cylindrical mirror. The collimation along the dispersion direction allows one to operate the monochromator at different values of c (=cosβ/cosα) by choosing the appropriate angle of incidence on the plane mirror. Large c values are used to improve resolution at the expense of flux. The CPGM design is almost free of aberrations, and the major contributions to its wavelength resolution are:

$$\Delta\lambda_{so} = \frac{2.7\,\Sigma_y \cos\alpha}{n\,k\,r_1}, \tag{11.7-1}$$

$$\Delta\lambda_{ex} = \frac{s\cos\beta}{n\,k\,r_2}, \tag{11.7-2}$$

$$\Delta\lambda_{Gr} = \frac{5.4\,\sigma_{Gr}}{n\,k}\cos\left(\frac{\alpha+\beta}{2}\right)\cos\left(\frac{\alpha-\beta}{2}\right), \tag{11.7-3}$$

and

$$\Delta\lambda_{PM} = \frac{5.4\,\sigma_{PM}\cos\alpha}{n\,k} \tag{11.7-4}$$

In the equation above, Σ_y is the RMS vertical source size, n is the diffraction order, k the grating line density, r_1 the distance from the source to the toroidal mirror, s the slit width, r_2 the distance from the refocusing mirror to the exit slit, and σ_{Gr} and σ_{PM} the RMS meridional slope errors on the grating and plane mirror, respectively. The slope errors on the collimating and refocusing mirrors also affect the resolution. However, their effect is very small due to the large "forgiveness factor," the cosine of the angle of normal incidence on the mirror.

The experimental stations to be installed at the end of the XRMS/RIXS beamline require a spot size in the micrometer range. Along the vertical direction this can be easily achieved with an elliptical cylinder demagnifying the exit slit width. Since the RMS horizontal size of the photon beam varies between 54 and 41 μm in the energy range 200 to 2500 eV, a demagnification of ≈2.35×50/5 =23.5 is required to obtain a spot with a horizontal FWHM of 5 μm. In the CPGM the horizontal demagnification of the source onto the slit is approximately 1. Therefore, the demagnification in this design needs to take place in between the slit and the sample. However, the requirement for a distance of ≈700 mm between the sample and the end of the refocusing mirror means that the entrance arm of the horizontally refocusing mirror needs to be larger than 10 m, which is impractical.

The very small horizontal divergence of the beam expected from a 4 m insertion device in the 5 m straight sections of NSLS-II, 32 μrad RMS at 200 eV, allows for a solution in which the beam diverges up to an elliptical cylindrical mirror located after the exit slit. This mirror then demagnifies the horizontal source down a few microns. One could implement this in the CPGM by replacing the toroidal mirror with a sagittal cylinder that provides the grating with a collimated beam along the dispersion direction. Unfortunately, the illumination of the refocusing cylinder after the grating by a divergent horizontal beam results in a large astigmatic coma aberration that significantly reduces the monochromator resolution.

The proposed monochromator [11.7.5] therefore uses a sagittal cylindrical mirror to collimate the beam along the vertical (dispersion) direction. The following optical element is a plane mirror that illuminates a variable line spacing plane grating. The line density of the grating is given by $k(w) = k_0 + 2b_2\,w + 3b_3\,w^2 \ldots$, where w=0 is at the grating center and is positive toward the exit slit. The linear coefficient term, b_2, can be chosen to zero the defocus term in the optical path function, i.e.,

$$f_{20} = \frac{\cos^2\beta}{dGrEx} + 2b_2\,n\,k\,\lambda, \tag{11.7-5}$$

at one wavelength, whereas b_3 can be chosen to zero the coma term in the optical path function, i.e.,

$$f_{30} = \sin\beta\frac{\cos^2\beta}{dGrEx^2} + 2b_3\,n\,k\,\lambda, \tag{11.7-6}$$

also at a single wavelength. In Eqs. 11.7-5 and 11.7-6, *dGrEx* is the distance between the grating and the exit slit. The important point in this design is the fact that the plane mirror can be used to zero f_{20} for all wavelengths by illuminating the grating at the required angle of incidence. Note that this design has one less mirror than the CPGM.

Eqs. 11.7-1–11.7-4 also give the contributions to the wavelength resolution in the proposed design, with r_1 being the distance from the source to the cylindrical mirror and by replacing r_2 with *dGrEx*.

11.7.2.2 Source Parameters

The machine parameters, the RMS electron beam sizes and divergences, and the insertion device parameters used in the calculations are listed in Tables 11.7.1 and 11.7.2. The flux emitted in the central cone by the two insertion devices with a 42 mm period when operated in phase to deliver linear polarized radiation is shown in Figure 11.7.1.

Table 11.7.1 Machine Parameters Used in the Calculations.

Energy (GeV)	3.0
Current [mA]	500
σ_x [μm]	40.2
σ_y [μm]	1.7
$\sigma_{x'}$ [μrad]	14.9
$\sigma_{y'}$ [μrad]	1.8

Table 11.7.2 ID Parameters Used in the Calculations.

	Beamline 1 and 2
ID type	2 x APPLE II
Length of each ID [mm]	2000
Period length [mm]	42

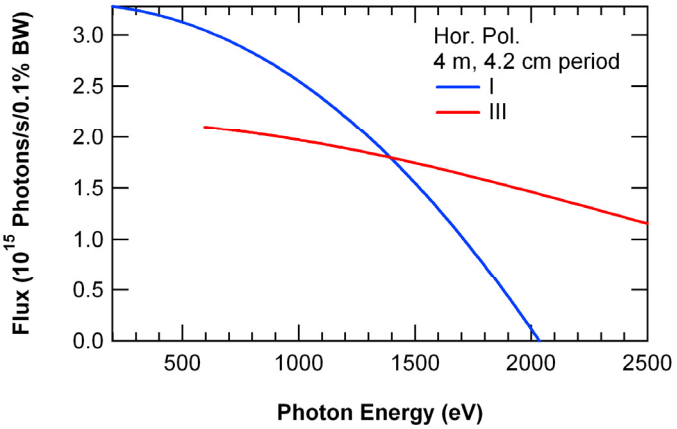

Figure 11.7.1 Flux emitted in the central cone by a 4 m undulator with a 4.2 cm period, operating in linear mode, as a function of the photon energy.

The total sizes and divergences used in the calculations were obtained as the vector sum of the electron beam parameters and the RMS values of the photon beam calculated using [11.7.6]:

$$\sigma_r = \sqrt{2\lambda L}/2\pi \text{ and } \sigma_\rho = \sqrt{\lambda/2L}\,, \tag{11.7-7}$$

where L is the undulator length and λ the radiation wavelength.

11.7.2.3 Monochromator Design

The discussion for the monochromator design will first consider the use of the two EPUs in-phase as a single insertion device. The modifications to the optical design required for canted operation will be presented at the end of the section.

A sketch of the proposed beamline is shown in Figure 11.7.2; the parameters of the optics are listed in Table 11.7.3. The first element (M1) is a sagittal cylindrical mirror located at 28 m from the source, outside the shield wall. The angle of normal incidence in this mirror (as well as that of M3 and M4) is determined as a compromise between the highest possible reflectivity in the energy range covered by the beamlines and a reasonable mirror length. Figure 11.7.3 shows a small set of the calculations performed [11.7.7] to determine the angle of incidence and the coating material on the mirrors. We selected an angle of incidence of 88.75° and a 30 nm coating of Au over the Si substrate. As shown in the figure, the selected parameters provide a good reflectivity up to 2.2 keV. We note that at this angle of incidence the *s* and *p* reflectivities are almost identical. Therefore, the beamline will not distort circular polarized radiation.

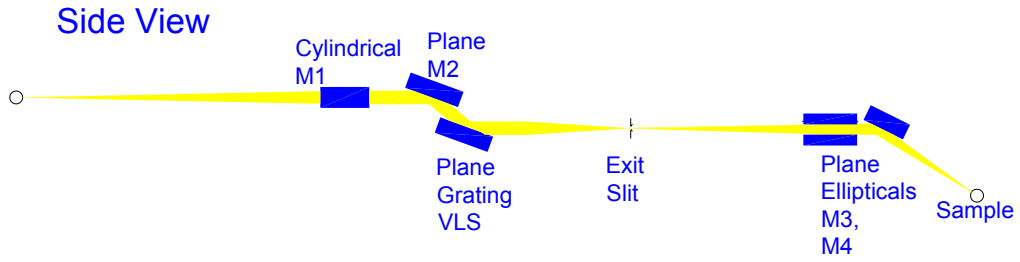

Figure 11.7.2 Sketch of the proposed soft x-ray resonant scattering and RIXS beamline.

Table 11.7.3 Attributes of the Optical Components for the XRMS / RIXS Beamline.

Element	Distance (mm)	Angle (deg)	Deflection
M1- Sagittal Cylinder	28000	88.75	Horizontal
M2- Plane	29611 to 29944	82.4-88.9	Vertical
Gr - Grating	≈30000	86.4- 89.6	Vertical
Slit	50000		
M3 - Plane Elliptical	51850	88.5	Horizontal
M4 – Plane Elliptical	52350	88.5	Vertical
Sample	53350		

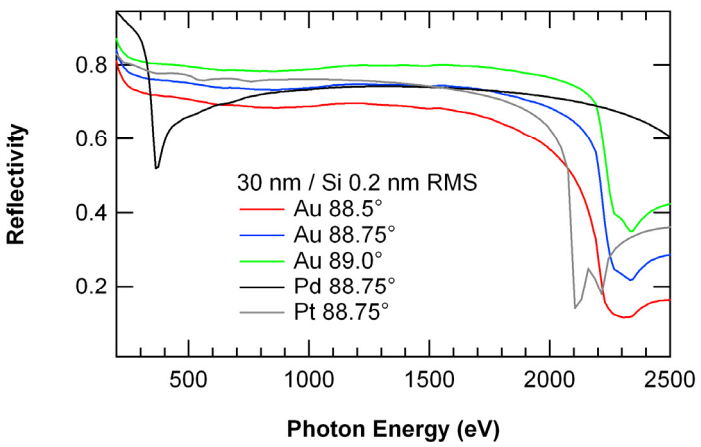

Figure 11.7.3 Reflectivities of possible coatings for s polarized light as a function of the photon energy. The substrate is Si and the coating is 30 nm thick. The RMS surface roughness is 0.2 nm.

The second optical element is the plane mirror (M2) that provides the required angle of incidence to the grating necessary to keep the selected energy in focus at the exit slit. The mechanical principle used in the PGM [11.7.8] can be used to achieve the required movements. The resolution in angle required in the current design (i.e., assuming five scanning steps at the highest resolution) is 0.03 μrad for the grating and 0.05 μrad for the plane mirror. These values are very close to the resolution of the angular encoder used in the CPGM (0.04 μrad).

Since the angle of incidence on the mirror for a given VLS grating is determined by the focusing condition and the grating equation at that energy, it is advantageous to have at least three gratings that allow exchanging resolution for flux keeping a fixed exit slit width.

11.7.2.3.1 Gratings for the XRMS/RIXS Beamline

We have specified a grating for ultra high resolution, one for high resolution and high flux, and one for moderate resolution and the highest flux). The parameters of the chosen gratings are listed in Table 11.7.4, assuming that the distance from the grating to the exit slit is 20 m. The gratings are operated in the +1 order.

Table 11.7.4 Parameters of the Gratings for Beamline 1.

	Ultra High Resolution (UHR)	High Resolution, High Flux (HR)	Medium Resolution, High Flux (HF)
k_0 [mm^{-1}]	3600	1200	300
b_2 [mm^{-2}]	5.1832×10^{-5}	6.288×10^{-5}	8.991×10^{-5}
b_3 [mm^{-3}]	2.57×10^{-9}	3.13×10^{-9}	4.49×10^{-9}
C	4.6-5.2	≈2.2	≈1.5

The UHR grating has 3600 lines per mm (l/mm) at its center and will operate with a c value increasing from 4.6 at 200 eV to 5.2 at 2.5 keV. The contributions to the resolving power for the UHR grating, calculated using Eqs. 11.7-1–11.7-4, and their vector sum are presented in Figure 11.7.4. The source size dominates the resolving power from 200 to 900 eV. At higher energies, the slope errors on the grating become the dominant term. A reduction of the grating RMS slope error to 0.05 μrad would improve the resolving power at 1 keV from 9.1×10^4 to over 11×10^4.

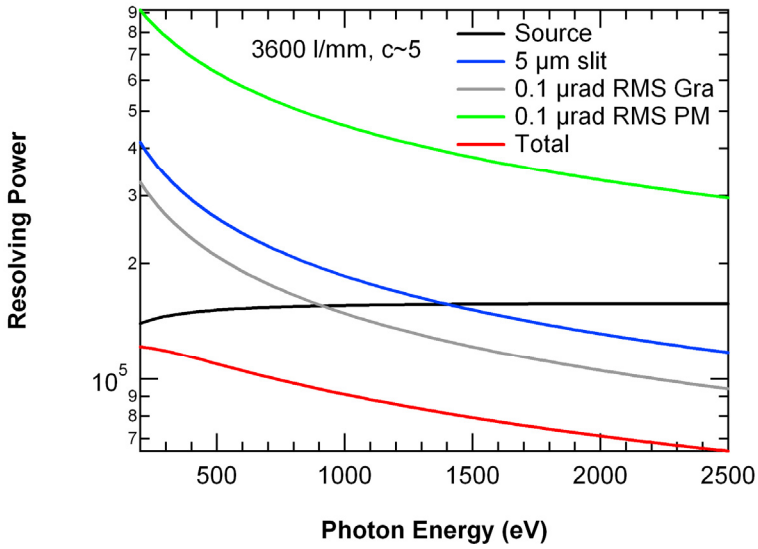

Figure 11.7.4 Contributions to the resolving power due to the source, 5 µm exit slit, 0.1 µrad RMS slope errors on the grating and M2, and their vector sum for the ultra high resolution (UHR) grating of the soft x-ray resonant scattering and RIXS beamline.

Figure 11.7.5 shows the contributions to the resolving power of the 1200 l/mm grating designed for high resolution. In this case the *c* value is approximately 2.2 and, as evident in the figure, the resolving power is dominated by the source size. A smaller slope error in this grating will not improve significantly the resolving power.

Figure 11.7.5 Contributions to the resolving power due to the source, 5 µm exit slit, 0.1 µrad RMS slope errors on the grating and M2, and their vector sum for the HR(high resolution, 1200 l/m) grating of the soft x-ray resonant scattering and RIXS beamline.

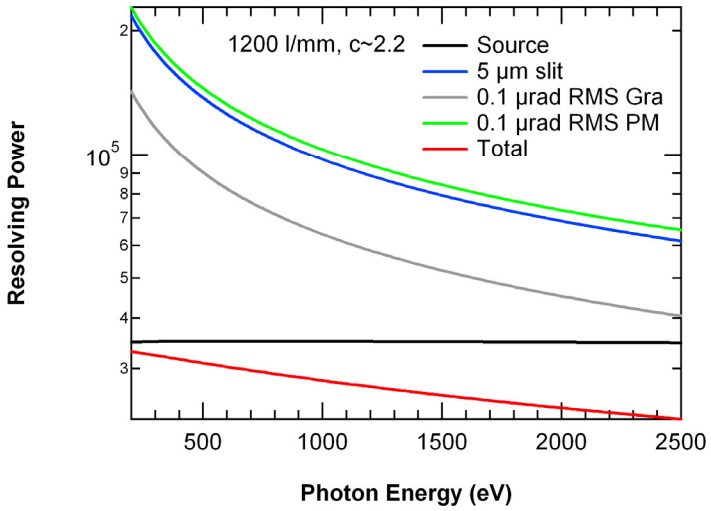

As for the HR grating, the total resolving power of the HF grating is also dominated by the source size (Figure 11.7.6). With a 5 µm exit slit width, even this grating provides a resolving power higher than 7000 between 200 and 2.5 keV.

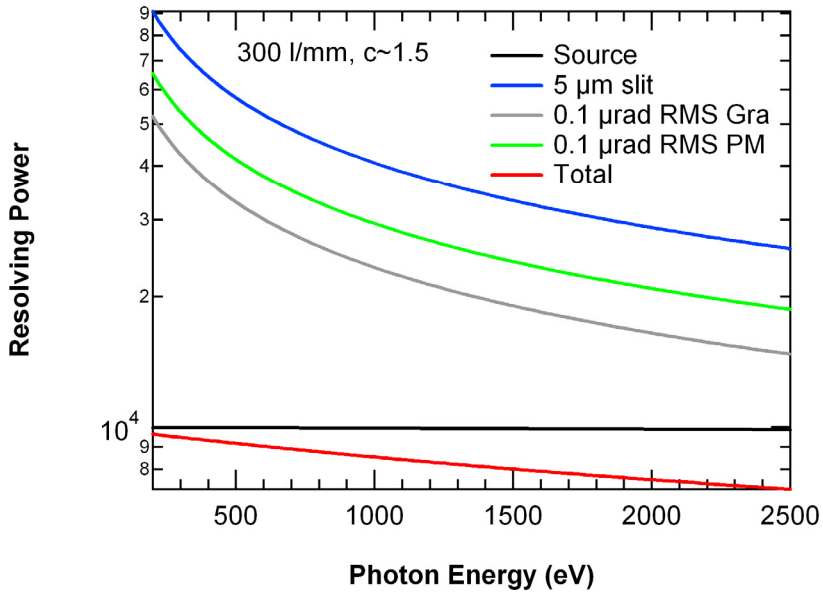

Figure 11.7.6 Contributions to the resolving power due to the source, 5 µm exit slit, 0.1 µrad RMS slope errors on the grating and M2, and their vector sum for the HF(high flux, 300 l/m) grating of the soft x-ray resonant scattering and RIXS beamline.

11.7.2.3.2 Refocusing

The refocusing onto the sample is performed with two elliptical cylinder mirrors. The first one (M3) is the horizontally refocusing mirror located at a distance of 51.850 m from the source with a nominal demagnification of 36. The vertically refocusing mirror (M4) is 0.5 m downstream of M3 and demagnifies the slit width by 2.3. The angle of incidence on both mirrors is 88.75°.

11.7.2.3.3 Flux

The absolute grating efficiencies were calculated using the differential formalism of the exact electromagnetic theory [11.7.9], assuming the central line density in each grating and blazed groove profiles. The results for the three gratings assuming Au coating and blazed angles of 1.8° for the UHR, 1.0° for the HR, and 0.4° for the HF grating are displayed in Figure 11.7.7. The high line density and high *c* value used in the UHR grating lead to an efficiency that varies only between 1.2 and 3.2%. The efficiency of the HR grating is higher than 10% between 300 eV and 2150 eV, whereas the efficiency of the HF grating is higher than 20% in the same energy range.

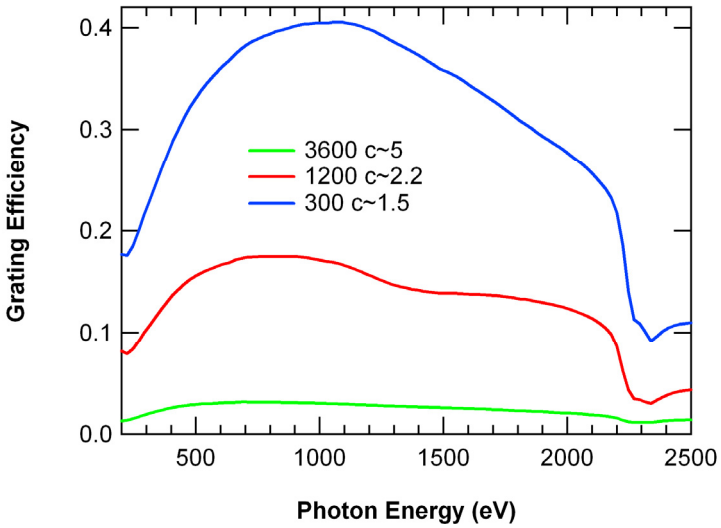

Figure 11.7.7 Absolute efficiencies of the three Au-coated, blazed, VLS gratings in the soft x-ray resonant scattering ant RIXS beamline, labeled by their central line density: UHR 3600 lines/mm, HR 1200 lines/mm, and HF 300 lines/mm.

The reflectivities of the Au coated plane mirror as a function of the photon energy when operated with each one of the gratings are shown in Figure 11.7.8. The penalty in reflectivity when very high resolution is required is evident in this figure. The total flux expected at the sample position with an exit slit width of 5 μm was calculated taking into account the undulator flux appearing in Figure 11.7.1 after correcting for the bandpass of the 5 μm exit slit width, the reflectivities of the Au coated M1, M2, M3, and M4, as well as the grating efficiencies. The results appear in Figure 11.7.9. For completeness, the resolving power expected with each grating is shown in the upper part of the figure. Switching from the UHR to the HR grating at 1 keV increases the flux 16 times while losing only a factor of 3 in resolving power. By switching from the HR to the HF grating, one gains an additional factor of 8 in flux with the same resolution loss.

Figure 11.7.8 Reflectivities of the (Au coated) plane mirror in the soft x-ray resonant scattering and RIXS beamline at the angle of incidence required for operation with each of the three gratings: UHR 3600 lines/mm, HR 1200 lines/mm, and HF 300 lines/mm.

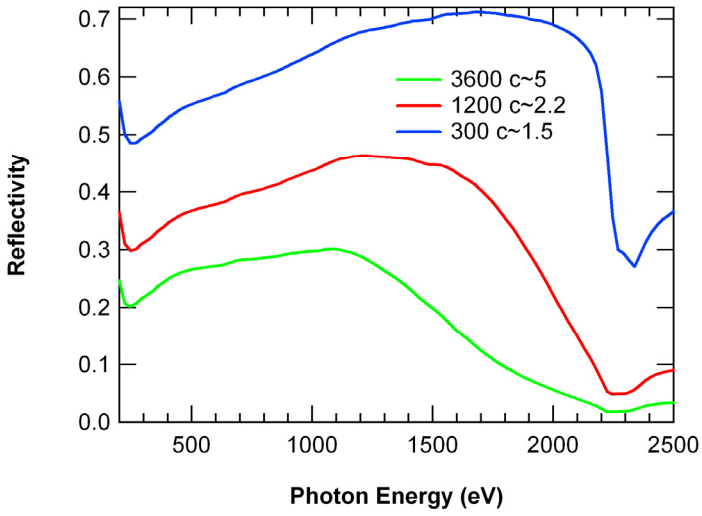

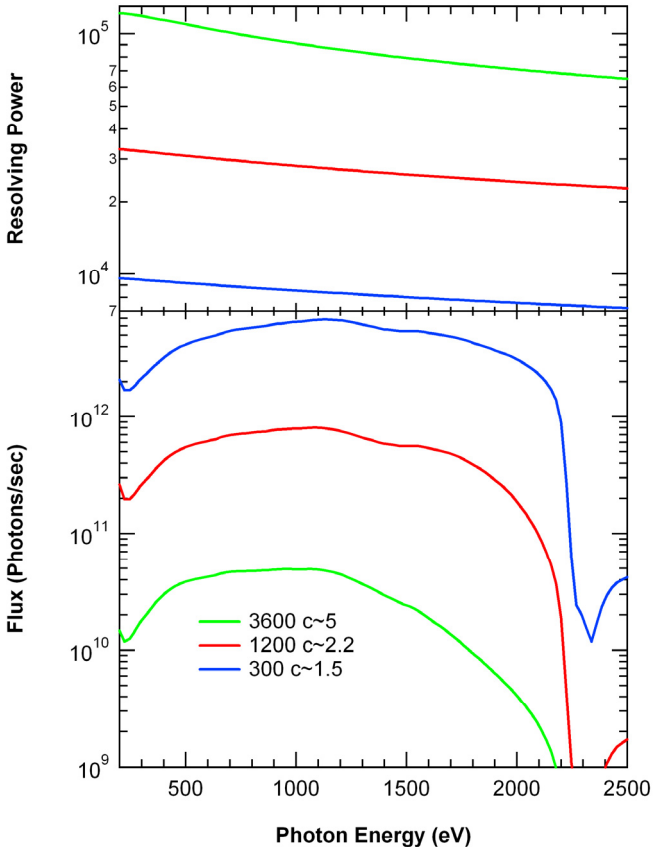

Figure 11.7.9 Flux (lower panel) and corresponding resolving power (upper panel) expected at the sample position for the three gratings of the soft x-ray resonant scattering and RIXS beamline, for a 5 μm exit slit width. The gratings are: UHR 3600 lines/mm, HR 1200 lines/mm, and HF 300 lines/mm.

The proposed design will result in a soft x-ray beamline with unparalleled performance. When operated in high flux mode, the beamline will provide close to 10^{13} ph/s, equal to any existing soft x-ray beamline, and still have a resolving power higher than the most recent soft x-ray beamlines at other DOE synchrotron facilities (i.e., beamline 11.0.02, the Molecular Environmental Sciences Facility, at ALS). When operating in high resolution mode, the beamline will have a resolving power close to 100,000 (an order of magnitude improvement over the capability of, for example, beamline 4-ID-C at APS), with a calculated flux of ~5 × 10^{10} ph/s, which is comparable to the flux at 4-ID-C.

11.7.2.4 Ray Tracing

The ray tracings for the XRMS/RIXS beamline were performed using the Shadow code [11.7.10]. The caption above the spot patterns gives the RMS values of the beam, either size or divergence, along the horizontal and vertical directions. The y-coordinate is along the dispersion direction at the exit slit and sample position and along the length of the optical elements. Slope errors (0.1 μrad RMS along the meridional direction of the plane elements and 0.5 μrad RMS along the meridional direction of the other optical elements) were included in the ray tracings by assuming a sinusoidal variation on the optical elements' surface. All the ray tracings were performed with sizes and divergences calculated as described in the description of the source.

Figure 11.7.10 shows the spot pattern at the cylindrical mirror (M1) when illuminated with 200 eV photons. As seen in the figure, a 300 mm-long mirror accepts most of the central cone radiation emitted by the undulator at this energy. The illumination of the plane pre mirror (M2) and the HR grating when they are tuned to 200 eV (Figure 11.7.11 and Figure 11.7.12) show that despite the divergence of the horizontal beam, the optical surfaces of these elements need to be approximately 7 mm wide. The total length of the plane

mirror, using the SX700 principle [11.7.8], needs to be approximately 400 mm. The gratings need to be less than 100 mm long. Figures 11.7.13 and 11.7.14 show the illumination of the refocusing elliptical cylinder mirrors (M3 and M4). The horizontally focusing mirror needs to be at least 400 mm long and the vertically focusing mirror needs to be less than 80 mm long.

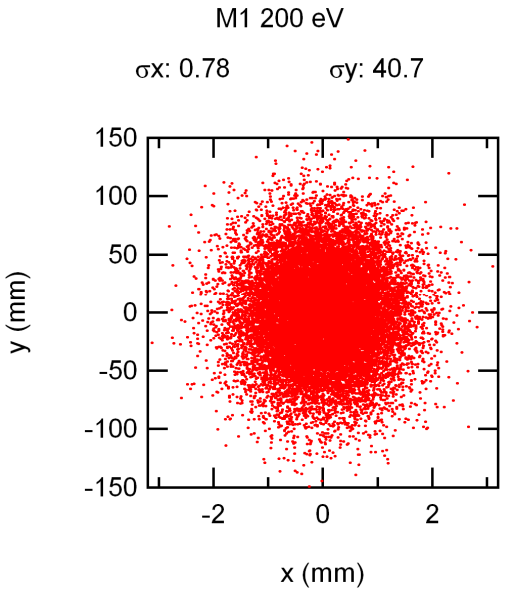

Figure 11.7.10 Spot pattern at M1 for 200 eV photon energy in the soft x-ray resonant scattering and RIXS beamline.

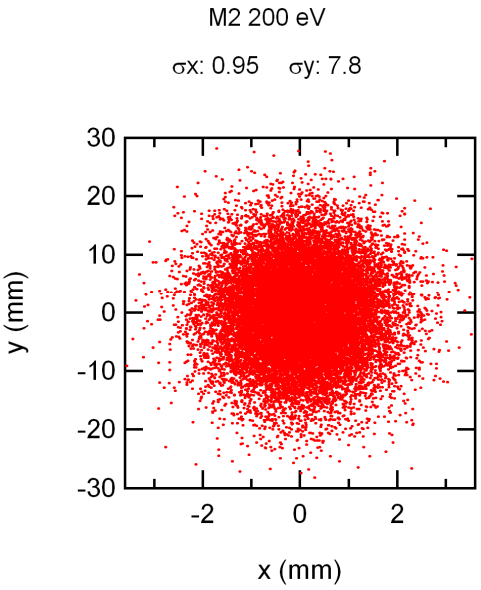

Figure 11.7.11 Spot pattern at M2 when tuned to 200 eV with the HR grating in the soft x-ray resonant scattering and RIXS beamline.

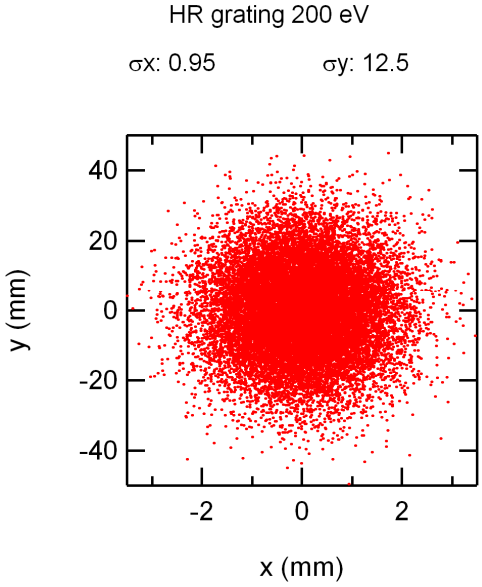

Figure 11.7.12 Spot pattern at the HR grating for 200 eV photon energy in the soft x-ray resonant scattering and RIXS beamline.

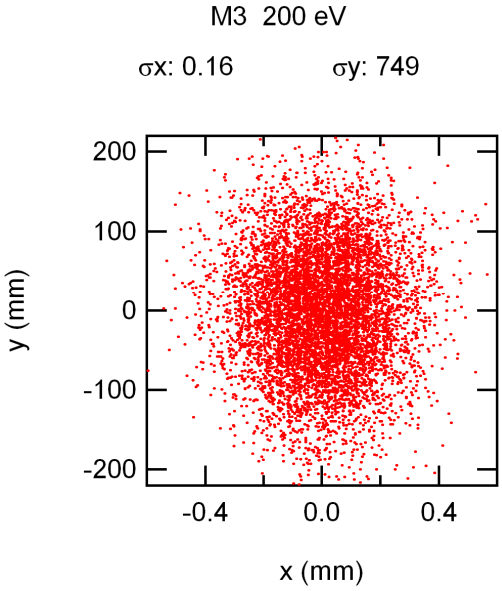

Figure 11.7.13 Spot pattern at M3 for 200 eV photon energy in the soft x-ray resonant scattering and RIXS beamline.

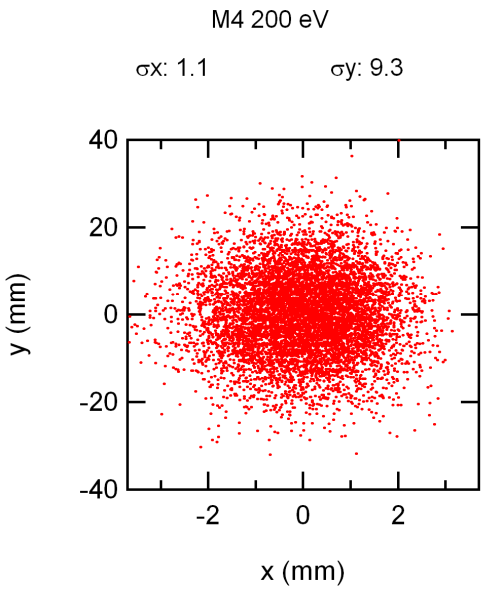

Figure 11.7.14 Spot pattern at M4 for 200 eV photon energy in the soft x-ray resonant scattering and RIXS beamline.

The resolution of the monochromator at 200 eV with the HR grating is demonstrated by the spot patterns shown in Figure 11.7.15. Clearly, the monochromator has a resolution better than 6 meV, in agreement with the analytical calculations (Figure 11.7.5) without including the contribution of the exit slit. The figure also shows that an exit slit length of 10 mm is required to let through the horizontally diverging beam. Another example showing the agreement between the analytical calculations and ray tracings results in the case of the UHR grating (Figure 11.7.4) is shown in Figure 11.7.16. This figure indicates that the resolution at 1 keV with these grating is better than 10 meV.

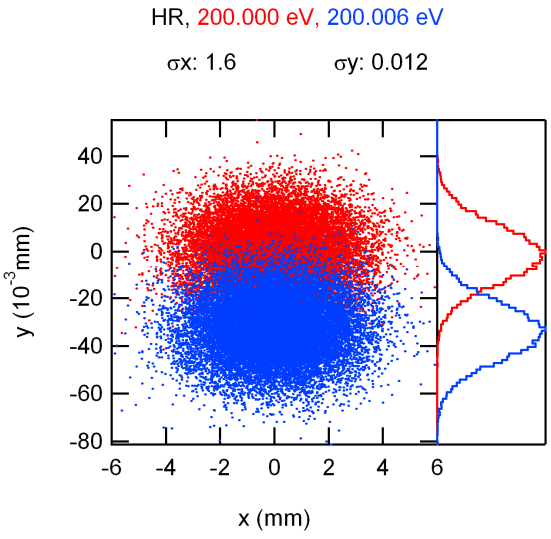

Figure 11.7.15 Spot pattern at the exit slit plane for 200 and 200.006 eV photon energies using the HR grating in the soft x-ray resonant scattering and RIXS beamline. The sigma values are for 200 eV.

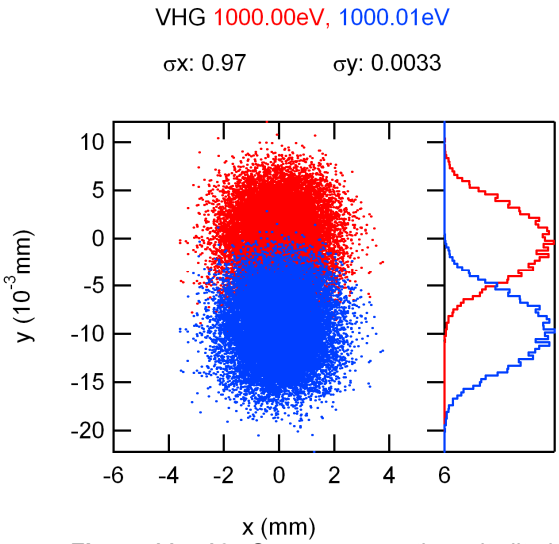

Figure 11.7.16 Spot pattern at the exit slit plane for 1000 and 1000.01 eV photon energies using the UHR grating in the soft x-ray resonant scattering and RIXS beamline. The sigma values are for 1000 eV.

The ray tracings illustrating the spot size and the divergence at the sample plane for 200 eV photons are shown in Figures 11.7.17 and 11.7.18, respectively. The RMS horizontal and vertical sizes and divergences shown in the figures are consistent with the values obtained from the vector sum of the source parameters (slit

for the vertical size) modified by the corresponding magnification and the contributions due to the assumed slope errors. Obviously, the RMS vertical size will not change with energy, while the RMS horizontal size will decrease from 2.3 μm at 200 eV to 2.0 μm at 2.5 keV. The largest vertical RMS divergence, less than 0.5 mrad, will occur when the UHR grating is used at 200 eV.

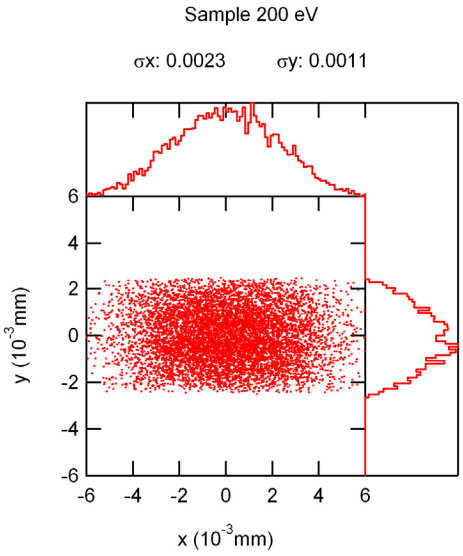

Figure 11.7.17 Spot pattern at the sample position at 200 eV photon energy for the soft x-ray resonant scattering and RIXS beamline.

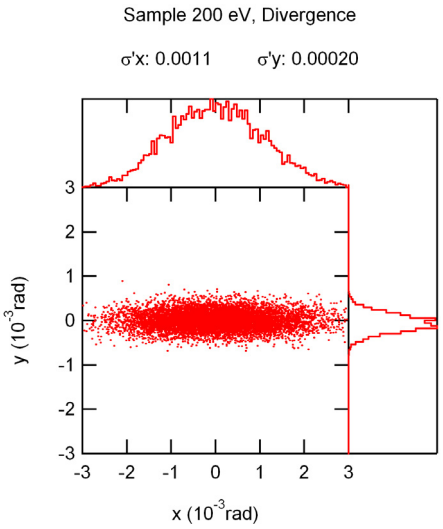

Figure 11.7.18 Spot divergence at the sample position at 200 eV photon energy for the soft x-ray resonant scattering and RIXS beamline.

11.7.2.5 Design for Use of Two Canted EPUs

In this mode of operation, the horizontal angle between the electron beam and the axes of the EPUs should be as small as possible to keep a reasonable exit slit length. On the other hand, the angle should be large enough that there is a minimal overlap between the two beams. We chose 0.17 mrad for the separation between the two beams, which corresponds to 4σ of the RMS divergence at 200 eV. Two sagittal cylindrical mirrors, designed to collimate along the vertical direction its respective source, replace M1. This ensures the two beams will be focused at the exit slit; but implies that the resolution of the far beam (upstream undulator) is a few percent better than that of the closer beam. The elliptical cylinder horizontally refocusing mirror (M3) also needs to be replaced with two elliptical cylinder mirrors when operating in the canted mode. The mirror refocusing the beam from the upstream undulator is designed to be slightly out of focus to obtain approximately the same horizontal beam sizes at the sample position.

Ray tracings were also performed for use of the canted EPUs, and Figures 11.7.19 through 11.7.26 summarize the results for 200 eV photons using the HR grating. The captions in the figures show the RMS beam sizes and their average positions. At 200 eV the "contamination" of the radiation from the upstream undulator on the downstream beam is less than 2.5%. This number decreases to practically zero at 1 keV. The contamination can be practically eliminated at the expense of some flux at lowest photon energies. This can be achieved by having a gap of 80 mm between the two M1 mirrors. This will reduce the flux at 200 eV by approximately 10% but will reduce the contamination to less than 0.3%. Practically no flux is lost for energies higher than 1 keV. With the above mentioned separation between the M1 mirrors, their length should be 240 mm, the plane mirror and the grating wider than 16 mm, each M3 at least 320 mm, and the exit slit length 20 mm. The latter means that some mechanism will need to be develop to control the slit to have the same opening at both extremes and be parallel to the floor to better than a few tens of a microradian. Comparing the spot size at the sample in the two cases (Figures 11.7.25 and 11.7.26) reveals that the horizontal sizes differ

by approximately 4% at 200 eV. From ray tracings performed at 1 keV, one obtains a 15% difference in the horizontal beam size.

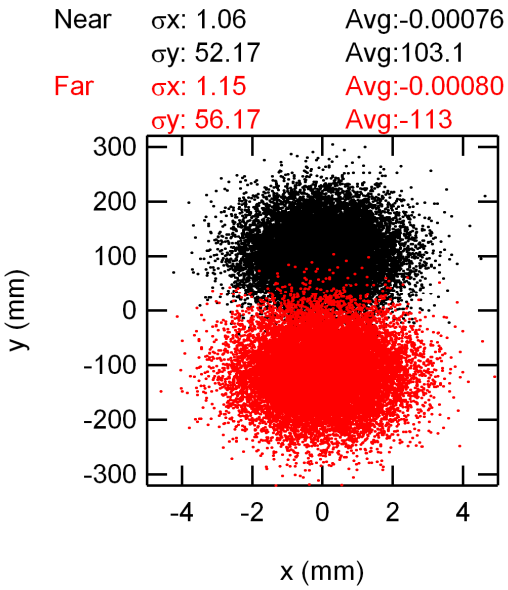

Figure 11.7.19 Illumination of the near and far M1 mirrors at 200 eV photon energy in the soft x-ray resonant scattering and RIXS beamline.

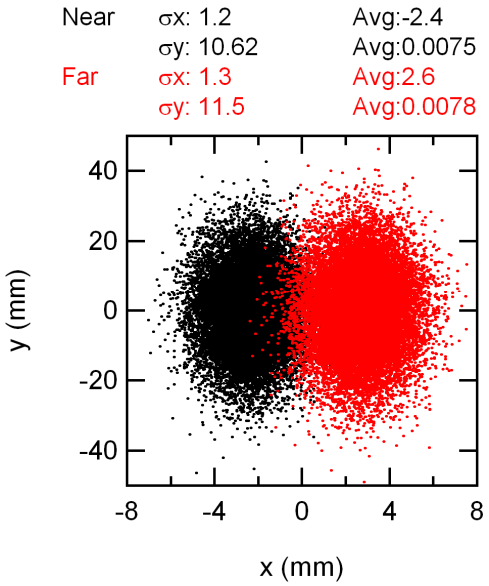

Figure 11.7.20 Illumination of the plane mirror (M2) with the two beams at 200 eV photon energy for the HR grating in the soft x-ray resonant scattering and RIXS beamline.

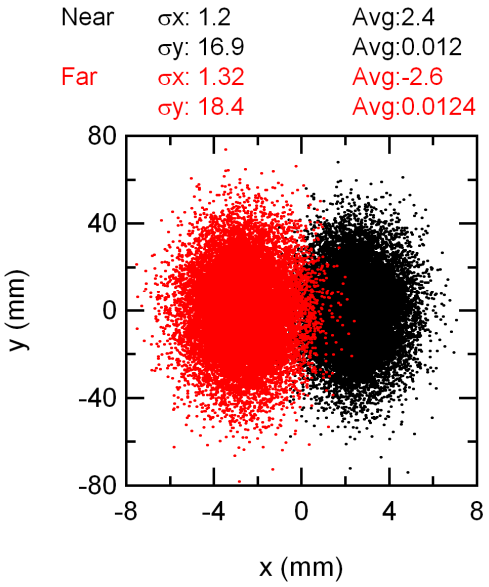

Figure 11.7.21 Illumination of the HR grating by the two beams at 200 eV photon energy in the soft x-ray resonant scattering and RIXS beamline.

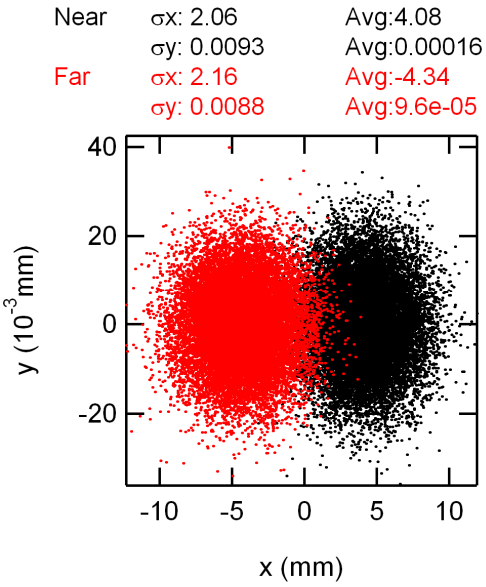

Figure 11.7.22 Illumination of the slit by the two beams at 200 eV photon energy for the HR grating in the soft x-ray resonant scattering and RIXS beamline.

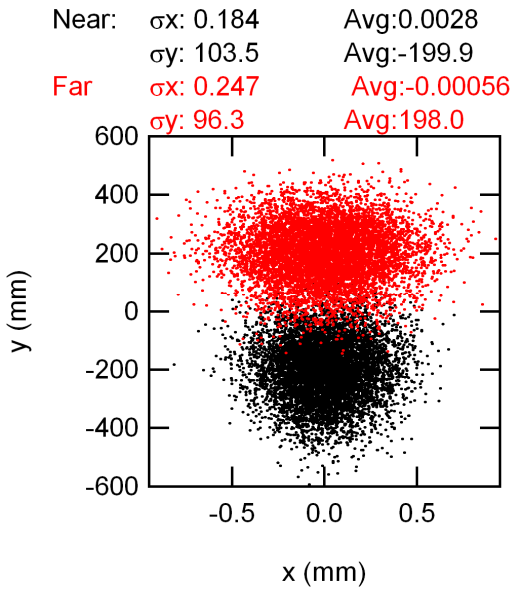

Figure 11.7.23 Illumination of the M3 mirrors by the two beams at 200 eV photon energy for the HR grating in the soft x-ray resonant scattering and RIXS beamline.

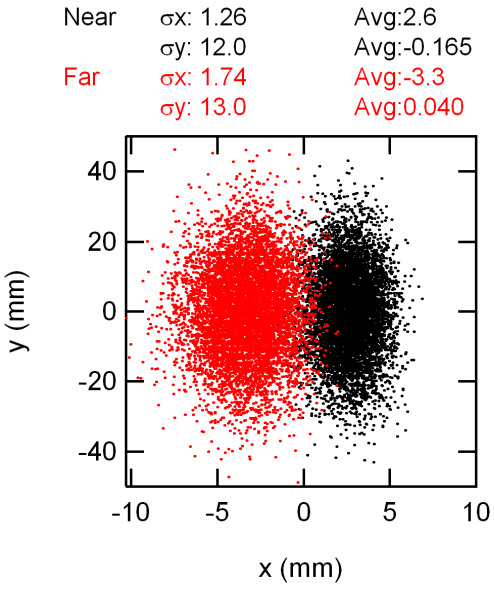

Figure 11.7.24 Illumination of M4 by the two beams at 200 eV photon energy for the HR grating in the soft x-ray resonant scattering and RIXS beamline.

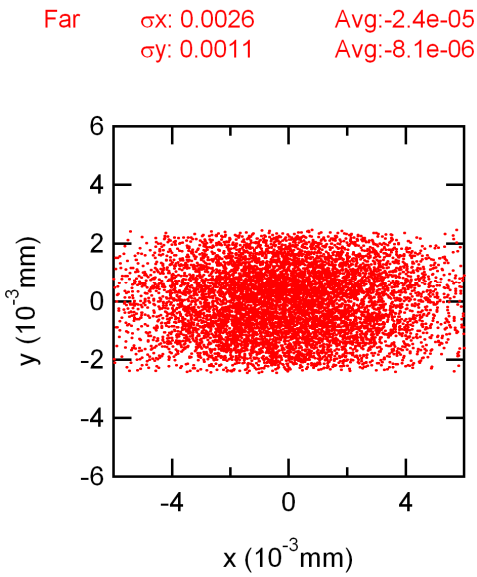

Figure 11.7.25 Sample illumination with the far beam at 200 eV photon energy for the HR grating in the soft x-ray resonant scattering and RIXS beamline.

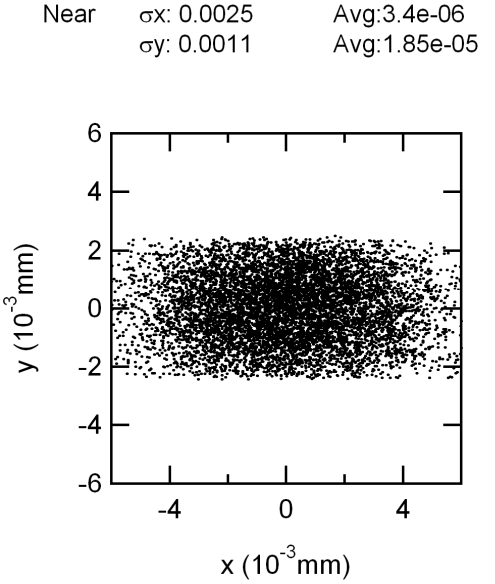

Figure 11.7.26 Sample illumination with the near beam at 200 eV photon energy for the HR grating in the soft x-ray resonant scattering and RIXS beamline.

11.7.2.6 Power Absorbed by Pre-Monochromator Mirrors

The calculated [7.19] power absorbed by the first optical element, i.e., the M1 mirror, when the two EPUs are phased to emit linear horizontally polarized radiation at 200 eV is shown in Figure 11.7.27. At 200 eV photon energy, for the UHR grating, the angle of incidence on the plane mirror is 82.4°, which is the smallest angle (largest grazing angle) required in the operation of the monochromator.

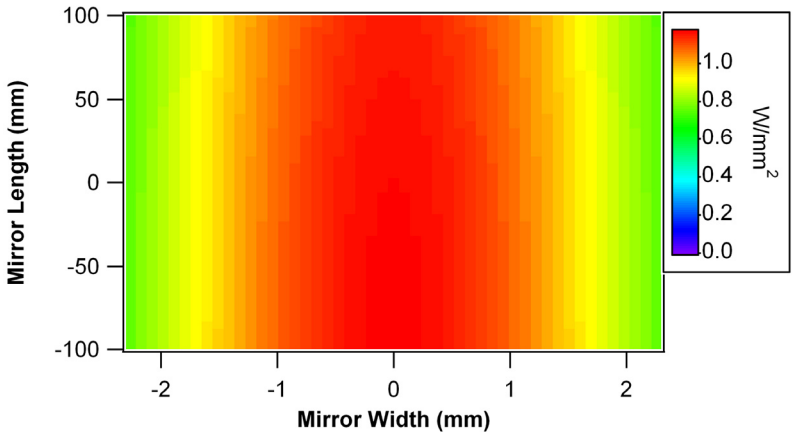

Figure 11.7.27 Power density absorbed by the M1 mirror of the soft x-ray XRMS/RIXS beamline when the EPU is tuned to 200 eV in linear polarization mode.

The maximum power density absorbed by M1 is 1.2 W/mm^2 (Figure 11.7.27) and the total power is almost 1 kW. The corresponding values for the plane mirror (M2) are 0.56 W/mm^2 and less than 100 W. The power, and power density, absorbed by the grating in this case is very small. Considerable cooling must be provided to both mirrors (M1 and M2) to avoid deformations of the ideal mirror shape. The cooling scheme for M1 needs to ensure that the heat-induced meridional RMS slope errors in M1 are below 0.5 μrad. In the case of the plane mirror (M2), a novel cooling design should be developed to preserve the ultra high resolving power. The development of such a cooling scheme will require iterations of finite element analyses and ray tracings performed with the calculated surface deformation.

11.7.3 Beamline Layout

Figure 11.7.28 depicts the proposed layout for the beamline. The M1 mirror tank and the M2 mirror + grating tank are contained in the front optics enclosure. After that, a horizontal diverting mirror separates the line into two branches. At an angle of incidence of 88.5º, a single mirror deflection would reduce the flux by only ~30% across the relevant energy range (see Figure 11.7.3). The RIXS branch takes the straight through beam to maximize the flux and the RIXS spectrometer points away from the shield wall. The XRMS station sits on the inboard branch. The large vacuum chambers just before the experimental chambers house the re-focusing mirrors.

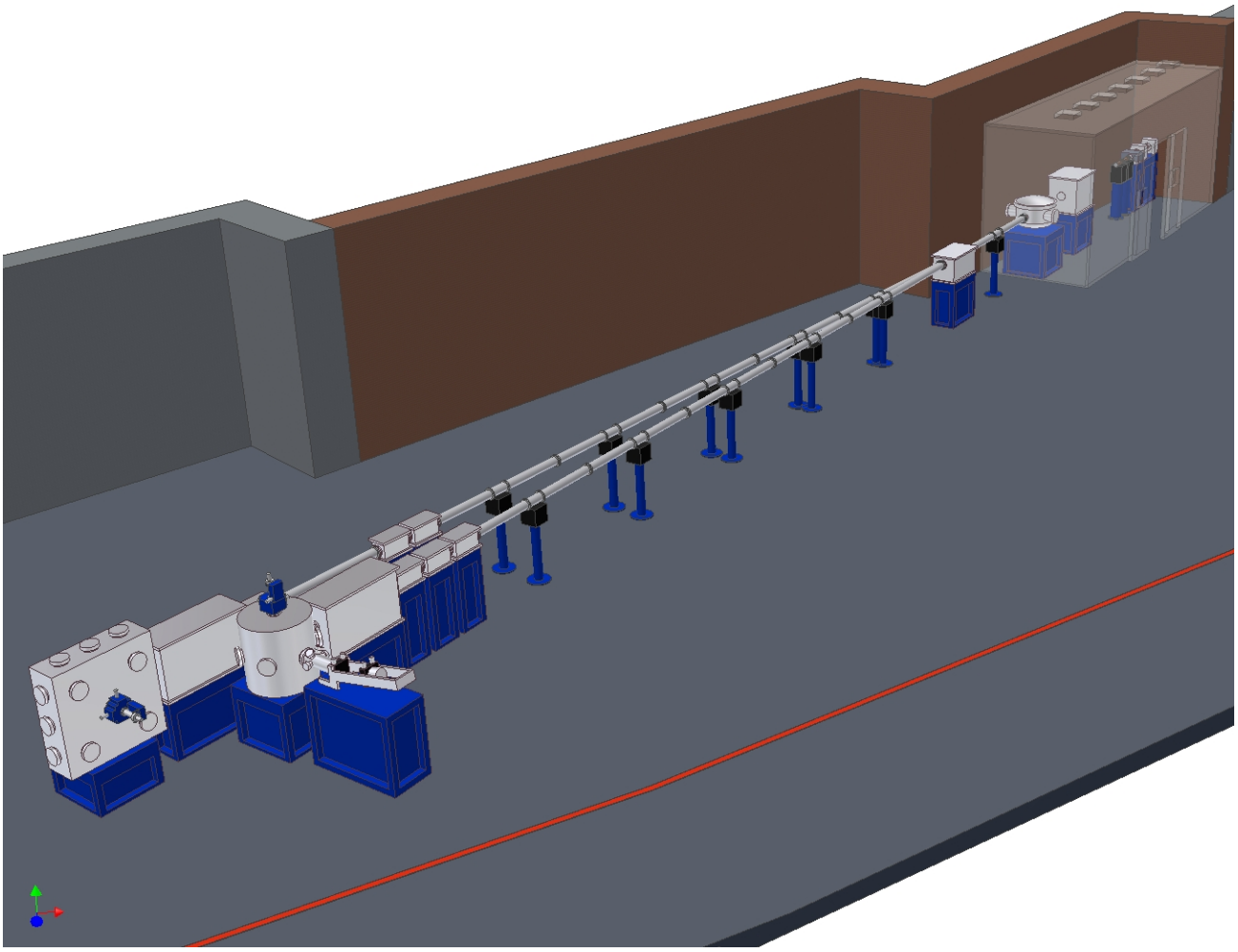

Figure 11.7.28 Proposed layout for a Soft X-Ray Resonant Scattering and RIXS Beamline.

11.7.3.1 XRMS End Station

To conduct measurements in the soft x-ray range, vacuum pressures of order 10^{-8} Torr or lower are necessary to eliminate scattering and absorption from residual gases, maintain the cleanliness of the sample and upstream optics, and prevent condensation onto sample surfaces during low-temperature operation. In essence, the XRMS end station is a good diffractometer contained in a vacuum vessel, which complicates the design of the instrument. The diffractometer must permit independent motions of sample θ to near 90°, detector 2θ to near 180° (back scattering), and as many other motions as is practical. The design goals for the XRMS end station will be to allow near 360° rotation of the sample azimuthal angle (ψ), and about ±10° on the sample flip axis (χ). Those motions would allow for specular scans along the Q_z direction (normal to the sample) and diffuse scans along Q_x (with the scattering plane parallel to the x-z plane). Of course, it would also be desirable to rotate the detector arm out of the scattering plane to conduct diffuse scans along the Q_y direction. In the past such motions have been difficult to attain as in-vacuum stepper motors generally were not available. However, in recent years, several suppliers have started offering such items. This development should simplify a design featuring detector motion out of the scattering plane. A conceptual sketch of the proposed diffractometer is presented in Figure 11.7.29.

On the detector side, it is envisaged that the detector arm will house a group of point detectors that are optimized for different dynamic ranges. In addition, a two-dimensional detector would be of great benefit for examining diffuse diffraction patterns as well as soft x-ray Small Angle X-ray Scattering, SAXS. The size and characteristics of the detector suite will be discussed in more detail in Section 11.7.4. However, all the detectors will require beam-defining slits between the sample and the detector to reduce the background counts. The slits also define the angular acceptance of the point detectors and being able to vary their acceptance angle would be beneficial. The most direct way of accomplishing this would be to have the detector and slit translate along the 2θ arm; the angular acceptance would increase as the detector approached the sample. For this implementation the detector stage or individual detectors should be mounted on a motorized linear translation stage.

As stated above, there are at least three related but separate user communities that would use the XRMS end station, and the sample environment required to support the science program in each group will be quite different. The correlated electron materials community would prefer, generally speaking, the ability to cool the sample as low as possible and also to be able to apply high magnetic fields on the order of 5 Tesla or larger. The large fields would be useful for driving complex materials across phase boundaries and then searching for ordering phenomena such as orbital ordering via the appearance of additional peaks in the scattering pattern. While such large fields and low temperatures would be useful for the magnetic multilayer and spintronics materials group, particularly in the case of magnetic semiconductors, a more useful ability for them would be to have more modest fields, on the order of 1 Tesla or lower, but have the ability to vary the field quickly by, for example, rotating the direction of the magnetic field both in-plane and out of plane. Also, since many of the properties of interest for these researchers involve interfacial chemical and magnetic ordering, the evolution of interface roughness could be studied via in-situ sample heating to at least several hundred degrees Celsius.

It is unlikely that a single experimental configuration would satisfy the needs of all the potential user communities. Therefore, having different inserts available for the XRMS chamber would provide the required sample environment. In the first configuration, the XRMS chamber would be equipped with a large field superconducting magnet with a maximum sustained field of 5 Tesla or greater. In all likelihood, this magnet would be of a split coil design and would be fixed (non-rotating), which would limit the angular range of the scattering. In the second configuration, the large magnet would be replaced by one with a smaller maximum field, on the order of ~1 T or so, but where the direction of the magnetic field could be varied. Also, the magnet should be designed to leave the scattering plane unobscured, perhaps by having the magnet poles rotate along with the sample θ angle. An in-vacuum octupole design might provide the solution that satisfies these requirements. In addition, the low-temperature cryostat could be replaced with a modest sample heating stage to permit in-situ annealing and subsequent measurement.

The sample environment should also provide for numerous electrical connections. These would be used to monitor sample temperature, conduct four-point conductivity and magneto-resistance measurements, and other probes. There should also be shielded cables capable of providing high voltage, which could be used to pole and de-pole ferroelectric and multiferroic materials. Similar shielded cables could be used for measuring sample current to conduct XAS measurements to complement the XRMS experiments. Finally, the sample manipulator and experimental chamber should be equipped with a load-lock device for rapid sample transfer.

11.7.3.2 RIXS End Station

The greatest design challenge for a RIXS spectrometer is to develop an instrument with the highest resolving power at soft x-ray energies while still maintaining a reasonable count rate. A RIXS instrument is a very good, compact soft x-ray spectrometer that is affixed to an experimental vacuum chamber (see Figure 11.7.30). The general characteristics and design tradeoffs of a RIXS instrument are:

- Plane Grating Monochromator or Rowland circle configuration
- several gratings to cover wide energy range and offer a choice of resolution

- blazed gratings to increase efficiency
- large area, 2D CCD detector that translates along the grating dispersion direction to increase accessible energy range
- entrance slit (higher resolution) vs. slitless entrance (requires small beam spot; provides more flux)

With regard to the last point, the exceptionally small emittance of NSLS-II results in a extremely small spot size on the sample (approx. 4 μm, vertical × 8 μm, horizontal) while still maintaining a high flux on the order of 10^{10} to 10^{12} ph/s. Thus it should be feasible to design a custom RIXS spectrometer with no entrance slit and achieve performance, in resolution and throughput, comparable to or better than the best instruments currently available. Alternatively, an entrance slit could be incorporated into the design to increase resolution further, but at the cost of decreased throughput. Of course, the entire instrument, as well as the sample environment, must be in continuous ultrahigh vacuum to maintain clean surfaces of cryo-cooled samples..

As mentioned above, one potential benefit of RIXS is dipole-allowed section rules that are present both in the photo-excitation process and in the radiative decay of the core hole. In principle, therefore, it should be possible to investigate, in an element-specific fashion, the valence-electron wave functions along different crystal symmetry directions. To accomplish this, it would be advantageous to have the RIXS spectrometer move with respect to the sample, thus accessing different momenta relative to the crystal while keeping fixed the polarization of the incident light. This will prove to be an engineering challenge as the RIXS spectrometer is likely to be at least 1 m to 2 m in length or longer. Moving such an instrument while maintaining vacuum in the 10^{-8} Torr range or better will be difficult. One candidate solution would have the RIXS chamber and spectrometer located on a rotary platform and connected to the beamline via a large diameter bellows. The sample would be mounted on a separate rotary seal. The whole chamber could thus rotate about the beam position while the sample counter-rotates to maintain its orientation relative to the photon beam.

The ability to vary the incident light polarization via use of the EPU insertion devices is of great utility. This will permit collection of RIXS spectra with the electric field vector of the incident radiation oriented horizontally and vertically without having to rotate the sample. Also, with the proposed rapid switching scheme, lock-in detection techniques become feasible, which would be of great utility in examining small spectral signals that might arise in linear dichroism effects. Finally, heretofore, RIXS measurements with circularly polarized soft x-rays have not been common. Such measurements could be quite useful, as they impose an additional selection rule on dipole-allowed processes, namely, the magnetic quantum number m_j should vary according to $\Delta m_j = \pm 1$ or 0. Such capabilities would be extremely useful in examining high-temperature superconductor and other correlated electron systems where ferromagnetic order either coexists or is nearly degenerate with other phases. Similar arguments would apply to novel materials such as multi-ferroic compounds

The sample environment should allow for as many perturbations on the sample as is practical. Certainly, the sample should be connected to a cryostat that can lower the temperature as low as possible. Closed-cycle, commercial cryostats that provide a temperature on the sample of 4.2K and are UHV compatible are currently available. Closed-cycle cryostats with a base sample temperature as low as 1.2K are also available, but they are not currently compatible with a good vacuum environment. However, commercial suppliers are currently investigating whether good vacuum performance and improved cooling is feasible.

In addition to the sample temperature, for many experiments it is critical to apply a large magnetic and /or electric field on the sample to drive a material across a phase boundary and examine the resulting changes on the RIXS spectra. Split core magnets with maximum sustained fields near 11 Tesla are commercially available. More complicated designs where the direction of the magnetic field can be varied are less common, but possible, at the cost of added expense and more limited field strengths. As with the XRMS chamber, the RIXS chamber should include numerous electrical connectors and suitable in-vacuum cabling for monitoring sample temperatures, applying fields, and recording sample currents. The chamber should also be equipped with a load lock and sample transfer mechanism.

11.7.4 Detectors

Three different classes of detectors will be required for the XRMS beamline: "point" detectors operating in current mode, "point" detectors operating in pulse counting mode, and 2D detectors. For the current-mode point detectors, we will use photodiodes whose response is optimized for the soft x-ray energies. These optimized silicon photodiodes, such as the AXUV series from International Radiation Detectors, Inc. have very high quantum efficiency (~50 – 200) in the soft x-ray range and a thinned silicon oxide junction that greatly reduces absorption in the nonresponsive oxide layer. Also, these photodiodes are inexpensive. They can be equipped with in-vacuum pre-amplifiers that reduce pick-up noise over the cabling to the data acquisition computer, which is indispensable for accurately recording low signal level. Alternatively, low-current GaAsP photodiodes are also available, but at increased expense. However, both types will be evaluated for use in the XRMS end station.

In addition to the current-mode photodiodes, we plan on installing pulse counting detectors suitable for extremely low-photon-flux detectors. These detectors are capable of single photon detection and they are extremely useful in examining weak, off-specular diffraction features; standard photodiodes are of limited use in those situations, as the count rate often approaches the noise floor. Two types of pulse counting detectors will be evaluated. The first is avalanche photodiodes, which are robust detectors operated at modest bias (~150 V), which provide internal gain. APDs are insensitive to repeated exposure to atmosphere, which makes them useful in situations such as the planned multiple configurations of the XRMS chamber, where the vacuum chamber is vented repeatedly. Also, they extend the accessible dynamic range down by one to two orders of magnitude over standard soft x-ray photodiodes. Modest cooling, to 0° to -20°C, improves the internal gain of the APDs by about an order of magnitude. Such temperatures are easily achieved using small Peltier cooling stages. A disadvantage of APDs is that strong absorption of incident x-rays occurs near the oxygen K edge; this limits their operating energies to above ~600 eV.

Another possible pulse counting detector is a channel electron multiplier (CEM) with a CsI photoelectric converter screen. These detectors are extremely sensitive, even more so than APDs, and they are sensitive over the entire spectral range covered by the beamline. However, the sensitivity of CEMs decreases with repeated exposure to atmosphere.

In addition to the point detectors, we will require high-efficiency 2D area detectors. Indeed, for the RIXS spectrometer, such detectors are crucial, as they permit designs of instruments that capture a much larger solid angle than would be possible with point detectors. Two types of detectors will be evaluated for use the two end stations. The first type is soft x-ray CCD cameras. These detectors have a reasonably high quantum efficiency of ~30% to 70% in the soft x-ray range. The current state-of-the-art CCD cameras have an active area of 25 mm × 25 mm with 2048 × 2048 pixels and a pixel size of 13.5 μm. In the near future, suppliers expect to produce CCD chips with 4096 × 4096 pixels with an active area of 50 mm × 50 mm. At the moment, the major soft x-ray CCD suppliers do not plan to reduce the pixel size below 13.5 μm, which would improve the resolving power of the RIXS spectrometer. Therefore, detector development should be monitored closely to ascertain whether improved detectors can be incorporated into the experimental design of the XRMS and RIXS apparatus.

For 2D detection of soft x-rays, CCDs offer the best dynamic range with the smallest pixel size. One disadvantage to CCD cameras is that they are rather bulky for in-vacuum use. A more serious limitation is that the cameras often require active water cooling. This is a bit inconvenient for the XRMS spectrometer, as it implies that the coolant supply pipes have to be inserted into the vacuum chamber and directed along the detector arm to the camera. Also, care must be taken so that the coolant lines do not limit the motion of the detector arm. An alternative 2D detector is a MultiChannel Plate detector with a delay line read-out. MCP detectors do not require cooling and typically have a lower dark count than the CCD cameras. The disadvantages are that the minimum spatial resolution of the MCPs is about 50 μm, they require high voltage, and the data rates are typically lower than CCDs. The lower spatial resolution would make the MCP detectors

more suitable for the XRMS diffractometer than the RIXS spectrometer, and developments in these detectors should be followed closely.

11.7.5 Laboratory and Conventional Facilities

Two laboratory spaces would be desired for such a high-resolution soft x-ray beamline. Some of these facilities, however, should be shared resources that will be used by other soft x-ray beamlines. The first laboratory space would be a clean lab where testing and assembly of the in-vacuum instrumentation and beamline components would occur. This should contain one or two laminar flow hoods, storage facilities (cabinets and drawer space) for various end station components and test equipment, ultrasonic agitators for component cleaning, and a generous number of lab benches. There should be specialized utilities such as deionized water and dry nitrogen gas available, and sufficient electrical capacity to run several rough pumps, ion pumps, turbo pumps, and other required instrumentation. The clean lab should also dedicate one laminar flow hood, lab benches, and storage for sample preparation and mounting. Clean tools should be supplied for this purpose. There should also be one or two vacuum desiccators for sample storage. Also, the clean lab will probably need a satellite storage area for temporary storage of waste solvents. Because of the necessity to guarantee cleanliness and availability of tools and instrumentation for UHV application, the clean lab should be accessible only via keyed access, with either electronic or mechanical keys.

The second laboratory would house sample characterization tools that complement the data collected on the XRMS and RIXS end stations. Many of the experiments on these end stations will be on samples where magnetism competes with or greatly influences other physics properties. Thus the support laboratory should include a suite of instruments to characterize the advanced samples measured on the beamlines. Candidate instrumentation should include MOKE (magneto-optic Kerr effect) in longititudinal, polar, and transverse modes, SQUID magnetometry, perhaps combined with AC susceptibility and PPMS (physical properties measurement system), which includes magneto-transport measurements, Hall effect, and critical current probes), high-frequency magnetic characterization (e.g., electron spin resonance or ferromagnetic resonance) and some form of magnetic microscopy (MFM or MOKE microscopy). The laboratory should also include a high-temperature vacuum furnace that can be used to anneal samples in a magnetic field to vary effects such as magnetic ordering and exchange bias, and also to produce magnetically soft pole pieces for specialized electromagnets used on the beamline.

11.7.6 Outstanding Issues

We propose the acquisition of a portable soft x-ray polarization analysis chamber, which could be mounted on any beamline. It is anticipated that the polarization analysis chamber could be shared between the two soft x-ray beamlines in the initial tranche of beamlines, and would support other soft x-ray beamlines at NSLS-II as they come on line.

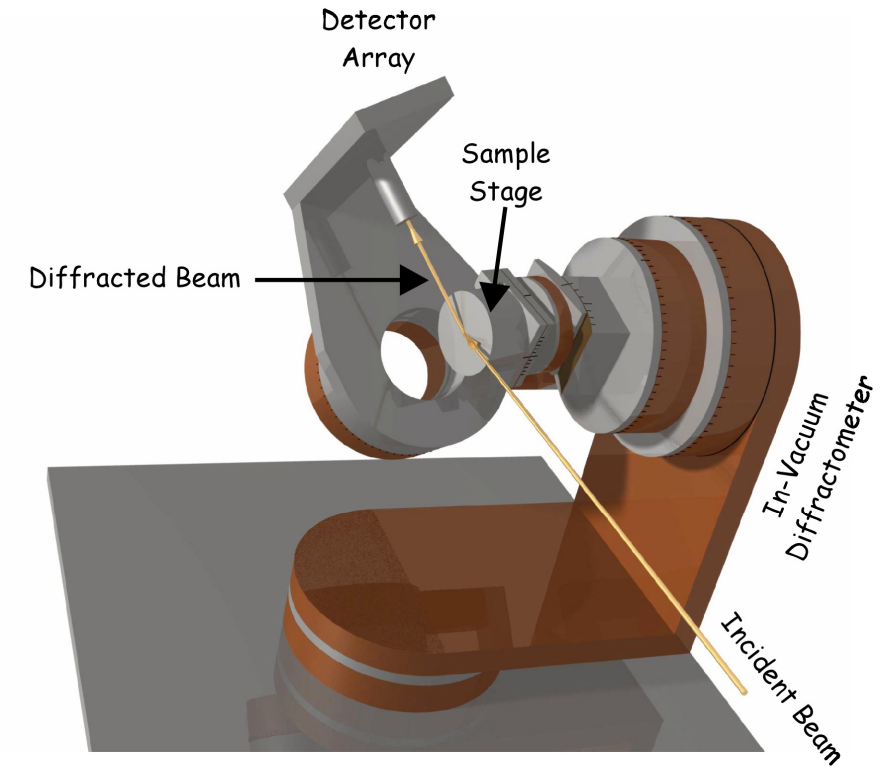

Figure 11.7.29 Schematic representation of a proposed XRMS in-vacuum diffractometer. The final design will incorporate multiple rotational degrees of freedom for sample and detector stages, sample cooling to LHe temperatures, and an electromagnet for applying an external magnetic field.

References

[11.7.1] C. Sanchez-Hanke, R. Gonzalez-Arrabal, J. Prieto, E. Andrzejewska, N. Gordillo, D. Boerma, R. Loloee, J. Skuza, R. Lukaszew, Observation of nitrogen polarization in Fe-N using soft x-ray magnetic circular dichorism, *J. Appl. Phys.* **99**, 08B709 (2006).

[11.7.2] B. Heinrich, et al., Dynamic exchange coupling in magnetic bilayers. *Phys. Rev. Lett.* **90**(18) (2003).

[11.7.3] M.G. Samant, et al., Induced spin polarization in Cu spacer layers in Co/Cu multilayers. *Phys. Rev. Lett.* **72** 1112 (1994).

[11.7.4] R. Follath, The versatility of collimated plane grating monochromators. *Nucl. Instr. & Meth. A* **467** 418 (2001).

[11.7.5] R. Reininger, and A.R.B. de Castro, "High resolution, large spectral range, in variable-included-angle soft X-ray monochromators using a plane VLS grating." *Nucl. Instr. & Meth. A* 538(1–3): pp. 760 (2005).

[11.7.6] P. Elleaume, Undulator Radiation, in *Undulators, Wigglers and their Applications*, H. Onuki and P. Elleaume, Eds. 2003, Taylor & Francis: London.

[11.7.7] R. Reininger, SRCalc, 2001–2006.

[11.7.8] F. Riemer, and R. Torge, Bessy Sx-700 Uhv Monochromator – Design-Features and Kinematic Concept. *Nucl. Instr. & Meth* **208**(1-3) 311(1983).

[11.7.9] M. Neviere, P. Vincent, and R. Petit, Theory of Conducting Gratings and Their Applications to Optics. *Nouvelle Revue D Optique* **5**(2) 65 (1974).

[11.7.10] C. Welnak, G.J. Chen, and F. Cerrina, "Shadow – A Synchrotron-Radiation and X-Ray Optics Simulation Tool." *Nucl. Instr. & Meth. A* **347**(1-3) 344 (1994).

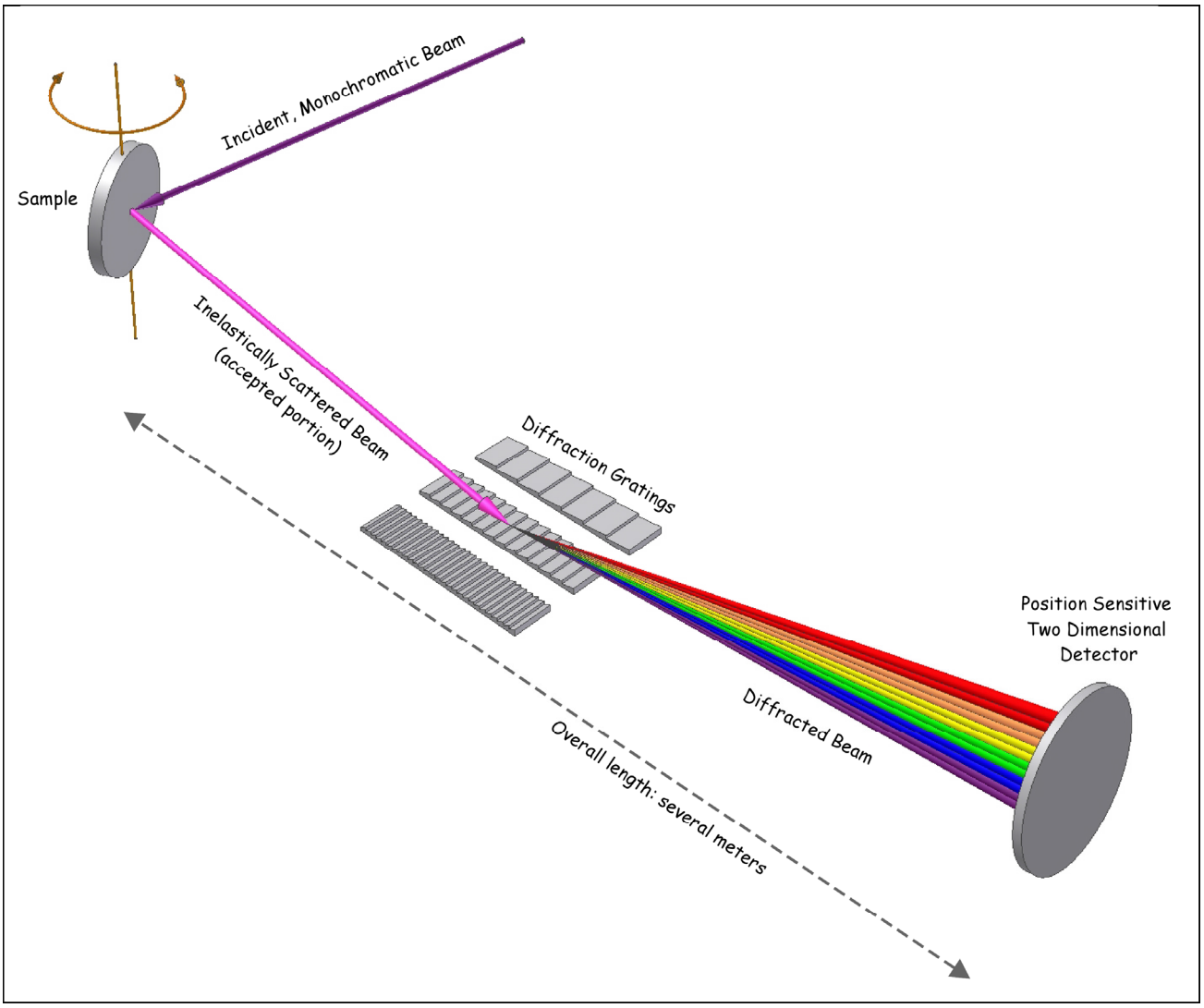

Figure 11.7.30 Schematic representation of RIXS spectrometer. The incident monochromatic beam undergoes inelastic scattering processes in the sample. A small portion of the emitted radiation (which is distributed over 2π steradians) is accepted by the RIXS spectrometer. User-selectable diffraction gratings cover different energy ranges and offer a choice of resolving power. The length of the overall instrument will be several m. In addition to sample rotation (shown in the figure), the entire RIXS spectrometer will rotate about the vertical sample axis to permit selection of different final states.

References (cont.)

[11.7.11] A. Remhof, et al., Shining light on magnetic microstructures. *Superlattices and Microstructures* 37(5) 353 (2005).

[11.7.12] V. Cvetkovic, et al., Observing the fluctuating stripes in high Tc superconductors. cond-mat/0607402 v1, 2006.

11.8 A High Flux Beamline for Soft X-Ray Coherent Scattering, Imaging, and Spectroscopy

The NSLS-II storage ring accelerator, fitted with appropriately matched undulators, will be an excellent source for soft x-ray beamlines that require either high brightness or high flux, or both. The high degree of transverse spatial coherence produced by these sources in the soft x-ray range will especially favor soft x-ray imaging and coherent scattering experiments. The additional concurrent capability to select the polarization of the soft x-ray beam, or to be able to switch the polarization rapidly between two polarization states, will greatly expand the scientific scope of this beamline.

The Soft X-Ray Coherent Scattering and Imaging Beamline is proposed to cover an energy range between 200 and 2000 eV with high flux at selectable resolving power from 4,000 to over 20,000. This beamline will provide x-rays of variable polarization with the important capability of fast switching between two polarization states. The combined properties of strong transverse spatial coherence and rapid polarization switching will be ideally suited to experiments that require either of these two properties, or both. Two experiments that require transverse spatial coherence are coherent imaging/scattering and scanning transmission x-ray microscopy. A class of experiments that benefit greatly from the magnetic sensitivity gained by rapid switching of the incident photon beam polarization is soft x-ray magnetic spectroscopy. This class of experiments includes soft x-ray magnetic circular dichroism (SXMCD), soft x-ray magnetic linear dichroism (SXMLD), and all of the variants of photoelectron emission microscopy (PEEM).

The beamline described in this section, based on optimally matched soft x-ray undulator sources described in Chapter 8, can serve all of the classes of experiments described above. Clearly, the number of end stations required to serve all of these experiments is too great to be housed at a single beamline. The actual buildout of soft x-ray undulator beamlines will be determined in a process that will involve input from all NSLS-II stakeholders. In addition to undulator beamlines, the NSLS-II bending magnets will be ideal sources for soft x-ray experiments, especially flux-driven soft x-ray experiments that require a larger étendue or illumination phase space than a coherent beam provides. One class of flux-driven experiments is full-field transmission x-ray microscopy (TXM), e.g., for tomography of biological specimens.

Coherent imaging and scattering involve the coherent illumination of a small specimen region (typically 5 to 10 μm, mapping pixel sizes of 2.5 to 10 nm into 1024^2 or 2048^2 detector pixels) with a spatially and spectrally coherent beam so that one records the Fourier transform of the exit wave on an area detector such as a CCD. In coherent scattering, the dynamics of this far-field intensity pattern can be used to monitor the dynamics of phase and absorption changes in the specimen, including over correlation distances as large as the illumination width. This is exploited in the Hard X-ray Coherent Scattering beamline described in Sec. 11.6, but the addition of coherent scattering capabilities in the soft x-ray region allows for coupling to the strong L-edge magnetic circular dichroism signal available for materials such as iron, nickel, and cobalt in the soft x-ray range, as well as to lower-Z elements in a coherent version of resonant scattering. In diffraction microscopy or coherent x-ray diffraction imaging (CXDI), partial information on the sample (such as knowledge or imposition of a "finite support," which is a region from which there is known to be, or is constrained to be, no scattering) is exploited to allow one to phase the far-field diffraction pattern and obtain a real-space image of the specimen without any resolution or efficiency limits imposed by lenses.

Scanning transmission x-ray microscopy (STXM) involves the use of a focusing optic to produce a microprobe beam through which the specimen is scanned. Whereas the hard x-ray nanoprobe described in Sec. 11.4 relies primarily on fluorescence detection due to low absorption, in the soft x-ray range, absorption dominates and the fluorescence yield for materials is low, so that transmission is the main signal used. As the resolution of soft x-ray focusing optics continues to improve, their diameter will increase dramatically, so in a STXM beamline it is generally preferred to have coherent illumination rather than a large beam diameter,

such as 100 to 500 μm. What has proven to be especially powerful is the coupling of spatial resolution with soft x-ray near-edge absorption spectroscopy in an approach termed *spectromicroscopy* [11.8.1] so that one can make nanoscale maps of chemical speciation for a number of low-Z elements for studies in biology, environmental science, polymer science, and a number of other fields. This requirement for high-quality spectroscopy drives the need for a high-energy resolution monochromator.

The classes of experiments which require rapidly switching source polarization but not a high degree of transverse spatial coherence, e.g., SXMCD, SXMLD, and PEEM, are generally based on flux-hungry techniques. Owing to the quest to measure ever smaller and ever more dilute samples, these techniques require ever smaller illuminated area. For example, modern PEEM end stations desire an illuminated spot size down to as small as 1 μm, thereby requiring the full brightness of an NSLS-II undulator source. At the same time, these classes of experiments require high, ~10^4, resolving power in order to provide selectivity among closely spaced (in photon energy) absorption features. The combined requirements of very high flux, high resolving power, small focused spot size, and rapid polarization switching make these experiments ideally suited to the undulator sources described in Chapter 8 and the beamline described here.

11.8.1 Soft X-Ray Spectromicroscopy

Scanning transmission x-ray microscopy with zone plate lenses was pioneered at NSLS by a group from Stony Brook led by Kirz [11.8.2]. The first instrument had a spatial resolution of about 300 nm, an energy resolution of about 1 eV, and a per-pixel dwell time of around 100 msec with a focused flux of 10^4 ph/s. Over twenty years, the Stony Brook group of Jacobsen, Kirz et al. have improved every figure of merit by one or more orders of magnitude simultaneously, while pioneering the development of various techniques of spectromicroscopy analysis. While the STXMs at NSLS beamline X1A continue to serve a vibrant community, STXMs at higher brightness soft x-ray sources such as the ALS have further improved the flux and energy tuning range.

The resolution that can be achieved in STXM is determined by three factors: the resolution of the optic, the resolution of the scanning system, and the radiation tolerance of the specimen. While the NSLS-II project proposes to push the development of multilayer Laue lenses (MLLs) and kinoform refractive lenses for the ultimate in image resolution with hard x-rays, these optics are not usable for soft x-rays due to absorption effects. Instead, all high-resolution STXMs employ Fresnel zone plate optics with finest outermost zone widths (and thus approximate spatial resolution) of 25 to 30 nm. As discussed in Chapter 12, there have been impressive recent demonstrations of 15 nm resolution soft x-ray zone plates; however, these zone plates had too small an efficiency and working distance to be usable in STXM. Instead, zone plate diameters of 100 to 500 μm are required to deliver a usable working distance for STXM experiments, and this requires the use of large-field-area electron beam lithography for optic fabrication. There is widespread consensus in the field that 10 nm resolution might be achievable in the coming years, though at that point sidescattering of even high-voltage electron beams in photoresists becomes the factor that limits the push to even finer zone widths. The extremely high brightness of an NSLS-II soft x-ray undulator should allow one to explore an alternative path toward achieving higher microscope resolution: the use of higher diffractive orders. For example, as one goes from first-order to third-order diffractive focusing in a zone plate, the resolution can, in principle, improve by a factor of three at a cost of a factor of 10 in focused flux. This loss of flux has been too severe, and the tradeoffs between optic diameter and focal length have been too daunting, for this to be exploited in present-day research, but with NSLS-II such a resolution/flux tradeoff might be more palatable.

A very attractive feature of the coherent scattering and imaging beamline is that the exit slit remains at a fixed position as the energy is tuned, yet its design is nearly aberration-free, so that high energy resolution is maintained. This is advantageous for STXM, because the beam must diverge from the exit slit to fill the aperture of the zone plate some distance away, where it is demagnified to a geometrical image that must be no larger than the diffraction-limited focus of the optic. By maintaining a constant exit slit position, this slit-to-zone plate distance can remain fixed as a function of photon energy.

The other two factors affecting ultimate resolution are the characteristics of the scanning system, and radiation tolerance of the specimen. While a STXM can benefit from the engineering of the hard x-ray nanoprobe end station described in Section 11.4, it will likely need to operate at considerably faster scanning speeds. The present-day NSLS STXM operates with pixel dwell times of about 1 msec, while the STXMs at ALS operate with 0.1 to 1 msec dwell times; in contrast, zone plate microprobes at APS typically operate with pixel dwell times of 0.1 to 1 seconds. (There are two reasons for the relative speed of soft x-ray STXMs over hard x-ray microprobes: the fact that spatially coherent flux scales as λ^2, and the fact that only a small fraction of incident photons get converted into fluorescent photons in hard x-ray microprobes). For NSLS-II, new scanning systems will need to be developed which can work with pixel dwell times as short as a microsecond. Indeed, the notion of "dwell time" is already inaccurate with present-day soft x-ray STXMs: they work not by stop-and-start motion of the specimen but by continuous scanning, with only the readout clocked at a specified pixel time. Even with this continuous scanning approach, the acceleration which the specimen undergoes in the "fast" scan direction will become more and more extreme at the turnaround point from each scanline. Possible solutions, such as double-mirror beam scanning systems similar to those used in confocal microscopy, bear consideration. We consider the scanning system speed and acceleration issues to be outstanding problems requiring further development.

Finally, radiation damage sets the ultimate limit on spatial resolution. The radiation exposure and thus dose needed to detect an object tends to increase as the fourth power of improvements in spatial resolution, so that it will become essential for a soft x-ray STXM to have cryo specimen capabilities for radiation sensitive specimens. Only one cryo STXM has been demonstrated, by the Stony Brook group; an improved version of this system will be key for exploiting the higher flux and tighter focus of a STXM at NSLS-II.

Ultimately, the growth of the x-ray microscopy user community is related to the straightforward understanding of the information delivered by the microscopes: "what you see is what you get." Such visualization depends on the spatial resolution of each microscope, allowing one to see in more or less detail the characteristics of the samples. The proof that this is a healthy, growing community is the fact that in the ALS five-year strategic plan presented in May 2006, two of the five beamlines that will be built or renovated in the next five years will feature microscopy-based instruments [11.8.3].

The NSLS-II soft x-ray beamline proposed here should provide higher brightness soft x-ray beams than are presently available, beams that are well-matched to the soft x-ray microscopes they will serve. The microscopy branch of the beamline proposed here will provide BNL with a 2013 state-of-the-art soft x-ray microscope. It will feature high spatial resolution with high photon flux at high resolving power and rapid-switching polarization, to serve the evolving needs of the NSLS-II scientific user community.

11.8.2 Coherent Scattering and Imaging

Coherence provides a known phase relationship between portions of a wavefield at different places across a specimen. This can be exploited to reveal patterns of long-range order in specimens, and to understand the dynamics of this ordering by correlation of the far-field diffraction intensity patterns acquired at various times. Fast point detectors can be used to explore short timescales, while area detectors can operate at much greater efficiency by collecting information from many "speckles" simultaneously. In addition, through the use of certain types of a priori knowledge of the specimen, the far-field intensity pattern can be inverted to yield a real-space image of the object.

Coherent scattering and imaging provides a simple benefit relative to the observation of real-space images using a lens: it dispenses with any of the limitations on resolution and transfer efficiency associated with lenses (which at present have a resolution limit of about 25 nm and an efficiency of about 10%). However, because coherent scattering and imaging provides a less direct measurement of real-space interactions in the specimen, its advantages are strongest when it is used to probe length scales finer than a lens can "see." As a result, coherent scattering and imaging experiments are generally performed with a requirement for purely coherent illumination over a field of view of only about 5 to 10 μm. In order to record the far-field diffraction

pattern at small scattering angles (as required for finite support image reconstruction, and measurements of long correlation distances), it is important to have the beam converge toward the detector so that the unscattered beam fills as few detector pixels as possible. As a result, while a STXM is best located several meters from an exit slit, a coherent scattering or imaging experiment is best done with the sample located essentially at the position of the exit slit or, even better, in an intermediate position between a coherence-preserving optic and a detector onto which an image of the exit slit is projected.

Because coherent scattering is well suited for studying micrometer-range correlations of nanostructure, it is of particular use for observing the dynamics of systems in response to a change in external condition. As an example, in the soft x-ray range one can study changes in thin-film magnetic media as a function of applied field, especially by working with circularly polarized radiation so as to exploit magnetic circular dichroism. The capability to control the magnetic field, temperature, stress/strain, and so on in the sample environment therefore becomes a key consideration in the design of the specimen chamber.

In diffraction microscopy or coherent x-ray diffraction imaging (CXDI), one seeks to obtain a real-space image of the object from its far-field diffraction intensity. This is fundamentally impossible due to the well-known phase problem unless one is able to compensate for the lack of experimental far-field phases in some way. The most common approach (used in remote sensing for nearly three decades) is to incorporate a priori knowledge of the specimen. The easiest is what is called a "finite support" constraint, which says that the specimen is known to fill only a small fraction of the illuminated region that contributes to the far-field diffraction pattern. This was first demonstrated for x-ray image reconstruction by Miao et al. [11.8.4] and there have been a number of important subsequent demonstrations by his group and others. At present the best 3D image resolution is 10×10×50 nm in soft x-ray experiments done by Chapman et al. [11.8.5] at ALS, and the first non-stained cell image has also been obtained there by the Stony Brook group [11.8.6]. Diffraction microscopy with hard x-rays allows one to image specific microcrystalline domains by recording diffraction not about the forward-scattered beam but diffraction about Bragg spots, and Pfeiffer et al. [11.8.7] have used this to map out strain in nanocrystals. Why then use soft x-rays with a longer wavelength and thus lower ultimate resolution? Because one needs a signal to be scattered at large angles, i.e., large momentum transfer, and soft x-rays undergo larger scattering from a given specimen size than hard x-rays do. As a result, it can be expected that one will use either the X-Ray Coherent Scattering Beamline described in Section 11.6, or this current beamline, depending on the total thickness and scattering strength of the specimen. By having both beamlines at hand, researchers at NSLS-II will be able to maximize the information they can obtain from any specimen through the use of diffraction microscopy.

11.8.3 Beamline Design

The scope of this beamline is to meet the need for soft x-ray spectromicroscopy, coherent imaging/scattering, and magnetic spectroscopy experiments to have the highest possible spatial resolution, high coherent flux (>10^{13} ph/s), high-energy resolving power, and rapid-switching polarization (linear, circular, or elliptical). These goals require the design of a coherence-preserving soft x-ray beamline that also provides the capability to switch rapidly between two polarization states. This beamline should also be able to provide the specific coherence, flux, and resolving power requirements of the potential target end stations: 1) transversely coherent illumination of large-diameter (100–500 μm) zone plates in a STXM end station, in order to reach optic-limited spatial resolution, 2) high coherent flux density delivered in a low-divergence beam with small (few μm) diameter for an imaging/scattering end station, and 3) very high flux in a ~1 μm spot for a polarization-sensitive soft x-ray spectroscopy end station. For all of these end stations/programs, it is our intent to reach photon energy resolving power of ~10.000 over the entire energy range.

11.8.3.1 Scope

This beamline will be designed to meet the needs of soft x-ray microscopy, coherent imaging/scattering, and magnetic spectroscopy experiments. To meet the goals anticipated for these experiments in 2013, the

beamline will need to provide very high coherent flux, $>10^{13}$ ph/s with spatial requirements described above, at a resolving power of 10^4 over the 200–2000 eV photon energy range, with rapid-switching polarization capability. The beamline we propose to meet these challenging goals is described in some detail below. It is served by a 4 m long elliptically polarized soft x-ray undulator that produces a brightness $>10^{20}$ ph/s/0.1%BW/mm^2/mrad^2 (see Chapter 8) over the 200–2000 eV photon energy range.

In addition to high flux and high resolving power, the beamline is designed to deliver beams of two distinct polarization states to a common focal spot, as provided by two canted (by ~0.25 mrad) 2 m long elliptically polarized undulators (EPUs) (see Chapter 8). These polarizations can be any that can be produced by the EPUs, which include circular, elliptical, and linear (along any in-plane axis). The beamline will provide the capability to rapidly switch the polarization between the polarizations states of the two EPUs, e.g., between σ and π linear polarization or between left and right circular polarization. The beamline design includes the capability to switch between the two selected polarization states, thereby enabling dichroism experiments to be performed under fixed sample conditions. Since the polarization switching is performed mechanically (chopper), the rate of switching can be high (up to kHz range), thereby significantly increasing the sensitivity of dichrosim measurements via phase-sensitive detection schemes. Rapid-switching polarization and phase-sensitive detection are crucial for detection of small dichroic signals, e.g., from low-cross-section processes or from small elemental concentrations in materials. The addition of rapid-switching polarization modulation capability to the flux, resolving power, and spot size properties of the proposed soft x-ray beamline will make it unique among existing DOE facilities.

In this beamline design, we pursue the goal of designing a beamline with the capabilities and the flexibility to perform state-of-the-art, highly demanding microscopy, coherent scattering/imaging, and magnetic spectroscopy experiments in the year 2013. These experiments require simultaneously high brightness, high photon flux, high energy resolution, and polarization modulation.

11.8.3.2 Choice of Fast-Switching EPW vs. Canted EPUs

We propose that this beamline be able to deliver two fast-switching polarization-modulated (e.g., left and right circularly polarized, or horizontal and vertical linearly polarized) beams of soft x-rays to a common focal spot. The soft x-ray polarization modulation can be produced by two main schemes. The first is the use of an electromagnetic insertion device that switches the polarization of the x-rays by changing the polarity of the current passing through the appropriate sets of magnets. The second scheme is the use of two identical insertion devices canted at an angle that allows the modulation of the soft x-rays to take place in space. This is the option taken by BESSY-II and SLS and recently also at SPring-8. Each of the two canted devices delivers one type of polarization, and the selection of the polarization takes place downstream of the beamline with a chopper. The chopper drives the switching frequency of the measurements.

Both polarization modulation schemes require a chopper to “clean” unwanted radiation from the signal. NSLS has a long experience in fast switching polarization experiments using an Elliptically Polarizing Wiggler. At present, the fast switching frequency of the NSLS EPW is 22 Hz, and an effort is ongoing to increase it up to 100 Hz [11.8.8]. We propose selecting the option with two canted insertion devices at NSLS-II. Electron beam stability is a critical goal of the NSLS-II storage ring and an electromagnet-based device could introduce beam instabilities via the constantly changing current in the electromagnets. The scheme based on two canted insertion devices involves canting the electron orbit but this orbit, when implemented, is time independent. Furthermore, the canted undulator scheme is capable of supporting much higher polarization switching rate than is the EPW scheme, owing to inductance-related limits on the ability to drive an electromagnet with a square-wave programming input.

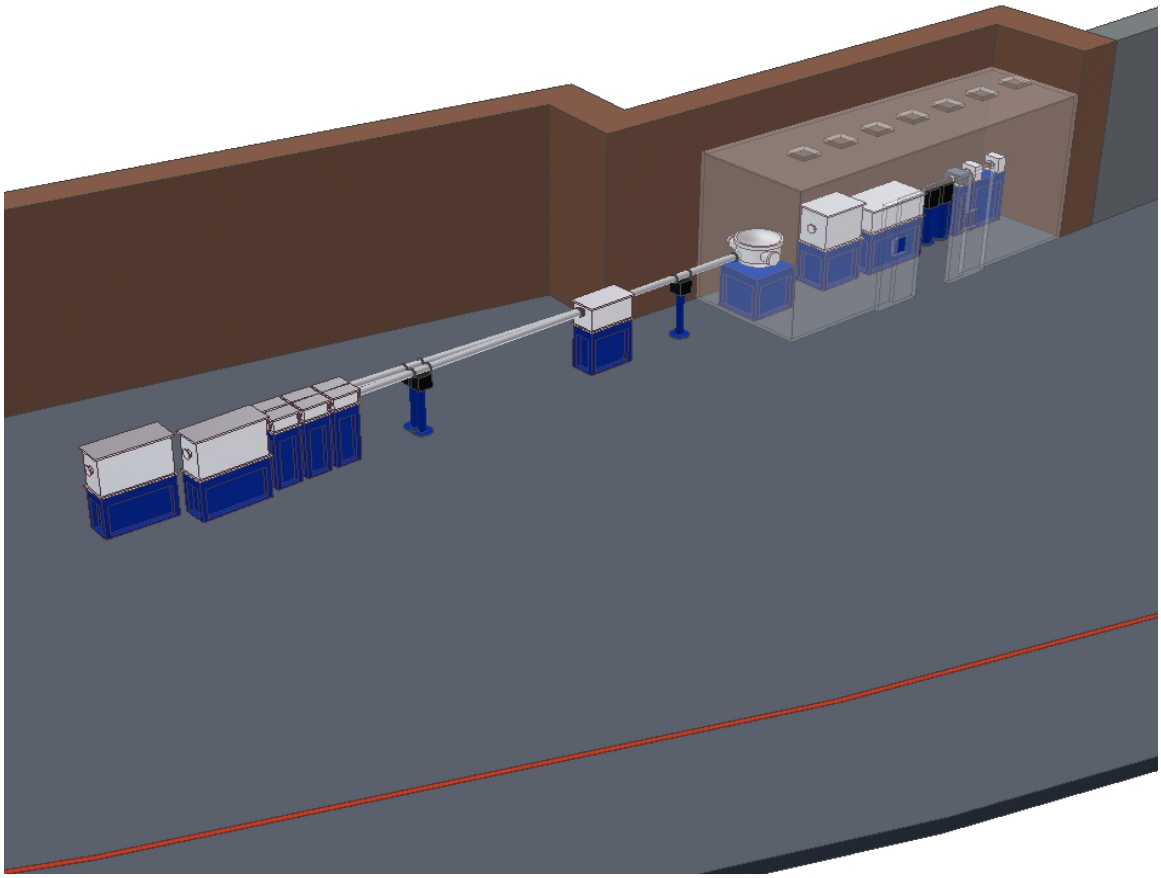

Figure11.8.1 Preliminary layout of soft x-ray beamline for soft x-ray coherent scattering, imaging, and spectroscopy.

11.8.3.3 Beamline Design

This section describes the optical design and the expected performance of a soft x-ray beamline optimized for coherent scattering, imaging, and spectroscopy. The source for this beamline would be the EPU45 elliptically polarized undulator described in Chapter 8. Two 2 m EPU45 undulators would be installed in a 5 m long ID straight section with provision for horizontal canting of the beams passing through the two EPU45s by an angle of 0.25 mrad or less. The two undulators could be operated, with proper phasing, as a single unit, providing horizontal, vertical, or circular polarized light, or independently, to provide two different polarizations for fast-switching dichroism experiments.

An alternative choice of ID straight section is an 8 m long ID. This choice would allow the undulator length to grow, but at the expense of larger source size owing to the larger beta function values in the 8 m ID straight compared to the 5 m IDs. Since the opening angles, both horizontal and vertical, of the electron beam in either the 5 m or 8 m ID straights is less than the diffraction-limited photon divergence angle, there is no angular divergence benefit to larger beta function for soft x-ray beamlines at NSLS-II. Therefore, we have chosen the 5 m ID straight sections for the soft x-ray beamlines, in order to provide the smallest possible focal spots on sample (or on other end station pinholes or focusing optics). One could envision providing the same spot size and flux using undulators in an 8 m ID straight, but only by fabricating longer undulators than proposed here and then throwing away photons spatially (via baffles or apertures), which is wasteful and not necessary.

The major components of this Soft X-ray Beamline monochromator design would be a cooled cylindrical first mirror, variable line spacing plane gratings (VLSPG), *no* entrance slit, and plane elliptical KB-type post-focusing mirrors. The beamline would be optimized for the energy range between 200 eV and 2.3 keV.

State-of-the-art optical elements would be required in order to simultaneously produce the very high flux, high photon energy resolution, and small focused spot size. A soft x-ray beamline would achieve a resolving power ~1.8×10^4 at 1 keV with a 10 μm exit slit width, if RMS slope errors of 0.1 μrad can be achieved over ≈100 mm usable meridional dimension on the plane optical elements. A spot size with FWHM of less than 5×5 μm^2 requires RMS slope errors of approximately 0.5 μrad along the meridional direction on the sagittal cylinder and the elliptical cylinders used in the proposed design. These mirror figure requirements are beyond the current state of the art and will therefore require research and development.

In the proposed soft x-ray beamline, ~4×10^{12} ph/s will illuminate a spot with FWHM of less than 6×4 μm^2 (hor×ver.) at 1 keV within a bandwidth of 56 meV (~18,000 resolving power). The calculated flux at 1 keV increases by an order of magnitude with a different grating delivering a resolving power of 4500 to the same spot size.

11.8.3.4 Beamline Optics

The requirements for the highest possible resolution and a fixed exit slit over a broad energy range can be fulfilled with the collimated plane grating monochromator proposed by Follath et al. [11.8.9]. Its optical design includes a horizontally deflecting toroidal mirror that collimates along the vertical (dispersion direction) and focuses the beam horizontally at the exit slit. The vertically collimated beam is deflected (vertically) by a plane mirror illuminating the plane grating at an angle of incidence α. The beam dispersed by the grating, at an angle β, is focused onto the exit slit plane by a sagittally focusing cylindrical mirror. The collimation along the dispersion direction allows operation of the monochromator at different values of c ($=\cos\beta/\cos\alpha$) by means of choosing the appropriate angle of incidence on the plane mirror. Large c values are used to improve resolution at the expense of flux. The CPGM design is almost aberration-free. The major contributions to its wavelength resolution are:

$$\Delta\lambda_{so} = \frac{2.7\,\Sigma_y \cos\alpha}{n\,k\,r_1}, \tag{11.8-1}$$

$$\Delta\lambda_{ex} = \frac{s\cos\beta}{n\,k\,r_2}, \tag{11.8-2}$$

$$\Delta\lambda_{Gr} = \frac{5.4\,\sigma_{Gr}}{n\,k}\cos\left(\frac{\alpha+\beta}{2}\right)\cos\left(\frac{\alpha-\beta}{2}\right), \tag{11.8-3}$$

and

$$\Delta\lambda_{PM} = \frac{5.4\,\sigma_{PM}\cos\alpha}{n\,k}, \tag{11.8-4}$$

where the suffixes on $\Delta\lambda$ refer to the source (*so*), the exit slit (*ex*), the grating (*Gr*), and the plane mirror (*PM*). In these equations, Σ_y is the RMS vertical source size, n is the diffraction order, k the grating line density, r_1 the distance from the source to the toroidal mirror, s the slit width, r_2 the distance from the refocusing mirror to the exit slit, and σ_{Gr} and σ_{PM} the RMS meridional slope errors on the grating and plane mirror, respectively.

The slope errors on the collimating and refocusing mirrors also affect the resolution. However, their effect is very small due to the large "forgiveness factor," the cosine of the angle of normal incidence on the mirror.

Some of the experimental stations to be installed at the end of the soft x-ray beamlines at NSLS-II require a spot size in the micrometer range. Along the vertical direction this can be easily achieved with an elliptical cylinder that demagnifies the exit slit width. Since the RMS horizontal size of the photon beam varies between 54 and 41 μm in the energy range 200-2500 eV, a demagnification of ≈2.35×50/5 =23.5 is required to obtain a horizontal spot size of 5 μm FWHM. In the CPGM, the horizontal demagnification of the source onto the slit is approximately one. Therefore, the demagnification in this design needs to take place in between the slit and the sample. However, the requirement for a distance of ≈700 mm between the sample and the end of the refocusing mirror means that the entrance arm of the horizontally refocusing mirror needs to be larger than 10 m, which is impractical.

The very small horizontal divergence of the beam expected from a 4 m long insertion device in a 5 m straight section of NSLS-II, 32 μrad RMS at 200 eV, allows for a solution in which the beam diverges up to an elliptical cylinder located after the exit slit. This mirror then demagnifies the horizontal source down a few microns. One could implement this in the CPGM by replacing the toroidal mirror with a sagittal cylinder that provides the grating with a collimated beam along the dispersion direction. Unfortunately, the illumination of the refocusing cylinder after the grating by a divergent horizontal beam results in a large astigmatic coma aberration that reduces significantly the monochromator resolution.

The proposed monochromator [11.8.10] uses a sagittal cylindrical mirror to collimate the beam along the vertical (dispersion) direction. The following optical element is a plane mirror that illuminates a variable line spacing (VLS) plane grating. The line density of the grating is given by $k(w) = k_0 + 2b_2 w + 3b_3 w^2 \ldots$, where w=0 is at the grating center and positive towards the exit slit. The linear coefficient term, b_2, can be chosen to zero the defocus term in the optical path function at a single wavelength,

$$f_{20} = \frac{\cos^2 \beta}{dGrEx} + 2 b_2 n k \lambda, \tag{11.8-5}$$

whereas b_3 can be chosen to zero the coma term in the optical path function, i.e.,

$$f_{30} = \sin\beta \frac{\cos^2 \beta}{dGrEx^2} + 2 b_3 n k \lambda, \tag{11.8-6}$$

also at a single wavelength. In Eqs. 11.8-5 and 11.8-6, *dGrEx* is the distance between the grating and the exit slit. The important point in this design is the fact that the plane mirror can be used to zero f_{20} for all wavelengths by illuminating the grating at the required angle of incidence. Note that this design has one less mirror than the CPGM, owing to the meridional focusing provided by the VLS plane grating.

Eqs. 11.8-1–11.8-4 also give the contributions to the wavelength resolution in the proposed design with r_1 being the distance from the source to the cylindrical mirror and by replacing r_2 with *dGrEx*.

11.8.3.5 Source

The undulator source for this beamline will be two canted soft x-ray EPUs, as described in Chapter 8. Either the EPU42 or the EPU45 will be chosen, depending on allowed magnetic gap considerations not finalized at the time of the writing of this document. Here we will assume an EPU42 source, but the baseline EPU45 device will provide similar performance. The EPU42 soft x-ray undulators cover the energy range between 200 and 2000 eV with pure circular polarization, and a larger energy range with linear polarization. In canted mode, the two undulators will generally be set to different polarizations, and a fast-switching chopper will be used to alternate the polarization delivered to the sample. In un-canted mode, the two

undulators are set to the same polarization and, if properly phased (e.g., by use of a "modulator" between the two devices), will act as a single long undulator.

The machine parameters, the RMS electron beam sizes and divergences, and the insertion device parameters used in the calculations are listed in Tables 11.8.1 and 11.8.2.

Table 11.8.1 Machine Parameters Used in the Calculations.

Energy (GeV)	3.0
Current (mA)	500
σ_x (μm)	40.2
σ_y (μm)	1.7
$\sigma_{x'}$ (μrad)	14.9
$\sigma_{y'}$ (μrad)	1.8

Table 11.8.2 ID Parameters Used in the Calculations.

	Soft X-ray Beamline II
ID type	2 x APPLE-II EPU
Length of each ID (mm)	2000
Period length (mm)	42

Figure 11.8.2 shows the flux emitted in the central cone by the two insertion devices with a 4 mm period when operated in phase to deliver linear polarized radiation.

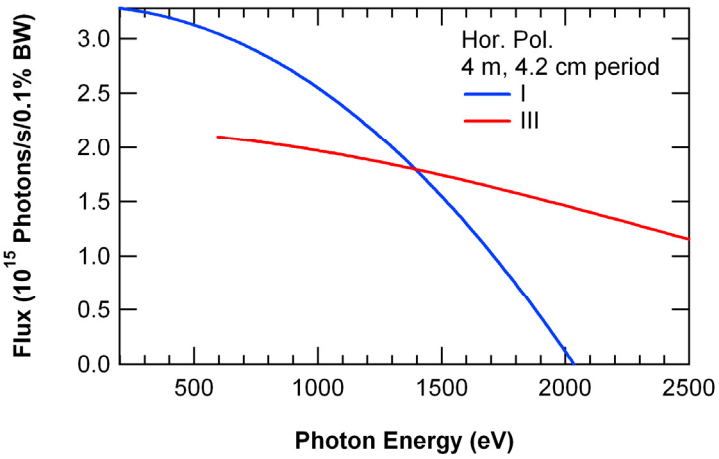

Figure 11.8.2 Flux emitted in the central cone by a 4 m ID linear device with a 4.2 cm period, as a function of photon energy.

The total sizes and divergences used in the calculations were obtained as the vector sum of the electron beam parameters and the RMS values of the photon beam were calculated using $\sigma_r = \sqrt{2\lambda L}/2\pi$ and $\sigma_\rho = \sqrt{\lambda/2L}$, where L is the undulator length and λ the radiation wavelength [11.8.11].

11.8.3.6 Beamline Layout

A soft x-ray beamline for imaging and coherent scattering requires very high flux, and spot sizes at the experimental stations in the micron range. The proposed monochromator can fulfill these requirements. To achieve high flux at good, but not the highest possible, energy resolution, the distance between the gratings and the exit slit is relatively short (~10 m) and low-line-density gratings are chosen. A cartoon of the proposed beamline is shown in Figure 11.8.3, with parameters listed in Table 11.8.3.

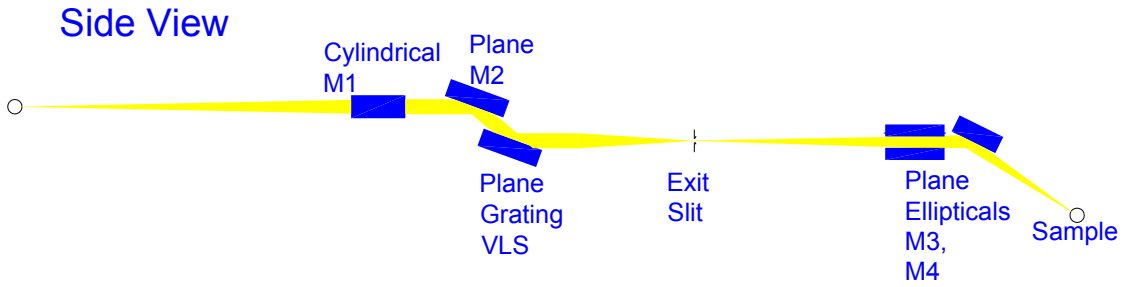

Figure 11.8.3 Sketch of a possible soft x-ray microscopy, coherent imaging/scattering, and magnetic spectroscopy beamline.

Table 11.8.3 Distance from the Source, Angle of Incidence, and Deflection of the Optical Components for a Soft X-Ray Beamline for Imaging and Coherent Scattering.

Element	Distance (mm)	Angle (deg)	Deflection
M1- Sagittal Cylinder	28000	88.75	horizontal
M2- Plane	29611-29944	82.4-88.9	vertical
Gr – Grating	≈30000.	86.4- 89.6	vertical
Slit	40000		
M3 - Plane Elliptical	41200	88.5	horizontal
M4 – Plane Elliptical	41700	88.5	vertical
Sample	42500		

There is space between the shield wall (25 m from the undulator source) and M1 to insert an experimental station to host coherent experiments that are illuminated directly by the undulator source, with no optics in between to degrade the coherence of the beam.

11.8.3.6.1 First Mirror

The first element in the beamline is a sagittal cylindrical mirror located at 28 m from the source, outside the shield wall. The angle of normal incidence in this mirror (as well as that of M3 and M4) is determined as a compromise between the highest possible reflectivity in the energy range covered by this beamline and a reasonable mirror length. Figure 11.8.4 shows a small set of the calculations performed [11.8.12] to determine the angle of incidence and the coating material on the mirrors. An angle of incidence of 88.75° and a 30 nm coating of Au over the Si substrate were chosen. As Figure 11.8.4 shows, the selected parameters provide good reflectivity up to 2.2 keV. Note that at this angle of incidence, the s- and p-reflectivities are almost identical. Therefore, the beamline will not distort circular polarized radiation.

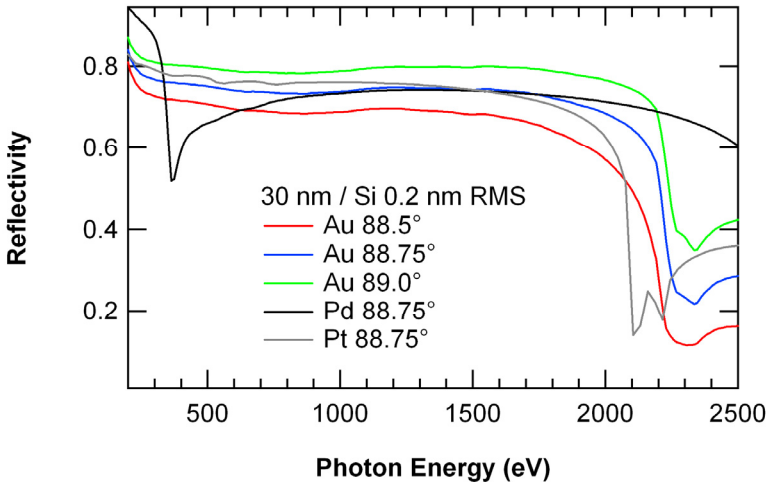

Figure 11.8.4 Reflectivities of possible coatings for s polarized light as a function of the photon energy. The substrate is Si and the coating is 30 nm thick. The RMS surface roughness is 0.2 nm.

11.8.3.6.2 Monochromator

The second optical element is the plane mirror that provides the required angle of incidence to the grating necessary to keep the selected energy in focus at the exit slit. The mechanical principle used in the PGM [11.8.13] can be used to achieve the required movements. The resolution in angle required in the current design[1] is 0.03 μrad for the grating and 0.05 μrad for the plane mirror. These values are very close to the resolution of the angular encoder used in the CPGM (0.04 μrad).

Since the angle of incidence on the mirror for a given VLS grating is determined by the focusing condition and the grating equation at that energy, it is advantageous to have at least three gratings that allow trading off resolution for flux while keeping a fixed exit slit width.

For this beamline we have chosen three gratings: One for ultra high flux (UHF), one for high flux and good resolution (HF), and one for high resolution (HR). The parameters of the chosen gratings are listed in Table 11.8.4 assuming that the distance from the grating to the exit slit is 10 m. The gratings are operated in the +1 diffraction order.

Table 11.8.4 Parameters of the Gratings for a Soft X-Ray Beamline for Imaging and Coherent Imaging/Scattering.

	UHF	HF	HR
k_0 [mm^{-1}]	150	400	1200
b_2 [mm^{-2}]	1.7991×10^{-4}	1.7977×10^{-4}	1.2576×10^{-4}
b_3 [mm^{-3}]	1.80×10^{-8}	1.80×10^{-8}	1.25×10^{-8}
C	≈1.5	≈1.5	≈2.2

The resolving power expected with these gratings when using a 10 μm exit slit width is shown in the upper panel of Figure 11.8.5. The HR grating will provide a resolving power higher than 10^4 in the full energy range, whereas the UHF grating resolving power is better than 4000 up to 1.7 keV.

[1] Obtained by requiring five scanning steps at the highest resolution.

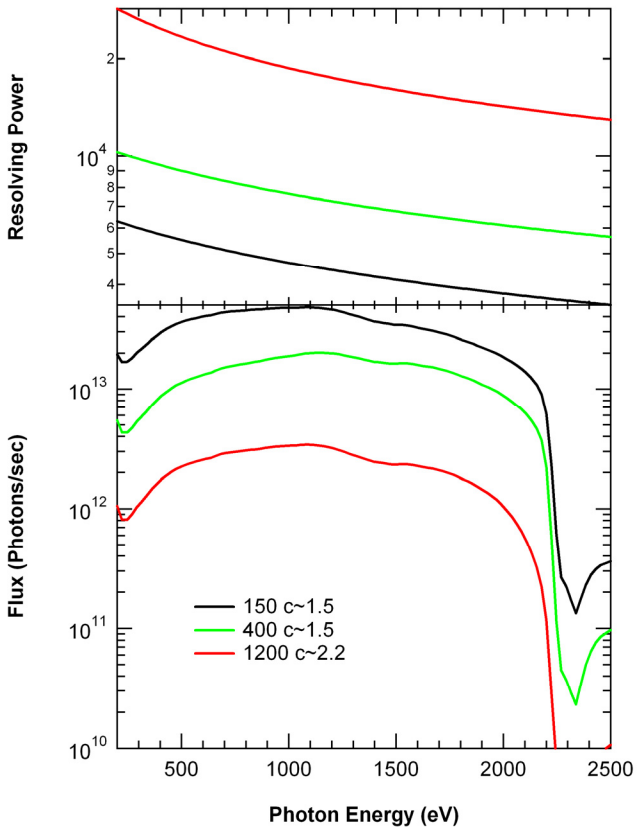

Figure 11.8.5 (upper panel) Flux expected at the sample position of a soft x-ray imaging, coherent scattering, and spectroscopy beamline with a 10 μm exit slit width and three gratings.

(lower panel) Flux and corresponding resolving power of a soft x-ray imaging, coherent scattering, and spectroscopy beamline with a 10 μm exit slit width and three gratings.

The ability to tune this monochromator to zero order is important for certain experiments envisioned for this beamline, as well as for setup and alignment. Since the VLS gratings provide vertical focusing only at soft x-ray wavelengths, the zero-order counterpart would be a vertically focusing mirror. Such a mirror could be provided as an additional in-vacuum-selectable choice in a multiple-grating instrument. Heat loading issues should be considered for components downstream of the monochromator, e.g., the exit slit, which could be illuminated by the intense focused zero-order light.

11.8.3.6.3 Refocusing Mirrors

The refocusing onto the sample is performed with two elliptical cylindrical mirrors. The first one (M3) is the horizontally refocusing mirror located at a distance of 41,200 mm from the source and has a nominal demagnification of 32. The vertically refocusing mirror M4 is 0.5 m downstream of M3 and demagnifies the slit width by a factor of 2.1. The angle of incidence on both mirrors is 88.75°.

11.8.3.6.4 Flux

The efficiencies of the gratings for this beamline were optimized for blazed groove profiles. The resulting blaze angle for the 150 l/mm grating is 0.3°, that of the 400 l/mm grating is 0.45°, and that for the 1200 l/mm grating is 1.0°.

The total flux expected at the sample position with a 10 μm exit slit width is presented in the lower panel of Figure 11.8.5. For the high-flux (HF) grating, more than 1.5×10^{13} ph/s are expected at the sample at a resolving power higher than 4000 for energies between 200 eV and 1.7 keV.

11.8.3.6.5 Ray Tracings

The ray tracings were performed using the Shadow code [11.8.14]. The caption above each spot pattern gives the RMS beam sizes and divergences along the horizontal and vertical directions. The y coordinate is along the dispersion direction at the exit slit and sample position and along the length of the optical elements. Slope errors (0.1 μrad RMS along the meridional direction of the plane elements and 0.5 μrad RMS along the meridional direction of the other optical elements) were included in the ray tracings by assuming a sinusoidal variation on the optical elements surface. All the ray tracings were performed with the source sizes and divergences shown in Table 11.8.1.

Figure 11.8.6 shows the spot pattern at the cylindrical mirror when illuminated with 200 eV photons. As seen in this figure, a 300 mm long mirror accepts most of the central cone radiation emitted by the undulator at this energy.

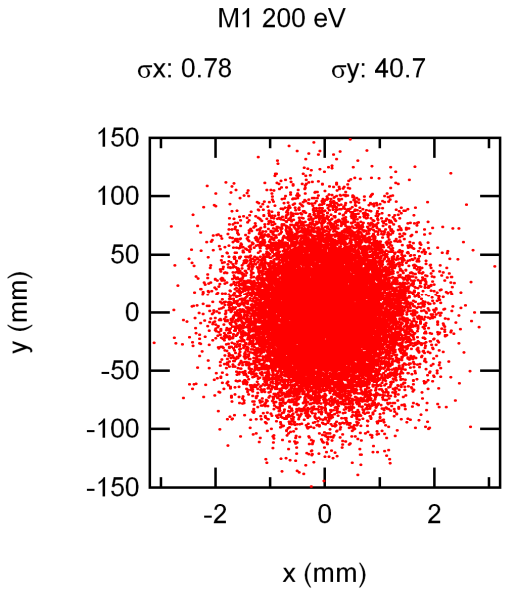

Figure 11.8.6 Spot pattern at M1 for 200 eV, for the soft x-ray coherent scattering, imaging, and spectroscopy beamline.

The illumination of the plane pre-mirror determines that its minimum dimensions are approximately 7 mm wide by 400 mm long. In contrast, the gratings need to be less than 100 mm long. An exit slit length of ~8 mm is required to let through the horizontally diverging beam. The illumination of the refocusing elliptical cylinders determines that the horizontally focusing mirror needs to be at least 300 mm long and the vertically focusing mirror needs to be less than 80 mm long.

As was demonstrated with ray traces for the soft x-ray monochromator in Section 11.7, the resolution of the monochromator for this soft x-ray beamline can be shown to match the analytically determined values shown in Figure 11.8.5.

The RMS horizontal and vertical sizes and divergences values obtained by ray tracing are consistent with the values obtained from the vector sum of tthehe source parameters (slit for the vertical size) modified by the corresponding magnification and the contributions due to the assumed slope errors. The expected RMS sizes at the sample are 2.3 μm horizontal and 1.6 μm vertical. The largest vertical RMS divergence at the sample, less than 0.5 mrad, will occur when the HR grating is used at 200 eV.

11.8.3.6.6 Canted IDs

In this mode of operation, the horizontal angle between the electron beam and the undulators' axes should be as small as possible to keep a reasonable exit slit length. On the other hand, the angle should be large enough that there is a minimal overlap between the two beams. We chose 0.17 mrad for the separation between the two beams, which corresponds to four times the 1-σ RMS divergence at 200 eV. Two sagittal

cylindrical mirrors, designed to collimate along the vertical direction its respective source, replace M1. This ensures that the two beams will be focused vertically at the exit slit, i.e., the photon energy of the two beams will be the same; but implies that the resolution of the far beam (upstream undulator) is a few percent better than that of the closer beam. The horizontally focusing M3 elliptical cylinder mirror focusing also needs to be replaced with two elliptical cylinder mirrorrs when operating in the canted mode. The mirror refocusing the beam from the upstream undulator is designed to be slightly out of focus to obtain approximately the same horizontal beam sizes, one from each of the two M3 mirrors, at the sample position.

Section 11.7.2.4 details the ray tracing results for 200 eV photon energy with the high resolution grating. The corresponding ray traces for the Soft X-Ray Coherent Scattering, Imaging, and Spectroscopy Beamline will be similar, and will be carried out as part of the NSLS-II Title I effort. At 200 eV photon energy, the "contamination" of the radiation from the upstream undulator on the downstream beam is less than 2.5%. See Figure 11.8.7, which presents the illumination spot diagrams for the near and far EPU beams on the M1 cylindrical mirrors.

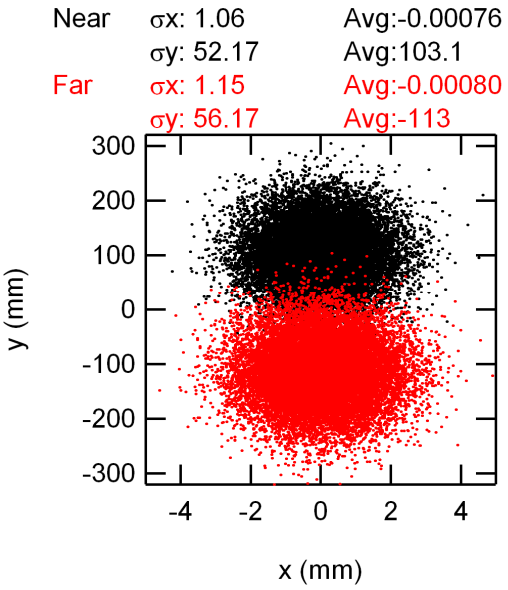

Figure 11.8.7 Illumination of the near and far M1 mirrors at 200 eV for the coherent imaging, scattering, and spectroscopy beamline.

This "contamination" value decreases to nearly zero at 1 keV, and can be practically eliminated at the expense of some flux at lowest photon energies by having a gap of 80 mm between the two M1 mirrors. This will reduce the flux at 200 eV by approximately 10% but will reduce the contamination to less than 0.3%. Practically no flux is lost for energies higher than 1 keV. With the above mentioned separation between the M1 mirrors, their length should be 240 mm, the plane mirror and the grating wider than 16 mm, each M3 at least 240 mm long, and the exit slit length 15 mm. The exit slit length is rather large, given the requirement of identical opening (to better than ~0.5 μm) across the entire 15mm length; the slit blades also must be aligned parallel to the floor to better than a ~20 microradians. Sample illumination spot diagrams for the far and near beams at 200eV photon energy are shown in Figure 11.8.8. The horizontal and vertical dimensions of both beams are identical to two significant figures and overlap to better than 0.02 μm.

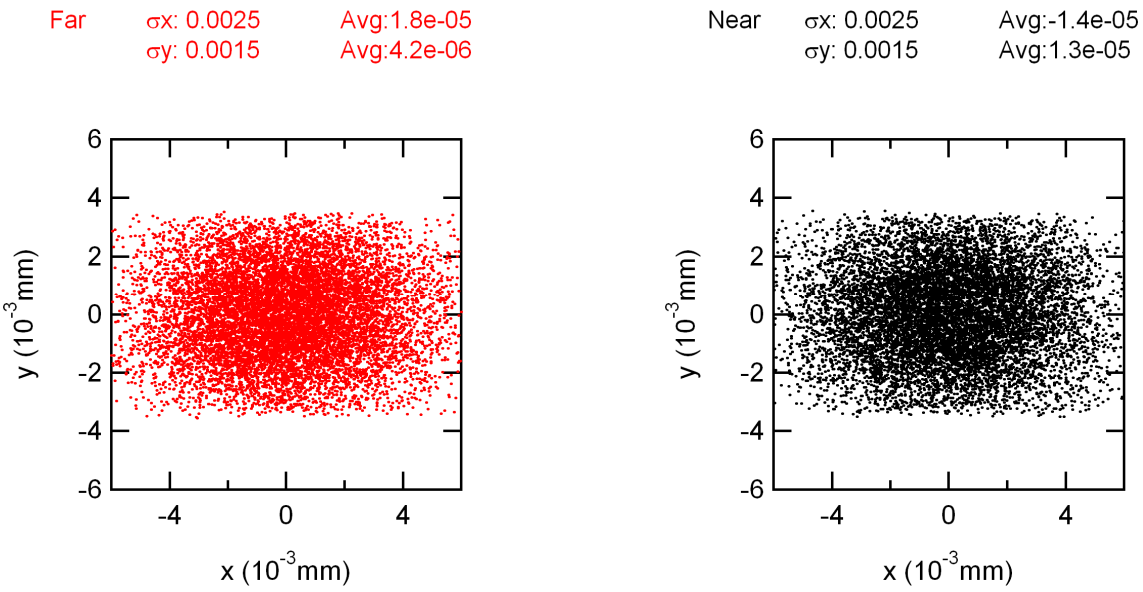

Figure 11.8.8 Sample illumination with the far beam (left) and near beam (right) at 200 eV for the coherent imaging, scattering, and spectroscopy beamline.

11.8.3.6.7 Polarization Selection: Variable Apertures and Chopper

The beamline would have variable-opening white beam apertures to define the sizes, and therefore intensities, of the polarized beams from the two canted undulators. A fast-switching, up to a few kHz, mechanical chopper would be installed downstream of these apertures, to alternately select one of the two polarized beams. The apertures and chopper could be located anywhere along the beamline, but would likely be located after the monochromator to minimize power loading issues. The horizontal location of the apertures and chopper would need to be precisely controlled to eliminate any overlapping polarized beams.

11.8.3.6.8 Calculated Power

The calculated power absorbed by the first three optical elements when the two IDs are phased tuned to emit linear horizontally polarized radiation at 200 eV is similar to the power distributions shown for the other proposed soft x-ray beamline (Section 11.7.2.4). The maximum power density absorbed by M1 is 1.2 W/mm^2 and the total power is almost 1 kW. The corresponding values for the plane mirror will also be close to those calculated for the soft x-ray XRMS/RIXS beamline: 0.56 W/mm^2 and less than 100 W. The power and power density absorbed by the grating in this case are very small.

The cooling scheme for M1 needs to ensure that the heat-induced meridional RMS slope errors in M1 are below 0.5μrad. In the case of the plane mirror, a novel cooling design should be developed to preserve the high resolving power. The development of such a cooling scheme will require iterations of FEA and ray tracings performed with the calculated surface deformation.

11.8.3.6.9 Vacuum Issues

A soft x-ray beamline for resonant scattering and imaging would be windowless (i.e., would share ultra high vacuum with the NSLS-II storage ring). All of its components would be UHV-compatible, including all of the end station components. As is the case for all UHV beamlines, this beamline would be divided into sections separated from each other by metal-sealed UHV gate valves. These valves would be part of the equipment protection system, acting to isolate beamline components from each other or the storage ring if the

constantly monitored vacuum readings rise above a maximum permitted level. The beamline would have approximately 15 sections, some of which require extra pumping speed owing to high undulator head loads and large total surface area of components.

Beam position (BPM) and intensity (I_0) monitors, as well as polarization ratio monitors, would be required upstream of each end station. The small lateral spatial dimensions of the beams would be a challenge for positioning all of these monitoring devices.

11.8.3.6.10 End Stations

As described in the introduction to this section, we anticipate this beamline will have two end stations, to be determined based on user input and demand, among three or more possible choices: 1) an end station optimized for scanning transmission x-ray microscopy, 2) an end station optimized for coherent scattering and imaging, and 3) an end station optimized for rapid-switching polarization-sensitive spectroscopies, including SXMCD, SXMLD, and PEEM. It is likely that the two chosen branch lines will experience heavy demand; why then put two end stations on one beamline when beam-sharing is precluded by the small phase space of the NSLS-II beam at soft x-ray wavelengths? The best experiments involve a combination of sample preparation, data collection, and on-line analysis; consequently, user productivity with 24 hour access to an experiment is not twice what it is with 12 hour access. If both end stations can be left with the specimen in place during the off-hours, and if experiment changeover can be made rapid, reliable, and reproducible such as by using a well-engineered switching mirror, then two different end stations can be accommodated with high productivity from each.

Based on user demand at the STXMs at the present-day NSLS, at the ALS, and elsewhere, it is reasonable to expect that NSLS-II will have several STXMs around the facility, since even the NSLS-II bending magnets are very bright sources and can be used for coherent soft x-ray experiments with appropriate spatial filtering. As a result, it is conceivable that NSLS-II will host one STXM optimized for handling room temperature specimens at atmospheric pressure for convenience and for the ability to work with specimens in wet chambers, another optimized for studies of frozen hydrated specimens in vacuum and at liquid nitrogen temperature, and another that is configured with various switchable fields for studies of magnetism. The current choice for the soft x-ray undulator beamline proposed here is a room temperature STXM with specimen at atmospheric pressure. Much of the engineering of this end station can be done in common with the Hard X-ray Nanoprobe described in Section 11.4. However, as noted above, a STXM is likely to require significantly faster scanning speeds than the hard x-ray nanoprobe will, and these engineering challenges must be addressed in the end station design. Fortunately an excellent base of experience exists based on the STXMs now operating at NSLS and ALS.

The same might be said of end stations for coherent scattering and imaging: there may ultimately be more than one beamline able to do these experiments at NSLS-II. One or more of there may be optimized for magnetic specimens while others are optimized for frozen hydrated biological specimens at liquid nitrogen temperature. The current choice for the soft x-ray undulator beamline proposed here is a chamber optimized for studies of magnetism, with a load lock for sample insertion and removal in a high vacuum environment, provision for ~1T magnetization of the sample along any axis (esp. in-plane and out-of-plane), and rapid energy tunability.

Since the STXM and coherent scattering experiments will work with a nearly fully coherent beam, there is no built-in tolerance to beam motion that would otherwise be provided by "overfilling" limiting apertures or focusing optics. For this reason, it is essential that the beamline have full diagnostics on the beam position and flux at multiple locations. For polarization-sensitive measurements, e.g., of magnetic samples, it is also crucial to monitor the beam polarization accurately. It is only with proper diagnostics that one can troubleshoot problems in flux variation or resolution loss in coherence experiments, variations that can otherwise render the data from an experiment worthless for quantitative analysis.

The key parameters for rapid-switching polarization-sensitive spectroscopy are well-defined, stable polarization of the beams from the two canted undulators and as close as possible to 100% overlap of the two polarized beams at the sample position. The development and characterization of diagnostics for these purposes, both in the ID straight section where the canting takes place, and in the beamline where the chopper provides the time-dependent polarization modulation, is crucial to the success of all of the spectroscopy end station experiments.

11.8.3.6.11 Alternatives to the Design

To maximize utilization of this flagship beamline, we propose to leave two well-engineered end stations more or less permanently in place, so that scientists can rely on a constant, always-aligned apparatus for carrying out their experiments. At the same time, one can expect that some dedicated users will bring their own end station equipment for specialized experiments. Experiments of this type surely need to be accommodated at NSLS-II. One alternative to the above design is to add a third, mirror-switchable end station to the beamline. Given the space constraints of fitting two permanent end stations around a small separation angle at the end of the beamline, this may be of questionable utility but this may change based on proposals received.

11.8.4 Detectors

Detectors for scanning transmission x-ray microscopy (STXM) must be able to handle high transmitted flux signal levels with fast readout time, since per-pixel dwell times might be as fast as a microsecond. Segmentation is also important to provide the ability to record dark field images from strongly scattering objects (such as immunogold labels in biological specimens), and to sense phase contrast, which provides a way to detect molecular resonances with less radiation damage than absorption contrast involves. Fortunately, a collaborative effort between Brookhaven, Stony Brook, and the Max Planck Institute silicon lab has already produced detectors that are able to perform these roles at sub-millisecond dwell times. With further development, it should be possible to have new versions of these detectors that are able to work at the microsecond dwell times anticipated for STXM research at NSLS-II. Additional detector capabilities that should be developed include total electron yield detectors when working with a sample at high vacuum, and visible light detectors for luminescence studies.

Coherent scattering and imaging place a different set of demands on detector performance. The preferred situation is to collect a large 2D measurement of scattered intensity, such as in a large-pixel-count area detector with at least 1024^2 but ultimately 2048^2 or even 4096^2 pixels. Because the scattered signal can be strongly concentrated near the forward direction for most specimens, a detector with very high dynamic range (or, alternatively, fast, low-noise readout to gain dynamic range through multiple signal measurements) is required. Backside-thinned, direct detection CCD cameras presently serve as the main detector for soft x-ray coherent scattering and imaging experiments, but they leave much to be desired both in terms of dynamic range (typically only around 10^3:1) and readout time (typically many seconds for low-noise operation). A much more promising approach is to use pixel array detectors with on-detector processing of the signal to provide high dynamic range and rapid readout time. Again, such detectors are already being developed at Brookhaven, so there is considerable in-house expertise to draw upon. For experiments exploring the fastest possible correlation times, one may instead turn to a speckle-sized aperture in front of a small area detector to record intensity fluctuations at a single location in the scattering plane. Several such detectors can be used to gain additional signal, but never to the same value as provided by a fast-readout area detector such as a pixel array detector.

11.8.5 Laboratory Space

The laboratory requirements for applications of soft x-ray microscopy and coherent dynamics are determined largely by those of the different application areas. For biology and environmental science, access to a nearby wet lab is essential, with fume hoods and wet chemical mixing areas, oxygen-free glove boxes for the study of anaerobic bacteria, sterile laminar flow hoods for handling cell and bacteria cultures, and high resolution light microscopes with transmission, phase contrast, and fluorescence capabilities plus a stage that can be indexed to allow for rapid location of pre-screened sample locations. Equipment for plastic and sulphur embedding of specimens, and an ultramicrotome for thin sectioning, should also be included. An additional area is needed in the wet lab room for the preparation of frozen hydrated specimens for cryo microscopy; this area should include a high-pressure freezer, cryo plunger, and cryo ultramicrotome.

Studies in magnetism require the preparation of thin films on transparent substrates such as silicon nitride, in some cases with nanopatterned structures. Fortunately the Center for Functional Nanomaterials at Brookhaven plans to have the necessary processing equipment, as well as complementary, non-synchrotron-based analytical tools such as scanning probe microscopes. However, proper studies of magnetic samples require access to additional complementary instrumentation such as P-MOKE, SQUID, Kerr microscope, and electron spin resonance spectrometer.

These soft x-ray beamlines will be especially demanding of ultra-high vacuum conditions, requiring continuous access to the NSLS-II vacuum group facilities. The beamline would require a clean environment (laboratory space) for the cleaning and assembly of ultra-high vacuum parts.

Shared access to sample preparation and mounting facilities is required. For handling cryo specimens, steady use of liquid nitrogen is required both at the end stations and in the sample preparation laboratory, including equipment for inspection and crystal orientation.

References

[11.8.1] H. Ade, X. Zhang, S.Cameron, C. Costello, J. Kirz, and S. Williams, *Science* **258**, 972 (1992).
[11.8.2] J. Kirz, *J. Opt. Soc. Am*. **64**, 301 (1974).
[11.8.3] http://www-als.lbl.gov/als/ourorg/strategicplan.html
[11.8.4] J. Miao, *Nature* **400**, 342 (1999).
[11.8.5] H.N. Chapman et al., *J. Opt. Soc. Am*., **A23**, 1179 (May 2006).
[11.8.6] D. Shapiro et al., Proc. Nat. Acad. Sci. **102**, 15343 (2005).
[11.8.7] S. Marchesiniet al.., *Phys. Rev. B* **68**, 140101-1 (2003).
[11.8.8] A. Friedmanet al., Proceedings of the Particle Accelerator Conference (1993) pp. 1599.
[11.8.9] R. Follath, *Nucl. Instr.& Meth. A* 467-468, 418 (2001).
[11.8.10] R. Reininger and A. de Castro, *Nucl. Instr. & Meth. A* **538**, 760 (2005).
[11.8.11] P. Elleaume, "Undulator Radiation," in *Undulators, wigglers and their applications*, H. Onuki and P. Elleaume, Editors. 2003, Taylor & Francis: London.
[11.8.12] R. Reininger, *SrCalc*, 2001-2006.
[11.8.13] F. Riemer and R. Torge, *Nucl. Instr. & Meth A.*, **208**, 313, (1983).
[11.8.14] C. Welank, G.J. Chen, and F. Cerrina, *Nucl. Instr. & Meth. A*, **347**, 344, (1994).

11.9 A Macromolecular Crystallography Beamline

11.9.1 Scientific Case for Macromolecular Crystallography

Understanding the living cell is the utmost challenge of modern biology. The expectation that a deeper understanding of the biological process can be achieved, once the three-dimensional structure of countless molecules and their functional roles have been conquered, is the driving force behind the revolution structural biology is undergoing today. Numerous cellular mechanisms are now being described at a molecular level. Examples of these are protein synthesis, RNA transcription, DNA replication, immune response, enzymatic metabolism, signal transduction, cellular division, and the production of energy, to name just a few. In addition we should emphasize the dramatic impact that structural biology has on the development of new drugs, wherein drug designers count upon being able to look in three dimensions at the molecular fit of their proposed drug into the active site of its target enzyme.

We're truly in a golden age for macromolecular x-ray crystallography (PX for short). The growing use of synchrotron sources for PX is in part due to the continuing hypothesis-driven investigations launched by structural biologists and drug-target studies performed by pharmaceutical scientists, and also to the recent organized efforts in structural genomics. More than three structures out of four deposited in the Protein Data Bank were solved using synchrotron data and this fraction keeps increasing [11.9.1.1]. The availability of brighter x-ray sources and the improved quality of instrumentation and methods that we see today has driven researchers to attempt increasingly difficult scientific problems. Indeed, the size and complexity of macromolecules that can be studied has increased by an order of magnitude in the last roughly 15 years.

The most difficult problems, which quite often are the most interesting ones, represent the pinnacle of the structural biologist's craft. Structure of large macromolecular assembly, such as the three-dimensional structure of the 150,000 atoms of the bacterial ribosome [11.9.1.2], gives detailed information about the machinery of the cell, e.g., protein synthesis. Also found in this category are the structures of viral particles which have possible application in treatment of diseases and nanotechnology. Major challenges also need to be overcome in working with membrane proteins which perform many cellular functions and responses, representing about 30% of all proteins produced in a cell (making them quite interesting to the pharmaceutical industry). To address this issue structural genomics effort specifically targeting membrane proteins have recently been launched. The work on the voltage-dependent K^+ channel, these "life's transistors" which control electrical activity in nerve and muscle, and for which Roderick MacKinnon, Rockefeller University, was co-awarded the 2003 Nobel Prize in Chemistry, is a perfect illustration of the exciting science obtained from structural studies on membrane proteins (Figure 11.9.1). More recently even structure determinations of macromolecular assemblies of membrane proteins are being conquered, e.g., a transient intermediate in the mechanism of nutrient uptake across Gram-negative bacteria [11.9.1.3].

NSLS-II will have a dramatic impact in structural biology. The two highest priorities are to handle very small weakly diffracting crystals, and to treat very large molecular assemblies; this is where dramatic progress in structural biology will lie. Investigators in the Northeastern United States are at a serious disadvantage: neither the current NSLS, nor CHESS at Cornell University, can provide the small beam size with high intensity and excellent collimation that is required for this sort of progress. The ultrahigh source brightness of NSLS-II, in combination with anticipated developments in optics, detectors, and computing power, will allow structural biologists to tackle macromolecular assemblies of exceptional complexity, bringing our understanding of the macromolecular machinery of the cell to an unprecedented level. Also, in selected cases, time-resolved studies of macromolecular dynamics and interactions down to microsecond time scales or beyond will be possible, adding an additional dimension to the value of the results.

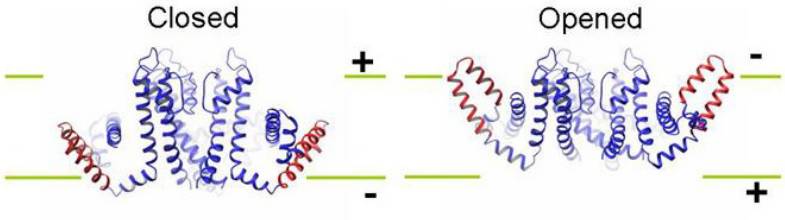

Figure 11.9.1 A model for control of passage of potassium ions through a channel in the cell membrane, in response to changes in the cell membrane voltage. From the work of Prof. Roderick MacKinnon, Rockefeller University.

References

[11.9.1.1] BioSync http://biosync.rcsb.org/BiosyncStat.html.

[11.9.1.2] Ban et al., (2000) *Science* **289**, 905; Harms et al., (2001) Cell **107**, 679; Wimberly et al., (2000) Nature **407**, 327; Pioletti et al., (2001) EMBO **20**, 1829; Yusupov et al., (2000) *Science* **292**, 883; B.S. Schuwirth et al., (2005) Science **310**, 827.

[11.9.1.3] Shultis et al., (2006) *Science* **312**, 1396; Pawelek et al., (2006) Science **312**, 1399.

11.9.2 X-Ray Damage to Biological Samples

One of the major problems facing the characterization of biological materials at NSLS-II will be damage to experimental samples. The damage to biomaterials from strong x-ray beams can be attributed to thermal effects, radiation effects, or a combination of both.

11.9.2.1 Thermal Damage

Thermal damage is the result of the local heating of the sample. Increased thermal vibrations cause atomic bonds to break and the subsequent destruction of the molecules [11.9.2.1]. Heating effects can be minimized by increasing the irradiated sample volume and by keeping the dose distribution within the sample as uniform as possible, or by proper cooling. Assuming a time-averaged power of the x-ray beam, i.e., a time-independent thermal input source, Kuzay et al. estimated that for an 8 keV x-ray beam and 10^{13} ph/mm^2/s^{-1}, a cryo-cooled protein crystal that is 100 μm thick will suffer a temperature increase of 6 K and stabilize in 4.5 s, while a 300 μm crystal will suffer a temperature increase on the order of 20 K and take more than 52 s to stabilize. Moreover, their results showed that gradient effects became negligible for thinner crystals. On the other hand, in each case, the sample temperature rise was estimated to be roughly linear in incident flux. Keeping the number of photons incident on the sample constant (at 10^{12} photons), this dose over 10 s led to a 6 K temperature increase, whereas exposures over 0.1 s led to a 40 K temperature increase. Conversely, if duration of the x-ray exposure is much shorter than the time the system takes to reach thermal equilibrium, then the maximum temperature is not reached and the system temperature will be smaller than the equilibrium temperature—as long as enough cooling time is provided through the entire data collection cycle.

Using finite element analysis, Nicholson et al. [11.9.2.2] modeled the heating of a 100-μm-cube protein crystal suspended in vitrified ellipsoidal cryosolution film, 300 μm long by 100 μm at its widest point, in a nitrogen and helium gas stream kept at 100K. Considering a 50 μm incident beam perpendicular to a plane where the thickness of the cryoprotectant was almost zero, these authors determined that a temperature difference of 4.1^{o}C in ~400 ms and 1.6^{o}C in ~100 ms, for nitrogen and helium respectively, can be expected between the “no beam” state and the “beam on” state. They further concluded that the most noticeable

changes would occur if beam and crystal sizes were comparable. This is borne out by experience at the ESRF multipole wiggler (10^{15} ph/s/mm^2), where up to 11 beam positions have been used on long, needle-shaped crystals.

11.9.2.2 Radiation Damage

Radiation damage results from the interaction of the ionizing photon beam and the electrons in the biological material, and is commonly classified into primary and secondary damage [11.9.2.3]. Primary damage is caused by the direct interaction of the x-ray beam and the electrons (photoelectric, Auger, and Compton effects), leading to a breaking of chemical bonds and the destruction of molecules. In contrast, secondary damage results from reactions caused by radiolytic products (e.g., free radicals generated by solvent atoms absorbing the ionizing radiation). Primary damage depends only on the photon energy, x-ray dose, and number of photons absorbed, but is independent of temperature [11.9.2.4]. Secondary damage varies with the nature of the radiolytic products and with other factors, such as temperature, reactivity, and mobility of the free radicals. To maximize the signal-to-noise ratio of the data collected and minimize local heating effects, the rate at which the dose is given and the lifetime of the free radicals in the biological sample need to be considered. It should be possible, at very high photon fluxes (10^{16} ph/s/mm^2), to capture all images before significant damage by the migrating radiolysis products [11.9.2.5, 11.9.2.6] can be observed. At these photon fluxes, the inverse dose effect (the probability of free radical recombination) should limit dose effects as the number of incident photons per unit time per unit area (dose rate) rises.

Ravelli's group at ESRF [11.9.2.7] have recently addressed the cause of radiation damage. Addressing the question of whether radiation damage in biological macromolecules is caused by dose accumulation or by dose rate, they concluded that the dose-rate effect observed is a secondary problem when compared with the compounding absorbed-dose radiation damage. This is consistent with results previously obtained by Sliz et al. (2003). However, at the atomic level these authors found that structural changes increase in magnitude as dose rates become higher. Why does a dose rate effect exist at all? The answer to this apparently trivial question is not easy. One possible explanation might be related to a free-radical steady-state. The formation, recombination, and diffusion of free radicals would all contribute to the total free-radical population, including electrons generated by x-ray exposure. As Leiros et al. speculate, at high dose rates the free radical recombination rate may not be fast enough and may lead ultimately to free radical diffusion and the creation of damage. As beams become more and more focused (micro and sub-micro focusing) and smaller sample volumes are probed, sample heating would foster radical diffusion and a free-radical steady-state may not be attained. It is not yet clear what implications there would be of such a non-equilibrium state for the radiation damage issues discussed here.

Radiation damage is a particularly severe problem for experiments that involve kinetics, as cryogenic mitigation techniques are usually not viable. As for semiconductors and demonstrated on a number of occasions for biomaterials [11.9.2.8], the chief source of radiation damage is mobile electrons and electron-holes, both of which pose considerable mobility at room temperatures as well as at cryogenic temperatures. The amount of damage suffered by a given material is commonly measured in terms of the amount of energy deposited, or *dose* (1 Gray [Gy] = 1 Joule/kg). Several authors agree that for biological samples, the upper limit is of the order of 10^7 Gy. Recently, Howells et al. [11.9.2.9] made an assessment of the maximum tolerable dose. They found that biological materials seem to be tolerant to a dose 10 to 1,000 times higher than that initially predicted by Henderson [11.9.2.10].

Table 11.9.1 is a summary of different approaches at third-generation sources. Under these conditions, O'Neill and others found that the total dose delivered by 12 keV photons in 10 s to an average protein crystal containing 50% solvent, $\mu/\rho = 2.6$ cm^2/g, through a sample area of 80 μm^2, will be 2×10^5 Gy. Using these values, the dose per second delivered to a similar sample was estimated for the flux observed by Henderson, Teng, Kuzav, O'Neil, and Sliz; the current flux at NSLS beamline X25; and the flux proposed for NSLS-II.

Table 11.9.1 Dose, Biomolecular Crystal Size, and Useful Lifetime for Different Photon Fluxes.

	Henderson [11.9.2.10]	Teng [11.9.2.3]	Kuzay [11.9.2.1]	O'Neil [11.9.2.5]	Sliz [11.9.2.11]	X25 (wiggler)	NSLS-II
Photon Energy [keV]	8	12	8	12	12	12	12
Flux [ph/s/mm^2]	2×10^{11}	3×10^{12}	$10^{13} - 10^{15}$	4×10^{13}	4×10^{15}	2×10^{13}	5×10^{18}
Dose [Gy]	2×10^{7}	1×10^{7}	10^{5}- 10^{3}	2×10^{15}	1×10^{6}(a)	1×10^{4} (a)	2.5×10^{9}(a)
Time to (1/e) death [s]	–	11×10^{3}	–	–	25	2.5×10^{3}	0.01
Dose to (1/e) death [ph/mm^2]	–	2×10^{16}	–	–	5×10^{16}	5×10^{16} (b)	5×10^{18} (b)
Minimal crystal size[μm]	–	35	–	–	20	–	–

(a) Estimated after O'Neil et al. [11.9.2.5] (b) Estimated after Sliz et al. [11.9.2.11].

Assume a cubic sample of size a and n_o incident photons on a cross-section of area A. The total dose (energy per mass) will be given by:

$$D = \frac{\Delta E}{m} = \frac{\Delta E}{\rho \times A \times a} \tag{11.9.2-1}$$

where $m = \rho$ x V . If it is assumed that all absorbed photons deposit energy in this volume and that the sample is thin:

$$n = n_o e^{-\mu d}; \quad n = n_o [1 - \mu d]. \tag{11.9.2-2}$$

The number of absorbed photons will be:

$$n = n_o \mu d \tag{11.9.2-3}$$

and the deposited energy for d=a and photon energy E in (keV):

$$\Delta E = n_o \mu a E \tag{11.9.2-4}$$

or

$$\Delta E(J) = n_o \mu a e E(eV), \tag{11.9.2-5}$$

where e is a conversion factor, 1.6×10^{-19} J eV^{-1}. Therefore, the dose per unit time is given by:

$$\frac{D}{t} = \frac{n_o \mu a e E}{\rho A a} \tag{11.9.2-6}$$

and the total dose is :

$$D = \frac{n_o t(\mu/\rho) eE}{A}. \qquad (11.9.2\text{-}7)$$

Assuming that the limit for data collection for a given protein crystal is reached when the contribution of the unit cells in the crystal to a Bragg reflection falls to *1/e* of its initial value at the 3.5 Å resolution, Sliz et al. estimated that the accumulated dose would be 5×10^{16} ph/mm^2. With the incident photon flux given in Table 11.9.3, these authors estimated that the crystal would survive for a total of 25 s in the beam. Using these approximations, we can estimate the dose that will be deposited in a crystal for the total intensity of Bragg reflections to decrease by 1/e. The values obtained are of the order of 10^{16} ph/mm^2 (Table 11.9.1). This allows us to estimate the useful life time of a crystal in a flux, such as observed currently at X25 and being proposed for NSLS-II. The values found are in good agreement with experimental observations at X25 and with the values found by Teng and Mofat [11.9.2.4].

Further, following the assumption that for each elastically scattered photon about 10 photons are absorbed by the sample (i.e., each unit cell will contribute one photon to the Bragg reflection before the crystal is declared dead [11.9.2.11]), it is possible to determine the minimum crystal size needed to obtain a complete data set. The value determined by these authors is in good agreement with the values obtained by Teng and Mofat [11.9.2.4] and other authors [11.9.2.12, 11.9.2.13].

Therefore, it should be possible to combine short exposures (in the μs range), proper crystal cooling, and improved detector technologies to study biological crystals at NSLS-II. An alternate strategy could be the exploitation of the improved resolution, via use of monochromator optics, that allow higher-energy resolution, such as, for example, Si (511) or (331), which incur lower dose rates.

References

[11.9.2.1] T.M. Kuzay, M. Kazmierczak, and B.J. Hsieh; *Acta Cryst.* **D57** 69 (2001).
[11.9.2.2] J.M. Nicholson, C. Nave, F. Khalid, B. Fell, and E. Garman; *Nucl. Inst. & Meth. A* **467** 1380 (2001).
[11.9.2.3] T.-Y. Teng and K. Moffat; *J. Sync. Rad.*. **7**, 313-317 (2000.)
[11.9.2.4] (T.-Y. Teng and K. Moffat; *J. Sync. Rad.* **9**, 198-201 (2002).
[11.9.2.5] P. O'Neill, D.L. Stevens, and E.F. Garman; *J. Sync. Rad.*. **9,** 329-332 (2002).
[11.9.2.6] V. Cherezov, K.M. Riedl, and M. Caffrey; *J. Sync. Rad.***9,** 333-341 (2002).
[11.9.2.7] K.S. Leiros, J. Timmins, R.B.G. Ravelli, and S.M. McSweeney; *Acta Cryst*. *D* **62** 125 (2006).
[11.9.2.8] Cherezov, K.M. Riedl, and M. Caffrey; *J. Sync. Rad.* **9** 333 (2002).
[11.9.2.9] R. Howells, T. Beetz, H.N. Chapman, C. Cui, J.M. Holton, C.J. Jacobsen, J. Kirz, E. Lima, S. Marschesini, H. Miao, D. Sayre, D.A. Shapiro, and J.C. Spence; arXiv:physics/0502059 v1 11Feb2005.
[11.9.2.10] Henderson; Proc. R. Soc. Lond. **B241** 6 (1990).
[11.9.2.11] Sliz, S.C. Harrison, and G. Rosenbaum, *Structure* **11** 13 (2003).
[11.9.2.12] Glaeser, M. Fracciotti,, P. Walian, S. Rouhani, J. Holton, A. MacDowell, R. Celestre, D. Cambie, and P. Padmore; *Biophys*. J. **78** 3178 (2002).
[11.9.2.13] P. Burmeister; *Acta Cryst.* **D56** 328 (2000).

11.9.3 Source and Optics

An intense and well-collimated source of x-rays, ideal for x-ray crystallography applications, will come from either the 2 m long, 14 mm period superconducting undulators, or the 3 m long, 19 mm period cold permanent magnet undulators,. The small angular divergence of the x-ray beam emitted by these undulators allows the collection of the entire photon beam with a relatively compact KB mirror assembly. For example, at ~35 m from the undulator source, the width of the horizontal fan of x-rays is ~2.2 mm (4σ) at a photon

energy of 12 keV (employing the fifth harmonic of a SCU), and a 74 cm horizontally focusing mirror would intercept the full beam at a grazing incidence angle of 3 mrad. These optics will allow the x-rays to be focused onto small crystals that are a few tens of microns in diameter with relatively small convergence angles—as low as 147 μrad (H) × 81 μrad (V). With typical mirror coatings, one can cover x-ray energies up to ~30 keV at this grazing angle. For comparison, this mirror acceptance is simply not possible on an undulator or wiggler beamline on the existing NSLS x-ray ring; at best, such a mirror could intercept only ~15% of the much wider horizontal beam fan.

The NSLS-II shield wall lies 25 m from the source point, and we would prefer to position the monochromator assembly (double-crystal monochromator based either on cryogenically cooled silicon crystals or water-cooled diamond crystals) immediately after the shield wall, followed by a KB focusing mirror assembly (shown conceptually in Figure 11.9.2; parameters are listed in Table 11.9.2). Placing the KB assembly here rather than further downstream allows these mirrors to be relatively short, thereby reducing their residual figure error. The KB mirrors would be outfitted with dynamical curvature adjustments, employing either conventional construction with purely mechanical bending, or segmented bimorph construction with electromechanical bending. This would allow them to produce a focused x-ray beam over a range of demagnifications from ~2:1 to ~10:1, depending on the preferred experimental configuration. One could either choose one focusing mode for each experimental station, or employ a long experimental hutch, within which the diffractometer could be moved to provide either mode or could be placed at an intermediate position with the optics demagnification adjusted to suit.

Table 11.9.2 KB System Parameters for an NSLS-II X-Ray Crystallography Beamline.

Mirror Coating	Rhodium and/or platinum			
Grazing Incidence angle	3 mrad			
Operating energy range	~5-30 keV			
Efficiency of KB system at 12 keV	90% (Rh), 75% (Pt)			
VFM Length (optical surface only)	37 cm			
HFM Length (optical surface only)	74 cm			
	High Demagnification Mode		Low Demagnification Mode	
VFM (undulator to mirror distance, 36 m)	Focal length	5 m	Focal Length	12 m
	Demagnification	7.2:1	Demagnification	3:1
HFM (undulator to mirror distance, 35 m)	Focal Length	6 m	Focal Length	13 m
	Demagnification	5.8:1	Demagnification	2.7:1

VFM = vertical focusing mirror; HFM = horizontal focusing mirror

11.9.3.1 Performance of the Optical System

A critical physical parameter determining the image quality of the focused beam, because of the ultra low emittance of NSLS-II, will be the residual figure errors of the KB mirror surfaces. Indeed, one reason to keep the distance from these KB mirrors to the focus relatively short is because their surface figure errors contribute to the focused spot size roughly proportional to this distance. On the other hand, the state of the art in x-ray mirror optics will continue to improve, with the ultimate goal being <0.1 μrad figure error. Table 11.9.3 shows the expected improvement in x-ray beam focus in relation to the surface figure error of the KB mirrors in these beamlines. The perfect mirror case is included as a point of reference. Typical figure errors that are routinely achieved in 2006 in long mirrors of this kind are about 2 μrad, although reports about much

lower figure error have appeared recently; for example, a mirror 78 cm long with a figure error of 0.8 μrad has just been installed on beamline ID23-1 at ESRF [11.9.1].

Table 11.9.3 NSLS-II Undulator-Based X-Ray Beamline Performance vs. Mirror Figure Error. The red (upper text line in each pair) signifies the "high" demagnification mode, and the blue (lower text line) signifies the "low" demagnification mode (see Table 11.9.2). The FWHM beam convergences for the low demagnification mode are 0.147 mrad (H) and 0.081 mrad (V), and for the high demagnification mode are 0.317 mrad (H) and 0.195 mrad (V).

RMS figure error [μrad]	0	0.1	0.5	1.0	2.0
Vertical focus size FWHM μm]	1.0	2.6	11.8	23.5	47.0
	2.4	6.1	28.3	56.5	112.8
Horizontal focus size FWHM [μm]	15.5	15.8	21.0	32.2	58.5
	33.6	34.2	45.4	69.7	126.7
Monochromatic intensity at 12 keV [ph/s/μm^2]	1.0×10^{13}	4.5×10^{12}	7.9×10^{11}	2.7×10^{11}	7.7×10^{10}
	2.0×10^{12}	8.6×10^{11}	1.5×10^{11}	5.2×10^{10}	1.5×10^{10}

Note: FWHM = Full Width at Half Maximum

Fairly frequently, experimenters have great difficulty growing crystals larger than a few microns in size. These situations would benefit from focused beam sizes (particularly in the horizontal direction) smaller than those quoted in Table 11.9.3. For these applications, a secondary optical element, placed in the experimental hutch just before the sample, could be used to focus the beam further, to a dimension as small as 1 μm. This could be another focusing mirror (or KB mirror pair, shorter than the KB mirror pair that would be used upstream in the beamline), a refractive lens system, a Fresnel zone plate, a tapered capillary, or simply an aperture (followed by a suitable guard). Setups of this kind are presently in operation at ESRF and SLS, and are being installed at a few beamlines at APS. This need not be a permanently installed feature; it can be inserted on demand.

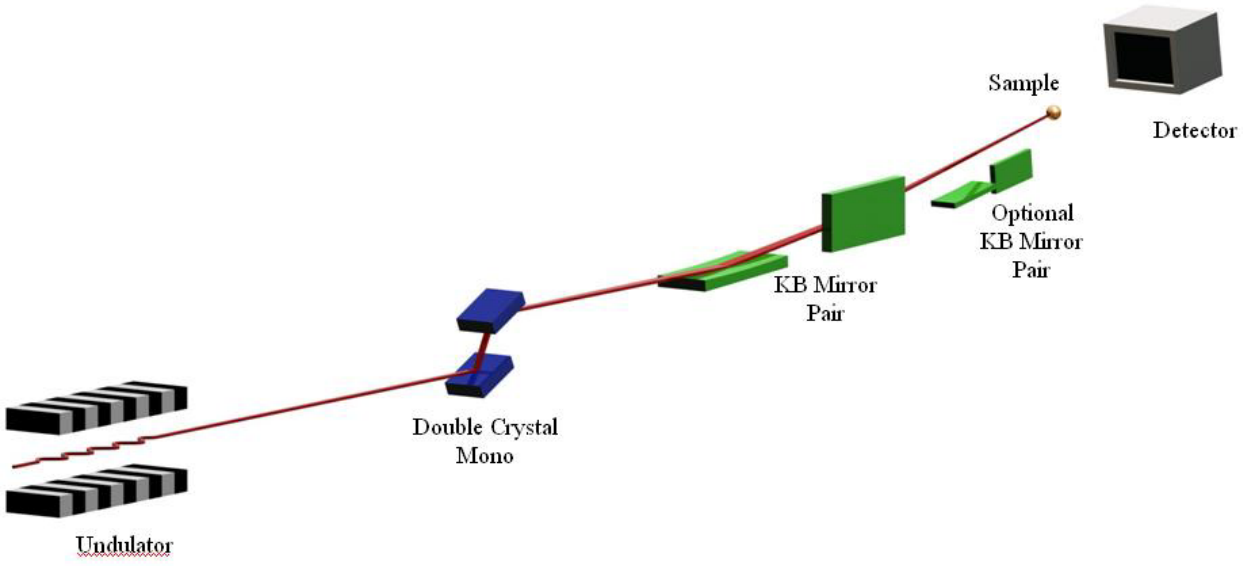

Figure 11.9.2 Conceptual layout of undulator-based crystallography beamline. The optional KB mirror pair may be inserted into the beam path before the sample to deliver a microbeam.

11.9.3.2 The Usefulness of Dual Undulators

Finally, we mention that crystallography beamlines, which have a fairly compact footprint in the direction perpendicular to the beam, are prime candidates for being placed to view multiple "canted" undulator sources installed in a single straight section of the storage ring. The concept of two canted undulators in one straight section has become the standard for new PX beamlines at APS, as demonstrated by GM/CA-CAT [11.9.2] and NE-CAT; the concept was also adopted at the ESRF [11.9.1].

The key accelerator parameter that influences the design of the beamline is the canting angle between the two undulator sources, because this defines the separation between the undulator beams along the sector length. We are envisioning a canting angle, between two successive undulator sources in a straight section, of between 0.25 and 2 mrad (this is discussed briefly elsewhere in the current CDR, and will be addressed in more detail in the Title I and Title II designs); at a later stage it will be determined what canting angle could be achieved. Canting angles used at APS and ESRF are 1.0 and 1.5 mrad respectively. A canting angle of 0.25 mrad would provide a horizontal beam separation between the two undulator beams of 7.5 mm at a distance of 30 m from the nominal source position, where the first optical element would be located. In this circumstance, a horizontally deflecting mirror or monochromator would probably need to act on one of the undulator beams to separate it far enough from the other beam to permit the construction of two independent beamlines farther downstream. A canting angle of 2 mrad, on the other hand, would provide a horizontal beam separation between the two undulator beams of 6 cm at a distance of 30 m from the nominal source position. This should be sufficient to allow the placement of a standard first optical element for one of the beams without disturbing the other beam. In this circumstance, the first optical element would be the double-crystal monochromator that would serve one of the two beamlines; the first crystal of this monochromator, probably to be cryogenically cooled silicon, will be somewhat substantive, underscoring the importance of providing adequate separation between the two undulator beams at the monochromator location. The other undulator beam would pass through this monochromator chamber undisturbed, and continue farther downstream before encountering the monochromator that would serve the other beamline. To give an acceptable horizontal separation of the two monochromatic beams at the location of the first experimental station (at least 0.5 m to accommodate an appropriate experimental apparatus), multiple horizontally deflecting mirrors could be used, as pursued by GM/CA-CAT. Alternatively, a rather large horizontal separation could be afforded by employing a horizontally deflecting monochromator, as pursued by NE-CAT at APS. Beamline designs that are compatible with canted undulator sources will be examined carefully.

11.9.3.3 End Stations

Below we describe the apparatus and software that would be developed or acquired to equip experimental stations where the principal scientific discipline is single-crystal x-ray diffraction studies on biological macromolecules, known as (not quite accurately) *PX,* for *protein crystallography*. We presume that there may be several NSLS-II straight sections available for PX, each of which might support more than one undulator. We also acknowledge that although PX is the principal target, the capabilities of the instruments, and likely the interests of the local scientists, could embrace broader disciplines, say powders of macromolecular crystals or highly ordered "crystalline" fibers of specimens such as filamentous viruses. To provide focus for this section, we will describe the sorts of experiments to be accommodated, and will show how NSLS-II can have a dramatic impact.

11.9.4 Experiments Driving This Development

No end is in sight for the paradigm of modern PX: single crystals grown from cloned components will be subjected to monochromatic x-ray diffraction measurements, and distinctive scattering from a few heavy atoms will provide information to allow calculation of the three-dimensional electron density. The possibilities provided by NSLS-II, especially its brightness, guide the variations one might play on this theme,

and suggest the importance each might have in the early years of its operation. Here is a list of experimental demands on the PX stations for NSLS-II, in approximately decreasing order of importance.

1. A critical and enduring need will be to wring the best from increasingly smaller crystals. Every experimental station will employ the brightness of NSLS-II to exploit crystals in the range down to 10 μm, and one station will be equipped to study crystals at the ultimate focusing limit of NSLS-II.
2. The trend in biological sciences is the study of increasingly large molecular assemblies. This is where the future lies. The current state of the art is on the order of 150,000 individual atoms in an asymmetric object, and atomic resolution requires the high-brightness synchrotrons. The brightness of NSLS-II will provide extraordinary collimation to provide excellent diffraction from these very large-unit-cell crystals
3. A significant value of NSLS, and potential value of NSLS-II, is simply being able to handle quite good crystals expeditiously, both for investigators who want to visit to take their own data, and for mail-in service. Rapid diffractometers with excellent shutter/axis synchronization and high-quality detectors should be able to provide automated crystal screening followed by full data collection and processing.
4. To provide phasing power from inherently weak signals from low-abundance heavy atoms, the brightness of NSLS-II can be focused on narrowing the bandwidth of radiation, and thereby enhancing the signal, of sharp K-shell transitions by use of high diffraction-order monochromators [11.9.3].
5. The exploitation of the sulfur and phosphorus edges to study DNA complexes is gaining increased interest as new generation synchrotrons are capable of delivering bright beams at longer wavelength. Longer and shorter wavelengths will be explored at NSLS-II to provide a larger range of possibilities to the user.
6. Something over 10% of proteins contain a transition metal that contributes to the molecule's biological function. Provision of a relatively simple energy-dispersive x-ray detector at each experimental station would provide a quick way to survey for these metals in any specimen.
7. A straightforward and inexpensive facility to provide at several stations would be a single-crystal UV/Visible spectrophotometer. This would find service for the monitoring of x-ray damage in crystals, examining redox states of chromophoric functional groups, and other similar tasks.
8. The crystal-growth "industry" has a continual need to assess the diffraction quality of newly grown crystals. We would provide a station with flexible means to couple crystal-growth automation with diffraction specimen automation to provide the rapid screening that is required.
9. Following on the aim to study the smallest possible crystals, we would provide a versatile environment to explore various avenues, such as performing short measurement sweeps on individual micro-crystals swept up and cryocooled together on a tiny mesh, or performing one-shot exposures on micro-crystals passing the beam in a flow cell.
10. In the context of study of micro-crystals, each of which might be capable of providing only a small fraction of a complete data set, one station would be capable of exploring innovative methods for their use. Examples might be use of increased angular divergence, or broader energy bandwidth, to integrate the diffraction rocking curve for stationary crystals.
11. A small fraction of investigators at NSLS-II will want to follow the time course of some reaction in their crystalline molecule. Use of the white-beam Laue method would not be particularly effective with the undulators we propose. However, to exploit freeze-trapping of intermediates and other methods we have not envisioned, there would be space to install flash lamps or lasers to trigger reactions. These will complement the sharp time structure of the ring and the UV/Vis spectrophotometer we propose above.

11.9.5 Experimental Apparatus

We propose equipment that might serve a suite of experimental stations that could be served by two canted NSLS-II undulators, each producing a hard x-ray spectrum in the range 5 – 30 keV. Components of this sector can be replicated in other sectors to serve expected demand. Since progress in automation is exploding right now, we plan that several of the beamlines will be fully automated, capable of following a sample-in/structure-out model.

The downstream undulator beam would be designed to deal with the most challenging problems, with a range of optical characteristics available, including the smallest possible microfocus that is accompanied by a convergence less than 1 mrad. It would be set up to attack any crystallographic problem, with multiple options for micro-focusing (KB mirrors, graded multilayers, refractive lenses, elliptical capillaries), a monochromator that can produce higher harmonics to narrow the bandwidth, full automation for high-throughput data collection, microspectrophotometer, energy-dispersive x-ray detector, and so forth.

The upstream undulator could provide a beam for two to three stations with fixed energy, say at 13.6 keV (just above the bromine K edge), one being an end station (similar to the station described above that uses the beam from the downstream undulator) and the others being side stations. Here are potential roles for the stations that use the beam from the upstream undulator:

- Station 1: Set up to serve as a crystal-screening station. There would be robotics for conventional specimens and for various crystal-growth apparatuses. Any economies in detectors and other components. can be taken here.
- Station 2: Setup to provide rapid throughput for fixed-wavelength operations: drug-binding studies, SAD structure solving, molecular replacement, and so on.
- Others: Likely there would be substantial demand for both of these, and they could be replicated.

We expect large demand for the sort of station defined for the downstream undulator. Most of the PX sectors should have two of these high performance stations. We explore each component of the experimental stations further, below.

11.9.5.1.1 Crystal Orienters

Every station would be equipped with quick orienters capable of holding a crystal on an axis within 2 μm, fully automated x-y-z alignment mechanism, and excellent crystal visualization. The current state of the art in crystal drives is represented by direct-drive servo-motor ω axes employing an air bearing that provides positional reliability on the few-micrometer scale. These rotate at about 30 rpm (180 deg/sec). Mechanized crystal-alignment mechanisms give accuracy on the same few-micron scale.

Several sources of software are available today that can automatically center crystals in the x-ray beam. These will be better by 2013. All stations would be equipped with a full ω-κ-φ orienter or equivalent. Already in 2006 there is software in use at ESRF that allows flexible use of a demountable κ-φ orienter. This code allows one to orient a crystal to a particular orientation, for example to rotate about the longest unit-cell edge, and to keep the crystal stationary in the x-ray beam while κ and φ are rotated to position the crystal. There are available computer-controllable front- and back-lighting systems, and automated microscope zoom mechanisms, to provide the best possible specimen visualization.

11.9.5.1.2 Detectors

By 2013, position-sensitive detectors will be available that will provide roughly $4k^2$-pixel images in a ~400 mm format with essentially continuous readout (no need to close the shutter nor to stop the rotation axis) on the 100–500 ms time scale. We would install the very best systems that we can afford. By that time, to store data that are produced at this pace should be straightforward.

11.9.5.1.3 Automation

Writing in 2006, the standard of mechanical specimen changing is to have individual crystals mounted, each on its own cartridge or pin, carried in a magazine or cassette, for automated cryogenic mounting and dismounting. The 2013 equivalent of this will be available at every station.

11.9.5.1.4 Ancillary Features

Modern PX would be impossible without cryogenic cooling of specimens, which are otherwise exquisitely sensitive to x-ray damage. Therefore, every station would have a cryogenic system appropriate for keeping specimens at ~100 K; there will be at least one system capable of ~20 K.

A particular problem with small specimens, especially when photon energies less than about 12 keV are used, is high x-ray background that results from scattering from air in the space between the exit aperture and the beam stop. Therefore, stations would be provided with helium chambers to surround the collimator / specimen / beam-stop volume, which would be used to minimize background from air scatter when it's appropriate.

Amplifying experiments 8–10 above, one can imagine inventive ways to employ multiple microcrystals to measure complete data sets. These might include ones picking up a few tens of microcrystals on a network or sieve, or flowing microcrystals through a flow cell, exposing each for one shot as it passes by. Each of these might require special optics, say a focusing capillary that would provide a wide convergence to sample a wide rocking curve, or white or pink radiation to perform Laue crystallography. One of the end stations could be made versatile enough to accommodate this work.

11.9.6 Experiment Control

All stations would have hardware for control of beamline components that is as similar as possible to minimize trouble shooting and maintenance of spare parts. Also the user software at every station would be recognizably similar to the others. There would be the transparent possibility for secure remote observation and operation. There would be easy-to-use software to allow automated assessment of crystal quality, data-collection strategy, and full processing of raw data. Examples of this exist now; the "dna" software package of the European consortium (http://www.dna.ac.uk) is one of the most complete. It incorporates the program BEST [11.9.4], which provides excellent analysis of quality and recommends data-collection parameters. There are other sources of this sort of evaluation. There will be invisible database software to provide complete tracking of every specimen, and collection of meta data for future publication and deposition of results into the Protein Data Bank.

11.9.7 Computing Environment

For the purchase of computing hardware, two principles would rule: 1) all of the stations at each sector employed for PX would have, inasmuch as possible, interchangeable computing and storage hardware; 2) computing hardware would be purchased to be replaced at the end of its practical lifetime (the three-year Moore's Law rule). Therefore, with a replacement plan on a three-year time scale, a similar style of computing engines would be selected for instrument control at all of the stations, and similarly for data reduction and processing. We have shown at the PXRR that this is an excellent use of a capital computing budget. A redundant supply of disk farms on the scale of several tens of TB would be available for interchangeable use by the individual stations. Depending on the climate of activity in the field, the possibility exists to archive raw data at NSLS-II.

11.9.8 User-Assistance Environment

Given the pace of modern PX, investigators must have access to synchrotron-based data collection when they need it. A model that assures users rapid access to beam time, already in place at NSLS, would be followed at NSLS-II. As technical developments allow, we envision that future users will take advantage of robotic and automation developments. The proposed facility would address the needs of the emergent user community, allowing for remote or virtual access with limited staff assistance and the use of modern teleconferencing technologies. In parallel, at least one station would provide full assistance to the user who chooses to address his or her studies locally at the facility.

Two other aspects of the user-assistance environment now in place at NSLS would also be in the makeup of the environment at NSLS-II. Night-time and weekend support would be provided by PX operators, assuring overall quality control of the experimental stations, facilitating communications among them, and giving investigators the ability to collect data at several different stations, when warranted. Also, modeled on the popular PXRR Mail-In program, there would be a program at NSLS-II whereby specimens can be sent by rapid courier to the facility and measured at the beamline either through collaborative assistance using local scientific staff, or through assistance by local technical staff to enable investigators to manage their experiments remotely.

11.9.9 Crystallography Conventional Facility Requirements

Here we describe the supporting biological laboratory and the equipment for sample preparation and characterization that would be required to support the proposed NSLS-II x-ray macromolecule crystallography beamlines. We also propose to establish a crystal-growth facility to serve a broader audience. We embrace the "Biology Village" concept proposed for the Diamond facility, in which beamlines for biology research are clustered at one section of the ring. This model would be cost effective, with users sharing centralized support. Not only would it avoid duplication in laboratory space and equipment, but also it would strengthen interactions among users and staff.

11.9.9.1 Protein Sample and Crystal Handling

11.9.9.1.1 Characterization

A laboratory with a cold room attached would provide basic biochemistry equipment to all users. The supporting laboratory for the proposed NSLS-II PX beamlines would include at least these instruments:

- balances, centrifuges, and pH meters
- gel electrophoresis apparatus
- UV/visible spectrometer
- dynamic light scattering system
- mass spectrometer
- chromatography equipment (FPLC)
- refrigerators and –20^{o}C and –80^{o}C freezers

11.9.98.1.2 Crystal Manipulation and Freezing

While most users will bring or send frozen samples for x-ray data acquisition, others will bring crystals still in crystallization chambers. They will need equipment and supplies to manipulate and cryopreserve the crystals for their studies. The best possible facilities will be provided to allow visitors to cryopreserve their own specimens. In addition to basic resources such as microscope, dewars, mounting pins, and cryobuffers, we would provide a resource to allow use of the high-pressure (~2 kBar) cryocooling technique developed by Cornell scientists [11.9.5].

11.9.9.2 Crystallization Facility

Standing on the shoulders of the NIH Protein Structure Initiative, we propose to serve the structural biological community more broadly by creating a high-throughput pipeline that will carry purified proteins to high resolution 3D protein structures in a high-throughput way. This would assist scientists in fields other than structural biology to obtain structure information for proteins of their interest. It would be established in the supporting biological laboratory adjacent to the NSLS-II PX beamlines. This pipeline would employ approaches and technologies that exist now to streamline and automate the steps of protein structure determination. Acting on protein samples that would have been prepared and characterized in advance, crystallization and optimization steps would be carried out through use of crystallization robotics. Technology exists for crystallization-plate bar coding, movement of crystallization plates into and out of a storage vault, and crystallization-plate imaging and image processing.

Technology that is missing, to which we would contribute, includes automated methods to screen for diffraction crystals still in their crystallization cells, and robotics to mount single crystals from these cells. The ultimate goal is to establish a system that allows the beamline scientific staff to determine molecular structures in a high-throughput manner with minimum of time and cost.

References

[11.9.1] D. Nurizzo et al., *J. Sync. Rad*. **13** 227 (2006).
[11.9.2] R. Fischetti et al., in Proceedings of 9th International Conference on Synchrotron Radiation, to be published as an AIP Conference Proceedings.
[11.9.3] J.L Smith, and A. Thompson, *Structure*, **6**, 815 (1998).
[11.9.4] A.N Popov, and G.P. Bourenkov, "Choice of data-collection parameters based on statistic modeling," *Acta Cryst.*, **D59** (Pt 7):1145-53, (2003).
[11.9.5] C.U. Kim, R. Kapfer, and S.M. Gruner, "High-pressure cooling of protein crystals without cryoprotectants," *Acta Cryst*., **D61** 881 (2005).

11.10 An Optics R&D Diagnostic Beamline

In addition to facility beamlines, which will focus on scientific innovation and productivity, we propose to establish a beamline dedicated to optics and instrumentation R&D. It is important to do so, since such developments can not be carried out at the facility beamlines due to the scheduling pressure from the user community. Experience shows that the conflict between carrying out user science and making beamline upgrades tends to minimize innovation in favor of productivity.

11.10.1 Conceptual Overview

An Optics R&D beamline should be kept simple. Its purpose is to develop new optical systems, so it should not, by definition, contain any permanent optics. It should have provision for inserting optics into the line at any point without major reconfiguration of safety systems. This implies a series of optics enclosures into which it should be possible to insert monochromators, mirrors, and other equipment relatively easily.

11.10.2 Source

The primary need is to have a source of radiation that matches closely the properties of a typical facility beamline, which is available for significant blocks of time to allow optics development to be pursued independently of a user program. Such beamlines have been available at all synchrotrons since one was established at NSLS in the mid 1980s.

Because the properties of most beamlines at NSLS-II will be determined by the type of insertion device used, it is not straightforward to decide on the appropriate source for the optics R&D beamline. The situation is made much more difficult by the fact that the bending-magnet radiation spectrum will be significantly different from that produced by undulators and wigglers. Most of the optics R&D beamlines installed at current machines are based on a bending magnet source. For most existing machines, the spectrum available at such a port is not much different in energy from the spectrum produced by insertion devices, so this is acceptable—although the spectra differ dramatically in brightness and intensity. For optics development, intensity is generally not as important as the ability to schedule large blocks of time.

It could be that the proper functioning of an optic depends on the angular and spatial properties of undulator light. In this case, it is essential that an undulator beamline be available. Since it is not anticipated that all of the beamlines will be populated immediately, then it may be reasonable to allocate one of them to optics R&D, locating a user program on the beamline when the need arises. If this option is chosen, it is important to plan for an alternative location for new developments to be able to continue to be made.

In summary, preference would be for an undulator source since that will be the most common Facility Beamline source. A bending magnet beamline would not have adequate spectral coverage in the hard x-ray range, and the few available wiggler beamlines will be in high demand for user science.

11.10.3 Beamline Optics

In order to keep the required flexibility in such a beamline, the beamline design would be exceptionally simple. Specifically, it would consist of series of well-shielded, white beam–compatible optics enclosures, threaded with a number of vacuum pipe sections. These would be easily removable, allowing optics test beds to be placed at any desired distance from the source point. The final enclosure should be larger than the others to accommodate extended optics setups. It is expected that computing and controls and conventional facility requirements would all be relatively standard for such a beamline.

11.10.4 Optics Test Beamline – Experiment Plan

The beamline outlined above would provide the facility for at-wavelength testing and R&D of synchrotron optics that is essential in the development of components that will utilize the full brightness and coherence of the NSLS-II source. There are four basic optical testing techniques that would be implemented at this beamline as soon as photons are available. These are described below.

An easily implemented at-wavelength test setup can be modeled after the work done at SPring-8 by Souvorov et al. [11.10.1] This group developed a measurement technique and an image inversion algorithm for reconstructing the surface profile of a reflector from a series of through-focus images recorded with a high resolution CCD camera. This technique works for flat as well as figured surfaces, and can be extended to look at wavefronts from focusing optics, such as Bragg-Fresnel optics and refractive lenses. The diagnostic capability of this technique will enable one to determine the source and location of phase errors in these optics, providing much more information to the fabricator than available from a simple image size measurement. Implementation of this technique requires a high resolution camera to extract intensity information as a function of position from the small image space area. Initial testing on this beamline can be done with prototype Bragg-Fresnel optics and kinoform optics, and with polished flats and spheres available from other optics suppliers.

Another test set-up that can be implemented rather easily is the wire or knife-edge scanning system, as reported by Yamauchi et al. [11.10.2]. This system was used to measure the focal quality of KB elliptical cylinder mirrors on the 1 km beamline at SPring8. By measuring the intensity profiles in various transverse planes around the point of focus, one can reconstruct the aberrated wavefront of the incident beam and learn something about the optical component that produced it. This measurement technique requires only a single element detector and a precision translation stage with nanometer positioning accuracy.

The third measurement technique that can be considered for implementation is an at-wavelength interferometry technique pioneered by Weitkamp et al. [11.10.3]. This technique involves development of a shearing-type interferometer based on Moiré patterns produced from the Talbot effect with two fine-pitched gratings. The instrument requires a high resolution camera to view the Moiré pattern produced by the Talbot effect system. The complete instrument is a small, robust unit that is insensitive to the usual vibrational instabilities of other interferometer techniques. It is ideally suited for direct measurement of wavefronts transmitted by refractive optics.

The fourth test method that can be implemented on this beamline is in-situ profilometry of optical surfaces under normal and accelerated heat load conditions. This entails using a portable Long Trace Profiler setup to view surfaces through a window as they are irradiated with the direct white beam or monochromatic beam. The LTP technique has been used to measure nanometer distortions in water-cooled mirrors on an APS beamline. It is an invaluable tool for validating thermal and mechanical designs of mirror substrates, coating materials, mounting mechanisms, and bending mechanisms. The portable LTPs are currently under development in the BNL Optical Metrology Lab. Implementation at NSLS-II would require the placement of viewports and mirror test chambers at the appropriate locations along the beamline.

References

[11.10.1] Souvorov et al., *J. Sync.Rad.* **9** 223 (2002).
[11.10.2] Yamauchi et al., *J. Sync. Rad.* **9** 313 (2002).
[11.10.3] Weitkamp et al., *Opt. Express* **13** 6296 (2005); SRI 2006 Workshop on Metrology for X-ray Optics, abstract No. 34050005, "X-ray Interferometric In-situ Characterization of Reflective and Refractive Optics."

11.11 A High-Magnetic Field Beamline

In addition to temperature and pressure, magnetic field is an important thermodynamic variable for studies of a variety of condensed matter systems ranging from molecular conductors to superconductors to heavy fermion systems. Ongoing improvements in magnet technology enable studies of such systems at ever increasing fields, and new phases with exotic and intriguing behaviors continue to be revealed. The coupling of high-field magnets and synchrotron radiation is an obvious avenue for high-resolution structural and spectroscopic studies of these new phases. Yet presently, there are few high-field magnets at synchrotron radiation facilities, and the highest DC field worldwide is 15 T. Given the size and complexity of high-field magnets, such a facility will require a dedicated beamline. In this section we consider a high-field magnet beamline for hard x-ray scattering and spectroscopy.

Figure 11.11.1 shows the schematic layout of a high-field magnet beamline.

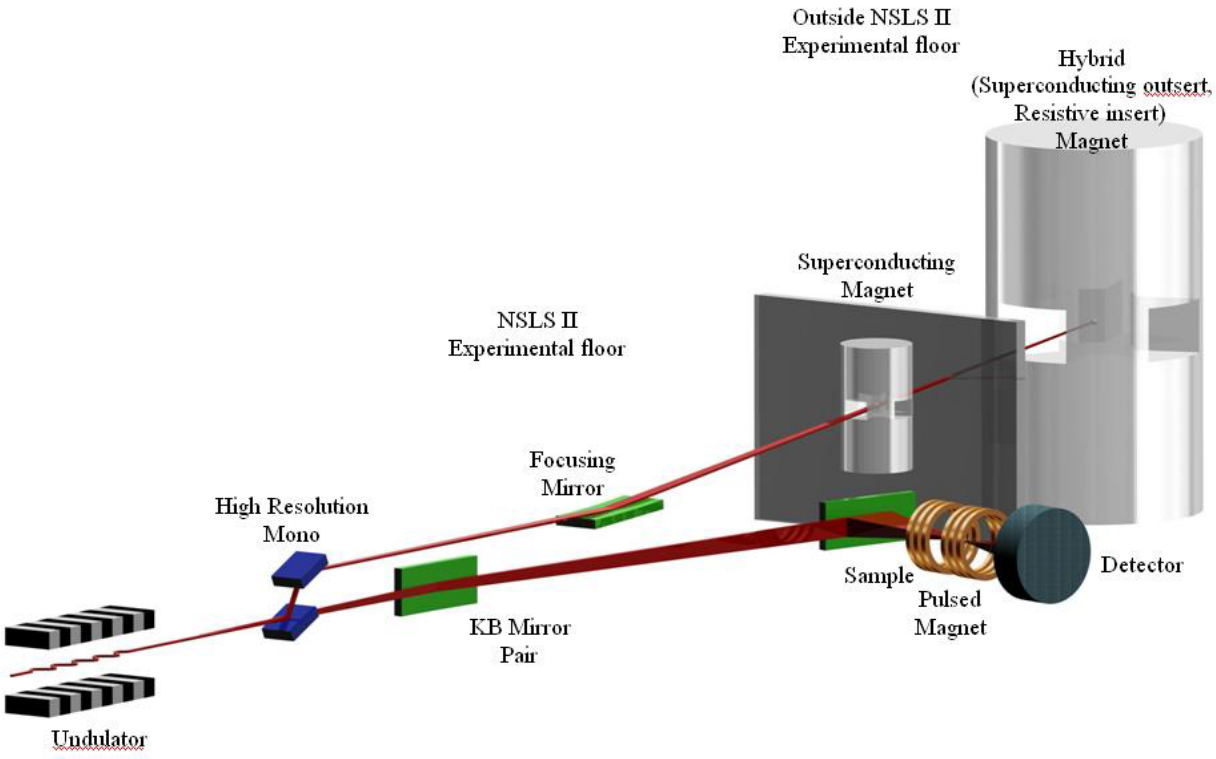

Figure 11.11.1 Conceptual layout of high magnetic field beamline. The large hybrid magnet would be located outside the experimental hall, the wall of which is denoted by the gray panel in the figure.

11.11.1 Source

The high-field magnet beamline would require an undulator source due to the need to have the DC hybrid magnet located outside of the main building (for size, safety, and stray field issues). A standard high-brightness undulator would meet the anticipated experimental needs, and no special requirements for the machine parameters are expected.

11.11.2 Optics

The optics for this beamline are expected to be relatively standard, with a double-crystal monochromator to allow an energy range of ~5–30 keV, with a spot size of ~1×1 mm^2 for either of the fixed field magnets. In addition, in-line phase retarders (for producing circularly polarized beam at rare earth L and transition metal K edges: ~5 – 10 keV) will be utilized. The monochromator would require a wide beam. A mirror that accomplishes this by defocusing the beam is shown in the beamline layout, Figure 11.11.1.

11.11.3 Beam Transport and Enclosures

There would be a single first-optics enclosure of size ~10(W)×20(L)×12 ft (H) for the aforementioned optics (except the dispersive mono, which would be in the first hutch for use with the pulsed magnet).

11.11.4 End Stations

A high-field magnet beamline would ideally consist of two hutches. The first, which would be located inside the main building, would accommodate “medium-field” magnets such as a 4 T cryogen-free magnet

that can be operated with vertical or horizontal field and a ≥13 T superconducting magnet as well as a ≥50 T pulsed magnet. Such magnets would make possible a variety of scattering experiments (PD, single-crystal XRD, SAXS, and GISAXS) and spectroscopy (XAS and XMCD). This would provide a versatile and relatively low-cost high-field magnet facility.

The second hutch, which would be housed in a separate building, would accommodate a 30 T, DC, split-coil, series-connected hybrid magnet. The utilities (e.g., power supply, water cooling components, and closed-cycle helium refrigerator/liquefier) for the hybrid magnet would be contained in a second building.

The specifications for the split-coil, series-connected, hybrid magnet (National High Magnetic Field Laboratory conceptual design) are: 30 T DC magnet with four 45-degree (11-degree vertical) ports, with vertical field. The magnet can be rotated ~15 degrees about a vertical axis. The magnet can also be rotated 90 degrees to provide a horizontal field, with four ~1-degree (32 mm diameter) windows appropriate for XAS and SAXS experiments.

11.11.5 Conventional Facility Requirements

The nonstandard requirements for the first hutch are its size and structural floor load limit. An in-line arrangement of magnets, which would simplify experimental changeovers, and sample insertion and liquid helium refills of the superconducting magnet, necessitate a longer and taller hutch: 16 ft (W)×30 ft (L)×16 ft (H). In addition, due to the weight of the capacitor bank for the pulsed magnet, a structural floor load limit of 200 psf is required.

The nonstandard facility requirements for the second hutch are 1) its size: 30(W)×30(L)×26 ft (H)— with a hutch 6 ft below ground and a 600 ft^2 structural floor load limit at the site of the magnet, 2) an auxiliary building to house a utility plant for the hybrid magnet, which would supply 10 MW of power and 120 l/s of cooling water for the resistive part of the magnet, and 3) a commercially available, closed-cycle helium refrigerator/liquefier, which requires an input of ~2 l/min of liquid nitrogen for the superconducting part of the magnet and the cryostat; this would also be housed in the utility plant.

11.12 A High-Energy Beamline

There are a number of advantages to using high-energy x-rays, including a larger q range and reduced absorption, allowing large samples to be studied and extreme conditions to be accessed. Focused high-energy x-rays are essential for high-resolution x-ray scattering of samples in multi-anvil and diamond anvil cells. Newly developed x-ray focusing optics and detectors can take advantage of the enhanced flux and brightness of the NSLS-II superconducting wiggler source to enable a myriad of crystallographic and spectroscopic measurements.

A **s**uper**c**onducting **w**iggler beamline would provide x-rays in the energy range 20 keV to 150 keV. While the damping wiggler sources will provide a harder source of x-rays than the undulators, the flux from a SCW is an order of magnitude higher than that provided by a damping wiggler, at typical high-energy x-ray scattering energy of 80 keV. SCWs are therefore the desired source for high-energy x-rays.

For the SCW wiggler proposed here, the radiation fan is about 10 mrad wide. Focusing of the x-rays is thus crucial to collect the large fan in order to increase the available flux at the sample. Recent developments in sagittal focusing Laue optics make it possible to focus a large divergence of high-energy x-rays.

The use of white radiation and energy-sensitive detectors for energy dispersive diffraction is an established technique for kinetic experiments in high-pressure (either in a diamond anvil cell or large-volume press) and high-temperature experiments. With the optical elements withdrawn from the center beam, the end station will accept white radiation, thus allowing for energy dispersive experiments.

11.12.1 Conceptual Overview

Figure 11.12.1 shows a sketch of a possible arrangement for beamlines utilizing one such wiggler source. The experimental stations would likely include two side stations utilizing fixed wavelength and two center stations that can utilize both the white beam and focused monochromatic beam.

Considerations have been given in the conceptual design to facilitate changing of configurations in the future in anticipation of unforeseen future needs. Beam can be passed through the hutches in a manner that allows experiments to run simultaneously.

11.12.2 Source

The highest energy photons are produced by very-high-field wigglers. The radiation is broadband with high power at high x-ray energies. The wiggler for the beamline would need to cover the 20 to 150 keV energy range, which requires a critical energy E_C of more than 20 keV, corresponding to a wiggler field of over 3.5 T at the NSLS-II energy of 3 GeV. The brightness should be as high as possible, which means the wiggler period length should be as small as possible. The combination of high field and small period requires a superconducting wiggler design. SCWs are available commercially with a peak field of up to 7 Tesla [11.12.1].

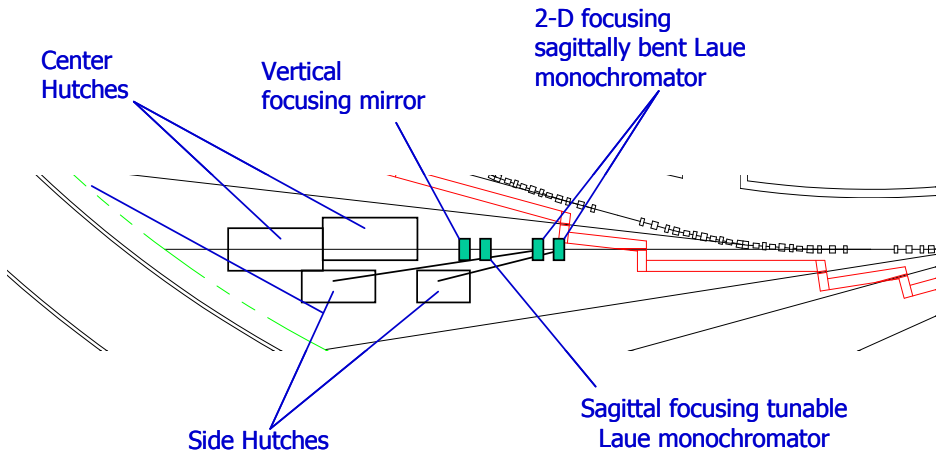

Figure 11.12.1. Layout of the superconducting wiggler beamlines. The length from the ID to the aisle is 60 m.

The wiggler for the beamline covers the 5 to 150 keV energy range, which requires a critical energy E_C of more than 30 keV and a wide beam fan with K of approximately 30. The specifications of the wiggler are listed in Table 11.12.1. Specifications of similar SCWs that are currently in service at medium-energy synchrotrons are listed in Table 11.12.2. A 1 m SCW with 60 mm period and 6.0 T peak field is proposed, as discussed in Chapter 8. We note that a radiation horizontal fan of 10 mrad is difficult to accommodate within the current design of the ring vacuum chamber. Thus accommodating multiple beamlines in this way may require a specialized design of that chamber. Such issues will be looked into in the title I design phase of NSLS-II.

The performance of the proposed wiggler for a 3.0 GeV ring energy was shown in Chapter 8. The wiggler outperforms other options at energies above 30 keV. The critical energy is almost twice that of the NSLS X17 superconducting wiggler (21.6 keV). Having substantial flux at energies above 100 keV is essential for strain mapping and MRT. The deflection parameter is chosen to be wide enough to generate a large horizontal beam profile of a more than 0.5 m at 50 m from the source point. This allows splitting of the fan into multiple

experimental hutches. In addition to the 29 full-size poles, a number of poles in the entrance and exit may be used for better electron beam orbit maintenance.

11.12.3 Optics

Sagittal focusing using Laue crystals was pioneered at NSLS [11.12.2, 11.12.3]. The concept is shown in Figure 11.12.2a. This new x-ray optics concept makes it possible to focus the large divergence of high-energy x-rays produced by the NSLS-II SCW. The extent of such focusing is similar to that of sagittal focusing by a Bragg crystal, except for a factor related to the asymmetry angle. The anticlastic bending facilitates the use of inverse-Cauchois geometry in the meridional plane to provide better energy resolution and to increase the photon flux by an order-of-magnitude compared to traditional sagittal focusing with Bragg crystals. Furthermore, sagittal focusing by a Laue crystal is preferred over a Bragg crystal at x-ray energies above 30 keV because, unlike Bragg crystals, the length of the beam's footprint on a Laue crystal is small and insensitive to energy. For many experiments, beam divergences on the order of 1 mrad at the sample will be tolerable. In diffraction experiments with a vertical scattering plane, a larger divergence in the horizontal plane can also be tolerated.

A double-crystal sagittally focusing monochromator based on this concept has been constructed and tested and has been in use at the X17B1 beamline for two years, providing 67 keV x-rays (Figure 11.12.6). It focuses a horizontal divergence of 3 mrad to a brightness-limited horizontal dimension of 0.2 mm. The x-ray flux density at the focus was a few hundred times larger than that of unfocused x-rays. Currently, using this device, flux on a small sample in a diamond-anvil cell is limited by the brightness of the NSLS storage ring. Combined with a vertically focusing mirror, the same monochromator can be implemented at the upgraded NSLS wiggler beamlines to provide 50 to 100 keV photons of about 10^{12} ph/s, with an energy resolution of 10^{-4} $\delta E/E$, in a spot of less than 50 microns in diameter. This intensity is two orders of magnitude larger than the current state of the art at NSLS X17B1 and will enable studies of smaller samples at higher pressures and higher temperatures.

The conditions imposed on the asymmetry angle of a sagittally bent Laue crystal to achieve 2D focusing have been determined. This simple design diffracts beam into side stations, providing a high-flux beam of 67 keV with moderate energy resolution of 10^{-3} $\delta E/E$ with a flux of about 10^{13} ph/s/mm^2, in a spot of less than 50 microns (V)×100 microns (H). This, when coupled with a matching bent-Laue crystal analyzer, allows high-resolution experiments at high energies. This arrangement is suitable for pair distribution function measurements and powder diffraction measurements in difficult environments, e.g., stainless steel reaction tubes and high temperature capillaries. It will also be valuable for certain single-crystal experiments, such as charge density studies, where data must be collected to very high q values.

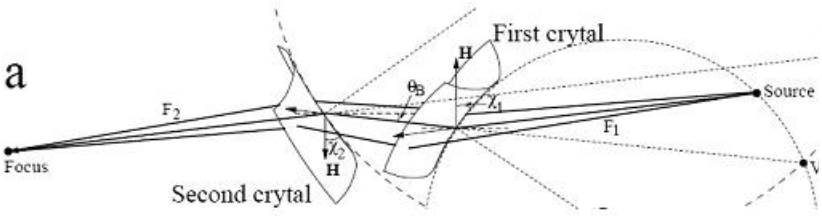

Figure 11.12.2

a) The mechanism of the sagittal focusing with asymmetric Laue crystals. Bending of the crystals causes precession of the diffraction vector (H) around the axis of sagittal bending, and the resulting focusing of the diffracted beams.

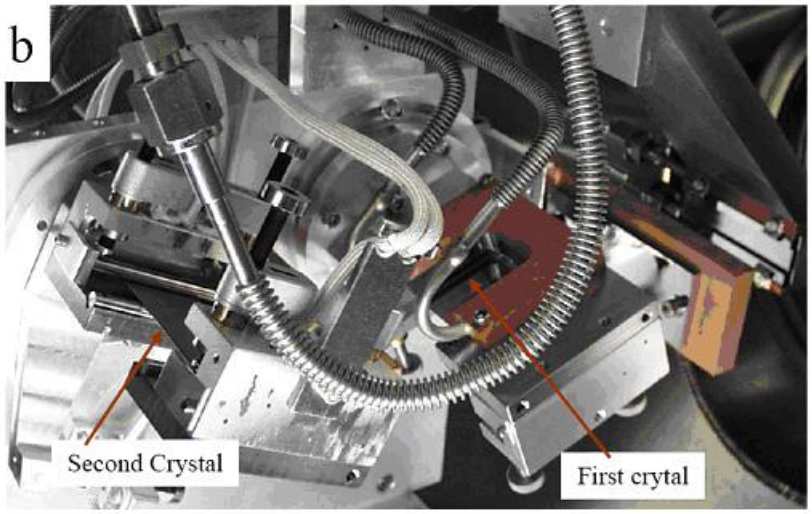

b) Photograph of a monochromator installed at the NSLS X17B1 beamline.

11.12.4 Beam Transport and Enclosures

The demand for the wiggler beamline for different experimental configurations is expected to be high, as has been the case with the X17 beamline at NSLS. The design of the beam transport and enclosures will therefore use the same principle as adopted at X17, to allow maximum flexibility both in terms of the science and in experimental configuration.

Due to the high energy of x-rays generated by the SCW, the entire beamline will be fully enclosed in radiation shielding, as is done at the NSLS X17 beamline. A single enclosure will house the beam-splitter, white beam filters, shutters, and monochromators for the four experimental hutches downstream. The effect of the high power of the wiggler on the optical components will be minimized by aggressive filtering of the white beam radiation with a few millimeters of aluminum or silicon material.

The monochromators for the sidescattering branches would be of the single-crystal, sagittal focusing Laue type described above. The monochromators for the inline hutches would be of the double-bounce Laue type, which can be withdrawn, thus allowing white beam to enter the inline experimental hutches. The same design has been in use at the X17 beamlines at NSLS.

11.12.5 End Stations

Four hutches, two inline with white beam capabilities and two sidescattering monochromatic-beam branches, are considered for the wiggler beamline. Each hutch will be served by a part of the wiggler fan of a few mrad wide. Each hutch will have its own shutter and can operate independently from other hutches. Note, only the first in-line hutch has a beampipe passing through it.

The first hutch will host a Diamond Anvil Cell instrument (first inline hutch in Figure 11.12.4) with both EDXD and low-resolution powder diffraction setup. The second hutch (first side branch in Figure 11.12.4) will host a high-resolution, high-energy x-ray diffraction instrument for pair distribution function and diffuse scattering measurement, and a separate liquid spectrometer for buried interface study. These two hutches will be 12-ft W × 16-ft L × 10-ft H on the floor level.

Two 16 -ft (W) × 24 -ft (L) x16 -ft (H) hutches, one inline for EDXD white beam experiments and one as a side branch for ADXD experiments, are 3 feet *below* floor level. The height of these hutches above the floor is 13 feet. Each will host a large-volume press of approximately 20 tons weight, on a pedestal of 10×10 ft, resulting in an average floor loading of approximately 500 psf. In addition to the large-volume press, the long inline hutch, which is the most downstream hutch at the beamline, will host a strain mapping instrument with in-situ deformation capability, a MRT and DEI setup. The three experimental arrangements will be a permanent setup but will operate on a time-share basis. This arrangement allows longer term experiments, such as creep and stress corrosion fatigue, or thermal crack growth studies that require intermittent monitoring on a time scale of days.

In addition to experiments currently ongoing at the NSLS SCW beamlines, the higher critical energy, higher brightness, and optimized experimental infrastructure at the NSLS-II wiggler beamline will allow a new range of exciting experiments currently not possible anywhere else in the world. These will include experiments to simulate service conditions experienced by real engineering components while their internal stress state and structures are continually monitored by diffraction.

References

[11.12.1] E. Weihreter, et al., Proc. EPAC 2004, Lucerne, Switzerland (2004) 324-326. http://accelconf.web.cern.ch/AccelConf/e04/PAPERS/MOPKF012.pdf

[11.12.2] Z. Zhong, C. Kao, D.P. Siddons, H. Zhong, and J.B. Hastings, "X-ray reflectivity of sagittally bent Laue crystals," *Acta. Cryst. A* **59** 1-6 (2003).

[11.12.3] Z. Zhong, C. Kao, D.P. Siddons and J.B. Hastings, "Rocking-curve width of sagittally bent Laue crystals," *Acta Cryst, A* **58** 487 (2002).

11.13 A Hard X-Ray Imaging Beamline

11.13.1 Introduction

In a variety of synchrotron applications in materials science and engineering as well as in biological and medical sciences, X-ray imaging is the key to the investigation of structures from nanometer to millimeter scales. The subject areas of x-ray imaging studies vary widely and include materials microstructure/properties research, bone and cartilage growth and formation, small animal and soft tissue research, biomedical research such as tumor detections, structure and development of foams, and dynamics of complex fluid flow and nanofluidics. Additional areas where x-ray imaging is expected to have a significant impact in the future include time-resolved imaging of materials processing such as electrodeposition, imaging of subcellular organelle structures in frozen-hydrated biological cells, and 3D nanocrystallites, nanoclusters, and other nanostructures.

To satisfy the growing needs in the scientific community for x-ray imaging and to perform state-of-the-art research to advance x-ray imaging techniques, we proposes to build a 300 m long beamline dedicated for full-field imaging research and applications (see below). The beamline will be furnished with three core capabilities:

- static and time-resolved Phase-Contrast Imaging
- Diffraction-Enhanced Imaging with density reconstruction
- Fresnel Diffraction Imaging with high-resolution image retrieval

All three core techniques will include 3D tomographic capability. With the synchrotron x-ray beam brightness and coherence proposed at NSLS-II, this long beamline with the above core capabilities will be a unique, premier x-ray imaging facility in the United States, and thus will offer the scientific community a powerful tool for advanced structural and dynamic imaging applications in materials and biological sciences that is not currently available at existing DOE synchrotron facilities.

This section summarizes the preliminary plans of the scientific scope and the preconceptual design of the x-ray imaging facility at NSLS-II.

11.13.2 Scope of Scientific Program

X-Ray Imaging covers a wide range of techniques and applications. The NSLS-II XRI facility will focus on the following core experimental techniques: 1) Phase-Contrast Imaging, in both static and time-resolved modes, 2) Diffraction-Enhanced Imaging capability, 3) coherent Fresnel Diffraction Imaging, and 4) image retrieval and tomographic 3D reconstruction as an integral part of the facility.

A good portion of the scientific program requires a highly coherent x-ray beam in an energy range of 7–50 keV, and a large field of view with minimal source-size smearing. In addition, time-resolved imaging experiments will make use of the pulsed nature of the NSLS-II synchrotron x-rays with an aim to achieve a single-pulse temporal resolution of ~50 ps and a simultaneous high spatial resolution of ~1 μm.

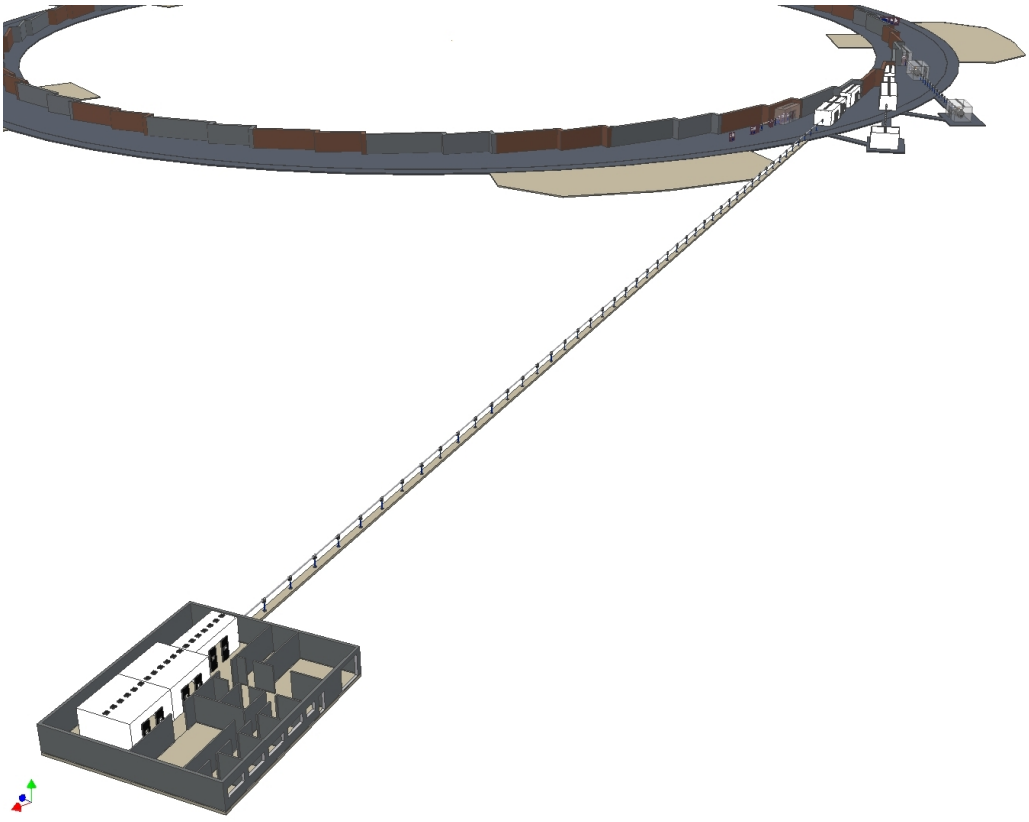

Figure 11.13.1 Conceptual layout of x-ray imaging facility showing a remote end station with three optical enclosures, the first of which is 300 m from the source.

11.13.2.1 Phase-Contrast Imaging

PCI is a coherence-based technique that makes use of the edge enhanced effects in near-field Fresnel diffraction and allows detections of weakly absorbing features in a specimen that are otherwise not observable in conventional absorption-based x-ray radiography. The spatial resolution with PCI is generally limited by the detector spatial resolution of 1–10 μm, which is well suited for many biological, medical, and materials science applications. A KB mirror system is planned, to provide a projection-imaging capability to allow increased spatial resolution down to 0.1–1 microns, if necessary.

Phase sensitivity directly depends on the source-to-specimen distance and the specimen-to-detector distance thus leading to the requirement of a long beamline for PCI applications, as illustrated in Figure 11.13.1. In addition, a long beamline provides an unobstructed larger field of view, which will be needed for imaging larger specimens in materials and medical sciences. Based on the designs and experiences of the existing synchrotron beamlines in the world, we propose to build a 300 m long beamline, which (assuming σ_x = 84.6 μm) will provide a phase sensitivity of 2 mrad within the typical spatial resolution of 1 μm, and will be able to detect minute refractive angular deviations of <1 μrad. These specifications will represent the state of the art in worldwide x-ray PCI capabilities.

PCI will be the work-horse facility of the XRI beamline, perhaps comprising 60 to 70% of the scientific work. Examples of anticipated research topics include:

- fracture mechanics of composites and biological materials
- materials microstructure/properties such as deformation and sintering
- bone and cartilage growth and formation
- small animal and soft tissue research on vascular and pulmonary functions
- porosity distribution in foods
- structure and development of plant seeds
- characterization of geological structures and microfossils
- cement mortar research
- structure and development of foams
- granular packing of non-equilibrium systems
- time-resolved studies of internal complex fluid flow and fluid sprays
- multi-phase fluid flow using particle image velocimetry

11.13.2.2 Diffraction-Enhanced Imaging

DEI, developed at NSLS by Dean Chapman et al. in the 1980s, makes use of a high-quality crystal analyzer to detect refracted or small-angle-scattered x-rays from the specimen. Because of high angular selectivity of the crystal analyzer, DEI can image very minute phase shifts due to density inhomogeneity in the specimen. In addition, in Ultra Small Angle X-ray Scattering (USAXS) mode, it can be used to image density inhomogeneities and fluctuations at a given spatial frequency of interest. Technically, DEI can be set up in one or all of three regimes: a) top of analyzer rocking curve for scattering background rejection, b) side of analyzer rocking curve to convert refraction-angle into intensity contrast, and c) far from analyzer rocking curve on direct beam to pick up USAXS signals at a given scattering angle. Examples of DEI applications include:

- microstructures and defects in materials
- deformation, sintering, and cracks formations
- porosity in bones and calcification effects
- soft tissue and vascular network detections in x-ray radiographs
- diagnosis of cancerous tumors in soft tissues

11.13.2.3 Coherent Fresnel Diffraction Imaging

Coherent FDI involves the collection of Fresnel or in-line holograms in near-field regimes and the reconstruction of original nonperiodic objects by image retrieval techniques. Compared to PCI, FDI seeks to record a complete set of Fresnel diffraction fringes at a greater detector-to-specimen distance, which allows quantitative determination of an object density function and permits spatial resolution reaching well beyond the detector pixel resolution. When working in the intermediate regime of a few Fresnel zones, FDI essentially becomes the far-field coherent diffraction imaging technique. Examples of potential applications include:

- structures of large biological functioning units (e.g., tissues, myocytes, muscles, bones, cartilage, etc.)
- identification of organelles and critical protein assemblies in biological cells
- self-assembly of macromolecule arrays with nano-templates and nano-grids
- structural imaging of multi-unit inorganic/small-molecule/biomolecule composites
- noncrystalline nanoparticles such as nanoclusters and nano-wire assemblies
- structural imaging of precipitates and defects in engineering materials
- topographic imaging of domain growths in ferroelectrics

11.13.2.4 Image Reconstruction

Image reconstruction software packages and associated user support will be an important and integral part of the XRI facility at NSLS-II. The software package will be developed either in-house or collaboratively with other research groups, and will include such programs as image analysis and pattern recognition in PCI, density reconstruction in DEI, phase-retrieval and reconstruction in FDI, and 3D tomographic capabilities in all three core research areas. Due to an extremely diverse scientific user community in this field, considerable user support and additional personnel are envisioned and will play a crucial role in enhancing the scientific productivity of the XRI facility.

11.13.3 Preliminary Conceptual Design

The proposed long x-ray imaging beamline (Figure 11.3.1) will consist of an undulator located on one of the low horizontal beta 5 m straight sections, a standard beamline front-end, a first optics enclosure, an experimental hutch at ~50 m from the source, a long beam transport, and a satellite XRI facility building that houses two experiment hutches at 300 m from the source. An optional second optic enclosure is included in the conceptual design to accommodate additional imaging optics in the future.

11.13.3.1 Undulator Source and Front End

The x-ray source for the XRI beamline will be an undulator 3 m long with a 1.9 cm period, producing a highly brilliant x-ray beam from 7–50 keV using third and higher harmonics in order to satisfy the partial coherence requirement for x-ray imaging applications. The undulator will be situated at a low-horizontal-beta straight section, producing a source size that is smaller than usual, with a correspondingly larger beam divergence. Based on experience at APS, this arrangement can improve phase contrasts considerably for low-density objects. Furthermore, it will increase the field of view to allow phase-contrast imaging of larger objects, such as an entire mouse.

The front-end will consist of standard beamline components, with special emphasis on beam position monitors and feedback to ensure a stable x-ray beam with <1 μrad angular variations.

11.13.3.2 X-Ray Optics and Window

The FOE will accommodate an x-ray beam aperture to filter unwanted radiation outside the undulator central cone, an adjustable white-beam slit, a liquid nitrogen–cooled, Kohzu-style Si (111) double-crystal

monochromator, and a harmonic-rejection double mirror with a low offset. Both the silicon crystals and the mirror will be highly polished with ultra-low slope errors (<1 μrad). The monochromator will cover a tunable energy range of 7–50 keV, while the mirror will consist of multiple coating stripes to provide fixed cut-off energies at 9 keV, 15 keV, 18 keV, and 24 keV. For higher energy applications (>24 keV), the mirrors will be moved out of the beam.

Both the monochromator and the double mirror optics, as well as other beamline components, will be designed to allow white beam to pass through. It is envisioned that all x-ray optics and beamline components will be in ultra-high vacuum, with an x-ray window at the upstream end of the hutches as the only vacuum barrier. The window will be made of highly polished beryllium or diamond or some other materials such as SiN_3 to minimize any phase contrast effects from inhomogeneities and/or imperfections.

11.13.3.3 Experiment Hutches

There will be three experiment hutches at the XRI beamline. Hutch B will be the first experimental enclosure downstream of the FOE and will be located at around 50 m from the source within the NSLS-II building. This hutch will be about 5×10 m in footprint and will be white-beam compatible. It will be used mostly for coherent FDI development and for time-resolved imaging using both monochromatic and pink beams.

Experiment hutches C and D will be located in the XRI satellite building at around 300 m and 315 m from the undulator source, respectively, both 5×15 m in footprint. Hutch C will focus on materials applications using direct PCI, while Hutch D will be dedicated to biological and biomedical imaging applications. The separation of the two experiment enclosures is necessary due to environmental safety concerns for certain biomedical and small animal specimens. It is also envisioned that Hutch D may be an integral part of a future expansion to form a clinical laboratory at the XRI facility, much like the existing enterprise at Elettra Light Source in Trieste, Italy.

The current plan is build the C and the D hutches as monochromatic enclosures so that the beam transport connecting the remote building and the main building will not require white-beam capability.

11.13.3.4 Second Optic Enclosure and Beam Transport

A Second Optic Enclosure just upstream of Hutch C will be designed and constructed inside the XRI facility building. This SOE will serve two purposes. First, it will offer the possibility of housing a second double-crystal monochromator in case the first monochromator in the FOE, more than 250 m upstream, introduces significant stability issues magnified by the long lever arm. Second, the SOE may house secondary focusing optics, such as a compound refractive lens or a pair of KB mirrors to allow projection imaging using a focused monochromatic x-ray beam.

11.13.3.5 Experimental Instrumentation

The proposed XRI facility will provide state-of-the-art instrumentation for coherent FDI, PCI, and DEI applications, with 3D tomographic and time-resolved capabilities. Essential instrumentation components include long (>3 m) optical tables, precision translation and rotation stages, precision polished adjustable slits and apertures, motion controls and signal detection electronics, and a variety of area detectors, including lens-coupled and direct-detection Charge-Coupled Device cameras with small pixel sizes (0.5–10 μm), low noise, and large dynamic range (>50,000). In addition to CCDs, fast area detectors such as pixel-array detectors with MHz frame rates will be essential for time-resolved imaging experiments. Other important instrumentation includes x-ray beam shutters and timing choppers, highly polished silicon single-crystals for DEI, and a computer cluster for image analysis and tomographic reconstruction and visualization.

11.13.3.6 Conventional Laboratories and Offices

The XRI facility in the satellite building will house one dry laboratory and one wet laboratory space, plus an enclosure or laboratory space that is suitable to accommodate live small animals. At least 10 standard office spaces and a small conference room will be included in the satellite building, along with a common area for users.

11.14 A Small-Angle X-Ray Scattering Beamline

The high-brightness x-ray beam of NSLS-II will greatly improve the capabilities of Small Angle S-ray Scattering. The lowest accessible scattering vector (q), a benchmark specification for SAXS instruments, will be significantly extended. This is true even with small beam sizes (on the order of microns) and at relatively high x-ray energies (>20 keV). A successful SAXS beamline will directly translate into an array of new scientific opportunities, such as the possibilities to follow dynamical events in biological systems with time resolution as fast as microseconds and to use SAXS as a scanning probe microscope to examine the local structures that underlay micro-textures.

11.14.1 Conceptual Overview

This beamline will be based on a 3 m long undulator source located in a high-β 8 m straight section. The beamline is expected to be ~90 m or longer and include two end stations. The main end station will have two hutches, with the extra downstream hutch housing the USAXS detector. The side station will only utilize part of the x-ray beam produced by the undulator. It will therefore have reduced performances compared the main station and will operate in a quick-access mode to accommodate preliminary study type of measurements.

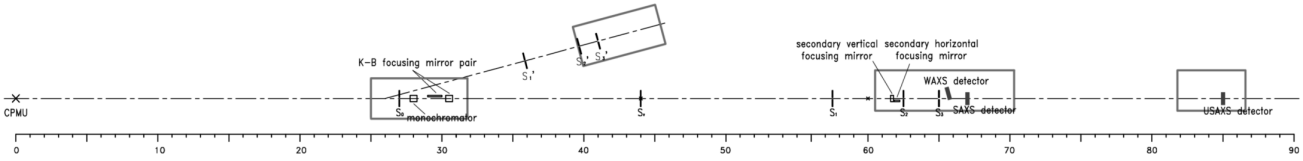

Figure 11.14.1 Conceptual layout of the SAXS beamline. See text for details.

The optical elements for the main SAXS station include a cryogenically cooled monochromator, two KB focusing mirror pairs and a series of collimating slits. This branch of the beamline will operate windowless to provide the best support for experiments at low x-ray energies (phosphorus and sulfur K-edges at ~2 keV) or those where beam coherence is a concern.

The side station is intended for simple exploratory measurements. Its monochromatic x-ray beam will be provided by a graded multilayer upstream of the main monochromator. Three sets of slits along the beam path provide beam collimation. No other optical component is necessary. Since the monochromator does not capture synchrotron radiation in the central cone and the x-ray beam continues to diverge after the monochromator, the flux at the sample will be much lower compared to that in the main station (a factor of ~100, depending on the position of the monochromator transverse to the beam direction). Nonetheless, this end station is still expected to provide performance similar to that of the current undulator-based SAXS beamline at NSLS—or better.

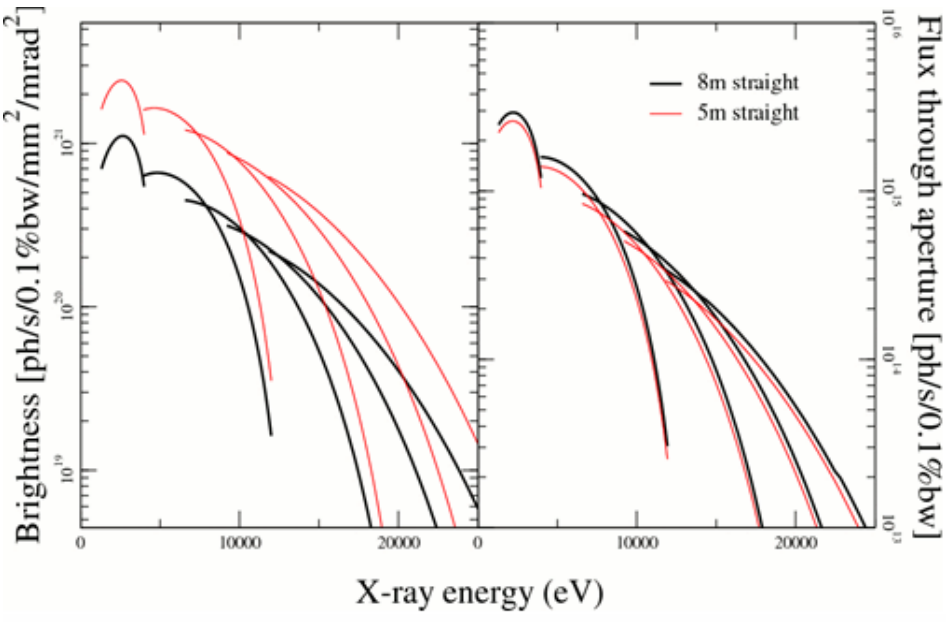

Figure 11.14.2 The characteristic of the 3 m CPMU. The aperture used in the calculation is 1.2 mm (H) by 0.6 mm (V) at 30 m from the source, corresponding to the beam size intercepted by the primary KB mirrors.

11.14.1.1 Radiation Source

The source will be a 3 m long CPMU, with 158 1.9 cm periods located in a high-β 8 mstraight section. Its brightness and flux through an aperture as calculated by SPECTRA are shown in Figure 11.14.2 (see also Section 11.2.). Note that due to the lower beam divergence, this device produces higher flux through the aperture in a high-β 8 m straight section than in a 5 m straight.

11.14.1.2 Focusing Optics

Tentatively, the focusing optics at this beamline will be a pair of KB mirrors. At 30 m from the source, the FWHM beam spot is ~0.53 mm (H) × 0.34 mm (V) (calculation by XOP/XUS, 12 keV, fifth harmonic). Assuming that the x-ray incident angle onto the primary KB mirror pair is 3 mrad, mirror lengths of 0.4 m (H) and 0.2 m (V) result in an effective aperture of 1.2×0.6 mm^2 and will capture most of the x-ray beam. With these short lengths, it is relatively easy to achieve low figure error.

Note that the field of x-ray focusing optics is quickly developing. By the time this beamline is built, alternative focusing optics such as compound refractive lenses may offer better performance then mirrors, especially for experiments that require relatively high x-ray energies (>20 keV).

11.14.2 Performance Estimate for the Main SAXS Station

The performance estimate below assumes 12 keV x-rays (K=1.322). At this energy, the flux captured by the primary focusing mirror, or an equivalent aperture of 1.2 mm × 0.6 mm at 30 m from the source is 3.7×10^{14} ph/0.1%BW. As this is only a preconceptual design, the figure error of the mirrors will be ignored in the simulations.

11.14.2.1 USAXS/SAXS/WAXS

For the majority of the SAXS/WAXS/GISAXS measurements, the primary KB pair will 1:1 focus the beam midway between S_1 and S_2. The sample will be located immediately after the guard slits, S_3. The SAXS detector will be located 2 m downstream of the sample. This detector will be specially designed so that the

scattering at very low angles will pass through the detector and reach the USAXS detector located at the end of the second hutch, 20 m from the sample. The following table shows two typical beamline configurations.

Table 11.14.1 Two Typical SAXS Configurations.

	SAXS/WAXS	USAXS/SAXS/WAXS
S_1 and S_2	0.4 mm (H) x 0.2 mm (V)	0.1 mm x 0.1 mm
S_3	0.8 mm (H) x 0.4 mm (V)	0.2 mm x 0.2 mm
Beamstop	2 mm (H) x 1 mm (V) at 2 m	3 mm at 20 m
q_{min}	$3x10^{-3}$ Å^{-1}	$5x10^{-4}$ Å^{-1}
Beam utilization*	91%	28%

* Percentage of the photons reflected by the KB focusing mirrors that reach the sample.

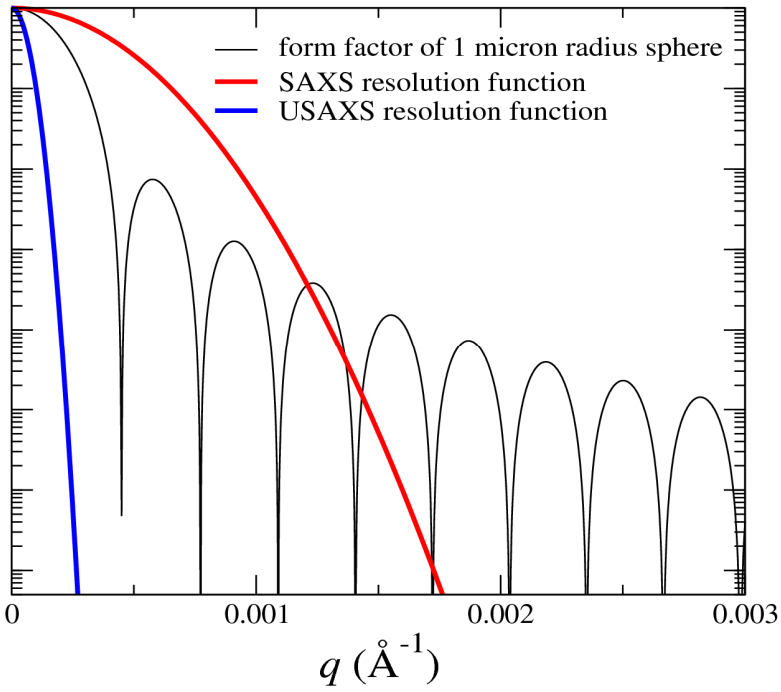

Figure 11.14.3 Width of the resolution for the SAXS and USAXS configurations. Clearly, at very small q, a sharp resolution function is necessary for measurements that involve near-micron length scale.

In the USAXS configuration, the lowest q of 5×10^{-4}Å^{-1} corresponds to more than 1 μm in real space and should be satisfactory for the vast majority of measurements. In fact, this is also roughly the lowest q achievable with Bonse-Hart cameras. For instance the UNICAT at APS advertises a q_{min} of 0.0001Å^{-1} , and corrected example data only go as low as 5×10^{-4}Å^{-1}. For samples with even larger characteristic lengths, topography, or scanning probe microscopy might work better than SAXS.

Note that the USAXS station is an inseparable part of this instrument. The angular resolution in SAXS measurements using slit collimators is determined by three factors. Both the detector point spread function and the beam spot size on the sample in effect smear out the scattering pattern and result in degraded angular resolution. So does the beam divergence seen by the sample. Increasing the sample-to-detector distance reduces the first two contributions; reducing the slits size improves the last two; increasing the distance between S_1 and S_2 improves the last. Although in principle the SAXS detector covers qs that are nearly as low as the USAXS detector, the long distance between the sample and the USAXS detector is necessary. This is because of the q-resolution due to the pixel size of the detector; the beam size on the sample improves with longer sample-to-detector distance. One way to visualize this q resolution improvement is the following. The

beam size and pixel size both smear out the scattering pattern on the detector. The degradation of the image is reduced if the pattern itself is magnified before smearing.

11.14.2.2 Microbeam SAXS

The second pair of KB mirrors provides beam sizes down to a few microns. This is done in combination with the primary KB pair, which first focuses the beam at S_B with ~2:1 demagnification. The second KB pair then images the virtual source defined by S_B to the sample position. The combined effective demagnification is ~10:1.

Since the FWHM source size is ~300 μm (H) and ~10 μm (V), a 10:1 demagnification is not sufficient to reduce the focused beam size to ~1 μm in both directions. Instead, the actual beam size at the sample will be tailored by adjusting the aperture size of S_B. On the other hand, the beam divergence, limited by the accepting angles of the first KB pair, is 0.04 (H) × 0.02 mrad (V) (1.2×0.6 mm at 30 m). The divergence of the beam focused at the sample will be therefore 0.4×0.2 mrad, translating into minimum qs of 0.005 $Å^{-1}$ (H) and 0.003 $Å^{-1}$ (V). The aperture size of S_0 provides control on the beam divergence. Again, the micro-focusing optics is not required to be a KB mirror pair, but it should have long working distance to allow space for auxiliary instruments such as an optical microscope to perform simultaneous multi-probe measurements.

11.14.2.3 USAXS with a Linear Detector

For measurements that request very low q, it is possible to use the beamline in a configuration similar to a Kratky camera. In this configuration, the beam is focused the vertical micro-focusing mirror to a linear detector at the end of the beamline. The FWHM beam size will be ~60 μm at the detector, mainly due to figure error of the focusing mirror (assumed to be 0.1 μrad, which will be the target of R&D). A beam stop size of 0.3 mm is feasible. The lowest q can therefore be reduced by a factor of 10 compared to the USAXS configuration described in Section 11.14.2.1, not considering the background scattering from the slits. Again, the discussion above on angular resolution still applies. A tight slit collimation or data de-smearing will be necessary.

11.14.2.4 USAXD with Long Working-Distance Focusing Optics

Compound refractive lenses can focus the x-ray beam into a sub-micron spot. As in visible optics, when the sample is positioned before the lens, the pattern at the back focal plane of the lens is the Fourier transform of the sample transparency. The resolution of the scattering pattern is limited by the size of the focused beam (in fact, this is always the case when focusing the beam at the detector in a diffraction experiment). It has been demonstrated [11.14.1] that, with long lens working-distance (3 m) and sufficient resolution of the detector, this method can record diffraction patterns from crystals of micron-sized and larger particles.

11.14.3 Supporting Facilities

Ideally there should be two labs associated with this beamline. One will be used for preparing biological samples that require wet chemistry. Beside a water purifier and several sinks, this lab should also be equipped with standard biochemistry instruments such as balances, pH m, refrigerators and incubators, etc. The second lab will be used for polymer type of work using organic solvents (e.g., chloroform) and must have one or two fume hoods that can handle these solvents. A shared clean room is also desirable.

Reference

[11.14.1] A.V. Petukhov, J.H.J. Thijssen, D.C. 't Hart, A. Imhof, A. van Blaaderen, I.P. Dolbnya, A. Snigirev, A. Moussaïd, and I. Snigireva, “Microradian X-ray diffraction in colloidal photonic crystals,” *J. Appl. Cryst.* **39**:137 (2006).

11.15 A Photoemission Beamline, ARPES, at 0.1 meV and 10 meV

11.15.1 Conceptual Overview

Strongly correlated electron systems present some of the biggest challenges in condensed matter physics today. The unscreened interactions between the electrons result in a range of exotic and poorly understood phenomena including high T_c superconductivity in the cuprates, colossal magneto-resistance in the manganites and giant thermoelectric effects in the cobaltates. Several factors can influence the properties of strongly correlated materials including dimensionality, competing orders, disorder and inhomogeneities. By way of example, the nature of the low-energy excitations in any system depends on the *dimensionality* of the system; in 3D systems, the excitations are typically well-defined quasiparticles, whereas in 1D systems, the elementary excitations are collective excitations that represent spin-charge separated entities. In 2D systems the situation is much less clear. Indeed, the nature of the low-energy excitations in the 2D cuprates remains a topic of considerable debate.

Driven by the quest to understand high T_c superconductivity, Angle-Resolved PhotoEmission Studies has again emerged as one of the key probes of the electronic structure and associated dynamics of condensed matter systems. Among the many spectacular successes using ARPES in the study of the cuprates, are the measurement of the doping dependent electronic structures and Fermi surfaces and their dramatic deviation from the conventional rigid band picture, the detection of the d-wave superconducting gap, the observation of an anisotropic pseudo-gap, and the discovery of a mass-renormalization associated with possible strong electron boson coupling. Indeed the latter observation has raised the hope that the mechanism of high temperature superconductivity may finally be resolved.

Outside of studies of the cuprates, the ARPES technique has had significant impact on a range of other problems in condensed matter including electron-phonon coupling, charge density wave transitions, and the formation of quantum well states in thin films and multilayers. In the latter area, the extension of the technique to include the capability of measuring spin polarization of the photoemitted electrons as well as energy and momentum has enabled the identification of spin-polarized quantum well states in the technologically important magnetic multilayers. Indeed, it was the Spin Polarized PhotoEmission Studies of these systems that first pointed to the importance of understanding the spin-dependent scattering at the interfaces in the multilayers. SPPES has also proven important in the study of a range of other low-dimensional magnetic systems, including surface and thin films.

The classical Fermi surface probes—such as de-Haas, van-Alphen, positron annihilation, and Compton scattering—apply only to the analysis of bulk materials but do not easily allow the mapping of the Fermi surfaces of 2D structures such as ultrathin films. Photoemission, on the other hand, can provide k-resolved maps of the Fermi surfaces of these interesting systems. This information is an important component in obtaining a full understanding of the physical behavior of such nanostructures. This is particularly true in the field of magnetic nanostructures, where the possibility of useful technological application has stimulated a considerable effort in generating remarkable spintronic devices.

Here we outline the preconceptual design for a beamline that will combine the unique capabilities of NSLS-II with further developments in these spectroscopies and with the use of Molecular Beam Epitaxy for the growth of thin oxide films. This latter capability will dramatically enhance the range of materials available for study as it will remove the current restrictions associated with the “cleavability” of samples and will also allow the detailed study of atomically engineered nanoscale systems with both magnetic and nonmagnetic ground states.

11.15.1.1 Source

Undulators to cover the range 8–1500 V must be slightly aperiodic to suppress higher orders and must be capable of circular polarized light over the range 400 to 2000 V, to cover the TM L edge and the RE N edge.

11.15.1.2 Optics

This beamline optics is essentially similar to the one for high-resolution soft X-rays, but extending its range down into the UV, from 8 – 1500 V. The design is with plane gratings of variable spacings. Energy resolution will be ~0.2 meV at 10 eV and ~15 meV at 1000 eV. The spot size for the first end station is 10 μm and for the second end station is 1 μm.

11.15.1.2.1 Motivations/Justifications for Source and Optics

The **very low energy range** (down to 8 eV) is required for bulk-sensitive measurements, because at the lower energies the escape depth of the photoemitted electrons is considerably longer. Furthermore, the very highest energy resolution will be achievable at the lowest energies.

The **high-energy r**ange (up to 1500 eV) allows the excitation of many core-levels and therefore permits XPS for sample characterization. However, the high energies can also be used as a means of achieving more bulk sensitivity, both in direct photoemission and in resonant photoemission. The latter technique will allow studies of the site-specific electronic structure. The limit of 1500 eV has been chosen as a compromise to cover the L edges of the TM and some of the N edges of the RE, but at the same time allow the dimensions of the (entrance) mirrors to be reasonable.

11.15.1.2.2 Circular Polarization

In the study of magnetic multilayers, is it very useful to have an element-sensitive probe of the magnetic properties of a multilayer; this also provides a bulk sensitivity that will complement the surface sensitivity of SPPES.

Well-focused photon beams on the samples will enable studies of nanoscale systems, with an emphasis on studies of the inherent inhomogeneities. This also recognizes that in the field of strongly correlated systems, many newly discovered materials are initially very small in size, on the order of tens of microns.

11.15.1.3 End Stations

The proposed beamline would have two photoemission end stations. The first would be optimized for ultrahigh-resolution photoemission for Fermi surface mappings and studies of low-energy excitations, and would have as its main components a 2D electron spectrometer coupled to a low-temperature cryostat for sample cooling down to 1K. It is also possible that the 2D electron spectrometer in this end station will be replaced by a new time-of-flight detector currently being investigated at BNL. The second end station will also be equipped with an electron spectrometer, but this will be coupled to a vectorial spin-detector for studies of magnetic systems. In this second end station the sample cryostat will cool down to approximately 10K. These two end stations will be in-line, separated by refocusing optics to further reduce the spot size in the second end station. A state-of-the-art MBE system for in-situ preparation and characterization of films and multilayers with atomic level control will be shared and accessible by the two end stations.

A schematic of the envisioned system is shown in Figure 11.15.1.

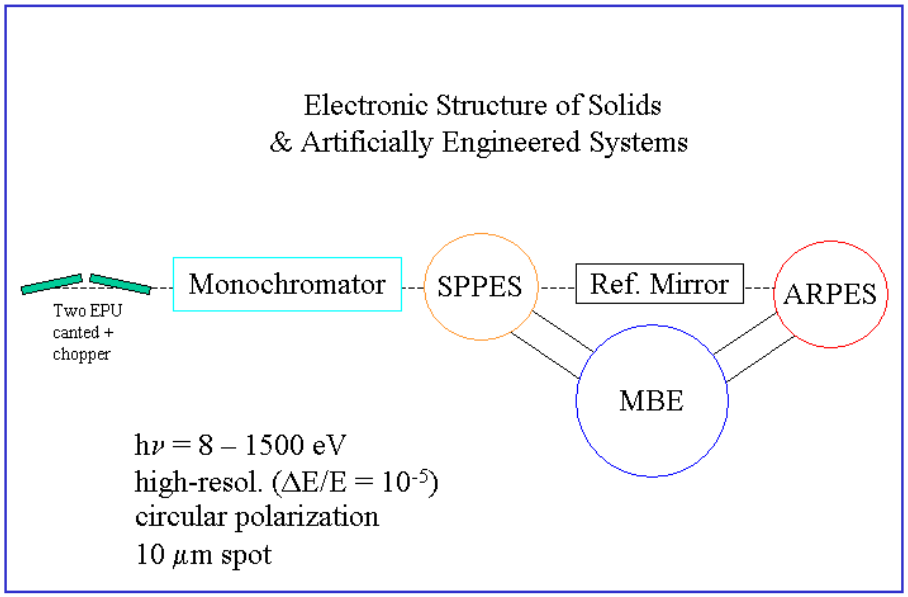

Figure 11.15.1 Schematic of the proposed photoemission beamline at NSLS-II.

11.16 X-Ray Bending Magnet and Damping Wiggler Beamlines

Three different general kinds of beamlines that view bending magnet or damping wiggler sources are envisioned.

One type of beamline would deliver white beam to the experimental station. X-ray topography and x-ray footprinting alike would benefit from access to such a beamline. A focusing mirror could be installed to increase the intensity of the white beam delivered to the sample and also tailor the spectrum (i.e., eliminate high photon energies).

A second type of beamline would be a tunable, monochromatic beamline using a double-crystal monochromator with no focusing elements. Various kinds of EXAFS, powder diffraction, x-ray standing wave, and x-ray topography experiments would benefit from access to such a beamline. Also, for experiments that require high photon energies (above ~20–25 keV), this sort of beamline might be useful, because focusing mirrors are unlikely to work well at such high energies, and sagittal focusing using the second monochromator crystal becomes more challenging using the Bragg geometry.

A third type of beamline would be a tunable, monochromatic beamline using a double-crystal monochromator with focusing elements, either focusing mirrors or sagittal focusing crystals, or both. EXAFS, photoemission, some x-ray standing wave, and some powder diffraction experiments would benefit from access to this beamline. X-ray crystallography and scattering experiments in general would also benefit, but those beamlines are addressed by other aspects of the proposed design. A tunable monochromatic beamline might also incorporate a collimating mirror upstream of the monochromator, to reduce the vertical beam divergence as much as possible, improving the energy resolution of the monochromator.

All three types of beamlines could be arranged to view bending magnet and damping wiggler sources alike. They would, however, possess distinguishing characteristics, depending on which kind of source is viewed. The beamlines that view the damping wiggler sources would require crystal monochromators and white beam mirrors (if desired) that must cope with the high heat load produced by such sources. The

beamlines that view the bending magnet sources, on the other hand, would not be faced with such a challenge, and crystal monochromators that are used on x-ray bending magnet beamlines might need only relatively minimal cooling. (NSLS-II bending magnet beamlines would have to deal with half the power of current NSLS x-ray bending magnet beamlines, and a beryllium window, if used, would absorb most of that power.)

Owing to the higher energy spectra produced by damping wiggler sources, the damping wiggler beamlines and hutches would need significantly more radiation shielding than the bending magnet beamlines would. In fact, for the bending magnet beamlines, the stainless steel vacuum beam tubes and chambers that will be used in these beamlines would probably provide sufficient shielding.

Finally, given the foreseen high demand for access to beamlines that will view damping wiggler sources, we are investigating the possibility of using canted damping wigglers installed in single straight sections, with each canted wiggler serving an independent beamline. We envision a canting angle, between successive damping wigglers, of between 3 and 5 mrad (this is discussed briefly elsewhere in the CDR, and will be addressed in more detail in the Title I and Title II designs); at a later stage it will be determined what canting angle could be achieved. Designing a sector of such beamlines could pose a significant challenge due to space restrictions, but could be simplified if one beamline in such a sector is designated to provide strictly white beam to the experimental station, without optical components (or perhaps just a single mirror). The white beam experimental station that terminates such a beamline could be positioned somewhat upstream in the sector, and beam tube(s) through which the adjacent canted wiggler beam(s) would transit could span through such a station, with the relevant optics positioned downstream. Also, horizontally deflecting optics such as mirrors or monochromator crystals could be installed to further separate the beams that are produced by the canted damping wigglers.

Because of the range of experimental techniques that would be addressed by these beamlines, in this section we address the implications of selected techniques for the beamline and end-station designs, beginning with EXAFS, which is likely to be the application most in demand on these beamlines. Thus, most of this section addresses EXAFS considerations for these beamlines. Many of these considerations apply also to the other techniques that would be addressed by these beamlines. X-ray photoemission would benefit from access to these beamlines as well, but would have end-station needs similar to those of photoemission setups on VUV and soft x-ray beamlines; therefore, the relevant considerations are not described here. In fact, photoemission setups would benefit from simultaneous access to the VUV, soft x-ray, and hard x-ray ranges, and therefore a photoemission beamline might incorporate optics that address each of these energy ranges.

11.16.1 EXAFS Considerations

The two paramount requirements for EXAFS are energy range and stability. EXAFS scans typically extend 1 keV above the absorption edge, and edges for elements of interest range from 1 to 35 keV. The available broad-spectrum ranges for damping wiggler and bending magnet sources (7–35 and 1–7 keV, respectively) combine to fit this requirement, with 80 to 90% of expected analyses needing a damping wiggler source.

Stability requirements include both energy and positional stability. Energy stability, the repeatability or energy drift over time, is vital to near-edge spectroscopy for speciation and oxidation-state identification. The required energy stability is <0.1 eV. Positional stability, critical for heterogeneous samples and for Grazing Incidence XAS applications, refers to the location of beam relative to the sample over time and over a 1000 eV energy scan. For bulk XAS, beam position should not vary by more than 50 μm, or 10% of the microbeam spot size. Both the required energy and positional stability can be achieved with a combination of engineered design and dynamic feedback within beamline optics. For example, NSLS beamline X15B achieves <10 μm positional and <0.1eV energy stability over 72 hours, 140–280 mA ring current, and 800 eV scans, with a 0.75 mm spot size at 2.15 keV [11.16.1]. It is anticipated that *ring* stability issues will be significantly improved at NSLS-II as a result of top-off mode and the increased attention placed on electron beam stability and noise mitigation (mechanical, thermal, and acoustic) throughout the facility. It is imperative, then, to

ensure that *beamline* design maintains that degree of stability, and does not introduce noise or variations with energy.

11.16.2 Configuration for Canted Damping Wiggler Sources

Here we describe an example beamline layout and optics configuration for two beamlines that view canted damping wiggler sources, as shown in Figure 11.16.1. The associated hutches are shown in Figure 11.16.2 These examples are optimized for 7–25 keV, the energy range applicable to most bulk XAS and microbeam applications, and illustrate some application-specific requirements (e.g., environmental science and geoscience). Beamline and end-station components in these examples are as follows:

1. A beryllium window isolates the beamline vacuum system from the ring vacuum, and absorbs much of the lowest-energy power/heat load. For a high-power damping wiggler source, it will also be necessary to provide carbon filters (described elsewhere in this document) before the beryllium window to absorb the lowest-energy portion of the wiggler spectrum, or to furnish a diamond window (instead of a beryllium window) that would also serve a filtering purpose (this is described elsewhere in the CDR).
2. There will be beam-defining apertures and beam diagnostic instrumentation.
3. A harmonic-rejection/collimating mirror conditions the beam prior to the monochromator to eliminate higher harmonics and to enable maximum energy resolution from the monochromator. This may not be needed for the higher energy ranges of the damping wiggler beamlines (where harmonics are not an issue and the source is already well collimated), but would be important for most XAS applications in the 7–25 keV range. For microbeam applications, the focusing optics can assume the harmonic-rejection role.
4. A double-crystal monochromator, water- or cryogenically cooled, will have the required energy and positional beam stability (a fuller description appears in Section 11.3). Current monochromators for conventional hard x-ray beamlines employ two nondispersive (parallel) Bragg reflections from an appropriate crystalline material, the most common being Si(111), suitable for 2–24 keV. Other materials include Si(311) for higher energies, and Ge, InSb, YB_{66}, quartz, and beryl for lower energies. For silicon monochromators it is possible to fabricate such double-crystal monochromators as a monolith (i.e., a channel-cut monochromator), although consideration must then be given to the change in exit-beam height with energy. New natural and synthetic crystalline and assembled multilayer or grating materials are being developed that will have improved resolution and stability, compared with materials currently in use. Because higher resolution naturally results in narrower bandpass (and lower flux), the brighter sources at NSLS-II will enable the use of these new materials.
5. Macro-focusing optics will be used to collect a substantial fan of radiation (up to ~1 to 2 mrad) and focus it to ~1 mm at the sample. This allows for smaller samples, lower concentration, and also provides a longer beamline length for the geometric considerations of having two canted damping wiggler beamlines separated by only a few mrad. Focusing can be achieved using either a mirror or sagittal focusing of the second crystal of the monochromator.
6. There will be a final beryllium window vacuum barrier.
7. Micro-focusing optics will consist of advanced KB mirror optics or hard x-ray zone plates. Variable focus (~10 to ~1 μm) will tailor resolution to specific experiments. Focal length needs to be long enough to accommodate a variety of sample types as well as fluorescence detection and optical imaging apparatus.
8. The sample stage will have important features including high translation and rotation resolution, cooling capability, high-quality optical imaging, and adaptability for various sample types, in-situ cells, solid or liquid samples, and different mounting materials. Motion should include rotation and should enable both horizontal and vertical sample orientations for Grazing-Incidence XAS. Detectors will include I_0, transmission and reference channels, advanced solid state detector arrays for high-throughput/low target

signal fluorescence detection, simultaneous powder/micro-diffraction, and available electron-yield detection.

9. The end-station enclosure (within the experimental hutch) will be suitable for experiments requiring a controlled atmosphere (e.g., environmental science and catalysis). This enclosure will be capable of operation open to air, as a vented fume hood, or as a "glove box" for sample manipulation and analysis under controlled atmospheres (especially for oxygen-sensitive samples). Both the stage and enclosure should be designed to accommodate radioactive samples, with respect to containment, survey, and decontamination.

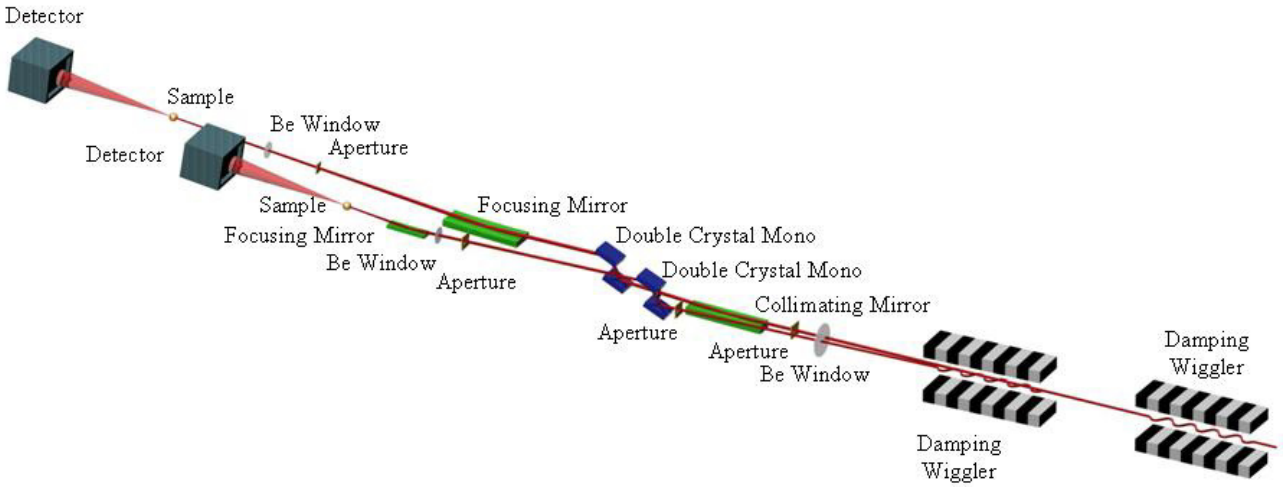

Figure 11.16.1 Conceptual view of canted damping wiggler beamlines.

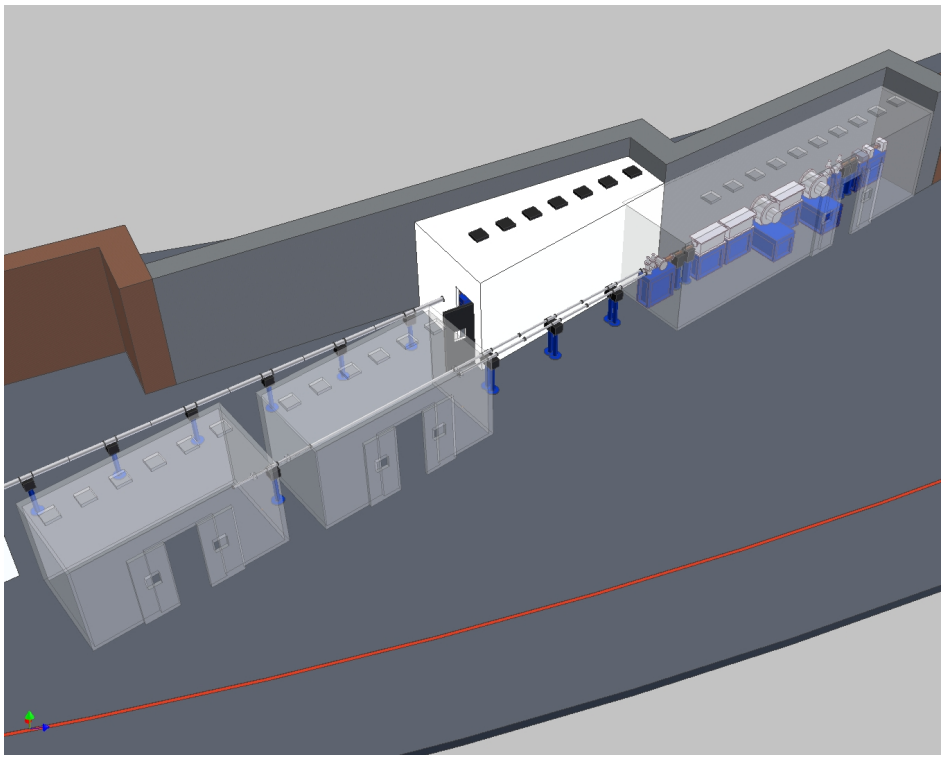

Figure 11.16.2 Conceptual layout of hutches associated with canted damping wiggler beamlines shown above. The white hutch illustrates a potential adjacent bending magnet first optics enclosure.

11.16.3 Configuration for Bending Magnet Sources

Here we describe an example beamline layout and optics configuration for beamlines that view bending magnet sources, as shown in Figure 11.16.2. Note that these examples are optimized for 1–7 keV, the energy range applicable to light element and specialized bulk XAS and microbeam applications (e.g., applications described in [11.16.2]). Here we call attention only to differences in the components compared with their counterparts in damping wiggler beamlines:

1. Bending magnet beamlines used below 4 keV cannot have a primary beryllium window. Instead, for these beamlines a thin (~2 μm) carbon foil would serve as a differential-pumping vacuum barrier and an absorber of very-low-energy power.

3. Harmonic rejection is especially important for lower energy ranges, where the harmonics are likely to reach absorption edges of transition metals or other common matrix elements. This mirror also protects monochromator crystals that are sensitive to radiation damage. For example, beryl crystals, used in the 800–1500 eV range, are destroyed by radiation of energy greater than 5 keV.

5. Macro-focusing optics on bending magnet beamlines would collect a wider (~3 mrad) fan than counterpart optics on damping wiggler beamlines. Essentially, this is made possible by the steeper incidence angles at lower photon energies used with focusing optics such as toroidal mirrors.

6. The final beryllium window vacuum barrier must be ultrathin and suitable for x-rays of energy >1 keV. A polymer-supported beryllium window 12 μm thick has been tested and is currently in use at NSLS beamlines X15B and X19A. This is essentially transparent above 1.8 keV and has acceptable transmission down to ~1 keV, while isolating high vacuum from He atmosphere (Moxtek Corporation).

7. There would be secondary focusing optics for microbeam.

8. This end-station enclosure would typically operate with a helium atmosphere for the transmission of low-energy beam.

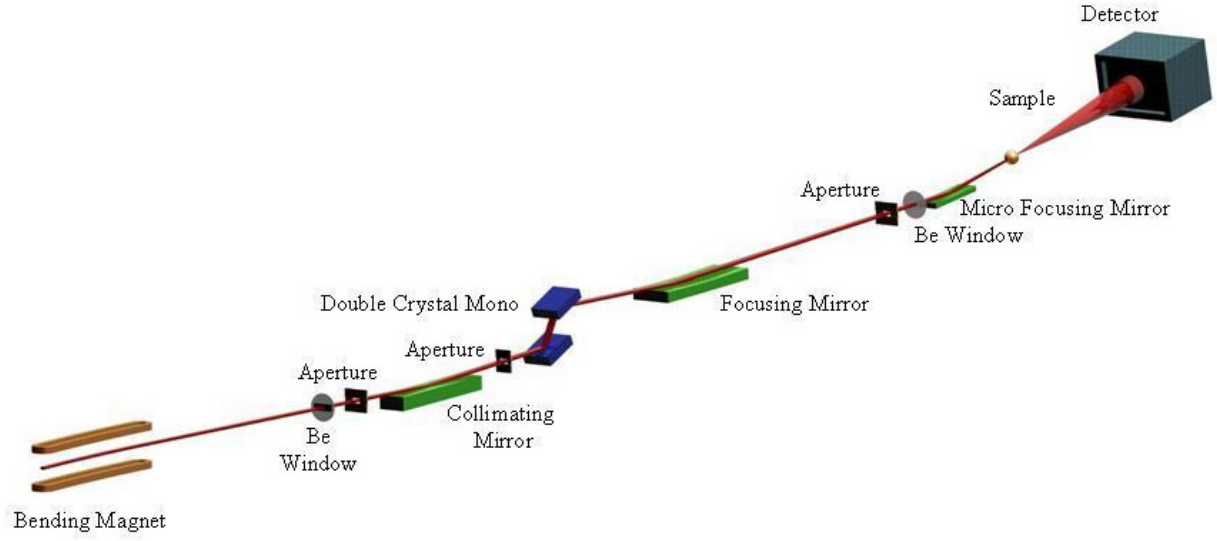

Figure 11.16.3 Conceptual view of a generalized bending magnet beamline. The second focusing mirror (“micro focusing”) is optional.

11.16.4 Computing and Controls

All NSLS-II beamlines will have a uniform control system interface, as described in Section 11.6. Specific operations for XAS and microbeamlines include control of monochromator energy, spot size and focus, sample position, optical image capture, and detector control. It will be useful to have capabilities for automation of a series of scans or sequence of samples, as well as for on-the-fly data evaluation. Quick-EXAFS data collection (i.e., very rapid scanning of the monochromator through the entire EXAFS scan range) will be important, as will 2D and 3D spectroscopic image analysis.

11.16.5 Conventional Facilities

Conventional laboratory facilities are needed for sample preparation, mounting, and characterization; microscopy with image capture; powder and solution mixing; anaerobic handling in a glove box (with anaerobic transport of samples to interface with the beamline end station enclosure); and handling of the BNL "benchtop dispersibles" classification of radioactive materials. These needs are expected to be met with the Laboratory Office Buildings of NSLS-II.

11.16.6 Special Considerations for Biological X-Ray Absorption Spectroscopy

X-ray Absorption Spectroscopy can be used to measure the transition of a metal atom from core electronic states to excited electronic states [11.16.3]. Spectral analysis near this transition, "X-ray Absorption Near-Edge Structure," provides information on the metal's charge state and geometry. Spectral analysis above the absorption edge (up to 10–15% above the edge in energy), "Extended X-ray Absorption Fine Structure," provides complementary structural information, such as numbers, types, and distances of ligands or neighboring atoms. Both techniques are valuable for studying a variety of metal sites in biological systems. Recently, these techniques have been extended to metallo-proteomics methods, where hundreds of proteins are assayed for their metal content [11.16.4]. The user group for biological XAS at the existing NSLS has been substantial and is expected to be productive for the foreseeable future.

Traditionally, XAS, like most other spectroscopies, has been used as a static probe of structure. NSLS-II, with the 100-fold higher flux densities available from damping wigglers compared to NSLS x-ray bending magnet sources, provides the opportunity to extend x-ray absorption measurements into the time-resolved realm, potentially revolutionizing the study of biochemical and bioinorganic systems. For example, proteins containing metal (hemoglobin is an example) react over extremely quick time scales, sometimes as fast as a picosecond. NSLS-II will allow much faster time scales to be probed than can be done currently with XAS; this capability will be provided by a combination of timing studies (pump-probe), fast mixers (on the microsecond timescale), and freeze–quench devices [11.16.5].

11.16.7 Anticipated Beamtime Demand vs. Capacity

Most EXAFS applications and demand will be for damping wiggler sources. Efforts to increase this capacity include using canted shorter damping wigglers to supply radiation to multiple beamlines, and using more creative beamline designs, such as beam-splitting optics. Although this is still under evaluation, as described elsewhere in the CDR, for canted damping wiggler sources the photon beams radiated by each may only be separated by up to a few mrad. This geometrical challenge can be addressed by sharing enclosures and shielding, staggering the position of optical elements and of end stations, and incorporating opposite vertical offsets for monochromators and mirrors to afford the greatest possible separation between beamlines.

While the NSLS-II damping wiggler beamlines will far outperform the current NSLS EXAFS and microprobe beamlines (as well as all second- and third-generation synchrotron bending magnet lines worldwide), that does not necessarily translate into faster throughput of experiments. The historic trend in

worldwide synchrotron development is that brighter beam enables more difficult experiments, which use as much, or more, beamtime.

11.16.8 Powder Diffraction Considerations

Powder diffraction is one of the most widely used techniques in modern materials science, and the advent of synchrotron radiation sources has enormously broadened the power of the technique. It is now nearly routine to solve complicated crystal structures from powder data alone, and time-resolved in-situ powder diffraction measurements of materials such as catalysts being formed are of great interest. These measurements are generally possible only with intense synchrotron sources. Every major synchrotron x-ray source in operation has a beamline dedicated to powder diffraction, and NSLS-II will be no exception.

We propose a station very similar to the successful (former) BM16 at ESRF or 11BM at APS. In general, bending magnet sources are suitable for general-purpose powder diffraction, because the experiments make use of rather large beams (on the order of millimeters in each dimension), and good angular resolution is required in only one (vertical) direction. The comparative flux characteristics of the NSLS-II damping wiggler and bending magnet sources, however, make it clear that the needs of powder diffraction at NSLS-II will mainly have to be addressed by damping wiggler sources. Requirements for a general-purpose powder diffraction beamline are as follows:

Tuning range of 5 to 50 keV to allow resonant diffraction experiments across a wide range of the periodic table and to be able to measure samples of high Z in capillaries.

Sufficient access to the sample to allow environmental chambers (e.g., cryostats, furnaces, reaction cells) to be used. With careful design, this can probably be realized from only one side, so that components of another beamline can be, say, 30 cm on one side of the sample position. This would permit the powder beamline to share floor space with another beamline using canted damping wigglers to provide radiation to both beamlines.

Two detector sets should be provided to permit high resolution ($\delta d/d \sim 10^{-4}$) and moderate resolution (5×10^{-3}), with the latter capable of providing continuous readout. We propose to equip the beamline with a tunable multi-analyzer stage, so that on the order of 10 diffraction angles, separated by approximately 2°, are read out simultaneously with an angular resolution on the order of 0.005°. The beamline would also have a position-sensitive detector such as a multichannel Si strip detector. Both detector sets would be permanently mounted on a single two-theta axis, so they could be used with negligible setup time. Siddons has demonstrated a technique to obtain high-resolution data sets in real time based on a bright converging beam, such as from a multilayer, with a detector in Rowland circle geometry; the proposed beamline could also be used in that mode, and it would be again developed to minimize setup time.

The source flux available from a damping wiggler, ranging from 4×10^{15} to 1×10^{14} ph/s/10^{-3}BW/mrad over the range of 5 to 50 keV, compares extremely favorably to that from bending magnets at ESRF (1×10^{13} to 5×10^{12}), APS, and current NSLS (1.5×10^{13} at 5 keV, 1×10^{12} at 30 keV). Proposed beamline optics would consist of an initial collimating/focusing mirror and a double-crystal monochromator containing a sagittally bent second crystal, providing a focal spot size on the order of 0.5 mm square (and unfocused beam could be provided by flattening the second crystal). The beam would be sufficiently intense that it could be easily masked down to ~100 $(\mu m)^2$ for diamond anvil cell experiments. Focusing could be relaxed for samples that are available in larger quantities, to reduce radiation damage, if needed.

11.16.9 X-Ray Topography Considerations

X-ray topography techniques benefit greatly from access to extended beam fan, continuous spectrum sources, such as bending magnet sources [11.16.6]. Most useful topography experiments are carried out using

photons in the energy range from 6 to 120 keV. To address the need for continuous spectrum, extended beam fan for this photon energy range, we envision that access to damping wiggler beamlines will be necessary.

Two types of beamlines would be useful for x-ray topography experiments. The first would be, simply, a beamline that delivers white beam to a five-circle goniometer at the experimental station. Small source size and long beamline length would be essential for such a beamline, to maximize both the spatial resolution capability and the area of the beam delivered to the experimental station. For example, beamline X19C at NSLS has a length of 25 m, which results in a very respectable spatial resolution capability of 0.1 μm per cm of specimen-film distance and a beam size of 5(H)×0.6(V) cm at the crystal. Beamline ID19 at ESRF (which has two undulators and one wiggler) has a length of 145 m, resulting again in submicron spatial resolution per cm of specimen-film distance and a beam size of 4.5×1.5 cm. The small source size and long beamline length also provide a high degree of coherence, which opens up the possibility of phase-contrast imaging supplemental to x-ray topography imaging.

The second type of x-ray topography beamline would be a tunable, monochromatic beamline using a double-crystal monochromator with no focusing elements. This would be suitable for monochromatic x-ray topography experiments and especially suitable for studies of relaxation in heteroepitaxial layers (particularly dynamic studies). This facility would be equipped with accurate slits (down to a few μm in width) to allow section topography imaging. On this beamline, a high-precision vertical diffractometer to allow high-resolution diffractometry in combination with diffraction imaging would also be very desirable, with the built-in possibility for small beam size spatial mapping of rocking curves.

Since high-resolution x-ray film is still the best large-area, high-resolution, continuous-contrast detector available, both types of beamline would require access to darkroom facilities located near the beamline. (X-ray topography is a very labor-intensive technique that requires constant online decision making based on the results of iterative changes in diffraction geometry.) Currently, high-resolution film is capable of 1 to 2 microns spatial resolution over a field of view as large as a sheet of 8×10 inch film (large fields of view become increasingly important as the size range of semiconductor wafers continues to expand). This, coupled with the dynamic range necessary to provide good defect contrast offered by these x-ray films, means that this type of detector will remain the one of choice for the foreseeable future.

11.16.10 X-Ray Footprinting Considerations

For several years, Synchrotron Footprinting technology has been used to map the solvent accessibility of reactive probe residues in proteins and nucleic acids as a function of binding interactions, conformational changes, and folding processes [11.16.7]. SF combines a number of state-of-the-art techniques. These include 1) the use of synchrotron radiation light sources, 2) the chemistry of radiolysis and interactions of hydroxyl radical with nucleic acids and proteins in aqueous solution, 3) mixing technologies to initiate rapid reactions, and 4) analytical tools for the detection of radiolysis products of nucleic acids and proteins. These technologies have been implemented at NSLS with great success. Footprinting studies of nucleic acids are routinely conducted with x-ray exposures of tens of milliseconds, which include studies of nucleic acid folding and their interactions with proteins. This technology can also be used to study protein structure and dynamics in solution as well as protein–protein interactions in large macromolecular complexes. Their success has stimulated adoption of these approaches at ESRF and the Brazilian synchrotron source, LNLS.

At NSLS-II, the higher white beam flux densities available at damping wiggler beamlines will allow highly enhanced footprinting studies to be carried out. These beamline improvements will overcome the effects of intrinsic and extrinsic scavengers and allow faster time-resolved experiments. Time-resolved measurements using SF, both in vitro and in vivo, would provide a unique approach to better understand fundamental processes relating to macromolecular folding and the assembly of nucleic acids and proteins and their complexes essential to cell biology. The timescales of these processes are seconds to milliseconds to microseconds, depending on the system under study. For in vitro studies, current technology can access the millisecond timescale, but many processes on the microsecond timescale are not amenable to study, due to

insufficient flux density. For in vivo studies, even structural examination on the seconds timescale is not achievable, in many cases. The new NSLS-II facility could allow structural probes on biologically relevant timescales (milliseconds or faster) in real time, in vivo. The SF technique continues to have unique capabilities, one of which is the prospect for examining macromolecular structure in vivo. Proof that such approaches are feasible was recently demonstrated by an NSLS user at X28C; this provides an exciting new avenue for technology development for the resource. However, the limitations of existing beamlines make it unlikely that these advances can be fully exploited without NSLS-II.

References

[11.16.1] See, for example, Brandes and Northrup (2006), "High-resolution phosphorus K-edge XANES of phosphate minerals," in prep for *American Mineralogist.*

[11.16.2] Akabayov et al., 2005 "Using softer X-ray absorption spectroscopy to probe biological systems" *J. Synchrotron Radiation* 12, 392).

[11.16.3] Ascone, I., et al., Metallogenomics and biological X-ray absorption spectroscopy. *J Sync. Rad*, 2005. **12**(Pt 1): p. 1–3; Ascone, I., R. Fourme, and S.S. Hasnain, Introductory overview: X-ray absorption spectroscopy and structural genomics. *J Sync. Rad*., 2003. **10**(Pt 1): p. 1–3; Lippold, B., et al., Towards an automated quality control of XAS data. *J Sync. Rad*, **12**(Pt 1) p. 45 (2005); Scott, R.A., et al., Bottlenecks and roadblocks in high-throughput XAS for structural genomics. *J Sync. Rad*. **12**(Pt 1) p. 19 (2005).

[11.16.4] Shi, W., et al., Metalloproteomics: High-throughput structural and functional annotation of proteins in structural genomics. *Structure* **13**(10) p. 1473 A9 (2005); Chance, M.R., et al., High-throughput computational and experimental techniques in structural genomics. *Genome Res*. **14**(10B) p. 2145 (2004).

[11.16.5] Kleifeld, O., A. Frenkel, and I. Sagi, Time-dependent XAS studies of trapped enzyme-substrate complexes of alcohol dehydrogenase from Thermoanaerobacter brockii. *J Sync. Rad*. **8**(Pt 2) p. 978 (2001).

[11.16.6] White beam synchrotron radiation topography. Miltat, J. NATO Advanced Study Institutes Series, Series B: Physics (1980), B63 (Charact. Cryst. Growth Defects X-Ray Methods), 401-20; Monochromatic synchrotron radiation topography. Sauvage, Michele. NATO Advanced Study Institutes Series, Series B: Physics (1980), B63 (Charact. Cryst. Growth Defects X-Ray Methods), 433-55.

[11.16.7] Maleknia, S.D., et al., Determination of macromolecular folding and structure by synchrotron x-ray radiolysis techniques. *Anal Biochem*. **289**(2) p. 103 (2001); Brenowitz, M., et al., Probing the structural dynamics of nucleic acids by quantitative time-resolved and equilibrium hydroxyl radical "footprinting". *Curr Opin Struct Biol*. **12**(5): p. 648 (2002); Guan, J.Q., et al., Structural reorganization of proteins revealed by radiolysis and mass spectrometry: G-actin solution structure is divalent cation dependent. *Biochemistry*. **42**(41) p. 11992 (2003); Guan, J.Q. and M.R. Chance, "Footprinting Methods to Examine the Structure and Dynamics of Proteins." *Encyclopedia of Molecular Cell Biology and Molecular Medicine*, 2nd ed., R. Meyers, Ed., Wiley Inc. (2004); Guan, J.Q., S.C. Almo, and M.R. Chance, Synchrotron radiolysis and mass spectrometry: A new approach to research on the actin cytoskeleton. *Acc Chem Res*. **37**(4): p. 221 (2004); Takamoto, K. and M. Chance, Footprinting Methods to Examine the Structure and Dynamics of Nucleic Acids. *Encyclopedia of Molecular Cell Biology and Molecular Medicine*, 2nd ed., R. Meyers, Ed., Wiley Inc., 521 (2004); Guan, J.Q. and M.R. Chance, Structural proteomics of macromolecular assemblies using oxidative footprinting and mass spectrometry. *Trends Biochem Sci*. **30**(10): p. 583 (2005).

11.17 VUV and Soft X-ray Bend Magnet Beamlines at NSLS-II

The NSLS-II bending magnets will be excellent sources for certain classes of experiments, particularly in the vacuum ultraviolet and soft x-ray range. The VUV/soft x-ray range provides unique capabilities which coincide with the interests of numerous, diverse research fields. These include investigations into complex materials / correlated electron systems, magnetic materials and spintronics, semiconductor materials and devices, nanomaterials, catalysis and surface science, geology and environmental sciences, polymers and soft matter, structural and cellular biology and other biosciences, planetary science, atomic and molecular electronic structure, and others. VUV and soft x-rays can probe the electronic structure of these materials (spectroscopy) and the physical distribution of spectroscopic features, either by collecting scattering data to arrive at a statistical representation of the sample or by performing real-space imaging using advanced microscopy techniques.

An example from cellular biology will serve to illustrate some of the unique aspects of this spectral range and the benefits of bending magnet sources. With appropriate instrumentation, such as a full-field transmission microscope, soft x-ray imaging can be used to acquire 3D tomograms, with unprecedented resolution, of complete cellular structures in a hydrated environment [11.17.1]. Three characteristics contribute to this capability: illumination by photons with much shorter wavelengths than visible light microscopes; incoherent illumination of the focusing optics, which avoids image speckle; and exploitation of the "water window," that is, the spectral range between the C K-edge (~285 eV) and the O K-edge (~540 eV). In this region, the penetration depth through water is several mm, while absorption of the cellular proteins can be an order of magnitude higher than the surrounding water. Improvements in soft x-ray optics and strategies of "tagging" proteins of interest with various elements, particularly transition metals, should lead to even better cellular imaging capabilities. Also, much of the instrumentation and technique development that is pursued for cellular imaging can be adapted for resonant imaging of other non-crystalline materials.

Of course, the damping wigglers anticipated for NSLS-II will provide very broad spectral coverage (see Chapter 8). In fact, they will be far more powerful sources, in terms of both flux and brightness, than the bending magnets, even in the soft x-ray range. However, the relatively low critical energy of the NSLS-II bending magnets (2.4 keV) severely limits their performance at high photon energies. Therefore, it is anticipated that the damping wigglers primarily will serve the needs of communities that require access to higher energy photons. Some hard x-ray beamlines may be developed on the NSLS-II bending magnets which will provide higher flux and brightness than the current NSLS bending magnets—up to ~4 keV and significantly higher brightness, up to ~12 keV. Nonetheless, it is expected that the available bending magnet ports will be allocated primarily to infrared (see Section 11.18) and VUV / soft x-ray uses.

11.17.1 Monchromator Options

Because of the large variation in wavelengths in the VUV / soft x-ray spectrum, different monochromator designs are required to cover the entire spectral range. Some options are reviewed below.

11.17.1.1 VUV Range: <10 eV–~50 eV

At the low-energy range, a standard monochromator is the Normal Incidence Monochromator design. The typical NIM implementation utilizes a fixed included angle between entrance and exit slits and pre-grating mirrors to focus the beam onto the entrance slit. Post-monochromator mirrors are used to provide a good beam focus at the sample. A major advantage of the design is compactness. For example, at beamline U13UB on the NSLS VUV/IR ring, the total length of the NIM is about 6.5 m and the instrument still provides an impressive resolving power of ~20,000 across its entire operating range (5 – 30 eV).

A major limitation of the NIM is the narrow energy range that it supports. Recently, an extension of the Variable Line Spacing – Plane Grating Monochromator has been proposed. This design, discussed more fully

in Section 11.7.2, has been developed to cover the soft x-ray range (around 100 eV and upwards). The monochromator can cover a lower energy range, down to ~8 eV, with the inclusion of suitable gratings and modifications to the motion of the mirror and grating. In future design stages, the VLS-PGM approach will be evaluated in greater detail to determine its suitability to a versatile bending magnet beamline that can span both the VUV and soft x-ray ranges.

11.17.1.2 Soft X-Ray Range: ~50 eV–2000 eV

In this energy range, compact designs are not feasible; the reflectivity of optical components becomes small at grazing angles larger than a few degrees and optical components are longer. The most common selections are either the fixed-included angle Spherical Grating Monochromator and its derivatives and the variable angle plane grating monochromator and its variants, particularly the VLS-PGM [11.17.2].

Most soft x-ray lines at NSLS use an SGM or variant (e.g., the double-headed dragon design used at beamline U4B). At the time these beamlines were designed, the SGM offered the best solution of design tradeoffs with the available optics; in particular, the figure errors of optics were ~1 arcsec or larger. The SGM approach usually requires the use of gratings at angles away from their most efficient point. Also, a characteristic of SGM designs is a wavelength-dependent focus of the monochromator, which produces a moving source point for downstream optics and end stations. A benefit of the SGM design is simplicity, which is particularly important in alignment of the optics and in operations.

The VLS-PGM approach offers a number of advantages over the earlier SGM designs. The variable incident angle on the gratings improves the efficiency of the monochromator and the gratings are used over a wider energy range. Also, the fixed exit slit provides a fixed source point for downstream components. However, the design requires higher quality optics, and the motions of the monochromator are more complex. Despite these obstacles, the VLS-PGM design and its variants has gained favor at third-generation synchrotron sources.

11.17.1.3 Medium X-Ray Energy Range: ~1000 eV–~5000 eV

This energy range is underutilized in many synchrotron sources. The efficiency of grating monochromators begins to drop off considerably above ~2.5 keV, but the x-ray wavelength at those energies is still not well matched with the lattice spacing of common monochromator crystals. Double-crystal monochromator designs at these energies typically use less common crystals with larger lattice spacings; a list of commonly used crystals is shown in Table 11.17.1. Often, several crystal sets are required to provide coverage across the desired energy range.

Table 11.17.1 Common Crystals in Medium Energy Monochromators [11.17.3].

Crystal type	2D spacing(Å)	Energy Range(eV)	Typical Absorption Edges
Beryl	15.954	800 - 1560	Cu *L*, Na *K*, Mg *K*
YB_{66}	11.76	1070 - 2000	Mg *K,* Al *K*
Quartz	8.512	1500 - 1830	Al *K*
InSb(111)	7.481	1680 - 4000	Si *K*, P *K*, S *K*
Ge(111)	6.532	1930 - 4000	P *K*, S *K,* Cl *K*
Si(111)	6.271	2010 - 4000	P *K*, S *K,* Cl *K*

11.17.1.4 Zone Plate Optics as Monochromators

Zone plates are diffractive lenses whose focal length is wavelength-dependent. In microscopy applications, zone plate lenses are often used as the monochromator as well as the magnification/demagnification optical elements. Zone plates provide modest energy resolution; E/ΔE is typically only around 500–700. Zone plate monochromators are therefore used primarily in situations where elemental contrast in the soft x-ray range is desired for imaging purposes, but detailed spectroscopy is not required.

11.17.2 BM Ports and Beam Extraction

The NSLS-II lattice will accommodate 30 DBA cells. In each DBA cell, however, only the downstream dipole chamber will contain a beam extraction port; an extraction port on the upstream dipole chamber would interfere with the front end of the preceding insertion device.

A choice that must be addressed early in the detailed design process is the location of the first mirror for the BM beamlines. The source divergence from the bending magnets in the vertical direction will be quite small (on the order of 1 μrad) and a mirror of reasonable size will capture all of the beam in the vertical direction. The situation is much different in the horizontal direction. Each dipole will have a horizontal source arc of approximately 105 mrad. At the current design stage, the beam extraction port in the dipole vacuum chamber will accept only 3 mrad of the horizontal fan, with the center of the accepted angle located approximately 10 mrad along the dipole bend. A mirror outside the shield wall will be ~20 m away from the dipole source.

At that distance, even a long (~1 m) mirror positioned at grazing angle of 2° to 3° will accept only ~1 to 2.5 mrad of the horizontal synchrotron radiation fan from the dipole. To decrease the distance to the source and hence increase the collection angle, the first mirror would need to be located inside the shield wall.

In the current design, the beam pipe from the dipole source will run adjacent to the shield wall. This precludes adding a second beam extraction port on a single dipole magnet, as the beam pipe would run inside the shield wall. If all the bending magnet dipoles at the NSLS-II are populated with beamlines, additional capacity may be developed by increasing the number of beam ports available from a single dipole, as is done, for example, at NSLS, SSRL, and ALS. Because of the constraints imposed by the shield wall, this would require the use of mirror optics inside the shield wall to increase the deflection angle and direct the beams through the shield wall.

Any beamline design that incorporates optical elements inside the shield wall may interfere with other components within the storage ring tunnel, and in particular the front end systems. Furthermore, such designs must have fully automated motion, adding cost and complexity. From an operational perspective, beamline modifications that are not automated and require access to the first optic must wait until scheduled maintenance periods. Finally, the higher radiation levels inside the shield wall may affect the optics over time. Should this option be considered in future design stages, a comprehensive assessment of potential radiation damage to the first mirror should be undertaken as soon as practical.

For the reasons outlined in the previous paragraph, it seems prudent to propose beamline designs for the soft x-ray bending magnet ports where the first optic is outside the shield wall. The topic of optics inside the shield wall, however, should be revisited in future design phases of the project.

11.17.3 UV Circular Dichroism

One class of experiments that deserves special consideration is structural biology measurements using UV **c**ircular **d**ichroism (UV-CD) spectroscopy. The wavelength range of interest here is around 150–400 nm (~3–8 eV). The UV-CD technique provides complementary information to protein crystallography and is used to determine, for example, the percentage of α-helix or β-sheet constituents in a protein sample, often in an aqueous environment. UV-CD is particularly useful in situations where protein crystals are not available.

However, signal levels are small and require sensitive polarization modulation and lock-in detection. The difficulty in migrating this program to NSLS-II is the large opening angle used in the collection optics for UV-CD experiments. For example, the two UV-CD beamlines operating on the VUV ring (U11 and U9) accept very large horizontal opening angles: 37 mrad for U9 and 55 mrad at U11. Even with the higher flux of NSLS-II dipoles, at least 20 mrad of horizontal fan will be required to provide a capability similar to current instrumentation. At the current design stage, plans for standard dipole chambers will only accept ~3 mrad of horizontal fan.

The approach envisaged for the NSLS-II infrared beam ports may provide a solution. A mirror that is integral to the dipole vacuum chamber can be inserted. The beam would be focused onto a smaller opening where a second mirror deflects the beam upwards; the beam can then be transported through the shield wall and on to the monochromator and experimental station. Because of the shorter wavelengths used in UV-CD, the number of mirror deflections should be minimized to maintain the flux. Also, the UV mirrors would require different coatings and a more stringent shaping and polishing requirements than IR mirrors.

References

[11.17.1] M.A. LeGros, G. McDermott, and C.A. Larabell, X-ray tomography of whole cells. *Current Opinion in Structural Biology* **15** p. 593 (2005).

[11.17.2] R. Follath, The versatility of collimated plane grating monochromators. *Nucl. Instr. & Meth. in Phys. Res. A*, **467** p. 418-425 (2001).

[11.17.3] From X-Ray Absorption Fine Structure Spectroscopy Group at Daresbury, http://srs.dl.ac.uk/XRS/index.html.

11.18 Infrared Beamlines

11.18.1 Introduction

Infrared synchrotron radiation is a high-brightness, continuum source that excels for microspectroscopy and other low-throughput infrared techniques (diamond anvil cell spectroscopy, very high spectral resolution, very far-infrared and THz spectroscopy) [11.18.1]. Dipole bending magnets serve as optimal long wavelength radiation sources (in contrast to insertion devices) [11.18.2]. Our plans for supporting infrared science are based on extracting long wavelength radiation from the NSLS-II ring. Our goal is to provide a level of performance comparable to, or exceeding, that of the existing facilities at the NSLS VUV/IR ring in terms of brightness and spectral range. Since the infrared performance of most synchrotron facilities is typically limited by beam motion and environmental noise, the NSLS-II facility offers the potential for outperforming the existing VUV/IR ring through significant reduction in these noise sources. With bunch lengths of a few tens of psec, the NSLS-II ring will also offer benefits for time-resolved spectroscopies.

Infrared spectroscopy senses both vibrational and electronic degrees of freedom in materials. The energy of mid-infrared photons matches the characteristic vibrations of molecules, making infrared spectroscopy an important tool for identifying chemical content and structure. Principle applications include investigating the chemical content of heterogeneous materials (e.g., diseases in biological tissues, soils in the environment, and interplanetary particles from comets) and in materials science. The far-infrared and THz spectral range is sensitive to phonons and other collective modes. This includes transport phenomena and the various interactions between electrons and other excitations in a solid, making infrared spectroscopy an important tool for studying complex electronic systems. Phenomena range from excitons in semiconductor nanoparticles to ferroelectricity, magnetoresistance, and superconductivity in complex metal oxides. In many cases, the information complements that obtained from higher energy photons (e.g., photoemission, x-ray spectroscopy, diffraction and scattering), yielding a more complete picture of a material's structure and behavior. The high-

brightness of infrared synchrotron radiation is crucial for a variety of low-throughput techniques. These include microprobes and imaging microspectroscopy, the study of materials at extreme pressures and temperatures in diamond anvil cells, millimeter wave spectroscopy and ellipsometry through high-field magnet cryostats, and ultra-high resolution spectroscopy (to ~100 nanovolt energy resolution). The science mission defines performance goals reaching from the mid-infrared (λ ~3 μm as needed for chemical imaging) to the very far-infrared (λ~5 mm) for magnetic resonance spectroscopies. Such an extremely broad spectral range (at times extending into the visible and beyond) is also crucial for analysis methods that employ Kramer Kronig and sum rule techniques. Dynamical processes can be investigated using any of these techniques by exploiting the pulsed nature of the synchrotron source. Though lasers can probe shorter time scales, no other source allows for such wide spectral coverage.

11.18.2 Conceptual Design

Our original plans called for re-building the existing VUV/IR ring and infrared beamlines into a dedicated source for low-energy radiation and short pulses. This plan was modified due to siting considerations within the NSLS-II facility and the recognition that NSLS-II bending magnets will provide a highly competitive source (and in some spectral ranges, world-leading) in terms of both flux and brightness. The infrared program can then benefit from the same ultra stable, high-brightness electron beam and environment available to x-ray users, including shorter pulses for time-resolved spectroscopies. The proposed front-end design will follow concepts similar to the existing IR extraction from the VUV/IR ring, including a first extraction mirror inserted into the dipole chamber and adjacent to the electron beam [11.18.3]. The balance of a given beamline will have a more robust design to exploit the lower noise environment of the NSLS-II facility. The number and types of infrared beamlines will be comparable to the existing program [11.18.1] on the NSLS VUV/IR ring, plus compatibility with future expansion of ~50%. Our source requirements dictate optimal performance to wavelengths approaching 5 mm, necessitating careful design of the infrared extraction and dipole chamber geometry. We also envision the synchrotron source serving two beamlines equipped with mid-IR microspectrometers having large area focal plane array detectors [11.18.4]. An extended source is suited better than a single point-like source for illuminating an array, so we anticipate using a large horizontal collection of bending magnet radiation for this application.

11.18.2.1 NSLS-II as an Infrared Source

NSLS-II will be a powerful source of IR radiation. See Section 8.4 for a full description of the IR radiation produced by NSLS-II bending magnets.

11.18.2.2 Infrared Beamlines

11.18.2.2.1 Capacity

We propose that the number and type of NSLS-II infrared beamlines roughly match the existing NSLS VUV/IR beamlines at the time of transition to NSLS-II, plus provide the capacity for at least 50% growth. We anticipate the following:

- three mid-IR microprobe beamlines for biological, chemical, materials science, and space sciences (These would share a single standard NSLS-II dipole extraction.)
- two mid-IR beamlines for biological and chemical imaging using FPA detectors, each with an entire horizontal extraction
- one far-IR beamline focusing mostly on magneto-spectroscopy
- one combined mid-IR and far-IR beamline for materials science, including time-resolved spectroscopy
- one combined mid-IR and far-IR beamline for studies of materials at extreme temperatures and pressures (diamond anvil cells with cryostats and laser heating)

As noted in Chapter 8, two or three mid-infrared microprobes can share a single dipole extraction. The mid-infrared imaging microscopes will need the entire 50 mrad of horizontal collection, so each imaging end station will require its own dipole extraction. The far-infrared beamlines will also each require a full dipole extraction, plus the modified, large-gap dipole and chamber to collect the ~32 mrad (or 48 mrad, if feasible) of vertical aperture. Thus, we envision three extraction ports on conventional-type dipoles (one for the three microprobes, two each for the FPA imaging beamlines) and three extraction ports on large-gap dipoles (one each for the three far IR and THz beamlines). A symmetric placement of the large-gap dipoles within the NSLS-II lattice offers potential benefits from an accelerator physics standpoint. Thus, we expect the large-gap dipoles to be arranged in pairs (both dipoles of a cell superperiod) and symmetrically around the ring itself. Installing three sets meets the DBA 30 overall symmetry, and by placing one of these sets immediately downstream of the injection or RF straight sections will allow both dipoles in that cell to be used for infrared extraction. Indeed, we may be able to use the upstream dipole in the other two large-gap cells by suitable construction of the first extraction optic to allow insertion device radiation to pass. Nonetheless, we foresee that a set of three dipole pairs will meet the expected need at the time of transition from NSLS-II plus provide a growth capacity of from one to three additional far-infrared beamlines. The situation for mid-infrared-only beamlines is less complicated, since they will employ conventional dipoles. Three extractions will meet the anticipated needs when NSLS-II begins operations, and the growth capacity for two or three additional extractions can be included to meet future needs.

11.18.2.2.2 Mid-IR Microprobe

The microprobe beamlines require only a small horizontal segment of source (~15 mrad), making these mid-infrared beamlines among the simplest to design and meet performance requirements. We expect to employ a design similar to our existing U2A/U2B ad U10A/U10B mid-IR beamlines on the NSLS VUV/IR ring, using off-the-shelf mirror optics for focusing and steering the beam from the extraction point to the microprobe end station. Small-aperture CVD diamond windows are sufficient for separating storage ring vacuum from the rough (or medium high) vacuum environment of the mid-IR transport optics leading to the end station. These transport optics will provide for horizontal separation of the beam into two or three segments for delivery to individual end stations. A KBr or CsI window at the end of these transport sections will provide added vacuum protection and still provide complete spectral coverage.

11.18.2.2.3 Mid-IR imaging

Here, we intend to use the full horizontal swath (50 mrad) of beam to produce an extended source having significant depth (due to the ~1 meter long source segment). Though segmented mirrors have been used to collect a large angular swath and match it the planar profile of a focal plane array detector, this approach may also introduce undesirable multiple-beam interference effects (between different beam segments). Therefore we will investigate contiguous optical designs (e.g., anamorphic) for reshaping the source and matching it to the square format of most FPAs, while simultaneously matching the large numerical aperture of the FPA objective across the entire field of view. Though the mirror surface may be complex, computer-assisted diamond-turned optics are expected to meet performance requirements. Similar to the microprobe end stations, we expect to use CVD diamond for the UHV window material, and KBr or BaF_2 for the last window before the end station. NSLS is currently attempting to procure a Bruker Hyperion 3000 imaging microspectrometer system with a 64×64 element FPA detector. When combined with a 74X objective, the total effective area sampled by the FPA is about 35 μm squared, and each FPA element corresponds to 0.51 μm, well beyond the diffraction limit. This provides spatial oversampling and enables point-spread-function deconvolution to enhance spatial resolution. Such a system was tested at NSLS beamline U10 in June of 2005 [11.18.4] in order to demonstrate the principles, including the ability to match an extended source to the 35 μm area being sampled. Based on developing interest at NSLS and other SR facilities, we expect the need for two such end stations at the time of NSLS-II operations startup.

11.18.2.2.4 Far-IR and THz

As with the mid-infrared, we will be extracting a large horizontal segment. Even though optical requirements are more relaxed for longer wavelengths, we anticipate using the same extraction system as designed for the mid-infrared imaging. The balance of the beamline can be assembled with conventional mirror optics (like the NSLS VUV/IR far-infrared beamlines). Diffraction loss from small apertures is of great concern, and we expect the beamline's optical transport system to consist of larger mirror optics and vacuum components than for mid-infrared beamlines. The window separating machine vacuum from beamline vacuum also requires special consideration. In situations where only the THz and near IR portions of the spectrum are needed, a crystalline quartz window performs well and allows for large apertures (50 cm or larger). A more likely approach will be to use thin (<1 mm) CVD diamond so as to include the mid-infrared. Though this limits the aperture to below 2 cm, fast optics can be used immediately before and after to achieve good performance into the millimeter wave region.

11.18.2.2.5 Extension to Visible and Near UV

We note that several UV beamlines currently exist on NSLS VUV/IR ring bending magnet ports, supporting experiments in biology, chemistry, materials science, and condensed matter physics. Techniques include absorption, spectral and diffuse scattering, natural and magnetic circular dichroism, linear dichroism, fluorescence excitation, and emission and polarization from solid, liquid, and gaseous samples. For these beamlines, high flux (rather than high brightness) is the important source characteristic. Though NSLS-II undulators can meet the flux requirements, they are better suited to experiments requiring their exceptionally high brightness. NSLS-II dipole bends provide a similarly large flux when 50 mrad of horizontal angle is collected. Fortunately, we expect the optical design for extracting 50 mrad horizontal of infrared radiation (described in Chapter 8) to perform well for photon energies approaching 20 eV, spanning both the visible and UV spectral ranges. We anticipate that the first mirror will require a more sophisticated optical figure and polishing to maintain optimal source brightness for these much shorter wavelengths, plus control of any surface oxidation. Thus, NSLS-II bends (standard gap) should be capable of meeting the needs of this particular research community.

11.18.2.3 Beam Transport and Distribution Optics

The optics for managing and delivering the infrared radiation will follow design principles developed for the existing NSLS VUV/IR ring beamlines. The typical optic set includes combinations of plane, toroidal, paraboloidal, and sometimes spherical or elliptical mirrors. These and other special optical surfaces can now be manufactured by diamond diamond-turning methods, yielding surface quality (smoothness and accuracy) that exceeds infrared requirements. The extraction optics (first few mirrors inside the storage ring UHV) will deliver the beam through a transparent UHV window such as diamond. The remaining optical components will transport the beam and match it to a particular end station. Infrared beam transport does not entail complex optical components, UHV conditions, or special considerations for radiation shielding. Achieving diffraction-limited performance at long wavelengths is reasonably straightforward, but attention must be paid to other issues, such as diffraction losses. A key concern is mechanical stability for all the optical components, and we plan to use robust mechanical systems for mounting optical components. These supports will provide for in-vacuum beam steering controls, plus dynamic feedback to further reduce any low-frequency beam motion. Thermal loading is an issue only for the very first extraction optic inside the ring dipole chamber (discussed in a previous section).

11.18.2.4 End Stations

We expect that, in most cases, the end stations for the NSLS-II infrared beamlines will be those already in existence on the NSLS VUV/IR beamlines. These are mostly commercial FTIR spectrometers, some with dry nitrogen purging, others operating in a rough vacuum environment. These spectrometer end stations are

normally paired with an optical system (instrument) used to bring light to the sample under study. Examples are scanning microprobes, imaging microscopes, optical cryostats, diamond anvil cells, and magnet cryostats. It is assumed that NSLS will be maintaining these instruments at the state-of-the-art level between now and the operational startup of NSLS-II. The current NSLS infrared beamlines and end stations are listed here for convenience.

U2A Bruker 66 mid and far IR spectrometer, plus diamond anvil cells and cryostats
U2B Nicolet 860 mid IR spectrometer and scanning microprobe end station
U4IR Bruker 66 mid and far IR spectrometer, plus optical cryostat with laser for time-resolved spectroscopy
U10A Spectra-Tech IR spectrometer with scanning microprobe and microstat cryo system for far IR
U10B Nicolet 860 mid IR spectrometer and scanning microprobe end station, with fluorescence
U12IR Bruker 125HR high-resolution far IR spectrometer, plus 16 T magnet cryostat

11.18.2.5 Hutch Enclosures

The last several years have brought the realization that climate control, especially humidity, is critical for most mid-infrared microprobe and imaging experiments. Following the example of other synchrotron facilities (ANKA, CLS, Soleil, etc.), we plan to implement complete hutch enclosures for beamline end stations and instruments. These hutch enclosures will provide not only a stable climate (temperature and humidity) but will also reduce the detrimental effects of acoustic noise from neighboring beamline systems and provide a dark environment for performing optical alignment. It should be noted that these hutches are designed to be occupied at all times, i.e., they play no role in radiation protection. However, they could also serve for access control to hazardous experimental conditions such as laser light, high magnetic fields, and biological toxins.

11.18.2.6 Computing and Controls

The infrared beamlines do not present any unusual requirements for beamline controls. A basic system will be necessary for monitoring vacuum integrity and controlling various valve protection systems. Few of the mirror systems require regular adjustment, and the beam's position on optical surfaces can be monitored using conventional CCD cameras to view the visible radiation that is collected with the infrared. Requirements for positioning accuracy can be managed with conventional optomechanics, including stepper and DC servo motors. To ensure optimal stability at the experiment end station, we plan to include a two-mirror stabilization control system in the design. Such a system has been in use at ALS for several years, and a similar system is under development for NSLS.

Most infrared beamlines utilize commercial Fourier-transform infrared spectrometer systems. FTIR systems and their commercial software will need to be interfaced with NSLS-II injection signals to avoid collecting data during a top-off cycle. Converting all the systems to an EPICS-type interface will be considered, to allow better control of the data collection. We can expect to benefit from the experience of other storage ring light sources planning top-off operation, e.g., SLS in Switzerland and Soleil in France. Other ring signal requirements (in addition to an injection signal) are 1) beam current, 2) bunch synchronization signal (RF, RF/N where N is the bucket population factor), and 3) ring orbit RF frequency (i.e., RF/1300). Beam current should be accurate to at least 1 part in 1000.

11.18.3 Conventional Facility Requirements

11.18.3.1 Support Labs

Each beamline will need conventional laboratory space for tasks such as cryogen handling (IR detector operations), cryostat modifications and preparations, sample mounting and handling with optical microscopes,

etc. We also anticipate that biological imaging beamlines will need access to refrigeration and other facilities associated with cell culturing and tissue preparation. Placing these beamlines in relative proximity to other biological beamlines will allow for commonality of equipment and optimization of laboratory space. In other cases, specialized space will be needed in association with a particular beamline or combination of beamlines. Examples include the preparation and setup of LHe-cooled detectors and cryostats, especially magnet cryostats, where the area must be controlled for both personnel and equipment safety. The operation of class IIIB and class IV lasers is also typical for materials science IR beamlines, whether for fluorescence in high-pressure cells, micro-Raman, or time-resolved spectroscopy. For these situations we expect the beamline hutches to be divided into two or more sections to provide independent control and personnel and equipment protection (interlocks).

11.18.3.2 User and Equipment Access

The infrared beamline end stations should be sited such that users can occupy them at all times (including during injection). Additionally, they must be 100% accessible to equipment such as electronic racks, large cryostats, and LHe storage dewars. This motivates placing the infrared beamlines on the experimental floor along with the other NSLS-II beamlines (and not on the storage ring tunnel shield wall or another elevated surface).

11.18.3.3 Services

The infrared beamlines will require local access to liquid nitrogen (LN_2) for detectors and cryostats, dry nitrogen gas (for continuous purging of mid-IR spectrometers and end stations), and He gas (for detectors and cryostats). Electrical power requirements are comparable to those of a small experimental physics laboratory. Chilled water is needed for the first mirror in the optical extraction. This water must be extremely "quiet" (no pressure fluctuations) to avoid introducing mechanical noise into any of the optic components.

11.18.4 Example Infrared Beamline Schematics

Though the purpose of a given infrared beamline varies, the overall extraction, beam transport, and spectrometer end station layout does not differ greatly. Figure 11.18.1 shows a generic beamline layout consisting of three sections: 1) extraction optics and vacuum protections systems that collect the light and bring it around the fixed radiation protective shielding and through a UHV window; 2) the optical system for matching the source to the particular spectrometer and end station requirements, compensate for any beam noise, and transport the beam (under vacuum); and 3) a hutch enclosure that contains the beamline's FTIR spectrometer and specialized end station (e.g., an imaging microscope with focal plane array detector, a diamond anvil cell system, an optical cryostat with laser excitation, or a high-field magnet cryostat). For these beamlines it is assumed that the full horizontal collection of the source is delivered to a single end station.

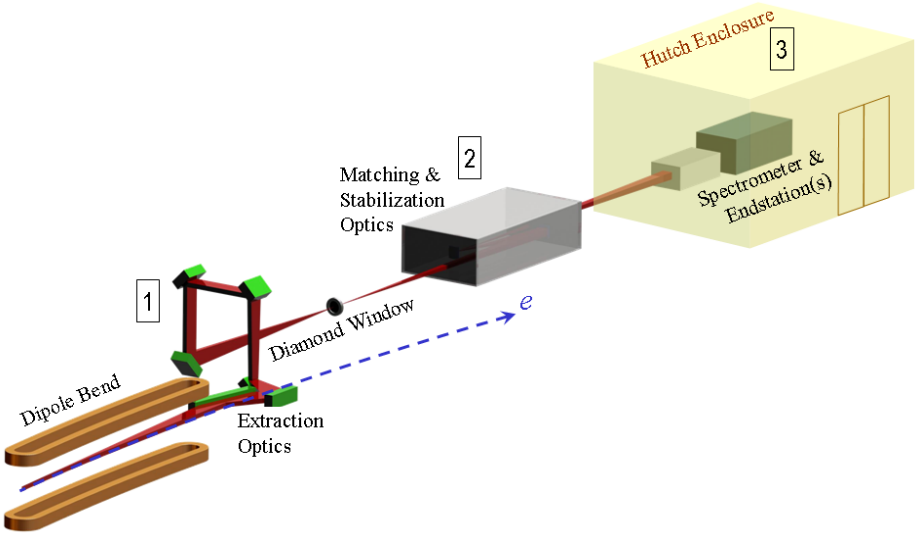

Figure 11.18.1 Schematic Infrared Beamline showing the three sections: 1) optics extract the infrared and bring it from the shielded storage ring enclosure and UHV environment out to the experimental hall and through a diamond window; 2) the optical system is designed to match the infrared beam to the experiment end station, plus provide for dynamic mirror alignment to eliminate mechanical beam movement, and 3) a hutch enclosure contains the FTIR spectrometer system and experiment end station.

The mid-infrared microprobe beamlines will require, typically, a horizontal collection that approximately matches the vertical collection (about 16 mrad for a standard dipole extraction). Thus, the 50 mrad of horizontal collection can be divided into two or three segments, delivered to independently operating microprobe end stations. Figure 11.18.2 illustrates a single extraction being split to serve three such end stations, where each receives about 15 mrad horizontal. This arrangement closely resembles the 40×40 mrad beamlines U2A/U2B and U10A/U10B on the VUV/IR ring where a ~90 mrad horizontal extraction is split to serve two beamlines.

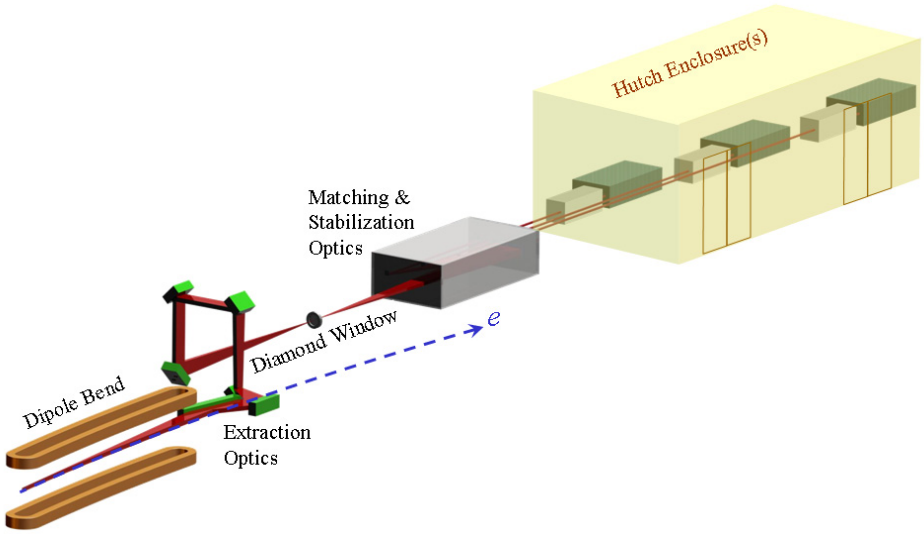

Figure 11.18.2 Multiple Microprobe End Stations. Same as the previous figure, but illustrating how the broad horizontal swath of infrared radiation can be split and fed to two or three simultaneously operating mid-infrared microprobe end stations. Each of the actual hutches would extend to the upper right a greater distance (deeper) than shown.

References

[11.18.1] See, for example, G.L. Carr, P. Dumas, C.J. Hirschmugl, and G.P. Williams, and other articles in *Infrared Synchrotron Radiation*, P. Roy and P. Calvani, eds. *Nuovo Cimento*, **20D** 375 (1998).

[11.18.2] W.D. Duncan and G.P. Williams, *Appl. Opt.* **22**, 2914 (1983).

[11.18.3] G. P. Williams et al., *Nucl. Instrum. & Meth. Methods Phys. Res.* A **246**, 165 (1986).

[11.18.4] G.L. Carr, O. Chubar, and P. Dumas, in *Spectrochemical Analysis Using Infrared Multichannel Detectors,* R. Bhargava & I. Levin, eds. (Blackwell Pub., 2005). Also R.L. Jackson, et al., WIRMS 2005, Rathen, Gy).

11.19 Time-Resolved Studies

11.19.1 Scientific Scope and Method

Synchrotron radiation, as a probe of physical (electronic, vibrational, structural) and chemical properties can serve to study the time-dependent properties of materials as well. The time scale of interest varies over many orders of magnitude, from femtoseconds to seconds and longer. In most cases, an event is triggered by some stimulus, and the properties are studied as a function of time following that stimulus. That time dependence can be followed using a sufficiently fast (gated) detector into the millisecond and shorter time range. However, fast detectors do not exist for all photon energy ranges of interest, and even when they do, there is always a tradeoff between speed and signal-to-noise. An alternative approach is to convert the temporal dimension into a spatial dimension that can be then sensed by a microprobe. The study of protein folding dynamics using flow/mixing cells and a synchrotron microprobe is an example of this approach, pushing into the microsecond time scale. In both of these cases, a higher brightness SR source provides increased performance, whether by simply increasing the signal-to-noise at the detector, allowing for smaller area (more sensitive, more rapid response) detectors to be used, or enabling a smaller area to be probed. These methods make use of specialized synchrotron beamline end station components, but do not require special or non-standard beamline designs.

A third approach exploits the time structure of the synchrotron storage ring source. Here, the individual pulses of synchrotron radiation (produced by the bunched electron beam) serve as a "strobe light" to capture an instant of time. This is the standard pump-probe technique commonly used to study fast and ultra fast processes and can completely relieve the detector of any requirement for time-resolution, thus providing the best combination of time resolution and signal-to-noise. There are, however, constraints to the technique. For example, the initiating stimulus must be synchronized to the SR pulses, and the specimen to be studied must allow for repetitive stimulus (within the limits of the pump and probe sources as well). Such issues are not unique to synchrotron radiation studies, and certainly not to NSLS-II. But the design of the NSLS-II accelerator system does present constraints on both the available bunch lengths and pulse patterns.

11.19.2 Review of Basic NSLS-II Properties

11.19.2.1 Bunch Length

The calculated bunch length (σ_z) for NSLS-II is 2.89 mm, which corresponds to σ_t=9.64 ps, or a FWHM of about 23 ps. These are zero current values. The bunch length for practical currents is more difficult to predict, but could be a factor of 2 larger (i.e., about 45 ps). This sets the limit for most time-resolved experiments without intentionally manipulating the electron bunches to produce shorter pulses. Those methods are discussed below.

11.19.2.2 Bunch Fill Patterns

The two factors that control the available pulse repetition frequency for a synchrotron radiation source are the RF frequency and harmonic number. The NSLS-II harmonic number of 1300 and RF frequency of 499.46 MHz allows for a variety of symmetric fill patterns to match the Pulse Repetition Frequency of common mode-locked lasers. The industry standard Ti:sapphire oscillator operates optimally around 80 MHz. Although NSLS-II does not have a symmetric fill for 83.2 MHz (499.46 MHz / 6), there are a number of fill patterns that yield PRFs matching Ti:sapphire oscillator subharmonics. Such subharmonics can be readily selected using Pockels-cell type electro-optic modulators. Except for its fundamental, a mode-locked laser at 76.84 MHz offers substantial flexibility for matching useful NSLS-II symmetric fill patterns.

Table 11.19.1 NSLS-II Fill Patterns Compatible with Mode-Locked Ti:Sapphire Laser Oscillators.

# of filled RF buckets	SR effective pulse repetition frequency (MHz)	Compatible laser oscillator frequency (MHz)	Laser divide by N (pulse selection)
1300	499.46		
650	249.73		
325	124.865		
260	99.892		
130	49.946		
100	38.42	76.84	2
65	24.973	74.919	3
52	19.9784	79.9136	4
50	19.21	76.84	4
26	9.9892	79.9136	8
25	9.605	76.84	8
20	7.684	76.84	10
13	4.9946	74.919	15
13	4.9946	79.9136	16
10	3.842	76.84	20
5	1.921	76.84	40
4	1.5368	76.84	50
2	0.7684	76.84	100
1	0.3842	76.84	200

Note that most storage rings operate with a gap in the fill pattern. This is not a problem when the SR serves as a probe, as long as the remainder of the fill pattern retains the overall symmetry. The only consequence is a loss of signal-to-noise, as some of the pump/excitation events are not probed.

Other mode-locked lasers (e.g., Er-doped fiber lasers, Nd:YAG, Nd:YLF, custom oscillators) will likely have other requirements or can be specially designed to work at these and other frequencies (e.g., 49.946, 99.892, 124.865 MHz). The optimal pulse rate for a given measurement depends on a variety of factors, but in very few cases are pulse rates much above 100 MHz useful, due mostly to limitations on extracting thermal energy from the sample. In situations where more laser power is required, an amplified system can be employed. Such systems usually operate at frequencies even lower than the orbital ring frequency (single bunch mode), in which case a gated detector is necessary to sample the appropriate synchrotron pulse.

Other “pump” stimuli can be employed, such as electrical. Since these are not constrained to an oscillator, the synchronization is usually much simpler than with a laser system. In any case, electrical synchronization signals, accurate to 5% of the electron bunch length, will be needed as a clock for the stimulus source.

11.19.2.3 Special Operating Modes for Timing

Timing experiments often have additional concerns beyond optimized flux and brightness. In timing measurements, the bunch length and PRF are critical. With regard to the PRF, for limited periods during the year, special operating modes are often employed at synchrotron facilities. Simplest among these modes is single-bunch or few-bunch operation, where a small fraction of the RF buckets are filled with more electrons than the standard bucket charge in normal operation. At NSLS-II, single-bunch operation would lead to a PRF of 384 kHz. This type of operating mode, or other few-bunch operations, might be useful for classes of experiments where the relaxation time of the samples is on the order of microseconds or where the detectors used have a long rise time or reset time. However, the cost in terms of overall flux for the general user community would be unacceptable. A common operating mode for timing operations that attempts to resolve this conflict is the so-called “camshaft” operation. In this mode, the majority of the RF buckets are filled as usual, but a large gap of unfilled buckets is placed in the distribution. In the middle of the gap, a single RF

bucket, the camshaft, is filled with several times the charge in the other buckets. Users can synchronize to the camshaft bucket and reject the contribution from the other filled buckets by using gated detection. The overall flux is not reduced much, as the proportion of the buckets in the gap to the number of filled buckets is relatively small. While potentially useful, this operating mode has not been studied in detail and should be evaluated more fully in future design phases.

11.19.2.4 Short Bunch Operations

The length of electron bunches in a storage ring can be reduced by adjusting several accelerator parameters. Examples include reducing the momentum compaction, reducing the ring energy, and increasing the RF slope (higher voltage, higher frequency). Unfortunately, most of these adjustments reduce the performance of the ring for other (non-time-resolved) users. Therefore, the availability of such modes will depend on the demand from the user community. Lowering the momentum compaction is usually accomplished at the expense of non-zero dispersion in the insertion device straight section. Should NSLS-II include a harmonic RF cavity to provide bunch stretching (to enhance the lifetime), such a cavity could be used, in reverse phase, to reduce the bunch length somewhat.

In addition, short photon bunches for a fraction of the NSLS-II beamlines may be generated by methods that preserve the beam properties for the majority of the (non-time-resolved) users. In general, these approaches provide short bunches to one or a few beamlines and do not provide reduced bunch length to the other beamlines. On the other hand, these approaches strive to provide short bunches while maintaining the desirable beam properties (low emittance and high flux and brightness) for most users. Two methods that have been implemented or proposed in recent years are laser time-slicing and implementation of additional accelerator RF systems (such as “crab” cavities).

Laser time-slicing, pioneered at Lawrence Berkeley National Laboratory, is the only accelerator-based method to date to demonstrate generation of femtosecond x-ray pulses. In this approach, high-power femtosecond laser pulses are synchronized with the electron bunches in the storage ring as they both propagate collinearly through an undulator. The interaction of the strong electric field from the femtosecond laser modulates the energy of a fraction of the electrons in the bunch, and the synchrotron radiation from these modulated electrons can be separated out in a subsequent dispersive section of the storage ring.

Crab cavities are RF cavities that impart a vertical deflection to the electron bunches. While the emitted radiation from the deflected bunch is larger in the vertical direction, the projection of the bunch along the time axis at given vertical position is considerably shorter than the undeflected pulse length. With suitable aperturing, a pulse on the order of one or a few ps can be generated at the cost of a reduction in flux by one to two orders of magnitude. Alternatively, asymmetrically cut crystals can be used without apertures to compress the entire bunch and preserve the flux. The attractive feature of crab cavities is that they can be operated in pairs where the second cavity applies a reverse deflection, which restores the electron bunches to their low emittance distribution. Thus crab cavities can produce short bunches with relatively high flux to several beamlines and straight sections while minimizing the impact on the general user community.

It must be stressed that the methods outlined above for producing short bunches have not been studied in detail. In future design stages, they must be evaluated more rigorously to determine the compatibility of the various options with the NSLS-II project goals.

11.19.2.5 Synchronization Signals

Generally, experiments on ultrafast timescales utilize a pump-probe architecture, where some excitation source, such as a high-power laser or an RF generator, perturbs the state of a sample and the subsequent response can be probed with the x-ray pulses from the storage ring. Accurate synchronization of the excitation is indispensable for these measurements, and the key to synchronization is the availability of accurate and fast bunch clock signals at the beamlines.

Signals from the storage RF system are an indirect measure of the photon bunch clock. While the frequency of the RF matches the frequency of the electron bunches in the storage ring, the phase between the RF and the electrons may shift for two reasons: 1) injection bumps during top-off may affect the relative phase of the RF and the electron bunches, and 2) for special operation modes that allow beam decay and re-injection (i.e., non- top off operations), the variable loading of the RF cavity as the beam decays will cause a shift in the phase of the cavity relative to the electron bunches. Thus RF signals are adequate for timing experiments involving gated detection and for samples with characteristic response times in the range of microseconds or longer. For ultrafast experiments where the systems responds in nanoseconds or less, a more direct measure of the electron bunches is required for synchronization.

The most precise manner of deriving a synchronization signal is to use the electron bunches as the source for the signal. This can be accomplished by either: 1) using an Avalanche PhotoDiode with a fast risetime to detect the visible light emitted as synchrotron radiation in the dipole magnets, or 2) inserting a floating stripline into the storage ring vacuum chamber and detecting the induced voltage on the stripline from the image charges that develop as the electron bunches pass in front of the stripline. The advantage to these methods over the RF signal is that the pulses derived from the electron bunches automatically correct for any phase drift between the electrons and RF.

Once generated, the signals from the APD or stripline must be discriminated and then distributed to the beamlines. We propose conversion of the signals to optical pulses and distribution over optical fiber rather than coaxial cable to minimize electromagnetic interference. Careful attention should also be given to minimizing any timing jitter that is introduced in converting timing signals and distributing the signals to the beamlines and end stations. In particular, it may be advantageous to have several sources of timing signals (APDs or striplines), with each source serving as a local timing signal for a cluster of beamlines.

12 RESEARCH AND DEVELOPMENT PROGAM

12.1 Introduction

The overall NSLS-II design philosophy is to use low-risk technology, requiring minimum research and development, to achieve the facility's baseline performance while, at the same time, having significant upgrade potential. Use of electron storage rings for photon production is a proven technology, and well understood; however, extending that technology to achieve unprecedented levels of brightness, flux, and stability imposes some technical risk. The major procurements require only limited R&D and present low technical risk. There are no known technical "show stoppers" in constructing NSLS-II.

R&D will be conducted in areas where opportunities exist for mitigating existing technical risk, achieving cost reductions, and/or enhancing performance. The following seven main areas have been identified for R&D:

- high spatial resolution optics
- nanopositioning instrumentation
- high energy resolution optics
- metrology and reflective optics
- advanced detectors
- advanced insertion devices
- stabilization of magnet–girder support systems

The R&D program for the first six items is described in this chapter. The R&D plan for the last item is described in Section 7.2.3.9. In addition to these principle R&D areas, there will also be important, but smaller scale, R&D efforts in several other areas. These are described in the appropriate sections of this CDR.

The R&D efforts supported by the NSLS-II project are targeted at meeting the needs of specific project deliverables. In the case of R&D related to experimental facilities, the approach taken is to first identify the specific technical requirements and then develop a solution to meet that defined need. In the case of the program on mirrors and detectors, these needs are expected to vary greatly depending on the specific experiment. Therefore, R&D efforts in these two areas that are specifically required to meet the needs of beamlines that are selected to be constructed out of the experimental facilities trust fund, discussed in Chapter 11, will also be funded out of the trust fund. As such, the initiation of efforts on mirrors and detectors will begin following identification of the suite of project beamlines.

12.2 High-Spatial Resolution Optics

12.2.1 Introduction and Overview

The goal of achieving ever-higher resolution in x-ray focusing is one that has been pursued by the worldwide x-ray optics community with impressive results. As Figure 12.2.1 shows, up until about a decade ago nearly all the progress in submicrometer focusing was accomplished with Fresnel zone plates as soft x-ray (<1 keV) optics. However, within the past decade, remarkable advances have been made in the development of a variety of optic types for focusing hard (8–20 keV) x-rays to sub-100 nm spot sizes. To surpass this historical trend and reach a 1 nm resolution target will require sustained effort as part of the NSLS-II project.

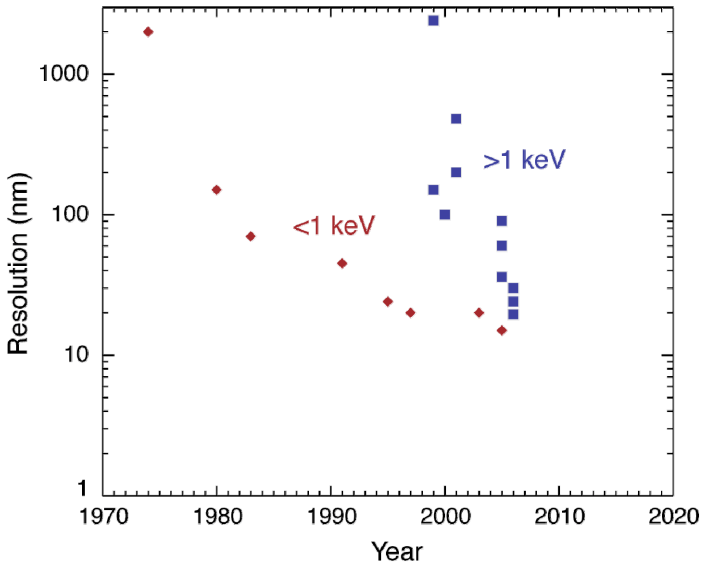

Figure 12.2.1 Historical trends in the best resolution of x-ray optics have involved rapid progress in the initial establishment of focusing techniques for a particular energy range, followed by progress resulting from sustained R&D efforts by the worldwide optics community. For E=1.24 keV, the limiting resolution is 1 nm. For hard x-rays, where we chose a characteristic energy of E=12.4 keV, λ and the limiting resolution is 0.1 nm.

In this section we provide some background on x-ray optics, and examine various possible approaches to achieving 1 nm spatial resolution.

12.2.1.1 Imaging Modes

We first consider the two major types of x-ray imaging systems in use today: those that use optics to form an image by collecting and focusing radiation scattered by an object, full-field imaging, and those that use optics to form a small focus through which the specimen is scanned (Figure 12.2.2). The types of information one can gain, and the requirements on specimen illumination, are very different between these two approaches. Full-field imaging is primarily restricted to transmission imaging, while scanned imaging allows one to use a greater range of signals (energy-resolved fluorescent photons, photo- and Auger-electrons, etc.). The same optics can be used as high-resolution objective lenses for both full-field and scanned image approaches. (There is an important difference: scanning systems can usefully employ optics with large off-axis aberrations, while full-field imaging systems cannot.) Here, we address optics that can produce a small point focus in scanning systems, since the flexibility of imaging signal (fluorescence, microdiffraction, etc.) is of great advantage to many hard x-ray studies of the properties of nanoscale materials.

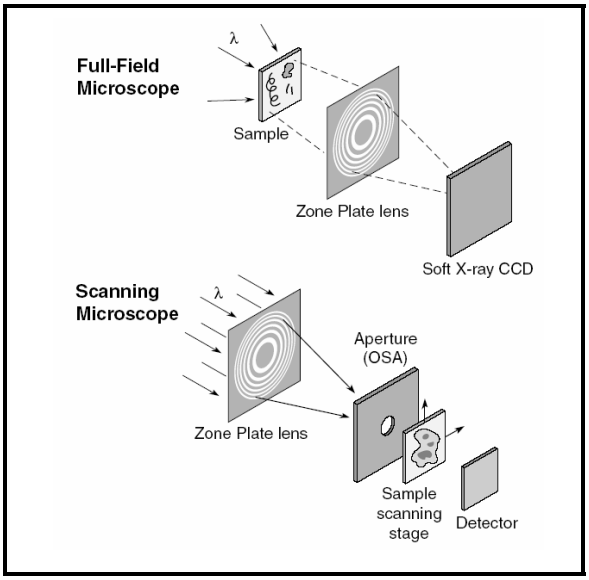

Figure 12.2.2 A schematic of two major kinds of x-ray microscope, the full-field microscope (top) and a scanning microscope (bottom). In the full-field case, the sample is illuminated incoherently, and a high resolution optic is placed downstream of the sample. The sample is imaged pixel by pixel onto the CCD. The scanning microscope has an optic upstream of the sample which is coherently illuminated, creating a small focused spot on the sample. The schematic representations of x-ray microscopes are reproduced with permission from Prof. D.T. Attwood, www.coe.berkeley.edu/AST/sxreuv.

12.2.1.2 X-Ray Interactions with Matter

The optical properties of materials in the photon energy range above about 30 eV are related quite directly to the atomic scattering factors. The index of refraction, n, of a material is typically written as $n = 1-\delta-i\beta$; the parameters δ and β are called the refractive index decrement and the absorption index, respectively. Many of the differences between x-ray and visible light optics are due to three facts 1) the real part of the refractive index $1-\delta$ is less than one, 2) δ is of order 10^{-6}, and 3) the ratio β/δ, which is related to the phase shift induced in an absorption length, is much smaller than for visible optics.

The index of refraction of a material is related to the scattering factors of the individual atoms:

$$n = 1-\delta-i\beta = 1-\frac{r_e}{2\pi}\lambda^2\sum_i n_i f_i = 1-\frac{r_e}{2\pi}\lambda^2\sum_i n_i(f_{1i}+if_{2i}), \qquad (12.2\text{-}1)$$

where r_e is the classical electron radius, λ is the wavelength, and n_i is the number of atoms of type i per unit volume. For photon energies larger than the electron binding energies, f_1 for an element tends to approximately Z, the number of electrons in the atom. f_2 is derived from the atomic photo-absorption cross-section, τ, and is defined as

$$f_2 = \frac{\tau}{2r_e\lambda}. \qquad (12.2\text{-}2)$$

The consequence of δ being small is that even the most dense material deflects x-rays only slightly. The critical angle, which is the maximum deflection angle a single mirror bounce can impart, is given by $\theta_c=\sqrt{(2\delta)}$, and is on the order of 10^{-3}. For both mirrors and refractive optics, this small θ_c results in limitations of the numerical aperture (see discussion below), and limits the resolution for a single optic t order λ/θ_c. As $\theta_c \propto \lambda$, this resolution is independent of energy and simply depends on the electron density of the material. For diffractive optics, the small δ also makes it difficult to fabricate the required zone plate thickness. A 2π phase-shift thickness is λ / δ, which can be in the microns or tens of microns range, making it necessary to fabricate zones that are just microns thick yet nanometers wide—an aspect ratio that is very large and difficult to fabricate.

12.2.1.3 Important Metrics of Focusing Optics

Here, we briefly summarize quantities that can be used to parametrize and compare the different optics; where possible, we estimate values.

12.2.1.3.1 Resolution and Numerical Aperture

As shown in Figure 12.2.3, the transverse resolution of any optic is limited by diffraction from its pupil function; for a circular lens with numerical aperture or semi-angle θ_{NA}, the Rayleigh resolution limit may be given by $\Delta_t = 0.61\lambda/\theta_{NA}$. (Strictly speaking, the numerical aperture is NA = $n\sin\theta_{NA}$, but $n \cong 1$, and for the regime considered here, the approximation NA$\approx \theta_{NA}$ is a good one.) For a wavelength of 0.1 nm, an optic of 1 nm resolution requires a numerical aperture of 0.06.

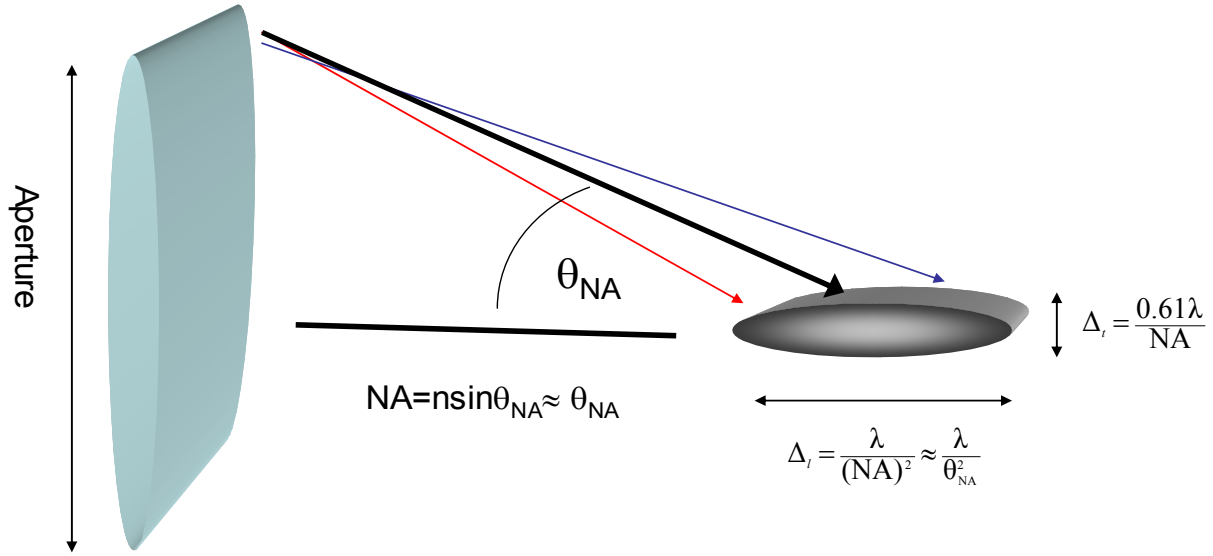

Figure 12.2.3 Illustrating the lens aperture, the numerical aperture (NA), the optics transverse resolution Δ_t, and the longitudinal resolution Δ_l, commonly referred to as depth of focus. Also shown schematically is the effect of a chromatic optic focusing different wavelengths, represented by the red, black, and blue arrows focusing at different focal lengths.

Fabricating hard x-ray optics with such large NA is a challenging task, compared with the state of the art in other methods of microscopy. For visible optical photons, one can commercially purchase microscope objectives with NA as large as 0.7 [12.2.1]. In the extreme ultraviolet with λ = 13.5 nm, a state-of-the-art mirror pair optic for lithography applications [12.2.2] has been constructed with NA = 0.3. For electron microscopes, the NA is on the order of tens of mrad, although here the significantly shorter wavelength compensates for the small NA. In comparison, commercially available zone plates for hard x-ray photons with 50 nm resolution currently have NA $\approx 10^{-3}$.

12.2.1.3.2 Depth of Field (DOF)

The depth of field for a coherently illuminated optic is $\Delta_l = \lambda/(\mathrm{NA})$. For NA of 0.1, we find the DOF is on the order of 10 nm. This sets important constraints on sample manipulators; one needs nm-precision translators of the sample in all directions. Furthermore, for diffraction-limited optics with a transverse resolution of $\Delta_t = 0.61\lambda/\theta$, the depth of focus also can be expressed as $\Delta_t = 2.7\Delta_t(\Delta_t / \lambda)$. Note that the DOF shrinks as the square of the transverse resolution, but grows linearly with photon energy.

12.2.1.3.3 Aperture

The aperture is the actual physical size of the optic, and determines the total photon flux arriving at the lens. It is *f**NA, where *f* is the focal length.

12.2.1.3.4 Efficiency

Most real optics do not have perfect transmission, and will not focus the entire flux incident on the optic into the focal spot. The role that optic efficiency plays is very different in scanning versus full-field imaging experiments. In a full-field imaging system, the optic is located downstream of the specimen; this means that if an optic with efficiency ε and numerical aperture θ is used to collect the photons emerging from the specimen, one will have to expose the specimen to an extra dose of

$$\frac{1}{\varepsilon}\frac{2\pi}{\pi\theta^2} = 2/\left(\varepsilon\theta^2\right) \tag{12.2-3}$$

to collect the same information that would have been obtained by a 100% efficient, 2π collection solid-angle optic. As a result, high efficiency, ε, large numerical aperture θ optics are essential for full-field imaging of radiation-sensitive specimens. In scanned imaging systems, the optic is located upstream of the specimen, so it is the efficiency of the detector that determines whether the specimen must undergo any extra exposure.

12.2.1.3.5 Chromatic Properties

An important characteristic of an optic is its behavior as a function of energy. Some optics have their best efficiencies for particular photon energies. For example, solid metal mirrors are relatively achromatic up to a critical energy before this efficiency drops off. Also, for solid metal mirrors the position of the focus is independent of energy. For zone plate optics the focal length varies with photon energy, and for purely refractive optics the focal length varies as the square of the photon energy.

12.2.1.3.6 Modulation Transfer Function

As Figure 12.2.4 shows, it is important to consider the fraction of energy that is delivered outside of the central focus, as that can lead to incorrect interpretation because information from other regions is mixed in with information from the selected area. The Modulation Transfer Function is a metric that allows one to compare quantitatively the spectral response of an optic. MTF is defined as the power recorded at a given spatial frequency, divided by the power present in the object at that frequency.

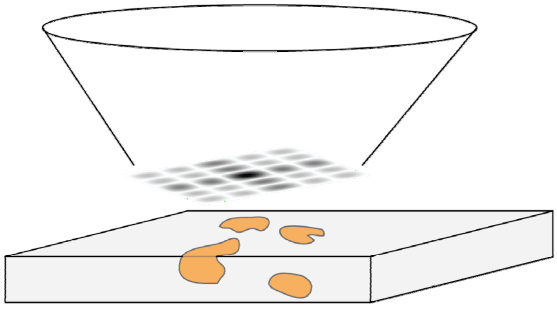

Figure 12.2.4 Illustration of the importance of having a "clean" central focus with minimal sidelobes for quantitative studies of heterogeneous materials. Excessive energy in the sidelobes can lead to mixing of signals from adjacent sample regions.

12.2.2. Basic Focusing Optics

12.2.2.1 Mirrors

The critical angle for total external reflection can be expressed in terms of a grazing critical angle relative to the surface normal as

$$\theta_C' = \sqrt{2\delta} = \lambda\sqrt{2\alpha f_1} \,. \tag{12.2-4}$$

This indicates that high-density materials and high energies give a slightly higher critical angle. More importantly, however, this relationship sets a fundamental limit to the resolution of reflective optics, because the maximum numerical aperture θ cannot exceed twice the critical angle. As a result, for a cylindrically symmetric reflective mirror, the Rayleigh resolution limit becomes

$$\Delta = 0.22/\sqrt{\alpha f_1} \,. \tag{12.2-5}$$

This limit is plotted for nickel and platinum in Figure 12.2.5.

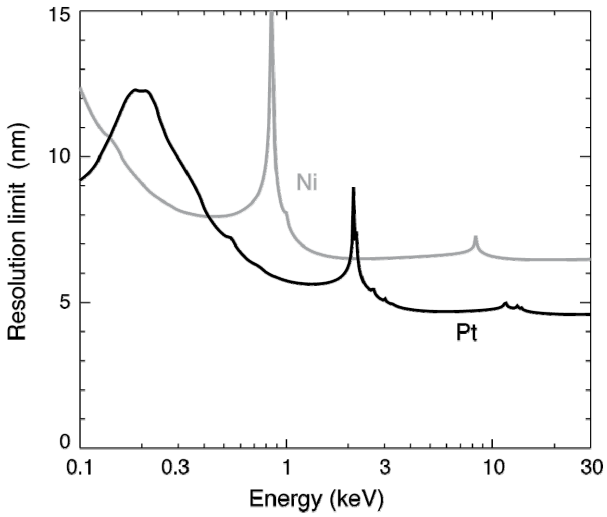

Figure 12.2.5 Theoretical resolution limit for grazing incidence single-bounce reflective optics with perfect figure and finish.

Reflective optical systems have achieved very impressive results for 1D focusing at the 30 nm level, and they have the advantage of being achromatic optics. However, we do not consider them to be a promising path to achieve 1 nm resolution, for several reasons. First, there is the intrinsic single-bounce resolution limit shown in Figure 12.2.6; in principle this could be overcome by using a multiple bounce system, or by using multilayer coatings to increase the critical angle. However, there still remain the challenges of producing the correct figure and finish over a very large optical area (see Figure 12.2.6), properly aligning the optic to avoid off-axis aberrations, and (for multiple-bounce systems) achieving the correct relative alignment of separate mirror segments. In a reflective system, the length of the mirror along the beam direction sets a limit to the lowest spatial frequencies that can contribute to the focus (rays from bottom left in Figure 12.2.6), and reductions in this length have the same effect as increasing the central stop fraction *a* and thereby introducing sidelobes about the central focus (Figure 12.2.4). In contrast, Figure 12.2.6 shows that for a transmission optic, all "ray bending" is accomplished in a more compact area, improving tolerance to fabrication inaccuracies.

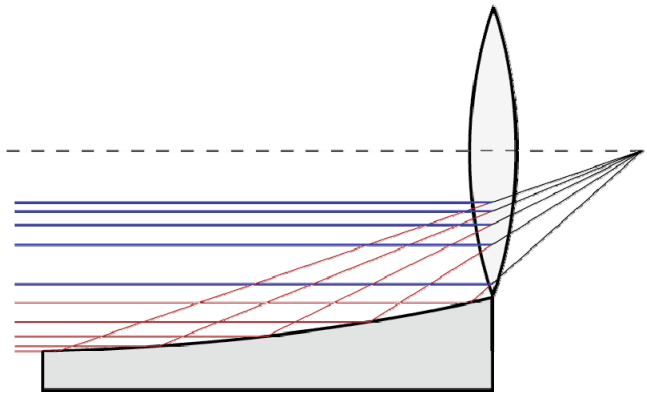

Figure 12.2.6 Illustration of the challenges faced by a reflective optical system relative to a transmission system.

In all sub 100 nm resolution demonstrations of x-ray focusing using reflective optics, anomalously strong sidelobes are observed around the central focus and often a diffuse scattering background signal, as well. For these reasons, we believe that while reflective optics will play a crucial role as achromatic optics at NSLS-II, they do not represent a viable path for 1 nm spatial resolution.

12.2.2.2 Fresnel Zone Plates and Multilayer Laue Lenses

Fresnel zone plates have provided the highest resolution x-ray foci for the past two decades, reaching 15 nm resolution in a recent demonstration [12.2.3]. FZPs are diffractive optics with a grating period $2\Delta_m$ that decreases with zone number n (and also with radius), so that from each local region of the zone plate an incident plane wave undergoes m^{th} order diffraction toward a point focus by an angle $\theta = m\lambda / (2\Delta_m)$, as shown in Figure 12.2.7. (The radius r_n of the nth zone boundary is well approximated by $r_n^2 = n\lambda f$, where f is the focal length).

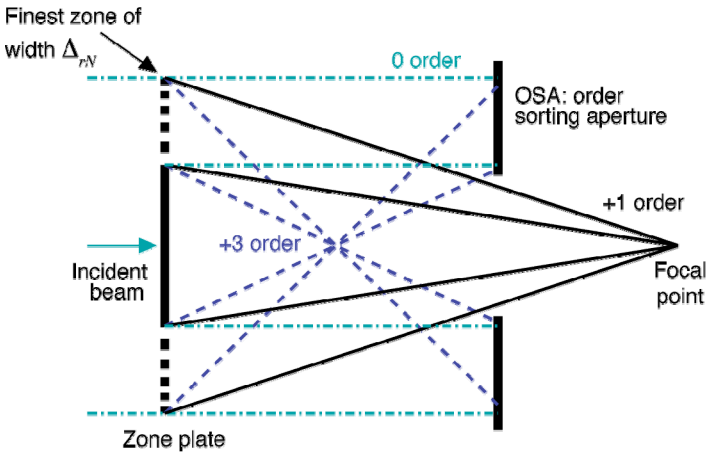

Figure 12.2.7 Schematic of a Fresnel zone plate as used in a scanned imaging configuration, where an order-sorting aperture (OSA) is used to isolate the first-diffraction-order focus.

As a result, the Rayleigh resolution Δ_t is set by the width of the N^{th}, narrowest, outermost zone as

$$\Delta_t = 0.61\lambda/\theta = 1.22\Delta_{rN}/m \,. \qquad (12.2\text{-}6)$$

In addition, the zones must be accurately placed to within about m/3 of their width to avoid phase errors that would otherwise degrade the focal spot. For a zone plate with diameter d, the m^{th} diffraction order focal length is given by

$$f = d\Delta_{rN}/(m\lambda) = d\Delta_t/(1.22\lambda). \tag{12.2-7}$$

The lens diameter required to achieve 1 nm resolution with a focal length of at least 1 mm is shown in Figure 12.2.8.

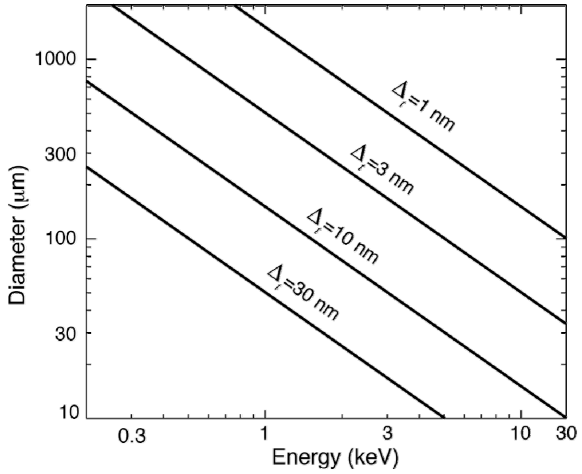

Figure 12.2.8 Diameter required of Fresnel zone plates designed to achieve a given Rayleigh resolution Δ_t as a function of x-ray energy.

The efficiency of thin, binary zone plates can be calculated using a relationship [12.2.4] that takes into account both phase shift and absorption in the zone material (see Figure 12.2.9). In general it is especially favorable to use materials at energies below particular absorption edges, to maximizes the ratio of phase shift to absorption. For energies below 1 keV, thicknesses of ~150 nm of gold or nickel give sufficient efficiency, and for energies above 1 keV, nickel becomes increasingly less practical due to the thicker films with correspondingly less favorable aspect ratios. For photon energies of 10 keV and higher it is more practical to use a high-density material such as gold with a thickness of 500 nm or more.

Most zone plates are fabricated by a process that involves 1) electron beam lithography to define the zone pattern, 2) reactive ion etching to transfer this pattern into a thick polymer plating mold, and 3) electroplating to produce the zone structures themselves. This fabrication procedure presents several challenges. To produce the highest possible resolution, the finest zone width Δ_{rN} must be as fine as possible, yet sidescattering of the electron beam in the photoresist makes lines below 10 nm extremely challenging to produce. At the same time, zones must be thick along the x-ray beam direction (indicated as zone thickness in Figure 12.2.9). This means that very high aspect ratio structures are desired. For 1 nm resolution from a zone plate operated in m=5th order at 10 keV, one would want to fabricate zones with a width of Δ_{rN}=4 nm and a height in gold of at least 600 nm, or an aspect ratio of 150:1. This is far beyond what has been achieved to date, which includes aspect ratios of 8:1 at Δ_{rN}=20 nm [12.2.5] and 14:1 at Δ_{rN}=32 nm [12.2.6]. Finally, the electron beam lithography system must be able to place zones with a 1σ absolute placement accuracy of Δ_{rN}/m over the entire optic diameter. For these reasons, circular zone plates do not appear to be a viable alternative for reaching 1 nm resolution.

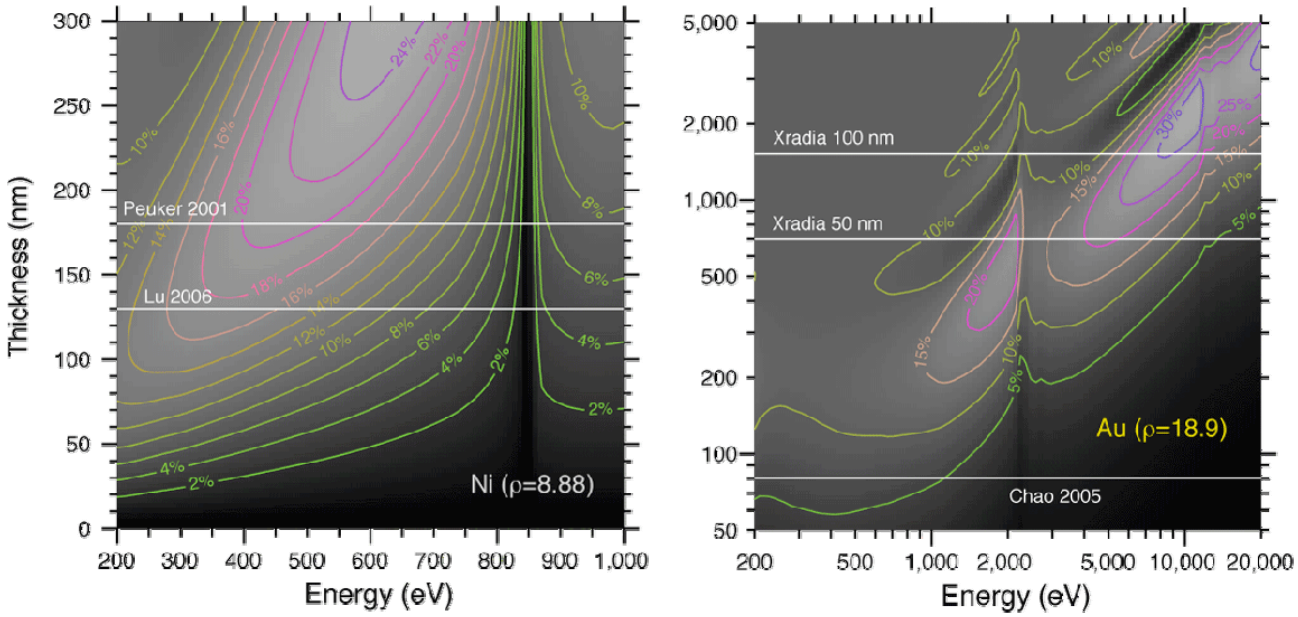

Figure 12.2.9 Diffraction efficiency of thin binary transmission zone plates as a function of material thickness and photon energy, based on the formula by Kirz [12.2.4]. In the soft x-ray range, zone plate thicknesses of 100 nm or more are required to achieve high efficiency, while at 10 keV, thicknesses of 500 nm or higher are required.

The above limitations to electron beam fabrication of zone plates have long been recognized. As early as 1980, Schmahl et al. [12.2.7] proposed an alternative approach to zone plate fabrication: Start with a wire, and deposit alternating layers of high and low-density materials to fabricate a zone plate pattern. The completed structure can then be sliced and thinned to yield a zone plate resembling a slice of a jelly-roll cake (Figure 12.2.10). While a number of researchers have pursued this approach over the years, the results obtained have not been encouraging: it is very difficult to produce a wire of the required roundness, and when sputtering multiple layers, any roughness and thickness errors accumulate to unacceptable values before one reaches the thinnest, resolution-determining outermost layers.

An alternative to this approach was proposed by Maser et al. in 2004 [12.2.8]. Optics of this new type have been given the name of Multilayer Laue Lenses. In MLLs, one starts from the outermost zones and works in. Rather than face the challenge of depositing thin films on the inside curvature of a cylinder with a radius of curvature of some tens of micrometers, a flat substrate is used to produce half of a linear zone plate (Figure 12.2.11). In this way one can start from a well-polished flat surface, with an error accumulation of zero at the thinnest, outermost zone; errors will build up only towards the innermost zones, which are coarser and thus more tolerant.

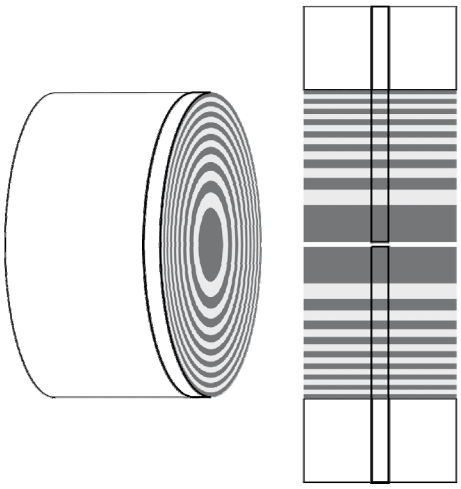

Figure 12.2.10 Sputter-sliced zone plates (left) and multilayer Laue lenses (right). For sputter-sliced zone plates, successive layers are deposited onto a wire in the order of coarser zone to finer zone. For MLL, successive layers are deposited onto a flat substrate in the order of finer zone to coarser zone. In each case, a slice of the structure yields the final optic. In the case of MLL, the result is half of a linear optic, which can be paired with its twin and put with a pair of orthogonal optics to yield a lens with 2D focusing properties.

Each half-linear zone plate produces a line focus, which appears like light coming from a slit; placing two half-linear zone plates next to each other therefore produces a double-slit interference pattern in the far field. As the two half-linear zone plates are brought into registry, the double-slit interference fringes in the far field overlap region become coarser and coarser until they disappear when the two half-linear zone plates are aligned. Since there is no horizontal focusing from the vertically focusing optics and vice versa, an orthogonal pair of half-linear zone plates produces a 2D focus with the characteristics of crossed linear lenses.

Producing zones using thin layer deposition techniques followed by slicing to obtain a zone plate with the desired thickness along the x-ray beam direction, removes any aspect ratio limit in the fabrication. However, the zones are now a volume grating, so that the Bragg condition must be met to yield high diffraction efficiency. For an optic of intermediate thickness, this can be achieved by giving each zone a "wedged" thickness, as shown in Figure 12.2.11. One can also satisfy the Bragg condition over a certain range of zone widths by taking a non-wedged optic and tilting it. This approach has been used by Kang et al. [12.2.9], who have demonstrated a 30 nm line focus at 19.5 keV.

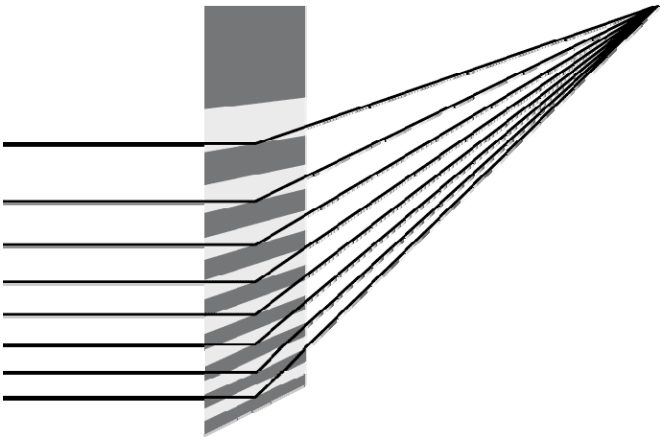

Figure 12.2.11 It is necessary to continuously adjust the tilt of individual zones in a multilayer Laue lens to meet the Bragg condition. We refer to this case (which applies to an optic of intermediate thickness) as having "wedged" zones.

12.2.2.3 Refractive Optics

Refractive optics and compound refractive optics for hard x-rays were discussed as far back as 1948 [12.2.10], but were dismissed at that time as being impractical. For a single refracting surface with a reasonable radius of curvature, since δ is so small, one obtains a relatively long focal length. For example, a 1 cm radius results in a focal length of order 10^4 m. Consequently, it was suggested by three groups independently [12.2.10, 12.2.11, 12.2.12] that compound lenses could bring the focal length down to

reasonable values. To first order, N lenses of focal length f_0 will have an effective focal length of f_0/N. The physical implementation of Snigirev [12.2.12] was a crossed array of cylindrical holes drilled in aluminum. Subsequently, a parabolic profile was suggested as a better approximation of an ideal lens, and this was also implemented [12.2.13].

However, for all practical variations of the refractive optic, absorption limits the aperture. If one considers the familiar parabolic profile with thickness t as a function of y, where y is the distance from the optic axis, then $t=y^2/(2\delta f)$ for a pure refractive optic. The lens absorption as a function of the radial lens coordinate is then given by $\exp(-4\pi\beta t/\lambda)$. One finds that the aperture is limited, and the effective lens aperture is proportional to $\sqrt{f}$. Consequently, the resolution is also proportional to $\sqrt{f}$, resulting in a gain that is dependent only on δ and β.To get a 1 nm spot, one finds for a focal length of order 1 μ an aperture of 100 nm, using silicon as a lens material; this aperture is clearly unacceptable.

12.2.2.4 Waveguides

One possible path to a 1 nm spot size on a sample is to use an optical path that includes a waveguide to serve as a secondary, coherent source. A conceptual arrangement is shown in Figure 12.2.12. The benefits of this arrangement are:

- a reduced requirement on the demagnification, and a resulting increase in potential working distance
- a source that is diffraction limited in both directions
- reduced sensitivity to beam motion

This path relies on the fact that a waveguide with a single mode illuminated radiates as a coherent source, and that the size of a waveguide that can carry a single mode is in the 30 to 50 nm range.

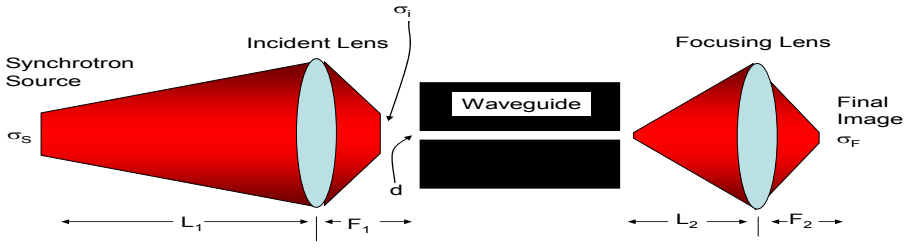

Figure 12.2.12 Schematic diagram showing the use of a waveguide in an optical system for achieving a 1 nm focal spot.

From an optics point of view, there are two disadvantages of synchrotron-based sources of radiation in comparison with visible light optics. First is the relative inaccessibility of the source. Due to heat load and radiation issues, it is difficult to adjust the source size with slits close to the source without perturbing the overall ring—and, in addition, the slits are engineering challenges. Secondly, all synchrotrons have relatively large electron beam source sizes, of the order of microns, which then also constrain the photon source size. To reach small x-ray spots requires a large demagnification factor, and leaves very little useful working distance.

Waveguides have been recognized as a possible mechanism to provide small beams. However, they have two drawbacks: waveguides need to work in the near field, and it has been difficult to couple light efficiently into the waveguide modes. Recent experiments with a direct coupling scheme as shown in Figure 12.2.12

have significantly improved the efficiency of coupling. In this scheme, the synchrotron source is demagnified by the incident lens on to the front of a waveguide with aperture *d*. The demagnification in this step,

$$\frac{L_1}{F_1}, \tag{12.2-8}$$

can be quite large with a small F_1. Since this illuminates only the waveguide, the working distance F_1 can be made as small as is necessary. As suggested in Figure 12.2.12, the incident lens focuses the source size σ_S to an image size σ_i, which is bigger than d, the width of the waveguide.

The waveguide, which only accepts a diffraction-limited fan, serves to pass the appropriate coherent fraction in the vertical, and since the source is close to diffraction limited in the vertical, most of the vertical fan can be coupled into the waveguide.

The portion of light that gets accepted by the waveguide propagates down the waveguide, with some loss due to wall roughness and wavefield overlap with the guiding materials. At the exit, the mode radiates coherently, with an effective size d, into another demagnifying lens. Since the source size is now 30 nm instead of 6 μ, the demagnification required is 30 instead of 10^4, and so one can have L2 be 3 m and F2 be 0.1 m, resulting in a significantly larger and more useful working distance than the 10 mm of a more conventional optics arrangement. Note that this would be most useful with broad bandpass optics. If one uses a square waveguide then, one can end up with a virtual source that is diffraction limited in both the vertical and horizontal.

Another advantage of this scheme is its potential stability. Given the dimensions listed above, it is possible to mount all the optics components and the sample stages on a single, vibrationally quiet table. The main disadvantage is that all the components introduce loss.

12.2.3 Basic Source Properties

12.2.3.1 Source Size, Divergence, and Estimate of Optic Size

In a 5 m, low-β straight section, NSLS-II is currently projected to have an effective vertical photon source size of 5.9 microns, a horizontal source size of 39 microns, and vertical and horizontal divergences of 12 and 18.6 μrad, respectively. We first consider a diffraction-limited optic focusing in just the vertical. The focused spot will be a convolution of the diffraction-limited spot with a demagnified image of the source; for Gaussian quantities, we can add in quadrature. Thus, to achieve a net 1 nm focus size we need √(1/2) nm from demagnification of the source, and √(1/2) nm from the diffraction-limited optic. The demagnification required is, therefore, 10^4 or better.

With the demagnification set, we now consider possible working distances (focal lengths). At 50 m, the focal length is 5 mm; at 100 m it is 10 mm. Using the beam divergence, we can estimate the size of the beam at these points and hence the size of the required optic. In the vertical, the 1σ size of the beam is 60 microns at 50 m and 120 microns at 100 m. In the horizontal, the 1σ sizes are 95 and 190 microns, respectively. As is discussed in Section 12.4, the approach to handling larger horizontal source size and divergence is to trade off flux for better a focal spot—for example, by slitting down the beam size in the horizontal.

12.2.3.2 The Smallest Spot Needs Coherent Illumination

Consider a beam from a distant source of width *a,* from which the optic subtends a full angle of ϕ (Figure 12.2.13). If the source distance, *s*, is many times the optic's focal length *f*, it will be imaged at a distance

$s' \approx f(1+f/s)$ so that the angle subtended by the optic from the image will be well approximated by the numerical aperture θ.

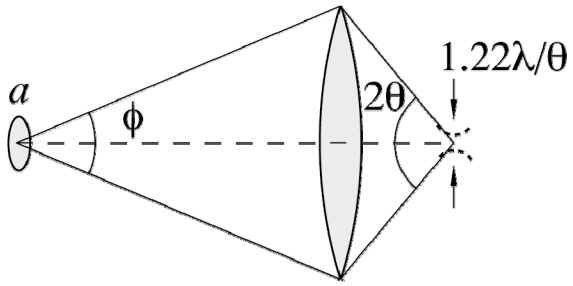

Figure 12.2.13 Illustration of the phase space area of scanned imaging, where one must restrict the product $a\phi$ to be less than λ.

By Liouville's theorem, the width of the geometrical image from this source will be b and the phase space product of the image will be $b\theta = a\phi$. We can then consider the ratio p of this spot size to that of the diffraction-limited focus, which is given by

$$p = \frac{b}{1.22\lambda/\theta} = \frac{a\phi/\theta}{1.22\lambda/\theta} = \frac{a\phi}{1.22\lambda}. \qquad (12.2\text{-}9)$$

A more detailed calculation involves convolution of the geometrical image with the diffraction-limited optic's point spread function; such a calculation for the case of incoherent brightfield imaging indicates that values of p of about 1 or less deliver nearly fully diffraction-limited image resolution (Figure 12.2.14). This leads to an important (and well-known) result: to obtain the finest possible focus spot from a lens, one requires either a spatially coherent source, or one must aperture an incoherent source to use only the spatially coherent fraction.

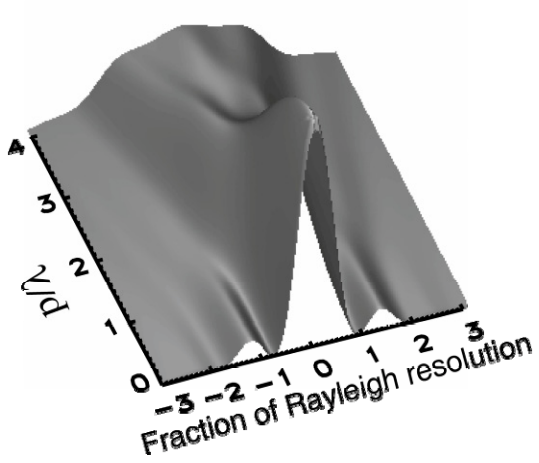

Figure 12.2.14 To achieve a perfect diffraction-limited focus in a scanned imaging system requires spatially coherent illumination; that is, the size-angle product p of the illumination must be restricted to about 1λ or less. NSLS-II will provide nearly coherent beams, making a large fraction of its flux available for achieving excellent spatial resolution in scanned imaging and microprobe experiments.

Figure: Winn et al. [12.2.14].

12.2.3.3 The Importance of Emittance

In this section, the effect of the electron beam emittance on determining the flux into a focused spot is considered. It is shown that for a diffraction-limited optic, improving the emittance of the ring increases the flux into a desired focus spot. When electron emittance is negligible, all the light goes into the focused spot.

By definition, for a diffraction-limited photon source,

$$\sigma\sigma' = \frac{\lambda}{4\pi}, \tag{12.2-10}$$

or, in terms of **f**ull **w**idth **h**alf **m**aximum, one finds $(d\times\theta)_{FWHM}\approx\lambda/2$, where d is the FWHM size of the source and 2θ is the FWHM angular divergence of the source.

For NSLS-II, the source is close to diffraction limited in the vertical, but in the horizontal the emittance is of order 1 nm. For ideal emittance preserving optics with a NA approaching 1 and a physical aperture larger than the beam, one could focus all the light into a 1 nm spot. However, optics with such perfection do not exist. In Figure 12.2.15 we consider the effect of finite emittance on the fraction of flux focused into the spot.

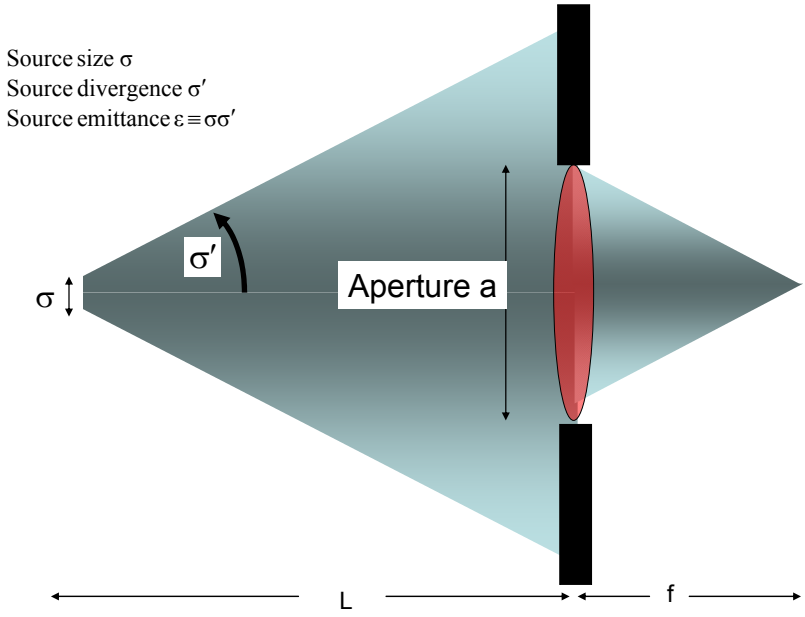

Figure 12.2.15
The requirement to coherently illuminate an optic results in reduced flux into the focused spot. The flux subtended by the optic is $\frac{a}{L}\frac{1}{\sqrt{2\pi}\sigma'_s} = \frac{a}{L}\frac{\sigma_s}{(\sqrt{2\pi})\varepsilon}$.

Then by replacing for σ_s with the constraint of coherent illumination, the fraction into the spot is $\frac{\lambda}{4\pi\varepsilon}$.

The effective emittance of the source is

$$\varepsilon = \sigma_s\sigma_s' = \sqrt{\sigma_e^{\,2} + \sigma_{ph}^{\,2}}\ \sqrt{\sigma_e'^{2} + \sigma_{ph}'^{\,2}}\ , \tag{12.2-11}$$

with σ_e representing the electron source size and σ_{ph} representing the photon source size, etc. As the electron emittance becomes vanishingly small, the source emittance simply becomes that of a diffraction-limited photon source, $\lambda/4\pi$. For NSLS-II, the electron beam is small in the vertical, but dominates in the horizontal.

To understand the role the emittance plays, consider a simple 1D model, shown in Figure 12.2.15 above, in which photons from a source of emittance, ε, are incident on an optic of size a, focal length f, at a distance L from the source, and hence with a NA of a/f. To obtain the smallest spot, d, allowed by an optic, it must be illuminated coherently, requiring

$$(d\ x\ 2\theta)_{FWHM} = (\sqrt{2\pi}\sigma_m\ x\ \frac{a}{L}) \le \frac{\lambda}{2}\ . \tag{12.2-12}$$

One can obtain a reduced source size of σ_m from the σ_s by slitting down, and this results in a reduction of the flux from the source to $(\sigma_m/\sigma_s)I_s$. Finally, if we consider the fraction of light that is incident on the optic, we find that the fraction is

$$\frac{a}{L}\frac{1}{\sqrt{2\pi}\sigma'_s}, \tag{12.2-13}$$

which compares the divergence of the source with angular size of the optic. The flux into the focused spot is then $(\sigma_m/\sigma_s)I_s(a/(L\sqrt{2\pi}\,\sigma_s')) = I_s\,(\lambda/4\pi\varepsilon)$.

The above arguments apply to the typical case of an aperture that is smaller than the full fan. For optics larger than the full radiation beam, the result is the same. In this case, the aperture size is $L\sqrt{2\pi}\sigma'_s$, from which we deduce that we need a source size

$$\sigma_m = \frac{\lambda L}{a2\sqrt{2\pi}} = \frac{\lambda L}{(L\sqrt{2\pi}\sigma')(2\sqrt{2\pi})} = \frac{\lambda}{4\pi\sigma'}, \tag{12.2-14}$$

and the fraction of flux into the focused (σ_m/σ_s), again becomes

$$\frac{\lambda}{4\pi\sigma\sigma'} = \frac{\lambda}{4\pi\varepsilon}. \tag{12.2-15}$$

In this limit, the fraction of flux into the focused spot is commonly referred to as the undulator coherent fraction.

As shown in Figure 12.2.16, the fraction of flux from the source that is focused into the spot tends to 1, as the electron emittance tends to 0, and the net (photon plus electron) emittance tends to $\lambda/4\pi$. From the figure we also see that the point of diminishing gains occurs when the electron emittance becomes less than the diffraction limit of $\lambda/4\pi$.

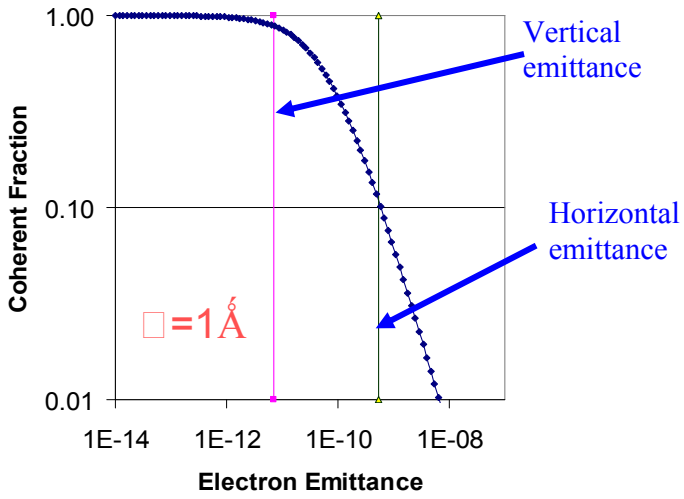

Figure 12.2.16 Effect of varying the electron beam emittance on the fraction of light delivered into a focused spot by a diffraction-limited optic for a photon energy of 12.4 keV.

These arguments indicate that if one is willing to sacrifice flux, a desired spot size can always be generated from a source of any emittance. However, improving the electron emittance allows more photons to be put into the focused spot. For NSLS-II, these considerations imply that there will have to be slits in the horizontal direction, but not in the vertical.

12.2.3.4 Incoherent Illumination is Better for Full-Field Imaging

The situation with full-field imaging is much different. Each pixel of the object acts as its own single-mode source for illuminating the objective lens, and for incoherent imaging (e.g., the generally preferred mode of transmission imaging, and fluorescence imaging systems) no optical phase correlation is desired from pixel to pixel. As a result, the challenge in full-field imaging is not one of providing the smallest possible phase space of the photon beam, but a much larger phase space. To illuminate a field of view corresponding to N pixels, one must provide N optical modes. It is for this reason that full-field imaging systems are often best suited to operation with incoherent sources such as bending magnets rather than undulators (Figure 12.2.17).

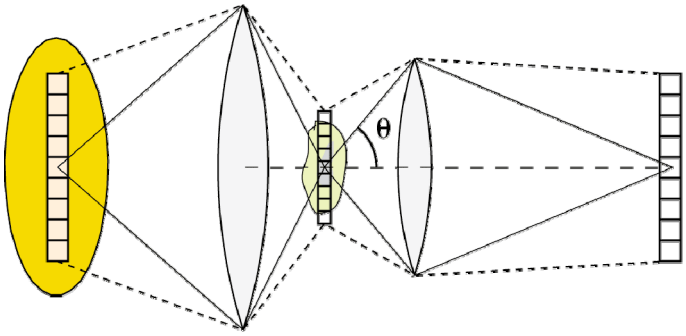

Figure 12.2.17 Illumination phase space requirements for full-field imaging. If the illumination of each pixel is to be uncorrelated with that of its neighbor (incoherent imaging), then the desired source phase space area is equal to the number of image pixels in each of two orthogonal directions.

12.2.4 Some Implications of Metrics, Source, and Optics

12.2.4.1 The Effect of Apodization on the Modular Transfer Function

Consider the case of optics that have a central obscuration, which is a fraction a of the optic diameter (such as the central stop-order sorting aperture pair required by Fresnel zone plates, as will be discussed below). A large central stop will slightly decrease the radius of the central focus while simultaneously putting a larger fraction of energy into sidelobes; this has the effect of reducing the MTF or fraction of specimen signal captured at various specimen size scales (Figure 12.2.18). Optics that allow work without central "stops" or at least with small values of a have very distinct advantages over optics with large central stops or large values of a.

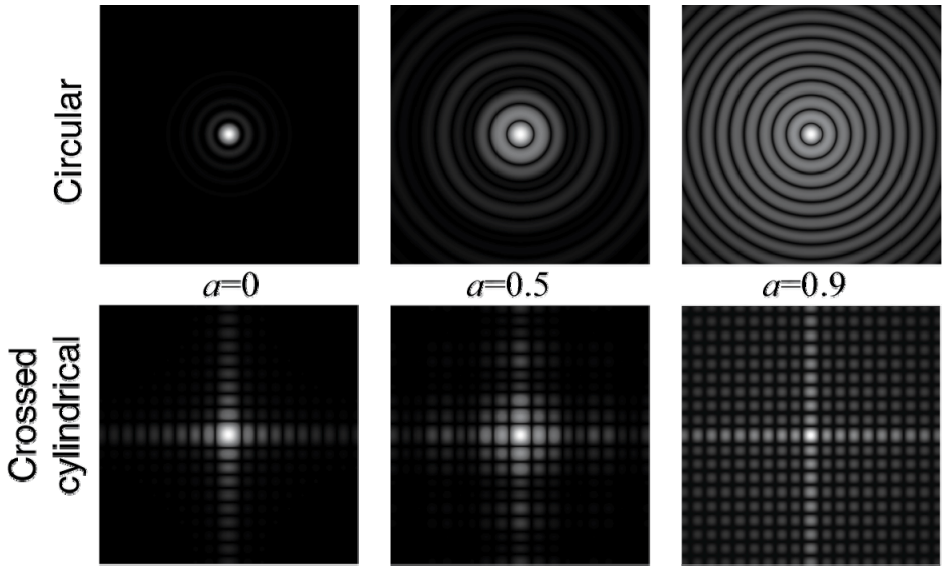

Figure 12.2.18 Point spread function for both circular and crossed cylindrical optics with various central stop fractions *a*. These images show the square root of the intensity as shades of grey, normalized to the peak value in the center. These images illustrate that it is not enough to simply achieve high numerical aperture; it is also important to have a lens with response reasonably near its center.

This is especially important when considering optical systems that use crossed cylindrical lenses to produce 2D focusing. (This is the case of MLLs and K-B mirrors, for example). In such systems, the loss of cylindrical symmetry in the optic naturally leads to a loss of cylindrical symmetry in the point spread function. When combined with a large fractional central obscuration, *a*, this can mean that the sidelobes beyond the central focus can be quite significant (Figure 12.2.18). There are likely to be experiments where users will choose a lower resolution but cylindricallysymmetric, low-*a* optic over higher resolution but crossed-orthogonal, high-*a* optics. While it may seem beneficial to narrow the central focus by increasing the diameter of a central stop, the contrast of an image (or, for example, the accurate fluorescent analysis of how much of an element is in what region of a specimen) will be degraded by the increasing presence of the sidelobes. This is especially problematic for imaging systems made up of orthogonal pairs of cylindrical lenses. As a result, circular optics with unobscured apertures will be favored for some experiments, even though a finer focus probe is available from orthogonal pairs of cylindrical optics with large central stops.

12.2.4.2 Limitations of Crossed Linear Lenses

A potentially serious limitation for the high-resolution optics of the types considered here is the use of the crossed-pair of 1 nm lenses to approximate a radially symmetric lens, and to produce a point focus. In this geometry, one focuses in one direction with one optic, and then places further downstream a lens focusing in the other direction. The leading optics candidates for high spatial resolution, Multilayer Laue Lenses and kinoforms, are each fabricated in a crossed linear geometry. For small NA, the Fresnel approximation is valid and the crossed lens is a good approximation to a radially symmetric lens. However, for large enough NA we expect the Fresnel approximation to break down, and the question is, in this new regime, are crossed lenses still a valid approach? Here we find that while there is some broadening of the central spot, the most significant effect is a reduction in contrast in the MTF, with less light in the central spot, and we therefore conclude that the crossed geometry is a reasonable, albeit not ideal, geometry.

In the Fresnel approximation, spherical secondary wavelets are replaced by wavelets with parabolic wavefronts. The starting point for such an analysis is the Fresnel-Kirchoff diffraction formula. With the usual approximation of a "thin" optic, then, following Goodman [12.2.16], the equation takes the form:

$$U(P_0) = \frac{1}{i\lambda} \iint_{(\xi,\eta)} U(P_1) \frac{\exp(ikr_{01})}{r_{01}} \cos\theta \, ds \,, \tag{12.2-16}$$

where

$$k = \frac{2\pi}{\lambda} \,, \tag{12.2-17}$$

and

$$r_{01} = \sqrt{z^2 + (x-\xi)^2 + (y-\eta)^2} \tag{12.2-18}$$

with (x, y, z) in the image plane and (ξ, η) in the "thin" object plane. One can expand r_{01} in a series, and retaining terms to the second order brings us to the Fresnel approximation for r_{01}:

$$r_{01} \approx z[(1 + \frac{1}{2}(\frac{x-\xi}{z})^2 + \frac{1}{2}(\frac{y-\eta}{z})^2] \tag{12.2-19}$$

showing the replacement of the spherical wave by a pair of orthogonal parabolic terms. Within this approximation then, the crossed linear pair of lenses are separable, and each lens focuses independently of the other. Examining higher order terms that were neglected, the limit of validity of this approximation is:

$$z^3 \geq \frac{\pi}{4\lambda}\left[(x-\xi)^2+(y-\eta)^2\right]^2 \qquad (12.2\text{-}20)$$

if we pick λ on the order of 0.1 nm and a physical aperture of 100 microns, which is a typical order of magnitude for the size of a hard x-ray focusing optic. We find that z, or the lens focal distance, is greater than or equal to 1 cm, corresponding to a diffraction-limited focused spot size of order 10 nm. In other words, for 100 micron aperture lenses, we expect a crossed lens pair to be able to focus at least down to 10 nm. However, this condition is sufficient, and is perhaps overly stringent; numerical simulations are required to clarify the true limits of the crossed pair.

Figures 12.2.19 and 12.2.20 show the results of such a simulation. Here we chose a cylindrically symmetric wave incident on an aperture. In the absence of a lens, the cylindrical wave results in a line focus at f_0 (not shown). The left panel shows that when a single cylindrical lens is placed in the aperture in a crossed geometry, the result is a 2D point focus. The same data are shown in the central and right panels. As we expect, for small NA for which the Fresnel approximation is known to hold, the sharp central component has approximately the same scaled width as a radially symmetric lens. Figure 12.2.20 shows a larger NA, on the order of 0.1. We can see that the sharp component maintains its width, but intensity shifts to the tails.

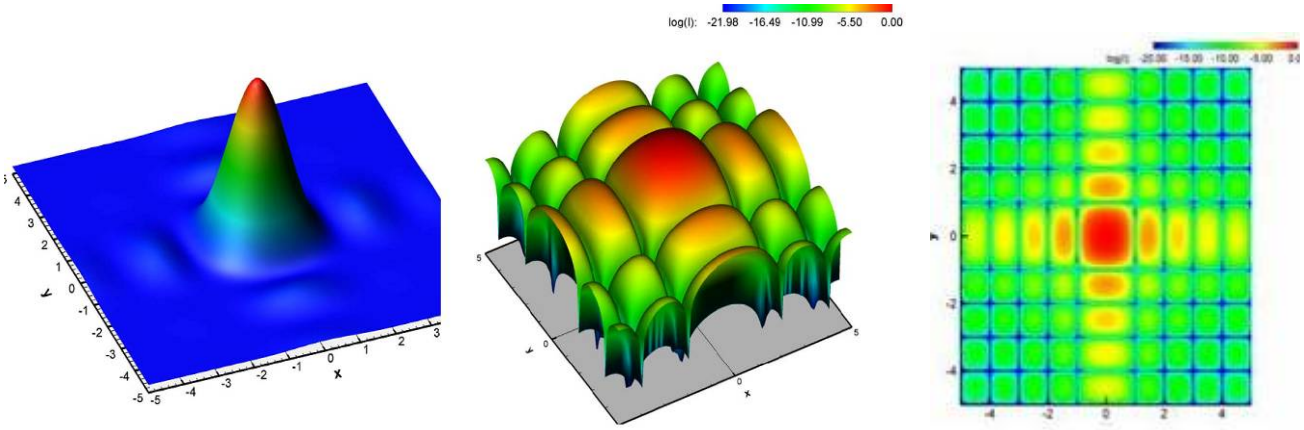

Figure 12.2.19 Results of simulations of a crossed linear lens arrangement in the limit of small NA (0.05). On the left are the data with the intensity on a linear scale showing the 2D focusing of a crossed pair. In the center we see the same data plotted in units of λ / NA with a log scale in order to highlight the subsidiary maxima; color represents intensity. The crossed geometry retains a sharp central focus, with a resolution very close to that of the radially symmetric lens. The right figure is the same data plotted as a 2D projection.

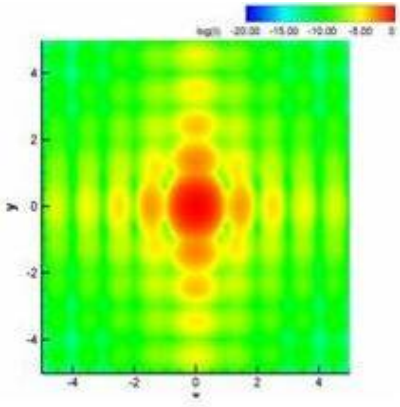

Figure 12.2.20 For NA=0.1 there is increased intensity in the tails surrounding the sharp central component. However, the sharp central component has approximately the same scaled width as the smaller NA shown in Figure 12.2.19.

12.2.5 Leading Candidate Approaches to Achieving 1 nm Resolution

Having outlined some of the fundamental issues associated with optics and achieving 1 nm spatial resolution at a synchrotron source, we now examine the leading candidates for approaches to achieve this, and the issues that are required to be solved for each. The first discussion concerns multilayer Laue lenses. Following that, kinoforms are discussed in detail.

12.2.5.1 Multilayer Laue Lenses (MLLs)

Because MLLs can be fabricated by depositing thin films on flat substrates, they offer a relatively straightforward route to high resolution x-ray focusing: in the simplest concept, one could deposit alternating atomic layers to obtain an x-ray focus with atomic dimensions. Such a simple picture, however, ignores factors such as focusing efficiency and the need to satisfy the Bragg condition.

In the discussion on planar Fresnel zone plates, we noted that the thickness of the zones along the x-ray beam direction plays a crucial role in determining the focusing efficiency of the optic (Figure 12.2.9). The aspect ratio of MLLs is even higher; while an exact calculation of the thickness can be found from considering the pendellösung phenomenon in dynamical diffraction theory, a good approximation at small numerical aperture for the desired thickness t of zones is given by

$$t = \lambda / \left(2\left[\delta_A - \delta_B\right]\right), \tag{12.2-21}$$

which works out to be about 5 μm for Mo as material A and Si as material B, at 10 keV. If the Bragg condition is also satisfied, a diffraction efficiency well above the theoretical limit of 40.1% for "thin" phase gratings can then be achieved. However, satisfying the Bragg condition introduces a new set of complications, shown in Figure 12.2.21.

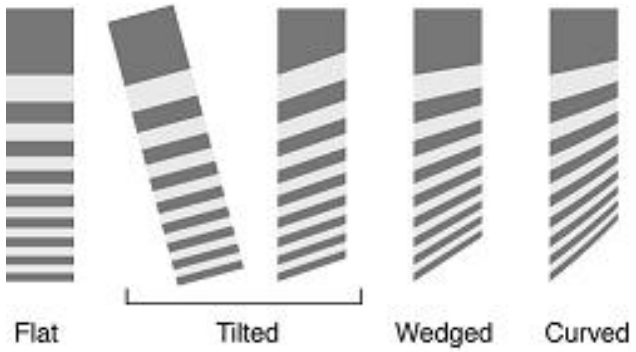

Figure 12.2.21 Types of MLL arrangements: flat, tilted, wedged, and curved. Tilted zones can be achieved either by tilting a straight cut from the substrate, or by cutting along the tilt angle.

If a simple perpendicular cut through a thin film stack is mounted perpendicular to the x-ray beam, each diffracting plane will be off-Bragg relative to the desired diffraction direction and the optic will have very low diffraction efficiency for all but the innermost zones (the "flat" case of Figure 12.2.21). If instead we tilt the perpendicular cut, or make a cut through the layer stack at a slight angle, this satisfies the Bragg condition for a particular set of zones only; this is called the "tilted" case in Figure 12.2.21. A better solution is to arrange for the zones at each radius to be at the proper tilt angle for satisfying the Bragg condition; this is called the "wedge" case in Figure 12.2.21. However, if the thickness of the optic exceeds the depth of focus [which is $\Delta_l = 2.7\Delta_t\left(\Delta_t / \lambda\right)$, giving $2\Delta_l$=54 nm for Δ_t=1 nm transverse resolution at λ=0.1 nm wavelength], then one must change the Bragg angle in depth through the optic, giving rise to the "curved" case of Figure 12.2.21. If such a curved-zone MLL could be fabricated, Schroer [12.2.17] has shown that it could, in principle, deliver a 1 nm resolution focus. The more realistic scenario involves making choices between tilted and wedged MLLs. As discussed further in Section 12.2.5.1.2, to go from 10 nm to 2 nm spatial resolution, it is essential to

develop approaches to fabricating wedged MLL zones. Unpublished calculations from Schroer's group show that this result holds down to 1 nm.

12.2.5.1.1 Characteristics of a Multilayer Laue Lenses

What are the characteristics of a multilayer Laue lens for 2D focusing? The optic would consist of four half-linear focusing components; at 10 nm resolution, each of these four components could be a tilted half-diameter linear focusing optic. The tilt would have to be set to the right value to meet the Bragg condition for the desired x-ray wavelength. Next, two such opposing optics would need to be aligned with respect to each other in translation and azimuthal rotation at nanometer precision so that their two line foci would completely overlap; the x-ray interference scheme shown in Figure 12.2.22 could be used to accomplish this, and then a laser interferometer could be used in a feedback loop to dynamically adjust the piezos to maintain alignment against thermal drifts. The orthogonal optic pair would then be aligned separately, and the two optics pairs would be combined to produce a crossed linear focus.

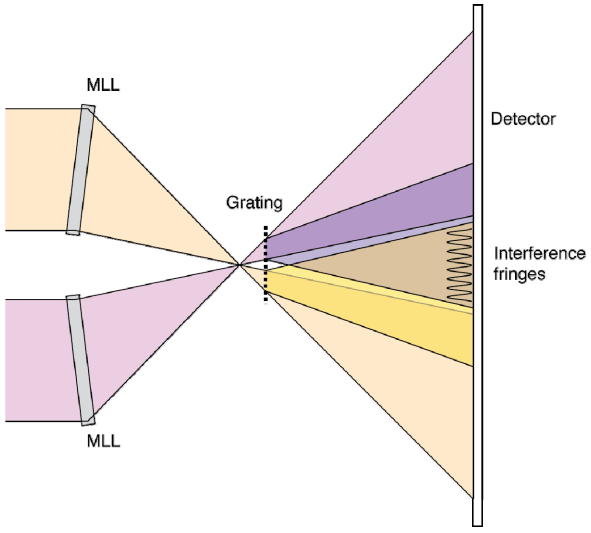

Figure 12.2.22 Possible alignment scheme for pairs of half-linear-focusing multilayer Laue lenses. A grating downstream of the focus could be used to cause the wavefield from each optic to interfere at a detector plane, and provide a diagnostic on the relative alignment of the two half-optics.

Such an optic might be used for tuning over a modest energy range, such as required for recording a XANES spectrum from the focal point. However, when tuning over a larger energy range, it would likely be necessary to readjust the tilt of each MLL, and then redo the translation and azimuthal orientation alignment. Note that because the optics would be tilted to be on-Bragg for a single incident beam direction, it is likely that they would have a very limited field of view when used as imaging rather than probe-forming optics.

12.2.5.1.2 Challenges Associated with Reaching 1 nm Resolution with Multilayer Laue Lenses

A number of significant challenges exist when contemplating extension of the MLL approach from values of ~10 nm toward the NSLS-II goal of 1 nm resolution focusing. Consider the case of a λ=0.1 nm optic with a focal length of only 1 mm (which is about as short as imaginable for practical experiments), the values of zone number n, distance of the zone from the optical axis r_n, zone width Δ_{rn}, and corresponding Rayleigh resolution are shown in Table 12.2.1.

Table 12.2.1 Resolution Dependence of MLL Optics Parameters.

Rayleigh resolution (nm)	Zone width Δ_{rn} (nm)	Zone number *n*	Distance of zone from optical axis r_n (μm)
10.0	8.2	370	6.1
5.0	4.1	1490	12.2
2.5	2.1	5,960	24.4
1.2	1.0	26,000	51.0
1.0	0.8	37,210	61.0

As the table shows, such an optic involves very thin zones throughout nearly its entire area. In fact, simply by going from a resolution of 5 nm to a resolution of 1 nm, one needs to go from 1,490 zones to 37,210 zones; the challenges in fabrication of the optic increase steeply with relatively small changes in the resolution goal. In fact, current examples of MLLs have all had less than 1,000 zones. (Note also that the monochromator resolving power, E/ΔE, should be comparable to the number of zones divided by 2 to achieve the desired spatial resolution.)

In addition, as discussed above, as the resolution is reduced below 10 nm, it will be necessary to move from tilted to wedged zones to keep all zones close enough to the Bragg condition to deliver uniform efficiency. (Further, if one does not meet the Bragg condition or have the proper thickness for each range of zone widths, both the amplitude and phase of the local exit wave from the optic will be degraded, which in turn will degrade the line spread focus profile of the optic.) An example of the need to move from tilted to wedged zones is shown in Figure 12.2.23; at 2.4 nm Rayleigh resolution corresponding to 2 nm zone width, only a narrow range of zones will be on-Bragg unless one can fabricate the MLL with wedged zones. Another way of illustrating the same conclusion is provided in Figure 12.2.24, which shows the calculated efficiency and Rayleigh-like resolution for flat, tilted, and wedged MLLs with various zone widths.

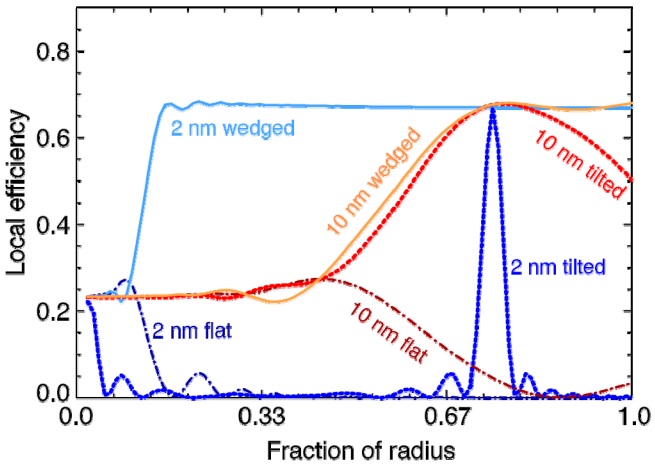

Figure 12.2.23 Local diffraction efficiency of zones at various radii as calculated for a Mo/Si MLL operating at 10 keV. For an outermost zone width of 10 nm, the simple tilted zone case gives high diffraction efficiency for a wide range of zone widths, although the 10 nm wedged case is superior. For an outermost zone width of 2 nm, the tilted zone case works only for a narrow range of zones which properly satisfy the Bragg condition; it becomes essential to fabricate wedged zones to achieve high focusing efficiency across the optic, to obtain a high-quality focus.

Figure adapted from Kang et al. [12.9].

The calculation for Figure 12.2.24 involves an estimate of the local diffraction efficiency from zones used as simple gratings to diffract light into a desired far-field diffraction order. In fact, this calculation is incomplete, in that since the optic thickness exceeds the depth of focus $2\Delta_l$, or about 54 nm for a 1 nm Rayleigh resolution optic at λ=0.1 nm, it will be necessary to move from wedged to curved zones because the Bragg condition will change through the depth of the MLL. The good news is that recent simulations by Schroer have indicated that curved-zone MLLs can, in principle, achieve a 1 nm resolution focus; however, no realistic scheme has yet been put forward for practical fabrication of curved 1 nm zones.

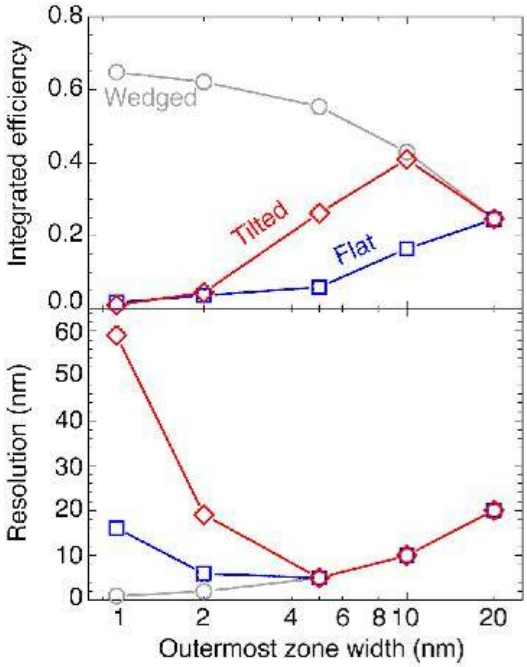

Figure 12.2.24 Calculated efficiency and Rayleigh-like resolution for MLLs with various values of outermost zone width for the flat, tilted, and wedged zone cases. As can be seen, a 5 nm resolution target with flat MLLs appears to be achievable at reduced efficiency. Better efficiency is attained if tilted zones are used. And if wedged zones are used, better efficiency and resolution are attainable.

The discussion thus far has assumed that layers of the proper thickness can be deposited with perfect thickness control, without thickness error or roughness accumulation, and with no interlayer diffusion. In recent years the EUV lithography program has been a huge driver in improving the quality of synthetic multilayer mirrors, and multilayer coatings as thick as 70 μm have been fabricated with roughness below 5 nm by a process of sputtering, interleaved with ion beam polishing. However, the fact that normal incidence reflectivity for sputtered multilayer mirrors continues to be poor at wavelengths below about 5 nm means that interlayer diffusion is likely limiting the performance of sputtered layers on dimensions of 1–2 nm, which is right at the ultimate resolution goal of the NSLS-II project. One possible solution to this problem is to use Molecular Beam Epitaxy rather than sputtering to fabricate the alternating zone layers, and preliminary calculations show that there are no significant focusing errors associated with forcing zone boundaries to line up with integer multiples of MBE monolayer thicknesses. In addition, while a key appeal of MLLs is the ability to start at the outermost zones so that error accumulation is zero when the zone width is the smallest, a glance at the table of zone widths and numbers in Table 12.2.1 reveals that for very high-resolution optics there is still ample opportunity for small fractional thickness variations to accumulate, leading to dephasing of zone positions from their proper values, which, in turn, will produce aberrations in the focus, or the choice of very large central stop fractions *a* that will provide a narrow focal spot at the cost of needing to tolerate very strong sidelobes.

12.2.5.1.3 Simulations for MLLs

For the leading candidate MLL optic, the push to a resolution of 1 nm raises a number of new questions. Any physical implementation of a MLL will deviate from the idealized structure, and it is important to understand if these imperfections would prevent the achievement of 1 nm resolution. In order to resolve these issues, or at least gain some physical intuition, some simulations have been performed. The optics imperfections addressed by these simulations are the 1) discreteness of the underlying material, 2) density contrast difference between the constituent layers, 3) interfacial roughness, 4) growth rate errors, and 5) apodization or elimination of the central portion of the optic. Briefly, these simulations suggest that many of these deviations from the ideal case do not prevent one from obtaining 1 nm resolution. Rather, most of the imperfections result in a reduction in intensity of the central high resolution feature but maintain the same width, with a concomitant growth of "tails" to the focused spot; in other words these imperfections lead to a

reduction of efficiency of the optic. However, one imperfection is quite disruptive to the high-esolution feature. If the growth rate for the constituent deviates significantly from the desired growth rate, the result is zones that are not placed at the idealized locations, leading to phase errors that destroy the focusing properties.

These results are consistent with existing intuition developed for standard binary zone plates; however, without these simulations it was not clear a priori that the extreme nature of these optics would not require different intuition. For example, for the most serious error, that of the growth rate, the standard intuition is that zones need to be placed to within an accuracy of one-third of the width of the zone in order to preserve the required phase accuracy. The other errors, such as randomization of boundary locations due to a discrete lattice or interface roughness, preserve the overall phase accuracy and hence preserve the optic resolution, albeit with some reduction of intensity. Note that there are limits to the simulations performed, because they are performed in the "thin" lens limit, which effectively compresses the optic into a single plane. We expect that this work will need to be reproduced in the "thick lens" limit to strengthen the conclusions.

Discrete Lattice Implementation

One potential physical implementation of a MLL is to grow these optics in a lattice-matched materials system. The single crystal nature of this implementation would have potentially significant advantages. First, the interfaces can be made atomically flat, as has been demonstrated [12.2.18]. Second, the single-crystal nature will result in reduced small-angle scattering. Third, these films can be made thinner as a result of the reduced roughness.

These advantages come at a price. The boundaries of transition between the different zones are fixed multiples of the materials chosen. For example if one chooses BaBiO3 and MgO as the materials pair from which to construct the MLL, the C-axis lattice parameters are 0.43 nm and 0.42 nm respectively, and so the thickness of any given zone can only be discrete multiples of these basic lattice units. However, the ideal zone plate functional form is $u_n = \sqrt{(n\lambda f + 0.25n^2\lambda^2)}$ and cannot be placed onto such a discrete lattice, leading inevitably to errors in the placement of the zone boundary placement. Numerically, the best choice v_n that approximates u_n using the underlying discrete lattice is chosen, and the simulation of the resulting profile is performed. What the simulations show is that in spite of the discretization of the zone profile, the width of the focused spot is not significantly different from an equivalent zone plate with the ideal zone profile. However, the intensity in the central component is reduced relative to the intensity in the tails.

Density Contrast Difference

The results obtained by varying the ratio of density contrast between the two layer compounds fit neatly with established intuition. The focus intensity is simply proportional to the contrast difference between the layers, with no effect on the optic resolution.

Interface Roughness

Here the results obtained by simulation are also consistent with naïve expectations. As long as the roughness is much smaller than the smallest zone width, the resolution of the optic is unchanged, though the intensity of the focus decreases with increasing roughness. The location of the diffuse scattering depends on the specific form of the roughness. For the Gaussian roughness chosen here, the unfocussed light goes into a uniform background. A conformal roughness will give a different distribution of the unfocused light. The numerical aperture of the optic will be limited to a size such that the smallest zone becomes comparable to the roughness. The net effect is that the numerical aperture is determined by the point at which the roughness becomes comparable to a zone width.

Growth Rate Errors

Growth rate errors are the most significant obstacle to the production of high resolution MLL optics. The reason is that growth rate errors can result in the center of mass being placed in a different location from its ideal location. This kind of error is in marked contrast with the other imperfections, which have the zone center of mass ideally placed, but with some randomness in the specific boundary location. This sort of error results in phase errors, and the simulations show that small errors can result in significant broadening of the focus.

Apodization

Existing examples of MLL optics are apodized, i.e., regions of the optics are blocked (effectively, there is a central stop). Our simulations show that increasing the central stop zone results in increased tails, but still maintains a sharp, high-resolution central feature. Figure 12.2.25 shows examples of simulations of five different sizes of central stops.

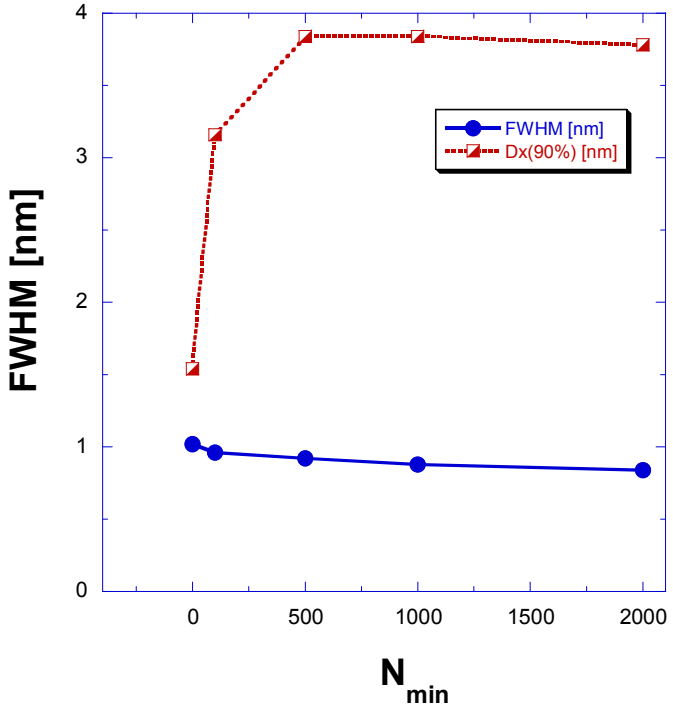

Figure 12.2.25 The blue curve shows the width of the central feature, extracted from the full width at half maximum (FWHM). The red squares and line include effects of the width of the tails or broad feature, determined by extracting the width containing 90% of the integrated intensity. The bottom axis is the size of the obstructed region measured by the number of zones. The full size of the zone plate is 20,000 zones.

Not shown in the figure is a reduced intensity of the central component with increased apodization. Clearly, while apodization results in increased intensity in the tails, the central FWHM is relatively unchanged. Consequently, apodization is not an obstacle to 1 nm resolution optics, but will result in a reduced sensitivity to high spatial frequencies.

Even with these potential limitations, MLLs offer one of the most promising paths toward focusing resolution on the nanometer scale. However, it is also likely that MLLs will not be the optic of choice for all experiments, as in some cases it may be preferable to use cylindrically symmetric optics with small central stop fractions *a* to minimize the energy distributed outside the central focus; in other cases, the achromatic nature of reflective optics may be preferred.

While Fresnel zone plates rely on the difference in optical properties between one material and vacuum, MLLs rely on the difference in optical properties between two different materials (typically with different densities and atomic numbers). Because the ratio of phase shift to absorption improves roughly as the square of increases in photon energy, this means that MLLs are not suitable for use at energies below a few keV. (The same argument apples to refractive lenses and kinoforms, as well.) As NSLS-II will be a powerful

source of coherent soft x-rays, it will be important to have available high-resolution Fresnel zone plates for soft x-ray focusing experiments at NSLS-II.

One final consideration involves thermal loading of the optic. Thermal engineering studies are required to set a limit on distortion of a MLL due to absorption of some fraction of the x-ray beam. Paradoxically, this is more of a problem at low photon energies than at high, because of the improvement of the ratio of f_1/f_2 at higher energies, so that a MLL becomes more and more of a pure phase optic.

In Figure 12.2.26, layer positions were measured using a standard Scanning Electron Microscope. While standard SEMs do well at measuring the size of small features within the field of view, current systems tend not to have very accurate absolute position measurement capabilities. For example, while one can observe that zones at the 10 μm layer position have a width of about 5 nm, one cannot determine that the boundary of zone 487 is at the required position of 10.0034 μm. Absolute zone placement errors must be kept to below about a third of a zone width (or 0.3 nm, which is the size of an atom) to meet the 1 nm resolution goal of NSLS-II.

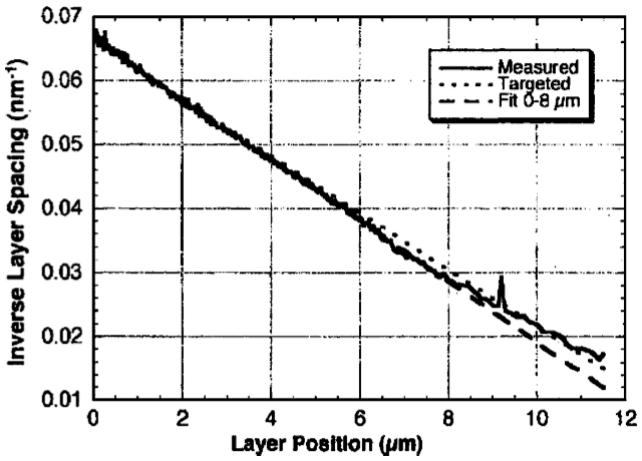

Figure 12.2.26 Example of present-day diagnostics used to evaluate zone placement accuracy in MLLs [12.2.21].

12.2.5.1.4 Effort Required to Reach 1 nm Resolution with Multilayer Laue Lenses

MLLs were first developed at Argonne National Laboratory, where there is an ongoing program to develop MLLs based on DC magnetron sputtering for layer deposition. We propose to complement the effort at Argonne, while keeping in contact with their efforts, in the following ways:

- BNL has unique capabilities in ultra precise layer deposition using Molecular Beam Epitaxy. With MBE, one can deposit material layers with a thickness that is controlled down to an integer number of crystallographic unit cells, offering the potential for improvement in the minimum zone width that one can really achieve without the compromising effects of interlayer diffusion, and also improved layer smoothness, which in turn can make zones stay in phase by being in the proper absolute position over a larger distance. We propose to embark on a program of MLL fabrication using BNL's existing MBE system to test the ability to produce MLLs with only a modest number of layer pairs (limited by the slow rate of deposition of MBE layers) but with high focusing efficiency. We will also examine the effects of producing layer boundaries at integer multiples of crystallographic unit cells, and compare the artifacts caused by this with numerical simulations that we are currently working on.
- We propose to explore new high-density/low-density materials pairs beyond those demonstrated by Argonne to check theory against calculation and to see if there are additional favorable materials pairs that should be considered.
- We propose to develop an MBE system with more rapid layer deposition.
- We propose to explore ways to fabricate wedged layers, such as by partial masking of the substrate during part of each deposition cycle.

- We propose to acquire or develop a system able to measure zone locations on an absolute position scale, rather than relying on a standard SEM. A good candidate for this is a scanning tunneling microscope with laser-interferometer scan axis control and in-situ electron diffraction.
- We propose to develop a system for mounting and aligning four MLLs to 1 nm tolerance using x-ray interferometry, and preserving their alignment using laser interferometer feedback on the MLL support mounts.

This effort will involve people with expertise in the fields of thick-film deposition, sectioning, numerical simulations, and engineering. It will be one of the major components of the NSLS-II R&D program and will explicitly complement and extend the related efforts at Argonne National Laboratory. We expect that the newly established group at BNL will keep in frequent contact with the Argonne effort.

12.2.5.2 Kinoforms

12.2.5.2.1 Introduction

Kinoforms [12.2.19] are computer-generated phase optics that, when illuminated, generate an image of a mathematically desired final object. It is possible to form a lens kinoform where the desired object is a single point and the incident illumination is a parallel plane wave; it is also possible to create kinoforms with other desired optical functions. Kinoforms (Figure 12.2.27) can be considered equivalently from two points of view; either as an array of coherently interfering lens-segments or as an optimally blazed zone plate.

.

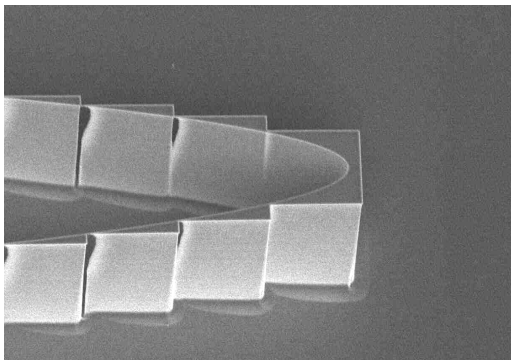

Figure 12.2.27 Kinoform structure etched into silicon with deep reactive ion etching. The step-like structure shows the material that is removed to give 2π phase shifts and is 30 microns for the designed energy of this lens. X-rays incident from the right will be focused to a line focus on the left.

Typical materials parameters of refractive lenses for hard x-rays result in an effective aperture that is limited by absorption in the thicker parts of the lens. The consequence of the absorption is that the numerical aperture, and hence the resolution, is limited. Kinoform lenses provide a route around this limitation. Shown in Figure 12.2.28 is a refractive lens and two kinoform lens equivalents of the refractive lens. For the refractive lens the mathematical derivation of the lens profile is straightforward. Given a refractive index δ, a focal length F, and a parallel beam illuminating the lens, the analog profile for a loss-less lens is

$$y^2+(2\delta-\delta^2)x^2-2\delta Fx=0\,, \qquad (12.2\text{-}22)$$

in other words, an ellipse. To obtain the kinoform structure, a volume of material is removed in integer multiples of λ/δ, where λ is the desired operating wavelength. There are two limiting kinoform structures, the "long" structure shown in Figure 12.2.28b, and the "short" structure shown in Figure 12.2.28c. The long structure is quite clearly related to the refractive lens, and the short structure has strong analogies to the standard zone plate. Both kinoform structures have a reduced absorption in comparison with the solid refractive structure shown in Figure 12.2.28a.

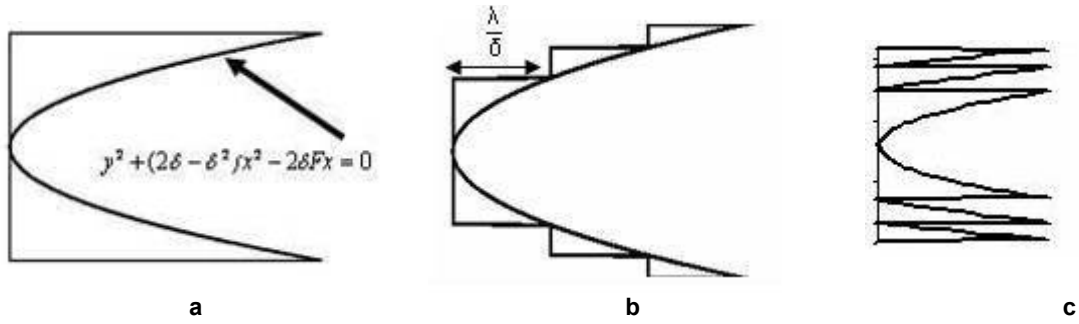

Figure 12.2.28 **a)** A solid refractive lens. **b)** Elliptical profile of "long" kinoform lens, and the sections removed from the solid refractive lens shown in **a** to reduce loss. A parallel beam comes from the left and the focused spot is on the right. **c)** A "short" kinoform lens, where the segments are folded into one plane; this is the more familiar kinoform structure, and the similarity to the binary zone plate is clear.

Shown in Figure 12.2.29 is a comparison of the absorption as a function of distance from the optic axis. On the left is the absorption of a solid refractive lens, and on the right is the same plot for the kinoform. The average transmission of the kinoform asymptotically approaches

$$T = e^{-\left(\frac{2\pi\beta}{\delta}\right)}, \qquad (12.2\text{-}23)$$

but the crucial difference is that the absorption is almost uniform across the lens aperture, and hence absorption no longer limits the NA and resolution of the lens. At 10 keV, for silicon T is 0.88, and for diamond T is 0.9937.

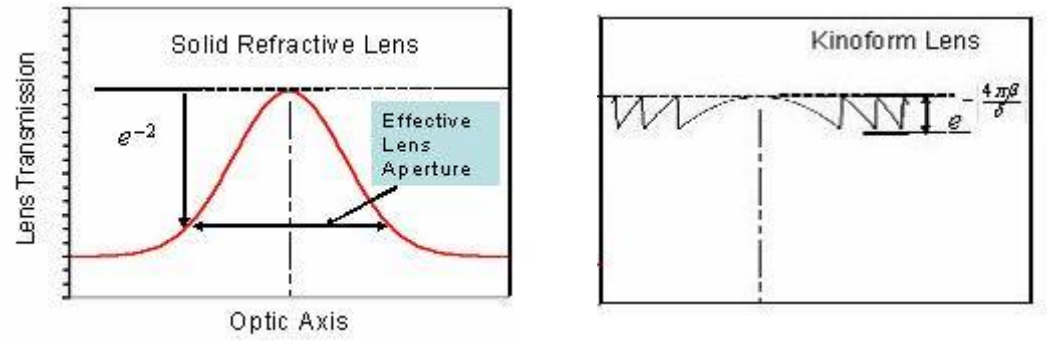

Figure 12.2.29 Comparison of the absorption across the aperture of a lens for a refractive lens on the left, and a kinoform lens on the right.

12.2.5.2.2 Analogy to the Zone Plate

While we obtained the kinoform structure by removing material of size integer multiples of λ / δ from a solid refractive lens, the resulting structure has strong analogies to a zone plate. Here we clarify the analogy to the zone plate, and then later we build on this to obtain some analytic results that have practical implications. y_m are the locations of the standard zone plate boundaries of a zone plate at x=0 for a focal length F and wavelength λ, where

$$y(0)_m = \sqrt{2mf\lambda + m^2\lambda^2}, \qquad (12.2\text{-}24)$$

as shown in Figure 12.2.30. If one evaluates the kinoform boundaries at x=$\frac{\lambda}{\delta}$, one finds that

$$y(\frac{\lambda}{\delta})_m = \sqrt{(2mf\lambda + \lambda^2(m^2 - (\frac{2m}{\delta}))} \ . \tag{12.2-25}$$

The first observation is that the boundaries $y(\lambda/\delta)_m$ correspond to the classic zone plate but with $F \rightarrow (F - (\lambda/\delta))$.

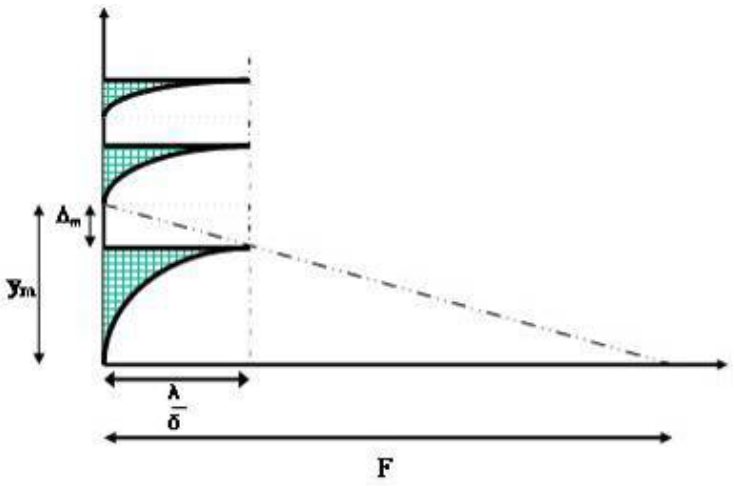

Figure 12.2.30 Connection between the kinoform and the zone plate. Evaluating the locations of the boundaries from the refractive point of view matches the zone plate boundaries if the limit δ is large.

Also, as δ tends to infinity, the thickness of the kinoform lens tends to zero, and the boundaries tend to the classic zone plate boundaries:

$$y(0)_m = \sqrt{2mf\lambda + m^2\lambda^2} \ . \tag{12.2-26}$$

This is consistent with the observation by Sweatt [12.2.22] that a thin holographic optical element can be considered as a "degenerate" lens, where the index of refraction approaches infinity, and curvatures and thicknesses approach zero for a fixed focal length.

12.2.5.2.3 The Kinoform as an Efficient Zone Plate

An ideal phase zone plate with no absorption can have ~40.4% of the light in the primary focus, and the higher order foci will have intensities

$$\frac{0.404}{n^2}, \tag{12.2-27}$$

where n is the index of the focus. In contrast, an ideal kinoform structure with no absorption operating at the primary or fundamental n=1 focus can have 100% efficiency. The reason for this difference is that for the binary zone plate, there is intensity in the higher order foci, whereas for the kinoform there is only one focus. As is shown later, the binary zone plate phase profile is a square wave profile within each Fresnel zone, which upon Fourier transforming allows the odd (±1, ±3, ±5,) harmonics to exist. In contrast, for the kinoform (which has a smoothly varying profile within each Fresnel zone), one can tailor the profile to have zeros at all

the alternate foci, resulting in all the light going into the fundamental, and giving a more efficient optic. We summarize the case for the kinoform graphically in the three panels of Figure 12.2.31.

In panel a, we show all the potential foci F/n that would result from a Fourier transform of the Fresnel zone structure of a lens. In the middle panel we show the "form factor" that is the result of the Fourier transform of the kinoform phase profile that repeats within each zone. The key feature of this panel is that the kinoform form factor has zeros at all the potential foci, except the one the kinoform phase profile is designed to maximize. In panel **c**, the bottom panel, is shown the product of the two terms, showing the only surviving focus, resulting in an efficiency of 100% for loss-less ($\beta = 0$) lens material. For real materials, β is not zero, and the net efficiency becomes

$$e^{-\left(\frac{2\pi\beta}{\delta}\right)}, \qquad (12.2\text{-}28)$$

as indicated above.

Figure 12.2.31 Normalized focal length.

a) All the allowed foci at 1/n in normalized units.

b) Form factor with zeros at most of these allowed foci.

c) The product, leaving a single focus.

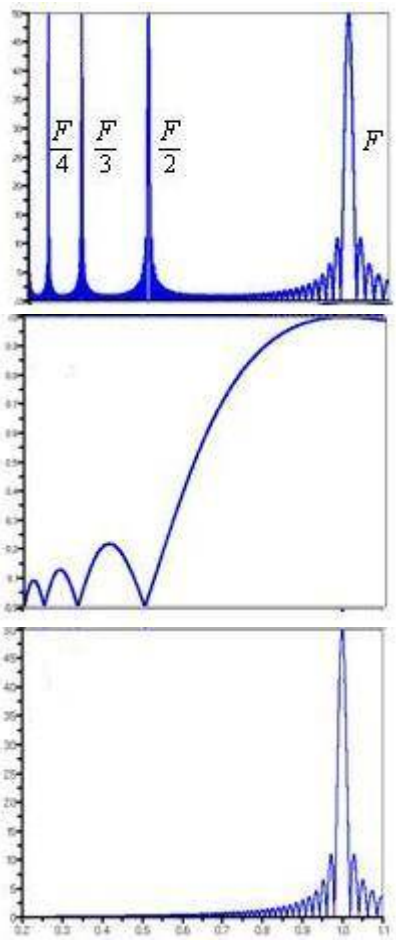

12.2.5.2.4 Higher Order Foci Enabled by the Efficient Kinoform

We briefly summarize here the analytic basis for the results illustrated in Figure 12.2.31, and extend it slightly, to show how to optimize not just the fundamental n=1 focus, but any focus of choice. This has an important practical implication. For the standard binary phase zone plate, the optic resolution is on the order of the size of the smallest zone. Most fabrication methods have a minimum feature size that can be fabricated with precision. One way to improve the resolution is to operate the zone plate at one of the higher order foci,

since the optic resolution or spot size of the nth order focus is 1/n times the size of the smallest zone. However, as we know from above, this comes at a substantial flux penalty: the n^{th} order focus has $1/n^2$ the intensity of the fundamental. The kinoform, by steering all the light into the chosen focus, allows us to efficiently operate with a resolution that can be significantly smaller than the smallest feature size in the lens. This is not un-physical; a classical optical lens is much bigger than the lens resolution.

To understand this analytically, we assume we have an optic with focal point *f* and aperture consisting of Fresnel zones with boundaries at

$$\sqrt{n2\lambda f}\ , \tag{12.2-29}$$

up to a maximum of N, i.e., a fixed maximum radius of

$$\sqrt{N2\lambda f}\ . \tag{12.2-30}$$

We will consider an optic consisting of kinoform or binary zone plate structures that are periodic in M multiples of Fresnel zones, and so the smallest feature is approximately M times larger than the smallest Fresnel zone. The new zone boundaries will be at

$$\sqrt{nM2\lambda f}\ , \tag{12.2-31}$$

where the dummy index n will run up to N/M, i.e.,the optic aperture stays fixed. In the paraxial limit, the phase shift required by the kinoform leads to a structure thickness

$$t(\rho) = \frac{\rho^2}{2\delta f} - nM\frac{\lambda}{\delta} \tag{12.2-32}$$

in the nth zone, where ρ is the radial distance from the optic axis. Using the Kirchoff Fresnel integral to find the amplitude A, at point z along the axis it can be shown that:

$$A(z) \propto \sum_n \frac{\left[e^{i\pi\alpha v}\right]_{v_n}^{v_{n+1}}}{i\pi\alpha} = \left\{\frac{2\sin(\pi\alpha M\lambda f)}{\pi\alpha}\right\}\left\{\sum_n e^{(i\pi\alpha M 2\lambda f)n}\right\}, \tag{12.2-33}$$

where

$$\alpha \equiv \frac{1}{\lambda}\left(\frac{1}{f} - \frac{1}{z}\right), \tag{12.2-34}$$

and v is ρ^2. One can consider the product of two terms as a "form factor"

$$\left\{\frac{2\sin(\pi\alpha M\lambda f)}{\pi\alpha}\right\} \tag{12.2-35}$$

and an array of "Bragg peaks"

$$\left\{\sum_n e^{(i\pi\alpha M 2\lambda f)n}\right\} \tag{12.2-36}$$

in the terminology of diffraction from crystalline arrays. In this case the Bragg peaks occur at the allowed foci. For M=1, the largest focal length is f, and the higher orders are f/n, with n = (± 1,± 2,± 3,…). For M=2 the largest focal length is 2f and the allowed foci are 2f/n; for M=3 the allowed foci are 3f/n, and so on. This makes physical sense; because we use zones of size M times the fundamental, the lowest order focal length is Mf.

However, the form factor term has zeros at all z = Mf/n with n = (±1,±2,±3,…), except for z = f, when, since in the limit α→o, we have

$$\lim_{\alpha \to 0} \frac{\sin(\beta\alpha)}{\alpha} = \beta\,, \tag{12.2-37}$$

which is nonzero. This focus at z = f, then, has nonzero intensity, and all the other foci have zero intensity. We have demonstrated in previous publications experimentally, and here analytically, that one can design kinoform hard x-ray optics to optimize the intensity of a higher order focal point. This is done to fabricate optics with resolution exceeding that allowed by the minimum size of a given fabrication method. Very few fabrication techniques and materials can give us the precision needed to fabricate the optical quality, nm-sized structures necessary to produce nm-sized beams. By using kinoforms in higher order, we anticipate an easier path for fabricating optics that can produce such focused beams.

12.2.5.2.5 Compound Kinoforms

A single kinoform lens has an aperture that is not limited by absorption. However, for hard x-ray photons, with the kinoform lens material refractive index <1, the optic resolution is limited by the critical angle, because of the required lens profile. Using Fermat's theorem, for a source infinitely far from a lens that is then focused to a point, the correct phase profile can be shown be an elliptical kinoform shape. Other source-to-lens and source-to-object distances will require other lens profiles that also can be deduced from Fermat's theorem. The elliptical shape immediately leads to the result that for a single lens there is a resolution limit ≈ λ/θ_c , because for a given focal length F, there is a maximum lens aperture = $F\theta_c$. For a single silicon lens at 11.3 keV, $0.61\lambda/\theta_c$ ~25 nm. The solution to this resolution limitation is to consider compound lenses, just as is done in conventional optical microscopy, and as shown in Figure 12.2.32. A single lens has a NA of θ_c, but an array of M lenses can have NA of $M\theta_c$. In fact, compound kinoform lenses have already been fabricated; however, these lens arrays consisted of identical parabolic kinoform lenses, and the resulting phase profile did not achieve the optimal performance. What is required is to create an array of kinoform lenses where each is designed to match the waveform from the lens prior to it to a new focus (i.e., from a virtual focus f_1 to a new focus f_2).

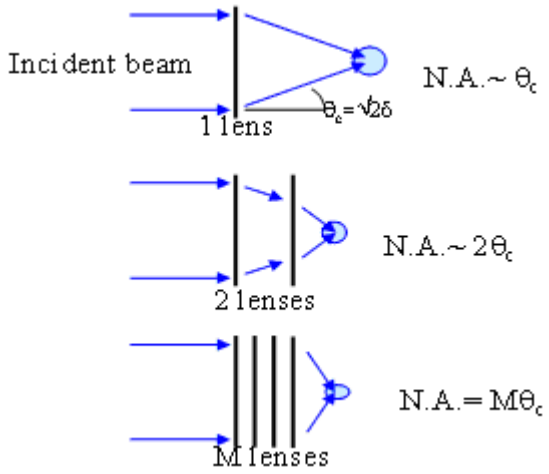

Figure 12.2.32 Using compound lenses to exceed the critical angle limit. A single lens has a maximum NA of θ_c, but M lenses can be arranged to have an NA of $M\theta_c$, resulting in a resolution of $0.61\lambda/M\theta_c$ for the array of lenses.

We have demonstrated a compound lens of this type. Shown in Figure 12.2.33 are results from a compound kinoform of four lenses, with a designed maximum deflection angle of $2\theta_c$, an expected lens resolution of 12.5 nm, and a lens aperture of 300 microns. The experimental data show a net deflection θ_d of $1.1\theta_c \pm 0.05\theta_c$, demonstrating that one can use compound kinoform lenses to focus down to below the critical angle limit.

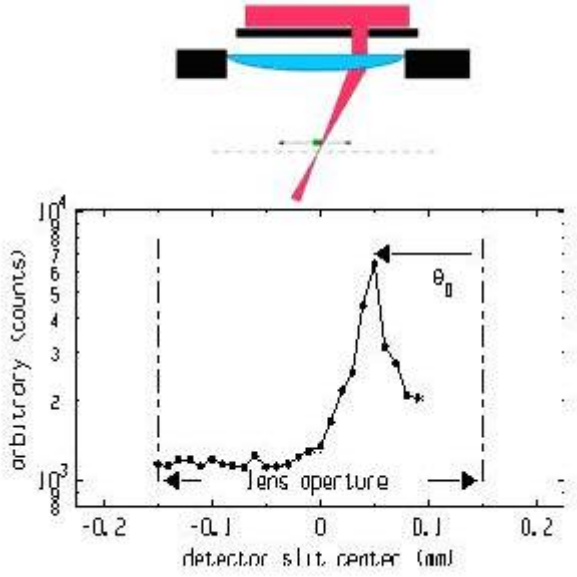

Figure 12.2.33 Experimental verification that one can exceed θ_c with an array of kinoform lenses. The top figure schematically describes the experimental layout, showing a slit limiting incident radiation to the outer part of the lens. A lithographically defined metal marker is scanned through the focus, and the fluorescent signal is shown as a function of position in the bottom panel of the figure.

The optic is an array of four lenses. The bottom panel shows that the array functions as a lens because of the peaked structure. If the peak structure were located at zero, it would function as designed. However, this lens has an aberration. When we measure the deflection angle θ_d, we find that θ_d of $1.1\theta_c = \pm 0.05\theta_c$, clearly larger than θ_c.

12.2.5.2.6 Challenges Associated with Reaching 1 nm with Kinforms

Shown previously in Figure 12.2.27 is a physical implementation of a kinoform structure in silicon. Silicon has been the material chosen to demonstrate many of the kinoform properties because of ease of fabrication. This structure is created by the following steps. A hard mask, typically SiO_2, is deposited as a uniform film onto the lens material. Using electron beam lithography methods, the desired pattern is written into a resist, and this pattern is now transferred into the hard mask. Next, using Reactive Ion Etching methods, the pattern is etched deep into the material, using the patterned hard mask to transfer the pattern. The Bosch process for deep RIE is used.

To move the technology beyond current state of the art and obtain 1 nm spots, we need to address the following issues: limitations of the crossed geometry, etching limitations, and alternative materials and refractive index metrology.

Crossed Lens Geometry

A lens of the type shown will give a line focus, as shown in Figure 12.2.34a. To create a spot, one uses a crossed pair (panel b). Shown in panel c is data showing a spot obtained from such a crossed geometry. The measured spot size was 0.6×4 microns^2, with most of the measured size due to the source and not due to intrinsic properties of the lens. In an earlier section we have addressed the limitations of the crossed geometry. The simulations suggest that the crossed geometry will result in reduced sensitivity to the sharpest spectral features as the numerical aperture of the lenses increases. We do not expect the crossed geometry to be a limitation for 1 nm resolution optics (though to go further one would need to develop radially symmetric lenses, not the linear ones considered here).

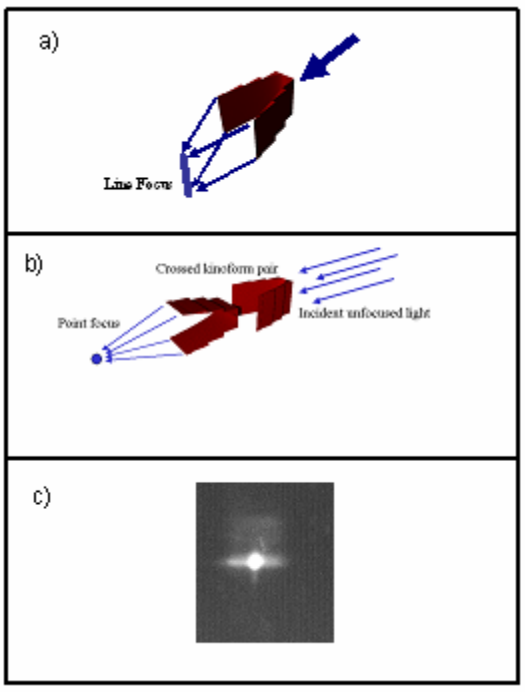

Figure 12.2.34 Use of linear, 1D kinoforms to obtain a focused spot.

a) Single 1D kinoform produces a line focus.

b) Two successive 1D kinoforms, operated as a crossed pair, produce a focused spot.

c) Experimental results from crossed lenses.

Etching Limitations

To obtain high-quality optics, the profile of the optic must match the ideal profile with phase errors less than $\pi/4$. Using micro-fabrication techniques, this is easily achievable due the precision of electron beam writers, which have a spatial placement error of the order of 1 to 10 nm over a 500 micron field. For a typical material with δ of order 10^{-6}, this precision corresponds to phase errors of order $(\lambda * 1\text{nm})/\delta$, approximately $10^{-4}\ \pi$, clearly more than adequate. In fact, the limitations of lens fabrication are primarily due to the etching processes that transfer the electron beam lithographic profiles to the substrate. Shown in Figure 12.2.35 are examples of the etching limitations.

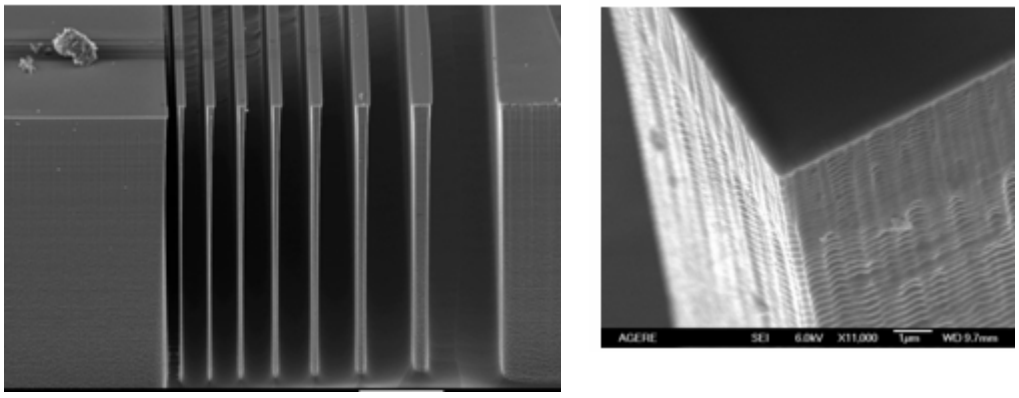

Figure 12.2.35 Two of the current limitations in Si etching technology. Left: Cut-away of a lens structure showing the depth of etching (88 microns, here). Right: Scalloping due to the Bosch process.

On the left is a structure that has been etched down 88 microns. The thinner features exhibit depth-dependent variation in thickness. For optics, it is important to keep a precise shape all the way down the etch depth; in other words, the sidewalls must have 90-degree angles. A further issue seen here is a rounding of the profile near the base. Finally, the right panel shows the scalloping results from the Bosch process. As shown, the scallops measure 200 nm, peak-to-valley.

We believe that both of these problems are solvable. For example, D. Olynick [12.2.23] at LBL has developed a smoother etch process that creates only 10 nm scalloping. Further, the RIE process routinely etches through whole wafers, a depth of 750 microns, and—depending on feature size—can produce the vertical and smooth sidewalls required. Finally, alternative etching methods, such as electrochemical methods, seem to have great potential but have not yet been evaluated for these types of applications.

Alternative Materials

Although silicon has been the material of choice up to this point, to achieve high spatial resolution with reasonable efficiencies requires materials with better optical properties than silicon. We have identified single crystal diamond as one of the better choices, since the transmission through a single lens is 99.4% at 10 keV. However, not only must the optical properties of the materials be better, the precision with which the required lens profiles can be transferred to the materials is just as important to the final lens performance. One must therefore develop fabrication methods for diamond, a project that is already underway. Diamond is a low-density alternative. Some high-density alternatives are Ge and InSb. The advantage of high-density materials is that fewer lenses are needed, which reduces the complexity. For each of these new materials all the steps have to be redeveloped: the deep etch, the hard mask, and the resist. However, for most materials of interest, other market pressures have already spurred some development; commercial etching recipes and tools for these materials are available. However, only in the case of silicon etching do the processes developed comfortably exceed our goals.

12.2.5.2.7 Achieving 1 nm Spot Sizes with Kinoform

There are three key features of kinoforms that potentially enable them to obtain 1 nm spots. First, the kinoform has a transmission function that is almost uniform as a function of increasing lens aperture, so the NA of the lens is not limited by absorption. This contrasts with the pure refractive lenses, which have a transmission function that decreases near the periphery of the lens.

Second, the kinoform does not have to be fabricated with structures as small as the resolution of the lens. This contrasts with the zone plate class of optics, where for efficient operation the smallest feature fabricated is the resolution of the lens. A refractive lens can be fabricated to operate in higher order, but there is a loss of efficiency. A kinoform profile can be optimized to maximize the higher-order focus.

Third, a compound kinoform lens sidesteps the issue of small δ that limits the focusing power of a single lens and otherwise limits the spatial resolution to $0.61\lambda/\theta_c$.

All the key items above have been demonstrated, and no new technology is required to fabricate these lenses. What will be required is to optimize existing fabrication and testing technology. In particular, the weakest link in the process is the quality of the etching process. While no new technology is required, improvements in technology will result in improved performance.

The kinoform lens would consist of an array of at least $(\theta_c\Delta_t)/(0.61\lambda)$ lenses—at least 25 lenses if the material were silicon, 20 lenses for diamond, and 14 for Ge. In all cases these are lower limits, and we expect to actually use approximately 1.5 times as many lenses as this, depending on the manufacturing tolerances. For a manufacturing process that allows smoother sidewalls and smaller feature sizes, the number of lenses will be close to the lower limit.

12.2.5.2.8 Effort Required to Reach 1 nm

To pursue this approach will require access to a high-precision electron beam lithography infrastructure and an etching research infrastructure. It is important that the lithography is precise over areas as large as possible. Usually this requires a stitching together of smaller areas, commonly referred to as the e-beam writing field. The precision of the stitching will limit the pattern placement accuracy, and this in turn will limit the optic resolution.

The etching research effort will have a main direction: using RIE methods on different materials. There will be a small effort to investigate alternative etching methods, such as electrochemical methods, that may have some advantages over RIE but are speculative.

A computational research program will be necessary to further understand the properties of these optics. All the simulation work pursued so far is in the thin lens approximation, and being able to simulate the 3D volume structure, will give increased confidence in understanding the properties and limitations of these optics.

In summary, the kinoform is one possible optics path to focus down to 1 nm. The aperture is not limited by absorption, the structures do not have to be as small as the optic resolution, and by using compound lenses one can exceed the critical angle limit to the numerical aperture. No new technology needs to be invented, but significant optimization and metrology will be required.

12.2.6 Testing of Optics

Traditional interferometric methods (such as those used for telescope mirrors and optical mirrors in state-of-the-art lithography systems) are not directly transferable to the fabrication of hard x-ray optics, because hard x-ray reflective optics must work at grazing rather than normal incidence, and diffractive and refractive optics depend on the transmission properties through a thickness of material rather than just a single surface profile measurement.

12.2.6.1 Investigating Modular Transfer Function

Several techniques have been used to measure the performance of x-ray lenses. Microfabricated test patterns (in particular, “Siemens star” patterns, which contain a broad range of spatial frequencies in a set of radial spokes) provide one approach, while the finest structure sizes can be achieved by viewing thin-film deposition layers end-on or as sliced cross-sections. Since the Modulation Transfer Function of an imaging system is given by the power recorded at a spatial frequency divided by the power present in the object at that frequency, objects of known structure can be used to measure the MTF. However, getting the “known” structure can have its own challenges, because test patterns suitable for x-ray imaging are usually too thick for transmitted electron characterization, and scanning electron microscopes are even more restricted to viewing only the surface layer of a test pattern. Since phenomena such as interlayer diffusion can affect materials’ boundaries at the 1 nm resolution level, it can be challenging to decouple the imaging system from the object. One simple alternative is to use a thin film with random point scatterers known to be smaller than the size of the probe; the power spectrum of an image of such a sample (which could also consist of high-contrast dopant atom clusters in a substrate) can be used to gauge the modular transfer function of the optical system. If there are distinct zeros in the contrast transfer function, one can even attempt to infer that there exist phase reversals in the imaging systems’ transfer function; this is an approach commonly used in electron microscopy.

12.2.6.2 Iterative Phasing Method

Another class of tests has begun to emerge, using iterative phasing methods to go from knowledge of the optic’s pupil function and measurement of the far-field diffraction pattern of the probe, to an estimate of the complex point spread function of the optical system [12.2.24]. These methods are strongly related to lens-less imaging. They offer a way to evaluate the focus of an optic without any need for a particular test pattern, and can be built on expertise available through nearby groups working in coherent diffraction x-ray imaging at Stony Brook University.

12.2.6.3 Coherent Illumination Methods

While incoherent illumination can provide powerful information on optics tested in a full-field imaging system, coherent illumination provides the best mechanism to map spatial frequency response versus position on the optic. (The loss of coherence means the loss of the ability to assign simultaneously precise position and direction values to ray paths in the optical system.) Therefore, it is crucial that NSLS-II have a coherent optics test beamline, and it will be important to develop improved hard x-ray coherent optics test capabilities now, using either NSLS or other sources until NSLS-II comes on line.

References

[12.2.1] Mitutoyo Corporation.

[12.2.2] K.A. Goldberg, P. Naulleau, P.E. Denham, S.B. Rekawa, K. Jackson, E.H. Anderson, and J.A Liddle, "At-wavelength alignment and testing of the 0.3 NA MET optic," *J. Vac. Sci. Technol*. B **22**(6), Nov/Dec 2004.

[12.2.3] W. Chao, B.D. Harteneck, J.A. Liddle, E.H. Anderson, D.T. Attwood, "Soft x-ray microscopy at a spatial resolution better than 15 nm." *Nature* **435**, (June 2005) pp 1210 ff.

[12.2.4] J. Kirz, *J. Opt. Soc. Am.*, **64** (1974).

[12.2.5] M. Panitz, G. Schneider, M. Peuker, D. Hambach, B. Kaulich, S. Oestereich, J. Susini, and G. Schmahl, "Electroplated Gold Zone Plates as X-ray Objectives for Photon Energies of 2–8 keV," AIP Conf. Proc. **507**, 676 (2000).

[12.2.6] Xradia, Inc.

[12.2.7] G. Schmahl, D, Rudolph, and N. Niemann, AIP Conf. Proc., **75** 255(1981).(1980).

[12.2.8] J. Maser, G.B. Stephenson, S. Vogt, et al., Proc SPIE **5539** 185(2004).

[12.2.9] H.C. Kang, J. Maser, G.B. Stephenson, C. Liu, R. Conley, A.T. Macrander, and S. Vogt, "Nanometer linear focusing of hard x rays by a multilayer Laue lens," *Phys. Rev. Lett*. **96**, 127401 (2006).

[12.2.10] P. Kirkpatrick, and A.V. Baez, *J. Opt. Soc. Am*., **38**, 766 (1948).

[12.2.11] S. Suehiro, H. Miyaji, and Hayashi, "Refractive lens for x-ray focus," *Nature* **352**, 385 (1991).

[12.2.12] A. Snigirev, V. Kohn, I. Snigireva, et al., *Nature* **384**, 49 (1996).

[12.2.13] B. Lengeler, C. Schroer, J. Tummler, et al., "Imaging by parabolic refractive lenses in the hard X-ray range," *J. Sync. Rad*. **6**, 1153 (1999).

[12.2.14] Winn et al., *J. Sync. Rad*. **7**, 395 (2000).

[12.2.15] Q. Shen, "X-Ray Flux, Brilliance, and Coherence of the Proposed Cornell High Energy-Recovery Synchrotron Source," CHESS Tech Memo, 01-002, March 2001,.

[12.2.16] J.W. Goodman, *Introduction to Fourier Optics*, McGraw-Hill (Standord Univ.)1996.

[12.2.17] Schroer, *Phys Rev B* **74** 0033405 (2000).

[12.2.18] Bozovic et al., *Nature* **421**, 873 (2003).

[12.2.19] J.A. Jordan, P.M. Hirsch, L.B. Lesem et al., "Kinoform lenses," *Applied Optics*, 9(8), 1883-87 (1970).

[12.2.20] A.I Erko, V.V. Aristov, and B. Vidal, *Diffraction X-Ray Optics*, IOP Publishing, Bristol, Philadelphia (1996).

[12.2.21] Lui et al., *J. Appl. Phys.* **98**, 113519 (2005).

[12.2.22] W.C. Sweatt, "Describing holographical optical elements as lenses," *J. Opt. Soc. Am*. **67** (6), 803-808 (1977).

[12.2.23] D. Olynick , private communication.

[12.2.24] H.M. Quiney, A. G. Peele, Z. Cai, D. Paterson, and K. A. Nugent, "Diffractive imaging of highly focused x-ray fields," *Nature Physics,* 2006.

12.3 Nanopositioning Instrumentation

At NSLS-II, the required instrument positioning performances and capabilities—such as resolution, dynamic range, repeatability, speed, and multiple axes synchronization—will exceed the limit of commercial availability. In this section, we present the nanopositioning instrumentation requirements and techniques to be developed for the NSLS-II project.

12.3.1 Real-Space Linear Nanopositioning for a Nanoprobe Scanning System

Given NSLS-II's outstanding brightness, a hard x-ray nanoprobe with nanometer scale resolution (Section 11.4) will be a very powerful x-ray characterization tool for the nanoscience community. This kind of unique instrument will also offer diverse capabilities in studying nanomaterials and nanostructures, particularly for embedded structures. The combination of diffraction, fluorescence, and phase contrast in a single tool will provide unique characterization capabilities for nanoscience. Multi-axis scanning stages with subnanometer, real-space positioning resolution are key components for the x-ray nanoprobe with 1 nm focal spot.

12.3.2 Requirements and Issues

The major technical challenge for the design of a scanning stage system for the NSLS-II nanoprobe is its requirement for positioning resolution and stability on the sub-nanometer scale, together with a travel range on the order of centimeters. With advances in the fabrication of novel x-ray optics and an optimized beamline design, we expect to be able to achieve a 1 nm focal spot at NSLS-II. Imaging and spectroscopy at this resolution will require staging of x-ray optics and specimens with a relative mechanical stability and repeatability of better than 0.3 nm.

Figure 12.3.1 shows a multidimensional scanning stage system for a typical scanning hard x-ray nanoprobe. As shown in the figure, the nanoprobe consists of three major component groups: a supporting base, a stage group for the x-ray focusing optics, and a stage group for sample holders.

The stages for x-ray focusing optics provide a 3D positioning capability with 0.3 nm resolution in a 12×12×12 mm travel range. An x-ray optics holder is mounted on the top of the stage group, which consists of two sets of mini stages: a pair of x–y stages for alignment of the optical Order-Sorting Aperture (OSA), and a set of hybrid micro stages for alignment of the x-ray focusing optics. The stage group for the sample holder is composed of x–y–z scanning stages and a rotary stage for x-ray tomography applications. Table 12.3.1 shows an expected design specification for the NSLS-II x-ray nanoprobe.

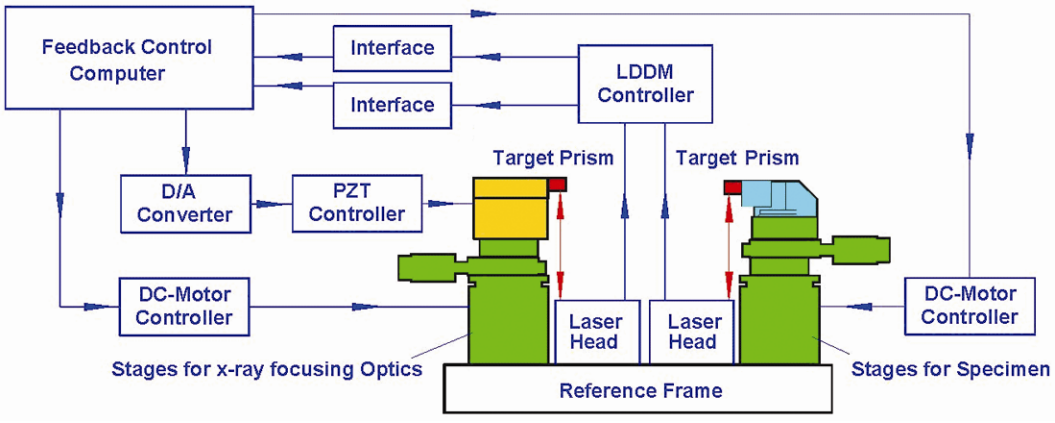

Figure 12.3.1 Schematic of multidimensional scanning stage system for a typical scanning hard x-ray nanoprobe.

Table 12.3.1 Expected Specifications for the NSLS-II Nanoprobe Scanning Stages.

	X-ray focusing optics scanning stages	Sample scanning stages
Overall dimension [mm]	230 (X) x 236 (Y) x 230 (Z)	230 (X) x 268 (Y) x 230 (Z)
Normal load capacity [kg]	3	3
Coarse motion stage type	DC-servo motor with gearhead	DC-servo motor with gearhead
Coarse motion dimension	3 linear	3 linear, 1 rotational
Coarse travel range [mm]	12 (X) x 12 (Y) x 12 (Z)	12 (X) x 12 (Y) x 6 (Z)
Coarse min. incremental motion [nm]	100	100
Coarse unidirectional repeatability [nm]	200	200
Fine motion stage type	PZT with motion reduction	Rotation stage range: Continuous
Fine motion dimension	2 linear	Min. incremental motion (μrad) 6.3
Fine travel range [mm]	2 (X) x 2 (Y)	Rotational repeatability (μrad) 50
Fine min. incremental motion [nm]	0.05	
Fine unidirectional repeatability [nm]	0.3	

Ambient vibrations will be a serious problem for such a facility. For example, at APS, the typical vibration level on the floor in the experimental station is about 10 nm in the frequency range below 10 Hz. This will be a major issue for operating of the scanning stage system in such an environment with a relative mechanical stability and repeatability of better than 0.3 nm. At NSLS-II, the facility will be designed literally from the ground up, to minimize sources and transmissions of vibration. Further, the sandy soil of the NSLS-II site has good vibration damping characteristics. Finally, a detailed finite element analysis of the entire facility, with particular attention to the nanoprobe beamline, will be carried out with a view to taking extra isolation measures for that beamline. Nevertheless, active vibration control on the subnanometer scale will be one of the key technical approaches for this project.

12.3.3 Survey of Technical Approaches

Subnanometer positioning resolution has been achieved by positioning stages for Scanning Tunneling Microscopes and various scanning Atomic Force Microscopes for many years. However, there are major specification differences between stages for STMs or AFMs and stages for scanning hard x-ray nanoprobes. As shown in Table 12.3.2, the working distance between the cantilevered working tip of an STM or AFM and the sample surface is on a nanometer scale, but the working distance between a hard x-ray focusing optic and its specimen for the NSLS-II hard x-ray nanoprobe will be ~10 mm. Further, the weight of a scanning microscope's cantilevered tip is typically in grams or significantly less. The weight of a single soft x-ray zone plate (for example) may be in the same range, but a group of such plates for a hard x-ray nanoprobe with its alignment structures and any optical OSA could weigh a few hundred grams. Finally, in the case of using hard x-ray focusing optics with multilayered diffractive lens techniques or advanced KB mirror systems, the weight of a hard x-ray optics system with 1 nm focal spot may weigh more than a kilogram, using today's commercially available stages.

Requirements for the stage's travel range also differ greatly between typical STM sand AFM stages and the stages for a hard x-ray nanoprobe. The travel range for a typical tip-tilt PZT scanning device is in the range of 50 microns. In contrast, required travel ranges are typically 10×10×10 mm for the stages carrying x-ray focusing optics. Based on these comparisons, it is clear that there are no simple solutions for mounting optics on a small, light, stiff scanning stage along the lines of the STM approach without a significant compromise on the stages specifications because of the 2 to 6 orders of magnitude difference between them.

Table 12.3.2 Comparisons of Scanning Stages for STMs, AFMs, and a Hard X-Ray Nanoprobe.

	Stages for STM and AFMs	Stages for hard x-ray nanoprobe
Working distance [mm]	< 0.00001	10–30
Load capacity [kg]	< 0.001	0.2–1
Travel range [mm]	< 0.1	> 10

A hard x-ray nanoprobe is currently being constructed at the Center for Nanoscale Materials at APS. The system is designed to accommodate x-ray optics with a resolution limit of 10 nm; therefore, it requires staging of x-ray optics and specimens with a mechanical repeatability of better than 5 nm [12.3.1]. A prototype of the APS/CNM nanoprobe, which is acting as an "Early User Instrument" or EUI, is operational. It demonstrated a relative mechanical stability and repeatability of better than 4 nm between its zone plate optics holder and sample holder [12.3.2]. Because this EUI stage system represents the current design, we use it as an example of the technical approaches for the development of an NSLS-II nanoprobe scanning stage system.

12.3.3.1 General Structure of the APS/CNM EUI

As shown in Figure 12.3.2, the EUI developed by APS/CNM consists of three major component groups: a supporting base with 2D differential laser Doppler displacement encoder system, a stage group for the x-ray optics, and a stage group for sample holders [12.3.2]. The entire scanning system was designed with high stiffness, high repeatability, low drift, flexible scanning schemes, and the possibility of fast feedback for differential active vibration control. To allow maximum flexibility in the design of the stage group for specimen holders, all high-precision positioning and scanning is performed by the optics stage group, whereas the specimen stage group is used for coarse positioning only.

Ideally, the base structure should be made from materials with good thermal stability, such as invar or Zerodur. The APS prototype is built of aluminum alloy. Four sets of laser heads and 16-reflection optics for the Laser Doppler Displacement Meter [12.3.3] were mounted on the base structure to perform 2D differential measurements between the x-ray optics holder and the sample holder. To ensure stability of the LDDM, a set of thermal and acoustic shields reduces the influence of heat from the laser heads.

The stages for zone plate optics provide 3D positioning capability with 0.125 nm resolution in the 12x12x12 mm range. The EUI includes three commercial DC-motor driven translation stages and two PZT-driven high-stiffness stages developed at Argonne using a redundantly constrained laminar structure weak-link mechanism for ultra precision motion control. A zone plate holder was mounted on the top of the stage group, which consists of two sets of mini stages: a pair of x–y commercial DC-motor stages for optical OSA alignment, and a set of picomotor-driven weak-link x–y–z stages developed at Argonne for aligning multiple zone plate optics.

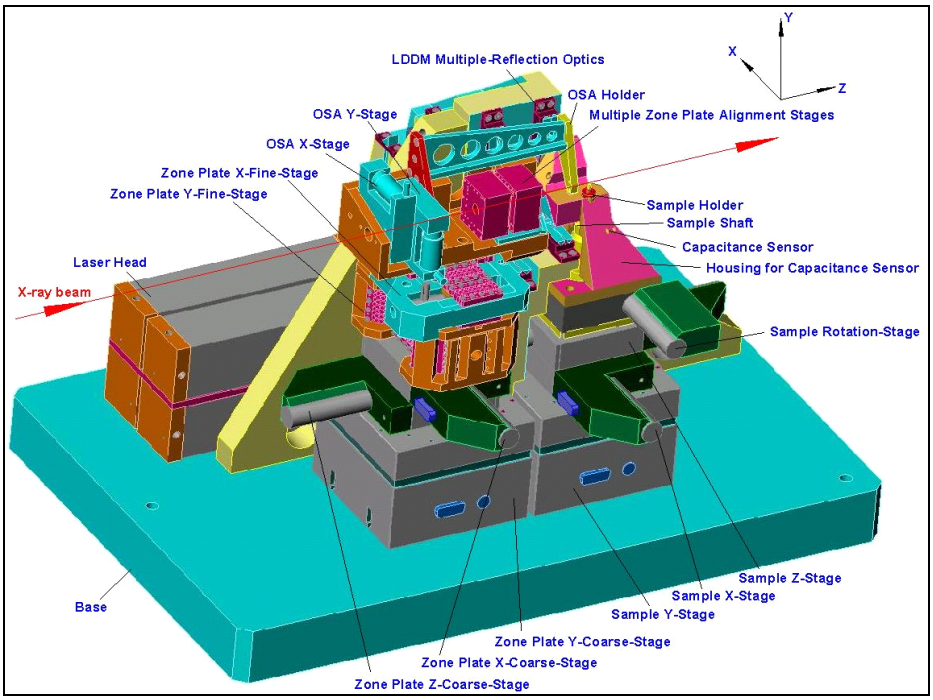

Figure 12.3.2 Model for the x-ray nanoprobe prototype at Argonne. Thermal shields are not shown.

The stage group for the sample holder is composed of three commercial DC-motor driven x–y–z scanning stages and a DC-motor-driven rotary stage for x-ray tomography applications. To improve the sample positioning accuracy, two pairs of capacitance sensors were used to dynamically measure the angular and displacement shifts of the rotation axis. The position of the sample will be determined by a combination of the LDDM system and the capacitance sensor system.

The APS/CNM EUI incorporates a number of design innovations that would also be utilized in any NSLS-II instrument. The first of these is to use a laser encoder system from Optodyne, Inc. with excellent performance (2 mm resolution) that is independent of polarization. This allows the use of multiple reflections (Figure 12.3.3) to create a novel design with subnanometer linear resolution [12.3.4–12.3.6]. In this design the optical path provides eight times greater resolution for linear displacement measurement and encoding. The travel ranges for these stages are ~12 mm, more than sufficient for these applications. Figure 12.3.3 shows the placement of the prisms on the optics stages and on the sample stages.

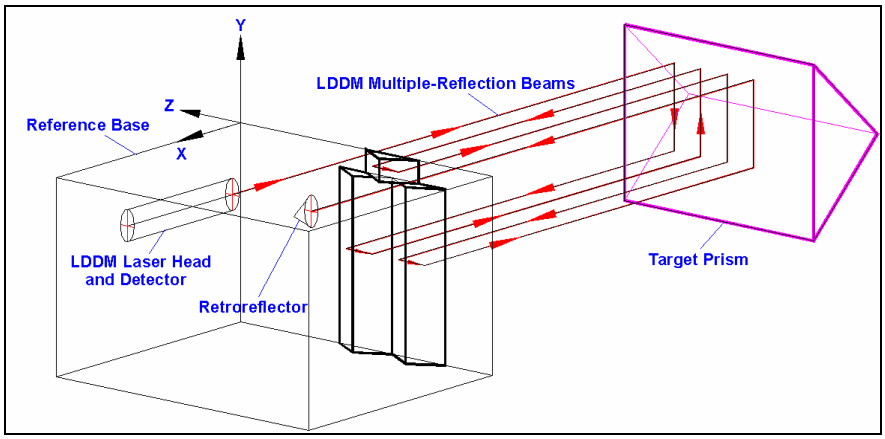

Figure 12.3.3 Schematic of the self-aligning multiple-reflection optical design. With the same laser source and detector electronics, this optical path provides eight times greater resolution.

The second design innovation is to use novel weak-link linear motion reduction mechanisms to perform linear motion closed-loop control at the sub 100 pm level with a micron-level travel range. The structure

consists of four groups of overconstrained, weak-link parallelogram mechanisms [12.3.7, 12.3.8]. The precision of the modern photochemical machining process using lithography techniques makes it possible to construct a strain-free (or strain-limited) overconstrained mechanism on a thin metal sheet. By stacking these thin metal weak-link sheets with alignment pins, a solid complex weak-link structure can be constructed at reasonable cost.

Two sets of piezoelectric-transducer-driven horizontal and vertical high-stiffness weak-link stages have been developed with different travel range and resolution for fine-motion control. The high-resolution, weak-link stages have a 0.02 nm resolution with a 1/15 motion-reduction mechanism and a travel range of 1.5 microns [12.3.7]. For the medium-resolution, weak-link stages, multiple PZT drivers are applied, to guarantee the linear motion trajectory accuracy in a specific direction. The resolution of the stage is 0.3 nm, with a travel range of 15 microns. Physik Instrumente™ PZT actuators with strain-gauge sensor servo-control modules were used to drive both high- and medium-resolution weak-link stages [12.3.9].

12.3.3.1.1 Gap between NSLS-II Requirements and Current EUI Achievement

The EUI differential scanning stage system with the high-resolution weak-link stages has been tested at APS [12.3.7]. As shown in Figure 12.3.4, a series of 1 nm and 3 nm vertical and horizontal differential displacement steps (between zone plate optics holder and specimen holder) have been demonstrated with closed-loop control.

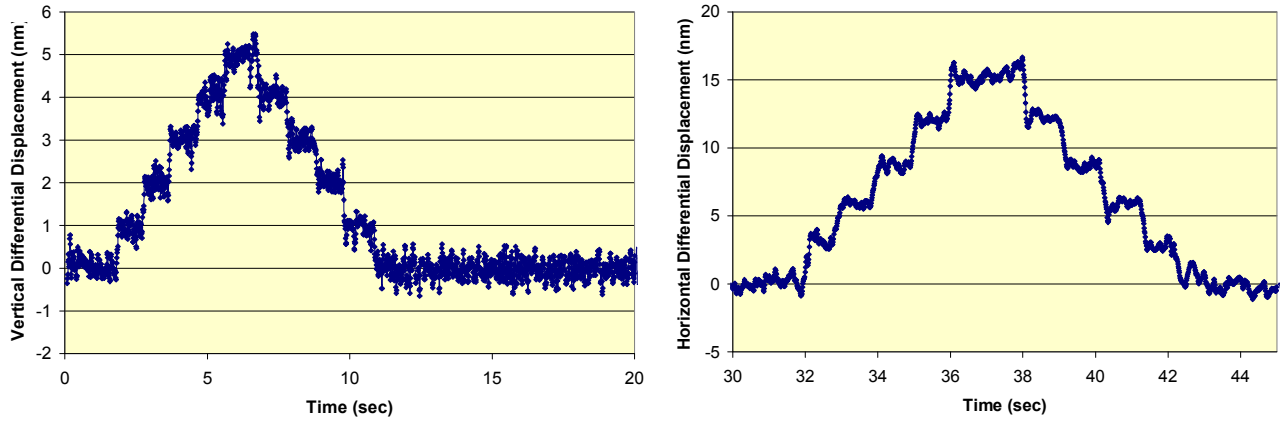

Figure 12.3.4 Closed-loop controlled differential displacement steps test with high-resolution weak-link stages.

Figure 12.3.5 shows an active vibration control test with the prototype system. During this test, the closed-loop control system performed a damping action in response to a single external mechanical disturbance (an 80 kg mass dropped to the floor from 0.2 m height at 3 m away).

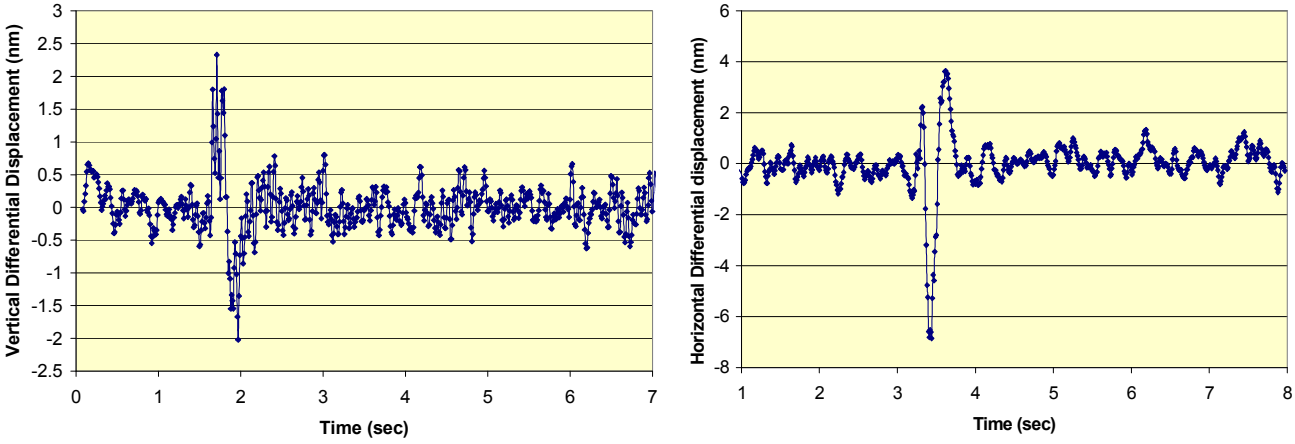

Figure 12.3.5 Active vibration control test with high-resolution weak-link stages.

It is obvious that there is a gap between the positioning resolution requirement for the NSLS-II nanoprobe and the test results from the APS/CNM EUI scanning stage system. For the differential positioning resolution in the vertical direction, the NSLS-II system will need a more than three-fold improvement. A 10-fold improvement will be required in the horizontal direction. Therefore, to meet the technical goal of the NSLS-II nanoprobe project, a significant research and development effort is necessary.

12.3.3.1.2 R&D Program

Figure 12.3.6 shows an active vibration control test result at APS with a 1D stage using a similar LDDM encoder system. A series of 0.1 nm, 0.2 nm, and 0.3 nm steps is demonstrated [12.3.2]. The laser beam is reflected back and forth 12 times between the fixed base and the moving target in this test. This result indicates that the goal of 0.3 nm positioning resolution is achievable in a 1D stage system with a rigid supporting structure. The challenge will be to duplicate this performance in a 3D stage system with significant travel. These results suggest that this is possible, but it will require detailed analysis and development work.

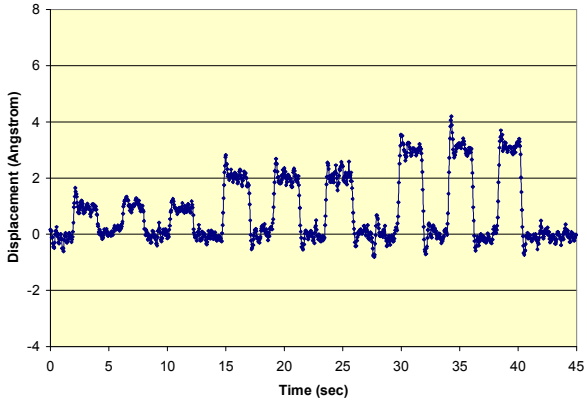

Figure 12.3.6 Closed-loop control scheme test for a 1D setup. A series of 0.1 nm, 0.2 nm, and 0.3 nm steps is demonstrated.

The R&D program will focus on the design, analysis, and development of a stage system with superb structural rigidity and advanced control strategy for multidimensional active vibration control. Specifically, a new prototype stage system will be built and tested under this R&D program to prove the design principle for

the NSLS-II scanning stage system and to ensure the success of the novel NSLS-II nanoprobe instrument. The tasks of this R&D program include:

- designing a scanning stage system that meets the system resolution and load capacity requirements with high stiffness and a 3D size as small as reasonably achievable
- optimizing the stage's motion trajectory accuracy to reduce the coupling motion between dimensions
- developing advanced control mechanism for multidimensional active vibration control

12.3.3.1.3 Real-Space Angular Positioning and 6D Angular/Linear Hybrid Positioning

Besides the 3D linear positioning stages, there are needs for high-precision angular positioning stages and 6D angular/linear hybrid positioning systems for the hard x-ray nanoprobe instrument. Most of these stages are commercially available for customization, such as a precision rotary stage for tomography applications and a 6D robot-arm-based detector manipulator for microdiffraction applications.

However, there are technical challenges in the design of angular positioning devices for the alignment of x-ray focusing optics with 1 nm focal spot, such as the MLL [12.3.10]. The challenges come from not only the level of precision and stability required by the x-ray optics, but also from the requirements of the structure for compactness and from the complexity of the multidimensional alignment system—because the motion tolerances needed to avoid crushing these tiny, fragile, expensive lenses are very tight. Moreover, since these alignment devices comprise the bulk of the load of the scanning stages, they must also be designed with high stiffness and to be as lightweight as possible.

Using MLL optics as an example, four linear Laue lenses are needed to obtain a 2D x-ray focus. Each lens requires individual remote 3D angular adjustment and 1D or 2D linear adjustment [12.3.11]. Since a typical lens has dimensions of 1×0.3×0.025 mm, the interface between the lens and the alignment stages needs a special, high-stiffness mounting coupling.

The 3D angular adjustment requires a resolution of 10 mrad that is achievable with a PZT-driven weak-link structure over a travel range of 1 to 2 degrees. Since one of the 3D angular motions requires a 22-degree travel range [12.3.11], a special high-stiffness rotary shaft must be developed.

12.3.3.1.4 R&D Program for Miniaturized Angular Positioning

This R&D program will focus on the development of a set of miniaturized goniometers to meet the needs of remote alignment for novel hard x-ray focusing optics such as the MLL. The tasks of this R&D program include:

- designing a 3D miniaturized motorized (or PZT-driven) goniometer system with high stiffness and a size as small as reasonably achievable
- optimizing the goniometer's structural dynamics performance to ensure the optics positioning stability for a 1 nm hard x-ray focal spot
- developing an equipment protection control strategy for the hard x-ray focusing optics

Two prototypes may be developed through this R&D program. The first prototype will provide an early working test-bed for the hard x-ray focusing optics. This first prototype will also provide the practical information for optimizing the design specifications for the second prototype, which will ensure that the final design goal for the NSLS-II nanoprobe project is achieved.

12.3.3.1.5 Absolute Accuracy at Subnamometer Scale

Finally, we note that for motion resolution on the 10 pm scale, with traceability to NIST standards, we have an existing strategy [12.3.12] that has been proven [12.3.13] to work, and is compatible with the NSLS-II environment. This would be most useful for measuring on an absolute scale the size of the focused spot, for

spot sizes ~1 nm. The x-ray interferometer was invented by Bonse and Hart [12.3.14] and has since found most application in x-ray physics to extremely precise measurements of x-ray scattering factors. It was immediately realized that its extreme sensitivity to displacements, down to 10 pm or less, makes it a very powerful metrological tool. Hart [12.3.15] showed that a suitable elastic translation could be built into the interferometer to give total displacements on the order of one micron, hence giving a useful overlap with larger-scale transducers, and this has been used to refer the silicon crystal spacing to the NIST optical (krypton) standard. Since silicon crystals are available with high perfection in bulk for the semiconductor industry, this provides a portable absolute length standard to a precision of 1 part in 10^6, referred to the krypton standard. Figure 12.3.7 shows a conceptual schematic of the interferometer for this application.

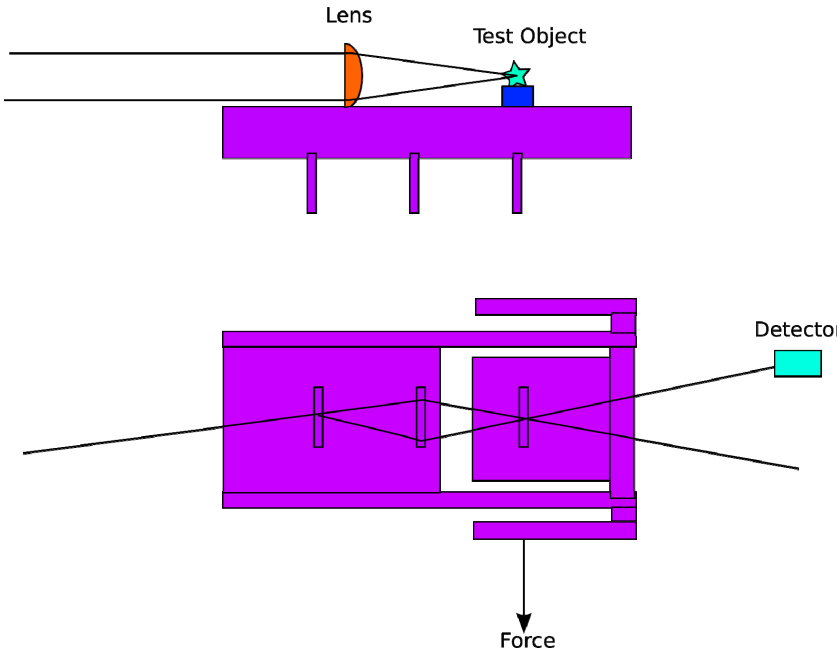

Figure 12.3.7 Conceptual schematic of an interferometer to precisely measure x-ray scattering factors.

References

[12.3.1] J. Maser, G. B. Stephenson, D. Shu, B. Lai, S. Vogt, A. Khounsary, Y. Li, C. Benson, G. Schneider, SRI 2003, AIP Conf. Proc. 705, (2004) 470-473.
[12.3.2] D. Shu, J. Maser, B. Lai, and S. Vogt, SRI 2003 Conf. Proc., 705, AIP (2004) 1287-1290.
[12.3.3] LDDM is a trademark of Optodyne, Inc., 1180 Mahalo Place, Compton, CA 90220, U.S.A.
[12.3.4] U.S. Patent granted No. 5,896,200, D. Shu, 1999.
[12.3.5] U.S. Patent granted No. 6,822,733, D. Shu, 2004.
[12.3.6] D. Shu, J. Maser, B. Lai, S. Vogt, M. Holt, C. Preissner, A. Smolyanitskiy, B. Tieman, R. Winarski, and G.B. Stephenson, to be published in the proceedings of X-ray Microscopy 2005, Himeji, Japan, July 2005.
[12.3.7] D. Shu, J. Maser, M. Holt, B. Lai, S. Vogt, Y. Wang, C. Preissner, Y. Han, B. Tieman, R. Winarski, A. Smolyanitskiy, and G. B. Stephenson, to be published in the proceedings of SPIE Optomechanics 2005.
[12.3.8] U.S. Patent granted No. 6,607,840, D. Shu, T. S. Toellner, and E. E. Alp, 2003.
[12.3.9] Instruction manual, Physik Instrumente GmbH & Co., Germany, 2003.
[12.3.10] H. C. Kang, J. Maser, G. B. Stephenson, C. Liu, R. Conley, A. T. Macrander, and S. Vogt, "Nanometer Linear Focusing of Hard X Rays by a Multilayer Laue Lens," *Phys. Rev. Lett*. **96**, 127401 (2006).
[12.3.11] J. Maser, private communication, May 2006.
[12.3.12] D. G. Chetwynd, D. P. Siddons, and D. K. Bowen, *J. Phys. E: Sci. Instrum*. **16**, 871 (1983).

[12.3.13] D. K. Bowen, D. G. Chetwynd, and D. R. Schwarzenberger, *Meas. Sci. Technol.* **1**, 107 (1990).
[12.3.14] U. Bonse and M. Hart, *Appl. Phys. Lett.* **6**, 155 (1965).
[12.3.15] M. Hart, J. Phys. D: *Appl. Phys*. **1**, 1405 (1968).

12.4 High Energy Resolution Optics

One of the goals of the NSLS-II project is to achieve 0.1 meV energy resolution for inelastic x-ray scattering experiments. This is an extremely challenging goal and represents more than an order of magnitude increase in resolution over the existing state-of-the-art. In addition to placing very high demands on the x-ray source to produce very high fluxes per unit bandpass, achieving this energy resolution will require new optics developments. In this section, we outline the R&D necessary to accomplish this.

12.4.1 Introduction

High-resolution inelastic x-ray scattering spectrometers are currently in use at all of the third-generation x-ray sources. The highest resolution achieved at these instruments to date is ~1 meV; routine resolution for practical experiments is 1.5 → 2 meV. Without exception, all these spectrometers (at ESRF, SPring-8, and APS) utilize high-order Bragg reflections from perfect Si crystals, operating at near-backscattering energies, to achieve the high resolution and high-angular acceptance that is required. Analyzer crystals used in these instruments are comprised of large numbers of perfect blocks glued to a spherical substrate to ensure the inelastically scattered x-rays are collected over a large solid angle (to increase count rates) without at the same time introducing the strain broadening that would otherwise be incurred by bending perfect crystals. This spherical curvature of the collection of small diced blocks acts to focus the reflected x-rays onto a detector located near the sample. Typically, several such analyzer–detector combinations are employed to increase data rates by collecting data from multiple positions in reciprocal space simultaneously.

In the left panel of Figure 12.4.1, the energy width of various Si reflections are plotted as a function of the photon energy for which these reflections occur in back-scattering. The size of the points is proportional to the reflectivity of that reflection. The general trend is very clear: to achieve high energy resolution, one is forced to utilize high photon energies. Further, the higher the resolution (smaller ΔE), the smaller the reflectivity. These fundamental facts have three negative consequences.

First, the higher photon energies mean that one is forced to utilize a non-optimum portion of the undulator spectrum—specifically, well beyond the maximum flux. This problem is particularly severe for a medium-energy ring such as NSLS-II. As can be seen from Figure 12.4.1, operating at ~1 meV resolution requires photon energies of >21 keV and to achieve 0.1 meV would require photon energies in excess of 31 keV. Figure 11.5.2 shows that at these energies the flux output from a U19 device, for example, is lower by more than two orders of magnitude at 30 keV compared to 10 keV, as measured in ph/meV, the figure of merit for an inelastic experiment. Second, the high-order Bragg reflections have increasingly smaller reflectivities, and thus any device based on such reflections will be increasingly inefficient—a real problem for this technique in which experiments are extremely photon-hungry. Third, operating at high photon energies, while offering some advantages in terms of penetration depth, also means inherently worse reciprocal space resolution for the same collection solid angle, relative to lower photon energies.

For these reasons, extending existing Si technology to use in inelastic analyzers operating at 0.1 meV energy resolution does not appear practical and it is necessary to seek alternatives.

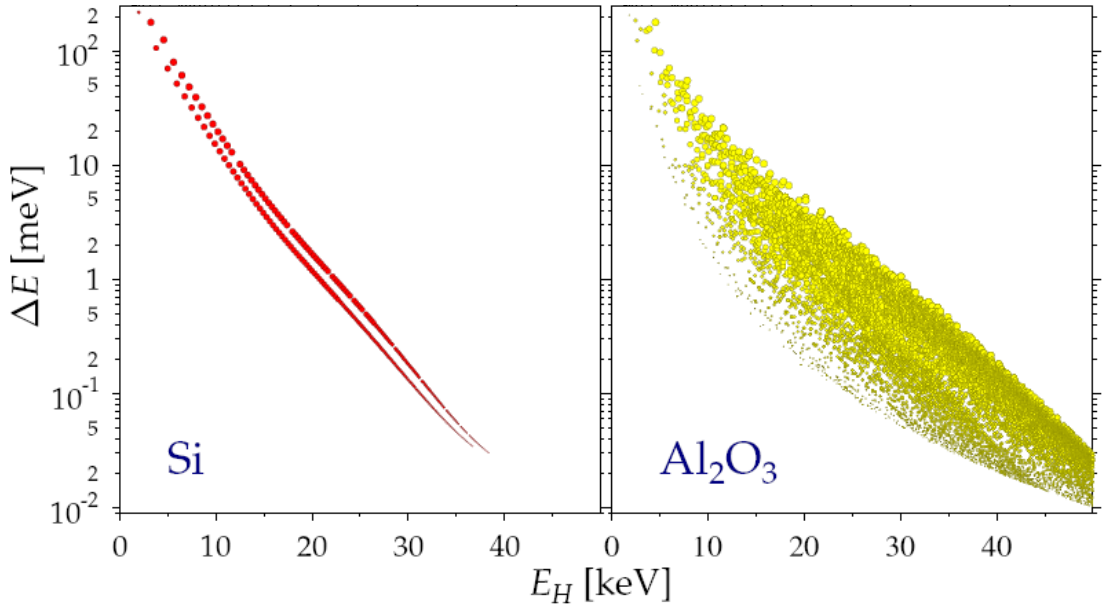

Figure 12.4.1 Energy bandpass for the Bragg reflections in Si and sapphire as a function of the photon energy for which these reflections occur in backscattering. In each case, the size of the point corresponds to the reflectivity of that reflection. The general trend in each case is that higher resolutions are achieved at higher photon energies and with smaller reflectivities.

One possibility is to continue to use perfect crystals in backscattering, but seek alternative (non-cubic) materials that have narrower energy bandpasses, at lower photon energies compared to Si. An example of this approach might be sapphire or quartz. As shown in the right panel of Figure 12.4.1, sapphire can offer reflections that have energy bandpasses as small as 0.1 meV (at high energies). However, sapphire does not appear promising for such very high resolutions, for two reasons. First, in order to get the very high resolutions for low-order reflections requires a very large extinction length—that is, the structure factor is small. From this it follows necessarily that the reflectivity (and hence the efficiency) is low. Further, since the extinction length is (at these resolutions) now comparable to the absorption length in the material, the reflections develop large angular tails (and therefore equivalent tails in energy scans) that would greatly complicate experimental measurements at small energy transfers. The second reason is that, in addition to these fundamental problems, there are severe technical challenges associated with the fabrication of large arrays of such crystals from these materials, challenges which may be insurmountable. We have chosen, therefore, not to pursue such approaches to reach 0.1 meV resolution. We note, however, that it may be useful to utilize quartz and sapphire, or related noncubic materials, for lower resolutions, perhaps >1meV at moderate photon energies.

12.4.2 Asymmetric Optics

Following the discussion above, we have chosen to pursue an alternative approach to achieving very high energy resolutions; that is, to utilize the angular dispersion of x-rays from highly asymmetrically cut crystals. This approach is based on the principle that any asymmetrically cut crystal operating at a Bragg reflection acts as a dispersive element with any wavelength spread in the incident beam, generating angular spread in the exit beam. This concept is illustrated schematically in Figure 12.4.2. Achieving high energy resolution then translates into the much simpler task of achieving high angular resolution, something that may be obtained with more conventional Bragg optics at relatively low energy. Furthermore, by choosing to operate in backscattering, one may tune the dispersive effects simply by tuning the asymmetry angle. Thus one may achieve very high energy resolutions (on the order of $\Delta E/E \sim 10^{-6}$–10^{-8}) even at moderate photon energies (5–10 keV). This approach has been discussed in several articles by Y Shvyd'ko and is discussed at length in [12.4.1].

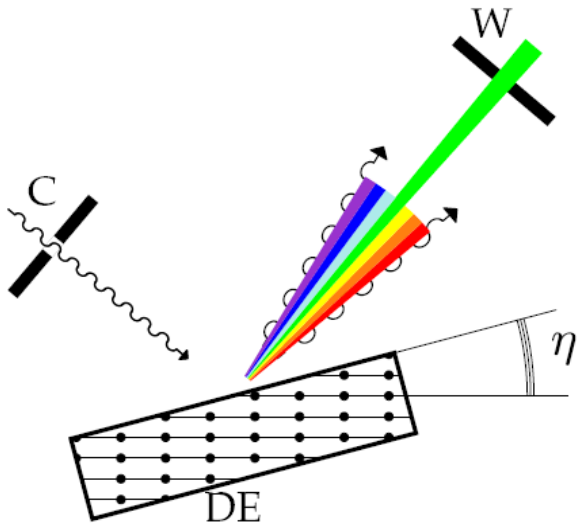

Figure 12.4.2 Schematic illustration of the concept of monochromatization through angular dispersion. An incident beam is collimated by C and Bragg diffracts from an asymmetrically cut crystal. Energy spread in the incident beam is transformed into angular spread in the exit beam. A wavelength selector (W) then selects a given energy bandpass by selecting a particular angular spread. The angular dispersion, and hence the energy resolution, is controlled by the asymmetry angle, η, not by the intrinsic width of the Bragg reflection.

With this approach, the goal of 0.1 meV energy resolution appears feasible. Further, there are a number of advantages inherent to working at lower photon energies, including improved reciprocal space resolution (for the same collection solid angle), proximity to transition metal K-edges (and their possible resonant effects), more efficient detectors, extremely steep wings in the resolution function, and, as discussed above, the intrinsic flux advantage of working closer to the peak of the undulator spectrum.

Chapter 11 discusses a possible spectrometer concept (including the monochromator, sample spectrometer, and analyzer) utilizing such asymmetric optics. However, there are significant risks associated with developing an instrument based on these untried principles today. We outline here an R&D program to mitigate these risks. The goal of this program is to demonstrate the feasibility of the asymmetric optics approach such that one may then design and construct an instrument with a high degree of confidence that it will function as intended.

This R&D plan has been informed by the early work of Shvyd'ko et al. at APS, who have recently taken the first steps in demonstrating the validity of the design principles mentioned here. Figure 12.4.3 shows a schematic of their experimental setup in which two Si(800) crystals, cut with an asymmetry angle of 88.5°, were tested, operating in backscattering at 9.1 keV. The two crystals (labeled D in the figure) were operated back-to-back such that one crystal acted as a monochromator (with a collimator, C, and wave-length-selector, W, collimating the beam and selecting the appropriate wavelength/angular spread, respectively) and the second crystal acted as an analyzer. The W and C crystals were fabricated from a single monolithic block of Si, as shown in Figure 12.4.4. The dispersive elements were comprised of Si(800) crystals 175 mm long, shown in Figure 12.4.5. The relative energy transfer between the two components can be tuned by varying the temperature of one of these dispersive elements with respect to the other. This changes the lattice constant of one piece of Si with respect to the other and hence the energy for which the backscattering condition is obtained. Thus energy scans are, in fact, temperature scans. Similar principles have been tried and tested in more conventional inelastic spectrometers.

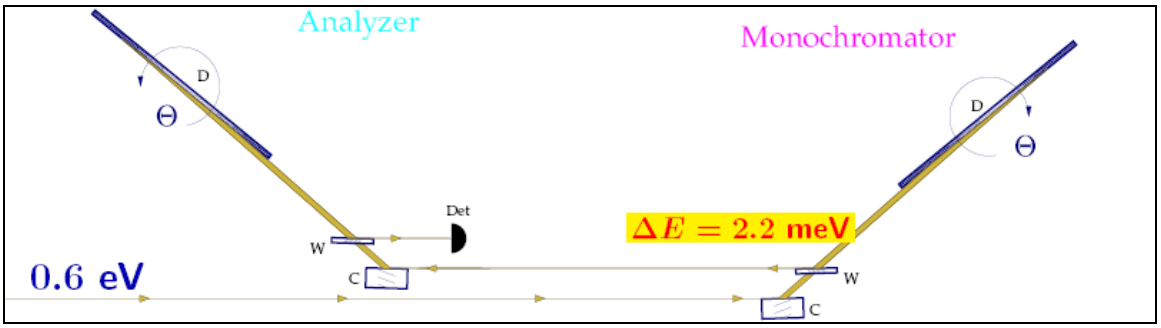

Figure 12.4.3 Arrangement of monochromator and analyzer crystals used in the initial experiments performed at 3ID at APS. The energy resolution of each component was found to be 2.2 meV at an incident photon energy of 9.1 keV.

The experiments, performed at 3ID at APS, demonstrated that the principles discussed above do indeed work—it is possible to construct a monochromator and analyzer based on angular dispersion effects.

However, these first steps remain a long way from making 0.1 meV spectrometers a reality. In particular, the overall resolutions of the instrument in Figure 12.4.3 was 3.1 meV, as show in Figure 12.4.6 [12.4.2, 12.4.3]; that is, each of the two components (monochromator and analyzer) contributed ~2.2 meV energy resolution. This is significantly larger than the theoretically calculated value of 0.7 meV.

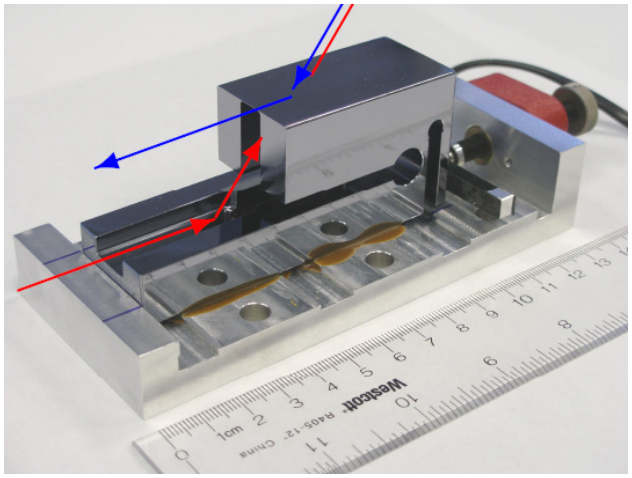

Figure 12.4.4 Monolithic Si crystal used as the collimator (C) and wavelength selector (W) in the experiments at APS. The incident beam (red line) is collimated by the first reflection, and passes through a 200 μm thick section of the crystal. It is then diffracted off a long dispersive element (not shown in this figure) and diffracted from the top surface of the thin section (blue line), which passes only a narrow angular (and therefore energy) spread to the detector.

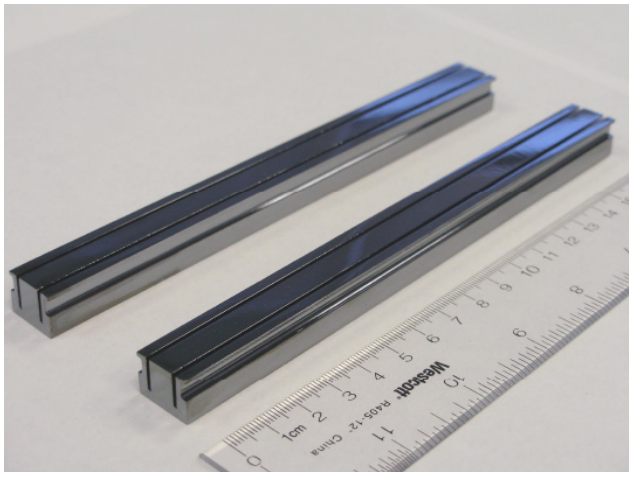

Figure 12.4.5 Si(800) crystals used as the dispersive elements in the experiments at APS. The crystals are 175 mm long and have an asymmetry angle of 88.5°.

The central questions of the R&D program will be to understand why the resolution is broadened beyond the theoretically expected result and then, based on this understanding, to construct prototype devices that demonstrate theoretical performance in resolution and throughput at the 0.1 meV level. Based on the preliminary experiments, a number of possible factors contribute to performance that is lower than expected. These are:

1. **Crystal imperfection**. This includes impurities or other defects that mean the lattice constant does not have the required degree of homogeneity over the length of the crystal.
2. **Strain due to the mounting scheme**. Strain effects associated with gluing or clamping of the dispersive elements crystals, or indeed even the way the angle of W is tuned relative to C via the weak links driven by the pico-motor (see Figure 12.4.4), could contribute to broadening of the Bragg reflections and hence worsening of the energy resolution.
3. **Strain effects due to crystal shape**. Particularly for the C/W combination crystal, there are many cuts close to diffraction surfaces that could introduce strain. Most obviously, the thin, 200 μm section, that allows for anomalous transmission of the beam diffracted from the collimator, C.
4. **Figure error in the surface polishing**. The required figure error for 0.1 meV resolution is less than 0.2 mrad.
5. **Temperature variation along the dispersive element**. Clearly, thermal gradients or inhomogeneities introduce lattice constant inhomogeneities that will broaden the reflections. The required temperature stability and homogeneity for 0.1 meV is 0.5 mK, which would contribute an energy broadening of 0.01 meV, well within tolerances.

Of these five possible factors, preliminary work suggests that the last of these is not important. Specifically, thermometry taken at three different places along the 175 mm dispersive crystal showed a total variation on the order of 4 mK, which would correspond to an energy broadening of 0.1 meV. This is small compared to the theoretically expected value of 0.7 meV and the experimentally observed value of 2.2 meV. Further, the thermal drift was equally small (~4 mK) over 2 days. Thus, at least at the 1 meV level, thermal effects do not yet represent a limiting factor.

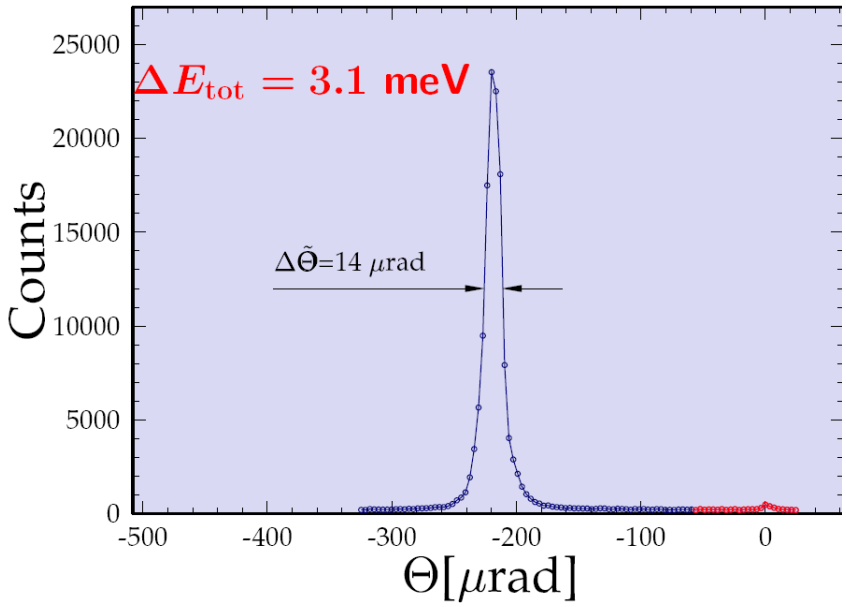

Figure 12.4.6 The effect of rocking the analyzer dispersive element through the aligned condition, with respect to the monochromator. The observed width corresponds to a total resolution of 3.1 meV, and results from the convolution of the monochromator and analyzer contributions.

The early portion of the R&D program will therefore focus on understanding the relative importance of factors 1–4. To this end, new high-purity Si has been purchased (resistivity of 50 kΩcm compared to the 1 kΩcm used in the experiment described above). This will be used as starting material for new crystals to be cut and polished with the required tolerances on "miscut" (<1 mrad) and surface figure error (<0.2 mrad). (Here, *miscut* refers to any deviation from the required asymmetry.) This work will be done at PTB, Germany. With these new crystals in hand, work first will be carried out to demonstrate theoretical performance in the existing temperature ovens. This work will include detailed high-resolution topographical studies of the crystals, both ex situ and in situ to understand any residual strain effects. Once the required performance has

been demonstrated in a pair of crystals, attention will be turned to solving the technical challenges associated with producing a working user instrument operating at 0.1 meV energy resolution based on these principles.

The technical challenges may be divided into four general areas.

1. **Crystal fabrication**. As discussed, it will be necessary to fabricate and mount large, strain-free, high-purity Si crystals. These will be 200 to 300 mm long with <1mrad miscut, and polished to a slope error of <0.2 mrad. In addition, the C/W crystal will be 80 mm long and require a 200 μm thin section, also with <1 mrad miscut. These challenges will be met as part of the initial phase of the R&D program.
2. **Temperature control**. As discussed, this is not believed to be a limiting factor in the current setup, but it will be a challenge to reach the 0.5 mK temperature homogeneity and stability required to reach 0.1 meV energy resolution. This is largely an engineering challenge, but it will require careful design and (probably) prototyping. As outlined in Section 11.5, it is presently envisaged that the analyzer will be broken into segments so that the temperature requirements need only be met over a 200 to 300 mm length, rather than a 2 m length, and a modular approach may be taken to temperature control. Nevertheless, it is clear that this will be one of the challenges associated with this instrument.
3. **Multi-crystal alignment**. The segmented analyzer crystals (up to 10 crystals in the final instrument) must be aligned to within 50 μrad of each other. Again, this is "only" an engineering and design challenge—and certainly there are rotational stages capable of these accuracies at these loads. Nevertheless, achieving this accuracy and maintaining it as the detector arm is rotated, for example, is a non-trivial matter that will require careful development work.
4. **Collimating optics**. Achieving the desired collection solid angle for the analyzer, discussed in Section 11.5 (namely, on the order of 5 to 10 $mrad^2$) will require special collimating optics capable of producing a collimated beam with a divergence of less than 50 μrad. There are a number of possible choices for such an optic, including graded multilayers. However, the design and fabrication work for this will likely be carried out by a vendor and not as part of the R&D program outlined here.

A final component of the R&D program will be the dynamical theory calculations simulating the performance of the monochromator and analyzer. These calculations will not only provide a basis against which to judge measured performance of these optics (including throughput, resolution, and lineshape), but will also allow us to assess sensitivity to various errors in fabrication and implementation, including those discussed here.

References

[12.4.1] Y. Shvy'ko, "X-ray Optics' High-Energy Resolution Applications," Springer Series in Optical Sciences, **89** (2004).

[12.4.2] Yu. Shvyd'ko, M. Lerche, U. Kuetgens, H. D. Rueter, A. Alatas, J. Zhao, "X-ray Bragg diffraction in asymmetric backscattering geometry," *Phys. Rev. Lett.* **97** 235502(2006).

[12.4.3] Yu. Shvyd'ko, U. Kuetgens, H. D. Rueter, M. Lerche, A. Alatas, J. Zhao, "Progress in the Development of New Optics for Very High Resolution Inelastic X-Ray Scattering Spectroscopy," AIP Conf. Proceedings Series, CP 879 (2006).

12.5 Metrology and Reflective Optics

Each new advance in SR source design has driven improvements in beamline optical components and associated metrology instrumentation and techniques. For example, prior to the commissioning of the NSLS x-ray ring early in the 1980s, cylindrical mirrors with RMS slope errors of 2 arcsec (10 μrad) were considered to be of excellent quality, capable of producing focal spots of several tens of microns in a typical soft x-ray beamline. The original NSLS x-ray mirror specifications in the early 1980s called for cylinder mirrors with slope errors of <1 arcsec (5 μrad). Mirrors of this quality could produce focal spots smaller than 10 μm, which was a great advance in the state of the art. Upgrades to NSLS in the 1990s and the advent of third-generation storage rings, such as APS at Argonne National Lab, significantly reduced the size of the electron beam source, enabling focal spot sizes in the range of 1 μm, with mirrors having slope errors of <1 μrad. Such mirror specifications are now routine for beamline optics. NSLS-II represents another leap in synchrotron performance, and a corresponding leap is therefore required of SR mirror fabricators and metrology developers to provide optics with slope errors on the order of 100 nrad.

Reflective optics will be used for many purposes in NSLS-II beamlines. The most widely used application will be for producing micron and sub-micron focal spots with a KB mirror pair. These mirrors will probably be made as long elliptical cylinders, up to 1 m in length, possibly as fixed or adaptive bent optics. Plane mirrors will be used as wavelength filters and first mirror power absorbers. There will be spherical collimating mirrors, grating for spherical grating monochromators, multilayer-coated bent cylinders for high-energy focusing, paraboloids, ellipsoids, toroids, etc. All of these mirrors will need to be produced with surface figure and finish tolerances significantly better than today's standards in order to make full use of the extremely small NSLS-II beam emittance. Excess surface slope error will degrade the performance of the beamline and make the ultimate performance unachievable.

The old optician's quip "If you can't measure it, I can make it," attributed to Norm Brown of LLNL, is absolutely true when mirrors are required that exceed the state of the art in both fabrication and metrology technology. When NSLS beamlines were first constructed 25 years ago, optical metrology techniques for measuring the figure of grazing incidence cylindrical aspheres, such as toroids and ellipsoids, did not exist or were grossly inadequate. The conventional tools that mirror fabricators used at that time to make spherical and flat surfaces, Fizeau interferometers, did not work well for nonspherical x-ray optics surfaces. Recognizing the need to improve metrology instrumentation capabilities for grazing incidence optics, BNL established the Optical Metrology Laboratory for the development of instrumentation and techniques that would allow one to easily characterize the finish and figure on aspheric optics. The success of the OML program has been demonstrated by the gradual improvement of SR optics over the years, enabling the mirror fabricators to keep up with advances in the quality of the storage ring beams. The Long Trace Profiler (Figure 12.5.1), developed at BNL, is now the de facto standard for SR mirror metrology at most large synchrotron facilities around the world. The current commercial version, the LTP V, has evolved over the past 15 years with improvements in optical and mechanical design, enabling measurements with accuracy at the 0.5 μrad level on meter-long mirrors. To achieve the next milestone—100 nrad accuracy—will require a multi-pronged approach to improvements in metrology instrumentation development and mirror fabrication technology.

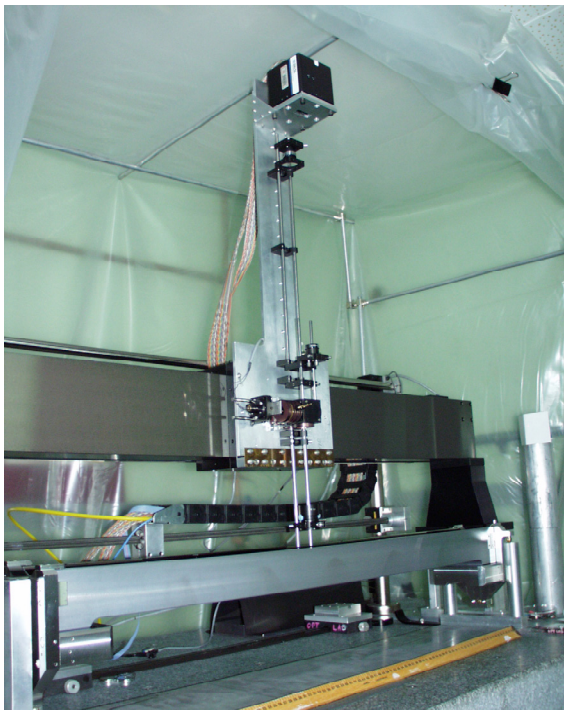

Figure 12.5.1 The current version of the Long Trace Profiler (LTP III) in the Optical Metrology Laboratory at BNL.

12.5.1 Challenges in NSLS-II Mirror Development

From experience over the past 20 years in dealing with various mirror fabricators, it is clear that one cannot expect vendors to develop dedicated metrology for fabricating SR optics at their own expense. This is especially true for small vendors with limited resources. Even for large vendors, the SR mirror market is quite small, and profit margins are not large enough to allow them to spend the resources to develop the proper metrology. Small vendors usually have customized measurement setups that are specific to the part being manufactured. We, as end users, must have a versatile measurement capability that can handle a large variety of optical component parameters. We need to have the metrology to ensure that the delivered optics meet the specified requirements. In the case of NSLS-II optics, we need to have the metrology to ensure that mirror surface slope errors are within 100 nrad of the desired shape and that figure errors are in the nanometer height range over the full length of the surface. We also need to ensure that surface roughness does not exceed a value, typically a few Å, that would cause excessive light to be scattered out of the core of the image. The goals of the reflective optics R&D program are:

- to develop the necessary metrology instrumentation to enable 100 nrad slope error and nanometer figure measurement accuracy
- to provide the manufacturer with the feedback needed so that he can adjust his process and improve the product delivered to us
- to assess the ability of new polishing methods to provide optics with the required surface accuracy

To achieve these goals we have identified five research tasks, the first three as near-term tasks to be initiated immediately and the last two as later-term tasks. The later-term tasks provide metrology capabilities at operating beamlines, while the near-term tasks deal with laboratory R&D issues needed for successful beamline development. These tasks include:

1. development of a next-generation Long Trace Profiler for accurate 100 nrad slope error measurements
2. development of a stitching interferometer system for high spatial resolution measurement of surface topography over the complete 2D surface area
3. evaluation of new polishing technologies for producing KB mirrors, in particular, magnetorheological finishing (MRF) technology that has been developed by QED Technologies in Rochester, NY
4. development of an at-wavelength wavefront metrology capability
5. development of an in-situ LTP for beamline diagnostics

12.5.2 Next-Generation Long Trace Profiler

The current Long Trace Profiler in the Optical Metrology Laboratory, the LTP III, is limited by systematic errors to an accuracy of 1 μrad. The commercial version of the instrument, the LTP V, manufactured by Ocean Optics, Inc. under license from BNL, incorporates a number of improved features and is capable of ~0.5 μrad accuracy. The source of systematic errors in both instruments has been traced to phase shifts in the laser probe beam produced by sub-nanometer surface roughness, and index inhomogeneity in the glass components with spatial period components in the range of 0.1 to 1 mm. In particular, the polarizing beamsplitter cube and the folding mirror flats are the major error sources. In order to increase the accuracy of LTP measurements beyond current state of the art, the quality of the internal glass components needs to be significantly improved. The current glass components are of commercial quality. We will need to have custom components made to extremely tight tolerances.

As with full-size SR mirrors, it is not sufficient to simply place an order for a glass component and expect it to meet the stringent surface and wavefront error specifications. We need to have the instrumentation available to perform the necessary metrology on the components ourselves. Transmitted and reflected wavefront errors are best measured with a conventional Phase-Measuring Interferometer. Recent advancements in commercial PMI technology have made available interferometers based on wavelength modulation phase shifting. For example, the Zygo Verifire MST 633 interferometer can separate the wavefront errors produced by the front and back surfaces of the glass from the glass thickness inhomogeneity errors. Acquisition of this type of interferometer will allow us to reduce the systematic error introduced by these glass components.

Other improvements are necessary to increase the reliability and repeatability of the LTP in the Optical Metrology Laboratory. The present aluminum air bearing translation stage in the OML needs to be replaced with a high-precision ceramic beam. The ceramic air bearing stages that are used in the commercial version of the LTP II have total slope errors on the order of 1 arcsec over the 1 to 2 m travel length. The current OML LTP translation stage has a slope error of ~20 arcsec. Reducing the magnitude of this large translation stage error signal will reduce the fraction of the error signal that leaks into the measured surface profile.

Further, improvements to the detector and control system will result in a more fully automated measurement system, requiring less operator intervention and consequent environmental perturbation of the measurement envelope. Use of a 2D camera instead of a 1D line scan camera will result in a more versatile system.

12.5.3 Stitching Metrology Development

The Osaka University group at the Center for Atomistic Fabrication Technology has demonstrated the necessity of measuring surface figure errors on KB mirrors down to 50 μm spatial periods, in order to produce nearly diffraction-limited nanofocusing optics. The elliptical cylinder shape precludes the use of a conventional PMI as the sole measuring tool. There is no single metrology instrument that can encompass the spatial period range from 0.5 m to 50 μm. The Osaka University group has shown that it is necessary to use stitching interferometry to extend the range of a micro-PMI into the long period region. This has enabled them to produce nearly diffraction-limited KB mirrors by elastic emission machining and plasma chemical

vapor machining, two of the several surface finishing technologies that have been developed at their laboratory over the past 20 years.

We will need to develop a sub-aperture stitching interferometry capability tailored to the types of optics that we anticipate will be used in NSLS-II beamlines. The Osaka system is optimized for 200 mm long mirrors. We will need to extend the range up to 1 m. To do this, we will likely combine a dedicated LTP optical head with a micro-PMI instrument, probably a Zygo NewView system that is normally used for surface roughness measurement. Both instruments will be mounted together on a scanning air bearing stage. A similar system has been developed by Zygo and QED Technologies for Canon in Japan. First results from the Canon Mid Spatial Frequency metrology tool were reported at the OSA OF&T workshop in Rochester earlier in October 2006 by M. Ohtsuka. The Canon system is optimized for spherical aperture optics and does not incorporate a scanning linear stage, but QED is confident that their stitching algorithm can be applied to the scanning head system. One of the unique features of the Canon system is the special Zygo NewView NV-R Optical Surface Profiler measurement head that is used to make the sub-aperture measurements. The internal optics are customized to optimize the instrument transfer function to provide more reliable data at high spatial frequencies. The improvement factor for the 20X objective is shown in Figure 12.5.2.

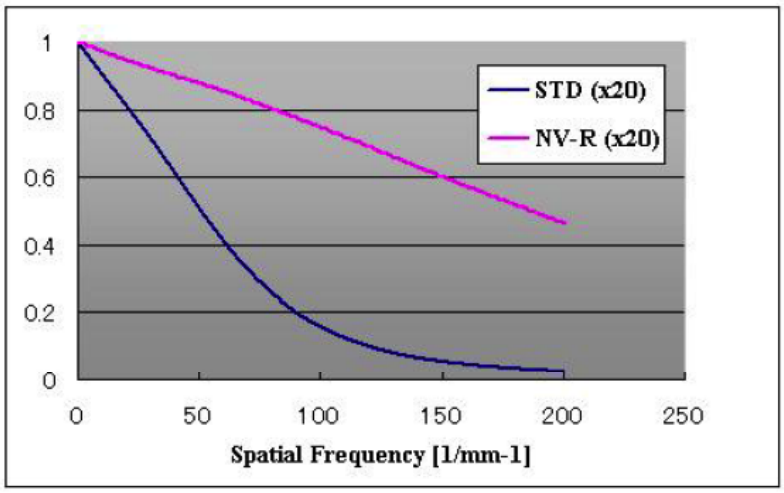

Figure 12.5.2 Improvement in frequency response of the Zygo NewView NV-R optical head used in the Canon lithography optics measurement system. Customized optical components replace standard components in this system.

Source: M. Othsuka, presented at OSA OF&T Topical Meeting, Rochester, NY, Oct. 2006

We will work with Zygo and QED to develop a stitching metrology instrument that incorporates the improved NV-R optical head and utilizes the QED stitching software algorithm. The hardware design and acquisition for this project should take about two years, and the assembly, installation, and commissioning should take another year.

12.5.4 Polishing Technology R&D

The recent developments by Osaka University in producing extremely smooth surfaces with nanometer figure errors are the result of more than 20 years of research into polishing technology, funded mainly by the Japanese semiconductor industry with the backing of the Japanese government. The KB mirrors produced by Osaka for SPring-8 hold the world record for smallest x-ray spot size. Only recently have the Japanese made these mirrors available outside of Japan through a local export company, but this company has not yet delivered any mirrors. The EEM process is so complex that it can only be done with the dedicated machine at Osaka University. The typical time required to polish a KB mirror with this process is 2 to 3 months. We need to explore other avenues for producing elliptically figured cylinder mirrors by other polishing techniques.

Magnetorheological finishing is a promising technique for producing mirrors with the required figure accuracy. MRF has been developed by QED Technologies as spinoff from work done at the Center for Optics Machining at the University of Rochester over the past decade. The MRF process utilizes a strong magnetic

field to change a liquid fluid stream into a relatively hard viscous stream in the vicinity of the workpiece. The MRF fluid carries a polishing compound that polishes the surface. Coupled with high-resolution metrology, the process converges rapidly to correct surface figure errors and produces extremely accurate surfaces, both spheres and aspheres. There is, however, a question about excess residual roughness remaining on the surface that may be an intrinsic property of the polishing process.

We are investigating establishing a collaboration with QED to explore the feasibility of the MRF process to produce KB mirrors suitable for use at NSLS-II beamlines. This is a three-part project. First, QED would demonstrate that they can produce a super-polished Si flat with nanometer figure error. This may involve fine-tuning the chemistry of the MRF fluid to lower the removal rate, since the Osaka work has shown that low removal rates are correlated with smoother surfaces. Second, QED would produce KB elliptical cylinders that will be evaluated at an NSLS or APS beamline. Third, QED would develop a sub-aperture stitching interferometry algorithm for producing long and narrow non-rotationally symmetric parts. This is a significant departure from the typical case of a small rotationally symmetric part, where the stitching algorithm contains a self-consistency check from closure. There is no closure with a rectangular grid-scanning algorithm. The sub-aperture stitching interferometry algorithm will be usable in our stitching interferometer so that we can perform our own metrology check on the delivered optics. If we pursue this effort and QED is successful in developing a polishing process that can produce nanometer quality optics for KB mirrors, they will transfer this technology to the many vendors who have QED polishing machines. We would then have a choice of vendors for custom KB mirrors. The resulting competition should act to produce a source of high-quality mirrors at reasonable cost.

12.5.6 At-Wavelength Metrology

A powerful topographic diagnostic technique for x-ray wavefront diagnostics, developed by Souvorov at SPring-8 and based on the phase retrieval algorithms of Jim Fienup at the University of Rochester, utilizes the information in interference patterns produced by coherent x-rays as seen at various distances downstream from an optical element that interacts with the incident beam. Souvorov has demonstrated that the topography of extremely smooth surface profiles of substrates polished by EEM at Osaka can be reconstructed with Å-level repeatability with this technique [12.5.1]. This wavefront reconstruction technique provides information about how the surface interacts with the x-ray beam under actual operating conditions at the actual operating wavelength. This measurement capability is invaluable for performing diagnostics on optical elements that cannot be characterized with surface profiling instruments at visible wavelengths. Examples of such components are kinoform refractive optics, zone plates, Bragg-Fresnel optics, and multilayer coated surfaces. An at-wavelength measurement technique for these kinds of optical elements is essential for assessing the quality of the fabrication process.

Developing this metrology technique here at BNL would require establishing a beamline for testing optics on NSLS-II. Such a beamline is very briefly discussed in Chapter 11. Initial work would need to be done in the two or three years prior to the start of beamline commissioning so that the methods and techniques would be in place as soon as coherent flux is available at the startup of the machine. The principal equipment needed for this measurement is a high-resolution image converter camera with 0.5 μm spatial resolution. Initial setup work could be done on an existing NSLS beamline and moved over to NSLS-II as soon as coherent photons are available. Other at-wavelength wavefront metrology techniques can also be explored. In particular, Talbot grating imaging, developed by T. Weitkamp at the Paul Scherrer Institute, is a potential candidate for x-ray wavefront distortion measurement. It requires the fabrication of grating structures with micron periods and very high aspect ratios for efficiency at high energies. These gratings can be fabricated by the facilities that will be available at the Center for Functional Nanomaterials. This measurement technique also has applications in imaging weakly absorbing biological structures [12.5.2].

A dedicated beamline for testing optics will have many uses, only a few of which are enumerated here. Other uses include testing multilayer coating uniformity by reflectometry and performing photometric calibration of various detectors.

12.5.7 In-Situ LTP Development

The original In Situ LTP measurements were performed at ELETTRA in 1996 [12.5.3]. Subsequent ISLTP measurements were made on a high heat load mirror at APS that showed significant transient distortion effects when the beam shutter was opened, showed the location of the 100 nm high thermal bump when the slits were nearly closed, and showed an unexplained residual curvature distortion when steady state equilibrium was reached after 15 minutes [12.5.4]. These measurements demonstrated the usefulness of in-situsurface slope error measurement as a diagnostic aid and alignment tool for positioning mirrors in the center of an x-ray beam. We have been developing improved versions of a compact LTP optical system that is easily portable and that can be set up at a beamline to monitor changes in the shape of a mirror in real time.

To take full advantage of the diagnostic capabilities afforded by the ISLTP, it is necessary to design the appropriate view ports into a particular mirror chamber or monochromator and to make provisions for mounting the ISLTP. These tasks should be performed during the design of the actual beamline hardware.

References

[12.5.1] A. Souvorov et al., *J. Sync. Rad.* **9**, p. 223-228 (2002).
[12.5.2] T. Weitkamp et al., *Opt. Exp.* **13** (16) p. 6296-6304 (2005).
[12.5.3] Qian et al., Proc SPIE **2856**, p 172-182 (1996).
[12.5.4] P.Z. Takacs et al., Proc. SPIE 3447, pp. 117-124 (1998).

12.6 Advanced Detectors

12.6.1 Detector Requirements and Challenges

Advanced detector systems will be required to take full advantage of NSLS-II's superlative performance. For a synchrotron experiment, the detector system is an especially critical component that often enables new science. One outstanding example is that of macromolecular crystallography. When the only viable area detector capable of quantitative interpretation was film, macromolecular crystallography was an esoteric pursuit, involving an exorbitant amount of labor to wet-process thousands of films for each experiment. The availability of synchrotron radiation sources made little impact. The development of new, large-area electronic detectors has transformed macromolecular crystallography into a high-throughput research powerhouse, providing key knowledge for the understanding of disease mechanisms and drug design.

In general, it is clear that the trend is toward higher levels of functionality integrated into the detector elements and readout systems. This will include digital signal processing of the analog sensor output as well as digital post-processing of events. These trends are already visible in the high energy physics field, and are beginning to be seen in synchrotron radiation systems. We can expect that pulse height histogramming, time and space correlations, and spectral corrections will all be integrated at the chip level in future detectors.

Conventional computing resources are also beginning to be embedded in more Application-Specific Integrated Circuits, ASICs. At least one programmable gate-array device manufacturer is selling a product with up to four PowerPC processors embedded in the center of a large programmable gate array. In the next years leading to NSLS-II, even more powerful devices can be expected. It is now almost as easy to embed a CPU into an ASIC as it is to include a subroutine in a software program. Modern simulation programs can

accurately simulate the performance of a complete ASIC before manufacture, giving a high degree of confidence that the final device will work as specified.

More sophisticated devices will inevitably lead to increased data capture rates. This is already a limitation for existing detectors, particularly those that deal with images. Add to the large pixel count, the need for energy spectra and/or time-correlation spectra per pixel, plus the need for tomographic information, and dataset sizes can easily expand to terabytes. It is not yet clear how to handle the gigabyte/second data rates expected from the next generation of area detectors, so these more sophisticated devices will need real innovation in data movement technology, or a great deal more customizing of readout systems to reduce data in real time, probably using the embedded intelligence described above.

At NSLS-II, the R&D program for detectors will be driven by the needs of the users for specific detectors. Here, we outline three examples of particular areas of challenge—imaging, spectroscopy, and high-spatial resolution detectors—and the R&D program that would be required to meet these challenges with next-generation detectors. The precise details of the actual R&D program will be determined in accordance with the requirements of the beamlines.

12.6.1.1 Imaging Challenges

Current detectors suitable for acquiring single-crystal and powder diffraction images are rather slow, with readout times of a second or more. This characteristic of 2D position-sensitive detectors is receiving significant attention, due to the large ready market offered by macromolecular crystallography. The Swiss Light Source has recently completed a silicon-based pixellated detector for this application, and it will soon be commercially available. At least one vendor has an independent but similar development underway. There are also detector R&D programs underway in support of Stanford's Linear Coherent Light Source x-ray free-electron laser project, and a program will soon begin in support of the European XFEL project. Consequently, an NSLS-II effort on the development of an imaging detector is not contemplated.

What has not been addressed by any developers so far is the problem of rapidly recording images with time-correlation. Time-correlation spectroscopy is a new technique showing great promise in the field of low-energy excitations in solids and liquids, such as thermal diffusion and critical phenomena. These experiments will be greatly improved by the high brightness of NSLS-II. However, the range of excitation energies accessible to the technique is determined by the time resolution of the detector. For a single-point detector, this can be on the nanosecond scale. Experimenters would like to sample a wide range of momentum transfer (i.e., length scales), so an area detector would be advantageous. Time resolution then translates into the readout speed of the detector. Of course, if each pixel of an area detector were read out photon-by-photon, then the time resolution would be limited by charge collection physics (typically hundreds of nanoseconds). Compared to the full-frame readout of a CCD, this is very fast. The events in each pixel need to be independently recorded in some way. One approach is to design a detector with an autocorrellator on each pixel. That possibility should be explored, making use of continuous increases in microelectronics density and using logarithmic variable time domain techniques to cover a wide range of time correlations in a relatively small footprint.

12.6.1.2 Spectroscopy Challenges

Pixel detectors equipped with energy-resolving capability will require the ability to put a complete energy-histogramming subsystem on each pixel of a large array. Such detectors will be the logical extension of devices currently reaching the experimental floor, which have hundreds of pixels, each with a complete signal-processing chain. These systems were designed for fluorescence detection in absorption spectroscopy experiments with dilute samples, where the experiment feasibility is dominated by the presence of a high parasitic flux of uninteresting radiation. This results in premature saturation of the detector chain, enforcing long acquisition times and eventually preventing a successful experiment. This situation will be worse with NSLS-II, and so we must plan for remedies. Increasing the parallelism even further is one way forward, and

on-chip intelligence to deconvolve acquired spectra on a photon-by-photon basis will be a significant enhancement, bringing improved separation between the desired and parasitic radiation. One could also imagine such a detector bringing a new lease of life to the Laue diffraction technique, since it becomes much simpler to perform the necessary diffracted intensity corrections if one knows the energy of the photon directly. This same knowledge also helps in indexing such Laue patterns, and removes the problem of harmonic overlap. Nevertheless, fabrication of such a detector is no simple undertaking. A high-speed ADC is power-hungry, and one would need on the order of 1 million of them for a reasonably sized detector. As CMOS technology continues to shrink, this will eventually be possible, at least for pixels of dimension 100 micrometers or more. Applications of such a detector might be in microbeam grain-mapping of polycrystalline materials, or high-pressure diffraction experiments. Such studies are important to provide a firmer basis for understanding the properties of real materials on all scales, and are ideally suited to a machine like NSLS-II.

12.6.1.3 Other Applications

Some of the highest demand from materials scientists is for polycrystalline diffraction—in particular, the type of instrument that uses a crystal analyzer to achieve very high angular resolution. Unfortunately, such instruments are intrinsically slow, since a large angular range must be scanned point-by-point with small angular steps. At NSLS, we have demonstrated a new instrumental arrangement that provides such high resolution without scanning, based instead on a focusing technique and using a high-resolution, high-speed linear position-sensitive detector. This detector is based on our silicon microstrip technology, and could easily speed up such data acquisition by a factor of 1,000. This would open up the field of time-resolved high resolution polycrystalline diffraction for the first time. This instrument could easily be combined with one of the high-rate spectroscopy detectors discussed above, to make a very powerful combined-function microprobe.

12.6.2 Infrastructure and Technologies

12.6.2.1 Sensor Fabrication and Novel Sensor Development

To develop the advanced detectors such as those described above, new technologies will be needed. The first requirement is the ability to produce complex, low-noise circuitry that is monolithic with the high-resistivity silicon detector element. Commercial foundries and processes do not routinely use high-resistivity silicon material, so processing it requires either a special agreement with a commercial foundry, or an in-house facility. Although BNL has a modest foundry for the production of simple sensor diodes, it is not adequate for a program to develop the new devices discussed above. However, there is significant in-house expertise in device design, both at the sensor level and at the integrated circuitry level. This BNL-based team is internationally recognized as among the leaders in the ionizing radiation detector field, having a long and successful track record.

The cost of establishing a foundry to provide the required capabilities at BNL is prohibitive, so we have begun discussions with IBM Research, based in Yorktown Heights, NY, on a collaboration to try to adapt standard foundry processes to our needs. These exploratory discussions are currently in the context of detector development for Stanford's LCLS, but the technology to be developed will be fully applicable to NSLS-II detectors. This approach requires a much smaller capital investment.

12.6.2.2 CAD Tools

The development of any electronic device at the chip level relies heavily on computer-aided design and engineering tools to handle the large and complex manipulations required. At the basic level, electric field profiles must be modeled within the volume of the silicon itself, a region in which the electrical properties of

the silicon varies on the nanometer length scale by orders of magnitude, and are not known from first principles. At a higher level, integrated components are formed by selective doping of areas of silicon through masks. The dimensions of these selected areas are sub micron, and are controlled by complex geometric rules, obtained through much R&D in device fabrication labs. The only way to perform such graphical manipulations efficiently is by liberal use of computers. Since these tools are the basis of the largest industrial enterprise in the world, they are sophisticated and expensive.

BNL has been involved in custom integrated circuit design for many years. The readout of signals from pixelated solid state sensors requires the use of such dedicated monolithic front-end electronics (i.e., ASICs) if the detector performance is to be optimal. Front-end ASICs can provide low-noise amplification, filtering, signal processing, efficient derandomization, sparsification, storage, and multiplexing of the signals from the individual segments of the sensors. Highly specialized ASICs were originally developed mainly as analog circuits, but the complexity and amount of digital circuitry has rapidly increased. For example, in the 10+ years that BNL has been developing state-of-the-art front-end ASICs, the transistor count grew from about 1,000 per ASIC to more than 600,000 per ASIC in 2005.

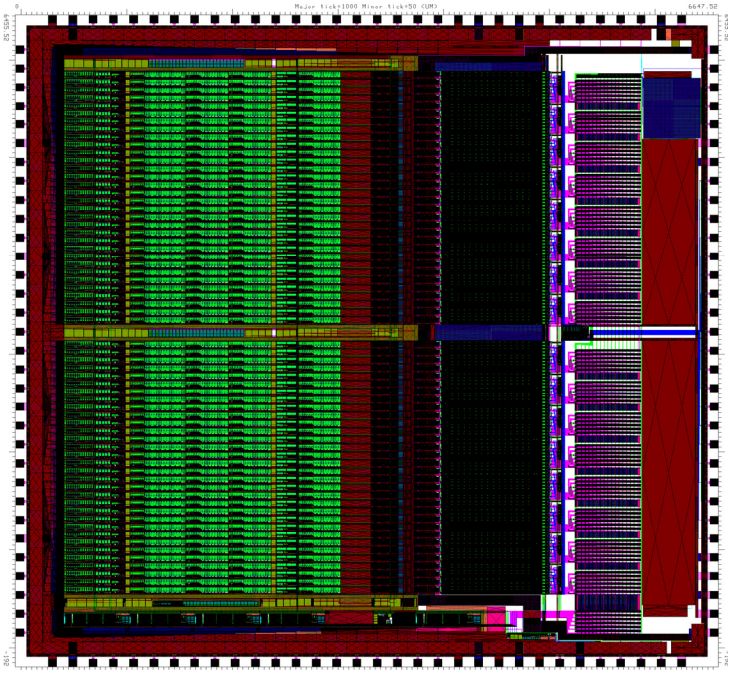

Figure 12.6.1 Layout of a 64-channel ASIC for high-rate counting with multiple energy discrimination. Size 6.65×6.65 mm², transistor count 601,000, layout tool MAGIC, design tool Capture/PSpice.

The development of a front-end ASIC starts from a conceptual diagram and proceeds with transistor-level design, advanced and extensive simulation, conversion of the schematics into a specialized layout, verification of the layout and parasitics extraction, and further iterations through the design and layout phases as needed. Once the layout is ready, the ASIC can be fabricated, in most cases using commercial foundries. The ASIC prototype, once fabricated, is thoroughly characterized without and with the sensors and, if needed, it undergoes more (typically one or two) additional review cycles of design and fabrication. Developing an ASIC requires, for each design phase, the use of specialized computer-aided design tools. The CAD tools currently adopted by the BNL ASIC design group have reached the limits of their capabilities.

As we progress to detectors which have such microcircuits directly integrated with the sensor, all of these CAD tools become necessary from the start, since we have effectively combined the sensor and front-end ASIC into a single monolithic structure. The following CAD tools will be acquired:

- analog and mixed signal transistor level design and simulation: Cadence Virtuoso Schematic Editor and Cadence Virtuoso AMS
- analog and mixed signal layout generation: Cadence Virtuoso Layout Editor

- layout extraction and layout vs. schematics comparison: Cadence Assura

12.6.2.3 Readout Electronics

Some form of electronic subsystem is required to take the signals from the detector and deliver them to the data acquisition system. This is conventional electronics, typically printed circuit boards in surface-mount technology, plus some mechanical enclosure.

12.6.2.4 Beamline Integration and Data Acquisition

It is extremely important that any detector be integrated into the user experiment through appropriate and adequate software. Since the NSLS-II control system will be EPICS-based, it is expected that all detectors will also conform to that standard, minimizing the amount of custom software necessary for this integration. Software to implement the scientific aims of the experiment is not considered in this section, but this should not be taken as minimizing its importance.

12.6.3 Detectors Needed for Proposed Beamlines

A range of standard, commercially available detectors will be useful for NSLS-II beamlines, but we do not discuss them here. They will be discussed in the description of each beamline. In addition to these currently available devices, the following are examples of new types that will be required. These, or other similar detectors, may be developed through focused efforts driven by specific needs identified by the scientific case and technical requirements for the beamlines constructed at NSLS-II.

- massively parallel Silicon Drift-Detector array for microprobe / fluorescence holography
- "speckle" detector with autocorellator
- large angular coverage silicon microstrip detector for polycrystalline diffraction

12.7 Insertion Devices

In Chapter 8 we specified the types of insertion devices that are needed to meet user requirements and to achieve the unprecedented brightness goals of NSLS-II. We presented the optical performance and spectral characteristics of these IDs. They are based on proven designs, and in some cases push the state of the art in what we believe to be rational and realizable extensions of existing technology. In this section we present conceptual magnetic designs of the various ID types that will meet the performance requirements and constraints. We also identify and describe the R&D and prototyping needed to verify each design concept, to resolve any unknowns, and to test advanced concepts for future upgrade paths. We describe novel mechanical concepts that may simplify ID designs and/or improve their performance. Finally, we describe magnetic measurement systems that will be developed to verify and optimize ID performance.

12.7.1 Tunable Hard X-ray Sources

A decade ago, the hard x-ray region of the spectrum by undulators could only be covered at high-energy machines, such as ESRF, APS, and SPring-8. The advent of a mini-gap, short-period in-vacuum undulator, dubbed IVUN, [12.7.1] in 1997 at the National Synchrotron Light Source has had a lasting impact on the design of synchrotron light source facilities all over the world. With the use of mini-gap, short-period undulators, a medium-energy ring (~3 GeV) can now produce tunable hard x-rays between 2 keV and 20 keV. Many years of successful operation of IVUs at SPring-8 [12.7.2], NSLS, and, more recently, at SLS and ESRF have demonstrated the reliability of IVUs. The NSLS currently has three IVUs in operation.

A long-standing concern in the ID community has been that the permanent magnets in small-gap IVUs would be gradually demagnetized and degraded by radiation, due to their proximity to the electron beam and exposure to synchrotron radiation. The conservative approach has been to use Sm_2Co_{17} magnets, rather than the higher field NdFeB magnets, because its lack of boron ought to make Sm_2Co_{17} more radiation resistant. However, after many years of successful operation at SPring-8, NSLS, and SLS without any signs of demagnetization, NdFeB IVUs with proper magnets have proven to be quite radiation resistant. The newest high-remanence, high H_{cj} grades of NdFeB (such as NEOMAX AH series), developed for use in hybrid car motors, should be particularly robust and radiation resistant. We have used this high-temperature NdFeB in our most recent IVU and have based our PM ID designs for NSLS-II on this same magnet material.

Curiously, some out-of-vacuum undulators at APS have experienced localized demagnetization, particularly those with smaller aperture vacuum chambers. Detailed simulations and radiation measurements suggest that the main source of the demagnetizing radiation is the tapered part of the aluminum vacuum chamber itself. Thus, out-of-vacuum IDs, such as the elliptically polarized undulators, may be more vulnerable to demagnetization than IVUs. Another contributing factor may be that the magnet grade used in APS undulators does not have particularly high H_{cj} and therefore does not withstand even localized radiation-induced head.

Advantages of IVUs over fixed-chamber, out-of-vacuum IDs are 1) that the former can be opened to provide a wide aperture during machine commissioning or beam studies, and 2) the lack of neutron-producing materials at transitions would mitigate magnet demagnetization.

A subject that needs further study is the impedance of the variable-gap IVUs. In Chapter 6, it was shown that the H-shaped space created by the gap space and the chamber forms a waveguide that contributes to transverse impedance. The RF transitions at the extremities of an ID must be properly tapered to reduce the geometric impedance. Modeling and RF measurements of real IVUs will be part of the R&D effort.

12.7.1.1 Cryo-Permanent Magnet Undulator

Recently the Cryo-Permanent Magnet Undulator (CPMU) has been proposed [12.7.3], as a simple means to enhance the performance of permanent magnet IVUs. The baseline design for a hard x-ray undulator for NSLS-II is based on a short-period linear undulator of the CPMU type. This is the U19 device described in Chapter 8.

The enhancement is based on the fact that NdFeB has a negative temperature coefficient of about –0.1%/K at 20°C for the remanent field (B_r), and also –0.5%/K for the intrinsic coercivity (H_{cj}). Therefore, one can expect higher field and higher radiation resistance simply by cooling the magnet array to lower temperature. However, NdFeB exhibits a spin orientation below somewhere around 150K and its B_r starts decreasing as the temperature goes below this value [12.7.6]. An obvious advantage of operating NdFeB at the plateau around 150K (in addition to gaining 11 to 13% higher field), is greatly reduced sensitivity of the field to temperature gradients.

To test the effect of cooling NdFeB undulators, we measured our decommissioned 0.3 m Prototype Small-Gap Undulator in dry ice at –71°C, and demonstrated that the field increased as expected at –0.1%/°C, or about 9% when cooled down by ~90°C. However, this measurement did not reach the plateau in the B_r vs. temperature that is expected at around –120°C. Analysis of the Hall probe data showed no significant increase in phase error, or in trajectory error, except in the end terminations. We also measured a 10-pole 13.5 mm period PM-hybrid prototype in dry ice with similar results.

The SPring-8 group recently compared warm and cold (130K) measurements of a 1 m long pure-permanent-magnet CPMU. They found that while the fields increased as expected, magnetic field errors scaled and tracked with temperature as well. This suggests that a CPMU can be shimmed at room temperature, and it will remain optimized when it is cooled. This also supports the notion that a CPMU is inherently “fail-safe,” in that it will still work well, albeit over a reduced tuning range, even if the cryocooling

fails. If this result holds true for a hybrid CPMU, we will save an enormous amount of time in the magnetic shimming and spectral optimization of CPMUs by avoiding multiple cool-downs and warm-ups during the iterative shimming process. An important R&D task will be to verify by cold and warm measurements that field errors track with temperature in a hybrid CPMU as well.

12.7.1.2 "Cryo-Ready" MGU Installed in NSLS

NSLS has recently constructed and installed a 1 m long "cryo-ready" MGU for beamline X25 (18 mm period, B_y = 0.95 T at 5.6 mm gap) [12.7.7]. It has provision for cryogenic cooling by circulating cold He gas from a refrigerator through channels embedded in the magnet array platens. For the test we were able to cool it to 130K by circulating boil-off N_2 gas. This test demonstrated that the mechanical features designed to accommodate the large differential thermal contraction of the cold magnet arrays relative to the warm vacuum vessel worked. We mapped the undulator before and after thermal cycling and found no measurable magnetic changes.

12.7.1.3 Optical Gap Measurement

First-order gap control is performed using four external stepper motors with a linear encoder feedback system that positions each magnet girder to a mean reproducibility of 1 micron. The 1 m magnet length required multiple structural feed-throughs in the vacuum envelope to assure continuity between rigid external structural girders and the in-vacuum magnet girders. However, magnetic and mechanical measurements indicated that gap-dependent nonlinear magnetic forces, environmental temperature gradients, and operational conditions caused deflections of the in-vacuum magnet girders exceeding specifications. The external linear encoders could not measure these effects, and correction by the primary gap control system would be ineffective. The CPMU direct measurements of the magnet gap differed by greater than 1 mm with respect to the gap, as inferred by the external linear encoders. These measurements indicated that relying exclusively on a conventional external linear encoder-based control system is insufficient under extreme conditions, and a direct means of gap measurement and a secondary means of gap control are necessary to maintain micron control of the magnet girders over the full range of environmental and operational conditions. An LED-based system (e.g., Keyence LS-7030) that has a measurement accuracy of ±2 μm and repeatability of ±0.15 μm can be employed to provide a secondary means of gap control, to permit correction over the regime of these tertiary effects for up to 100 microns of nonlinear gap control. Very fine taper/bow control can be achieved by embedding temperature-controlled heaters for each post. This method successfully worked for the X25 MGU at NSLS.

12.7.1.4 Optimizing the CPMU Design

Table 12.7.1 shows the possible combinations of period length, achievable peak field, and effective values of deflection parameter ($K_{y\,eff}$) at the undulator gap of 5 mm for warm (20ºC) and cold (–120ºC) in-vacuum devices calculated by the same Radia [12.7.8] model used for the X25 MGU. These are all hybrid structures with vanadium permendur poles. In this table, the effective K value for the non-sinusoidal field is calculated as

$$K_{x,y\,eff}{}^2 = 2\,\langle \gamma^2 \frac{v_{x,y}{}^2}{c^2} \rangle , \qquad (12.7\text{-}1)$$

where c is the speed of light in vacuum, γ is the Lorentz factor, and v is the velocity of the electrons.

Table 12.7.1 Period-Length vs. Maximum Flux Density and Effective K Value for IVU at Room Temperature and 150K.

Period Length (mm)	Warm (B_r = 1.29 T) B_{peak} (T)	Warm K_{eff}	Cold (B_r = 1.45 T) B_{peak} (T)	Cold K_{eff}
16.0	0.88	1.28	0.98	1.43
17.5	1.00	1.57	1.11	1.74
19.0	1.11	1.86	1.21	2.03
20.0	1.17	2.05	1.26	2.22
21.0	1.22	2.22	1.31	2.40

All of the NSLS MGUs have severe limitations in their length. Therefore, the ideal magnetic termination at the extremities has to be compromised in order to increase the number of full-field-strength periods. Hybrid devices tend to have an inherently larger gap dependence of integrated field strength, due to the nonlinear characteristics of pole materials and anisotropy of permanent magnets. Various termination schemes that minimize the gap dependence for pure permanent magnet devices have been developed [12.7.9]. However, designs for hybrid devices have limited effectiveness. End effects tend to be less important for small-gap undulators than for large-gap, high-field wigglers.

12.7.1.5 Minimizing Phase Error

A critical requirement for short-period, in-vacuum MGUs in a medium-energy storage ring is retaining high spectral brightness, up to the 7th or even the 9th harmonic. Loss of spectral brightness is well correlated with optical phase error. Phase error can be defined as the cumulative path length difference between the electron's actual trajectory and an ideal trajectory, expressed in degrees of phase at the fundamental optical wavelength. Cumulative optical phase error of 2° RMS is considered state of the art and will be the target for all NSLS-II undulators. This is an especially challenging requirement for small-gap, short-period IDs, as shown below.

Phase error arises from three sources: 1) systematic gap error, 2) trajectory wander, and 3) random phase errors. We will next describe the techniques we have developed and use routinely to minimize phase error from these three sources.

Systematic phase error can be caused by a) bowing of the magnet arrays due to attractive magnetic forces, b) gap taper, and c) nonflatness of the magnet mounting surfaces. These are long-range gap variations, on the scale of many undulator periods, which cause a gradual variation of field amplitude, wiggle amplitude, and therefore trajectory path length, without trajectory steering. To obtain a mechanical tolerance budget for these effects in the X25 MGU, we started with a finite-element analysis of an initial mechanical design for the magnet support beams, suspended on two hangers, under a distributed magnetic load of 8,000 N (due to the peak field of I T at a 5.6 mm gap). The resulting deflection profile was scaled to a field amplitude profile, which was numerically integrated to obtain the trajectory and, finally, a cumulative phase error profile. Figure 12.7.1 is a plot of the gap error (blue) and resulting cumulative phase error (magenta) vs. longitudinal position Z. The peak-to-valley deflection of 3 microns results in a RMS phase error of 0.75°. The figure shows that two supports per meter can induce a phase error of 0.75 degrees, due to deflection resulting from B = 1 T. Solid aluminum platens are assumed in this simulation.

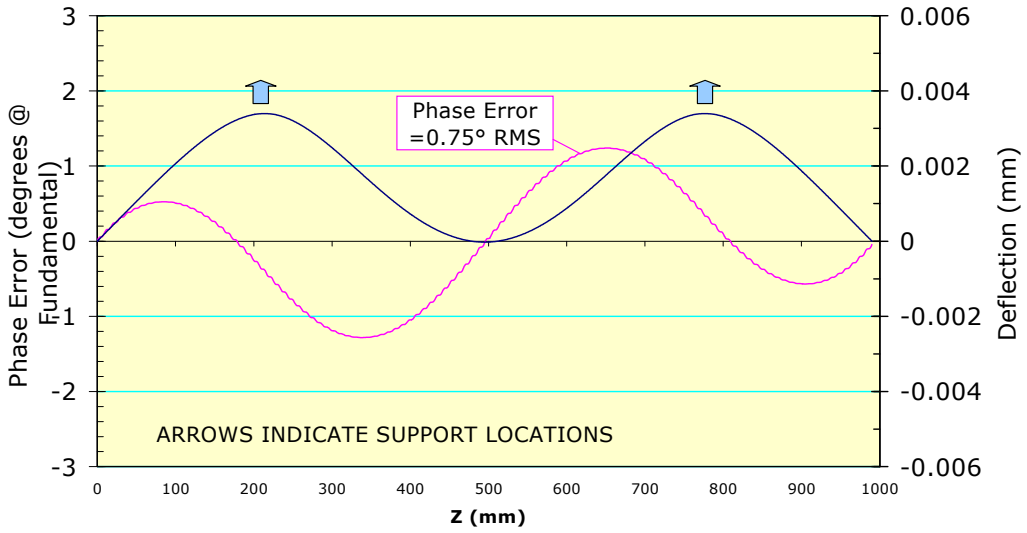

Figure 12.7.1 Phase error created by the mechanical deflection of aluminum magnet platens, due to the magnetic force of B = 1T.

The phase error created by 3.3 microns of linear tapering in 1 m is presented in Figure 12.7.2.

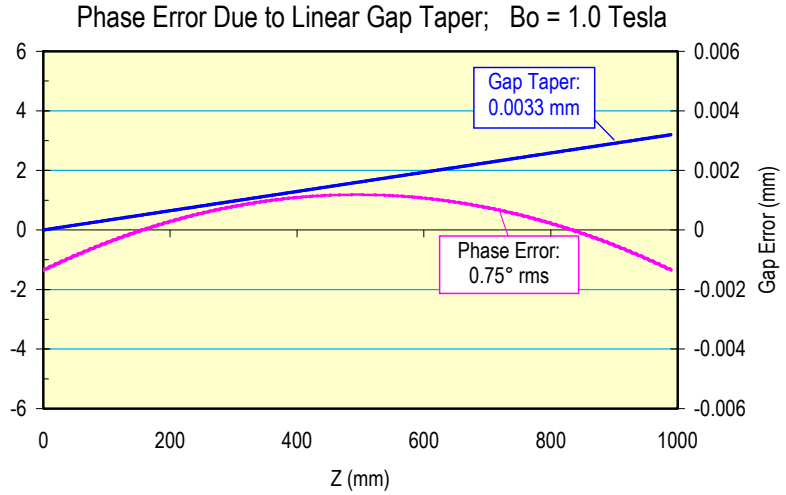

Figure 12.7.2 Phase error created by linear gap taper. B_0 = 1.0T.

Trajectory wander is caused by local, random field amplitude errors, which cause the trajectory to deviate from a straight line. The longer path is reflected in a phase error. Local steering errors can also accumulate over the length of the undulator as both integrated dipole (first integral error) and trajectory offset (second integral error). We routinely use the Pulsed Wire technique to quickly visualize the trajectory in undulators, identify the location and magnitude of steering errors, and apply steering shims to correct them. The pulsed wire easily displays both the horizontal and vertical components of a trajectory, including the contribution of the Earth's field.

Random phase errors are nonsteering errors that remain following trajectory straightening and the removal of systematic phase errors. In a PM-hybrid undulator, random phase errors are mainly caused by variations in the strength of individual magnets, as well as by pole positioning errors. To minimize these, the individual magnets are first measured, then sorted, paired, selected, and assigned to specific locations in the arrays. Various manual and computer-aided sorting and selection algorithms have been developed and are considered standard practice.

Earth's field causes significant trajectory deflection in long undulators. The measured local Earth's field is about 0.4 Gauss with an inclination of about 14° from the vertical. The vertical component contributes an

integrated (horizontally deflecting) dipole error of about 40 Gauss-cm/m. In a 3 m long CPMU, that adds up to a nontrivial dipole error of 120 Gauss-cm. The horizontal component is about 0.1 Gauss and oriented toward magnetic North. The effective (vertically deflecting) dipole error is <10 Gauss-cm/m and depends on the azimuthal orientation of the ID in the ring. The effect of Earth's field is readily visible on the pulsed wire as a parabolic trajectory component. It can be compensated by distributed trajectory shimming, or with external Helmholtz coils. In the X25 MGU we added a pair of 10-turn horizontal coils around the undulator vacuum vessel, powered by the end-pole trim supply from the old X25 wiggler previously residing at that location. Using the pulsed wire, we determined the optimal current to cancel Earth's field in the X25 MGU to be about 3.5 A. The small horizontal component was not compensated.

Other error specifications, such as maximum first and second integral and allowable integrated multipole requirements, will be specified before the engineering design phase.

12.7.1.6 Effect of Magnetic Field Errors on the Undulator Harmonics

The performance of real undulators is known to be poorer than the ideal case owing to magnetic field errors, despite valiant efforts to minimize such errors. It is generally accepted that the parameter which best relates magnetic field errors to spectral output is the RMS phase error ϕ. The RMS phase error ϕ is defined as the RMS path length difference between the real and ideal electron trajectories. It is calculated at the poles of the undulator and normalized to the wavelength of the fundamental harmonic (n = 1). (At higher harmonics (n >1), the RMS phase error is $n\phi$.) To date there has been no complete analytic treatment of the spectral effects of the phase errors. It has been argued that, for a zero-emittance electron beam, the relative on-axis brightness of the odd undulator harmonics n = 1, 3, 5, … emitted by an undulator with uncorrelated and Gaussian distributed phase errors is given by

$$B(n,\phi)/B(n,0) = e^{-n^2\phi^2} \tag{12.7-2}$$

where ϕ is the RMS phase error.

Recently, we have found empirically that this formula tends to underestimate the effect of phase errors for real undulators. For the two LCLS undulators discussed below, the expression above for a zero-emittance beam can be made to agree reasonably well with the result derived from magnetic measurements only if the RMS phase error is increased by ~20% from the measured value ($\phi \rightarrow 1.2\phi$). This is a large "correction" factor; more accurate results can be obtained by feeding the measured magnetic field profiles directly into undulator codes, such as UR or SPECTRA. Moreover, there is no analytical formula for phase error effects when the emittance needs to be taken into account, so we need to resort to numerical calculations.

Simulations were performed using measured magnetic field data from a set of undulators with RMS phase errors spanning a range from 2.0° to 3.7°. The measured magnetic field profiles and the storage ring parameters for NSLS-II were used as inputs to the undulator code UR in order to simulate realistic undulator spectral performance. If the results are a well-behaved function of phase error, one can then make a determination of the maximum tolerable RMS phase error required to achieve a particular level of undulator spectral performance. As discussed below, the results confirm the intuition that achieving a 2° RMS phase error, or better, is important for maintaining high spectral brightness for the high NSLS-II harmonics (7, 9, and 11). These results also confirm the idea that the phase error effects become more significant as the ring emittance decreases.

12.7.1.6.1 Relative On-Axis Brightness for Harmonics 7, 9, and 11 vs. RMS Phase Errors for NSLS-II Undulators

Computer simulations of the relative on-axis brightness as a function of the RMS phase error were performed using the NSLS-II emittance and real measured magnetic fields of three undulators. Comparisons

were made to the spectral performance of the same undulators with hypothetical ideal magnetic fields. The results are detailed below and show, for example, that the 9th harmonic undulator radiation degrades by about 15% if the RMS phase error increases from 2.0° to 3.0°.

12.7.1.6.2 Conditions

The NSLS-II storage ring parameters for a 5 m long low-β insertion device straight section were used for these simulations. The following parameter values were used: emittances ε_h=0.55 nm, ε_v=0.01 nm, energy spread δE/E=0.1%, and β-functions β_h = 2.7m, β_v=0.945m. The resultant electron beam sizes and divergences are σ_h=38.5 μm, σ_v=3.1 μm, σ_h'=14.2 μrad, and σ_v'=3.2 μrad.

The following three undulators were studied:

- Linac Coherent Light Source undulator number 1 (LCLS #1), period length=3.0 cm, 113 periods; K and ϕ measured at 6.8 mm gap: K=3.50 and ϕ=3.54°
- Linac Coherent Light Source undulator number 2 (LCLS #2), period length=3.0 cm, 113 periods; K and ϕ measured at 6.8 mm gap: K=3.49 and ϕ=4.21°
- APS short undulator A (APS #40), K = 2.80, period length = 3.3 cm, 62 periods; K and ϕ measured at 10.5 mm gap: K = 2.80 and ϕ = 3.68°

Numerical calculations of the on-axis brightness for these three undulators were performed. In order to study the dependence on the RMS phase error, the LCLS undulator fields were scaled in both field strength (uniformly to a lower value) and period length to simulate a change of the RMS phase error (the RMS phase error decreases when the K value becomes smaller). Very minor adjustments to the on-axis view angle were applied, and as such, those fields represent real devices with true magnetic field errors. It is worth noting that for the LCLS undulators, the period length was scaled from 3.0 cm to 1.9 cm to simulate a shorter period-length undulator, such as the NSLS-II U19 CPMU hard x-ray undulator. This procedure allowed us to study undulators which have RMS phase errors covering the range 2.0° to 3.7°.

12.7.1.6.3 Results

The on-axis brightness of the 7th, 9th, and 11th harmonics, relative to the brightness of the corresponding harmonics of a hypothetical, ideal magnetic field undulator, is plotted in Figure 12.7.3 for the three undulators described above, simulated for their performance in the NSLS-II storage ring. The relative brightness of the 3rd and 5th harmonics is much closer to 100% and is not shown in this figure.

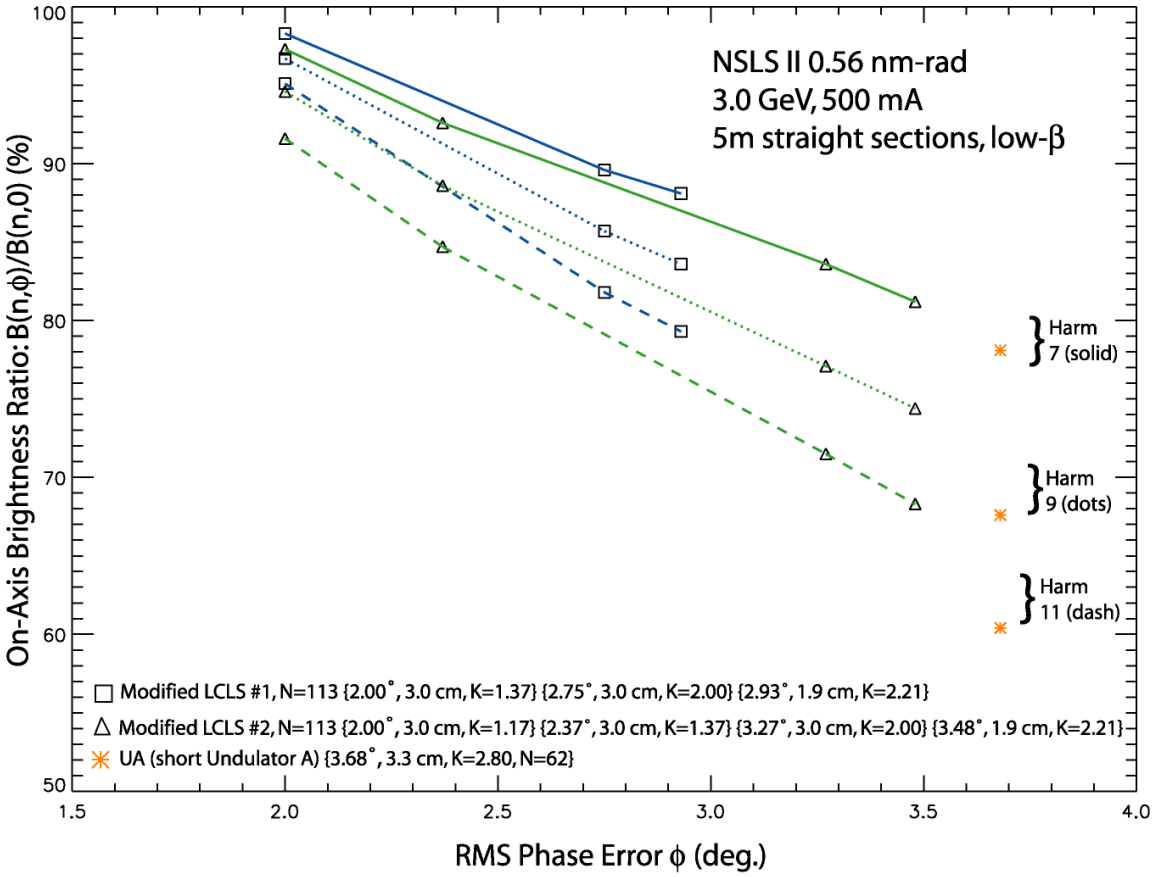

Figure 12.7.3 On-axis brightness of the 7th, 9th, and 11th harmonics of three undulators relative to the brightness of the corresponding harmonics of an ideal magnetic field undulator, as a function of the RMS phase error.

The key results of these simulations are as follows: improving the RMS phase error from 3.0° to 2.0° changes the relative brightness of the 7th harmonic from 86 to 98% (Δ_7 = 12% points), the 9th harmonic from 81 to 96% (Δ_9 = 15% points), and the 11th harmonic from 75 to 93% (Δ_{11} = 18% points).

12.7.1.6.4 Conclusions

The relative brightness of the NSLS-II undulator harmonics depends sensitively on the RMS phase error. The higher the harmonic number and the higher the RMS phase error, the faster is the rate of reduction. The rate of reduction is somewhat sensitive to the actual distribution of phase errors for real devices, but is much less sensitive to the actual K value or the undulator period length. For example, by improving the RMS phase error from 3.0° to 2.0°, the 9th harmonic would gain about 15%.

The effect of phase error becomes greater as the emittance of the storage ring decreases. For example, the performance drop for NSLS-II undulators would be 2 to 5% greater for harmonics 7–11 than for the same devices at APS, as a result of the smaller emittance of NSLS-II.

Future work on this subject should include simulations using the measured fields from recently built undulators around the world, including the 18 mm period undulator installed at NSLS beamline X25 in December 2005, which has a period length very close to the U19 CPMU proposed for NSLS-II and has a measured RMS phase error close to 2°.

12.7.1.7 Baseline CPMU Magnetic Design

The baseline design for the NSLS-II hard x-ray planar device is derived from the NSLS cryo-ready undulator developed for X25. The X25 mini-gap in-vacuum undulator has an 18 mm period length, a minimum magnetic gap of 5.6 mm and length of 1 m, and is designed to be operated at 150 K. The NSLS-II U19 CPMU will have a minimum gap of 5 mm and will be 3 m long, but most of its other requirements are similar to those for the X25 MGU. The main parameters are given in Table 12.7.2.

Table 8.2.3 shows the expected mechanical tolerances of the magnetic arrays.

Table 12.7.2 Mechanical Tolerances.

Item	Tolerance
Magnet/pole width [μm]	±100
Magnet height [μm]	± 25
Magnet thickness [μm]	±25
Pole height [μm]	± 25
Pole thickness [μm]	± 10
Pole-to-pole flatness [μm]	±10
Period [μm]	±10
Magnet array pitch/yaw/roll (relative) [μrad]	± 25
Magnet array horizontal/vertical rack [μm]	± 5
Gap control [μm]	± 5
Gap repeatability [μm]	± 5

The phase error for the device is required to be less than two degree RMS. Slight tapering, platen bowing, and other factors must be carefully controlled to achieve this level of phase error. As mentioned above, a novel gap measurement system using a commercial, high-precision, LED-based optical micrometer was incorporated in the X25 MGU to back up the linear encoders and to correct for gap changes due to differential contraction during cryogenic operation. The system monitors the magnet gap optically through viewports at either end of the MGU, ensuring gap accuracy of ±2 μm.

Figure 12.7.4 shows an isometric rendering of the MGU magnet arrays by Radia. Blue magnets have identical size and two different sized magnets are shown in green. Pieces in magenta represent permendur poles.

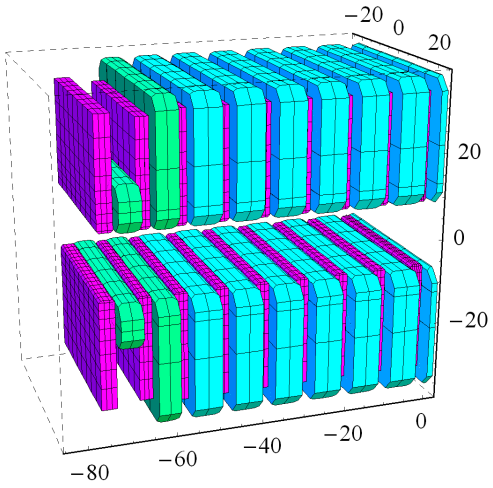

Figure 12.7.4 MGU magnet arrays. Only the first few periods are shown, for clarity. Units are millimeters.

The Radia simulations shown here were performed with a symmetrical model so the angular kick could be estimated. In the actual device we are likely to use an anti-symmetric structure to minimize the residual first integral. The values of magnet susceptibilities used are χ_m (para) = 0.02, χ_m (perp) = 0.42. The field and trajectory computed from the model are plotted in Figure 12.7.5 for gaps of a) 5.0 mm and b) 11.0 mm. The trajectory is calculated by a particle-tracking Runge-Kutta routine. The particle is launched with zero offset and angle (x = 0, x' = 0), and its position and angle are calculated every 0.53 mm (36 points per period). The gap dependence of the first integral is shown in Figure 12.7.6. The amount of change in the first integral found here can be easily compensated by external coils.

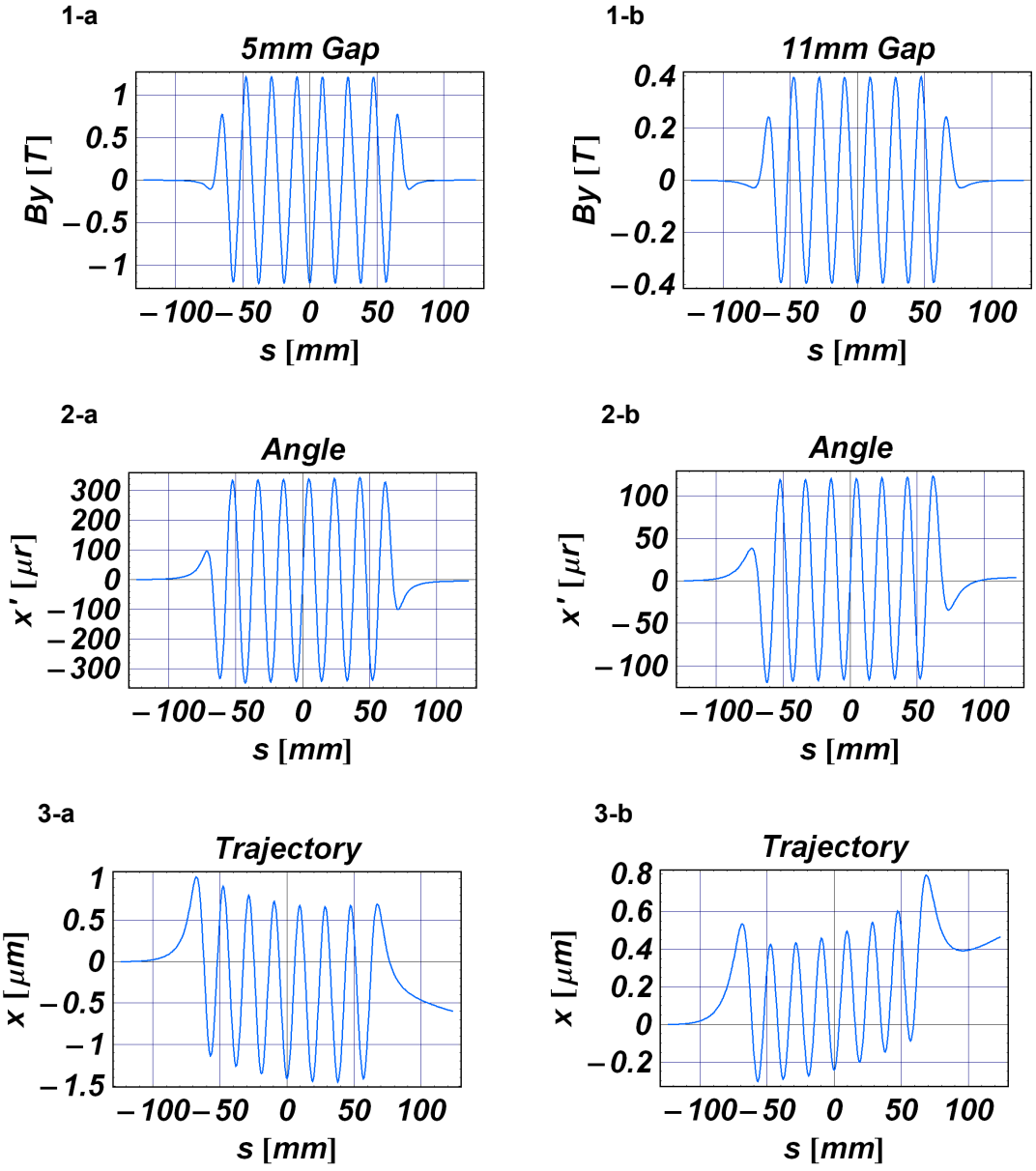

Figure 12.7.5 Gap dependence. Field, angle, and trajectory plots for the 7-period model for (column **a**) minimum gap (5.0 mm) and (column **b**) maximum operating gap (11.0 mm).

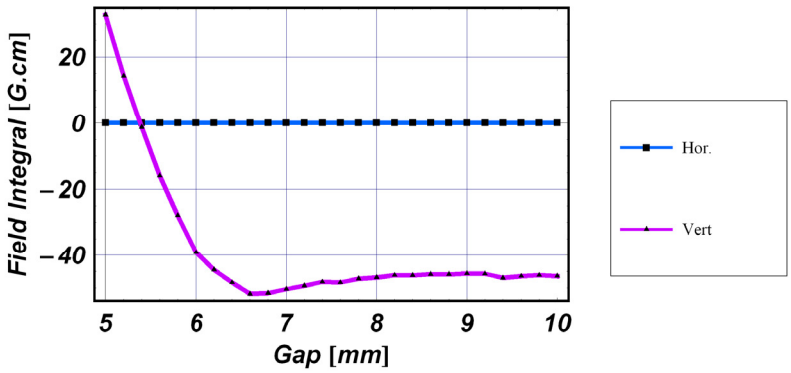

Figure 12.7.6 Gap dependence of the first integrals simulated for U19.

12.7.1.8 New Magnetic/Pole Materials Development

An avenue of further development of CPMUs is to investigate other rare-earth magnets that do not exhibit the spin re-orientation transition at 150K. For example, PrFeB has similar Br as NdFeB at room temperature, but its Br continues to increase further all the way down to 4K. PrFeB would permit use of liquid nitrogen to cool the CPMU to 77K and thereby attain an additional 5 to 7% increase in field. NEOMAX produced a few research samples of PrFeB several years ago, and again just recently. Although the material is not available commercially, we are discussing with NEOMAX and with SPring-8 the possibility of a PrFeB development project.

We will also investigate the use of exotic pole materials, such as oriented dysprosium, with a reported saturation flux density up to 3.5 Tesla at cryogenic temperatures. This opens the possibility of a CPMU built with PrFeB magnets and Dy poles, operating at 77K or lower with significantly higher performance than with NdFeB and permendur poles. This may ultimately reduce or eliminate the need for the complexity of superconducting undulators. This project will draw on the expertise in dysprosium and permanent magnet materials at the BNL Materials Science Department. If development of both PrFeB magnets and oriented Dy poles is successful, a short prototype undulator magnet module could be constructed and tested in our existing Superconducting Undulator Vertical Test Facility.

12.7.1.9 Vacuum and Mechanical Systems Development

A 3 m device will be constructed with three 1 m modules that are similar to the X25 MGU. The vacuum chamber is rectangular and opens along its length to facilitate magnetic field measurements and shimming. Most of the required vacuum components are mounted to this cover for easy access and for a cost-effective design. These components include ion pump/titanium sublimators, getter pumps, an RGA analyzer, a glow discharge cleaning system with associated pumping and view ports, an ion gauge, and bleed-up ports. The X25 system successfully achieved a pressure of less than 5×10^{-10} Torr, including magnets, after bakeout. The conceptual design in a CAD model is shown in Figure 12.7.7.

Techniques first demonstrated in the cryo-ready X25 MGU will be optimized and incorporated for the NSLS-II development program for the control system of the CPMU. Systems such as an in-vacuum gap separation system will be modeled that can provide precision gap control with negligible effects from external temperature fluctuations and ultimately demonstrate a cost-effective alternative to more conventional gap separation and control systems.

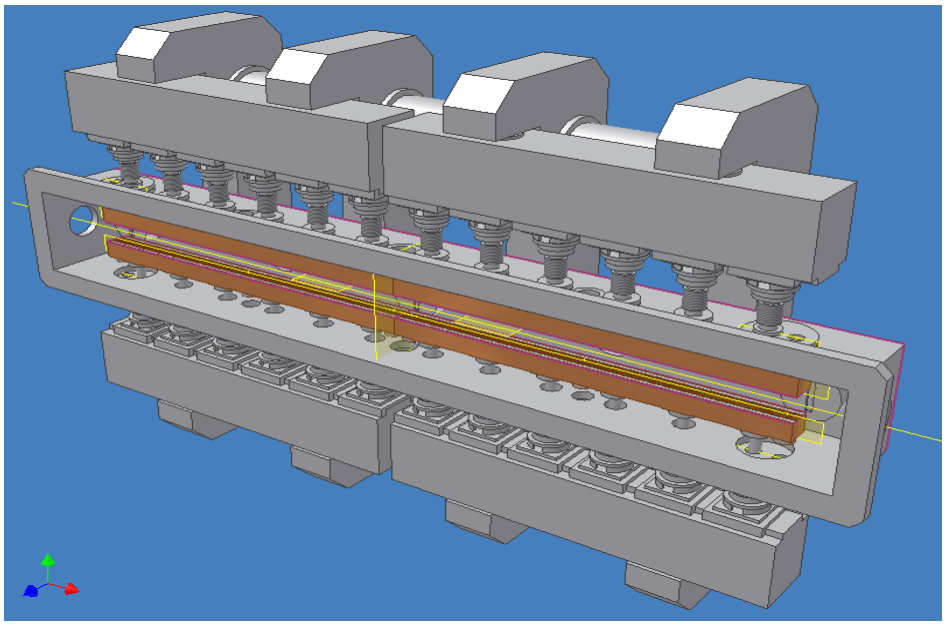

Figure 12.7.7 Conceptual design of U19.

12.7.1.10 CPMU Magnetic Measurement Systems Development

Two types of measurement systems are used to characterize the field quality of an insertion device at the magnetic measurement laboratory at NSLS. The first is a pulsed-wire measurement system that can be used to check the trajectories in both horizontal and vertical directions. It is also used to find the correct coil current of a Helmholz coil to cancel the earth field. The second type is a Hall probe mapping system. The Hall probe scan is done "on-the-fly," starting from a precise home position, acquiring the desired number of samples per undulator period.

One of the challenges for CPMU development is to establish an accurate low-temperature field measurement system. For properly designed undulators, the differences in field quality between room temperature and low temperature are expected to be small. However, it is essential that the field quality be verified at the actual operating temperature. A vertically oriented cryogenic magnetic measurement apparatus for prototype undulator models up to 0.4 m in length has been developed and used at NSLS [12.7.10]. In order to measure full-length devices in a horizontal orientation, a new measurement scheme must be developed. The magnetic measurement should be done in the vacuum vessel at the cold operating temperature, but not necessarily in UHV. Figures 12.7.8 and 12.7.9 delineate the concept of an in-vacuum, in-situ Hall probe mapper. It is mounted on the large rectangular front flange of the chamber. Hall probe position accuracy is maintained by a laser tracker and piezo controller.

For field integral measurements, an in-vacuum moving wire system has already been developed by ACCEL and ESRF. A similar mechanism can be used for a pulsed-wire system.

There is no convenient way to make in-situ (i.e., in-vacuum) field error corrections unless a remote-control magnet adjustment mechanism is incorporated in the magnetic arrays. In the absence of this development, field error correction must be performed iteratively, where each iteration requires a lengthy series of warm-up, venting, measurement, adjustment, pump-down, and cool-down steps. Our goal is minimize the number of such iterations by 1) designing the mechanical components to minimize the systematic field errors resulting from warm-up and cool-down, and 2) developing an efficient scheme of warm shimming and cold measurement. Ideally, field errors may track with temperature, so shimming at room temperature may suffice.

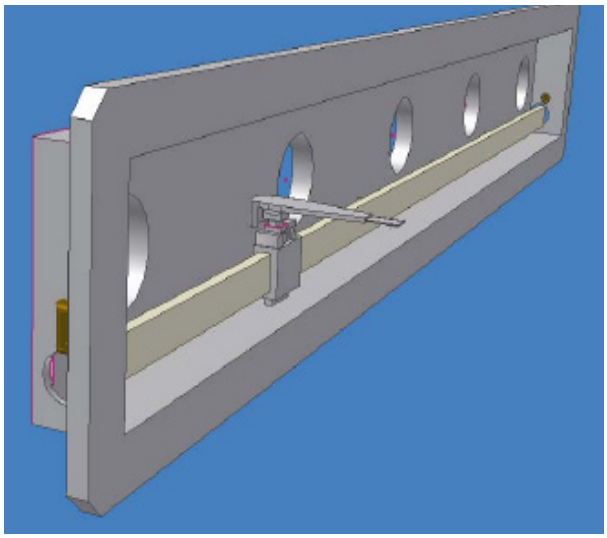

Figure 12.7.8 Hall probe mapper mounted on the flange cover.

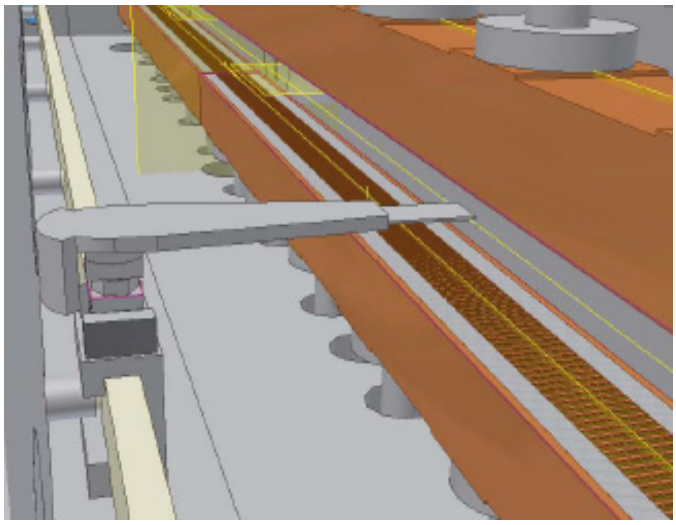

Figure 12.7.9 Mapper position with respect to the magnet arrays.

This cold magnetic field mapping system is essential for CPMU or HTSCU development. This system will be designed to be used primarily in the measurement laboratory but can also be used to perform in-situ measurements of insertion devices in remote locations such as a synchrotron tunnel. This system will incorporate a horizontal vacuum chamber that could accommodate either a CPMU or HTSCU that is 3+ m long and that demonstrates efficient installation of in-situ shimming and measurement of the magnet modules without the need for chamber reassembly. Cryogenic hall probe, pulsed/vibrating wire, and moving wire will be investigated. The research phase will demonstrate the incorporation of an in-vacuum measuring system with the vacuum vessel and precision gap separation mechanisms.

The goal of this development is to demonstrate cryogenic undulator measurement concepts that will ultimately be used in the characterization, shimming, and in-situ measurements of all the production in-vacuum and cryogenic insertion devices.

12.7.2 Variable Polarization Device

The variable polarization undulator, also known as an elliptically polarized undulator, EPU, is becoming more popular, as its impact on beam dynamics can now be controlled to an acceptable level. Currently, no in-vacuum EPU has been constructed, because of the difficulty of having moving parts and a strong force in a UHV environment. Therefore, the baseline design for NSLS-II will be the permanent magnet out-of-vacuum EPU45 and EPU100 devices described in Chapter 8, but R&D will be carried out to investigate in-vacuum EPU designs.

Various schemes to generate variably polarized light from an insertion device have been proposed. An electromagnet-based design that switches the polarity cannot cover the required photon energy range (250 eV–2 keV). The most popular design, based on PM technology, is the Advanced Planar Polarized Light Emitter (APPLE) type [12.7.11]. It has been popular because it can generate all the possible polarization states with the minimum number of magnets. However, it also has a few deficiencies. Strong multipole components inherent to the design would reduce the dynamic aperture of the machine. This effect is due to the fact that horizontal field and vertical field are coupled, so static optimization for different gap and phase is difficult. In long-period devices, the electron's wiggle amplitude can be large enough for the field rolloff to affect the trajectory and result in a so-called "dynamic field integral," which is not measured by stretched

wires or long coils. Recent efforts by various laboratories have mitigated these problems for limited types of operations [12.7.12].

There is an alternative design proposed for HiSOR by SPring-8 [12.7.13]. It separates the magnets for horizontal and vertical field, for ease of tuning as well as more moderate skew multipoles, at the expense of weaker achievable horizontal field. Detailed tracking studies will be carried out to decide which type of device is appropriate for NSLS-II.

Another concern for NSLS-II EPUs is the possible demagnetization of the permanent magnets by the use of the APS-style narrow gap vacuum chamber. Improvements to the vacuum chamber design will be investigated in order to minimize the source of radiation at the extremities of the chamber.

12.7.2.1 Anisotropy of Permanent Magnets

Rare-earth magnets used for insertion devices have permeability close to unity, so that, to first order, the magnetic induction from individual magnet blocks can be superposed to obtain the total field. However, more careful analysis shows that there is anisotropy in those magnets. The components of the permeability that are parallel to the preferred direction of magnetization (easy axis), and perpendicular to this direction, are different and lager than unity. The magnetic susceptibility χ_m and polarization J are defined as follows:

$$B = \mu H = \mu_0 \mu_r H = \mu_0 (\chi_m + 1) H , \quad (12.7\text{-}3)$$

$$J = \mu_0 \chi_m H \quad (12.7\text{-}4)$$

where B is magnetic induction, H is magnetic field strength, μ_0 the permeability of vacuum, and μ_r is the relative permeability defined for convenience.

The permeability can vary at different points on the hysteresis curve. For example, the value at the beginning of magnetization is termed initial permeability, and the largest gradient in the B-H curve is called maximum permeability. What is important in a magnetic circuit is the reversible or recoil permeability, which is the slope of a minor loop in the second quadrant. The recoil permeability is usually approximated by the slope of the major loop at H = 0. For NEOMAX 42AH, the susceptibility is estimated by the slope of the J-H curve around H = 0. The estimated values of susceptibilities from these curves are:

$$\chi_m \text{ (para)} = 0.02, \ \chi_m \text{ (perp)} = 0.42. \quad (12.7\text{-}5)$$

These values indicate that in the region where the magnetic flux lines deviate from the preferred direction of magnetization, the material can be nonlinear. For planar insertion devices, this region corresponds mostly to end sections, which determines the gap dependence of the field integral, in practical terms. However, in most EPUs, the field directions inside magnets vary greatly, depending on the array phase. For the CPMU these values will need to be measured at the operating temperature, in order to be valid.

12.7.2.2 Advanced Options

In-vacuum EPU is still an R&D subject. The performance of any type of ID strongly depends on the available minimum magnetic gap. Development of a 2.5 m long in-vacuum EPU is under consideration. If initiated, BNL would assemble magnet and pole materials, develop in-vacuum gap separation and magnet module axial position actuators, and procure a vessel and undulator support system. Measurements and characterization of the EPU fields under various gaps and phases would be made, as well as field corrections. The in-vacuum EPU could then be installed for the X-1 beam line of NSLS to verify performance prior to the move to NSLS-II. The goal of this development would be to advance the state of the art in EPU technology, to demonstrate the first in-vacuum EPU, to resolve the uncertainty in the methods of measurement and

shimming of EPUs to permit reliable and cost-effective operation, and to perfect a new class of insertion device, the in-vacuum EPU, that can be offered to meet the needs of NSLS-II users.

To switch the helicities at higher than 1 Hz, a tandem structure is needed so that light with opposite helicities is produced simultaneously for various switching schemes. In this case, each ID is located away from the center and the required beam stay-clear gap would increase. If a slower switching frequency is tolerated, one longer device with mechanical phase change is possible. Another possibility is to set up two helical undulators in tandem and have a phase shifter between them to change the resulting polarization [12.7.14]. In this case, two helical undulators can be in-vacuum type if limited tuning range can be tolerated. Table 12.7.3 shows the characteristics of an APPLE-II type EPU.

Table 12.7.3 Characteristics of an APPLE-II Type EPU. Assumed Br of the magnets is 1.35T.

Period Length (mm)	Magnetic Gap (mm)	Helical ModePeak Field (Bx = By)	EffectiveKx / Ky	Linear ModeEffective Ky
40	6.5	0.87	3.2	4.87
42	8	0.77	3.0	4.76
45	10	0.68	2.87	4.67
45	11	0.62	2.6	4.38

12.7.2.3 EPU45 (APPLE-II) Magnetic Design

One possibility is to install twin devices in an 8 m straight section. Assume that we can have a 5 mm vertical aperture for a 3 m device placed at the center of the 5 m straight, with vertical beta function equal to 1 m at the insertion center. In this case, the ring aperture (A) is:

$$A = \frac{gap}{\sqrt{\beta(end)}} = \frac{gap}{\sqrt{\beta_0 + (end)^2 / \beta_0}} = \frac{5mm}{\sqrt{(1+1.5^2)m}} = 2.77mm/\sqrt{m}\,. \tag{12.7-6}$$

We must verify that this is sufficient, but once we determine that this is acceptable, the required aperture y for an insertion device of length L placed at the center of a straight with beta-function β_0 at the center is determined to be

$$y = A\sqrt{\beta_0 + \frac{(L/2)^2}{\beta_0}} \tag{12.7-7}$$

For the 8 m straights β_0 = 3 m, we find the required vertical aperture is 7.4 mm at the half length of 3. 5 m. An 8 mm aperture chamber at APS allows 2.5 mm extra for the magnetic gap of their insertion device. Therefore, we will assume that the magnetic gap of the NSLS-II insertion device is close to 10 mm.

The minimum photon energy to be covered is 250 eV. An EPU45 with an APPLE-II type configuration shows the characteristics listed in Table 12.7.4. Here, the remanent fields of the NdFeB magnets are assumed to be 1.35 T.

Table 12.7.4 APPLE-II Type EPU45 Parameters.

Period length [mm]	45
Peak field (helical mode: v/h) [T]	0.68 / 0.68
Effective K	2.87
Minimum photon energy in helical mode [eV]	206
Minimum gap [mm]	10
Magnet horizontal size [mm]	50
Magnet vertical size [mm]	45
Remanent field (B_r) [T]	1.35

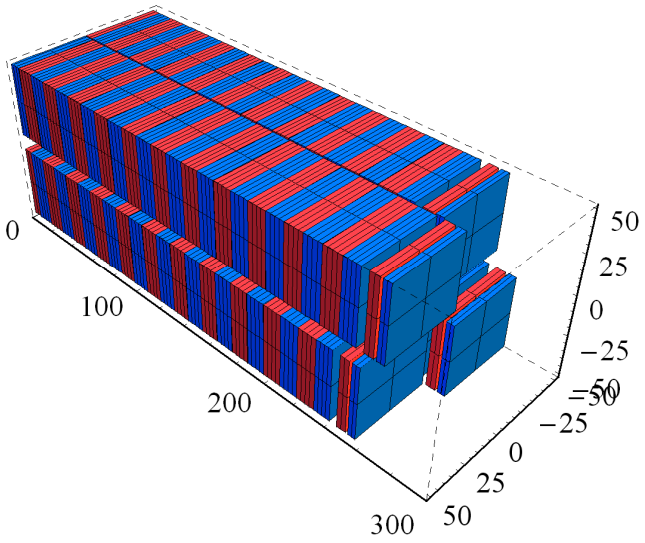

Figure 12.7.10 Magnet arrays of EPU45. Only the first few periods are shown for clarity. Units are millimeters. Vertically magnetized magnets are in red and horizontally magnetized magnets are in blue.

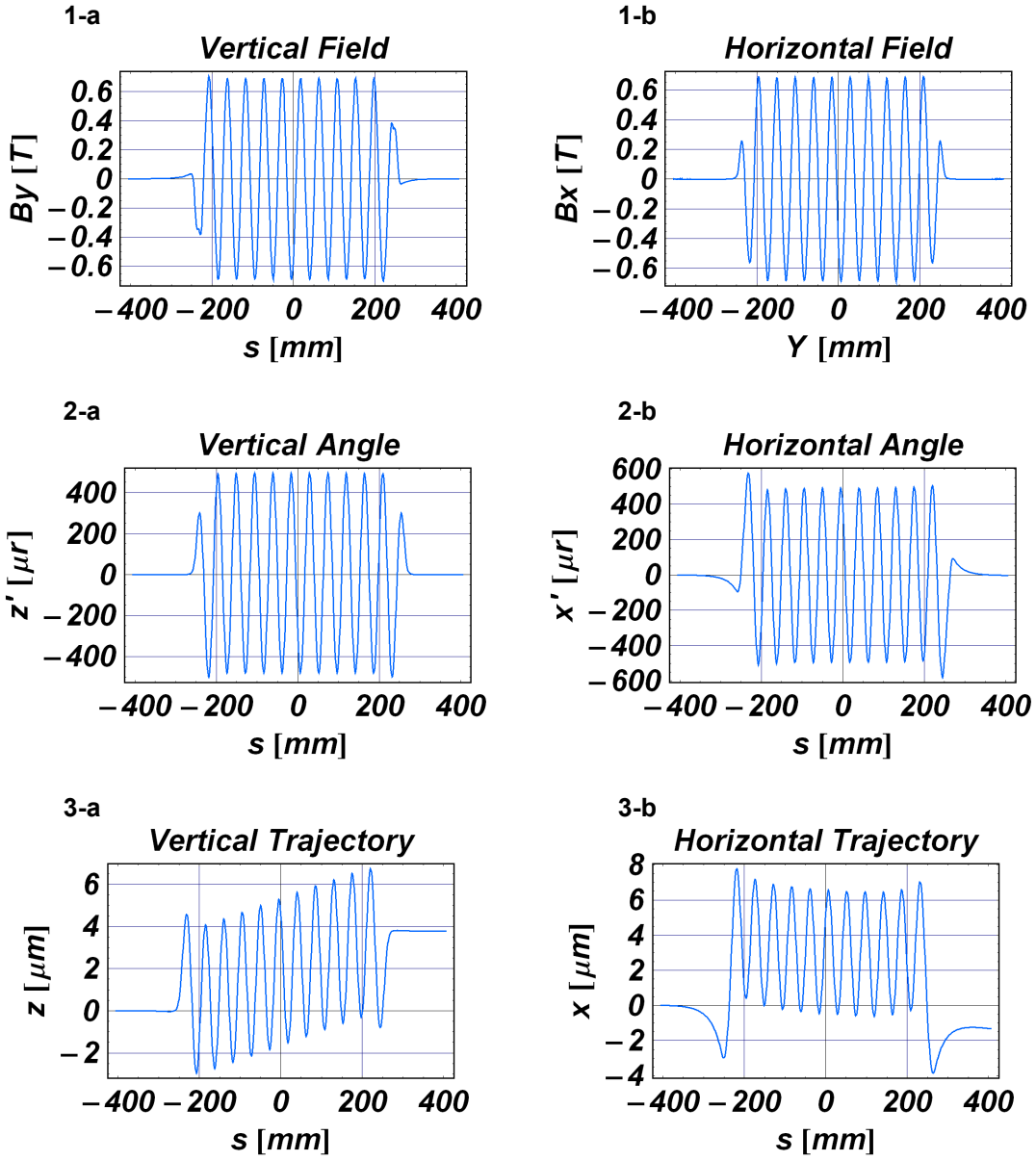

Figure 12.7.11 Field, angle and trajectory plots for the 11-period model of EPU45 in helical mode. **a)** vertical field, horizontal angle, horizontal trajectory and **b)** horizontal field, vertical angle, and vertical trajectory at a gap of 10 mm.

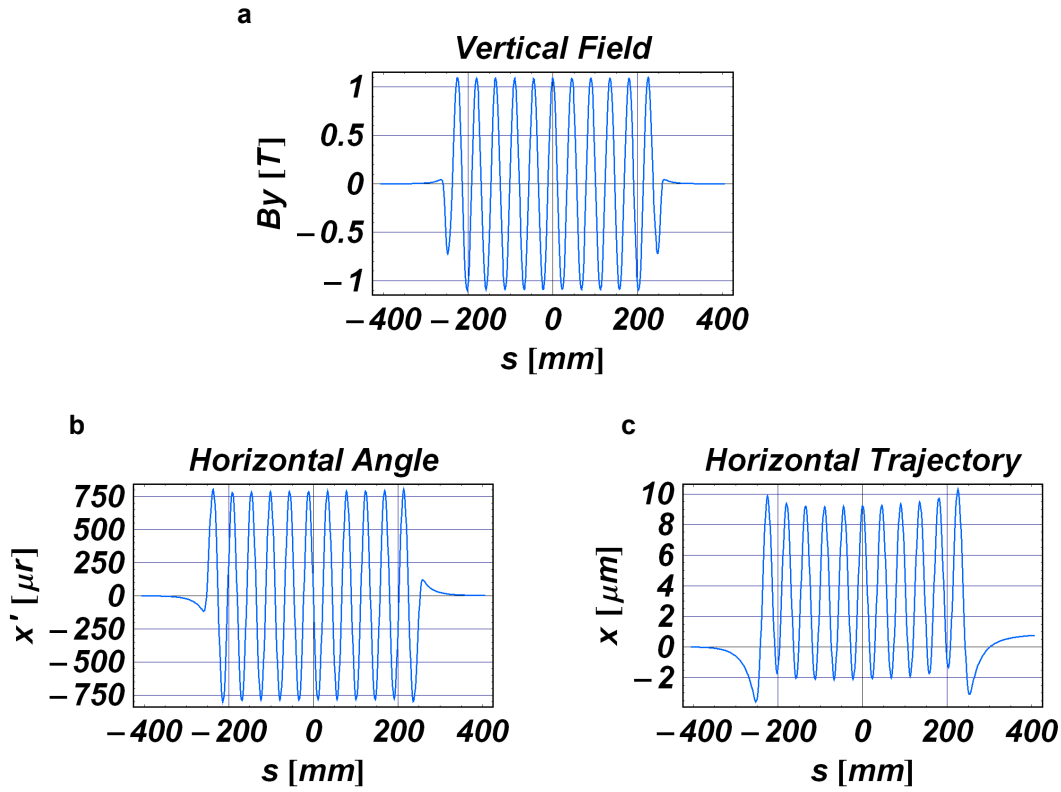

Figure 12.7.12 Field, angle, and trajectory plots for the 11-period model of EPU45 in linear mode. **a)** vertical field, **b)** horizontal angle, **c)** horizontal trajectory at a gap of 10mm.

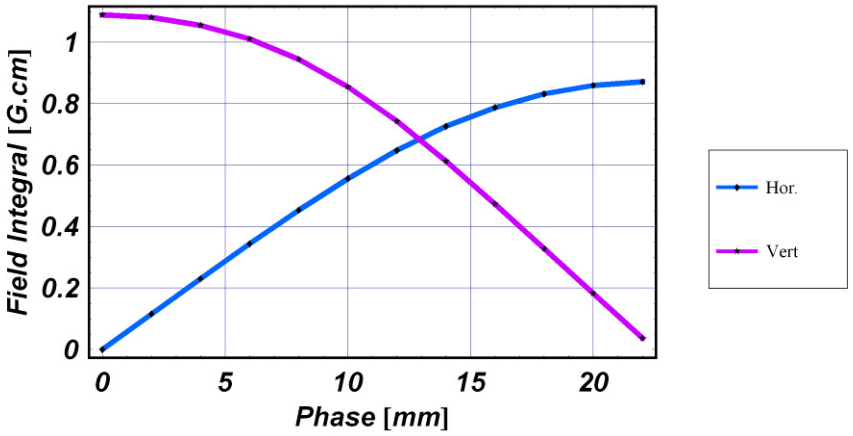

Figure 12.7.13
Fields vs. phase.

F

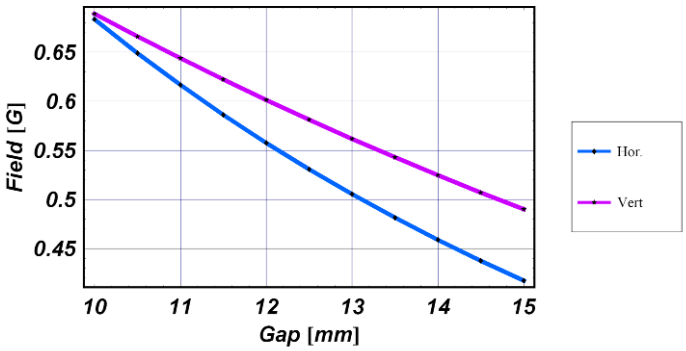

Figure 12.7.14 Fields vs. gap in helical mode.

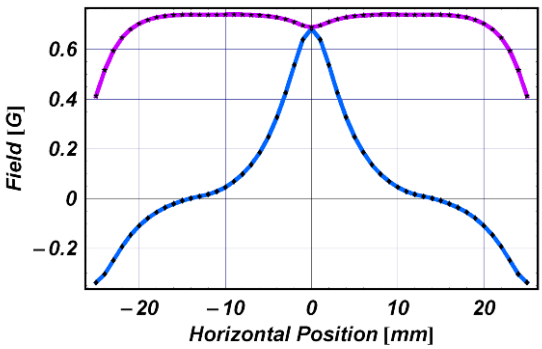

Figure 12.7.15 Fields vs. horizontal position at the origin in helical mode.

12.7.2.4 EPU50 (HiSOR) Magnetic Design

To alleviate a highly sharp horizontal field profile and the coupling of vertical and horizontal fields from the same magnet, a new design with three magnet arrays in each jaw has been proposed and implemented at UVSOR and HiSOR in Japan. Unlike the APPLE-II design, one array in the center produces vertical field and two arrays on the sides generate horizontal field. Therefore, each type can be separately shimmed to perfection. The horizontal field profile is more benign than that from APPLE-II. The parameters for the HiSOR design are shown in Table 12.7.5, and a Radia drawing shows the design (see Figure 12.7.16).

Table 12.7.5 HiSOR-Type EPU50 Parameters.

Period Length	5 mm
Peak Field (helical mode: v/h)	0.53 / 0.53T
Effective K	2.49
Minimum photon energy in helical mode	240 eV
Minimum gap	10 mm
Side Magnet Size (H/V)	50 / 45 mm
Center Magnet Width	14 mm
Remanent Field (Br)	1.35T

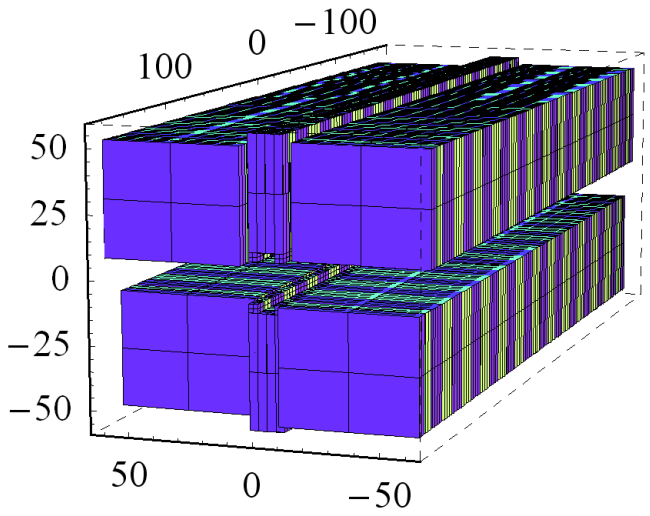

Figure 12.7.16 Magnet arrays of HiSOR-EPU50. Only the first few periods are shown, for clarity. Units are millimeters. Vertically magnetized magnets are in light green and horizontally magnetized magnets are in purple.

One disadvantage of the HiSOR design is that the maximum horizontal field is weaker than that of the APPLE-II for the same period length, due to the increased distance between the two arrays. Hence, slightly longer period length is required to obtain the same photon energy as with the APPLE-II design. If vertical linear polarization is needed, the vertical arrays can be shifted out of phase. However, some longitudinal components remain at the extremities, and tracking studies are needed to determine the detrimental effect.

The grooved-shape magnets in the center arrays improve the vertical field uniformity (see Figure 12.7.17).

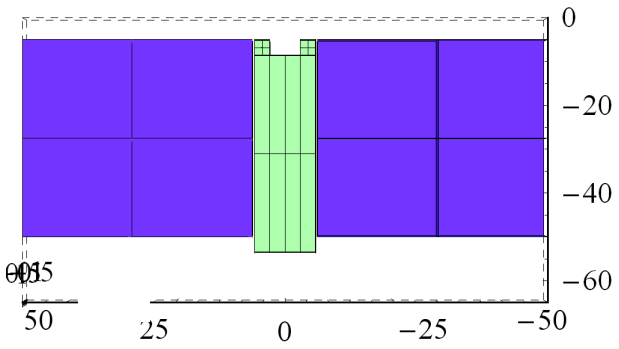

Figure 12.7.17 Cross-section of a magnetic array. Light green is for the vertical field and purple is for the horizontal.

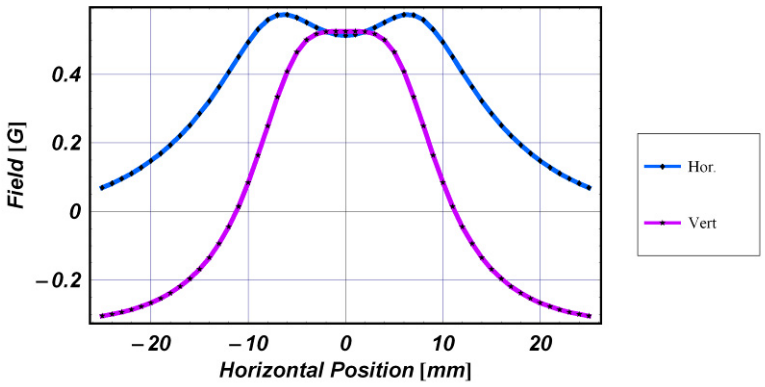

Figure 12.7.18 Field profile vs. horizontal position in helical mode.

12.7.3 Damping Wigglers

In Chapter 7 we defined two key parameters of the Damping Wigglers (DWs): a peak field of 1.8 T and an eventual total length of 35 m. The peak field value was chosen to be high enough to radiate sufficient power for adequate emittance damping, but not so high as to create excessive energy spread. The DWs are also useful as high-flux, high-brightness broadband sources in the hard x-ray range.

The initial installed length of DWs will be 21 m, composed of three wigglers, each 7 m long. A third key design parameter is the minimum magnetic gap. The estimated vertical stay-clear aperture at ±3.5 m from the center of the 8 m straight section is 10 mm. Allowing for beamtube wall thickness of 1.5 mm, plus 1 mm clearance between the beamtube and the magnet poles, we obtain a minimum magnetic gap of 15 mm. From empirical design formulas developed by Elleaume for various planar undulator (wiggler) technologies [12.7.15], we find that 1.8 T peak field can be produced at that gap by a conventional PM-hybrid wiggler with a period of 100 mm, using high-field NdFeB magnets (Br = 1.35 T) and vanadium permendur poles. With less expensive low-carbon steel poles, a somewhat longer period (~110 mm) would be required. In either case, these parameters are in the realm of wigglers that have been produced by industry. Of course, the 7 m length may be comprised of two 3.5 m long DWs, or three 2.3 m long units in tandem.

Unlike users of undulator radiation, wiggler users expect a broad, dipole-like spectrum. Therefore, minimizing phase errors is not important. Shimming of DWs is concerned mainly with trajectory straightness. In fact, gap taper, or variation in pole periodicity are sometimes introduced in wigglers intentionally to spoil coherence and to smooth the spectrum.

DWs must meet the same integrated dipole and multipole error specifications imposed on all IDs. However, since they will operate at fixed gap, these errors can be shimmed out more easily than in variable-gap IDs, without concern about gap-dependence. The next sections discuss some additional design considerations for DWs.

12.7.3.1 Dynamic Field Integral

The integrated field seen by sinusoidally wiggling electrons [12.7.16] is

$$\int B_y ds \approx \frac{-L}{2k^2 B\rho} B_y(x_i) \frac{dB_y(x_i)}{dx} , \qquad (12.7\text{-}8)$$

where L is the device length, k_w is the 2ρ/period length, ρ is the radius of curvature of the trajectory, and x_i is the horizontal displacement of the electron. This is called dynamic field integral, and it scales as ID period squared and as the derivative of the transverse field roll-off. An important aspect of optimization of long-period wiggler magnetics is how to determine the necessary transverse pole width to minimize the effect of the dynamic field integral effect while minimizing attractive force, which is proportional to the magnet area, and keeping the cost as low as possible. Beamtracking reveals the detrimental effect of this integral on the beam dynamics.

12.7.3.2 Attractive Force and Size/Cost Challenges of the Damping Wigglers

For NSLS-II, the damping wigglers will be used as a broadband source. The design calls for 7 m of damping wiggler in an 8 m straight. In reality, it is easier to combine two 3.5 m devices or five 1.4 m units. The approximate attractive force of a linear device is given as follows:

$$F_{ID} \approx \frac{B_y^2 WL}{4\mu_0}, \tag{12.7-9}$$

where W is the horizontal width of poles or magnets, L is the total length of the device, and μ_0 is the permeability of the vacuum. With W = 100 mm and B_{oy} = 1.8 T, the attractive force per meter is about 65 kN. A variable-gap device must have a structure that is rigid enough to not create an intolerable multipole field due to defection. As this is an out-of-vacuum device, many different designs have worked properly in storage rings.

Wigglers of this type, from 2 to 4 meters in length, have been designed and build to specification by industry for many synchrotrons. The mechanical structures to support and control the gap of these wigglers are generally massive and expensive. A detailed design study will consider alternative magnet configurations that could lessen the need for these massive structures. The goal of this project is to design a magnet configuration that can utilize a relatively compact, lower-cost magnet support system that ultimately could reduce the cost of these wigglers significantly.

12.7.3.3 Non-Sinusoidal Field Effect

Another issue for long-period undulators is the deviation from sinusoidal field, which effectively reduces the deflection parameter. (This is not an issue for wigglers, where the critical energy depends on peak field only.) We examine a hybrid undulator with permendur poles with the parameters shown in Table 12.7.6.

Table 12.7.6 U100 Wiggler Parameters.

Period length [mm]	100
Nominal peak field [T]	1.8
Remanent field (B_r) [T]	1.35
Gap [mm]	1 5
Magnet horizontal size [mm]	150
Magnet vertical size [mm]	100
Pole horizontal size [mm]	100
Pole vertical size [mm]	75
Air gap [mm]	0.1
Chamfer (magnet) [mm]	2.0
Chamfer (pole) [mm]	1.5
Corner cut (magnet) [mm]	3.0
Gap offset (magnet) [mm]	0.25

By varying the pole thickness while keeping fixed the total period length, we have calculated the peak magnetic field (induction) and effective K_y, as shown in Table 12.7.7. When the pole thickness is reduced from 19 to 18 mm, the peak field increases from 1.80 to 1.82 T and effective K_y decreases from 15.8 to 15.7. This indicates that the field deviates too much from the sinusoidal form.

Table 12.7.7 Comparison of Peak K_y and Effective K_y with Varying Pole Width.

Pole Thickness (mm)	Peak Field (T)	Peak Ky	Effective Ky
18	1.82	17.0	15.7
19	1.80	16.8	15.8
20	1.77	16.5	15.8
21	1.72	16.1	15.6

There are various ways to obtain a field closer to pure sinusoidal shape than the example above. One relatively simple solution is to add side magnets to boost the field while the pole thickness is increased. Wedge-shaped poles are another way to boost the field, in contrast to simple rectangular pieces. In either case, the cost would increase due to extra complexities.

12.7.3.4 Baseline Damping Wiggler Design

A conventional hybrid structure with permendur poles has been chosen for the NSLS-II device. Soft iron poles are significantly cheaper than permendur but produce inferior results, requiring complicating compensations such as side/back magnets or nonrectangular poles and magnets to achieve the required field (1.8 T) with a given magnet gap (15 mm). Figure 12.7.19 is an isometric rendering of the U19 magnet arrays by Radia. The magnets shown in magenta magnets have identical size; two different sized magnets are shown in green. Pieces in yellow represent permendur poles. Figure 12.7.20 shows the end view of the array.

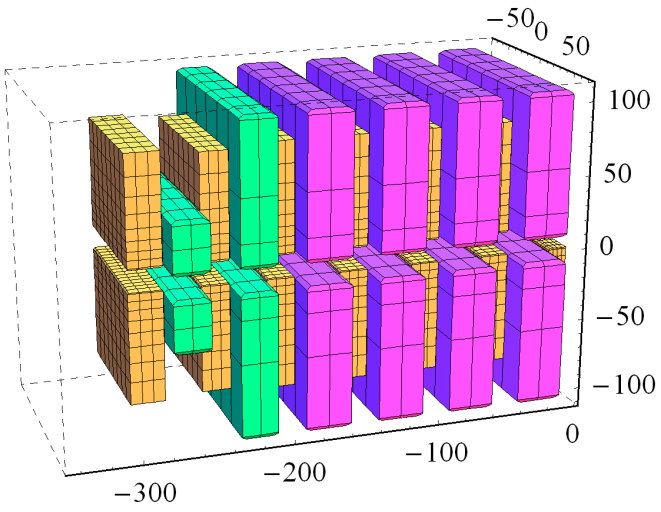

Figure 12.7.19 Magnet arrays of U100. Only the first few periods are shown, for clarity. Units are millimeters.

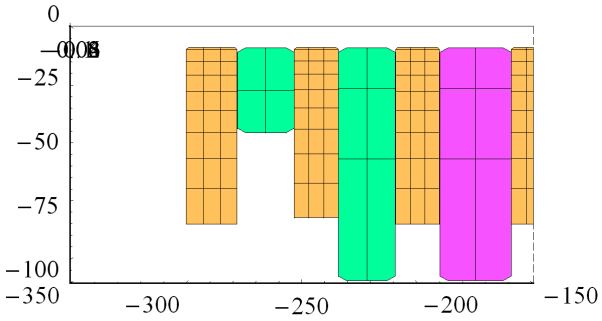

Figure 12.7.20 End view of U100.

The field and trajectory computed from the model are plotted in Figure 12.7.21, for a gap of 15 mm. The trajectory is calculated by a particle-tracking Runge-Kutta routine. The particle is launched with zero offset and angle (x = 0, x' = 0), and its position and angle are calculated every 2.78 mm (36 points per period). Gap dependence of its first integral is shown in Figure 12.7.22. The amount of change in the first integral can be easily compensated by external coils.

a

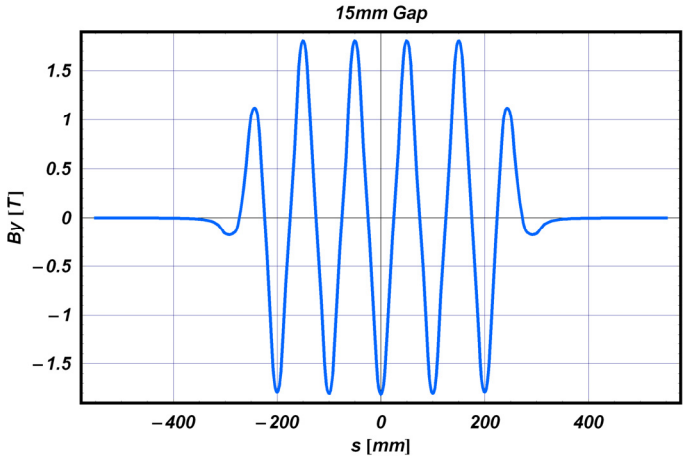

Figure 12.7.21 Field, angle, and trajectory plots for the five-period model of U100.

a) Vertical field.

b

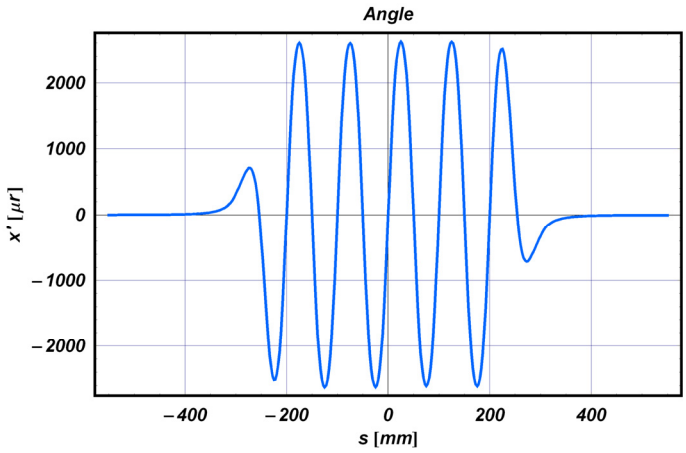

b) Horizontal angle.

c

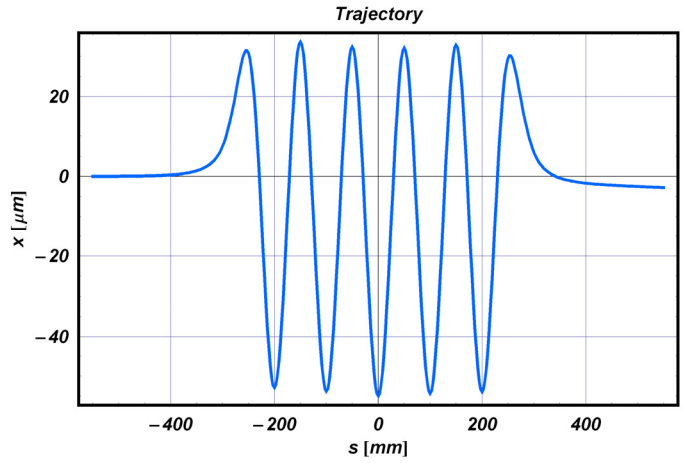

c) Horizontal trajectory at a gap of 10 mm.

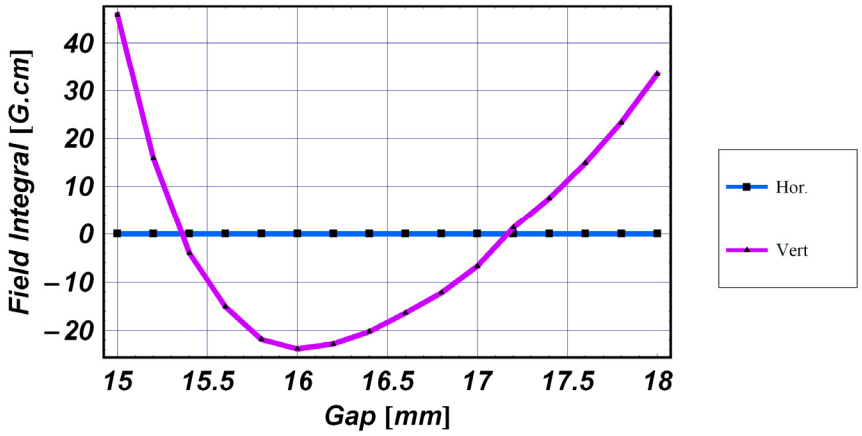

Figure 12.7.22 First field integral dependence on the gap.

12.7.3.5 R&D Elements for DW Development

Superconducting devices, especially HTSC versions, can be considered as an alternative choice for DWs. However, these DWs are an integral part of the light source lattice and any failure would result in the degradation of emittance, which affects all the users in the facility. Therefore, it is essential to achieve extremely high reliability for the HTSC-based DWs to be considered as an alternative for PM-based DWs. Extensive reliability studies will be necessary if this option is pursued.

Another subject is a novel gap separation mechanism, which should simplify the mechanical structure of the device. Attractive force for wiggler magnets is much larger than that by an undulator, so conventional structures tend to be very rigid and heavy in order to avoid deflection. As NSLS-II DWs are presumed to be fixed-gap devices, no strict requirement for gap parallel is required for the open position. One option is the scheme employed at the Source Development Laboratory at BNL, which utilizes inner and outer cages with roller bearings. Other possibilities will be considered.

12.7.4 Insertion Devices for Future Consideration

In this section we briefly discuss three other types of insertion devices that will be explored in our R&D program. If these prove feasible, they would provide a number of benefits and will be considered for future installation at NSLS-II.

12.7.4.1 Quasi-Periodic Undulator

Undulators designed to produce tunable vacuum ultra-violet and soft x-rays are of necessity long-period devices with period lengths of 40 to 100 mm or more. Because the characteristic K-parameter is proportional to the product of peak field and period, long-period undulators have necessarily high K values. Planar and elliptical undulators with high K-values produce spectra rich in harmonics (primarily odd-integer harmonics, since even harmonics are suppressed on-axis). In fact, the first few harmonics produced by high-K IDs have higher brightness and generate more SR power then the fundamental. If the user's monochromator is tuned to the fundamental, unwanted harmonics corresponding to higher orders of the monochromator pass through the exit slit unimpeded, polluting the monochromatic light and imposing an excessive heat load on optical components.

The Quasi-Periodic Undulator [12.7.17] was developed to overcome this problem. As the undulator's field amplitude pattern is altered, integer harmonics can be suppressed and replaced by noninteger harmonics. The latter do not coincide with higher orders of the monochromator and do not pass through the exit slit. The transmitted light is then purely monochromatic, and sensitive optics are protected. The monochromator must still absorb the unwanted harmonic power somewhere, but this can be accomplished by cooled absorbers at the exit slit. As with a conventional undulator, the monochromator can be tuned to any of the noninteger harmonics of the QPU to extend the spectral coverage of the instrument.

To date, several Pure Permanent Magnet QPU structures have been built. The QPU concept has been applied to both planar and APPLE-II type IDs. In circular polarization mode, the APPLE-II generates only fundamental radiation on-axis, so the QPU is of no benefit in that case. But in planar and elliptical modes, the quasi-periodicity helps manage the harmonic power and improves spectral purity, as described above.

12.7.4.2 Superconducting Wiggler

Higher photon energies (above 20 keV) can be effectively covered by a superconducting wiggler at NSLS-II. For a field range of 3.5 T, 60 mm period length, and a 10 mm magnetic gap, low-temperature SCW technology is now well established. However, achieving 6.0 T with the same period and gap will be a challenging task. In contrast, devices based on the use of **h**igh-**t**emperature **s**uper**c**onductors are a very promising approach for medium-field wigglers and would reduce the cost of both construction and operation. However, the current density now available for HTSC wire remains inadequate to produce the necessary field. Thus, the baseline design for the NSLS-II SCU will be the SCW60 device described in Chapter 8, which is based on conventional LTSC technology, but R&D will be carried out to investigate HTSC wiggler designs.

12.7.4.3 Superconducting Undulator

The first superconducting undulator in an electron storage ring was installed at LURE, Orsay in 1979. Since then, various devices for FELs have been developed [12.7.19]. In the past fifteen years, IVUs have been the primary device for short-period undulators. One of the reasons for not using SCUs in the storage ring is the difficulty of opening the necessary gap for injection. A new SCU with a variable gap mechanism has been in operation at ANKA [12.7.20] for the past few years. It has a rather complicated two-vacuum vessel structure, one vacuum for UHV and the other for insulation. The vessels are separated by 300μm stainless steel foil. The required performance was barely achieved due to 1) excessive heat load, which reduced the critical current achievable, and 2) a structural problem that contributed to the degradation of phase errors.

SCUs with conventional NbTi wire face serious problems to reduce the heat load onto the device's cold mass to a level manageable with modern cryocoolers. Unfortunately, state-of-the-art cryocoolers have a cooling capacity of less than a few watts at 4K. What is needed is a different type of LTSC wire that can withstand higher operating temperatures. One approach is to use Nb_3Sn; this is being pursued by the ALS group [12.7.21]. This type of wire is best suited for high-field applications. However, it is difficult to create the precise structure required for undulators, due to the wind and react process. Another approach is to use APC NbTi wire, which is supposed to be operated at much higher current density than conventional NbTi wire. Using this approach, extra space for heat shielding may be available for a fixed-gap vacuum chamber.

Even with these developments, SCUs based on LTSC technology will still have substantial thermal challenges. It may be that SCUs will not be viable until future developments in HTSC technology make it possible to manufacture an HTSC device. There is reason to be optimistic about this, and the NSLS-II project will monitor HTSC industry developments.

Another issue for SCUs is field correction. Extra wiring to correct phase errors has been attempted, but distributed integrated multipole corrections appear to be difficult. They might require correction at the end of the device. These also are issues for future development.

12.7.4.4 Revolver Type

If one type of magnetic array cannot satisfy the user's requirement, two or more different arrays could be used interchangeably, in a "revolver" type undulator system [12.7.18]. Revolver designs have been built at SPring-8 and ESRF and are operating reliably. In-vacuum revolver undulator was also developed by SPring-8 and installed at Pohang Light Source in Korea. This is a subject for future consideration, depending on the user requirements.

References

[12.7.1] T. Tanabe, et al., "Development of an In-Vacuum Minipole Undulator Array for National Synchrotron Light Source In-Vacuum Undulator," *Rev. Sci. Instrum*. 69 (1), pp 18 – 24, (1998).

[12.7.2] H. Kitamura, "Recent development of insertion devices at SPring-8," *Nuc. Instr. & Meth. A* 467-468 (2001) p 110.

[12.7.3] T. Hara, et al., "Cryogenic permanent undulators," *Phys. Rev. ST*, Acc. and Beam, Vol. 7, p.050720 (2004).

[12.7.4] R. Rossmanith, et. al., "A Year's Experience with a Superconducting Undulator in the Storage Ring Anka," Proc. 2006 European Particle Accelerator Conference, Edinburgh, Scotland (2006).

[12.7.5] S. Chouhan, et al, "Research and Development of Variable Polarization Superconducting Undulator at theNSLS," Proc. 2005 Particle Accelerator Conference, Knoxville, USA (2005).

[12.7.6] M. Sagawa, et al., "Magnetic properties of rare-earth-iron-boron permanent materials," *J. Appl. Phys.* 57 (1985) pp 4094.

[12.7.7] T. Tanabe, et al., "X-25 cryo-ready in-vacuum undulator at the NSLS," AIP SRI2006 conference proceedings (to be published).

[12.7.8] O. Chubar, P. Elleaume, and J. Chavanne, *J. Sync. Rad*. 5, pp. 481–484 (1998).

[12.7.9] J. Chavanne, et al., "End field structures for linear/helical insertion devices," Proc. 1999 Particle Accelerator Conference, New York p 2665 (2005).

[12.7.10] D. Harder, et al., "Magnetic measurement system for the NSLS superconducting undulator vertical test facility," Proc. 2005 Particle Accelerator Conference, Knoxville, USA (2005).

[12.7.11] S. Sasaki , et al., "A new undulator generating variably polarized radiation," *Jpn. J. Appl. Phys*. 31 (1992) L1794.

[12.7.12] J. Bahrt, et al., "Preparing the BESSY APPLE-undulators for top-up operation," AIP SRI2006 conference proceedings (to be published).

[12.7.13] A. Hiraya, et al., "Undulator at HiSOR–A compact racetrack-type ring," *J. Sync. Rad.* (1998) 5, pp 445.

[12.7.14] T. Hara, et. al., "SPring-8 twin helical undulator," *J. Sync. Rad*. (1998) 5, pp426.

[12.7.15] P. Elleaume, et. al., "Design considerations for 1 Å SASE undulator," *Nuc. Instr. & Meth A* 455 (2000) p. 503.

[12.7.16] J. Safranek, et. al., "Nonlinear dynamics in a SPEAR wiggler," *Phys. Rev. ST*, Acc. and Beam, Vol. 5, p.010701 (2002).

[12.7.17] S. Sakaki, et al., "Conceptual design of quasiperiodic undulator," *Rev. Sci. Instrum*. 66 (2), p 1953 (1995).

[12.7.18] H. Kitamura, et. al., "Recent developments of insertion devices at SPring-8," NIM-A, 467, (2001), pp 110.

[12.7.19] G. Ingold, et al., "Fabrication of a high-field short-period superconducting undulator," *Nuc. Instr. & Meth. A* 375 (1996) p. 451.

[12.7.20] A. Bernhard, et al., "Planar and Planar Helical Superconductive Undulators for Storage Rings: State of the art," Proc. 2004 European Particle Accelerator Conference, Lucerne (2004).

[12.7.21] S. Prestemon, et al., "Design and evaluation of a short period Nb3Sn superconducting undulator prototype," Proceed. 2003 Particle Accelerator Conference, Portland, U.S.A. p 1032 (2003).

13 CONVENTIONAL FACILITIES

13.1 CONVENTIONAL FACILITIES OVERVIEW

13.1.1 Introduction

The NSLS-II conventional facilities will provide the structures and systems necessary to enable installation and operation of the accelerator and experimental beamlines. The conventional facilities must be designed and constructed to enable the world-leading performance objectives of the project mission. Furthermore, the conventional facilities must be constructed on an aggressive schedule that enables installation of the accelerator systems and experimental beamlines in accordance with the project schedule goals. Lastly, the conventional facilities must meet the functional and aesthetic goals of creating an economically vibrant research facility that achieves technical excellence and is adaptable to the varied and changing requirements of the user community. This chapter describes the scope and design considerations for the NSLS-II conventional facilities.

13.1.2 Project Goals

The goals of the conventional facilities portion of the project support the overall goals of the NSLS-II project. These goals provide the guiding principals for conceptual design of the conventional facilities.

- World-class scientific capability
- Promote collaborative interaction
- Flexible building capability
- Economic construction and operation
- Sustainable design
- Section of the Ring Building available for accelerator installation by July 2010
- Ring Building beneficial occupancy by September 2011

13.1.3 Project Description

The NSLS-II conventional facilities will be designed to support the needs of the technical construction portion of the project. The selected site is the southeast corner of the intersection of Brookhaven Avenue and Groves Street. The existing NSLS building is diagonally across the intersection and the new Center for Functional Nanomaterials (CFN) is across Groves Street to the west.

The conventional facilities will consist of a Ring Building to house the accelerator and associated beamlines, a Central Lab Office Building (CLOB), up to four Lab Office Buildings (LOB), a Linac and RF Building with an associated service building, and four two story service buildings containing mechanical and electrical equipment. Additionally, the overall building complex is being planned to include a Guest House and the Joint Photon Sciences Institute Building. Both buildings are considered future construction and are not included in the Program or Cost of the NSLS-II project.

An architectural rendering of NSLS-II is shown in Figure 13.1.1. Figure 13.1.2 indicates the floor plan of the base scope NSLS-II complex and Figure 13.1.3 shows the complex with added conference center and LOB's 2, 3 & 4. The approximate gross area for each of these buildings is shown in Table 13.1.1. The building program is discussed more fully in Sections 13.4 and 13.5.

Table 13.1.1 NSLS-II Gross Area.

Building Component	Gross Area (ft^2)
Central Lab Office Building	52,748
Conference Center (optional)	15,000
Ring Building	244,663
Service buildings	32,000
Linac & RF Buildings	21,000
Lab Office Buildings (33,000 ft^2 optional)	44,000
Total NSLS-II	**409,411**

Figure 13.1.1 Architectural rendering of NSLS-II.

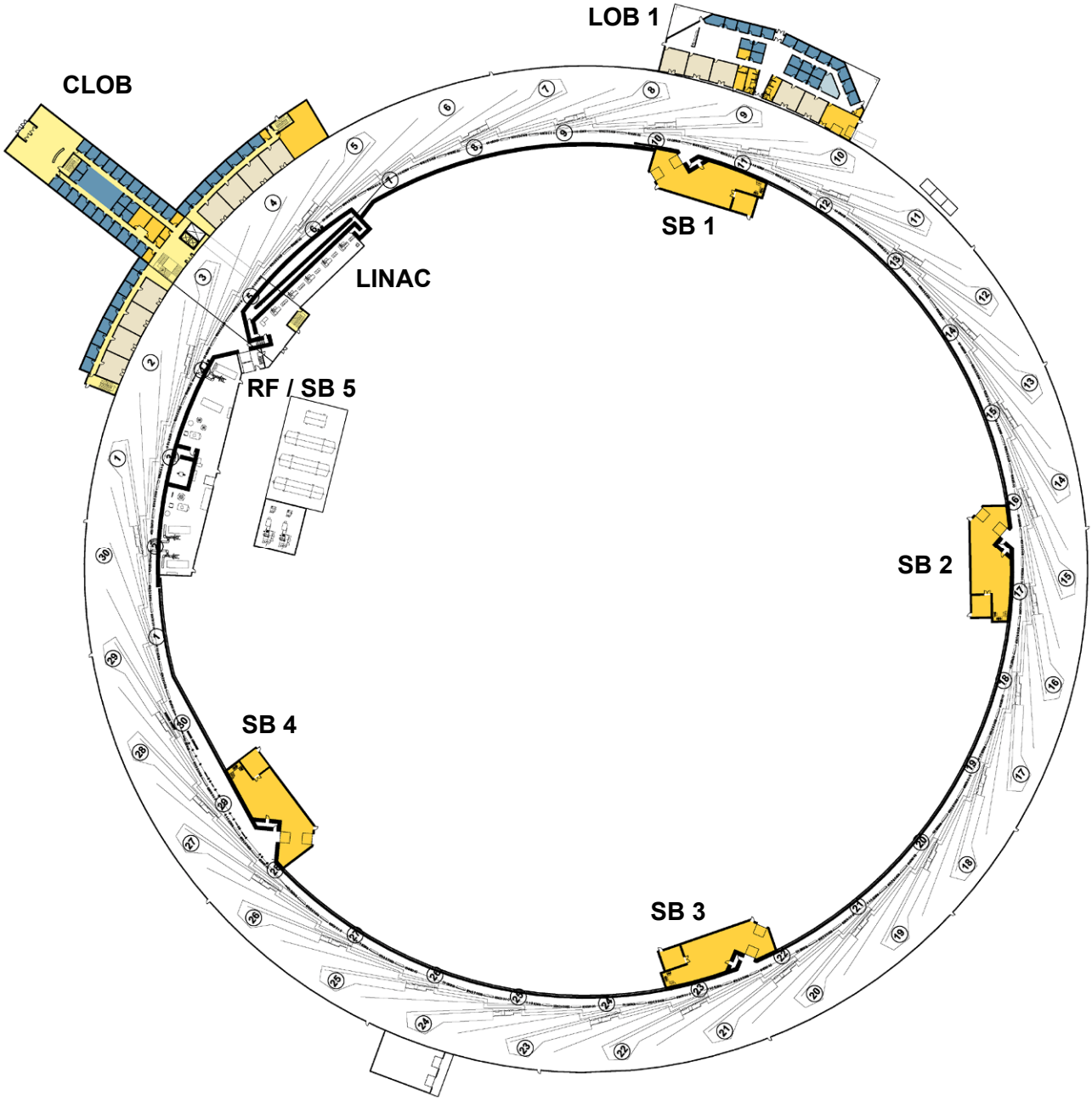

Figure 13.1.2 NSLS-II Complex Layout – First Floor Plan, base scope.

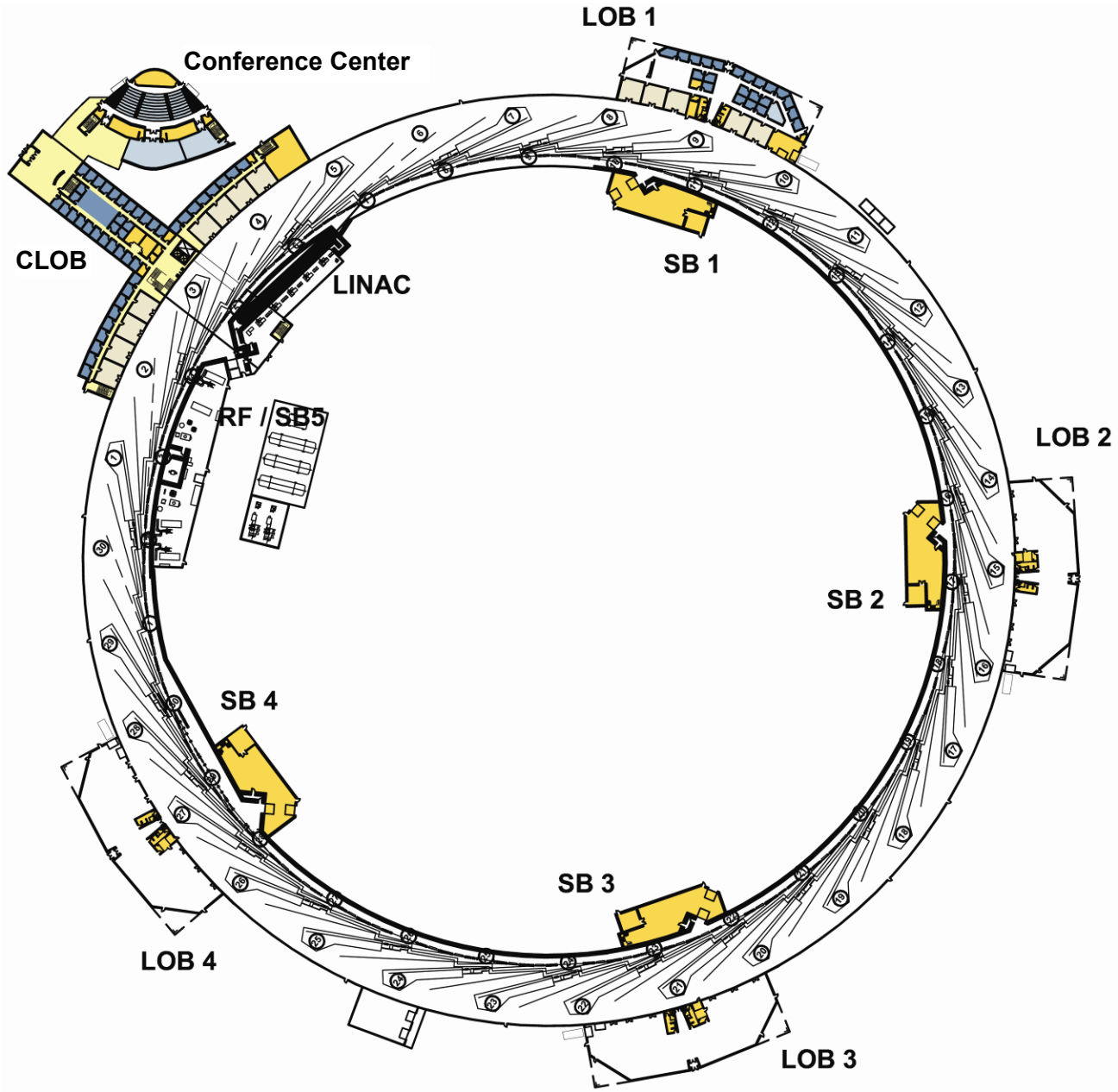

Figure 13.1.3 NSLS-II Complex Layout – First Floor Plan, with optional conference center and “warm shelled” LOBs 2, 3, and 4.

13.2 SITE ANALYSIS

13.2.1 Building Site Alternatives

13.2.1.1 Site Analysis Criteria

Five potential building sites were evaluated for the NSLS-II facility on the BNL campus. A site analysis has been prepared for each potential site. Evaluation criteria include:

- Overall campus planning – does placing the facility on the site promote the BNL master plan and enhance the overall character of the campus.
- Proximity to the Center for Functional Nanomaterials – is the site relatively near to CFN to facilitate collaborative research between the two facilities.
- Proximity to the existing NSLS facility – is the site relatively near the NSLS building to facilitate the transition of science from one to the other, and the potential reuse of the NSLS building for related programs.
- Technical suitability – does the site exhibit favorable ambient characteristics with regard to vibration, noise, traffic, electromagnetic or radiofrequency interference, or other characteristics that might detract from facility performance.
- Expansion capability – does the site promote expansion of lab/office space and allow for the extension of beamlines up to a length of 600 meters.
- Utility availability – are site utilities accessible to the site.
- Impact on existing facilities/infrastructure – does utilizing the site require operational or costly impacts on existing facilities and infrastructure.
- Environmental protection – does the site require negative environmental impacts to construct or operate.

A map of the potential sites is shown in Figure 13.2.1 and the evaluation matrix for each site is tabulated in Table 13.2.1.

Figure 13.2.1 Proposed site locations on the BNL campus with possible long beamlines.

Site 1: Southeast corner of Brookhaven Avenue and Groves Street
Site 2: Southwest corner of East Fifth Avenue and First Street
Site 3: Blue's Pond location, north of East Princeton Avenue
Site 4: South of East Princeton Avenue at Fawn Path
Site 5: East of William Floyd Parkway between Nineteenth Street and Upton Road

Table 13.2.1 Site analysis scoring matrix.

Criteria	Campus Planning		Vibration Characteristics		Proximity to NSLS, CFN, Other		Technical Suitability		Expansion Capability		Utility Availability		Impact on Existing Facilities		Environmental Concerns		EMI / RFI Characteristics		TOTAL WEIGHTED SCORE
Weight	3		3		2		2		3		1		2		2		1		
Score	Raw	Weighted	Raw	Weighted	Raw	Weighted	Raw	Weighted	Raw	Weighted	Raw	Weighted	Raw	Weighted	Raw	Weighted	Raw	Weighted	
Site 1	5	15	4	12	5	10	5	10	5	15	4	4	4	8	4	8	3	3	**85**
Site 2	3	9	3	9	3	6	3	6	5	15	3	3	4	8	4	8	3	3	**67**
Site 3	1	3	3	9	1	2	3	6	4	12	4	4	3	6	1	2	3	3	**47**
Site 4	1	3	4	12	1	2	2	4	5	15	1	1	5	10	2	4	5	5	**56**
Site 5	0	0	4	12	0	0	1	2	5	15	2	2	5	10	1	2	4	4	**47**

Note: Criteria weighting is on a scale of 1 to 3, with 3 being “Very Important” and 1 being “Somewhat Important.” Raw Score is on a scale of 0 to 5, with 5 being “Strongly Meets Criteria” and 0 being “Does Not Meet Criteria.” The Weighted Score is the product of those two values. The Total Weighted Score for each site is the cumulative value of all weighted scores for that location.

13.2.1.2 Alternative Site Analysis

Positive and negative attributes of each site are listed below.

13.2.1.2.1 Site 1 – Southeast of Intersection of Groves St. and Brookhaven Ave.

Positive Factors

- Location highly promotes BNL site master plan and development plan for Brookhaven Avenue.
- Pre-design survey indicates site has favorable vibration characteristics.
- Highly proximate to both the existing NSLS and CFN.
- Site is generally level, which should minimize need for off-site fill material.
- Site is only partially treed, which reduces clearing costs and environmental impacts.
- Undeveloped space on east and south sides of site will allow for installation of beamlines up to 600 m long.
- Utility mains with sufficient capacity for NSLS-II are available near the site.
- No identified environmental issues.
- A NEPA Environmental Assessment has been completed for the site and a Finding of No Significant Impact declared by DOE.
- Pre-design survey indicated favorable background EMI conditions. Requires relocation or remediation of power feeder along Seventh Street south of Brookhaven Avenue.

Negative Factors:

- Site requires completion of BNL shipping/receiving relocation project prior to construction.

13.2.1.2.2 Site 2 – Southwest of Intersection of East Fifth Ave. and First St.

Positive Factors

- There are no existing buildings on the site, so no demolition would be necessary.
- There is room for future beam extensions of up to 600 m.

Negative Factors

- Location is in relative proximity to Brookhaven Avenue, but it does not promote the BNL site master plan.
- The site is far from NSLS and CFN.
- The site is heavily wooded, has rolling grade, and major tree clearing and earthwork would be required.
- More access roads and infrastructure would have to be brought to the site.
- The site is located nearer to the weather station with potential EMI concerns caused by the Doppler radar.

13.2.1.2.3 Site 3 – The Blue's Pond Location, North of East Princeton Ave.

Positive Factors

- The site is close to NSLS and CFN, although not as conveniently situated as Site 1.
- There are no existing buildings on the site, so no demolition would be necessary.
- There is room for future beam extensions of up to 600 m.
- The site is located near Chilled Water Storage.
- The site is slightly farther from the Doppler radar than Site 1.

Negative Factors

- Location is in relative proximity to Brookhaven Avenue, but it does not promote the BNL site master plan.
- The site is wooded with rolling grade, and extensive tree clearing and earthwork would be required.
- Future long beams would have to extend over East Princeton Ave.
- More access roads and infrastructure would have to be brought to the site.
- Environmental impact: Existing Blue's Pond – a natural feature would have to be removed.

13.2.1.2.4 Site 4 – South of East Princeton Ave at Fawn Path

Positive Factors

- There are no existing buildings on the site so no demolition will be necessary.
- There is room for future beam extensions of up to 600 m.
- No identified environmental issues.

Negative Factors

- The site is very remote, at the southern edge of the BNL Campus.
- Proximity to Long Island Expressway could cause increased vibration impacts.
- The site is far from NSLS and CFN.
- The site is moderately wooded and some tree clearing would be required.
- More access roads and infrastructure would have to be brought to the site.

13.2.1.2.5 Site 5 – East of William Floyd Parkway, between Nineteenth St. and Upton Rd.

Positive Factors

- There are no existing buildings on the site so no demolition will be necessary.

Negative Factors

- The site is very remote, far from NSLS and CFN at the western end of Brookhaven Ave., and it does not promote the campus master plan.
- The site is very heavily wooded and major tree clearing would be required.
- There are minimal options for future beam extensions and additional tree clearing would be required.

13.2.2 Selected Site Analysis

Based upon the above analysis, Site 1 has the highest ranking of the 5 sites and is therefore the preferred building site. The location for the proposed NSLS-II site is based upon several criteria and includes the ability to comply with environmental requirements; the ability to meet research mission objectives; the physical proximity to collaborative BNL research facilities in the new Center for Functional Nanomaterials (CFN) and the existing NSLS, constructability factors related to site conditions; economic factors affecting project cost; conformance with BNL strategic planning goals and the ability to support future expansion and long beam lines. The site selected for construction of the NSLS-II meets all of the criteria indicated above and is superior to all alternative locations. The site design will respond to these criteria. The NSLS-II site plan at the selected site is shown in Figure 13.2.2.

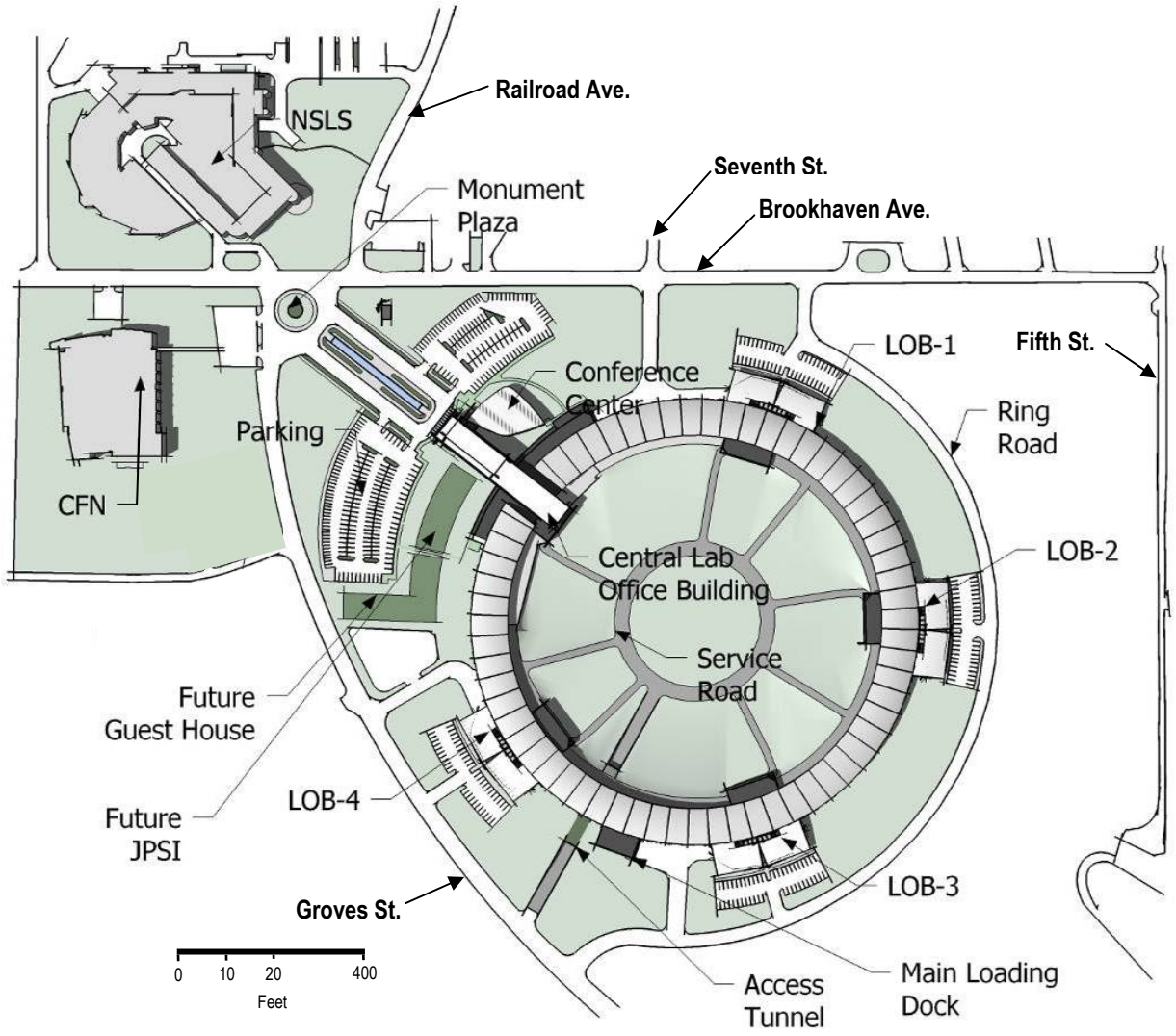

Figure 13.2.2 NSLS-II Site Plan.

13.2.2.1 Campus Planning

The site is a 50 acre parcel located at the intersection of Brookhaven Avenue and Groves Street on the BNL campus. Current master planning envisions Brookhaven Avenue becoming the primary east–west arterial street through the campus. Parcels adjacent to Brookhaven Avenue are considered preferred sites for current and future building projects, including NSLS-II. The architectural vocabulary along this axis will transform in character from a traditional masonry aesthetic in the west to an advanced technology image in the east.

The preferred site is located at a strategic location along Brookhaven Avenue consistent with the campus master plan. Together with CFN, NSLS-II will form a science focal point along Brookhaven Avenue emphasizing the site's commitment to new facilities promoting leading-edge science.

Locating NSLS-II in this parcel will allow for the future addition of extended beamlines of up to 600 m long. These may project eastward along Brookhaven Avenue, to the southeast, or to the south. This site allows for many future options.

13.2.2.2 Adjacencies

The adjacencies that NSLS-II will leverage at the preferred site are highly advantageous. The existing NSLS is diagonally located across Brookhaven Avenue, which will promote ease of interaction between the buildings, particularly during the science transition phase when both accelerators are operating. It will also simplify the relocation of equipment and staff between the two facilities. Additionally, the preferred site is directly across Groves Street from CFN. This adjacency will provide an unparalleled opportunity for collaborative research between two of the nation's premier science facilities.

13.2.2.3 Access, Traffic, Parking

The preferred site is bounded by Brookhaven Avenue on the north, Groves Street on the west and Fifth Street on the east. This configuration will provide easy access to all parts of the facility. The main entrance of the Central Lab Office Building will face the intersection of Brookhaven and Groves. Traffic into the primary facility parking lot will be from either of these roads, and a drop-off loop will be provided to the main entrance of the facility.

A Loop Road will be constructed around the outer perimeter of the building site. It will have access points from Brookhaven Avenue and Groves Street. The Loop Road will serve each of the Lab Office Buildings and also serve as the main service road around the site.

Each of the Lab Office Buildings will have an entrance serving the occupants of that building. Parking will be provided within convenient walking distance. Bicycle racks will also be provided near each building entrance.

Service vehicles will access the center of the Ring Building via a tunnel under the Ring Building. The tunnel will allow emergency vehicles as well as delivery of large equipment to enter the center of the ring. It will comply with NYDOT requirements and be 20 ft wide by 14 ft deep in height. The ramps in and out will have a slope not steeper than 12:1.

Pedestrian traffic will be accommodated by sidewalks between NSLS-II, CFN, and the existing NSLS buildings. Covered walkways or enclosed passages are envisioned between the Central Lab Office Building and both the Joint Photon Sciences Institute and the Guest House.

13.2.2.4 Vibration Survey

A pre-design vibration survey of the preferred building site was conducted by Colin Gordon Associates on June 14, 2006, with supplemental data collected on August 31 and September 1 [13.1]. The purpose of the survey was to evaluate the ability of the proposed NSLS-II building to meet the stated vibration criteria on the preferred building site. The site demonstrated no particular vibration characteristics that would adversely affect the performance of the NSLS-II scientific equipment. The results indicate that the preferred site is a "quiet" site vibrationally. A minimum 100 ft setback will be used between the building and both Brookhaven Avenue and Groves Street to minimize the vibration impact of passing traffic. Specific vibration criteria for the NSLS-II building are described in Section 13.3 Functional Requirements of this document.

13.2.2.4.1 Experimental Hall

Data were collected in mid-afternoon at six locations on the NSLS-II site and processed to obtain one-third octave band velocity spectra. The results indicate that the preferred site will easily meet vibration criteria VC-E but does not meet NIST-A criteria below a frequency of 5 Hz. It is believed that the low-frequency component which exceeds NIST-A is due to traffic, probably on the Long Island Expressway.

It is anticipated that the heavy floor slab of NSLS-II will reduce the amplitude at most frequencies, yielding a more favorable comparison to the criteria. Additional data was therefore taken on the floor slab of

the nearby, partially constructed Center for Functional Nanomaterials in the late evening hours. The analysis indicates that the slab of CFN will meet NIST-A criteria during the nighttime hours. These data are thought to be representative of the eventual nighttime performance of the Experimental Hall in NSLS-II.

13.2.2.4.2 Accelerator Tunnel

To evaluate the Accelerator Tunnel, the survey data were transformed to displacement Power Spectral Density (PSD) spectra. This is the desired format for the storage ring vibration criteria. When calculated over the range of 4 to 50 Hz, the calculated R values do not meet the stated criteria of R less than 25 nm. However, it was noted that the data below 6 or 7 Hz was contaminated by system noise due to an instrument cable. If the criteria are modified slightly to calculate R from 6 to 50 Hz or from 8 to 50 Hz, and thereby eliminate the questionable data, the R values do generally meet the stated criteria of less than 25 nm.

Supplemental data collected in the CFN microscopy lab again validates the hypothesis that the heavy building slab will make a significant difference in the vibration data. Measurements taken at 7:30 pm and at 11:40 pm both yielded results that met the RMS amplitude criteria for NSLS-II of 25 nm. Again, it is anticipated that the improvement in vibration results due to the floor slab at CFN will translate to improvements in the NSLS-II data.

Overall, the vibration study indicates that following the installation of the floor slab for the Accelerator Tunnel and the Experimental Hall, which will significantly stiffen the site, the vibration environment will be comparable to that of other world-leading light source facilities.

13.2.2.5 EMI/RFI Survey

Pre-design electromagnetic interference surveys were conducted on June 14th and September 19th, 2006 by VitaTech Engineering, LLC [13.2]. Several types of measurements were taken to characterize the site:

- AC Extremely Low Frequency Electromagnetic Interference (ELF EMI)
- DC Electromagnetic Interference
- Radiofrequency Interference (RFI)

The site demonstrated no ambient electromagnetic or radio frequency interference that would adversely affect the performance of the NSLS-II scientific equipment. The nearby NWS Doppler radar facility does not appear to have a problematic effect with respect to RFI.

The site is generally undeveloped and therefore should be relatively free of large electromagnetic fields above the ambient background. Buried electrical power feeders running east-west along Brookhaven Avenue and north-south along Seventh Street are sources of EMI that need to be considered. The 100 ft building setback from Brookhaven Avenue will allow fields to largely decay without impacting the building performance. The feeder along Seventh Street will need to be relocated away from the building footprint.

13.2.2.5.1 AC ELF Electromagnetic Interference

AC ELF EMI fields are substantial along Brookhaven Avenue, due to the existing underground electrical feeders, ranging up to 3.36 mG. These flux densities drop off rapidly south of Brookhaven to approximately 0.1 mG at the 100 ft setback line and drop further to essentially zero beyond that point. Likewise, flux density peaks at approximately 0.4 mG above the buried electrical power lines at Seventh Street but drop off very rapidly to the east. As a point of reference, flux densities of up to 0.3 mG are acceptable for high-accuracy instruments such as TEMs, SEMs, and E-beam writers, which will be used in CFN.

13.2.2.5.2 DC Electromagnetic Interference

DC Electromagnetic Interference is caused by ferromagnetic masses in motion, typically objects such as elevators, trains, cars, buses, etc. There is a potential for DC EMI due to traffic along Brookhaven Avenue to the north of the site and along Fifth Avenue to the east. Analysis by VitaTech [13.2] indicates that between 40 ft and 130 ft south of Brookhaven, the DC fields will be such that instrumentation with dB/dt differential DC EMI resultant RMS thresholds between 1 mG and 0.1 mG will meet specification. Between 130 ft and 200 ft, instruments with a threshold of 0.1 mG to 0.01 mG will meet specification (197 ft is the predicted 0.01 mG isoline). Similar separation distances will apply to north–south traffic along Fifth Street.

13.2.2.5.3 Radiofrequency Interference

The RFI site measurements indicated very low electric field strength across a range of frequencies from 100 kHz to 18 GHz. The NEXRAD Doppler weather radar that is located only 2200 ft away operates at a frequency of 2877 MHz. The existing NSLS has experienced RFI impacts from the NEXRAD radar and has installed RF shielding around select laboratory and research areas to reduce the problem. A similar remediation approach will be used at NSLS-II if needed; shielding will be provided at the hutches based on scientific requirements rather than general shielding of the building.

Electric field strength RF levels were recorded on September 19, 2006 by VitaTech Engineering [13.2] at a point approximately in the center of the proposed NSLS-II site. Data over a broad spectrum of frequencies indicated elevated RF levels at a number of frequencies from various sources including the NEXRAD radar. In all cases, the electric field strength RF levels were below 1V/m, which is the typical threshold for scientific instrumentation.

13.2.2.6 Geotechnical Survey

A geotechnical survey of the preferred site was conducted in July of 2006 [13.3]. The explorations included 12 cone penetrometer test (CPT) soundings and four test borings. The results indicate that 2 to 12 in. of topsoil overlays medium dense and very dense sand, with pockets of fill in some locations near buildings and roadways. The sand deposit will work well for spread footings, and the existing fill material is generally suitable for use around the site and under the floor if compacted properly. Differential settlement is estimated to be less than 0.75 in. with footings designed for 2.5 tons psf and at least 3 ft wide.

Soils at the site are classified as Site Class D, “Stiff Soil Profile,” in accordance with the New York State Building Code. Specific data relating to the subsurface conditions are described in Section 13.3, Functional Requirements.

13.2.2.7 Topographical Survey

A topographical survey was conducted in June of 2006. The survey indicates that the preferred site is relatively flat and well suited for the NSLS-II building. Site elevation does vary from 10 ft above the Experimental Floor elevation to 6 ft below the finished floor; however, most of the site is near the proposed floor elevation. The level grade will minimize the requirement for cut and fill operations and will work to the benefit of potential future long beam lines extending up to 600 m onto the adjacent grounds.

13.2.2.8 Existing Site Utilities

Site utilities consist of electric, chilled water, steam, potable water, sanitary and storm sewer, and dry compressed air. Electrical power is wheeled to the site at 69 kV by the local electrical utility company (LIPA). This tie line has sufficient capacity for the NSLS-II loads. The other utilities are generated at BNL’s central utility plants and distributed underground for use throughout the site. The distribution systems for these utilities are of sufficient capacity to serve the NSLS-II complex; however, additional generating

capacity is required for chilled water and cooling tower water. Additional chiller capacity and cooling tower capacity will be added at the existing central utility plant. A separate cooling tower system for process water cooling will be located near NSLS-II.

The most significant impact NSLS-II will have on the current BNL utility infrastructure is the central chilled water system, which is currently at maximum capacity and does not have spare capacity to meet the additional load of NSLS-II. As part of the NSLS-II project, additional chilled water capacity will be added to the existing central chilled water plant. Expanding the central chilled water plant in lieu of constructing dedicated local capacity provides advantages in reliability and reduced cost to the project [13.4].

Existing sanitary sewers are located parallel to and south of Brookhaven Avenue (6 in. VTP) and parallel to and west of Seventh Street (10 in. VTP). The system along Brookhaven Avenue can remain as is and the northerly and easterly Lab Office Buildings can be connected to this sewer line. The system along Seventh Street, which extends further south parallel to and east of Groves Street, must be relocated, as it conflicts with the proposed NSLS-II construction.

Preferred access and routing of utilities is along Brookhaven Avenue. Utilities along Brookhaven have adequate capacity and connection here enables routing of these utilities through a common utility vault or basement beneath the Ring Building floor and into the interior of the ring. This approach provides good access for maintenance while minimizing the effects of noise and vibration, compared to running utilities through the building.

13.2.2.9 Existing Facilities

BNL has an on-going program to remove excess facilities and consolidate operations from WW-II vintage wood structures into more permanent buildings. Consistent with this program, there is a project underway to relocate BNL warehousing, shipping, and receiving operations from the WW-II era buildings at the western edge of the proposed NSLS-II site. BNL will remove buildings and structures associated with these operations prior to construction of NSLS-II.

13.3 FUNCTIONAL REQUIREMENTS

13.3.1 Codes and Standards

The latest edition of the codes, standards, orders, and guides referred to in this section will be followed. All work will be in accordance with BNL's Implementation Plan for DOE 413.3, "Program and Project Management for the Acquisition of Capital Assets."

13.3.1.1 DOE Orders

DOE O5480.4 – Environmental Protection, Safety and Health Protection Standards
DOE O413.3A – Program and Project Management for the Acquisition of Capital Assets
DOE O414.1C – Quality Assurance
DOE O420.1B – Facility Safety
DOE O420.2B – Safety of Accelerator Facilities

13.3.1.2 Codes, Standards, and Guides

Building Code of New York State (NYSBC) – 2002 Edition
Building Code Requirements for Structural Concrete (ACI 318-99)
Specification for Structural Steel Buildings – Allowable Stress Design and Plastic Design, 1989 Edition
BNL Standards Based Management System Subject Areas
New York State and Suffolk County Department of Health Codes
American Concrete Institute
American National Standards Institute
ANSI 117.1 Accessible and Useable Buildings and Facilities
American Society of Mechanical Engineers
American Society for Testing Materials Standards
American Society of Heating, Refrigeration, and Air Conditioning Engineers (ASHRAE) Design Guidelines
ASHRAE Standard 90.1-2001 Energy Standards for Buildings Except Low-Rise Residential Buildings
American Water Works Association
American Welding Society
ANSI/ASHRAE Standard 62-2001 Ventilation for Acceptable Indoor Air Quality
ANSI/AIHA Z9.5-1992 Standards for Laboratory Ventilation
ANSI/ASHRAE 110-1985 Method of Testing Performance of Laboratory Fume Hoods
Factory Mutual
ICEA Insulated Cable Engineering Association
Industrial Control Standards (NEMA)
IEEE Institute for Electrical and Electronic Engineers
IEEE C2-1997 National Electric Safety Code (NESC)
IES Illuminating Engineers Society
Mechanical Code of New York State
National Institute of Standards and Technology
National Electrical Code (NFPA 70 2005)
Standard for Electrical Safety in the Workplace (NFPA 70E)
National Fire Protection Association (NFPA) Standards
Sheet Metal and Air Conditioning Contractors' National Association (SMACNA) Standards for Ductwork Design
Occupational Safety and Health Administration (OSHA)

Underwriters Laboratory
New York State Plumbing Code - 2002 Edition
New York State Fire Prevention Code - 2002 Edition
Energy Conservation Code of New York State - 2002 Edition
Americans with Disabilities Act Accessibility Guideline (ADAAG)
Leadership in Energy and Environmental Design (LEED) 2.2
LEED for Labs

13.3.2 Code Analysis

A Preliminary Life Safety Code Analysis has been prepared and is available as a Technical Reference [13.5].

13.3.3 Site/Civil

13.3.3.1 Existing Conditions

A current topographical survey was conducted in June 2006. The survey drawing identifies 1 ft contours and major surface features. It will be the basis for the site/civil design.

The proposed construction site is relatively level with mostly open field previously used as recreational fields. As indicated on Figure 13.3.1, there are warehouse buildings on the western edge of the site that are in the process of being removed under a separate BNL project (see section 13.2.2.9). There are some trees in the developed footprint that will require removal. Additionally, there is a railroad spur running parallel to Groves Street that enters the site from the south that will be cut back to a point outside the developed footprint of the facility. This rail spur will be available for use during construction for delivery of bulk materials if needed. The tree removal and cut back of the railroad spur are part of the NSLS-II site preparation work.

Site storm drainage is available along the western edge of the site however, consistent with sustainable design principles, on-site recharge will be maximized with only overflow conditions going to the existing storm drainage system.

13.3.3.2 Site Utilities

The following site utilities are available at or near the site and will used for the NSLS-II facility:

- Potable water
- Sanitary sewer
- Storm drain
- Chilled water
- Steam and condensate
- Compressed air
- Electrical power
- Telephone/data
- Fire alarm

13.3.3.2.1 Potable Water

Existing potable water lines are located around the perimeter of the site as follows:

- Along the north side of Brookhaven Avenue (12 in. and 10 in. TRANS [“Trans.”])
- Parallel to and west of Seventh Street (8 in. Trans.) and extending south beyond the NSLS-II site

- Parallel to and east of Groves Street (8 in. Trans.)

The 8 in. line west of Seventh Street will need to be relocated around the footprint of the building. Connection of fire protection water and domestic water for the NSLS-II loop system will be from the relocated 8 in. line west of Seventh Street and the 12 in. line at Brookhaven Avenue and North Sixth Street.

13.3.3.2.2 Sanitary

Existing sanitary sewer lines are adjacent to the site on two sides. A six in. VTP line parallels Brookhaven Avenue on the north of the site and a 10 in. VTP west of Seventh Street meets with the 6 in. line at MH-163. The sanitary line then crosses Brookhaven to a 20 in. VTP line. The NSLS-II will connect to the 6 in. line from the CLOB and one LOB. The remaining services will be routed to a new underground pumping station and pumped into the 10 in. VTP line.

13.3.3.2.3 Storm Water

Storm water drainage will be provided for on site. Retention ponds will be utilized to the maximum extent practicable as encouraged by the LEED standard. Any excess storm water will utilize existing drainage structures.

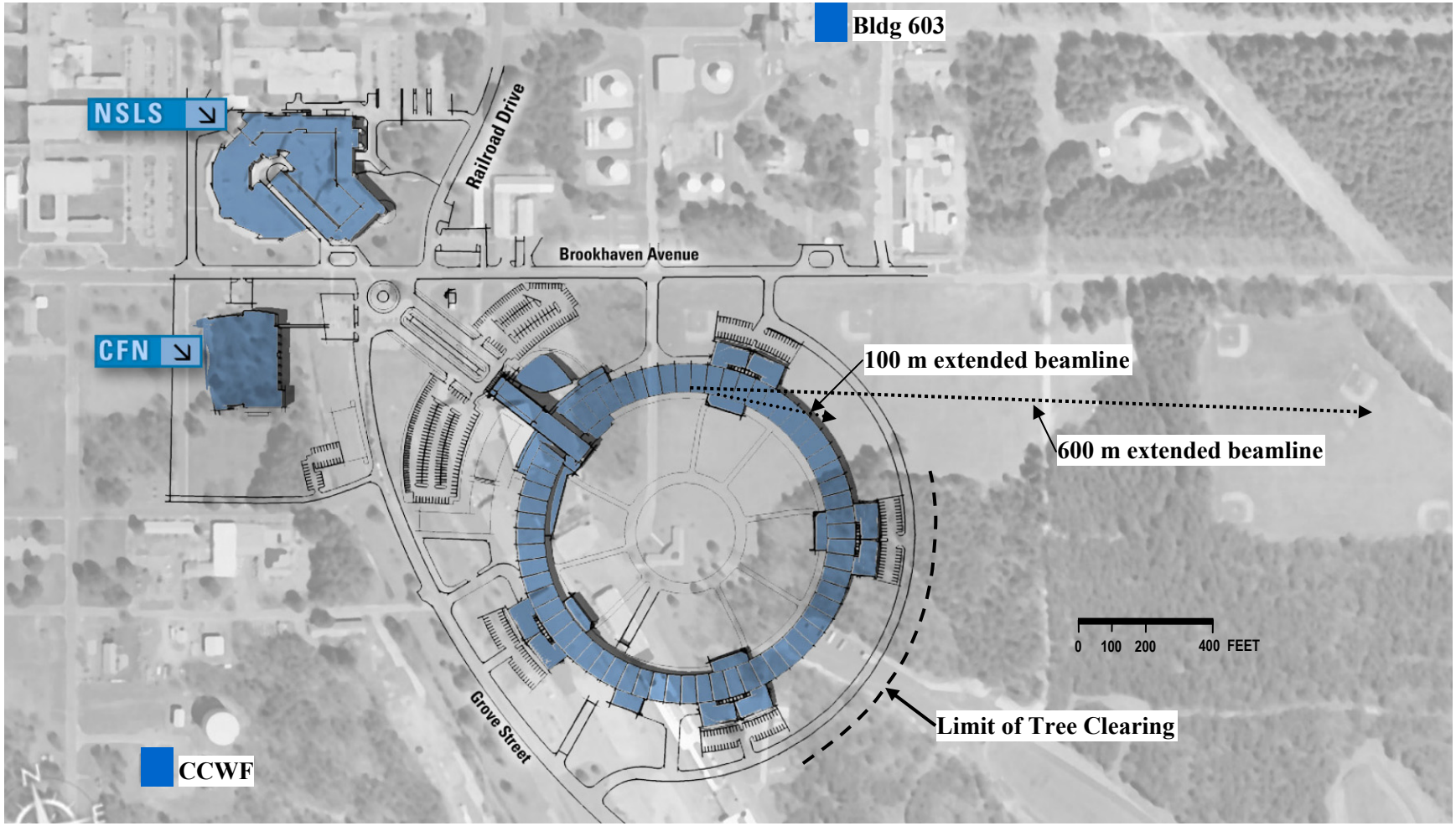

Figure 13.3.1 Proposed construction site for NSLS-II, showing existing conditions, including the limit of tree clearing required, and the locations of the BNL Central Chilled Water Facility (CCWF) and the Bldg 603 Electrical Substation that will supply chilled water and electrical power, respectively, to NSLS-II. Examples of possible extra long beamlines, extending outside the Ring Building, with lengths of 100 m and 600 m are also shown.

13.3.3.2.4 Chilled Water

Chilled water is a sitewide distributed utility. The NSLS-II project will tie into existing site chilled water at Rochester Street. A 24 in. chilled water supply and return header will be routed underground to the Ring Building and pass under the ring through the traffic access tunnel.

13.3.3.2.5 Steam & Condensate

A 10 in. steam line and a 4 in. condensate line are located just north of Brookhaven Avenue. The NSLS-II system will connect to these lines at MH-47.

13.3.3.2.6 Compressed Air

Compressed air is a sitewide distributed utility. The NSLS-II project will tie into existing site compressed air at Brookhaven Avenue. A 3 in. compressed air line will be routed underground to the Ring Building and pass under the ring through the traffic access tunnel.

13.3.3.2.7 Electrical Power

For a description of electrical site utilities, see Section 13.3.8, Electrical Engineering.

13.3.3.2.8 Telephone / Data

For a description of telephone and data utilities, see Section 13.3.8.14.2, Telephone and Data Communications.

13.3.3.2.9 Fire Alarm

For a description of fire alarms, see Section 13.3.8.14.1, Fire Alarm System.

13.3.4 Architecture

13.3.4.1 Building Envelope

The building envelope will be designed to meet at a minimum the prescriptive requirements of the Energy Conservation Code of New York (ECCNY). Brookhaven National Laboratory is located in Climate Zone 11B of the ECCNY. The thermal design parameters for envelope elements are dependent on the ratio of fenestration to overall wall area. The Ring Building has a window-wall ratio of less than 10 % and the LOBs and the CLOB have window-wall ratios greater than 10%. This ratio affects the prescriptive requirements of the ECCNY, as shown in Tables 13.3.1 and 13.3.2. Window to wall ratios of 0 to 10% are considered low fenestration area buildings and ratios or 25 to 40% are high fenestration area buildings.

Table 13.3.1 R-Values for High Fenestration Area Buildings – ECCNY

Building Component	Prescriptive R-Value
Exterior wall	R-11
Exterior wall below grade	R-11
Glazing	R-2 (U=0.5)
Roof (continuous insulation)	R-24
Slab on grade edge	R-8

Table 13.3.2 R-Values for Low Fenestration Area Buildings – ECCNY

Building Component	Prescriptive R-Value
Exterior wall	R-11
Exterior wall below grade	R-11
Glazing	No requirement
Roof (continuous insulation)	R-19
Slab on grade edge	No requirement

More stringent criteria will be used in most locations as required to meet the temperature stability performance of the building and to help achieve sustainability (LEED) goals. Targeted design R-values for wall and roofing systems are significantly higher than the prescriptive values shown above:

- Target R-value for Exterior wall system R-20
- Target R-value for Roofing system R-30

13.3.4.2 Building Occupancy

NSLS-II will be in operation 24 hours a day, 7 days a week; however, occupied hours for most staff are 8:00 AM to 5:00 PM. The overall building will be classified, per the Building Code of New York State, as a Business ("B") Occupancy. The anticipated populations of the various areas are shown in Table 13.3.3:

Table 13.3.3 Building Office Capacity

Building	Population
Central Lab Office Building	190
Ring Tunnel	0
Lab Office Building 1	30
Lab Office Building 2	30
Lab Office Building 3	30
Lab Office Building 4	30
Linac Building	0
RF Building	0

13.3.4.3 Parking

Parking will be provided for the Central Lab Office Building and for each of the four Lab Office Buildings. Each LOB will have one parking space for each occupant and 10 additional spaces for visitors. The CLOB will provide one parking space for each employee plus 80 visitor spaces to accommodate day-to-day visitors and seminar participants. Parking for the future JPSI and Guest House is allocated for future paving. A drop-off loop will be provided to the entrance of the CLOB. Each parking lot will be barrier free and provide the required number of ADA-compliant parking spaces to meet current LEED requirements. Requirements for parking spaces are as shown in Table 13.3.4.

Table 13.3.4 Parking Requirements.

Building	Parking Spaces
Central Lab Office Building	280
Future JPSI*	*120*
Future Guest House*	*52*
Lab Office Building 1	40
Lab Office Building 2	40
Lab Office Building 3	40
Lab Office Building 4	40
Total	612
*Not part of NSLS-II Project	

13.3.4.4 Vibration Criteria

The vibration limits of the Experimental Hall are those criteria associated with the user-supplied research instruments, which are not well defined at this time. Therefore, the vibration requirements of this space will be established to meet general vibration criteria for similar physical science research centers. The vibration requirements of the vast majority of research equipment available today would be satisfied by a floor meeting vibration criterion VC-E or the more stringent NIST-A. The NIST-A criterion is more stringent than VC-E at frequencies less than 20 Hz. A minimum target of VC-E will be established for the Experimental Hall.

The vibration requirements for the accelerator tunnel have been provided in a much different manner. The storage ring is most sensitive to frequencies in the range of 4 to 50 Hz. The criterion for the storage ring vibration is defined in terms of R, the area beneath the power spectral density (PSD) spectrum $\Delta(f)$, between cutoff frequencies f_1 and f_2. The RMS amplitude, R, is to be less than 25 nm. R is defined as

$$R = \sqrt{\sum_{f_1=4}^{f_2=50} \Delta(f) \times \delta f}$$

where $\Delta(f)$ is the displacement power spectral density spectrum (in units such as m^2/Hz, where the frequency term in the denominator is the measurement bandwidth) and δf is the frequency resolution of the spectrum, 0.25 Hz. The lower and upper bounds of the summation are 4 and 50 Hz, respectively. Frequency components outside this range may be neglected.

13.3.4.5 Noise Criteria

The facility will have two primary groups of noise sources: 1) the facility's mechanical systems, such as air handlers, and 2) the user-provided research equipment. The noise control associated with the first group is within the purview of the NSLS-II design team, but the ability to mitigate noise associated with the second group is somewhat limited. It can be anticipated via passive room noise control measures incorporated into the design, but it cannot be controlled via mechanical constraints such as airflow velocities, fan selection, or silencers, concepts typically employed for the first group.

Studies carried out during the design of the Advanced Photon Source determined that final operational room noise in the Experimental Hall would be a mix of sound from both groups of sources, and that NC-60 to NC-65 would be achievable from a combination of mechanical system noise control measures on the proposed air handling system and room absorption incorporated into walls and ceiling. This is the noise range found in many industrial cleanrooms. In the absence of absorptive material, the noise at APS was predicted to be on the order of NC-70. NSLS-II will utilize absorptive material and appropriate mechanical system design to achieve NC 60-65.Noise Criteria (NC) level guidelines for other spaces in the facility will be as shown in Table 13.3.5.

Table 13.3.5 Acoustic Noise Criteria.

Space Type	Noise Criteria (NC) Level
Office	35–40
Laboratory	45–50
Conference rooms	30
Interaction space	40
Common use areas	40–45
Accelerator tunnel	None
Experimental Hall	60–65
Mechanical / electrical rooms	Per OSHA
Seminar room	30

13.3.4.6 EMI / RFI Criteria

No universal EMI/RFI design criteria has been established for the NSLS-II facility, although individual beamlines or experiments may have specific requirements. Shielding, if required will be the responsibility of the researcher at the individual beamline or laboratory.

13.3.5 Functional Program

Adjacencies of the various functional areas within the NSLS-II complex have been established through detailed discussions with the user groups. These groups include the Accelerator Team, the Experimental Team, Facilities Engineering, Environmental Safety & Health, Maintenance, and Management.

The Ring Building and LOBs will be divided into four Control Areas to safely accommodate a range of chemicals and hazardous gases that may be used within NSLS-II. These CAs are as follows:

- CA 1 –Ring Building and the Linac/RF Building
- CA 2 –Lab Office Building 1
- CA 3 –Lab Office Building 2
- CA 4 –Lab Office Buildings 3 and 4

The Central Lab Office Building will be considered a second fire area zone. It will be separated from the Ring Building by fire wall construction meeting the New York State Building Code Section 707. This allows the CLOB to have an additional four control areas on its first floor separate from those in the Ring Building and LOBs.

The control areas will be separated from each other with a fire-rated barrier wall. There will also be storage rooms located near LOB 1 that are classified as H Occupancies for Hazardous Chemical and Gases that exceed the quantities allowed by the Building Code of New York State under “B” occupancy. The amount of gas and chemicals allowed per control area is provided in Tables 13.3.6 and 13.3.7.

Table 13.3.6 Allowed Quantities of Hazardous Gas.

Gas Type	Allowed Storage	Allowed Usage
Flammable	2,000 ft^3	2,000 ft^3
Pyrophoric	100 ft^3	20 ft^3
Highly toxic	40 ft^3 (in approved cabinets)	40 ft^3
Toxic	1,620 ft^3	1,620 ft^3
Oxidizing	3,000 ft^3	3,000 ft^3

Note: Quantities include all allowed increases for building automatic sprinkler system.

Table 13.3.7 Allowed Quantities of Hazardous Chemicals.

Gas Type	Allowed Storage	Allowed Usage
Flammable Class 1-B	240 gal	120 gal
Flammable Class 1-C	360 gal	180 gal
Combined Flammables	480 gal	240 gal
Water Reactive Class 1	No Limit	No Limit
Water Reactive Class 2	20 gal	10 gal
Oxidizer Class 1	800 gal	400 gal
Oxidizer Class 2	20 gal	50 gal
Oxidizer Class 3	4 gal	0.5 gal

Note: Quantities include all allowed increases for building automatic sprinkler system.

Relationships between the areas will meet the requirements outlined in the following sections.

13.3.5.1 Ring Tunnel

- Requires access from the Ring Building infield for tunnel equipment installation.
- Shielding is required on the inboard, outboard, and top of the ring tunnel. This can be achieved with high-density concrete, normal weight concrete, or soil. This can also be achieved with a combination of materials.
- Access from tunnel to active beamlines is not a requirement but may be desirable in some applications.
- Storage ring and booster ring power supplies will be located on the tunnel mezzanine directly above the ring tunnel.
- Easy access from the CLOB control room to the ring tunnel is desirable.
- Access from the Experimental Floor to the ring mezzanine will be from stairs or ships ladders running parallel to the interior ring tunnel ratchet wall at locations where there is no active beam line.
- Walls of the ring tunnel must provide radiation shielding from the rest of the facility.

13.3.5.2 Experimental Hall and Access Corridor

- The Experimental Hall will have 30 sectors (a sector includes a straight section and the adjacent bending magnet) and must accommodate 25 to 30 60 m insertion device beamlines and hutches and another 25 to 30 bending magnet beamlines..
- The Experimental Hall must be able to accommodate future beamlines that will extend outside the building.
- Floor height with respect to the tunnel must allow beamlines to be 1.4 meters above the finished floor in the Experimental Hall. The floor must be constructed to limit differential settlement, as the beamlines must be maintained at 1.4 meters along their entire length.
- The Experimental Hall must have line-of-sight portals into the tunnel for beamline set-up.
- A perimeter access corridor for equipment and personnel access to the beamlines is required. A continuous trench drain between the access corridor and the Experimental Floor is provided for water removal, in lieu of floor drains in the Experimental Floor.
- Beamlines must have easy access to nearby LOBs and CLOB.
- The access corridor should provide space for informal interaction between researchers.

13.3.5.3 Central Lab Office Building

- The CLOB needs a seminar room for approximately 400 people and adjacent breakout rooms.
- It should provide visitors viewing gallery overlooking the Experimental Floor.

- The control room, operators' offices, small conference room, and computer room should be grouped together on the second floor with easy access to the RF/LINAC and Ring Tunnel areas.
- Provision for future enclosed access should be provided to both the Joint Photon Sciences Institute building and the Guest House.
- HVAC for the CLOB will be by penthouse air handling units.
- The CLOB should have an entry lobby for displays and a reception area for new users and guests.

13.3.5.4 Lab Office Buildings

- Laboratory space and offices should be near to their respective beamlines.
- Each LOB needs an entrance and parking lot to accommodate 40 cars.
- Individual laboratories in the LOBs should have access to the Experimental Hall through double doors.
- Informal interaction space should be provided in each LOB, as well as a conference room.
- Laboratory space within a LOB will be shared by all six sectors using the LOB.
- Laboratories will require chemicals and gases to be delivered to them. Provision for delivery and storage of these materials is required. A high hazard storage area is provided in LOB-1.
- LOBs must be configured to allow for future expansion requiring additional labs and offices.
- Each LOB will have an at-grade loading area.
- Each LOB will have a gas bottle storage area.
- HVAC for the LOBs will be air handling units in each LOB mechanical room.
- Each LOB will have at least one HEPA-filtered laboratory fume hood for working with nanomaterials.

13.3.5.5 Service Buildings

- Service buildings will house mechanical and electrical equipment supporting the Ring Building and must therefore be equally spaced around the interior side of Ring Building.
- Service buildings require access for large equipment moves.
- Access to the ring tunnel for both equipment and personnel will be provided through the service buildings from both the tunnel mezzanine and the Ring Building infield.
- Service buildings must be located so utilities can be easily and efficiently routed to them.

13.3.5.6 Linac/RF Buildings

- The Linac /RF Building must be adjacent to the ring tunnel.
- The Linac area must be shielded due to radiation during linac operation.
- The Linac area floor should be elevated to enable Linac to Booster alignment
- The RF area must have a shielded test area
- The RF area must have a small cryo equipment enclosure nearby (but separate for vibration isolation) and concrete pad for associated Helium storage tanks

13.3.6 Structural Engineering

13.3.6.1 Codes and Standards

Refer to Section 13.3.1, Codes and Standards..

13.3.6.2 Soil Conditions

13.3.6.2.1 Laboratory Testing

A geotechnical study of the proposed NSLS-II building site was performed which included 16 grain size distribution analyses on soil samples recovered from the test borings [13.3].

13.3.6.2.2 Subsurface Conditions

The subsurface explorations encountered up to 6 ft of fill overlying a sand deposit that extends to more than 100 ft deep. Subsurface conditions consist of topsoil lying above a layer of fill which is over a thick layer of stratified sand.

Topsoil ranging in thickness from 2 to 12 in. was encountered in borings drilled in landscaped areas. Topsoil was not encountered in borings drilled in paved/developed areas.

Each of the borings encountered fill ranging in thickness from 3.3 to 7 ft. This fill is characterized as silty sand. Several explorations experienced refusals, indicating buried objects within the fill.

A layer of stratified sand, sand with silt, and sand with gravel was encountered below the fill in all of the borings and CPT soundings. The sand is light brown to brown, with density ranging from medium dense to very dense.

Subsurface explorations were terminated within the sand at maximum depths of about 100 ft. A 1999 report on the stratigraphy and hydrogeologic conditions at the lab prepared by the United States Geologic Survey refers to the sand as the "Upper Glacial Aquifer," and states that the thickness at BNL is about 185 ft. Confining clay units and additional sand and gravel aquifers overlie bedrock, which reportedly occurs at a depth of about 1,500 ft.

The depth to groundwater appears to range from about 23 to 37 ft below ground surface, depending on the location at the site. This is based on the boring and CPT observations, as well as data collected in 2003 for CFN.

Soils at the site are classified as Site Class D, a "Stiff Soil Profile," in accordance with Table 1615.1.1 of the New York State Building Code. This class is based on the shear wave velocity measurements in the CPT soundings and SPT N-Values in the test borings. The soils are not considered susceptible to liquefaction.

It is recommended that foundations be designed as spread footing foundations with slab-on-grade floors. Fill should be removed below footings so they bear directly on the sand deposits. Recommended bearing pressure is 2.5 tons psf on footings at least 3 ft wide.

The site contours indicate that the Experimental Hall floor will range from 9 ft below grade to 6 ft above grade. Floors are well above groundwater levels encountered in the explorations. It is recommended that the slab-on-grade floors bear on a minimum of 6 in. of compacted structural fill placed over the natural sand deposit or suitable existing fill that has been compacted. Adequate densification should be accomplished using a heavy roller for both the native sand as well as the structural fill. This will provide a base for the Experimental Hall floor and should yield a low differential settlement when combined with the floor slab design.

13.3.6.3 Building Design Loads

The building structure will be designed based on the following building load conditions.

Table 13.3.8 Live Loads

Location	Load (psf)
Laboratories	125
Experimental Hall	250 (to be confirmed in final design)
Ring Tunnel	250 (to be confirmed in final design)
Tunnel mezzanine	125
Ring Building access corridor	125 (or wheel loads from fork lift trucks)
Corridors	100
Stairs and lobbies	100
Offices	100 (includes 20 psf for partitions)
Light storage areas	125
Mechanical rooms	150 (or actual weight of equipment)

Table 13.3.9 Building Snow Loads

Factor	Value
Ground snow load Pg	45
Snow importance factor I	1.1 for Central Lab Office Building and Conference Center 1.0 for all other buildings
Snow exposure factor Ce	0.9 for Ring Building 1.0 for all other buildings
Thermal Factor Ct	1.0
Design snow load	30 psf (min) + Drift where applicable

Table 13.3.10 Building Wind Loads

Factor	Value
Basic wind speed (3-sec gust)	110 mph
Wind load importance factor	1.15 for Central Lab Office Building and Conference Center 1.00 for all other buildings
Wind exposure	B

Table 13.3.11 Building Earthquake Loads

Factor	Value
Short-period acceleration Ss	0.25 g
1 sec period acceleration S1	0.08
Site Class	C
Seismic Use Group	II for Central Lab Office Building and Conference Center I for all other buildings
Seismic Design Category	B
Seismic Importance Factor IE	1.25 for Central Lab Office Building 1.00 for all other buildings

13.3.7 Mechanical Engineering

13.3.7.1 Codes and Standards

Refer to Section 13.3.1, Codes and Standards.

13.3.7.2 Mechanical Systems

The NSLS-II facility will require the following mechanical systems:

Table 13.3.12 Mechanical Systems.

Mechanical Utility	Central Lab Office Bldg	Experimental Hall	Tunnel Mezzanine	Service Bldg	Linac / RF	Lab Office Buildings
HVAC	■	■	■	■	■	■
General exhaust	■	■	■	■		■
Chilled water	■	■		■	■	■
Process Cooling Tower water		F		■		
Steam and condensate	■			■		■
Heating water	■			■	■	■

F= Future

13.3.7.3 Outdoor Design Conditions

Outdoor design conditions are based on the 2005 American Society of Heating, Refrigeration, and Air-Conditioning Engineers (ASHRAE) Fundamentals Handbook. Data are for LaGuardia Airport, New York and is the same criteria used for the adjacent CFN building on the BNL campus.

Elevation: 82 Ft

Weather Data – Summer:

Design Dry Bulb: 95°F
Design Wet Bulb: 76°F

Weather Data – Winter:

Design Dry Bulb: 0°F
Wind Speed: 15 mph

13.3.7.4 Indoor Design Conditions

Office Space

Cooling: 75 deg F +/- 5 deg F; 50 % RH ±10 % RH
Heating: 72 deg F +/- 5 deg F; 30 % RH ±10 % RH

Laboratory Space

Cooling: 75 deg F +/- 5 deg F; 50 % RH ±10 % RH
Heating: 72 deg F +/- 5 deg F; 30 % RH +/-10 % RH

Ring Tunnel

Cooling: 78 deg F +/- 0.18 deg F; 50 % RH ±10 % RH
Heating: 78 deg F +/- 0.18 deg F; 30 % RH ±10 % RH

Experimental Hall

Cooling: 75°F ±1°F; 50% RH ±10% RH
Heating: 75°F ±1°F; 30% RH ±10% RH

Linac Building

Cooling: 75°F ±1°F; 50% RH ±10% RH
Heating: 72°F ±1°F; 30% RH ±10% RH

RF Building

Cooling: 75°F ±1°F; 50% RH ±10% RH
Heating: 72°F ±1°F; 30% RH ±10% RH

13.3.7.5 Facility Cooling Load

Cooling loads for the facility can be broken down between loads cooled by the HVAC air cooling systems and the process cooling water systems, as shown in Table 13.3.13.

Table 13.3.13 Estimated Cooling Load.

	Heat Rejection to HVAC Units (Tons)	Heat Rejection to Process Cooling Water (Tons)
Ring tunnel	98	281
RF Building	160	238
Linac Building	6	10
Cryo Building	10	138
Tunnel mezzanine	374	267
Experimental Hall	1156	0
Lab Office Buildings	237	0
Central Lab Office Building	170	0
Total Load	**2211**	**934**

13.3.7.6 Existing Utilities

Sitewide utilities are distributed throughout the BNL campus and will be used for the NSLS-II facility. These utilities are available as follows:

Table 13.3.14 Existing Utilities.

Utility	Pressure (psig)	Temperature (F)
Potable water	60-70	N/A
Chilled water supply	60-100	45
Chilled water return	40	57
Steam	125	353
Compressed air	100	N/A
Sanitary sewer	N/A	N/A

13.3.7.7 Ventilation

- Outside air will be supplied to all spaces in accordance with the requirements of ASHRAE Standard 62.1-2004.
- Supply air for dry laboratories will be sized to meet the HVAC thermal load.

- Wet laboratories airflow will be once through, 100% exhausted. Supply air will be determined to meet the worst case of the following:
  - Fume hood or other exhaust requirements
  - Thermal load of the space
  - Minimum of twelve air changes per hour
- Supply air to the ring tunnel will be designed to meet the temperature stability requirements, but not less than six air changes per hour.
- The experimental hall's air flow requirements will be based on the temperature stability requirements of the space, but not less than six air changes per hour.
- Locker and shower rooms will receive twelve air changes per hour and will be 100% exhausted.

13.3.7.8 Chemical Fume Hoods

Chemical fume hoods will be designed for a maximum airflow based upon a 100 fpm air velocity with the sash open to 18 in. height. The Laboratory HVAC system will be a constant volume design utilizing air valves. Fume hoods identified for nanomaterials research will be provided with bag-in bag-out HEPA filtration rated at 99.9995% efficiency, with gel seal type filter housing. At least one such hood will be furnished for each LOB. Wet laboratories will also be provided with ventilated chemical storage cabinets integral to the fume hood.

13.3.7.9 Radioisotope Fume Hoods (if required)

Radioisotope fume hoods will be designed for a maximum airflow based upon a 100 fpm air velocity with the sash open to 18 in. height. They will have bag-in-bag-out HEPA filtration equipment on the exhaust.

13.3.7.10 Bio-Safety Cabinets

The need for these is yet to be determined.

13.3.7.11 Building Pressurization

- The NSLS-II building will be maintained at a positive pressure to minimize infiltration of outside air into the facility. Specific areas within the facility will have pressurization that is positive or negative with respect to this building baseline pressure.
- The ring tunnel will be maintained at a positive pressure with respect to the building baseline pressure.
- Laboratories will be maintained at a negative pressure with respect to their surrounding corridors or adjacent spaces.
- Experimental hutches on the beamline floor may be positive or negative to the experimental floor depending on specific requirements of each experiment. An ESH review will be performed for each beamline experiment to determine the appropriate air balance for the application.
- Toilets, locker rooms, and showers will be maintained at a negative pressure with respect to their adjacent corridors.

13.3.7.12 Supply Air Filtration

All air handling units will have 30% pre-filters. Air handling units serving the ring tunnel, experimental areas, and laboratories will have 95% final filters upstream of the cooling coils. Special filtration requirements for experimental hutches are not included in the base construction.

13.3.7.13 Vibration Isolation

Vibration isolation will be required for some mechanical equipment in order to meet the vibration requirements of the accelerator and beamline experiments. Rotating equipment such as air-handling units, pumps, fans, compressors, etc., are of particular concern and will be isolated. Additionally, large ductwork and piping systems will also require isolation. Specific strategies for isolation are included in the vibration consultants' report [13.1]

13.3.7.14 Process Systems

Process systems are those systems that are provided primarily to support the experimental equipment rather than the building itself. The NSLS-II accelerator, beamlines, and laboratories will require the following Process systems.

Table 13.3.15 Process Systems.

Process System	Central Lab Office Bldg	Experimental Hall	Tunnel Mezzanine	Service Bldg	Linac / RF	Lab Office Buildings
Gaseous nitrogen	■	■	■			■
Liquid nitrogen		■			■	
Compressed air	■	■		■		■
DI water - consumable	■					■
DI water make-up				■		
Process cooling water - Cu		■	■			
Process cooling water - Al			■			

13.3.7.15 Plumbing Systems

The NSLS-II facility will require the following plumbing systems:

- Domestic cold water
- Domestic hot water
- Sanitary sewer
- Tempered water (for emergency eye wash and shower)

These services will be distributed within the CLOB, the LOBs, the Experimental Hall, and the Linac and RF Buildings.

13.3.7.16 Fire Protection Systems

All of the NSLS-II buildings will be protected by wet pipe automatic fire sprinkler systems. Fire detection and alarms will be provided as described in the Electrical section of this document. The NSLS-II facility will require the following fire protection systems:

- Fire water
- Automatic fire sprinklers

13.3.8 Electrical Engineering

13.3.8.1 Codes and Standards

Refer to Section 13.3.1, Codes and Standards.

13.3.8.2 Utilization Voltages

- 13,800 V, 3-phase, 3-wire, grounded wye, 60 Hz:
  - site distribution
- 480Y/277 V, 3-phase, 4-wire, 60 Hz:
  - lighting
  - motors greater than or equal to ½ HP
  - selected pieces of equipment
- 208Y/120 V, 3-phase, 4-wire, 60 Hz:
  - receptacles
  - motors less than ½ HP
  - selected pieces of equipment

13.3.8.3 Utilities

13.3.8.3.1 Relocation and/or Demolition of Existing Utilities

The extent of electric and communication utilities to be relocated and/or demolished shall be based on a utility survey and the final building footprint. In general, all existing utilities under the building footprint shall be relocated if active or removed if inactive. Inactive utilities outside the footprint may be abandoned in place.

13.3.8.3.2 Power

Building 603 Substation Expansion

The existing campus substation at Building 603 located near the intersection of Cornell Avenue and North Sixth Street, has adequate 69 kV power capacity but does not have adequate transformation capacity to 13.8 kV to serve the currently estimated loads of the NSLS-II project, and will require upgrading. Upgrades of additional 66 kV/13.8 kV transformers and related switchgear are required.

The existing substation yard includes 69 kV overhead structure with two incoming utility lines, three 20.0/26.7/29.9 MVA 66.0/13.8 kV transformers, and space for one additional transformer. Inside Building 603 are the 15 kV metal-clad switchgear lineups for Bus 1, Bus 2, and Bus 3.

The upgrade shall include modifying the existing 69 kV support structure, and providing a new 69 kV SF6 breaker, and a 20.0/26.7/29.9 MVA 66.0/13.8 kV transformer, 2000 A 15 kV overhead busway, and 15 kV SF6 metal-clad switchgear within Building 603, to be designated Bus 0. A new fire separation wall shall be provided between the existing transformer #3 and the new transformer.

There is not adequate space within Building 603 to house the new switchgear. Therefore, the building will require modification and expansion to house the new gear.

The new switchgear shall include a main breaker, three tie breakers to connect to Bus 1, Bus 2, and Bus 3, one outgoing breaker to feed the NSLS-II project.A new tie breaker at each of the existing Bus 1, Bus 2, and Bus 3 switchgear lineups will connect to Bus 0.Each new breaker shall be provided with relaying, metering, and communication for remote monitoring and control.

Campus Distribution

The existing campus manhole and ductbank system has two spare 5 in. ducts between Building 603 and the NSLS-II site which can be utilized to route a new 800A 15 kV feeder from the Bus 0 switchgear to manhole MH-E5 via manholes MH-E1, E2, E3, E4, and E5 along North Sixth Street. The feeder shall consist

of two sets of 3-1/c, 1000 kcmil, 15 kV, 100% EPR copper conductors. A redundant feeder may be provided in the future. This future feeder will require a new ductbank to be installed.

13.3.8.3.3 Telephone and Data Communications

Copper service is available at Building 537 at the northwest corner of the NSLS-II site. New cable may be routed in the existing ductbank to manhole MH-84 via MH-85. A new four-way 4 in. ductbank will be provided from MH-84 to the NSLS-II BDF (building distribution frame) within the CLOB.

Fiber service is available at Building 515 near the intersection of Brookhaven Ave and Rochester Street New cable may be routed in the existing manhole and ductbank system from Building 515 to the existing manhole MH-84 at the NSLS-II site via manholes MH-14B, 14H, 87, 86, and 85. The new cable may share the same new four-way 4 in. ductbank with the copper service cable from MH-84 to the NSLS-II BDF.

13.3.8.3.4 Street Lighting

Street lighting will be provided along Brookhaven Avenue and Groves Street from their intersection to the last vehicle entry point into the site.

13.3.8.4 Normal Power Distribution

The on-site normal power distribution system shall be configured in a primary selective scheme which will be fully utilized once the future redundant feeder is provided.

An eight-way 5 in. concrete-encased ductbank will be provided between MH-E5 and a new manhole within the Ring Building. Infield from this manhole, a six-way 5 in. concrete-encased ductbank will be provided clockwise and counterclockwise around the infield to each substation. Two sets of 3-1/c, 1000 kcmil, 15 kV, 100% EPR copper conductors will be provided from MH-5E to the "A" switch of each substation. A 480 V feeder utilizing one active and one spare 4 in. duct will be provided from Switchgear #1 to the process cooling tower facility on the north side of Brookhaven Avenue via MH-E5B, E5A, E5, and E4.

The feeder shall have the capacity to support 6000 kVA of additional load at the RF Building, which would be required if the storage ring were upgraded in the future to operate at an energy of 3.6 GeV. At this time, installation of supporting infrastructure shall be limited to the 15 kV primary feeder. All associated substations, switchgear, and distribution needed for operation at 3.6 GeV would be provided in the future.

Each substation shall include an outdoor metal enclosed switchgear close coupled to a 13,800-480Y/277 V 2000, 2500, or 3000 kVA oil-filled substation type transformer with a secondary air terminal section. The primary switchgear shall consist of two key-interlocked duplex load interrupter switches in series with one set of fuses. Each transformer shall be triple rated 55˚ OA, 65˚ OA, and 65˚ FA. A ductbank and secondary feeder shall be extended to 480 V switchgear located in the electrical room of each service building.

13.3.8.5 Emergency Power Distribution

Two on-site diesel generators will provide emergency and optional standby power during interruptions of the normal power distribution system. Each generator shall be provided with a weatherproof, reach-in, sound attenuated enclosure.

Fuel oil storage capacity shall provide 12 hour full-load operation and may be stored in a double wall, sub-base fuel tank with remote alarm panel. The fuel storage system shall comply with Suffolk County DHS Article 12 requirements.

Emergency power shall be provided to the following loads:

- Egress and exit lighting

- Fire alarm system
- Fire suppression system
- Selected exhaust and make-up systems
- Selected HVAC controls
- Mechanical control system

Standby power shall be provided to the following loads:

- Telecommunication system
- Security system
- Sump pumps, sewage ejectors, etc.
- Selected lab equipment

The intent is to limit the amount of laboratory equipment on generator power to that equipment which is necessary to prevent equipment damage or the loss of an experiment that will take several days to reproduce.

13.3.8.6 Uninterruptible Power

An Uninterruptible Power Supply system shall be provided to backup equipment associated with the control room. At this time, there are no other requirements for a central UPS system. If uninterruptible power is required, it will be provided by the user via point-of-use UPS units.

13.3.8.7 Design Loads

13.3.8.7.1 Equipment Loads

For initial planning, the following estimated loads have been used. However, as the machine design is refined and/or the equipment list is developed, the most current information available and/or the manufacturer's published data for the selected equipment or best approximation from similar equipment will be used.

Accelerator Tunnel and Tunnel Mezzanine

- Single magnet circuits
  - Total demand load = 2220 kW (74 kW/cell x 30 cells)
  - Each cell shall be served by approximately:
    30 – 3-phase, 208 V circuits
    20 – 1-phase, 208 V circuits
    20 – 1-phase, 120 V circuits
  - All loads are located in the mezzanine above the tunnel. Ten equipment racks will be located at 30 equally distributed locations.
  - Panel boards serving this rack-mounted equipment may be surface mounted on the mezzanine wall.
- Ring-wide power supplies (locations will be defined during the preliminary design phase)
  - One 480 kW, 480 V, 3-phase load
  - One 100 kW, 480 V, 3-phase load
  - One 10 kW, 480 volt, 3 phase load. Location will be defined during the preliminary design phase.
- Transfer line magnet power supplies (locations will be defined during the preliminary design phase)
  - Linac to booster ring: 30 – 3-phase, 208 V circuits
  - Booster to storage ring: 70 – 3-phase, 208 V circuits
- Insertion devices
  Currently undefined. Assume low power consumption.

- Vacuum instrumentation
  - Total demand load = 300 kVA (10 kW/cell x 30 cells)
  - Mostly 120 and 208 V, some 480 V
  - All loads are located in the mezzanine above the tunnel.
- Tunnel instrumentation
  - Total demand load = 300 kVA (10 kW/cell x 30 cells)
  - Mostly 120 and 208 V, some 480 V
  - All loads are located in the tunnel. Generally for portable equipment.
- Tunnel power and signal support
  Separate power and signal cable trays shall be provided within the tunnel throughout its entire length as well as above the racks at the mezzanine level. Additional tray shall be provided from the mezzanine to the control room.

Experimental Hall

- Total demand load = 2850 kW (75 to 95 kW/sector x 30 sectors)
- Equipment loads will generally be 120 and/or 208 V.
- Panel boards serving Experimental Hall equipment may be surface mounted on the adjacent walkway wall.

Linac/RF Building

- Linac RF system: 20 kW
- Booster RF system: 160 kW, 480 V, 3-phase
- RF transmitter: 700 kW, 480 V, 3-phase
- Cryogenic plant: 500 kW, 480 V, 3-phase

Central Lab Office Building

- Lab equipment: 25 VA per net square ft connected
- Office equipment: 5 VA per net square ft connected

Lab Office Buildings

- Lab equipment: 25 VA per net square ft connected
- Office equipment: 5 VA per net square ft connected

13.3.8.7.2 Demand Factors

A 1.0 demand factor will be used at electrical distribution equipment serving tunnel and Experimental Hall equipment. NEC code demand factors will be used at all other locations.

13.3.8.7.3 Spare Capacity

- Branch circuit panels and distribution panels serving tunnel equipment will provide 10% spare capacity.
- Branch circuit panels serving Experimental Hall equipment will provide 25% spare capacity.
- Branch circuit panels serving labs within the LOBs will provide approximately 50% spare capacity.
- Other panels and switchgear will provide approximately 25% spare capacity.

13.3.8.8 Grounding

13.3.8.8.1 Grounding Electrode System

- The grounding electrode system shall consist of underground metal piping, building steel, a 250 kcmil bare copper Ufer ground embedded in the concrete foundation around the perimeter of the building with cross-connecting conductors at approximately 100 ft spacing under the Ring Building, and the ground rods associated with the lightning protection system.
- The 250 kcmil concrete embedded conductor shall be exothermically welded to the foundation rebar at 20 ft increments.
- All underground connections shall be exothermically welded.
- The ground grid shall be designed to provide <5 ohms of resistance to earth.

13.3.8.8.2 Power System Safety Grounding

- The power system safety grounding shall be in accordance with the NEC and IEEE 142 Grounding of Industrial and Commercial Power Systems.
- The Building 603 substation upgrade and each of the NSLS-II unit substations shall be grounded in accordance with IEEE 80 AC Substation Grounding.
- Lab equipment shall be grounded in accordance with IEEE 1100 Powering and Grounding Electronic Equipment.
- A separate green insulated equipment grounding conductor shall be provided in all feeder and branch circuits.
- Branch circuits serving sensitive electronic equipment shall be provided with a green with yellow strips isolated equipment grounding conductor in addition to the green equipment grounding conductor.

13.3.8.8.3 Instrument Reference Grounding

Provide one instrument reference ground bus at each beamline to be used by users only for the purpose of grounding sensitive electronic and/or communication circuits. The bus shall be connected directly to the grounding electrode system and bonded to the local transformer(s) which provide power to that beamline equipment. It shall be considered the beamline's single point ground for all user equipment.

13.3.8.8.4 Static Dissipation Grounding

Selected labs may require static dissipative flooring and/or bench tops. Verify requirements and provide grounding as necessary.

13.3.8.8.5 RF Shield Grounding

If a shield is required to attenuate nearby radar emissions, the shield shall be bonded and grounded as recommended by the shielding consultant.

13.3.8.8.6 Telephone and Data Communication Grounding

Telephone and data communication grounding shall be provided in accordance with EIA/TIA 607.

13.3.8.8.7 Lightning Protection

A complete lightning protection system shall be provided in accordance with NFPA 780 and UL 96A.

13.3.8.8.8 Cathodic Protection

Typically, cathodic protection has not been provided on other campus projects. Therefore, it is assumed that it will not be required at the NSLS-II project. However, this requirement should be verified with the recommendations contained in the soils report.

13.3.8.9 ELF EMI and RFI Mitigation

At this time, there is no requirement to mitigate magnetic fields produced by electrical/mechanical distribution equipment which could effect sensitive lab equipment.

Similarly, there is no identified requirement to mitigate radio frequency interference from lighting fixtures, adjustable frequency drives, or other mechanical/electrical equipment that operate at higher frequencies.

There will be provision to shield the experimental floor from RFI generated by the RF cavities. Local shielding will be provided in the accelerator tunnel in these areas. Any additional shielding will be provided on an as-needed basis as part of the experimental apparatus. Most hutches have inherent EMI/RFI shielding by nature of their construction.

13.3.8.10 Vibration Isolation

At this time, vibration isolation of electrical equipment will include upgraded spring isolators on the generators, neoprene pads under transformers, and prohibiting the use of any conduit under or within vibration isolation slabs.

13.3.8.11 Radiation Protection

Conduit penetrations in to the tunnel shall be limited in quantity and located only through the tunnel ceiling. All penetrations shall include offsets that prevent line-of-sight through the high-density concrete. Spare penetrations shall be provided for future use.

Refer to Chapter 17, Radiation Safety and Shielding, for information regarding shielding material and thickness requirements.

13.3.8.12 Exterior Lighting

- Exterior lighting shall be provided along the interior and exterior roadways, parking lots, walkways, and building exits. Illumination levels shall be in accordance with DOE and IES standards.
- Fixtures shall be full cut-off type using metal halide light sources at a mounting height generally not exceeding 20 ft.
- Exterior lighting controls shall provide photocell on, photocell off controls with the ability to turn off the lights at a selectable time of day.
- The exterior lighting system shall comply with LEED Sustainable Site Credit #8 - Light Pollution Reduction and ASHRAE 90.1.

13.3.8.13 Interior Lighting

- Interior lighting shall be provided primarily from fluorescent sources. Incandescent lighting may be provided in labs where very low-level lighting is required or where RF interference may be a concern. Metal halide may be considered in the Experimental Hall.
- Fluorescent lamps shall be T8, 32 W, 4100K with a minimum CRI of 75. Fluorescent ballast for T8s and compact lamps shall have a minimum ballast factor of 0.85 and a total harmonic distortion of <10%.

- Exit lights shall be LED type.
- Occupancy sensors shall control lighting in all spaces other than lab and experimental areas. Offices, storage, and similar spaces shall be provided with override off switches at the door. Lab and experimental areas shall be provided with a low-voltage control system with local on/off override switches.
- Photo sensors shall be provided in perimeter offices and other spaces with natural lighting.
- Interior illumination levels shall be in accordance with DOE and IES standards. Egress and exit lighting shall comply with the New York State Building Code (NYSBC) and NFPA.
- The interior lighting system power consumption shall comply with ASHRAE 90.1 limitations.

13.3.8.14 Special Systems

13.3.8.14.1 Fire Alarm System

- A complete manual and automatic, supervised, fire detection, and voice evacuation system shall be provided. It shall be a non-coded, addressable, microprocessor-based fire alarm system with initiating devices, notification appliances, and monitoring and control devices. Initiating and appliance circuits shall be Class B. The fire alarm system shall be in accordance with DOE and NY State Code requirements.
- Smoke detection shall be provided in labs in the CLOB and the LOBs, throughout the Experimental Hall and tunnel, electrical rooms (including switchgear rooms in the service buildings), telephone and data communications rooms, and in elevator lobbies, shaft, and machine room. Consideration should be given to the use of air sampling detectors. Provisions shall be provided for connecting future smoke detectors located within the future experimental hutches. Smoke detectors in elevator lobbies, shaft, and machine room shall initiate elevator recall. Duct smoke detectors shall be provided in air handling systems as required by NYSBC and NFPA 90A.
- Heat detectors shall de-energize elevator power in accordance with ANSI 17.1 Elevator Code.
- The fire alarm control panel shall be located at the CLOB main entrance.
- Common alarm and trouble signals will be transmitted via dedicated fiber optic cable to the campus fire alarm system.
- The fire alarm system shall match campus standards.

13.3.8.14.2 Telephone and Data Communication Systems

- A complete pathways, spaces, and structured cabling distribution system shall be provided and consist of telecommunication rooms, plywood backboards, racks, cabinets, cable tray, conduit, back boxes, copper cable, fiber optic cable, connectors, cover plates, termination blocks, cross connect cables, patch panels, and all necessary accessories and shall be provided in accordance with applicable EIA/TIA standards.
- Cable tray shall be provided in LOB corridors and above the walkway around the Experimental Hall. Conduit shall be provided between the cable tray and each outlet or raceway.
- Each voice/data outlet shall be provided with one Cat 6 voice jack and one Cat 6 data jack.
- Each data outlet shall be provided with one Cat 6 data jack.

13.3.8.14.3 Security System

- The security system shall consist of an access control system only. Intrusion detection and CCTV systems are not required.
- Card readers shall be located at each building entrance, at each corridor entrance to a lab, at each entrance to the Experimental Hall, at each entrance to the tunnel, and at each entrance to other selected spaces.
- To match campus standards, security equipment components (card readers, controllers, locks, door contacts, etc.) will be owner furnished, contractor installed. Security system cabling and raceways shall be contractor provided and installed. Door exiting devices, power transfer hinges, etc. shall be coordinated with the door schedule.

13.3.9 Sustainable Design & LEED

The goal for the NSLS-II facility is to incorporate a wide range of sustainable strategies and objectives throughout the design and construction process while meeting the functional requirements of an advanced technology facility and creating a workplace that is environmentally friendly, energy-efficient, and both healthy and pleasant to be in. The NSLS-II facility will be designed to achieve a minimum LEED Certification Level of LEED Certified and higher if possible.

13.4 PROGRAM

13.4.1 Building Program

NSLS-II will have distinct components that make up the final building plan. They are the Ring Building, the Central Lab Office Building, the Lab Office Buildings, the Service Buildings, and the Linac/RF Buildings. Each of these buildings has separate space and utility requirements.

13.4.1.1 Definitions

Net Square Feet (NSF): The sum of all areas that are required to meet general or specific functional needs. NSF is calculated based on the interior dimensions of the rooms and spaces.

Gross Square Feet (GSF): The total area of all spaces in the building including wall thicknesses. GSF is calculated based on the exterior face of the building spaces and includes non-assignable spaces such as building circulation, mechanical/electrical rooms, restrooms, janitor closets, and the area of interior and exterior walls.

Building Efficiency: Building efficiency is calculated as the ratio of NSF/GSF.

Table 13.4.1 Summary Program of Spaces.

Space Description	NSF	GSF
Central Lab Office Building	36,900	52,748
Conference Center*	13,440*	15,000*
Ring Building	228,118	244,663
Service Buildings	28,696	32,000
Linac & RF Buildings	15,862	21,000
Lab Office Buildings* (4 @ 11,000 GSF ea.)	30,480*	44,000*
Total Square Feet	**353,496**	**409,411**
Building Efficiency: 86%		

* 15,000 GSF Conference Center and 33,000 GSF of Lab Office Building space are optional and not in base scope

13.4.2 Ring Building

The Ring Building, shown in Figure 13.1.2, will consist of four space components, the ring tunnel, the tunnel mezzanine, the Experimental Hall, and the access corridor.

The ring tunnel, housing the booster ring and the storage ring, occupies the inner most area of the Ring Building. The beamlines used by the experimental stations extend tangentially from the ring at select locations. The Experimental Hall is designed to accommodate beamlines that are approximately 60 m long from the center of the straight section to the end of the beamline. Outboard of the Experimental Hall will be the access corridor.

Above the ring tunnel is the tunnel mezzanine. Power supplies for the accelerator will be located on the tunnel mezzanine with electrical power feeds dropping through the floor into the tunnel.

Beyond the ring tunnel is the experimental floor. The experimental floor is the space where the beamlines and hutches for the experiments are located. The floor in this area will be designed to reduce transmission of vibration and prevent differential settlement of the floor which can be detrimental to the performance of the beamlines.

The outermost ring of the Ring Building is the access corridor which is approximately 10 ft wide and designed for fork truck and pedestrian traffic. This will be a continuous aisle that runs the circumference of the Ring Building. It is from this aisle that the CLOB and LOBs will be accessed.

Table 13.4.2 Ring Building Program of Spaces.

Space Number	Room Name	Size NSF	No. of Spaces	Total NSF	GSF	Notes
RB-101	Ring tunnel	34,824	1	34,824		
RB-102	Experimental Hall/Access corridor	143,820	1	143,820		
RB-103	Tunnel mezzanine	46,624	1	46,624		
RB-104	Loading dock	2400	1	2,400		
RB-105	Hazardous materials storage	450	1	450		Located near LOB 1
	Ring Building		**5**	**228,118**	**244,663**	
	Efficiency: 93%					

13.4.3 Central Lab Office Building

The Central Lab Office Building will be a three-story structure that serves as the focal point of the facility. Figures 13.4.1, 13.4.2, and 13.4.3 show the floor plans for the first, second, and third floors, respectively, of the CLOB. It will include an entry lobby for reception and displays, administrative offices, offices for operating staff, and workshop and lab space to support NSLS-II operations staff and users. It will include approximately 160 enclosed offices and 30 open plan offices. There will also be a director's suite with director's office and conference room..

The CLOB will have provision for connection to an optional separate Conference Center that can accommodate 400 occupants utilizing ground floor and mezzanine seating areas. The Conference Center will include lobby display areas and toilet facilities for seminar attendees.

The CLOB will also have 3 breakout/conference rooms on the second floor that can be accessed from the optional Conference Center mezzanine lobby area to serve as breakout rooms or used as conference rooms if the Conference Center is not constructed.

Incorporated into the CLOB is space equivalent to one Lab Office Building to serve user and NSLS-II staff beamlines in the CLOB area. Approximately 20 of the enclosed offices and 10 of the open plan offices will be for this staff. Eight laboratories will be available to support NSLS-II staff requirements and/or beamlines in the area.

The CLOB will contain the accelerator control room with associated conference and computer rooms and a viewing gallery located on the second level to view the Experimental Floor.

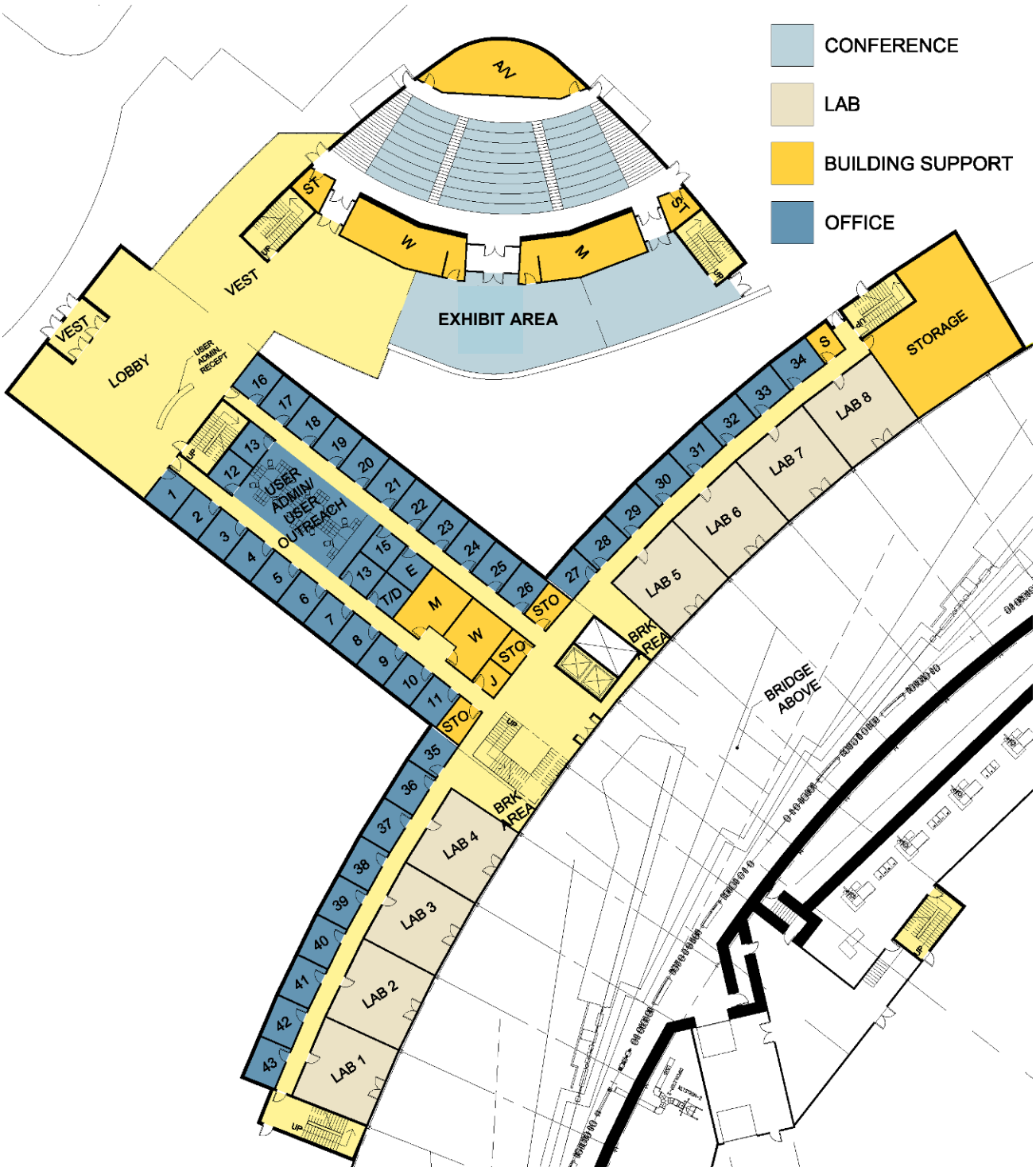

Figure 13.4.1 CLOB 1st Floor Plan.

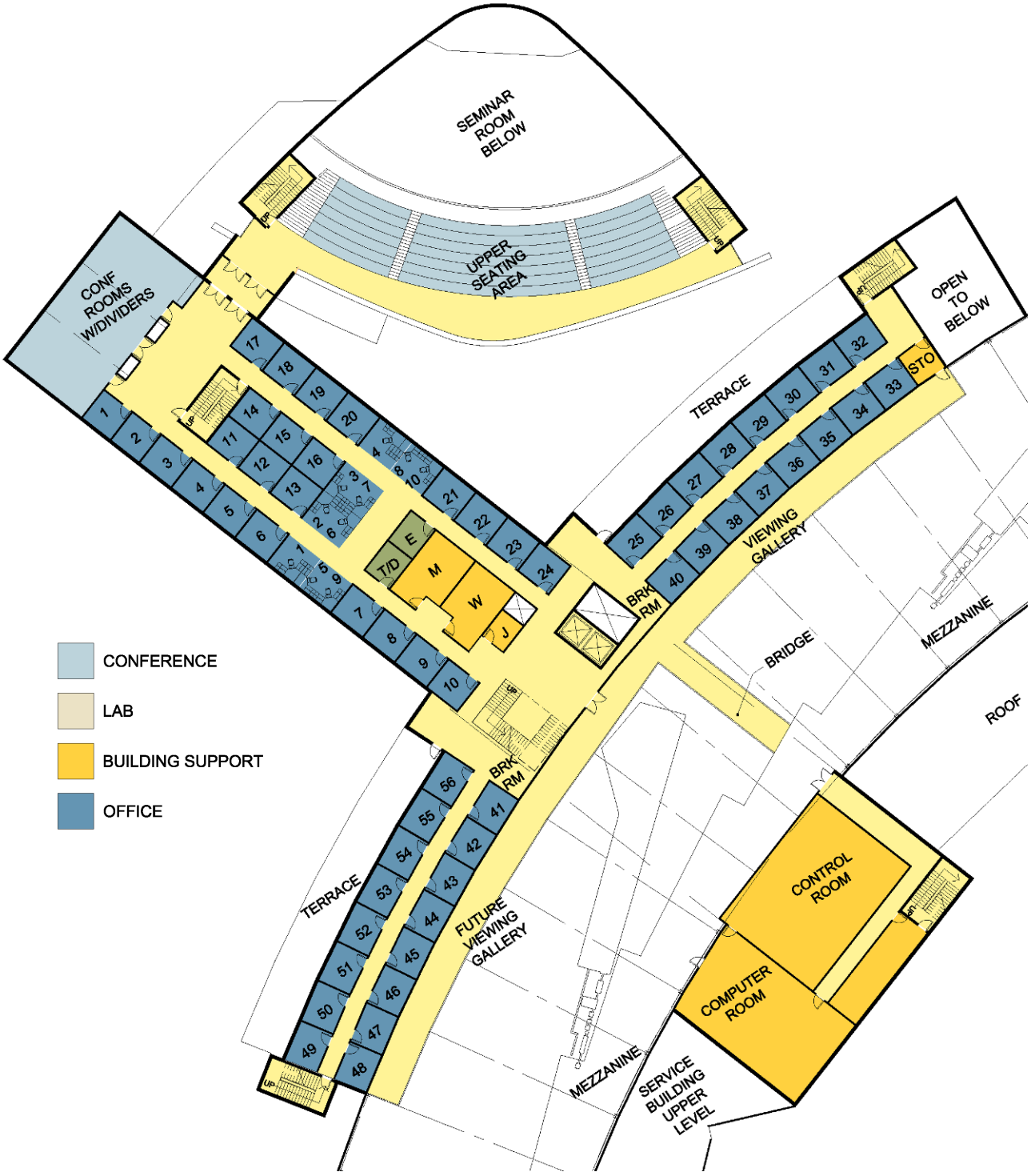

Figure 13.4.2 CLOB 2nd Floor Plan.

Figure 13.4.3 CLOB 3rd Floor Plan.

Table 13.4.3 Central Lab Office Building Program of Spaces.

Space Number	Room Name	Size NSF	No. of Spaces	Total NSF	GSF	Notes
CB-101	Private office	110	160	17,600		
CB-102	Open office	90	30	2,700		
CB-103	Director's office	240	1	240		
CB-104	Director's conference room	200	1	200		
CB-105	Storage	480	1	480		
CB-106	Breakout/ conf. rooms	500	3	1,500		
CB-107	Lobby	2,400	1	2,400		
CB-108	Break / kitchenette room	200	2	400		
CB-109	Control conference room	240	1	240		
CB-110	Control room	1,600	1	1,600		
CB-111	Computer room	800	1	800		
CB-112	Toilet room and shower	350	6	2,100		
CB-113	Viewing gallery	1,600	1	1,600		
CB-114	Laboratories (16 modules)	240	16	3,840		8 double-module labs
CB-116	Stock room	1,200	1	1,200		
CB-117	Auditorium, 1st floor	3,900	1	3,900		Not in Base Scope
CB-118	Auditorium, mezzanine	5,200	1	5,200		Not in Base Scope
CB-129	Exhibit breakout	3,340	1	3,340		Not in Base Scope
CB-120	Toilet rooms	400	2	800		Not in Base Scope
CB-121	AV room	200	1	200		Not in Base Scope
	Central Lab Office Bldg		**226**	**38,900**		
	Conference Center		**6**	**13,440**		Not in Base Scope
	Building Total		**232**	**50,340**		
	Efficiency – CLOB: 70%				**52,748**	
	Efficiency – Conference: 90%				**15,000**	
	Efficiency – Combined: 74%				**67,748**	

13.4.4 Lab Office Buildings

There will be a maximum of four single-story Lab Office Buildings. These will include 22 enclosed offices and eight open-plan offices. Each LOB will also have 10 laboratory modules plus interaction areas, conference rooms, and storage. The floor plan for LOB 1 is indicated on Figure 13.4.4.

Figure 13.4.4 LOB 1 floor plan.

Table 13.4.4 Lab Office Buildings Program of Spaces.

Space Number	Room Name	Size NSF	No. of Spaces	Total NSF	GSF	Notes
	Lab Office Building				**55,000**	Building Target GSF
LOB-101	Private office	110	22	2,420		
LOB-102	Flexible office space	90	8	720		
LOB-103	Laboratory module	240	10	2,400		5 double-module labs
LOB-104	Storage	480	1	480		
LOB-105	Conference room	200	1	200		
LOB-106	Lobby & interaction space	500	1	500		
LOB-107	Break room	200	1	200		
LOB-108	Loading/staging	200	1	200		
LOB-109	Toilet/shower	250	2	500		
LOB -110	Mechanical penthouse	0	0	0		Not currently included in program.
			45	**7,620**		
	4 Lab Office Buildings		**180**	**30,480**		
	Efficiency: 69%				**44,000**	

13.4.5 Laboratory Design

Each LOB will have five laboratories, which will be shared with all the beamlines associated with that particular LOB. These labs are based on a 12 ft wide and 20 ft long lab planning module with each lab being two modules wide. A typical laboratory layout is shown in Figure 13.4.5. These labs will have access to the Experimental Hall through recessed double doors 6 ft wide (two 3 ft wide leaves). The labs will be accessed from the LOB by a single recessed 3 ft wide door.

At least two labs in each LOB will be wet labs, either chemistry or biology, which will require a fume hood. At least one of these hoods will be HEPA filtered in each LOB. Additionally, each LOB will have the capability to provide at least one HEPA filtered fume hood designated for nanomaterials work. The other labs will be dry labs with cabinetry and equipment but no fume hoods. These labs may be equipped with elephant trunk exhausts or glove boxes as needed by the laboratory type. Two of the labs within each LOB may be designed to be upgradeable to an H5 Occupancy in the future, where Hazardous Production Materials (HPM) are used (per the New York State Building Code).

Chemistry wet labs will include ventilated chemical storage cabinets (possibly incorporated into the fume hood base). Each wet laboratory will also be furnished with a safety shower/eyewash station. Floor drains will not be provided in laboratory space though a sump pit may be provided to collect liquids and allow testing prior to pumping to sanitary waste.

These same general requirements will apply to the eight laboratories located in the Central Lab Office Building. Two of the labs in the CLOB will be wet labs, either chemistry or biology, which will require a fume hood. At least one of these hoods will be HEPA filtered.

Other types of labs will be accommodated either in JPSI or elsewhere at BNL:

- X-ray source/crystal polishing (located in JPSI)
- Metrology lab (located in BNL Instrumentation Division)
- Sample characterization labs (located in JPSI and LOBs)
- Electronics labs (located in JPSI and LOBs)
- Magnet characterization lab (located in BNL Building 832)
- Ultra high vacuum lab (located in BNL Building 905)

Since the LOB labs are going to be shared labs, it is necessary to make the labs as generic as possible while still serving the requirements of the research being performed.

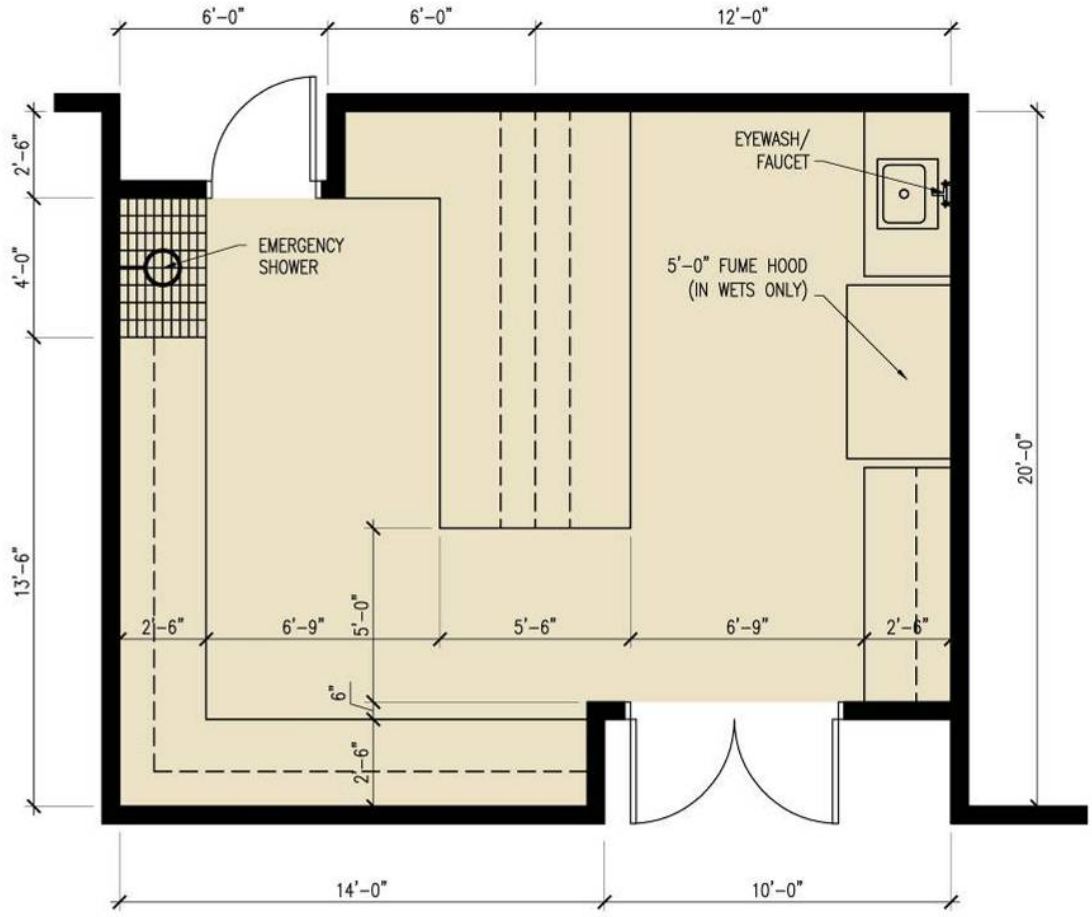

Figure 13.4.5 Typical laboratory layout.

13.4.6 Service Buildings

There will be five two-story service buildings and one single-story service building, located within the Linac/RF Building. These buildings will house the mechanical and electrical equipment to service the experimental floor, the ring tunnel, and the ring mezzanine. The Service Building 1st floor (see Figure 13.4.6) will provide personnel access to the ring tunnel through a labyrinth, and equipment access to the ring tunnel at two of these service buildings through a shielded door. The Service Building 2nd floor (see Figure 13.4.6) will house air handlers for the experimental floor area and will provide equipment access to the ring mezzanine via an at grade roll-up door.

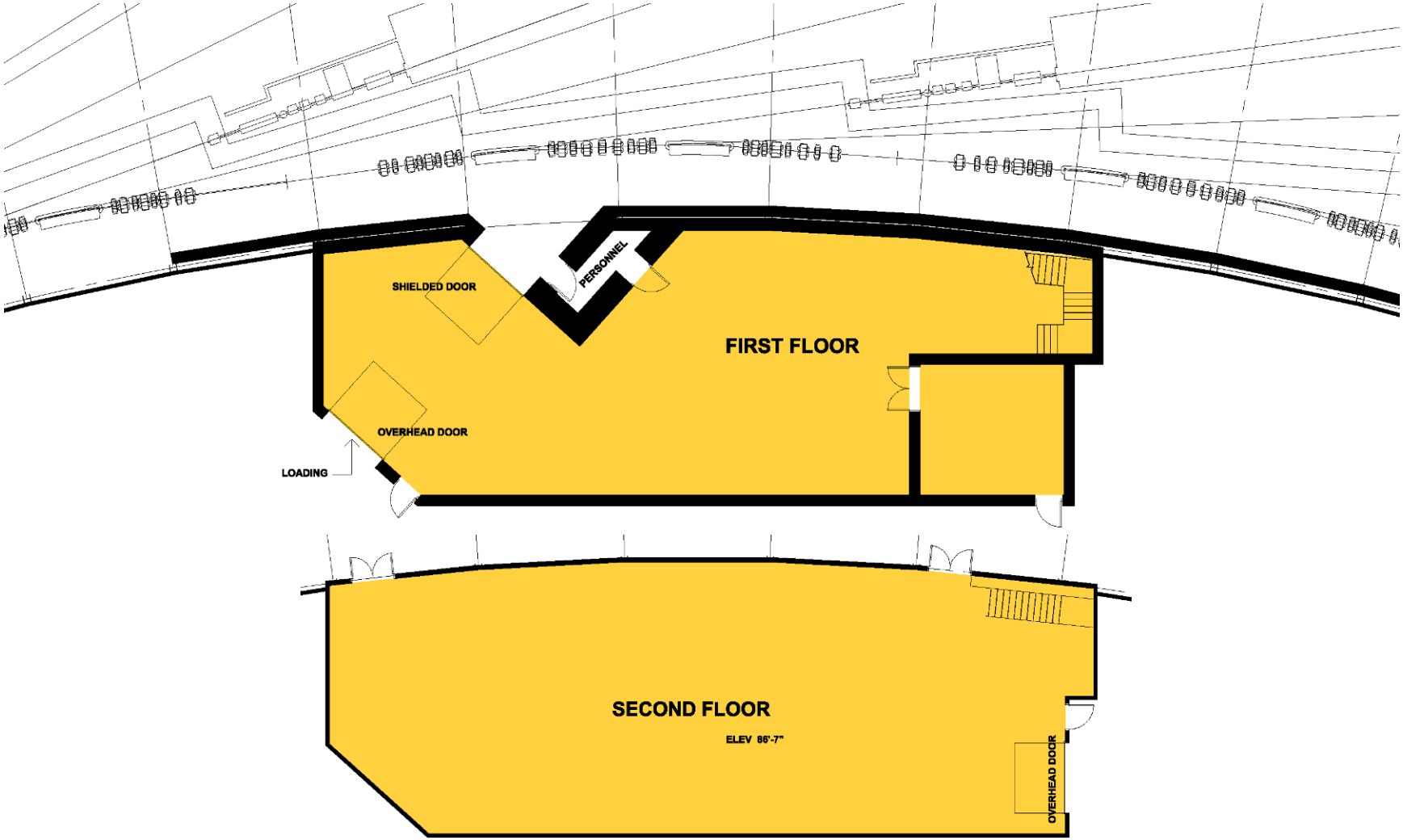

Figure 13.4.6 Service Building. Top figure shows first floor and bottom figure shows second floor.

Table 13.4.5 Service Buildings Program of Spaces.

Space Number	Room Name	Size NSF	No. of Spaces	Total NSF	GSF	Notes
	Service Buildings				**20,000**	Building Target GSF
SB-101	Mech./Elect. equip. room, lower level	3,277	4	13,108		
SB-201	Mech./Elect. equip. room, upper level	3,897	4	15,588		
			8	**28,696**		
	Efficiency: 90%				**32,000**	

13.4.7 Linac/RF Buildings

The Linac/RF Building consists of five spaces for the Linac and RF equipment and a single story Service Building. The space will be located on the opposite side of the ring from the Central Lab Office Building and will be accessed from the Central Lab Office Building via a bridge. The Linac area finished floor will be approximately 5 ft higher than the experimental floor to enable Linac alignment with the booster Ring. The RF area will include a concrete shielded RF cavity test enclosure. Above the RF area will be a second floor service area to provide space for mechanical and electrical equipment equivalent to that provided in Service Building SB1 – SB4. Figures 13.4.7 and 13.4.8 show the Linac and RF area floor plans, respectively.

Table 13.4.6 Linac and RF Buildings Program of Spaces.

Space Number	Room Name	Size NSF	No. of Spaces	Total NSF	GSF	Notes
	Linac and RF Buildings				12,900	Building Target GSF
LB-101	Linac Room	1,730	1	1,730		
LB-102	Klystron Galley	2,216	1	2,216		
LB-103	Service Building	6,150	1	6,150		
LB-104	RF Cavities	5,340	1	5,340		
LB-105	RF Testing	426	1	426		
	Linac and RF Buildings		**5**	**15,862**		
	Efficiency: 76%				**21,000**	

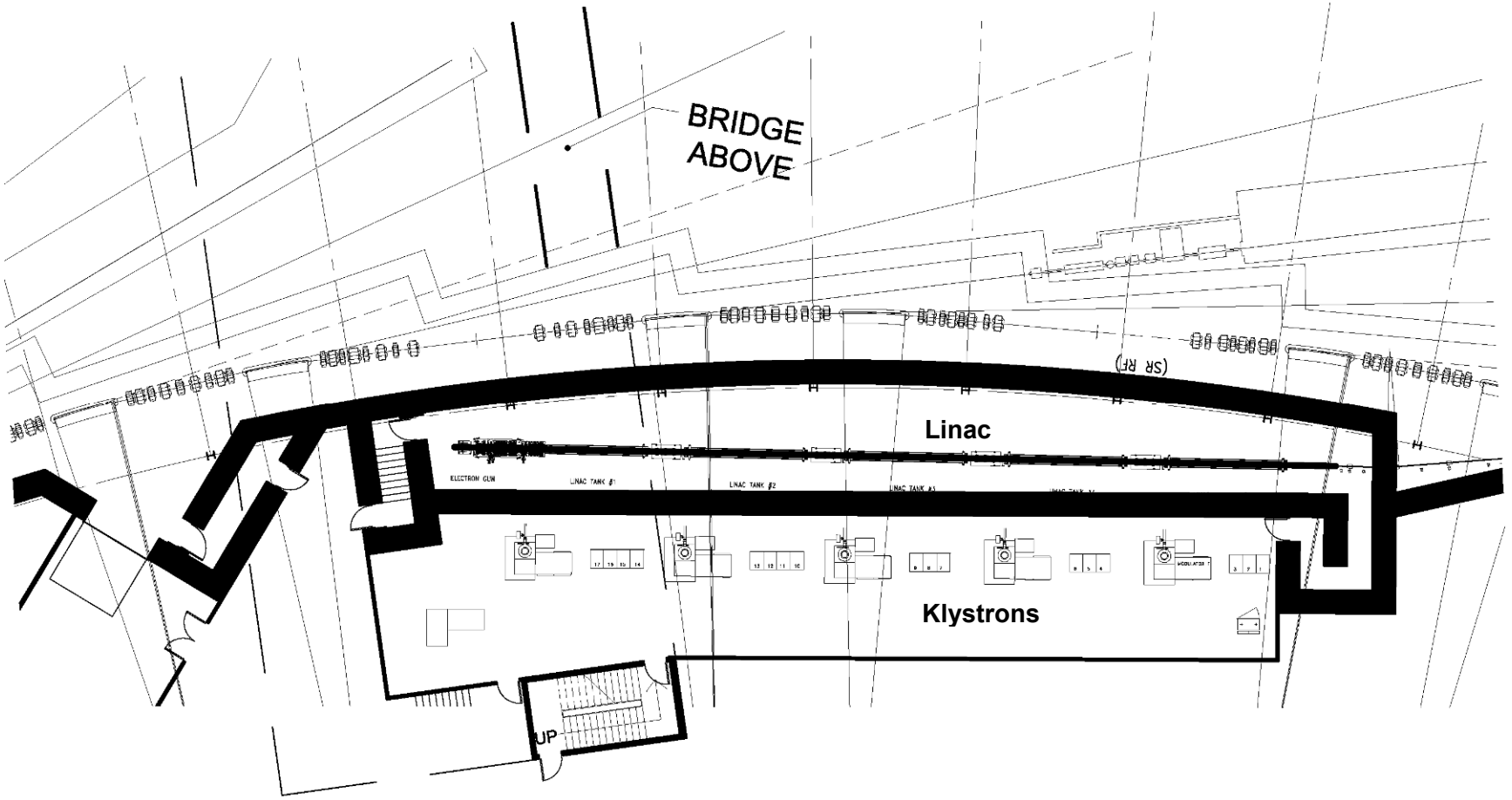

Figure 13.4.7 Linac area.

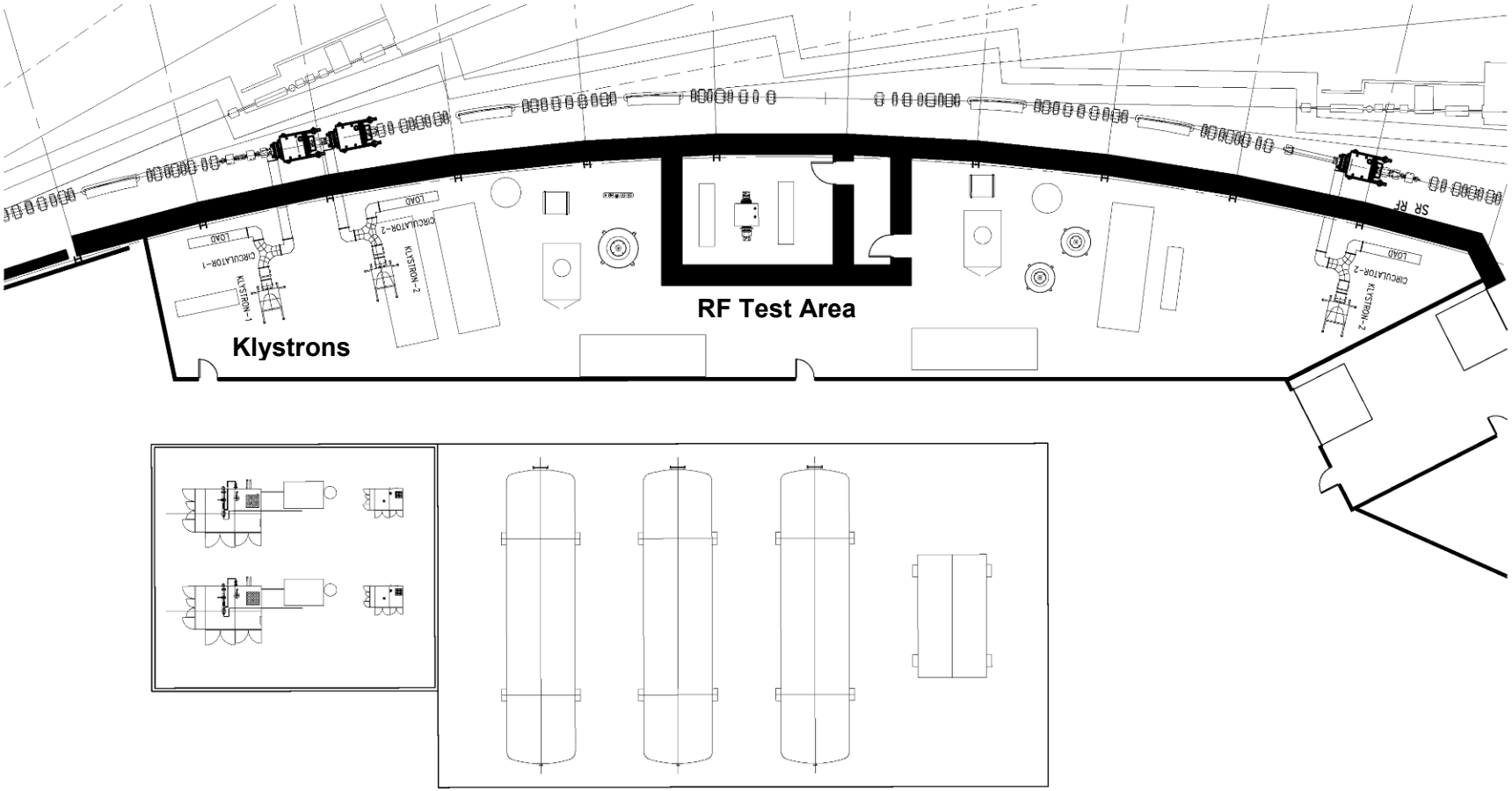

Figure 13.4.8 RF area.

13.4.8 Circulation

Entry points into the Ring Building are provided around the circumference of the building both from the outside and the inside of the ring. The main entrance to the Ring Building will be from the Central Lab Office Building. Other entrances to the complex are available from the LOBs and from the service buildings. Within the three-story CLOB, two elevators will provide vertical transportation.

When the accelerator is operating, access to the ring tunnel is not allowed, for safety reasons. Doors into the ring tunnel will be interlocked with the accelerator to prevent entry into the tunnel when the beam is operating.

Primary circulation within the Ring Building will be provided by the access corridor that circumscribes the outside of the building. It will provide for both pedestrian and vehicular (bicycle, forklift, etc.) traffic. The access corridor will have points of entry from each LOB and from each laboratory within the LOBs. If future beamlines are extended across the access corridor, provision will be made at that time for an elevated bridge across the beamline sized for all anticipated traffic.

Control room personnel require ready access to the tunnel mezzanine and the ring tunnel itself. A pedestrian bridge will be provided from the CLOB second floor across the Experimental Hall to the tunnel mezzanine. Entrance to the accelerator tunnel will be via the service buildings. Stairs in the service buildings will provide circulation between the mezzanine level and the tunnel level. Personnel will access the accelerator tunnel through a personnel labyrinth on the first level. Entry into the Ring Building from the LOBs, service buildings, and the CLOB will be restricted by card-reader controlled access.

13.4.9 Building Floor Elevations

The floor elevation for the Ring Building (experimental floor) is the functional baseline for the elevations of the adjoining buildings and spaces. This elevation is set to balance cut and fill on the site while also minimizing the need for engineered fill. The floor elevations for the components are given in Table 13.4.7.

Table 13.4.7 Building Floor Elevations.

Building Component	Floor Elevation
Experimental floor and access corridor	+ 73 ft
Ring tunnel	+ 74 ft 4 in.
Tunnel mezzanine	+ 86 ft 7 in.
Lab Office Building	+ 73 ft
Central Lab Office Building	--
First floor	+73 ft
Second floor	+ 88 ft
Third floor	+103 ft
Service buildings	--
Ring tunnel access	+ 74 ft 4 in.
Upper level	+ 86 ft 7 in.
Linac Building	+ 78 ft
RF Building	+ 74 ft 4 in.

13.4.9 Building Cross Sections

Figure 13.4.9-13.4.14 show typical cross-sections through the Ring Building and adjoining structures as follows: Figure 13.4.9 – in-between LOBs and MERs; Figure 13.4.10 – at the location of a LOB and MER; Figure 13.4.11 – at the location of the center of the CLOB; Figure 13.4.12 – to the side of the CLOB; Figure 13.4.13 – at the RF building; and Figure 13.4.14 – at the Linac building and experimental hall.

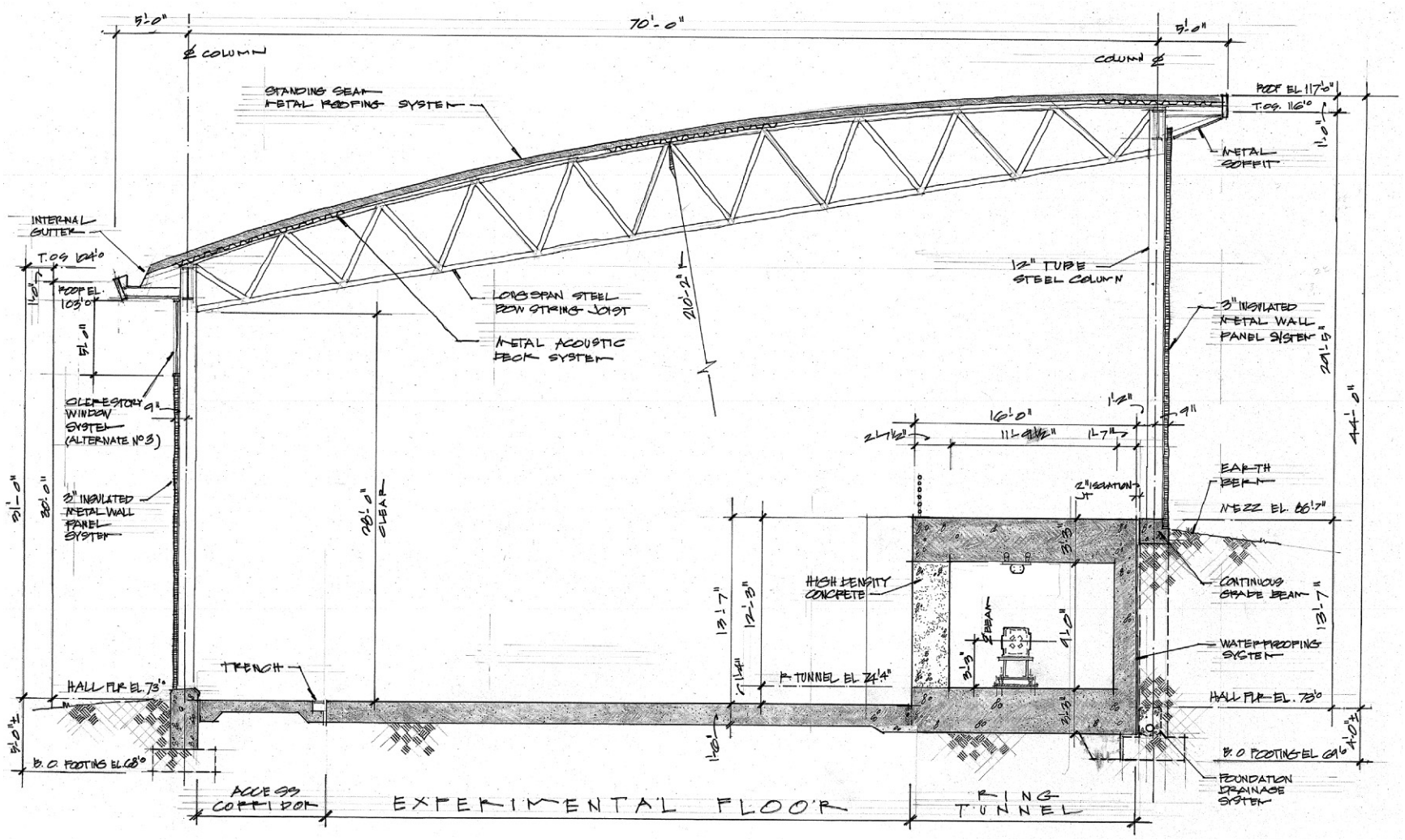

Figure 13.4.9 Cross-section through Ring Building in-between LOBs and MERs.

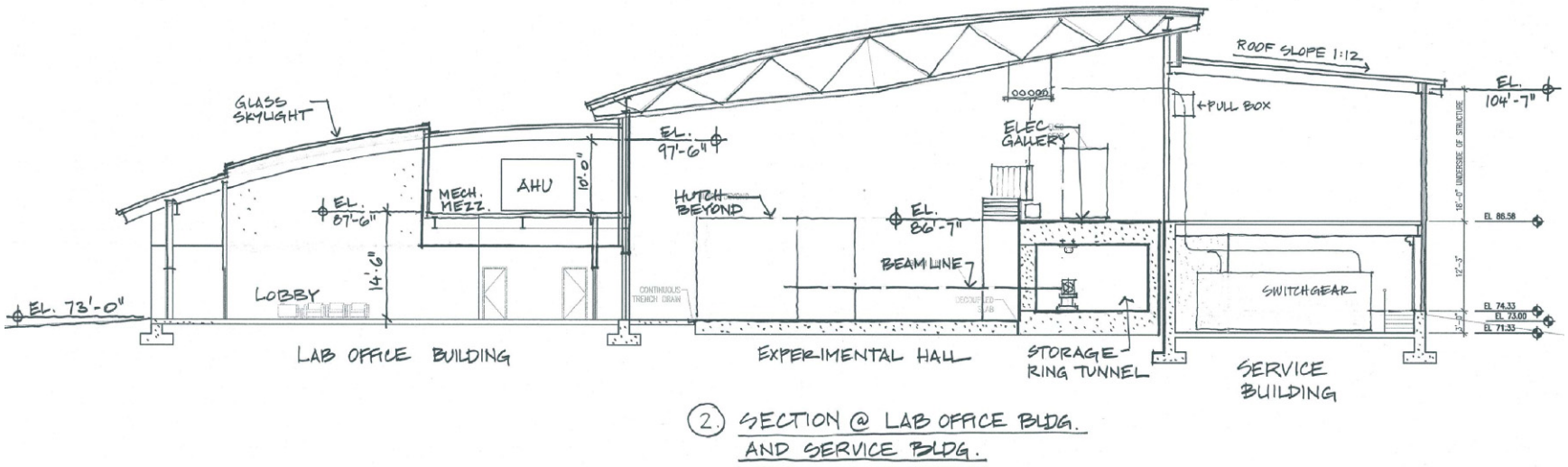

Figure 13.4.10 Cross-section through Ring Building in vicinity of an LOB and MER.

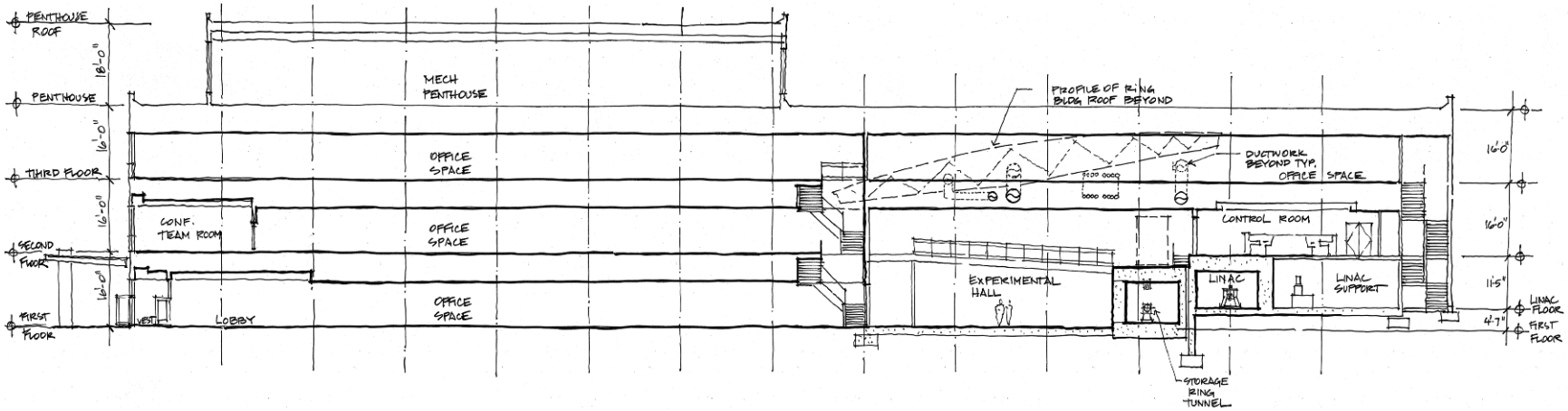

Figure 13.4.11 Cross-section of Ring Building through center of CLOB and MER.

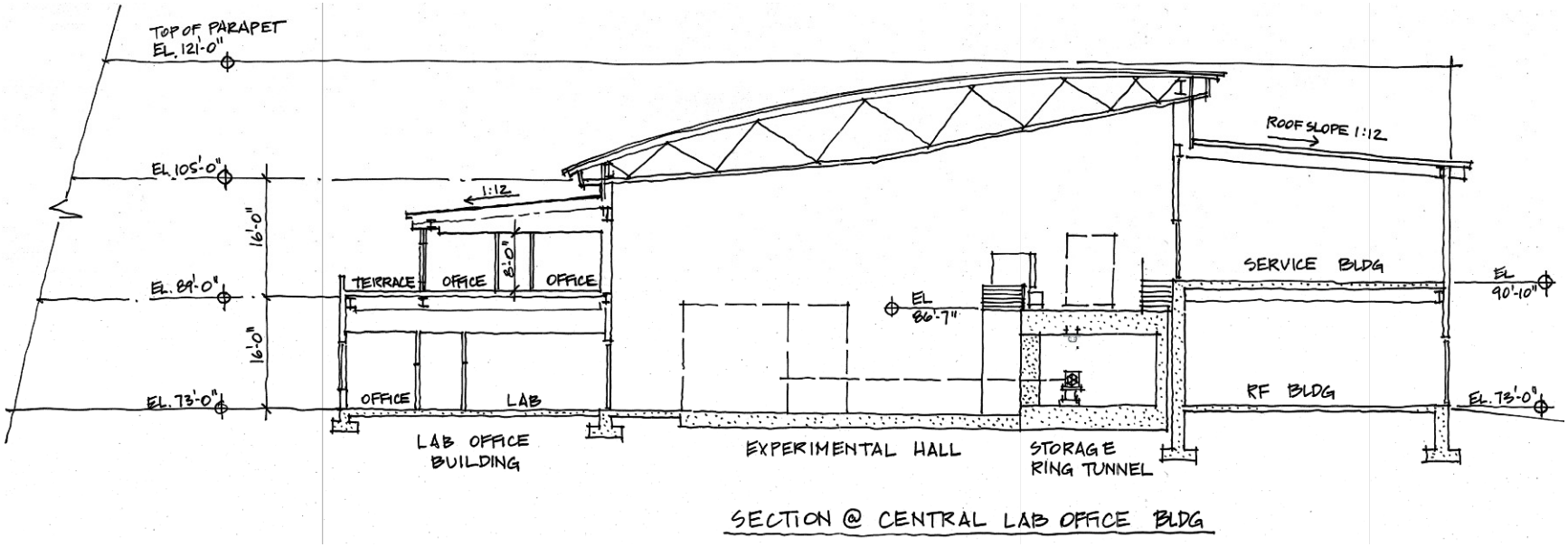

Figure 13.4.12 Cross-section of Ring Building through side of CLOB, showing second floor offices above LOB 1, which is integrated into the CLOB.

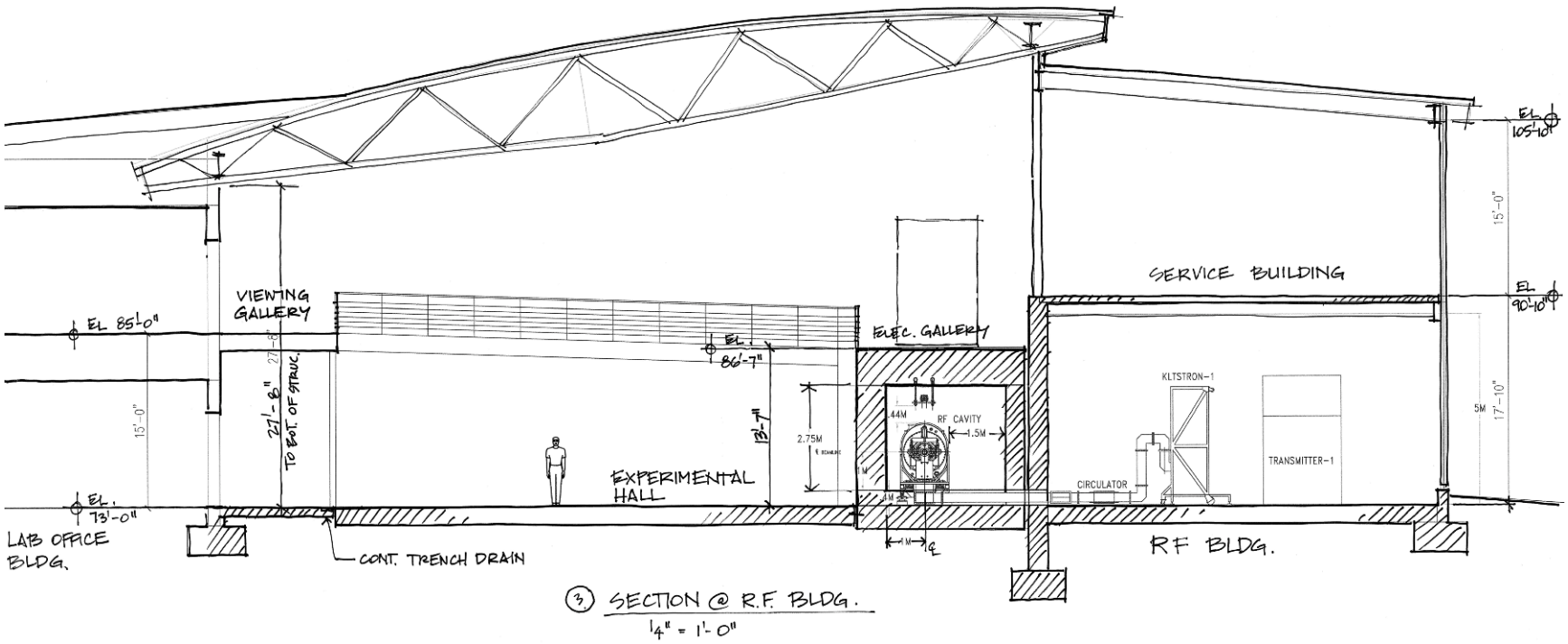

Figure 13.4.13 Cross-section through Ring Building in vicinity of RF building.

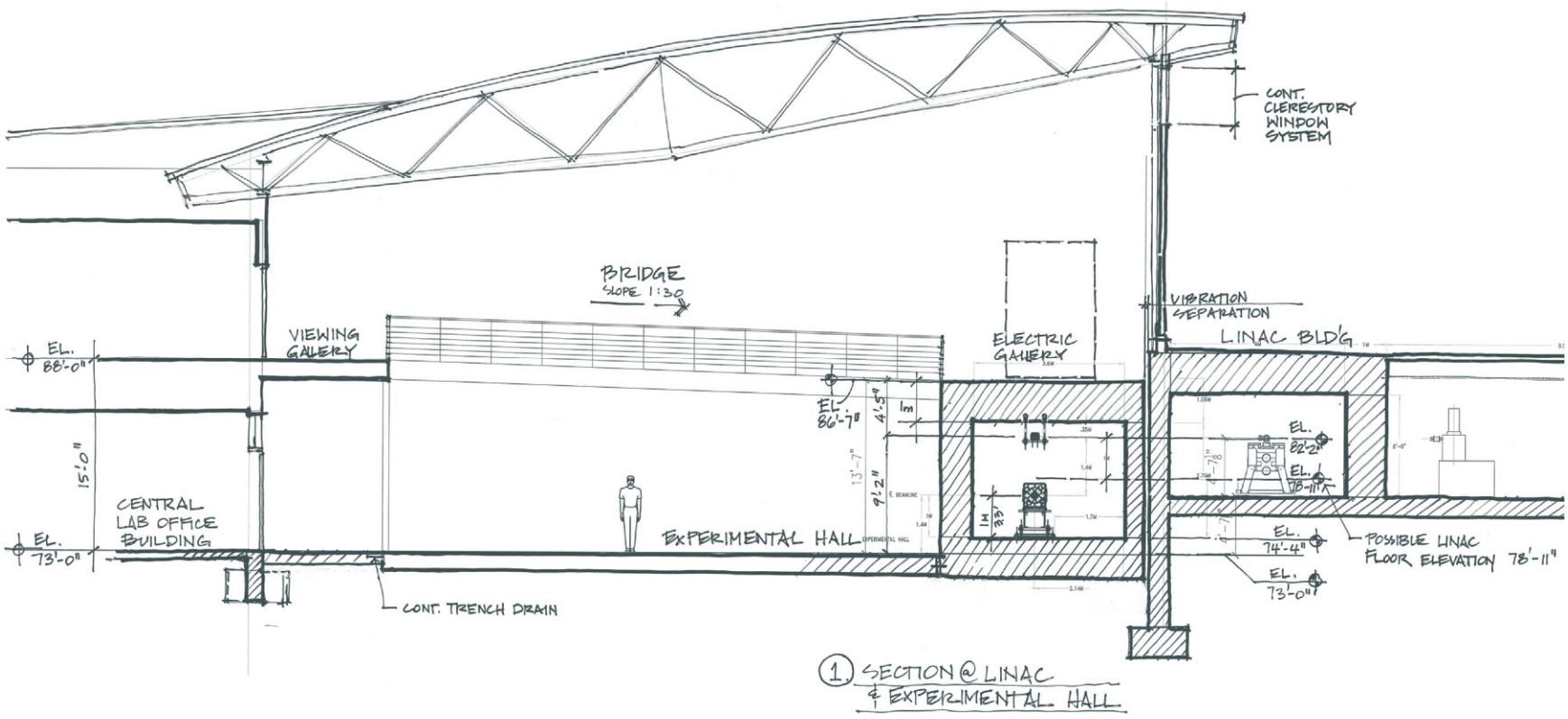

Figure 13.4.14 Cross-section through Ring Building in vicinity of Linac Building. The bridge from the CLOB to the electrical gallery on the tunnel mezzanine is also shown.

13.5 SCOPE AND CONCEPTUAL DESIGN

13.5.1 Improvements to Land (WBS 1.6.3.2)

Improvements to land includes removal of existing structures, pavement, abandoned utilities, rail spur, and unsuitable fill, then re-grading and installation of new paving, drainage, site lighting, and landscaping. This WBS element will consist of two work packages:

- WBS 1.6.3.2.1 – Site Preparation which will encompass site clearing, cutting to grade, removal of unsuitable fill, routing of utilities, and build-up and compaction to grade with suitable fill;
- WBS 1.6.3.2.2 – Site Restoration, which will be included in the Ring Building contract and will include the installation of all new paving, drainage, site lighting, and landscaping.

13.5.1.1 Existing Structures

Removal of the existing building foundations will be required as part of the NSLS-II site work. Additionally, any underground utilities serving these buildings will also be removed back to the utility mains.

13.5.1.2 Pavement

Removal of existing pavement will be required for Railroad Street and Seventh Street. Both roadways will be removed to a point that enables tie-in to new roads and parking areas constructed as part of the project.

13.5.1.3 Abandoned Utilities

Existing site utility systems that are not being used or have been abandoned in place will be removed as part of the NSLS-II project. The site plan identifies several underground utility pipes that will be removed back to an approved location and terminated.

13.5.1.4 Railway Spur

The existing railway spur that runs parallel to Groves Street will be removed to a point south of the building site. Approximately 500 ft of track will be removed.

13.5.1.5 Site Work

Site clearing will be required to remove trees to the west of Seventh Street and in the southeast corner of the site. The geotechnical report indicates a one foot layer of topsoil above sand, gravel, and silt. The topsoil will be removed for construction and retained for berm construction and replacement topsoil. Any other unsuitable fill identified by the geotechnical report will also be removed and replaced by material from the on-site borrow pit. Final site grading will level the site to the elevations shown on the site plan.

13.5.1.6 Paving

New paving for NSLS-II will include:

- Curbed drive and entrances from Brookhaven Avenue and Groves Street
- Curbed drop-off loop for the CLOB
- Parking (uncurbed) for the CLOB
- Ring Road (uncurbed) around the outer perimeter of the NSLS-II site

- Access to the Loop Road from Groves Street, Brookhaven Avenue
- Parking (uncurbed) for each of the LOBs
- Truck access to the main loading dock and loading platforms at each LOB
- Access tunnel under the Ring Building into the infield area
- Service road (uncurbed) around the infield including drives to each service building
- Campus sidewalks

13.5.1.7 Storm Water

Storm water drainage from buildings and paved areas will be collected in retention basins to the extent possible as encouraged by the LEED guidelines. Basins will be constructed both outside the Ring Building perimeter and within the infield of the Ring Building. Collected storm water will be disposed of onsite with percolation beds or will be discharged into existing drainage structures which will be enlarged as needed to meet 100 year storm criteria. Special drainage accommodation will be required for the access tunnel under the Ring Building.

13.5.1.8 Landscaping

After construction, the site will be reseeded and landscaping will be provided for the LOBs and the CLOB. The landscape design will enhance streetscapes and pedestrian circulation routes, and create buffers to screen unsightly views such as service yards. A building sign and landscaping elements will be used to screen the existing small communications building that will remain near the corner of Brookhaven Avenue and Groves Street.

13.5.1.9 Erosion and Sedimentation Control

Erosion and sedimentation control systems will be installed and utilized for the duration of the construction phase of the project. Silt fencing and stabilized construction entrances will be installed prior to the commencement of construction activities. Disturbed areas within the construction site will be stabilized as soon as practical and subsequently maintained with appropriate methods to minimize erosion of exposed earth. Temporary seeding, mulching, or crushed stone will be used to achieve stabilization.

13.5.2 Central Lab Office Building (WBS 1.6.3.3)

13.5.2.1 Architectural Concepts

The Central Lab Office Building will serve as the front door to the NSLS-II complex. It is envisioned to be a three-story building that will interface with the future Guest House and Joint Photon Sciences Institute buildings planned for the site. The building will house the Director’s office, a conference center, control room and office space, and will incorporate a lab office complex serving users for six sectors.

13.5.2.1.1 Alternatives – Building Configuration

- Two story building without integral LOB
- Three story building without integral LOB
- Three story building with integral LOB

13.5.2.1.2 Selected Concept – Three-Story Building with Integral LOB

The selected concept consists of a three story building that overlaps the Ring Building radially to provide a strong entrance to the facility as well as a connection across the Ring Building for easy access to the Accelerator Tunnel and Tunnel Mezzanine.

13.5.2.1.3 Future Expansion

It is not envisioned that the CLOB will expand in the future. The design does not provide for future expansion horizontally or vertically. However, connectivity to future adjacent buildings is envisioned. It is anticipated that the Lab Office Building area may expand in the future to accommodate future beamlines. In this case, the LOB portion of the Central Lab Office Building will expand horizontally, which allows the labs and offices to be on the same level as the Experimental Hall.

13.5.2.2 Space Program

The first floor will consist of the lobby with space for displays, a user reception area, staff offices and labs, user group labs and offices, shower facilities, loading area, stock room, and an access point for the future conference center. The second floor includes additional staff offices, breakout/conference rooms, a viewing gallery overlooking the Experimental Hall, a bridge across the Experimental Hall, and the control center inboard of the Ring Building that includes the control room, computer room, conference room, and kitchenette. The third floor will house the director's suite and continues with staff office space and a viewing space/terrace overlooking the inside of the ring.

The future conference center will be located on the first floor of the complex as a semi-attached space with its own identity. It will consist of a 400-person sloped-floor auditorium with exhibit space in the lobby and full audiovisual capabilities. Three breakout conference rooms will be provided on the second floor to support seminar activities. It will be located directly off the open, two-story lobby atrium where social events can be hosted.

13.5.2.3 Circulation

The primary point of entry will be the main entrance and lobby that will draw in pedestrian traffic from the parking lot and drop-off loop. Sidewalks are envisioned for pedestrian traffic to and from the adjacent future JPSI and Guest House buildings. Interaction areas will be incorporated adjacent to key circulation areas of the building. The building also provides primary entrance into the Experimental Hall. A bridge accessed from the second floor will span across the Experimental Hall and provide access to the control room as well as the accelerator tunnel, tunnel mezzanine, Linac and RF Building. Two elevators will provide vertical circulation within the building.

13.5.2.4 Quality of Life

Building orientation, sustainable materials, and the use of natural light will be integrated into the design to promote a comfortable and productive environment. Unlike the Ring Building, the Central Lab Office Building's envelope will consist of large areas of glass, allowing for visual transparency and providing an inviting front door to the NSLS-II complex. The lobby will be a space for informal interaction and social events. A shower facility will be provided to encourage exercise in off hours, which is a highly valued benefit for many employees and accommodates the 24/7 nature of NSLS-II operations, as well as support LEED sustainable design objectives.

13.5.2.5 Foundations

Building foundations are expected to be spread footings for columns and continuous strip footings for walls based on a similar foundation system used for the CFN Building in the immediate vicinity.

13.5.2.6 Building Superstructure

The Central Lab Office Building will be a three-story structure. All levels will be braced structural steel frames. The third level will include a Vierendeel truss structure to span across the Experimental Hall.

The second and third floor construction will typically consist of 20 GA – 2 in. thick composite steel deck with 3 in. lightweight concrete topping (total slab thickness = 5 in.) supported on a framework of steel beams and girders.

The roof will be comprised of structural steel framing or open web steel joists supporting 20 GA – 1 ½ in. thick steel roof deck.

13.5.2.7 Building Construction

The exterior of the CLOB will be constructed of an insulated metal wall panel and stud system. The system will be comprised of 2 in. insulated metal panels, exterior sheathing, air barrier, 6 in. metal studs, fiberglass batt insulation, and interior gypsum board. The minimum thermal resistance of the system will be R-20.

The roof of the CLOB will be a flat TPO membrane roofing system that meets current LEED requirements and the energy code minimum R-value.

The curtain wall windows at the CLOB will consist of 1 in. clear tempered insulated glass with a low-E coating in a thermally broken aluminum frame. The thermal transmission value for the glazing will be a U value of 0.30 in the summer and 0.30 in the winter. The visible light transmission will be 69% and the shading coefficient will be a maximum of 0.44.

The exterior doors will be curtain wall aluminum insulated doors to match the windows, or insulated hollow metal doors and frames.

13.5.2.8 Interior Finishes

The CLOB will have gypsum board walls with wood doors and hollow metal frames. The offices will have a side light or interior window to allow natural light into the interior spaces. The interior finishes are as follows:

- Floor finishes office area and conference rooms – carpet tile
- Floor finishes laboratories, control room, and computer room– sheet linoleum
- Floor finishes lobby – porcelain ceramic tile
- Exterior walls - painted
- Interior walls offices and labs – painted
- Interior walls conference rooms – paint or wall coverings
- Ceiling system – suspended acoustical tiles and grid
- Doors – wood, stained
- Door frames – painted

13.5.3 Ring Building (WBS 1.6.3.4)

13.5.3.1 Architectural Concepts

The Ring Building is the scientific and visual focal point for the NSLS-II facility. The halo-shaped building will dominate the site by its sheer breadth (937 ft in diameter), although its height (approx. 30 ft) is not proportionally commanding.

13.5.3.1.1 Future Expansion

The Ring Building is designed for future expansion by the addition of LOBs or support buildings to its outer or inner periphery. It is also possible that future beamlines will be added with a length of up to 600 m, which will extend substantially beyond the limits of the building. The facility is being designed to allow these long beamlines to be installed in the future with minimal impact on the current building. Accommodation for the long beamlines will be made when and if they are required.

13.5.3.1.2 Space Program

Within the Ring Building is the linac module, the RF module, the ring tunnel, the tunnel mezzanine, and the Experimental Hall. Service buildings connected to the inboard side of the Ring Building will provide HVAC, mechanical, and electrical services to the building components.

13.5.3.2 Circulation

The access corridor around the outside perimeter of the Ring Building provides the primary circulation route for the building. It will be designed to handle both pedestrian and forklift traffic. The corridor will provide access to the CLOB, all of the LOBs, individual laboratories within the LOBs, and the adjacent Experimental Hall. Stairs from the Experimental Hall will provide access to the tunnel mezzanine and the service buildings. The pedestrian bridge spanning the Experimental Hall will allow operators to conveniently walk between the control room and the tunnel mezzanine. Stairs within the service building will provide a means of accessing the ring tunnel from the tunnel mezzanine level.

Egress from the Experimental Hall will be through the four LOBs, the CLOB, across the tunnel mezzanine and through the service buildings, or through intermediate emergency exit doors spaced around the exterior perimeter of the Ring Building.

13.5.3.3 Quality of Life

Although the focus of the Ring Building is the enhancement of scientific inquiry, it is desirable to make the space an environment that researchers will enjoy occupying. Comfort facilities for the Ring Building are provided in the CLOB and in the four LOBs within a reasonable distance from all beamlines. As an add-alternate, natural lighting will be brought into the space via perimeter windows. Exterior shading will prevent direct sunlight from impacting experimental performance.

13.5.3.4 Foundations

The foundations for the walls along the outside perimeter of the Ring Building will consist of spread footings for columns and continuous strip footings for walls. The walls on the inboard side of the ring will have spread footings with concrete piers to the height of the tunnel roof and a concrete ring beam tying the piers together at the top.

13.5.3.5 Building Superstructure

13.5.3.5.1 Experimental Hall

The building structure will be a braced steel frame with a curved roof supported by steel joists and 72'-0" trusses or joist girders spanning radially. The roof structure will be supported by columns spaced along the inner and outer perimeters at a maximum spacing of 24'-0". The roof deck will be 20 GA – 1 ½ in. thick steel deck.

The Experimental Hall will have 18 in. thick reinforced concrete slab, poured in place over compacted sub-grade and a vapor barrier. This slab will be poured against and tied to the tunnel foundation wall with rebar dowels to prevent differential settlement. Isolated from this slab, will be the 8 in. reinforced concrete access corridor slab, poured over compacted sub-grade near the outer perimeter and designed for fork lift truck wheel loads.

13.5.3.5.2 Ring Tunnel

Within the Ring Building is the ring tunnel that houses the booster ring and accelerator ring. The exterior wall of the tunnel (inboard) will be a minimum of 0.5 m thick standard weight concrete with no less than 1 m of earth bermed against the wall. In locations where the exterior wall of the tunnel is not bermed, for instance adjacent to service buildings or the linac building, the wall will be 1 m thick standard weight concrete to provide adequate radiation shielding. The interior tunnel wall (ratchet wall) will be constructed of 0.8 m of high-density concrete for the entire height of the wall. The tunnel roof slab will be approximately 1 m thick standard weight concrete, designed to support the electrical gear above. In areas where potential radiation is increased due to transition, injection, or beam stop areas, thicknesses will be increased as indicated in Chapter 17, Radiation Safety and Shielding. The tunnel floor slab will be a 1 m thick standard weight reinforced concrete slab-on-grade poured in place over compacted sub-grade and a vapor barrier. The ring tunnel floor will not be vibrationally isolated from the Experimental Hall floor.

The interior shield wall of the tunnel or "ratchet wall" is currently planned to be constructed of pre-cast high-density concrete panels that will be procured as early as possible in the project. This provides potential advantages in reduction of schedule risk as well as possible cost savings to the project. The precast sections will be designed to be assembled from a few standardized panel sizes, to ease installation. The panels will be sized to be readily handled and transported by truck or rail or may be pre-cast on site prior to installation.

13.5.3.5.3 Service Buildings

Five service buildings along the inner perimeter of the Ring Building will be two-story structures with concrete exterior walls at the lower level supporting a braced steel frame for the second floor above. The concrete side walls will be designed for lateral earth pressure from the berms.

The second floor construction will typically consist of 20 GA – 2 in. thick composite steel deck with 3 in. lightweight concrete topping (total slab thickness = 5 in.) supported on framework of steel beams and girders.

The roof will be constructed of structural steel framing or open web steel joists supporting 20 GA – 1 ½ in. thick steel roof deck.

The first floor construction will consist of 6 in. thick slab on grade reinforced with 6x6 – W2.9 x W2.9 WWF over 6 in. of compacted granular fill and a vapor barrier. Final design of the first floor will be consistent with vibration mitigation needs of the facility.

Each service building will have a personnel labyrinth from the lower level into the ring tunnel. Additionally, an opening will be provided for installation of a large shield door (super door) for tunnel access for girders and other large assemblies as part of the technical facilities.

13.5.3.5.4 Linac Building

The Linac Building consists of the linac room and the klystron gallery.

The klystron gallery is a single-story structure with framed/braced structural steel construction. The roof will consist of a 20 GA - 1 ½ in. thick steel roof deck supported on structural steel beams and girders.

The linac room requires shielded walls and roof consisting of 1 m thick concrete. A personnel labyrinth will be proved at each end of the room for access.

The floor construction of both spaces will consist of 6 in. thick slab on grade reinforced with 6x6 – W2.9 x W2.9 WWF over 6 in. of compacted granular fill and a vapor barrier.

13.5.3.5.5 RF Building

This is a two-story structure with the RF area on the lower level and a mechanical/electrical equipment room above. It will have framed/braced structural steel construction. The roof will consist of a 20 GA 1 ½ in. thick steel roof deck supported on structural steel beams and girders.

The RF test room walls and roof will have radiation shielding consisting of 1 m thick concrete and a personnel labyrinth into the space will be provided.

The floor construction will consist of 6 in. thick slab on grade reinforced with 6x6 – W2.9 x W2.9 WWF over 6 in. of compacted granular fill and a vapor barrier.

13.5.3.5.6 Access Tunnel

There will be an access tunnel 20 ft wide and 14 ft high (clear height) that will go under the Ring Building for service vehicles. The tunnel retaining walls will be approximately 18 in. thick reinforced concrete walls and will also support the tunnel roof/Experimental Hall floor, which will consist of eight continuous one-way reinforced concrete slabs supported on concrete beams spanning between the tunnel walls.

13.5.3.6 Lateral Load Resisting System

Lateral loads will be mainly resisted by braced frames wherever possible, otherwise by moment frames where bracing location would become architecturally prohibitive.

13.5.3.7 Building Construction

13.5.3.7.1 Experimental Hall

The Ring Building exterior walls will be comprised of a built-up metal wall panel system with insulating batts and interior metal liner panel. The minimum thermal resistance of the system will be R-20.

The roof of the Ring Building will be a curved standing seamed metal roof system. The system will be comprised of the standing seamed roof over R30 rigid insulation, gypsum board sheathing, and structural metal roof deck.

The optional clerestory windows at the Ring Building will consist of 1 in. clear tempered insulated glass with a low-E coating in a thermally broken aluminum frame. The thermal transmission value for the glazing will be a U value of 0.30 in the summer and 0.30 in the winter. The visible light transmission will be 69% and the shading coefficient will be a maximum of 0.44. Clerestory windows will be an additive alternate but are not in the base scope.

The exterior doors of the Ring Building will be insulated hollow metal doors and hollow metal frames.

Acoustical treatments will line the ceiling and walls to maintain an acceptable noise level in the Experimental Hall.

13.5.3.7.2 Ring Tunnel

The ring tunnel will be constructed of poured in place or pre-cast concrete as described above in the Building Superstructure section.

13.5.3.7.3 Service Buildings

The service buildings' lower level will be constructed of poured in place concrete walls with a soil berm to the height of the second level. The second level exterior walls will be a built-up metal wall panel system with insulating batts and interior metal liner panel. The minimum thermal resistance of the system will be R-20.

The roof of the service buildings will be a TPO membrane roofing system. It will consist of a standing seamed roof over R30 rigid insulation, gypsum board sheathing, and structural metal roof deck.

The exterior doors of the service buildings will be insulated hollow metal doors and hollow metal frames.

Each service building will be provided with a 10 ft x 10 ft opening that may be filled with concrete block as portable shielding, or be used for a superdoor (borolated polyethelene-filled steel door) installation. The superdoors are not included in the conventional facilities portion of the project.

13.5.3.7.4 Linac and RF Buildings

The exterior walls of the Linac and RF Buildings will be 3 in. insulated metal wall panels, on a steel girt system. The minimum thermal resistance of the system will be R-20. Interior walls shared with the ring tunnel will be concrete of sufficient thickness to provide adequate radiation shielding.

The roof of these buildings will be a TPO membrane roofing system. It will consist of a standing seamed roof over R30 rigid insulation, gypsum board sheathing, and structural metal roof deck. In specific locations over the linac and the RF test room, shielding with 1 m thick concrete roof will be required.

The exterior doors of the Linac and RF Buildings will be insulated hollow metal doors and hollow metal frames.

13.5.3.8 Interior Finishes

13.5.3.8.1 Experimental Hall

The Experimental Hall will have the following interior finishes:

- Floor finishes – sealed concrete
- Exterior walls – factory-finished wall panels
- Interior walls – factory finished steel or concrete or gypsum board walls – painted
- Acoustic treatment on ceiling and walls
- Steel – painted
- Roof Structure – painted
- Doors – painted

13.5.3.8.2 Ring Tunnel

The ring tunnel will have the following finishes:

- Floor finishes – sealed concrete
- Interior and exterior concrete walls – painted
- Concrete roof structure – painted

13.5.3.8.3 Service Buildings

The service buildings will have the following finishes:

- Floor finishes – Sealed concrete
- Exterior wall – Factory-finished wall panels
- Interior and exterior concrete walls – painted
- Steel – painted
- Doors and frames– painted or factory finished.

13.5.3.8.4 Linac and RF Buildings

The Linac and RF Buildings will have the following finishes:

- Floor finishes – Sealed concrete
- Exterior wall – Factory-finished wall panels
- Interior walls – factory-finished steel or concrete or gypsum board walls – painted
- Steel – painted
- Roof Structure – painted
- Doors – painted

13.5.4 Lab Office Buildings (WBS 1.6.3.5)

13.5.4.1 Architectural Concepts

Five LOBs will be spaced around the exterior of the Ring Building. Four will be independent modules and one will be incorporated into the CLOB. The LOBs will be the primary entrance for many researchers. A focus on interactive spaces will provide an environment where collaboration is encouraged.

13.5.4.1.1 Alternatives – Building Configuration

Single-story buildings – Single-story buildings with labs along the Ring Building access corridor and offices and other spaces outboard of the labs. Ground level entrance from adjacent parking provides convenient access for research staff and visitors. This is the preferred alternative.

Two-story buildings – Two-story buildings with labs along Ring Building access corridor and offices above the labs on the second level. This alternative was not selected because of difficult circulation between labs and offices, and each LOB would require stairs and an elevator to meet ADA requirements.

Integral long beamlines – This concept was a single-story LOB design with integral beamline hutches built into the LOB to accommodate potential long beamlines. This configuration was not selected because the beamlines caused discontinuities in the LOB floor plan and because of the uncertainty of needing 100 m beamlines. Additionally, the LOB size had to increase to accommodate the hutches, adding cost to the conventional facilities.

13.5.4.1.2 Future Expansion

The five Lab Office Buildings are being designed with the intent of future expansion. Each LOB is being initially programmed to support six sectors, with one insertion device and one bending magnet beamline per

sector. If additional beamlines are added by canting insertion device beamlines, the LOBs will need to expand to support these. The LOBs are designed to expand horizontally along the outside of the Ring Building as future need demands. Services to any expansion, including HVAC, plumbing, power, etc. will be added at the time of the expansion. They are not included in the initial scope of the project.

13.5.4.2 Space Program

Each LOB will contain 30 offices, 10 laboratory modules, a conference room, storage, a kitchenette, and a loading platform. The intent of the Lab Office Buildings is to provide support space for experimentation that is close to the beamlines. Each LOB will support six sectors in the Experimental Hall. The LOB will provide five offices for each supported sector. The five laboratories will be shared by all six sectors to minimize duplication of space requirements and lab equipment. Each laboratory will have direct access to the Experimental Hall access corridor via double doors for moving equipment between them.

13.5.4.3 Circulation

Each Lab Office Building will be one story high and have a parking lot adjacent to the building and an exterior entrance that will be the primary entrance for most researchers and visitors. Direct access to the Experimental Hall will be provided from the lobby/interaction area and will be a secure entrance. Equipment and materials will be brought into the building from a loading platform that will also allow equipment to be conveniently moved into the Experimental Hall. Pedestrian traffic to other LOBs or to the CLOB will be via the access corridor around the perimeter of the Ring Building.

13.5.4.4 Quality of Life

The Lab Office Buildings will be home to staff and visitors who frequently work long and irregular hours. The glass storefront exterior walls will bring natural light into the office space. The glass façade and the relatively small size of the LOBs will create a contrast to the massive form of the Ring Building and will break down the scale. Open space with comfortable seating will encourage cooperative interactions between research teams. Covered outdoor seating will provide additional space to unwind and interact. A kitchenette will include a sink, refrigerator, and microwave for preparing simple meals. Comfort facilities will include toilets and a shower in each LOB. The building materials and use of natural lighting will provide the Lab Office Buildings with a pleasant work environment.

13.5.4.5 Foundations

Foundations are expected to be spread footings for columns and continuous strip footings for walls, based on similar foundation system for the CFN Building in the immediate vicinity.

13.5.4.6 Building Superstructure

These are single-story structures with framed/braced structural steel construction. The roof will be a 20 GA 1 ½ in. thick steel roof deck supported on structural steel beams and girders. The use of steel beams/girders will provide better support for the mechanical roof top units.

The first floor construction will consist of 6 in. thick slab on grade reinforced with 6x6 – W2.9 x W2.9 WWF over 6 in. of compacted granular fill and a vapor barrier.

13.5.4.7 Building Construction

The exterior walls of the LOBs will be comprised of a 3 in. insulated metal wall and exterior metal stud system. The system will be comprised of the insulated metal panel, 6 in. exterior metal studs, and interior gypsum board. The minimum thermal resistance of the system will be R-24.

The roof of the LOBs will be a standing seamed metal roof system. The system will be comprised of the standing seamed roof over R30 rigid insulation, vapor barrier, and structural metal roof deck. There will be an AHU mezzanine within the roof space for air-handling equipment serving the LOB.

The curtain wall windows at the LOBs will consist of 1 in. clear tempered insulated glass with a low-E coating in a thermally broken aluminum frame. The thermal transmission value for the glazing will be a U value of 0.30 in the summer and 0.30 in the winter. The visible light transmission will be 69% and the shading coefficient will be a maximum of 0.44.

The exterior doors will be curtain wall aluminum insulated doors to match the windows or insulated hollow metal doors and frames.

13.5.4.8 Interior Finishes

The LOBs will have gypsum board walls with wood doors and hollow metal frames. The offices will have a side light or interior window to allow natural light into the interior spaces. The interior finishes of the LOBs are as follows:

- Floor finishes, office area and conference rooms – carpet tile
- Floor finishes, laboratories – sheet linoleum
- Floor finishes, lobby – porcelain ceramic tile
- Exterior walls - painted
- Interior walls, offices and labs – painted
- Interior walls, conference rooms – paint or wall coverings
- Ceiling system – suspended acoustical tiles and grid
- Doors – stained wood
- Door frames – painted

13.5.5 Structural Materials

This section covers structural materials for all buildings included in the NSLS-II scope. This includes work in WBS numbers 1.6.3.2 – Site Preparation, 1.6.3.3 – Central Lab Office Building, 1.6.3.4 – Ring Building, 1.6.3.5 – Lab Office Buildings, and miscellaneous structural materials for WBS 1.6.3.6 – Mechanical Utilities, and 1.6.3.9 – Electrical Utilities.

13.5.5.1 Concrete (normal weight, unless noted otherwise)

- Foundation and slab on grade: f'c = 4000 psi
- Piers, walls, grade beams, slabs and stairs on grade: f'c = 4000 psi
- Light weight concrete for Second Level Floor: f'c = 4000 psi
- High density concrete for radiation shielding: f'c = 4000 psi; density = 250 lb/ft^3 nominal

13.5.5.2 Reinforcing Steel

- Deformed: ASTM 615, Grade 60
- Welded wire fabric: ASTM A185

13.5.5.3 Structural Steel

- Wide flanges and tees: ASTM A992, Fy = 50 ksi
- Channels, angles and plates: ASTM A36, Fy = 36 ksi
- Steel pipes: ASTM A53, Type E or S, Grade B, Fy = 35 ksi
- Structural tubes: ASTM A500, Grade B, Fy = 46 ksi
- Anchor bolts: ASTM F1554, 3/4 in. dia. min.
- Bolts: ASTM A325, 7/8 in. dia. min.

13.5.6 Mechanical Utilities

This section includes all site mechanical utilities identified as WBS 1.6.3.6 as well as building mechanical utilities systems included as a part of WBS numbers, 1.6.3.3 – Central Lab Office Building, 1.6.3.4 – Ring Building, 1.6.3.5 – Lab Office Buildings.

13.5.6.1 Mechanical Systems

Mechanical HVAC and piping systems will be provided to meet the environmental control needs of NSLS-II. The following systems are included:

- General HVAC
- Accelerator tunnel HVAC
- Experimental Hall HVAC
- Linac and RF Buildings HVAC
- General exhaust – Experimental Hall
- General exhaust – Lab Office Buildings
- Chilled water
- Process Cooling Tower water
- Steam
- Condensate
- Heating water

Specific details of each of these systems are described below.

13.5.6.1.1 General HVAC

Scope/Major elements	Air handling units
	Ductwork and accessories
	Controls
Redundancy	No redundancy
Humidification type	Steam
Coverage	Central Lab Office Building
	Lab Office Buildings
	Service buildings
Materials of construction	
Plenum	Galvanized steel
Filters	30% pre-filters and 95% final filters
Coils	Copper
Ductwork and accessories	Galvanized steel, insulated

Air handling units serving the Central Lab Office Building and the Lab Office Buildings will be commercial grade units. They will have 2 in. double wall construction, galvanized steel interior liner, and stainless steel condensate drain pan. Air handling units will be located in enclosed penthouse or mezzanine areas on top of their respective buildings.

Air handling units will have return fan, relief air section, mixing section, 30 % pre-filters, 95% pre-filters upstream of coils, steam preheat coil, cooling coil, centrifugal fan, and humidifier.

All units will be installed in draw-through configuration providing good dehumidification and even air flow through the cooling coil.

Supply and return fans will be centrifugal, belt-driven and will have high efficiency airfoil blades and AMCA label. They will be dynamically balanced after installation on the job site. Air filters will be replaceable cartridge type with filter efficiencies based on NBS Atmospheric Dust Spot Method. Their sizes will be standardized 24 x 24 and 12 x 24 in. where possible. Supply and return fans of all air handling units will have Adjustable Frequency Drives. All air handling units will have economizer cycle controls.

13.5.6.1.2 Accelerator Tunnel HVAC

Scope/Major elements	Air handling units
	Ductwork and accessories
	Controls
Redundancy	No redundancy
Temperature control	±0.1 °C (±0.18 °F)
Humidification type	Steam
Coverage	Accelerator tunnel
Materials of Construction	
Plenum	Galvanized steel
Filters	30% pre-filters and 95% final filters
Coils	Copper
Ductwork and accessories	Galvanized steel, insulated

The building/accelerator tunnel HVAC systems consist of multiple air handling units located in the five service building Mechanical Equipment Rooms (MER), each servicing one fifth of the tunnel circumference. The tunnel supply and return ducts are shown in Figure 13.5.1 and the corresponding HVAC equipment in the MER is shown in Figure 13.5.2. The air handling units will have 2 in. double wall construction, galvanized steel interior liner, and stainless steel condensate drain pan. The AHU serving the tunnel will include a return fan, relief air section, outside air intake, 30% pre-filter, 95% final filter, steam preheat coil, cooling coil, supply fan, humidifiers, hot water reheat coil, and duct-mounted low heat density electric reheat coil for final accurate temperature control and an SCR controller. The supply and return fans will have Adjustable Frequency Drives (AFD) for future flexibility and to provide ease of adjustment during balancing. Air will be cooled to as low as 50°F for proper dehumidification, and reheated to required discharge temperature. Cooling temperature will be reset based upon tunnel relative humidity to maintain RH setpoint and save energy. Most of the reheat will be with hot water. The final discharge temperature will be controlled by electric reheat coils responding to duct sensors in the main supply duct. Tunnel sensors will reset the discharge temperature setpoint to maintain the tunnel section temperature.

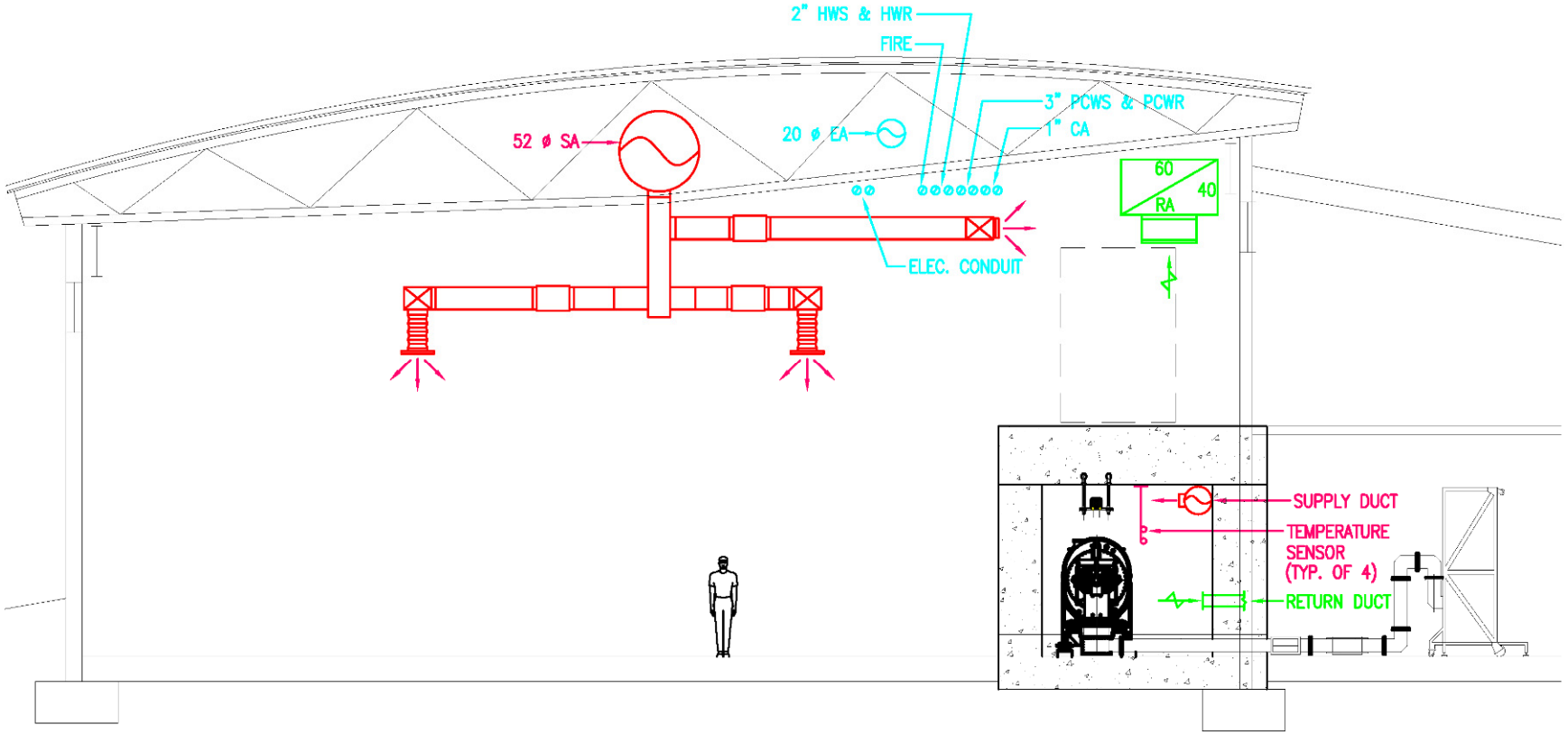

Figure 13.5.1 Cross-section view of Experimental Hall and storage ring tunnel HVAC supply and return ducts.

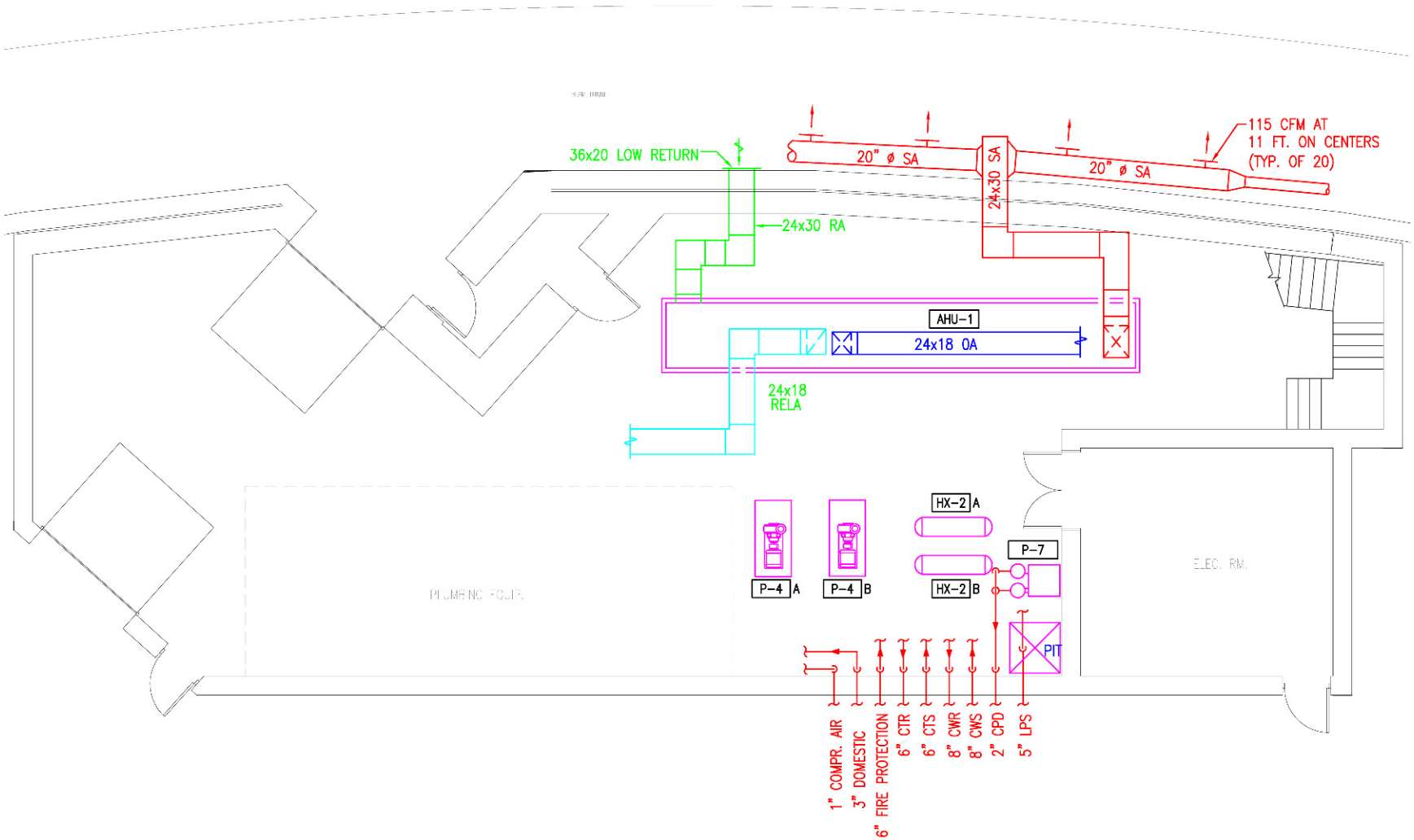

Figure 13.5.2 HVAC units servicing accelerator tunnel, located in lower level of MER.

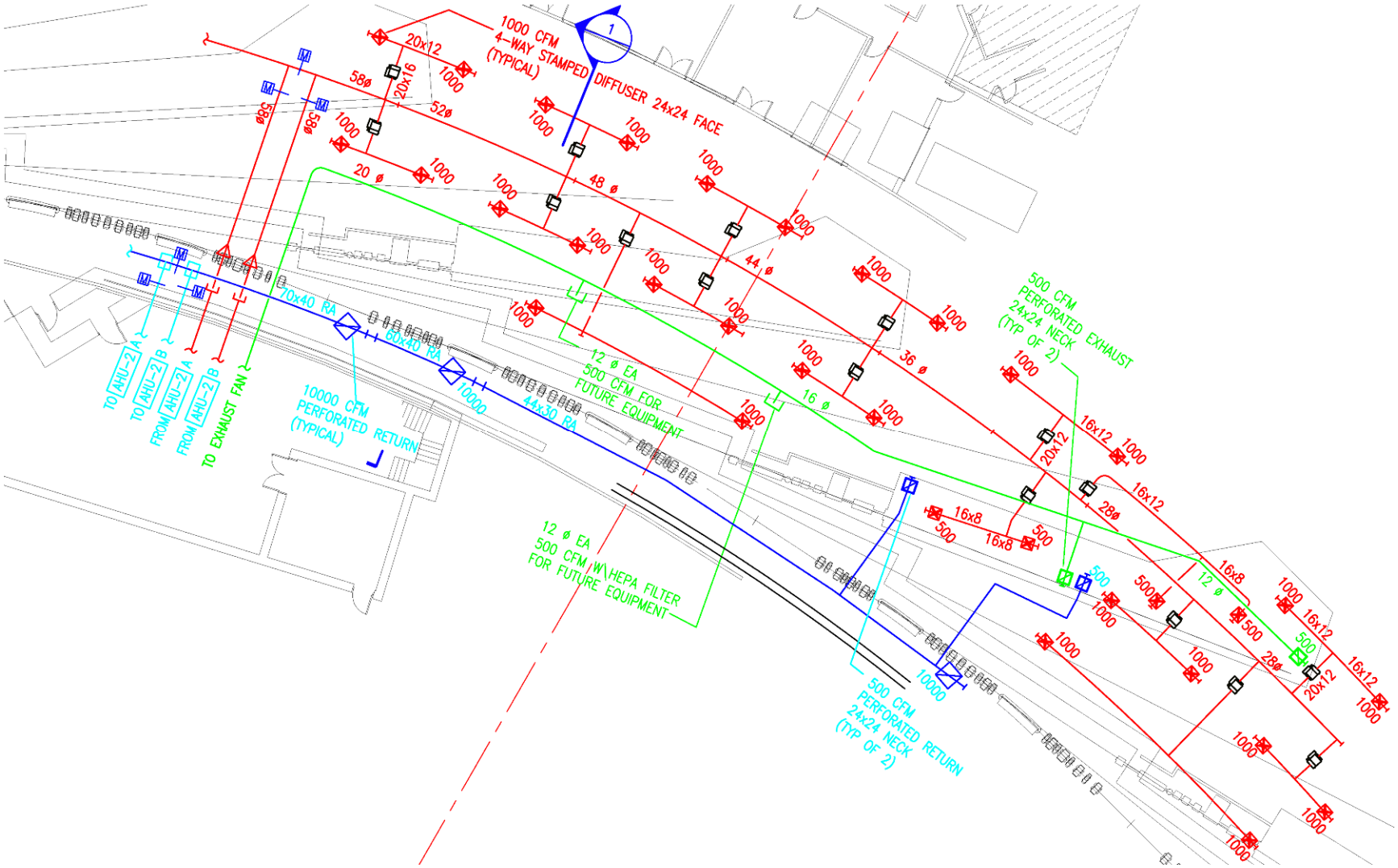

Figure 13.5.3 Floor plan layout of one half of HVAC supply and return ducts for Experimental Hall from AHU in one MER.

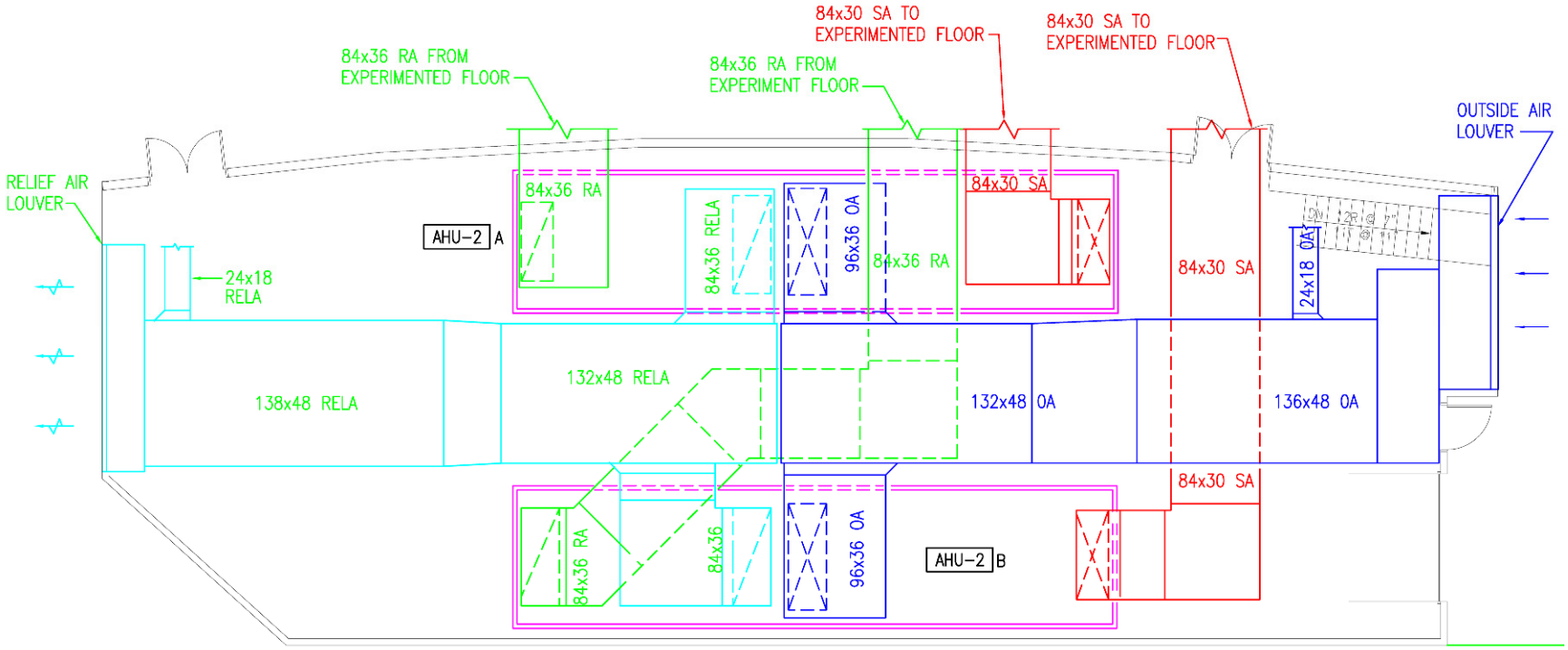

Figure 13.5.4 HVAC units servicing Experimental Hall, located in upper level of MER.

13.5.6.1.3 Experimental Hall HVAC

Scope/Major elements	Air handling units
	Ductwork and accessories
	Controls
Redundancy	No redundancy
Temperature control	±1.0 °F
Humidification type	Steam
Coverage	Experimental Hall
Materials of construction	
Plenum	Galvanized steel
Filters	30% pre-filters and 95% final filters
Coils	Copper
Ductwork and accessories	Galvanized steel, insulated

The Experimental Hall HVAC systems consist of multiple air handling units located in the five service building Mechanical Equipment Rooms (MER), each serving one fifth of the Experimental Hall. A radial cross-section view of the Experimental Hall supply and return ducts is shown in Figure 13.5.1 and the floor plan layout of one half of the HVAC supply, return, and exhaust ducts is shown in Figure 13.5.3. The corresponding HVAC equipment in the MER is shown in Figure 13.5.4.The AHUs will have 2 in. double-wall construction, galvanized steel interior liner, and stainless steel condensate drain pan. The potential for using heavier construction to minimize noise and vibration will be evaluated further in Title I design. The air-handling units will include return fan, relief air section, outside air intake, 30% panel filter, 95% pre-filter, steam preheat coil, cooling coil, supply fan, humidifiers, hot water reheat coil, and sound attenuators. The supply and return fans will have Adjustable Frequency Drives (AFD). Air will be cooled to as low as 50°F for proper dehumidification, and reheated to required discharge temperature. Temperature control in the Experimental Hall will be achieved using VAV boxes with hot water reheat coils.

The building/accelerator tunnel HVAC systems consist of multiple air handling units located in the five service building Mechanical Equipment Rooms (MER), each servicing one fifth of the tunnel circumference. The tunnel supply and return ducts are shown in Figure 13.5.1 and the corresponding HVAC equipment in the MER is shown in Figure 13.5.2.

13.5.6.1.4 Linac and RF Building HVAC

Scope/Major elements	Air handling units
	Ductwork and accessories
	Controls
Redundancy	No redundancy
Temperature control	±1.0°F
Humidification type	Steam
Coverage	Linac and RF Buildings
Materials of construction	
Plenum	Galvanized steel
Filters	30% pre-filters and 95% final filters
Coils	Copper
Ductwork and accessories	Galvanized steel, insulated

The Linac and RF buildings will be served by an air handling unit to provide fresh air ventilation and provide cooling to the space. The unit will be sized for 6 air changes per hour but will normally deliver two air changes per hour. Air handling units will have direct chilled water cooling.

13.5.6.1.5 General Exhaust – Experimental Hall

Scope/Major Elements	Exhaust fans
	Ductwork and accessories
Redundancy	N+1
Coverage	Experimental Hall - beamlines
	Hazardous material storage
	Other areas requiring exhaust
Materials of Construction	
Ductwork and accessories	Galvanized steel, insulated

Exhaust for the Experimental Hall will be provided by 10 exhaust fans – 2 in each service building. Each set of two fans will be tied together to provide full redundancy. Exhaust branches will have flow control devices to minimize balancing requirements as new loads are brought on line. This system will be available to provide general exhaust for the Experimental Hall, hutches, chemical storage cabinets, and specific equipment as needed. Other special exhaust requirements will be addressed individually as they are identified.

13.5.6.1.6 General Exhaust – Lab Office Buildings

Scope/Major elements	Exhaust fans, non-sparking
	Ductwork and accessories
Redundancy	N+1
Coverage	Laboratories with fume hoods
	Hazardous material storage
	Mechanical equipment rooms
	Toilets and showers
	Other areas requiring exhaust
Materials of construction	
Ductwork and accessories	Galvanized steel, insulated

Each Lab Office Building, including the CLOB, will be provided with an independent exhaust system. General exhaust mains and hood exhaust branches will have flow control devices to minimize balancing requirements during future changes. Exhaust fans will discharge the air at high velocity to prevent re-circulation. In each LOB, one of the laboratory exhausts will be HEPA filtered. Fume hood and hazardous materials storage cabinet exhaust systems will be segregated from toilet and general room exhaust systems.

13.5.6.1.7 Chilled Water

Scope/Major elements	Piping and accessories
Redundancy	Redundant chillers and pumps provided at the Central Utility Plant
Capacity	2400 ton peak load
Chilled water supply temperature	45°F
Chilled water return temperature	57°F
Differential pressure	35 psig
Piping velocity	4-6 FPS maximum
Coverage	Tunnel and Experimental Hall AHUs
	General air handing units – CLOB & LOB
Process cooling water heat exchangers	
Materials of construction	
Piping	Carbon steel, insulated
Valves	Butterfly or globe, carbon steel

The central chilled water system has primary pumps associated with each chiller in the central utility building and secondary pumps to circulate chilled water through the campus distribution system. The NSLS-II facility will be served by 24 in. chilled water supply and return fed by the campus distribution system. There will be no tertiary pumping in the building. Secondary chilled water pumps will have AFDs. Chilled water will enter NSLS-II and will be distributed underground in the interior annulus of the building and distributed underground to each service building. A flow meter will be located at the building entry point to monitor total chilled water flow to NSLS-II. Chilled water will serve air handling units, process cooling water heat exchangers, and miscellaneous cooling equipment. See Figure 13.5.5 for the location and routing of chilled water utilities to the site.

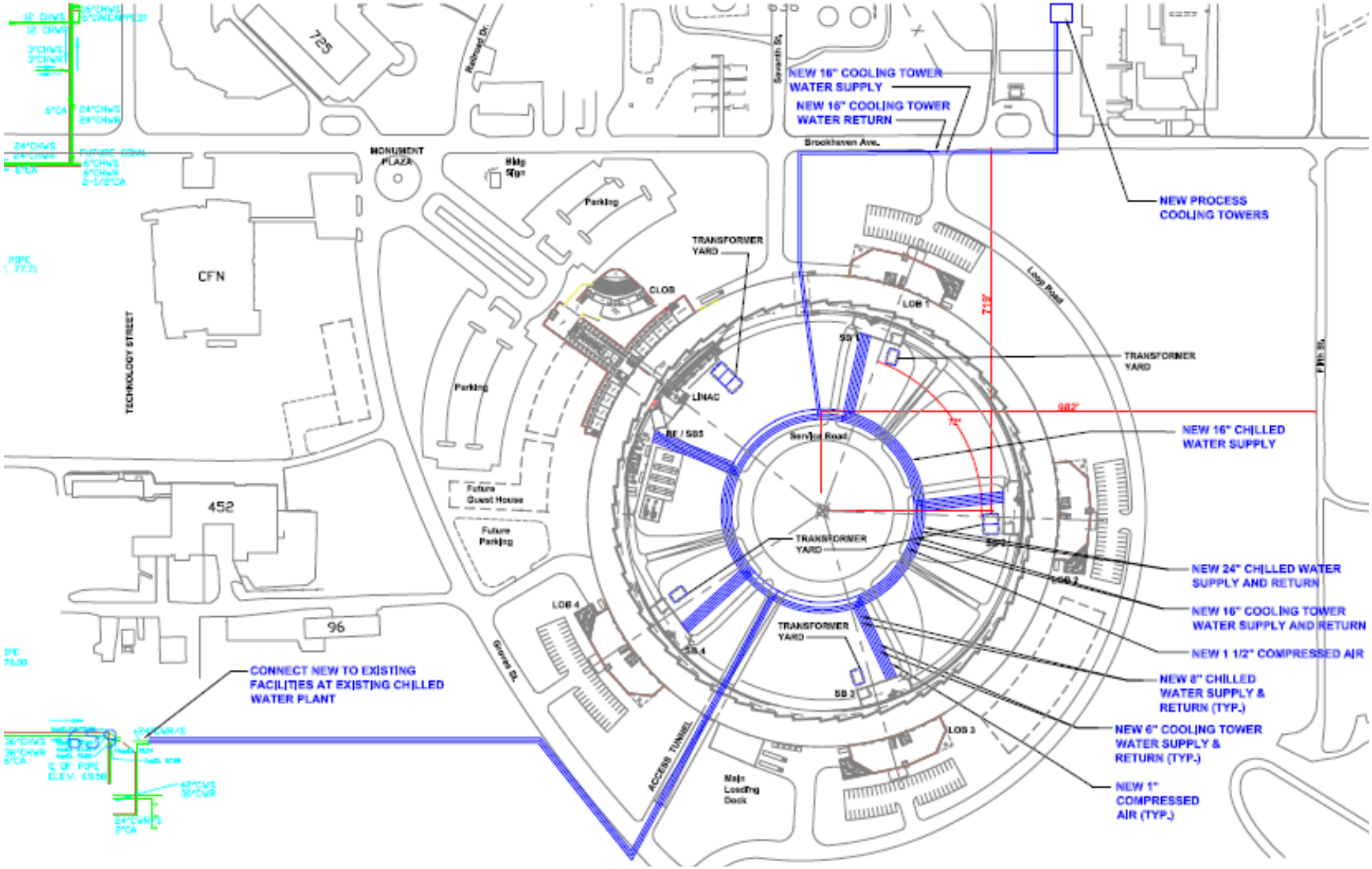

Figure 13.5.5 Chilled water utility plan.

13.5.6.1.8 Process Cooling Tower Water

Scope/Major Elements	Cooling towers
	Pumps
	Mechanical strainers/ side stream filtration
	Piping and accessories
Redundancy	N+1 tower cells and pumps
Capacity	2700 Ton peak load (three cells at 1350 ton each)
Tower water supply temperature	82°F
Tower water return temperature	97°F
Make-up source	Potable water
Coverage	Process cooling water system
Materials of Construction	Galvanized steel with "Baltibond" finish, PVC fill
Basins	Stainless steel
Fans	GRP
Piping	Carbon steel
Valves	Butterfly or globe, carbon steel
Pumps	Bronze impeller
	Carbon steel shaft
	Cast ion casing
Filters	Carbon steel shell and mesh
	Freeze protection, AFD for fans

The process cooling tower water system will provide primary cooling for the process cooling water system. This system will be designed to operate year-round. The process cooling water heat exchangers and piping systems are not part of conventional construction.

13.5.6.1.9 Steam

Scope/Major elements	Underground steam piping in conduit
	Pressure reducing valve (PRV)
	Hot water generator
	Humidifiers
	Piping and accessories
Redundancy	Dual PRV station
Capacity	17,000 lb/hr
Steam supply pressure in two stages	125 psig reduced to 15 psig in the service buildings
	125-50 psig; 50-15 psig
Coverage	AHUs in Ring Building, LOBs, and CLOB
	Hot water generator
Materials of Construction	
Piping	Carbon steel, insulated
Valves	Gate or globe, carbon steel
Heat exchanger	Carbon steel shell, copper tubes

Steam is available at the site from the Central Steam Plant at 125 psig and will be reduced to 15 psig at NSLS-II. The estimated peak steam load of the new building is 17,000 lbs/hr. The size of the underground

steam supply into the building is 6 in. Steam flow will be measured for energy calculations. See Figure 13.5.6 for routing of steam and condensate utilities.

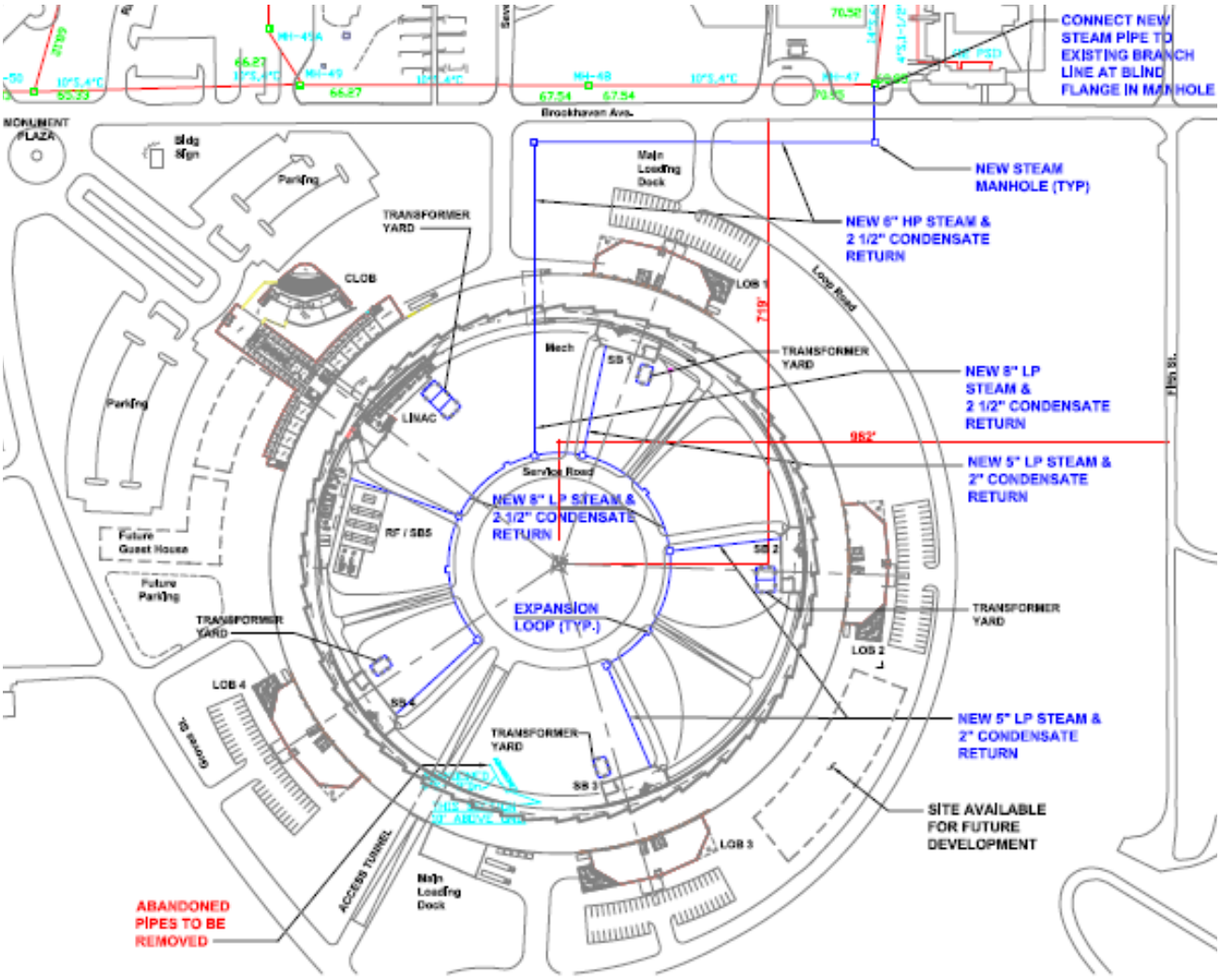

Figure 13.5.6 Steam Utility Plan.

13.5.6.1.10 Condensate

Scope/Major elements	Receivers
	Piping and accessories
Redundancy	Duplex pumping sets
Coverage	AHUs in Ring, LOBs, and CLOB
	Hot water generator
Materials of construction	
Piping	Sch. 80 carbon steel, insulated
Valves	Globe, carbon steel

The condensate will be collected in duplex receivers and returned to the Central Steam Plant via the site 40 psig pumped main in a 3 in. schedule 80 carrier pipe.

13.5.6.1.11 Heating Water

Scope/Major elements	Heat exchangers
	Pumps
	Piping and accessories
Redundancy	N+1 equipment
Capacity	
Heating water supply temperature	180°F
Heating water return temperature	160°F
Piping velocity	4-6 FPS maximum
Coverage	Tunnel and Experimental Hall AHUs
	CLOB and LOB
Service buildings	
Materials of construction	
Heat Exchanger	Copper tubes, carbon steel shell
Piping	Carbon steel, insulated
Valves	Butterfly or ball, carbon steel
Pumps	Bronze impeller
	Carbon steel shaft
	Steel Casing

Steam will be used to produce heating water in shell and tube heat exchangers located in the service buildings. Heating water will be distributed to the terminal re-heat coils.

13.5.6.2 Plumbing Systems

13.5.6.2.1 Potable Water

Scope/Major elements	Water heaters
	Piping and accessories
	Safety showers/ eye washes
Redundancy	Two mains, with multiple connection points to the site system will connect to form a looped system feeding the building.
Cold water supply temperature	Ambient
Hot water supply temperature	See Narrative below
Coverage	Experimental Hall
	CLOB
	LOB
Service buildings	
Materials of construction	
Piping	4 in. and over: Ductile iron, cement lined (buried)
	3 in. and under: Copper (above ground)
Valves	Ball, globe or gate, bronze
Pumps	Stainless steel impeller, shaft
	Mechanical seals
	Ductile iron casing
Tanks	Galvanized steel (storage)
	Stainless steel or glass lined (water heaters)
Remarks	Disinfected to code requirements

The existing potable water system along the north of the site along Brookhaven Avenue connects to a 12 in. line at North Sixth Street. The 8 in. line parallel to Seventh Street will be relocated away from the footprint of the NSLS-II buildings. A new 8 in. water line will be constructed under the parking lot to the west of the building footprint and reconnect to the Seventh Street line south of the site. See Figure 13.5.7 for location of potable tie-in points and routing of piping.

One tie-in will be installed in the 12 in. line at Brookhaven Avenue and North Sixth Street. The second tie-in will be to the 8 in. relocated line west of Seventh Street. These two 8 in. lines will feed the potable water loop in the Ring Building infield.

A section of the 8 in. water line east of Groves Street interferes with the proposed location of the future Guest House building footprint. This line will also need to be relocated for the Guest House to be constructed.

Potable water serving the facility will be used for both the domestic and laboratory plumbing fixtures and equipment. The available pressure is estimated at 60 PSI. All mains into the building will be protected by a backflow prevention device. Water filtration will be at point of use if needed.

Laboratory faucets will incorporate integral vacuum breakers, and make-ups to mechanical and laboratory equipment will be provided with appropriate backflow prevention devices.

Domestic hot water will be provided at each laboratory building MER and include a circulated piping system. Hot water will be produced by a storage type electric water heater. The hot water will be stored at 140°F and distributed to lavatories and laboratory fixtures at 120°F through a thermostatic mixing valve.

A tempered (85°F) water distribution piping system will be provided through a thermostatic mixing valve and used as the source for the emergency fixtures located throughout each laboratory building. The system will be circulated.

Type "L" copper tubing with wrought copper or cast brass fittings and solder joints will be the pipe material. The pipe joints will be formed with 95-5 tin-antimony solder or code approved "lead free" solder and flux having a chemical composition equal to or less than 0.2-percent lead. Piping 2 in. and smaller may be joined with fittings utilizing a copper crimping system such as the Rigid/Viega ProPress System. 2½ in. piping and over may be schedule 40 galvanized steel with threaded or mechanical couplings (Victaulic style connections). The piping will be insulated with fiberglass pipe insulation having an all service jacket and self-sealing lap.

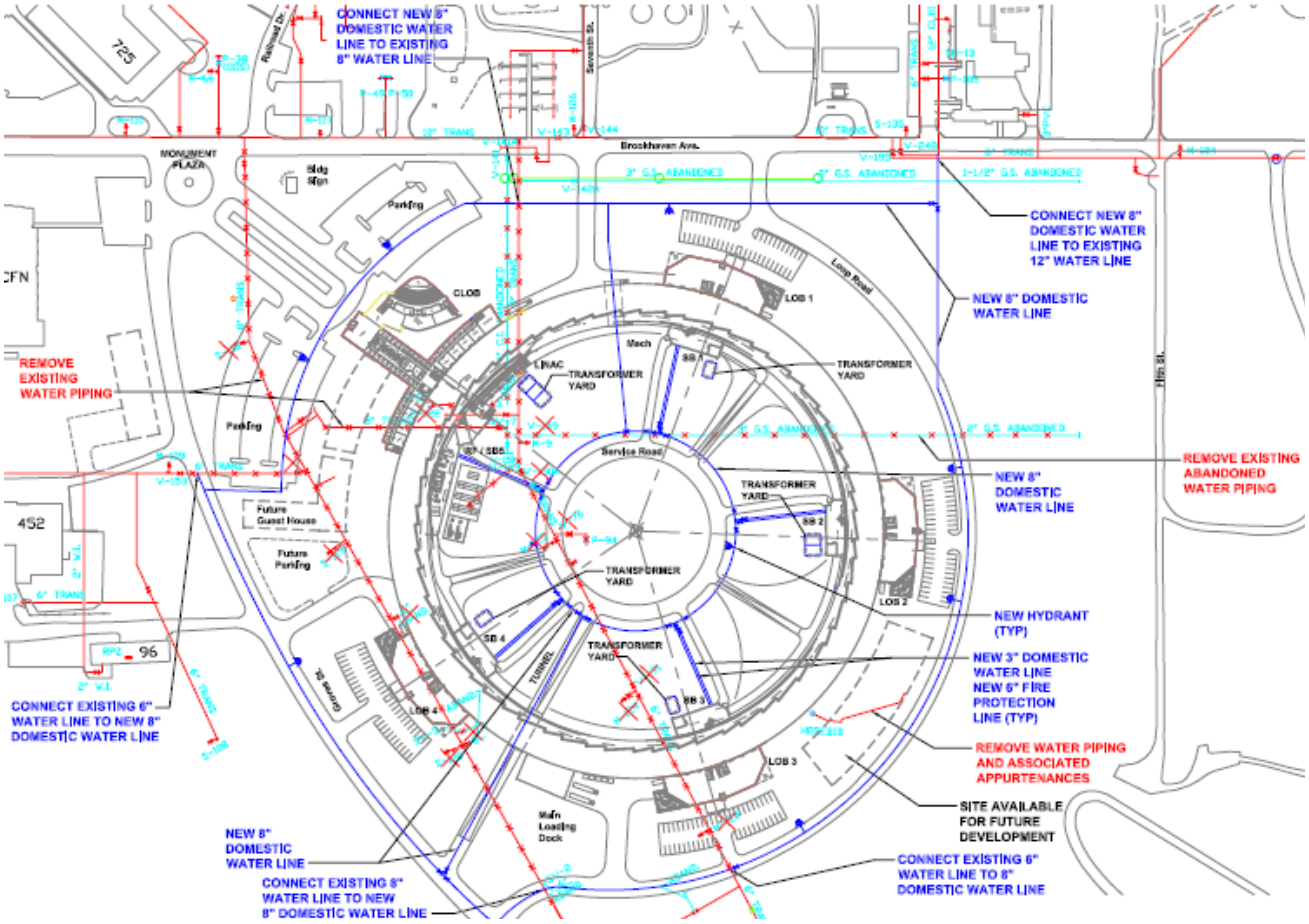

Figure 13.5.7 Potable Water Utility Plan.

13.5.6.2.2 Sanitary

A new 10 in. sanitary line will be constructed in the proposed parking lot to the west of the existing sewer. The new line would extend as a gravity line to just east of Groves Street and be located to the north of the future Guest House. The extension of the existing system to the south includes an underground pumping station, which is located in close proximity to the proposed layout of the outer ring road. The pumping station would be relocated to just to the east of Groves Street and a forced main would connect to the new 10 in. sanitary line. Construction would involve roughly 1000’ of 10 in. sanitary sewer, 2000’ of 6 in. sanitary sewer, 500 ft of 6 in. force main and one new underground pumping station.

13.5.6.3 Process Systems

Process systems will be provided to NSLS-II to meet the needs of the accelerator, beamlines, and laboratories. The following process systems are included:

- Nitrogen
- Liquid nitrogen
- Compressed air
- Deionized water
- Deionized water make-up (technical facilities)
- Process Cooling Water (technical facilities)

13.5.6.3.1 Nitrogen

Scope/Major elements	Site nitrogen skid, evaporator
	Piping and accessories
Redundancy	None
Supply pressure	100 psig
Coverage	Experimental Hall
	Central Lab Office Building
	Lab Office Buildings
Materials of construction	
Piping	Type L hard-drawn copper, oxygen cleaned
Valves	Ball, full port, brass, 3-piece, oxygen cleaned

The source for gaseous nitrogen will be vaporizers installed at the liquid nitrogen tank. Primary distribution will occur in the Ring Building. Secondary mains serving the lab/office buildings will be valved to permit isolation for maintenance and modifications. Branches serving individual laboratory modules will be valved.

Piping material will be type L copper tubing with wrought copper fittings and solder joints utilizing 95-5 tin-antimony solder.

The gaseous nitrogen distribution system will be designed to maintain a maximum pressure drop of 10-percent from the point of discharge to the farthest outlet.

13.5.6.3.2 Liquid Nitrogen

Scope/Major elements	Site nitrogen skid
	Piping and accessories
Redundancy	None
Coverage	Experimental Hall
	RF Building
Materials of construction	
Piping	Vacuum jacketed

Liquid nitrogen will be stored in a centrally located tank (location to be determined). Primary distribution will occur in the Ring Building with connection points available for beamline use. Filling stations will be provided at each lab/office building to permit dewars to be filled.

The piping distribution system will be through vacuum jacketed piping with either a dynamic or static vacuum. The piping shall contain an inner carrier tube and an exterior jacket. The annular space shall be

under vacuum and have appropriate spacers. The system components (piping, fittings, valves, etc.) shall be products manufactured by, or provided by, a single manufacturer and not built up assemblies.

13.5.6.3.3 Compressed Air

Scope/Major elements	Filter / dryer skids
	Piping and Accessories
Redundancy	100 scfm oil free back-up compressor / dryer skid
Capacity	100 scfm
Supply pressure	100 psig from site system
	95 psig after regulator
Quality	Oil free
Moisture	-20°F dew point
Particulate	1 micron
Coverage	Experimental Hall
	Central Lab Office Building
	Lab Office Buildings
	Service buildings
Materials of construction	
Piping	Hard-drawn copper, brazed
Valves	Ball, full port, brass

The source for the laboratory compressed air will be the site wide 100 PSIG system. The site system is oil free, filtered, clean, and dried to minus 20°F dew point.

To assure clean, dry compressed air delivery to the laboratories, the incoming service will be provided with a 1 micron coalescing filter to collect moisture and/or particulates originating in the site distribution piping. The filter will be designed to remove all particulates 1 micron and larger, and 100% of liquid water. A pressure regulator will be installed downstream of the filter and set for a discharge pressure of 95 PSIG. Individual connection points for personnel use will be provided with a regulator set limiting the pressure to 30 psig.

Piping for the system will be Type L copper tubing (ASTM B819) with wrought copper fittings and brazed joints. All components including valves will be cleaned for oxygen service and capped and/or bagged by the manufacturer for delivery to the site for installation. Assembly will be with brazing filler alloy without the use of flux.

13.5.6.3.4 Deionized Water

Scope/Major elements	DI water
	Point-of-use systems
Redundancy	
Capacity	
Supply temperature	78 F
Supply pressure	
Make-up water source	Potable water make-up system
Coverage	Lab Office Buildings Laboratories
Water quality	
Resistivity	1 mega-ohm/cm (min)
Materials of construction	
Piping	Sch. 80 polypropylene
Tanks	GRP, stainless steel
Valves	Diaphragm or ball, polypropylene
Pumps	Stainless steel

Each Lab Office Building that requires DI water as a consumable will be provided with a separate point-of-use water system. The system will include polishing, storage, and distribution components. Point-of-use polishing units will be installed in the laboratory designated for "wet use" in each LOB.

13.5.6.3.5 Deionized Water Make-up

Scope/Major elements	Pre-treatment plant
	DI water plant
DI water polishing skid	
	Pumps
	Piping and accessories
Redundancy	N+1 equipment
Capacity	TBD
Supply temperature	Ambient
Make-up water source	Potable water
Coverage	Process cooling water systems
	Deionized water system
Water quality	
Resistivity	1 mega-ohm/cm (min)
Materials of Construction	
Piping	Sch. 80 polypropylene
Tanks	GRP, stainless steel
Valves	Diaphragm or ball, polypropylene
Pumps	Stainless steel

The deionized water make-up system provides deionized quality water to both the DI water system used as a consumable in laboratories and to the process cooling water systems. The deionized water make-up system is included in the Technical Construction portion of the NSLS-II project. It is discussed in the Conventional Facilities chapter of the CDR for coordination purposes.

13.5.6.3.6 Process Cooling Water

Scope/Major elements	Heat exchangers
	Pumps
Filters	
	Piping and Accessories

The Linac, Aluminum and Non-Aluminum Process Cooling Water systems are included in the Technical Construction portion of the NSLS-II project. They are discussed in the Conventional Facilities chapter of the CDR for coordination purposes.

The process cooling tower water system will reject the majority of the process loads captured by the process water systems. Chilled water will be used to finely control the cooling water temperature. Plate and frame heat exchangers located in the MER spaces will reject heat to both the process cooling tower water system and the chilled water system. Process cooling water piping will be distributed around the perimeter of the Ring Building. Chilled water piping will be insulated to prevent condensation at low supply water temperatures. Cooling tower water and process cooling water systems will not require insulation.

13.5.6.4 Fire Protection Systems

13.5.6.4.1 Fire Water

Scope/Major elements	Fire water main
	Hydrants
	Piping, sprinkler heads and accessories
Redundancy	System loop is fed from two connection points to the site system
Capacity	Per Code
Coverage	Entire NSLS-II complex
Hazard classifications	
Accelerator tunnel	See narrative
Experimental Hall	See narrative
Office / Public spaces	Light hazard
Utility areas	See narrative
Gas cabinets	See narrative
Chemical storage areas	Extra hazard (Group 2)
Fire hose allowance	Per NFPA 13
Fusible link rating	As required for application
Minimum supply pressure	Main: TBD
Materials of construction	
Piping	Ductile iron, cement lined (buried)
	Sch. 40 black steel (above ground)
Valves	Butterfly or OS&Y
Pumps	

Two 8 in. fire services with post indicator valves will be extended from the site water mains. The actual available pressure has not been verified at this time. Fire flow data will be obtained during design. Each service will be provided with an Underwriters Laboratory and Factory Mutual listed reduced pressure backflow prevention device. A single combined full size bypass with a normally closed valve will also be provided. An additional site main will be extended below the building through a basement utility vault to the ring interior and provide the supply to fire hydrants located within the enclosed area.

A sprinkler system will be designed to provide 100-percent protection of the facility. Where the piping installation will be subject to freezing temperatures, dry sprinklers will be employed.

Interior piping will be Schedule 40 steel pipe. No other piping material will be acceptable. The piping will be joined by welding, threaded fittings, or cut groove fittings and couplings. Pipe and fittings used in dry pipe portions of the system will be galvanized inside and outside.

Unless otherwise indicated, the entire sprinkler system will be designed as an Ordinary Group 1 Hazard occupancy with 0.15 GPM/SF density. The remote hydraulic area will be calculated at 2500 ft^2.

A fire standpipe system is not required for this facility based on the Building and Fire Codes of New York State. However, per BNL's standards, 2-1/2 in. fire department valves connected to the sprinkler mains will be installed in each of the stair towers. The 2-1/2 in. fire department valves will have 2-1/2 in. x 1-1/2 in. reducers. Additional fire department valves may be located as required to achieve additional coverage.

Fire hydrants will be located along the Loop Road outside of the Ring Building and along the Service Road inboard of the Ring Building at distances meeting DOE and code requirements and not more than 300 ft from all building entrances.

13.5.6.5 Automatic Temperature Controls

NSLS-II will have an automatic temperature control system serving all buildings within the complex. The system shall be compatible with the existing WebCTRL Energy Management System (EMCS) as manufactured by Automated Logic Corp. The system shall have calibrated precision instruments for all critical environmental control points. The system shall interface with the EPICS-based control system utilized for control of accelerator systems.

13.5.7 Electrical Utilities

This section includes all site Electrical Utilities identified as WBS 1.6.3.9 as well as building electrical utilities systems included as a part of WBS numbers, 1.6.3.3 – Central Lab Office Building, 1.6.3.4 – Ring Building, 1.6.3.5 – Lab Office Buildings. See Figure 13.5.4 for location of electrical utilities to the NSLS-II site.

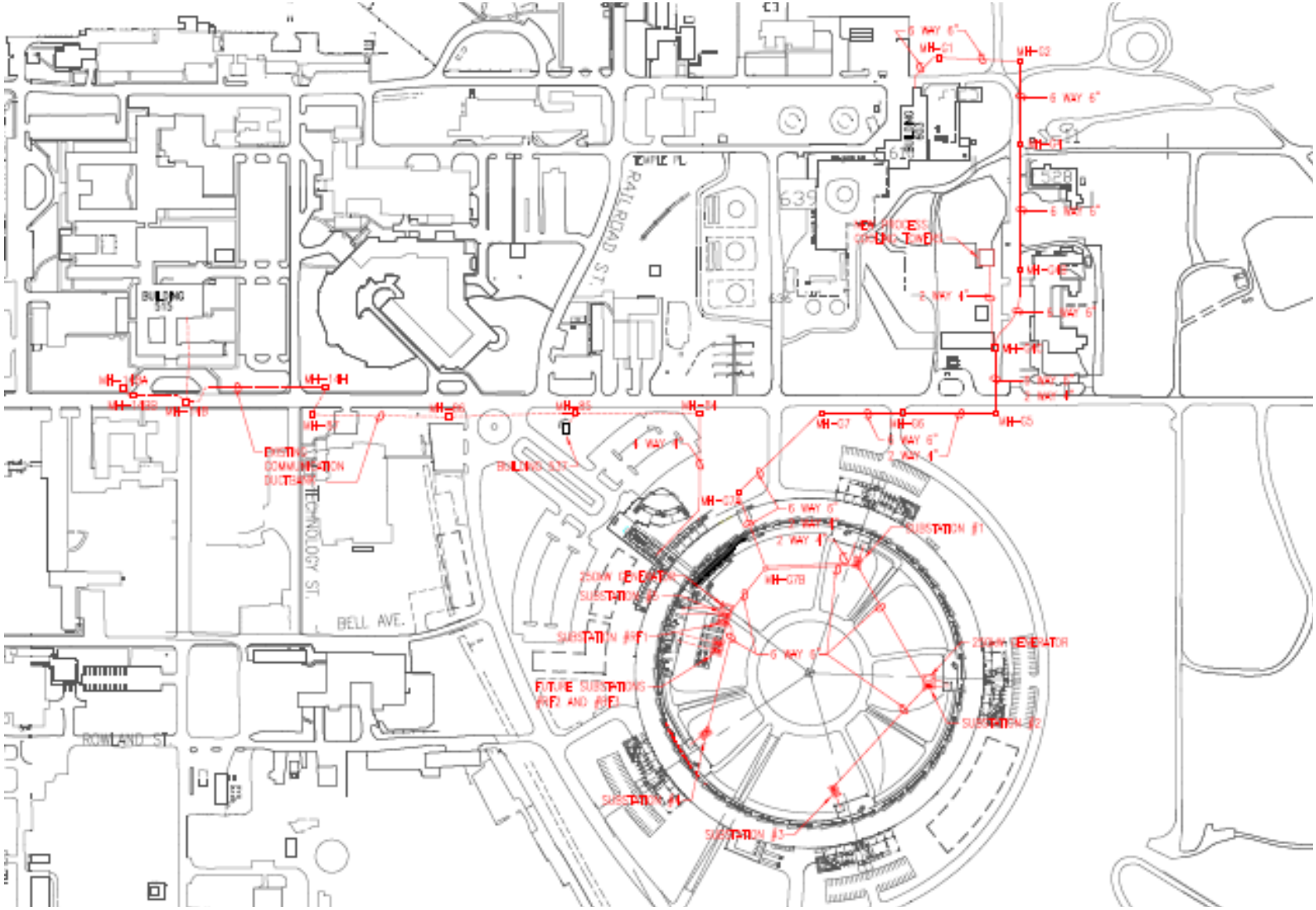

Figure 13.5.8 Electrical Site Utilities Plan

13.5.7.1 Site Utilities

13.5.7.1.1 Relocation and/or Demolition of Existing Utilities:

The scope of relocation and/or demolition of existing electric and communication utilities will be based on a utility survey and the final building footprint. At this time, it is assumed that existing utilities around the perimeter of the site are active and will remain, and that utilities across the site are abandoned and will be removed where they cross under the footprint of the building.

13.5.7.1.2 Power

Building 603, Campus Substation Expansion

The Building 603 campus substation will be expanded to include a fourth transformer to support the NSLS-II project.

The existing 69 kV substation yard will be modified to serve the new equipment. The two existing 69 kV potential transformers will be relocated. A new 69 kV SF6 breaker and a new 20.0/26.7/29.9 MVA, 66.0-13.8 kV transformer will be provided. A new fire separation wall will be provided between the existing transformer #3 and the new transformer.

Within Building 603, the existing walls around the storage room will be removed and a new 275 ft^2 addition with a roll-up door will be provided to house the relocated supplies.

The new Bus 0 15 kV SF6 metal-clad switchgear will be located over the existing cable trench and adjacent to the existing Bus 2 switchgear.

The Bus 0 switchgear will include a 2000 A main breaker, three 2000 A tie breakers to Bus 1, Bus 2, and Bus 3, one 1200 A outgoing breaker to feed the NSLS-II project, and three cells for future 1200 A outgoing breakers.

A new 2000 A tie breaker will be provided in each of the existing Bus 1, Bus 2, and Bus 3 switchgear lineups.

Modifications to existing switchgear will match their respective manufacturer's standards.

2000 A, 15kV busway will be utilized between the new transformer and the new switchgear, and to interconnect the new switchgear to each of the existing lineups.

Campus Distribution

The primary distribution system will be configured in a primary selective scheme. However, only one feeder will be provided with the base construction. The second feeder and new ductbank from Building 603 to MH-5E will be provided as an alternate or at some time in the future.

A new 800 A feeder consisting of two sets of 3-1/C, 1000 kcmil, 15 kV, 100% EPR copper conductors will be routed through the existing manhole and ductbank system from the Bus 0 switchgear in Building 603, along North Sixth Street to existing manhole MH-E5 at the intersection of Brookhaven Avenue and North Sixth Street. 100% insulation is provided in order to utilize the existing 5 in. ducts.

NSLS-II Site Distribution

An eight-way 5 in. concrete-encased ductbank will be routed from manhole MH-E5 to a manhole in the infield of the Ring Building via the basement utility room. A six-way 5 in. ductbank will than be routed around the infield interconnecting all the substations. Three ducts will serve the "A" switches and three ducts

will serve the "B" switches of the primary selective switchgear. An 800 A feeder consisting of two sets of 3-1/c, 1000 kcmil, 15 kV, 100% EPR copper conductors will be routed from MH-5E to the "A" switch of each substation. A 480 V feeder in two 4 in. ducts (minimum one spare) will be provided from switchgear #1 to the process cooling tower facility on the north side of Brookhaven Avenue via MH-E5B, E5A, E5, and E4.

One substation will be located at each service building 1 through 4. Two substations will be located at service building 5, which is associated with the Central Lab Office Building and the Linac and RF Buildings.

Each substation will consist of a primary switchgear, a 13,800-480Y/277 V, 2000, 2500, or 3000 kVA oil-filled substation type transformer, and a secondary air terminal section. The primary gear will be 15 kV outdoor, non-walk-in metal-enclosed switchgear with a key-interlocked duplex switch in series with one set of fuses. Each transformer will be triple rated 55˚ OA, 65˚ OA, and 65˚ FA. A ductbank and secondary feeder will be extended from the secondary air terminal cabinet to the switchgear located in the main electrical room of each service building.

13.5.7.1.3 Telephone and Data Communication

A new four-way 4 in. concrete-encased ductbank will be provided from existing manhole MH-84 to the BDF room in the Central Lab Office Building. The ductbank will be used for both copper and fiber optic cables.

Copper cables will be routed from Building 537 to the BDF via manholes MH-84 and 85.

Fiber optic cables will be routed from Building 515 near the intersection of Brookhaven Avenue and Rochester Street through existing ductbanks and manholes MH-14B, 14H, 87, 86, 85, and 84 and through the new four-way 4 in. ductbank from MH-84 to the BDF.

13.5.7.1.4 Street Lighting

New street lighting, matching the Brookhaven standard, will be provided along Brookhaven Avenue between Groves Street and the last vehicle entry point into the site, and along Groves Street between Brookhaven Avenue and its last vehicle entry point into the site. Lighting will also be provided in the parking lots, major pedestrian walkways, and the entrance to the CLOB.

The street lights will be circuited to building lighting panels via the building low-voltage lighting control panels.

13.5.7.2 Normal Power Distribution

13.5.7.2.1 Service Buildings Power Distribution

One 3000 A or 4000 A, 480Y/277 V, 3-phase, 4-wire switchgear will be located in each of the five service building main electrical rooms. A sixth switchgear will be located in the main electrical room of the service building associated with the Linac/RF Building. Each switchgear will include a main breaker section, and two or more distribution sections. The main sections will contain a drawout power air circuit breaker, CTs, digital meter with communication, and surge suppression equipment. Feeder devices in the distribution sections will also be drawout power air circuit breakers.

480 V distribution panels will be located in the mechanical rooms to serve mechanical equipment.

Lighting and receptacle panels will be located in the main electrical room to serve fixtures and devices within the service building.

13.5.7.2.2 Tunnel and Tunnel Mezzanine Power Distribution

Most of the equipment that supports the booster ring and storage ring is located on the mezzanine above the tunnel and operates at 208 V. With the large number of circuits, three double section 208Y/120 V branch circuit panelboards will be provided to serve the equipment racks housing the single magnet power supplies, vacuum instrumentation, tunnel instrumentation, and insertion devices. These panels will be located at each of the 30 cells around the Mezzanine, and served by a 112.5 kVA transformer located above the ratchet adjacent to the panels.

Power to the ring-wide power supplies will be provided by one or more dedicated 480Y/277 V panels fed directly from the switchgear. The panel location(s) will be verified during the design phase.

Power to the transfer line magnet power supplies will be provided by one or more 208Y/120 V panel(s) fed from the 480 V panel serving cell equipment or directly from the switchgear.

Empty cable tray will be provided through out the length of the tunnel and above the racks at the mezzanine level. Separate cable trays will be provided for power and signal. Tray locations will be coordinated with other utilities.

Lights and miscellaneous receptacles will be circuited to panels located in the adjacent service building.

13.5.7.2.3 Experimental Hall Power Distribution

Each beamline will be provided with one double section 208Y/120 V panelboard, served by a 75 kVA transformer and located at the mezzanine level at each of the 60 ratchets. Future branch circuits can drop out of the panel and be routed across the Experimental Hall on framing members to equipment located along the beamline.

Lights and miscellaneous receptacles will be circuited to panels located in the adjacent service building.

13.5.7.2.4 Linac/RF Building

A second switchgear will be located in the service building associated with the Linac/RF Building. This switchgear will be dedicated to equipment within the Linac and RF Buildings.

13.5.7.2.5 Central Lab Office Building Power Distribution

The Central Lab Office Building will be provided with an 800 A, 480Y/277 V panel fed directly from the switchgear in the associated service building. This panel will serve mechanical equipment and lighting and receptacle panels on each floor. Double section panels will serve the labs on the first floor.

Within each lab, two-compartment surface mounted raceway will be provided at bench tops and around the perimeter of the lab. Equipment in the center of the room will be served by surface-mounted raceways mounted on overhead ceiling mounted service carriers.

13.5.7.2.6 Lab Office Building Power Distribution

Each LOB will be provided with a 400 A, 480Y/277 V panel fed directly from the switchgear in the associated service building. This panel will serve mechanical equipment and lighting within the Lab Office Building, and will sub-feed two 208Y/120 V double section panels via a single 150 kVA transformer. The 208Y/120 V panels will serve devices in the lab and office areas.

Within each lab, two-compartment surface mounted raceway will be provided at bench tops and around the perimeter of the lab. Equipment in the center of the room will be served by surface-mounted raceways mounted on overhead ceiling-mounted service carriers.

13.5.7.3 Emergency Power

Because of the building's large size, two generators will be provided, one each at service building #2 and at the Linac/RF Building. The assumed size of each generator is 250 kW. A sub-base fuel tank in compliance with Suffolk County Article 12 will be provided with a 12-hour full load capacity. To reduce noise and vibration, a weatherproof, sound attenuated reach-in enclosure will be provided.

Two automatic transfer switches will be provided; one to serve code required emergency loads, and one to serve optional standby loads. The emergency loads include egress and exit lighting, the fire alarm system, fire suppression system, selected lab exhaust and make-up systems, and select HVAC control systems. The emergency loads will be reenergized within 10 seconds of sensing a power outage.

The optional standby loads are not defined, but will likely include selected laboratory equipment, one switched light fixture in each lab, and the communication and security systems. Optional standby loads may be delayed to limit motor starting kVA.

13.5.7.4 Uninterruptible Power Supply

A UPS will be provided to support the Control Room. The preliminary size is 30 kVA. If uninterruptible power is required for a specific piece of lab equipment, point-of-use UPS units will be provided by the users.

13.5.7.5 Voltage Utilization

- Building lighting - 277 V
- Motors 1/2 horsepower and larger - 480 V, 3-phase
- Motors less than 1/2 horsepower - 120 V
- Equipment – As required by nameplate, except special voltages and frequencies including 220 V, 230 V, 240 V, 380 V, DC, 50 Hz, 400 Hz, 415 Hz, etc. will require user provided point-of-use transformers and/or frequency converters.

13.5.7.6 Voltage Drop

Voltage drop will be limited to 2% in feeders and 3% in branch circuits.

13.5.7.7 Feeders and Branch Circuits

- All conductors will be copper installed in conduit. Conductors #3 and smaller will have THWN insulation. Conductors #2 and larger will have XHHW insulation.
- Conductors #10 AWG and smaller will be solid. Conductors #8 AWG and larger will be stranded. Minimum size conductors will be #12 AWG for branch circuits, #14 AWG for control wiring and #18 for signal cables.
- All feeder and branch circuit conductors will be provided with color coded insulation throughout their entire length.
- Separate neutral conductors will be provided for each receptacle circuit. Insulation of neutrals will be provided with three colored strips matching their associate phase conductors. Insulation of neutrals serving two or three pole circuits will be solid.
- All feeders and branch circuits will be provided with a green insulated equipment grounding conductor.
- All branch circuits serving sensitive electronic laboratory receptacles and equipment will be provided with a green with three yellow strips isolated equipment grounding conductors.
- Generally, conduit will be electrical metallic tubing with compression fittings. Conduit below grade will be concrete encased schedule 40 PVC. No conduit will be imbedded within slabs on or above grade.

13.5.7.8 Grounding

13.5.7.8.1 Grounding Electrode System

- The grounding electrode system will consist of underground metal piping, building steel, concrete encased 250 kcmil Ufer ground within all exterior wall foundations with direct buried cross connecting 250kcmil conductors 100 ft on center, and 10 ft ground rods spaced at approximately 100 ft on center around the perimeter.
- A 10 x 10 ft 250 kcmil ground grid will be provided at the Building 603 substation expansion, and at each unit substation transformer at the project site to reduce earth resistance and to limit step and touch potential.
- All underground connections will be exothermically welded.
- The ground grid shall be designed to provide <5 ohms of resistance to earth.
- A main ground bus will be located in the main electrical room at each service building. The grounding electrode conductors, interior metal pipe grounds, and the telecommunication ground will be connected to the main grounding bus.

13.5.7.8.2 Power System Grounding

- All power system grounding will be in accordance with the NEC.
- The secondary of each 13,800-480Y/277 V substation transformer will be grounded at the substation. The grounded neutral will be re-bonded at each switchgear main breaker.
- The generator neutral will be grounded at each generator. Four-pole automatic transfer switches will be provided.
- The secondary of each 480-208Y/120 V transformer will be connected to the nearest building steel via a local power system ground bus.
- A separate green insulated equipment grounding conductor will be provided in all feeders and branch circuits.
- Branch circuits serving sensitive electronic equipment will be provided with a green with yellow strips isolated equipment grounding conductor in addition to the green equipment grounding conductor.

13.5.7.8.3 Instrument Reference Ground

An instrument reference ground bus will be provided at each beamline to be used by users only for the purpose of grounding sensitive electronic communication circuits. The bus will be connected directly to the grounding electrode system and bonded to the local transformer(s) which provide power to that beamline equipment. The instrument reference ground bus will be considered the beamline's single point ground for all user equipment.

13.5.7.8.4 Electrostatic Dissipation

At this time, there are no known requirements for static dissipative flooring and/or bench tops.

13.5.7.8.5 RF Shield Grounding

Bonding plates will be provided in the RF shield at 100 foot increments and connected to the building counterpoise with #4/0 conductors.

13.5.7.8.6 Telephone and Data Communication Grounding

Telephone and data communication grounding will be provided in accordance with EIA/TIA 607.

13.5.7.8.7 Lightning Protection

A complete lightning protection system will be provided in accordance with NFPA 780 and UL 96A.

13.5.7.8.8 Cathodic Protection

It is assumed that no cathodic protection will be provided.

13.5.7.9 ELF EMI and RFI Mitigation

- No specific provisions have been incorporated to mitigate magnetic fields; however, routing of cables in and around laboratory spaces will be minimized, where feasible, to reduce fields in these areas.
- Further evaluation of planned RF cavity installations during subsequent design phases may identify local shielding requirements.

13.5.7.10 Vibration Isolation

The generators will be provided with spring isolators as recommended by the vibration consultant. All transformers will be mounted on neoprene pads. No conduit will be installed under or within vibration isolation slabs.

13.5.7.11 Radiation Protection

Conduit penetrations in to the tunnel will be limited in quantity and located only through the tunnel ceiling. All penetrations will include an off-set to eliminate line of sight through the high density concrete. See radiation protection section for additional detail.

Spare penetrations will be provided for future use.

13.5.7.12 Exterior Lighting

- Exterior illumination levels will be as indicated in DOE/IES standards.
- Parking lots and access drives will be lit by 175 W metal halide cut-off fixtures mounted on 20 ft aluminum poles.
- Walkways will be lit by 100 W metal halide cut-off fixtures mounted on 12 ft aluminum poles and 50 W metal halide bollards.
- Building-mounted exterior lighting will be provided at entrances and exits and at loading docks.
- No architectural/façade lighting will be provided.
- Site lighting will be circuited via low-voltage control panels with photocell on/off control.

13.5.7.13 Interior Lighting

- Lighting design will be accomplished with energy efficient fluorescent lamps and electronic ballasts. Downlights and accent lights will be provided by compact fluorescent lamps. Incandescent lamps will not be utilized except in selected labs where low level illumination is required or where electromagnetic interference may occur.
- Fluorescent lamps for troffers and pendant type fixtures will be T8, 32 W, 4100K with a CRI of at least 75.
- Fluorescent ballasts for T8 lamps shall be electronic type with a ballast factor of 0.85 minimum and total harmonic distortion of less than 10%.
- Compact fluorescent lamps will be used in downlights and wall wash fixtures.
- Exit lights will be LED type.

- Fluorescent fixtures in labs will be controlled by a low-voltage control system with low-voltage switches at the entrances.
- Occupancy sensors will be provided in enclosed offices and in open office areas, corridors, restrooms, and in support spaces.
- Photo sensors will be provided in perimeter offices and in spaces with natural lighting to de-energize lights when sufficient daylight is present.
- Footcandle levels will be in accordance with DOE standards where applicable and with the IES Handbook for other spaces:
  - Tunnel: 30 FC
  - Mezzanine: 30 FC
  - Experimental Hall (above beam-lines): 50 FC general illumination
  - Laboratories: 50-75 FC general with 75 FC on work surfaces
  - Offices: 30–50 FC general with 50 FC on work surfaces
  - Conference rooms: 30 FC
  - Attended support spaces: 30 FC
  - Unattended support spaces: 15 FC
  - Corridors: 10–15 FC
  - Restrooms: 10–15 FC general with 30 FC at the mirror/sink area
  - Mechanical/electrical equipment rooms: 15 FC
  - Telephone/communication rooms: 50 FC

Egress and exit lighting will be provided in accordance with NYSBC and NFPA 101

13.5.7.14 Special Systems

13.5.7.14.1 Fire Alarm

A complete manual and automatic, supervised, fire detection and voice evacuation system will be provided. It will be a non-coded, addressable, microprocessor-based fire alarm system with initiating devices, notification appliances, and monitoring and control devices. Initiating and appliance circuits will be Class B. The fire alarm system will be in accordance with DOE requirements and NFPA 72.

Manual stations will be programmable and located at all building exits, at all exit stairs, and at 300 foot intervals in egress corridors.

Photoelectric area smoke detectors will be located in all labs, through out the Tunnel and Experimental Hall, and in elevator lobbies, shaft and machine room. Provisions will be made for smoke detectors to be located within the future hutches. Smoke detectors in elevator lobbies, shaft and machine room will initiate elevator recall. Duct smoke detectors will be provided in air handling systems as required by NYSBC and NFPA 90A.

Heat detectors will be located adjacent to sprinkler heads in elevator shafts and machine room and will de-energize elevator power in accordance with ANSI 17.1, Elevator Code.

Post indicating valves, sprinkler flow and tamper switches, and pre-action and dry-pipe systems will be monitored.

Combination audio/visual and/or visual only devices will be provided throughout the corridor system, in each lab, and in most rooms other than single person offices. A minimum of two indicating circuits will be provided in each area with devices connected alternately.

The fire alarm control panel will be located at the main entrance of the Central Lab Office Building.

Notification appliance circuit power supplies will be distributed throughout the facility to provide power for the audible/visual appliances and to reduce voltage drop. The power supplies will be located in easily accessible locations.

Common alarm and trouble signals will be transmitted via dedicated fiber optic cable to the campus fire alarm system.

The fire alarm system will match campus standards.

13.5.7.14.2 Telephone and Data Communication System

A complete pathways, spaces, and structured cabling distribution system will be provided that consists of telecommunication rooms, plywood backboards, racks, cabinets, cable tray, conduit, back boxes, copper cable, fiber optic cable, connectors, cover plates, termination blocks, cross connect cables, patch panels, and all necessary accessories and will be provided in accordance with applicable EIA/TIA standards.

The Building Distribution Frame room will be located in the Central Lab Office Building. The BDF room will also serve as the Intermediate Distribution Frame room for the Central Lab Office Building, and the associated service building and sector of the tunnel and Experimental Hall.

Four 4 in. conduits will be routed from the BDF to Manhole MH-85 on the south side of Brookhaven Drive.

One IDF will be located in each Lab Office Building to serve its associated outlets.

Cable tray will be provided at lab and office corridors and around the Experimental Hall to route riser cable between the BDF and IDFs and to route station cables to outlets in the tunnel, Experimental Hall, and service building. Conduit will be provided between the cable tray and each outlet or raceway.

Each voice/data outlet will be provided with one Cat 6 voice jack and one Cat 6 data jack.

Each data outlet will be provided with one Cat 6 data jack.

Voice and data riser cabling will be provided from the BDF to each IDF. Voice riser cables will be multi unshielded twisted pairs, 24 gauge, solid copper and terminated on the terminal block in each closet. Data riser cabling will be 12 multi mode and 12 single mode fiber optic cables terminated at each end in a patch panel with a type SC connector. Voice will be terminated directly on rack-mounted termination panels. Patch panels will be mounted in 19 in. equipment racks.

Station cabling from each voice/data will consist of two four-pair Category 6 cables terminated at the devices and on the rack mounted telephone terminal blocks. Cables will be labeled at each device, terminal block, and patch panel.

13.5.7.14.3 Security System

The security system will consist of an access control system only. Intrusion detection and CCTV systems will not be provided.

Card readers will be located at each building entrance, at each corridor entrance to a lab, at each entrance to the Experimental Hall, at each entrance to the tunnel, and at each entrance to other selected spaces.

To match campus standards, security equipment components (card readers, controllers, locks, door contacts, etc.) will be owner furnished, contractor installed. Door exiting device, power transfer hinges, etc. will be coordinated with the door schedule. Security system cabling will be contractor installed and terminated by the owner.

13.5.8 Sustainable Design (LEED)

13.5.8.1 Approach

Sustainable design is an approach that addresses how design decisions will impact the natural environment, building occupants, construction methods and materials, and long term operations and maintenance. Incorporating sustainable design in new buildings is a DOE requirement that must be balanced with other program objectives such as cost, schedule, and technical performance. As such, sustainable design is an additional set of criteria on which design decisions for NSLS-II must be based.

The goal for the NSLS-II facility is to incorporate a wide range of sustainable strategies and objectives throughout the design and construction process while meeting the functional requirements of an advanced technology facility and creating a workplace that is environmentally friendly, energy-efficient, and both healthy and pleasant to be in. The NSLS-II facility will be designed to obtain a minimum of a LEED Certified Level as well as meet sustainable goals outlined in The Federal Leadership in High Performance and Sustainable Buildings Memorandum of Understanding (MOU).

LEED™ (Leadership in Energy and Environmental Design) is a voluntary, consensus-based national rating system developed by the U.S. Green Building Council that provides a complete framework for assessing building performance and meeting sustainability goals. Its current version, LEED Version 2.2 for New Construction and Major Renovations (NC) is being proposed for this project.

Consistent with the USGBC LEED program, the project team identified five key principles that will define and guide our sustainable approach. These principles will continue to be monitored throughout the design and construction and include the following:

- Site: Sustainable Site Design
- Water: Protecting and Conserving Water
- Energy: Designing for Energy Efficiency and Considering Alternative Energy Sources
- Materials: Optimizing the Environmental Life Cycle of Materials
- IEQ: Enhance Indoor Environmental Quality

The project will be evaluated against each LEED criteria. Those which receive either a ‘Prerequisite’ or ‘Credit’ marking result in a point score for certification:

Prerequisites: This category is based on minimum requirements and all must be met. No further points will be awarded unless the minimum is achieved. There are a total of seven Prerequisites.

Credits: Credits are evaluated and result in a point score. The total points possible under LEED-NC v.2.2 are 69 points.

The certifications levels are available as follows:

Table 13.5.1 LEED Certification Points.

Certification Level	Points Required
LEED Certified	26-32 Points
LEED Silver	33-38 Points
LEED Gold	39-51 Points
LEED Platinum	52-69 Points

13.5.8.2 Sustainable Site

Maximizing the benefit of the existing site can be accomplished though a number of sustainable measures, one of which is storm water management. The volume of storm water generated on the site depends

on the area of impervious surfaces. To control the quantity of storm water run-off, detention ponds have been designed to capture excess and reduce the impact on the BNL site system.

The possibility of utilizing bio-retention ponds or pervious pavement to treat storm water runoffs is proposed. In addition to controlling quantity, these strategies help to promote infiltration, and capture and treat the storm water runoff.

Bicycle racks and other site amenities will be included to ensure compliance with as many LEED credits as possible. Other possible amenities include designated preferred parking for car/van pools and fuel efficient vehicles and showers for bikers.

13.5.8.3 Water: Protecting and Conserving Water

Implementing water efficiency measures can reduce potable water use, and often save building owners operating costs. In addition, sustainable water use protects natural water bodies from contamination. To reduce potable water consumption, no permanent irrigation will be provided for the NSLS-II site. The plantings will be native to the region and will require little or no additional water after new growth has been established.

Further, we believe that the use of water-conserving fixtures can, in aggregate, provide savings of 20 to 30% when compared to water usage requirements under the Energy Policy Act 1992. These types of fixtures will be considered for NSLS-II.

13.5.8.4 Energy: Designing for Energy Efficiency and Using Alternative Sources of Energy

The impact that energy use has on the environment is broad and long-lived. Almost every aspect of conventional energy use poses some threat to the natural environment. Instituting energy efficient strategies like daylighting, high energy efficiency equipment, EMS optimization, ENERGY STAR roof, and building commissioning will all contribute to a building which will perform at a higher level, ultimately reducing overall energy consumption and reducing operating and maintenance costs. To further meet the sustainable requirements outlined in the MOU we will establish a whole building performance target that takes into account the intended use, occupancy, operations, plug loads, other energy demands, and design to earn the Energy Star7 targets for new construction and major renovation where applicable.

This project will eliminate the use of ozone-depleting compounds during and after construction where alternative environmentally preferable products are available, consistent with either the Montreal Protocol and Title VI of the Clean Air Act Amendments of 1990, or equivalent overall air quality benefits that take into account life cycle impacts.

13.5.8.5 Materials: Optimizing the Environmental Life Cycle of Materials

Almost 70% of all energy invested in a building's construction is embodied in the materials themselves. Embodied energy is the energy required to extract, transport, process, install, recycle, or dispose of these materials. The project team will evaluate the environmental impact, resource efficiency, and performance of the proposed building materials. Non-toxic materials from local and renewable sources will be considered.

The material selection process will focus on life-cycle issues rather than solely on aesthetic or first cost. Use of recycled content materials and those that are manufactured regionally will be maximized. For all EPA designated products we will use products that meet or exceed EPA's recycle content recommendations.

Material recycling will be facilitated to reduce waste and conserve resources. The design will provide for an area dedicated to the separation, collection, and storage of materials for recycling by the building occupants.

A Construction Waste Management Plan will be required for this project. A minimum of 50% of construction, demolition, and land clearing waste will be recycled and/or salvaged to meet LEED requirements as well as goals included in the MOU agreement.

13.5.8.6 IEQ: Enhance Indoor Environmental Quality

The quality of the indoor environment has a significant impact on human health, productivity and quality of life. Sustainable indoor environments promote daylighting, natural ventilation, and interiors that are free of toxins. The result is an interior environment that safeguards occupant health, and reduces operating costs. We will comply with ASHRAE Standard 55–2004 and ASHRAE Standard 62.1-2004 Ventilation for Acceptable Indoor Air Quality. Other strategies will include CO_2 monitoring System, low VOC and non-toxic materials, as well as permanent air monitoring systems.

A large contributor to the quality of the indoor environment is the indoor air quality. An Indoor Air Quality (IAQ) Management Plan will be developed and implemented during construction and pre-occupancy.

After construction and prior to occupancy, a minimum 72-hour flush-out will be conducted with maximum outdoor air consistent with achieving relative humidity no greater than 60 percent. After occupancy, flush-out will continue as necessary to minimize exposure to contaminants from new building materials.

In addition to industry standard sustainable initiatives, the NSLS-II team will propose specific innovations in sustainability pertaining to IEQ and human comfort. These innovations include using furniture systems which follow the LEED for Commercial Interiors (LEED CI) Guidelines and meet the Greenguard Air Quality Certification.

13.5.8.7 LEED Status

In order to track the LEED prerequisites and credit point status of the project, a tracking spreadsheet has been developed that include the following information:

- LEED Prerequisite/Credit. Title and Intent of each prerequisite/credit taken directly from LEED. What the credit/prerequisite is meant to achieve.
- Requirement. Requirement necessary to meet LEED prerequisite or credit requirement, taken directly from LEED.
- LEED Points Available. Notes the number of points available for each LEED credit. If REQ'D appears in the column, this indicates a prerequisite for which there are no associated points.
- "Yes" / "Maybe?" / "No" Status
  "Yes" The credit can be achieved.
  "Maybe?" The credit will be pursued but there is not enough information at this time to assume it will be earned.
  "No" The credit is not achievable.
- Responsibility: Person or group of people responsible for preparation of documentation, calculation, and/or information research.
- Comment. Provides general comments regarding possible impacts to cost, schedule, design, etc.

Based on the Total Point Summary, the NSLS-II project is currently estimated to have 25 Yes and 22 Maybe points, as shown in Table 13.5.2. To meet the goal of a LEED Certified level, the project is required to have a minimum of 26 points. Thus, we aniticipate no difficulty in achieving LEED Certified Certification and depending on how many Maybe points we obtain, it is possible that we may achieve LEED Silver or LEED Gold Certification, in accordance with Table 13.5.1.

Table 13.5.2 NSLS-II Preliminary LEED Points.

Point Category	Score
Yes	25 points
Maybe	22 points
No	22 points
Total Possible	69 points

13.6 METHOD OF ACCOMPLISHMENT

13.6.1 Design

Title I and Title II design will be performed by an A/E firm under contract to BNL. The A/E firm will be competitively selected based on best technical qualifications for this project. The A/E firm will also optionally provide Title III support services for construction monitoring, start-up, and commissioning.

13.6.2 Construction

Conventional construction will involve construction of the NSLS-II complex of buildings and improvements to land and utilities including expansion of the existing Central Utility Building. These will be procured generally as a lump-sum competitively procured contract to a general contractor. Certain aspects of the site preparation work will be contracted as an early package to allow for required settling of earthworks prior to physical construction of the facility. Early procurement of the shield wall high density concrete will also mitigate schedule risk. Four construction packages are planned: site preparation; shield wall early procurement; the main Ring Building (and all associate structures and utilities); and expansion of the CCWF. The contractors will be selected based on an evaluated bid whereby the award is given to the firm meeting all technical, management, financial, past performance record, and safety qualifications for the project at the best value.

13.6.3 Quality Assurance

The project will be conducted in accordance with BNL's site-wide Quality Assurance Program (QAP) that applies to all work conducted at BNL. The BNL QAP conforms to the requirements of Department of Energy (DOE) Order 414.1, Quality Assurance, and 10CFR 830 Subpart A, Quality Assurance Requirements. BNL's QAP consists of the following ten criteria:

- Program
- Personnel Training and Qualification
- Quality Improvement
- Documents and Records
- Work Processes
- Design
- Procurement
- Inspection and Acceptance Testing
- Management Assessment
- Independent Assessment

BNL's approach to satisfying the requirements of these criteria are delineated in the BNL Quality Assurance Program Description within the BNL Standards-Based Management System (SBMS). The NSLS-II design, construction and operation are subject to the QAP. A key element of the QAP is the concept of

"Graded Approach", that is, applying an appropriate level of analysis, controls, and documentation commensurate with the potential to have an environmental, safety, health, radiological, or quality impact.

13.6.3.1 NSLS-II QA Plan

The NSLS-II QAP has been developed and addresses both the conventional and technical aspects of the project. This plan addresses project activities from design through construction, as well as commissioning and startup. The sections of the NSLS-II QAP applicable to conventional facilities address the basic design and construction of the building and utilities systems executed by the NSLS-II Conventional Facilities Division. Requirements of the NSLS-II QAP will flow down to contractors performing design and construction of conventional facilities.

13.6.4 Bid Strategy

The bid environment on Long Island is expected to remain very competitive for the next several years, a timeframe that includes the bid period for NSLS-II. The project team recognizes the challenge of this bid environment and of the rapidly escalating costs of concrete and steel, primary materials for the project, and has developed a bid strategy to deal with it. A base building package has been identified along with a series of additive alternates that may be constructed if within the overall project budget. Some of the items listed as add alternates are features that are highly desirable for a world-class research facility but not absolutely essential for basic operation. Other items are building components that can be constructed in phases as the experimental floor is filled with beamlines over the course of several years.

As a result of beamlines being phased in over a period of time, portions of the experimental floor will not be used initially and the LOBs supporting future beamlines will not be fully occupied. The user group requirements for these future beamlines are not known at this time. It has been decided that optional Lab Office Buildings 2, 3, and 4 could be constructed in a warm-shell configuration for future fit-out by the user groups as needs dictate. The construction would include finishes on exterior walls, electrical power, HVAC, plumbing and other essential services. The LOBs would be useable, but not be ready for final occupancy until the space is programmed with the final user groups.

13.6.4.1 NSLS-II Base Scope

The base scope consists of the following building components:

- Ring Building
- Central Lab Office Building
- Lab Office Building 1
- Linac and RF Buildings
- All five Service Buildings.

The base scope will include the Ring Road, the loop road, the access roads to the service buildings and parking lots for the CLOB and LOB 1.

The base scope will include a curved standing seamed roof over the Ring Building and LOBs. The full design includes two AHUs in each service building to serve the Experimental Hall. All HVAC and mechanical systems required for the ring tunnel from all five service buildings will be included in the base bid.

13.6.4.2 Bid Alternates

In addition to the items listed above, there are several building components that will be included as design alternates. These include but are not limited to the Conference Center and Exhibit areas, Lab office Buildings

2, 3, and 4 and associated systems, and parking. Table 13.6.1 identifies the proposed bid alternates for the project.

Table 13.6.1 Base Bid and Bid Alternate Components.

Building Component		Base Bid	Bid Alternate
Ring Building including ring tunnel, ring mezzanine, Experimental Floor, and access corridor.		■	
Central Lab Office Building and associated mechanical electrical and fire protection.		■	
Lab Office Building No. 1 and associated mechanical electrical and fire protection systems.		■	
RF Building and associated mechanical electrical and fire protection.		■	
Linac Building and associated mechanical electrical and fire protection.		■	
Service Buildings 1 through 5.		■	
All AHUs and duct work serving the Ring Tunnel from Service Buildings 1 through 5.		■	
All AHUs and ductwork serving the Experimental Floor and ring mezzanine from Service Buildings 1 through 5.		■	
Process utilities serving the Ring Building to be built out for all experimental areas.		■	
Ring Building curved standing seam roof.		■	
Road and parking curbing at building entrances only.		■	
Paving of Ring Road and parking for CLOB and LOB 1.		■	
Grass seeding of site.		■	
Alternate # 1	Conference Center.		■
Alternate # 2	Lab Office Buildings 2, 3 and 4.		■
Alternate # 3	Clerestory windows on Ring Building.		■
Alternate # 4	Ring Building sloped (not curved) standing seam roof (deduct).		■
Alternate # 5	Parking lots for LOBs 2, 3, and 4.		■
Alternate # 6	Finish layer of asphalt to parking lot and roads.		■
Alternate # 7	Provide trees and shrubs for landscaping as well as grass seeding.		■
Alternate # 8	TPO roof on Ring Building (deduct).		■
Alternate # 9	Preinsulated Metal Panel		■

13.6.5 Value Management

Value Management (VM) will be performed for this project as required under DOE Order 413.3A, "Program and Project Management for the Acquisition of Capital Assets." An independent value management team will perform VM review during Title I design. A VM report will be provided to the NSLS-II Project Director and DOE/BHSO Federal Project Director for consideration and, where feasible, incorporation into project design documents.

The VM review will be a systematic review of the mature Title I design performed by an independent team of qualified consultants. The team will comprehensively review design elements and material selections with regard to their needed level of performance and quality. Alternate methods, elements and selections that meet the necessary performance and quality will be considered. The comparative first cost and life cycle cost of these alternatives will be determined and compared to the original design. A VM report will be prepared indicating alternatives considered, their respective costs and recommendations as to which alternatives should be implemented in the project design.

13.6.6 Commissioning

An important element in the ultimate success of the NSLS-II will be proper commissioning of the facilities systems and instruments. The extreme sensitivity of the storage ring and research beamlines requires that all systems and instruments achieve their maximum performance capability to fulfill the research mission. Additionally, any systems or equipment that can create environmental disturbance must be properly

calibrated, balanced, tuned, or shielded to prevent detrimental impact to the research. During the Title I design phase, a detailed facility commissioning plan will be prepared to assure that appropriate commissioning requirements have been included in the NSLS-II design. The commissioning plan will:

- Present a schedule and sequence for start-up of building systems and instruments, including dependencies linked to the conventional or technical construction schedule.
- Identify safety approvals required prior to start-up
- Identify systems and instruments at the equipment level that will require commissioning.
- Identify references and sources of start-up procedures and performance, test and acceptance criteria for the instruments and equipment.
- Identify whether the equipment will be commissioned by BNL staff, contractor staff, vendor staff, or if the services of a specialty commissioning contractor are warranted.
- Identify the point at which equipment has been accepted and can be turned over to operations staff.
- Be updated during the Title II and Title III phases as appropriate to reflect changes in equipment selection and performance.

13.7 CONCEPTUAL DESIGN DRAWINGS

Conceptual design drawings of the NSLS-II site and buildings are provided in a separate volume of drawings. The drawings are organized into four sections:

- Site/civil engineering
- Architectural
- Mechanical engineering
- Electrical engineering

Drawing lists for each of these sections follows.

13.7.1 Site/Civil Concept Design Drawings

Site/civil drawings are identified in the drawing list below:

Table 13.7.1 Site/Civil Concept Design Drawing List.

Site / Civil Concept Drawings
Site Layout & Grading Plan
Sanitary Sewer Plan
Storm Sewer Plan
Potable Water Plan
Steam Plan
Chilled Water, Cooling Tower Water and Compressed Air Plan

13.7.2 Architectural Concept Design Drawings

Architectural drawings are identified in the drawing list below:

Table 13.7.2 Architectural Concept Design Drawing List.

Architectural Concept Drawings
Site Plan
Building View
Base Building Site Plan
Base Building Floor Plan
Building View
Building View
Building View
Overall NSLS-II Floor Plan
Ring Building Plan
Beamline Cluster (6 beamlines)
Central Lab Office Building (CLOB) - First Floor
Central Lab Office Building (CLOB) - Second Floor
Central Lab Office Building (CLOB) - Third Floor
Seminar/Exhibit Area Plan
Building View
Building View
Building View
Building View
Building View
Lab Office Building (LOB) - Full Build-out (LOB 1)
Lab Office Building (LOB) - Shell Build-out (LOBs 2, 3 and 4)
Building View
Service Building - Second Floor
Service Building - First Floor
Linac Building
RF Building
Typical Section at Ring Building
Section at Lab Office Building and Service Building
Section at Central Lab Office Building
Section at RF Building
Section at RF Building
Section at Linac and Experimental Hall

13.7.3 Mechanical Concept Design Drawings

Mechanical drawings are identified in the drawing list below:

Table 13.7.4 Mechanical Concept Design Drawing List.

Mechanical Drawings
Typical Experimental Floor - HVAC
Mechanical Section
Service Building – Lower Level – Mechanical Room
Service Building – Upper Level – Mechanical Room
RF Building – Upper Level - Mechanical Room
Typical Experimental Floor - Piping
Accelerator Tunnel AHU Control Diagram
Process Cooling - Condenser Water Diagram

13.7.4 Electrical Concept Design Drawings

Electrical drawings are identified in the drawing list below:

Table 13.7.5 Electrical Concept Design Drawing List.

Electrical Drawings
Site Electrical Plan
Building 603 Campus Substation Upgrade, Switch House And Yard Plan
Campus Substation And Site Distribution One-Line Diagram
Cluster #3 Electrical Floor Plan
Cluster#3 Normal Distribution One-Line Diagram

References

[13.1] BNL Site Vibration Study, 2006.
[13.2] VitaTech Engineering EMI/RFI Site Assessment Study, 2006.
[13.3] Geotechnical Report for NSLS-II site, 2006.
[13.4] BNL Chilled Water Alternatives Study, 2006.
[13.5] NSLS-II Preliminary Life Safety Code Review, 2006.

14 ENVIRONMENT, SAFETY, & HEALTH, AND QUALITY ASSURANCE

14.1 INTRODUCTION

Brookhaven National Laboratory is committed to the success of the mission objectives of the National Synchrotron Light Source II and to the safety of its users, staff, and the public. The NSLS-II Project Director is responsible for achieving this objective. The NSLS-II Environmental Safety and Health Manager is responsible for ensuring that an ES&H system is established, implemented, and maintained in accordance with requirements. The ES&H Manager will provide oversight and support to the project participants to ensure a consistent ES&H program.

It is our vision to provide a "Best in Class" safety program. We view such a program as essential to the safety of the workers as well as the successful completion of the project. We will seek to provide an injury free work environment and will measure our performance by comparison with only those who have achieved recognition as "Best in Class." To achieve this vision, safe working conditions and practices are an absolute requirement for all staff and contractors. We expect all design and work to be performed with this goal in mind. We will not be satisfied unless our ES&H program as well as our new facility are both recognized as "Best in Class." To accomplish this vision, it is essential that ES&H be fully integrated into the project and be-managed as tightly as quality, cost and schedule.

An ES&H Program Plan [14.1] with this vision in mind has been prepared by the ES&H Manager and approved by the NSLS-II Project Director. This plan specifies that the program implemented for NSLS-II shall satisfy its ES&H commitments by:

1. Establishing an Integrated Safety Management Program that implements the DOE Policy, DOE P 450.4, "Safety Management System Policy," the BNL Subject-Based Management System topic areas, and the requirements of the DOE "Accelerator Safety Order." The program will protect the environment and the safety of workers and the general public by assuring that:
    a. Facilities, systems, and components needed to meet mission requirements are fully defined and are designed, constructed, and operated in accordance with applicable BNL and DOE requirements
    b. Potential hazards to personnel associated with all NSLS-II systems, structures, and components are identified and controlled through the timely preparation of safety assessment documents
    c. Potential risks to the environment are addressed through the timely and comprehensive preparation of appropriate National Environmental Protection Act documentation
    d. ISO 14001 and OHSAS 18001 criteria are implemented to assure that all ES&H risks are identified and addressed
    e. Requirements in 10 CFR Part 835, part 850, and Part 851 are fully implemented to protect worker safety and health
2. Implementing a QA program that follows DOE Order 414.1-2A, "Quality Assurance Management System Guide," and incorporates quality requirements from BNL's SBMS subject areas Quality Management and Graded Approach for Quality Requirements.
3. Implementing an effective construction safety programs to ensure worker safety on the NSLS-II site during construction. All work performed on the NSLS-II site will be conducted in accordance with the NSLS-II Environmental, Safety, and Health Plan.

4. Performing Independent Design Reviews on systems, structures, and components designated as "safety significant" or "safety class" in the SAD or as defined through QA classifications described in the NSLS-II QA Plan.
5. Providing appropriate training to ensure that project staff are adequately trained and qualified to perform their assigned work safely. Job training assessments will be conducted for all staff to ensure knowledge of job-related hazards and their controls. All project staff are responsible for ensuring that their training and qualification requirements are fulfilled, including continuing training to maintain proficiency and qualifications.
6. Developing and implementing operating procedures to control work on NSLS-II technical systems.
7. Performing and documenting safety inspections of all project facilities and work areas, and ensuring prompt correction of any issues identified in the inspection.
8. Reporting and investigating occurrences and incidents in accordance with the BNL Occurrence Reporting Policies and Procedures as defined in the BNL SBMS. Any incident, accident, or other abnormal event will be properly communicated and investigated via established procedures.

Policies and requirements to ensure implementation of these expectations will be established and communicated to all staff, contractors, and vendors.

14.2 PRELIMINARY HAZARDS ANALYSIS (PHA)

A principal component of an effective ES&H program is to ensure that all hazards have been properly identified and controlled through design and procedure. To ensure that these issues are understood at the conceptual phase, a Preliminary Hazards Analysis [14.2] has been conducted to identify the hazards that will be encountered during the project's construction and operational phases. In addition, the PHA was also used to make the Facility Hazard Categorization; NSLS-II was determined to be an "Accelerator Facility," as defined in DOE Order 420.2B, "Safety of Accelerator Facilities."

Generally, all the hazards and their risks anticipated to be encountered at NSLS-II as identified in the PHA are well known to the accelerator community. Years of experience with such facilities at BNL and within the DOE complex have generated well-defined design criteria and controls to eliminate and/or control these risks. Table 14.1 summarizes the hazards that have been considered and the codes and standards that apply to the reduction of risk associated with each hazard.

This PHA process began concurrent with the conceptual design, to ensure that all significant hazards were identified and adequately addressed in the early design work. Each of these issues will be followed as design advances and as construction and installation work commence. A Baseline Hazards List [14.2] was developed as the first step in identifying the potential hazards. This list utilized the best available information, encompassing data from the NSLS-II conceptual design, existing NSLS safety-basis documentation, subject-matter expertise (with conventional facilities, accelerator systems, and ES&H) and lessons-learned from the DOE's accelerator community covering design criteria, regulatory requirements, and related occurrences. It also included a preliminary (pre-mitigation) risk assessment at the subsystem level that identified a risk category before incorporating the ES&H-related design and operational controls that are postulated to mitigate those risks. The identified hazards then were further developed in the PHA, where the proposed ES&H design enhancements were taken into consideration. The PHA re-analyzed the risks, including these enhancements and, in certain cases, operational controls, to establish a post-mitigation risk category. This category affords a realistic assessment of the residual ES&H risks posed by the NSLS-II facility and is input to the Title I design.

Eleven of the hazards reviewed in the PHA are mitigated to low risk or below through design and procedure, and five hazards remain at a moderate level. The latter include: Construction, Electrical, Chemical/Hazmat, Material Handling, and Experimental Operations. While the PHA adequately addresses all

risks, those remaining above a low post-mitigation category will require more attention during the Title 1 design process to ensure that they are adequately controlled.

A brief review of each hazard and the means of mitigating risks are provided in the following sections.

Table 14.1 Hazards Considered in PHA and Applicable Codes and Standards.

PHA Identifier	Hazard List	Applicable NSLS-II ES&H Regulations, Standards, Codes, Order
NSLS-II – PHA-1	Construction hazards Site clearing Excavation Work at elevations (steel, roofing) Material handling Utility interfaces, (electrical, steam, chilled water) Misc. finishing work Weather-related conditions Transition to Operations	29 CFR 1926, Safety and Health Regulations for Construction
NSLS-II – PHA-2	Natural phenomena hazards Seismic Flooding Wind Snow Lightning	DOE Order 420.2B Safety of Accelerator Facilities DOE Guide 420.2-1 Accelerator Facility Safety Implementation Guide DOE Order 420.1B Facility Safety DOE STD 1020-2002 Natural Phenomena Hazards Design and Evaluation Criteria for Department of Energy Facilities DOE STD 1021-93 Natural Phenomena Hazards Performance Categorization Guidelines for Structures, Systems and Components. DOE STD 1022-94 Natural Phenomena Hazards Site Characterization Criteria. DOE STD 1023-95 Natural Phenomena Hazards Assessment Criteria. New York State Building Code
NSLS-II – PHA-3	Environmental hazards Construction impacts Storm-water discharge (construction and operations) Operations impacts Soil activation Air activation Cooling-water activation (HVAC and machine) Oils/chemical leaks Discharge/emission points (atmospheric/ground)	BNL Subject Areas NYSDEC Petroleum bulk storage, SCDHS Article 12 40 CFR 61 - Subpart A, National Emissions Standards for Hazardous Air Pollutants (NESHAPS) 6 NYCRR 200 – 234 – NYSDEC Prevention and Control of Air contamination and Air Pollution
NSLS-II – PHA-4	Waste hazards Construction phase Facility maintenance Experimental operations Industrial Hazardous Radiological	BNL Subject Areas 6 NYCRR Part 371, Identification and Listing of Hazardous Wastes 6 NYCRR Part 374.3, Standards for Universal Waste 40 CFR 262.11, Hazardous Waste Determination (EPA 1987) 40 CFR 273, Standard for Universal Waste Management 6 NYCRR Part 374-2 and 225-2, Used Oil Specifications
NSLS-II – PHA-5	Fire Hazards Facility occupancy classification Construction materials Storage Flammable/combustible liquids Flammable gasses Egress/access Electrical Lightning	BNL Subject Areas NFPA 101 Life Safety Code NFPA 45 Fire Protection for Laboratories Using Chemicals Elevator Std

PHA Identifier	Hazard List	Applicable NSLS-II ES&H Regulations, Standards, Codes, Order
NSLS-II – PHA-6	Electrical hazards Facility Experimental Job-built equipment Low voltage/high current High voltage/high power Maintenance Cable tray overloading/mixed utilities	BNL Subject Areas NFPA 70 National Electrical Code NFPA 70 E Standard for Electrical Safety in the Workplace NFPA 70 B Recommended Practice for Electrical Equipment Maintenance
NSLS-II – PHA-7	Noise/Vibration	BNL Subject Areas OSHA 29 CFR 1910.95 Occupational Noise Exposure
NSLS-II – PHA-8	Cryogenic Oxygen deficiency Thermal Cryogenic distribution system Pressure	BNL Subject Areas American Society of Mechanical Engineers (ASME) Boilers and Pressure Vessel Code, sections I through XII including applicable Code Cases, (2004). * ASME B31 (ASME Code for Pressure Piping) as follows: (i) B31.1—2001—Power Piping, and B31.1a—2002—Addenda to ASME B31.1—2001; (ii) B31.2—1968—Fuel Gas Piping; (iii) B31.3—2002—Process Piping; (iv) B31.4—2002—Pipeline Transportation Systems for Liquid Hydrocarbons and Other Liquids; (v) B31.5—2001—Refrigeration Piping and Heat Transfer Components, and B31.5a—2004, Addenda to 29 CFR 1910.134, OSHA Respiratory Protection Standard
NSLS-II – PHA-9	Confined space hazards	BNL Subject Areas 29 CFR 1910.146, Permit-required confined spaces
NSLS-II – PHA-10	Ozone hazards	BNL Subject Areas DOE G 420.2-1, Accelerator Facility Implementation Guide
NSLS-II – PHA-11	Chemical/hazardous material inventory Toxic Extremely toxic Compressed gas Carcinogens, mutagens, teratogens Combustibles Explosives Flammable gases Lead (shielding)	BNL Subject Areas 49 CFR Department of Transportation ANSI Z358.1-2004 Emergency Eyewash and Shower Equipment OSHA 1910
NSLS-II – PHA-12	Accelerator/Beamline hazards Vacuum/Pressure Cooling water Compressed gas Electrical Heavy equipment handling Magnetic Cryogenic Shielding Mechanical (moving shutters, valves and actuators)	BNL Subject Areas DOE Order 420.2B Safety of Accelerator Facilities DOE G 420.2-1, Accelerator Facility Implementation Guide
NSLS-II – PHA-13	Ionizing radiation hazards Prompt radiation (synchrotron radiation scatter, neutrons, bremsstrahlung) Radioactive contamination Activation (equipment) Radioactive material (dispersible use, storage)	BNL Subject Areas 10CFR 835

PHA Identifier	Hazard List	Applicable NSLS-II ES&H Regulations, Standards, Codes, Order
NSLS-II – PHA-14	Non-ionizing radiation hazards RF & microwave Magnetic fields Laser Visible light	BNL Subject Areas ANSI Z136.1-2000 Safe Use of Lasers
NSLS-II – PHA-15	Material handling hazards Overhead cranes/hoists Fork trucks Manual material handling Delivery area distribution Manual movement of materials	BNL Subject Areas ASTM B30 Overhead Cranes
NSLS-II – PHA-16	Experimental operations Electrical equipment Transportation of hazardous materials Biological materials Chemicals (corrosive, reactive, toxic, flammable) Nanomaterials (particulates) Elevations Dark-room hazards Clean-room hazards Ionizing radiation Ozone production Slips, trips, falls Machine tools/hand tools Stray static magnetic fields Research gasses (corrosive, reactive, toxic, flammable)	BNL Subject Areas

14.2.1 Construction Hazards (NSLS-II PHA – 1)

BNL has a mature construction safety program, with recent experience in constructing the Research Support Building (64,000 sq ft) and the Center for Functional Nanomaterials (94,000 sq feet). Lessons-learned from these two projects, as well as from other construction projects in the DOE complex, coupled with the existing program, will control risk at the NSLS-II facility. Typical construction hazards anticipated at the NSLS-II construction site include the following:

- Site clearing
- Excavation
- Work at elevations (steel, roofing)
- Utility interfaces, (electrical, steam, chilled water)
- Material handling
- Miscellaneous finishing work
- Weather-related conditions
- Transition to Operations

14.2.1.1 Construction Hazards – Mitigating Factors (Design)

- Engineered and approved excavation systems
- Engineered and approved fall-protection systems
- Permanent fall-protection systems incorporated into facility's roof systems (for future maintenance)
- Modern code-compliant construction equipment with the required safety controls (e.g., backup alarms, seatbelts, load capacity readouts)

14.2.1.2 Construction Hazards – Mitigating Factors (Operational)

- Strict adherence to 29 CFR 1926, OSHA Construction Standard
- Integrated Safety Management (contractually flowed down to subcontractors)
- Contractor-Required Health and Safety Plan (flowed down to subcontractors)
- Pre-qualification of contractors and subcontractors based on their Experience Modification Rate, Days Away, Restricted, Transfer rate, and Total Recordable Case rate
- Independent third-party inspections of construction safety program
- Dedicated onsite construction safety professionals
- Phase hazards analysis for high-risk activities (e.g., site clearing, work at elevations)
- Contractor-safety incentive program
- Frequent ES&H communication with contractor and subcontractors at plan-of-day, "tool box" meetings
- Major construction equipment inspected before arriving on site

14.2.2 Natural Phenomena Hazards (NSLS-II PHA-2)

Natural Phenomena Events, including high winds, floods, and earthquakes, were investigated and documented in the plan DOE Accelerator Order 5480.25, "Implementation Plan for BNL Natural Phenomena Hazards Evaluation – 1994" [14.3]. The data confirmed that all accelerator facilities at BNL were built to the appropriate national consensus codes and standards at the time of their construction. The NSLS-II design will be governed by the Building Code of the State of New York, which is more restrictive than prior codes. The BCNY specifies design criteria for wind loading, snow loading, and seismic events. Furthermore, all accelerator facilities were determined to be low hazard and Performance Category 1 (per DOE STD-1021-93). NSLS-II also was determined to be a Performance Category 1 facility. It will contain only small quantities of activated, radioactive, and hazardous chemical materials. If a NPH were to cause significant damage, the impact would be mission related and would not pose a hazard to the public or the environment.

14.2.2.1 NPE Mitigating Factors (Design)

- Performance Classification designation PC-1
- Strict conformance to Building Codes State of New York
- Snow-loading criteria: 45 psf ground, 30 psf+ for drift design
- Wind design: 120 mph (with 3-second gust)
- Seismic design: to 0.20g acceleration velocity
- Lightning-protection system per NFPA (National Fire Protection Association) 780
- Pitched roofs on structures to preclude localized flooding/roof leaks
- Site drainage designed to shed water

14.2.2.2 NPE Mitigating Factors (Operational)

- Limited and controlled quantities of hazardous materials
- BNL Site Emergency Plan
- NSLS-II site emergency plan (to be developed)
- Emergency drills
- U.S. Weather Service dopplar radar facility on BNL site for early notification of severe weather

14.2.3 Environmental Hazards (NSLS-II PHA 3)

Environmental hazards from NSLS-II include the potential for releasing, in amounts beyond regulatory limits, oils, solvents, chemicals, and radioactive material to the soil, groundwater, air, or sanitary system. The

principal initiators for such a release would be the failure of equipment, impact from a natural phenomenon, fire, or a violation of procedures/processes.

The NSLS-II facility established a goal of obtaining Leadership in Energy and Environmental Design certification that contains requirements for sustainable design principles, pollution prevention, and waste minimization during construction and operations.

14.2.3.1 Environmental Hazards – Mitigating Factors (Design)

- Recirculating (closed-loop) cooling systems
- Minimal need for the regeneration of filter beds, through the use of water-treatment chemicals and disposable pre-filters
- Handling and storage facility for control of waste water
- Design to Suffolk County Article 12 (secondary containment) requirements
- NSLS-II will include sustainable design principles with the goal of obtaining LEED certification

14.2.3.2 Environmental Hazards – Mitigating Factors (Operational)

Implementation of an environmental management program designed to international standards (ISO 14001), where chemical use is minimized through review and less hazardous chemicals and processes are substituted where possible. Controls are based on the following:

- Process Assessments
- ES&H Committee, Beamline Review Committee, design reviews
- Work Planning, Experimental Safety Reviews, Tier I inspections
- Training/qualification
- NSLS-II Environmental Assessment
- NESHAP evaluation (to be developed)

14.2.4 Waste Hazards (NSLS-II PHA-4)

Waste-related hazards from NSLS-II include the potential for releasing waste materials (oils, solvents, chemicals, and radioactive material) to the environment, injury of personnel, and a possible reactive or explosive event. Typical initiators would be transportation accidents, incompatible materials, insufficient packaging/labeling, failure of the packaging, and a natural phenomenon.

The types and volume of wastes that will be generated by NSLS-II are not anticipated to differ markedly from those generated by the existing NSLS. During a typical year of operation, NSLS-II will generate 3,000 to 5,000 pounds (1,400 to 2,300 kilograms) of waste.

14.2.4.1 Waste Hazards – Mitigating Factors (Design)

- Two 90-day waste accumulation areas on opposite sides of ring
- 90-day areas are designed with 2-hr fire rating, independent exhaust ventilation, fire detection, alarm pull box, communications (phone) system, access control (card reader), and secondary containment

14.2.4.2 Waste Hazards – Mitigating Factors (Operational)

- NSLS-II chemical use and waste production will be minimized through review; less hazardous chemical and processes will be substituted where possible
- Local Satellite Accumulation Areas in laboratories or at beamlines

- 90-day weekly inspections
- Periodic New York State Department of Environmental Conservation inspections of the 90-day areas and Satellite Accumulation Areas
- Hazardous Waste Generator training
- Experimental Safety review process
- Work planning and control
- Facility-Specific safety orientation
- Tier I inspections
- Process Assessment forms
- Tritium sampling program for accelerator's cooling-water systems
- Waste reduction, pollution prevention, and recycling
- HazMat transportation procedures per DOT and site Transportation Safety Document

14.2.5 Fire Hazards (NSLS-II PHA – 5)

Operational experience at accelerators throughout the DOE complex has demonstrated that most fires in accelerator facilities are electrically initiated, typically by component failure. However, other sources of fire are considered in the design of the NSLS-II facility. They include the combustibility of building construction materials, the accumulation of combustible materials by occupants, the use of pyrophoric or reactive materials, improper storage or use of flammable materials, lightning storms, and static discharge.

14.2.5.1 Fire Hazards – Mitigating Factors (Design)

- Design to BCNY and appropriate NFPA standards
- Preliminary Fire Hazards Analysis
- Noncombustible construction throughout facility
- Early-warning fire-detection systems (e.g., smoke detectors, rate of rise detectors)
- Automatic fire suppression (e.g., sprinkler system)
- Emergency power supply for essential systems
- Hazardous material storage areas: rated, vented, alarmed
- Lightning protection system for facilities
- Adequate grounding systems

14.2.5.2 Fire Hazards – Mitigating Factors (Operational)

- Manual fire suppression provided by sufficient portable fire-extinguishers
- Alarm systems to alert occupants and summon fire department (e.g., fire alarm bells/strobes, manual pull stations, connected to on-site fire department)
- Full-time, BNL Fire/Rescue Group with mutual aid arrangements with local fire departments
- Ongoing inspection program to minimize combustibles and ignition sources
- Ignition-source control programs (cutting/welding permits, no smoking policy)
- Experimental Safety Review to minimize fire hazards of experiments by design features
- Fire evacuation drills

14.2.6 Electrical Hazards (NSLS-II PHA – 6)

The NSLS-II will have a large amount of facility-related and experimental electrical equipment. Electrical hazards from NSLS-II include the potential for serious injury, death, and equipment damage. Electrical shock and arc flash can be caused by exposed conductors, defective and substandard equipment, lack of adequate training, or improper procedures.

14.2.6.1 Electrical Hazards – Mitigating Factors (Design)

- Design to NFPA 70 and 70 E National Electric Code
- Adequate power distribution (beamlines and laboratories)
- Segregated power and utility distribution (cable/utility trays)
- Electrical and mechanical equipment rooms adequately sized and accessible from outside of ring
- Electrical distribution/disconnect equipment located in unobstructed areas (physically marked to provide clear access)
- Where possible, NRTL-certified equipment

14.2.6.2 Electrical Hazards – Mitigating Factors (Operational)

- Non NRTL-certified equipment inspected and certified by competent person
- Engineering and beamline design reviews
- Operation of equipment at <50 volts where feasible
- SBMS procedures for electrical safety
- Electrical safety training
- Operational procedures to keep electrical equipment unobstructed
- Ongoing inspection program

14.2.7 Noise and Vibration Hazards (NSLS-II PHA – 7)

Hazards from noise and vibration include overexposure of personnel to OSHA noise limits and permanent hearing loss, also known as Permanent Threshold Shift. The vibration of equipment can contribute to high noise levels, as well as potentially damage or interfere with sensitive equipment.

NSLS-II will incorporate a wide variety of equipment that will produce a range of noise and vibration. Support equipment (e.g., pumps, motors, fans, machine shops, and general HVAC) all contribute to point source- and overall ambient-noise levels. While noise will typically be below the OSHA 8-hr time-weighted average, certain areas with mechanical equipment could exceed that criterion and will require periodic monitoring, posting, and the use of Personal Protective Equipment. Ambient background noise is of a greater concern from the standpoint of users' comfort, stress level, and fatigue. Background noise in the accelerator and experimental areas at the existing NSLS is a common quality-of-life complaint and interferes with broadcast safety announcements and alarm systems.

14.2.7.1 Noise and Vibration – Mitigating Factors (Design)

- Separate mechanical/utility areas from work areas
- Isolate operations and experimental process equipment (e.g., pumps); utilize service chase concept, hutches, or individual equipment enclosures
- Use low-noise fans in HVAC systems
- Incorporate sound-absorbing materials into structure (wall and ceiling panels, baffles)

14.2.7.2 Noise and Vibration – Mitigating Factors (Operational)

- Baseline and periodic area noise surveys
- Personnel noise dosimetry
- Noise-exposure medical protocol where required
- New equipment reviews for noise and vibration levels as part of procurement process

14.2.8 Cryogenic Hazards (NSLS-II PHA – 8)

Cryogenic hazards at NSLS-II will include the potential for oxygen-deficient atmospheres due to catastrophic failure of the cryogenic systems, thermal hazards (cold burns) from cryogenic components, and pressure hazards. Initiators could include the failure or rupture of cryogenic systems from overpressure, failure of insulating vacuum jackets, mechanical damage or failure, deficient maintenance, or improper procedures.

Large volumes of inert cryogen liquid (nitrogen and possibly helium) will be piped into and around the NSLS-II facility from a centralized distribution point. In addition, dewar vessels (typically up to 500 liters) will be used locally in experiments.

Liquid nitrogen and liquid helium will be used for cooling experimental samples such as protein crystals, and also to cool beamline equipment, such as detectors, for enhanced sensitivity. Similarly, liquid coolants will chill accelerator components such as magnetic insertion devices, to make them superconducting (i.e., have zero resistance to electrical current).

14.2.8.1 Cryogenic Hazards – Mitigating Factors (Design)

- Design piping systems and pressure vessels per ASTM and ANSI codes or equivalent
- Install oxygen sensors and alarms
- Install interlocks and automatic exhaust system/quench
- Relief mechanisms in all piping and dewar systems

14.2.8.2 Cryogenic Hazards – Mitigating Factors (Operational)

- Develop the review process
- Pressure-test initial systems
- Cryogenic Safety Committee reviews and tests as required by SBMS
- Prepare and conduct NSLS-II facility-specific access training
- Conduct compressed-gas safety training
- Conduct cryogen safety awareness training
- Conduct Oxygen Deficiency Hazard training
- Maintain ODH classification and controls
- Conduct system-specific training

14.2.9 Confined Space Hazards (NSLS-II PHA – 9)

Hazards from confined spaces could result in death or injury due to asphyxiation, compressive asphyxiation, smoke inhalation, or impact with mechanical systems. Initiators would include failure of cryogenic systems releasing gas, fire, or the failure of mechanical systems.

Two types of confined spaces should be considered for the NSLS-II facility. The first are those associated with the facility's support/maintenance and typically include sump pits and HVAC plenums that would only be accessed by Plant Engineering's maintenance personnel or vendor personnel. The second category is those confined spaces created by the experimental programs and may include pits for support equipment or large tanks installed to recover inert gases.

14.2.9.1 Confined-Space Hazards – Mitigating Factors (Design)

- Definition of confined space criteria for designers – "design out," where possible
- Design of multiple means of egress, where possible

- Adequately size mechanical enclosures to allow maintenance

14.2.9.2 Confined-Space Hazards – Mitigating Factors (Operational)

- Identification and posting of all confined spaces
- Facility-specific safety orientation to identify spaces
- Work Planning and Control program
- Site's maintenance personnel identify their confined spaces

14.2.10 Ozone Hazards (NSLS-II PHA-10)

Synchrotron radiation can generate significant levels of ozone when the unattenuated beam passes through air. Experience at the current NSLS demonstrated that in some instances, ozone concentrations may approach or exceed the ACGIH Threshold Limit Values and precautions are needed to control potential exposures.

14.2.10.1 Ozone Hazards – Mitigating Factors (Design)

- Direct the beam path through evacuated or inert gas atmosphere containing pipes
- Minimize beam's horizontal and vertical dimensions
- Minimize beam path's length
- Filter beam to eliminate lower photon energies
- Scrub air round beam path with ozone filters
- Install ozone monitoring at potential problem areas

14.2.10.2 Ozone Hazards – Mitigating Factors (Operational)

- Experimental and beamline review program
- Delay personnel entry time to allow ozone to degrade

14.2.11 Chemicals and Hazardous Materials (NSLS-II PHA – 11)

The use of chemical and hazardous materials (HazMat) at NSLS-II could result in injury and death, or in exposures that exceed regulatory limits. Initiators could be experimental operations, transfer of material, failure of packaging, improper marking/labeling, failure of fume hood or glove box, reactive or explosive event, improper selection (or lack) of personal protective equipment, or a natural phenomenon.

14.2.11.1 Chemical and HazMat Hazards – Mitigating Factors (Design)

- Dedicated Chemical Storage Area with segregation, ventilation, fire-protection system, flammable, and O_2 monitors and access control
- Chemical delivery area located adjacent to loading dock
- Vented chemical storage cabinets in laboratories with lab quantities of hazardous material
- Gas cabinets for toxic and highly toxic gasses, individual venting and purging capacity and exterior access
- Double-wall stainless tubing for distributing toxic and highly toxic gasses
- Dedicated storage for biological- and infectious-materials
- Bulk gas piped in, (Liquid Nitrogen, Gaseous Nitrogen, Air) number of individual bottles limited
- Exhausted fume hoods in laboratories, (specialized hoods, e.g., HEPA where necessary)
- Covered centralized location for storing gas. (Satellite location due to size of ring)

- Safety showers and eyewashes in each laboratory (tepid water)
- Loading dock with leveling system to reduce material handling
- All lead material encapsulated/painted
- Hutches with exhaust ventilation to exterior of building

14.2.11.2 Chemical and HazMat Hazards – Mitigating Factors (Operational)

- Chemical Inventory control system (barcode); Chemical Management System (CMS)
- Lab Standard/Hazcom Training
- Transport of materials per DOT and BNL Hazardous Material Transportation Manual (HMTM)

14.2.12 Accelerator/Beamline Hazards (NSLS-II PHA – 12)

Hazards from the accelerator and beamlines include the cooling water, chemicals, compressed gas, electrical, material handling, and magnetic/cryogenic/ radiation.

The accelerator and beamlines will have various electrical equipment and associated power supplies. High-power equipment includes vacuum pumps, vacuum gauges, detectors and beam-position monitors (higher voltage-biased system).

Two important hazards are synchrotron scatter from beamline optics and bremsstrahlung radiation from loss of high-energy electrons from the orbit. Both hazards are found along the beamline. Synchrotron scatter will mostly be from the first optical elements. Bremsstrahlung radiation is confined to the beamline vacuum chamber with lead collimators until it can be directed into a beam stop. On many beamlines, the synchrotron light is offset from the bremsstrahlung cone at the monochromator and can be stopped there. For lines that have insufficient offset, a backstop is placed in the hutch behind the endstation.

14.2.12.1 Accelerator/Beamline Hazards – Mitigating Factors (Design)

- Engineered safety-systems in place will protect the ring and beamlines from vacuum, cooling-water flow, extreme temperatures, and compressed air faults
- Vacuum faults will cause the accelerator's interlock systems to close the sector and front-end valves, thus dumping beam; beamline interlocks will close a beamline valve and/or a front-end valve; insertion device beamline interlocks will close the fast valve and dump RF
- Any reduced flow of cooling water is sensed, causing the accelerator's interlocks to dump RF and the beamline interlocks to close the safety shutters
- Elevated magnet temperature sensors will turn off the magnet's power supply. If sensed on ring components, RF will be dumped. If sensed in the pump room water, RF and magnet power supplies will be dumped.
- Loss of primary compressed air supply from the Central Chilled Water Facility will activate the NSLS-II backup supply and alert the control room
- Loss of backup compressed air supply (affecting operation of front-end masks, safety shutters, and fast valves) will alert the control room

14.2.12.2 Accelerator/Beamline Hazards – Mitigating Factors (Operational)

- Safety Analysis Document and Accelerator Safety Envelope (to be developed)
- Operational procedures
- Systems design review

14.2.13 Ionizing Radiation Hazards (NSLS-II PHA – 13)

Potential hazards from ionizing radiation include prompt radiation (x-rays, neutrons, bremsstrahlung) produced during machine operation, induced activity in machine components, and radioactive material (use, storage). Typical initiators of radiation exposure would include operating machines, maintenance work, and using radioactive materials. Accidental exposure could result from failure of an interlock or other protective system, inadequate design or control of shielding, or an inadequate procedure.

To address these issues, the NSLS-II design will incorporate the requirements specified in 10 CFR 835 and the accelerator-specific safety requirements as set by DOE Order 420.2B, Safety of Accelerator Facilities. The facility will be designed and operated in a manner to maintain radiation exposure to staff, users, and the general public personnel within DOE and BNL dose limits and control levels [14.4]–[14.8].

A full discussion of radiation shielding at NSLS-II is given in Chapter 15.

14.2.13.1 Ionizing Radiation – Mitigating Factors (Design)

- Shielding for accelerators and beamlines to reduce dose to design levels
- Redundant interlock systems for accelerator enclosures and beamline hutches
- Redundant radiation safety critical devices (e.g., transfer line beam stops, beamline safety shutters)
- Real-time beam loss monitoring systems for injection and storage-ring operation
- Routine area monitoring of dose levels by passive dosimeters for neutrons and gammas on the experimental floor

14.2.13.2 Ionizing Radiation – Mitigating Factors (Operational)

- Radiological protection program incorporating requirements of 10 CFR 835 and BNL SBMS Radiological Control Manual
- Strict configuration control of shield systems
- Radiological safety training (e.g., GERT, Radiation Worker I)
- Facility-specific Safety Orientation and ES&H Orientations
- Work control procedures ensuring adequate planning and ALARA reviews before work authorizations

14.2.14 Non-Ionizing Radiation Hazards (NSLS-II PHA – 14)

Anticipated non-ionizing radiation hazards at NSLS-II include radio frequency, microwave, magnetic and laser hazards. The NSLS-II accelerators and storage rings will depend on the reliable operation of pulsed klystrons and continuous-wave high-power radio-frequency (RF) systems for injecting electrons and maintaining the stored beam. Both of these devices generate electromagnetic radiation within the RF and microwave energy ranges (30 KHz – 300 GHZ) and also pose significant electrical hazards. The devices typically are operated and maintained such that these energies will be shielded and, therefore, will not thermally or electrically expose nearby personnel.

The NSLS-II experimental program will use Class 1, 2, 3a, 3b, and 4 lasers. Many of them will occupy permanent locations, while others will be part of short-term beamline experiments, in place for just days to weeks at a time. Lasers, particularly those in Class 3b and 4, have associated electrical hazards, and some laser procedures require the use of solvents, dyes, and halogen gasses, which can also be hazardous.

14.2.14.1 Non-Ionizing Radiation Hazards – Mitigating Factors (Design)

- Equipment designed with integral shielding and interlock systems, as needed
- Laser interlock systems
- Gas cabinets for lasers using halogens (fluorine gas) vented outside the building

14.2.14.2 Non-Ionizing Radiation Hazards – Mitigating Factors (Operational)

- Baseline and routine surveys for stray magnetic fields, RF, and microwave
- Training for static magnetic fields, RF, microwave, and laser hazards
- Equipment ES&H review during installation
- Laser Safety Officer reviews
- Personnel protective equipment

14.2.15 Material-Handling Hazards (NSLS-II – 15)

The consequences of hazards encountered in material handling include serous injury or death to equipment operators and bystanders, damage to equipment, and interruption of the program. These hazards could be initiated by a dropped or shifted load, equipment failure, improper procedures, or insufficient training or qualification of operators.

14.2.15.1 Material-Handling Hazards – Mitigating Factors (Design)

- Hoists and attach points designed to ASTM/ANSI standards
- Piped-in gasses to reduce material handling of cylinders

14.2.15.2 Material-Handling Hazards – Mitigating Factors (Operational)

- Routine inspection and maintenance of all material-handling equipment
- Only trained and qualified personnel allowed to use equipment
- Equipment is locked to prevent unauthorized use
- Daily and annual inspection as required by supervisors to assure proper condition of equipment.

14.2.16 Experimental Hazards (NSLS-II – 16)

The consequences from experimental operation hazards range from minor to severe injuries, possible death, and danger to the experimental, accelerator, or facility equipment, as well as a programmatic impact. Initiators would include the release or unexpected reaction of hazardous material, the failure of protective systems, laser hazards, the use of radioactive materials and of biological materials, operators' error, lack of training, poorly designed/installed equipment, failure of equipment, unexpected chemical reactions, and undefined hazards or risks from material not considered in experimental safety reviews. Many of the anticipated hazards are discussed in the specific hazard-analysis sections (e.g., ozone, non-ionizing radiation).

Inert and various research gases will be used in experiments; inert gases include nitrogen, helium, and argon. Small amounts of flammable gasses, such as hydrogen, propane, and butane, may be required. Various toxic gases, such as hydrogen sulfide, carbon monoxide, or nitrogen oxides might also be used in liter quantities. Small-scale use of oxygen and the halogens also is anticipated. Liquid nitrogen and liquid helium will be used to cool experimental samples such as protein crystals.

The NSLS-II team continues to work with the DOE "nano" community to share the latest information on the hazards of nanoparticles and to fully implement the Secretarial Policy Statement on Nanoscale Safety (DOE P 456.1). Future changes in design guidance and equipment/systems may be necessary due to emerging information.

14.2.16.1 Experimental Hazards – Mitigating Factors (Design)

- Each laboratory will have a tailored design (be "programmed") based on its anticipated use and possible future use (user input in design process, historical inventories/hazards considered).
- The NSLS-II facility will be designed for Bio-safety Level 2.
- Chemical fume hoods installed in laboratories will be appropriate to experimental work, (based on the design programming).
- HEPA filtered hoods will be used for work with nanomaterial particulate and radiological dispersible materials (once-through systems).
- An adequate power supply (GFCI protected) will be designed into the laboratories to support anticipated equipment needs and future growth.
- Equipment bonding system will be installed.
- There will be provisions for adequate chemical storage.
- Outdoor-vented cabinets for storing flammable gasses in laboratories
- Laboratories designed for easy access/egress, process flow, ease of cleaning
- Laboratories located near beamlines, reducing movements with experimental materials
- Facility and laboratories designed to meet OSHA 1910 (walkways, stairs, egress)
- Safety shower and eye wash in each chemical laboratory (hands-free, tepid water)

14.2.16.2 Experimental Hazards – Mitigating Factors (Operational)

- Experimental safety review program
- Control of hazardous materials (inventory, storage)
- ES&H support staff (subject-matter experts, monitoring technicians)
- Principal Investigator's R2A2 and training
- Adequate beamline staffing

14.3 NEPA COMPLIANCE

In compliance with the National Environmental Protection Act (NEPA) and its implementing regulations (10 CFR 1021 and 40 CFR 1500-1508) and in accordance with the requirements of DOE Order 451.1B, an Environmental Assessment (EA) was prepared to evaluate the potential environmental consequences of constructing and operating NSLS-II at DOE's preferred site (BNL) has been carried out [14.9]. The EA analyzed the potential environmental consequences of the facility and compared them to the consequences of a No Action alternative. The assessment included detailed analysis of all potential environmental, safety, and health hazards anticipated as the design, construction, and operation of the facility progresses. The EA determined that there would be no significant impact from the construction and operation of the proposed facility and that an Environmental Impact Statement (EIS) was not required. A Finding of No Significant Impact (FONSI) was approved by the DOE Brookhaven Site Office (BHSO) Manager and made available to the general public and project stakeholders [14.10].

14.4 QUALITY ASSURANCE

NSLS-II management will design and build a world-class user facility for scientific research with the assistance of a fully involved Quality Assurance (QA) Program.

The NSLS-II Project Director is responsible for achieving performance goals. The NSLS-II Quality Assurance Manager is responsible for ensuring that a quality system is established, implemented, and

maintained in accordance with requirements. The QAM will provide oversight and support to the project participants to ensure a consistent quality program.

A QA Program Plan [14.11] has been prepared by the QA Manager and approved by the NSLS-II Project Director. This plan specifies the program requirements that apply to all NSLS-II work. The primary objective of the QA program is to implement quality assurance criteria in a way that achieves adequate protection of the workers, the public, and the environment, taking into account the work to be performed and the associated hazards. The objectives include:

- "Designing in" quality and reliability
- Assuring that all personnel involved in the project uphold the NSLS-II Quality Assurance Plan
- Promoting early detection of problems to minimize failure costs and impact on schedule
- Developing appropriate documentation to support construction and operational requirements
- Assuring that personnel have the necessary training as needed before performing critical activities, especially activities that have environmental, safety, security, or health consequences
- Defining the general requirements for design and readiness reviews, including environmental, safety, security, and health issues related to NSLS-II and contractor hardware, software, and processes.

References

[14.1] NSLS-II Environment, Safety, and Health Plan.
[14.2] NSLS-II Preliminary Hazards Analysis.
[14.3] DOE Accelerator Order 5480.25 Implementation Plan for BNL Natural Phenomena Hazards Evaluation – 1994.
[14.4] NSLS-II Technical Note 00012; "Preliminary Radiological Considerations for the Design and Operation of NSLS-II Linac"; PK Job and WR Casey July25, 2006.
[14.5] NSLS-II Technical Note 00013; "Preliminary Radiological Considerations for the Design and Operation of NSLS-II storage Ring and Booster Synchrotron; PK Job and WR Casey July25, 2006.
[14.6] NSLS-II Technical Note 00014; "Preliminary Shielding Estimates for NSLS-II Beamlines and Front Ends"; PK Job and WR Casey July 25, 2006.
[14.7] J. Pankkal, W.R. Casey, "Preliminary Activation Analysis of Accelerator Components and Beam Stops at the NSLS-II"; NSLS-II Technical Note 00015; August 1, 2006.
[14.8] NSLS-II Technical Note 00016; "Preliminary Activation Analysis of Soil, Air and Water near the NSLS-II Accelerator Enclosures"; PK Job and WR Casey August 15, 2006.
[14.9] NSLS-II Environmental Assessment.
[14.10] Finding of No Significant Impact for NSLS-II Project, approved by BHSO, September 27, 2006.
[14.10] NSLS-II Quality Assurance Plan.

15 RADIATION SAFETY AND SHIELDING

15.1 SHIELDING OBJECTIVES

NSLS-II is subject to the DOE radiation protection standards. The primary document that defines the DOE radiation protection standards is the Code of Federal Regulations 10 CFR 835. In addition, the accelerator-specific safety requirements are set by DOE Order 420.2B, Safety of Accelerator Facilities. All radiation protection policies and guidelines at NSLS-II must be in compliance with these regulations along with the BNL Radiation Control Manual and other pertinent documents in the BNL Standards Based Management System.

The maximum annual exposure to radiation workers and members of the public is limited in 10 CFR Part 835 to 5,000 mrem and 100 mrem, respectively. To keep radiation exposures well below regulatory limits, BNL maintains an annual administrative control level of 1,250 mrem for its workers and 5 mrem per year from any single facility to the public off-site. An additional control level of 25 mrem/year from NSLS-II operations is established for personnel working in non-NSLS-II facilities on site.

The dose to workers and to the members of the public from NSLS-II operations will be kept well below federal limits and within BNL administrative levels through shielding, operational procedures, and review of all experiments and other use of radioactive materials. In accordance with 10 CFR 835.1001, measures will be taken to maintain radiation exposure as low as reasonably achievable (ALARA) through shielding design and administrative controls. The primary method of radiation control will be through physical design features such as shielding and barriers to radiological areas. Administrative controls will only be employed as supplemental to control radiation exposure. An internal control level for the facility will be to keep the annual dose equivalent, as the result of NSLS-II operations, <100 mrem/year for all NSLS guests, users and staff members working at the facility.

Shielding for the accelerators and the storage ring will be provided through a combination of various materials (e.g. concrete, lead, polyethylene, and soil) and will be designed for normal operations using conservative beam loss assumptions to limit the maximum dose to 500 mrem when in contact with the shield for 2,000 hours per year. Occupational exposure of personnel is most likely to occur in the vicinity of experimental hutches along the beam lines. Shielding of these areas will be designed to maintain exposures when in contact with the hutch wall to <100 mrem/year for 2,000 hours of exposure per year.

The adequacy of the shielding for abnormal conditions, including a maximum credible incident (MCI) will be evaluated. The MCI is defined as a credible fault condition with the maximum or worst-case radiological consequences. Depending upon the severity of the radiological conditions created during the MCI, additional shielding or other engineering controls (e.g. interlocked radiation monitors) may be needed. The likelihood of an incident creating a dose to an individual exceeding the administrative control level must be determined to be low and any exposure exceeding the annual limit because of inadequate shielding will be prevented.

Effectiveness of the shielding will be actively monitored by radiation instruments located on the experimental floor and by frequent area-surveys performed by the health physics personnel. Additional local shielding will be provided to reduce the radiation field as needed. Passive area monitors will also be used to integrate doses in various areas. The results will be analyzed for trends, and shielding will be improved as appropriate.

15.2 SHIELDING ESTIMATES FOR THE ACCELERATOR ENCLOSURES

Radiological conditions for the design and operation of the NSLS-II linac, storage ring, and booster synchrotron have been analyzed using the currently available design parameters. The booster synchrotron will be housed in the same tunnel as the storage ring at NSLS-II. Calculations of the resulting radiation fields and required shielding have been made for normal loss of stored beam and loss of beam during injection at the septum/extraction magnets. The shielding estimates are based on conservative assumptions, including several modes of operations that involve normal beam loss mechanisms as well as certain abnormal beam loss scenarios. These situations are drawn from experiences and assumptions used at existing accelerator and synchrotron radiation facilities. Shielding requirements for the storage ring and booster synchrotron are based on maintaining exposure to personnel to less than 500 mrem/year assuming a occupancy of 2,000 hours per year for a worker at NSLS-II. The calculated shielding for the occupiable regions during operation is for a dose rate of <0.25 mrem/h, at the exterior of the accelerator enclosures on contact. Sufficiently conservative factors are included in these estimates to provide additional margin of safety.

15.2.1 Sources of Radiation Hazard

For the radiological analysis of NSLS-II accelerator enclosures, the following radiation components were considered:

- bremsstrahlung radiation created during electron beam loss
- neutron production by high-energy bremsstrahlung
- synchrotron radiation from the insertion devices

High-energy electrons produce bremsstrahlung [15.1] when intercepted by the accelerator components or residual gas molecules in the vacuum chamber. Bremsstrahlung, or “breaking radiation,” is emitted by a high-energy electron as it decelerates due to inelastic radiative interaction with the coulomb field of atomic nuclei of the medium it traverses. Subsequent pair production and bremsstrahlung production can generate an electromagnetic shower. The radiation originating in the shower is highly forward-peaked in the forward direction of the electron beam. However the transverse component is significant and cannot be ignored. The lateral shielding for the accelerator enclosures is designed to protect personnel from the transverse component of the electromagnetic shower. In addition to bremsstrahlung radiation, two other radiation components need to be considered. These are Giant Resonance Neutrons and High Energy Neutrons originating from the interaction of bremsstrahlung with heavy metals [15.2]. GRN are produced by photonuclear interactions when the photon energy is above the threshold energy of 7 to 20 MeV. This component has an average effective energy of about 2 MeV and is emitted isotropically. If the photon energy is above 50 MeV, high-energy neutrons (>25 MeV) are also emitted. The high-energy neutron component is not isotropic. To estimate the shielding and other requirements for the NSLS-II accelerator enclosures, these sources of radiation have been considered, across a range of possible conditions.

15.2.2 Shielding Design Methodology for the Accelerators

15.2.2.1 Radiation Attenuation Factors for the Shielding Materials

The radiation attenuation factors used for the materials in the current shielding calculations are given in Table 15.2.1. These data have been obtained from various sources in the literature [15.3–15.6]. A number of references which discuss these attenuation factors have been reviewed. We have chosen conservative values for these factors to provide an additional safety margin for the shielding calculations.

Table 15.2.1 Radiation Attenuation Factors of Shielding Materials.

Radiation Component	Shielding Material	Density [g/cm^3]	Attenuation Length [g/cm^2]
Bremsstrahlung	Concrete	2.35	49
	Heavy Concrete	3.70	50
	Lead	11.34	25
	Iron	7.80	37
	Earth	1.60	70
	Polyethylene	1.01	70
Giant Resonance Neutrons (E <25 MeV)	Concrete	2.35	40
	Heavy Concrete	3.70	45
	Lead	11.34	161
	Iron	7.80	100
	Earth	1.60	33
	Polyethylene	1.01	6.3
High-Energy Neutrons	Concrete	2.35	65 (<100 MeV) 115(>100 MeV)
	Heavy Concrete	3.70	125(>100 MeV)
	Lead	11.34	191
	Iron	7.80	138
	Earth	1.60	90
	Polyethylene	1.01	62

15.2.2.2 Dose Equivalent Factors of Radiation Components

Effective Dose Equivalent factors for the unshielded source terms at 1 meter in the transverse direction from a 3.0 GeV electron beam interaction on a thick copper or iron target are given in Table 15.2.2. The data are taken from Sullivan [15.7]. Note that the dose equivalent factors in the transverse direction (90 degrees) are independent of the electron beam energy, but dependent on the beam power.

Table 15.2.2 Dose Equivalent Factors (Fi) Used for Shielding Calculations.

Radiation Component	Dose Equivalent Factor [mrem-m^2/Joule]
Bremsstrahlung	1.39
Giant Resonance Neutrons	0.27
High-Energy Neutrons	0.043

In the absence of any shielding, the bremsstrahlung component will include low-energy particle component (e^- and e^+), which can be disregarded, since shielding for bremsstrahlung will ensure attenuation of the particle component. In the forward direction with respect to the electron beam (zero degrees), the dose equivalent factor for bremsstrahlung [15.8] is 8.3 × E mrem-m^2/J, where E is the electron energy in MeV. The bremsstrahlung dose rate at 1 m near zero degrees, but not within the forward spike [15.8], is taken as 850 mrem-m^2/J. The GRN component is assumed to be isotropic from the loss point. These forward dose equivalent components are important for the design of ratchet wall shielding of the storage ring.

15.2.2.3 Shielding Calculations for NSLS-II Accelerator Enclosures

The bulk shielding for the accelerator enclosures has been calculated using the following expression [15.9]:

$$H = \sum_i \frac{F_i J}{R^2} e^{-t/\lambda_i} \qquad (15\text{-}1)$$

where H = Dose Equivalent Rate summed over all components, in mrem/h, F_i = Radiation Dose Equivalent Factors for the corresponding radiation component (i^{th} component), J = electron energy dissipation in joules/hour, R = total distance of the dose point from the source in meters, t = thickness of bulk shielding in g/cm^2, and λ_i = attenuation length of the i^{th} radiation component in g/cm^2.

The equation is solved using a parameter search for the thickness of the bulk shielding (concrete), such that H <0.25 mrem/h. The shielding strategy employed is to use concrete as bulk shielding, to provide global shielding of accelerator enclosures for distributed losses in the system. This shielding needs to be supplemented by additional local shielding, employing lead for bremsstrahlung or polyethylene for neutrons, to reduce radiation fields from the high loss points to acceptable limits of <0.25 mrem/h (500 mrem/2,000-hour work year).

15.2.3. Shielding Estimates for the Linac Enclosure

15.2.3.1 Linac Parameters

For NSLS-II, a linac will be providing 200 MeV electrons into the booster synchrotron. In the current calculations the linac tunnel is assumed to be 60 meters long, 4 meters wide, and 3 meters high. The salient features of the linac system are as follows:

- beam energy: 200 MeV
- beam current: 20 nA
- bunch pattern: 500 pC/ 40 bunches
- frequency: 1 Hz
- tunnel length: 60 m
- tunnel width x height: 4 m x 3 m
- position of beam from floor: 1 m
- power: 4 W

15.2.3.2 Bulk Shielding for the Linac Tunnel

For the linac system, the bulk shielding computations are based upon normal operation beam losses of certain fractions of beam power. Table 15.2.3 gives the estimated losses of beam energy in the linac system components.

Table 15.2.3 Estimated Losses in the Linac System Components.

Component	Charge [nC/s]	Loss [%]	Energy [MeV]	Power Loss [W]
Accelerator system	20	1 % distributed	200	0.04
Injection septum	0.25	50 %	200	0.05
Linac beam stop	20	100 %	200	4.0

To estimate the bulk shielding for the linac tunnel, a distributed loss of 1% of the beam energy is assumed along the length of the tunnel. The shielding requirement for the lateral walls and the roof of the linac tunnel is calculated based upon this beam loss scenario. The occupiable regions are shielded for a dose rate of 0.25 mrem/h (500 mrem for 2,000 work hours per year). The roof is considered as a fully occupiable region in the current calculations. The distance of the lateral walls and the roof is taken as 2 m from the beam.

The bulk shielding estimates of the concrete thickness for the linac tunnel is given in Table 15.2.4. 90cm-thick standard concrete with a density of 2.35 g/cm^3 will limit the dose rate to <0.25 mrem/h at the exterior of the lateral wall and the roof, for an assumed 1% distributed beam loss scenario.

The injection septum for the linac injection to the booster synchrotron is in the storage ring enclosure.

Table 15.2.4 Bulk Shielding Estimates for the Linac Tunnel.

Component	Lateral wall Concrete Equivalent[1] Thickness [cm]	Roof Concrete Equivalent[1] Thickness [cm]
Non-injection region	90	90
Linac downstream wall	220 100 cm + 15 cm (Pb)	100

[1] A density 2.35 g/cm^3 is considered standard for concrete.

The bulk shielding estimates in the forward direction of the linac should be estimated if an occupiable region exists in the forward direction of the extraction magnet. The calculations are based on the forward direction bremsstrahlung dose equivalent rates provided by Sullivan [15.7]. These estimates are given in Table 15.2.4. The estimated concrete equivalent thickness for bulk shielding is 220 cm. Local shielding of lead in the forward direction can be provided to save on the concrete bulk shielding. A factor of 8 with respect to standard concrete can be applied to calculate the equivalent thickness of lead. Local shielding by the equivalent thickness of lead may replace concrete in the forward direction at the extraction region of the linac.

15.2.4 Design of the Linac Beam Stop

When the linac is not injecting into the booster, the beam is dumped at the linac beam stop. This beam stop will be located at the end of the linac accelerator tunnel closer to the extraction region. Since the detailed layout of the building is not currently available, it is assumed that the concrete bulk shield, which separates the occupiable regions, is 2 m away in all directions from the beam stop. 100% of the 4-W electron beam is dissipated on the beam stop. The shielding strategy in this case will be to shield the stop locally in addition to the linac concrete bulk shielding available at the injection/extraction region.

When 200-MeV electrons interact with the material of the beam stop, an electromagnetic shower will be generated within the material, due to successive bremsstrahlung and pair-production interactions. A shower is developed in the material when the primary electron energy is much greater than the critical energy of the material. The critical energy, E_c, is the electron energy for a given element at which the average energy loss from bremsstrahlung production is equal that from ionization. The lateral and longitudinal shower dimensions within the material are determined by the Moliere radius and the radiation length of the material [15.10] Table 15.2.5 gives the shower parameters for various shielding materials that are also used for beam stops.

Table 15.2.5 Electromagnetic Shower Parameters for Various Materials.

Material	Density [gm/cm^3]	Critical Energy [MeV]	Radiation Length [cm]	Moliere Radius [cm]
Aluminum	2.70	51.0	8.89	3.70
Iron	7.87	27.4	1.76	1.40
Copper	8.96	24.8	1.43	1.22
Tungsten	19.3	10.2	0.33	0.73
Lead	11.35	9.5	0.56	1.25
Concrete	2.35	51.0	10.9	4.5

The material considered for the linac stop is iron, for various qualities such as sturdiness, thermal stability, conductivity, and relative compactness of shower dimensions. Iron being a low Z material, the photo-neutron yield and the resulting activation will also be minimal.

The theory of electromagnetic showers stipulates that material of dimensions of approximately 20 radiation lengths in longitudinal and 3 Moliere radii in transverse will contain 99.99% of the electromagnetic shower [15.10]. Thus, an iron cylinder of 35 cm length and 8.5 cm diameter will be sufficient to effectively contain the electromagnetic shower in the linac stop. The scattered low-energy photon radiation will require additional lead shielding, but will be well below the critical energy and photo-spallation reaction threshold. The neutrons created in the shower will escape isotropically from the stop and require additional shielding.

Table 15.2.6 shows the dose rate due to various radiation components around the linac beam stop at the exterior of the 1m concrete shield wall without local shielding. Since the exact layout of the storage ring-linac tunnel is not available at present, the concrete shield wall is assumed to be 2 m away from the iron beam stop. Table 15.2.6 also provides the dose rates on the exterior of the concrete shield wall with a local shielding of 15 cm of Pb and 25 cm of polyethylene (density = 1 g/cm^3). The local shielding limits the dose rate at the exterior of the concrete bulk shielding to <0.25 mrem/h. The stop will be in the linac enclosure; personnel will have no access to the enclosure when there is the potential for beam acceleration.

Table 15.2.6 Dose Rates at the Exterior of the Concrete Shield Wall around the Linac Beam Stop.

Radiation Component	Unshielded Dose Rates [mrem/h]	Dose Rates with 15 cm Pb and 20 cm Poly [mrem/h]
Bremsstrahlung	18.37	0.0142
Giant Resonance Neutrons	1.21	0.0079
High Energy Neutrons	1.85	0.2172
Total Dose Rate	21.43	0.2393

15.2.5 Shielding Estimates for Booster and Storage Ring

15.2.5.1 Storage Ring Parameters

The operations goal for the NSLS-II storage ring is to store a 500 mA current of 3.0 GeV electrons injected by the booster synchrotron. However, it may be desirable to increase either the electron energy or the stored current in the future if the user program requires it. Since it is very difficult and costly to increase the shielding after construction, the initial shielding will be sized to enable safe operation for a 500 mA current stored at an electron energy of 3.5 GeV. The estimated lifetime of the beam in the storage ring is 2 hours. In the current calculations the storage ring tunnel is assumed to be 780 meters in circumference. The maximum assumed operating parameters of the storage ring system are thus:

- beam energy: 3.5 GeV
- beam current: 500 mA
- beam lifetime: 2 hr
- tunnel circumference: 780 m
- stored charge: 1.3 μC
- stored electrons: 8.1×10^{12}
- stored energy: 4,540 J

15.2.5.2 Bulk Shielding for the Storage Ring Enclosure

With two hours of beam lifetime in the storage ring, ~ 50% stored beam loss occurs in one hour. 10% of this beam loss is assumed to occur at any one location of the storage ring. The shielding requirements for the storage ring at regions other than the injection/extraction region are calculated based on this beam loss scenario. Table 15.2.7 summarizes the various beam loss scenarios considered.

Table 15.2.7 Estimated Beam Losses in the Storage Ring - Booster Components.

Accelerator component	Loss [%]	Energy [MeV]	Power Loss [W]
SR Accelerator System	10%	3,500	0.075
Booster Accelerator system	2%	3,500	0.0175
Injection/Extraction, booster to storage ring	50%	3,500	0.82
Injection/Extraction linac to booster	50%	200	0.05
Booster beam stop	100%	3,500	0.874

The lateral wall of the storage ring on the experimental floor side is assumed to be 1 meter from the storage ring vacuum chamber. The roof and the inboard walls are assumed to be 2.5 meters from the vacuum chamber. The ratchet wall in the forward direction is assumed to be 20 meters from the middle of the insertion device straight section. The ratchet wall shielding thickness is calculated using the forward-peaking component of the Dose Equivalent Factors available in the literature [15.8]. The occupied regions on the experimental floor side of the storage ring are shielded for a dose limit of <0.25 mrem/h for 2,000 hours of occupancy per year. The roof and inboard wall are also considered as fully occupied regions in the current calculations.

The bulk shielding estimates in terms of concrete thickness for the storage ring and booster synchrotron system are given in Table 15.2.8. Shielding wall thickness in standard concrete equivalent is given for the lateral wall and roof. The standard concrete can be replaced by a high density concrete. Shielding thickness is also given in terms of heavy concrete of density 3.7 g/cm^3. However, if concrete of a different density is used, shielding thickness will need to be scaled accordingly.

The ratchet wall shielding thicknesses at the first optics enclosure side of the beamlines are also given in Table 15.2.8. These walls are assumed to be 20 meters from the center of the straight section of the insertion devices. These walls are thicker (160 cm standard and 102 cm high-density concrete) due to the bremsstrahlung forward component that needs to be shielded.

15.2.5.3 Bulk Shielding: Booster-to-Storage Ring Injection/Extraction Region

Injection from the booster synchrotron to the storage ring takes place approximately every 1 minute. Taking into account the storage ring lifetime as 2 hours, 0.83% of the beam is lost in 1 minute. In 1 hour, 49.77% of the beam is lost and an equivalent amount is injected into the storage ring to keep the ring current at 500 mA—an operation known as "top-off." During injection, 50% injection efficiency is assumed. Therefore, twice the amount of charge is injected into the storage ring and half as much of the injected charge is lost on the injection/extraction septum magnets. The shielding requirement at the injection/extraction region is calculated taking into account this beam loss scenario. There may be a higher rate of injection during other modes of operation, such as accelerator performance evaluation or during injection to fill the storage ring from zero current. Assuming that top-off is the prevailing mode of operation in the long run, shielding calculations are performed for an average injection frequency of once every minute and 50% of the injected beam energy being dissipated at the injection/extraction septum region. The lateral wall on the experimental floor side and the roof is assumed to be 1 meter from the septum.

The bulk shielding estimates in terms of concrete thickness for the storage ring enclosure at the booster-to-storage-ring injection/extraction region are also given in Table 15.2.8. 160cm-thick standard concrete with a density of 2.35 g/cm^3 will limit the dose rate to <0.25 mrem/h at the exterior of the lateral wall of the storage ring. 150 cm of concrete on the roof will limit the dose rate to the same level at the exterior on contact. Part of the concrete can be replaced with an equivalent thickness of lead as additional local shielding, if needed. A factor of 8 with respect to standard concrete can be applied to calculate the equivalent thickness of lead required. The extraction region can be shielded locally with an additional 10 cm of lead all around to maintain uniformity of the storage ring roof thickness around the ring. A berm (of earth) with a density of 1.6 g/cm^3 may be used as shielding to partially replace the inboard concrete wall. A berm/standard concrete factor of 2.1 can be applied to estimate the necessary thickness for this berm.

15.2.6 Bulk Shielding Estimates for the Booster Enclosure

At NSLS-II, the booster synchrotron will be housed in the storage ring enclosure. A top-off injection from the linac to the booster synchrotron will take place approximately every minute. The injected beam energy is 200 MeV and the injected charge is 15 nC. These electrons are accelerated to 3.5 GeV and injected into the storage ring. There may be a higher rate of injection during other modes of operation, such as accelerator

performance evaluation or during injection to fill the storage ring from zero current. Assuming that top-off is the prevailing mode of operation, shielding calculations are performed for an average injection frequency of one in every minute and 2% of the beam energy being dissipated at any single point in the booster synchrotron during acceleration. The salient features of the booster synchrotron are given below.

- beam energy: 3.5 GeV
- repetition rate: 1 Hz
- ring circumference: 780 m
- accelerated charge: 15 nC
- no of electrons per fill: 9.36×10^{10}
- total energy in the booster: 52.5 J

In the current design, the booster system will be suspended from the roof of the storage ring. The roof and lateral wall are each assumed to be 1 meter from the booster vacuum chamber. Bulk shielding for the booster synchrotron is calculated based on the algorithm given in Section 15.2.2.3. The results are given in Table 15.2.5.2. Storage ring shielding estimates are also given in the same table. The bulk shielding thickness for both standard concrete and high density concrete are given. Note that the required shielding in all directions is less than the shielding of the storage ring enclosure. Therefore, the booster synchrotron can be safely housed inside the storage ring enclosure with the current configuration without any additional radiological consequences. It must be emphasized that the distance from the source to the bulk shielding is critical in determining dose rates outside the shielding. The stated distances in the current calculations need to be maintained in the civil construction design, and any change warrants rescaling of the bulk shielding thickness.

15.2.6.1 Bulk Shielding for the Linac-to-Booster Injection/Extraction Region

Injection to the booster from the linac takes place once per minute during top-off mode. This injection frequency can be temporarily higher during machine studies periods. Assuming that top-off is the prevailing mode of operation, shielding calculations are carried out for an average injection frequency of once per minute. 15 nC of charge is injected to the booster in every minute. During the injection, 50% injection efficiency is assumed. This results in 50% of the injected beam energy being dissipated at the injection/extraction region and twice the quantity of charge being injected into the booster to achieve filling.

The linac injection septum to the booster is housed in the storage ring injection region. The bulk shielding estimates of the concrete thickness for the linac to booster injection region are also given in Table 15.2.8. 115 cm-thick standard concrete with a density of 2.35 g/cm^3 will limit the dose rate to <0.25 mrem/h at the exterior of the bulk shielding on contact for the lateral wall and the roof for the assumed 50% injection loss. In the current calculations, the distance from the loss points to the lateral walls and the roof is assumed to be 1 meter. The distance from the septum to the inboard wall is assumed to be 2 meters. These assumptions can be modified when a more detailed layout of the tunnels is available. If the septum is located at the booster to storage ring injection region, the available bulk shielding of the storage ring at the injection region will limit dose rates to <0.25 mrem/h. Additional local shielding can replace concrete, if bulk shielding is deficient.

Table 15.2.8 Bulk Shielding Estimates for the Storage Ring and Booster Synchrotron Enclosures.

Component	Expt. Floor Wall Concrete Equivalent Thickness [cm]	Roof Concrete Equivalent Thickness [cm]	Inboard Wall Concrete Equivalent Thickness [cm]
Storage ring non-injection region	120[a] or 76[b]	100[a]	100[a]
Booster to storage ring Injection/Extraction	160[a] or 102[b]	150[a] or (100[b] + 8 Pb)	150a or (100b + 8 Pb)
Storage ring ratchet wall (forward direction)	160[a] or 102[b]	100[a]	---
Booster non-injection region	95[a] or 60[b]	95[a]	80[a]
Linac to booster Injection region	115[a]	115[a]	100[a]

[a]Concrete of density 2.35 g/cm^3 is taken as standard concrete.

[b]Corresponding thickness with concrete of density 3.7 g/cm^3.

15.2.7 Booster Beam Stop Design Calculations

15.2.7.1 Booster Beam Stop

When the booster is not injecting into the storage ring, the beam is dumped at the booster beam stop. This beam stop will be located on the floor of the storage ring enclosure closer to the extraction/injection region. As the detailed layout of the building is currently not available, it is assumed that the concrete bulk shield, which separates the occupiable regions, is 1 m away at the experimental floor side and 3 meters away from the roof. The lateral wall of the storage ring at the injection region of the storage ring is assumed to be 160 cm of standard concrete equivalent and the roof is 100 cm of concrete equivalent without any additional local shielding. 100% of the 0.87 W electron beam is dissipated on the beam stop. The shielding strategy in this case will be to shield the stop locally in addition to the concrete bulk shielding available at the injection extraction region.

The electromagnetic shower parameters for various materials considered for the booster beam stop are given in Table 15.2.5. Iron is the preferred material for the stop, due to various qualities such as sturdiness, thermal stability, conductivity, and relative compactness of shower dimensions. As iron is a relatively low-Z material, the photo-neutron yield and the resulting activation will also be minimal.

The theory of electromagnetic showers (Table 15.2.5) stipulates that material approximately 20 radiation lengths long and 3 Moliere radii in transverse will contain 99.99% of the electromagnetic shower [15.10]. Thus, an iron cylinder 35 cm long and 8.5 cm in diameter will be sufficient to effectively contain the electromagnetic shower in the booster beam stop. The scattered low-energy photon radiation will require additional lead shielding, but will be well below the critical energy to further propagate the shower and the photo-spallation reaction threshold. The neutrons created in the shower will escape isotropically from the stop and require additional shielding.

Table 15.2.9 shows the dose rates due to various radiation components around the booster beam stop with no local shielding in place. This table also provides the dose rates on the exterior of the concrete shield wall with a local shielding of 10 cm of Pb and 10 cm of polyethylene (1g/cm3). As the exact layout of the storage ring injection region is not currently available, the distance from the iron beam stop to a) the concrete shield wall at the floor side, b) the roof, and c) the inboard wall is assumed to be 1 meter, 3 meters, and 2 meters, respectively. It can be seen that the dose rates after local shielding are primarily due to high-energy neutrons. With the proposed local shielding, the dose rates come down to <0.25 mrem/h on contact at the exterior of the concrete shield walls. (The possible effect of neutrons slowing in polyethylene is neglected in the current calculations.) The stop is inside the storage ring enclosure, and personnel have no access when the beam is in the storage ring.

Table 15.2.9 Dose Rates on Contact : Exterior Concrete Shield Walls near the Booster Beam Stop.

Radiation Component	Dose Rate on Lateral wall [mrem/h]		Dose Rate on Roof [mrem/h]		Dose Rate on Inboard Wall [mrem/h]	
	No local shielding	Pb+Poly 10+10 cm	No local shielding	Pb+Poly 10+10 cm	No local shielding	Pb+Poly 10+10 cm
Bremsstrahlung	0.3011	0.0028	2.2600	0.0208	4.0189	0.0369
Giant Resonance Neutrons	0.0104	0.0010	0.1493	0.0151	0.2653	0.0268
High Energy Neutrons	0.0616	0.0178	0.2277	0.0660	0.4048	0.1174
Total Dose Rate	0.3731	0.0216	2.6370	0.1019	4.6890	0.1811

15.3 SHIELDING ESTIMATES FOR BEAMLINES AND FRONT ENDS

NSLS-II is subject to DOE radiation protection rules established in 10 CFR 835. Operating with an administrative control level of 100 mrem per year, NSLS-II will be well within the legal limits established in 10 CFR 835. Shielding for NSLS-II beamlines will be designed to maintain levels through the shielding to less than 0.05 mrem/hr. A worker could work immediately adjacent to the shielded enclosure along the beamline for 2,000 hours per year and not exceed 100 mrem/year, such that the individual beamline scientist dose will be ALARA.

15.3.1 Sources of Radiation Hazard in the Beamlines

The radiation present on the experimental floor can be separated into sources that come through the ratchet wall penetration and those that come through the ratchet wall itself.

15.3.1.1 Radiation through the Ratchet Wall

In the process of operating the storage ring, as well as producing the desired synchrotron radiation [15.11], there is considerable generation of other radiation behind the storage ring wall. The shielding for this parasitic radiation is achieved by the concrete shield wall and the local shielding at various locations inside the storage ring. During the commissioning of the storage ring, surveys will be made to determine if any "hot spots" exist and, if so, additional local shielding will be employed to reduce the dose rates on the experimental floor to acceptable levels.

15.3.1.2 Radiation through the Ratchet Wall Penetration

The radiation through the ratchet wall penetration falls into the following categories:

- radiation from electron beam hitting storage ring components
- gas bremsstrahlung created from electron interaction with the residual gas molecules in the vacuum chamber
- synchrotron radiation created by the bending magnets and the insertion devices [15.11]

To estimate the shielding and other requirements for NSLS-II beamlines, these sources of radiation have been considered across a range of possible conditions. The neutron dose estimates done by the PICA neutron shield program [15.12] and confirmed by the measurements in other synchrotron radiation facilities [15.13] determined that the neutron dose hazard on the experiment floor is insignificant for all credible scenarios. Therefore, neutron shielding on the experiment floor for the beamlines has not been recommended other than for specific instances.

15.3.1.3 Interaction of Stored Beam with Storage Ring Components

If the stored electron beam collides with any storage ring component, a bremsstrahlung shower will be produced. Only a small portion of this radiation makes it through the synchrotron radiation apertures. In addition, bremsstrahlung collimators in the front end will severely limit the line of sight through the ratchet wall penetration. These collimators allow only radiation scattered in small angles to the beam path to exit onto the experimental floor. The beamline shielding present to account for other radiation sources will be more than sufficient to stop the radiation from beam losses inside the storage ring components.

Initial operations at NSLS-II will require that the beamline safety shutters (located inside the ratchet wall) be closed during injection. The closed shutters will keep any radiation that might come through the ratchet wall penetration. When NSLS-II begins operating in the top-off mode, in which the safety shutters are left

open, the additional radiation due to this mode of operation needs to be addressed. Preliminary analysis and experience at the other facilities indicates that it is not expected to be a problem [15.14].

15.3.2 Shielding Design Simulations

15.3.3.1 Simulation Tools

Bremsstrahlung dose scattering calculations for NSLS-II ID beamlines were carried out using the EGS4 electron-gamma shower simulation program [15.15]. This implementation is part of the CALOR program package distributed by the Radiation Shielding Information Center (RSIC) of the Oak Ridge National Laboratory. EGS4 simulates the coupled interactions of photons and electrons with materials over an energy range from a few keV to several TeV. It also includes a standalone program, PEGS4, which creates parameterized cross sections to be used by EGS4. Physical processes simulated by this program include bremsstrahlung production, positron annihilation at rest and in flight, Moliere multiple scattering, Moller and Bhabha scattering, Compton scattering, pair production, photoelectric effect, and continuous energy loss by Bethe-Bloch formalism. The photoneutron production and transport is not simulated by EGS4, but measurements at the other third-generation light source facilities have confirmed that photoneutrons are not a radiation hazard at the synchrotron radiation beamlines.

The synchrotron radiation scattering calculations for NSLS-II beamlines have been performed using the STAC8 program [15.16]. STAC8 was developed at the Spring8 facility and has been used extensively at other third-generation synchrotron radiation facilities during design and operation. STAC8 generates insertion device radiation spectra and monochromatic beams with a fixed band width. The program simulates photon transport by Compton scattering (with anisotropy), Rayleigh scattering, and photo-absorption. It calculates scattered photon flux as a function of energy and angle, and converts photon flux to dose rates. Build-up factors in the shielding materials are taken into account, but the effect of polarization has not been considered.

15.3.3 Bremsstrahlung Source Estimates in the ID Beamlines

Gas bremsstrahlung is produced by interaction of the storage ring electron beam with residual gas molecules in the ring vacuum chamber. Such interactions are sources of stored beam loss, which results in beam decay and occurs continuously during storage ring operation. Gas bremsstrahlung interactions take place all around the storage ring, but are a particular problem in the straight sections for the insertion devices. Gas bremsstrahlung is produced in a very narrow beam in the straight path and sums up for the entire straight path in the line of sight of the beamlines. The NSLS-II straight beam paths are 16 m long. (The straight beam path length is longer than the insertion device straight section length.)

The total beam integrated bremsstrahlung dose rate D (rem/h) from the straight particle trajectory in the vacuum chamber of the storage ring at a distance L from the straight path is usually approximated by semi-empirical equations. Three common empirical relations have been in use historically. The semi-empirical equation proposed by Frank [15.17] had been successfully utilized at the Advanced Photon Source and other similar facilities. Using the equation developed by Frank, the dose rate due to primary bremsstrahlung is described as at a distance L from the end of the straight path is

$$\text{dose rate (rem/h)} = \frac{3.0\times10^{-4}}{\pi\times X_0}\ \frac{E^2}{0.511^2}\ \frac{l\times I}{L(L+l)}\ , \qquad (15\text{-}2)$$

where X_0 = radiation length of air at 10^{-9} Torr = 2.34×10^{16} cm, l = effective length of the straight path (16 meters), I = beam current in e/s (3.1×10^{18} electrons/s for 500 mA), and E = electron beam energy in MeV. L is nominally taken as 20 meters. This equation yields a primary bremsstrahlung dose rate of 240 rem/hour.

Another analysis developed by Ferrari [15.18], et al., gives the following expression for dose rate produced by the primary bremsstrahlung in the ID beamlines at a distance of L from the straight path.

$$\text{dose rate (rem/hour)} = 2.5 \times 10^{-25} \; \frac{E^{2.67}}{0.511^{2.67}} \; \frac{l \times I}{L(L+l)} \; \frac{P}{P_0}, \tag{15-3}$$

where l = effective length of the straight path (16 meters), I = beam current in e/s (3.1×10^{18} electrons/s for 500 mA), E = electron beam energy in MeV, P = operating pressure in the vacuum chamber in nTorr, and P_0 = 1 nTorr. L is nominally taken as 20 meters. This equation yields a primary bremsstrahlung dose rate of 280 rem/hour.

Chronologically, the first expression developed in this regard is by Rindi and Tromba [15.19]. This simple expression provides the dose rate at 10 meters from the straight path as

$$\text{dose rate (rem/hour at 10 m)} = 1.7 \times 10^{-14} \, E^{2.43} \; \frac{P}{P_{atm}} \; I \, l, \tag{15-4}$$

where l = effective length of the straight path (16 meters), I = beam current in e/s (3.1×10^{18} electrons/s for 500 mA), E = electron beam energy in MeV, P = operating pressure in the vacuum chamber, and P_{atm} = atmospheric pressure. This expression yields a primary bremsstrahlung dose rate of 450 rem/h at 10 meters and 112 rem/h at 20 meters.

Table 15.3.1 gives the estimated primary bremsstrahlung dose rates in the NSLS-II beamlines calculated by the three semi-empirical expressions at 20 meters from the straight path for a straight path length of 16 meters and vacuum chamber pressure of 1 nTorr. Methods 1 and 2 give similar results, in contrast to method 3. Being conservative, methods 1 and 2 are used to estimate the primary bremsstrahlung dose rates for the NSLS-II insertion device beamlines.

Table 15.3.1 Primary Bremsstrahlung Dose Rates at the NSLS-II ID Beamlines.

	Bremsstrahlung Dose Rate [rem/h]	Notes:
Method 1 (Lure-APS)	240	Beam Energy = 3.5 GeV Beam Current = 500 mA Straight section Path Length = 16 m Distance to the dose point = 20 m Straight section vacuum = 10^{-9} Torr
Method 2 (Ferrari)	280	
Method 3 (Rindi-Tromba)	112	

15.3.4 Design of Shutters/Stops

15.3.4.1 Geometry Used for the Calculations

The primary bremsstrahlung dose rates at the insertion device beamlines determine the thickness of bremsstrahlung shutters, stops, and collimators in the beamlines and front ends. Figure 15.3.4.1 shows the geometry used in the EGS4 simulations to calculate the thickness of lead and tungsten required to attenuate the dose rate <0.25 mrem/h at the downstream side of the stop/shutter on contact. These shutters will be located inside the shielded enclosures. The primary bremsstrahlung source term was estimated using the empirical formulae from Table 15.3.1 to scale the dose rate results. The bremsstrahlung beam from the NSLS-II straight section is incident on a lead or tungsten block with transverse dimensions of 20 x 20 cm^2. The heavy metal is followed by the ICRU tissue [15.20] of 30 cm thick to score the dose at the downstream side of the shutter/stop. The ICRU tissue is binned into 1 cm^3 bins for scoring the dose, and the maximum dose is taken as the dose index.

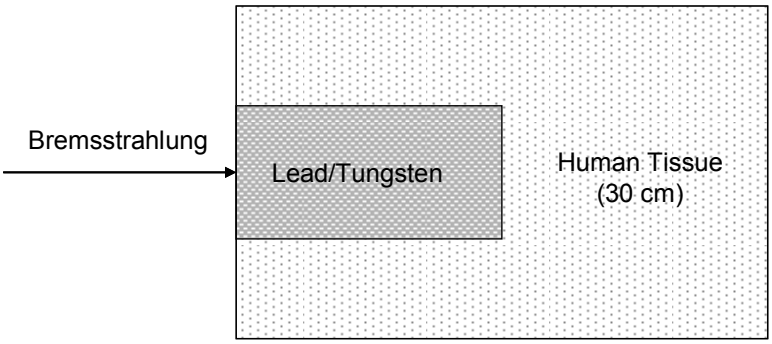

Figure 15.3.1 Simulated EGS4 geometry of the NSLS-II safety shutters.

15.3.4.2 Thickness of Shutters/Stops

Table 15.3.2 shows the primary bremsstrahlung dose rates predicted by the two conservative methods, and the thickness of lead or tungsten required to reduce the radiation dose rate at the back of the shutter/collimator to less than 0.25 mrem/h (<2.5 μSv/h). The dose rates at the downstream surface in the ICRU tissue were calculated as a function of lead or tungsten thickness and fitted using an effective exponential attenuation factor. The results are also plotted in Figure 15.3.2 for source calculated by method 1. Note that a lead thickness of > 30 cm or a tungsten thickness of >20 cm are required as stops/shutters at NSLS-II beamlines to reduce the dose rate to less than 0.25 mrem/h (<2.5 μSv/h), taking into account the conservative primary bremsstrahlung source term.

Table 15.3.2 Shutter/Collimator Thickness for NSLS-II Insertion Device Beamlines.

	Method 1 (LURE-APS)	Method 2 (Ferrari-CERN)
Bremsstrahlung dose rate [rem/h]	240	280
Lead thickness required [cm]	28.9	29.2
Tungsten thickness required [cm]	19.6	19.8
Dose rate behind the stop/shutter [mrem/h]	0.25	0.25

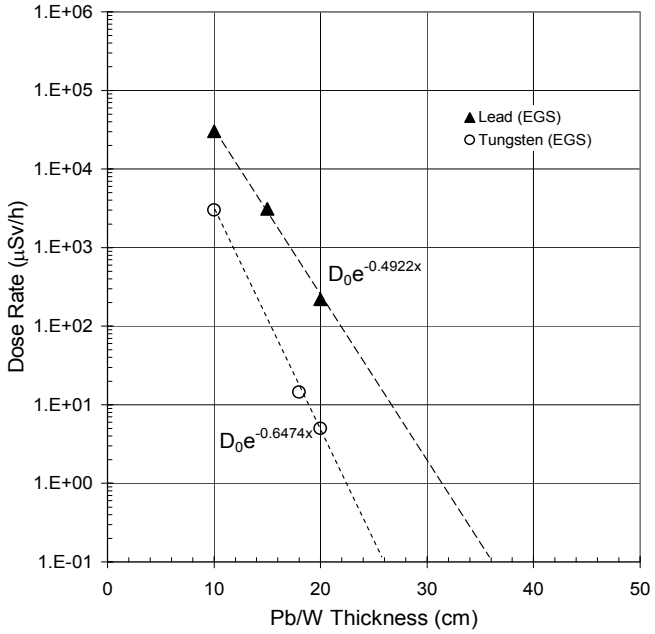

Figure 15.3.2
Contact dose rates at the downstream surface of the shutters/stops. Bremsstrahlung source was calculated by method 1.

15.3.5 Shielding Estimates for Experimental Stations

15.3.5.1 Computation for Bremsstrahlung and Synchrotron Radiation Scattering

The synchrotron radiation and bremsstrahlung can be scattered from any potential component in the beamlines and front ends. Such components include windows, slits, monochromators, mirrors, and so forth, and vary from beamline to beamline. Therefore, calculations were performed with a worst-case potential scatterer upstream of the first optics enclosure (Figure 15.3.3), of typical dimensions (2.0 m wide, 3 m high, and 10 m long). Figure 15.3.4 shows the results of the calcuations. The worst-case potential scatterer for bremsstrahlung is 3 cm thick copper, and for synchrotron radiation is 0.1 cm thick aluminum with small transverse dimensions. In addition to this, 10 meter air in the station is also a potential scatterer for synchrotron radiation. The EGS4 calculations were performed for bremsstrahlung, and STAC8 calculations were performed for synchrotron radiation.

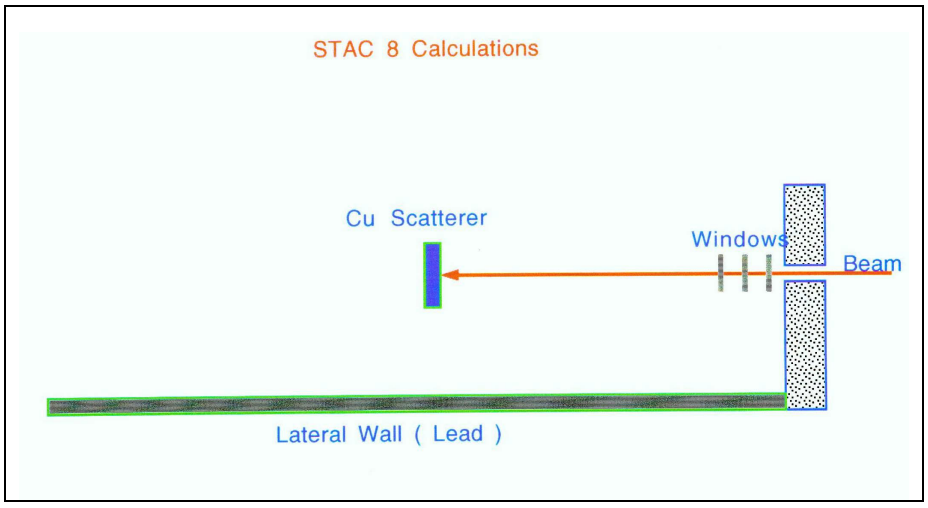

Figure 15.3.3 EGS4 and STAC8 geometry for bremsstrahlung and synchrotron radiation scattering calculations.

15.3.5.2 Shielding Estimates for the First Optics Enclosures

Preliminary shielding estimates for the NSLS-II First Optics Enclosures are calculated using the available beamline and insertion device parameters. For each shielding situation, the synchrotron and bremsstrahlung shielding have been calculated for the representative station geometry. The shielding simulations for bremsstrahlung were done using the EGS4 program and for synchrotron radiation using the STAC8 program. In most cases, one of the sources (bremsstrahlung or synchrotron radiation) dominates for the shielding requirement and the contribution of the other becomes negligible; thus, the calculated shielding for the dominant source can be implemented. All bremsstrahlung and synchrotron radiation calculations were done at 500 mA of beam current, at 3.5 GeV electron beam energy. Also, all the doses are scored in the ICRU tissue on contact unless otherwise mentioned, instead of at a distance of 30 cm from the dose point. Occupational exposure of personnel is most likely to occur in the vicinity of experimental stations along the beamlines. Shielding of these areas is designed to maintain individual exposures when in contact with the hutch wall as <100 mrem/year for 2,000 hours of exposure per year. Thus, the experimental station shielding is designed to meet or exceed this criterion to ensure that occupational radiation doses are ALARA.

15.3.5.3 Shielding Estimates for Secondary Bremsstrahlung

Bremsstrahlung scattering calculations for the representative geometry of the NSLS-II FOE were performed using EGS4. The computational geometry given in Figure 15.3.1 was used. EGS4 calculates integral energy deposition per particle at various regions of the geometry. The radiation dose (energy deposited per unit mass) at any given location per particle was calculated from the 3D energy deposition profile in the standard ICRU tissue placed at the location, taking the maximum energy deposition per unit mass**.** Once energy deposition per particle at each region is available, the absolute dose rate at any region can be scaled, using the primary bremsstrahlung dose rate provided by the empirical formulae.

Figure 15.3.4 gives the scattered bremsstrahlung dose rates 1 meter away from a 3 cm thick copper scatterer in terms of μSv/h (× 0.1 mrem/h). The bremsstrahlung forward-beam direction in this figure is 90 degrees. The transverse directions are 0 degrees and 180 degrees. Calculations are for a 240 rem/h primary bremsstrahlung dose rate. Note that the scattered bremsstrahlung beam is highly forward peaked.

To calculate the shielding requirements for the downstream wall of the FOE, the calculated dose rates (DR) from Figure 15.3.4 were used. The minimum distance from the copper scattering target to the downstream wall is taken as 10 meters. For small angles, a constant distance of 10 m to the wall is assumed, and the distance-adjusted dose factor is taken as 10^2. The required lead thickness for the downstream wall of the FOE, as a function of the scattering angle to achieve the design dose limit of <0.05 mrem/h, is calculated using the expression

$$\text{lead thickness (cm)} = [\ln (0.01 \times DR) - \ln 0.05\ ] / 0.473. \quad (15\text{-}5)$$

The minimum attenuation coefficient of 0.473 cm^{-1} for lead has been used in these calculations for bremsstrahlung attenuation.

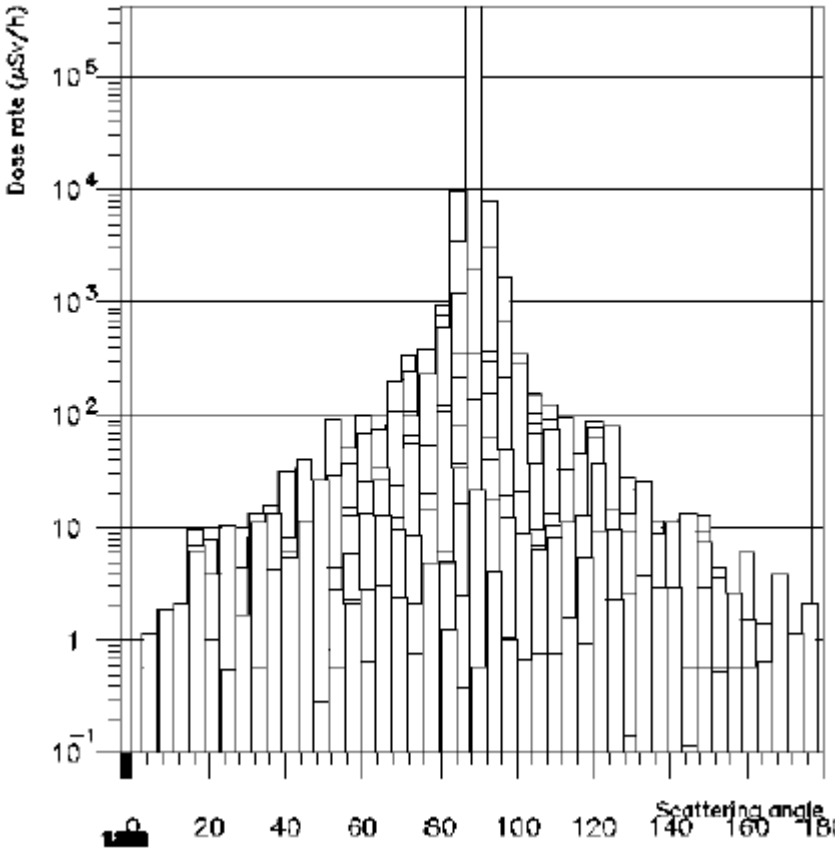

Figure 15.3.4
Scattered bremsstrahlung dose rates for the NSLS-II beamlines. (Primary bremsstrahlung scattered from a Cu target of 3 cm thickness with small transverse dimensions.)

Table 15.3.3 provides the calculated lead thickness for the panels of the FOE as a function of the scattering angle to achieve the design dose limit of <0.05 mrem/h. Because of the forward-peaking nature of the high-energy bremsstrahlung scattering, the lead shielding thickness required at small angles along the beam direction is large. In practice, this will be satisfied by the presence of collimators or bremsstrahlung stops approximately from 0 to 2 degrees. Considering a uniform downstream wall thickness of 5 cm, additional shielding will be required for scattering angles <4 degrees. This can be satisfied by placing the appropriate lead local shielding around the beam transport pipes. The exact transverse dimensions of these local shields can be calculated once the station dimensions are available. Currently, a uniform downstream wall thickness of 50 mm is recommended.

Table 15.3.3 Shielding Estimates for the FOE for Bremsstrahlung Scattering[a].

Angle [deg]	Dose Rate [mrem/m^2-h]	Lead Thickness Back Wall [cm][b]	Lead Thickness Side Wall [cm]	Lead Thickness Roof [cm]	Half Width of Local Shielding Required [cm]
1	5.0 x 10^3	14.6	2.3	0.4	17
2	1.5 x 10^3	8.65	2.3	0.4	34
3	7.0 x 10^2	7.04	2.3	0.4	52
4	4.0 x 10^2	5.86	2.3	0.4	69
5	2.2 x 10^2	4.59	2.3	0.4	87
6	1.5 x 10^2	3.78	2.3	0.4	100
8	1.0 x 10^2	2.93	2.3	0.4	140
10	7.0 x 10^1	2.17	2.3	0.4	170

[a] Lead thickness required to reduce the dose rate to <0.05 mrem/h for bremsstrahlung scattering from a 5 x 5 x 3 cm^3 Cu scatterer at the upstream of the experimental station, beam current 500 mA, beam energy 3.5 GeV. Experiment station is 10 meters long.

[b] A uniform thickness of 5.0 cm is recommended. Additional shielding in the forward direction can be achieved by the stop/collimator and local shielding.

The lateral wall (side wall) shielding for the FOE can be calculated using the same equation:

$$\text{lead thickness (cm)} = [\ln DR - \ln 0.05] / 0.473. \quad (15\text{-}6$$

Because of the relatively large statistical fluctuation of calculated DR at 180 degrees and 0 degrees in Figure 15.3.4, an average DR of 0.15 mrem/h (1.5 μSv/h) has been used to calculate the required lead thickness for the side wall to achieve the design dose limit of <0.05 mrem/h. This gives a lead thickness of

$$\text{lead thickness (cm)} = [\ln 0.15 - \ln 0.05] / 0.473 = 2.3 \text{ cm}. \quad (15\text{-}7)$$

A side wall thickness of 23 mm is recommended for the insertion device beamlines. The roof of the experimental stations is assumed to be at distance of 1.5 m from the beam. The distance adjustment factor for DR in this case is $1/1.5^2$. The shielding thickness for the roof can be calculated by the expression

$$\text{lead thickness for roof (cm)} = [\ln (DR \times 0.4) - \ln 0.05] / 0.473. \quad (15\text{-}8)$$

Taking an average transverse DR of 0.15 mrem/h, the expression yields a roof thickness of 4 mm for the insertion device experiment stations. This thickness is less than the lead thickness required for synchrotron radiation shielding, in most cases.

It must also be emphasized that the bremsstrahlung production is linear with respect to the pressure in the vacuum chamber. In the current calculations for primary bremsstrahlung source term, a vacuum chamber pressure of 1 nTorr is assumed. It is imperative to maintain a vacuum of <1 nTorr in the storage ring to minimize bremsstrahlung production during the storage ring operation.

15.3.5.4 Synchrotron Radiation Scattering Calculations with STAC8

Synchrotron radiation scattering calculations to estimate the shielding requirements for the NSLS-II FOE were performed using the STAC8 shield program. The worst-case scatterer, 0.1 cm aluminum, is used as the potential scatterer upstream of the station. In addition to this, 10 meters of air along the length of the station were also considered as a potential scatterer of the synchrotron radiation in the station.

The source spectrum for the NSLS-II insertion devices for this calculation was generated by the STAC8 program. Four kinds of IDs were considered for the NSLS-II beamline station shielding design. The salient features of these insertion devices, calculated by the STAC* program, are given in Table 15.3.4.

Table 15.3.4 NSLS-II Insertion Device Parameters for Beamline Shielding Calculations.

Device Type	No. of Poles	B_{eff} [Tesla]	Period [mm]	Power at 500 mA [kW]	Critical Energy [keV]	Aperture in FOE [mm]
DW	120	1.8	100	75.25	14.66	4 x 10
U19	316	1.0	19	11.64	6.26	4 x 4
U14	286	1.4	14	15.46	8.75	4 x 4
SCW	10	3.5	150	35.57	28.47	4 x 8

Station dimensions of 2 x 3 x 10 meters are assumed. All calculations for 3.5 GeV beam energy at 500 mA.

The lateral walls of the experimental stations were assumed to be 1 meter distant and the roof was 1.5 meter. Shielding for these areas was calculated to maintain individual exposures, when in contact with the experimental station wall, at less than100 mrem/year for 2,000 hours of exposure per year. This converts to an effective dose rate of <0.05 mrem/h at the occupiable areas.

Table 15.3.5 gives the preliminary shielding estimates for the FOE at NSLS-II for four insertion device beamlines. Required shielding estimates for the side panel, roof, and the upstream panel are given only for calculations of synchrotron radiation scattering.

Table 15.3.5 Preliminary Shielding Estimates for NSLS-II White Beam Stations (SR Only).

	Lead Thickness [mm]		
Insertion Device	Side Panel	Roof	Upstream Panel
U19	8	7	8
U14	10	9	10
SCW	16	14	16
DW	14	12	14

SR = Synchrotron radiation. All calculations are done for Beam Energy of 3.5 GeV at 500 mA. Insertion Device parameters are used from Table 15.3.5.2. Station dimensions are assumed to be 2.0 x 3.0 x 10.0 m^3. Side panels are at a distance of 1 m and roof at 1.5 m away from the beamline.

15.3.5.5 Shielding Recommendations for NSLS-II First Optics Enclosures and White Beam Stations

Table 15.3.3 provides the shielding estimates for the FOE and white beam stations for NSLS-II from bremsstrahlung scattering calculations. Table 15.3.5 provides the shielding estimates from scattering calculations of synchrotron radiation. In each case, the shielding requirement for the dominant source must be implemented.

To summarize, bremsstrahlung shielding dominates for the back wall and side wall, and synchrotron radiation dominates for the roof and upstream wall. Table 15.3.6 compiles the shielding requirements for the NSLS-II FOE and white beam stations. Shielding requirements for the four kinds of ID beamlines are given. Lead shielding of 50 mm is needed for the entire downstream wall of all ID beamlines to shield the forward-peaking bremsstrahlung scattering source. An additional 50 mm of lead (100 mm total) is needed for the central portion around the beam penetration. This lead shielding can be achieved by the appropriate design of the local shielding around the beam pipe. It is also desirable to design bremsstrahlung collimators at appropriate locations upstream of the FOE, near the potential scattering components.

Table 15.3.6 Summary Shielding Requirements for NSLS-II First Optics Enclosures.

Insertion Device	Side Panel [mm]	Roof [mm]	Upstream Panel [mm]	Downstream Panel[a] [mm]
U19	23	7	8	50
U14	23	9	10	50
SCW	23	14	16	50
DW	23	12	14	50

[a] An additional 50 mm of lead locally around the beam pipe penetration.

15.4 RADIOLOGICAL CONSEQUENCES OF ACCIDENTAL BEAM LOSS

15.4.1 Consequences of Accidental Linac Beam Losses

Shielding calculations for the linac enclosure have been carried out assuming a 1% distributed beam loss during beam acceleration (0.66% at any given point). Shielding thickness has been calculated for a dose rate of <0.25 mrem/h, at the exterior of the concrete bulk shielding. In the unlikely event of 100% linac beam loss during beam acceleration at any given point of the accelerator system, the dose rate on contact at the exterior shielding wall will be ~150 times more than the limiting value. The dose rate will be <37.8 mrem/h at the exterior of the concrete bulk shielding of the enclosure due to this beam loss event.

15.4.2 Consequences of Linac-to-Booster Injection Losses

The shielding calculations for the storage ring and the booster assume an average injection frequency from the linac into the booster of once per minute. An unlikely situation was conceived where 20 nC/s, which is the capacity of the linac, would be injected into the booster continuously and all of it be lost at the injection septum. The total charge lost at the septum in this case in an hour would be 7.2×10^4 nC/h. Assuming 50% loss of injected beam at the injection/extraction region (15 nC every minute), 900 nC/h would be lost at the region for which the shielding design calculations were carried out. The shielding is designed for a dose rate of <0.25 mrem/h at the occupiable regions. Therefore, the dose rate during this accident scenario at the exterior of the concrete bulk shielding on contact near the injection region would be less than 0.25 (7.2×10^4/900) = 20 mrem/h.

15.4.3 Consequences of Booster-to-Storage Ring Injection Losses

The shielding calculations for the booster to storage ring injection assume an average injection frequency of once per minute. A scenario was developed where 20 nC/s, the capacity of the linac, was injected continuously into the booster and the storage ring, and all of it was lost at the injection septum. The total charge lost in this case in an hour would be 7.2×10^4 nC/h. Assuming a 50% loss of injected beam at the injection/extraction region, 750 nC/h would be lost at the region for which the shielding design calculations were carried out. The shielding for the accelerators is designed for a dose rate of <0.25 mrem/h at the occupiable regions, on the exterior of the bulk shielding. Therefore, the dose rate at the occupiable regions during this accident scenario would be less than 0.25 (7.2×10^4/750) = 24 mrem/h at the exterior of the shield wall.

15.4.4 Maximum Credible Incident Analysis

In the shielding estimates of NSLS-II injection losses, the average injection frequency from the booster into the storage ring is assumed to be once per minute. A highly unlikely scenario would be if 20 nC/s, the capacity of the linac, were injected into the storage ring continuously and 100% were lost at the septum. This scenario was considered for the radiological consequences of injector loss at the booster septum.

In addition to the scenario described above, a situation was conceived where a dipole magnet downstream of the injection septum shorts and the 100% injected beam proceeds along the direction of one of the beamlines. However, the mis-steered electron beam would generally be unable to proceed farther than a collimator or a front end shutter, where it would create an electromagnetic shower. If this accidental scenario were to persist, it would result in higher dose rates in the first optics enclosure of the beamlines. The shielding wall of the storage ring is designed for a beam loss charge of 77.5 nC/h, 10% of the stored beam loss at any given location. The shielding for the storage ring is designed for a dose rate of <0.25 mrem/h at the occupiable regions. Dose rates during this particular accident scenario would be a factor of 929 greater than

the limiting dose rates. The dose rates would be $<(7.2\times10^{4}/77.5)\ 0.25 = 232$ mrem/h at the exterior of the shield wall of the storage ring on contact near the optics enclosure regions.

Loss of vacuum in the insertion device straight path is another credible incident that can cause higher dose rates around the FOE of the beamlines. In the bremsstrahlung source calculations in Section 15.3.3, a straight section pressure of 10^{-9} Torr is assumed. A sudden loss of vacuum to 1 Torr in the straight section would increase bremsstrahlung production by a factor of 10^{9}. We further assumed that this scenario would last for <1 millisecond (approximately 1,000 revolutions of the beam) before the beam would be completely absorbed. No credit was given to the engineering controls that trip the beam at vacuum loss. The FOEs are designed for a dose rate of <0.05 mrem/h on contact at the exterior of the shield panels. The dose rate during this accident scenario would be higher by a factor of 10^{9}, but would last for only a millisecond. The total dose commitment to an individual beamline scientist due to one such incident can be estimated as $<(0.05\times10^{9})/(3.6\times10^{6}) = 14$ mrem.

The probability of these failure scenarios to occur simultaneously is extremely small and the radiological consequences of these incidents are insignificant. In addition, sufficiently conservative factors are included in the shielding estimates to provide additional margins of safety. Dose rates in the current estimates are calculated on contact at the exterior of the bulk shielding, which is conservative. It is also prudent to assume a time period for each event duration, such that the total dose commitment to personnel during such an unlikely scenario can be estimated. Continuous injection for prolonged periods can also be limited by the engineering controls.

15.5 ACTIVATION ANALYSIS OF ACCELERATOR COMPONENTS

Bremsstrahlung is generated in accelerator systems of synchrotron radiation facilities by the radiative interaction of the circulating electron beam with accelerator components and with residual gas molecules in the vacuum chamber. The photoneutron interaction of bremsstrahlung with materials leads to the radioactivation of accelerator components through neutron emission and the production of radioisotopes. However, this activation interaction is a second-order effect, because it involves the intermediate process of bremsstrahlung production. Photoneutron interaction takes place above the threshold bremsstrahlung energy of 7–20 MeV; the cross section for photoneutron interactions is in millibarns. Therefore the electron beam activation of materials is not as abundant as the proton beam activation, because electrons do not cause direct spallation interaction with the nuclei.

Photospallation is another process (with comparable cross sections) by which radioisotopes are produced. The particular radionuclides produced in a material will depend on (γ, n), (γ, 2n), and photospallation cross sections of the material. These interactions can potentially activate various accelerator components. Isotopes and their saturation activities are listed in IAEA 188 [15.21]. The materials of interest for NSLS-II operations are aluminum, iron (in steel), copper, tungsten, and lead.

Radioactivity builds up during the operation of accelerator systems. When operations cease, there is an initial rapid decay of shorter-lived isotopes; after a waiting period, only the longer-lived isotopes remain. For routine operations of NSLS-II, short-lived isotopes will be of interest, because residual activity in the accelerator components and beam stops may be high enough to limit access time to the area.

15.5.1 Residual Activity Estimates of Accelerator Components

15.5.1.1 Methodology for Estimating Activation in Materials

The methodology of estimating activity of a radionuclide formed by (γ,n) reaction is to assume that the yield of neutrons is also the yield of radionuclide atoms [15.9]. The neutron yield in the accelerator components and in the beam stops is based on the equation from Swanson:

$$Y^1 = 1.21 \times 10^8 \, Z_1^{0.66} \text{ neutrons/joule,} \tag{15-9}$$

where Z_1 = atomic number of the element. The equation can be modified for a given isotope as

$$Y = F(1.21 \times 10^8 \, Z^{0.66}) \text{ n/J,} \tag{15-10}$$

where F is the fractional abundance of a given isotope with atomic number Z. Therefore, the change in the number of radioactive nuclides (N) due to (γ,n) interactions per unit time is given by

$$dN/dt = WYf - \lambda_R N \text{ atoms/sec,} \tag{15-11}$$

where W = dissipated electron beam power in watts, f = fraction of electron beam power which converts to bremsstrahlung, and λ_R = radioactive decay constant of the radionuclide in s^{-1}. By solving the equation and applying the initial boundary condition N = 0 for t = 0,

$$N = \frac{WYf}{\lambda_R} (1 - e^{-\lambda R t}) \text{ atoms.} \tag{15-12}$$

Since the activity is $\lambda_R N$

$$\text{Activity} = WYf\,(1 - e^{-\lambda R t})\ \text{disintegrations/sec}, \tag{15-13}$$

the saturation activity of the radionuclide, as t tends to be large, is

$$A = WYf\ \text{disintegrations/sec} \tag{15-14}$$

This is the saturation activity of a radionuclide with a given half life if the continuous operation time of the accelerator system is about three times the half life of the radionuclide formed. For each of the potential activated materials, Swanson (IAEA 188) has prepared tables listing the saturation activities of the (γ,n), (γ,2n) and photospallation products in (Ci/kW), and the exposure rate in (R/h) at 1 meter from the saturation activity.

The data in these tables have been used to estimate the saturation activity and the radiation fields following certain operation periods and the residual radiation field after shutdown.

15.5.1.2 Radioactivation of the Linac Iron Beam Stop

Approximately 4 watts of electron beam power are dissipated in the linac beam stop during the continuous beam dump on the stop. The radioactive materials formed in the iron beam stop have a range of half lives from a few seconds to a few years. Continuous operation for 1 hour of the iron beam stop results in about 90% of the saturation exposure rate. The main activities are due to ^{52}Mn(m), ^{56}Mn, ^{54}Mn, ^{52}Fe, and ^{53}Fe. The estimated combined exposure rate at 1 meter from the beam stop for a power dissipation of 4 watts is about 2.21 mR/h, contributed mainly by ^{52}Mn (m) (half life 21.1 min) and ^{53}Fe (half life 8.51 min). After about an hour of shutdown, the exposure rate would be ~0.046 mR/h at 1 meter. ^{54}Mn, the long-living isotope formed in the iron beam stop with a half life of 303 days, will not attain saturation activity until about three years of continuous operation. After 200 hours of continuous operation of the beam stop, the activity due to ^{54}Mn in iron would be 0.05 mR/h. ^{55}Fe, produced from ^{54}Fe, will not pose any substantial exposure hazard, due to the low-energy x-ray emission of 5.95 keV. Activation of the linac beam stop during NSLS-II operations is not a serious radiological hazard.

15.5.1.3 Radioactivation of the Booster Iron Beam Stop

Approximately 0.87 watts of electron beam power is dissipated in the booster beam stop during the continuous beam dump on the stop. Continuous operation of 1 hour of the iron beam stop results in about 90% of the saturation exposure rate. The main activities are due to ^{52}Mn(m), ^{56}Mn, ^{54}Mn, ^{52}Fe, and ^{53}Fe. The estimated combined exposure rate at 1 meter from the beam stop is about 0.48 mR/h, contributed mainly by ^{52}Mn(m) (half life 21.1 min) and ^{53}Fe (half life 8.51 min). After about an hour the exposure rate would be ~0.01 mR/h at 1 meter. ^{54}Mn, the long-living isotope formed in the iron beam stop with a half life of 303 days, will not attain saturation activity until about three years of continuous operation. After 200 hours of continuous operation of the beam stop, the activity due to ^{54}Mn in iron would be 0.01 mR/h. ^{55}Fe, produced from ^{54}Fe, will not pose any substantial exposure hazard, due to the low-energy x-ray emission of 5.95 keV. Activation of the booster beam stop during NSLS-II operations is not a serious radiological hazard.

Saturation activity and the resulting radiation field, due to the activation of iron in the septum magnet from injection losses, will be comparable to or less than at the booster beam stop.

15.5.1.4 Radioactivation of the Tungsten Injection Stop

There is a stop between the linac and booster, made of tungsten. This stop will not normally see any beam, but should an incident occur, the entire 4-watt electron beam would be directed to it. Tungsten has four

isotopes that can be activated: ^{182}W [0.264], ^{183}W [0.144], ^{184}W [0.306], and ^{186}W [0.284] (the fractions in brackets indicate isotopic abundance). Only ^{182}W and ^{183}W contribute the relatively long-lived radionuclides of ^{181}W (half life 140 days) and ^{182}Ta (half life 115 days). These isotopes contribute residual activity after prolonged operation. Because this stop normally will not see beam, a generous 1-hour operation time was used in calculations of radioactivation: This scenario would produce the activities ^{180}Ta(m), ^{182}Ta(m), ^{184}Ta, ^{185}Ta, ^{183}W(m), and ^{185}W(m). The essential exposure rate at 1 meter is 4.9 mR/h (IAEA188), mainly from ^{183}W(m) (half life 5.3 s), and ^{185}W(m) (half life 1.62 min). After a decay of 1 hour, the estimated exposure rate will be 0.05 mR/h. The short-term radiation field for this material is not a radiation hazard.

The front end safety shutters and the beamline bremsstrahlung stops will also be made up of tungsten. These shutters/stops intercept the bremsstrahlung beam from the straight section coming along the beamlines. The bremsstrahlung power incident on these stops/shutters is a few microwatts and will not create any detectable activation of the beamline and front end safety shutters and stops.

15.5.1.5 Radioactivation of Copper at the Injection Septum

The injection septum consists of copper conductor with iron. As the septum is a high beam-loss point, the copper in the injection septum can become activated during continuous operation, as happens during top-off. Most of the isotopes formed during this process are short-lived except ^{60}Co (half life 5.26 years) and ^{63}Ni (half life 93 years). Other short-lived isotopes produced are ^{58}Co (half life 71.3 days), ^{58}Co(m) (half life 9.2 h), ^{61}Cu (half life 3.32 h), ^{62}Cu (half life 9 min), and ^{64}Cu (half life 12.8 h). After 100 hours of continuous operation, these isotopes will attain saturation activity. After shutdown, the initial activity will be mainly due to ^{62}Cu. The initial combined activity after 100 hours of continuous operation is estimated <5.8 mR/h at 1 m from the septum. After 200 hours of operation, ^{60}Co will achieve only 0.3% of the saturation value. The radiation field attributable to this isotope will be negligible. After about an hour of waiting time, the activity from short-lived isotopes will decay and the corresponding radiation field will be <0.09 mR/h.at 1 meter from the septum.

15.5.1.6 Radioactivation of Lead at the Injection Septum

The injection septum is a high beam-loss point. This region is heavily shielded with lead, which becomes activated and results in the production of ^{206}Tl, ^{207}Tl, ^{207}Tl(m), ^{202}Pb(m), ^{203}Pb(m), and ^{204}Pb(m). Most of these isotopes are relatively short lived and attain saturation activity in a few hours of continuous operation of the septum. After prolonged operation of the septum, the estimated initial radiation field from lead activation at 1 meter from the septum shielding will be 1.6 mR/h. After a few minutes of waiting time, the activity will be 0.36 mR/h, mainly from ^{204}Pb(m), which has a half life of 67 minutes.

Lead is also used as bremsstrahlung beam stops and collimators in the beamlines and front ends. These stops and collimators intercept the bremsstrahlung beam from the straight section coming along the beamlines. The bremsstrahlung power incident on these stops/collimators consists of a few microwatts. This bremsstrahlung energy will not create any detectable activation of the safety stops and collimators in the beamlines and front ends.

15.5.1.7 Radioactivation of the Aluminum Vacuum Chambers

The vacuum chambers of the accelerator system are made of aluminum. Stored beam loss occurs continuously during storage ring operations. For shielding calculations of the storage ring, a stored beam loss of 10% is assumed to take place at any given location of the storage ring. Part of his beam loss energy will dissipate on the aluminum vacuum chamber, possibly activating it. The main activation products are ^{11}C, ^{13}N, ^{15}O, ^{24}Ne, ^{25}Al, and ^{26}Al(m). The isotopes will attain saturation activity after a few hours of operation. ^{22}Na, the long-living isotope produced by activation, will not attain saturation activity until about seven years. After a few hours of operation, the combined exposure rate due to saturation activity is estimated as <0.2 mR/h, at 1 meter from the vacuum chamber. The major contribution is from ^{26}Al(m) (half life 6.37 s). After a few

minutes, the exposure rate will come down to less than 0.02 mR/h at 1 meter from the vacuum chamber. After 200 hours of continuous operation, ^{22}Na will attain only 0.5% of the saturation value and the corresponding radiation field will be <0.1 mR/h at 1 m from the vacuum chamber.

Table 15.5.1 summarizes the results of the activation analysis for various accelerator components that can be potentially activated at NSLS-II. For each component, activity and the resulting exposure rates have been calculated for the assumed beam loss scenario.

Table 15.5.1 Activation Results for Various Accelerator Components at NSLS-II.

Accelerator Components	Activity after 200 hours of operation [mCi]	Immediately after shutdown, exposure rate at 1 m [mR/h]	1 hour after shutdown, exposure rate at 1 m [mR/h]
Linac iron beam stop	3.45	2.21	0.05
Booster iron beam stop	0.75	0.48	0.01
Linac tungsten injection stopper	17.7	4.9	0.05
Copper at injection septum	11.0	5.8	0.09
Lead at the septum shielding	4.28	1.6	0.44
Storage ring aluminum vacuum chamber	0.56	0.20	0.05

The foregoing analysis shows that the activation of accelerator and beamline components is not a serious radiation hazard during NSLS-II operations, although it is good practice to conduct a complete radiation survey of each accelerator enclosure prior to permitting access after prolonged operation. Based on this survey, access requirements are to be specified at various locations inside the accelerator enclosures.

15.5.2 Activation of the Soil

The potential for soil activation is limited at the electron accelerators, since the main radiation component, bremsstrahlung, is mainly in the forward direction of the electron beam and gets absorbed by machine components such as magnets, absorbers, and so forth. The soil berms are generally at very large angles (almost at right angles) to the forward direction of the electron beam. However, there exists a potential for the high-energy neutron component to penetrate through the transverse concrete shield and produce radioisotopes in the soil. These isotopes can migrate to the groundwater systems. Therefore, it is desirable to assess this risk in detail at a large installation like NSLS-II to reassure the staff and the public.

The soil activation analysis for the NSLS-II design has been carried out at three distinct locations of the accelerator enclosures where the probability for beam loss is significant. These are at the linac beam stop, booster beam stop, and booster-to-storage-ring injection septum.

15.5.2.1 Results of Soil Activation Calculations for NSLS-II

Table 15.5.2 gives the activity in the soil created by ^{3}H and ^{22}Na at various beam-loss locations, for 5,000 hours of NSLS-II operation. The potential activity created by leachables in the groundwater is also shown. Leachability rates of 100% and 7.5% are assumed for ^{3}H and ^{22}Na, respectively. A water concentration factor of 1.1 is used. Although the average annual local rainfall is 55 cm, the soil beneath the concrete floor is not exposed to rainfall and the potential leachability of radioactive isotopes from the soil to the water table at these locations is minimal.

Table 15.5.2 Activity in the Soil Created by ^{3}H and ^{22}Na at Various Beam Loss Locations.

Beam loss Location	Average HEN Flux in soil [Φ_{av}]	^{3}H Soil Activity [Ci/cm^3]	^{3}H Leachable to water [pCi/liter]	^{22}Na Soil Activity [Ci/cm^3]	^{22}Na Leachable to water [pCi/liter]
Linac beam stop (floor)	0.22×10^{2}	2.77×10^{-15}	2.97	2.47×10^{-14}	2.04
Linac beam stop (inboard)	0.39×10^{2}	4.91×10^{-15}	5.40	4.38×10^{-14}	3.61
Booster beam stop (floor)	0.05×10^{2}	0.62×10^{-15}	0.68	0.56×10^{-14}	0.46
Booster beam stop (inboard)	0.08×10^{2}	1.00×10^{-15}	1.10	0.90×10^{-14}	0.74
Storage ring septum (floor)	0.04×10^{2}	0.50×10^{-15}	0.55	0.45×10^{-14}	0.37
Storage ring septum (inboard)	0.06×10^{2}	0.76×10^{-15}	0.84	0.67×10^{-14}	0.55

15.5.3 Activation of Air in the Accelerator Enclosures

Routine accelerator operations at NSLS-II would generate small amounts of air activation at high beam-loss locations, due to photoneutron reactions of bremsstrahlung in air. The isotopes produced by air activation are ^{13}N (half life 10 min), ^{11}C (half life 20 min), and ^{15}O (half life 2.1 min). These isotopes would be produced within the accelerator enclosure and would attain saturation activity within hours of operation, but would decay quickly because of their short half lives and would remain primarily within the confines of the enclosure.

The air activation analysis for NSLS-II has been carried out at three distinct locations of the accelerator enclosures where the probability for beam loss is significant. These are at the linac beam stop, booster beam stop, and booster-to-storage-ring injection septum.

15.5.3.1 Results of Air Activation Calculations for the Accelerator Enclosures

Table 15.5.3 gives the activity in air at various beam-loss locations inside the accelerator enclosures of NSLS-II. For the linac tunnel, an effective bremsstrahlung straight path of 30 m is assumed. The linac tunnel volume is taken as $3\times3\times60 = 540$ m^3. A half chord of length 23 meters from the source inside the storage ring tunnel is considered as the maximum bremsstrahlung path length inside the tunnel. For the purpose of calculating activity per unit volume, a corresponding volume of air $3\times3\times 46$ m^3 = 414 m^3 is assumed inside the storage ring.

Table 15.5.3 Saturation Activity in Air at Various Beam Loss Locations.

Beam loss location	Beam loss [Watts]	Volume of air [m^3]	^{13}N [pCi/cm^3]	^{15}O [pCi/cm^3]	^{11}C [pCi/cm^3]
Linac beam stop	4.0	540	0.083	0.009	0.002
Booster	0.87	414	0.019	0.002	0.0004
Beam stop					
Storage ring septum	0.63	414	0.484	0.052	0.010

The computed concentration of radionuclides in air at various beam loss locations inside the accelerator enclosures is orders of magnitude smaller than the derived air concentration for environmental exposure in DOE Order 5400.5. Once the operation is shut down, this concentration will rapidly decrease, due to both radioactive decay and air ventilation.

15.5.4 Activation of Cooling Water

Activation of water for cooling the magnets and the other accelerator components may be estimated by the similar method as the estimation of air activation inside the accelerator enclosures. The primary reactions leading to the activation of cooling water are the bremsstrahlung interactions with ^{16}O in water. The most abundant of the radionuclide produced by this process is ^{15}O. Other activation products that are formed include ^{11}C (4.4 % of ^{15}O), ^{3}H (at saturation, 2.2 % of ^{15}O) and ^{13}N (about 1% of ^{15}O). ^{15}O has a radioactive

half life of 2.05 minutes and attains saturation during a short period of operation. ^{3}H will not attain saturation until several decades of accelerator operation.

15.5.4.1 Results of Cooling Water Activation Estimates

Among the accelerator components which require cooling, the storage ring septum is a maximum beam loss location. The saturation activity of radionuclides in the cooling water is estimated at the storage ring septum. A closed-loop inventory of 100,000 gallons (3.785×10^{8} cm^3) of water is assumed in the system. Table 15.5.4 provides the saturation concentrations of the radionuclides in the cooling water of the storage ring septum. As mentioned earlier, ^{3}H will attain saturation only after decades of operation. After 5,000 hours of continuous operation, the concentration of ^{3}H will be only 3% of the saturation value.

Table 15.5.4 Saturation Activities of Radionuclides in the Cooling Water at the Storage Ring Septum.

Beam loss [Watts]	^{15}O [pCi/cm^3]	^{11}C [pCi/cm^3]	^{13}N [pCi/cm^3]	^{3}H [pCi/cm^3]
0.63	0.24	0.01	0.002	0.005

The computed concentration of radionuclides in cooling water of the storage ring septum is orders of magnitude smaller than the derived concentration for environmental discharge limits in the DOE Order 5400.5. Once the operation is shut down, concentration of all nuclides, except that of ^{3}H, will rapidly decrease, due to radioactive decay of the short-lived isotopes.

15.6 SKYSHINE ESTIMATES AND SITE BOUNDARY DOSES

The term skyshine refers to the radiation that is initially directed skyward from a source but, due to scattering reactions with air nuclei, then is directed back to the earth. The neutron component of the radiation will be the major contributing factor to the skyshine dose. Any location in the accelerator where there is a probability for potential beam loss can be a source of skyshine. However, the potential beam loss and the resultant photo-neutron production at any given location in the accelerator system is small. The neutron component is well shielded at NSLS-II for personnel protection. Therefore, most beam losses do not cause significant skyshine.

15.6.1 Estimates of Skyshine Created at the Linac Beam Stop

Some skyshine radiation will be produced at the linac beam stop, where four watts of electron power will be dissipated. For the skyshine calculations, it is assumed that the linac beam stop is completely unshielded locally, aside from the 1 meter of concrete shielding on the roof.

The skyshine dose rates due to neutron radiation are calculated using the method developed by Rindi and Thomas [15.22]. The unshielded neutron dose at the concrete roof is taken as the source term. The skyshine at a given distance is calculated by the following algorithm.

$$\text{skyshine dose rate} = (a \times H / r^2)\, e^{-r/\lambda} \qquad (15\text{-}15)$$

Where a = 7 (constant), H = unshielded dose rate on the concrete roof (source term), r = distance of the dose point from the source in meters, and λ = 3300 meters, effective air attenuation factor.

Table 15.6.1 gives the calculated skyshine estimates for the linac beam stop at 100 meters and 1 mile (1,600 meters) from the linac stop. For a conservative operational period of the linac, 5,000 hours a year, the annual skyshine dose estimates are well within the acceptable limits. With the additional local shielding of the linac stop, the skyshine doses will be comparable to background levels.

Table 15.6.1 Estimates of Skyshine Created at the NSLS-II Linac Beam Stop.

Neutron source component	Skyshine Dose at 100 m		Skyshine Dose at 1 mile	
	[mrem/h]	[mrem/year]	[mrem/h]	[mrem/year]
Giant resonance neutrons	8.2×10^{-4}	4.1	2.0×10^{-6}	0.010
High-energy neutrons	1.3×10^{-3}	6.3	3.0×10^{-6}	0.015
Total skyshine dose	2.1×10^{-3}	10.4	5.0×10^{-6}	0.025

15.6.2 Estimates of Skyshine Created at the Booster Beam Stop

Some skyshine radiation will be created at the booster beam stop. However, these dose rates will be lower than the skyshine dose rates produced at the linac beam stop because only 0.874 watts of electron power are dissipated at the booster beam stop, versus 4 watts at the linac beam stop. For the booster beam stop skyshine calculations, it was assumed to be unshielded locally, except for the 1-meter concrete bulk shielding.

Table 15.6.2 gives the calculated skyshine estimates for the booster beam stop using the same algorithm as in the previous section. The skyshine estimates at 100 meters and 1 mile (1,600 meters) from the beam stop have been calculated. For a conservative operational period of 5,000 hours a year, the annual skyshine dose estimates are well within the acceptable limits. With the additional local shielding of the booster beam stop, the skyshine doses will be comparable to background levels.

All other skyshine dose rates that result from beam losses in the accelerator systems will be comparable to background dose rates.

Table 15.6.2 Estimates of Skyshine Created at the NSLS-II Booster Beam Stop.

		Skyshine Dose at 100 m	Skyshine Dose at 1 mile	
Neutron Source component	[mrem/h]	[mrem/year]	[mrem/h]	[mrem/year]
Giant Resonance Neutrons	1.0×10^{-4}	0.5	2.5×10^{-7}	0.001
High Energy Neutrons	1.6×10^{-4}	0.8	3.7×10^{-7}	0.002
Total Skyshine Dose	2.6×10^{-4}	1.3	6.2×10^{-7}	0.003

References

[15.1] Perkins, D.H., Introduction to High Energy Physics, Third Edition, Addison-Wesley Publishing (1984).

[15.2] J.S. Levinger, "Theories of photonuclear reactions," *Ann. Rev. of Nucl. Sci*., 4 (1954).

[15.3] Hubbel, J.H., Photon Cross Sections and Attenuation Coefficients from 10 keV to 100 GeV, NSRDS-NBS 29 (1969).

[15.4] Schaeffer, N.M., Reactor Shielding for Nuclear Engineers, NTIS, Springfield, VA (1973).

[15.5] R.G. Alsmiller, and J. Barish, "Shielding against neutrons produced when 400 MeV electrons are incident on thick copper target," *Particle Accelerators*, **5** (1973).

[15.6] Fasso, A. et al., Radiation Problems in the Design of LEP Collider, CERN 84-02 (1984).

[15.7] Sullivan, A.H., A Guide to Radiation near High Energy Particle Accelerators, Nucl. Tech. Publishing (1992).

[15.8] Swanson, W.P., et.al. Aladdin Upgrade Design Study, University of Wisconsin Report, AUS14 (1985).

[15.9] Moe, H., Advanced Photon Source - Radiological Design Considerations, APS-LS-141 (1991).

[15.10] Basic Aspects of High Energy Particle Interactions and Radiation Dosimetry, ICRU -28 (1978).
[15.11] Schwinger, J., Classical Radiation of Accelerated Electrons, *Phys. Rev*. **75** (1949).
[15.12] Gabriel, T. A., PICA, Intra-nuclear Cascade Calculations, ORNL 4687 (1971).
[15.13] M. Pisharody et.al., "Dose measurements of Bremsstrahlung produced neutrons," *Nucl.Instr.& Meth*. A230 (1999) p 542.
[15.14] H. Moe et al., Radiological Considerations for TopUp at APS, APS-LS 276 (1998).
[15.15] EGS4 Code System, User's Manual, SLAC265 (1985).
[15.16] STAC8 Program Manual, Y.Asano, SPring-8 Publication (1998).
[15.17] Frank, J.C., LURE EP 88-01 (1988).
[15.18] Ferrari, et.al., Estimation of Gas bremsstrahlung, Health Physics, 68 (1995).
[15.19] Tromba, G. and A.Rindi, "Gas bremsstrahlung from Electron Storage Ring," *Nucl.Instr. & Meth*., A292 (1990).
[15.20] Photon, Electron, Proton and Neutron Interaction Data in Body Tissues, ICRU Report 46 (1992).
[15.21] Swanson, W.P., Radiological Safety Aspects of Electron Linear Accelerators, IAEA 188 (1979).
[15.22] Rindi, A. and R.H. Thomas, "Skyshine - A Paper Tiger," *Particle Accelerators* **7** (1975).